Science Engineering & Environment

VOLUME 1

Edited by

Zakaria Hossain

Satoshi Kaneco

SEE 2015,TSU, MIE, JAPAN
SCIENCE, ENGINEERING AND ENVIRONMENT

PROCEEDINGS OF FIRST INTERNATIONAL CONFERENCE – SEE 2015
SCIENCE, ENGINEERING & ENVIRONMENT TSU, MIE, JAPAN 19-21 NOVEMBER, 2015

Science, Engineering and Environment

Edited by

Prof. Zakaria Hossain
Graduate School of Bioresources
Mie University, Japan

Prof. Satoshi Kaneco
Graduate School of Engineering
Mie University, Japan

THE GEOMATE INTERNATIONAL SOCIETY

Copyright @ 2015 by The GEOMATE International Society

All rights reserved. In principle, no part of this publication or the information contained herein may be reproduced in any form or by any means, translated in any language, stored in any data base or retrieval system, or transmitted in any form or by any means without prior permission in writing from the publisher.

Disclaimer: The editors and the publisher have tried their best effort to ensure the integrity and the quality of this publication and information herein. However, they give no warranty of any kind, expressed or implied with regard to the material contained in this book, and will not be liable in any event for the consequences of its use.

Published by:
The GEOMATE International Society
Tsu city, Mie, Japan
E-mail: society@geomate.org
http://www.geomate.org/

ISBN Number: 978-4-9905958-5-2 C3051

Table of Contents

Preface

On behalf of the SEE 2015 Organizing Committee, it is our great pleasure to welcome you to the International Conference Science, Engineering & Environment, held at the Center Palace Grand Hotel, Tsu, Mie, Japan organized in conjunction with Mie University Research Center for Environmental Load Reduction, The GEOMATE International Society, Useful Plant Spread Society, Glorious International, AOI Engineering, HOJUN, JCK, CosmoWinds and Beppu Construction, Japan.

The conference covers three major themes with many specific themes including:

Engineering	Science	Environment
· Environmental Engineering	· Environmental Sciences	· Environmental Technology
· Chemical Engineering	· Chemistry and Chemical Sciences	· Recycle Solid Wastes
· Civil and Structural Engineering	· Fisheries and Aquaculture Sciences	· Environmental dynamics
· Computer Software Web Engineering	· Astronomy and Space Sciences	· Meteorology and Hydrology
· Electrical and Electronic Engineering	· Atmospheric Sciences	· Atmospheric and Geophysics
· Energy and Thermal Engineering	· Botany and Biological Sciences	· Physical oceanography
· Aerospace Engineering	· Genetics and Bacteriology	· Bio-engineering
· Agricultural Engineering	· Forestry Sciences	· Environmental sustainability
· Biological Engineering and Sciences	· Geological Sciences	· Resource management
· Biological Systems Engineering	· Materials Science and Mineralogy	· Modelling and decision support tools
· Biomedical and Genetic Engineering	· Statistics and Mathematics	· Institutional development
· Bioprocess and Food Engineering	· Microbiology and Medical Sciences	· Suspended and biological processes
· Geotechnical Engineering	· Meteorology and Palaeo Ecology	· Anaerobic and Process modelling
· Industrial and Process Engineering	· Pharmacology	· Modelling and numerical prediction
· Manufacturing Engineering	· Physics and Physical Sciences	· Interaction between pollutants
· Mechanical and Vehicle Engineering	· Plant Sciences and Systems Biology	· Water treatment residuals
· Materials and Nano Engineering	· Psychology and Systems Biology	· Quality of drinking water
· Nuclear Engineering	· Zoology and Veterinary Sciences	· Distribution systems on potable water
· Petroleum and Power Engineering		· Reuse of reclaimed waters
· Forest Industry Engineering		

This year we have received many submissions from different countries all over the world. The technical papers were selected from the vast number of contributions submitted after a review of the abstracts. The final papers in the proceedings have been peer reviewed rigorously and revised as necessary by the authors. It relies on the solid cooperation of numerous people to organize a conference of this size. Hence, we appreciate everyone who support as well as participate in the joint conferences.

Last but not least, we would like to express our gratitude to all the authors, session chairs, reviewers, participants, institutions and companies for their contribution to SEE 2015. We hope you enjoy the conference and find this experience inspiring and helpful in your professional field. We look forward to seeing you at our upcoming conference next year.

Best regards,

Prof. Dr. Zakaria Hossain, Conference Director

Prof. Dr. Satoshi Kaneco, Conference Chairman

Organization

Scientific Committees:

Honorary Chairman: Dr. Sohji Inoue, E/Prof. Mie University, Japan
Conference Chairman: Dr. Satoshi Kaneco, Prof., Mie University, Japan
Conference Director: Dr. Zakaria Hossain, Prof. Mie University, Japan

Conference Organizing Committee:

Dr. Satoshi Kaneco, Prof., Mie University, Japan (Chair)
Dr. Zakaria Hossain, Prof. Mie University, Japan (Director)
Dr. Sohji Inoue, E/Prof. Mie University, Japan (Co-Chair)
Dr. Toshinori Sakai, Prof. Mie University, Japan (Co-Chair)
Dr. Takamitsu Kajisa, Prof. Mie University, Japan (Co-Chair)
Dr. Masaaki Kondo, A/Prof. Mie University, Japan (Co-Chair)

National & International Advisory Committee:

Dr. Fumio Tatsuoka, Prof., Tokyo University of Science, Japan
Dr. Junichiro Takeuchi, Prof., Kyoto University, Japan
Dr. Kingshuk Roy, Prof., Nihon University, Japan
Dr. Nakib Dan Khan, A/Prof. Mie University, Japan
Dr. Sai Vanapalli, Prof., University of Ottawa, Canada
Dr. Musharraf Zaman, Prof. Univ. of Oklahama, USA
Dr. Rafiqul Tarefder, Prof. University of New Mexico, USA
Dr. M. Bouassida, Prof., National Sch. of Engg. of Tunis
Dr. L.R. Austriaco, Prof., Angles Univ. Found., Philippines
Dr. A.S.M. Abdul Awal, Prof., Univ. Technology Malaysia
Dr. M. Ibn Ibrahimy, Prof., Int. Islamic Univ., Malaysia
Dr. Mohammad Shariful Islam, Prof., BUET, Bangladesh.
Dr. Bujang B.K. Huat, Prof., Univ. Putra Malaysia
Dr. Nemy Banthia, Prof., UBC, Canada
Dr. Ian Jefferson, Prof., Univ. of Birmingham, UK
Dr. John Bolander, Prof., Univ. of California, USA
Dr. Shamsul Chowdhury, Prof., Roosevelt Univ., USA
Dr. Isabel Pinto, Prof., University of Coimbra, Portugal
Dr. Mark Jaksa, Prof., University of Adelaide, Australia
Dr. Jim Shiau, A/Prof., USQ, Australia
Dr. Hj. Ramli Bin Hj. Nazir, A/Prof., UTM, Malaysia
Dr. H.M. Shahin, Prof., Islamic University of Technology, Bangladesh
Dr. Md. Ariful Islam, A/Prof. Dhaka University, Bangladesh
Dr. Md. Nurul Amin, Prof. Dhaka University, Bangladesh
Dr. D.K. Chauhan, Prof. Noida International Univ., India
Dr. Chan Chee-Ming, A/Prof. Universiti Tun Hussein Onn Malaysia
Dr. Ahmed H. A. Dabwan, A/Prof. TATI Univ. College, Malaysia

International Technical Program Committee:

Prof. Zachary Senwo, Alabama A&M University, United States
Prof. Essaid Bilal, Ecole Nationale Superieure Des Mines De Saint Etienne, France
Prof. Adolf Heinrich Horn, Geological Institute - Federa University of Minas Gerais, Brazil
Prof. Bang-Fuh Chen, National Sun Yat-sen University, Taiwan
Prof. Bindeshwar Singh, Kamla Nehru Institute of Technology, India
Prof. Catherine Mulligan, Concordia Institute of Water, Energy and Sustainable Systems, Canada
Prof. Daffalla Rabih, Kenana Sugar Company, Sudan
Prof. Ibrahim Maiyza, National Institute of Oceanography & Fisheries, Egypt
Prof. Marilia Hagen, Indiana University, United States
Prof. Md. Abdul Baset Mia, BSMR Agri. Univ., Bangladesh
Prof. Mohamed Abdou, Faculty of Education Department of Mathematics, Egypt
Prof. MOHAMED TAHIRI, Présidnce de l'Université Hassan II de Casablanca, Morocco
Prof. Nazar Oukaili, University of Baghdad, Iraq
Prof. Radim Cajka, Technical University Ostrava, Faculty of Civil Engineering, Czech Republic
Prof. Rajaraman Jambunathan, AMET University, India
Prof. Saad Farhan Ibrahim Alabdullah,University Of Almustansiriyah, Iraq
Prof. Salem Alsanusi, Benghazi, Libya
Prof. Sudhir Kumar Das, Retired Senior Project Manager of Indian Railways, India
A/Prof. Abdull Halim Abdul, OIl and Gas department, Malaysia
A/Prof. Abdull Halm Abdul, 537 Jalan Jasmin 17, Malaysia
A/Prof. Baoping Cai, China University of Petroleum, China
A/Prof. Dariusz Jakóbczak, Koszalin University of Technology, Poland
A/Prof. Lakhveer Singh, Universiti Malaysia Pahang (UMP) Malaysia, Malaysia
A/Prof. Lidia Sas Paszt, Research Institute of Pomology, Poland
A/Prof. Mahmood Barbooti, University of Yechnology, Iraq
A/Prof. Majid Mirzaei, Universiti Tunku Abdul Rahman, Malaysia
A/Prof. Sarawut Thepanondh, Mahidol University, Thailand
A/Prof. Yasir Al Hussein, Jerash University, Faculty of Engineering, Jordan
A/Prof. Bindeshwar Singh Kamla, Nehru Institute of Technology, India
A/Prof. Namir Alkawaaz, University of Almustansiriyah, Iraq
Dr. Akinola Johnson Olarewaju, Federal Polytechnic Ilaro, Ogun State, Nigeria, Nigeria
Dr. Alexandre Costa, Federal University of the valleys of Jequitinhonha and Mucuri, Brazil
Dr. Bashir Dar, University of kashmir Delina Baramulla J&K India, India
Dr. Bassam Abdellatif, National Authority for Remote Sensing and Space Sciences, Egypt
Dr. Binh Phu Nguyen, National University of Singapore, Singapore
Dr. Evgeni Starikov, KIT, Karlsruhe, Germany; Chalmers, Gothenburg Sweden, Germany
Dr. Iskhaq Iskandar, Dept. Physics, University of Sriwijaya, Indonesia
Dr. Loc Nguyen, Sunflower Soft Company, Vietnam
Dr. Mohd Afendi Rojan, Universiti Malaysia Perlis, Malaysia
Dr. Mohd Altaf, University of kashmir Delina Baramulla J&K India, India
Dr. Mostafa Khater, Egypt - El sharqia - Zagazig, Egypt
Dr. Mostafa Khater, Egypt - El sharqia - Zagazig, Egypt
Dr. Nashrul Fazli Mohd Nasir, Universiti Malaysia Perlis, Malaysia
Dr. Rolando Javellonar, Romblon State University, Philippines
Dr. Suphaphat Kwonpongsagoon, Mahidol University, Thailand
Dr. Wei Hong Tan, Universiti Malaysia Perlis, Malaysia
Dr. Yoshiro Fujii, Shin Kobe Dental Clinic, Japan
Dr. Yuk Feng Huang, Universiti Tunku Abdul Rahman (UTAR), Malaysia
Dr. Jingwei Zhao, University of Wollongong, Australia

Conference Correspondence:

Prof. Dr. Zakaria Hossain (Director)
Dept. of Environmental Science and Technology, Mie University, Japan
Mr. Md. Aminul Islam (Secretary)
Dept. of Environmental Science and Technology, Mie University, Japan
E-mail: conference@geomate.org
Tel & Fax: +81-59-231-9578

Editorial and Executive Committee:

Prof. Dr. Zakaria Hossain
Prof. Dr. Satoshi Kaneco

Note- A: Associate, E-Emeritus

Keynote Papers

First International Conference on Science, Engineering & Environment,
Tsu City, Mie, Japan, Nov.19-21, 2015, ISBN: 978-4-9905958-5-2 C3051

SUSTAINABLE HYDROGEN PRODUCTION WITH ZINC OXIDE

Satoshi Kaneco
Department of Chemistry for Materials, Graduate School of Engineering, Mie University, Japan

ABSTRACT

Nonmetal (N and B) doped ZnOs were developed for hydrogen production from aqueous sacrificial anion, S^{2-}−SO_3^{2-}, solution. In the present work, N− and B−doped ZnO nanomaterials were successfully prepared by a simple, effective, high yield, and low cost mechanochemical combustion technique, with addition of urea or boric acid to a zinc acetate and oxalic acid mixture. The prepared oxides were characterized by X−ray diffraction (XRD), BET surface area analysis, X−ray photoelectron spectroscopy (XPS), scanning electron spectroscopy (SEM), UV−visible diffuse reflectance spectroscopy (UV-DRS), and photoluminescence spectroscopy (PL). The photocatalytic hydrogen production was observed with 880 μmol g^{-1} for undoped ZnO with 0.4 M Na_2S + 0.4 M Na_2SO_3 solution, due to in-situ formation of a ZnS/ZnO heterojunction. The doped ZnO materials had better activity than undoped ZnO. The photocatalytic H2 evolution with B−doped ZnO (1730 μmol g^{-1}) was larger compared with those obtained with N−doped ZnO. The photocatalytic H_2 productions with B−doped ZnO were affected by parameters such as calcination temperature, calcination time, and doping concentrations. The B−doped ZnO demonstrated higher activity due to small particle size, large surface area, and reduction of electron−hole recombination.

First International Conference on Science, Engineering & Environment,
Tsu City, Mie, Japan, Nov.19-21, 2015, ISBN: 978-4-9905958-5-2 C3051

WHAT CAN BE KNOWN REGARDING EVAPOTRANSPIRATION LEVELS OF HERAT IN AFGHANISTAN IN 120 DAYS VIA WIND - EFFORTS TOWARDS RESEARCH IN REGARD TO EVAPOTRANSPIRATION LEVELS IN WAR-TORN AFGHANISTAN -

Takamitsu Kajisa
Department of Environmental Science and Technology, Graduate School of Bioresources,
Mie University, Japan

ABSTRACT

The only place we know of that has a higher level of evapotranspiration than Afghanistan's Herat is the area made famous by gambling, Las Vegas. In both areas, on a summer day, evapotranspiration levels will be over 10mm/day. This is more than double what the average evapotranspiration level is in Japan. I've heard that Las Vegas was built on land that couldn't be used for farming, so it became a gambling town. The weather data for Herat is as strange as that. Results garnered from comparisons of many calculation methods have been announced by many researchers, however, for example, in reference to Herat, the evapotranspiration level we got from the Hargreaves-Samai method (heretofore, HS method) was greater than that which we got from the Penman-Monteith method (heretofore PM method, the standard calculation method in FAO). We were able to confirm that the difference was more than double in fall and spring in Herat, when there is no high wind. In summer, for 120 days almost from July to September, there is high wind. This difference shows that the demand for water from the river, via a difference in calculation method, differed by double and that there were growing concerns that this would be the start of a conflict. Differing from the PM method, the HS method does not use wind speed data, and it's said that it is the proposed calculation method for semi-arid and arid land. Therefore, the treatment of wind speed might be constant or be changing as corresponding to air temperature or sun-shine. However, the spring and fall seasons at Herat have a low wind speed close to that of mid-winter. Therefore, we are studying the obvious faults in the HS method in spring and fall concerning the result. In this way, we're not simply reporting an example that shows a comparative scale of evapotranspiration based on many calculation methods. While paying respect to the original work, we're going one by one through the hypotheses introduced when each calculation method was proposed and through comparison to Herat's weather data, we are able to confirm the practicality of the PM method while recognizing the special characteristics of each suggested calculation method and Herat's weather. In this way, this is a set of comparisons not using any tools, relying only on logic. At present, these are the efforts we are putting into the research of evapotranspiration levels in war-torn Afghanistan.

Technical Papers

Science

First International Conference on Science, Engineering & Environment,
Tsu City, Mie, Japan, Nov.19-21, 2015, ISBN: 978-4-9905958-5-2 C3051

POTENTIAL EFFECTS OF MELALEUCA HONEY ON ORAL STREPTOCOCCI BIOFILM

Wen-Jie, NG[1, 2*], and Ricky, RACK[1]

[1]Faculty of Science; [2]Centre for Biodiversity Research,

Universiti Tunku Abdul Rahman, 31900, Perak, Malaysia

ABSTRACT

Various pharmacognosy studies of honey have been conducted in different regions worldwide. Ever since the discovery of antibacterial activity of honey in 1892, honey has been selected as one of the treatment remedies against bacterial infections. On the other hand, oral *Streptococcus* species has been known to be the main causative agent leading to dental caries. The formation of biofilm by these bacteria is one of the main causes of their detrimental effects on teeth surface. Hence, the objectives of this study were to isolate oral viridans streptococci and to determine the potential effects of Melaleuca honey on the cariogenic bacterial biofilm. In this study, twenty salivary samples were collected and a total of three identified streptococci isolates were obtained. These bacterial isolates were then subjected to biofilm assays with different concentrations of honey samples (100%, 50%, 25%, 12.5% and 6.25%, w/v). Results showed the strongest effects of Melaleuca honey were observed at 50% (w/v) concentration that inhibited 54.8% of biofilm formation and also reduced 75.5% biomass of the established biofilm. In brief, obtained outcomes demonstrated the potential effects of Melaleuca honey against cariogenic streptococci biofilm and it could be recommended for further analyses as a potent inhibitory agent against dental caries.

Keywords: Melaleuca, Streptococci, Cariogenic, Biofilm

INTRODUCTION

Honey is a common natural sweetener created from the enzymes found in bees and propolis. Differences in the nectar source may be accountable to variety in the color and flavor of honey [1]. Reports recorded the medicinal usage of honey as an antimicrobial agent turns out to be a good remedy without any other observable complications [1, 2]. Literatures propose that the antibacterial properties of honey are mainly contributed by its high osmolarity, viscosity, acidic pH and also the presence of hydrogen peroxide [1]. However, the potency of honey against bacteria differs among different types of honey. Differences in botanical origins, geography, season as well as processing and storage conditions may contribute in variations of active components in honey [3].

In Southeast Asia, Melaleuca honey or commonly known as Gelam honey, originated from *Melaleuca cajuputi* Powell or Gelam trees which can be found naturally in swamp forests [4], possesses the ability to promote wound healing process [5]. Other than reducing the levels of inflammatory mediators, such as tumor necrosis factor-α (TNF-α) and cyclooxygenase-2 (COX-2) in inflamed wounds, Melaleuca honey was found to exhibit cytotoxic effect against HT29 human colon cancer cells as well [6, 7]. In addition, Melaleuca honey also showed potent antibacterial activity against *Klebsiella pneumoniae*, *Staphylococcus aureus*, *Escherichia coli*, *Salmonella* spp. and vancomycin-resistant enterococci [8]. Study showed this honey contains phenolic compounds which exhibit free radical scavenging activities that lead to oxidative damage on bacterial cells [9, 10].

Despite the awareness about dental hygiene, dental caries remains one of the top chronic problems in the world. Dental caries is always associated with lack of fluoridation, poor hygiene and formation of plaque [11]. The formation of bacterial plaque is commonly caused by a heterogenous group of α-haemolytic streptococci that present in the oral cavity. Some examples of viridans streptococci are *Streptococcus mutans, Streptococcus salivarius, Streptococcus mitis* and *Streptococcus sanguis* [12]. These bacteria along with other bacterial species colonize the tooth surface, forming oral biofilm or plaque. Furthermore, biofilm causes a bacterial cell changes its gene expression and could become 1000 times more resistant to the antibiotics and other antimicrobial agents than its planktonic counterparts

[13]. Hence, in this study the potential effects of Melaleuca honey against cariogenic bacterial biofilm were assessed.

MATERIALS AND METHODS

Honey Sample

Melaleuca honey sample was collected by authorized bee farmers under the supervision of the Ministry of Agriculture and Agro-based Industry, Malaysia and kept in the dark at room temperature to prevent reduction of glucose oxidase content by photo-oxidation [14]. Honey was serially diluted with distilled water to achieve concentrations of 100%, 50%, 25%, 12.5% and 6.25% (w/v).

Isolation of Oral Streptococci

Twenty salivary samples were collected and each sample was diluted to 1/1000. The diluted samples were then cultured on nutrient agar plate and incubated overnight at 37°C. Single colonies formed were further identified with biochemical tests.

Biochemical Identification Tests

Preliminary identification of the single colonies was carried out with Gram staining and catalase test, whereby only isolates with Gram-positive cocci in chains and catalase-negative were further subcultured on sheep blood agar for the determination of haemolytic activity. Then, the α-haemolytics (partial haemolysis) isolates were further identified using the API 20 Strep system. The 7-digit numerical profile was entered into the api*web*^{TM} identification software database to obtain the bacterial identity. These isolates were then used in the biofilm assays.

Biofilm Assays

Inhibitory effect of honey on the formation of biofilm

By referring to previous study [15], 0.5 McFarland bacterial suspension was inoculated into each honey sample. Then, 200 µl of the mixture was dispensed into a sterile flat-bottomed microtitre plate and incubated for 24 hours at 37°C without shaking to allow the establishment of biofilm. After incubation, the liquid phase or planktonic bacteria was gently discarded and the remaining attached biofilm was then fixed by with 10% (v/v) formaldehyde for 5 minutes to prevent further bacterial growth. The fixative was then discarded and the wells were washed gently with phosphate-buffered solution (PBS) twice. Crystal violet (0.1%, v/v) was used to stain the attached biofilm for 5 minutes.

Then, the stained microtitre plate was left to dry overnight and the dye was solubilized with acetone-ethanol solvent. Twenty microliters of the resulting solution was added to 180 µl of solvent contained in a second microtitre plate. The extent of biofilm formation was determined with the absorbance at 570 nm wavelength. Each assay was conducted in triplicate and average values were obtained. The reduction of the biofilm biomass was calculated:

Reduction of biofilm formation (%) =

$$b / a \times 100\%$$

Whereby, a = absorbance of negative control
b = absorbance of bacterial suspension with honey

Reducing effect of honey on established biofilm

With modifications [15], prepared 0.5 McFarland bacterial suspension was dispensed into a sterile flat-bottomed microtitre plate and incubated for 24 hours at 37°C without shaking. The planktonic bacterial suspension was then discarded, followed by the inoculation of 200 µl of honey samples and incubated again for 24 hours at 37°C.

After incubation, the planktonic bacteria was gently removed and the remaining attached biofilm was then fixed with 10% (v/v) formaldehyde for 5 minutes. The fixative was then removed and the wells were washed gently with PBS solution twice. The attached biofilm was stained with 0.1% (v/v) crystal violet for 5 minutes and excessive dye was discarded. Then, the stained microtitre plate was left to dry overnight and 200 µl of acetone-ethanol solvent was added to solubilize the dye. Twenty microlitres of the resulting solution was added to 180 µl of solvent contained in a second microtitre plate. The extent of biofilm biomass was determined from the absorbance at 570 nm wavelength. Each experiment was conducted in triplicate and the average values were obtained. The reduction of the established biofilm biomass was calculated based on the following formula:

Reduction of established biofilm biomass (%) =

$$b / a \times 100\%$$

Whereby, a = absorbance of negative control
b = absorbance of biofilm treated with honey

RESULTS

Isolation of Oral Streptococci Species

As shown in Table 1, the three isolates are Gram-positive cocci, in chains, catalase-negative and exhibited partial haemolysis on sheep blood agar, indicating their α-haemolytic property. Table 2 shows the identification percentage of the streptococci isolates based on the numerical profile of API 20 Strep System.

Table 1 Preliminary identification screening of bacterial isolates

Isolate	Gram stain	Shape and arrange-ment	Catalase test	Haemoly-tic property
J	+	cocci, in chains	-	α-haemolysis
N	+	cocci, in chains	-	α-haemolysis
P	+	cocci, in chains	-	α-haemolysis

Note: + positive; - negative.

Table 2 The API 20 Strep identification of viridans streptococci

Isolate	Numerical profile	Percentage of identification (%)
J	0040440	*Streptococcus mitis* 87.8
N	5040670	*Streptococcus mutans* 97.0
P	5040770	*Streptococcus mutans* 99.9

Biofilm Assays

Figure 1 summarizes the effect of Melaleuca honey on the biofilm formation of three different oral streptococci isolates. Based on the figure, it can show that all concentrations of honey were able to inhibit biofilm formation. Generally, as honey concentration increased, the percentage inhibition of biofilm formation was increased as well. However, the inhibitory effect of 100% (w/v) honey was reduced drastically, reaching a biofilm reduction as low as 1.4% for Isolate J. The greatest biofilm inhibition was observed at 50% (w/v) honey concentration with a peak of 54.8% on Isolate P followed by reductions of 50.7% and 25.0% on Isolate N and Isolate J, respectively. On the other hand, the lowest inhibition was exhibited by honey concentration of 6.25% (w/v), on Isolate J at 2.7%.

Figure 2 illustrates the effect of Melaleuca honey on 24-hour established biofilm of three different oral streptococci isolates. Based on the figure, all concentrations of honey were able to reduce biofilm with more concentrated honey samples exhibited greater reduction. However, the percentage reduction of biofilm biomass was reduced significantly at 100% (w/v) concentration of honey. The greatest biofilm reduction can be observed at 50% (w/v) honey concentration with a peak of 75.5% on Isolate P, followed by reduction of 57.2% and 34.6% for Isolate N and Isolate J, respectively. On the other hand, the lowest biomass reduction was exhibited by honey concentration of 6.25% (w/v) on Isolate N with only 5.6% reduction.

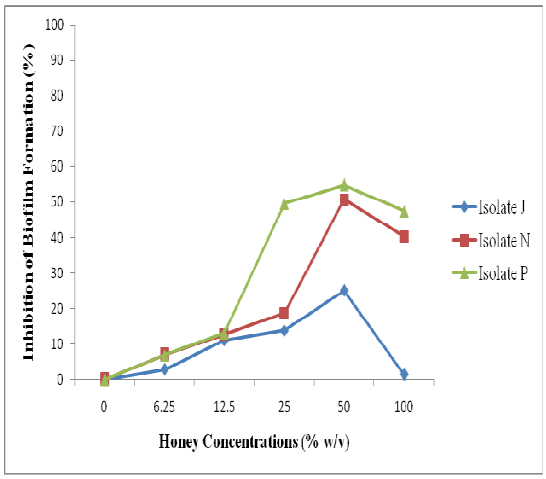

Fig. 1 Inhibitory effect of Melaleuca honey on biofilm formation.

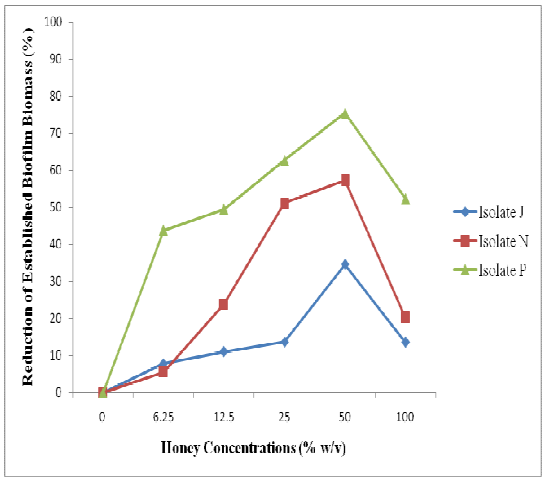

Figure 2: Reducing effect of Melaleuca honey on established biofilm.

DISCUSSION

The major bacterial populations that contribute to the plaque formation on teeth are Gram-positive viridians streptococci such as *Streptococcus mutans*, *Streptococcus mitis* and others which is a part of the normal flora in oral cavity [12]. Based on the outcomes, Melaleuca honey was shown to be able to inhibit biofilm formation of all oral streptococci isolates. The efficacy of honey in reducing biofilm formation is believed due to many antibacterial properties as well as its involvement in inhibiting bacterial quorum sensing [9]. One of the postulated mechanisms which inhibit the formation of biofilm is

through the repression of signaling molecules [9, 12]. Previous study showed that chestnut honey was able to inhibit *N*-acyl-*L*-homoserine lactones that repressing quorum sensing, thus inhibiting biofilm formation of *Aeromonas hydrophilia*, *Yersinia enterocoliticia* and *Erwinia carotovora* [9]. In a similar way, this may explain how Melaleuca honey was able to inhibit bacterial biofilm formation of viridans streptococci [16].

In addition, Melaleuca honey contains phenolic compounds such as gallic acid and ferulic acid that can manifest free radical scavenging activities which are also able to exert antibacterial effects [9]. Hence, the presence of these compounds is believed to contribute in the antibacterial action of Melaleuca honey against viridans streptococci. Consequently, the presence of higher amount of phenolic compounds in more concentrated honey explains the greater inhibitory effect on biofilm formation [17].

Many studies also attribute the antibacterial effect of honey to its acidic nature. To place things in perspective, the viridans streptococci grow well at a pH of 6.75 to 7.25, which is the pH of the oral cavity [18]. Thus, due to the presence of gluconic acid, honey with its average pH of between 3.2 and 4.5 is able to inhibit the growth of bacterial cells [3]. However, the acidity is reduced in highly diluted honey which explains the inhibitory effect on biofilm formation was lower at 6.25% (w/v) honey concentration [10].

Furthermore, honey as a highly concentrated solution of sugars can reduce the availability of water necessary for bacterial growth as the sugar molecules in honey bind with water molecules [14]. Secondly, the presence of honey creates a hypertonic condition which causes water to diffuse out from bacterial cell [19]. The bacterial cell will not be able to sustain its growth in concentrated honey with higher osmolarity effect, thus biofilm formation is inhibited. However, the antibacterial mechanism of natural honey is not solely due to its high sugar content [20].

The highest reduction in biofilm biomass for all isolates was found at honey concentration of 50% (w/v) but the reduction dropped significantly at 100% (w/v) concentration. Such outcome could be attributed by the presence of hydrogen peroxide in honey which is an oxidizing agent that can inhibit bacterial growth and metabolism [14]. Hydrogen peroxide is generated in a reaction involving the endogenous enzyme glucose oxidase which oxidizes glucose to gluconic acid and hydrogen peroxide [3, 14]. However, water is needed to activate glucose oxidase in this reaction [14]. In this study, at the highest concentration of honey sample, there was insufficient water for the activation of enzymatic activity to generate hydrogen peroxide that explains the reduction rate of established biofilm was lower at 100% (w/v) than 50% (w/v).

CONCLUSION

In general, Melaleuca honey was shown to exert antibiofilm effects on all oral cariogenic streptococci isolates. Further studies are needed to evaluate its therapeutic potential against cariogenic bacteria for the prevention of dental caries.

ACKNOWLEDGMENTS

The authors appreciate the facilities and financial support provided by the university.

REFERENCES

[1] Singh MP, Chourasia HR, Agarwal M, Malhotra A, Sharma M, Sharma D, Khan S, Honey as complementary medicine: a review, International Journal of Pharma and Bio Sciences, Vol. 3(2), 2012, pp. 12-31.

[2] Molan PC, Honey: antimicrobial actions and role in disease management, New Strategies Combating Bacterial Infection, In I. Ahmad & F. Aqil, Eds. Weinheim: Wiley VCH; 2009, pp. 229-53.

[3] Mandal S, DebMandal M, Pal NK, Saha K, Antibacterial activity of honey against clinical isolates of *Escherichia coli, Pseudomonas aeruginosa* and *Salmonella enterica* serovar Typhi, Asian Pacific Journal of Tropical Medicine, Vol. 3(12), 2010, pp. 961-4.

[4] Zainol MI, Yusoff KM, Yusof MYM, Antibacterial activity of selected Malaysian honey, BMC Complementary & Althernative Medicine, Vol. 13(129), 2013, 1-10.

[5] Tan MK, Adli DSH, Tumiran, MA, Abdulla MA, Yusoff, KM, The efficacy of Gelam honey dressing towards excisional wound healing, Evidence-Based Complementary and Alternative Medicine, Vol. 2012, 2012, pp. 1-6.

[6] Tey CPW, Hussein SZ, Abdullah S, Karim NA, Makpol S, Yusof YAM, Gelam and Nenas honeys inhibit proliferation of HT 29 colon cancer cells by inducing DNA damage and apoptosis while suppressing inflammation, Asian Pacific Journal of Cancer Prevention, Vol. 13(4), 2012, pp. 1605-10.

[7] Vallianou NG, Gounari P, Skourtis A, Panagos J, Kazazis C, Honey and its anti-inflammatory, anti-bacterial and anti-oxidant properties, General Medicine, Vol. 2(2), 2014, pp. 1-5.

[8] Ng WJ, Ken KW, Kumar RV, Gunasagaran H. Chandramogan V., Lee YY, *In-vitro* screening of Malaysian honey from different floral sources for antibacterial activity on human pathogenic bacteria, African Journal of Traditional, Complementary and Alternative Medicines, Vol. 11(2), 2014, pp. 315-8.

[9] Lee KY, Abdul Razak SL, Ismail N, Ng CF, Asyraf MH, Goon JA, Sharif NM, Jubri Z, Malaysian Gelam honey reduces oxidative damage and modulates antioxidant enzyme activities in young and middle aged rats, Journal of Medicinal Plants Research, Vol. 5(23), 2011, pp. 5618-25.

[10] Ng WJ, Chin TJ, Khoo BHY, Antioxidant properties, enzyme activities and inhibitory effects of Melaleuca honey against cariogenic bacteria growth and biofilm formation, Advances in Environmental Biology, Vol. 8(18), 2014, pp. 1-7.

[11] Xie H, Cook GS, Costerton JW, Bruce G, Rose TM, Lamont RJ, Intergeneric communication in dental plaque biofilms, Journal of Bacteriology, Vol. 182(24), 2000, pp. 7067-9.

[12] Sweeny LC, Dave J, Chambers PA, Heritage J, Antibiotic resistance in general dental practice-a cause for concern? Journal of Antimicrobial Chemotherapy, Vol. 53(4), 2004, pp. 567-576.

[13] Proal A, Understanding Biofilms, Bacteriality — exploring chronic disease, 26 May, 2008, Web. 13 March 2013, http://bacteriality.com/2008/05/26/biofilm/

[14] Molan PC, The antibacterial activity of honey. 2. Variation in the potency of the antibacterial activity, Bee World, Vol. 73, 1992, pp. 59-76

[15] Cooper R, Jenkins L, Rowlands R. Inhibition of biofilms through the use of Manukan honey, Wounds, Vol., 7(1), 2000, pp. 24–32.

[16] Wang R, Starkey M, Hazan R, Rahme LG, Honey's ability to counter bacterial infections arises from both bactericidal compounds and QS inhibition, Frontiers in Microbiology, Vol. 3(144), 2012, pp. 1-8.

[17] Ng WJ, Lim KY, Chong JY, Low KL, *In vitro* screening of honey against *Enterococcus* spp. biofilm, Journal of Medical and Bioengineering, Vol. 3(1), 2014, pp. 23-8.

[18] Ahmed M, Djebli N, Aissat S, Khiati B, Meslem A, Bacha, S, *In vitro* activity of natural honey alone and in combination with curcuma starch against *Rhodotula mucilaginosa* in correlation with bioactive compounds and diastase activity, Asian Pacific Journal of Tropical Medicine, Vol. 3(10), 2013, pp. 816-21.

[19] Cooper RA, Molan PC, Harding KG, Antibacterial activity of honey against strains of *Staphylococcus aureus* from infected wounds, Journal of the Royal Society of Medicine, Vol. 92, 1999, pp. 283-5.

[20] Nassar HM, Li M, Gregory RL, Effect of honey on *Streptococcus mutans* growth and biofilm formation, Applied Environmental Microbiology, Vol. 78(2), 20112, pp. 536-40.

INDUCED EARTHQUAKES CORRELATIONS WITH EARTH'S CRUSTAL THICKNESS

Marilia Hagen
Department of Geological Sciences, Indiana University, USA

ABSTRACT

In this paper we carried out an investigation about the possible causes for enhancement of earthquakes in USA over the last seven years. From our calculations, indications set forth that the increased evolution of the quakes in the country is due to the human actions. For further analysis we divided the country into three main seismological regions: western, central and, eastern. We roughly classified the areas by their thickness of Earth's crust in a variation 25-45-25 km. The thickest area is in the mid- continent and most of this region are part of the Great Plains. In our study we are going to investigate the reason for the Mississippi Lime in Oklahoma a very thick area, started an unusual earthquake activity since 2010, most at Oklahoma/ Kansas border. In this region also there are many anthropogenic activities concerning with the waste water wells and more than 4000 of them active at the moment in the state. The enhancement of earthquakes cluster is investigated in other locations in the USA. Those studies elsewhere indicated that the anthropogenic reasons vary; one of the most important is the deep waste water disposal used to recycle contaminated water extracted from the gas and oil wells, and other independent sources will be examined. We intend to explain why not all the waste wells are triggering earthquakes and how it would be strongly attached to the unevenness of the Earth's crust.

Keywords: Earth's crust, waste wells, Oklahoma

INTRODUCTION

There are many ideas and speculations on why intraplate events occur, but no consensus has emerged on how they are generated or how they continue to occur over many earthquake cycles. Intraplate earthquakes also present significant seismic hazards, especially because they can affect densely populated regions with little preparation for seismic shaking. The existence of intraplate earthquakes remains a deep scientific mystery with strong social implications that needs to be solved by innovative approaches. In this paper we are trying to explain how intraplate earthquakes are associated with the thickness of the earth's crust, and how the manmade earthquakes would represent a threat for the society.

Ellsworth [1] agreed the number of earthquakes related to fracking has been increased and the industries should monitor them better, it agrees with our observations in locations as Oklahoma as we are going to discuss later. McGarr et al., [2] made a study about the anthropogenic seismicity and described that in some regions manmade earthquakes are more obvious because background seismicity is low. Our research find out that places as the midcontinent are easier to checkout human activity than California coast.

Scientists [3] speculated that wastewater wells could be responsible for creating a wave of pressure that crawled through the subsurface and triggered the earthquakes far from the wells, some as far as 35 kilometers away. Wastewater can result from a variety of processes, including those related to energy production. For example, water is usually present in rock formations containing oil and gas and therefore will be co-produced during oil and gas production. Wastewater can also occur as flow back from hydraulic fracturing operations that involve injecting water under high pressure into a rock formation to stimulate the movement of oil and gas to a well for production.

Wastewater injection increases the underground pore pressure, which may, in effect, lubricate nearby faults thereby weakening them. If the pore pressure increases enough, the weakened fault will slip, releasing stored tectonic stress in the form of an earthquake. Even faults that have not moved in millions of years can be made to slip and cause an earthquake if conditions underground are appropriate. Although the disposal process has the potential to trigger earthquakes, not every wastewater disposal well produces earthquakes. In fact, very few of the more than 30,000 wells designed for this purpose appear to cause earthquakes. In this paper, we investigated why and where the disposal wells would trigger earthquakes.

RESULTS

Our registers showed earthquakes with magnitude ≥ 4 are a rare occurrence on the middle of USA covering the period 1965- 2015. Those rare events happened most near the known fault as

New Madrid. One exception is in Oklahoma/ Kansas border which since 2010 has shown an increase of seismological events on the Mississippi Lime and the following characteristics magnitude ≥ 4 and depth ≤ 5. Once this pattern on Oklahoma was delineated by our maps it needed more clarification and research so we narrowed our period of search to 2009- 2015. There were two reasons to collected the information on this period, one it is an implement of great number of waste water wells injection in the country and other the excellent records at the same interval in USA, about earthquakes. The Fig.1 shows the earthquakes events in Oklahoma / Kansas last seven years. The quake activity in this region was observed during last fifty years with more details since 2009, and it was notice an accumulation point or a cluster of earthquakes last years with Magnitudes 4-6 which happened most on the Mississippi lime, the exact location is at the border region Oklahoma/ Kansas determining the highest activity in the middle continent, sometimes above California. Historically this region was transformed through uplifting erosion and exposure to weathering and other geologic processes all before being buried again in subsequent periods. This place is called 'Chat' has served as a reservoir rock and its weakness make it fragile for the stress and pressure applied in the region. Events on the area happened most at depth 0-7 km and the same depth remarks occurred in other states analyzed. It is a possibility of subsurface faults, fractures in this region. Wells there produces lots of water; produced water is many times saltier than ocean water. It also can contain toxic metals and radioactive substances. Water disposal underground is the most inexpensive solution; other treatment methods would costs much more.

The uncommon activity in the region points out a discrepancy for others places in the middle country. In order to better understand for the location we defined a central region with the following coordinates 37.87N, 33.60S,-94.52E,-102.95 W, and considered only earthquakes with magnitude ≥ 4. Before 2000 the region did not assist any earthquake above magnitude 3 however, the frequency and the magnitude has been increase last seven years. We also search for the number of wells conventional and unconventional opened in this location and they have decreased last two years. Even though the number of waste water wells is now, 3,000 wells distributed on all the state, the earthquakes happened preferably in Mississippi lime region**.** This location has many conventional and unconventional wells since 2007 and waste water wells since 2009. It is a thick limestone section differing slightly from other plays and have a bigger shale component as part of their interbedded zones. The oil and natural gas play of that name focuses on a specific part of this area centered along the Kansas/Oklahoma border, with some experts estimating it to extend as far as southern Nebraska. While the largest oil activity has been in northern Oklahoma, areas now considered as part of the shale stretched farther north and west within Kansas. Earlier descriptions put the area of interest at around seven million acres, but with extension to the north and west, estimates now rage to 17 million acres. This area in Oklahoma is one of the most disturbed since 2009 when the number of earthquakes started to increase.

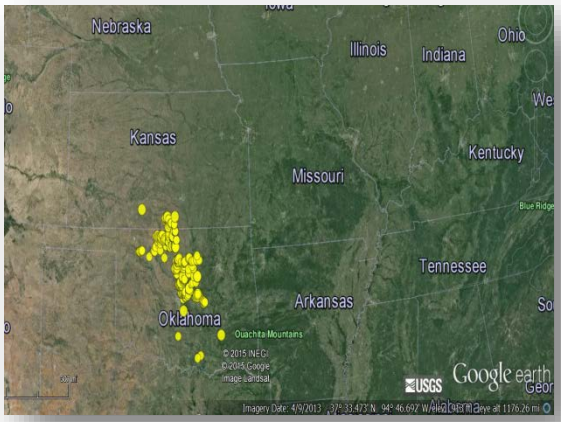

Figure 1 - Earthquakes with magnitude equal or above 4 in the period 2009-2015 in the Oklahoma/Kansas region.

Waste water wells disposal started around 2009 in Oklahoma. In 2011 an earthquake happened in the area with magnitude, 5.7 and depth around 5 km, reminding that depth $\leq$ 5km is one of the characteristics in what we understood as an induced earthquake in some areas midcontinent. At that time it was dismissed as connected with the injection wells by scientists and by oil/ gas companies.

In Virginia, also in 2011, an earthquake which caused much of damage in the area occurred with magnitude 5.7 in the Richmond basin which is far from the Marcellus shale coincident with an introduction in 2010 of a new technic to exploit coal bed methane that especially in that area is very hard and explosive. Coal bed methane is a natural gas trapped in the seams of coal deposits, and when it is sucked from the earth it brings up enormous amount of water with salt and it can't be legally disposed on the ground surface. Therefore it is drilled in deeper wells, up to 1,5 kilometers down injecting the water into deeper geologic formations. At those depths you have natural occurring faults.

You put water there increases the pressure, reduces the strength and makes the fault lines clamped together. Also depending on the rocks formation it could increase the probability of the brittle material under strain break under the applied pressure near the faults. This pressure is directly dependent of the Young's modulus (modulus of elasticity) and varies for different materials under strain. Coal beds in the Triassic Basin near Richmond and Farmville were formed 205 to 245 million years ago, when Pangea was splitting up rather than colliding. In the Triassic Basin, pressure to convert organic plant material into coal came from just the weight of overlying sediments, without tectonic squeezing - that is why the Chesterfield County coal is bituminous, rather than semi-anthracite.

The area of our interest is located is located at north of Richmond and extends across the Virginia coastal Plain in the tide water region of the state, it is Taylorsville basin. Since 2009 studies indicated that could contain as much as 1,6 trillion cubic feet of natural gas. At this time they introduced a new technic in the area known as micro wave fracking since the production have decreased with conventional wells. Both areas, Oklahoma and Virginia were dealing with the waste water wells, at the time and it is possible that the big earthquakes were due to that.

In our other paper [4], we also discussed the mechanism for hydraulic fracturing which involves to injecting mixture of water, sand and chemical additives into a subsurface petroleum reservoir at high pressure. The initial stage of a well shows small earthquakes caused by the strain to break the rocks to construct the well. However, each place pursue different geological formation, it means that some are harder to break as the coal bed methane in Virginia, and the stress-strain on the rocks will be much higher than for example, the one used to exploit marine limestone in Oklahoma. The Young modulus varies for each material under pressure, therefore it will be more damage depending how brittle is the material under pressure. Then, for each geological formation a different pattern for earthquakes will be delineated. The crustal thickness on USA varies is denser in the mid - continent in the ten states were covered by the Great Plains. Apparently it is the reason because the mid-continent has smaller earthquakes with some exceptions nearby known faults. The second conclusion will be the thinner crust will cause higher magnitude and more frequent earthquakes. Figure 2 showing the Earth's crust variations in USA.

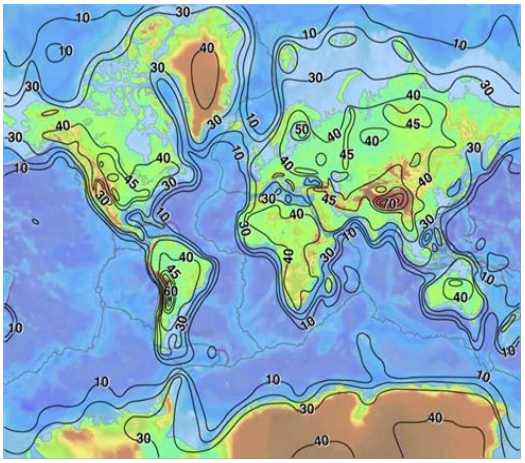

Figure 2- This contour map of the thickness of the Earth's crust was developed from the CRUST 5.1 model. The contour interval is 10 km; we also include the 45 km contour for greater detail on the continents. [7]

Observe that midcontinent is thicker as 45 km and greatly varies at the Western side near the Pacific coast where it is thinner as 25 km. In our previous study we found out that the thickness of the crust is the most important factor in the surge of earthquakes in different locations since the crust is uneven in all the continent with variations between 20 -45 km in the midcontinent being less thick at the Western and Eastern boundaries. Our study considered not only those two events, but also the researching on the enhancement of quakes in other points of USA, obeying the magnitude ≥ 3.5. From these studies the USA response for events allowed to divide the country in three main regions seismically active. The central region formed by most of states in the Great Plains, west and eastern sides. The three areas presented diverse geological formation, implying varied earthquakes characteristics. The period comprehended 2009-2015 showed that the Western side near of San Andreas Fault earthquakes $M \geq 7.0$ was not uncommon. However, in the Central and Eastern side seldom times earthquakes were $M \geq 5.0$ The western side has a history of higher quake activity partially because is the boundary of two tectonic plates , formed by subduction zones, faults known and unknown , fractures and a thinner crust. The Central part is very thick sometimes reaching 45 km, and events has lower magnitude. The eastern side has a complicated geological history mixing thicker and thinner places, younger and older crust, the magnitude of earthquakes is not higher than M 6.0; however the intensity of earthquakes at eastern side is much more destructive than the western with the same magnitude. Recently Hennings et al.

[5] discussed the relationship between stress, stress heterogeneity, and the permeability of subsurface fractures and faults. They analyzed a Sumatra region, Indonesia. They find out that reservoir potential is most enhanced in areas with large numbers of fractures with high ratios of shear to normal stress. This occurs in areas of the field that are in strike-slip stress style. Comparatively, reservoir potential is lower in areas of the field that are in a thrust- fault stress style where fewer fractures with high shear- to - normal stress ratios exist. Working on this direction we find out that many earthquakes happen near of some wellbores, and none happened near others. Therefore, it showed a clear connection between stress, stress variability, active faults, and the permeability of natural fracture systems in the subsurface. An extensive analysis in other USA states showed that the enhancement of earthquakes were most observed in the central part of the country as indicating non natural causes. Even though the other localities would have a small enhancement would be harder to detect those events as unnatural. At the New Madrid seismic zone small earthquakes with magnitudes between M2 and M4 increased last seven years with a special increase in 2011which source we could not find. As a following research we studied Arkansas because is a state part of New Madrid fault system. In the first period analyzed 1965-2008 there were only 3 medium events in this area $M \geq 3$ by year. After 2009 small and medium earthquakes increased. A location Greenbrier/Guy where 160 earthquakes happened between small, medium magnitudes with depths 0- 10km.This location has a minor Greenbrier fault nearby earthquakes swarm location. There is also a great number of waste water wells disposal due the coalbed methane wells.

The next location is Colorado in the period 1965-2009 the events started to be recorded in 1973 with an explosion reported in East Tavputs Plateau, unknown origin. A location of Paonia experiment a swarm of earthquakes reported as rock burst; the first detection officially was reported in 2001 in the West Elk Mountain. Since 2009 there is an enhancement earthquakes clusters due to the rock burst those are all small earthquakes. Other point in Colorado with rise of occurrences is located in Trinidad, near Sangre de Cristo Mountain. Trinidad is situated on Raton Basin, at the foothills of the Rocky Mountain. Colorado also is part of the four corner region, the larger US methane anomaly, and highly methane exploration is being done. Several waste water disposals are located there. The sedimentary beds are Paleozoic, Mesozoic, and Paleogene age. The eastern part of the basin, the sedimentary section is covered by flours of basalt of Miocene age as observed in Richmond, Virginia. Those two locations in Colorado had an increase activity due not only for the waste water disposal wells, but the heavy coal bed exploration. [6]

Texas had three important regions with the increasing of earthquakes one was in Dallas observed since 2009, the main characteristic of those earthquakes is the depth location reported as 5 km. In 2015 it is reported some events with depth $\geq$ 8 km. The activity is possible attached for a higher number of unconventional wells in the region. However, the magnitude of those events did not surpass M4. In 2015, there were 50,000 waste water wells in Texas. Only one earthquake above M4 was reported in Dallas, in 1999. The place is a stage of increasing small earthquakes but they are not above M4, in this location is a rare occurrence, and the depths are shallow, seldom times the depth is above 5 km. The other point targeted for earthquakes is San Antonio all them at 5 km depth, in the period 2009-2015. In 2011 the place was stroked by a magnitude 4.8. Still working on Texas State, there was another cluster of earthquakes located in Snyder. It was discovered some years ago a new shale in Snyder called Cline shale, it is a Permian basin comprised of three parts: the eastern Midland Basin, the central basin Platform and the western Delaware basin. This area is covered by black shale, organic -rich, deep water materials that would become source rocks in later geologic intervals this material is similar as the Mississippi lime reported in Oklahoma. It is supposed to be an enormous reservoir and they are preparing a heavy hydraulic fracking next years. The records provided about 57 small earthquakes up to a depth 7km. In this particular area of Texas, the events had increased 2010- 2014. All in all, there are 50,000 waste water wells officially reported in Texas and it covers most of the state. However, the quakes activity was observed more into the three areas Dallas, San Antonio, and Snyder. Finalizing our analysis states near New Madrid fault, Arkansas, Missouri and Tennessee, displayed a pattern with cluster of small earthquakes with epicenter bellow 8 km with small and medium magnitudes. Other States further was of New Madrid had different characteristics happened in cluster as well, but shallower depth (0-5 km).

The formation of middle US created diverse scenarios as unfolded and folded structures, unconformities as sub surface fractures and faults hided and unidentified so far. Some regions as Oklahoma have subsurface faults or fractures that under intense strain from the directional wells break or move creating the small events observed. The analysis on the increased seismicity last few years provided the following results:

a) Prior 2009, the regions targeted had no history or minor seismicity. b) Magnitude of

earthquakes middle of USA had seldom cases of M ≥ 5 therefore; these earthquakes also occur in shallower depths most 0-5 km. On the other hand events near New Madrid fault for example even though rarely happen with M ≥ 5, are able to have profounder depth.

c) Regions with enhancement in seismicity last years presented clusters or swarms of intermittent earthquakes with M ≥3. Some regions have quakes reaching M≥4 when previously it was no event in the area. d) Susceptible areas to present major number of small or medium quakes in general share a general composition of black, organic- marine formation in the mid-US. e) The contaminated water injected underground under high pressure has a strain effect in the materials underground and depending of the nature of the material reached it will ignite earthquakes in subsurface faults. Because the discrepancies in the Earth's crust thickness, under stress different locations will provide diverse intensity, magnitude and depth event. Therefore, three reasons will explain why some places with waste water wells have low earthquake activity, one is the volume and pressure applied to the injection, the second one which material injection water will reach and the third on is how thick the crust is in this area. One last reason or cause it would be the presence of subsurface faults or fractures unknown. Nowadays, information about waste water wells locations are incomplete, we guess that the contaminated, salty water released by methane gas exploration has a first cheaper discharge the drill of deeper wells near the gas exploration sites as Virginia, Oklahoma, Colorado, California and Wyoming. Those wells are the first responders for the increasing of earthquakes in those states.

On the western side is harder to distinguish the origin of earthquake unless having instruments that would supply some extra data providing the source quakes as natural or unnatural. Therefore analysis to the western side (California) of country has provided partial data.

The eastern side has a complicated geological history and contributes with larger earthquake events, seldom times. However, for the explained before earthquakes at the eastern side are more destructive in nature than in the western.

The formation, depth and thickness as the deposits in each location exploited make an individual well replies in a unique way to seismological stress. Our analysis on USA showed an enhancement of small magnitude earthquakes over the entire land. Many states presented locations with swarm of small earthquakes with different magnitudes. So far, there are magnitudes most in the range M3 - M4. The exception it is the western where the earthquakes reach magnitudes ≥ 4, easily.

About the catalogues investigated and used in this research there were discrepancies between the numbers of events, the sets rarely matches with each other in the period of one year. In the period 2009-2015 only one year USGS reported higher number of documented events than IRIS (2010). They remained with different quantities on 2015. The data categorized as anthropogenic or different sources started to be classified and released, by USGS two years ago. On the other hand, several small earthquakes with depth zero were not reported by USGS, only IRIS had all of them recorded, though IRIS is unable to distinguish anthropogenic sources. Both catalog provided that small events magnitudes 0-3 in 2009 were a total of 2145 in average covered California. In 2014 this number has increased to approximately 5340 events, with a leadership of Oklahoma and second California. Oklahoma showed a bizarre behavior in 2009 no event M ≥ 4, however in 2014 the number suddenly is 22 events, last seven years earthquakes magnitude ≥ 4 are becoming common in Oklahoma. Apparently everything indicates that this increase in the Mississippi lime area is due to the unconformities of the crustal surface at this particular location. In this study we mentioned two earthquakes Oklahoma, Virginia both with M5.7 both happened in 2011. In the region they occurred has unfrequently stories of large earthquakes. However, since 2009 those places added waste water wells due the exploitation of coal bed methane that needed to dispose the waste water that will be deposed in deeper wells in geological formations. However, this method increases the pressure underground, and depending the thickness of the Earth's crust in the region, as well the material of rocks will lead to earthquakes. Those quakes are not necessarily close to the wells depending of what disturbance the injection makes bellow the ground. A physical model that would input data and variables, as pressure, Young module, and also considerate the presence of faults are impossible nowadays some of those faults are unknown. We are also dealing with different kind of shale material, porosity, permeability, density of oil , gas or coal , dissimilar thickness of crustal surface , such factors play different rules on the hazard events observed and compiled. Unconventional wells close associated with waste water wells, are greatly responsible in the increase of small and medium earthquakes in some specific area in the midcontinent. However states that reported to not have wells experimented an increase of small superficial /shallower earthquakes as Georgia and Maine. Nevertheless, Georgia reported some waste water wells in their territory, some years ago. Besides those facts there is also

big events that are manmade as in Nevada during the period 1970-1980 or more recently due to nuclear explosions. After 2000, Nevada earthquakes M≥ 5 are a very rare occurrence; although at the moment the western side of Nevada has an enhancement of events, probably associated with waste water injection.

DISCUSSION

The causes of the enhancement of small/ medium earthquakes during the period 2009-2014 in USA were due to different human activities. How those actions influence the ground and will respond to these interferences is dependent most of the thickness of the earth's crust in the region analyzed. The presence of the subsurface faults or fractures dormant or half active also will change the increase in magnitude and the frequency of events. The western side contributes with the highest level of magnitude, during the period observed. California contributed with the events M ≥ 6, the biggest events observed thirty years ago in Nevada were nuclear experiments, nowadays west side of Nevada showing cluster M ≥ 4, not totally identified by human activity so far. The western side of USA is the thinnest and younger geological region with some places reaching less than 25 km; therefore events powerfully increase in these locations. Central part of USA is the thickest one, around 45 km, and also more stable geological formations, the reason for the exception active Oklahoma / Kansas relays in the awaken subsurface fractures due to the human activity.

CONCLUSION

The main issue on our research was to investigate the enhancement of earthquakes intraplate and the possible causes and sources for that. Our conclusion it was that waste water disposal wells in the country the ones known as deeper disposal wells are responsible for this increase. Unfortunately, there is no available catalog for the waste water disposal wells in the country. Some states reported waste water wells and the location but not all of them. Oklahoma recently released a map with waste water wells and earthquakes, both maps did not match, it meant from the 3,000 wells constructed earthquakes happened near some of them and some place were uneventful. We found out that most of the higher activity middle continent area occurred last seven years was anthropogenic interference and sometimes partially connected with drilling.

Many places presented the events in clusters in different scenarios, and far from drilling places in varied areas of the country; most of them have been clear attachment with waste water wells. The most important factor to earthquakes it is the thickness of the Earth's crust, places thicker has less events, than locations thinner. The midcontinent is thicker than western edge; therefore there are fewer occurrences of earthquakes and smaller magnitudes in the central region. The eastern side has an uneven structure in the Earth's crust however at contrary of western side is far from the border of a tectonic plate, therefore events rise smaller magnitudes than the western side. Events look connected most to waste water wells used for coal bed methane and oil, mining, and nuclear explosions; some events were not reported by both catalogues, many places showed superficial quakes in a depth 0-1km, those events are mostly small magnitudes varying 1 ≤M ≤ 3.

The dependence between magnitude and depth of earthquakes rely on the ground thickness, thinner ground will create larger magnitude quakes, the distribution of crust thickness in US is the follow it is thicker in the middle, thinner in the western, and variable at eastern. At western side magnitudes usually reach M ≥ 7, in the middle of country and eastern seldom times will be M ≥ 5, the exception would be New Madrid, and Charleston. As a final point, the Oklahoma/Kansas activity experimented last period 2009- 2014 most at the depth 0-5 km with medium magnitude (M≥ 3.5) indicates that there is an unknown subsurface fractures in a region identified as Mississippi Lime, called as the Chat. This region is similar for the one observed in Arkansas (with similar earthquakes swarm, M≥3.5) nearby New Madrid fault.

ACKNOWLEDGEMENTS

I am thankful to my adviser in Japan, Sigeo Hamada, from the Nihon University, Tokyo, Japan, whom was my doctorate adviser period 1986/1988. I would like to thank Mr. Charles W. Hagen who corrected some of English. I would like to thank Dr. M. Hamburger (Indiana University) who helped me with important suggestions along this research.

REFERENCES

[1] Ellsworth W.L. , Injection - induced earthquakes, Science , 34 (6142),2013

[2] McGarr A., Maximum magnitude earthquakes induced by fluid injection, Journal of Geophysical Research: Solid Earth- 119, 1008-1019, 2014

[3] Hagen M, Natural Science, 2015, 7, 459-474 Published Online September 2015 in SciRes. http://www.scirp.org/journal/ns -Mechanism of Intraplate Earthquakes and Anthropogenic Causes in USA

[4] Hand, E., Injection wells blamed in Oklahoma earthquakes, Geoscience - July/2014- vol. 345- issue 6192
[5] Hennings P., Allwardt.P, Paul P., Zahm C, Reid Jr. R, Alley H., Kirschner R., Lee B.,Hough E., Relationship between fractures, fault zones, stress, and reservoir productivity in the Suban gas field, Sumatra, Indonesia- AAPG 81111, v 96. No 4, PP 753- n2, 2011
[6] Rubinstein J.L., Ellsworth W, McGarr A and Benz H.M. - The 2001 - present induced earthquake sequence in the Raton Basin of Northern New Mexico and Southern Colorado, Bulletin of seismological society of America, vol.104, n 5, pg1-20, 2014
[7] http://earthquake.usgs.gov/data/crust/ (**Figure 2**)

First International Conference on Science, Engineering & Environment,
Tsu City, Mie, Japan, Nov.19-21, 2015, ISBN: 978-4-9905958-5-2 C3051

GEOCHEMICAL ASSESSMENT OF LATE PALEOGENE SYNRIFT SOURCE ROCKS IN THE SOUTH SUMATRA BASIN

Edy Sutriyono, Endang Wiwik Dyah Hastuti, Budhi Kuswan Susilo
Geology Study Program of Engineering Faculty of Sriwijaya University
Jl. Srijaya Negara, Bukit Besar, Palembang, Sumatera Selatan,
Indonesia

ABSTRACT

The potential of Late Paleogene synrift source rocks in generating hydrocarbons within the South Sumatra basin has been evaluated using geochemical and pyrolytic techniques. The samples were collected from the outcropping shales of different layers constituting the Upper Oligocene Talang Akar Formation. Results of TOC analysis reveal minor quantities of organic carbons, indicating poor to fair potential source rocks. The S_2/S_3 ratios indicate two apparent kerogen types. The majority of the samples is type III kerogen; however, there appears minor type IV kerogen, implying the oxydized organic matter and no expulsion. The S_1+S_2 measurement of all the pyrolysed rocks, except one sample LP 12A, yields less than 1 mg HC/g rock, supporting the proposed scenario of little potential to generate hydrocarbons. Evaluation of hydrogen and oxygen indices confirms a gas prone source, but all the shales analyzed, disregarding one sample LP 18, provide a direct evidence that the rock section is immature to early mature to expel oil. Important notes can be made that the early stage of organic maturation might have occurred due to heating, as a result of deeper burial during Miocene time prior to the subsequent uplift in response to the Plio-Pleistocene orogeny.

Keywords: geochemistry, outcrops, pyrolysis, source rock, thermal maturity

INTRODUCTION

The organic geochemical study reported in the present paper aimed to evaluate potential source rocks, and to assess thermal maturity of the rock succession in the Paleogene South Sumatra basin. Tectonically, the study area lies in the South Palembang subbasin, situated around the southern part of South Sumatra basin (Fig. 1). The initial subsidence of the basinal area has commonly been attributed to extensional forces occurred in the southwestern margin of Sundaland during the Late Eocene [1]. Several workers have suggested that an early episode of depression began in the Early Tertiary as rifts, in which the synrift clastic materials accummulated in a terrestrial environment [2]-[3].

The synrift sedimentation in the basin continued as the rifting event proceeded, and the shoreline migrated landward because of the occurring transgression during Late Oligocene-early Middle Miocene times. This transgressive phase resulted in successively from lower to upper units the Talang Akar Formation, the Baturaja Formation, and the Gumai Formation. At this time, the basin was mostly under the influence of tensional stresses responsible for widening the depocenter area. In the late Middle Miocene a transgressive event in the basinal area ceased, the sea level dropped, a regressive regime commenced, and the region was predominantly controlled by compressive strain fields for the rest of Tertiary times. This regime formed consecutively the Air Benakat Formation, the Muara Enim Formation, and the Kasai Formation (Fig. 2). In the Plio-Pleistocene, the whole sedimentary successions of the region were uplifted due mainly to orogeny. The late Tertiary orogenic event is considered to be the latest tectonic deformation that has been responsible for the present geologic configuration of the Paleogene South Sumatra basin. A particular interest of the present study is the Talang Akar Formation. This work has employed conventional geochemical analyses and pyrolysis measurements for the sampled sections.

METHODS

Organic geochemistry is an important tool to identify the quality of prospective source rocks with respect to hydrocarbon generation [5]-[6]. The present study has employed the widely used geochemical technique to determine total organic carbon (TOC wt. %), and pyrolysis measurements to gain the values of hydrogen index (HI mg HC/g C), oxygen index (OI mg CO_2/g C), and maximum temperature (T_{max} ºC). In interpretation of the TOC data, this study implements the accepted geochemical model [7], suggesting that the TOC content of 1.0 wt. % is the lower limit for identifying hydrocarbon expulsion from source rocks.

The measurement of pyrolytic contents utilizes Rock-Eval instrument to calculate the following parameters:

- Hydrogen Index (HI) = (S_2/TOC) x 100 (mg HC/g C)
- Oxygen Index (OI) = (S_3/TOC) x 100 (mg CO_2/g C)
- Hydrocarbon type (HT) = S2/S3 (mg HC/g rock)
- Production Index (PI) = $S_1/(S_1+S_2)$

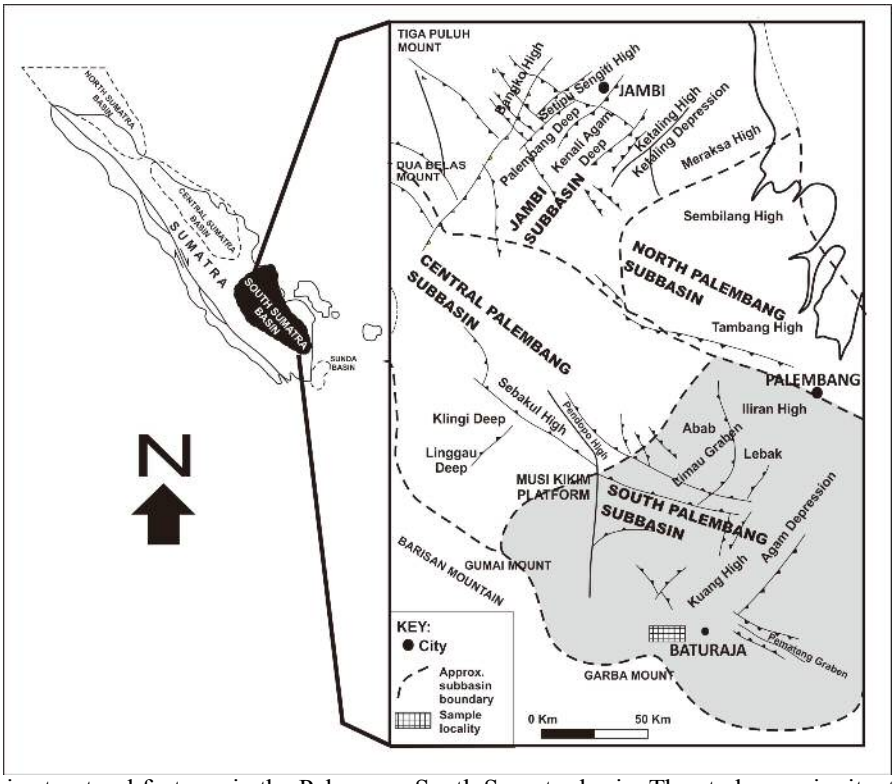

Fig. 1 Main structural features in the Paleogene South Sumatra basin. The study area is situated in the South Palembang subbasin (modified from [4])

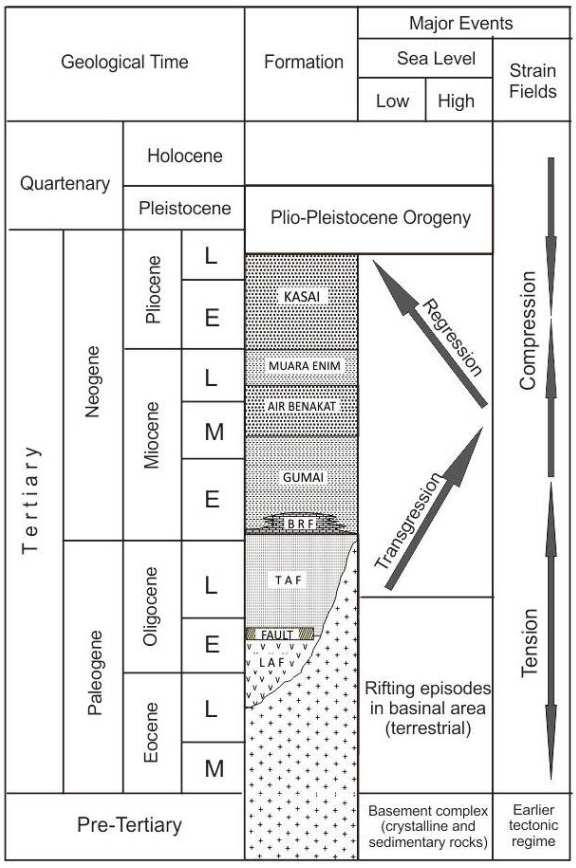

LAF: Lahat Formation; TAF: Talang Akar Formation;
BRF: Baturaja Formation

Fig. 2 Generalized stratigraphy of South Sumatra basin

Determination of hydrocarbon types follows the accepted values [5]. According to this author, the HT value of less than 2.5 mg HC/g rock is defined as dry gas, ranging from 2.5 to 5.0 mg HC/g rock is classified as wet gas, and higher than 5.0 mg HC/g rock is considered as oil. The sum of S_1+S_2 components define genetic potential for hydrocarbon yield due principally to heating, hence the given values suggest the amount of total hydrocarbons. In this respect, S_1 represents the amount of free hydrocarbons (mg HC/g rock) released by volatilization at elevated temperatures, whereas S_2 is the value of HC quantity (mg HC/g rock) resulted from further heating of kerogen during experimental work. Assessment for total potential of source rock refers to as the published classifications [7] as follows:

- values of less than 2.0 mg HC/g rock are classified as little potential for oil generation, possibly some potential for gas prone
- values ranging from 2.0 to 6.0 mg HC/g rock are considered to be moderate or fair source potential
- values of higher than 6.0 mg HC/g rock are typical indicators of good to excellent source potential

In order to assess thermal maturity of the source section, the present study used T_{max} data and PI values, and compared the resulted interpretations to the previously reported models cited elsewhere in many published works [7]. This study has also compiled the geological data available, such as regional geology and stratigraphy to support interpretations of geochemical data and pyrolytic parameters.

SAMPLE DETAILS

Varieties of strata constituting the Upper Oligocene Talang Akar Formation have been observed in the studied region. Nine rock specimens were collected from this section, particularly from exposures along Lengkayap river (LP 04, LP 11, LP 12A, LP 12B, 24, and LP 25) and Napalan river (LP 16, LP 17, and LP 18). Fig. 3 shows the locality of shale outcrops sampled for geochemical analyses discussed in this article. The outcrops were investigated based mainly on lithologic and sedimentologic characteristics. Shales in the Talang Akar sequence are commonly silty or sandy and coaly, and these rocks are mostly brown and gray. Details of the rock samples such as locality, stratigraphic age, stratigraphic unit, and types of lithology are displayed in Table 1.

Table 1 Sample details showing locality, stratigraphic age, stratigraphic unit, and lithology

Sample No.	Locality			Stratigraphic Age	Stratigraphic Unit	Lithology
	River	Longitude (ºE)	Latitude (ºS)			
LP 04	Lengkayap	104º 05' 54.9"	4º 19' 48.7"	Upper Oligocene	Talang Akar Formation	Brown shale
LP 11	Lengkayap	104º 06' 04.9"	4º 19' 52.9"			Gray shale
LP 12A	Lengkayap	104º 06' 07.3"	4º 19' 52.2"			Brown shale
LP12B	Lengkayap	104º 06' 07.3"	4º 19' 52.2"			Gray shale
LP 16	Napalan	104º 06' 54.9"	4º 22' 47.5"			Brown shale
LP17	Napalan	104º 06' 57.5"	4º 22' 37.5"			Gray shale
LP18	Napalan	104º 06' 57.0"	4º 22' 35.3"			Gray shale
LP 24	Lengkayap	104º 05' 26.5"	4º 19' 45.3"			Brown shale
LP 25	Lengkayap	104º 05' 26.2"	4º 19' 45.6"			Brown shale

GENERAL GEOLOGY

The study area is situated in the South Palembang subbasin, which is one of four subbasins within the Paleogene South Sumatra basin (Fig. 1). The basin has long been recognized as one of hydrocarbon producing basins in Sumatra. The island of Sumatra is part of Sundaland located in the southwestern portion of SE Asian continent. The tectonic evolution of the region during Tertiary times has been discussed in many published works [1], [8]-[9]. The more recent overview of the development of Sundaland from the Late Palaeozoic to the Late Mesozoic has also been presented [10]. However, discussion in details the regional tectonics of this landmass is beyond the main aims of the present study.

Regional geology of the South Sumatra basin has been presented elsewhere, and commonly discussed on the basis of a wide variety of views. The basin is an asymmetric depocenter, bounded by the Barisan Mountains to the southwest, the Sunda platform to the northeast, the Tigapuluh Mountains to the northwest, and the Lampung High to the southeast [2]. It has generally been acknowledged that subsidence in basinal area was initiated by tensional stresses occurring in the southwestern margin of Sundaland during Late Oligocene to Early Miocene times [3], [11].

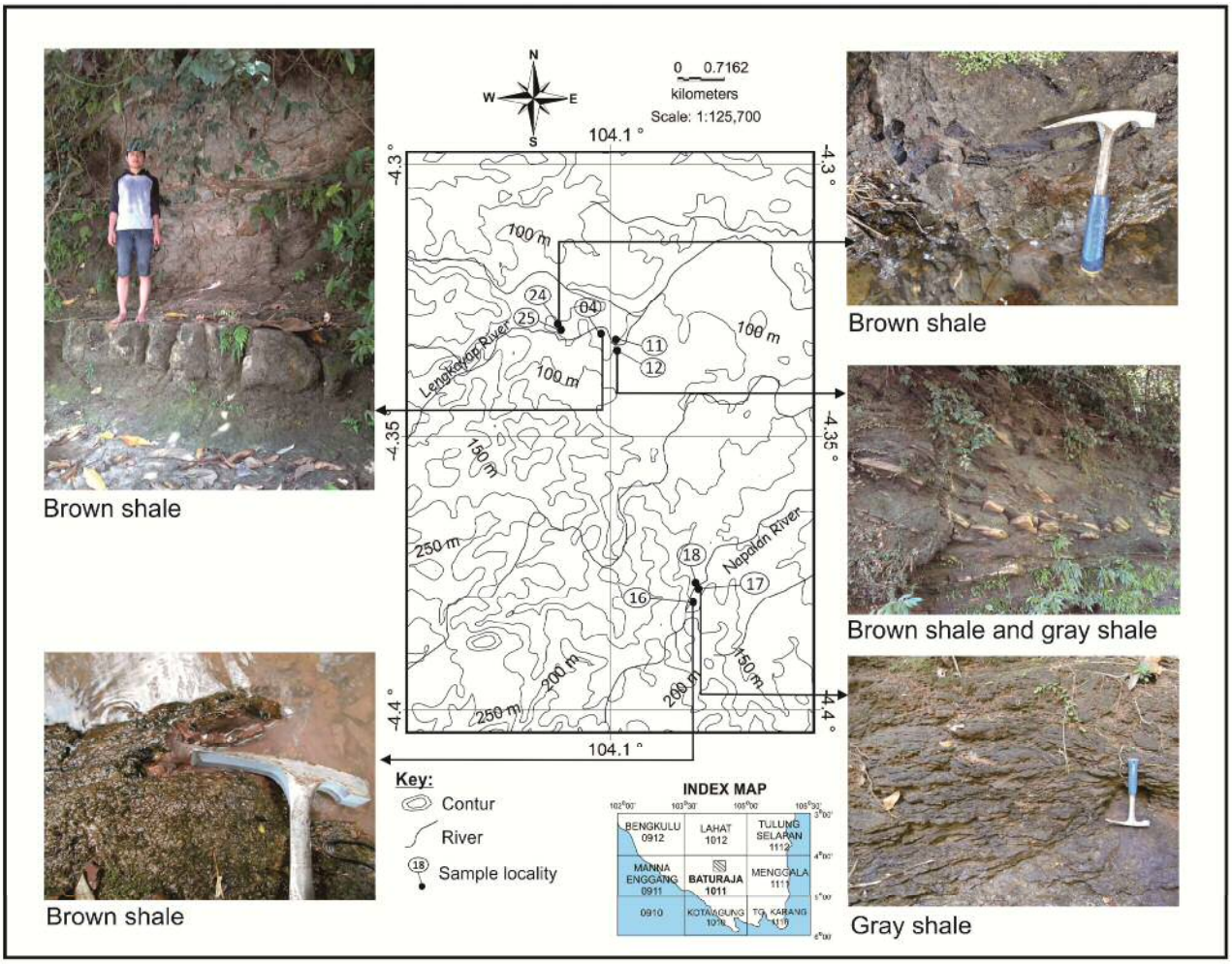

Fig. 3 A topographic map showing the locality of shale beds collected for geochemical analyses. Also shown are the sample numbers and some outcrop photographs

The tension is considered to have been responsible for the commencement of rifting in a back-arc setting. The back-arc basins extending along the eastern section of the island, namely North Sumatra basin, Central Sumatra basin, and South Sumatra basin, were formed during the Late Eocene or at ~40 Ma [1]. There were at least three stages of rifting within the basinal area [12]. These authors suggest that the early-, middle-, and late-rift episodes were followed respectively by the deposition of predominantly non-marine sediments, deep and broad lacustrine clastics, and coarse clastic fluvio-deltaic facies. In the case of Talang Akar Formation, the deposition of rock sequence commenced during the early rift stage in the Late Oligocene. The generalised stratigraphic column of the basin has been presented elsewhere by various workers [2], [13]-[16].

In terms of a regional structural setting, the basin comprises at least two main components. These include (1) half graben, horst, and faulted blocks involving the Mesozoic basement [2], [17], and (2) the NW-SE trending structures and depression to the northeast. The structures in the region were broadly resulted from the Late Neogene Barisan orogeny due to oblique convergence between the Indo-Autralian and Eurasian plates [2]-[3], [11], [17]. These structural features, especially folds and faults appear to have controlled a general pattern of stratigraphic exposures, involving both the pre-Tertiary basement sequence and the Tertiary sedimentary cover [3]. The basement exposures occur particularly in areas of block faulting, whereas the overlying successions tend to follow the regional strike of anticlinoria.

RESULTS AND INTERPRETATIONS

A number of selected outcrops of the Upper Oligocene Talang Akar Formation have been analyzed to obtain organic geochemical data and pyrolysis values. Results of the present analysis were compared with those of the published work [18] in order to better understand geochemistry of the source system throughout the region. Table 2 shows the analytical results of geochemical analysis and pyrolysis measurements of the rock samples.

Table 2 Geochemical and pyrolysis analytical results from the sampled rock sequence

Sample No.	TOC	S_1	S_2	S_3	HI	OI	TP (S_1+S_2)	HT (S_2/S_3)	PI S_1/(S_1+S_2)	OM
LP 04	0,11	0,06	0,09	0,06	81,52	54,35	0,15	1,50	0,40	421
LP 11	0,90	0,06	1,04	0,62	115,57	68,90	1,10	1,68	0,06	415
LP 12A	0,61	0,04	0,31	0,75	51,01	123,42	0,35	0,41	0,11	417
LP12B	0,81	0,05	0,46	0,52	56,83	64,25	0,51	0,89	0,10	412
LP 16	0,08	0,02	0,05	0,04	61,65	49,32	0,07	1,25	0,29	380
LP17	1,55	0,03	0,10	0,25	6,44	16,09	0,13	0,40	0,23	407
LP18	1,16	0,04	0,07	0,17	6,06	14,72	0,11	0,41	0,36	514
LP 24	1,00	0,06	0,74	0,86	73,79	85,75	0,80	0,86	0,08	396
LP 25	1,04	0,06	0,91	0,72	87,37	69,12	0,97	1,26	0,06	411

Key: TOC: total organic carbon (wt. %); S_1: amount of free hydrocarbon (mg HC/g rock); S_2: amount of hydrocarbon from heating (mg HC/g rock); S_3: organic carbon dioxide; HI: hydrogen index [(S_2/TOC)x100] (mg HC/g C); OI: oxygen index [(S_3/TOC)x100] (mg CO_2/g C); TP: total potential (mg HC/g rock); HT: hydrocarbon type (mg HC/g rock); PI: production index; OM: organic maturity or T_{max} (ºC).

TOC values range from 0.08 to 1.55 wt. %, and a median content of 0.81 wt. %. Of these, five rocks LP 04, LP 11, LP 12A, LP 12B, and LP 16 yielded TOC content of less than 1.0 wt. %, and four samples LP 17, LP 18, LP 24, and LP 25 resulted in TOC content of more than 1.0 wt. %. These values do not vary significantly, suggesting that the source section is poor to good in quality. This interpretation is principally to follow the previously proposed geochemical models [5], [7], [19]-[20]. It has also been reported that the source facies of Talang Akar unit in Kuang area has poor to fair potential, whereas the rock sequence in Limau area has good potential [18].

The apparently low TOC content is likely to determine a minor quantity of organic carbons in the source beds. In contrast to marine black shales, in which the organic matter is commonly abundant [21], all of the shales studied are mostly light to medium brown and gray, implying a general lack of organic component. This may be a direct reflection of terrestrial environment, where the silty or sandy shales of the Talang Akar Formation accummulated. The previously published studies have also reported that the oil source rocks for the majority of back-arc basins in the western region of Indonesia were deposited in fluvio-deltaic environments [22]-[23]. In addition, it has been confirmed that oils in Sumatra were generated from terrestrial-rich marsh or swamp coals and coaly shales [24]. The more recent studies suggest that the Paleogene South Sumatra basin has terrestrial source rocks, consisting mainly of carbonaceous shales and coals [12].

There are two kerogen types based on the S_2/S_3 ratios. The majority of samples yielded the S_2/S_3 values of equal to or more than 1.0 mg HC/g rock, suggesting type III kerogen, whereas the minority of rocks resulted in less than 1.0 mg HC/g rock, indicating type IV kerogen. The later type of kerogen is also supported by the HI values of less than 50 mg HC/g C derived particularly from samples LP 17 and 18. Type IV kerogen is more likely negligible with respect to expulsion, and it is commonly resulted from other kerogen types that have been reworked or oxidized [6]. Evaluation of total potential of hydrocarbon generation relies principally on the measurement of pyrolytic yield (S_1+S_2). The pyrolyzed rock samples resulted in low values, ranging from 0.07 to 1.10 mg HC/g rock and a median value of 0.96 mg HC/g rock. Therefore, the data provide a direct evidence of little or no potential for source rocks to expel oil. This interpretation is consistent with the results of previous studies [7], [18].

Hydrogen indices range from 6 to 116 mg HC/g C, and average 60 mg HC/g C. All but one sample LP 11 yielded HI values of less than 100 mg HC/g C (Table 2). Organic facies with low HI values (<300 mg HC/g C) and low S_2/S_3 ratios is referred to as gas prone [25]. The present values are identical with the existing pyrolytic data [18]. Hence, the HI data confirm a gas prone source in the Talang Akar unit. Given the low HI values, there existed the effects of weathering on source rocks [26]. In this case, the Talang Akar succession may have undergone any surface weathering since the commencement of basin inversion following the Late Neogene orogeny [11]. Oxygen indices range from 15 to 123 mg CO_2/g C, and average 61 mg CO_2/g C. Several samples yielded S_2 ≥0.4 mg HC/g rock, suggesting that the formation has reliable HI and OI indices and an organic composition characterized by the type III variety of kerogen. Fig. 4 displays the HI vs OI plot constructed on the basis of the Talang Akar pyrolytic data, confirming a strong indication of gas prone and type III kerogen.

Excluding LP 18, the eight of nine samples yielded T_{max} ranging from 380º to 421ºC, suggesting that the source beds are immature to expel oil. In oppose to the T_{max} data [18], the values here are considerably low.

According to these authors, the Talang Akar section in Limau area is mature with T_{max} values of 436º-450ºC, while that exposed in Kuang area is early mature with T_{max} values of 425º-433ºC. The source rocks with T_{max} less than 435ºC are immature, T_{max} between 435º and 465ºC may result in oils, and T_{max} higher than 465ºC enable to generate gases [5]. Based on this category, the Talang Akar shales are mostly immature. Fig. 5 shows the HI vs T_{max} values of the Talang Akar samples, which indicates that the eight of nine samples are immature, whereas one specimen with an extremely high T_{max} yield is apparently odd and thus disregarded in the interpretation of the resulted data.

However, coal-bearing sequence such as the studied formation is able to expel liquid hydrocarbon at T_{max} above 360ºC [27]. In this regard, the present data suggest that the Talang Akar section is oil-prone generation, implying that the rock unit has possibly entered the top zone of maturation. This interpretation agrees with the result of studies on the low rank coal of the South Sumatra basin [28], suggesting that the T_{max} value of the coal bearing source rock has reached approximately the upper limit of oil generating window. To compile the existing and present data, the Late Paleogene source section in the basin appears to be well constrained geochemically as poor to good yield in generating liquid hydrocarbons (Table 3).

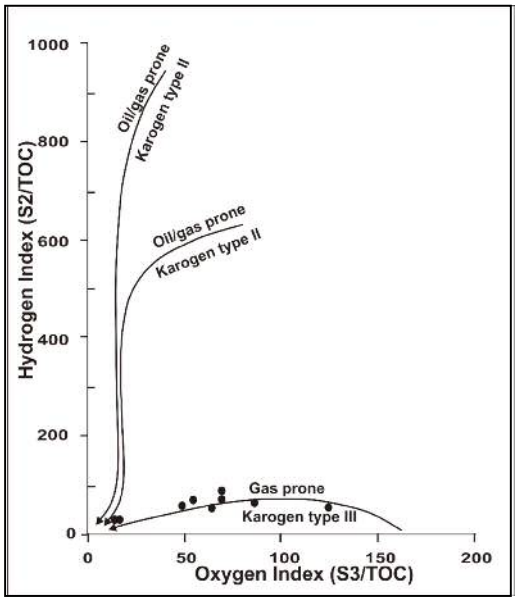

Fig. 4 Modified van Krevelen diagram showing the HI vs OI plot based on the Talang Akar pyrolytic data, indicating that the source section is gas prone and type III kerogen

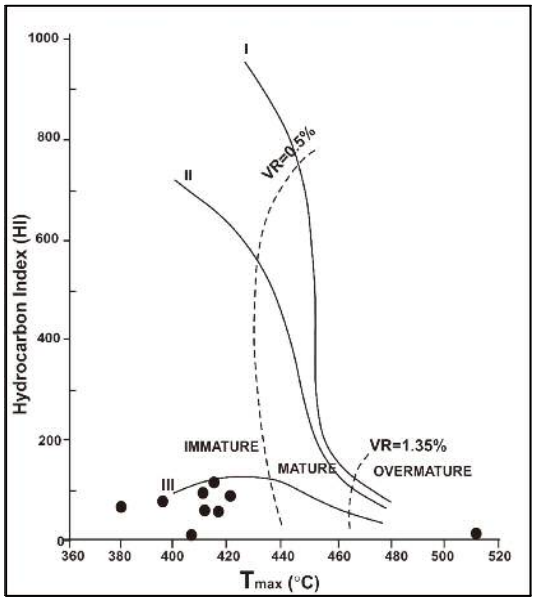

Fig. 5 Diagram showing the HI vs Tmax yield of the Talang Akar samples. Also shown are the range of thermal maturities based on the accepted vitrinite reflectance (VR) values (dashed line). One sample in the right extremity (T_{max} 514ºC) is unlikely and considered here as an erroneous T_{max} yield

Table 3 Comparison of experimental results between the previously reported geochemistry of well rocks and the present geochemical analysis of outcrops

Parameters	Area within the South Palembang subbasin				Interpretations
	Well rocks (1)		Outcrops (2)		
	Limau	Kuang	Napalan River	Lengkayap River	
TOC (wt. %)	1.5-8.0	0.3-0.9	0.08-1.55	0.11-1.04	(1) fair to good potential, and early mature to mature [18].
S_1 (mg HC/g rock)	0.5-2.1	0.1-0.5	0.02-0.04	0.04-0.06	
S_2 (mg HC/g rock)	1.5-8.0	0.2-4.0	0.05-0.10	0.09-1.04	(2) poor to fair potential, and disregarding the T_{max} value of 514ºC, the present study suggests immature based on the existing classification [5], and early mature following the other model [27].
T_{max} (ºC)	436-450	425-433	380-514	396-421	

In a regional context, the proposed scenario is also consistent with the result of fission track study conducted in the adjacent Sunda basin [29]. This author suggests that the Late Paleogene Talang Akar source section has been exposed to the zone of thermal annealing, which is coincident with the top of oil window [30]. In the South Sumatra basin, the thick Miocene overburden seems to have provided the necessary burial depth for organic maturity in the shale beds. In addition, several workers suggest that the upward emplacement of dioritic and granitic magmas underneath the sedimentary cover was somehow responsible for the paleo-high heat flow in the basin [31]-[32]. The heat influx might permit significant heating favourable for an early stage of maturation.

It seems interesting that one sample TP 18 yielded the T_{max} value of 514ºC, suggesting that the sequence is overmature (Fig. 5). The appearence of such a very high temperature is unlikely, and discordant with the existing analytical results of thermal maturity observation and their corresponding interpretations [18], [23]-[24]. More importantly, the overmature level as suggested by the one sample only obviously disagrees with independent thermal maturity constraints such as vitrinite reflectance (VR) measurements. The VR data derived from the Talang Akar well samples indicate that the maturity degree of the source sequence ranges from immature (VR = 0.3-0.4%) to mature (VR = 0.45-0.94%) [18]. Thus, it is technically sound to disregard the T_{max} yield of this particular sample in the interpretation of organic maturity data, and this single value is considered here as a result of incorrect T_{max} readings, but the possible causes of the technical false remain uncertain.

CONCLUSIONS

On the basis of the above discussion, the present geochemical study draws some concluding remarks as follows:

1. The Late Paleogene Talang Akar shales contain lack of organic carbons based on the TOC data and the S_1+S_2 values, suggesting poor to fair potential source rocks for generating a significant amount of oils.
2. The HI/OI ratio of all the rock samples analysed suggests that the source sequence is gas prone or type III kerogen.
3. The source rocks are attributed to differences in thermal maturity ranging from immature to early mature with respect to oil expulsion.
4. The succession has been subjected to the zone of early mature, principally caused by heating via deeper burial as a result of the Early Neogene deposition.

ACKNOWLEDGEMENTS

The authors are grateful to the University of Sriwijaya for research fund. This paper is part of geochemical and paleontological studies carried out in the South Sumatra basin. We also thank our colleagues Idarwati, ST. MT., Elisabet Dwi Mayasari, ST. MT., and Harnani, ST. MT., who have been involved in the field reconnaissance.

REFERENCES

[1] Daly, M. C., Cooper, M. A., Wilson, I., Smith, D. G., and Hooper, B. G. D. “Cenozoic plate tectonics and basin evolution in Indonesia”, Marine and Petroleum Geology, v. 8, 1991, p. 2-21.

[2] de Coster, G. L. “The geology of the Central and South Sumatra basins”, Proceedings 3rd Annual Convention, IPA, 1974, p. 77-110.

[3] Pulunggono, A. “Tertiary structural features related to extensional and compressive tectonics in the Palembang basin, South Sumatra”, Proceedings 5th Annual Convention, IPA, 1986, p. 187-213.

[4] Bishop, M. G. “South Sumatra basin province, Indonesia: the Lahat Talang Akar Cenozoic total pretroleum system”, US Department of the Interior, Geological Survey, 2001, p. 3-22.

[5] Peters, K. E. “Guidelines for evaluating petroleum source rock using programmed pyrolysis”, AAPG Bulletin, v. 60, 1986, p. 318-329.

[6] Peters, K. E. and Cassa, M. R. “Applied source rock geochemistry. In L. B. Magoon and W. G. Dow (editors): The petroleum system – from source to trap”, AAPG Memoir 60, 1994, p. 93-120.

[7] Tissot, B. P. and Welte, D. H. “Petroleum formation and occurrence”, New York, Springer-Verlag, 1984, 699 pp.

[8] Hamilton, W. “Tectonics of the Indonesian region”, US Geological Survey Professional Paper, 1078, 1979, 345 pp.

[9] Malod, J. A., Karta, K., Beslier, M. O., and Zen, M. T. Jr. “From normal to oblique subduction: tectonic relationships between Java and Sumatra”, Journal of SE Asian Earth Sciences, v. 12, 1995, p. 85-93.

[10] Hall, R. “The origin of Sundaland. Proceedings of Sundaland Resources”, MGEI Annual Convention, 2014, p. 1-25.

[11] Simanjuntak, T. O. and Barber, A. J. “Contrasting tectonic styles in the Neogene orogenic belts of Indonesia”, Geological Society Special Publication, no. 106, 1996, p. 185-201.

[12] Sudarmono, Suherman, T., and Eza, B. “Paleogene basin development in Sundaland and its role to the petroleum systems in the western Indonesia”, Proceedings of the Petroleum Systems of SE Asia and Australasia Conference, IPA, 1997, p. 545-560.

[13] Adiwidjaja, P. and de Coster, G. L. “Pre-Tertiary paleogeography and related sedimentation in South Sumatra”, Proceedings 2nd Annual Convention, IPA, 1973, p. 89-103.

[14] Sitompul, N., Rudiyanto, Wirawan, A., and Zaim, Y. “Effects of sea level drops during late Early

Miocene to the reservoirs in South Palembang subbasin, South Sumatra, Indonesia", Proceedings 21st Annual Convention, IPA, 1992, p. 309-324.

[15] Tamtomo, B., Yuswar I., and Widianto, E. "Transgressive Talang Akar sands of the Kuang area, South Sumatra basin: origin, distribution and implication for exploration play concept", Proceedings of the Petroleum Systems of SE Asia and Australasia Conference, IPA, 1997, p. 699-708.

[16] Riadhy, S., Ascaria, A., Martono, D., Sukotjo, A., Hernadi, D., Kruniawan, M., and Luthfi, N. "Carbonate play concept in Sopa and surrounding areas: an alternative model for hydrocarbon occurrence, Musi platform, South Sumatra basin", Proceedings 27th Annual Convention, IPA, 1999, p. 1-13.

[17] Pulunggono, A., Haryo, A. S., and Kosuma, C. G. "Pre-Tertiary and Tertiary fault systems as a framework of the South Sumatra basin: a study of SAR-maps", Proceedings 21st Annual Convention, IPA, 1992, p. 339-360.

[18] Sarjono, S. and Sardjito. "Hydrocarbon source rock identification in the South Palembang subbasin", Proceeedings 18th Annual Convention, IPA, 1989, p. 427-467.

[19] Graham, S. A., Brassell, S., Carroll, A. R., Xiao, X., Demaison, G., Mcknight, C. L, Liang, Y., Chu, J., and Hendrix, M. S. "Characteristics of selected petroleum source rocks, Xianjiang Uygur Autonomous region, Northwest China", AAPG Bulletin, v. 74 (4), 1990, p. 493-512.

[20] Bordenave, M. L. "Applied petroleum geochemistry", Editions Technip, Paris, 1993, 524 pp.

[21] Ryder, R. T., Burruss, R. C., and Hatch, J. "Black shale source rocks and oil generation in the Cambrian and Ordovician of the Central Appalachian Basin, USA", AAPG Bulletin, v. 82 (3), 1998, p. 412-441.

[22] Gordon, T. L. "Talang Akar coals – Ardjuna subbasin oil source", Proceedings 4th Annual Convention. IPA, 1985, p. 91-120.

[23] Robinson, K. M. "An overview of source rocks and oils in Indonesia", Proceedings 16th Annual Convention, IPA, 1987, p. 97-122.

[24] Robinson, K. M. and Kamal, A. "Hydrocarbon generation, migration and entrapment in the Kampar block, Central Sumatra", Proceedings 17th Annual Convention, IPA, 1988, p. 211-256.

[25] Mann, U. and Stein, R. "Organic facies variations, source rock potential, and sea level changes in Cretaceous black shales of the Quebrada Ocal, Upper Magdalena Valley, Colombia", AAPG Bulletin, v. 81 (4), 1997, p. 556-576.

[26] Uphoff, T. L. "Precambrian Chuar source rock play: an exploration case history in southern Utah", AAPG Bulletin, v. 81 (1), 1997, p. 1-15.

[27] Teerman and Hwang. "Evaluation of the source rock potential of Sumatran coals by artificial maturation of coal", Proceedings 18th Annual Convention, IPA, 1989, p. 469-489.

[28] Amijaya, H. "Indonesian low rank coal as petroleum source rock: high petroleum potential but no expulsion?", Proceedings 34th Annual Convention, IPA10-G-071, 2010.

[29] Sutriyono, E. "Cenozoic thermotectonic history of the Sunda-Asri basin, southeast Sumatra: new insights from apatite fission track thermochronology", Journal of Asian Earth Sciences, v. 16 (5-6), 1998, p. 485-500.

[30] Gleadow, A. J. W., Duddy, I. R., and Lowering, J. F. "Fission track analysis: a new tool for the evaluation of thermal history and hydrocarbon potential", The APEA Journal, v. 23, 1983, p. 93-102.

[31] Carvalho, H. D. C., Purwoko, Siswoyo, Thamrin, M., and Vacquier, V. "Terrestrial heat flow in the Tertiary basin of Central Sumatra", Tectonophysics, v. 69, 1980, p. 163-188.

[32] Kusumajana, A. H. P., Noeradi, D., Sapiie, B., and Priono, A. "The role of hydrocarbon maturation modeling, a case study: South Sumatra basin", Proceedings 34th Annual Convention, IPA10-G-147, 2010.

First International Conference on Science, Engineering & Environment,
Tsu City, Mie, Japan, Nov.19-21, 2015, ISBN: 978-4-9905958-5-2 C3051

TOXIC EFFECT AND MECHANISMS OF NANOPARTICLES ON FRESHWATER INFUSORIA

Kosyan D.B. [1], Rusakova E.A. [2], Sizova E.A. [3], Yausheva E.V. [4], Miroshnikov S.A.[5]
[1] Laboratory of Agroecology and technogenic nanomaterials,
State Educational Institution All-Russian Research Institute of Beef Cattle Breeding RAAS, Russia
[2] Orenburg State University, Russia
[3] Orenburg State University, State Educational Institution All-Russian Research Institute of Beef Cattle Breeding RAAS, Russia
[4] State Educational Institution All-Russian Research Institute of Beef Cattle Breeding RAAS, Russia
[5] State Educational Institution All-Russian Research Institute of Beef Cattle Breeding RAAS, Russia

ABSTRACT

Nanoparticle toxicology works toward establishing the hazard of nanoparticles, and therefore their potential risk, in light of the increased use of exposure. The current study was research proper characterization of the nanoparticles for understanding of their toxic effects and mechanisms at the cellular level. Dose and time as a main parameters is essential in hazard identification and risk assessment of nanomaterials. Material for the evaluation of toxic effects was used 20 samples of commercially available and laboratory preparations of metals and nanocarbon, divided into main groups: carbon nanoparticles, metal oxide nanoparticles and metal nanoparticles in different concentration. Fresh water infusoria *Stylonychia mytilus* (wild strain) in exponential growth phase was used as the test object.

Analysis of data on oxides of the metals showed higher toxicity than metal nanoparticles. In groups the maximum toxicity was observed in iron oxides (Fe3O4, Fe2O3), copper (CuO) and molybdenum (MoO3) (0,1; 0,025; 0,0125 M) after 24 hours of incubation with the test object Analysis of the effect of metal nanoparticles on the cells of infusoria showed that the maximum toxic effect was observed when exposed to Cu, Fe, Ag (0,025- 0,0015625 M). Statistical analyses showed a high correlation between concentration and time ($P \leq 0{,}001$).

The issue of accessibility of nanomaterials released in the environment for living organisms has been poorly studied. The toxic effects of nanoparticles can be associated with their size and their physicochemical properties.

Keywords: Nanoparticles, Ttoxic Effect, Stylonychia Mytilus, Cytotoxicity, Ecology

BACKGROUND

Active development of researches in nanomaterials leaves open the question of their safety. The safety of nanostructures for environment and human health becomes the top priority. Because of their properties, nanostructures react easier and are able to form complex compounds with unknown properties. This fact adds technological perspective to nanoparticles. At the same time we have to pay special attention for the ecological risks connected with nanostructures [1].

Nanotechnologies represent the convergence of techniques and molecular biology that lead to the development of structures, equipment and systems. Nanoparticles have new functional properties with sizes in range from 1 to 100 nm [2]. At present, there is not enough information for a full understanding of the interaction of nanostructures with biological systems and, thus, it is unclear whether nanostructures have negative effects that cause harmful biological reactions [3], [4].

Some authors point to the risk of carcinogenic effects of nanoparticles. They also note the ability to generate reactive oxygen species (due to the presence of the reaction centers). The nanoparticles are stable and do not undergo biotransformation. They are not removed from the cell that causes stress in cells and their breakage. Also, literature comprises data that nanoparticles may have protective effect on living organisms, increasing the body's resistance to various toxicants [5], [6].

Particle size and surface area are important characteristics of a material with toxicological prospects. When size of particles decreases, the surface area increases, it enables a large number of atoms or molecules to be deposited on the substrate surface. Nanoparticles differ from molecules and ions of the same composition not only in size but also in a higher specific surface and high adsorption and cumulative ability. Their chemical potential increases at the phase interface, thereby changing the solubility, reactivity and catalytic ability [7]. The degree of activity may also depend on the type of nanoparticles (metals, oxides, mixtures, etc.). Thus, the change of physical, chemical and

structural properties of nanomaterials due to the decrease in size may cause a number of interactions that might lead to toxicological effects.

OBJECTIVES

Therefore, the objective of this work is the assessment of toxic influence of different particles on the cell of test object.

MATERIALS AND METHODS

Fresh water infusoria *Stylonychia mytilus* (wild strain) in exponential growth phase was used as the test object. The studied test functions include survival rate, number (biomass). Primary culture of *Stylonychia mytilus* was cultivated in a Lozin-Lozinsky saline solution, (1 g in 1 liter of distilled water). Yeast (*Saccharomyces cerevisiae*) was added: NaCl-0,1%; KCl-0,01%; $CaCl_2$-0,01%; $MgCl_2$-0,01%; $NaHCO_3$-0,02.

The following nanoparticles were used in the study (presented below in Table 1):

Table 1 Characteristics of the used nanoparticles

Name	Size [nm]	Phase and chemical composition	Production method	Surface (m^2/g)
		Metals		
Fe	90	Metallic iron (not less than 99.8% of the mass.) and sorbed gases: CH4, CO2, Ar, N2	Method of electric explosion of a conductor in air	7,7
Cu	97	crystal copper 96,0 ± 4,5%, copper oxide - 4,0 ± 0,4%	High-temperature condensation with subsequent modification of oxygen	24
Zn	90	90%, the rest sorbing gases, zinc oxide and H2O	The electric explosion of wire in an argon atmosphere	5,34
Ag	70	99.99% of metallic silver adsorbed gases to 0,01% - CH4, CO2, Ar, N2	The electric explosion of wire in an argon atmosphere	6,5
Ni	70	Metallic nickel:Ni=99,758%, Mg=0,041%, Al=0,058%, Si=0,049%, S=0,005%, Ti=0,010%, Fe=0,047%, Co=0,032% (electronsand microanalysis)	Method of electric explosion of a conductor in air	4,5-6,0
Mo	50	Mo: 99,7%, O_2: 0,3%	Plasma-chemical method	14
W	50	W: 99.7%;O2: less than 0.3%	Plasma-chemical method	6,5
		Metal oxides		
CuO	90	cupric oxide, CuO 99,6% mass	Plasma-chemical method	14
ZnO	95	ZnO: 96%; Oxides of other metals less than 4%	Plasma-chemical method	9
Fe_3O_4 (I)	65	Fe3O4 at least 99 wt.%, about 1% of the mass. - adsorbed gases: CH4, CO2, O2, N2	Method of electric explosion of a conductor in air	10
Fe_3O_4 (II)	65	Fe3O4 99 % of mass.	Chemical	20
Al_2O_3	54	95% mass. α- Al2O3. 3%, 2% - sorbing gases (nitrogen, hydrocarbons), water	Electrical explosion of aluminum wire in oxygen atmosphere	40
NiO	94	oxide of bivalent nickel NiO: 99,6%	Plasma-chemical method	12
MoO_3	92	MoO_3 : 99,8% mass	Plasma-chemical method	12
		Composite		
FeCo	62,5	70% iron, 30% cobalt	Gas-phase	8,2
CuZn (I)	65	60% copper and 40%zinc	The electric explosion of wire in an argon atmosphere	5-6
CuZn (II)	96,5	60% copper and 40%zinc	Gas-phase	10
		Carbon nanomaterials		
k-SWCNT-90A	1,5	SWCNTs: 90 wt. %	Electric arc evaporation	400

These materials were assessed (particle size, polydispersity, volume, quantitative content of fractions, surface area) by electron scanning, transmission and atomic force microscopy using the following equipment: a LEX T OLS4100, a JSM 7401 F and a JEM-2000 FX("JEOL", Japan).The size distribution of particles was investigated using a Brookhaven 90Plus /BIMAS and ZetaPALS Photocor Compact (Russia) in lysols after dispersing the nanoparticles using an ultrasonic disperser UZDN-2T (Russia) at f-35 kHz, N 300 W, and A-10 μa for 30 min. Toxic effects of the samples were assessed in a wide range of equimolar concentrations (4M - 6 × 10-6 M). The size of nanoparticles was determined with the help of electronic microscope JSM-740 IF.

Action of toxic substances was studied in a wide range of concentrations (3.2M-6*10^{-6}M).

The sensitivity of *Stylonychia mytilus* to the action of toxicant was determined according to the time of their death. It was registered when protozoa stopped moving, which was accompanied by a violation of the integrity of the cells and lysosomes. The number of cells in 5 ml of medium containing intact infusoria (without nanoparticles) was a control group in all experiments. The total number of cells in 5 ml of medium containing infusoria was counted using a light microscope (MT 5300L). Cells in the stationary phase were incubated at 20 ± 2◦C in medium with toxicants within 24 hours in a concentration range - 3,2-6 × 10-6 M.

ANOVA statistical analysis was utilised and then using the Tukey test (SPSS вер. 17,0). Differences were c onsidered significant if P < 0,05.

RESULTS AND DISCUSSION

The results of studies demonstrated that the maximum toxic effect was achieved after the influence of Ag nanoparticles on protozoa. Cell death was observed after 10 minutes of incubation of the test object with the toxicant. The toxicity was observed up to a concentration of 1 * 10-5 M. Nanoparticles of Cu and Fe also caused cell death, but their effect was less potent than that of Ag. Toxic effect caused 100% cell death. Fe toxicity occurred in 24 hours. Cu and Ag toxicity occurred in 10 minutes of incubation. Action other nanometals was characterized by less mortality in comparison with Ag, Cu and Fe. Thus, Zn was less toxic, 100% mortality was observed up to 0.003125 M. When concentration of the element decreased, the number of living cells increased and reached 21% of the total amount in the final concentration (0.0001953125M). Minimal death rate was registered after the influence of Ni and W solutions. Toxicity of Ni was observed at a concentration of 0.005 M and W – at concentration of 0.2 M. The number of dead cells varied from 70 to 100% at other concentrations. This effect can be explained by the small size of Cu, Ag and Fe nanoparticles as compared with Mo, Ni, Zn, W (Fig. 1)

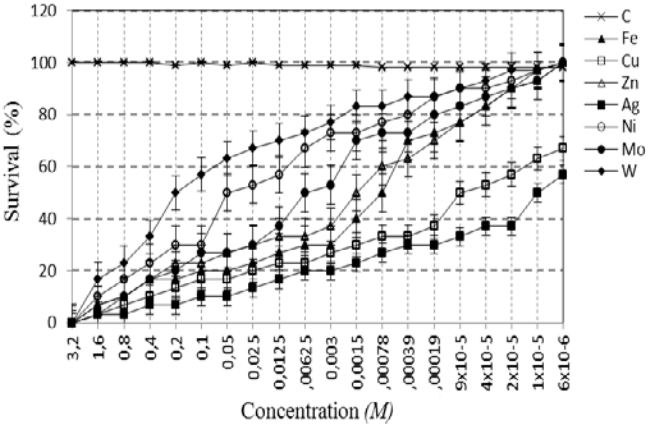

Fig. 1. Influence of metal nanoparticles at different concentration on *Stylonychia mytilus* survival

It is proven that nanoparticles in size of 2-50 nm will have greater cytotoxicity as compared with larger particles. There are a lot of experimental data are available about nanoparticles of silver and copper. Toxic effects of metal nanoparticles were demonstrated in the studies on other water test objects. For example, Ag and Cu nanoparticles are highly toxic to daphnia (the LD50 over 48 h was 0.06 and 0.04 mg/l) [8]. Studies of Ag and Cu on Danio rerio demonstrated the increased mortality and disease process [9], [10]. The effect of colloidal nanosilver on growth and structure of laboratory populations of *Scenedesmus quadricauda* (Turp.) *Bréb*. and *Monoraphidium arcuatum* (Korsch.) *Hind*. at concentrations ranging from 0.0001 to 1 mg/l. The toxicity of colloidal silver was expressed at a concentration of 0.1 mg / l and above. Moreover, algostatic effect was observed, its duration was directly dependent on the concentration of silver in the environment [11], [12].

Rather different data were obtained by a toxicity analysis of metal oxide nanoparticles. Maximum toxicity was registered in oxides of iron (Fe3O4 (I), Fe3O4 (II)), copper (CuO) and molybdenum (MoO3). 100% mortality of infusorias was observed under the influence of iron oxide. It is also possible to ascertain the negative chemotaxis (movement of the attractant), because most of the dead cells were located around the perimeter of the

main nanoparticle concentrations. No changes in the cells of infusorias were identified in the earlier periods. The influence of copper oxide in comparison with iron oxides was less pronounced. The toxic effect (100% death) was observed in 6 hours. In 24 hours it attained a maximum at 0.1, 0.025 and 0.0125 M in nanoparticle solutions. When concentration decreased, the number of surviving cells increased from 3% to 10% (at concentration of 0,0001953125M). The assessment of MoO_3 toxicity demonstrated that cell death occurred in 10 minutes of contact with a solution of nanoparticles (at a concentration of 0.0125 M). This situation remained throughout the whole time period. ZnO, TiO_2 and NiO possessed minimal toxicity. Their action was manifested only in the initial concentration (0.1 M) (Fig. 2)

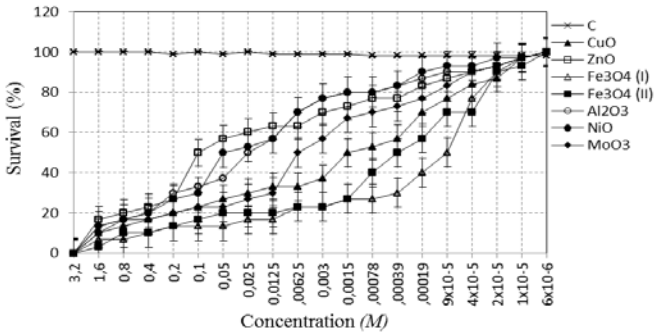

Fig. 2. Influence of metal oxide nanoparticles at different concentrations on survival of *Stylonychia mytilus*

Toxicity of metal oxides (TiO_2, ZrO_2, Al_2O_3, and CeO_2) was assessed on green algae (*Pseudokirchneriella subcapitata*) and the effect on the photosynthetic activity was demonstrated [13]. It is also noted that the zinc oxide inhibits the growth of test object at a concentration of 600 μg / l [14]. The negative impact of oxides of zinc, aluminum and titanium was shown on embryos of *Danio rerio*. It was revealed that ZnO has the maximum influence [15]. The lethal dose (LD50) of zinc oxide nanoparticles was 1.8 mg / l after 96 h of incubation.

Assessment of mixtures toxicity demonstrated that CuZn mixture causes the maximum cell death. At all concentrations 100% cell death was detected. In comparison with this mixture, brass was characterized by less toxicity; total death of infusoria was observed up to a concentration of 0.0015625 M. Moreover, this effect was expressed in 10 minutes of incubation and remained until the end of the period. The number of surviving cells varied from 10 to 25% of the total number. FeCo was less toxic, total cell death was observed in 24 hours and up to a concentration of 0.05 M, no toxic effect was observed in other concentrations (Fig. 3).

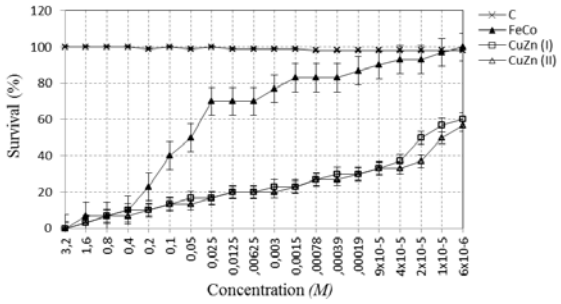

Fig. 3. Influence of mixtures of metal nanoparticles at different concentrations on survival of *Stylonychia mytilus*

Toxic effect at concentrations up to 0.0125 M was observed for the whole time period after the analysis of the first group. Test objects were still be able to move in further dilutions, 100% of infusoria were alive. The relative resistance to carbon nanomaterials can be explained by the fact that protozoa used them as food [16], [17] and [18]. In a recent study, the toxicity of fullerenes C60 for two aquatic species (*daphnia* and *Pimephales*) caused lipid peroxidation (LPO) in brain. LPO significantly increased in the gills. And the result is a significant increase in the expression of genes associated with the inflammatory response and metabolism. In contact with water, C60 spontaneously forms stable set (nanoC60) with dimensions D = 25-500 nm. Prokaryotic effect of these aggregates inhibits the growth (0.4 ppm) even at relatively low concentrations and reduces the rate of aerobic respiration (4 ppm) [19]. In addition, chronic effects of carbon nanoparticles, fullerenes C60 were studied using midges in *Chironomus riparius* at different periods of life. The influence of fullerenes C60 on growth of 10-day and 42-day species was studied at a nominal concentration of 0.0004-80 mg / kg of dry weight. The body length decreased at a concentration of 0.0025-20 mg / kg, but no effect occurred at higher concentrations. Stunt was observed at a concentration of 0.5 mg / kg. The observed effects correlate with the analyzed sizes of particles in sediment indicating that small agglomerates of fullerene cause more serious consequences for *C. Riparius*, than larger agglomerates that was observed at higher doses of C60. The results have demonstrated that fullerenes can be dangerous for sediment dwellers; it is manifested in changing ecotoxic parameters that influence the survival of water organisms [20].

The study of nanoparticle toxic action demonstrated that the studied samples had different toxic action towards test cells (Table 2).

Table 2 Biological effect of nanoparticles on *Stylonychia mytilus*

Name	Concentration (M)			
	Tox	LC50	LOEC	NOEC
Metals				
Fe	3,2 - 0,0015	0,00075	0,00039	0,00019 - 6×10^{-6}
Cu	3,2 - 0,00019	9×10^{-5}	4×10^{-5} - 2×10^{-5}	1×10^{-5} - 6×10^{-6}
Zn	3,2 - 0,003	0,00015	0,00078 - 0,00039	0,00019 - 6×10^{-6}
Ag	3,2 - 2×10^{-5}	1×10^{-5}	6×10^{-6}	-
Ni	3,2 - 0,1	0,05	0,025 - 0,0125	0,00625 - 6×10^{-6}
Mo	3,2 - 0,0125	0,00625	0,003	0,00015 - 6×10^{-6}
W	3,2 - 0,4	0,2	0,1	0,05 - 6×10^{-6}
Metal oxides				
CuO	3,2 - 0,003	0,00015	0,00078 - 0,00019	9×10^{-5} - 6×10^{-6}
ZnO	3,2 - 0,2	0,1	0,05	0,025 - 6×10^{-6}
Fe_3O_4 (I)	3,2 - 0,00019	9×10^{-5}	4×10^{-5}	2×10^{-5} - 6×10^{-6}
Fe_3O_4 (II)	3,2 - 0,00078	0,00039	0,00019	9×10^{-5} - 6×10^{-6}
Al_2O_3	3,2 - 0,05	0,025	0,0125	0,00625 - 6×10^{-6}
NiO	3,2 - 0,1	0,05	0,025 - 0,0125	0,00625 - 6×10^{-6}
MoO_3	3,2 - 0,00625	0,003	0,0015	0,00078 - 6×10^{-6}
Composite				
FeCo	3,2 - 0,1	0,05	0,025	0,0125 - 6×10^{-6}
CuZn (I)	3,2 - 4×10^{-5}	2×10^{-5}	1×10^{-5}- 6×10^{-6}	-
CuZn (II)	3,2 - 2×10^{-5}	1×10^{-5}	6×10^{-6}	-
Carbon nanomaterials				
k-SWCNT-90A	3,2 - 0,0125	0,00625	0,003	0,00015 - 6×10^{-6}

Note: Tox – the concentration causing 0-39 % survival object; LC50 – the concentration causing 50% survival of object; LOEC – the concentration causing 40-69 % survival of object; NOEC – the concentration causing 70-100 % survival of object [21].

Hydrophobic properties and zeta potential (ζ-potential) of particles in solution are the main parameters that help to assess the toxicity (except for the size of nanoparticles). Smaller particles and positively charged particles have a pronounced toxic effect. The zeta potential, electrical potential that is produced by the motion of particles between the adsorption layer of ions located on the surface of the particles and the diffusion layer of ions surrounding the particles determine the interaction of nanoparticles with membrane of cell, its damage and lethal effect. For example, chitosan nanoparticles and chitosan nanoparticles containing copper ions inhibit bacterial growth. The toxic effect is expressed in violation of membrane structure and cell aggregation. Aggregation of bacteria occurs in the presence of chitosan nanoparticles with a positive zeta potential, but when there is no copper. [22].

Studies on microorganisms showed that in the case of substances, which have a bactericidal effect, such as silver or zinc, the increase of surface plays an important role when the material is presented in the form of nanoparticles. Nanoparticles also release copper ions more actively than the usual surface. But this does not exclude other mechanisms of action. Silver nanoparticles penetrate into cells; interact with proteins, particularly with proteins containing sulfur and DNA. They inhibit the fission process and cause cell death. At the same time, membranes damage under the action of silver ions. Free radicals that evolve under their action can damage DNA. The antibacterial effect of ZnO is also associated with the release of hydrogen peroxide and membrane damage. And it is the main reason of their toxicity. The main mechanism of action for silver nanoparticles is DNA damage. In both cases, the nanoparticles disrupt the structure of the membrane by physical interaction. ZnO inhibits the growth of bacteria, primarily Gram-positive. In contrast, the

silver nanoparticles are more active against Gram-negative bacteria [23].

The iron oxide is non-toxic for the bacteria. Iron oxide nanoparticles are able to penetrate into the cell and cause the formation of reactive oxygen species, so they can lead to death of bacteria. In the case of iron oxide nanoparticles not only to their anti-bacterial properties can be used for combating microorganisms, but also their ability to affect the movement of body due to their charge. Antimicrobial agents may be bound with these particles, and their delivery will be the main function of these nanoparticles.

Thus, studies have shown that the toxicity of nanoparticles of metals, oxides and mixtures varies and depends on physical and chemical properties. Size of particles also influences on it. It concerns metal nanoparticles and cationic properties in case of oxides and mixtures.

CONCLUSIONS

Processes that control transport and removal of nanoparticles in an aqueous medium are not clearly understood. The future of nanomaterials in aquatic ecosystems is controlled by a number of biotic / abiotic processes such as dissolution, dispersion, interaction between nanomaterials and natural chemicals, human impact in the ecosystem. Moreover, assessing the environmental risk, it is important to understand the environmental consequences of the impact of nanomaterials. Before unconscious dumping of huge amounts of hazardous nanomaterials in the environment, the questions of solubility and degradation of nanomaterials in water needs to be studied. The initial information on the safety, toxicity and adaptation of aquatic environment shall be gained.

Due to the growth of nanotechnology, regardless of the potential benefits, the researchers need to anticipate and characterize the potential risks associated with the new technology. Despite this, currently there are not enough convincing data that indicate that these effects will become a serious problem, and that they cannot be solved by a rational scientific approach. At the same time, it is impossible to ignore the safety assessment of nanomaterials.

ACKNOWLEDGEMENTS

This study was supported by the Russian Science Foundation, Russia. No. 14-36-00023.

REFERENCES

[1] Zou X, Shi J, Zhang H. «Coexistence of silver and titanium dioxide nanoparticles: enhancing or reducing environmental risks?», Aquat Toxicol., Vol. 154, Sep. 2014, pp. 168-75.

[2] Borm P, Robbins D, Haubold S, «The Potential Risks of Nanomaterials: A Review Carried out for ECETOC, Particle», Fibre Toxicol., Vol. 3(1), 2006, pp. 1743–8977.

[3] Luo J, «Toxicity and Bioaccumulation of Nanomaterial in Aquatic Species», J. U.S. SJWP, Vol. 2, 2007, pp. 1–16.

[4] Ikuma K, Decho AW, Lau BL., «When nanoparticles meet biofilms-interactions guiding the environmental fate and accumulation of nanoparticles», Front Microbiol., Vol. 16, Jun. 2015, pp. 560-591

[5] Rocha TL, Gomes T, Sousa VS, Mestre NC, Bebianno MJ, «Ecotoxicological impact of engineered nanomaterials in bivalve molluscs: An overview», Mar Environ Res., Vol. 1136(15), Jun. 2015, pp.30002-7

[6] Moreno-Garrido I, Pérez S, Blasco J, «Toxicity of silver and gold nanoparticles on marine microalgae», Mar Environ Res., Vol. 1136(15), May 2015, pp. 00075-6.

[7] Canesi L, Ciacci C, Balbi T,Interactive effects of nanoparticles with other contaminants in aquatic organisms: Friend or foe?», Mar Environ Res., Vol. 1136(15), Mar. 2015, pp. 00046-9.

[8] Park MV, Neigh AM, Vermeulen JP, de la Fonteyne LJ, Verharen HW, Briedé JJ, van Loveren H, de Jong WH, «The effect of particle size on the cytotoxicity, inflammation, developmental toxicity and genotoxicity of silver nanoparticles», Biomaterials, Vol. 32(36), 2011, pp. 9810-7.

[9] Griffitt RJ, Luo J, Gao J, «Effects of Particle Composition and Species on Toxicity of Metallic Nanomaterials in Aquatic Organisms», Env. Toxicol. Chem., Vol. 27(9), 2008, pp. 1972–1978.

[10] Griffitt RJ, Weil R, Hyndman KA, «Exposure to Copper Nanoparticles Causes Gill Injury and Acute Lethality in Zebrafish (Danio rerio)», Env. Sci. Techn., Vol. 41(23), 2007, pp. 8178–8186.

[11] Ипатова ВИ, Спиркина НЕ, Дмитриева АГ, «Устойчивость микроводорослей к коллоидному наносеребру», Физиология растений, Vol. 62(2), 2015, pp. 273-282.

[12] Piccapietra F, Allué CG, Sigg L, Behra R, «Intracellular silver accumulation in Chlamydomonas reinhardtii upon exposure to carbonate coated silver nanoparticles and silver nitrate», Environ. Sci. Technol., V. 46, 2012, pp.7390−7397.

[13] Velzeboer I, Hendriks AJ, Ragas AM, van de Meent D, «Aquatic Ecotoxicity Tests of Some

Nanomaterials», Env. Toxicol. Chem., vol. 27(9), 2008, pp. 1942–1947.
[14] Franklin NM, Rogers NJ, Apte SC, «Comparative Toxicity of Nanoparticulate ZnO, Bulk ZnO, and ZnCl2 to a Freshwater Microalga (*Pseudokirchneriella subcapitata*): The Importance of Particle Solubility», Environ. Sci. Technol., 2007, Vol. 41(24), pp. 8484–8490.
[15] Zhu X, Chang Y, Chen Y, «Toxicity and Bioaccumulation of TiO2 Nanoparticle Aggregates in Daphnia magna», Chemosphere, Vol. 78(3), 2010, pp. 209–215.
[16] Oberdorster G, Oberdorster E, Oberdorster J, «Nanotoxicology: An Emerging Discipline Evolving from Studies of Ultrafine Particles», Env. Health Perspect., Vol. 113(7), 2005, pp. 823–839.
[17] Templeton RC, Ferguson PL, Washburn KM, « Life Cycle Effects of Single Walled Carbon Nanotubes (SWNTs) on an Estuarine Meiobenthic Copepod», Environ. Sci. Technol., Vol. 40(23), 2006, pp. 7387–7393.
[18] Zhu X, Zhu L, Chen Y, and Tian S, «Acute Toxicities of Six Manufactured Nanomaterial Suspensions to Daphnia Magna», J. Nanopart. Res., Vol. 11, 2009, pp. 67–75.
[19] Pakarinen K, Petersen EJ, Alvila L, Waissi-Leinonen GC, Akkanen J, Leppänen MT, Kukkonen JV, «A screening study on the fate of fullerenes (nC60) and their toxic implications in natural freshwaters», Environ Toxicol Chem., Vol. 32(6), Jun. 2013, pp.1224-32.
[20] Waissi-Leinonen GC, Nybom I, Pakarinen K, Akkanen J, Leppänen MT, Kukkonen JV, «Fullerenes (nC60) affect the growth and development of the sediment-dwelling invertebrate Chironomus riparius larvae», Environ Pollut., Vol. 3, Jul. 2015, pp. 17-23.
[21] Jackson P, Raun Jacobsen N, Baun A, Birkedal R, Kühnel D, Alstrup Jensen K, Vogel U, Wallin H, «Bioaccumulation and ecotoxicity of carbon nanotubes», Chemistry Central Journa, Vol. 7(1), 2013, pp. 131-154.
[22] Auffan M., Rose J., Bottero J.-Y., Lowry G.V., Jolivet J.-P., Wiesner M.R.. Towards a definition of inorganic nanoparticles from an environmental, health and safety perspective. Nature Nanotechnology., Vol 4, 2009, pp. 634–641.
[23] Kolesnikova T.A., Khlebtsov B.N., Shchukin D.G., et al. Atomic Force Microscopy Characterization of Ultrasound-Sensitive Nanocomposite Microcapsules. Nanotechnologies in Russia. V.3(9/10). 2008. pp.554–563.

DIELECTRIC SPECTROSCOPY ON MIXTURE OF RICE HUSK, RICE HUSK ASH AND RICE BRAN FROM 4 Hz TO 1 MHz

S. F. Khor[1], M. H. A. Md Yusoff[1], E. M. Cheng[2], M. A. Rojan[2], B. Johar[3], A. Chik[3], Z. A. Talib[4], M. F. Abd Malek[1]
[1]School of Electrical Systems Engineering, Universiti Malaysia Perlis, Malaysia; [2]School of Mechatronic Engineering, Universiti Malaysia Perlis, Malaysia; [3]School of Materials Engineering, Universiti Malaysia Perlis, Malaysia; [4]Faculty of Science, Universiti Putra Malaysia, Malaysia.

ABSTRACT

There is approximately 120 million tons of Rice Husk (RH) and 76 million tons of Rice Bran (RB) is produced in the world annually. Most of the husk and bran is either burnt or dumped as waste or used as animal feed due to less commercial interest by majority of rice producing countries. In this study, mixtures of rice husk/rice husk ashes (RHA) with RB on different ratios were prepared. Dielectric permittivity (ε'), loss factor (ε'') and AC conductivity (σ') were measured in the frequency range of 4 Hz to 1 MHz in ambient temperature. Results for mixture of RHA and RB indicate that a dipolar relaxation occurring between 10^3 – 10^5 Hz and the peak is depressed and shifted to lower frequency as the RB content increases in the mixture. Moreover, AC conductivity decreases as the RB content increase. This may attributed to production of natural oil content from RB. In contrast, a dielectric characteristic for RH is generally not affected by the RB contents. This study explore dielectric characteristic of mixture between RH/RHA and RB in low frequency range because lack of literature is reported on low frequency response. Additionally, the potential application of RH/RHA and RB could be explored in effort to diminish waste disposal and enhance environmental protection.

Keywords: Rice Husk, Rice Bran, Dielectric Permittivity, Dielectric Loss Factor, Frequency

INTRODUCTION

The commercial rice-milling process produces approximately 120 million tons of raw rice husk (RRH) [1] and 76 million tons of raw rice bran (RRB) in the world annually [2]. However, the production of rice by-products increase due to the growth of demand for rice from year to year in sequence of the population growths in Africa and Asian countries [3]. The main compositions in RRH are silica, cellulose and lignin [1], while fresh RRB is rich of micronutrients like oryzanols, tocopherols, tocotrienols, phytosterols, 20% oil and 15% protein, 50% carbohydrate dietary fibers. However, the natural oil content can be easily degraded to glycerol and free fatty acid by lipase enzyme which cause a rancid smell [4]. This lipases hydrolyze process is endogenously produced as a result of microbial activity during the milling process [5].

Hence, less commercial interest and low nutrition value render the RRH and RRB are being discarded which is either burnt or dumped as waste or utilized for non-energy related low value applications, e.g. animal roughage [6], mulching [7] and bedding materials [8] by majority of rice producing countries. Such improper disposal methods constitute to land detriment and air pollution that violates environment protection legislation.

These works turn this liability into asset by determining the dielectric properties of RH, RHA and RB in order to find possible utilization in the electrical industry. Moreover, this study would extend the knowledge of dielectric characteristic of RRB, RRH, and mixture between RHA and RRB in low frequency range since available information on low frequency response is very scarce in the literature.

METHODOLOGY

Samples Preparation

RRH and RRB used in this work were supplied by a local rice milling factory at Perlis, Malaysia. After removing clay and rock, the RRH was milled into 0.03 mm particle size using a RT-34 pulverize machine. Next, the grinded RRH was incinerated at a controlled temperature of 500°C for 3 hours and cooled in 1 hour by using muffle furnace. Next, the obtained RHA was ground and mixed with RRB at different contents. A disk-form pellet with 13 mm diameter was formed by using hydraulic press model 769YP-15A. The composition of pellets in this study is listed in Table 1 with the designation for the respective mixture fraction.

Table 1 Mixture fraction of the RRH, RHA and RRB.

Sample Code	Weight (±0.001 g)	
	Rice Husk	Rice Bran
RRB	-	0.600
RRH	0.600	-
H500B0	0.600	-
H500B1	0.500	0.100
H500B3	0.300	0.300
H500B5	0.100	0.500

X-ray Diffraction Analysis

The amorphous phases of the RRB, RRH, and RHA were identified by XRD analysis, Bragg angle 2θ in angular range of 10° to 80° at 5°/min in steps of 0.02 with Cu-Kα radiation. Model of X-ray Diffractometer is XRD-6000 (Shimadzu, Japan).

Dielectric Measurement

Dielectric measurement was performed at room temperature by using HIOKI IM 3570 with L2000 4-terminals probe in the frequency range of 4 Hz to 1 MHz with an oscillation voltage of 1.0 V.

RESULTS AND DISCUSSION

The XRD spectrums of RRB, RRH and RHA on 500◦C combustion temperatures are shown in Fig. 1. It presents a broad baseline at around 22° which means those materials has significant content of amorphous compounds. As reported by [9], RHA is very sensitive to the combustion temperature and time duration in a furnace. The appearance of RHA is white colour indicating the residual carbon content is low.

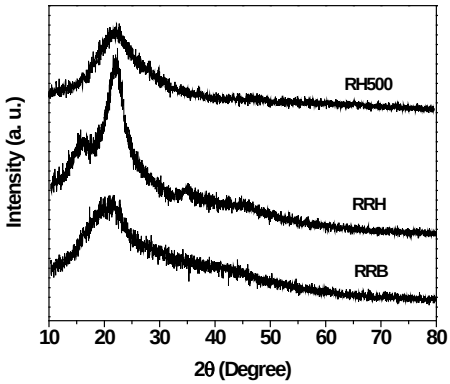

Fig. 1 X-ray diffraction pattern of RRB, RRH and RHA after thermal treatment made at 500◦C.

Dielectric properties are important in predicting the behavior of the materials when they are subjected to the low frequency electric fields in order to design component for the application of microelectronics, optoelectronics and cryoelectronics [10]. The dielectric properties of usual interest in such applications are the dielectric permittivity, ε', and the dielectric loss factor, ε'', respectively the real and imaginary parts of the complex permittivity,

$$\varepsilon^* = \varepsilon' - j\varepsilon'' \quad (1)$$

Basically, the dielectric permittivity represents the polarizability response of a material to the applied field, while the dielectric loss factor represents the energy loss because of the retarding or friction forces of the rotating dipoles during the movement of charges in an alternating electromagnetic field [11].

Figure 2 and 3 show the frequency dependence of the real (ε') and imaginary (ε'') part of the complex permittivity, respectively for the prepared samples measured at ambient temperature.

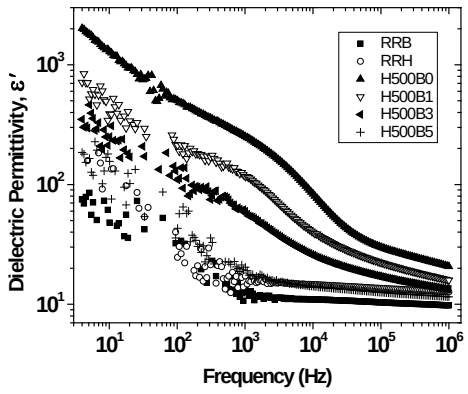

Fig. 2 Frequency dependence of dielectric permittivity of RRB, RRH and mixture of the RHA with RRB at different fractions.

In Fig. 2, it shows an electrode polarization at low frequencies and continuous with a relaxation dispersion around 1 kHz. It can be observed that the dispersive behavior reduced as RB content increase. The sample with the highest RB content, i.e., H500B5 has almost similar trend with RRH and RRB, which exhibit a general plateau above 1 kHz indicating the mobile carriers able to follow the rapid alternation of the electric field. In the meanwhile, a corresponding dielectric loss peak is observed in Fig. 3 where the peak shifts to lower frequency as the RB content increases. This may due to the free fatty acid that content in RB inhabit the movement of mobile carrier and leads to lagging in

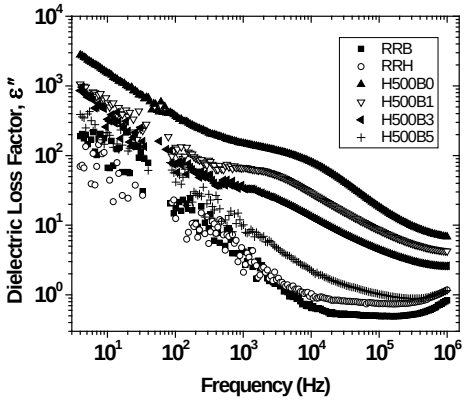

Fig. 3 Frequency dependence of dielectric loss factor of RRB, RRH and mixture of the RHA with RRB at different fractions.

dipole polarization with respect to changing electrical field. Beyond the loss peak frequency, ω_p the charges cannot oscillate as quickly as the alternating field, dispersion takes place and eventually decrease to a constant value of $\varepsilon^{'}$ at higher frequencies. This is due to dipole polarization mechanism ceases to contribute to the net polarization of the dielectric.

The loss factor of the RRB, RRH and H500B5 decreased with increasing frequency from 4 Hz to 10 kHz, reached a minimum, and then increased as frequencies were further increased to 1 MHz. The dielectric spectrum for RRB are in good agreement with earlier results of [12] in which authors reported the frequency dependence of the $\varepsilon^{''}$ of fresh soybean oil at 25°C. These variations may associate to high content of free fatty acid. Free fatty acid fraction of RRB contained highest oleic acid followed by linoleic acid and linolenic acid [13] [14].

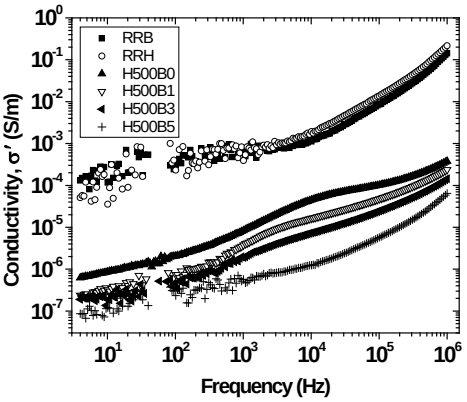

Fig. 4 Frequency dependent of real conductivity of RRB, RRH and mixture of the RHA with RRB at different fractions.

Figure 4 shows the variation of real conductivity as a function of applied frequency for the RRB, RRH and mixture of RHA with different RB content, which calculated from equation as shown below.

$$\sigma^{'} = \omega\varepsilon_{\circ}\varepsilon^{''} \tag{2}$$

where ω is the angular frequency, $2\pi f$, and $\varepsilon_{\circ}$ is the dielectric permittivity of free space, 8.854×10^{-12} F/m.

As seen in Fig. 4 the present of conductivity disperse at low frequencies is associated with the lack of external force where motion of charges is reduced to weak oscillation within its neighborhood vacant site instead of having long-range transport motion under the influence of an applied field. At higher frequencies, the conductivity spectra exhibit a stronger dispersive region before reach the relaxation frequency, which could be attributed to short-range transport due to motion of mobile carriers over limited distance on short time scales [15] [16]. Beyond the relaxation frequency, further increment of conductivity can be assigned to the fact that mobile carriers vibrates more frequently within the allowed localized sites [16].

Both RRB and RRH have similar trend of conductivity spectra as depicted in Fig. 4. The high conductivity of RRH was contributed by potassium (K), which is metal element that contented at the outer and inner surface of RRH. After combustion process, the potassium content reduced significantly as decomposed [17]. Generally, RRB has high calcium content in addition to micronutrients [18], which may leads to high conductivity characteristic.

Figure 4 also clearly shows that conductivity increase with increases of RHA content. Silica is a major element in RHA [9], [17], [19]-[23] which may react with element calcium from RB, forming a compound with greater insulation properties. The result also indicated that mobile carriers were mainly contributed from RHA. In other words, the amount of mobile carries was subjected to the RHA content. Basically, diffusion coefficient, D and mobility, $\mu = eD/kT$ are connected by Nernst-Einstein relation and lead to conductivity, σ [24]

$$\sigma = \frac{ne^2D}{kT} \tag{3}$$

where n is charge carrier density, e is carrier charge, k is Boltzmann constant, and T is absolute temperature. Decrement of conductivity with RB contents may correlated with enhancement of activation energy in diffusion for electrical transport process. Activation energy for electrical conductivity can be explained by Anderson and

Stuart model [25]. There are two possibilities of hindrance for diffusion mechanism. The conduction pathway being strained and the mobile carriers may induce electrostatic binding energy with other elements within the sample. Hence, diffusion movement of mobile carriers encountered more difficult steps and resulting in an overall decrease of conductivity with the increase of RB content.

CONCLUSION

The dielectric permittivity, dielectric loss factor and conductivity with different rice bran content are frequency dependence. From the thorough analysis of the experimental data, short-range transport of carries predominant conductivity spectra and dipolar type relaxation occurs at higher frequency regions as observed in the dielectric loss factor plot. Dielectric permittivity, dielectric loss factor and conductivity decreases with an increase in RB content. Such a behavior may attribute to decrease number of mobile carriers and formed a compound with lower conduction effect. Besides, Anderson-Stuart model has been used to describe the variation of the conductivity by inducing activation energy. This work demonstrates that dielectric properties of RHA can be effectively tailored by mixing RB possessing vary electrical characteristics. In addition, there is a potential to change these abandoned agriculture waste into renewable energy resource for electrical field applications.

ACKNOWLEDGEMENTS

The authors wish to express a grateful acknowledgement to rice milling factory in Perlis Malaysia for supplying rice husk and rice bran to the present research. Authors are thankful to laboratory assistants in Universiti Malaysia Perlis for technical supports.

REFERENCES

[1] Ajay K, Kalyani M, Devendra K, Om P, “Properties and industrial applications of rice husk: A review”, International J. of Emerging Technology and Advanced Engineering, Vol. 2, Oct. 2012, pp. 86-90.

[2] Susan SC, Priscilla S, “Chapter 14: Production composition functionality and food applications physiological benefits”, Fiber Ingredients: Food Applications and Health Benefits, CRC Press, 2009, pp. 305-318.

[3] Mohanty S, Rice crisis: The aftermath. Rice Today 7, International Rice, Research Institute, 2008, pp. 40-41.

[4] Nagendra PMN, Sanjay KR, Shravya KM, Vismaya MN, Nanjunda SS, “Health benefits of rice bran - A review”, J. of Nutrition & Food Science , Vol. 1, Sept. 2011, pp. 1-7.

[5] Hoogenkamp H, “Rice bran reinvented”, Asia Pacific Food Industry, Vol. 21, Nov. 2009, pp. 36-39.

[6] Norhaizan ME, Tan BL, Loh SP, “By-products of rice processing: An overview of health benefits and applications”, J. of Rice Research, Vol. 1, Aug. 2013, pp. 1-11.

[7] Rwezaula GJ, Loth SM , Christine GI, Shazia OWMR, Susan NM, Amon PM, Paul JRN, Ashimogo GC, Tiisekwa T, Mvena T, Henry SL, “Effect of organic mulch types on common biotic, abiotic factors and components of yield in determinate and indeterminate tomato (Lycopersicon esculentum Mill) commercial cultivars”, Asian J. of Plant Science, Vol. 4, 2005, pp. 580-588.

[8] Shah MK, Nepali DB, Devkota NR, Yadav JL, “Effect of stocking density, bedding materials and probiotics on the performance of broiler”, Nepalese J. of Agricultural Sciences, Vol. 11, Sept. 2013, pp. 78-85.

[9] Chen GY, Du GY, Ma WC, Yan BB, Wang ZH, Gao WX, “Production of amorphous rice husk ash in a 500 kW fluidized bed combustor”, Fuel, Vol. 144, March 2015, pp. 214–221.

[10] Singh R, Ulrich RK, “High and low dielectric constant materials”, The Electrochemical Society Interface, 1999, pp. 26-30.

[11] Saltas V, Triantis D, Manio T, Vallianatos F, “Biomonitoring of environmental pollution using dielectric properties of tree leaves”, Environmental Monitoring and Assessment, Vol. 133, Oct. 2007, pp. 69–78.

[12] Hu LZ, Toyoda K, Ihara I, “Dielectric properties of edible oils and fatty acids as a function of frequency, temperature, moisture and composition”, J. of Food Engineering, Vol. 88, Sept. 2008, pp. 151–158.

[13] Katsuharu Y, Shintaro M, “Fatty acid compositions of rice lipid and their changes during storage”, Agricultural and Biological Chemistry, Vol. 28, Aug. 1964, pp. 257-264.

[14] Orthoefer, FT, "Chapter 10: Rice bran oil". Bailey's Industrial Oil and Fat Products, 6th ed. Vol. 2, Shahidi F: John Wiley & Sons, Inc., 2005, pp. 465-489.

[15] Funke K, Banhatti RD, Bruckner S, Cramer C, Krieger C, Mandanici A, Martiny C and Ross I, “Ionic motion in materials with disordered structures: conductivity spectra and the concept of mismatch and relaxation”, Physical Chemistry Chemical Physics, Vol. 4, May 2002, pp. 3155-3167.

[16] Nageswara R, Padmaraj O, Narsimulu D, Venkateswarlu M, Satyanarayana N, “A.C conductivity and dielectric properties of spinel LiMn2O4 nanorods”, Ceramics

International, accepted. July 2015.

[17] Bie RS, Song XF, Liu QQ, Ji XY, Chen P, "Studies on effects of burning conditions and rice husk ash (RHA) blending amount on the mechanical behavior of cement", Cement and Concrete Composites, Vol. 55, Jan. 2015, pp. 162–168.

[18] Simone ADSCF, Priscila ZB, Marilene DVCP, "Nutritional composition of rice bran submitted to different stabilization procedures", Brazilian J. of Pharmaceutical Sciences, Vol. 48, Oct./Dec., 2012, pp. 651-657.

[19] Haslinawati MM, Matori KA, Wahab ZA, Sidek HAA, Zainal AT, "Effect of temperature on ceramic from rice husk ash", International J. of Basic and Applied Sciences, Vol. 9, Oct. 2009, pp. 22-25.

[20] Della VP, Kühn I, Hotza D, "Rice husk ash as an alternate source for active silica production", Materials Letters, Vol. 57, Dec. 2002, pp. 818–821.

[21] Zahedi M, Ramezanianpour AA, Amir MR, "Evaluation of the mechanical properties and durability of cement mortars containing nanosilica and rice husk ash under chloride ion penetration", Construction and Building Materials, Vol. 78, March 2015, pp. 354–361.

[22] Antiohos SK, Papadakis VG, Tsimas S, "Rice husk ash (RHA) effectiveness in cement and concrete as a function of reactive silica and fineness", Cement and Concrete Research, Vol. 61–62, July–Aug. 2014, pp. 20–27.

[23] Ismail NAA, Azmi MA, Ahmad S, Taib H, "Effect of rice husk firing temperature on synthesis of silica (SiO_2)", Int. Conf. on ICXRI, 2014, pp. 183-184.

[24] Wei G, Nigel MS, An Introduction to Electronic and Ionic Materials. London: World Scientific Publishing Co. Pte. Ltd., 1999, ch. 11.

[25] Anderson OL, Stuart DA, "Calculation of activation energy of ionic conductivity in silica glasses by c1assical methods", J. of American Ceramic Society, Vol. 37, Dec. 1954, pp. 573 – 580.

First International Conference on Science, Engineering & Environment,
Tsu City, Mie, Japan, Nov.19-21, 2015, ISBN: 978-4-9905958-5-2 C3051

REFLECTION AND DIELECTRIC MEASUREMENT FOR SALINITY OF WATER USING MICROSTRIP LOOP SENSOR/ANTENNA AND DIELECTRIC PROBE

E.M. Cheng[1], M. F. Abdul Malek[2], S. F. Khor[2], K. Y. You[3], K.Y. Lee[4], M. A. Rojan[1], S. Abu Bakar[1], N. F. Mohd Nasir[1], Z. Zakaria[1], and W. H. Tan[1]

[1]School of Mechatronic Engineering, Universiti Malaysia Perlis, Malaysia; [2]School of Electrical System Engineering, Universiti Malaysia Perlis, Malaysia; [3]Faculty of Electrical Engineering, Universiti Teknologi Malaysia, Malaysia; [4]Faculty of Engineering and Science, Universiti Tunku Abdul Rahman, Malaysia.

ABSTRACT

This study was conducted to investigate the feasibility of loop sensor in gauging level of salinity of water via electromagnetic wave reflection. High salinity cause adverse effect to environment. When high levels salinity of water diffuse into soil, the salinity of soil will be subsequently cause degeneration to vegetation and fertile land to be barren. At the worst case scenario, the extinction will be occurred on low self-resistant species and hence lead to interruption of biodiversity and ecosystem of a territory. In addition, the diminished groundcover exposes soil to erosion, which can lead to landslide and pollution of water. It would decline the value of land for human and animal consumption. These impacts of salinity can cause tremendous lost in money because the restoration of impaired agricultural production, corroded landmark and infrastructure, as well as water treatment is extremely costly. Therefore, a reliable detection system for salinity of water source is very crucial. In this work, reflection measurement was conducted by using loop antenna in conjunction with Agilent E8362B P-series network analyser (PNA) for water salinity detection. Dielectric probe will be then used in conjunction with PNA for dielectric characterization due to different salinity of water. It comes to learn that the different level of salinity of water exhibit different dielectric properties through reflection measurement. The increment of salinity leads to increment and decrement of dielectric constant and loss factor, respectively. Similar observation can be found through reflection coefficient in terms of magnitude and phase.

Keywords: Keywords: Loop Sensor, Salinity, Reflection Coefficient, Dielectric Properties, Water

INTRODUCTION

Salinity of water source is very crucial in determining the quality of our environment, either for residential purpose or habitat for flora and fauna. Salinity is referred to the quantity of salt in water which will affect its acidity. Disturbance of acidity of water may cause inconvenience to human race, flora and fauna. The prehistoric case during 2400–1700 B.C. in ancient Mesopotamia which cause several negative issues due to disturbance of salinity were occurred. Their negative effect, e.g. soil erosion, landslide, water pollution and some other environmental issues were even extended to disrupt civilization. The recent one is occurred in southern Iraq [1].

Agricultural activity is backbone of economy for certain ASEAN countries, e.g. Thailand, Malaysia, Indonesia, Vietnam and etc. The disruption of acidity of water can be extended to soil salinity. Water and soil for plantation and agricultural activity is closely related. Salinity of soil and water must be preserved at optimum salinity, in order to provide the best environmental condition for agricultural activity. Suffice to say, the salinity of water is not merely disrupt the ecosystem, but its effect may even connect to economy of an agricultural-based countries. As a result, a fast and accurate salinity detection method is required for precaution.

In this work, water in different degree of salinity which is presented in molarity will be characterized dielectrically by Agilent E8362B PNA Microwave Network Analyzer in conjunction with Agilent 85070E slim probe from 2 GHz to 20 GHz. In addition, complex reflection coefficient in terms of magnitude and phase are measured by using Agilent E8362B PNA Microwave Network Analyzer. However, measurement of loop sensor/antenna on salinity will be conducted within 2.3 GHz to 2.5 GHz where ISM band appear within this frequency range, i.e. 2.45 GHz. The relationship among the salinity, dielectric properties and reflection coefficient will be discussed.

Past Researches

Researches for salinity analysis have been conducted

in recent years [2]-[3]. Immense number of publication can be found especially implementation of microwave method [4]-[5]. Kundra et al. (1992) [6] measure dielectric properties of milk due to effects of dissolved salts. Gadani et al. (2006) [7] proved the effect of salinity and frequency on dielectric constant where dielectric constant decreases when concentration of saline water increase. Whereas, increment of frequency cause decrement in loss factor. On the other hand, Thomas M. Dauphi et al. (1983) [8] reported that a salinometer which was designed with principle of the conductivity for ratio of sample to standard seawater in dual cell. Satellite was even used for complex dielectric analysis on pure and sea water [9].

Loop Antenna/Sensor

In telecommunication industry, loop antenna is well known as one of the efficient receiver of radio signals if compare with other antennas, e.g. monopole antenna, dipole antenna, Uda-Yagi antenna and etc. It is due to its mobility, compatibility wide range of frequencies, and low electricity consumption. The performance of a loop antenna's performance is crucially determined by its design, specification and placement.

Loop antennas can be a wideband transmitter and receiver. It has high portability because it can be easily miniaturized [10] for many portable and small wireless devices. On the other hand, loop antennas are also low cost, ergonomic, and commonly used for various purposes, e.g. as sensor or antenna sensing system.

Basic principle of loop antenna

Agilent 85050E Slim Probe

A loop antenna is made of a loop of copper as shown in Fig. 1. The loop antenna's capacitance is proportionally varies with operating frequency. In other word, the loop's capacitance increase with frequency and vice versa. The equivalent loop's capacitor maintains electric voltage by holding the deposited charge. Charge will be release and causes the flow of current after time constant, τ. It implies that the longer τ lead to higher efficiency of antenna to propagate the waves into free space. Lower frequency can be easily implemented in such a case. Albeit lower frequency cannot propagate farther, its signal of wave can be stronger.

METHODOLOGY

Samples Preparation

In this project, the saline water with different molarity is prepared for reflection-based saline water measurement. The sodium chloride (NaCl) with different quantity (weight) is dissolved in water, in order to prepare different molarity of saline water. The samples were prepared in molarity of 0.00 M, 0.34 M, 0.69 M, 1.03 M, 1.38 M, 1.72 M, 2.07 M, and etc. The molarity can be defined as the molar concentration that denotes the number of moles of a given substance per liter of solution. The formula for molarity can be expressed as

$$\text{molarity}\left(\frac{\text{mol}}{\text{L}}\right) = \frac{\text{mole of solute(mol)}}{\text{Volume of solution(L)}} \tag{1}$$

$$\text{moles of NaCl(mol)} = \frac{1\,\text{mol}}{\text{Relative weight of NaCl(g)}} \times \text{Weight of NaCl(g)} \tag{2}$$

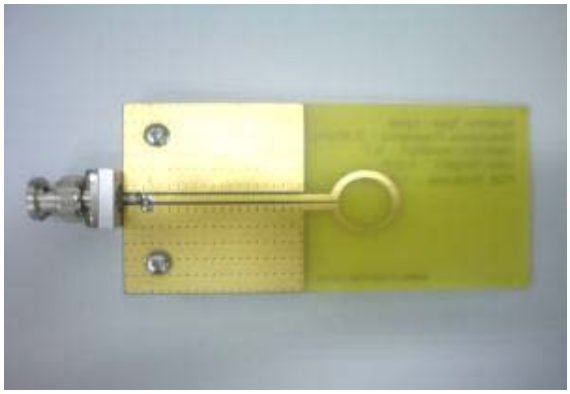

Fig. 1 Microstrip Loop Antenna/Sensor.

Reflection and Dielectric Measurement

Reflection measurement

The reflection measurement for complex reflection coefficient using loop antenna is as shown in Fig. 2. Short, open, load, and known-thru standards (SOLT) in Agilent 85050B standard mechanical calibration kit are used for calibration prior to reflection measurement [11]. The calibration procedure is conducted to get rid systematic errors and drift errors.

During reflection measurement, the loop antenna which connects with Agilent E8362B PNA Microwave Network Analyzer is used to measure reflection coefficient in terms of magnitude and phase. The antenna was fully dipped in the various molarity of saline water. The measured magnitude and phase for various molarity of saline water as exhibit on PNA were recorded for analysis.

Dielectric measurement

Agilent 85070E slim probe (Fig. 3) is an open-ended type of dielectric sensor which works with Agilent microwave PNA for dielectric characterization in terms of dielectric constant (ε') and loss factor (ε").

Fig. 2 Reflection measurement for salinity using loop antenna.

Fig. 3 Agilent 85070E slim probe [12].

Calibration is conducted through slim form probe calibration short, pure water and free space. The method of measurement is similar with reflection measurement where the slim probe is dipped into saline water. Both ε' and ε" will be computed through Agilent 85071E material measurement software. Both ε' and ε" are needed to explain the measured complex reflection coefficient.

RESULTS AND DISCUSSIONS

The Effect of Salinity on Dielectric Properties (Agilent 85052D Slim Probe)

Figure 4 and 5 illustrated the variation of dielectric measurement using Agilent 85052D slim probe in conjunction with PNA. Figure 4 indicates that the dielectric constant, ε' of all saline water with different molarity decreases when frequency increase from 5 GHz to 20 GHz, overall. The incomplete polarization due to the delay of response to the change of applied field causes the decrement of ε'. In addition, the measured dielectric constant for free space is as expected which present in unity.

In Fig. 5, the loss factor, ε" shown constant in null value for free space. is merely almost level off when exceeding 15 GHz. It might due to the delay response of molecules in saline water to applied time-varying field. The synchronous polarization among the molecules in saline water reduce the friction occurred among molecules. The loss factor is determined by asynchrony of relaxation and operating frequency. The highly dispersion of relaxation frequencies among the molecules in saline water cause the asynchrony. The rotations of molecules due to time-varying applied field cause the friction. Subsequently, the heat is generated and dissipated. As a result, the loss factor for different molarity exhibit different gradient of trendline as shown in Fig. 4.

Generally, it can be observed from Fig. 4 that dielectric constant decreases when molarity of saline water increases. When Sodium Chloride (NaCl) dissolved in water, water molecules (H_2O) will bind with the molecule of NaCl to form hydrogen bonding. It increases the inertia of molecules. Subsequently, the mobility of water molecules is degraded and so for polarization. The mobility of these molecules is constraint during polarization and hence cause the descending of ε' when molarity increases. Higher molarity implies less free water molecule. Hence, ε' decreases when salinity (molarity of NaCl) in water increases. In contrast, ε" increases with molarity of NaCl.

The dispersion of relaxation frequencies among bound molecules and free water molecules due to inertia increase the asynchronous of rotation. Hence, the rotational losses or friction among molecules rise up. It can be justified through Fig. 5 where ε" increase with molarity of NaCl in saline water. However, it starts to be level off because most of the free water molecules have been bound by NaCl. It enhances the synchrony of all molecules during the polarization. Low dispersion of relaxation frequencies and operating frequencies might be the main reason for this phenomenon.

In addition, the higher molarity also exhibit lesser gradient. It is attributed to insufficiency of free water molecule. Pure water exhibit the highest ε' due to the presence of free water molecule is high. It can be easily polarized when field is applied because the mobility of free water molecules has not been constraint. When free water molecule is bound with NaCl in solution, free water molecule loss its mobility and its inertia is high. Hence, it leads to low ε'.

In the meantime, higher molarity also results lower gradient of ε' over frequency. It is due to high inertia of bound molecules where these molecules lost its capability to polarize synchronously with operating frequency. Therefore, its ε' is presented constantly in Fig. 4. Meanwhile, dispersion of frequency among the applied field, bound molecules and free water molecules are lead to variation of ε" over frequency. At low frequencies, bound molecule

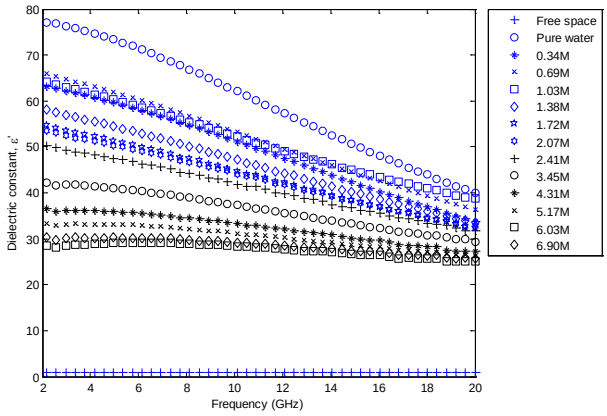

Fig. 4 The variation of dielectric constant over frequency for various molarity of saline water.

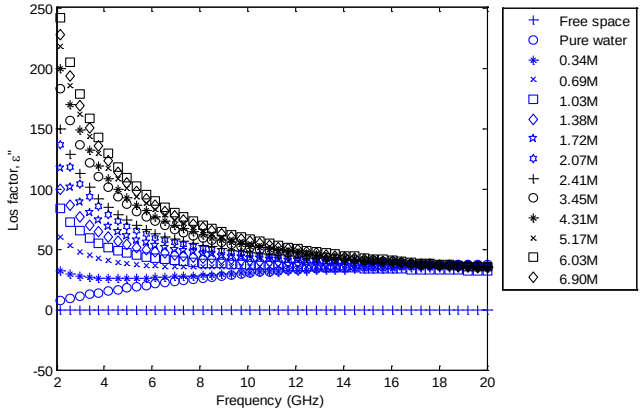

Fig. 5 The variation of loss factor over frequency for various molarity of saline water.

which are major component in saline water are still capable to follow the oscillation of applied field. When frequency increases, they might be oscillate insignificantly because the frequency of oscillation is too high. Less friction among molecules are taken place, therefore, it exhibits lower gradient of ε" over frequency range beyond 15 GHz.

The Effect of Salinity on Reflection Coefficient (Loop Antenna/Sensor)

From Fig. 6, it can be observed that the magnitude of reflection coefficient decreases when frequency increases. Actually, it is in line with the variation of ε' over frequency as shown in Fig. 4. Reflection coefficient, Γ can be expressed as

$$\Gamma = \frac{Z_L - Z_0}{Z_L + Z_0} \tag{3}$$

where Z_L is impedance of load/sample and Z_0 is a constant which refer to characteristic impedance of transmission line on loop antenna. In this work, Z_L is defined as impedance of saline water. Generally, Z_L can be expressed as

$$Z_L = j\frac{1}{\omega C} \tag{4}$$

$$C = \varepsilon C_0 \tag{5}$$

where ω is angular velocity and C_0 is capacitance for free space. If Z_L is closer with Z_0, Γ will show lesser. As a result, it can be deduced that the decrement of magnitude of reflection coefficient over frequency might due to approach of Z_L to Z_0. It can be explained by the mismatch impedance where the smaller $Z_L - Z_0$ at numerator of Γ as expressed in Eq. (3). The loop antenna is designed to drive the electromagnetic wave to propagate into free space. When the loop antenna was dipped into saline water, the propagation environment is

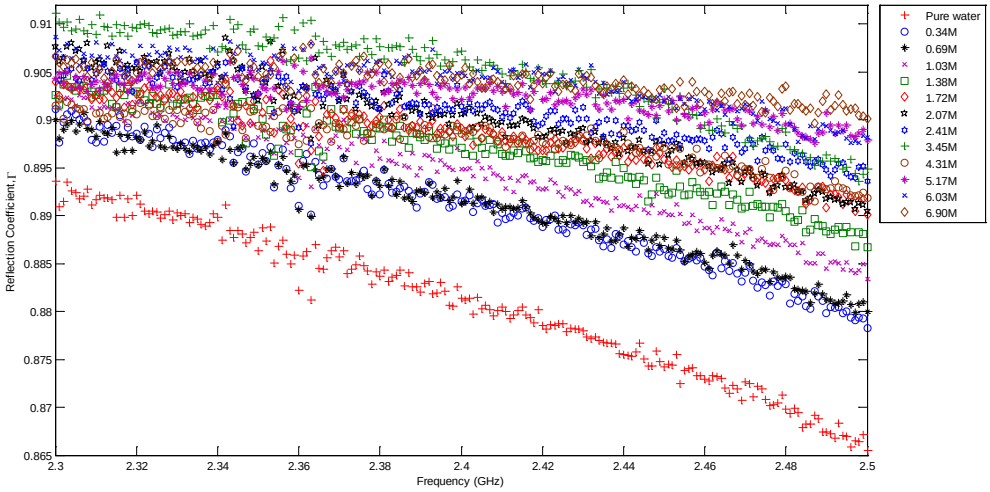

Fig. 6 The variation of magnitude of reflection coefficient over frequency.

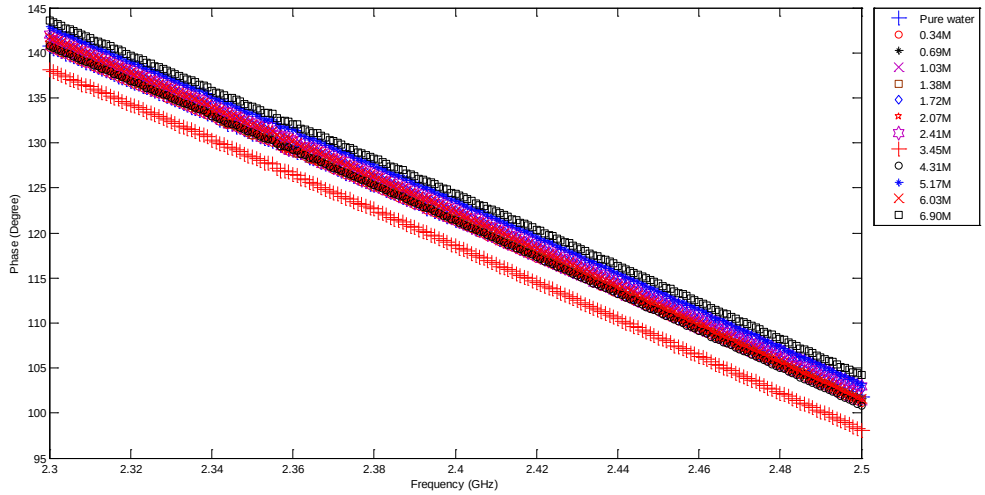

Fig. 7 The variation of phase of reflection coefficient over frequency.

different from the free space. It causes the reflection where it meets the mismatch impedance at interface of two media. The higher degree of mismatch implies the greater reflection is occurred. It can be inferred that when the dielectric constant decreases with frequency (Fig. 4), it leads to the decrement of mismatch impedance. Hence, it can be noticed that magnitude of reflection coefficient decreases over frequency too as shown in Fig. 6.

Withal, phase of reflection coefficient plummet as frequency increases. It can be clearly seen in Fig. 7. The phase for all molarity of saline water cannot be distinguished significantly. It might due to the insignificant delayed time of incident wave and reflected wave. When the incident wave transmits from antenna impinges on interface, the time delay is occurred before reflection. In Fig. 7, time delay during the reflection on interface is mitigated over frequency. Therefore, the phase angle has shown decreases with frequency, as increment of frequency shorten time delay during the polarization. Time is delay because time is taken for process polarization. When the frequency increases, the dielectric constant decreases. The depth of wave from the interface to be reflected might be smaller. As a result, the resultant phase shift due to reflection on surface and internal depth of saline water will be smaller. Delayed time is closely related to the depth which the internal reflection occurred. It can be seen that depth for internal reflection does not change significantly over frequency

CONCLUSION

A reflection-based microwave measurement system which consists of dielectric slim probe and loop

antenna/sensor in conjunction with PNA is developed for the sake of salinity measurement. PNA in conjunction with dielectric slim probe are used to measure the dielectric constant, ε' and loss factor, ε" of saline water with different molarity (salinity). Reflection measurements using loop antenna/sensor were also conducted for reflection coefficient. Then, the measured reflection coefficient is presented as magnitude and phase. It can be observed that both dielectric constant and loss factor decrease when frequency increases. Meanwhile, dielectric constant, ε' decreases when frequency increases. Nevertheless, loss factor, ε" increases with frequency. The measured reflection coefficient in terms of magnitude and phase decrease when frequency increases. The effect of molarity on the dielectric properties is different if compared with the variation of dielectric properties over frequency. The ε' is in decrement when molarity (salinity) increases while the ε" shown increment over molarity. RG405 has better agreement with Agilent 850520 High Temperature Probe in measuring reflection coefficient for all selected frequency in salinity measurement. Meanwhile, RG405 performed consistently with High Temperature Probe. The variation of reflection coefficient over percentage of sugar content in solution is maintained at certain accuracy. RG402 performed inconsistently in sugar content detection comparing with RG405.

ACKNOWLEDGEMENTS

The authors gratefully acknowledge Universiti Malaysia Perlis (UniMAP) for supporting this work financially. In the meantime, author would like to deliver the deepest gratitude to Research Cluster of Embedded Computing, UniMAP for the research equipments.

REFERENCES

[1] Jacobsen T, Adams RM, "Salt and silt in ancient Mesopotamian agriculture", Science, Vol. 128, 1958, pp. 1251-1258.

[2] Timothy B, Sydney L, Hernan G, Ricardo AL, Cathy S, John A, "Objective analyses of annual, seasonal, and monthly temperature and salinity for the world ocean on A 0.25° grid", Int. J. Climatol, Vol. 25, 2005, pp. 931–945.

[3] Connors BM, Juarez-Colunga E, Dill LM, "Effects of varying salinities on Lepeophtheirus salmonis survival on juvenile pink and chum salmon", J. of Fish Biology, Vol. 72, 2008, pp. 1825–1830.

[4] Cheng EM, Fareq M, Shahriman AB, Mohd Afendi R, Lee YS, Khor SF, Tan WH, Nashrul Fazli MN, Abdullah AZ, Jusoh MA, "Development of microstrip patch antenna sensing system for salinity and sugar detection in water", Int. J. of Mechanical & Mechatronics Engineering, Vol. 14, 2014, pp. 31-36.

[5] Cheng EM, Fareq M, Shahriman AB, Mohd Afendi, Zulkarnay Z, Khor SF, Liyana Z, Nashrul Fazli MN, Tan WH, Noorpi NSM., Mukhtar NM, Othman M, "Development of low cost microwave detection system for salinity and sugar detection", Int. J. of Mechanical & Mechatronics Engineering, Vol. 14, 2014, pp. 59-71.

[6] Kundra T, Raghavan SV, Akyel C, Bosisio R, van de Voort FR, "Electromagnetic properties of milk and its constituents at 2.45MHz", J. of Microwave power, Vol. 27, 1992, pp. 199-204.

[7] Gadani DH, Rana VA, Bhatnagar SP, Prajapati A N, Vyas AD, "Effect of salinity on dielectric properties of water", Indian J. of pure & Applied Physics, Vol. 50, 2006, pp. 405-410.

[8] Thomas MD, John A, Peter Klein H, John Phillips M, "The electrical conductivity of weight diluted and concentrated standard seawater as a function of salinity and temperature", IEEE J. of Oceanic Engineering, Vol. OE-5, 1980, pp. 28-41.

[9] Meissner T, Wentz FJ, "The complex dielectric constant of pure and sea water from microwave satellite observations", IEEE Transactions on Geoscience and Remote Sensing, Vol. 42, 2004, pp. 1836-1849.

[10] Wheeler HA, Great Neck NY, "Fundamental limitations of small antennas", Proc. of the IRE, Vol. 35, 2006, pp. 1479 – 1484.

[11] Keysight Technologies. "Specifying calibration standards and kits for Keysight Vector Network Analyzers" Application Note, 2014.

[12] Agilent Technologies. "85070E Dielectric probe kit", Printed Version of 85070E Help File, 2013.

First International Conference on Science, Engineering & Environment,
Tsu City, Mie, Japan, Nov.19-21, 2015, ISBN: 978-4-9905958-5-2 C3051

THE INFLUENCE OF LOCAL LAND USE ON THE WATER QUALITY OF URBAN RIVERS

Juan Carlos Covarrubia[1], Scott Rayburg[1], Melissa Neave[2]
[1]Swinburne University of Technology, [2]Centre for Urban Research, RMIT University

ABSTRACT

Urban rivers are often heavily degraded in terms of their physical and biological forms and functions. This has occurred because, until recently, urban rivers in many cities were viewed as either 'problems' to be managed (e.g., for flood control) or as a means for waste disposal, rather than as aesthetic and/or ecological resources. An inherent property of all cities is the relationship between urban runoff and the rivers that receive this runoff. Urban river flows are often highly variable and extremely polluted, which limits their potential for recreational use and as habitat for terrestrial and aquatic organisms. This study investigates how different urban landuses are reflected in the water quality of a specific river. To accomplish this, the study adopts a longitudinal approach and assesses water quality at multiple points along a single system that has three distinct land uses: 1) rural and agricultural; 2) residential; and 3) industrial. The study shows that water quality is relatively good in the rural and agricultural region, shows signs of impairment in the residential region, and becomes heavily impaired in the industrial region—despite having very similar stream side environments (good riparian vegetation cover and a floodway reserve) for its entire length. This study identifies which portions of the catchment are most responsible for non-point source pollution in urban rivers and therefore can be used to target remediation strategies to help improve the overall quality of these systems.

Keywords: Non-point source pollution; nutrient pollution; heavy metals; river management

INTRODUCTION

Urban rivers are major assets to communities as they provide numerous benefits, including fresh water, recreation, landscape amenity, habitat provision and flood control. Humans have long recognized the value of urban rivers, with most human settlements having been established along riverbanks [1]. However, as cities grow their associated rivers can experience changes to their ecosystems as a consequence of pollutants that originate in the urban environment. This leads to a degradation of stream ecological functioning and the loss of other river resource amenities. To mitigate these problems, numerous regulations and initiatives have been enacted at local and national scales to protect urban rivers [2]. Despite these, urban river pollution and degradation continue to be a problem worldwide.

Urban river water quality is mainly affected by human activities that either directly modify stream form and/or function or introduce pollutants into the stream. In terms of pollutants, these may arrive in the stream from either "point" or "non-point" sources. Point source pollution can be attributed to one specific cause and as such tends to be more easily managed (i.e., if the point source can be identified the pollution can be eliminated or reduced through direct action) while non-point source pollution derives from catchment runoff, and as such is highly dispersed and largely untraceable. This aspect of non-point source pollution makes it much more difficult to manage [3]. According to an investigation by [4] non-point source pollution from agriculture, forests and developed urban areas contributes around 74-75% of nitrogen and 80-82% of phosphorous to total pollution loadings in rivers. This demonstrates how difficult it can be to eliminate these pollutants, as the sources are distributed and hard to manage while their contribution to overall pollutant loads is very high. Another example of the problems associated with non-point source pollution can be found in research by [5]. They showed that the main causes of urban river pollution were the discharge of non-point source industrial and agricultural wastes and domestic sewage (such as people and livestock excrement) throughout the watershed. Such pollutants typically alter the properties of urban rivers including their colour, odour, acidity and the ecosystems contained within them [6].

To combat these problems, both monitoring and mitigation (i.e., ensuring a certain level of water quality) need to be undertaken to maintain the ecological balance of urban rivers and to avoid any public health problems [7]. To achieve this, water quality is often monitored, using a variety of physical-chemical, chemical and biological indicators [8]. These indicators are then assessed to determine whether the observed levels reflect

anthropogenic factors (which can be managed) or to natural processes such as erosion, climate, hydrological conditions, topography, catchment area, tectonic and or edaphic factors (which normally cannot be managed).

In addition to monitoring, there are some methods for enhancing the water quality of urban rivers (i.e., mitigation). For example, [9] show how employing wetlands in an urban river system can partially remove nutrients and other elements that affect the ecosystem of a river. Likewise, [10] show that vegetation improves and maintains waterways and that sites with good riparian vegetation typically have better water qualities than those lacking riparian vegetation. Thus, monitoring and mitigation are used in combination to improve the health of urban rivers.

To achieve the best outcomes for urban rivers, it is clear that further research needs to be done to determine where pollutants are coming from (e.g., how different land uses impact on the delivery of non-point source pollutants to adjacent waterways) and how different river configurations (e.g., natural and artificial streams; vegetated and non-vegetated riparian areas; parklands or urban flood corridors, etc.) affect water quality. This project aims to investigate these issues. Specific aims of the project include determining which land use types most impact on urban water quality and what affect, if any, stream and streamside form and character have on the quality of an urban stream.

SITE DESCRIPTION

Kororoit Creek is located in the city of Melbourne in the southern part of the state of Victoria, Australia (Fig. 1), originating in the rural foothills of the Great Divide near Gisborne and Sunbury. The river then flows into the western suburban areas of Melbourne.

A variety of animals, including fish, birds, mammals, amphibians and arthropods, make their homes in Kororoit Creek. For example, wetlands along the creek are home to the endangered Growling Grass Frog and remnant native grasslands in the lower sections of the river provide habitat for the endangered Striped Legless Lizard. There is also a large population of native water rats and significant remnant stands of saltmarsh and white mangroves in the lower sections of the river, which are used by a wide range of rare and/or endangered waterbirds. Thus, Kororoit Creek provides habitat for a diverse range of species, including many that are at risk of extinction.

METHODS

To establish how land use is affecting the water quality of Kororoit Creek a longitudinal study was conducted along the river's length. Multiple field sites were investigated and compared with data from two long-term monitoring sites (Fig. 2). Thus, this study investigates two sources of data: 1) long term data collected by Melbourne Water at two sites along Kororoit Creek (low spatial but high temporal resolution data); and 2) field data collected at eight sites for this study (high spatial but low temporal resolution data). The original objective was to collect data from nine sites (Fig. 2) but there was insufficient flow at the uppermost site (Site 9) to enable analysis. Thus, only data from sites 1-8 are reported here. Sites 7-9 were located within a section of the catchment that was dominated by agricultural landuse. Sites 3-6 were located within a section of the catchment that was largely urban housing. Sites 1-2 were in an industrial sector of the catchment.

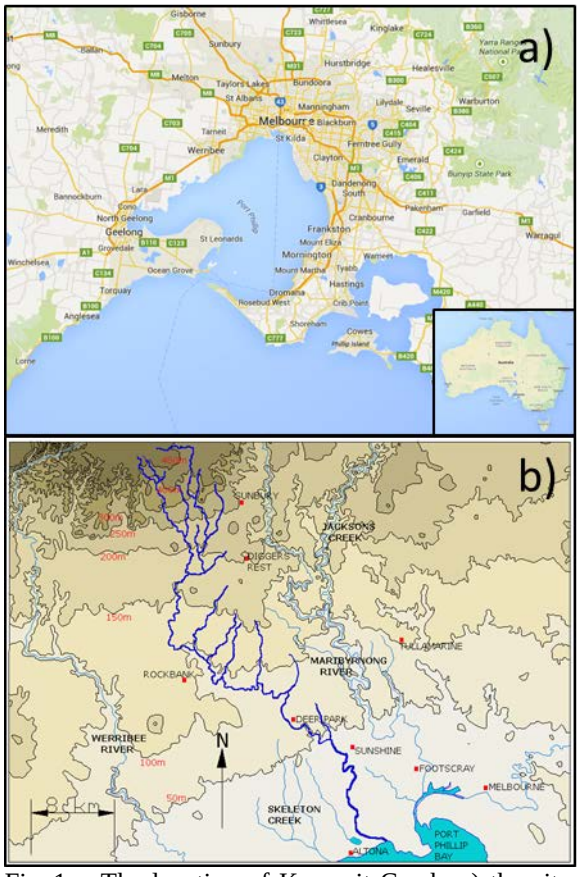

Fig. 1 The location of Kororoit Creek. a) the city of Melbourne, and its location within Australia (sourced from Google Maps); b) Kororoit Creek in western Melbourne (Sourced from Wikipedia).

Data were collected from the eight study sites between April 25, 2015 and May 10, 2015. In each case, a HI 9828 water quality multimeter (Hanna Instruments) was used to analyse the following variables: acidification (pH), turbidity (ppm), dissolved oxygen (%), and electrical conductivity (µS⁄cm).

Fig. 2 The nine fields sites (sites 1-9) and two Melbourne Water monitoring sites (WBKOR0227 and WBKOR0278) assessed in this study (sourced from Apple Maps).

Existing water quality data were also obtained for two Melbourne Water Sampling sites on Kororoit Creek that had been monitored since the early 1990's (Fig. 2). These high quality, laboratory processed data included a wide range of water quality indicators, although they are limited in their spatial extent. The parameters available for these two sites from Melbourne Water include:

1. Ammonia (NH_3)
2. Total Nitrogen (N)
3. Total Phosphorus (P)
4. Dissolved Oxygen (DO) (%)
5. Electrical Conductivity (EC) ($\mu S/cm$)
6. Acidity (pH)
7. Escherichia Coli ($cfu/100ml$)
8. Heavy Metals: *Arsenic (As), Cadmium (Cd), Chromium (Cr), Copper (Cu), Lead (Pb), Nickel (Ni), Zinc (Zn).* (ppm)
9. Nitrate (NO_3)
10. Nitrite (NO_2)
11. Phosphate (PO_4)
12. Temperature (℃)
13. Suspended Solids (mg/L)
14. Turbidity (NTU)

All data were analysed using simple graphical means. For the eight field sites, three samples were collected and the data from these were plotted against on the same graph to visually determine how water quality varied between sites and between sampling dates. The data for the two Melbourne Water monitoring sites were plotted together to ascertain how water quality at each site had changed through time and to illustrate which of the two sites had poorer water quality for the variable in question. Finally, the water quality data from both sources were compared to guideline values [11] to determine whether the water quality was deemed safe for each variable at each site and at each sampling time.

RESULTS AND DISCUSSION

This project investigated how land use impacts the water quality of urban rivers. The study included a wide range of water quality parameters and many of these showed at least some sensitivity to land use.

Standard water quality measures in urban environments include pH, total dissolved solids, dissolved oxygen and electrical conductivity. These standard parameters were measured at the eight field sampling sites and the results are presented in Fig. 3 and Table 1.

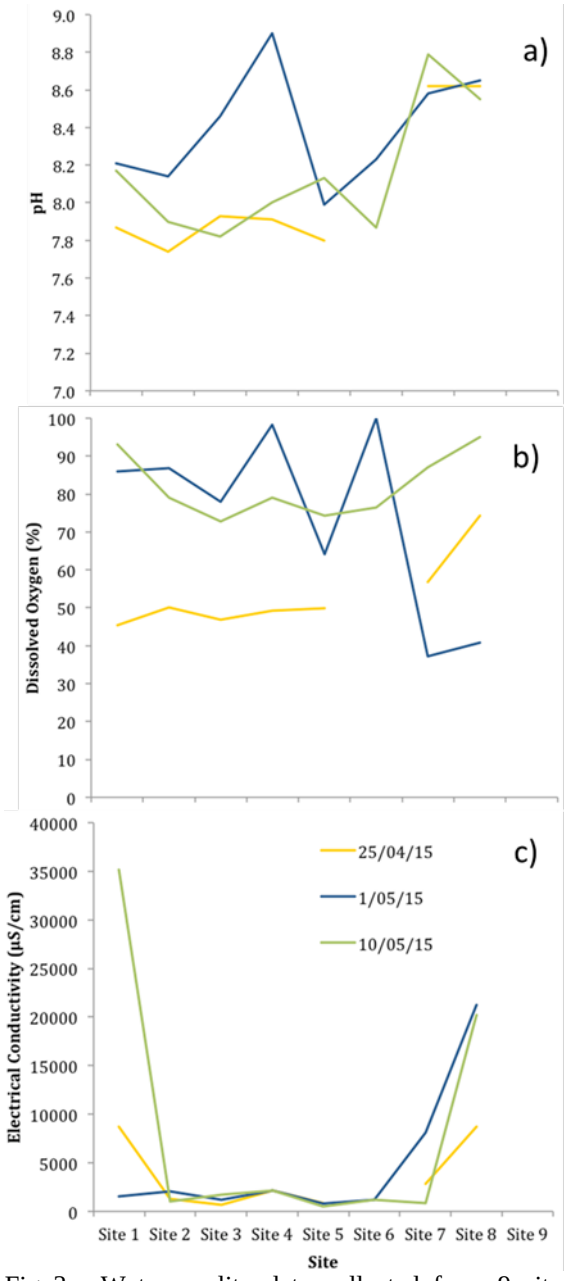

Fig. 3 Water quality data collected from 9 sites along Kororoit Creek in the winter of 2015. a) pH; b) dissolved oxygen; c) electrical conductivity.

In terms of pH, all samples were relatively similar, ranging from approximately 8.6 at the most upstream site (Site 8) to about 8.2 in the downstream sites. For all samples the pH was basic (above 7). The dissolved oxygen (DO) results were quite varied between sampling periods. DO was relatively low (~50%) for most sites on the first sample date (25/04). The following two dates returned higher values for most sites except for Sites 7 and 8, which neared 40% on 01/05/2015. Electrical conductivity was low for all dates for Sites 2 to 6 but varied considerably between samples for Sites 1, 7 and 8.

Table 1 Comparison between the data obtained for nine field sites along Kororoit Creek and the standards given by [11].

	Parameter guideline values			
	pH	TDS (ppm)	DO (%)	EC (μScm^{-1})
Sites	6.8 – 8.3	1000	85 – 110	500
1	X	X	X	X
2	✓	✓	X	✓
3	✓	✓	X	✓
4	X	X	X	X
5	✓	✓	X	✓
6	✓	✓	X	✓
7	X	X	X	X
8	X	X	X	X
9	-	-	-	-

Note: TDS = total dissolved solids; DO = dissolved oxygen; EC = electrical conductivity.

According to [11] guideline levels, the pH should be between 6.8 and 8.3. At sites 1, 4, 7 and 8 the pH exceeded guideline values (Table 1). Similarly, these four sites were outside guideline values for electrical conductivity, DO and total dissolved solids. All of the remaining sites were within guideline values for all of these variables except DO, with every site being deficient in oxygen relative to guideline levels for at least one sample. For each of these variables, there does not appear to be a clear and consistent link between land use type and water quality.

A total of 20 variables were measured over a period of 20 years at the two Melbourne Water monitoring sites. Generally speaking, variables of particular categories (such as metals and nutrients) behaved similarly between these two sites. For this reason, only representative plots are included in this paper and these were chosen to display the general pattern in variable levels at each site.

In terms of the standard water quality parameters of pH, DO and electrical conductivity, the results from the Melbourne Water sites tend to confirm the results from the field data with the downstream site (equivalent to field Site 1) exceeding guideline values for pH and electrical conductivity (but somewhat surprisingly not for DO) while the upstream site (equivalent to field Site 5) only exceeded guideline values for DO (Table 2).

Table 2 Comparison between the data obtained by Melbourne Water in two monitoring sites along Kororoit Creek and the standards given by [11].

Parameter	**Guideline Values**	**WBKO R0227**	**WBKO R0278**
pH	6.5 - 8.3	✓	X
Dissolved Oxygen (%)	85% - 110%	X	✓
Electrical Conductivity	500 μScm^{-1}	✓	X
Temperature	15 - 35 °C	X	X
Turbidity	10 NTU	✓	X
Suspended Solids	NR	-	-
NO_3	0.7 mg/L	✓	X
NO_2	NR	-	-
NH_3	0.9 mg/L	✓	✓
Total N	0.6 mg N L^{-1}	X	X
PO_4	0.02 mg P L^{-1}	✓	X
Total P	0.025 mg P L^{-1}	X	X
Escherichia Coli	NR	-	-
Arsenic	0.013 mg/L	✓	X
Cadmium	0.0002 mg/L	X	X
Chromium	0.001 mg/L	✓	X
Copper	0.0014 mg/L	X	X
Lead	0.0034 mg/L	✓	X
Nickel	0.011 mg/L	✓	X
Zinc	0.008 mg/L	✓	X

✓. The parameter is within the permitted levels; X. The parameter is not within the permitted levels; **NR.** No guideline recommended.

Fig. 4 presents data for two key nutrients, Total Nitrogen (TN) and Total Phosphorous (TP) for the two Melbourne Water sites. These data show that the downstream site was consistently higher than the upstream site for both of these key nutrients. This result demonstrates a clear link between nutrient concentrations and industrial land uses (as nutrient levels are low upstream in the residential area). These findings are consistent with previous research that has shown that nutrient levels can increase in industrial areas. However, it is important to mention that the results are contrary to previous investigations that have found nutrient levels to be high in agricultural areas [14].

This result may be related to the distance

between the furthest upstream monitoring site (WBKOR0227) and the agricultural zone (which is several km upstream) or to a relatively low fertilization regime in the agricultural areas of Kororoit Creek. To confirm whether nutrient pollution is not a problem upstream, it is recommended that an additional long term water quality monitoring site be added in this area to complement those already available. In any case, it is clear that the residential areas of Kororoit Creek do not contribute significant quantities of nutrients to the stream but industrial areas do.

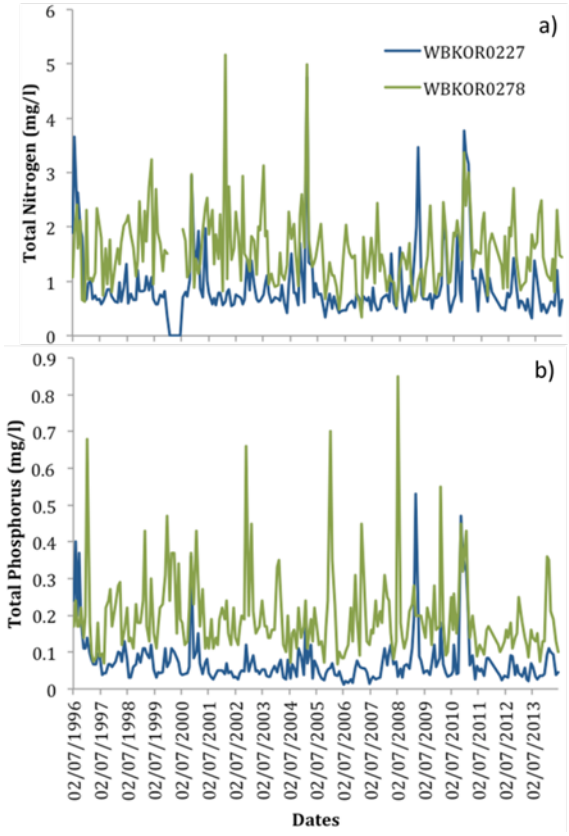

Fig. 4 Nutrient data from Melbourne Water quality assessment sites. a) total nitrogen; b) total phosphorus.

The downstream site also consistently displayed higher metal concentrations than the upstream site (Fig. 5). These results suggest that the industrial zone is a major source of metals to the river system while the residential area is not. These results are consistent with previous research. For example, [12] accredited the presence of heavy metals to factories in and around urban rivers, a pattern that is also reflected in this study. Hence, both nutrients and metals seem closely linked to industrial land uses.

In contrast, the upstream site displayed higher concentrations of E. Coli (Fig. 6) than the downstream site. In this case, then the source of E. Coli appears to be residential land uses. In these types of regions, one of the main water quality threats is the discharge of faecal matter, which is a primary contributor to E. Coli levels [13]. In contrast, the downstream site is situated in a predominantly industrial area, and so is unlikely to have a ready source of faecal matter that would cause elevated levels to be present there. Thus, for E. Coli there appears to be a clear link between land use and pollutant load, with residential areas generating high E. Coli levels and industrial areas generating low E. Coli levels.

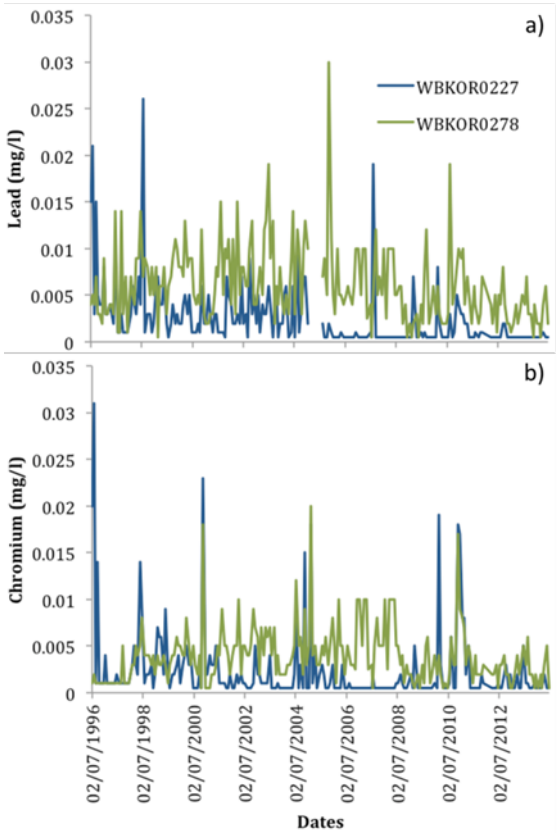

Fig. 5 Metal data from Melbourne Water quality assessment sites. a) lead; b) chromium.

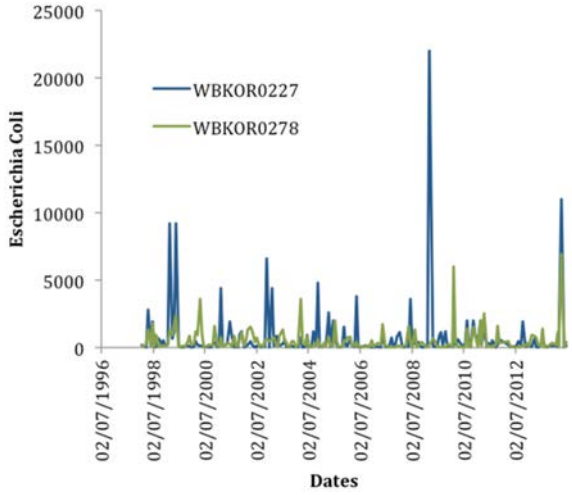

Fig. 6 E. Coli data from Melbourne Water quality assessment sites.

The performance of all of the parameters monitored by Melbourne Water against [11] guideline levels are presented in Table 2. These data show that for nearly every variable (the exceptions being NH_3 and DO) the downstream site breaches [11] guidelines, indicating that the river is extensively polluted at its outlet. However, the river is in relatively good condition further upstream with only six variables (DO, temperature, total nitrogen, total phosphorus, cadmium and copper) regularly exceeding guideline levels. A current focus on tree planting in the upstream reaches should help to improve these values even further, resulting in a relatively safe and healthy upstream riverine environment. However, there appears to be little prospect of improved water quality downstream unless the adjacent industries are encouraged or compelled to reduce their discharges to the creek.

CONCLUSION

The results of this study reveal a strong relationship between water quality and land use. Of the land uses investigated in this research, industrial areas are by far the biggest contributors to poor water quality, with nutrients and metals being especially high in and around these areas. In contrast, residential water quality was relatively good, although elevated levels of E. Coli could be found in these areas. It is hoped that a current wave of tree planting along the banks in the residential areas will help to improve the water quality in these parts of the river further in coming years. However, it is unlikely that the water quality in the industrial areas will improve without a concerted effort to reduce the flow of pollutants into the river from the surrounding industries.

ACKNOWLEDGEMENTS

The authors gratefully acknowledge Melbourne Water for providing data for this project.

REFERENCES

[1] Mouri, G. (2015). Assessment of land cover relocation incorporating the effects of human activity in typical urban and rural catchments for the design of management policies. Env. Sci. and Policy, 50, 74-87.

[2] Spänhoff, B., Dimmer, R., Friese, H., Harnapp, S., Herbst, F., Jenemann, K., Müller, U. (2012). Ecological status of rivers and streams in Saxony (Germany) according to the water framework directive and prospects of improvement. Water (Switzerland), 4, 887-904.

[3] Rezaei, A., & Sayadi, M. (2015). Long-term evolution of the composition of surface water from the river Gharasoo, Iran: A case study using multivariate statistical techniques. Env. Geochem. and Health, 37, 251-261.

[4] Choi, J. Lim, K. & Won, C. (2013). Catchment water quality management planning for sustainable development of tidal areas. Irrig. and Drain., 62, 18-23.

[5] Yan, C., Zhang, W., Zhang, Z., Liu, Y., Deng, C., & Nie, N. (2015). Assessment of Water Quality and Identification of Polluted Risky Regions Based on Field Observations & GIS in the Honghe River Watershed, China. Plos ONE, 10, 1-13.

[6] Kai, D., Jianguo, W., Jianqiang, W., Wang, C., Changjun, Z., & Xiaoyan, W. (2015). Treatments to Control Urban River Pollution in Water Source City of South to North Water Diversion Project. Polish J. of Env. Stud., 24, 501-504.

[7] Matysik, M., Absalon, D., & Ruman, M. (2015). Surface water quality in relation to land cover in agricultural catchments (Liswarta river basin case study). Polish J. of Env. Stud., 24, 175-184.

[8] Leščešen, I., Pantelić, M., Dolinaj, D., Stojanović, V., & Milošević, D. (2015). Statistical Analysis of Water Quality Parameters of the Drina River (West Serbia), 2004-11. Polish J. of Env. Stud., 24, 555-561.

[9] Rai, U., Upadhyay, A., Singh, N., Dwivedi, S., & Tripathi, R. (2015). Seasonal applicability of horizontal sub-surface flow constructed wetland for trace elements and nutrient removal from urban wastes to conserve Ganga River water quality. Eco. Eng., 81, 115-122.

[10] Valle Junior, R. F., Varandas, S., Pacheco, F., Pereira, V., Santos, C., Cortes, R., & Sanches Fernandes, L. (2015). Impacts of land use conflicts on riverine ecosystems. Land Use Policy, 43, 48-62.

[11] ANZECC / ARMCANZ, 2000, 'Australian and New Zealand Guidelines for Fresh and Marine Water Quality, Vol 1.

[12] Dumas, C., Ludwig, W., Aubert, D., Eyrolle, F., Raimbault, P., Gueneugues, A., & Sotin, C. (2015). Riverine transfer of anthropogenic and natural trace metals to the gulf of lions (NW mediterranean sea). App. Geochem., 58, 14-25.

[13] Titilawo, Y., Obi, L., & Okoh, A. (2015). Antimicrobial resistance determinants of escherichia coli isolates recovered from some rivers in osun state, south-western nigeria: Implications for public health. Sci. Total Env., 523, 82-94.

[14] Ahearn, D., Sheibley, R., Dahlgren, R., Anderson, M., Johnson, J., & Tate, K. (2005). Land use and land cover influence on water quality in the last free-flowing river draining the western Sierra Nevada, California. J. of Hyd., 313, 234-247.

First International Conference on Science, Engineering & Environment,
Tsu City, Mie, Japan, Nov.19-21, 2015, ISBN: 978-4-9905958-5-2 C3051

ESTIMATION OF PERMEABILITY OF POROUS MEDIA WITH MIXED WETTABILITIES USING PORE-NETWORK MODEL

Junichiro Takeuchi, Wataru Sumii, Hidetaka Tsuji, and Masayuki Fujihara
Graduate School of Agriculture, Kyoto University, Japan

ABSTRACT

Water flow through porous media is involved with physical factors such as size and configuration of pores, contact angle of grain surface, and connectivity of pores. To deal with these factors, pore-scale modeling is essential. Pore aggregate referred to as pore-network is extracted from randomly packed spherical grains with the modified Delaunay tessellation method. Water flow in a pore-network is formulated in terms of a network flow problem in hydraulics, in which friction and local losses such as contraction and enlargement of pipes are explicitly treated, while those are implicitly included in the hydraulic conductance of capillary tubes in existing works. Through the numerical experiments, it was confirmed that the effect of the local loss on the hydraulic conductivity could be negligible. Furthermore, the relative permeabilities of porous media with mixed wettabilities along the primary drainage and imbibition processes were estimated.

Keywords: Relative Permeability, Network Flow, Friction Loss, Local Loss

INTRODUCTION

The constitutive relationship, which is a set of relationships between capillary pressure and saturation, and capillary pressure and relative permeability, is essential for simulations of variously saturated seepage flows. Some functional models such as the van Genuchten model [1] for saturation and the Mualem model [2] for relative permeability are generally utilized in many works. However, since these functional models describe REV (representative element volume)-scale relationships, they cannot treat entrapped air and residual water in pores dynamically. The approaches that enable to deal with interface between water and air are divided into two main groups: one is a continuum-based two-phase flow model and the other is a discrete model which tracks movement, generation, and disappearance of interfaces. The former solves the equations for the mass and momentum conservations numerically in a porous space [3], and the latter simulates water and air intrusion in bond-percolation and invasion-percolation manners in a pore-network [4]. In this study, the latter approach is used since required computational load is relatively small. Another reason for usage of the pore-network approach is hydrophobic grains in a porous medium. It is well known that hydrophobic grains change the hydraulic properties such as water retention characteristics and permeability drastically [5], and the altered hydraulic properties are beyond an applicable scope of the functional models.

In the framework of pore-network model, permeability of an objective medium is estimated on the basis of a flow in pore segments. The flow rate in a pore segment is described by a proportional relation to hydraulic gradient between the ends of a segment. It is the hydraulic conductance that is used as a proportionality coefficient between the flow rate and the hydraulic gradient. Some works derive the conductance from mathematical or numerical analysis of a cross-section, in which the segment is assumed as a pipe with a constant cross-section [6-8]. Another derive it from longitudinal or 3-D analysis of a segment, in which a shape of the cross-section varies along the flow path [9], [10]. From a standpoint of hydraulics, the total head loss, which corresponds to the difference of piezometric heads in the segment ends, is described as the summation of the friction loss and local losses such as the enlargement, contraction, entrance, exit, and turning losses, and the equation does not show a linear relationship between the head loss and the flow rate. By the transformation of the equation for the flow rate, it is proved that the conductance derived from the cross-sectional analysis is related to the friction loss when the flow is laminar (APPENDIX). Furthermore, in a case of the conductance derived from the longitudinal or 3-D analysis, the relation between the flow rate and the hydraulic gradient should not be represented linearly in a strict sense, because it contains enlargement and/or contraction losses. Then another question arises: if the relation between the flow rate and the pressure gradient could not be described as a linear equation, why is the Darcy's law represented as a linear equation? In the presented study, an equations system for the pore-network flow is reconstructed in terms of a network flow problem in hydraulics, and the effect of local losses on the hydraulic conductivity is

investigated through numerical experiments. And the constitutive relationship between the matric potential and the relative permeability, and the saturation and the relative permeability of porous media mixed with hydrophobic grains at various fractions are estimated.

MODEL DESCRIPTION

Generation of Pore Network Model

In this study, a virtual pore-networks is extracted from randomly packed spherical grains like glass beads, which are computed with the discrete element method (DEM). From the computed porous media, pore bodies which are relatively large voids and pore throats which are relatively small voids connecting pore bodies are extracted by the modified Delaunay-tessellation approach proposed by Al-Raoush et. al. [11]. In the extraction process, location and size of pore bodies and throats are identified based on the 3-D coordinates of grains. A pore body is represented as an inscribed sphere in the void surrounded by grains, and a pore throat as a cylindrical tube in this study. When the cross-section of a pore throat is represented by a circle, there are three representative circles, (1) the inscribed circle in the void surrounded by grains, (2) the equivalent circle whose area is equal to that of the void, and (3) the effective circle whose hydraulic conductance is equal to that of the void [6] as illustrated in Fig. 1. In some works, the effective radius is given as the arithmetic mean of the inscribed and equivalent radii based on the mathematical and numerical analyses [6], [12], but it might be underestimated since they analyzed the minimum cross-section along the pore throat. In alternate cross-sections other than minimum one, the hydraulic conductivity becomes larger due to the presence of slip walls. Hence, the effective radius is treated as a fitting parameter in this study. Figure 2 shows a computed porous medium with about 58 hundreds uniform spherical grains 0.2 mm in diameter and an extracted pore-network, which consists of 14,522 pore bodies and 36,761 pore throats. The histograms of pore sizes in the pore-network is shown in Fig. 3.

Formulation Based on Network Flow Problem

In advance to calculation of porous network flow, connected pore-networks whose pore bodies and throats are filled with water are computed in an invasion percolation manner under various conditions relevant to initial states, imposed pressures on the bottom, and mixture fractions of hydrophilic and hydrophobic grains. The detail of the processes is described in the work by Takeuchi (2015) [13]. Using the water-filled pore-networks, which are sub-networks of the original pore-network, hydraulic conductivity of each sub-network is calculated under the condition where same pressure is imposed on the top and bottom faces of the sub-network. The interfaces between air and water in

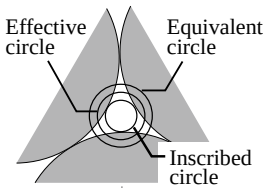

(a) At the minimum cross-section

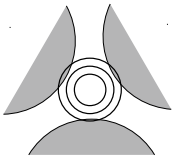

(b) At alternate cross-section

Fig. 1 Representative circles for a pore throat

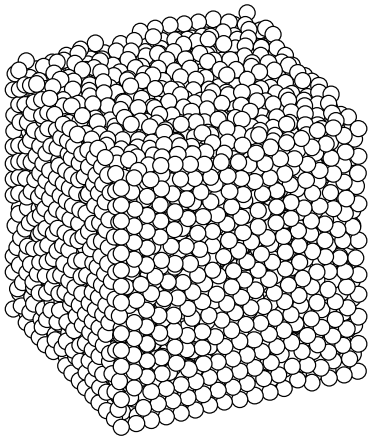

(a) Porous medium model

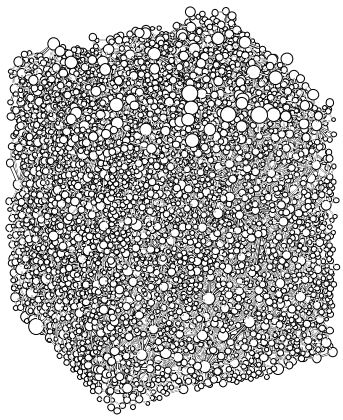

(b) Pore network model

Fig. 2 Extraction of pore network

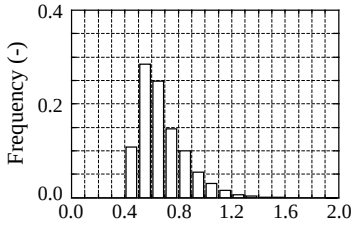

(a) Pore body radius (0.1 mm)

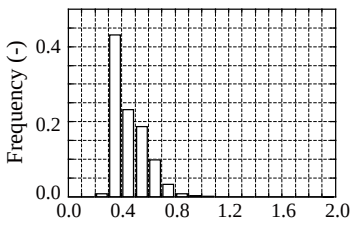

(b) Pore throat radius (0.1 mm)

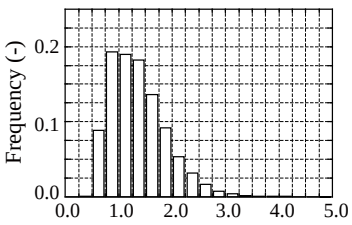

(c) Pore throat length (0.1 mm)

Fig. 3 Histograms of pore sizes

pores are fixed at the computed location.

Water flow in pore-networks is calculated based on the pipe network analysis, in which local head losses such as enlargement and contraction are considered. In a network flow problem, flow rates in each pipe segment (pore throat and a part of each pore body in this case) and piezometric head at each junction (the center of pore body) are unknown. For simplicity, a segment is represented as a pipe whose cross-section is abruptly contracted and enlarged in this study, and the segment is divided into three parts as illustrated in Fig. 4. Then the total head loss along the segment is described by the empirical equations as follows [14].

$$h_i - h_j = \kappa_k |q_k| q_k \tag{1}$$

with

$$h_m = \frac{p_m}{\rho g} + z_m \qquad (m = i, j) \tag{2}$$

$$\kappa_k = \left(\sum_{m=i,j,k} \frac{f_m l_m}{2 g d_m A_m^2} + \frac{k_S}{2 g a_k^2} + \frac{k_E}{2 g a_k^2} \right) \tag{3}$$

$$d_m = \frac{4 a_m}{P_m} \qquad (m = i, j, k) \tag{4}$$

$$l_i + l_k + l_j = l_{ij} \tag{5}$$

where h_i is the piezometric head at the center of the pore body i, κ_k is the coefficient that includes friction and local losses, f_m is the friction factor, k_S and k_E are the loss coefficients for sudden contraction and sudden enlargement, respectively, l_m is the length of the part $m\,(m = i, j, k)$, d_m is the hydraulic diameter, a_m is the cross-sectional area, q_k is the flow rate in the pore throat k (the segment ij), g is the gravitational acceleration, p_m is the pressure, z_m is the height from a datum, ρ is the water density, P_m is the wetted perimeter, and l_{ij} is the length of the segment ij. When the flow in the pipe is laminar, the friction factor is represented as

$$f_m = \frac{\alpha}{\mathrm{Re}_m} \tag{6}$$

with

$$\mathrm{Re}_m = \frac{\rho d_m |q_k|}{\mu a_m} \tag{7}$$

where α is a constant that depends on the shape of the cross-section and its value is 64, 56.908, and 53.333 for the circular, square, and equilateral-triangular cross-section, respectively [15]; Re_m is the Reynolds number; and μ is the water viscosity. Equations (6) and (7) indicate that the coefficient κ_k depends on the flow rate q_k, that is $\kappa_k = \kappa_k(q_k)$.

The mass balance at each junction (pore body here) except for inflow and outflow pore bodies is described as follows.

$$\sum_{k \in \eta_i} q_k = 0 \tag{8}$$

where η_i is the set of pore throats connecting the pore body i.

In addition to Eqs. (1) and (8), the piezometric heads in the inflow and outflow pore bodies, into or from which water flows freely depending on the prescribed head, are given as follows.

$$h_m = h_m^* \qquad (m \in \eta^{\mathrm{IN}}, \eta^{\mathrm{OUT}}) \tag{9}$$

where η^{IN} and η^{OUT} are the sets of the inflow and outflow pore bodies, respectively.

The network flow problem in a pore space, which is described by Eqs. (1) through (9), is a non-linear equations system, and it is solved by the Newton method. The coefficient $\kappa_k(q_k)$ is estimated from the previous q_k in the iterative process of the Newton method in the same way with a linearization technique for the Richards equation [16], and when the flow rates in some pores are zero or extremely small, a sufficiently small value (e.g., 10^{-20}) is given to q_k since q_k is included in denominator (Eqs. (6), and (7)) in this study to avoid crashes in computing.

When the local losses (sudden contraction and enlargement losses here) are negligible compared with the friction loss, Eq. (1) becomes the conductance-based equation, which is generally used in different works (e.g., [6]-[10]), and described as follows (See APPENDIX for details).

$$h_i - h_i = \frac{l_{ij}}{\rho g \Theta_{ij}} q_k \tag{10}$$

where Θ_{ij} is the hydraulic conductance between the nodes i and j. Then the equations system becomes linear.

The above mentioned formulation indicates that the hydraulic conductance Θ_{ij} is related to the friction losses and the shape of the cross-section, and it does not include other local losses. Furthermore, it implies that the conductance derived from longitudinal or 3-D analysis should not be used, since it contains some local effects like contraction, enlargement, and turning losses. If these effects are considered, the equation relating to the flow rate and head loss (the pressure difference) becomes non-linear as shown by Eqs. (1) through (7).

The hydraulic conductivity of the sub-network, which is the unsaturated one, is estimated based on the Darcy's law.

$$K = \frac{QL}{A \Delta H} \tag{11}$$

with

$$Q = \sum_{k \in \eta_{\mathrm{PT}}^{\mathrm{IN}}} q_k = \sum_{k \in \eta_{\mathrm{PT}}^{\mathrm{OUT}}} q_k \tag{12}$$

where K is the hydraulic conductivity of variously saturated porous media, Q is the total flow rate through the medium, $\eta_{\mathrm{PT}}^{\mathrm{IN}}$ and $\eta_{\mathrm{PT}}^{\mathrm{OUT}}$ are the sets of

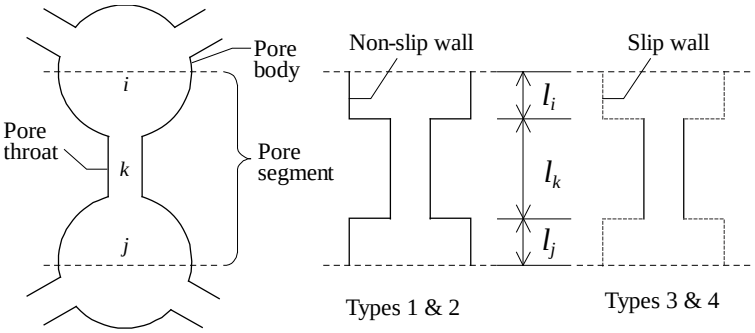

Fig. 4 Configurations of pore segment

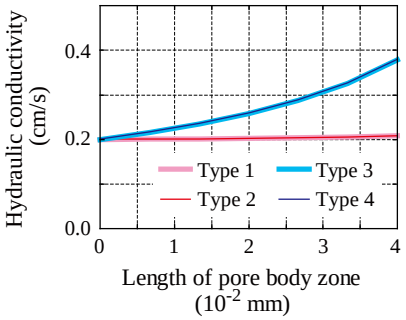

Fig. 5 Relation of hydraulic conductivity and pore segment configuration

the pore throats connecting to the inflow and outflow pore bodies, L and A are the length and the cross-sectional area of the medium, and ΔH is the difference of the piezometric head between the inflow and outflow faces. The saturated hydraulic conductivity K_S is computed from the pore-network in which all the pore bodies and pore throats are filled with water, and the relative permeability K_r is obtained by the following relation.

$$K_r = \frac{K}{K_S} \tag{13}$$

NUMERICAL EXPERIMENTS

Configuration of Pore Segments

Firstly, an effect of configuration of pore segments between pore bodies on the hydraulic conductivity is investigated. In this study, four types of segment, which are designed to consider how the pore bodies are dealt, are tested (Fig. 4). In the all types, pore bodies on both ends are treated as relatively large circular tubes, and a pore throat as relatively narrow circular tube. In Type 1, the friction losses of both large and narrow tubes and the local losses for sudden contraction and enlargement are considered, while only friction losses are considered in Type 2. In Types 3 and 4, the large tubes are assumed to have slip walls. Type 3 has the local losses for sudden contraction and enlargement, and Type 4 does not have such local losses.

The saturated hydraulic conductivities of the extracted pore-network (Fig. 1) are computed, as the lengths of the large-tubes vary from 0 to 0.04 mm. The tube with a constant cross-section ($l_i = l_j = 0$) is treated as a standard, and the effective radius r^{eff} of tubes is adjusted based on the inscribed radius r^{ins}, i.e., $r^{\mathrm{eff}} = \omega r^{\mathrm{ins}}$, where ω is a coefficient, in order that the hydraulic conductivity becomes about 2×10^{-2} cm/s. For the objective pore-network the value of the coefficient is identified as 1.38, and the hydraulic conductivity is reproduced as 2.006×10^{-2} cm/s. The values of k_s and k_E are given as 0.5 and 1.0, respectively, and each value becomes maximum when the sudden contraction and enlargement are supposed to be the entrance and exit, respectively.

The obtained result is shown in Fig. 5. It is found that all the hydraulic conductivities increase at accelerated paces as the length of large tubes increases, and the increasing pace of Types 3 and 4 is large compared with Types 1 and 2. This indicates that the friction losses in pore bodies need to be introduced, but the effect is limited. Furthermore, it is shown that the effects of the local losses are negligible. Actually, the ratio of the local losses and the friction loss in a typical segment ($r^{\mathrm{ins}} = 0.03$ mm, $l_k = 0.1$ mm) is about 6×10^{-3} if the Reynolds number is 0.17, which is a half of the maximum Reynolds number.

Relative Permeability

To calculate the relative permeability of variously saturated pore-networks, various states along drainage and imbibition processes are needed. Then, water retention curves for the primary drainage and the primary imbibition of the extracted pore-network are computed in an invasion percolation manner, which is the same way with our previous work [13]. The objective porous media are presumed to include hydrophilic and hydrophobic grains in various proportions. The mixture fraction of hydrophobic grains ranges from 0% to 100% at 25% interval. The contact angles of the hydrophilic and hydrophobic grains, which are essential factors that determines the water retention properties, are identified by a trial-and-error adjustment so as to fit the observed results. The identified values are listed in Table 1, where different values are given to the contact angles for the drainage and imbibition processes.

Table 1 Contact angles (deg)

Process	Mixture fraction	Hydrophilic grain	Hydrophobic grain
Drainage	0%	46	74
	25%	50	
	50, 75, 100%	60	
Imbibition	0%	58	110
	25%	92	
	50, 75, 100%	98	

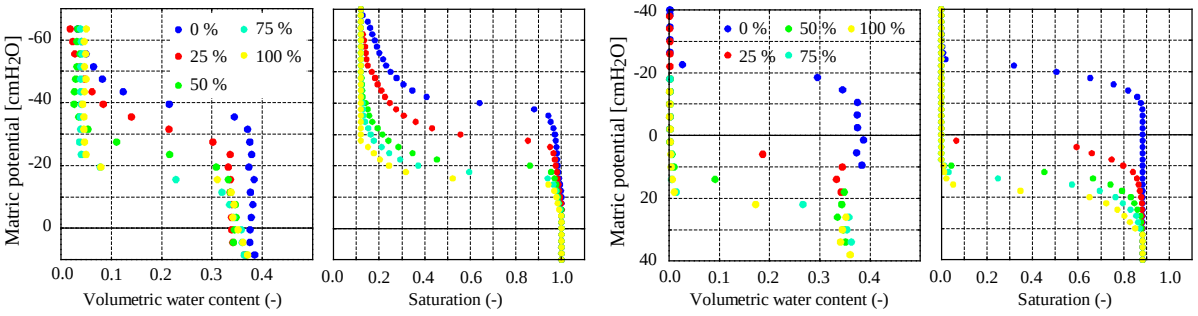

(a) Measurement (b) Computation (a) Measurement (b) Computation

6-1 Drainage process 6-2 Imbibition process

Fig. 6 Water retention curves

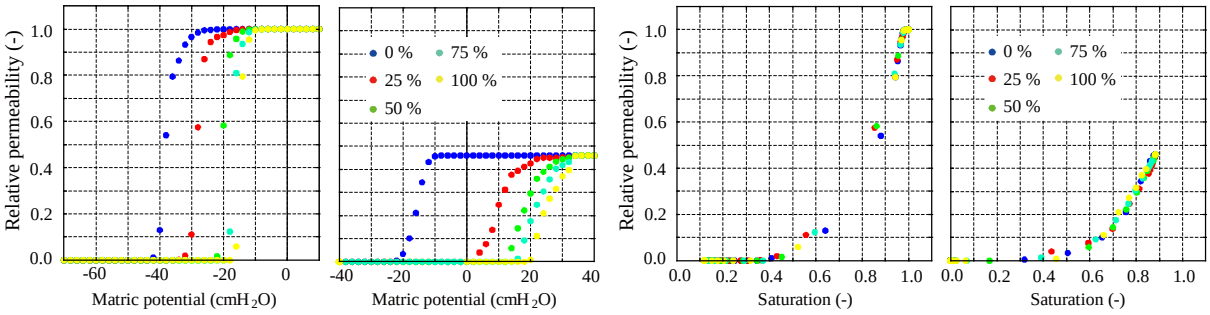

(a) Drainage process (b) Imbibition process (a) Drainage process (b) Imbibition process

7-1 Relative permeability vs. matric potential 7-2 Relative permeability vs. saturation

Fig. 7 Relative permeability

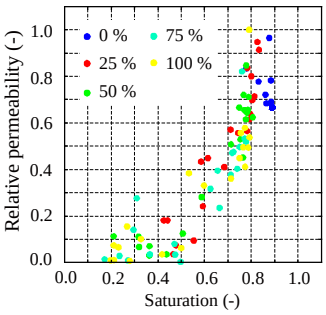

Fig. 8 Measured relative permeability

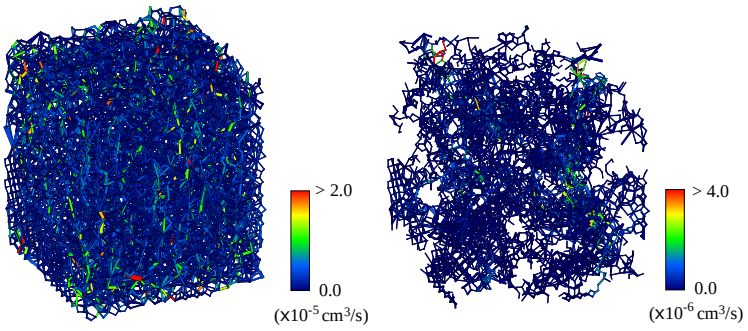

(a) 0%, -22 cmH2O (b) 50%, -22 cmH2O

Fig. 9 Flow distributions (drainage process)

These are considered to correspond to the receding and advancing contact angles. Besides, in the drainage or imbibition process different values are given to hydrophilic grains even in accordance with the mixture fraction. It is considered that the hydrophilic (original) glass beads are partially hydrophobized by the redundant coating material (octyltrichlorosilane, OTS) that remains on the hydrophobized grain surfaces. This speculation is consistent with our experiments on measurements of the water drop penetration time, the apparent contact angle, and the water-entry pressure [17]. The computed and measured water retention curves are shown in Fig. 6.

At each point along the primary drainage and imbibition processes, sub-networks in which pores are filled with water are withdrawn, and the hydraulic conductivity is computed if the sub-network stretches out from the bottom up to the top. Here, the constant-radius tubes without sudden contraction and enlargement ($l_i = l_j = 0$, and $\omega = 1.38$) are used. Common pressure head is imposed to the pore bodies on the bottom and top faces, then the hydraulic gradient becomes unit. Therefore, water flows down by the gravity through the porous medium.

Figure 7-1 shows the relation of the relative permeability and the matric potential in the drainage and imbibition processes. This figure corresponds to the water retention curves in Fig. 6. Figure 7-2 shows the computed relation of the relative

permeability and the saturation, and it indicates similar tendency with measured one (Fig. 8). The measured one was obtained with the constant head method (Daiki, DIK-4012). Although the method is normally used for measurement of the saturated hydraulic conductivity, variously saturated glass beads of diameter 0.1 mm with mixed wettabilities are used in this study.

Figure 9 shows some typical flow distributions in pore-networks. These figures indicate water flows in only a minority of pores especially in unsaturated states since many terminals are included in the pore-network.

CONCLUSION

Water flow through porous media is re-formulated in terms of a network flow problem in hydraulics, where friction and local losses such as sudden contraction and enlargement are incorporated. The equations system becomes nonlinear in contradiction to the Darcy's law, which expresses a linear relation between flow rate and hydraulic gradient, if the local losses are introduced. Through the numerical experiments with a virtual pore-network extracted from randomly packed spherical grains, it is confirmed that the system could be regarded as a linear system because the local losses are negligible compared with the friction loss. Furthermore, relative permeabilities of porous media with mixed wettabilities along primary drainage and imbibition processes are estimated, and the results indicated a similar tendency with the measured one.

APPENDIX

When the local losses are negligible compared with the friction loss, Eq. (1), which stands for total loss in the segment between the nodes i and j becomes as follows.

$$h_i - h_j = \left(\sum_{p=i,j,k} \frac{l_p}{\rho g \Theta_p} \right) q_k \tag{14}$$

with

$$\Theta_p = \frac{2 d_p^2 A_p}{\alpha \mu} \tag{15}$$

When the harmonic average is taken between the nodes i and j, the hydraulic conductance Θ_{ij} of the segment becomes as follows.

$$\frac{l_{ij}}{\Theta_{ij}} = \frac{l_i}{\Theta_i} + \frac{l_k}{\Theta_k} + \frac{l_j}{\Theta_j} \tag{16}$$

Then, the flow rate q_k is represented as follows.

$$q_k = \Theta_{ij} \frac{\rho g \left(h_i - h_j \right)}{l_{ij}} \tag{17}$$

ACKNOWLEDGEMENTS

This work was supported by JSPS KAKENHI Grant Number 24780232.

REFERENCES

[1] van Genuchten MT, "A closed form equation for predicting the hydraulic conductivity of unsaturated soils", Soil Sci. Soc. Am. J., Vol. 44, 1980, pp. 892-898.

[2] Mualem Y, "A new model for predicting the hydraulic conductivity of unsaturated porous media", Water Resour. Res., Vol. 12, 1976, pp. 513-522.

[3] Ferrari A, Jimenez-Martines J, Borgne TL, Mehuest Y, and Lanati I, "Challenges in modeling unstable two-phase flow expriments in porous micromodels", Water Resour. Res., Vol. 51, 2015, doi:10.1002/201WR016384.

[4] Gharbi O, Blunt MJ, "The impact of wettability and connectivity on relative permeability in carbonates: a pore network modeling analysis", Water Resour. Res., Vol. 48, 2012, doi:10.1029/2012WR011877.

[5] DeBano LF, "Water repellency in soils: a historical overview", J. Hydrol., Vol. 231-232, 2000, pp. 4-32.

[6] Bryant S and Blunt M, "Prediction of relative permeability in simple porous media", Phys. Rev. A, Vol. 46, 1992, pp. 2001-2011.

[7] Patzek TW and Silin DB, "Shape factor and hydraulic conductance in noncircular capillaries I. One-phase creeping flow", J. Colloid Interface Sci., Vol. 236, 2001, pp. 295-304.

[8] Valvatne PH and Blunt MJ, "Predictive pore-scale modeling of two-phase flow in mixed wet media", Water Resour. Res., Vol. 40, 2004, doi:10:1029/2003WR002627.

[9] Koplik J, "Creeping flow in two-dimensional networks", J. Fluid Mech., Vol. 119, 1982, pp. 219-247.

[10] Dagan Z, Weinbaum S, and Pfeffer R, "An infinite-series solution for the creeping motion through an orifice of finite length", J. Fluid Mech., Vol. 115, 1982, pp. 505-523.

[11] Al-Raoush R, Thompson K, and Willson CS, "Comparison of network generation technique for unconsolidated porous media", Soil Sci. Soc. Am. J., Vol. 67, 2003, pp. 1687-1700.

[12] Bryant S, King PR, and Mellor DW, "Network model evaluation of permeability and spatial correlation in a real random sphere packing", Trans. Porous Media, Vol. 11, 1993, pp.53-70.

[13] Takeuchi J, Sumii W, and Fujihara M, "Modeling of fluid intrusion into porous media with mixed wettabilities using pore network", in Proc. 5th Int Conf. on GOEMATE, accepted, 2015.

[14] Larock BE, Jeppson RW, and Watters GZ, Hydraulics of Pipeline Systems, CRC Press, 2000, p. 537.

[15] Shah RK, "Laminar flow friction and forced

convection heat transfer in duct of arbitrary geometry", Int. J. Heat Mass Transfer, Vol. 18, 1975, pp. 849-862.

[16] Huyakorn PS and Pinder GF, Computational Methods in Subsurface Flow, Academic Press, 1983, p.473.

[17] Takahashi T, Hydraulic properties of porous media with mixed wettabilities, Graduation Thesis of Kyoto University, 2013, p.45 (in Japanese).

First International Conference on Science, Engineering & Environment,
Tsu City, Mie, Japan, Nov.19-21, 2015, ISBN: 978-4-9905958-5-2 C3051

MORPHOFUNCTIONAL CHARACTERISTICS AND ELEMENTAL COMPOSITION OF RAT LIVER UNDER DIFFERENT NUTRIENT PROVISION

Rusakova E.A. [1], Kvan O.V. [2], Miroshnikov S.A.[3], Korotkova A.M.[4], Skuridina I.V.[5]
[1] Department of Biological Science, Orenburg State University, Russia
[2] Orenburg State University, Russia
[3] SSI All-Russian Scientific Institute beef cattle, Russia
[4] Orenburg State University, Russia
[5] Perm National Research Polytechnic University, Russia

ABSTRACT

The article presents research of structural and functional changes in the liver in the conditions of modeling of micronutrient deficiencies in the organism of experimental animals with subsequent inclusion of complex minerals into their food ration. The object of the study was the liver of rats «Wistar». The elemental composition of biological substrates has been studied using atomic emission and mass spectrometry (ICP-AES and ICP-MS) in the test laboratory ANO «Center for Biotic Medicine».

It has been established that the addition of selenium to the ration increases the concentration of this element in the liver by 15,0% ($p \leq 0,05$) against the background of lowering nickel by 50,0% ($p \leq 0,05$) in the experimental group I relative to control. When you turn on zinc into the ration, the concentration of it increases by 14,3% ($p \leq 0,05$) in the experimental group II relative to the control. Inclusion of iodine in the ration contributed to the increase of the iodine concentration by 4,52% in the experimental group III relative to the control group.

Thus, the intake by the animal organism of toxic elements (lead and cadmium salts) leads to a change in the structural elements of the liver, resulting in depletion of hepatocyte in glycogen, or its complete disappearance, in offensive vacuolization and necrosis of hepatocytes and in changes in vessels diameter microvasculature, i.e. structural and functional changes in the liver are identified. Introduction into the ration of complex of essential trace elements (I, Se, Zn) involves an increase in functional activity of the liver.

Keywords: Liver Glycogen, Hepatocytes, Rats, Essential Elements.

BACKGROUND

In terms of socio-economic instability and increasing anthropogenic load on territories protection of public health becomes a priority [1]. Hypo - and giperelementozies are one of the major causes of bad health. Deviation in the entry into the body of the macro-and micronutrients, violation of their correlation in the food ration affects the vital activity of the organism. We know a number of diseases, caused by deficiency of essential trace elements, which lead to serious disorder in health status [2], [3].

Xenobiotics are biotransported in the liver involving cellular enzyme systems. For the normal activity of the latter the optimal amount of essential trace elements (zinc, selenium, iodine) [4], [5] must enter the organism. Micronutrients deficiencies in the food ration lead to disruption of the activity of cellular enzyme systems.

Zinc helps to stabilize cell membranes, it is a strong antioxidant protection factor [6], [7]. The activity of more than 40 intracellular enzymes [8] disrupts because of the lack of zinc in food ration.

Iodine deficiency statuses causes the lack of iodine in the environment and food [9].

Selenium is involved in the metabolism of iodine, so selenium deficiency leads to disruption of iodine metabolism [10], [11], because a deficiency of selenium, production of glutathione and glutathioneperoxidase is disrupted and they reduce the sensitivity of hepatocytes to free radical damage [12].

Glutathione is found in high concentrations in the liver (up to 5 millimole), 90 % of it is contained in the cytosol, the rest – in the mitochondria. In the latter glutathione is an antioxidant, it restores hydrogen peroxide and prevents lipid peroxidation by hydroxyl radical. At low concentration of glutathione in a cell, its sensibility to free radical damage increases [13], [14].

In centrolobular hepatocytes higher levels of cytochrome P-450 [15] are noted which is involved in the metabolism of various xenobiotics. Thus, according to the literature data, the process of biotransformation is attributable largely to the activities of centrolobular hepatocytes. However, as studies show, hepatocytes of this zone are more vulnerable to the toxic effects of some products, as

glutathione and glutathione peroxidase localize predominantly in periportal cells [16].

Taking into account that the area is a biogeochemical province deficient in the above listed elements, the purpose of our study was to identify the structural and functional changes in the liver under the conditions of creating a model of micronutrient deficiencies in organism of experimental animals with subsequent inclusion in the ration of complex minerals [17]. As the liver is the main organ of biotransformation, in which a significant amount of cellular enzyme systems is actively involved, the normal activity of the latter requires entry of the optimal amount of essential trace elements into the organism. Micronutrient deficiencies in the ration lead to a disruption of the functions of the body's enzyme systems [18].

OBJECTIVES

Studies were done in the experimental-biological clinics (vivarium) of the Orenburg State University on the model rats «Wistar». The object of the study was the liver. 100 bimonthly rats – females – were selected for the experiment.

MATERIALS AND METHODS

To equalize the status of animals and to create elemental chemical elements deficient state, for three weeks they were nourished by specially prepared polished rice (boiling for 15 minutes in distilled water followed by washing and removing the broth). For prevention of avitaminosis (vitamin deficiency) states in animals, multivitamin complex was administered in the ration in accordance with the recommendations of the Institute of Nutrition (Russian Academy of Medical Sciences) (2001). The animals were watered by twice-distilled water.

The study was conducted as follows (Table 1).

Table 1 The scheme of the experiment

Group	The period of the experiment, weeks	
	Preparatory ration 2-4 week	Basic ration 4-8 week
Control	BR – basic ration (feed, diet);	BR
I	SR	SR + Se
II	SR	SR +Zn
III	SR	SR + I
IV	SR	SR + Se, Zn, I

Note: BR - basic ration (feed, diet); SR - semisynthetic ration (diet).

After a period of equalization the animals were divided into seven groups by the method of analogues pairs: one control and four experimental (n=20) and then transferred to the regimen of the main accounting period. The only difference was that the semisynthetic ration, developed by the Institute of Nutrition (2001), for the animal units of group I was supplemented per os by selenium – (selenopyran – 0,0001 g/head per day); of group II – zinc – (zinc sulfate – 0,042 mg/head per/ day; of the III group – iodine (potassium iodide in an amount of 0,332 g / day head per / day) and of the IV– trace complex I, Se, Zn.

During the experiment, slaughters of animals were practiced by decapitation under ether anesthesia-Rausch. Samples were taken to perform histological studies of the liver. The material was fixed in 10 % neutral formalin, followed by preparation of serial paraffin sections, with the thickness of 5 – 7 microns. Deparaffinized sections were imbued with hematoxylin-eosin. To identify glycogen and glycoproteins histochemical (periodic acid – йодная кислота) Schiff-reaction was used. The material was examined by the method light microscopy. The relative area of sinusoidal capillaries was determined with the help of ocular dot mesh-insert, and the eyepiece – with the help of the micrometer –first the diameter was measured and then the volume of hepatocyte nuclei and nucleoli calculated.

The elemental composition of biological substrates has been studied using atomic emission and mass spectrometry (ICP-AES and ICP-MS) in the test laboratory ANO «Center for Biotic Medicine», Moscow (accreditation certificate – SSES. RU.TSOA.311, registration number in the state register – Ross. RU 0001.513118 from May 29, 2003; Registration Certificate of ISO 9001: 2000, Number 4017 - 05/04/06). The investigation was fulfilled by the ICP-AES and MS- ICP methods, biosubstrates ashing was carried out using microwave decomposition system MD-2000 (USA). Evaluation of the content of elements in the resulting ash was performed by a mass spectrometer Elan 9000 (Perkin Elmer, USA) and atomic emission spectrometer Optima 2000 V (Perkin Elmer, USA). In total, the content of 14 chemical elements was determined, including Cu, Fe, Li, Mn, Ni, As, Cr, Zn, I, V, Co, Se, Si, B.

The obtained data are expressed as mean values±standard deviation (mean±σ). The results were worked up using the program Statistica 10.

RESULTS AND DISCUSSION

Our studies have shown that in the control group of animals the distribution of glycogen, detected by Schiff-reaction and verified by control pigmentation after treatment with amylase, was

little dependent on the internal localization of hepatocytes. The reaction differs among centrolobular and peripheral hepatocytes. The arrangement of cells rich in glycogen is mosaic.

When adding selenium, clear zonal location of cells rich in glycogen was observed. Centrolobular hepatocytes are deprived of glycogen, and Schiff-reaction is significantly expressed in peripheral cells. At this small glycogen granules merge to form large in size clumps of reserve glycogen. Sinusoid capillaries widen significantly near the central veins. In the number of cellular elements there are many small cells with round nuclei, which are found along clearly oriented hepatic beams, composing the wall of sinusoidal capillaries.

There exists an assumption that these Pit-cells are granular lymphocytes, which possess natural killer activity and simultaneously perform endocrine function. Due to this, they can (depending on conditions) have opposite effect: when the liver is damaged they as killers destroy the damaged hepatocytes, and during recuperation period they stimulate proliferation of hepatic cells similar to endocrine cells.

The addition of zinc to a balanced ration, after creating in an organism micronutrient deficiency, leads to a significant increase in the intensity of Schiff-reaction in all hepatocytes both in centrolobular, and in peripheral. Schiff-positive granules in the cytoplasm of the hepatocytes are fine, powder-like indicating that glycogen in these cells is more labile. The structure of hepatic beams is not broken, but sometimes there is lymphoid infiltration. We can assume that these are Pit-cells.

When you add iodine to a balanced ration the structure of liver beams is not broken, so as it is in the liver of control group of animals, location of rich in glycogen hepatocytes is mosaic, but the intensity of the reaction is more expressed.

In cells, lacking glycogen, vacuolization of the cytoplasm is observed, especially among binucleated hepatocytes.

Cytoplasm of most hepatocytes is enriched with glycogen with the insertion in the ration of the complex of micronutrients. Schiff-reaction was expressed more than in control especially in peripheral hepatocytes. Although in centrolobular hepatocytes reaction is less, expressed difference in color between centrolobular and peripheral cells is not observed.

Compared with the control the number of cells with medium and large in volume nuclei increases among hepatocytes, the number of nucleoli in them also enlarges, nuclear-nucleolar index reaches the minimum value (Table 2).

Table 2 Indicators of microstructures of centrolobular zone of liver

Group №	Relative area of sinusoidal capillary, %	Number of binucleated cells	Volume of the nucleus, mu³	The volume of the nucleolus, mu³	Nuclear-nucleolar index
Control	10,1 ± 1,30	2,66 ± 0,88	373,9 ± 0,83	1,34 ± 0,33	279,0
I experimental	20,1± 1,26***	5,16 ± 0,40	438,4 ± 0,74	4,59 ± 0,22	95,5
II experimental	14,6 ± 1,02	5,5 ± 0,42 *	447,7 ± 1,00	5,54 ± 0,21	80,8
III experimental	13,7 ± 0,88	4,83 ± 0,87	679,2 ± 0,46*	6,67 ± 0,30	101,8
IV experimental	17,3 ± 1,20	5,3 ± 0,49*	735,6 ± 0,74	9,28 ± 0,47	79,3

Note: * – $p \leq 0,05$, ** – $p \leq 0,01$, *** – $p \leq 0,001$

Morphometric analysis of liver structures denoted the mobility of these indicators depending on the mineral security.

In particular, the introduction of selenium in the ration was marked by the maximum increase of the observed relative area of sinusoidal capillaries by 10 % ($p \leq 0,001$) in the test group I relative the control group. Additional incorporation of zinc in the ration led to an increase in the number of binucleated cells twice in the experimental group II relative to the control. The maximum increase in the core was traced with the introduction of iodine in the ration. Thus, the core volume in test group III was 81,7 % ($p \leq 0,001$) higher relative the control. Volume of the nucleolus in the experimental group IV was the maximum value (9,28 mu^3), which was the result of lower nuclear-nucleolar index relative the control group.

This fact indicates an intensification of structural and metabolic processes in cells. Hepatic structure of beams is not broken.

Additional inclusion of the complex of essential elements in the ratio of rats, kept on deficient mineral ration, affects not only the morphofunctional structure of the liver, but also the quantitative composition of chemical elements in the studied organ (Table 3).

Table 3 Concentration of chemical elements in the rat liver, ug/g DS

Element	Group				
	Control	I	II	III	IV
Essential and conditionally essential microelements					
As	0,207± 0,025	0,205± 0,020	0,203± 0,025	0,200± 0,027	0,201± 0,024
B	0,039± 0,006	0,037± 0,005	0,033± 0,002	0,038± 0,001	0,036± 0,004
Co	0,079± 0,012	0,070± 0,011	0,080± 0,016	0,060± 0,009	0,062± 0,010
Cr	0,103± 0,012	0,102± 0,016	0,103± 0,013	0,100± 0,018	0,102± 0,012
Cu	5,10±0, 51	5,12 ±0,44	5,07±0, 41	5,09±0, 54	5,11±0, 52
Fe	469,0 ± 47,0	463±51 ,0	445,9± 48,9	451,3± 50,2	459,3± 48,9
I	0,199± 0,024	0,197± 0,022	0,188± 0,026	0,208± 0,028*	0,207± 0,020
Li	0,0019 ±0,000 37	0,020± 0,0003	0,0018 ±0,000 29	0,00±0, 0002	0,00019 ±0,000 35
Mn	2,98±0, 30	3,00±0, 31	3,04±0, 28	2,88±0, 29	3,0±0,3 1
Ni	0,02±0, 003	0,01±0, 002*	0,02±0, 007	0,03±0, 006	0,02±0, 004
Se	0,505± 0,061	0,581± 0,067*	0,506± 0,059	0,502± 0,063	0,597± 0,062
Si	33,77± 3,38	31,1±3, 22	33,2±3, 25	31,7±2, 93	33,4±3, 19
V	0,0016 ±0,000 32	0,0014 ±0,000 25	0,0016 ±0,000 19	0,0013 ±0,000 21	0,0014 ±0,000 28
Zn	29,4±2, 94	29,7±2, 67	33,6±2, 23*	28,3±3, 03	4,3 ± 3,01*

Note: * – $p \leq 0,05$, when comparing the control and experimental groups

It has been established that the addition of selenium to the ration increases the concentration of this element in the liver by 15,0% ($p \leq 0,05$) against the background of lowering nickel by 50,0% ($p \leq 0,05$) in the experimental group I relative to control. When you turn on zinc into the ration, the concentration of it increases by 14,3% ($p \leq 0,05$) in the experimental group II relative to the control.

Inclusion of iodine in the ration contributed to the increase of the iodine concentration by 4,52% in the experimental group III relative to the control group.

Feeding of complex essential elements contributed to increasing concentrations of iodine, manganese, selenium and zinc by 4,02; 3,36; 18,2 and 16,7% ($p \leq 0,05$) against the background of lowering concentrations of arsenic and vanadium by 2,90 and 12,5%.

CONCLUSIONS

Thus, the intake by the animal organism of toxic elements (lead and cadmium salts) leads to a change in the structural elements of the liver, resulting in depletion of hepatocyte in glycogen, or its complete disappearance, in offensive vacuolization and necrosis of hepatocytes and in changes in vessels diameter microvasculature, i.e. structural and functional changes in the liver are identified. Introduction into the ration of complex of essential trace elements (I, Se, Zn) involves an increase in functional activity of the liver. Additional administration of a complex of essential elements in the ration increases the concentration of iodine, manganese, selenium and zinc in the liver against the background of lowering nickel, vanadium and arsenic.

ACKNOWLEDGEMENTS

Research was done with financial support of the Russian Science Foundation №14-16-00060.

REFERENCES

[1] Avtandilov GG, «Medical morphometry», M.: Medical, 1990:384 p.

[2] Kanamura S, Asada-Kubota M, «The heterogeneity of heap tocytes during the postnatal development of the mouse», Anat. Embriol, 1980;158:151-59.

[3] Lebedev SV, «Morfofunction of the condition of the liver upon toxic organism loading of doses of cadmium and lead in diets with mineral substanses», Cell Biology and Toxicology, 2008; 24 (Suppl 1):87-9.

[4] Kedderis GL, «Biochemical basis ofhepatocellular injury», Toxicol. Pathol, 1996; 24:77-83.

[5] Lu H, Hu J, Li J, Pang W, Hu Y, Yang H, Li W, Huang C, Zhang M, Jiang Y, «Optimal dose of zinc supplementation for preventing aluminum-induced neurotoxicity in rats», Neural Regen Res. 2013;8(29):2754-62.

[6] Tinkov AA, «Adipose tissue chromium and vanadium disbalance in high-fat fed Wistar rats», J Trace Elem Med Biol., 2014; Aug 2. pii: S0946-672X(14)00137-0.

[7] Erkekoglu P, Arnaud J, Rachidi W, Kocer-Gumusel B, Favier A, Hincal F, «The effects of

di(2-ethylhexyl) phthalate and/or selenium on trace element levels in different organs of rats», J Trace Elem Med Biol., 2014 Aug 19. pii: S0946-672X(14)00156-4.

[8] Monedero-Prieto MJ, «Effects of selenium on liver and muscle contents and urinary excretion of zinc, copper, iron and manganese», Biol Trace Elem Res., 2014 May;158(2):224-9.

[9] Churin BV, Trunova VA, Sidorina AV, Zvereva VV, Astashov VV, «Effects of zinc on the content of chemical elements in the liver of rats during early stages of obesity», Bull Exp Biol Med. 2013 Dec;156(2):196-200.

[10] Permenter MG, Dennis WE, Sutto TE, Jackson DA, Lewis JA, Stallings JD, «Exposure to cobalt causes transcriptomic and proteomic changes in two rat liver derived cell lines»,
PLoS One. 2013 Dec 30;8(12):e83751.

[11] Charradi K, Mahmoudi M, Elkahoui S, Limam F, Aouani E, «Grape seed and skin extract mitigates heart and liver oxidative damage induced by a high-fat diet in the rat: gender dependency» Can J Physiol Pharmacol. 2013 Dec;91(12):1076-85.

[12] Fatima SN, Mahboob T, «Role of selenium in protection of liver cirrhosis», Pak J Pharm Sci. 2013 Nov;26(6):1097-102.

[13] Pal A, Badyal RK, Vasishta RK, Attri SV, Thapa BR, Prasad R, «Biochemical, histological, and memory impairment effects of chronic copper toxicity: a model for non-Wilsonian brain copper toxicosis in Wistar rat», Biol Trace Elem Res. 2013 Jun;153(1-3):257-68.

[14] Ergen K, Ince H, Düzova H, Karakoç Y, Emre MH, «Acute effects of moderate and strenuous running on trace element distribution in the brain, liver, and spleen of trained rats», Balkan Med J. 2013 Mar;30(1):105-10.

[15] Fatmi W, Kechrid Z, Nazıroğlu M, Flores-Arce M, «Selenium supplementation modulates zinc levels and antioxidant values in blood and tissues of diabetic rats fed zinc-deficient diet», Biol Trace Elem Res. 2013 May;152(2):243-50.

[16] Sivrikaya A, Akil M, Bicer M, Kilic M, Baltaci AK, Mogulkoc R, «The effect of selenium supplementation on elements distribution in liver of rats subject to strenuous swimming», Bratisl Lek Listy. 2013;114(1):12-4.

[17] Kim KH, Funaba M, Yoshida M, Matsui T, «The effects of magnesium deficiency on molybdenum metabolism in rats», Biol Trace Elem Res. 2013 Jan;151(1):100-4.

[18] Medici V, «The evolving scenario of copper and fatty liver», Metab Syndr Relat Disord. 2013 Feb;11(1):4-6.

First International Conference on Science, Engineering & Environment,
Tsu City, Mie, Japan, Nov.19-21, 2015, ISBN: 978-4-9905958-5-2 C3051

A NOVEL QUANTIFICATION OF THE COMPLEX GEOMETRIES OF LOW LIGHT SURVIVING PLANTS USING FRACTAL ANALYSIS TO INVESTIGATE A BASIS OF A NEW AND UNIQUE ALLOMETRIC MEASURE OF PLANTS

Chaitanya D. Karamchedu[1]
[1]Jesuit High School, Portland, OR – 97225, USA

ABSTRACT

This study explored plant architecture and growth using a novel application of mathematical tools. Fractal analysis of plant architectures was performed to quantify and describe functional obligations of plants, photosynthesis in particular. The methods used for this study included a) the assimilation of various plant species' profiles from the USDA database, b) computation of fractal dimensions and derived measures and c) statistical analysis of these measures. Initial results from this study suggests that a) plants surviving in low light conditions have fractal dimensions within a characteristic range of 1.6 - 1.85, suggesting that the fractal dimension strongly reflects a branching and photosynthesis strategy to maximize available light for energy production. b) Plants exhibit distinct fractal geometries at the leaf level and the whole plant level. The fractal dimensions of the plant (FDP), the leaf (FDL) and the ratio of the two (FDR=FDL/FDP) may serve as numeric descriptors of the photosynthesis strategy of related plants, suggesting its use as a new taxonomic descriptor. c) This study also suggests that there is a correlation between the fractal dimensions and the metabolic demand of a plant and could help identify deviations from the expected metabolic demand predicted by its expected FDR values due to growth. d) The fractal measures including the fractal dimension ratio is potentially a new and useful allometric tool. This could aid in refining biomass calculations and in the estimation of carbon sequestration potential of plants, as current models may be overestimating these values.

Keywords: Allometry, Biomass, Fractal Analysis, Photosynthesis

INTRODUCTION

Plants that survive in low light conditions are known to have complex geometries represented in their foliage, particularly in relation to plants that don't survive in lower light conditions [1]. These adaptations suggests that they are critical to the plant fulfilling its functional obligations under the specific environmental constraints that it operates in. One such functional obligation that the plant needs to fulfil is photosynthesis under the specific environmental constraint of low light availability.

While many of the adaptations in plants are biochemical and molecular in nature, there are also significant geometric adaptations in the form and growth of such plants [2]. Irregularity and complexity is a defining characteristic, not merely of such adaptations in plants, but of the very general form of plants itself. Pioneering work by Mandelbrot introduced fractal mathematics, a mathematics of understanding the irregular forms and structures in nature [3]. One central concept in this form of analysis is that of the fractal dimension, also known as the Hausdorff-Besicovitch dimension. This is a measure of irregularity or fracture of a form under consideration.

The primary question that motivates this study is - what is the relationship between the fractal geometry of the form of plants and the plant's functional obligations?

Prior research in these areas have considered a) the distinct complex geometries of low light surviving plants[1], b) the features and consequences of shade tolerance [2] [4], c) the mathematical analysis of tree architecture to aid in the understanding of a trees structure-function relationship [5] [6] and d) the use of allometric analysis in biomass estimations. [7][8]. Some of these studies have investigated the use of fractal geometries[9] to better specify and understand the varied effects of form and function and acclimation to light availability, such as leaf thickness, mesophyll thickness, shoot modifications and age dependent changes [10].

These studies inspire questions about underlying mathematical traits of such complex geometries. Can we quantify this complex geometry in precise mathematical terms? How does this complexity compare to plants that do not thrive with leaves in low light conditions? How does the measure of the complex geometries of low light surviving plants aid in the understanding of the functional obligations of

the plant.

Several of the studies mentioned above attempt to infer biomass of plants based on allometric measures [8]. These studies attempt to increasingly refine biomass estimation techniques, but some of the underlying models such as 3D tomography [10] do not allow for the practical incorporation over vast areas in a non-destructive manner. Furthermore, these studies ignore the effects of seasonal change, age, and disease or habitat degradation on the structure of the plant. The main questions that this study seeks to answer are:

A) Can the complex geometry of the foliage of low light surviving plants be identified by a quantifiable measure?

B) Is the plant's overall architecture represented by such quantifiable measures?

C) Beyond the descriptive value of these measures, do such measures have a predictive value? Does such a measure help to predict the metabolic demand of a plant?

D) Is there a value for such measures in helping to assess biomass distributions?

MATERIALS AND METHODS

Compilation of Data

Several techniques were employed to compile data for this study.

Compilation of Empirical Field Data

Direct field work was done using a digital camera to assimilate photographs of a wide variety of plants in the Pacific Northwest region of the United States. The plants photographed included shade tolerant and intolerant plants and plants with winter foliage.

Compilation of plant photographs and details from USDA & Wikipedia.

Wikipedia and the USDA's online database of plants (http://plants.usda.gov/gallery.html) was used to compile taxonomic, allometric and geographic data about a variety of plants.

For a smaller subset, photographs of saplings of these plants were also compiled where available.

Compilation of Plant Biomass

Above ground tree mass was compiled from two separate sources. The online resource from the "Hubbard Brook Ecosystem Project" [11] operated by the USDA was used to compile biomass for plants that were catalogued in that database. Above ground tree biomass was also compiled from the online resource of the Canadian Forestry Service [12].

Compilation of Fractal Dimension of Plants

Fractal dimension of photographs were evaluated and compiled for all the photographs using the box counting method. Two software tools were considered, the first was a tool developed by the Japanese National Food and Agricultural Organization and the other was a tool developed by the Charles Sturt University of Australia [13], (http://seit.unsw.adfa.edu.au/staff/sites/dcornforth/Fractop/index.html).

Data Analysis Methods Used in This Study

For question A, fractal dimensions of the various plants that were either low light surviving or not were plotted against the survivability criteria and visually examined to identify any discernable pattern. ANOVA tests were performed on this data to test any discernable variation in the fractal dimensions.

For question B, the fractal dimension of the whole plant and leaf structures were distinctly computed and used to derive their interrelationship, designated as the 'Fractal Dimension Ration' (FDR). ANOVA analysis was performed to ascertain if the whole plant fractal dimension revealed a distinct measure compared to the fractal dimensions of the leaf structures, and to identify any discernable changes in these measures for related species.

For question C, the fractal dimension of the saplings were compared against those of the mature tree to discern any significant deviation between the two.

For question D, linear multi-variable regression analysis was performed to determine the effect of the FDR on the biomass of the plant

DATA ANALYSIS, RESULTS & DISCUSSION

A. Can the complex geometry of the foliage of low light surviving plants be identified by a quantifiable measure?

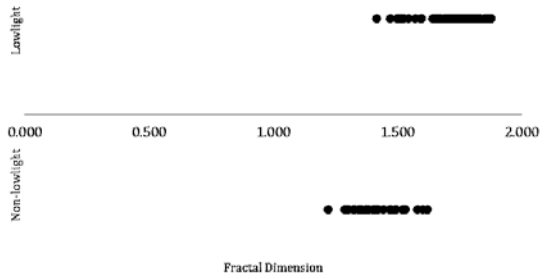

Fig. 1 Lowlight Survivability: Fractal dimensions of plants based on their ability to thrive in lowlight

The operating assumption for the hypothesis of this question was that the complex adaptations of the leaves of plants that thrive under low light conditions must be reflected in the fractal geometry of the plant. In the absence of any such distinction of fractal geometries between the groups of plants that thrive in low light versus those that do not, there should not be any significant variance of the means of these groups. Preliminary ANOVA analysis of the data shows that there is indeed a variance of the means among these groups. As reflected above, the low p-values and the high ratio of F to F-crit suggest

a strong distinction in the fractal dimension and hence in the architecture, of low light thriving plants compared to those that do not.

TABLE I
STATISTICAL ANALYSIS OF FRACTAL DIMENSIONS OF LOWLIGHT AND NON-LOWLIGHT PLANTS

Groups	Count	Average	Variance
Lowlight	61	1.7130	0.0124
Non-lowlight	25	1.422	0.0108

Anova

Source of Variation	*SS*	*df*	*MS*	*F*	*P-value*	*F crit*
Between Groups	1.5	1	1.5	125.173	2.51×10^{-18}	3.954
Within Groups	1.006	84	0.012			
Total	2.506	85				

Examination of the frequency distribution of the fractal dimension of plants reveals bi-modal distribution, suggesting the operation of clearly distinct forces on the fractal dimension of the plants. The sample dataset chosen for this analysis contained an assortment of plant species, with the only common distinction between the groups being their ability to thrive in low light, and the bimodality in the distribution appears to reinforce the effect of this adaptation on the fractal dimension of the plants.

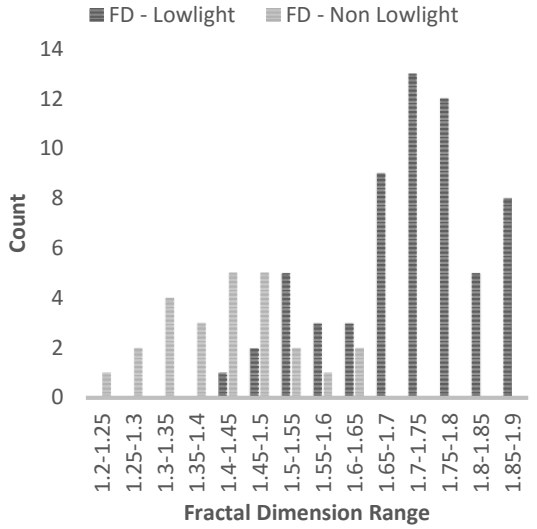

Fig. 2 Bi-modal distributions of fractal dimensions

Questions arise regarding the reasons why low light survivability must affect the fractal dimension of the plant. The plant's ability and adaptations to survive in low light is confounded with the fact that many of these plants also survive winter. The plant's own foliage structures are clearly governed by many such factors including its genetic constitution. This inspires the following question - what could be the reason for a common effect on the fractal dimension, when there are many underlying factors that controls the foliage geometry?

One potential argument is the nature of competing functional obligations of the plant. Regardless of the genetic constitution and winter adaptations, all plants that thrive in low light probably have selective pressures to maximize photosynthesis under depleted light availability. Expansive foliage, with a broad and flat surface, limits the ability to maximize sunlight due to the limiting effects on surface areas. This is because, it further casts a shadow and renders the volume under the leaf useless for photosynthesis. Plants that allowed for sinuses and fractures in the foliage would therefore make more light available to the lower layers to also participate in photosynthesis, thereby conferring a potential advantage to survivability. However, such a fracture or sinus architecture cannot be maximized beyond a limit, because the very nature of the fracture reduces the per leaf photosynthesis potential, thereby creating a competing force. The range of geometric variations for these competing forces therefore appear restricted. This mutually limiting set of constraints for photosynthetic efficiency could account for the narrower range of allowable fractal dimensions. Initial data suggests that the optimal range of fractal dimension to balance these competing interests in between 1.6 – 1.85.

This argument does not make the claim that a plant's fractal dimension in the 1.6-1.85 automatically confers lowlight survivability. Nor does it make the claim that low light surviving plans cannot have fractal dimensions outside this range. Further research is necessary to identify counter examples for the putative optimal range identified here, and the implications thereof.

B. Is the plant's overall architecture represented by such quantifiable measures?

The fractal dimension of the overall foliage (FDP) reflects the degree of fracture of the whole plant. The fractal dimension of the specific leaf arrangement (FDL) reflects the fracture geometry of the local leaf arrangement. In idealized shapes for fractal analysis, the fractal dimensions of the whole and part are scale invariant, and hence should not be distinct.

TABLE II:
FDL AND FDP REPRESENT DISTINCT MEASURES OF THE PLANTS GEOMETRIC ADAPTATION

Groups	*Count*	*Average*	*Variance*
FDL	76	1.650	0.025
FDP	76	1.729	0.013

However, ANOVA

analysis reveals that there is a very clear distinction in fractal dimensions of the whole plant foliage versus that the fractal dimension of the leaf arrangements by themselves (F/F-crit = 3.1, p=0.0005), suggesting distinct forces directing the degree of fracture for the whole plant, versus the degree of fracture of smaller leaf level units, hence the FDL and FDP are distinct and important measures. Significantly, these values tend to be close to each other leading to ratio significantly clustered around 1.

Fig. 3 Photosynthesis strategy of Pinaceae

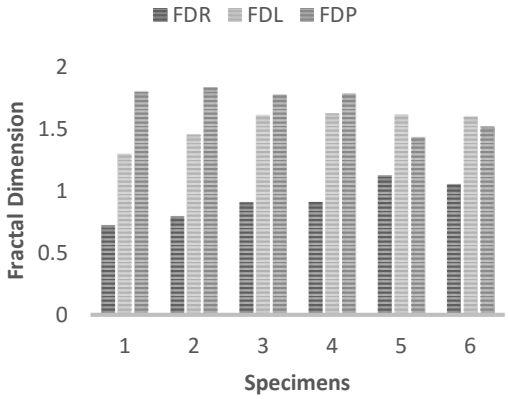

Fig. 4 Photosynthesis strategy of Fagaceae

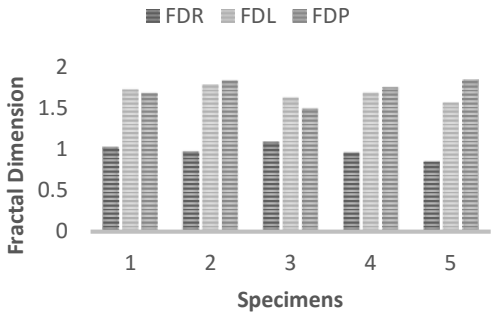

Fig. 5 Photosynthesis strategy of Sapindaceae

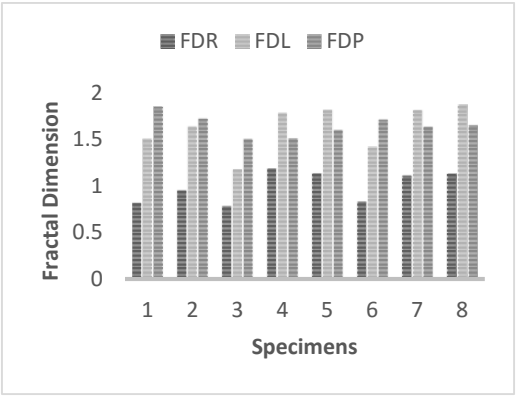

Fig. 6 Photosynthesis strategy of Betulaceae

TABLE III:
FDL AND FDP REPRESENT DISTINCT MEASURES OF THE PLANTS GEOMETRIC ADAPTATION

Groups	*Count*	*Average*	*Variance*
FDL	76	1.650	0.025
FDP	76	1.729	0.013

ANOVA

Source of Variation	*SS*	*df*	*MS*	F	*P-value*	*F crit*
Between Groups	0.239	1.000	0.239	12.366	0.001	3.904
Within Groups	2.900	150.000	0.019			
Total	3.140	151.000				

Larger values of FDL indicates flatter leaves, versus thinner leaves for lower values of FDL. Larger values of FDP indicate more dense foliage, versus lower values for more open foliage. This suggests four categories of photosynthesis architectures that the combination of FDL and FDP lead to, as represented by Table IV.

TABLE IV
PHOTOSYNTHESIS STRATEGY CATEGORIES

	Thin – Low FDL	Flat – High FDP
Dense – High FDP	Sieve – A dense canopy with thin leaves	Basket – A dense canopy with flat leaves
Open – Low FDP	Lattice – An open canopy with thin leaves	Mosaic – An open canopy with flat leaves

Within each photosynthesis strategy, the ratio of FDL to the FDP indicates whether the plant's overall foliage arrangement is more fractured (FDR>1) than the leaves themselves, or whether the leaves are more fractured. Examination of the FDR of a wide variety of plants, both low light surviving and others suggests that the FDRs tend towards a value of 1; an indication of the mutually compensatory nature of the fracture of leaves and overall foliage. Extending the discussion from Question 1, this FDR, along with the FDP and FDL appears to characterize the overall plants photosynthesis architecture.

In the discussion for question 1, we considered the mutually competing pressures of maximizing photosynthetic efficiency of a leaf, while allowing for effective photosynthesis for lower or inner layers

of leaves in the plant. The plant's branching pattern and bifurcation strategy in combination with the leaf arrangement affects the overall degree of fracture of the plants foliage, the FDP. The leaf's arrangement around the twig affects the degree of fracture of the leaf structures, the FDR. The ratio, FDR, then indicates whether the leaves are more fractured than the plant or vice-versa.

The combination of FDL and FDP suggests a classification of the plant's photosynthesis strategy into the categories mentioned above. This, in conjunction with FDR, then appears to be a fundamental descriptor of the plants architecture and branching strategy in relation to its foliage and photosynthetic obligation. This study suggests that the FDR, FDP and FDL are a potentially useful and comprehensive descriptor of the plant architecture in addition to the bifurcation ratios currently being studied [6].

C. Beyond the descriptive value of these measures, do such measures have a predictive value? Does such a measure help to predict the metabolic demand of a plant?

So, assuming no fundamental change in the efficiency of photosynthesis, maintaining steady state metabolic demand would cause an increase in surface area due to scaling up. Central to this question is whether the fractal dimensions of the plant foliage, suggestive of the photosynthetic strategy of the plant, are predictive of the metabolic demands of the plant.

Basic geometry of scaling [5] suggests a power law in operation, where a scaling up in the form of the plant results only in a fractional increase in surface area for a unit increase in volume. Various studies have estimated this to be the $2/3^{rd}$ power of the volume [5]. This analysis makes the simplifying assumption that the surface area is representative of the photosynthetic capacity, and the volume of the plant is representative of the metabolic demand of the plant. Hence, in the hypothetical scenario where there are no additional functional obligations of the plant, an idealized scaling up would create a deficit in the photosynthetic output of the plant, for its corresponding increase in volume, hence its metabolic demand. This deficit can only be met either by a change in the surface geometry of the plant to compensate for the deficit in surface area, or by a fundamental change in the energy efficiency of the leaves themselves. Conversely, any variation from the expected compensatory change in surface area is indicative of a proportionate change in the metabolic demand of the plant itself.

Preliminary data from this study reveals that the fractal dimension of saplings are distinctly different from their corresponding mature state. There is a discernable difference in the mean of these two groups as well, indicated by the F and F crit values of the data. Curiously, the sapling stage of the plants have a lower fractal dimension, indicating that the saplings are more fractured that the adult form, and therefore have relatively more surface area than the mature form of the plant. This is clearly a significant deviation from the norm in an idealized Euclidean shape, where the smaller scaled object has a lower surface area than the larger one relative to its volume. Based on the prior discussion on the compensatory increase in surface area to meet the metabolic demand, this suggests that the sapling stages have a relatively higher metabolic demand compared to the plants mature form.

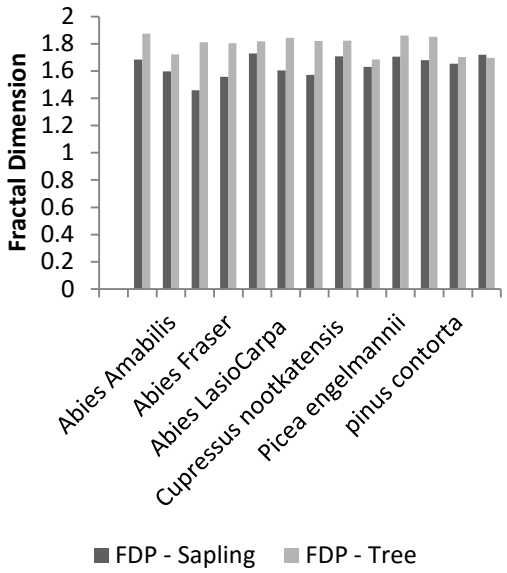

Fig. 7 Differences between saplings and mature plants

TABLE V
DIFFERENCES BETWEEN SAPLINGS AND MATURE PLANTS

Groups	*Count*	*Sum*	*Average*	*Variance*
FDP - Sapling	14	23.043	1.645929	0.006493
FDP - Tree	14	24.931	1.780786	0.006496

ANOVA

Source of Variation	*SS*	*df*	*MS*	*F*	*P-value*	*F crit*
Between Groups	0.127	1	0.127	19.6	0.00015 2	4.225
Within Groups	0.168	26	0.006			
Total	0.296	27				

D. Is there a value for such measures in helping to assess biomass distributions?

Techniques for accurate and non-destructive estimation of biomass in becoming increasingly important. Current techniques employ models that

account for the effects of plant diameter and height in the calculations of biomass. [8]. A basic form some of these models use is $M = aD^b$, where M is the mass of the plant, D is the diameter and D^b includes the effect of the height, [7].

One consequence of this model is it ignores the wide range of consequences shading and light availability has on the overall biomass. Studies have shown the significant effects of light availability and the plants adaptations to light availability on biomass [2].

One possible method to incorporate the effects of light availability to the plant on the overall estimation of biomass is to use the FDR and develop a new regression model. In such a model, the straightforward use of the power b to adjust for of the effect of height may seem premature, as the plants adaptations vary with height [2]. A regression model that distinctly considers all these three variables was developed based on the data of this study.

TABLE VI
REGRESSION ANALYSIS

ANOVA					
	df	*SS*	*MS*	*F*	*Significance F*
Regression	3	16.706	5.569	58.396	$1.05x10^{-13}$
Residual	35	3.338	0.095		
Total	38	20.044			

R Square 0.833

	Coefficients	*Upper 95%*	*Standard Error*	*t Stat*	*P-value*
Intercept	3.320	4.141	0.404	8.217	$1.105x10^{-09}$
FDR	-0.807	-0.022	0.387	-2.087	0.044
Height L	0.007	0.018	0.005	1.372	0.178
Diameter	0.008	0.010	0.001	7.654	$5x10^{-09}$

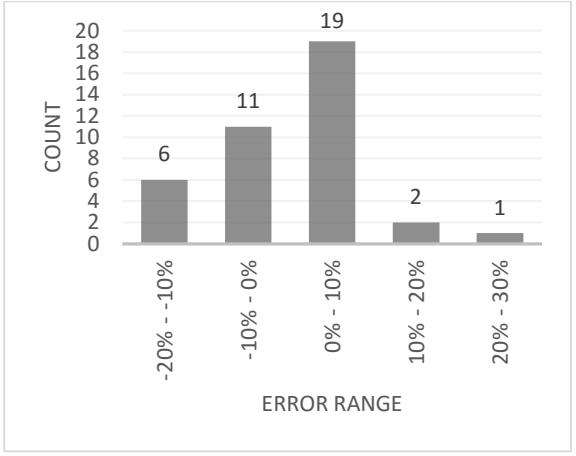

Fig. 8 Distribution of deviations from current biomass predictions

The results suggest that:

a) The FDR is strongly predictive and negatively correlated with the above ground biomass of the plant (p-value of .04, and a negative slope).
b) The height of the plant is not strongly predictive (p-value 0.17) of the above ground biomass
c) The diameter of the plant is strongly predictive of the biomass (p-value $5.5x10^{-09}$)This regression model also suggests that the form of the biomass as

$$M = k1^{aD} * k2^{b*FDR} * k3^{c*H} \quad (1)$$

Leading to a form

$$\boldsymbol{Log(M) = K_0 + K_1(D) + K_2(FDR) + K_3(H)} \quad (2)$$

Where K_0 = 3.32(P<0.0001),
K_1= 0.008(p=$5.59x10^{-9}$),
K_2=-0.807(p=0.044) & K_3=0.007(p=0.178)

REFERENCES

[1] U. Niinemets, "Photosynthesis and resource distribution through plant canopies," Plant, Cell and Environment, 2007, pp. 1052-1071,.

[2] F. V. a. U. Niinemets, "Shade Tolerance, a Key Plant Feature of Complex Nature and Consequences," The Annual Review of Ecology, Evolution, and Systematics, 2008, pp. 39:237-257.

[3] B. B. Mandelbrot, The Fractal Geometry of Nature, Freeman, 1997.

[4] D. Westmoreland, "Developmental Plasticity in Oak Leaves," in Proceedings of the 16th Workshop/Conference of the Association for Biology Laboratory Education (ABLE), 1995.

[5] K. J. Niklas, Plant Allometry - The Scaling of Form and Process, Chicago, London: The University of Chicago Press, 1994.

[6] R. B. a. N. A. Slade, "Bifurcation Ratios And The Adaptive Geometry Of Trees," Botanical Gazette, 1981, pp. 142(3):394-401.

[7] M. M. Dimitris Zianis, "On Simplifying Allometric Analysis of Forest Biomass," Forest Ecology and Management 187, 2004, pp. 311-332.

[8] David Pare', "Estimating stand-scale biomass, nutrient contents, and associated uncertainities for tree species of Canadian forests," Canadian Journal of Forest Resources, 2013, pp. 43:599-608.

[9] Y. Peitgen, Fractals For The Classroom, New York: Springer-Verlag, 1992.

[10] Pierre Dutilleul, "Plant Light Interception Can Be Explained via Computed Tomography Scanning: Demonstration with Pyramidal Cedar (Thuja occidentalis, Fastigiata)," Annals of Botany , p. 101: 19–23, 2008.

[11] "Interactive Biomass Program," [Online]. Available: http://www.hubbardbrook.org/w6_tour/biomass-stop/single-tree-biomass.htm.

[12] "Natural Resources Canada," [Online]. Available: https://apps-scf-cfs.rncan.gc.ca/calc/en/calculateur-calculator.

[13] "FracTop," [Online]. Available: http://seit.unsw.adfa.edu.au/staff/sites/dcornforth/Fractop/index.html.

First International Conference on Science, Engineering & Environment,
Tsu City, Mie, Japan, Nov.19-21, 2015, ISBN: 978-4-9905958-5-2 C3051

COMPARATIVE ISOTHERMS STUDIES ON ADSORPTIVE REMOVAL OF METHYL ORANGE FROM WASTEWATER BY WATERMELON RINDS AND NEEM-TREE LEAVES

Sadiq Sani[1] and Muhammad Bashir Ibrahim[2]
[1]Faculty of Science and Education, Federal University Dutsinma, Nigeria; [2]Bayero University Kano, Nigeria

ABSTRACT

Powdered watermelon rinds (WRP) and neem leaves (NLP) adsorbents were used for equilibrium adsorption isotherms studies for detoxification of methyl orange dye (MO) from simulated wastewater. The applicability of the process to various isotherm models was tested. All isotherms from the experimental data show excellent linear reliability (R^2: 0.9487-0.9992) but adsorptions onto WRP are more reliable (R^2: 0.9724-0.9992) than onto NLP (R^2: 0.9487-0.9989) except for Temkin's Isotherm where reliability is better onto NLP (R^2: 0.9937) than onto WRP (R^2: 0.9935). Dubinin-Radushkevich's monolayer adsorption capacities for both WRP and NLP (q_D: 20.72 mg/g, 23.09 mg/g) are better than Langmuir's (q_m: 18.62 mg/g, 21.23 mg/g) with both capacities higher for adsorption onto NLP (q_D: 23.09 mg/g; q_m: 21.23 mg/g) than onto WRP (q_D: 20.72 mg/g; q_m: 18.62 mg/g). While values for Langmuir's separation factor (R_L) for both adsorbents suggest unfavourable adsorption processes (R_L: -0.0461, -0.0250), Freundlich constant (n_F) indicates favourable process onto both WRP (n_F: 3.78) and NLP (n_F: 5.47). Adsorption onto NLP has higher Dubinin-Radushkevich's mean free energy of adsorption *E* (0.13 kJ/mol) than WRP (0.08 kJ/mol) and Temkin's adsorption heat (b_T) is better onto NLP (b_T: -0.54 kJ/mol) than onto WRP (b_T: -0.95 kJ/mol) all of which suggest physical adsorption.

Key words: Watermelon rinds, Neem leaves, Methyl orange, Adsorption isotherms, Isotherm parameters.

INTRODUCTION

The dependence of humans on water as an essential necessity for survival has been threatened by water scarcity which affects 40% of the world population (about 1.2 billion) projected to reach 2.7 billion by 2025, water borne diseases claiming annual death rate of 5 to 10 million and pushes global water demand to double every 21 years [1,2]. Of the about 71% of the earth surface occupied by water, only about 0.05% is accessible for human consumption while the bulk of the remaining comprises of the inaccessible seawater, groundwater, swamps and frozen polar ice caps [1]. The scarcity of water is due to rapid population growth, increased industrialization and decreased amounts of rainfall in the previous decades [3]. More so, water pollution by untreated synthetic dye effluents released from industries has been identified as one of the consequences of worsening situation of water scarcity in the society.

Dyes are complex chemical substances that bear stable aromatic rings synthesized to impart strong and persistent colour that does not degrade on exposure to light [4,5]. Although natural dyes are still in rare use, almost all dyes in use today are synthetic with annual production of over $\mathbf{7 \times 10^5}$ tonnes of which azo dyes account for 60–70% [6]. About 10-15% of these dyes are discharged as untreated effluents during the dyeing process [7,8].The untreated effluent discharged from textile, cosmetics, pulp and paper, paint, pharmaceutical, food, carpet and printing industries is highly coloured due to large amounts of unfixed dyes that remained during colouring and washing [9,6]. Untreated dye effluents are toxic and non-biodegradable environmental pollutants that prevent re-establishment of microbial populations, degrade water quality permanently, cause allergy, dermatitis, cancer, skin irritation, dysfunction of kidneys, liver and reproductive system in humans [10,11]. In other words, it could leach into and pollute surface and ground waters used for drinking; affect the photosynthesis of aquatic plants by hindering penetration of light into the water; and may cause suffocation of aquatic flora and fauna due to anaerobic degradation of azo dyes into highly lethal substances [12-14].

Thus, to overcome the challenges of water scarcity and ensure safe water exploitation, much attention has been devoted to developing cost-effective technologies for water/wastewater treatment for sustainable industrial and agricultural development. Traditional and conventional techniques usually employed for the treatment of dye wastewater consist of biological, physical and chemical methods which are mostly inadequate, ineffective, expensive, complicated, time-consuming and require highly-skilled personnel especially at 1-100 mg/L levels of dissolved dye adsorbates [15].

Conventional adsorption methods using activated carbons pose disadvantages of sludge disposal problems, high costs of operation, maintenance, adsorbent purchase and sludge regeneration [16,17].

However, proposed non-conventional techniques using agricultural wastes materials and by-products as adsorbents are relatively cheaper, environmentally friendlier and more efficient than conventional adsorbents for the removal of dyes even at trace level. The methods utilize the ability of the waste materials to accumulate dye pollutants from waste streams by purely physico-chemical pathways of uptake. Their adsorption capacities are studied and evaluated using adsorption equilibrium isotherms under optimized conditions of agitation time, adsorbent dose, adsorbents particle size, initial dye concentration and initial pH of dye [17-19]. The substrates are renewable resources available in large quantities with little or no value in most countries. Their utilization in dye removal poses the dual advantages of effective wastewater treatment and waste management. They usually have high molecular weight due to the presence of lignin, cellulose and hemicelluloses components [20]. Many agricultural waste adsorbents (rice husks, corncob, coir-pith, plum kernels, bagasse pith, nut shells, fruit peels, leaf powders, spent tea leaves, fruit shells, seed husk, saw-dust, hyacinth root, etc.) were reported as cost-effective alternative low cost adsorbents for dyes removal from wastewater in the recent past decades [21]. The aim of this study is to compare various adsorption isotherms for the adsorption of methyl orange dye from simulated wastewater.

MATERIALS AND METHODS

Adsorbents and adsorbate reagent

Adsorbents used in this work were derived from the fresh agricultural solid wastes of watermelon (*Citrullus lanatus*) rinds and neem-tree (*Azadirachta indica*) leaves. The watermelon rinds were collected from local fruit vendors at Kofar Kaura and Central Market in Katsina Metropolis while neem-tree leaves were collected from twigs of matured neem-trees within and near the main campus of Umaru Musa Yar'adua University, Katsina.

Methyl orange (*p*-dimethylamino-azobenzenesulphonic acid sodium salt), its structure shown in Figure 1, is a mono-azo dye supplied from Fluka Chemicals. Its 1000 mg/L stoke solution was prepared by dissolving accurately weighed 1.0 g of the dye solute in 1000 cm^3 of de-ionized water and all desired concentrations in the subsequent experiment were obtained by further dilution [22].

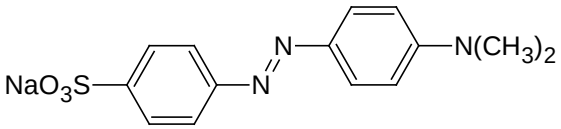

Fig. 1 Structure of Methyl Orange Dye

Adsorbent Samples Preparation

Neem leaves samples collected were excessively washed with tap-water, rinsed copiously with distilled water to remove dust and any other soluble substances. The leaves were allowed to dry for seven days under a shade at room temperature until they become crisp. The dried leaves samples were then pulverized with a mechanical electronic grinder into fine powdered form; and then dried overnight for 16 hours in an oven at a temperature range of 65℃ as heating beyond the range of $35 - 45$℃ above the ambient temperature may decompose the active sites on the samples. The oven-dried neem-tree leaves powder (NLP) samples were sieved to the size range of 75 – 300 μm using electronic sieve shaker and the fractions preserved in separately labelled air-tight plastic containers according to their particle sizes for use as adsorbents in adsorption experiments. Similar procedure was carried out on sliced pieces of fresh watermelon rinds samples with the powdered fractions (WRP) separately preserved in labelled plastic containers for use as adsorbents in the adsorption experiments [21,23].

Batch adsorption experimental procedure

Experiments on the adsorption of methyl orange by WRP and NLP were carried out by batch method and the influence of various parameters such as contact time (5 – 240 min), adsorbent dosage (100 – 500mg), particle size ($\leq 75\mu m$, $\leq 150\mu m$, $\leq 250\mu m$, $\leq 300\mu m$ and $> 300\mu m$), initial dye concentration (5 – 300mg/L) and initial dye pH (2-12) were studied at constant agitation speed of 300 rpm and room temperature (25°C) in triplicates. The adsorption measurements were conducted by mixing various amounts of adsorbent in 150-cm^3 Erlenmeyer glass flasks containing 50 cm^3 of dye solution of known concentration. The initial pH of the dye solutions were adjusted to the desired values by adding few drops of 0.1M HCl or 0.1M NaOH aqueous solutions [24]. The solutions were agitated using orbital shaker for a predetermined time to attain equilibrium. At the end of predetermined or equilibrium time intervals, the samples were taken out and the supernatant solution was separated from the adsorbent by filtration with Whatman No. 41 filter paper, discarding the first few volume (3-4 drops) of the filtrate [24]. The filtrates were used for analyses using UV-vis spectrophotometer, reporting each data point as an average value of the triplicates recorded. In each case, the percentage adsorption

and substrate's equilibrium adsorption capacity, q_e (mg/g) were evaluated using Equations 1 and 2.

$$\%\,\text{Adsorption} = \left[\frac{C_O - C_e}{C_O}\right] \times 100 \quad (1)$$

$$q_e = \frac{V(C_O - C_e)}{W} \times 100 \quad (2)$$

where $\boldsymbol{C_o}$ (mg/L) is the initial dye concentration, $\boldsymbol{C_e}$ is the concentration at equilibrium or predetermined time *t*, $\boldsymbol{V}$ (L) is the volume of dye solution used and $\boldsymbol{W}$ (g) is the weight of the adsorbent.

Equilibrium adsorption isotherm models

The various isotherms used in this study were enumerated in Table 2. Langmuir adsorption isotherm is the most widely used two-parameter model to explain the monolayer adsorption of dyes from aqueous solutions in testing the possible adsorption mechanism by adsorbents. The dimensionless equilibrium parameter called the separation factor, R_L in Equation (3), is an extension of Langmuir's Equation introduced to predict the favouravility of adsorption process (Bhattacharyya and Sharma, 2004). For favourable adsorption isotherm $0 < R_L < 1$, irreversible if $R_L = 0$, linear if $R_L = 1$ and unfavourable if $R_L > 1$ [25,26].

$$R_L = \frac{1}{1 + K_L C_e} \quad (3)$$

Freundlich's empirical isotherm Equation is often used to describe non-specific adsorption (Table 2). It is valid for $1 < |n| < 10$ [25]. Temkin adsorption isotherms are used to study the heat of adsorption and the adsorbent-adsorbate interaction on surfaces which suggest a linear decrease of sorption energy as the degree of completion of the sorptional centers of an adsorbent is increased [27,24]. The Dubinin-Redushkevich isotherm model is used to study relationship between the characteristic sorption curve and the porous structure of the sorbent [28,27] and estimate the characteristic porosity of the adsorbent as well as the apparent energy of adsorption [29]. The Harkins-Jura adsorption isotherm accounts for multilayer adsorption and explains the existence of heterogeneous pore distribution [27,24].

$$\varepsilon = RT \ln\left(1 + \frac{1}{C_e}\right) \quad (4)$$

The sorption mean free energy per mole of sorbate, E (J/mol), is computed from $\boldsymbol{B_D}$ (mol^2/J^2) using Equation 5 [28].

$$E = \frac{1}{\sqrt{2B_D}} \quad (5)$$

Table 1 Linear Plot Details of Various Adsorption Isotherm Models Used

Linear Form	Plot Variables
Langmuir Isotherm Model	
$\frac{\boldsymbol{C_e}}{\boldsymbol{q_e}} = \frac{\boldsymbol{1}}{\boldsymbol{K_L q_m}} + \frac{\boldsymbol{C_e}}{\boldsymbol{q_m}}$	$\boldsymbol{C_e/q_e}$ versus $\boldsymbol{C_e}$
Freundlich Isotherm Model	
$\boldsymbol{q_e = lnK_F + 1/n\ lnC_e}$	$\boldsymbol{lnq_e}$ versus $\boldsymbol{lnC_e}$
Temkin Isotherm Model	
$\boldsymbol{q_e = B_T lnA_T + B_T lnC_e}$	$\boldsymbol{q_e}$ versus $\boldsymbol{lnC_e}$
Dubinin-Redushkevich Isotherm Model	
$\boldsymbol{lnq_e = -B_D \varepsilon^2 + lnq_D}$	$\boldsymbol{lnq_e}$ versus $\boldsymbol{\varepsilon^2}$
Harkins-Jurah Isotherm Model	
$\frac{\boldsymbol{1}}{\boldsymbol{q_e^2}} = \left(\frac{\boldsymbol{B_{HJ}}}{\boldsymbol{A_{HJ}}}\right) - \left(\frac{\boldsymbol{1}}{\boldsymbol{A_{HJ}}}\right) \boldsymbol{log_{10} C_e}$	$\boldsymbol{1/q_e^2}$ versus $\boldsymbol{log_{10} C_e}$

If the values of the plot variables for each linear form of the isotherm Equations in Table 1 are plotted against each other, a straight line graph should be obtained giving room for the computation of all other constants from the resulting slopes and intercepts of the plots [24]. From the Equations q_e is the amount of dye adsorbed per unit mass of adsorbent in a single monolayer, $K_L (= k_a/k_d)$ the Langmuir equilibrium constant (k_a and k_d are rate constants for adsorption and desorption at equilibrium, MO + Adsorbent = MO…Adsorbent), C_e the equilibrium liquid phase concentration of the dye [25], K_F Freundlich constant for relative adsorption capacity of adsorbent, n_F the quasi-Gaussian energetic heterogeinety or intensity of the adsorption surface [25-31], $B_T (= RT/b_T)$ constant related to the heat of adsorption, T (K) is the absolute temperature, R the universal gas constant (8.314 $Jmol^{-1}K^{-1}$), b_T ($kJmol^{-1}$) adsorption energy variation, A_T (Lmg^{-1}) equilibrium binding constant, q_D (mg/g) the D-R's theoretical monolayer saturation capacity of an adsorbent, ε (J/mol) is the Polanyi potential given in Equation 4 and B_D (mol^2/J^2) is D-R's isotherm activity coefficient related to the mean free energy of sorption per mole of sorbate, E (J/mol), as it is transferred to the surface of the solid from infinite distance in solution [28], B_{HJ} is the isotherm constants and A_{HJ} the Harkins-Jura isotherm parameter.

RESULTS AND DISCUSSION

To have an insight into the adsorption behaviours of MO dye onto watermelon rinds and neem leaves samples and to gain the optimal fitting of theoretical model, the experimental data from batch experiment were analyzed using five two-parameter isotherm Equations (Langmuir, Freundlich, Dubinin-Radushkevich (D-R), Temkin and Harkins-Jura), in which linear regression analysis was used to evaluate whether the theoretical models have better or worse fitted the experimental data. The respective parameters of these isotherm models have been enumerated in Table 2.

Langmuir Isotherm

Based on the relationship of adsorption capacity for MO dye adsorption onto the adsorbents and the equilibrium concentrations, the Langmuir adsorption isotherms are modeled and presented in Figure 2. According to these isotherm curves, the Langmuir isotherm parameters are calculated and listed in Table 2. The experimental data for adsorption on both adsorbents show high linear reliability with isotherm from WRP (R^2: 0.9992) being more reliable than that of NLP (R^2: 0.9989) with the Langmuir's isotherm model [32]. This finding indicates that MO adsorption on watermelon rinds and neem leaves follow the Langmuir monolayer adsorption very well [32].

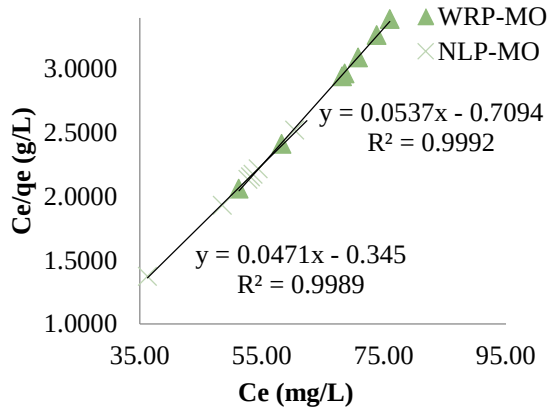

Fig. 2 Langmuir Isotherm Plot for MO Adsorption onto WRP and NLP.

Freundlich Isotherm

Based on the relationship of adsorption capacity for MO dye adsorption onto the adsorbents and the equilibrium concentrations, the Freundlich adsorption isotherms are correlated and given in Figure 3. The Freundlich isotherm parameters are calculated and tabulated in Table 2. Though experimental data for adsorption on both adsorbents, it show high linear reliability with isotherm from WRP (R^2: 0.9956) being more reliable than that of NLP (R^2: 0.9910) with the Freundlich's isotherm model [32]. This demonstrates that the experimental data fitted well with the Freundlich isotherm Equation. Moreover, it was reported that the Freundlich isotherm constant can be used to explore the favourability of adsorption process. The adsorption process is said to be favourable when the value of n_F satisfies the condition $|1| < n_F < |10|$, otherwise it is unfavourable [32]. While the n_F values in Table 2 for adsorption of MO on watermelon are situated outside the range of 1–10 indicating unfavourable adsorption process, the values for MO adsorption on neem leaves are within the range of 1–10, demonstrating favourable adsorption process.

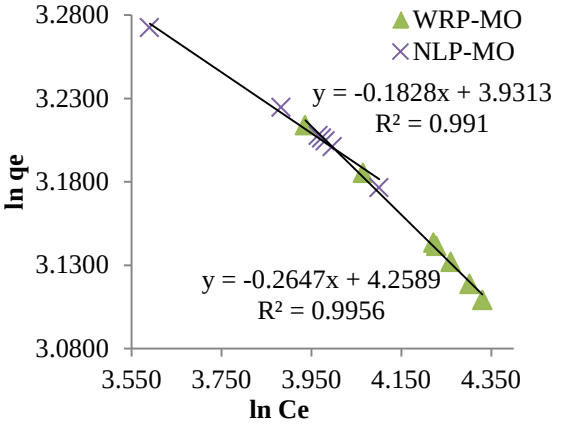

Fig. 3 Freundlich Isotherm Plot for MO Adsorption onto WRP and NLP.

Temkin Isotherm

Figure 4 illustrates the Temkin isotherm model for MO adsorption on watermelon rind and neem leaves samples. The relevant isotherm parameters are listed in Table 2. Although the experimental data for adsorption on both adsorbents were reliable, Temkin isotherm model indicated high linear reliability with isotherm from NLP (R^2: 0.9937) being more reliable than that of WRP (R^2: 0.9935) with the [32]. This outcome suggests that the experimental data fitted well with the Temkin isotherm model [32]. Furthermore, it can also be discovered in Table 2 that the heat of MO adsorption is higher on NLP samples (-0.54 kJ/mol) than on WRP samples (-0.92 kJ/mol).

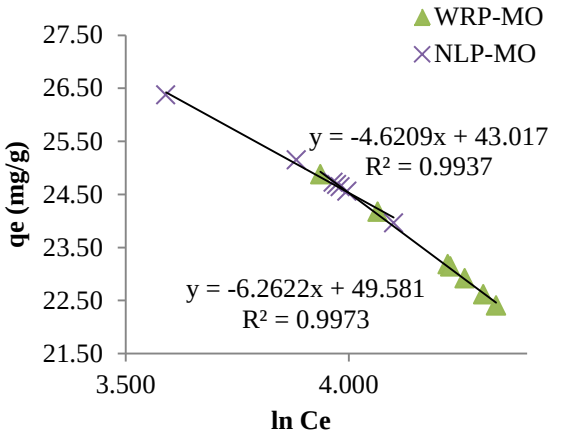

Fig. 4 Temkin Isotherm Plot for MO Adsorption onto WRP and NLP.

Table 2 Langmuir, Freundlich, Dubinin-Radushkevich (D-R), Temkin and Harkins-Jura Isotherm Parameters for MO Adsorption onto WRP and NLP

Sorption Parameters	WRP	NLP
Langmuir Isotherm		
q_m (mg/g)	18.62	21.23
K_L	-0.0757	-0.1365
R_L	-0.0461	-0.0250
R^2	0.9992	0.9989
Freundlich Isotherm		
$\|n_F\|$	3.78	5.47
K_F	70.7321	50.9732
R^2	0.9956	0.9910
Temkin Isotherm		
b_T (kJ/mol)	-0.9469	-0.5362
B_T	3.3597	-4.6209
A_T	$\mathbf{3.56 \times 10^{-2}}$	$\mathbf{9.06 \times 10^{-5}}$
R^2	0.9935	0.9937
Dubinin-Redushkevich Isotherm		
B_D (mol^2/J^2)	$\mathbf{8 \times 10^{-5}}$	$\mathbf{3 \times 10^{-5}}$
E (kJ/mol)	0.0791	0.1291
q_D (mg/g)	20.72	23.09
R^2	0.9724	0.9487
Harkins-Jura Isotherm		
A_{HJ}	-455	-769
B_{HJ}	0.9545	0.4615
R^2	0.9909	0.9837

Dubinin-Redushkevich Isotherm

The Dubinin-Radushkevich (D-R) adsorption isotherm linear plots for MO dye adsorption onto the adsorbents (presented in Figure 5) were prepared according to their adsorption capacity and equilibrium concentrations., the D-R isotherm parameters Corresponding to these linear plots were calculated and summarized in Table 2. The experimental data for adsorption on both adsorbents showed higher linear reliability with isotherm from WRP (R^2: 0.9724) than that of NLP (R^2: 0.9487) [32]. Moreover, it was reported that when the value of E was below 8kJ/mol, the adsorption process could be considered as a physical adsorption. In contrast, if the value of E is located in the range of 8–16kJ/mol, it would be a chemical adsorption [32]. From Table 2, it can be observed that the mean free energy, E, of adsorption on NLP (0.13 kJ/mol) is higher than that on WRP (0.08 kJ/mol). Thus, the effect of physical adsorption plays a dominating role in the process of MO dye adsorption onto the adsorbents [32].

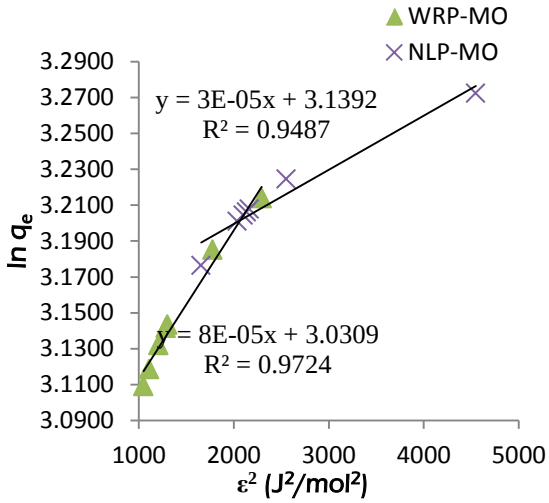

Fig. 5 Dubinin-Redushkevich Isotherm Plot for MO Adsorption onto WRP and NLP.

Harkins-Jura Isotherm

The Harkins-Jura isotherm models for MO adsorption onto watermelon rinds and neem-tree leaves samples are presented in Figure 6 and the relevant isotherm parameters are calculated and summarized in Table 2. Experimental data for adsorption on both adsorbents was good, but it showed higher linear reliability with isotherm from WRP (R^2: 0.9909) than that obtained with NLP (R^2: 0.9837) [32]. This result reveals that MO adsorption onto watermelon rinds and neem-tree leaves samples is in support of the multilayer adsorption rule [32].

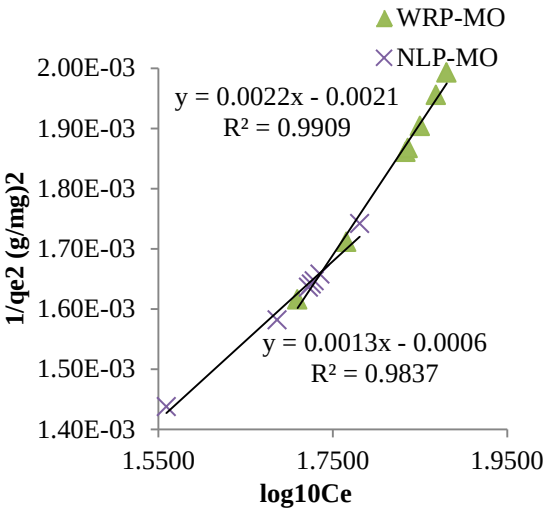

Fig. 6 Harkins-Jura Isotherm Plot for MO Adsorption onto WRP and NLP.

CONCLUSIONS

Adsorption of MO dye onto watermelon rinds- and neem leaves-derived adsorbents has been modeled using five two-parameter isotherm Equations . The results achieved suggested that all the experimental data of both adsorption processes on these samples followed the Langmuir, Temkin, Freundlich, Harkins-Jura and Dubinin-Radushkevich (D-R) isotherm models as evidenced by the values of the correlation coefficient, R^2 (0.9359-0.9998), with the first and last models being the most fitting and the least fitting respectively ofor adsorption on both adsorbents. The values of monolayer maximum adsorption capacity for Langmuir's q_m (24.75-24.81mg/g) and Dubinin-Radushkevich's q_D (20.72-26.06mg/g) are comparable. While values of the Langmuir's separation factor R_L suggest that both adsorption processes are unfavourable, the values of Freundlich constant n_F for adsorption of MO onto neem leaves indicates unfavourable dyes adsorption on heterogeneous surfaces. The mean free energy of adsorption, *E*, calculated from Dubinin-Radushkevich (D-R) isotherm Equation, was in the range of 0.29-0.32 kJ/mol, suggesting that the process is a physical adsorption. Calculated multilayer heat of adsorption (b_T) from the Temkin isotherm Equation was restricted within -0.95 kJ/mol for WRP to -0.54 kJ/mol for NLP. The three models namely D-R, Temkin and Harkins-Jura models show that the dye is removed from aqueous medium by a multilayer adsorption process.

REFERENCES

[1] Rijsberman FR, "Water scarcity: Fact or fiction", *Agricultural Water Management*, Vol. 80, 2006, pp. 5-22.

[2] Ahuja S, Handbook of water purity and quality, IWA Publishing, Great Britain, 2009, pp. 1-7.

[3] Lee B, Preston F, Kooroshy J, Bailey R and Lahn G, "Resources futures – A Chatham House report", The Royal Institute of International Affairs, London, United Kingdom, 2012.

[4] Damarji B, Khalaf H, Duclaux L and David B, "Preparation of TiO_2-pillard montmorillonite as photocatalyst part II: Photocatalytic degradation of a textile azo dye", 2009, *Applied Clay Science*, Doi: 10.1016/j.clay.

[5] Unuabonah EI, Adebowale KO and Dwodu FA "Equilibrium, kinetics and sober design studies on the adsorption of aniline blue dye by sodium tetraborate-modified kaolinite clay adsorbent", J. of Hazardous Materials, Vol. 157, 2008, pp. 397-409.

[6] Zohra B, Aicha K, Fatima S, Nourredin B. and Zoubir D, "Adsorption of Direct Red 2 on bentonite modifies by cetyltrimethylammonium bromide", Chemical Engineering J., Vol. 136, 2008, pp. 295-305.

[7] Gómez V, Larrechi, MS and Callao MP, "Kinetic and adsorption study of acid dye removal using activated carbon" Chemosphere, Vol. 69, 2007, p. 1151.

[8] Gupta VK, Kumar R, Nayak A, Saleh TA and Barakat M.A, "Adsorptive removal of dyes from aqueous solution onto carbon nanotubes: A review", *Advances in Colloid and Interface Science*, Vol. 193-194, 2013, pp. 24–34.

[9] Santos SCR and Boaventura RAR, "Adsorption modelling of textile dyes by sepiolite", Applied Clay Science, Vol. 42, 2008, pp. 137-145.

[10] Bulut E, Ozcar M and Sengil IA, "Equilibrium and kinetic data and process design for absorption of Congo red on bentonite", J. of Hazardous Materials, Vol. 154, 2008, pp. 613-622.

[11] Ozcan AS and Ozcan A, "Adsorption of acid dyes from aqueous solution onto acid-activated bentonite", J. of Colloidal and Interface Sciences, Vol. 276, 2004, pp. 39-46.

[12] Acemioglu B, "Adsorption of Congo red from aqueous solution onto calcium-rich fly ash", J. of Colloid and Interface Science, Vol. 274, 2004, pp. 371-379.

[13] Purkait MK, Maiti A, DasGupta S and De S "Removal of Congo red using activated carbon and its regeneration", *J. of Hazardous Materials*, Vol. 145, 2007, pp. 289-295.

[14] Song YL, Li JT and Chen H, "Degradation of C.I. acid red 88 aqueous solution by combination of Fenton's reagent and ultrasound

irradiation", *J. of Chemical Technology and Biotechnology*, Vol. 84, 2009, pp. 578-583.

[15] Liu C, Ngo HH, Guo W and Tung K, "Optimal conditions for preparation of banana peels, sugarcane bagasse and watermelon rind in removing copper from water", Bioresource Technology, Vol. 119, 2012, 349-354.

[16] Yadla SV, Sridevi V and Lakshmi MVVC, "A review on adsorption of heavy metals from aqueous solution", *J. of Chemical, Biological and Physical Sciences*, Vol. 2, No. 3, 2012, pp. 1585-1593.

[17] Gönen F and Serin DS, "Adsorption study on orange peel: Removal of Ni (II) ions from aqueous solution", *African J. of Biotechnology*, Vol. 11, No. 5, 2012, pp. 1250-1258.

[18] Neomagus HWJP, "Bio-Polymeric heavy metal adsorbing materials for industrial wastewater treatment" 2005 (WRC Report No. 1072/1/05): http://www.wrc.org.za/Knowledge%20Hub%20Documents/Research%20Reports/1072-1-05.pdf (accessed 23rd December, 2012).

[19] Nită I, Iorgulescu M, Spiroiu MF, Ghiurea, M., Petcu, C. and Cintezã, O. (). The adsorption of heavy metal ions on porous calcium alginate microparticles. *Analele Universităt din Bucureşti – Chimie, Anul XVI* (serie nouă), Vol. 1, 2007, pp. 59–67.

[20] Salleh MAM, Mahmoud DK, Karim WA and Idris A, "Cationic and anionic dye adsorption by agricultural solid wastes: A comprehensive review. *Desalination*, Vol. 280, 2011, pp. 1-13.

[21] Sharma N, Tiwari DP and Singh SK, "Decolourization of Synthetic Dyes by Agricultural Waste - A review", *International J. of Scientific & Engineering Research*, Vol. 3, No. 2, 2012, pp. 1-10.

[22] Haddadian Z, Shavandi MA, Abidin ZZ, Fakhru'l-Razi A and Ismail MHS, "Removal of methyl orange from aqueous solutions using Dragon Fruit (*Hylacereusundatus*) foliage", *Chemical Science Transactions*, Vol. 2, No. 3, 2013, pp. 900-910.

[23] Gopalakrishnan, K., Manivannan, V. and Jeyadoss, T., "Comparative study of Zn(II), Cu(II) and Cr(VI) from textile dye effluent using sawdust and neem leaves powder", *E-J. of Chemistry*, Vol. 7, No. *S1*, 2010, pp. S504-S510.

[24] Suyamboo BK and Perumal RS, "Equilibrium, thermodynamic and kinetic studies on adsorption of a basic dye by Citrullus Lanatus rind", *Iranica J. of Energy & Environment*, Vol. 3, No. 1, 2012, pp. 23-34.

[25] Bhattacharyya KG and Sharma A, "*Azadirachta indica* leaf powder as an effective biosorbent for dyes: a case study with aqueous Congo red solutions. *J. of Environmental Management*, Vol. 71, 2004, pp. 217-229.

[26] Asiagwu AK, Omuku, PE and Alisa CO, "Kinetic model for removal of methyl orange (dye) from aqueous solution using avocado pear (*Persea Americana*) seed", *J. of Chemical, Biological and Physical Sciences*, Vol. 3, No. 1, 2012-2013, pp. 48-57.

[27] Samarghandi, M.R., Hadi, M., Moayedi, S. and Askari, F.B., "Two-parameter isotherms of methyl orange sorption by pinecone derived activated carbon", *Iranica J. of Environmental Health, Science and Engineering*, Vol. 6, No. 4, 2009, pp. 285-294.

[28] Abdul-Hameed HM, "Comparison study between Dubinin-Redushkevich and Temkin model for adsorption of mercury onto activated carbon", *J. of Engineering*, Vol. 14, No. 1, 2008, pp. 2331-2336.

[29] Khan TA, Dahiya S and Imran Ali I, "Removal of Direct Red 81 dye from aqueous solution by native and citric acid modified bamboo sawdust - kinetic study and equilibrium isotherm analyses", *Gazi University J. of Science*, Vol. 25, No. 1, 2012, pp. 59-87.

[30] Abdullah NM, Othaman R, Abdullah I, Jon N. and Baharum A., "Studies on the adsorption of phenol red dye using silica-filled enr/pvc beads", *J. of Emerging Trends in Engineering and Applied Sciences* (JETEAS), Vol. 3, No. 5, 2012, pp. 845-850.

[31] Murugan T, Ganapathi A and Valliappan R, "Removal of dyes from aqueous solution by adsorption on biomass of mango (*Mangifera indica*) leaves", *E-J. of Chemistry: http://www.e-J.s.net*, Vol. 7, No. 3, 2010, pp. 669-676.

[32] Liu J and Wang X, "Novel silica-based hybrid adsorbents: Lead(II) adsorption isotherms**",** *The Scientific World J.*, Article ID 897159, 2013, 6 pages: http://dx.doi.org/10.1155/2013/897159.

First International Conference on Science, Engineering & Environment,
Tsu City, Mie, Japan, Nov.19-21, 2015, ISBN: 978-4-9905958-5-2 C3051

DETERMINATION OF PHYTOCHEMICAL COMPOUND FROM *Spirogyra* sp. USING ULTRASONIC ASSISTED EXTRACTION

Pornphan Champa[1,2], Kanda Whangchai[1,3], Niwooti Whangchai[4],
Somkiat Jaturonglumlert[5] and Nomura Nakao[6]

[1] Department of Biology, Faculty of Science, Chiang Mai University, Chiang Mai, Thailand
[2] The Graduate School, Chiang Mai University, Chiang Mai, Thailand
[3] Postharvest Technology Research Institute, Graduate School, Chiang Mai University, Chiang Mai, Thailand
[4] Faculty of Fisheries Technology and Aquatic Resources, Maejo University, Chiang Mai, Thailand
[5] Faculty Engineering and Ago-Industry, Maejo University, Chiang Mai, Thailand
[6] Graduate School of Life and Environmental Science, University of Tsukuba, Tennodai, Tsukuba, lbaraki, Japan

ABSTRACT

Currently, the use of phytochemical compounds from macro algae for cosmetic and pharmaceutical purposes is popular. This study aimed to evaluate ultrasound assisted-extraction (UAE) method on phytochemical components (gallotannin, total flavonoids content, total saponin content and total phenolic compounds) in *Spirogyra* sp.. The ultrasonic devices with same input power of 5 watts and varying 3 frequencies (45 kHz, 210 kHz and 1 MHz) of UAE coupled with 3 solvents (ethanol, methanol and acetone) were investigated. Treated samples were collected after sonication for 120 min. The results revealed that UAE method showed the highest performance in yield extraction compared with hot water. The highest yields of gallotannin and total flavonoids content were obtained by sonication at 45 kHz with 2.7 mg/g and 3.5 mg/g acetone but the highest yield of total phenolic compounds was found when sonicated at 45 kHz with methanol and total saponin content was found with ethanol. Thus, UAE at 5 watts, 45 kHz. showed the best result in yields extraction of those phytochemical compounds. While the suitable solvents for phytochemical compounds extraction differed and depended on the purpose and phytochemical type. UAE in combination with acetone had a suitable effect on *P. digitatum* inhibition while UAE in combination with acetone, ethanol and methanol showed non significantly different on *E.coli* inhibition.

Keywords: Ultrasound assisted-extraction, Phytochemical, Spirogyra sp., Escherichia coli, Penicilium digitatum

1. INTRODUCTION

Ultrasound-assisted extraction (UAE) has proved to be a particularly effective extraction method to reduce the extraction temperature, amount of solvent and the extraction time. This method is especially useful for the extraction of bioactive compounds. Usually, hot water treatment at 80°C for 4 hr. has been used for extraction of *Spirogyra* sp. [1]. However, hot water extraction in polysaccharides is associated with long duration and high temperature which lead to the degradation. [2] found that using ultrasonic at a frequency of 3 2 0 KHz with water extraction of polysaccharides in *Codinopsis pilosula* was effective to increase polysaccharide.[3] investigated different solvents in phytochemical extraction of *Canna indica* by UAE method. It was shown that acetone extract contained highest antioxidant activity, high amount of flavonoid and phenolic compounds. Combination of high frequency with extraction method is the technique of using ultrasonication combine with organic solvent or water solution to extract the substances from proposed materials. Ultrasonic enhances the high frequency through the carrier likes water or organic solvent. This leads to bubbles formations which form the shrinking and expanding of bubbles cycle. During bubble expansion, the substances were pulled out from materials then dissolved in the extracted solvent. Also, the bubble collapse causes high pressure and high temperature which leads to cell destruction which better increases antioxidant extraction by the solvent. There are many factors afferhing the efficiency of this method such as ultrasonic frequency, time and extraction solvent.

Tao (*Spirogyra* sp.) is a genus of filamentous freshwater green algae in the Division Chlorophyta, Order Zygnematales, Family Zygnemataceae. It is named after the helical or spiral arrangement of the chloroplasts. There are more than 400 species of *Spirogyra* in the world [4]. The algae grow in the clean standing water. For moderate quality of clear water, the turbidity would not exceed 10 NTU,

temperature 15-27°C and pH 6-7.8. *Spirogyra* sp. is consumed by people in the north and northeast of Thailand as a traditional food. It contains high amount of nutritional compositions including basic nutrients such as carbohydrates, fats, proteins, multivitamins, minerals and antioxidants [5]. *Spirogyra* sp. was screened against three bacteria: *Pseudomonas solanacearum*, *Escherichia coli* and *Clavibacter michiganense* and three plant pathogenic fungi: *Fusarium oxysporum*, *Curvularia* species and *Aspergillus niger*. Its antimicrobial property was found to be effective against the entire test organisms [4]. Moreover, *Spirogyra* phytochemical components (alkaiods, steriods, flavonoids, tannins, terpanoids) exhibit antimicrobial activity against *Escherichia coli* and *Candida albicans* [6].

In this study aimed to evaluate ultrasound assisted-extraction (UAE) methods on phytochemical components (gallotannin, flovoniods and total phenolic compounds) in *Spirogyra* sp.

2. MATERAILS AND METHODS

2.1 *Spirogyra* sp. preparation

Fresh *Spirogyra* sp. were collected from the low flowing stream located at SobPerng, MaeTeang, Chiang Mai Provinces and transported to the Postharvest Physiology Research Laboratory, Chiang Mai University. The algal samples were cleaned with distilled water and dried by hot air oven at 60 °C for 24 hr.

2.2 Preparation of extracts

Five gram of each *Spirogyra* sp. sample was out roughly and extracted by different methods as the following; hot water (95˚C), UAE (45 kHz, 210 kHz and 1 MHz) with same ultrasonic input power of 5 W in combination with various solvents (ethanol, methanol and acetone). Treated samples were collected at 120 min. during extraction period. Then, the extract of each sample was analyzed for the phytochemicals components.

2.3 Phytochemical analysis

2.3.1 Determination of Gallotannin

Algal extracts (50µl), in test tubes were made up to 1 ml with distilled water. One hundred µl of 0.4 N sulphuric acid and 600 µl of rhodanine were added to the diluted extracts. After 5 min, 200 µl of 0.5 N potassium hydroxide was added followed by 4 ml distilled water after a further 2.5 min. The mixtures were left for an additional 15 min at room temperature and evaluated by UV-vis spectrophotometer (520 nm) which methanol was used as a blank. The mixtures were analyzed in triplicates to measure gallotannin concentration by gallic acid equivalents (GAE) Makkar (1999) [7].

2.3.2 Determination of Total Saponin content

Algal extract (0.25 ml) was pipetted and put into a test tube then, 0.25 ml of vanillin reagent and 2.5 ml of 72% H_2SO_4 were added (in ice bath). The mixture was heated in water bath at 60˚C for 10 min, and then cooled. The absorbance of mixture was measured with spectrophotometer at 544 nm. Diosgenin was used as a reference standard. The test was performed in duplicate. Determination of total sapogenin was carried out according to the method of Hiai *et al.* [8].

2.2.3 Determination of Total phenolic content

Total phenolic content was determinated by the Folin–Ciocalteu colorimetric method, based on the procedure, gallic acid was used as standard phenolic compound. Briefly, 50 µl (two replicates) of the filtered extracts were mixed with 450 µl of distilled water and 2.5 ml of 0.2 N Folin–Ciocalteu reagent. After 5 min, 2 ml of saturated sodium carbonate (75 g/l) was added. The blue-colour solution was measured by spectrophotometer at 765 nm after incubation at 30˚C for 1.5 h with intermittent shaking. Quantitative measurements were performed, related to standard calibration curvet 20, 100, 200, 300, 400, 500 mg/l of gallic acid in 80% methanol. The total phenolic content was expressed by gallic acid equivalents (GAE) as milligrams per game of dry material.

2.2.4 Determination of Total Flavonoid content

Total flavonoid content was measured by aluminum chloride colorimetric assay. An aliquot (1 mL) of the extracts or standard solution of (+)-catechin (20, 40, 60, 80 and 100 mg/L) was added to 10 mL volumetric flask, containing 4 mL of distilled deionized water (dd H_2O). The flask was added with 0.3 mL 5% NaNO2. After 5 min, 0.3 mL 10% $AlCl_3$ was added. At the sixth minute, 2 mL 1 M NaOH was added and the total volume was made up to 10 mL with dis trilled water. The solution was mixed and the absorbance was measured against by UV-VIS Spectrophotometer Lambda 5 (510 nm). 5. Total flavonoid contents were expressed as milligrams of (+)-catechin equivalents (CE) per 100 g dry weight

(mg CE/100 g dw). All samples were analyzed in triplicate.

2.4 Antibacterial activity

Antibacterial activity was evaluated using gram negative bacteria *E.coli* 0157:H7 as a propose bacterial. First, bacteria strains were sub-cultured (37˚C, 24 hr). The effects of various extracts against bacterial strains were determined by zone of inhibition (ZOI) method. The $1x10^6$ of cell suspension per ml was spread in the plates then drilled by sterile cork borer (3 mm in diameter). After that, each drilled plate was filled with 100 µl of *Spirogyra* sp extracts after UAE in combination with different solutions (ethanol, methanol and acetone) extraction method. Amoxicillin was used as a positive control while water was used as a negative control. Then, plates were incubated at 37˚C for 24 hr. The diameter of zone inhibition was measured in millimeter (mm.). All experiments were performed in triplicate.

2.5 Antifungal activity

7-days-old *Pennicillium digitatum* spore on potato dextrose agar (PDA) plate was washed then suspended in the sterile distilled water to produce a final concentration of $1x10^6$ spores per ml. The volume of 20 µl spore suspension was spread on PDA with the mixture of 5000 mg/l *Spirogyra* sp. extracts. All experiments were performed in triplicate.

RESULTS AND DISCUSSION

3.1 Phytochemical analysis

3.3.1 Effect on Gallotannin Yield

Table 1 Phytochemical yields (wt.%) of *Spirogyra* sp. extract by Ultrasound assisted extraction

Frequency of UAE	Solvents	Gallotannin Contents	Total Saponin Contents	Total Phenolic Content	Total Flavonoids Contents (mg/g)
	Hot water	0.03a	0.44a	0.002a	1.52a
	Ethanol	0.65b	2.55b	0.001b	1.62a
45 kHz	Methanol	0.62b	2.38b	0.001b	1.52a
	Acetone	0.51b	2.23b	0.001b	1.25a
	Ethanol	0.87bc	2.02bc	0.004a	3.12c
210 kHz	Methanol	0.81bc	1.97bc	0.004a	2.21b
	Acetone	0.70bc	1.88c	0.003a	2.03b
	Ethanol	2.74d	0.88d	0.002ab	2.62bc
1 MHz	Methanol	2.17d	0.78d	0.001b	2.48b
	Acetone	1.93d	0.74d	0.001b	2.31b

The data followed by the same letter within the column are not significantly different (*P = 0.05)

Gallotannin yield by UAE in combination with different kind of solvents were determined. All UAE treatments at 5 watt, 45 kHz for 120 min. showed higher performance on gallotannin extraction than hot water treatment. Sonication affected cell membrane breakdown reduced on extraction time and increased the yield increased the UAE produced cavitation that gave highest efficiency at low frequency range (20 to 100 kHz) and high power or high intensity ultrasound [9]. In addition to UAE, the phytochemical yields depended on solvents (Table 1). UAE combined with acetone treatment showed the highest yield on gallotannin extraction (2.7 mg/g). UAE extraction combined with methanol and ethanol treatments (0.87 mg/g and 0.65 mg/g.) showed no significant difference. (Fig. 1)

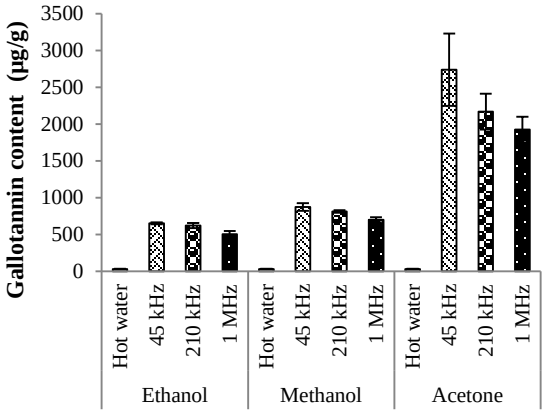

Fig. 1 Gallotannin yields of *Spirogyra* sp. extracted by UAE

3.3.2 Effect on Total Saponin Contents

For most of the *Spirogyra* sp. samples, the highest yield (2.5 g/g) of total saponin contents was UAE in combination with ethanol at 5 watt, 45 kHz for 120 min. (Fig. 2) followed in UAE in combination with methanol and acetone, the yields were 2.0 and 0.8 mg/g. effectively total saponin contents from UAE treatment was higher these treatment with than hot water The UAE extraction technique incombination with ethanol was developed for the fast extraction of saponins from *Eclipta prostrasta* L. [10] UAE has an advantage of accelesating the extraction process, causing less damage to the structural and molecular properties of the samples. Moreover, UAE require shorter time, less solvent and fine, higher exraction yield.

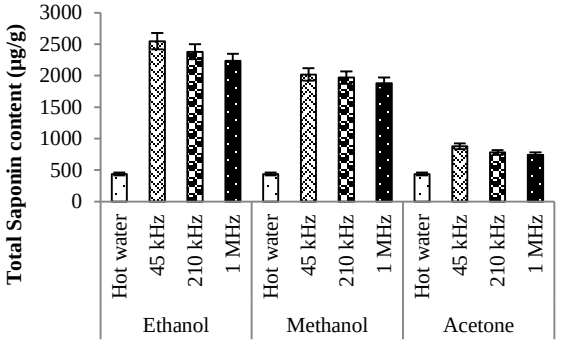

Fig. 2 Total saponin content of *Spirogyra* sp. extracted by UAE.

3.3.3 Effect on Total Phenolic Content

UAE combined with methanol treatment at 5 watt, 45 kHz for 120 min. had the best performance on yield extraction as 3.6 mg/g which was significantly different when compared with ethanol and acetone combination treatments ($p<`0.05$). While UAE combined with ethanol and acetone treatments showed 1.4 and 1.7 mg/g respectively on yields extraction with no significant difference on the frequency of UAE treatments (Fig. 2). Methanol is one of the most frequently used solvent for extraction. It has a polarity of 6.6 compare with 5.2 for ethanol and 5.1 for acetone. This difference in polarity has demonstrated the amount of total phenolic content in the extract [11]. In this case, [9] reported that methanol had higher ability on total phenol extraction for *Mesembryanthemum edule* L. *Aizoaceae* shoot than ethanol at the levels of 104.7 and 74.2 mg GAE.g^{-1}DW respectively.

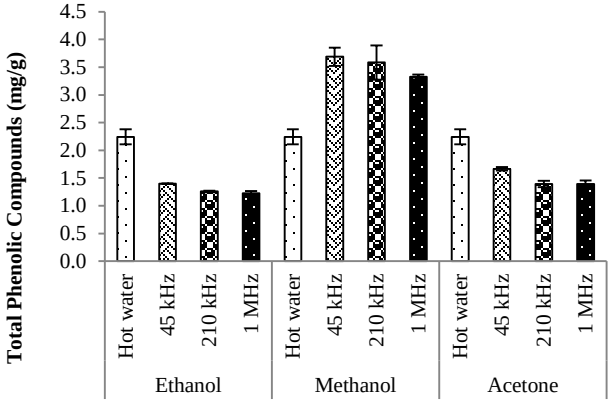

Fig. 3 Total phenolic compounds yield in *Spirogyra* sp. extracted by UAE

3.3.4 Effect on Total Flavonoids Contents

Flavonoids are strong antioxidants capable of reacting with scavenging oxygen species because of their phenolic hydroxyl groups [12]. The highest yield of total flavonoids was 3.1 g/g by UAE at 5 watt, 45 kHz for 120 min. in combination with methanol. While UAE in combination with acetone and ethanol gave the yield of 2.6 and 1.6 g/g respectively. All of the frequencies showed no significant difference on yield extraction of total flavonoids contents (Fig. 4).

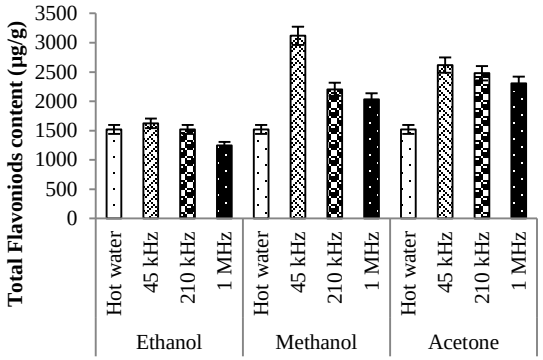

Fig. 4 Total flavonoids content of *Spirogyra* sp. extracted by UAE

3.4 Antibacterial activity

The effect of *Spirogyra* sp. extracts on *E.coli* 0157:H7 growth inhibition showed that *Spirogyra* sp. extracts by UAE (45 kHz, 5 watt for 120 min.) in combination with different solutions (ethanol, methanol and acetone) extraction method inhibited the growth of *E.coli* 0157:H7. The *Spirogyra* sp. extracted from UAE in combination with ethanol and acetone showed the highest results on *E.coli* 0157:H7 growth inhibition as 11.7 mm next is UAE in combination with methanol as 11.0 mm while the *Spirogyra* sp. extract from hot water method showed the negative result on *E.coli* 0157:H7 growth inhibition (Fig. 5) This is relevant to Rutikanga *et al.* [6] who reported that *Spirogyra* sp. extract from methanol extraction method showed the best inhibition on *E. coli* and *Candida albicans* growth rate. Opposite with the *Spirogyra* sp. extract from hot water method.

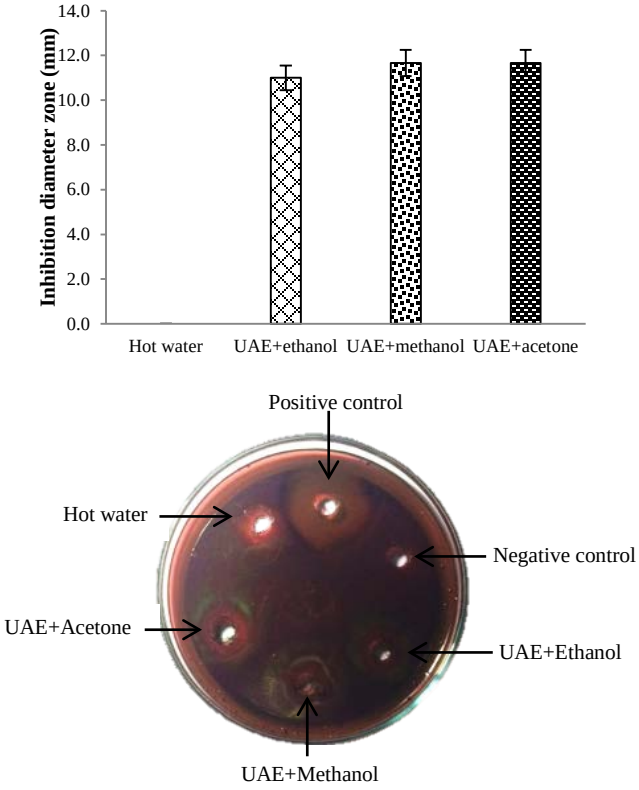

Fig. 5 Antimicrobial activity of *Spirogyra* sp. extracted by UAE in combination with deference solvents on *E.coli* 0157:H7

3.5 Antifungal activity

The effect of *Spirogyra* sp. extracts on *P. digitatum* growth inhibition showed that *Spirogyra* sp. extracts by UAE (45 kHz, 5 watt for 120 min.) in combination with different solutions (ethanol, methanol and acetone) extraction method inhibited the growth of *P. digitatum*. The *Spirogyra* sp. extract from UAE in combination with acetone showed the best results on *P. digitatum* growth inhibition with non-microbial growth. Next is UAE in combination with methanol and ethanol with the number of colony forming at 134 and 286 cfu respectively. While the *Spirogyra* sp. extracts from hot water method showed microbial growth rate similar to control treatment with no significantly different in results. (Fig.6)

Phytochemical has the effective on antibiotic. [13] reported that flavonoid and phenolic compound inhibited the growth of *Aspergillus niger*, *Bacillus subtilis*, *Candida albicans*, *Escherichia Coli*, *Micrococcus luteus*, *Pseudomonas aeruginosa*, *Saccharomyces cerevisiae*, *Staphylococcus aureus* and *Staphylococcus epdermidis*. Furthermore, type of solvent is one of the important factor that optimize the extraction ability in many plant bioactive [14]. The result showed the relevant between type of solvent and UAE extraction method. The solvents that have best result on tannin and saponin extraction also gave the positive results on microbial inhibition these because saponin and tannin are bioactive substances which have the effective on microbial inhibition

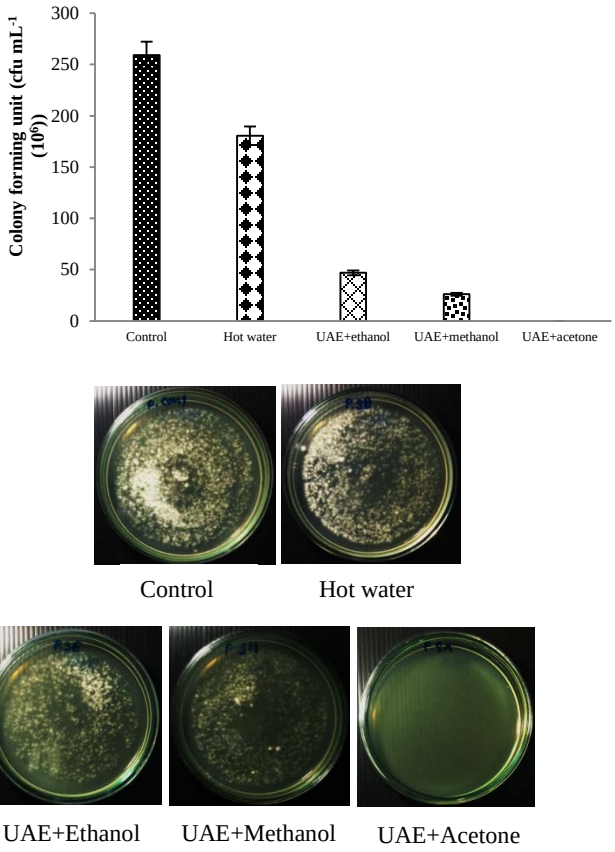

Fig.6 Antifungal activity of *Spirogyra* sp. extracts by UAE in combination with deference solvents on *P. digitatum*

3. CONCLUSION

Ultrasound Assisted-Extraction (UAE) with the electric power of 5 watt, frequency of 45 KHz for 120 min is the optimum condition for phytochemical extraction in *Spirogyra* sp. Methanol is the appropriate solvent for total phenolic extraction.While acetone is the appropriate solvent for gallotanin and flavonoid extraction in *Spirogyra* sp. UAE in combination with acetone had an suitable effect on *P. digitatum* inhibition while UAE in

combination with acetone, ethanol and methanol showed had no significantly different on *E.coli* inhibition.

4. ACKNOWLEDMENTS

This work was supported by National Innovation Agency. The authors are sincerely grateful to Department of Biology, Faculty of Science Chiang Mai University, Faculty Engineering and Ago-Industry, Maejo University, Chiang Mai and School of Life and Environmental Sciences, University of Tsukuba for providing the laboratory facilities.

5. REFERECES

[1] Peerapornpisal Y, Punyoyai T and Amornlerdpison D, "Antioxidant and anti-inflammatory activities of *Spirogyra neglecta* (Hassall) Kützing". Khon Kaen University Science Journal, Vol.40, No. 1, 2012, pp. 228-235.

[2] Zao Y, Chen, X, Yang W and Liu S, "Response surface methodology for optimization of the ultrasonic extraction of polysaccharides from Codonopsis pilosula Nannf. var. modesta L.T.Shen", Carbohydrate Polymers, Vol. 84, 2011, pp. 503-508.

[3] Padma SV and Jyoti S, "Ultrasound-Assisted Extraction in Different Solvents for Phytochemical Study of Canna indica", International Journal of Food Engineering, Vol. 6, No. 3, 2010, pp.1-6.

[4] Naik AA, Hemavani C and Thippeswamy B, "Evaluation of antimicrobial property of *Spirogyra* species", International Multidisciplinary Research Journal, Vol. 2, No. 2, 2012, pp. 13-15.

[5] Peerapornpisal Y, "Edible freshwater macroalgae in Northern Thailand", Journal of Fisheries Technology Research, Vol. 1, 2008, pp. 178-189.

[6] Ratikanga A, Gitu LM and Oyaro N, "Mineral composition, antioxidants and antimicrobial actibities of freshwater algae (*spirogyra genus*) from Jomo Kenyatta University of Agriculture and Technology (JKUAT)", World Rural Observations, Vol. 6, No. 2, 2014, pp.86-91.

[7] Makkar HPS, "Quantification of tannins in tree foliage: a laboratory manual for the FAO/IAEA Co-ordinated Research project on "Use nuclear and Related Techniques to develop simple tannin assay for predicting and improving the safety and efficiency of feeing ruminants on the tanniniferous tree foliage: Joint FAO/IAEA Division of Nuclear Techniques in Food and Agriculture", Vienna, 1999.

[8] Hiai S, Oura H and Nakajima T, "Color reaction of some sapogenins and saponins with vanillin and sulphuric acid", Planta Medica, Vol. 29, 1976, pp. 116-122.

[9] Hanan F, Riadh K, Marrie-Elizabeth L, Chedly A and Christian M, "Ultrasound-assisted extraction: Effect of extraction time and solvent power on the levels of polyphenols and antioxidant activity of Mesembryanthemum edule L. Aizoaceae shoot", Tropical Journal of Pharmaceutical Research, Vol. 11, No. 2, 2012, pp. 243-249.

[10] Ting H, Yan-Yun G, Qin-Fan Z, Xian-Ke Z, Liang Z, Jin-Hua P, Jian C and Jian-Guo J, "Optimization of ultrasonic-assisted extraction of total saponins from Eclipta prostrasta L. using response surface methodlogy", Journal of Food Science, Vol. 77, No. 9, 2012, pp. C975-C982.

[11] Betancourt AO, "Analyse, extraction at recuperation de poly-3-hydroxybutyrate present dans la biomasse", Université du Québec á Montréal Tesis, 2008, pp.45-55.

[12] Cao G, Sofie E and Prior RL, "Antioxidant and pro-oxidant behavior of flavonoids: Structure activity relationships", Free radical Biology and Medicine, Vol. 22, 1997, pp. 749-760.

[13] Jussi-Pekka R, Susana R, Marina H, Anu H, Marja K, Tytti K, Kalevi P, Heikki V and Pia V, "Antimicrobial effects of Finnish plant extracts containing flavonoids and other phenolic compounds, Vol. 56, 2000, pp. 3-12.

[14] Lafka TI, Sinanoglou V and Lazoa ES, "On the extraction and antioxidant activity of phenolic compounds from winery wastes", Food Chemistry, Vol. 104, 2007, pp. 1206-1214.

First International Conference on Science, Engineering & Environment,
Tsu City, Mie, Japan, Nov.19-21, 2015, ISBN: 978-4-9905958-5-2 C3051

EFFECT OF TiO_2-COATED SUBSTRATE PHOTOCATALYSIS ON CHLOPYRIFOS INSECTICIDE DEGRADATION

Kanda Whangchai[1,2,3*], Trid Sriwichai[2], Niwooti Whangchai[4] and Nakao Nomura[5]

[1] Postharvest Technology Research Institute, Graduate School, Chiang Mai University, Chiang Mai, Thailand
[2] Postharvest Technology Innovation Center, Commission on Higher Education, Bangkok, Thailand
[3] Department of Biology, Faculty of Science, Chiang Mai University, Chiang Mai, Thailand
[4] Faculty of Fisheries Technology and Aquatic Resources, Maejo University, Chiang Mai, Thailand
[5] Graduate School of Life and Environmental Science, University of Tsukuba, Tennodai, Tsukuba, lbaraki, Japan

ABSTRACT

The efficiencies of photocatalysis using TiO_2-coated substrates to reduce chlorpyrifos insecticides was evaluated. Three different glass substrates (glass ball, glass slide and glass bead) were prepared and tested with KI solution for efficiency of oxidation test. It was found that TiO_2-coated glass beads at 45 mg/ml for 60 min had the highest iodine liberation rate. A 1 mgL^{-1} standard chlorpyrifos was subjected to those TiO_2-coated substrates photocatalysis for 15, 30, 45 and 60 minutes. The percentage reduction of chlorpyrifos was calculated. It was shown that TiO_2-coated glass bead photocatalysis had high reduction rate of chlorpyrifos concentration within 15 minutes, which correlated with an increase in iodine liberation rate. The effectiveness of TiO_2 in photocatalysis to reduce contaminated chlorpyrifos in Chinese kale was determined by treatments with different TiO2-coated substrate photocatalysis and sampled every 15 minutes for 60 minutes. It was found that TiO_2-coated glass bead reduced chlorpyrifos concentration to 53% when compared with the control. In addition, in the quality of Chinese kale after treatment withTiO_2 in photocatalysis and stored for 12 days at 5 ˚C was also investigated. There was no significant difference in the quality of Chinese kale in weight loss, leaf color, total soluble solids and ascorbic acid content.

Keywords: Chlorpyrifos, Degradation, Titanium Dioxide, Photocatalysis

1. INTRODUCTION

Exporting countries are concerned with increasing crop production with constraints on available agricultural land. Increasing the use of pesticides in the future is one way to achieve this goal. Thai Agricultural Commodity and Food Standard in 2006 reported that the residual pesticides is the detected at higher concentration than the Maximum Residue Limit (MRL by importers). Among vegetables, chlorpyrifos residue was the most commonly found in Chinese kale. [Chlorpyrifos is an organophosphate insecticide and is widely used for pest control on vegetable crops [1]. The most common method for reducing chemical residues is by washing with detergent, sodium hypochlorite or potassium permanganate. However, this method creates chemically polluted water as a byproduct and has a high cost and limited effectiveness. The Good Agricultural Practices (GAPs) certification program has been a strategy for limiting pesticide residue on crops. However, chlorpyrifos contamination of chilli is still a critical problem to be solved because of over usage by growers. Titanium dioxide (TiO_2) belongs to the family of transition metal oxides [2, 12]. There are four commonly known polymorphs of TiO_2 found in nature, namely: anatase (tetragonal), brookite (orthorhombic), rutile (tetragonal) and TiO_2 (B) (monoclinic) [5, 15]. Only TiO_2 powder was stated in this report. TiO_2 powder has high photocatalytic activity due to their higher specific surface area. It is relatively economical, photostable in solution, highly stable chemical, nontoxic, redox selective and strong oxidizing power [1, 5] and can be as a photocatalyst. When TiO_2 absorbs ultraviolet (UV) radiation from sunlight or illuminated light source (fluorescent lamps), pairs of electrons and holes will be produced [3]. The positive-hole of TiO_2 breaks apart the water molecule to form hydrogen gas and hydroxyl radical. The negative-electron reacts with oxygen molecule to form super oxide anion. This cycle continues when light is available. Hydroxyl radicals were claimed to the extremely powerful oxidation agent due to their oxidizing strength. In the environmental aspect, this mechanism was utilized to oxidize hazardous organic pollutant into nontoxic materials [4]. TiO_2 has been proved for its advantages in removing toxic substances [7] such as malathion[17], methamidophos, chlorfenapyr, phoxim, dichlofenghion, bromophos ethyl, bromophos methyl, atrazine, cyanazine, irgarol, prometryne, propazine, chlorotoluron, metobromuron, isoproturon cinosulfuron, triasulfuron [5], fenamiphos [5], pirimiphos-methyl [10], dichlorvos and phosphamidon [13],diquat, paraquat [14], triclopyr, daminozid [16], parathion [19], 4-bromoaniline, 3-nitroaniline, pentachlorophenol, 1,2,3-trichlorobenzene and diphenylamine. However, the potential and appropriate applications of TiO_2 including oxidative degradation should be further studied. Currently,

utilization of TiO_2 photocatalysis as an oxidation process for water treatment increases. The advantage of photocatalysis is that, the photogeneration of •OH radical is not harmful to the environment. This study was conducted to determine the degradation of chlorpyrifos in Chinese Kale by washing with various TiO_2-coated with substrate photocatalyst.

2. MATERIALS AND METHODS

2.1 Photocatalyst

Commercial TiO_2 powder was purchased from Ajax Finecham®, Australia)

2.2 Photoreactor and Light Source

All photocatalytic experiments were carried out in dark acrylic box of (30× 50 × 40 cm) operated with two UVA lamps with light intensity 10 watt each. The TiO_2-coated glass substrates were packed between the lamp and tube. Two reaction tubes were placed on the bottom of the reactor. A schematic diagram of the experimental set up is shown in Fig. 1

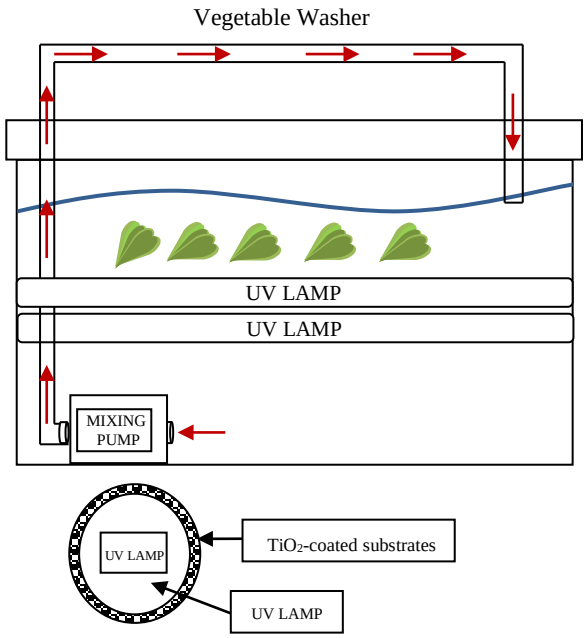

Fig. 1 Schematic of reaction system of TiO_2 coated substrate combined with photocatalysis in degradation of chlorpyrifos residue in Chinese Kale

2.3 Study of Various TiO_2-Coated Substrates Photocatalysis for Oxidative degradation activity and Reducing Standard Chlopyrifos Solution

Standard chlopyrifos at the concentration of 1 mg L^{-1} or 2% KI solution was prepared in a flask and then placed inside different types of glass substrates coated with TiO_2 (glass ball: 1 cm in diameter, glass slide (2.5 x 7.5 cm) and glass bead: 1 mm in diameter prepared by coating with TiO_2 powder at 45 mg mL^{-1} (with almost the same surface area) by FCVAD (Filterred Cathodic Vacuum Arc Deposition) at oxygen 10^{-2} Torr and 250 volt. Each TiO_2 coated substrate was put in photocatalysis reactor for 15, 30, 45 and 60 minutes. The concentration of iodine liberation from 2% potassium iodine was measured at 354nm using digital spectrophotometer. Finally, triplicates of chlopyrifos samples were analyzed. Using a gas chromatograph equipped with a flame photometric detector (GC-FPD). The percent removal of chlopyrifos was calculated at each collection time. Chlopyrifos concentrations were determined by gas chromatography. The analysis was performed using Agilent Technologies (Wilmington, DE) with model 6890 gas chromatograph equipped with a flame photometric detector (GC-FPD). The GC column was a fused silica capillary column HP-5, 5% phenylmethylsiloxane, with the dimensions of 30 m × 0.32 mm i.d. and a 0.25 µm film thickness (Agilent Technologies). The temperature was programmed to increase at 10ºC min^{-1} from an initial 100ºC to 200ºC and then at 4ºC increase to the final temperature of 220ºC. A purified helium gas carrier was used at a flow rate of 3.6 mL min^{-1}. The detector temperature was 250ºC. Sample solution (1.0 µL) was injected in splitless mode. Quantification of chlopyrifos was performed using chlopyrifos standard as reference.

2.4 TiO_2-Coated substrates Photocatalysis on the Reduction of Chlorpyrifos Insecticide in Chinese Kale and Its Quality Changes During Storage

Chinese Kale were purchased from an organic agriculture farm in MaeTaeng district, Chiang Mai, Thailand. They were cleaned with distilled water and those with uniform shape and lesion free were selected. Each sample was dipped into 10 mgL^{-1} chlorpyrifos solution for 3 0 minute. and left to dry at room temperature. Then washed in photocatalysis reactor (Fig. 1). For 15, 30, 45 and 60 minute the reduction in percentage of pesticide residue was then determined by gas chromatography.

2.4.1 Quality Changes during Storage

Chinese Kale were washed in the reactor for 15, 30, 45 and 60 minute in the previous experiment and then kept in sealed PE bags. All the treated samples were stored at 5°C for 12 days and were selected to measure the quality changes at the end of storage. The percentage of weight loss, leaf color change, total soluble solids (TSS) content and ascorbic acid content (AOAC) were determined.

2.4.2 Statistic Analysis

All the experiments were done in triplicates and evaluated with regression procedure, using SPSS version 17. The differences between the treatments were analyzed, using Duncan's multiple range test (*$P < 0.05$).

3. RESULTS AND DISCUSSION

3.1 Study of Various TiO_2-Coated substrates Photocatalysis for Oxidative Degradation Activity and Reducing Standard of Chlorpyrifos Solution

Iodine liberation by 2 % KI increased in of all TiO_2-coated treatments (Fig. 2). The increase in iodine liberation promoted oxidation efficiency by the reaction time.The active hydroxyl free radical which generated

from the reaction react with potassium iodide which resulting in iodine liberation[9]. Reduction in standard chlorpyrifos by different TiO_2-coated glass substrates with photocatalysis is shown in Fig. 3. The concentration of chlorpyrifos solution decreased and time of exposure increased. Within the first 15-minnute, a rapid reduction in chlorpyrifos concentration was obvious in all treatments. However, most effective method of reducing the amount of chlorpyrifos was observed when TiO_2-coated glass bead was used and treated for 15-min. It was able to reduce significantly almost 50% of chlorpyrifos from 1.0 mgL^{-1} to4.6 mgL^{-1} while the concentration of other treatments slightly decreased with increasing time. The increase in iodine liberation promoted oxidation efficiency by the reaction time. It's hypothesized that high density and surface area of TiO_2-coated glass bead as determinated by BET (BRunaver Emmett-Teller) analysis (data not shown) are able to increase the photocatalytic efficiency by increasing reactive species generation. These confirmed with a study of an organophosphate pesticide exposed longer to UV decomposed better [6]. This is because when the irradiation time by UV lamp increases, lots of free radicals and formed in the liquid, causing much decomposition of the pesticides [8, 18].

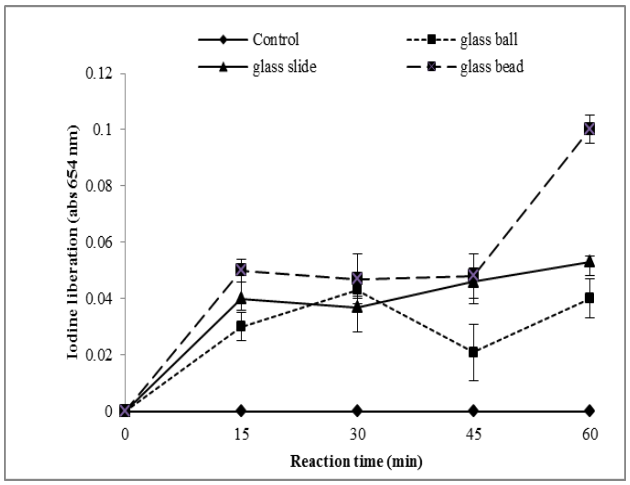

Fig. 2: Oxidative degradation activity (Iodine liberation) after treatment with different TiO_2- coated glass substrates

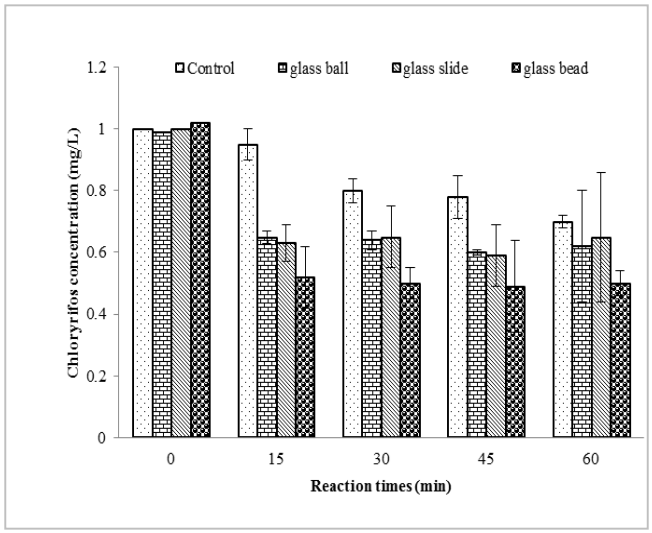

Fig. 3: Degradation efficiency of chlorpyrifos under different TiO_2-coated glass substrates

Previous studies had shown many intermediates of the photocatalytic degradation identified according to the reaction [11]. Oxidant attack of the OH^- on the P=S bond occurred first, resulting in the formation of oxon derivatives. Continuous attack of OH^- followed by the rupture of P-O bond resulted in the formation of corresponding phenols and different alkyls or phosphate esters [6, 7].

3.2 TiO_2-Coated Glass Substrates Photocatalysis on the Reduction of Chlorpyrifos Insecticide in Chinese Kale and its Quality Changes During Storage

Chinese kale were washed in different TiO_2-coated substrate to remove residual chlorpyrifos. It was found that degradation percentage of chlorpyrifos in Chinese kale when washed in TiO_2-coated glass bead increased with increasing time. The highest rate of reduction occurred in 60 minutes when compare with the control, which was immersed in distilled water. It was found that the TiO_2 photocatalysis reduced chlorpyrifos concentration to 53 % when compared with the control which was 11.5 % (Fig. 4). Similarly, the decomposition rate of 17-β-oestradiol treated by immobilized TiO_2 was 98% in 3.5 h. [20]. In addition, two organophosphorus insecticides, dimethyl-2,2-dichlorovinyl phosphate (DDVP) and dimethyl-2,2,2-trichloro-hydroxy ethyl phosphonate (DEP), were photocatalytic degraded by illumination with a super-high pressure mercury lamp or by exposure to sun light[21]. All of these treatments were observed to have no effect on fruit quality, as determined by on weight loss, leaf color, total soluble solids and ascorbic acid (Table 1)

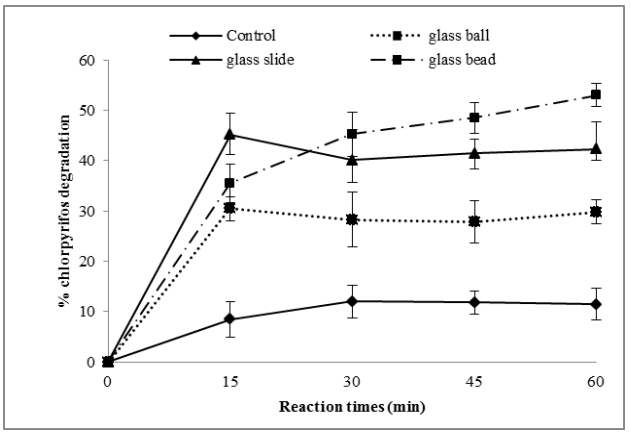

Fig. 4: Chlorpyrifos degradation in Chinese kale when treated with various TiO_2-coated substrates for 60 minutes

Table 1 Effect of TiO_2-coated substrates phytocatalysis on quality of Chinese Kale after Storage at 5°C for 12 days

Columns with different letter of each parameter indicate significant differences by Duncan's multiple range test (*$P < 0.05$*)

Treatment	Weight loss (%)	TSS (% brix)	Peel color			Ascorbic acid mg/100 g
			L*	a*	b*	
Control	6.5 [ab]	8.8 [a]	23 [a]	-4.5 [a]	3.5 [be]	40.5 [ab]
glass ball	6.1 [ab]	9.0 [ab]	22.5 [ab]	-3.9 [ab]	4.2 [ab]	39.0 [bc]
glass slide	5.9 [bc]	7.8 [ab]	21.0 [ab]	-3.83 [bc]	4.3 [ab]	37.5 [c]
glass bead	6.3 [ab]	9.0 [ac]	23.7 [a]	-4.12 [ab]	4.9 [a]	42.8 [a]

4. CONCLUSION

Photocatalysis using TiO_2-coated glass bead had high performance on the degradation of chlorpyrifos insecticide. In addition, it was confirmed that this technique could improve vegetable quality with no adverse effects on quality of Chinese kale in weight loss, leaf color, total soluble solids and ascorbic acid content.

5. ACKNOWLEDGEMENTS

The authors would like to acknowledge Postharvest Technology Innovation Center, Commission on Higher Education Bangkok and Faculty of Science ChiangMai University for financial support. This research study was undertaken in Department of Physics and Materials Science and Department of Biology, Faculty of Science, ChiangMai University, Thailand.

6. REFERENCES

[1] Fujishima A, Rao TN and Tryk DA, "Titanium dioxide photocatalysis", Journal of Photochemistry and Photobiology C: Photochemistry Reviews, Vol. 1, 2000, pp.1-21.

[2] Jian C, "Advanced oxidation technologies: Photocatalytic treatment of wastewater", PhD Thesis, 1997, Wageningen, Netherlands.

[3] Philippopoulos CJ. and Nikolai M D, "Photocatalytic processes on the oxidation of organic compounds in water", 2013, http://www.intechopen.com (Access: July 2013)

[4] Ravelli D, Dondi D, Fagnoni M and Albini A, "Titanium dioxide photocatalysis: An assessment of the environmental compatibility for the case of the functionalization of heterocyclics", Applied Catalysis B: Environmental, Vol., 99, 2010, pp.442–447.

[5] Mital GS and Manoj T, "A review of TiO_2 nanoparticles", Chinese Science Bulletin, Vol. 16, 2011, 56, pp. 1639-1657.

[6] Mountacer H, Nemmaoui SM, Rafqah S, Voyard G and Sarakha M, "TiO_2 Photocatalysis of the Organophosphorus Fenamiphos: Insight into the Degradation Mechanism", ISRN Environmental Chemistry, Article ID 319178, 2013, pp. 1-8.

[7] Konstantinou IK and Albanis TA, "Degradation pathways and intermediates of photocatalytic transformation of major pesticide groups in aqueous TiO_2 suspensions using artificial and solar light: A review**",** 3rd European Conference on Pesticides and Related Organic Micropollutants in the Environment, Halkidiki, Greece, 2004, pp.320-324.

[8] Konstantinou I K. and Albanis TA, "Photocatalytic transformation of pesticides in aqueous titanium dioxide suspensions using artificial and solar light: intermediates and degradation pathways", Applied Catalysis B: Environmental, Vol. 1310, 2002, pp. 1-17.

[9] Hart E.J. and Henglein A, "Free radical and free atom reaction in the solnolysis of aqueous iodine and formate solutions",Journal of Physical Chemistry,Vol.89,1985,pp 4342-4347.

[10] Herrmann JM, Guillard C, "Photocatalytic degradation of pesticides in agricultural used waters", Chemistry, Vol. 3, No. 23, 2000, pp. 417–422.

[11] Herrmann JM, Guillard C, Arguello M, Agüera A, Tejedor A, Piedra L and Fernández-Alba A, "Photocatalytic degradation of pesticide pirimiphos-methyl: Determination of the reaction pathway and identification of intermediate products by various analytical methods", Catalysis Today, 1999, 54, 353–367.

[12] Hashimoto K, Irie H and Fujishima A, "TiO_2 photocatalysis: A Historical overview and future prospects", Japanese Journal of Applied Physics, Vol. 44, No. 12, 2005, pp. 8269-8285 (Part 1).

[13] Rahman MA and Muneer M, "Photocatalysed degradation of two selected pesticide derivatives, dichlorvos and phosphamidon, in aqueous suspensions of titanium dioxide", Desalination, Vol. 181, 2005, pp. 161-172.

[14] Tariq MA, Faisal M, Muneer M and Bahnemann D, "Photochemical reactions of a few selected pesticide derivatives and other priority organic pollutants in aqueous suspensions of titanium dioxide", Journal of Molecular Catalysis A: Chemical, Vol. 265, 2007, pp. 231–236.

[15] Florencio MH, Pires E, Castro AL, Nunes MR, Borges C and Costa F M, "Photodegradation of Diquat and Paraquat in aqueous solutions by titanium dioxide: evolution of degradation reactions and characterisation of intermediates", Chemosphere, Vol. 55, 2004, pp. 345–355.

[16] Lomora M, Draghici C and Enesca Al., "Intermediary compounds in advanced oxidation processes for wastewater treatment", in " Bulletin of the Translvania University of Brasov, Series K: Engineering Sciences Vol. 4 (53) No. 1-2011, 2011, pp. 51-58.

[17] Shayeghi M, Dehghani MH, Alimohammadi M and Goodini K, "Using ultraviolet irradiation for removal of malathion pesticide in water", Journal of Arthropod-Borne Diseases, Vol.6, No.1, 2012, pp. 45–53.

[18] Carp O, Huisman C L and Reller A, "Photoinduced reactivity of titanium dioxide", Progress in Solid State Chemistry, Vol. 32, 2004, pp. 33–177.

[19] Calza P, Medana C, Pazzi M, Baiocchi C and Pelizzetti E, "Photocatalytic transformations of

sulphonamides on titanium dioxide", Applied Catalysis B: Environmental, Vol. 53, 2004, pp.63–69.

[20] Harada K, Hisanaga T and Tanaka K, "Photocatalytic degradation of organophosphorous insecticides in aqueous semiconductor suspensions", Water Research, Vol. 24, 1990, pp. 1415-1417.

[21] Evgenidou E., Konstantinou I., Fytianos K. and Albanis T. "Study of the removal of dichlorvos and dimethoate in a titanium dioxide mediated photocatalytic process through the examination of intermediates and the reaction mechanism", Journal of Hazardous Materials. Vol. B137, 2006, pp. 1056-1064.

SHORT-TERM EFFECTS OF COURT-TYPE TRADITIONAL THAI MASSAGE ON PRESSURE PAIN THRESHOLD AND PAIN INTENSITY IN PATIENTS WITH CHRONIC TENSION-TYPE HEADACH

Peerada Damapong[1], Naowarat Kanchanakhan[2], Wichai Eungpinichpong[3], Prasobsook Putthapitak[4], and Pongmada Damapong[1]

[1]College of Allied Health Science Suan Sunandha Rajabhat University, Bangkok 10300, Thailand
[2]College of Public Health Sciences, Chulalongkorn University, Bangkok 10330, Thailand
[3]Research Center in Back, Neck, and Other Joint Pain, and Human Performance, Faculty of Associated Medical Sciences, Khon Kaen university, Khon Kaen 40002, Thailand
[4]Bamnet Narong Hospital, Amphur Bamnet Narong, Chaiyaphum Province 36160. Thailand

ABSTRACT

This study aimed to evaluate the short-term effects of the court-type traditional Thai massage (CTTM) on pressure pain threshold and pain intensity to treat patients suffering from chronic tension-type headaches (CTTHs) comparing with amitriptyline taking. A randomized controlled trial was conducted. Sixty patients diagnosed with CTTH were evenly divided into the treatment and control group. The treatment group received a 45-minute course of court-type traditional Thai massage the control group was prescribed to take 25 mg of amitriptyline once a day before bedtime lasted. The results were evaluated in short-term day 1 after intervention, The measurement consisted of Visual Analog Scale (VAS), Tissue hardness and pressure pain threshold (PPT). The results demonstrated that there was a significant decrease in pain intensity for the CTTM group at different assessment while a significant difference occurred between-group comparison ($P<0.05$). Moreover, the PPT of the CTTM group was significantly increased ($P<0.05$). It can therefore be concluded from the findings that CTTM seems to be an effective therapy for stress-related variables and increased the PPT as well as reducing pain intensity for the CTTHs.

Keywords: Effects ,Traditional Thai Massage, Tension-type Headache

INTRODUCTION

Tension-type headache (TTH) is the most common form of primary headache [1]. The International Classification of Headache Disorders (Headache Classification Subcommittee of the International Headache Society (HIS) 2004) that strongly suggest a neurobiological basis, at least for the more severe subtypes of tension-type headache, the division into episodic and chronic types [1]. The lifetime prevalence of TTH was as high as 78% in a population-based study in Denmark [2]. Globally, the percentages of the adult population with an active headache disorder are 42% for tension-type headache [3]. However, for some individuals, the difference based primarily on the frequency of attack with the episodic tension-type headache (ETTH) or chronic tension-type headache (CTTH), difference between these two types of headache is that the former involves pain that lasts no longer than 15 days per month, whereas the latter causes pain that continues at least 15 days per month for over six months[1]. However, the aggregate societal impact is large because the disorder is highly prevalent. The individual impact of CTTH is greater than that of ETTH, but the disorder is greater than that of ETTH, but the disorder is less common [4].

TTH treatment involves both pharmacologic and non-pharmacologic approaches [1]. Non-pharmacologic approaches have been widely used and proven effective but with fewer risks and undesirable side effects, a survey by the WHO on headache treatment indicated that the three most popular types of alternative or complementary therapies were physical therapy (44%), acupuncture (39%), and naturopathy (25%) [5]. Among complementary therapies, traditional Thai massage is an alternative treatment. It can be classified into two types: the popular type traditional Thai or Chaloeisak massage and the Court-type Traditional Thai Massage (CTTM) employing polite gestures and emphasizing pressing on points for treatment purposes [6] - [8]. Despite the popularity of traditional Thai massage, there have been some studies investigating its effects on alleviating TTHs carried out in Thailand, including the single-group studies employing a quasi-experimental design of Wattakeecharoen, [9] Udompittayason, [10] Meechana, [11] and the randomized controlled clinical trials of Kruapanich et al [12]. and Sooktho [13]. The results yielded inconclusive evidence on

the likelihood of traditional Thai massage in reducing TTHs, thus calling for further research.
A pilot study on the effectiveness of the court type traditional Thai massage in CTTH treatment on a sample of 10 subjects using the inclusion criteria developed by the HIS. The subjects received two massage therapies for 45 minutes each over a period of one week with evaluations being done before and after each treatment. The findings showed that the majority of the patients were comparison before and after the treatment revealed a significant reduction in CTTH symptoms after the treatment at $p < 0.05$ (Visual Analog Scale (VAS) before and after the treatment were 6.80 and 2.70 respectively). It was also found that the post-treatment angles of movement in all directions were enhanced at $p < 0.05$ [14]. Nevertheless, to ensure the short-term effects of CTTM on pressure pain threshold (PPT) and pain intensity in treating CTTHs, it is necessary to carry out a randomized controlled trial and compare the results with those obtained from the prescription of amitriptyline.

MATERIALS AND METHODS

Design

A randomized controlled trial was conducted at the Department of Traditional Thai Medicine, Bamnet Narong Hospital, Amphur Bamnet Narong, Chaiyaphum Province, Thailand. This study was approved by the 1st Ethics Review Committee For Research Involving Human Subjects, Health Science Group, Chulalongkorn University (COA No. 052/2557).

Subjects

The patients aged 18-65 years at Bamnet Narong Hospital diagnosed with CTTH according to the criteria of IHS [1] with the inclusion and exclusion criteria below. The sample consisted of 60 patients with CTTH as identified by the score on the VAS of 4 or above [12]. They were randomly assigned to the treatment group or the control group, each with 30 subjects.

The main inclusion criterion was CTTH diagnosed by criteria of IHS [1], for any of the following: Headache occurring on ≥ 15 days per month on average for over six months, Headache lasts hours and could also be continuous, Suffer from at least two of the following symptoms: a. bilateral location, b. pressing/tightening (non-pulsating) quality, c. mild or moderate intensity, d. not aggravated by routine physical activity such as walking or climbing stairs, experience headache without the following symptoms: a. no more than one of photophobia, phonophobia or mild nausea, b. neither moderate nor severe nausea nor vomiting, not attributed to another disorder, suffer from headaches at least twice a week, experience pain with a severity of greater than or equal to 4 on the VAS, be willing to participate, no prior experience with the CTTM, amitriptyline and other treatments or prior experience dating back more than 1 week.

Patients were excluded for any of the following: other types of headache not classified as CTTH, history of the following illnesses or disorders: a. cervical disorders, such as cervical spondylosis, or herniated disc, b. neurological disorders, such as hemiplegia or paresis, c. skin diseases, such as chickenpox or herpes zoster, no communicative ability or inability to follow instructions and a fever of 38.5°C.

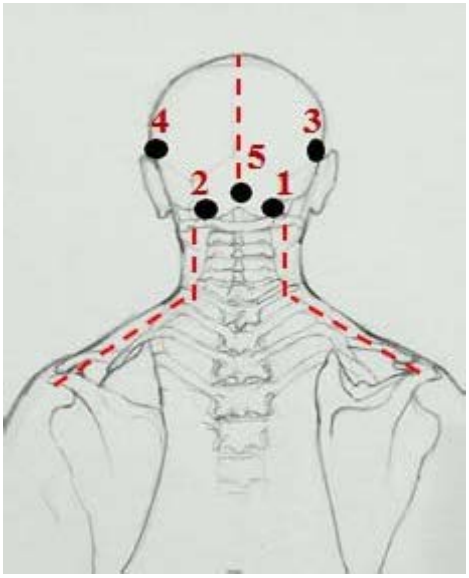

Figure 1:The massage points 1–5 on the back of the head of CTTH patient [15].

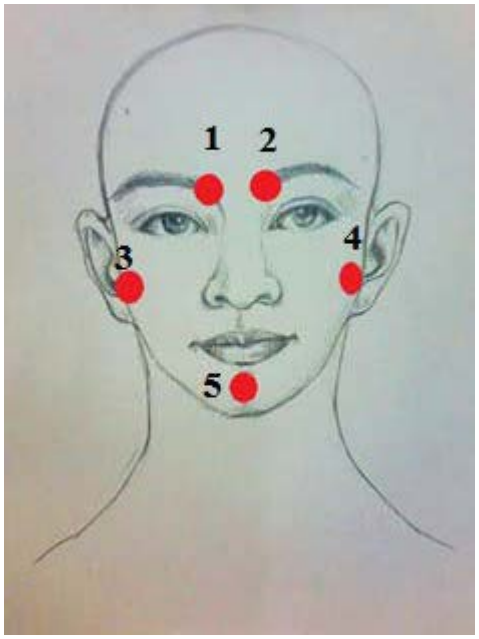

Figure 2:The massage points 1–5 on the forehead of CTTH patient[15].

Assessment

Outcome measures including the VAS, tissue hardness meter and algometer, were assessed before the first treatment, assessed was conducted again in short-term day 1.

Measurement instruments

The VAS is an instrument for measuring perception of current pain, rated from 0 (no pain) to 10 (most severe pain ever experienced). In this study, the VAS was assessed before the first treatment as well as after the treatment at short-term day 1. Tissue hardness and PPT were measured using a Tissue Hardness meter-and-algometer (OE-220, ITO /JAPAN). Tissue hardness measurement involved pushing the force sensor of the device on the skin over the trapezius muscle until the beep sound was noted, then stop pushing and read the recorded number giving the percentage of tissue hardness. PPT was measured using the algometer mode of the device. The 1-cm2 sensor knob was gradually pushed down on the skin over the muscle until the patient feel a little discomfort without pain. At this time, the patient was informed to push the hand-held switch with a beep sound to stop the procedure and read the recorded force for PPT. The reliability of measurement were tested at the beginning of the study and found high for tissue hardness (ICC = 0.97) and PPT (ICC = 0.92) [15]. The tissue hardness and the PPT were assessed before the first treatment as well as after the treatment at short-term day 1.

Intervention

Sixty patients aged 18-65 years who were diagnosed with CTTH according to the criteria of the International Headache Society (IHS) participated. They were randomly allocated into a treatment group and control group. After the preliminary diagnosis, the randomization, and signing of the consent form, the patients were given a 1 day treatment according to the group to which group they belonged. The details are as follows.

The 30 patients who were randomly allocated in the treatment group received the CCTM. Lasting 45 minutes for each session, the treatment. The CCTM involved using thumb pressures along the massage meridian lines and points of CCTM.

In details, the method for alleviating TTH using CCTM comprised of seven steps lasting 45 minutes, starting from the shoulders (15 minutes), both sides of the upper back (5 minutes), the area connecting the neck and the shoulders (10 minutes), the tips of the shoulders (3 minutes), the back of the head (5 minutes) (Figure 1), the middle line of head (2 minutes), and the forehead (5 minutes) (Figure 2).

The other 30 patients who were randomly allocated into the control group were given Amitriptylene by a licensed medical practitioner. They were prescribed to take 25 mg once daily. Each of them was informed that the medication could cause drowsiness, and recommended that strict adherence to the prescribed time of consumption was required.

Randomization

The patients meeting the inclusion criteria were assigned to either the treatment group (receiving CTTM) or the control group (taking amitriptyline) using the simple random sampling technique. The randomization was performed using a lottery by the researcher assistant.

Statistical Analysis

The data was analyzed in terms of mean and standard deviation (SD) for continuous variables and percentage for categorical variables. The study aimed to analyze each session of treatment separately at different time points: before the first treatment, after day 1.

An analysis of Paired t-tests were used to compare the within-group variables at baseline with outcome measures short-term day 1 after the treatment or control period within each respective group, and analysis of covariance (ANCOVA) was also be conducted to compare the differences between the two groups as well as estimate the adjusted difference between the two groups at 95% confidence level.

RESULTS

Details of demographic data and health status were presented in table 1. The average age 37 to 50 year classify from class interval of CTTM group was 13(43.30) and of the control group was 13(43.30). Most baseline characteristics were equally balanced between the two groups. Table 2 shows compare the within-group VAS means of the CTTM group and the control group at baseline, short-term day 1. The results showed a statistically significant decline in the VAS means for both the groups ($P < 0.05$). Tissue hardness and PPT not statistically significant for both the groups. Table 3 shows compare between groups the CTTM group and the control group were compared at baseline, short-term day 1, it was found that after adjustment for baseline levels, the means for VAS and PPT were statistically different at short-term day 1 ($P < 0.05$). The VAS mean of the CTTM group was 5.03 compared to 5.13 for the control group with the difference between the two groups equaling 0.32 (95% confidence interval, 0.07-0.57, $P < 0.05$). The PPT mean of the CTTM group was 3.40 compared to 2.89 for the control group with the difference between the two groups equaling 5.38 (95% confidence interval, 5.53 - 0.55, $P < 0.05$).

Table 1 Demographic and baseline clinical characteristic

Characteristics	CTTM	Control	P-value
Gender			
Female	26(86.70)	29(96.70)	<0.05
Male	4 (13.30)	1 (3.30)	
Aged (year)			
23–36 years	6 (20.00)	1 (3.30)	
37–50 years	13(43.30)	13(43.30)	0.350
51–64 years	11(36.70)	16(53.30)	
Mean = 49.75; SD = 10.93; median= 48			
Classify from class interval			
Baseline of clinical outcome measure			
Visual analog scale (VAS 0–10 cm); mean □ ± SD	6.30 ± 1.20	6.06 ± 0.94	0.105
Tissue hardness (%); mean ± SD	59.89 ± 11.04	57.16 ± 8.50	0.159
Pressure pain threshold (kg/cm2); mean ± SD	3.17 ± 0.69	2.85 ± 0.79	0.264

Note: CTTM is court-type traditional Thai massage.

Table 2 Comparison of the outcome measures between baseline (pre-test) and post-test assessments in the CTTM and control groups (paired t-tests).

Outcome	Group	Baseline	Short-term day 1 (Mean ± SD)	P-value
Visual analog scale (VAS 0–10 cm); mean □ ± SD	CTTM	6.30 ± 1.20	5.03± 1.24	<0.05
	Control	6.06 ± 0.94	5.13± 1.04	<0.05
Tissue hardness (%); mean ± SD	CTTM	59.89 ± 11.04	56.88±1 1.55	0.198
	Control	57.16 ± 8.50	56.93±8 .40	0.896
Pressure pain threshold (kg/cm2); mean ± SD	CTTM	3.17 ± 0.69	3.40±0. 78	0.056
	Control	2.85 ± 0.79	2.89±0. 65	0.697

Note: CTTM is court-type traditional Thai massage. NA is not available. $P < 0.05$ is statistically significant differences from baseline.

Table 3 Comparison of the adjusted mean and 95% CI outcome measures (adjusted for baseline using ANCOVA)

Outcome	Short-term day 1 (Mean ± SD)			
	CTTM	Control	Difference (95% CI)	P-value
Visual analog scale (VAS 0–10 cm); mean □ ± SD	5.03±1.24	5.13± 1.04	0.32 (0.07 to 0.57)	<0.05
Tissue hardness (%); mean ± SD	56.88± 11.55	56.93 ± 8.40	-5.59 (-4.50 to 3.66)	0.625
Pressure pain threshold (kg/cm2); mean ± SD	3.40± 0.78	2.89± 0.65	5.38 (5.53 to 0.55)	<0.05

Note: CTTM is court-type traditional Thai massage. NA is not available. $P < 0.05$ is statistically significant differences from baseline.

DISCUSSION

This study aimed to evaluate the short-term effects of the CTTM on PPT and pain intensity to treat patients suffering from CTTH comparing with amitriptyline taking. Assessment was conducted at the VAS, tissue hardness meter and PPT, were assessed before the first treatment, assessed was conducted again in short-term day 1. The headache pain intensity scores reduced from baseline at short-term day 1 for both the CTTM group and the control group, the VAS, a comparison between the two groups indicated statistically significant differences. Similar findings were also reported, Cathcart S, et al. study Pain sensitivity mediates the relationship between stress and headache intensity in chronic tension-type headache, results shows pain sensitivity significantly mediated the relationship between stress and headache intensity [16]. This study similar findings were Chatchawan and colleagues, on the effects of Thai traditional massage on pressure pain threshold and headache intensity in patients with chronic tension-type and migraine headaches, the results shows in both groups, headache intensity decreased significantly ($P < 0.05$) [17].

A comparison of the tissue hardness reduced for CTTM groups but not statistically significant for within-group and between the groups. differed findings are also reported elsewhere. Zheng et al.

[18] evaluated the therapeutic effectiveness of lumbar tender point deep massage in treating chronic nonspecific low back pain.

The PPT compare between groups of the CTTM group increased was significantly higher than that of the control group. The results are consistent with those of other researches carried out earlier. Walton, DM., et al. study Clinical Pressure Pain Threshold Testing in Neck Pain: Comparing Protocols, Responsiveness, and Association With Psychological Variables, the results suggest that PPT is adequately reliable and that 3 measurements should be taken to maximize measurement properties[19]. Similar findings were also reported, Toro-Velasco et al. [20], which investigated the effectiveness of a head-neck massage protocol in alleviating CTTHs compared to placebo ultrasound. An assessment of PPT at both sides of temporalis muscles immediately and 24 hours after the treatment did not demonstrate an improvement in the patients' conditions. It should be noted, however, that Toro-Velasco et al.'s research is different from the present study in terms of research design, sample size, and the form and area of massage. and Similar findings are also reported, Chatchawan and colleagues [17], on effects of Thai traditional massage on pressure pain threshold and headache intensity in patients with chronic tension-type and migraine headaches. After the treatment and at 3 and 9 weeks of follow-up, the TTM group showed a significant increase in PPT ($P < 0.01$) compared with the sham ultrasound group.

CONCLUSIONS

The results showed the VAS a statistically significant decrease in headache pain intensity for the CTTM group at at baseline, short-term day 1 and a statistically significant difference between the CTTM group and the control group at each assessment at at baseline, short-term day 1. As for tissue hardness, the value for the CTTM group was significantly lower than that of the control group at short-term day 1, and the value for both the groups reduced at short-term day 1, although not statistically significant. Additionally, the PPT compare between groups of the CTTM group increased was significantly higher than that of the control group. It can therefore be concluded from the findings that CTTM seems to be an effective therapy for stress-related variables and increased the PPT as well as reducing pain intensity for the CTTHs.

ACKNOWLEDGEMENTS

This study was supported by the Thai Traditional Medical Knowledge Fund. This publication has been supported by Suan Sunandha Rajabhat University, Bangkok, Thailand.

REFERENCES

[1] WorldHealthOrganization, "*The International Classification of Headache Disorders 2nd Edition*," Cephalalgia, vol. 24, 2004.
[2] Martelletti, P. and T.J. Steiner, *Handbook of Headache practical management*. 2011, London New York Springer Milan Heidelberg Dordrecht
[3] Stovner, L., et al., *The global burden of headache: a documentation of headache prevalence and disability worldwide.* Cephalalgia, 2007. **27**(3): p. 193-210.
[4] Stephen, D. S., Richard B., and Donald J.D. L., *Wolff 's Headache and Other Head Pain*, Oxford University, Oxford, UK, 2001.
[5] World Health Organization, *Atlas of headache disorders and resources in the world 2011*. 2011.
[6] The Foundation for the Promotion ofThai TraditionalMedicine Ayurved School, *Traditional Massage (Court-type Thai Traditional Massage)*, Pickanesprinting, Bangkok, Thailand, 2005.
[7] The Foundation for the Promotion ofThai TraditionalMedicine and Ayurved Thamrong School Center of Applied Thai Traditional Medicine Faculty of Medicine Siriraj Hospital Mahidol University, *Traditional Massage (Court-type Thai Traditional Massage) Basic Massage*, Mahidol University, Bangkok, Thailand, 2011.
[8] AyurvedThamrong School Center of AppliedThai Traditional Medicine Faculty of Medicine Siriraj Hospital Mahidol University, *Traditional Massage (Court-Type Thai Traditional Massage)Massage Point*, Mahidol University, Bangkok, Thailand, 2014.
[9] Wattakeecharoen, J., *Comparison the effects of modified Thai traditional massage and management by paracetamol on level of pain and duration of decreasing pain level in tension-type headache patients.* , in *Master Thesis in nursing*. 1991, Mahidol University.
[10] Udompittayason, W. and W. Tanchaiswad, *Effect of Thai massage on reduction of tension-type headache.* Thai J Nurs Res 2001. **5**: p. 156-68.
[11] Meechana, R., *The comparison of the effects of Thai traditional massage and the use of paracetamol for reducing tension of persons with headache.*, in *Master Thesis in Public health*. 2001, Mahidol University.
[12] Kruapanich, C., et al., *The immediate effect of Traditional Thai massage for reducing pain on patients related with Episodic tension-type headache.*, in *Master of Science Thesis in Physical Therapy*. 2010, KhonKaen university.
[13] Sooktho, S., et al., *Therapeutic Effectiveness of Traditional Thai Massage on Patients with Chronic-*

Tension Type Headache And Migraine., in Master of Science Thesis in Physical Therapy. 2012, KhonKaen university.
[14] Damapong, P. Kanchanakhan, N. Eungpinichpong, W., and Damapong, P., *Effectiveness of Court-type Traditional Thai Massage in Patients with Chronic Tension-type Headache: A Pilot Study*. Journal of Health Research. vol. 29, no. 5, 2015.
[15] Damapong, P. Kanchanakhan, N. Eungpinichpong, W., Putthapitak, P., and Damapong, P., *A Randomized Controlled Trial on The Effectiveness of Court-type Traditional Thai Massage versus Amitriptyline in Patients with Chronic Tension-type Headache*. Evidence-Based Complementary and Alternative Medicine Article. In press, 2015.
[16] Cathcart S, PhD., Bhullar N, PhD., Immink M, PhD., Vedova CD, PhD., Hayball J, PhD. *Pain sensitivity mediates the relationship between stress and headache intensity in chronic tension-type headache/La sensibilité à la douleur médiatrice entre le stress et l'intensité des céphalées de tension chroniques.* Pain Research & Management : The Journal of the Canadian Pain Society 2012 Nov;17(6):377-80.
[17] Chatchawan, U. Eungpinichpong, W. Sooktho, S. Tiamkao, S., and Yamauchi, J. *"Effects of thai traditional massage on pressure pain threshold and headache intensity in patients with chronic tension-type and migraine headaches,"* The Journal of Alternative and Complementary Medicine, vol. 20, no. 6, pp. 486–492, 2014.
[18] Zheng, Z. Wang, J. Gao ,Q., et al., *"Therapeutic evaluation of lumbar tender point deepmassage for chronic non-specific low back pain,"* Journal of Traditional Chinese Medicine, vol. 32, no. 4, pp. 534–537, 2012.
[19] Walton DM, Levesque L, Payne M, Schick J. *Clinical Pressure Pain Threshold Testing in Neck Pain: Comparing Protocols, Responsiveness, and Association With Psychological Variables*. Phys Ther 2014 06;94(6):827-37.
[20] Toro-Velasco, C. Arroyo-Morales, M. Fern๑andez-de-las-Pe˜nas, C. Cleland, J. A. and Barrero-Hern๑andez, F. J. *"Short-term effects of manual therapy on heart rate variability, mood state, and pressure pain sensitivity in patients with chronic tensiontype headache: a pilot study,"* Journal of Manipulative and PhysiologicalTherapeutics, vol. 32, no. 7, pp. 527–535, 2009.

First International Conference on Science, Engineering & Environment,
Tsu City, Mie, Japan, Nov.19-21, 2015, ISBN: 978-4-9905958-5-2 C3051

XANTHAN GUM FROM SUGAR CANE RESIDUE

Nittaya Ngowatana[1] and Kanokwan Rudisirisak[1]
[1]Department of Chemistry, Faculty of Science and Technology, Rajamangala University,
Thunyaburi, Pathumtani,12110, Thailand

ABSTRACT

Xanthan gum is polysaccharide that is used as the component to increase the viscosity and stability of the food product and other product. Some microorganisms could produce xanthan gum. This project focused on the xanthan gum production by using sugarcane residue, as law material, and *Xanthanmonas campertris TISTR 840*. We found that incubation time of *Xanthanmonas campertris TISTR 840* at room temperature was 48 hours. Sugarcane residue extraction that composed sugar 15.5g./100 mL. , pH 7, incubated with *Xanthanmonas campertris TISTR 840* for 144 hours at room temperature and 200 rpm. shaker speed could produce xanthan gum in highest amount.. Precipitation of xanthan gum was added KCl 4 g to 100 mL of incubation media that removed microorganism . We dried xanthan gum at 100^0 C ,30 min. and collected 1.5g. of xanthan gum. The produced xanthan gum was soluble in water, 95% ethanol, 5% NaOH, 8% HCl, iso-propyl alcohol and glycerol. It was stable in 5% NaOH, 8% HCl , 2% NaCl. The produced xanthan gum that was soluble in water;2g./100mL.; was stable at 120^0C. Infrared spectroscopy showed that both of produced and commercial xanthan gum were the same pattern of IR spectrum . Salad cream added with produced xanthan gum was stable in acid-base property and viscoscity for 4 weeks.

Keywords: Xanthan gum, Xanthanmonas campertris TISTR 840, Sugarcane residue, Polysaccharide, Microorganism production

INTRODUCTION

We made artificial paper from sugarcane residue.We found that if we boiled the residue before paper production , we could reduce amount of NaOH that extracted cellulose. *Xanthanmonas campertris* can grow on rice, barley, corn flour, acid whey, molasses and sugarcane,etc,[1] and produce xanthan gum.[1],[2]. Xanthan gum is use as additive in food, cosmetic and medicine industry because its suitable property, such as a high degree of pseudoplasticity, a high viscosity at low concentration[2].The FDA (Food and Drug Administation in 1996) allowed to use xanthan gum as food additive[3]. This project focused on the xanthan gum production by using sugarcane residue, as law material for production of xanthan gum from *Xanthanmonas campertris TISTR 840*.

MATERIALS AND METHODS

Preparation Of *Xanthanmonas campertris TISTR 840*

Freeze-dried culture of *Xanthanmonas campertris TISTR 840* was inoculated in nutrient broth under aseptic conditions and incubated at room temperature and 200 rpm. shaker speed. Turbidity at 600 nm. used to determined growth rate of *Xanthanmonas campertris TISTR 840*. The activated *Xanthanmonas campertris TISTR 840* was keep in slant at low temperature.

Sugarcane Residue Extraction

Sugarcane residue 1 kilogram was cut into small pieces and boiled in 1,000 mL.of water about 3 hrs.The extraction was light yellow, evaluated pH and amount of reducing sugar by DNSA. The sugarcane residue extraction was sterilized and stored at low temperature under aseptic conditions throughout the entire experiment.

Determination Of The Reducing Sugar Content

The reducing sugar content was determined with DNSA that measured at 520 nm using a glucose solution (100-500 mg/dm^3) as the standard.

Growth Rate Of *Xanthanmonas campertris TISTR 840* In Sugarcane Residue Extraction

The activated *Xanthanmonas campertris TISTR 840* was inoculated in sterile sugarcane residue extraction 50 mL. and incubated at room temperature ,shaking rate 200 rpm., 144 hrs.. This inoculated extraction , 5 mL., was inoculated in sterile sugarcane residue extraction 250 mL and incubated at the same condition anddetermined growth rate by turbidity measuring at 600nm..

Factors Effected Xanthan Gum Production

The reducing sugar content

The sugarcane residue extraction was adjusted the

reducing sugar content to 0.5, 0.75, 1.5 and 3.0 g/100mL., pH7 by using NaOH and sterilized. The activated *Xanthanmonas campertris TISTR 840* was inoculated in 100 mL. of this extraction and incubated at room temperature ,shaking rate 200 rpm., 24 hrs.. This inoculated extraction , 5 mL., was inoculated in sterile sugarcane residue extraction 95 mL and incubated at the same condition. At 0, 48, 96, 144 hrs., we measured pH, viscosity by using 4cm.diameter probe at 100 rpm. Separated micro-organism from media by centrifuge. After sterilized media , measured amount of reducing sugar and used 1% KCl to coagulate xanthan gum.

Acid- base condition

The sugarcane residue extraction was adjusted the reducing sugar content to 1.5 g/100mL., pH 5, 7and 9 by using NaOH. The extraction that were primary pH and adjusted pH were sterilized. The activated *Xanthanmonas campertris TISTR 840* was inoculated in 300 mL. of each extraction and incubated at room temperature ,shaking rate 200 rpm., 24 hrs.. Each inoculated extraction 10 mL., was inoculated in sterile sugarcane residue extraction 90 mL,respectively and incubated at the same condition. At 0, 48, 96, 144 hrs., we measured pH, viscosity by using 4cm.diameter probe at 100 rpm. Separated micro-organism from media by centrifuge. After sterilized media , measured amount of sugar and used 1% KCl to coagulate xanthan gum.

Shaking rate

The sugarcane residue extraction was adjusted the sugar content to 1.5 g/100mL., pH 7 by using NaOH. The extraction was sterilized. The activated *Xanthanmonas campertris TISTR 840* was inoculated in 120 mL. this extraction and incubated at room temperature ,shaking rate at 150, 200 and 250rpm., 24 hrs.. Each inoculated extraction 10 mL., was inoculated in sterile sugarcane residue extraction 90 mL,and incubated at the same condition. At 0, 48, 96, 144 hrs., we measured pH, viscosity by using 4cm.diameter probe at 100 rpm. Separated micro-organism from media by centrifuge. After sterilized media , measured amount of reducing sugar and used 1% KCl to coagulate xanthan gum.

Concentration of KCl

The sugarcane residue extraction was adjusted the sugar content to 1.5 g/100mL., pH 7 by using phosphate buffer. The extraction was sterilized. The activated *Xanthanmonas campertris TISTR 840* was inoculated in 120 mL. this extraction and incubated at room temperature ,shaking rate at 150, 200 and 250rpm., 24 hrs.. Each inoculated extraction 10 mL., was inoculated in sterile sugarcane residue extraction 90 mL,and incubated at the same condition. At 0, 48, 96, 144 hrs., we measured pH, viscosity by using 4cm.diameter probe at 100 rpm. Separated micro-organism from media by centrifuge. After sterilized media , measured amount of reducing sugar and used KCl 2%, 3% and 4% to coagulate xanthan gum.

Properties Of Produced Xanthan Gum

Color of xanthan gum

Solubility in solvent

Comparison solubility of 2%xanthan gum, 2% starch, 2% gum arabic in H_2O, ethyl alcohol, 5%NaOH, 8%HCl , isopropylalcohol and glycerol.

Stability in solutions

Prepare 2% of xanthan gum in 2%NaCl, 5%NaOH and 8%HCl.Measure viscosity of these solutions by using 4 cm.probe at 100rpm., room temperature and recorded at 24, 48,72 and 96 hrs.Compare with 2% starch, 2% gum arabic.

Stability at temperature

Prepare 2% of xanthan gum in 2%NaCl, 5%NaOH and 8%HCl.Measure viscosity of these solutions by using 4 cm.probe at 100rpm.,at 40, 60, 80 and 100^{o}C..Compare with 2% starch, 2% gum arabic.

Property Of Produced And Commercial Xanthan Gum

Viscosity

Measured viscosity of 1% of each produced and commercial xanthan gum by using 4 cm.probe at 100rpm.

Acid-base value

Measured pH of 1% of each produced and commercial xanthan gum at room temperature.
.

Comparison melting point of produced and commercial xanthan gum by using Staurt Melting Point Apparatus SMP3.

Infrared spectrum

Comparison infrared spectrum of produced and commercial xanthan gum.

RESULT AND DISCUSION

Growth Rate Of *Xanthanmonas campertris TISTR 840* In Sugarcane Residue Extraction

Figure 1 was shown that the stastionary phase of the activated *Xanthanmonas campertris TISTR 840* in sterile sugarcane residue extraction was 48-144 hrs..

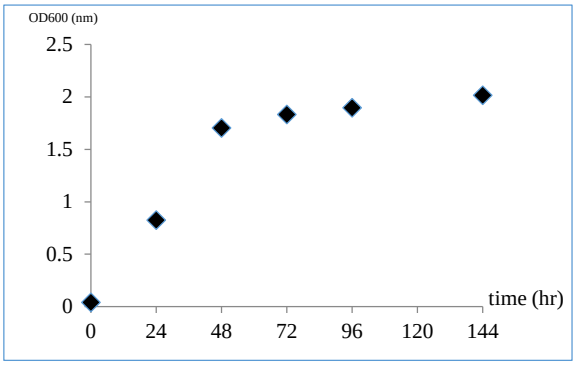

Fig.1 Growth curve of The activated *Xanthanmonas campertris TISTR 840*

Factors Effected Xanthan Gum Production

The Reducing sugar content

Figure 2 was shown that the sugarcane residue extraction; amount of 1.5 and 3.0 g/100mL.reducing sugar, pH 7; similar effected to growth rate of *Xanthanmonas campertris TISTR 840* at room temperature,shaking rate 200 rpm., This profile wasshown that the higher amount of reducing sugar, the higher growth rate of *Xanthanmonas campertris TISTR 840*.

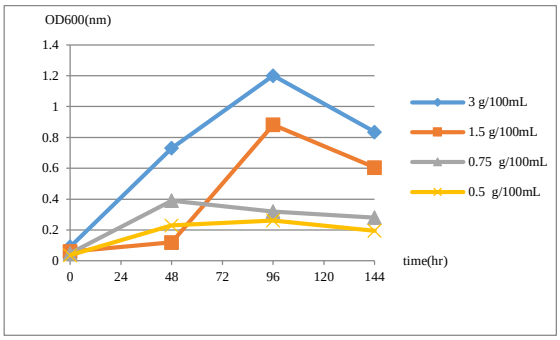

Fig. 2 The reducing sugar content of the sugarcane residue extraction , 0.5, 0.75, 1.5 and 3.0 g/100mL. effected to growth rate of *Xanthanmonas campertris TISTR 840*.

Figure 3 was shown that the amount of reducing sugar of all of the sugarcane residue extraction at pH 7 ,room temperature and shaking rate 200rpm..had the same profile in the growth of *Xanthanmonas campertris TISTR 840*. This profile indicated that *Xanthanmonas campertris TISTR 840* used the sugarcane residue extraction as carbon source.

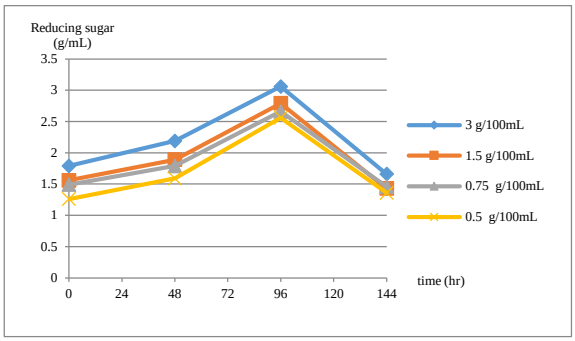

Fig. 3 Profile of the amount of reducing sugar in growth rate of *Xanthanmonas campertris TISTR 840*.

Figure 4 was shown that the *Xanthanmonas campertris TISTR 840*. could produce the higest xanthan gum in the 1.5 g/100mL. of reducing sugar of sugarcane residue extraction pH 7 at room temperature and shaking rate 200rpm. that recipitated by 1%KCl.

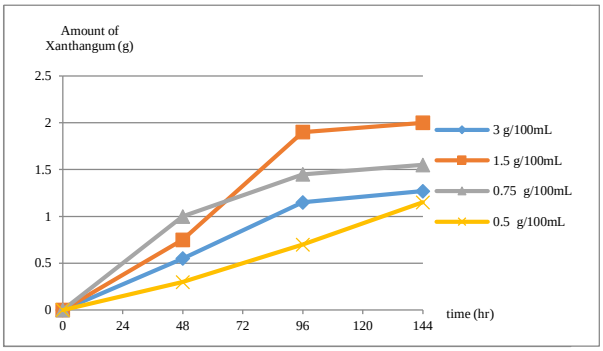

Fig. 4 The *Xanthanmonas campertris TISTR 840*. could produce the higest xanthan gum in the 1.5 g/100mL. of reducing sugar of sugarcane residue extraction

Acid- base condition

Adjusted pH of the sugarcane residue extraction; pH 5 by acetate buffer, pH 7 by phospate buffer and pH 9 by Tris buffer. The primary pH was the origin sugarcane residue extraction. Figure 5 was shown that the sugarcane residue extraction ; amount of 1.5 mg./100mL.reducing sugar; at the primary pH and pH 7 were the similar effect to growth rate of *Xanthanmonas campertris TISTR 840*.at room temperature and shaking rate 200rpm..

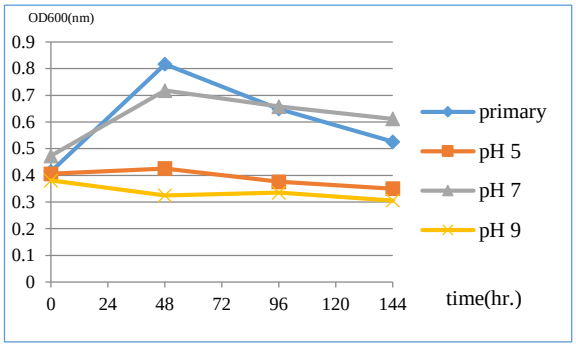

Fig.5 Effect of pH of the sugarcane residue extraction at amount of 1.5g/100mL. reducing sugar to growth rate of *Xanthanmonas campertris TISTR 840.*

Figure 6 was shown that the primary pH sugarcane residue extraction; amount of 1.5 g./100mL.reducing sugar at room temperature and shaking rate 200rpm. Was the highest viscosity.

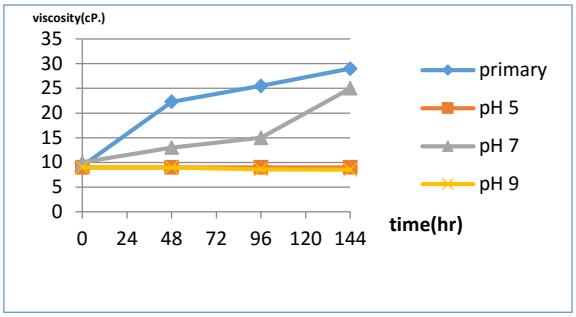

Fig. 6 The highest viscosity of sugarcane residue extraction; 1.5 g/100mL.of reducing sugar , primary pH,at room temperature and shaking rate 200 rpm..

Figure 7 was shown that the primary pH sugarcane residue extraction; amount of 1.5 g./100mL.reducing sugar ,adjusted pH 7 at room temperature and shaking rate 200rpm. could produce the highest amount of xanthan gum that precipitated by 1% KCl.

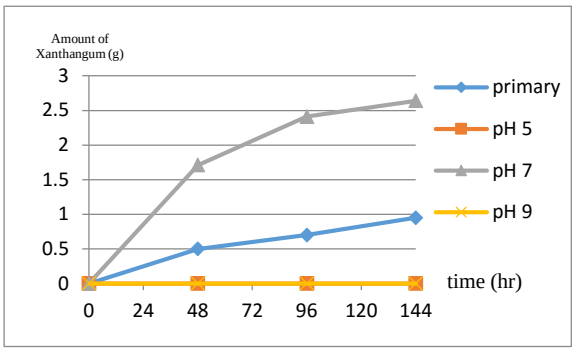

Fig. 7 The highest amount of xanthan gum from the sugarcane residue extraction; 1.5 g/100mL.of reducing sugar, adjusted pH 7at room temperature and shaking rate 200 rpm..

Shaking rate

Figure 7 was shown that shaking rate at 200 rpm. was suitable for production xanthan gum from the sugarcan residue extraction; amount of 1.5 g./100mL reducing sugar ,adjusted pH 7 at room temp and precipitation by 1% KCl.

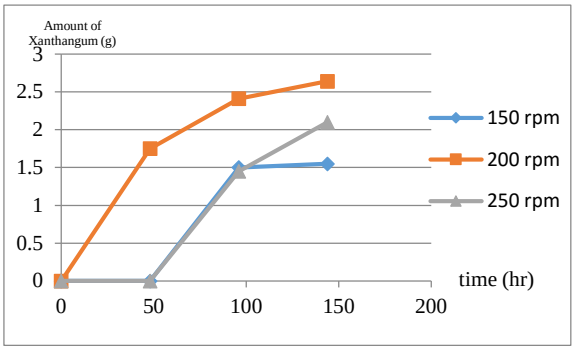

Fig. 7 The highest amount of xanthan gum from the sugarcane residue extraction; 1.5 g/100mL.of reducing sugar, adjusted pH 7 at room temperature and shaking rate 200 rpm..

Concentration of KCl

Figure 8 was shown that the 4%KCl was suitable to precipitate xanthan gum from the sugarcan residue extraction; amount of 1.5g./100mL reducing sugar, adjusted pH 7 at room temp and shaking rate at 200 rpm.

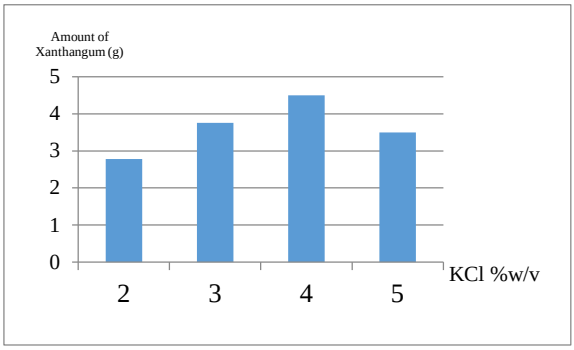

Fig. 8 The highest precipitation of xanthan gum by using 4%KCl from the sugarcane residue extraction; 1.5 g/100mL.of reducing sugar, adjusted pH 7 at room temperature and shaking rate 200 rpm..

The Suitable Conditions For Production Xanthan Gum From The Sugarcane Residue Extraction

From figure 1-8 and results indicated that we could produce xanthan gum from the 1.5 g/100mL.of reducing sugar of sterilized sugarcane residue extraction that adjusted to pH 7 by phosphate buffer[4] because phosphate was energy source[5], shaking rate 200 rpm. with 4 cm.diameter probe at

room temperature

Properties Of Produced Xanthan Gum

Produced xanthan gum was light yellow powder.We found that the properties of produced xanthan gum were similar to the other gums.

Solubility in solvent

2% produced xanthan gum, 2% starch and 2% gum arabic could dissolve well in H_2O, ethyl alcohol, 5%NaOH, 8%HCl , isopropylalcohol and glycerol .

Stability of solutions

Figure 9-11; the viscosity of 2% produced xanthan gum, 2% starch, 2% gum arabic.in 2%NaCl, 5% NaOH and 8%HCl measured by using 4 cm.probe at 100rpm., room temperature and recorded at 24, 48,72 and 96 hrs. indicated that the solutions of produced xanthan gum weremore stable than the other .

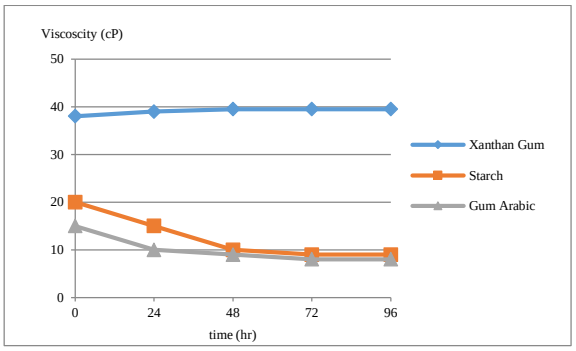

Fig.9 Stability of 2% of xanthan gum, 2% starch and 2% gum Arabic in 2%NaCl

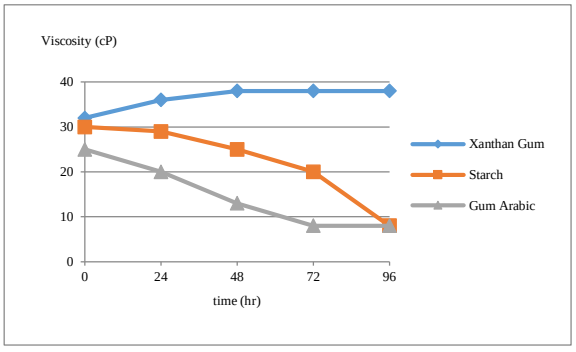

Fig.10 Stability of 2% of xanthan gum, 2% starch and 2% gum arabic in 5%NaOH

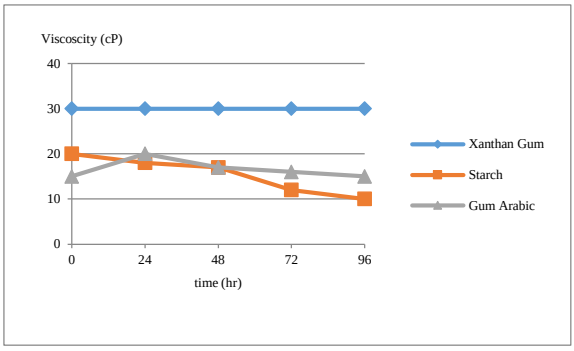

Fig.11 Stability of 2% of xanthan gum, 2% starch and 2% gum arabic in 8%HCl

Stability at temperature

Figure 12 ; the viscosity of 2% produced xanthan gum, 2% starch and 2% gum arabic in 2%NaCl, 5%NaOH and 8%HCl measured by using 4 cm. probe at 100rpm. at 40, 60, 80 and 100ºC. indicated that the 2% produced xanthan gum was more stable than the other.

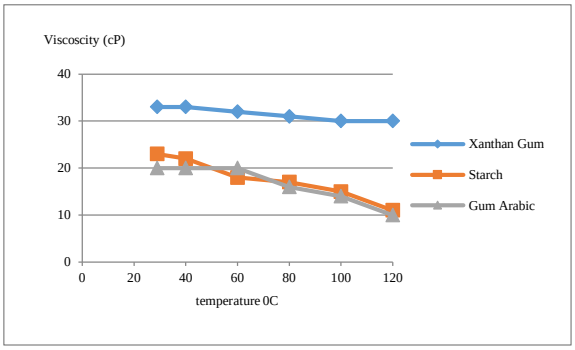

Fig.12 Stability of 2% of xanthan gum, 2% starch and 2% gum arabic in 8%HCl at 40, 60,80 and 100ºC.

Properties Of Produced And Commercial Xanthan Gum

Viscosity , acid-base valueand melting point

Table 1 Properties of produced and commercial xanthan gum

Property	Produced xanthan gum	Commercial xanthan gum
viscosity(cP.)	600	580
pH	7	7
melting point	170	>145

Table1 indicated that the properties of produced and commercial xanthan gum were similar; viscosity of 1% of produced and commercial xanthan gum measured by using 4 cm.probe at 100rpm.

Infrared spectrum

Figure 13 and 14 indicated that infrared spectrum of produced and commercial xanthan gum.were similar.

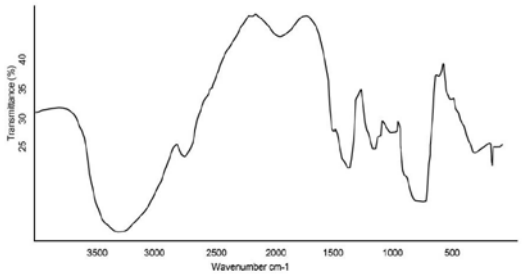

Fig.13 Infrared spectrum of produced xanthan gum.

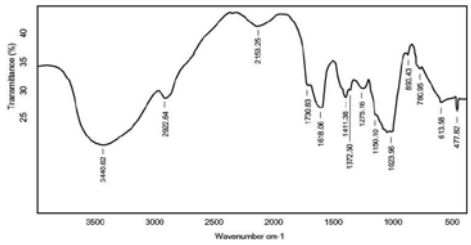

Fig.14 Infrared spectrum of commercial xanthan gum.

REFERENCES

[1] Rosalam,S., England, R. "Review of xanthan gum production from unmodified starches by *Xanthomonas campestris* sp."Enzyme and Microbial Technology,39,(2006)pp 197-207

[2] Sandra,F et.al,Characterization of xanthan gum produced from sugar cane broth.Carbohydrate polymers.volumn 86,Issue 2, 15 August 2011,pp 469-476.

[3] FAO/WHO(Food and Agriculture Organization of the United Nation).1990.Production yearbook 1989.Roma,Codebook.ECON-109(1990).

[4] Salah,R.B.,et.al.Production of xanthangum from *Xanthomonas campestris* nrrl B-1459 by fermentation of date juice palm by-product.(*Phoenix dactylifera* L.) J.of Food process Engineering,34(2011),pp457-474.

[5] Vuyst L.De.,Vermeire,A. Use of industrial medium components for xanthan production by ***Xanthomonas campestris.***Applied microbiology and biotechnology,42 (1994),pp187-191

First International Conference on Science, Engineering & Environment,
Tsu City, Mie, Japan, Nov.19-21, 2015, ISBN: 978-4-9905958-5-2 C3051

EXACT TRAVELING WAVE SOLUTIONS FOR THE GENERALIZED HIROTA-SATSUMA COUPLE KDV SYSTEM USING THE $\mathbf{EXP}\left(-\phi\left(\zeta\right)\right)$ -EXPANSION METHOD

Mostafa M.A. Khater[1] and Emad H. M. Zahran[2]

[1]Department of Mathematics, Faculty of Science, Mansoura University,
35516 Mansoura, Egypt;
[2] Department of mathematical and physical engineering, college of engineering Shubra,
University of Benha, Egypt

ABSTRACT

In this research, we find the exact traveling wave solutions involving parameters of the generalized Hirota-Satsuma couple KdV system according to the $\boldsymbol{exp}(-\boldsymbol{\varphi}(\boldsymbol{\xi}))$ -expansion method and when these parameters are taken to be special values we can obtain the solitary wave solutions which is derived from the exact traveling wave solutions. It is shown that the proposed method provides a more powerful mathematical tool for constructing exact traveling wave solutions for many other nonlinear evolution equations.
Keywords: The $\boldsymbol{exp}(-\boldsymbol{\varphi}(\boldsymbol{\xi}))$ -expansion method; The generalized Hirota-Satsuma couple KdV system; Traveling wave solutions; Solitary wave solutions.

INTRODUCTION

No one can deny the important role which played by the nonlinear partial differential equations in the description of many and a wide variety of phenomena not only in physical phenomena, but also in plasma, fluid mechanics, optical fibers, solid state physics, chemical kinetics and geochemistry phenomena. So that, during the past five decades, a lot of method was discovered by a diverse group of scientists to solve the nonlinear partial differential equations. Such methods are tanh - sech method [1]-[3], extended tanh - method [4]-[6], sine - cosine method [7]-[9], homogeneous balance method [10, 11],F-expansion method [12]-[14], exp-function method [15, 16], trigonometric function series method [17], (G'/G)-expansion method [18]-[21], Jacobi elliptic function method [22]-[25], The $\boldsymbol{exp}(-\boldsymbol{\varphi}(\boldsymbol{\xi}))$ -expansion method [26]-[28] and so on.

The objective of this article is to apply the $\boldsymbol{exp}(-\boldsymbol{\varphi}(\boldsymbol{\xi}))$ -expansion method for finding the exact traveling wave solution of the generalized Hirota-Satsuma couple KdV system which plays an important role in mathematical physics.

The rest of this paper is organized as follows: In Section 2, we give the description of the $\boldsymbol{exp}(-\boldsymbol{\varphi}(\boldsymbol{\xi}))$ -expansion method In Section 3, we use this method to find the exact solutions of the nonlinear evolution equations pointed out above. In Section 5, conclusions are given.

DESCRIPTION OF METHOD

Let us we have the following nonlinear evolution equation

$$P(u, u_t, u_x, u_{tt}, u_{xx}, \ldots\ldots) = 0, \tag{2.1}$$

Since, P is a polynomial in $u(x,t)$ and its partial derivatives. In the following, we give the main steps of this method

Step 1. We use the traveling wave solution in the form

$$u(x,t) = u(\xi), \qquad \xi = x - ct, \tag{2.2}$$

Where c is a positive constant, to reduce Eq. (2.1) to the following ODE:

$$p(u, u', u'', u''', \ldots\ldots) = 0, \tag{2.3}$$

Where P is a polynomial in u (ξ) and its total derivatives.

Step 2. Suppose that the solution of ODE (2.3) can be expressed by a polynomial in $exp(-\varphi(\xi))$ as follow

$$u(\xi) = a_m(\exp(-\varphi(\xi))^m + \cdots, a_m \neq 0 \tag{2.4}$$

Where $\varphi(\xi)$ satisfies the ODE in the form

$$\varphi'(\xi) = \exp\left(-\varphi(\xi)\right) + \mu \exp\left(\varphi(\xi)\right) + \lambda, \tag{2.5}$$

The solutions of ODE (2.5) are

When $\lambda^2 - 4\mu > 0, \mu \neq 0,$

$$\varphi(\xi) = ln\left(\frac{-\sqrt{\lambda^2-4\mu}\, tanh(\frac{\sqrt{\lambda^2-4\mu}}{2}(\xi+c_1))-\lambda}{2\mu}\right), \quad (2.6)$$

When $\lambda^2 - 4\mu > 0, \mu = 0,$

$$\varphi(\xi) = -ln\left(\frac{\lambda}{exp(\lambda(\xi+C_1))-1}\right), \quad (2.7)$$

When $\lambda^2 - 4\mu = 0, \mu \neq 0, \lambda \neq 0,$

$$\varphi(\xi) = ln\left(-\frac{2(\lambda(\xi+C_1)+2}{\lambda^2(\xi+C_1)}\right), \quad (2.8)$$

When $\lambda^2 - 4\mu = 0, \mu \neq 0, \lambda = 0,$

$$\varphi(\xi) = \ln(\xi + C_1), \quad (2.9)$$

When $\lambda^2 - 4\mu < 0$

$$\varphi(\xi) = ln\left(\frac{\sqrt{4\mu-\lambda^2}\, tan\,(\frac{\sqrt{4\mu-\lambda^2}}{2}(\xi+c_1))-\lambda}{2\mu}\right), \quad (2.10)$$

Where $a_m, \ldots, \lambda, \mu$ are constants to be determined later.

Step 3. Substitute Eq. (2.4) along Eq. (2.5) into Eq. (2.3) and collecting all the terms of the same power $exp\,(-m\varphi(\xi))$, (m = 0,1,2,3 ...) and equating them to zero, we obtain a system of algebraic equations, which can be solved by Maple or Mathematica to get the values of it.

Step 4. Substituting these values and the solutions of Eq.(2.5) into Eq.(2.3) we obtain the exact solutions of Eq.(2.1).

It is to be noted here that the construction of the $exp(-\varphi(\xi))$ –expansion method is similar to the construction of the $\left(\frac{G'}{G}\right)$ -expansion. For better understanding of the duality of both methods we cite [29], [30] and [31].

3 APPLICATIONS

Here, we will apply the $\boldsymbol{exp}(-\boldsymbol{\varphi}(\boldsymbol{\xi}))$ -expansion method described in Sec.2 to find the exact traveling wave solutions and the solitary wave solutions of the generalized Hirota-Satsuma couple KdV system[32]. We consider the generalized Hirota-Satsuma couple KdV system

$$\begin{cases} u_t = \frac{1}{4}u_{xxx} + 3u\,u_x + 3\left(-v^2+\omega\right)_x, \\ v_t = -\frac{1}{2}v_{xxx} - 3u\,v_x, \\ \omega_t = -\frac{1}{2}\omega_{xxx} - 3\,u\,\omega_x. \end{cases} \quad (3.1)$$

When $\omega = 0,$ Eq. (3.1) reduce to be the well-known Hirota-Satsuma couple KdV equation. Using the wave transformation $u(x,t) = u(\zeta),$ $v(x,t) = v(\zeta),$ $\omega(x,t) = \omega(\zeta)$ and $\zeta = k(x - \lambda_1 t)$ carries the partial differential equation (3.1) into the ordinary differential equation

$$\begin{cases} -\lambda_1 k\,u' = \frac{1}{4}k^3u''' + 3k\,u\,u' + 3k\left(-v^2+\omega\right)', \\ -\lambda_1 k\,v' = -\frac{1}{2}k^3v''' - 3k\,uv', \\ -\lambda_1 k\,\omega' = -\frac{1}{2}k^3\omega''' - 3k\,u\,\omega'. \end{cases} \quad (3.2)$$

Suppose we have the relations between $(u \,\&\, v)$ and $(\omega \,\&\, v) \Rightarrow \left(u = \alpha v^2 + \beta v + \gamma\right)$ $\left(\omega = Av + B\right)$. Where α, β, γ, A and B are arbitrary constants. Substituting this relations into second and third equations of Eq. (3.2) and integrating them, we get the same equation and integrate it once again we obtain

$$k^2v'^2 = -2\alpha v^4 - 2\beta v^3 + 2\left(\lambda_1 - 3\gamma\right)v^2 + 2c_1v + c_2, \quad (3.3)$$

where c_1 and c_2 is the arbitrary constants of integration, and hence, we obtain

$$\begin{aligned} k^2u'' &= 2\alpha k^2v'^2 + k^2\left(2\alpha v + \beta\right)v'' \\ &= 2\alpha\begin{bmatrix} -\alpha v^4 - 2\beta v^3 + 2\left(\lambda_1 - 3\gamma\right)v^2 \\ +2c_1v + c_2 \end{bmatrix} \\ &\quad + \left(2\alpha v + \beta\right)\begin{bmatrix} -2\alpha v^3 - 3\beta v^2 \\ +2\left(\lambda_1 - 3\gamma\right)v + c_1 \end{bmatrix}. \end{aligned} \quad (3.4)$$

So that, we have

$$P'' + lP - mP^3 = 0. \quad (3.5)$$

Where $c_1 = \dfrac{1}{2\alpha^2\left(\beta^2 + 2\lambda_1\alpha\beta - 6\alpha\beta\gamma\right)},$

$$v(\zeta)=\mathrm{a}\,\mathrm{P}(\zeta)-\frac{\beta}{2\alpha},\ \alpha=\frac{\beta^2-4}{4(\gamma-\lambda_1)},$$

$$A=\frac{4\beta(\lambda_1-\gamma)}{\beta^2-4},$$

$$B=\frac{1}{6(-\gamma+\lambda_1)(\beta^2-4)^2}\times$$

$$\begin{pmatrix}16c_3\lambda_1\beta^2-2c_3\lambda_1\beta^4-16c_3\gamma\beta^2+3c_3\gamma\beta^4\\+56\lambda_1^2\gamma\beta^2-48\gamma^2\lambda_1\beta^2-16c_2+c_2\beta^6\\-12c_2\beta^4+12c_2\beta^2-16\gamma^2\lambda_1-32\lambda_1^2\gamma\\-8\lambda_1^3\beta^2+\beta^4\gamma^3-2\beta^4\lambda_1^3+32c_3\gamma\\-32c_3\lambda_1+48\gamma^3+\beta^4\gamma^2\lambda_1\end{pmatrix},$$

$$l=\frac{-a}{k^2}\left(\frac{3\beta^2}{2\alpha}+2\lambda_1-6\gamma\right),m=\frac{-2\alpha a^3}{k^2}.$$

Balancing between the highest order derivatives and nonlinear terms appearing in P'' and P^3 $\Rightarrow$ $(N+2=3N)\Rightarrow(N=1)$. So that, by using Eq.(2.4) we get the formal solution of Eq.(3.5)

$$P(\zeta)=\mathrm{a}_0+a_1\exp(-\phi(\zeta)),\qquad(3.6)$$

Substituting Eq. (3.6) and its derivative into Eq. (3.5) and collecting all term with the same power of $\boldsymbol{exp}(-\mathbf{3}\boldsymbol{\varphi}(\boldsymbol{\xi}))$, $\boldsymbol{exp}(-\mathbf{2}\boldsymbol{\varphi}(\boldsymbol{\xi}))$, $\boldsymbol{exp}(-\boldsymbol{\varphi}(\boldsymbol{\xi}))$, $\boldsymbol{exp}(\mathbf{0}\boldsymbol{\varphi}(\boldsymbol{\xi}))$ we get:

$$2a_1-m\,a_1^3=0,\qquad(3.7)$$

$$a_1\lambda-3m\,a_0\,a_1^2=0,\qquad(3.8)$$

$$2a_1\mu+a_1\lambda^2+l\,a_1-3m\,a_0^2\,a_1=0,\qquad(3.9)$$

$$a_1\lambda\mu+l\,a_0-m\,a_0^3=0.\qquad(3.10)$$

Solving above system by using maple 16, we get:

$$l=\frac{\lambda^2}{2}-2\mu,\ a_0=\pm\frac{\lambda}{2}\sqrt{\frac{2}{m}},a_1=\pm\sqrt{\frac{2}{m}},\ \text{where}\ (m>0).\ \text{thus the solution is}$$

$$P(\zeta)=\pm\frac{\lambda}{2}\sqrt{\frac{2}{m}}\pm\sqrt{\frac{2}{m}}\exp(-\phi(\zeta)).\qquad(3.11)$$

Let us now discuss the following cases:

When $\lambda^2-4\mu>0,\mu\neq0,$

$$P_{(1,2)}=\pm\frac{\lambda}{2}\sqrt{\frac{2}{m}}\pm\sqrt{\frac{2}{m}}\times$$

$$\left(\frac{2\mu}{-\sqrt{\lambda^2-4\mu}\tanh\left(\frac{\sqrt{\lambda^2-4\mu}}{2}(\zeta+C_1)\right)-\lambda}\right),\qquad(3.12)$$

and

$$P_{(3,4)}=\pm\frac{\lambda}{2}\sqrt{\frac{2}{m}}\pm\sqrt{\frac{2}{m}}\times$$

$$\left(\frac{2\mu}{-\sqrt{\lambda^2-4\mu}\coth\left(\frac{\sqrt{\lambda^2-4\mu}}{2}(\zeta+C_1)\right)-\lambda}\right),\qquad(3.13)$$

When $\lambda^2-4\mu>0,\mu=0,$

$$P_{(5,6)}=\pm\frac{\lambda}{2}\sqrt{\frac{2}{m}}\pm\sqrt{\frac{2}{m}}\frac{\lambda}{\exp(\lambda(\zeta+C_1))-1}.\qquad(3.14)$$

When $\lambda^2-4\mu=0,\mu\neq0,\lambda\neq0,$

$$P_{(7,8)}=\pm\frac{\lambda}{2}\sqrt{\frac{2}{m}}\pm\sqrt{\frac{2}{m}}\frac{2(\lambda(\zeta+C_1)+2)}{\lambda^2(\zeta+C_1)}.\qquad(3.15)$$

When $\lambda^2-4\mu=0,\mu\neq0,\lambda=0,$

$$P_{(9,10)}=\pm\frac{\lambda}{2}\sqrt{\frac{2}{m}}\pm\sqrt{\frac{2}{m}}\frac{1}{\zeta+C_1}.\qquad(3.16)$$

When $\lambda^2-4\mu<0$

$$P_{(11,12)}=\pm\frac{\lambda}{2}\sqrt{\frac{2}{m}}\pm\sqrt{\frac{2}{m}}\times$$

$$\left(\frac{2\mu}{-\sqrt{\lambda^2-4\mu}\tan\left(\frac{\sqrt{\lambda^2-4\mu}}{2}(\zeta+C_1)\right)-\lambda}\right),\qquad(3.17)$$

and

$$P_{(13,14)} = \pm\frac{\lambda}{2}\sqrt{\frac{2}{m}} \pm \sqrt{\frac{2}{m}} \times \left(\frac{2\mu}{-\sqrt{\lambda^2-4\mu}\cot\left(\frac{\sqrt{\lambda^2-4\mu}}{2}(\zeta+C_1)\right)-\lambda} \right), \quad \textbf{(3.}18\textbf{)}$$

- **Note that**:

All the obtained results have been checked with Maple 16 by putting them back into the original equation and found correct.

4 PHYSICAL INTERPRETATIONS OF THE SOLUTIONS

In this section, we depict the graph and signify the obtained solutions to the generalized Hirota-

Satsuma couple KdV system. Now, we will discuss all possible physical significances for parameter.

- **Case1.** when: $\left(\lambda^2-4\mu>0\right)$.

1- $\left(\lambda>0,\mu>0\right)$ For example λ = 3, μ = 2 the solution P_1 and P_2 in Eq. (3.12) represent kink shape soliton solutions.

2- $\left(\lambda>0,\mu<0\right)$ For example λ = 3, μ = -2 the solution P_1 and P_2 in Eq.(3.12) represent singular multi soliton solutions. (Dark and bell shaped).

3- $\left(\lambda<0,\mu>0\right)$ For example λ = -3, μ = 2 the solution P_1 and P_2 in Eq. (3.12) represent kink shape soliton solution.

4- $\left(\lambda<0,\mu<0\right)$ For example λ = -3, μ = -2 the solution P_1 and P_2 in Eq. (3.12) represent singular multi soliton solutions. (Bell and dark shaped).

5- $\left(\lambda=0,\mu<0\right)$ For example λ = 0, μ = -4 the solution P_1 and P_2 in Eq. (3.12) represent singular multi soliton solutions. (Dark and bell shaped).

6- $\left(\lambda>0,\mu>0\right)$ For example λ = 3, μ = 2 the solution P_1 and P_2 in Eq. (3.13) represent singular multi soliton solutions. (Bell and dark shaped).

7- $\left(\lambda>0,\mu<0\right)$ For example λ = 3, μ = -2 the solution P_1 and P_2 in Eq. (3.13) represent kink shape soliton solution.

8- $\left(\lambda<0,\mu>0\right)$ For example λ = -3, μ = 2 the solution P_1 and P_2 in Eq. (3.13) represent singular multi soliton solutions. (Dark and bell shaped).

9- $\left(\lambda<0,\mu<0\right)$ For example λ = -3, μ = -2 the solution P_1 and P_2 in Eq. (3.13) represent kink shape soliton solution.

10- $\left(\lambda=0,\mu<0\right)$ For example λ = 0, μ = -4 the solution P_1 and P_2 in Eq. (3.13) represent kink shape soliton solution.

- **Case2.** When: $\left(\lambda^2-4\mu>0,\mu=0\right)$.

1- $\left(\lambda>0\right)$ For example λ = 3 the solution P_3 and P_4 in Eq. (3.14) represent singular multi soliton solutions. (Dark and bell shaped).

2- $\lambda<0$ For example λ = -3 the solution P_3 and P_4 in Eq. (3.14) represent singular multi soliton solutions. (Dark and bell shaped).

- **Case3**. when: $\left(\lambda^2-4\mu=0\right)$, $\left(\lambda\neq0,\mu\neq0\right)$ For example λ = 1, μ = 0 the solution P_5 and P_6 in Eq. (3.15) represent singular kink soliton solutions.

- **Case4.** When: $\left(\lambda^2-4\mu=0\right)$, $\left(\lambda=0,\mu=0\right)$ The solution P_7 and P_8 in Eq. (3.16) represent singular kink soliton solutions.

- **Case5.** When: $\left(\lambda^2-4\mu<0\right)$.

1- $\left(\lambda>0,\mu>0\right)$ For example λ = 2, μ = 4 the solution P_{11} and P_{12} in Eq. (3.17) represent bell shape soliton and dark periodic solutions.

2- $\left(\lambda<0,\mu>0\right)$ For example λ = -1, μ = 2 the solution P_{11} and P_{12} in Eq. (3.17) represent singular multi soliton.

3- $\left(\lambda=0,\mu>0\right)$ For example λ = 0,

μ = 2 the solution P_{11} and P_{12} in Eq. (3.17) represent (Dark and Bell) periodic soliton solutions.

4- $(\lambda > 0, \mu > 0)$ For example λ = 2, μ = 4 the solution P_{13} and P_{14} in Eq. (3.18) represent multi soliton solutions (Bell and Dark).

5- $(\lambda < 0, \mu > 0)$ For example λ = -1, μ = 2 the solution P_{13} and P_{14} in Eq. (3.18) represent multi soliton solutions (dark and bell).

6- $(\lambda = 0, \mu > 0)$ For example λ = 0, μ = 2 the solution P_{13} and P_{14} in Eq. (3.18) represent multi soliton solutions (Dark and Bell).

Figures:

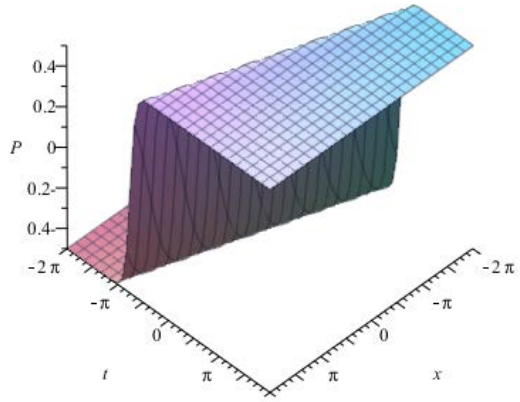

$P_1 \Rightarrow Case\,1.$

Eq. (3.12)

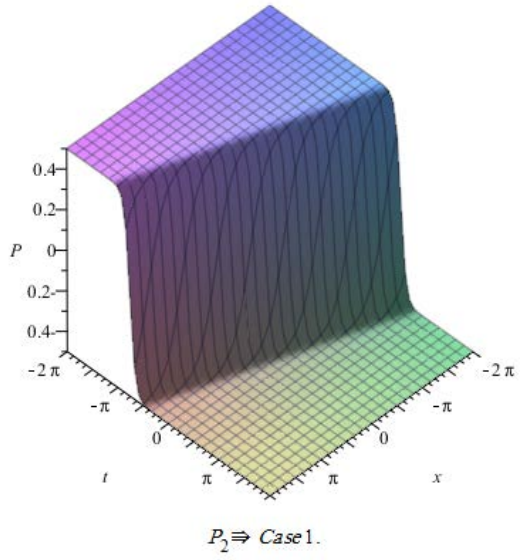

$P_2 \Rightarrow Case\,1.$

Eq. (3.12)

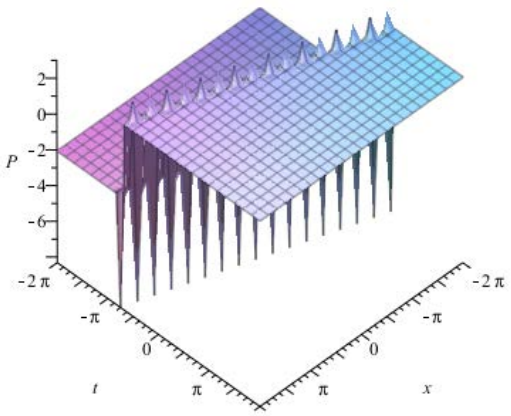

$P_1 \Rightarrow Case\,2$

Eq. (3.12)

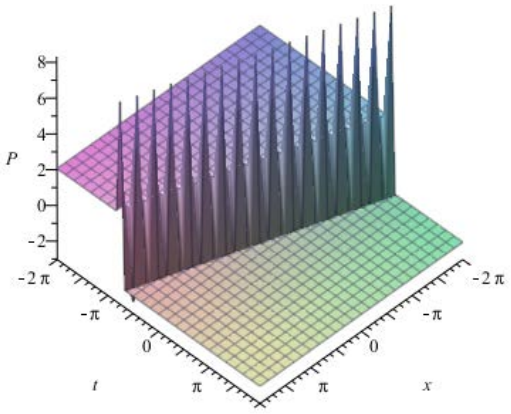

$P_2 \Rightarrow Case\,2$

Eq. (3.12)

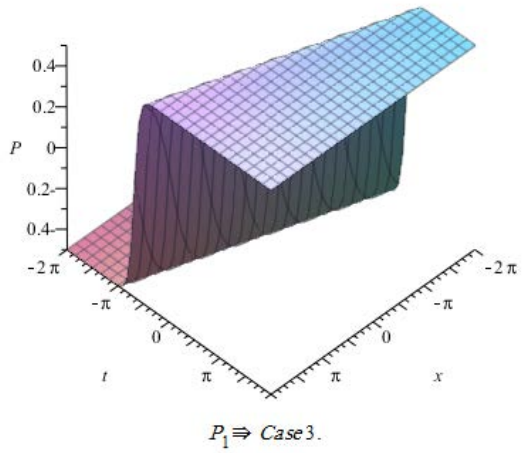

$P_1 \Rightarrow Case\,3.$

Eq. (3.12)

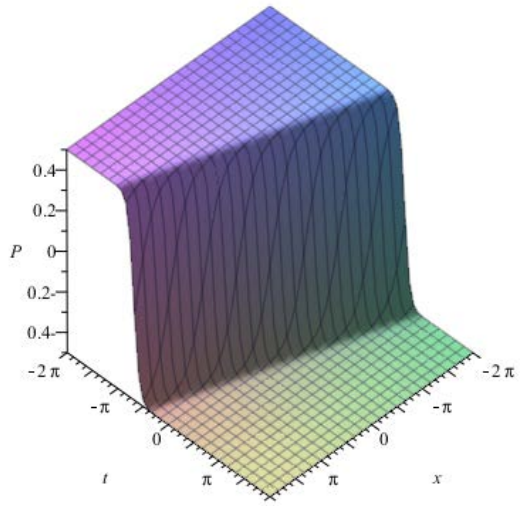

$P_2 \Rrightarrow$ *Case* 3.

Eq. (3.12)

Eq. (3.12)

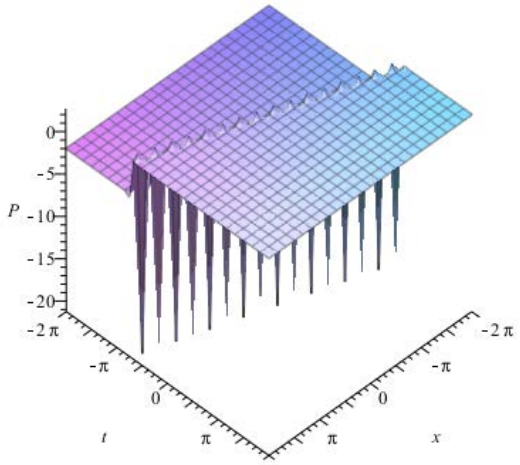

$P_1 \Rrightarrow$ *Case* 5.

Eq. (3.12)

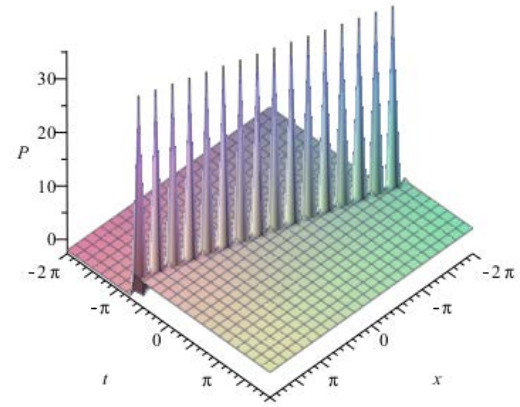

$P_1 \Rrightarrow$ *Case* 4.

Eq. (3.12)

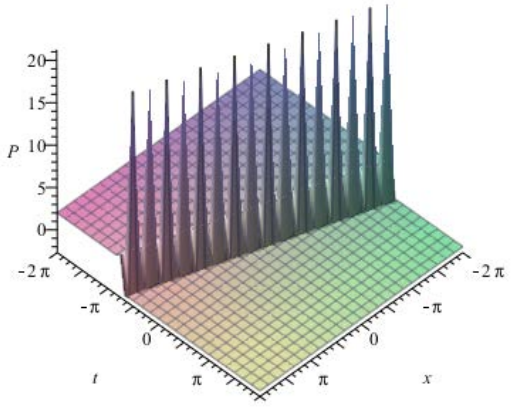

$P_2 \Rrightarrow$ *Case* 5.

Eq. (3.12)

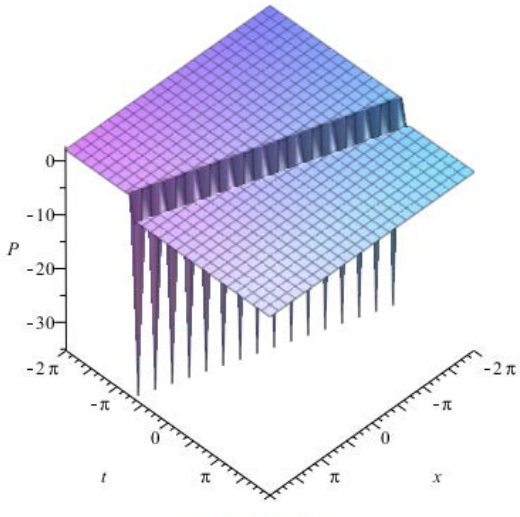

$P_2 \Rrightarrow$ *Case* 4.

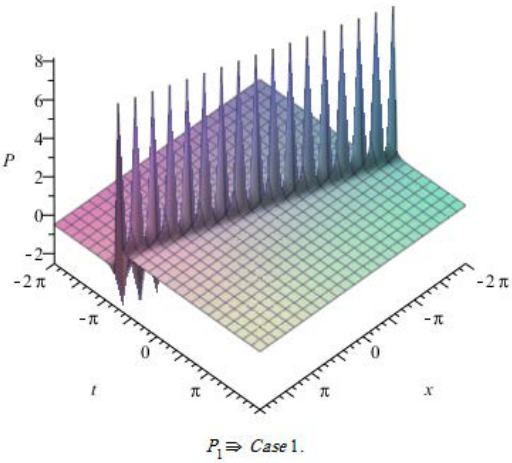

$P_1 \Rrightarrow$ *Case* 1.

Eq. (3.13)

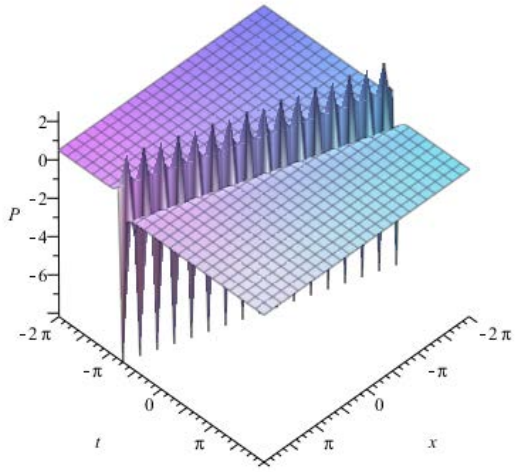

$P_2 \Rightarrow$ *Case* 1.

Eq. (3.13)

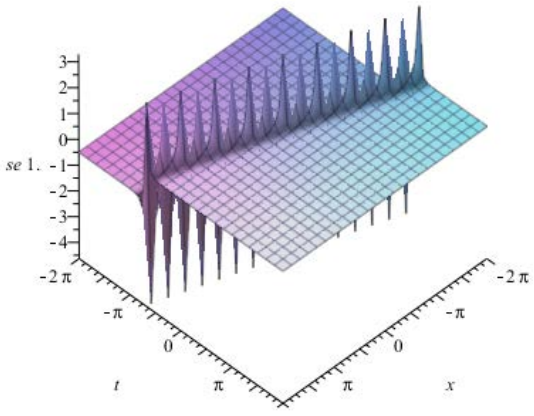

$P_1 \Rightarrow$ *Case* 3.

Eq. (3.13)

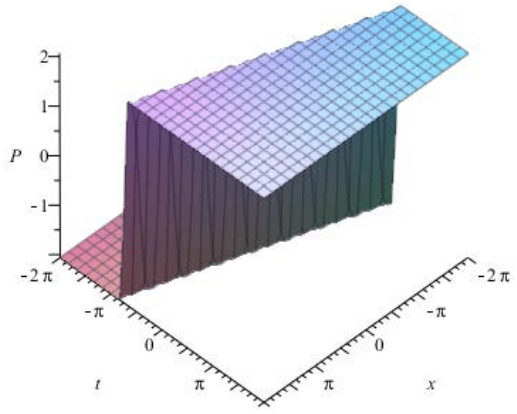

$P_1 \Rightarrow$ *Case* 2.

Eq. (3.13)

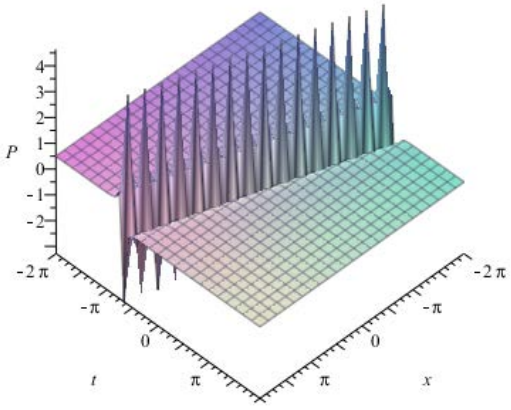

$P_2 \Rightarrow$ *Case* 3.

Eq. (3.13)

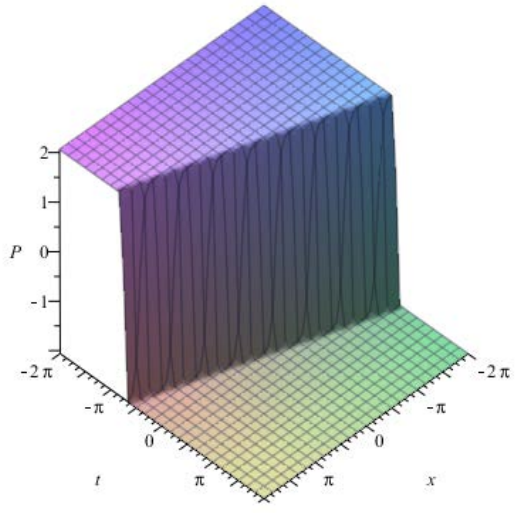

$P_2 \Rightarrow$ *Case* 2.

Eq. (3.13)

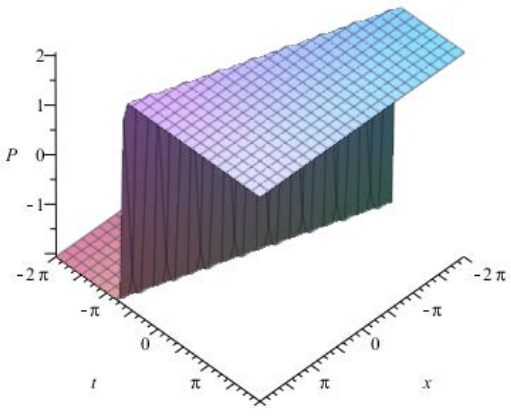

$P_1 \Rightarrow$ *Case* 4.

Eq. (3.13)

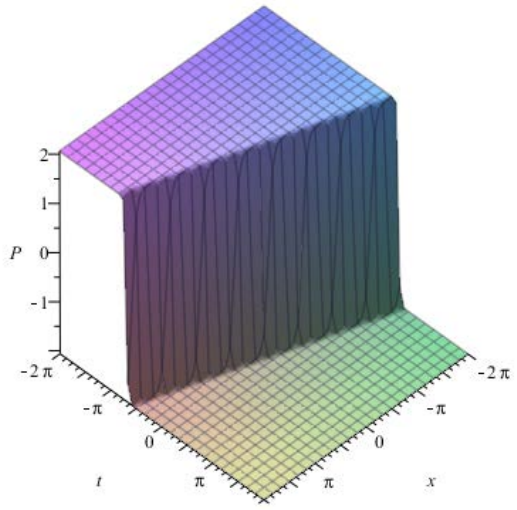

$P_2 \Rightarrow$ *Case* 4.

Eq. (3.13)

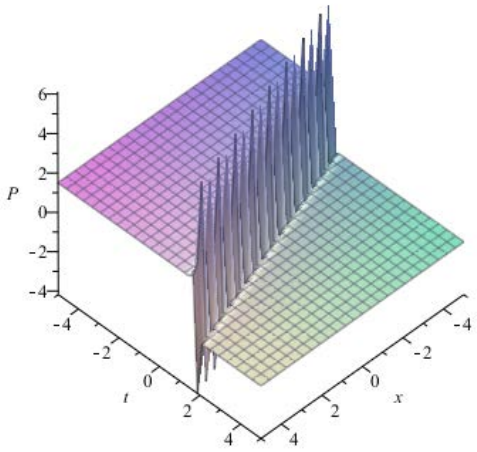

$P_3 \Rightarrow$ *Case* 1

Eq. (3.14)

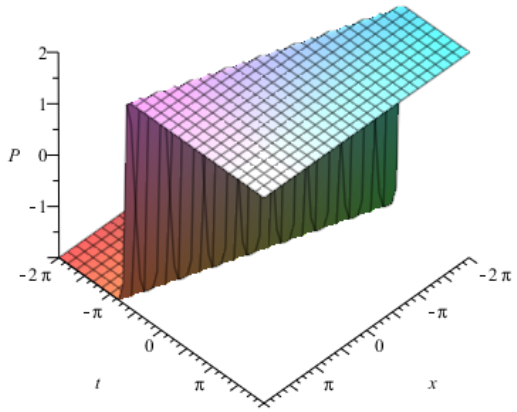

$P_1 \Rightarrow$ *Case* 5.

Eq. (3.13)

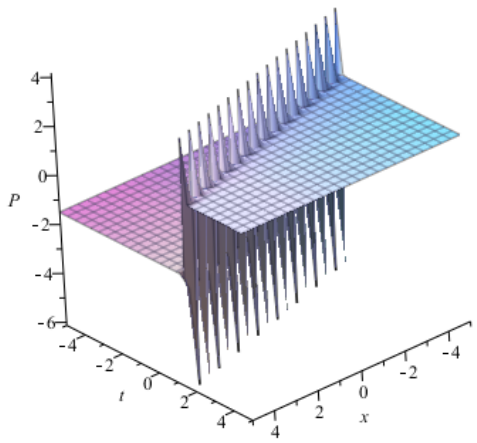

$P_4 \Rightarrow$ *Case* 1

Eq. (3.14)

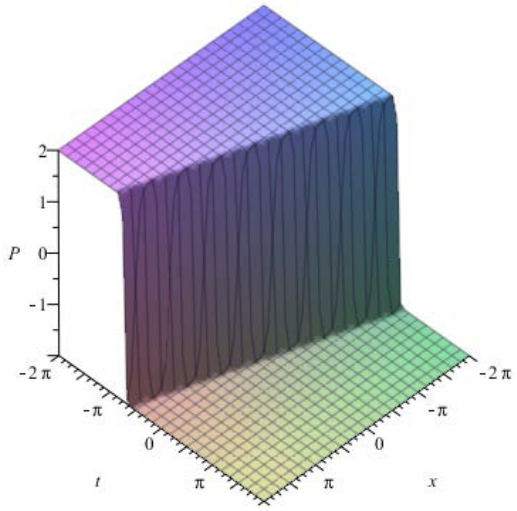

$P_2 \Rightarrow$ *Case* 5.

Eq. (3.13)

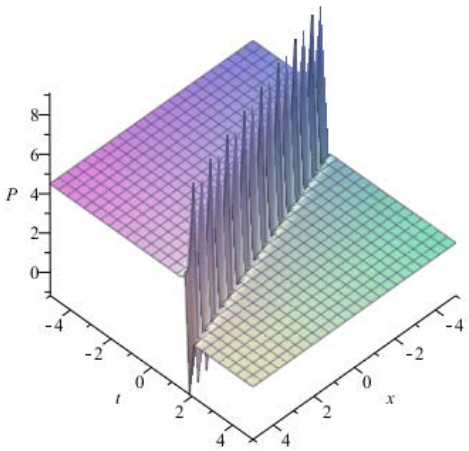

$P_3 \Rightarrow$ *Case* 2.

Eq. (3.14)

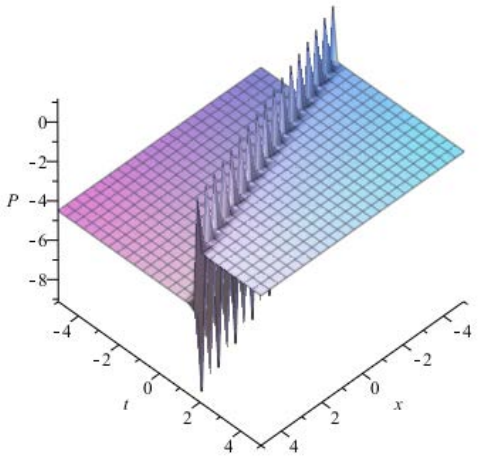

$P_4 \Rightarrow Case\,2$

Eq. (3.14)

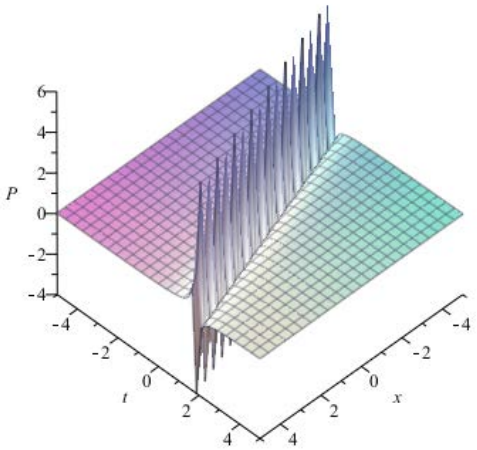

$P_9 \Rightarrow Case\,1.$

Eq. (3.16)

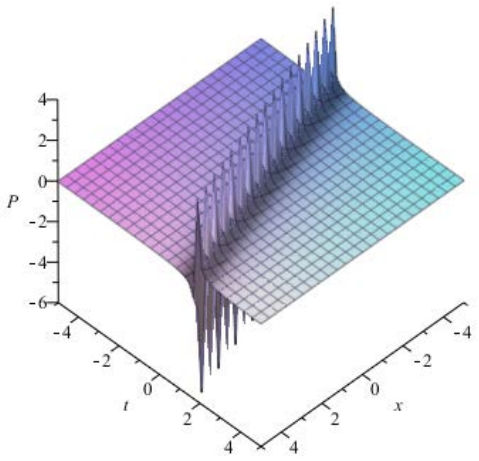

$P_7 \Rightarrow Case\,1.$

Eq. (3.15)

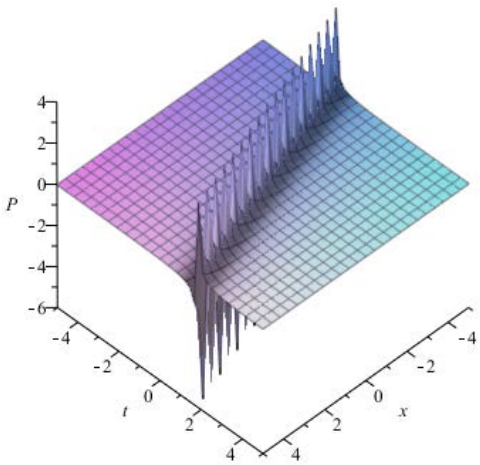

$P_{10} \Rightarrow Case\,1.$

Eq. (3.16)

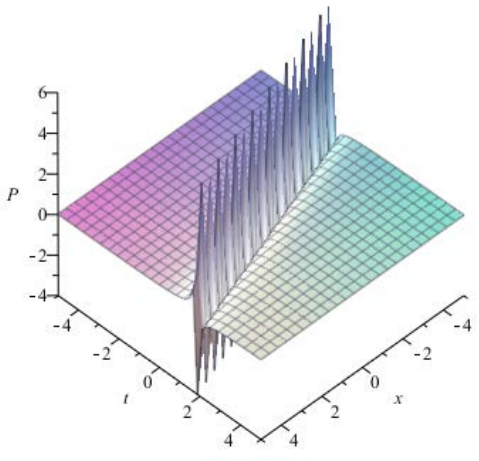

$P_8 \Rightarrow Case\,1.$

Eq. (3.15)

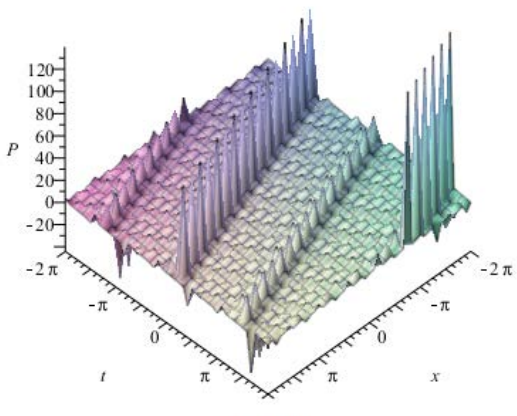

$P_{11} \Rightarrow Case\,1.$

Eq. (3.17)

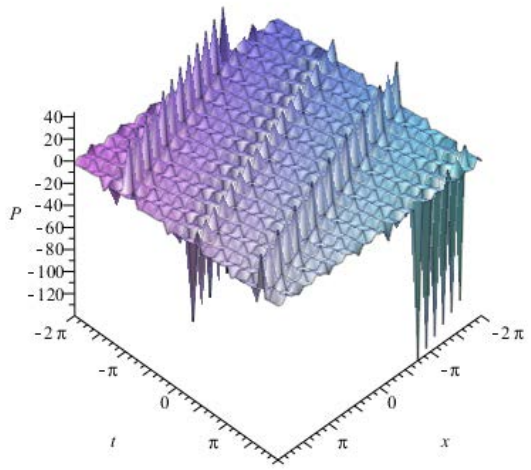

$P_{12} \Rightarrow$ *Case* 1

Eq. (3.17)

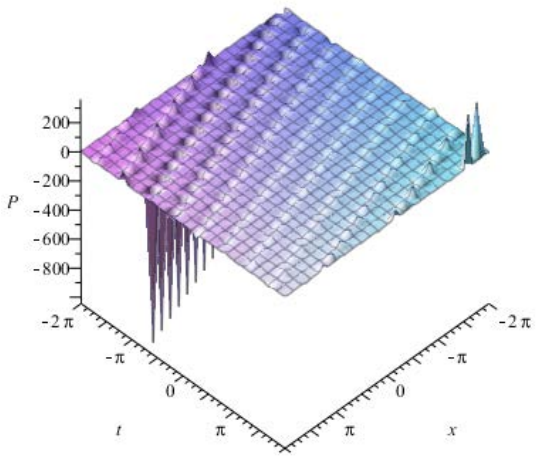

$P_{11} \Rightarrow$ *Case* 3.

Eq. (3.17)

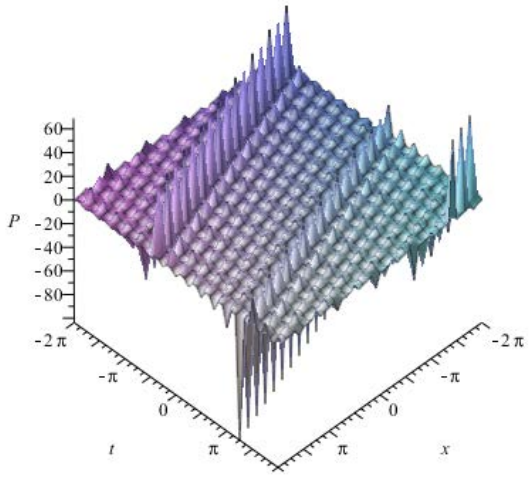

$P_{11} \Rightarrow$ *Case* 2.

Eq. (3.17)

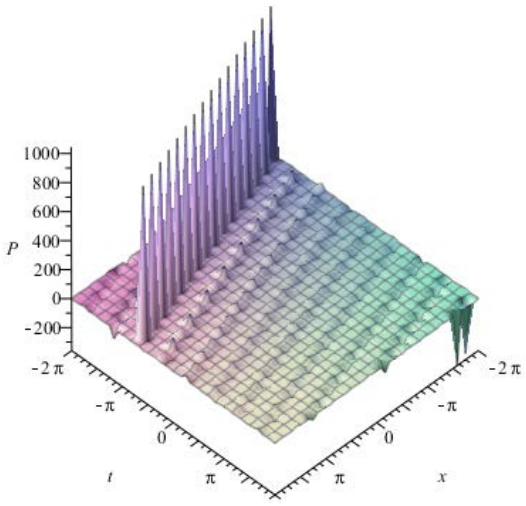

$P_{12} \Rightarrow$ *Case* 2.

Eq. (3.17)

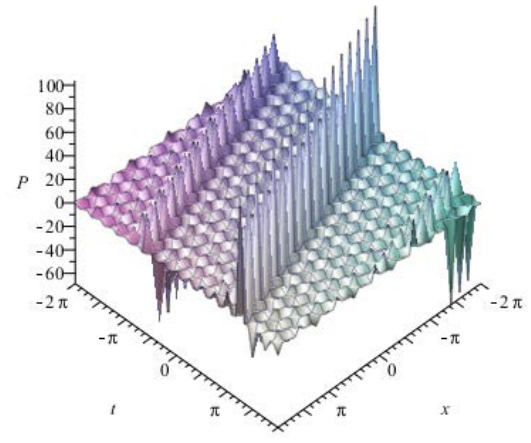

$P_{12} \Rightarrow$ *Case* 2

Eq. (3.17)

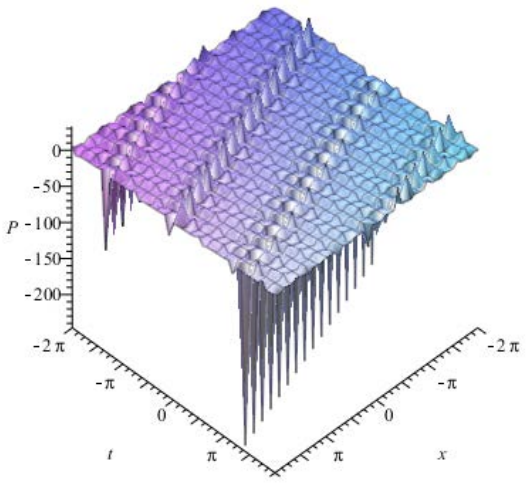

P_{13}, *Case* 1.

Eq. (3.18)

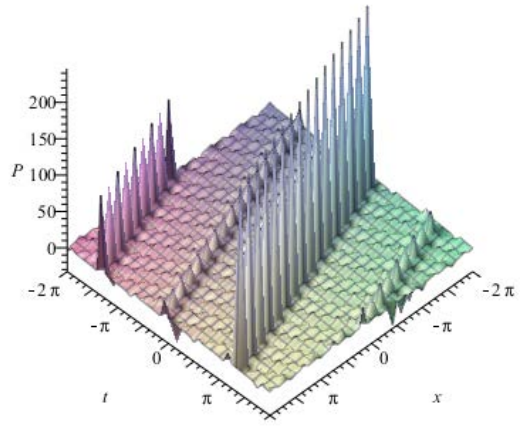

P_{14}, *Case* 1.

Eq. (3.18)

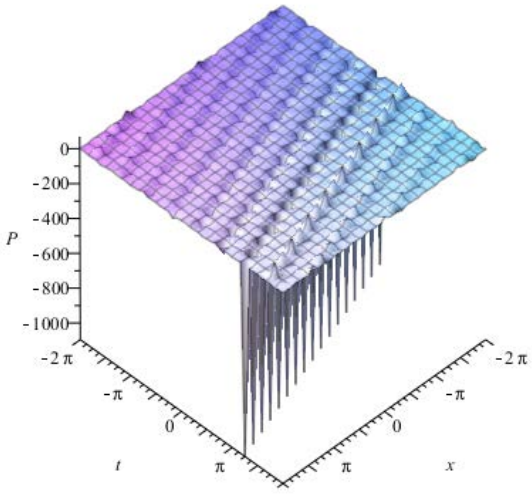

P_{13}, *Case* 3.

Eq. (3.18)

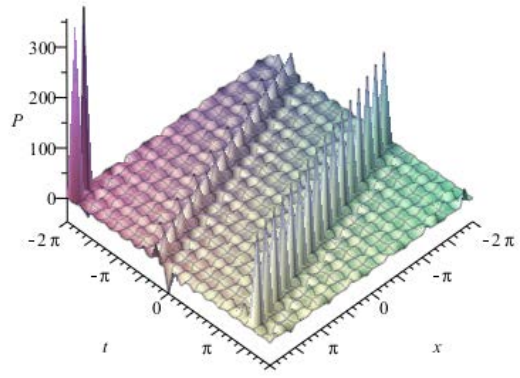

P_{13}, *Case* 2.

Eq. (3.18)

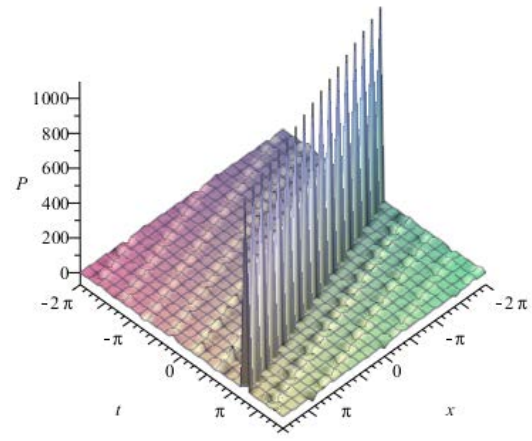

P_{14}, *Case* 3.

Eq. (3.18)

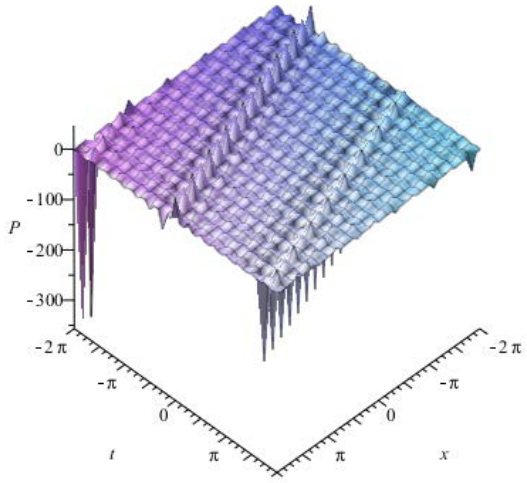

P_{14}, *Case* 2.

Eq. (3.18)

5 CONCLUSIONS

The $\boldsymbol{exp}(-\boldsymbol{\varphi}(\boldsymbol{\xi}))$ -expansion method has been applied in this paper to find the exact traveling wave solutions and then the solitary wave solutions of the generalized Hirota-Satsuma couple KdV system. Let us compare between our results obtained in the present article with the well-known results obtained by other authors using different methods as follows: Our results of nonlinear dynamics of the generalized Hirota-Satsuma couple KdV system are new and different from those obtained in [32], and figs. [1-16], show the solitary traveling wave solution of the generalized Hirota-Satsuma couple KdV system . We can conclude that the $\boldsymbol{exp}(-\boldsymbol{\varphi}(\boldsymbol{\xi}))$ -expansion method is

is a very powerful and efficient technique in finding exact solutions for wide classes of nonlinear problems and can be applied to many other nonlinear evolution equations in mathematical physics. Another possible merit is that the reliability

of the method and the reduction in the size of computational domain give this method a wider applicability.

REFERENCES

[1] W. Maliet, Solitary wave solutions of nonlinear wave equation, Am. J. Phys., 60 (1992) 650-654.
[2] W. Maliet, W. Hereman, The tanh method: Exact solutions of nonlinear evolution and
wave equations, Phys.Scr. 54 (1996) 563-568.
[3] A. M. Wazwaz, The tanh method for travelling wave solutions of nonlinear equations, Appl. Math. Comput. 154 (2004) 714-723.
[4] S. A. EL-Wakil, M.A.Abdou, New exact travelling wave solutions using modified extended tanh-function method, Chaos Solitons Fractals, 31 (2007) 840-852.
[5] E. Fan, Extended tanh-function method and its applications to nonlinear equations, Phys.
Letts. A 277 (2000) 212-218.
[6] Mahmoud A.E. Abdelrahman, Emad H. M. Zahran and Mostafa M.A. Khater, Exact Traveling Wave Solutions for Modified Liouville Equation Arising in Mathematical Physics and Biology, International Journal of Computer Applications (0975 8887) Volume 112 - No. 12, February (2015).
[7] A. M. Wazwaz, Exact solutions to the double sinh-Gordon equation by the tanh method and a variable separated ODE. Method, Comput. Math. Appl., 50 (2005) 1685-1696.
[8] A. M.Wazwaz, A sine-cosine method for handling nonlinear wave equations, Math. Comput. Modeling, 40 (2004) 499-508.
[9] C. Yan, A simple transformation for nonlinear waves, Phys. Lett. A 224 (1996) 77-84.
[10] E. Fan, H.Zhang, A note on the homogeneous balance method, Phys. Lett. A 246 (1998) 403-406.
[11] M. L. Wang, Exact solutions for a compound KdV-Burgers equation, Phys. Lett. A 213 (1996) 279-287.
[12] Emad H. M. Zahran and Mostafa M.A. Khater, The modified simple equation method and its applications for solving some nonlinear evolutions equations in mathematical physics,
(Jokull journal- Vol. 64. Issue 5 - May 2014).
[13] Y. J. Ren, H. Q. Zhang, A generalized F-expansion method to find abundant families of Jacobi elliptic function solutions of the (2+1)-dimensional Nizhnik-Novikov-Veselov equation, Chaos Solitons Fractals, 27 (2006) 959-979.
[14] J. L. Zhang, M. L. Wang, Y. M. Wang, Z. D. Fang, The improved F-expansion method and its applications, Phys.Lett.A 350 (2006) 103-109.
[15] J. H. He, X. H. Wu, Exp-function method for nonlinear wave equations, Chaos Solitons
Fractals 30 (2006) 700-708.
[16] H. Aminikhad, H. Moosaei, M. Hajipour, Exact solutions for nonlinear partial di_erential equations via Exp-function method, Numer. Methods Partial Differ. Equations, 26 (2009)
1427-1433.
[17] Z. Y. Zhang, New exact traveling wave solutions for the nonlinear Klein-Gordon equation, Turk. J. Phys., 32 (2008) 235-240.
[18] M. L. Wang, J. L. Zhang, X. Z. Li, The (G'/G)-expansion method and travelling wave
solutions of nonlinear evolutions equations in mathematical physics, Phys. Lett. A 372
(2008) 417-423.
[19] S. Zhang, J. L. Tong, W.Wang, A generalized (G'/G)- expansion method for the mKdv equation with variable coefficients, Phys. Lett. A 372 (2008) 2254-2257.
[20] E. M. E. Zayed and K. A. Gepreel, The (G'/G)-expansion method for finding traveling wave solutions of nonlinear partial differential equations in mathematical physics, J. Math. Phys., 50 (2009) 013502-013513.
[21] E.H.M.Zahran and mostafa M.A. khater, Exact solutions to some nonlinear evolution equations by the (G'/G)- expansion method equations in mathematical physics, Jokull Journal, Vol. 64, No. 5; May 2014.
[22] C. Q. Dai , J. F. Zhang, Jacobian elliptic function method for nonlinear differential difference equations, Chaos Solutions Fractals, 27 (2006) 1042-1049.
[23] E. Fan , J .Zhang, Applications of the Jacobi elliptic function method to special-type
nonlinear equations, Phys. Lett. A 305 (2002) 383-392.
[24] S. Liu, Z. Fu, S. Liu, Q.Zhao, Jacobi elliptic function expansion method and periodic wave solutions of nonlinear wave equations, Phys. Lett. A 289 (2001) 69-74.
[25] Emad H. M. Zahran and Mostafa M.A. Khater, Exact Traveling Wave Solutions for the
System of Shallow Water Wave Equations and Modified Liouville Equation Using Extended
Jacobian Elliptic Function Expansion Method, American Journal of Computational Mathematics (AJCM) Vol.4 No.5 (2014).
[26] Nizhum Rahman, Md. Nur Alam, Harun-Or-Roshid, Selina Akter and M. Ali Akbar, Application of exp $\boldsymbol{exp}(-\boldsymbol{\varphi}(\boldsymbol{\xi}))$ expansion method to find the exact solutions of Shorma-Tasso-Olver Equation, African Journal of Mathematics and Computer Science Research Vol. 7(1), pp. 1-6, February, 2014.
[27] Ra_qul Islam, Md. Nur Alam, A.K.M. Kazi Sazzad Hossain, Harun-Or-Roshid and M.
Ali Akbar, Traveling Wave Solutions of Nonlinear Evolution Equations via $\boldsymbol{exp}(-\boldsymbol{\varphi}(\boldsymbol{\xi}))$ Expansion Method, Global Journal of Science Frontier Research Mathematics and Decision Sciences. Volume 13 Issue 11 Version 1.0 Year 2013.
[28] Mahmoud A.E. Abdelrahman, Emad H. M. Zahran Mostafa M.A. Khater, Exact traveling

wave solutions for power law and Kerr law non linearity using the $\boldsymbol{exp}(-\boldsymbol{\varphi}(\boldsymbol{\xi}))$expansion
method . (GJSFR Volume 14-F Issue 4 Version 1.0).
[29] M. Alquran, A. Qawasmeh, Soliton solutions of shallow water wave equations by means of expansion method. Journal of Applied Analysis and Computation. Volume 4(3)
(2014) 221-229.
[30] A. Qawasmeh, M. Alquran, Reliable study of some new _fth-order nonlinear equations by
means of (G'/G)- expansion method and rational sine-cosine method. Applied Mathematical Sciences. Volume 8(120) (2014) 5985-5994.
[31] A. Qawasmeh, M. Alquran, Soliton and periodic solutions for (2+1)-dimensional dispersive long water-wave system. Applied Mathematical Sciences. Volume 8(50) (2014) 2455-2463.
[32] Yan, Zhenya. "The extended Jacobian elliptic function expansion method and its application in the generalized Hirota–Satsuma coupled KdV system." Chaos, Solitons & Fractals 15.3 (2003): 575-583.

First International Conference on Science, Engineering & Environment,
Tsu City, Mie, Japan, Nov.19-21, 2015, ISBN: 978-4-9905958-5-2 C3051

EFFECT OF THE BIOEXTRACT TO CONTROL THE CURVULARIA LEAF SPOT (*Curvularia. sp*) AND CANKER OF LEMON (*Xanthomonas campestris citri*)

Vithaya Tavenooth,
Faculty of Agricultural Technology, Rajamangala University Of Technology Thanyaburi, Thailand

ABSTRACT

Effect of the bio-extract to control the Curvularia Leaf Spot (*Curvularia. sp*) and Canker of Lemon (*Xanthomonas campestris citri*) under laboratory operations. Faculty of Agricultural Technology Rajamangala University of Technology Thanyaburi [RMUTT] Thailand between June and July 2015 by Bio-extract obtained from the fermentation of sugar mixed with one part of water and one part of chip plant species. Three ingredients, bio-based formulation with agar. 4 different types of plants, names Galangal, chili, basil, alata are used in these experiments and mixed in 4 formula [I-IV] with control distill water.The growth rate and sizing of colony are determine at 1,3,5,7and 14 days by Randomized Complete Design (CRD) with four replications five treatments is used. The results shown that *Curvularia sp* growth effect to all formula at 3 days. All formula prohibit growth the *Curvularia sp* for all formula and shown non- different diameter of colony below 1.4 centimeter . Effect of bio-extract control of the citrus canker (*Xanthomonas campestris citri*) on agar NA. found that growth of bacteria *Xanthomonas campestris citri* on food do not mix bio-extract was higher than on the water extract bio-extract and bacteria *Xanthomonas campestris citri*) growing at least 1,2 formula shows that bio-extracted from plants tend to control plant diseases.

Keywords : Bio-extract, Curvulatia.sp, Xanthomonas campestris citri, Galangal, Chili, Basil, Alata

INTRODUCTION

Many small farmers in Northeast Thailand have been using the bio-extracts (BE) produced from plant and animal residues to reduce or replace chemical fertilizer and pesticide use. They use bio-extract either singly or in combination with other organic amendments in crop production. Chemical pesticide widely used for plant cultivation and control plant disease including lemon production. However, chemical pesticide cause high cost and effect to quality of soil in long term use to prevent plant disease by using chemicals. In farming, in addition to causing problems with toxic chemicals in the environment, then it may be left to farmers who use and includes a certain chemical residues to consumers of agricultural products [1,6] Currently imports are found to be bio–extract in many, whether it is a fermented in accelerating the growth of plants, the use of bio-fermentation to enhance the quality of the output, for better for water. Bio-extract fertilizer becomes one of the alternative compound for reduction of chemical treatment or Biological insect repellent to pests control and the use of Effective Microorganisms in Plant Disease[1,2] therefore, recognizes the importance of crop quality, thus leading Microorganisms used as a test plant diseases caused by bacterial leaf spot. This is caused by *Curvularia sp*. And canker is

The aim of current study was to apply the bio-extracts to top margin is 30mm while the left, right, caused by bacteria *Xanthomonas campestris citri.* The study found that the bio-organic substances that are qualified to serve as a deterrent to prevent plant disease control, and also can be used instead of chemicals

MATERIALS AND METHODS

The experiment was conducted at Rajamangara University of Technology Thunyaburi, Pathumthani province. Randomize Complete Design (CRD) was applied for this experiment with 5 treatments viz. bio-extract formulas of formula 1. galangal, Chili, basil, alata. formula 2 galangal, chili, basil, formula 3. galangal, chilies, formula 4. Galangal, chili, basil, alata and leavening P.D. 2 and 5 recipes do not mix fermented foods by measuring the growth of the mycelium fungus on a PDA was to apply the bio-extracts to find a formula to control Curvularia sp. causes leaf spot of corn. to control bio-fermentation bacteria *Xanthomonas campestris citri* causes citrus canker.

Bio-extract preparation

Stems and leaves of galangal, chili, basil , alata . leaves were cut or ground into small pieces and mixed with molasses at the ratio of 3:3: Clean water (20liters)was added to each 3 kg of mixture. The mixture was left to ferment in a 20-L closed bucket (anaerobic conditions) for 3 month (department of agriculture, 2015). Then, the product, or bio-extract,

was released into plastic bottles wrapped in foil and kept at 4°C as a stock solution for experimentation from 4 different types of plants names; galangal(*Alpinianigra.L.Burtt*) , chili (*Capsicum frutescens L*) , basil (*Ocimu sanctum linn*) alata(*Sennaalata L.Roxb.)* obtained from the fermentation of sugar mixed w)ith one part of water and one part of chip plant species. and water was added to the mixture to make 20 L. The fermentation was allowed for 3 months Three ingredients, bio-based formulation with agar. 4 different types of plants names:galangal(*Alpinianigra.L.Burtt*,) chili*(Capsicum frutescens L*.), basil(*Ocimu sanctum linn)*,alata(Sennaalata(L.) Roxb.) are used in **.**

Table1 Doses of herbs used in making fermented in each recipe

each recipe	The amount of herbs used in making fermented			
	Galanga (Alpinia nigra.)	Chili (*Capsicsicum frutescens L* .)	basil(Ocimu sanctum)	Alata (Sennaalata)
1 kg	3kg	3 kg	3kg	3kg
2 kg	3kg	3 kg	3kg	-
3 kg	3kg		-	-
4 kg	3kg	3 kg	3kg	-

These experiments and mixed in 4 formulas I-IV **(**with control**)** distill water**(**.The growth rate and sizing of colony are determine at 1,3,5,7and 14 days by Randomized Complete Design (CRD) with four replications five treatments is used. Bring bio-fermentation to test effect to inhibit fungal ***(****Curvularia sp* ***)*** growth and bacteria ***(****Xanthomonas campestris citri***)** by the agar well diffusion method for each plant extract and filtered through Muslin cloth and 100% plant extract solution was prepared. The extracts were poured in the flasks plugged with cotton and heated at 100°C for 10 minutes to avoid contamination [3]. The bio-extract formulas of formula 1. galangal, chili, basil, alata formula 2 galangal, chili, basil, formula 3. galangal, chili, formula 4. galangal, chili, basil, alata poison food technique was applied [4] by ratio PDA concentrations: bio-extract: 10 ml: 1ml prepared using PDA in test tubes and stored in (ratio:10:1**)** of bio extracts was incorporated to potato refrigerator at 4°C. Curvularia leaf spot pathogen was isolated from dextrose medium agar for inoculation of the test pathogen infected corn plants and was identified as per in sterilized petridish. The pathogen was monograph and standard procedures. grown on potato dextrose agar medium was placed at center of petridish containing different formula .The growth rate and sizing of colony are determine at 1,3,5,7and 14 days The agar dilution assay was carried out according to **[5]** with a slight modification. Thirty nine grams of potato dextrose agar (PDA) powder was boiled until the agar completely dissolved in 1 L of distilled water. The solution was then sterilized using autoclave at 121°C for 15 min. 10 ml of the sterilized PDA and 1 ml of bio- extract were mixed and plated on the sterilized petridish (8.5 cm in diameter). 7.0 mm diameter of mycelia discs were inoculated at the centre of the medium. The antifungal assay was divided into4. different treatments as bio-extract of 4 formula The colony growth was determined on the

Statistical analysis

The experimental data were statistically analyzed .The significance of differences between the treatments was evaluated by one way analysis of variance at the significance level of 95 % .The Statistical software SPSS version 17.0 was used in the analysis. All the data were analyzed with students 't' test .The value of growth parameter and disease data were statistically analyzed .In the test of significant *($P \leq 0.05$),**($p \leq 0.01$),***($p \leq 0.001$) indicate the treatments were significant at probability level respectively.

RESULTS

The Data recorded during the course of investigation has been subjected to three-way classification. The conclusion was drawn on the basis of analysis of variance. The calculated value of F was compared with table value of F at 5% levels of significance for an appropriate degree of freedom The result shown that *Curvularia sp.* growth effect to all formula at 3 day. All formula prohibit .The growth of *Curvularia sp* on all formula shown that non- different diameter of colony below 1.4 centimeter .Effect of bio-extract all formula on disease *Curvularia sp* in general disease incidence (Table-1) The growth of *Curvularia sp* on all formula 1. galangal, chilli, basil,alata was size of colony 1.33 centimeter.formular2,1.43 centimeter formula 3,1.5 centimeter formular4,1.45 centimeter while other formular5(control) 5.99 centimeter on 14day, The growth of *Curvularia sp* on all formula

1. galangal, chilli, basil,alata was size of colony 1.30 centimeter. Formula 2,1.35 centimeter formula 3,1.38 centimeter formula 4,1.35 centimeter while other formular5 (control) 4.05 centimeter on 7 days

Fig. 1 The Growth rate of *Curvularia sp.*on PDA mixed bio-extract 5 formulas at 1,3,5,7,and14 days

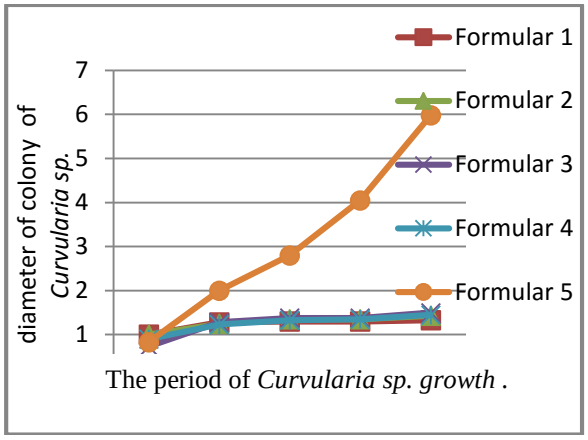

Table1 Average diameter colony of *Curvularia sp.* Growth on PDA mixed 5 formulas at 1,3 5,7 and 14 days

Date / Formular	1	3	5	7	14
1	1	1.28	1.3	1.3	1.33
2	1	1.25	1.35	1.35	1.43
3	0.73	1.28	1.38	1.38	1.5
4	0.9	1.2	1.3	1.3	1.4
5	0.83	2	2.8	4.05	5.98

Effect of bio-extract control of the citrus canker (*Xanthomonas campestris citri*) on agar NA. found that growth of bacteria *Xanthomonas campestris citri* on food do not mixed bio-extract was higher than on the water extract bio-extract and bacteria (*Xanthomonas campestris citri*) growing at least 1,2 formula

Figue.2 The growth rate of *Xanthomonas campestis citri* on PDA mixed bio-extract 5 formulas at 1,3,5,7,and 14 days.

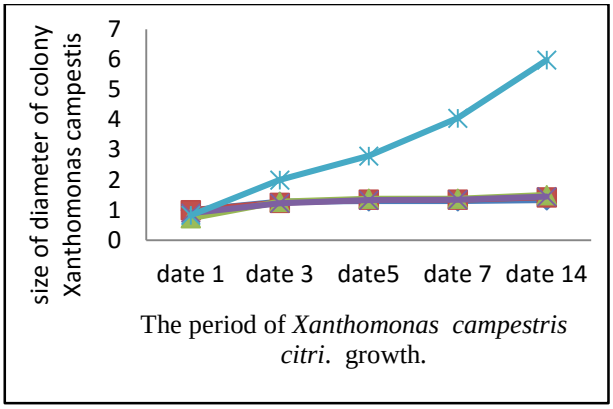

Table 2 Average diameter colony of of *Xanthomonas campestris citri* . Growth on PDA mixed 5 formulas at 1 ,3,5.7 and 14 days

Formula	The diameter of colony				
	1	3	5	7	14
1	0.7b	0.7c	0.7d	0.7c	0.7d
2	0.7b	0.78c	0.78d	0.78c	0.85cd
3	0.7b	0.98b	1.03c	1.1b	1.1bc
4	0.7b	1.13b	1.2b	1.2b	1.28b
5	0.78a	1.48a	1.53a	1.6a	2.65a

DISCUSSION

Effect of bio-extract control of *Curvularia sp.* growth effect to all formula at 3 days. All formula prohibit growth the *Curvularia sp* for all formula and shown non- different diameter of colony below 1.4 centimeter . Effect of Bio-extract control of the citrus canker (*Xanthomonas campestris citri*) on agar NA. found that growth of bacteria(*Xanthomonas campestris citri*) on PDA mixed the water do not mix bio-extract was diameter colony of *Xanthomonas campestris citri* higher than bio-extract and bacteria(*Xanthomonas campestris citri*) growing at least 1,2 formula shows that bio-extracted from medicinal plants tend to control plant diseases. The bio-extracts indicate the potential of selected plant species as a source of natural fungicidal material and bactericide material. Antifungal and antibacterial activity was confirmed by all of the selected plant species .The results of this research as well as provides results of the research [6].The results revealed that different formula extracts do not varied in their efficacy for inhibiting the mycelia growth and bacterial growth of tested pathogens .

Acknownledgement
Author are thankful to Faculty of Agricultural Technology, Rajamangala University of Technology Thanyaburi ,Thailand for research funding , providing necessary facilities and help.

REFERENCES

[1] Ashwani Tapwal, Nisha Shipra Garg, Nandini Gautam, Rajesh Kumar .In Vitro antifungal potency of Plant extracts again five phytopartogen.Braz. arch.biol.technol.vol.54 no.6 uritiba Nov./Dec.2011

[2] Bajwa, R., Shafique, S., Anjum, T. and Shafique, S. (2004), Antifungal Activity of Allelopathic Plant Extracts IV: Growth Response of *Drechslera hawaiiensis, Alternaria alternata* and *Fusarium monilifrome* to Aqueous Extract of *Parthenium hysterophorus. Int. J. Agri. Biol.*, 6: 511516.[Links]

[3] Kiran, K., S. Linguraju and S. Adiver, 2006. Effect agents against Drechslera sorokiniana In: Asian of plant extract on *Sclerotium rolfsii,* the incitant Cong. Mycol. Pl. Pathol., Indian Soc. Mycol. Pl. of stem rot of ground nut. J. Mycol. Pl. Pathol., Pathol. University of Mysore (Abst) Oct.1-4, pp: 2 4 1 .

[4] Madavi, S. and R.P. Singh, 2005. Management of Production productivity and export of vegetables.mushroom pathogens through botanicals. Ind. Technical Bulletin 7 Indian Institute of Vegetable Phyto. Pathol., 58: 189-193. Research, Varanasi.

[5] Nene, Y. and L. Thapilyal, 2000. Poisoned foodtechnique of fungicides in plant disease control3rd Edn. Oxford and IBH Pu**[5**Alam SJ, *Chem Sci*, 2004, 116, 325.

[6]Chalermwut, Noisopa, Benjaphorn Prapagdee, Chalie Navanugraha and Rungjarat Hutacharoen :2010,Kasetsart J. (Nat. Sci.) 44(5) 809

First International Conference on Science, Engineering & Environment,
Tsu City, Mie, Japan, Nov.19-21, 2015, ISBN: 978-4-9905958-5-2 C3051

OPTIMAL MIXING RATIOS OF SILICA AND HYBRID RESIN WITH EPOXY RESIN FOR CONCRETE FLOOR SURFACE COVERING

Kyuhwan Oh[1], Choi Woo Byung[2] and Sang Keun Oh[3]
[1]Faculty of Architectural Engineering, Seoul National University of Science and Technology, Seoul
[2]Faculty of Engineering, **,** Research head at Dootop C&C (Inc.), Seoul
[3] Faculty of Architectural Engineering, Seoul National University of Science and Technology, Seoul

ABSTRACT

The goal of this study was to find the optimal mixing ratios of silica with a silane coupling agent for using them as cover materials for concrete floors. The Epoxy resin is currently used as the floor-finishing materials. However, the epoxy resin has many disadvantages such as peeling, decreased bond strength in wet conditions, weakness upon impact, poor film rigidity, susceptibility to corrosion, and environmentally-unfriendliness, when used in underground structure parking lots.

Accordingly, this study carried out experiments to determine the viability of using hybrid-finishing materials for floors, with 3-glycidoxypropyltrimethoxysilane as the silane coupling agent. The results of adhesion strength, impact resistance, flexural strength, compressive strength, and length change tests were used to determine the optimal mixing properties. Based on these results, the best mixture ratio (mass ratio) was found to be 1:1.75.

Keywords: Epoxy Resin, Silane Couplig Agent, Silica, Concrete Floor Finishing Materials

INTRODUCTION

As the population density increases, more and more large buildings and apartment complexes are being constructed in South Korea. Even the already congested areas now have high-rise buildings. To maximize the land utilization, most of the buildings now have underground parking lots. However, these underground parking lots are subjected to repetitive live loads caused by pedestrians and vehicles. As a result, floor-finishing materials rapidly degrade because of factors such as floor impact, friction, and tire wear.

In particular, the bond strength of the epoxy-resin-based finishing materials become susceptible to various forms of degradation and damage due to relatively high humid environment. Additionally, most epoxy-resin-based floor-finishing materials are only 2–3 mm thick, causing problems such as low impact resistance, low abrasion resistance, low flexural strength, and frequent occurrences of brittle fracture.`

The maintenance and repair of the damaged finishing materials cost additional time and money. From an eco-friendly viewpoint, the epoxy-resin-based floor-finishing materials, which use solvents such as paint thinners (acetone, naphtha, methyl ethyl ketone, etc.) and toluene, do not create a safe environment in the closed underground parking lots.

Despite these factors, inorganic finishing materials that do not use such solvents are not actively used because of the certain material weaknesses such as shrinkage and low abrasion resistance during the curing process.

In order to ameliorate the material and environmental issues associated with epoxy-resin-based floor-finishing materials, the development of a hybrid resin using silane coupling agent has been recently attempted. The hybrid resin would improve physical performance as well as bond strength between the heterogeneous materials. However, thus far hybrid resins have had limited application in the field because of their poor bond strength on a wet surface and lifting and peeling caused by long-term effects of live loads.[2]

To overcome these problems, a major objective has been made through this study to improve the basic physical properties of floor-finishing materials by finding an optimal mixing ratio of the hybrid resin and silica, mixed with a hydrolyzed silane coupling agent (hereafter referred to as “hybrid resin”) to increase the thickness of the coating material and improve its overall physical performance, i.e., increased bond strength, impact resistance, and compressive strength.

MATERIALS

Epoxy Resin

The base of the epoxy resin used in this experiment was a liquid resin comprising diglycidyl-ether, type bisphenol A; a polymide-amine-based material was used as the curing agent for the epoxy resin. The following Table 1. shows the physical properties of epoxy resin.

Silane Coupling Agent

3-Glycidoxypropyltrimethoxysilane (GPTMS) was chosen as the silane coupling agent. Its chemical structure consists of organic chains in which one

terminal has a methoxy functional group where three hydrolysis reactions are possible and the other has an epoxy functional group. GPTMS also chemically binds organic and inorganic materials.

Table 1. Epoxy Resin Properties

Properties	Typical Value
Epoxy Equivalent Weight, g/eq	180-190
Viscosity(cPs at 25℃)	700-1,100
Hy-Cl(wt%)	0.1
Specific Gravity(20℃)	1.14

In order to improve the weak affinity between the organic matrix and the inorganic filling material in floor-finishing materials, silane coupling agents can be used for improving the performance and quality of inorganic and organic composite materials by enhancing their mechanical and electrical characteristics, water resistance, bond strength, resin modification, and surface modification of the filling materials. Table 2 lists the physical characteristics of the silane coupling agent used in this study.

Table 2. Properties of GPTMS

Properties	Typical Value
Molecular Weight	236.4
Viscosity(cPs at 25℃)	3
Specific Gravity(25℃)	1.069
Refractive Index, n25℃	1.427
Flash point(℃)	110
Boiling point(℃)	290

Silica

The average particle size of the fine silica, made by SIBELCO Inc, used for preprocessing the silane coupling agent was 6–9 μm. Silica No. 7 and No. 10, numbered and made by Kyung-In material Inc, were 0.1–0.35mm and 0.01–0.05mm used as the filling materials in the epoxy resin that contains the silane coupling agent.

Determination of Optimal Content Ratio of Epoxy and Silane Coupling Agent

GPTMS was added to an ethanol solution for preprocessing the silica by the silica wet process. Silica was immersed in a hydrolyzed solution at pH 4, followed by filtration, drying, and then blended with the epoxy resin.

After preprocessing, the hardened body of the silane coupling agent resin, blended with epoxy, was analyzed using scanning electron microscopy (SEM). The silane coupling agent was added to the samples that showed the best dispersibility. The results showed that 4 wt% GPTMS had the best dispersibility and was therefore chosen as the basic resin for testing.

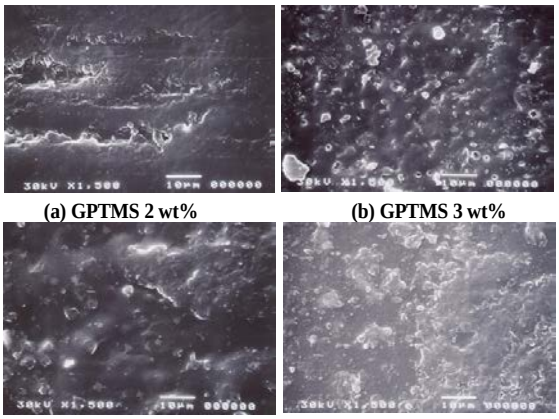

(a) GPTMS 2 wt% **(b) GPTMS 3 wt%**

(c) GPTMS 4 wt% **(d) GPTMS 6 wt%**

Fig. 1. Dispersion level of silica in GPTMS

TEST RESULTS AND DISCUSSION

Resin-based and silica composite material (C.R.)

Flow value and interfacial de-adhesion

The mixing ratio of the epoxy resin and silica (No. 7 and No. 10) for the flow values and interfacial de-adhesion test was set; the basic mixing ratio was fixed as 4:1 (base: curing agent) and the mixing ratio of silica increased by 0.5 g from 5.0 g to 7.5 g, giving six values of resin: silica (1:1.0 to 1:1.5). Figs. 2 and 3 show the results of the flow values and the occurrence of interfacial de-adhesion per mixing ratio of C.R._A and C.R._B.

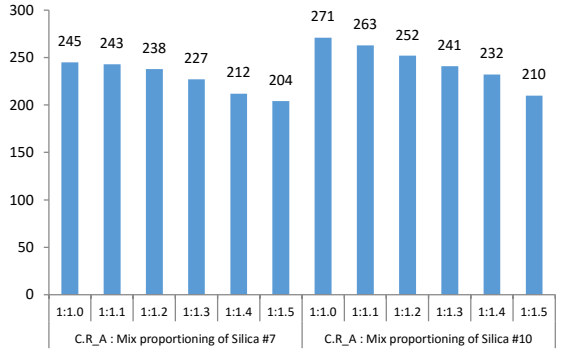

Fig. 2 Test results for flow values and material separation of C.R._A

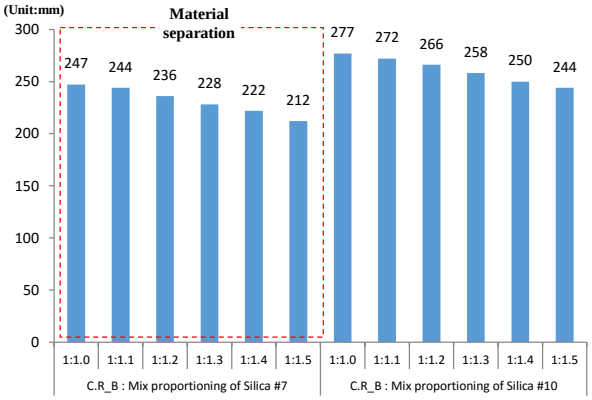

Fig. 3 Test results for flow values and material separation of C.R._B

For the mixing ratio of C.R._B, silica No. 7 showed that interfacial de-adhesion occurred in all the mixing ratios, but silica No. 10 had no interfacial de-adhesion.

Therefore, in a 1:1.3 mixed sample, shown in No. 7 part of Fig. 2, interfacial de-adhesion did not occur. However, a somewhat good flow value was seen. Interfacial de-adhesion also did not occur in the 1:1.3 mixed sample in No. 10 part of Fig. 9, which also had a good flow value. As a result, an additional test was conducted to select the appropriate mixing ratio for No. 7 and No. 10 to suppress shrinkage after curing.

For the C.R._A, a mixing mass ratio of epoxy: silica (No. 7 and No. 10) was fixed at 1:1.3 ratio, while the ratio of silica No. 7 and No. 10 was adjusted to determine the flow values and interfacial de-adhesion. Because the interfacial de-adhesion results were the same with both types of silica for C.R._B, the best flow value, observed for the S.R._B: silica ratio of 1:1.0, was used and the mixing ratio (mass ratio) of silica No. 7 and No. 10 was adjusted to determine the flow values and interfacial de-adhesion presence.

For the C.R._A n2 mix, it was found that while the flow value had a high flexibility of 257 mm, no interfacial de-adhesion was found. For the C.R._B n1 mix, the flow value showed 249 mm of flexibility and no interfacial de-adhesion. Therefore, in the C.R_A, to obtain an appropriate ratio of No. 7 and No. 10, the ratio of silica added to epoxy resin was 1:1 (mass ratio). In the C.R_B, to obtain an appropriate ratio of No. 7 and No. 10, the ratio between the silica added to the epoxy and silane coupling agent synthesis resin was 2:3 (mass ratio).

In the subsequent tests conducted to investigate the physical properties (bond strength, impact resistance, flexural strength, compressive strength, length change rate, etc.), the mixing ratio of silica No. 7 and No. 10 used in all the C.R._A mixtures was C.R._A n2, shown in Table 6, and for C.R._B the mixing ratio of C.R_B n1 was used. A mixing ratio of epoxy resin and mixed silica was increased by adding 0.25 weight between 1:1 and 1:2 (mass ratio) to have five levels for manufacturing the specimens.

Bond strength test

Bond strength test method was followed by KS F 4937. The test results of the bond strength of C.R._A are shown in Figs. 4 and 5.

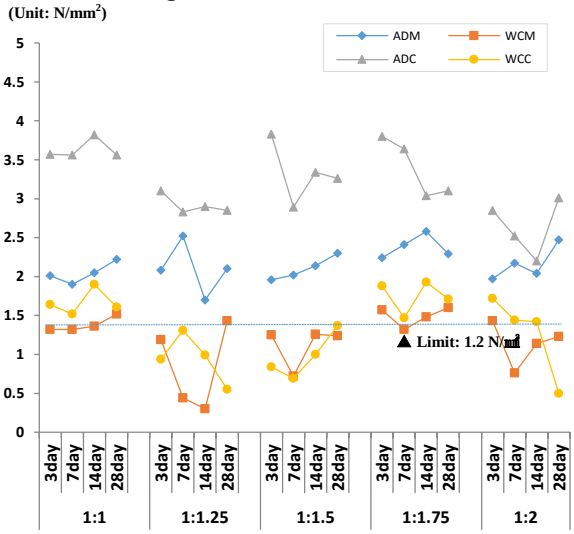

Fig. 4 Test results of the mixing ratio and bond strength at each curing age of C.R._A

(Unit: N/mm²)

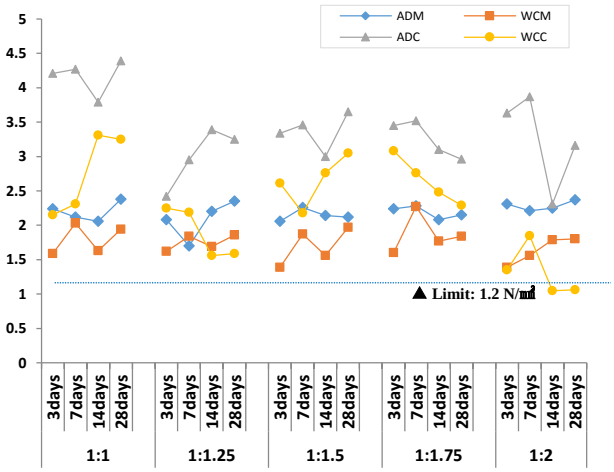

Fig. 5 Test results of the mixing ratio and bond strength at each curing age of C.R._B

In C.R._A, the broken floor material, together with the floor concrete, was shown in the dried mortar (ADM) and dried concrete (ADC), regardless of changes in the silica addition amount, once it exceeded 1.2 N/mm^2, the quality criteria of KS F 4937 was above 179.87% and 265.29%, on average, respectively. On the other hand, the wet mortar (WCM) and wet concrete (WCC) showed overall interfacial falling off, regardless of the changes in the added amount of silica, and all the mixing ratios other than 1:1 and 1:1.75 were below the KS standard. Therefore, for the wet mortar and concrete base, the epoxy resin and silica additions to the epoxy resin do not improve the bond strength.

At the 1:1.75 mixing ratio, the bond strength improved in the wet concrete, but gradually decreased as the curing continued, as shown in the dried concrete. This phenomenon is disadvantageous in terms of long-term durability of the floor. At the mixing ratio of 1:1.25 and 1:1.2, a similar trend was seen in the wet concrete.

In the C.R_B, the overall strength increased by compared to that of the C.R_A. The bond strength in the dried mortar and dried concrete destroyed the base, exceeding the KS quality standard by approximately 181.67% and 283.83%, respectively. Further, in the C.R_B:silica = 1:1–1:1.75 (mass ratio) range at the wet mortar and concrete base, the bond strength result exceeded the standard by approximately 145.88% and 188.04%; all the samples showed the falling apart of the floor material together with the floor concrete.

In the case of the wet concrete (WCC), a mixing ratio of 1:1, 1.:1.5, and 1:1.75 except for strength at the curing ages of 14 d and 28 d in the 1:2 mixing ratio showed higher bond strength distribution compared to that of the dried mortar (ADM). This result occurred because the hybrid resin reacted with fine moisture in the surface of the adherent, thereby creating a cross-linking between the resin-based coating film, which did not form strong roots, and the concrete base to improve the bond strength in the C.R_B in a wet-base condition compared to that in the C.R_A.

Impact resistance test

The impact resistance test of C.R was conducted at the curing age of 14 days after coating on the wet concrete and wet concrete bases by KS F 2622. The test result was summarized Figure 6.

For the C.R_A. the samples in which silica was added to the epoxy resin showed cracks around the edge of the hollow hole, regardless of the fall height in the concretes under dried and wet conditions, regardless of change in the amount of added silica.

This was because dispersion was not easy owing to the interfacial de-cohesion in the epoxy matrix when silica was simply added to the epoxy resin so that cross-linking density at that region degraded, thereby creating cracks on the area of impact. Therefore, the addition of silica alone cannot solve the problem of brittle fractures that occur often with conventional epoxy resin materials.

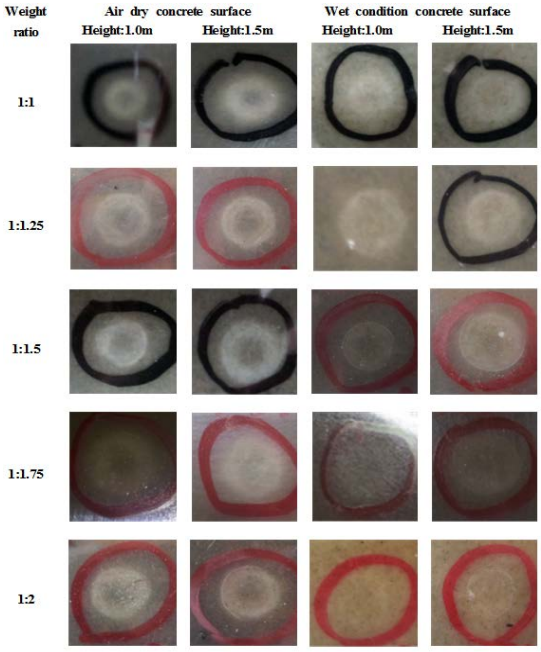

Fig. 6 Surface Condition after impact resistance test

For the C.R_B, the impact of a spherical weight fallen from the height of 1 m showed no damage to the concrete base under the dried and wet conditions, regardless of the amount of the silica addition added to the hybrid resin. However, near the hybrid resin:mixing silica ratio of 1:2 (mass ratio), cracks were found around the hollow hole owing to the impact of the spherical weight fallen from the height of 1.5 m.

This result can be explained based on the fact that the silane coupling agent contained in the hybrid resin connected the epoxy matrix and silica to form interfacial force by a chemical bond between them so that the stability of the silica particles increased and a uniform dispersion phase formed, facilitating the buffering action owing to absorption and dispersion against the external impact. As observed for mixing ratio of hybrid resin:mixing silica=1:2 (mass ratio), this phenomenon can also be explained by fact that increase in the silica contents can decrease the cross-linking density because of the aggregation of silica owing to the high-specific surface area of silica.

Compressive strength and flexural strength test

Compressive strength and flexural strength test method was followed by KS L 5105, KS F 2408. Figs. 7-8 show the result of the compressive strength test of the C.R.

The compressive strength of the specimens of C.R_A and C.R_B showed somewhat increasing trend as the curing ages increased. In the C.R_A, all the mixing ratios except for 1:1 exceeded 100 N/mm^2 at 28 d of curing age, whereas in the C.R_B, all the mixing ratios had values below 100 N/mm^2.

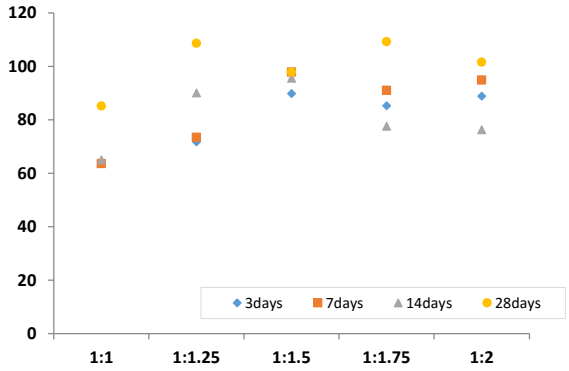

Fig. 7 Test result of compressive strength of C.R_A

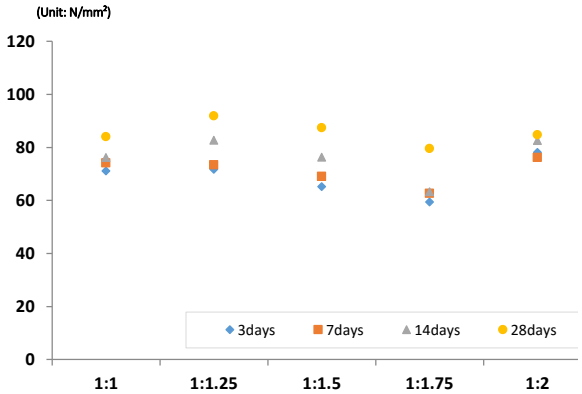

Fig. 8. Test result of compressive strength of C.R_B

This result showed that the mesh structure of the C.R_B having diversified tissue structure because of the addition of silica was somewhat disadvantageous in terms of compressive strength compared to the C.R_A that has fine tissue structure as it consists of only the polymer resin.

The difference of the mixing ratio showed that in the C.R_A, the relatively high compressive strength was observed for the mixing ratios of 1:1.25 and 1:1.75, while in the C.R_B, the mixing ratio of 1:1.25 showed the highest compressive strength. In particular, both C.R_A and C.R_B showed increased compressive strength up to a mixing ratio of 1:1.25 based on the amount of the added silica. However, for ration more than 1:1.25, no compressive strength increase was observed. Even in the C.R_B, the compressive strength decreased up to a mixing ratio of 1:1.75. Based on this result, increasing the amount of the silica added minimally affected the compressive strength and 1:1.25 should be considered as the appropriate level.

The flexural strength of C.R_A showed that samples with added silica had somewhat higher result in the range 29.45–48.30 N/mm^2 at 3 d of curing age. It also showed increasing distribution up to 7 d of curing, followed by a decrease till the 14th day of curing age. Then, at 28 d of curing age, the flexural strength varied in the range 22.24–34.04 N/mm^2. Therefore, the overall flexural strength showed less distribution than that observed at 3 d of curing age. At 28 d of curing age, the strength increased as the amount of the added silica was changed; however, the degree of change was minimal.

On the other hand, in the case of C.R_B, most of the mixing ratios showed values above 30 N/mm^2 of the flexural strength, thus showing overall improvement in the flexural strength compared to that observed in the C.R_A. The mixing ratios of 1:1.25 and 1:1.75 indicated better flexural strength compared to other mixing ratios. In particular, the initial strength at 1:1.75 was approximately 34% higher than that at 1:1.25. At all the aging conditions, deviation of less than ~4% was observed, which suggested stable flexural strength values. This flexural strength characteristic can reduce the crack occurrence probability with regard to the initial deformation (behavior and deflection) after the completion of construction and can accelerate the overall project schedule, including the subsequent operations, which was considered as advantageous.

In the case of 1:1.25 mixing ratio, its initial strength was lower than that observed for the 1:1.75 mixing ratio; however, it increased gradually as the material age increased by approximately 6% at 28 d.

Although this result was within the error range, a mixing ratio of 1:1.25 can maintain stable performance better than a mixing ratio of 1:1.75, which demonstrated gradual decrease as the material age increased after the initial strength.

Conclusively, flexural strength was greatly affected as mesh structure formed by adding mixed silica into the hybrid resin. This result was consistent with the previous study result, which reported more than 20% increase because of silica addition.

This result indicated that while compressive strength of the epoxy resin increased as the material age increased, it became vulnerable to brittle fracture as confirmed by the impact resistance test. In the case of C.R_B, flexural strength improved owing to the buffer action of the silane coupling composite resin.

CONCLUSION

The results of the study that aimed to derive the optimal mixing ratio of an epoxy resin for concrete floor constructed with a silane coupling agent and silica are as follows:

The bond strength test result showed in the case of silica addition to the epoxy and hybrid resins, all values of flexural strength at all mixing ratios (1:1–1:1.75) except for 1:2 mixing ratio at 14 d and 28 d of the curing age under the wet-base condition showed improved bond strength in the wet base, thus exhibiting clear improvement effect on reducing the difference with the dried base.

The impact resistance test result on the resin-based specimens showed that no change was found when silica was added. Brittle fracture characteristic of the epoxy resin improved through the addition of the silane coupling agent. Abrasion resistance also clearly improved owing to silane coupling synthesis because of the bond formation between GPTMS and the curing agent, which caused coupling action between the epoxy bond and the silica interfacial to form a strong interfacial force.

The measurement result of the compressive strength on the hybrid resin showed that the compressive strength of the epoxy and hybrid resins had an overall lower compressive strength than that of the epoxy resin. In terms of mixing ratio, the compressive strength increased up to 1:1.25, but showed no change as the silica mixing rate increased and then decreased later, which showed irregular change. Therefore, improvement in the compressive strength cannot be obtained by hybrid resin and silica mixing. On the other hand, in the flexural strength test, the improvement owing to the hybrid resin was shown clearly. For example, at the mixing ratios 1:1.25 and 1:1.75, consistent high flexural resistance performance was observed from 3 days strength and 28 days strength.

Based on the conclusions mentioned above, the optimal mixing ratio of the epoxy and hybrid resins as well as mixing silica was 1:1.75 (mass ratio) when the dried condition of the concrete base cannot be secured because of the broad investing region and shortening of the schedule. However, when a size is relatively small and a field where dried condition of the concrete base surface can maintain well, its optimal ratio shall be 1:1.25(mass ratio) for a long-term basis viewpoint.

In the future, when floor-finishing materials are applied to a field, securing performance through test evaluation such as wheel load resistance performance, noise occurrence, slide resistance, and chemical resistance will be evaluated. It needs to be further reviewed and studied for extending its application range to various purposes apart from the construction of finishing materials.

ACKNOWLEDGEMENTS

This research was supported by a grant(15RERP-B082204-02) from Residential Environment Research Program funded by Ministry of Land, Infrastructure and Transport of Korean government.

REFERENCES

[1] Chae, Woo-byung et al., “A Study on the Performance Evaluation of Surface Finishing Material for Parking Slab Mixed with Cemetitious Powder Component to Polyurethane Resin ”, Journal of the Architectural Institute of Korea(Structure system), Volume 27 No.1 (Total volume 267), 2011, pp.111-118

[2] Chae, Woo-byung , Ph.D thesis, Physical Performance Evaluation of Hybrid Finishing Material for Concrete Slab using Silane Coupling Agent, Architectural Engineering, Graduate School of Architectural Engineering, Chungbuk National University, 2013, 02

[3] Xi-e Cheng, Shiyong Liu, Wenfang Shi , “Synthesis and properties of silsesquioxane-based hybrid urethane acrylate applied to UV-curable flame-retardant coatings,” Progress in Organic Coatings, 65, 2009, pp.1–9

[4] J. J. Benkoski, E. J. Kramer, H. Yim, M. S. Kent, and J. Hall, “The Effects of Network Structure on the Resistance of Silane Coupling Agent Layers to Water-Assisted Crack Growth,” Langmuir, Vol. 20. No.8, 2004, pp.3246–3258

[5] Cornelius CJ, Marand E, “Hybrid inorganic-organic materials based on a 6FDA-6FpDA-DABA polyimide and silica: physical characterization studies,” Polymer, Vol. 43, No.8, 2002, pp.2385–2400

[6] Cevdet Kaynaka, Cengiz Celikbileka, Guneri Akovalia , “Use of silane coupling agents to improve epoxy–rubber interface,” European Polymer Journal, Volume 39, Issue 6, 2003, pp.1125–1132

First International Conference on Science, Engineering & Environment,
Tsu City, Mie, Japan, Nov.19-21, 2015, ISBN: 978-4-9905958-5-2 C3051

STATISTICAL MECHANICS IN BAYESIAN REPRESENTATION: HOW IT MIGHT WORK AND WHAT OUGHT TO BE THE PROBABILITY DISTRIBUTION BEHIND IT.

E. B. Starikov[1,2]
[1] Institute for Theoretical Solid-State Physics, KIT, Wolfgang-Gaede-Str. 1, D-76131 Karlsruhe, Germany;
E-mail: starikow@tfp.uni-karlsruhe.de; [2] Department of Physical Chemistry, Chalmers University of Technology, SE-41296 Gothenburg, Sweden.

La statistique n'est qu'une addition correcte de chiffres faux.
(*The statistics is just the correct addition of the false numbers*.)

Charles-Maurice de Talleyrand-Périgord

ABSTRACT

Statistical mechanics is clearly being restricted by its fuzzy basement, namely its assumption as for the 'large number of microscopic particles'. This communication tries to show and discuss some handy and useful way of how to circumvent such a restriction.

Keywords: Entropy, Enthalpy, Thermodynamics, Statistical Physics, Bayesian Statistics.

INTRODUCTION

In our most recent review paper devoted to the ultimately true interpretation of the ideas by N. L. S. Carnot [1] we have posed the following question as for the statistical interpretation of thermodynamics: Was it just a plain success or solely a sheer despair? To our mind, the correct answer would be – the both. Why?

Indeed, one of the two basic thermodynamics laws (the 1st one) cannot be considered a kind of statistical regularity, whereas another one (the 2nd one) – could nonetheless be made to obey the statistical regularities. Then, how it could be possible to combine this fact with the clear dialectic interrelationship between the two laws in question (cf. the work [2] for more detailed discussion of this important topic)?

The first (to the best of our knowledge) interesting suggestion as to a possible way out of the above-mentioned logical blind alley came from Johannes Diderik van der Waals – as early as in 1911 [3]. In his short note Prof. Dr. van der Waals had discussed the interrelationship between the probability and entropy notions, as it appeared from the considerations by L. Boltzmann and J. W. Gibbs.

Specifically, what Prof. Dr. van der Waals had suggested was in no way just a speculation – but a clearly formulated, substantiated, justified and fully competent suggestion to employ the Bayesian approach in deriving the relationship between the entropy and probability notions. The only serious and effectual obstacle on the way to the practical embodiment of that ingenious suggestion by van der Waals was the fact that the Bayesian approach to the probability notion wasn't really 'trendy' – not only at his time – but even approximately until the time of after the Second World War – it had to succumb to the '*frequentist*' train of thoughts…

Still, fortunately, van der Waals' valuable suggestion has not experienced just a traceless dissolution in the whirlpool of the 'trendy' medium – it had still been employed in the work by George Augustus Linhart [4-7], and, moreover, it is being further developed in the most recent time (cf. the work by Preety Aneja and Ramandeep S. Johal [8] – as well as all the recent work from this very active and successful group [9-13]), as well as the references therein).

Meanwhile, the 'frequentist' statistical-physical approach is based upon the long known and over-all accepted atomistic representation of the Matter, which makes us to operate with "extremely large number of atoms/molecules", and therefore we have seemingly no other reasonable way than just to apply to the conventional statistical treatment …

With this in mind, it is extremely important to note that the very possibility to avoid the conventional explicit microscopic consideration could be rather helpful, for notions like "extremely large number of atoms/molecules" are in fact FUZZY, in accordance with the well-known SORITES paradox. Indeed, it's a practically difficult task to achieve a universally strict definition of what exactly the "large number" is and hence, operating with such notions and their derivatives, like "thermodynamic limit", isn't really a productive approach.

Thus, the aim of our present communication should be to demonstrate how Bayesian approach might be handy and useful in circumventing the SORITES paradox, as well as to show the way of establishing mathematical/logical interconnection between its results and the well-known, tried and true products of the 'frequentist' train of thoughts.

ENTROPY CONSIDERATIONS

First of all, we start with the expression for entropy formally derived by G. A. Linhart [4-7], which is in fact nothing more than a temperature-dependent expression for the conventional Boltzmann's entropy:

$$S = \frac{C_\infty}{K}\ln\left(1+x^K\right);\; x \equiv \frac{T}{T_{ref}}. \tag{1}$$

Now, we employ the reasoning used for Eq. 2 by Aneja-Johal [8], namely, that the difference between the 'final' and 'initial' entropies is equal to zero. With this in mind and making use of Eq. 1 here, we get the following interdependence between the temperatures *T1* and *T2* of the both interacting systems (T1 and T2 here – are the relative temperatures (divided by T_{ref}), like *x* in Eq. 1 above, whereas $TP \equiv T+$; $TM \equiv T-$ (also – the both – are divided by T_{ref})):

$$T2 = \left(\frac{-T1^K + TP^K + TM^K\left(1+TP^K\right)}{1+T1^K}\right)^{\frac{1}{K}}. \tag{2}$$

Thus, Eq. 2 here casts T2 as a function of T1, and *vice versa*. This is why, we differentiate T2 by T1 and simplify the expression of the resulting derivative, to get the following formula:

$$\frac{dT2}{dT1} = -\frac{T1^{-1+K}\left(1+TM^K\right)\left(1+TP^K\right)\left(\frac{-T1^K+TP^K+TM^K\left(1+TP^K\right)}{1+T1^K}\right)^{-1+\frac{1}{K}}}{\left(1+T1^K\right)^2}. \tag{3}$$

Now, we can rearrange Eq. 3 a little bit in such a way, that we get a product of two functions, F(T1) and G(T2), to apply formula (1) by Aneja-Johal [8].

$$\begin{aligned} &T1^K - T1^K + \left(1+TM^K\right)\left(1+TP^K\right) \\ &\equiv 1+TP^K+TM^K\left(1+TP^K\right)+T1^K-T1^K \\ &= \left(1+T1^K\right)+\left(-T1^K+TP^K+TM^K\left(1+TP^K\right)\right) \\ &= \left(1+T1^K\right)\left(1+\frac{-T1^K+TP^K+TM^K\left(1+TP^K\right)}{1+T1^K}\right) \\ &= \left(1+T1^K\right)\left(1+T2^K\right). \end{aligned} \tag{4}$$

That is, our Eq. 3 can be recast as follows:

$$\frac{T2^{-1+K}\,dT2}{\left(1+T2^K\right)} = -\frac{T1^{-1+K}\,dT1}{\left(1+T1^K\right)}. \tag{5}$$

And, if we assume that $dT2 = -dT1$, then, the desired prior, as a function of temperature (Pr(*T*)) is unique – for all the subsystems under study – and then (in G. A. Linhart's representation !) reads, in effect, as a specific heat capacity at constant volume, divided by temperature:

$$\Pr(T) = \left(\frac{T^{K-1}}{1+T^K}\right) = \frac{C_V(T)}{T}. \tag{6}$$

Interestingly, when the expectation (average) temperature is calculated, using the latter form of prior, we get exactly this same form of the Gaussian hypergeometric function ${}_2F_1$ – as we obtain, when calculating the internal energy within G. A. Linhart's approach (see Eq. 8 in the work [14]) … Thus, we readily see that Aneja-Johal approach fits well into the general framework of the G. A. Linhart's 'Bayesian' statistical mechanics … But there is also a clear technical (mathematical) complication – to work out some closed formulas for the work, the efficiencies etc. – we have to approximate the available special transcendent functions … But, to our mind, it shouldn't constitute any principal complication …

WORK, EXPECTATION TEMPERATURE, INTERNAL ENERGY CONSIDERATIONS

To find the expression for the work done, we start with the formulation by Aneja-Johal [8]. Thus, we can extract the work (*W*) in some process

involving the both systems in question, which is equal to the decrease in internal energy (U) of the total system, $W = -\Delta U$, where $\Delta U = U_{\text{fin}} - U_{\text{ini}}$.

Then, using the Linhart's expression for the internal energy (see the work [14], Eq. 8), we get the following formula for the work:

$$W = C_{\infty} T_{ref} \left[\begin{array}{l} \left(xP\left(1 - {}_2F_1\left(1, \frac{1}{K}, 1+\frac{1}{K}; -xP^K\right)\right) \right. \\ \left. + xM\left(1 - {}_2F_1\left(1, \frac{1}{K}, 1+\frac{1}{K}; -xM^K\right)\right)\right) \\ - \left(x1\left(1 - {}_2F_1\left(1, \frac{1}{K}, 1+\frac{1}{K}; -x1^K\right)\right) \right. \\ \left. + x2\left(1 - {}_2F_1\left(1, \frac{1}{K}, 1+\frac{1}{K}; -x2^K\right)\right)\right) \end{array} \right], \quad (7)$$

where:

$$xP \equiv \frac{TP}{T_{ref}};\ xM \equiv \frac{TM}{T_{ref}};\ x1 \equiv \frac{T1}{T_{ref}};\ x2 \equiv \frac{T2}{T_{ref}}.$$

We see that Eq. 7 is formulated in terms of the special function, namely – the Gauss' Hypergeometric function ${}_2F_1$, which complicates a lot its practical usage … Thus, we would need to simplify Eq. 7. So then, first, we use one of the Pfaff's transformations:

$$ {}_2F_1\left(1, \frac{1}{K}, 1+\frac{1}{K}; -z^K\right) = \left(1+z^K\right)^{-\frac{1}{K}} {}_2F_1\left(\frac{1}{K}, \frac{1}{K}, 1+\frac{1}{K}; \frac{z^K}{1+z^K}\right); \quad (8)$$

and on the other hand, we employ the well known interconnection between the Gauss' Hypergeometric and incomplete Beta functions:

$$ py^{-p} B_y(p,q) = {}_2F_1(p, 1-q, 1+p; y) $$
$$ \Rightarrow \frac{1}{K}\left(\frac{z^K}{1+z^K}\right)^{-\frac{1}{K}} B_{\frac{z^K}{1+z^K}}\left(\frac{1}{K}, 1-\frac{1}{K}\right) \equiv {}_2F_1\left(\frac{1}{K}, \frac{1}{K}, 1+\frac{1}{K}; \frac{z^K}{1+z^K}\right) \quad (9)$$

And now, if we recall the definition of the incomplete Beta function, we can cast it as follows:

$$ B_y(a,b) = \int_0^y t^{a-1}(1-t)^{b-1} dt; \quad a>0; b>0. \quad (10)$$

Then, it is possible to recast the right-hand part of Eq. 8, using Eq. 10, in the following way:

$$ {}_2F_1\left(1, \frac{1}{K}, 1+\frac{1}{K}; -z^K\right) = \left(1+z^K\right)^{-\frac{1}{K}} \frac{1}{K}\left(\frac{z^K}{1+z^K}\right)^{-\frac{1}{K}} B_{\frac{z^K}{1+z^K}}\left(\frac{1}{K}, 1-\frac{1}{K}\right) \equiv \frac{z^{-1}}{K} B_{\frac{z^K}{1+z^K}}\left(\frac{1}{K}, 1-\frac{1}{K}\right); \quad (11)$$

All these results can be properly checked using the software *Mathematica* …

Therefore, it is in principle possible to express the Gauss hypergeometric functions in Eq. 7 *via* regularized incomplete Beta functions, as soon as we notice that:

$$ I_y(a,b) = \frac{B_y(a,b)}{B_1(a,b)}, \quad (12)$$

where I_y – is the regularized incomplete Beta function and B_1 – the conventional complete Beta function. Then, taking Eq. 12 into account, it is in general possible to rewrite the right hand side of Eq. 11 as follows:

$$ {}_2F_1\left(1, \frac{1}{K}, 1+\frac{1}{K}; -z^K\right) \equiv \frac{z^{-1}}{K} B_{\frac{z^K}{1+z^K}}\left(\frac{1}{K}, 1-\frac{1}{K}\right) \equiv \frac{z^{-1}}{K} \frac{B_{\frac{z^K}{1+z^K}}\left(\frac{1}{K}, 1-\frac{1}{K}\right)}{B_1\left(\frac{1}{K}, 1-\frac{1}{K}\right)} B_1\left(\frac{1}{K}, 1-\frac{1}{K}\right) \equiv \frac{z^{-1}}{K}\left(\pi \csc\left(\frac{\pi}{K}\right)\right) I_{\frac{z^K}{1+z^K}}\left(\frac{1}{K}, 1-\frac{1}{K}\right), \quad (13)$$

where $\mathbf{csc \equiv 1/sin}$ stands for the conventional *cosecant* function.

And, therefore, Eq. 7 might essentially be simplified in such a way:

$$W = C_{\infty} T_{ref}$$

$$\left[\begin{array}{l} \left(xP\left(1 - \frac{xP^{-1}}{K}\left(\pi \csc\left(\frac{\pi}{K} \right) \right) I_{\frac{xP^{K}}{1+xP^{K}}}\left(\frac{1}{K}, 1 - \frac{1}{K} \right) \right) + \right. \\ \left. xM\left(1 - \frac{xM^{-1}}{K}\left(\pi \csc\left(\frac{\pi}{K} \right) \right) I_{\frac{xM^{K}}{1+xM^{K}}}\left(\frac{1}{K}, 1 - \frac{1}{K} \right) \right) \right) \\ - \left(x1\left(1 - \frac{x1^{-1}}{K}\left(\pi \csc\left(\frac{\pi}{K} \right) \right) I_{\frac{x1^{K}}{1+x1^{K}}}\left(\frac{1}{K}, 1 - \frac{1}{K} \right) \right) + \right. \\ \left. x2\left(1 - \frac{x2^{-1}}{K}\left(\pi \csc\left(\frac{\pi}{K} \right) \right) I_{\frac{x2^{K}}{1+x2^{K}}}\left(\frac{1}{K}, 1 - \frac{1}{K} \right) \right) \right) \end{array} \right] \quad (14)$$

The important mathematical point here is that the function $I_Y(a,b)$, the regularized incomplete Beta function, represents nothing more than the cumulative probability function for some random number Y obeying the Beta distribution. Hence, interestingly, all this does boil down to nothing more than just the Bayesian approach to statistics – as it originally ought to be – for, as well known, that was Reverend Thomas Bayes himself, who started employing the continuous Beta distribution function as a prior for the discrete binomial distributions …

Well, and physically this means that we ought to consider the heat capacity at constant volume to be a random variable. Would the latter conclusion be a kind of heresy – and ought we to be immediately condemned by all the researchers' community? Not at all, God bless, for such a seemingly unexpected standpoint could still be throughout plausible (see, for example, the work [15], the references therein, as well as the corresponding discussion in the work [14]).

Indeed, the (statistical-mechanical) physical sense of heat capacity consists in that it shows how the 'sum' of all the possible elementary excitations in the system would describe the macroscopic state of the system. Linhart's formula (please, cf. Eq. 5 in [14]) is just the mathematical expression of this property – moreover, it shows, how the experimentally measurable heat capacity, that is, in our notations, $Y \equiv \mathbf{C}$, might well be expressed in terms of the standard probability theory ($\frac{C}{C_{\infty}}$) …

To sum up, Eq. 14 here is expressing the work to be done *via* the probabilities to achieve some definite value of the heat capacity (or, generally speaking, some definite macroscopic state of the system under study) at some particular temperature value.

Thus, from here on, the only way to handle Eq. 14 in terms of elementary functions would be to introduce some proper, pertinent approximations for the function $I_Y(a,b)$. In this case there are just two possibilities, namely: Y – around *0*, as well as Y – around *1*.

Then, we get:

$$\begin{array}{l} I_Y(a,b) \propto \frac{Y^a}{aB(a,b)}\left(1 + \frac{a(1-b)Y}{a+1} + O\left(Y^2\right) + \ldots \right); \\ Y \to 0 - \text{and} - a \notin \mathbf{N}; \\ I_Y(a,b) \propto 1 - \frac{(1-Y)^b Y^a}{bB(a,b)}\left(1 - \frac{(a+b)(Y-1)}{b+1} + O\left((Y-1)^2\right) \right); \\ Y \to 1 - \text{and} - b \notin \mathbf{N}. \end{array} \quad (15)$$

And, finally – the last, but not the least …

CONCLUSION

The above considerations clearly show us that statistical mechanical inferences could be pretty well – and in a completely straightforward way – handled within the Bayesian approach. This occurs to be possible, since we are closely following the approach by G. A. Linhart [4-7].

The immediate profit on this way consists in that our considerations are absolutely not restricted to the throughout fuzzy notion of some "large number" of atoms/molecules, as it is normally the case for the conventional treatment (see, for example, [16] and the references therein). And this profit is definitely achievable within the framework of Bayesian approach, which enables us to get rid of the fuzziness introduced by the straightforwardly and blindly adopted atomistic hypothesis. So, here we might get an opportunity to significantly widen the actual horizons of the conventional statistical thermodynamics, to include not only strictly macroscopic, but also meso- and even nanoscopic levels of studies …

However, there is the only serious and crucially important poser that still remains unanswered:

What ought to be the formal logical links between the Bayesian representation outlined above and the conventional Gibbs ensembles described by the Normal (Gaussian) distribution function, the tried and true Boltzmann exponential distribution etc., which are already long and very well known to be really faithful and useful mathematical instruments of theoretical physics ?

Well, the immediate and clear answer is: Surely, we do not have to overthrow or, that is to say, completely refurbish all the conventional statistical mechanics ! But we just ought to widen the horizons of the latter and carefully look after the

detailed conceptual links between its different chapters…

…Regretfully, the short format of the present communication doesn't really allow us to dwell on this important topic, but we would at least like to point out here that:

The Beta Density is anyway of extreme importance in the formal mathematical derivation of the conventional Canonical Distribution [17].

The Beta Probability Distribution is the tried and true method of successful statistical evaluation in the cases where fuzzy sets are at work [18].

ACKNOWLEDGEMENTS

I greatly appreciate expressing my sincere gratitude to Dr. Ramandeep Singh Johal, Associate Professor (Physics), Indian Institute of Science Education & Research, Mohali, for detailed and thorough discussions on the above theme of our common research interest.

REFERENCES

[1] E. B. Starikov, *What Nicolas Léonard Sadi Carnot wanted to tell us in fact*. Pensée Journal, v. 76, pp. 171-214, 2014.

[2] E. B. Starikov, *Valid Entropy-Enthalpy Compensation: Its True Physical Meaning*. J. Appl. Solut. Chem. Mod., v. 2, pp. 240-245, 2013.

[3] J. D. van der Waals, *Über die Erklärung der Naturgesetze auf statistisch-mechanischer Grundlage*. Phys. Z., v. XII, pp. 547-549, 1911.

[4] G. A. Linhart, *NOTE. The Relation Between Entropy and Probability. The Integration of the Entropy Equation*. J. Am. Chem. Soc., v. 44, pp. 140-142, 1922.

[5] G. A. Linhart, *Correlation of Entropy and Probability*. J. Am. Chem. Soc., v. 44, 1881-1886, 1922.

[6] G. A. Linhart, *Additions and Corrections – Correlation of Entropy and Probability*. J. Am. Chem. Soc., v. 44, 2968-2969, 1922.

[7] G. A. Linhart, *Correlation of Heat Capacity, Absolute Temperature and Entropy*. J. Chem. Phys., v. 1, pp. 795-797, 1933.

[8] P. Aneja, R. S. Johal, *Prior information and inference of optimality in thermodynamic processes*. J. Phys. A, Math. Theor., v. 46, p. 365002, 2013.

[9] R. S. Johal, *Models of Finite Bath and Generalized Thermodynamics*. In: *Studies in Fuzziness and Soft Computing*. A. Sengupta, Ed., v. 206, pp. 207-217, 2006.

[10] P. Aneja, R. S. Johal, *Prior Probabilities and Thermal Characteristics of Heat Engines*. Cent. Eur. J. Phys., v. 10, pp. 708-714, 2012.

[11] R. S. Johal, *Efficiency at Optimal Work from Finite Reservoirs: A Probabilistic Perspective*. J. Non-Eq. Thermodyn., v. 40, pp. 1-12, 2015.

[12] P. Aneja, R. S. Johal, *Form of Prior for Constrained Thermodynamic Processes*. Eur. Phys. J. B, v. 88, pp. 129-138, 2015.

[13] R. S. Johal, Renuka Rai, G. Mahler, *Reversible Heat Engines: Bounds on Estimated Efficiency from Inference*. Found. Phys., v. 45, pp. 158-170, 2015.

[14] E. B. Starikov, *Many Faces of Entropy or Bayesian Statistical Mechanics*. ChemPhysChem, v. 11, pp. 3387-3394, 2010.

[15] R. L. Scott, *The Heat Capacity of Ideal Gases*. J. Chem. Educ., v. 83, pp. 1071-1081, 2006.

[16] A. R. Khokhlov, A. Yu. Grosberg, V. S. Pande, *Statistical Physics of Macromolecules (Polymers and Complex Materials)*. AIP Press, New York, USA, 1997.

[17] B. H. Lavenda, "*Statistical Physics. A Probabilistic Approach*", Wiley-Interscience Publication, New York, Chichester, Brisbane, Toronto, Singapore, 1991, pp. 224-230.

[18] M. Smithson, J. Verkuilen, "*Fuzzy Set Theory. Applications in the Social Sciences*", Sage Publishing, Thousand Oaks, CA, USA, 2006, pp. 41-43.

First International Conference on Science, Engineering & Environment,
Tsu City, Mie, Japan, Nov.19-21, 2015, ISBN: 978-4-9905958-5-2 C3051

ADOMIAN DECOMPOSITION METHOD FOR SOLVING OF FREDHOLM INTEGRAL EQUATION OF THE SECOND KIND USING MATLAB

Dalal Adnan Maturi[1]

[1]Departement of Mathematics, Faculty of Science, King Abdulaziz University, P.O.Box 42664,Jeddah 21551, Saudi Arabia

ABSTRACT

In this paper, we will be find exact solution of Fredholm Integral equation of the second kind through using Adomian Decomposition Method by using MATLAB program, so all calculations can be easily using MATLAB to find that exact solution.

Keywords: Fredholm integral equation of the second kind; Adomian Decomposition Method; MATLAB.

INTRODUCTION

In this paper, we consider the Fredholm integral equation of the second kind

$$y(x) = f(x) + \lambda \int_a^b K(x,t)y(t)\,dt \qquad (1)$$

The unknown function $y(x)$, that will be determined, occurs inside and outside the integral sign. Th kernel $K(x,t)$ and the function $f(x)$ are given real-valued functions, and λ is aparameter.

In this paper, we present the computation of exact solution of Fredholm integral equation of the second kind using MATLAB.

ADOMIAN DECOMPOSITION METHOD

In this section, we use the technique of the Adomian Decomposition Method [4,9,13,14] . The Adomain Decomposition Method consists of decomposing the unknown function $y(x)$ of any equation into a sum of an infinite number of components defined by the decomposition series

$$y(x) = \sum_{n=0}^{\infty} y_n(x), \qquad (2)$$

Or equivalenty

$$y(x) = y_0(x) + y_1(x) + y_2(x) + y_3(x) + \cdots \qquad (3)$$

Where the components $y_n(x), n \geq 0$ will be determined recurrently. The Adomain Decomposition Method concerns itself with finding the components $y_0(x), y_1(x), y_2(x), y_3(x), \cdots$ individually.

To establish the recurrence relation, we substitute (2) into the Fredholm integral equatin (1) to obtain

$$\sum_{n=0}^{\infty} y_n(x) = f(x) + \lambda \int_a^b K(x,t)\left(\sum_{n=0}^{\infty} y_n(t)\right) dt, \qquad (4)$$

or equivalenty

$$y_0(x) + y_1(x) + y_2(x) + y_3(x) + \cdots = f(x) + \lambda \int_a^b K(x,t)\,[\,y_0(t) + y_1(t) + y_2(t) \cdots]dt \qquad (5)$$

The zeroth component $y_0(x)$ is identified by all terms that are not included under the integral sign . (This means that the components $y_n(x), n \geq 0$ of the unknown function $y(x)$ are completely determined by setting the recurrence relation

$$y_0(x) = f(x), \quad y_{n+1}(x) = \lambda \int_a^b K(x,t)y_n(t)\,dt, \quad n \geq 0 \qquad (6)$$

or equivalenty

$$\begin{aligned} y_0(x) &= f(x), \\ y_1(x) &= \lambda \int_a^b K(x,t)y_0(t)\,dt \\ y_2(x) &= \lambda \int_a^b K(x,t)y_1(t)\,dt \\ y_3(x) &= \lambda \int_a^b K(x,t)y_2(t)\,dt \\ y_4(x) &= \lambda \int_a^b K(x,t)y_3(t)\,dt \end{aligned} \qquad (7)$$

And so on for other component's.

In view of (7), the components $y_0(x), y_1(x), y_2(x), y_3(x), \cdots$ are completely determined. As a result, the solution $y(x)$ of the Fredholm integral equation (1) is readily obtained in a series form by using the series as assumption in (2).

EXAMPLE

Example1. Consider the Fredholm integral equation of second kind

$$\boldsymbol{y(x) = \cos x + 2x + \int_0^{\pi} xty(\mathrm{t})dt}\,.$$

Applying the Adomian Decomposition Method we find

$$\boldsymbol{\sum_{n=0}^{\infty} y_n(x) = \cos x + 2x + \int_0^{\pi} xt \sum_{n=0}^{\infty} y_n(t)\, dt}\,.$$

To determine the components of $\boldsymbol{y(x)}$, we use the recurrence relation

$$\boldsymbol{y_0(x) = \cos x + 2x},$$
$$\boldsymbol{y_{n+1}(x) = \int_0^{\pi} xt\, y_n(\mathrm{t})dt}, \qquad \boldsymbol{n \geq 0}.$$

This in turn gives

$$\boldsymbol{y_0(x) = \cos x + 2x},$$
$$\boldsymbol{y_1(x) = \int_0^{\pi} xt\, y_0(\mathrm{t})dt = \frac{2x(\pi^3 - 3)}{3}},$$
$$\boldsymbol{y_2(x) = \int_0^{\pi} xty_1(\mathrm{t})dt = \frac{2627688692113193x\pi^3}{422212465065984}},$$
$$\boldsymbol{y_3(x) = \int_0^{\pi} xty_2(\mathrm{t})dt = \frac{565797518176089x\pi^3}{8796093022208}},$$
$$\boldsymbol{y_4(x) = \int_0^{\pi} xty_3(\mathrm{t})dt = \frac{1461939532799565x\pi^3}{2199023255552}},$$
$$\boldsymbol{y_5(x) = \int_0^{\pi} xt\, y_4(\mathrm{t})dt = \frac{5666162705481445x\pi^3}{824633720832}},$$
$$\boldsymbol{y_6(x) = \int_0^{\pi} xt\, y_5(\mathrm{t})dt = \frac{228758604898117x\pi^3}{3221225472}},$$
$$\boldsymbol{y_7(x) = \int_0^{\pi} xt\, y_6(\mathrm{t})dt = \frac{1773238149117601x\pi^3}{2415919104}},$$
$$\boldsymbol{y_8(x) = \int_0^{\pi} xt(\mathrm{t})dt = \frac{2290896361316795x\pi^3}{301989888}},$$
$$y_9(x) = \int_0^{\pi} xty_8(\mathrm{t})dt = \frac{138734700048595x\pi^3}{1769472},$$
$$y_{10}(x) = \int_0^{\pi} xt\, y_9(\mathrm{t})dt = \frac{1433882164955047x\pi^3}{1769472},$$
$$y_{11}(x) = \int_0^{\pi} xty_{10}(\mathrm{t})dt = \frac{694677298961617x\pi^3}{82944},$$
$$y_{12}(x) = \int_0^{\pi} xty_{11}(\mathrm{t})dt = \frac{1346209783445453x\pi^3}{15552}.$$

And so on. Using (2) gives the series solution

$$\begin{aligned}\boldsymbol{y(x)} &= \boldsymbol{\cos x + 2x + \frac{2x(\pi^3 - 3)}{3}} \\ &+ \boldsymbol{\frac{2627688692113193x\pi^3}{422212465065984}} \\ &+ \boldsymbol{\frac{565797518176089x\pi^3}{8796093022208}} \\ &+ \boldsymbol{\frac{1461939532799565x\pi^3}{2199023255552}} \\ &+ \boldsymbol{\frac{5666162705481445x\pi^3}{824633720832}} \\ &+ \boldsymbol{\frac{228758604898117x\pi^3}{3221225472}} \\ &+ \boldsymbol{\frac{1773238149117601x\pi^3}{2415919104}} \\ &+ \boldsymbol{\frac{2290896361316795x\pi^3}{301989888}} \\ &+ \boldsymbol{\frac{138734700048595x\pi^3}{1769472}} \\ &+ \boldsymbol{\frac{1433882164955047x\pi^3}{1769472}} \\ &+ \boldsymbol{\frac{694677298961617x\pi^3}{82944}} \\ &+ \boldsymbol{\frac{1346209783445453x\pi^3}{15552}} + \cdots\end{aligned}$$

$$\begin{aligned}&\boldsymbol{y(x)} \\ &= \boldsymbol{\cos x + 2x + \frac{2x(\pi^3 - 3)}{3}} \\ &+ \boldsymbol{\frac{32774555302931703282193785 37x\pi^3}{34199209670344704}} + \cdots\end{aligned}$$

Then the gives the exact solution

$$\boldsymbol{y(x) = \frac{3387389766011857539636662 1689x}{11399736556781568} + \cos x}$$

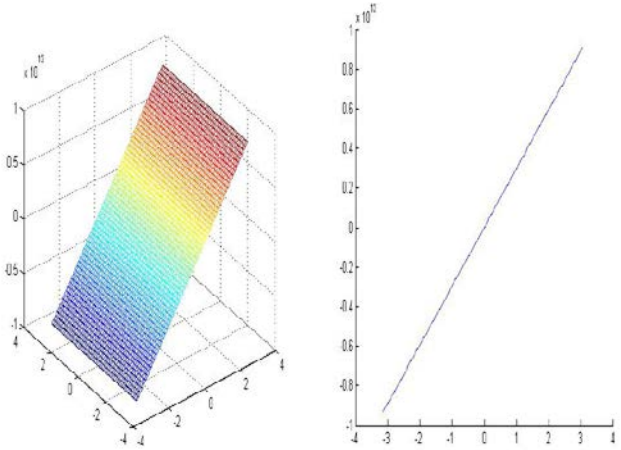

Fig. 1 Plot 3D and 2D of the exact solutions result Of Fredholm integral equation for example 1

CONCLUSION

In this paper, Adomain Decomposition Method, for solving Fredholm integral equations of the second kind, is studied successfully. The computations associated with example were performed using MATLAB.

REFERENCES

[1] V. Balakumar, K. Murugesan, Numerical Solution of Systems of Linear Volterra Integral Equations Using Block-Pulse Functions, Malaya Journal of Matematik, S(1)(2013)77-84.

[2] L.C. Becker and M. Wheeler, Numerical and Graphical Solutions of Volterra Equations of the Second Kind,Maple Application Center, 2005.

[3] R.L.Burden and J. Douglas Faires, Numerical Analysis, 8th ed., Thomson Brooks/Cole, Belmont, CA, 2005.

[4] T. A. Burton, Volterra Integral and Differential Equations, 2nd ed., Mathematics in Science & Engineering, 202, Elsevier, 2005.

[5] M.I. Berenguer, D. Gamez, A. I. Garralda-Guillem,M. Ruiz Galan, and M.C. Serrano Perez, Biorthogonal Systems for Solving Volterra Integral equation Systems of the Second Kind, Journal of Computional and Applied Mathematics,235(7)(2011),1875-1883.

[6] J. Biazar and M. Eslami, Modified HPM for Solving Systems of Volterra Integral Equation of the Second Kind, Journal of King Saud University-Science, 23(1)(2011),35-39.

[7] P. Linz, Analytical and Numerical Methods for Volterra Equations, Studies in Applied Mathematics 7, SIAM, Philadelphia, 1985.

[8] F. Mirzaee, Numerical Computional Solution of the Linear Volterra Integral Equations System Via Rationalized Haar Functions, Journal of King Saud University- Science, 22(4)(2010),265-268.

[9] A.M.Wazwaz, Linear and Nonlinear Integral Equation: Methods and Applications, Springer, 2011.

[10] S. Effati and M.H. NooriSkandari, Optimal Control Approach for Solving Linear Volterra Integral Equations, I.J.Intelligent Systems and Applications, 2012,4,40-46.

[11] D.A.Maturi, Numerical Solution of System of Two Nonlinear Volterra Integral Equations,International Journal of Computers & Technology, Vol12,No.10,pp.3967-3975,2014.

[12] D.A.Maturi, A.Z.Bajamal, B.M.AlGethami, Numerical Solution of Volterra Integral Equation of Second Kind Using Implicit Trapezoial , Journal of Advances In Mathematics, Vol8,No.2,pp.1540-1553,2014.

[13] D.A.Maturi,, Adomian Decomposition Method of Fredholm Integral Equation of the Second kind using Maple, Journal of Advances In Mathematics, Vol9,No.1,pp.1868-1875,2014.

[14] D.A.Maturi,, Application of Adomian Decomposition Method of Fredholm Integral Equation of the Second Kind , European Journal of Science and Engineering, Vol2,No.2,pp.1-9,2014.

First International Conference on Science, Engineering & Environment,
Tsu City, Mie, Japan, Nov.19-21, 2015, ISBN: 978-4-9905958-5-2 C3051

THE EFFECT OF CROSS-LINKED AGENTS ON KERATIN FILMS PROPERTY

Weerasak Songeon and Prasong Srihanam

[1]Faculty of Science, Mahasarakham University, Maha Sarakham 44150, Thailand

ABSTRACT

This research aimed to investigate the effect of cross-linking agents on the properties of keratin films. The films were prepared by mixing all solutions until homogeneous before pouring them into polystyrene plates and oven drying them at 40 °C for three days. The obtained films were characterized for their morphology and secondary structure using a scanning electron microscope (SEM) and Fourier transform-infrared (FT-IR) spectrophotometer. The native keratin film had smooth surfaces and was slightly fragile throughout the film area. Considering all the cross-linking agents, the keratin film cross-linked with glutaraldehyde had the smoothest surface. In addition, the differences in the cross-linking agents resulted in different morphologies of the films. The secondary structure analysis found that the random coil structures of the films had been changed into β-sheets after blending with the cross-linking agents. This resulted in an increase to a denser texture, strength and thermal stability of the films. The results suggest that the morphology, secondary structure and thermal stability of the keratin films were dependent on the content and type of cross-linking agent used.

Keywords: Film, Keratin, Morphology, Secondary structure

INTRODUCTION

Keratin is a structural protein that has unique biological and chemical properties [1], [2]. It can be extracted from several original sources. Recently, keratin has been used in many applications [3], [4]. It can be prepared in many forms, especially as a film. It has also exhibited a high potential as a scaffold material for several tissue engineering applications. Previous reports have developed novel keratin by cross-linking the disulfide bonds. The recycled keratin biomaterials could be fabricated into films to be used as drug release carriers. However, a keratin film with this composition has limited applications due to its high fragility, low strength and flexibility [5]. As an alternative, polymer blends, as cross-linking agents, have been used to improve some of the limitations of the keratin material [6], [7]. However, the effect of cross-linking agents on the keratin properties has not been fully studied. Therefore, the objective of this work was to study the effect of different cross-linking agents on keratin film properties, especially the morphology, secondary structure and thermal stability.

METHODOLOGY

Human hair was gathered from a local hair salon in Maha Sarakham Province, Thailand. The hair was wormed at 40 °C before being immersed in n-hexane for 12h to remove the external lipid. All chemical reagents used were analytical grade.

Preparation of Keratin Solution

Human keratin was extracted using a modification of Shindai's method [26]. Briefly, 10g of hair sample was dissolved using a mixture solution of 7g urea, 2g sodium dodecyl sulfate (SDS) and 0.8g sodium hydroxide (NaOH) in 100 mL distilled water at 70 °C while being stirred until homogeneous dissolution. The obtained solution was then dialyzed against distilled water for three days.

Preparation of Keratin Blend Films

A 1% wt keratin solution was firstly mixed with different ratios of cross-linking agents in beakers. The mixture solutions were then poured into polystyrene plates with diameters of 9 cm. The plates were then dried in an oven at 40 °C for three days to obtain the blend films.

Characterizations

Morphological observation

All of the films were dehydrated and cut (~ 1cm in length) before observing their morphology under a scanning electron microscope (SEM) (JEOL, JSM-6460LV, Tokyo, Japan). The samples were sputter coated with gold on double sided carbon tape for enhancing surface conductivity. Current and

voltage were adjusted to give a power of 2W (3mA, 15 kV) for 3 min.

Secondary structure analysis

All of the films had their secondary structures investigated using attenuated total reflection infrared (ATR-IR) spectroscopy (Perkin Elmer-Spectrum Gx, USA) in the spectral region of 4000-400 cm^{-1} at a 4 cm^{-1} spectral resolution and 32 scans.

Thermal properties study

The keratin/sericin blend films with 8-10 mg were loaded in a platinum crucible. The thermogravimetric analysis (TGA) was then performed using a TA instruments SDT Q600 (Luken's drive, New Castle, DE). The samples were non-isothermally heated from 50 °C to 800 °C at a heating rate of 20 °C/min. The TGA was performed in nitrogen with a flow rate of 100 mL/min.

RESULTS

Morphological study

The morphology of the films was investigated using a scanning electron microscope (SEM). The results showed that keratin (Fig. 1a) had a smooth surface with a homogeneous texture of the cross-section without phase separation. Keratin blended with PEGDE resulted in a rougher surface as well as cross-section (Fig. 1b) in comparison to the native keratin film. In contrast, the keratin blended with glutaraldehyde (Fig. 1c) and genipin (Fig. 1d) had smoother surfaces than the native keratin film. Considering the edge of the films, the keratin blended with genipin showed some slight phase separation, which was not found in the other films.

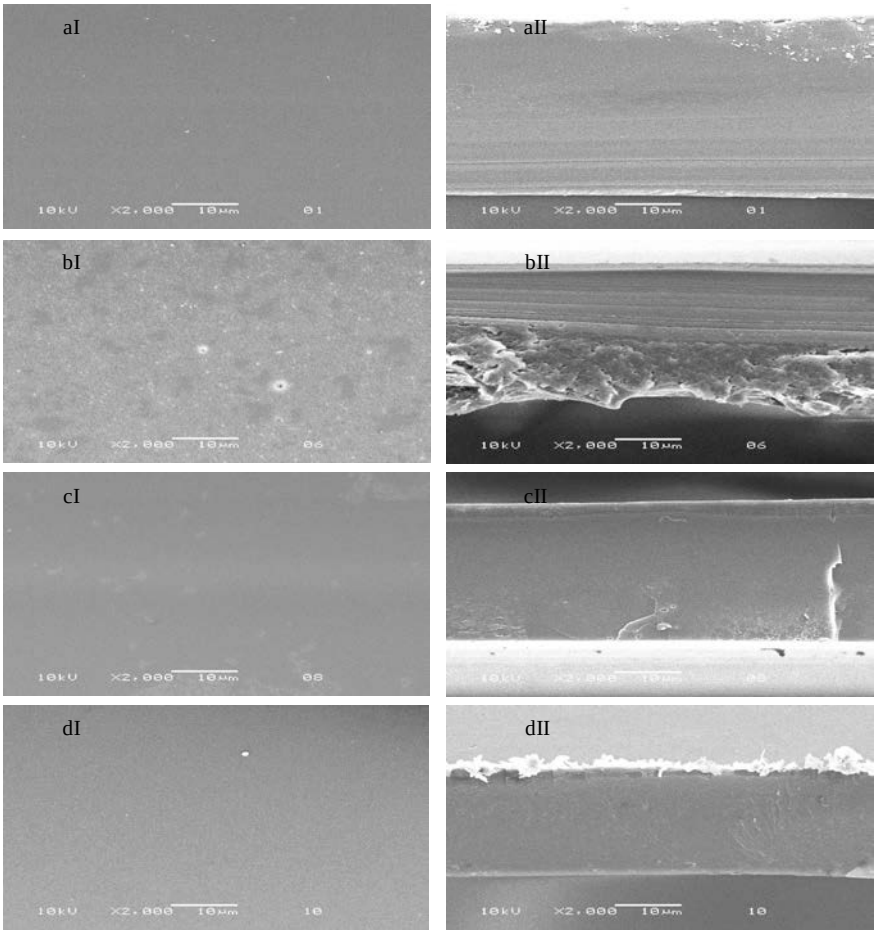

Fig. 1 SEM micrographs native keratin film (a) and keratin blended with PEGDE (b), glutaraldehyde (c) and ginipin (d). Column I present as the surface and column II a cross-section of the films. (All bars =10μm).

Secondary structure

The results showed that the native keratin film had absorption peaks at 1671, 1539 and 1232 cm^{-1} [Fig. 2a]. The keratin film blended with PEGDE had absorption peaks at 1664 and 1234 cm^{-1} [Fig. 2b], while glutaraldehyde showed them at 1622, 1571 and 1236 cm^{-1} [Fig. 2c]. In addition, the keratin blended genipin showed absorption peaks at 1628, 1553 and 1236 cm^{-1} [Fig. 2d].

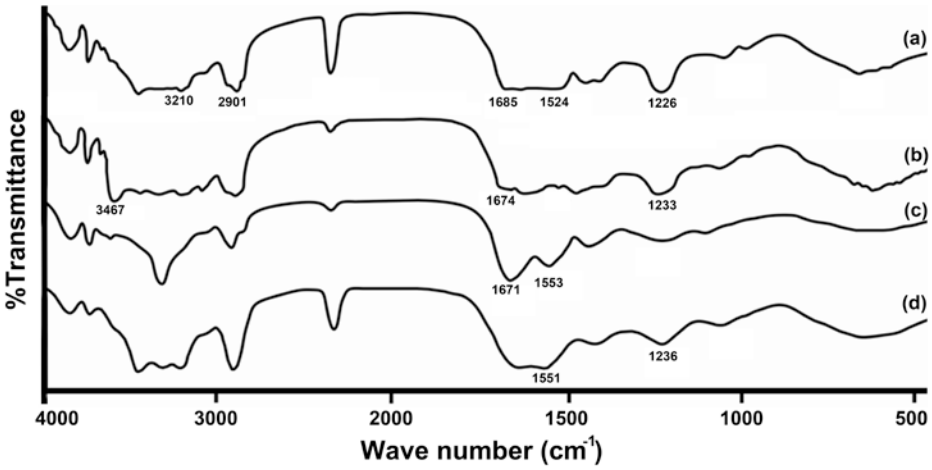

Figure 2 FTIR spectra of native keratin (a), keratin blended with 0.1% PEGDE 0.01 g (b), keratin blended with genipin (c) and keratin with glutaraldehyde (d).

Thermal stability

The thermal stability of the films as indicated by DTG curves is shown in Fig. 3, which shows the maximum temperature of decomposition ($T_{d,max}$), which are summarized in Table 1. The native keratin started weight lose at about 105 °C and had a $T_{d,max}$ at 311 °C (Fig. 3a). Among the cross-linking agents, keratin blended genipin showed the highest $T_{d,max}$ at 316 °C (Fig. 3f,g), then PEGDE at 314 °C (Fig. 3b,c) and glutaraldehyde had the lowest of $T_{d,max}$ at 304 °C (Fig. 3d,e).

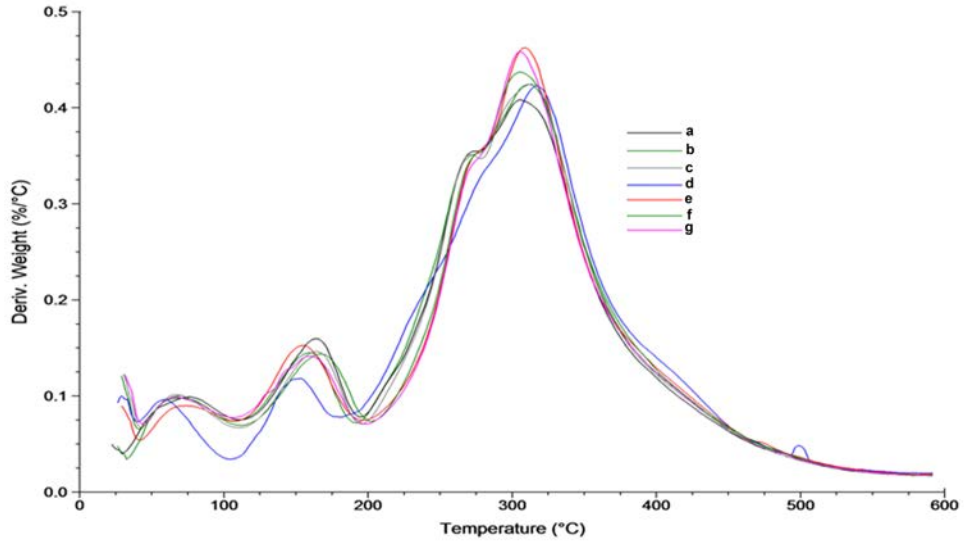

Figure 3. DTG curve of native keratin (a), keratin blended with PEGDE of 0.01 g (b) and 0.02 g (c), glutaraldehyde of 0.01 g (d) and 0.02 g (e) and genipin of 0.01 g (f) and 0.02 g (g).

Table 1 Temperature of maximum decomposition of keratin films blended with different cross-linking agents.

Type of films	$T_{d,max}$ (°C)
Keratin	311
Keratin/PEGDE	314
Keratin/glutaraldehyde	304
Keratin/genipin	316

DISCUSSION

The SEM micrographs showed the different surfaces and textures of the cross-sections according to the unique characteristics of each cross-linking agent. Generally, the keratin varied in size, molecular weight and amino acid components. The cross-linking agents influenced the dense texture of the film. This was due to their acting as a binder between the keratin molecules to hold them more closely together. The secondary structure of the protein was mainly observed in the amide I, II and III regions [8]. Amide I was the stretching of the carbonyl group (-C=O) while amide II was the blending of the –NH group and stretching of –CH. On the other hand, amide III was the stretching of –CN and the plane of –NH as well as the stretching of –CC and –C=O [9]. The FTIR spectra suggested that the native keratin was composed of α-helix and random coil structures. Glutaraldehyde, the smallest chemical structure, helped to decrease the crystallinity of the keratin film and resulted in a decrease in the thermal stability of the keratin film. However, the keratin films that were blended with PEGDE and genipin had increased thermal stability. This might suggest that PEGDE and genipin are complex chemical structures that interacted with the keratin molecules more than the glutaraldehyde and caused an increase in the α-helix and β-sheet structures. The decomposition of all the films showed at least two steps with the $T_{d,max}$ higher than 300 °C (300-330 °C). This temperature was the decomposition of the amino acid side chain and peptide bonds between the amino acids [10].

CONCLUSION

The native keratin had smooth surfaces with some particles with homogeneous textures without phase separation. The keratin film blended with cross-linking agents had altered textures and increased thermal stability due to changes in their secondary structure, except for glutaraldehyde. The results obtained in this work may be used for the preparation of keratin films for several applications, especially biomedical and controlled drug release.

ACKNOWLEDGEMENTS

The authors would like to thank the Faculty of Science, Mahasarakham University, Thailand for financial support for this work.

REFERENCES

[1] Katoh K, Shibayama M, Tanabe T, Yamauchi K, "Preparation and physicochemical properties of compression-model keratin films," Biomaterials, Vol. 25, 2004, pp. 2265-2272.
[2] Yamauchi K, Hojo H, Yamamoto Y, Tanabe T, "Enhanced cell adhesion on RGDS-carrying keratin film," Mater. Sci. Eng. C, Vol. 33, 2003, pp. 467-472.
[3] Yamauchi K, Maniwa M, Mori T, "Cultivation of fibroblast cells on keratin-coated substrata," J. Biomater. Sci. Polym., Vol. 9, 1998, pp. 259-270.
[4] Balaji S, Kumar R, Kakkar P, Ramesh D, Vijaya Ramesh R, Reddy PNK, Sehgal PK, "Preparation and comparative characterization of keratin-chitosan and keratin-gelatin composite scaffolds for tissue engineering applications," Mater. Sci. Eng., Vol.32, 2012, pp. 975-982.
[5] Fujii T, Ogiwara D, Arimoto M, "Convenient procedures for human hair protein films and properties of alkaline phosphatase incorporated in the film," Biol. Pharm. Bull., Vol.27, 2004, pp. 89-93
[6] Vasconcelos A, Fredi G, Cavaco-Paulo A, "Biodegradable materials based on silk fibroin and keratin," Biomacromolecules, Vol. 9, 2008, pp. 1299-1305.
[7] Tonin C, Aluigi A, Vineis C, Varesano A, Montarsolo A. and Ferrero F, "Thermal and structural characterization of poly(ethylene-oxide)/keratin blend films," J. Therm. Anal. Calorim., Vol. 89, 2007, pp. 601-608.
[8] Sun P, Liu ZT, Liu ZW, "Particles from bird feather a novel application of an ionic liquid and waste resource," J. Hazard Mater., Vol. 170, 2009, pp. 786-790.
[9] Wang Y-X, Cao X-J, "Extracting keratin from chickens by using a hydrophobic ionic liquid," Process Biochem., Vol. 47, 2012, pp. 896-899.
[10] Kweon HY, Um IC, Park YH, "Structural and thermal characteristics of *Antheraea pernyi* silk fibroin-chitosan blend film," Polymer, Vol. 42, 2001, pp. 6651-6656.

First International Conference on Science, Engineering & Environment,
Tsu City, Mie, Japan, Nov.19-21, 2015, ISBN: 978-4-9905958-5-2 C3051

THE EFFECT OF STARCH ON PROPERTY OF SILK FIBROIN/KERATIN BLEND FILMS

Yaowalak Srisuwan and Prasong Srihanam

Faculty of Science, Mahasarakham University, Maha Sarakham 44150, Thailand

ABSTRACT

This work aimed to study the effect of starch on silk fibroin (SF)/keratin (K) blend film properties. The SF and K solutions were mixed with starch, homogeneously stirred and poured into polystyrene culture plates. The mixture solution was then dried in an oven at 40 °C for three days. The films were then investigated for their morphology, secondary structure and thermal properties using a scanning electron microscope (SEM), Fourier transform-infrared (FT-IR) spectrophotometer and Thermogravimetric analysis (TGA). The results showed that each film had different surface patterns depending on the ratio used. Almost all the films co-existed with random coil and α-helix structures, which resulted in an increase in the flexibility of the film. The structure of the films changed to β-sheet after blending the SF and K according to the H-bond formation and increased the thermal stability of the films. This result indicated that starch helped to decrease the crystalline structure of the film, which increased their flexibility.

Keywords: Biopolymer, Morphology, Secondary structure, Thermal property

INTRODUCTION

Silk is a natural fibrous protein produced from silkworms that has a unique characteristic. It has been proven that silk fiber has several excellent biological properties, including high strength, biocompatibility, low inflammatory response and biodegradability [1]. Recently, silk has been of increasing interest for applications, especially biomedical and controlled drug release [2],[3]. The silk component, fibroin, has been reported as an important biomaterial that can be constructed in various forms [4]. In addition, silk fibroin has been blended with other materials to obtain novel materials, such as collagen [5], PLGA and alginate [6] or hyaluronan [7]. Keratin, a kind of high cystein content fibrous protein, has been applied in various fields, include tissue engineering [8]. Little information is available about silk fibroin/keratin blend materials. However, the structural proteins have some limiting properties with regard to their use, which are their fragility and low flexibility. Therefore, we chose starch, a polysaccharide with high polarity, for improving the properties of the silk fibroin (SF)/keratin (K) blend films. The properties of the blended films, such as morphology, secondary structure and thermal stability, were investigated.

METHODS

Preparation of Silk Fibroin Solution

SF solution was prepared by firstly boiling twice the cocoons of *Bombyx mori* in 0.5% (w/v) Na_2CO_3 solution at 90 °C for 30 min each time, and then washing with distilled water to obtain SF. The pure SF was then dissolved using a tertiary system of $CaCl_2$:ethanol:H_2O (1:2:8 by mol) at 70-75 °C for 60 min. The hydrolysate SF was dialyzed against distilled water with a dialysis membrane (MW cut off 10 kDa) for three days to exclude the salt. The concentration of the SF solution was adjusted to 1% (w/v) by distilled water.

Preparation of Keratin Solution

K was extracted from human hair that was collected from a hair salon in Maha Sarakham Province, Thailand. The hair was immersed in hexane solution for 12 h to remove some lipid components, and then air-dried at room temperature for one day. Then 1 g of dried hair was dissolved in 20 mL of a mixture solution of 0.02 M sodium hydroxide (NaOH), 0.5 M urea, 0.26 M sodium dodecyl sulfate and distilled water at 70 °C with stirring until the hair was completely dissolved. The solution was then dialyzed against distilled water for three days with a dialysis tube (MW. cutoff = 3,500 Da) to obtain the k solution. The k concentration was diluted to 2% w/v against distilled water before use.

Silk Fibroin/Keratin Blend Film Preparation

The SF/K blend films were prepared by mixing 1% wt. of SF solution and 1% wt. K solution at different ratios: 1:1, 1:3 and 3:1. The 21 mL of the mixture was then mixed with 0.25g starch. The solution was boiled to dissolve the starch before pouring onto the polystyrene plates. They were placed in an oven at 40 °C for three days to obtain the blend films. In addition, the native SF and K films were also prepared for comparisons of the film properties.

Characterization of Films

All films were cut and their morphology observed under a scanning electron microscope (SEM) (JEOL, JSM-6460LV, Tokyo, Japan). The samples were sputter coated with gold and placed on double sided carbon tape for enhancing surface conductivity. The secondary structures of the films were analyzed using FTIR spectroscopy (Perkin Elmer-Spectrum Gx, USA) in the spectral region of 4000-400 cm^{-1} at a 4 cm^{-1} spectral resolution and 32 scans. Thermal properties were also measured using a thermogravimetric analyzer (TGA), TA instruments, SDT Q600 (Luken's Drive, New Castle, DE). The films with weights of 8-10 mg were prepared and loaded in a platinum crucible. The samples were non-isothermal heated from 50°C to 1000 °C at a heating rate of 20 °C/min. The TGA was carried out in nitrogen with a flow rate of 100 mL/min. The TG and heat flow were recorded with TA Instrument's Q series explorer software. The analyses of the data were done using TA Instrument's Universal Analysis 2000 software (version 3.3B).

RESULTS AND DISCUSSION

Morphology of Films

Native SF film had slightly rough surfaces with a homogeneous texture observed in the cross-section (Fig. 1a); as did the native K film (Fig. 1b). The surfaces of the blended films were rougher than the native films and particle like-beads covered the film surfaces and textures (1:3 ratios, Fig. 1e). It was also found that the surfaces and texture of the blend films depended on the ratios of SF/K used. The most compatible film textures and surfaces were in the blend ratio at 1:1 (Fig. 1d) compared to the other ratios (Fig. 1c and 1e).

The morphology of the film was affected by the chemical composition of each material [9]. SF is mainly composed of similar monomers that resulted in a smooth surface and homogeneous texture. K is mainly composed of many different protein sizes that resulted in the rough surface of the film. In case of the blend films, unequal ratios caused particles of starch granules to appear in the film. This suggested that there might be more starch molecules than the ratio needed to interact with the SF and K molecules.

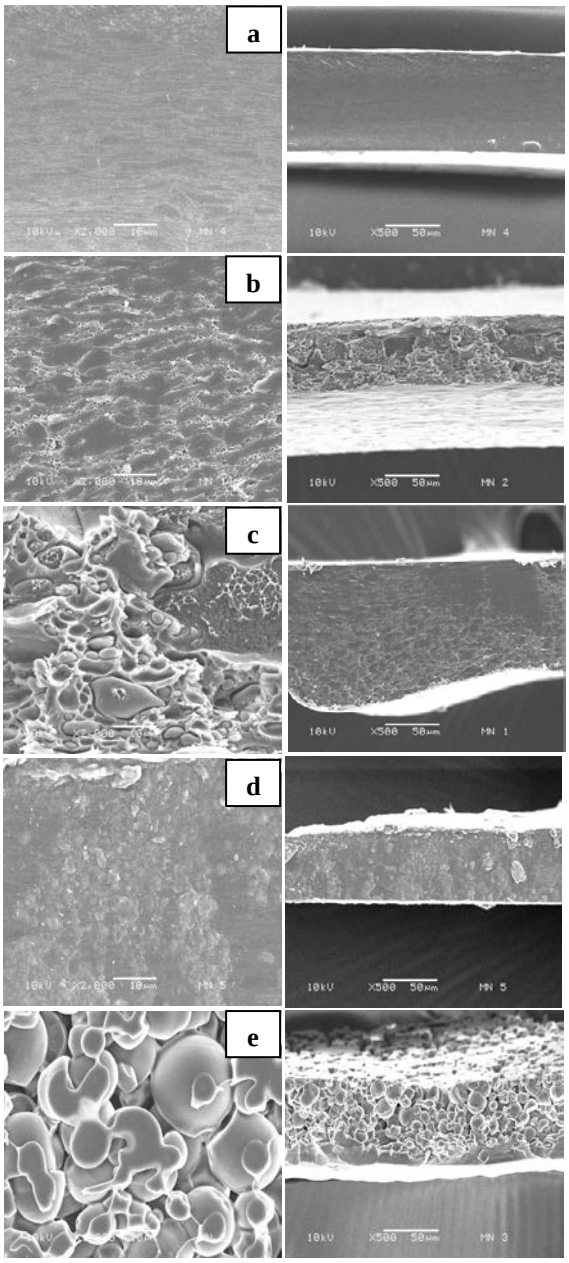

Fig. 1 SEM micrographs of various films: native silk fibroin (d), keratin (b) and silk fibroin/keratin blend in different ratios of 3:1 (c), 1:1 (d) and 1:3 (e) with 0.25g starch added. Left presented as surface and right as cross-section. (All bars = 50μm)

Secondary Structure of Films

Figure 2 shows the FTIR spectra of the various types of films. In general, the films had varied absorption peaks. The native SF film showed absorption peaks at 1660, 1548 and 1249 cm^{-1}, whereas the native keratin film had absorption peaks at 1652, 1547 and 1242. The absorption peaks of the blend films showed different patterns according to the blend ratios. At the SF/K ratio of 1:3, the absorption peaks were found at 1659, 1525 and 1249 cm^{-1}. The 1:1 ratio had absorption peaks at 1649, 1525 and 1312cm^{-1}. At the SF/K ratio of 3:1, the absorption peaks were at 1691, 1526 and 1228 cm^{-1}.

The results indicated that SF/K blended with starch had increased the strength of the films. This was observed from the absorption peaks at amide II (1525 cm^{-1}), which dominantly appeared after mixing with starch. This peak was designated as a β-sheet structure [10]. Moreover, the absorption peaks at about 100-900 cm^{-1} also appeared. These peaks were the response of the saccharide structure [11].

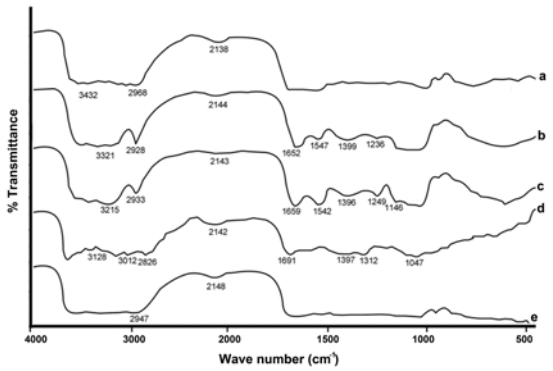

Fig. 2 FTIR spectra of various films: native silk fibroin (a), native keratin (e) and SF/K blend in the ratios of 1:3 (b), 1:1 (c) and 3:1 (d) with 0.25g starch added.

Thermal stability

The thermal stability of the films was illustrated by TG curves (Fig. 3). Generally, the films started to decompose at about 100 °C, which was the water evaporation temperature. The main decomposition temperatures of all the films were higher than 300 °C, which was clearly indicated by the DTG curves (Fig. 4). The maximum temperature of decomposition ($T_{d,max}$) peaks are summarized in Table 1. The native SF had a $T_{d,max}$ at 310 °C, while the native K had a $T_{d,max}$ at 309 °C. Among the blend ratios, SF/K at 1:3 had the highest $T_{d,max}$ of 315 °C, while the ratios of 3:1 and 1:1 had similar $T_{d,max}$ vales at 311 °C.

The increases in the $T_{d,max}$ could be a result of the interaction via H-bonds between the hydroxyl groups of the starch and amino or carboxylic groups of the protein [12].

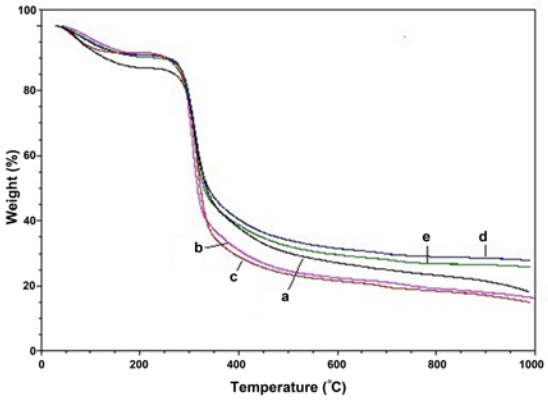

Fig. 3 TG curves of various films: native silk fibroin (a), native keratin (b) and SF/K blend in the ratios of 1:3 (c), 3:1 (d) and 1:1 (e) with 0.25g starch added.

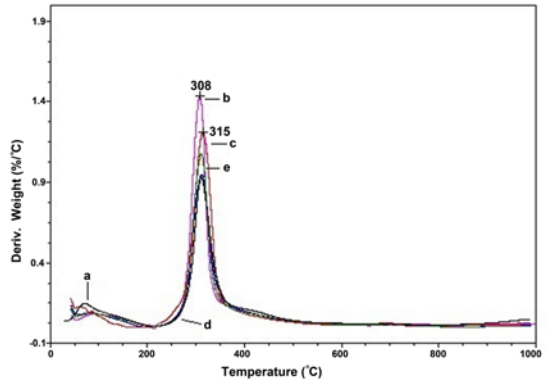

Fig.4 DTG of various films: native silk fibroin (a), native keratin (b) and SF/K blend in the ratios of 1:3 (c), 3:1 (d) and 1:1 (e) with 0.25g starch added.

Table 1 $T_{d,max}$ of several films.

Film type	$T_{d,max}$ (°C)
Silk Fibroin (SF)	310
Keratin (K)	308
SF:K (1:3)	315
SF:K (3:1)	311
SF:K (1:1)	311

CONCLUSION

Starch helped to increase the flexibility of the SF/K blend films as it caused a change in the secondary structure of the films from β-sheet into random coil. The surfaces and texture of the SF/K blend films varied due to the blending ratios and were composed of particles within the cross sections of the films that also increased the surface roughness. The blended film at a 3:1 ratio had the highest stability after mixing with starch. The different properties of the SF/K blend films should enable the preparation of novel materials for medical and pharmaceutical applications.

ACKNOWLEDGEMENTS

The authors would like to thank the Faculty of Science, Mahasarakham University, Thailand for financial support of this presentation.

REFERENCES

[1] Altman GH, Diaz F, Jakuba C, Calabro T, Horan RL, Chen J, Lu H, Richmond J, Kaplan DL, "Silk-based biomaterials," Biomaterials, Vol. 24, 2003, pp. 401-416.

[2] Chen J, Minoura,N, "Transport of pharmaceuticals through silk fibroin membrane," Polymer, Vol. 35, 1994, pp. 2853-2856.

[3] Hofmann S, Wong Po Foo CT, Rossetti F, Textor M, Vunjak-Novakovic, G, Kaplan DL, Merkle HP, Meinel L, "Silk fibroin as an organic polymer for controlled drug delivery," J. Control Release, Vol. 111, 2006, pp. 219-227.

[4] Zhou J, Cao C, Ma X, Hu L, Chen L, Wang C, "In Vitro and in vivo degradation behavior of aqueous-derived electrospun silk fibroin scaffolds," Polym. Degrad. Stab., Vol. 95, 2010, pp. 1679-1685.

[5] Zhou J, Cao C, Ma X, Lin J, "Electrospinning of silk fibroin and collagen for vascular tissue engineering," Int. J. Biol. Macromol., Vol. 47, 2010, pp. 514-519.

[6] Wang X, Wenk E, Castro GR, Meinel L, Wang X, Li C, Merkle H, Kaplan, DL, "Silk coatings on PLGA and alginate microspheres for protein delivery," Biomaterials, Vol. 28, 2007, pp. 4161-4169.

[7] Garcia-Fuentes M, Meinel AJ, Hilbe M, Meinel, L, Merkle HP, "Silk fibroin/hyaluronan scaffolds for human mesenchymal stem cell culture in tissue engineering," Biomaterials, Vol. 30, 2009, pp. 5068-5076.

[8] Reichi S, "Films based on human hair keratin as substrates for cell culture and tissue engineering," Biomaterials, Vol. 30, 2009, pp. 6854-6866.

[9] Teresa K-K, Justyna B, "Biodegradation of keratin waste: Theory and practical aspects. Waste Manage., Vol. 31, 2011, pp. 1689-1701.

[10] Wang Y-X, Cao X-J, "Extracting keratin from chickens by using a hydrophobic ionic liquid," Process Biochem., Vol. 47, 2012, pp. 896-899.

[11] She Z, Jin C, Huang Z, Zhang B, Feng Q, Xu Y, "Silk fibroin/chitosan scaffold: Preparation, characterization and culture with HepG2 cell," J. Mater. Sci. Mater. M., Vol. 19, 2008, pp. 3545-3553.

[12] Srihanam P, "Silk fibroin/chitosan blend films loaded methylene blue as a model for polar molecular releasing: Comparison between Thai silk varieties," J. Appl. Sci., Vol. 11, 2011, pp. 2592-2598.

First International Conference on Science, Engineering & Environment,
Tsu City, Mie, Japan, Nov.19-21, 2015, ISBN: 978-4-9905958-5-2 C3051

AN ALGEBRAIC AND COMBINATORIAL APPROACH TO THE CONSTRUCTION OF EXPERIMENTAL DESIGNS

Julio Romero[1] and Scott H. Murray[2]
[1]Department of Information Sciences and Engineering, University of Canberra, Australia;
[2]Department of Mathematics and Statistics, University of Canberra, Australia.

ABSTRACT

Experimental design is a well-known and broadly applied area of statistics. The expansion of this field to the areas of industrial processes and engineered systems has meant interest in an optimal set of experimental tests. This is achieved through the use of combinatorial and algebraic approaches. As such, the present study states the theoretical basis to construct and enumerate experimental designs using non-isomorphic mathematical structures in the form of matrix arrangements called orthogonal arrays (OAs). These entities are characterized by their number of rows, columns, entries (symbols), and strength. Thus, each different column could represent some measurable feature of interest (temperature, pressure, speed). The runs, expressed through OA rows, define the number of different combinations of a particular design. Similarly, the symbols allocated in OAs' entries could be the distinct levels of the phenomenon under study. During the OA construction process, we used group theory to deal with permutation groups, and combinatorics to create the actual OAs following a particular design. The enumeration process involved the use of algebraic-based algorithms to list all possible combinations of arrays according to their isomorphic equivalent. To test isomorphism, we used graph theory to convert the arrays into their corresponding canonical graph.

The outcomes for this study are, firstly, a powerful computational technique to construct OAs from 8 to 80 runs; and secondly, additions in the published list of orbit sizes and number of non-isomorphic arrays given in [1] for 64, 72, and 80 runs.

Keywords: Orthogonal arrays, Combinatorics, Experimental design, Engineered systems.

INTRODUCTION

The engineering or scientific method is the approach of solving problems through the efficient application of scientific principles based upon a well-structured theoretical knowledge [2]. In applying the aforementioned approach, engineers undertake experiments or tests as an intrinsic and natural part of their jobs. As such, sound statistical-based experimental designs are extraordinarily useful within the engineering profession aiming to improve process and systems characterized by suitable engineering specifications. These specifications are described as several "controllable" variables associated with the overall system/process performance. Therefore, knowing the main factors and their interactions, the engineer is able to analyze, for instance, process yield, process variability, development time, and operational costs [3], [4].

Latest implications in using experimental tests are related with *engineering parameter design*. Within this discipline, it is possible not only to develop new products/processes, but also to enhance the existing ones. To cite some examples in parameter design, we have the evaluation and comparison of basic design configurations; the appraisal of different alloys in strength of materials; the selection of design parameters to make the product / process to work within a specified tolerance range under a wide variety of field conditions (we say the design is being robust); and the determination of the key factor combinations affecting a particular product performance.

Besides their flexibility of being easily implemented in engineering design [2], our arrays are mathematically made so we can perform their combinatorial "enumeration". This last idea is the one presented in this paper. Our interests in following a purely mathematical point of view in dealing with experimental designs are, firstly, the development of algorithms which actually calculate the objects we are defining theoretically; secondly, to answer concrete questions in group theory to explore more of it; and thirdly, to deal with complexity theory such as to able to answer the problem whether two graphs, given by their adjacency matrix, are in fact, isomorphic [5].

We initially present the main concepts of group theory which underlie the algorithms used to construct the arrays. We move further with the tools provided by the theory of graphs, to map an array into its equivalent canonical graph to be able to

indirectly assess isomorphism between the arrays. We then present a pseudo code to implement a backtrack search algorithm to look through the different *orbits* which conform the *orbit space* of a particular array of design type *t*.

COMBINATORIAL SETTING

Orthogonal arrays (OAs) are related to combinatorics, finite fields, geometry, and error correcting codes. Fig. 1 shows an example of an OA of strength two (transposed).

$$F^T = \begin{vmatrix} 0 & 0 & 1 & 1 & 2 & 2 & 0 & 0 & 1 & 1 & 2 & 2 \\ 0 & 1 & 0 & 1 & 0 & 1 & 0 & 1 & 0 & 1 & 0 & 1 \\ 0 & 0 & 0 & 1 & 1 & 1 & 1 & 1 & 1 & 0 & 0 & 0 \end{vmatrix}$$

Fig. 1 Strength two OA (transposed)

Each of the four possible rows does appear in the array, and they appear the same number of times (picked them in groups of $t = 2$ columns). This is the fundamental property that defines an OA [6]. In the previous example, only three *symbols* appeared, 0, 1, and 2. Thus, we say the array has 3 *levels*. Note that each level may represent a particular combination of physical properties: fuel with additive or not, 20°C or 80°C, machine running or stopped, and so forth. Following the same example, we have 3 columns each representing a variable under study (additive, temperature, machine's condition). In a similar way, our array F has 12 rows or *runs*, each representing a particular combination of the different variable levels. Mathematically, we represent an OA of strength t, s levels, N runs, and a variables as: $OA(N, S_i^{a_j}, t)$. For our particular array F, we have $OA(12, 3^1 2^2, 2)$ or equivalently, a design type $U(3^1, 2^2)$ [6], [7].

A strength-*t* OA assures that all possible combinations of the levels in a variable of up to *t* occur together equally often [6]. Thus, the strength of the array defines the *effects of each individual variable* (factor) that can be taken in consideration when assessing the design [6], [8]. Also, according to the strength *t* required, we will be able to calculate some *interactions* between factors as well. Such experiments are called *fractional factorial designs* [7]. Our particular interest is in OAs of strength 3, which can model all main factors in a particular phenomenon under study and up to two interactions between the factors.

MATHEMATICAL BACKGROUND

This section shows how we performed the construction and enumeration of strength three orthogonal arrays. We initially explain the mathematical approach used for the permutation computational implementation.

We applied group theory to define the full group of factor transformations and the corresponding automorphism group. Furthermore, we used graph theory to represent the orthogonal array as a colored graph. This approach allowed us to define a canonical representative of an orbit of OAs using the canonical graph [9]. This leads to improve the computational time and memory usage for the calculations. We also implemented the backtrack search and the lexicographical least run algorithms to find the arrays and as a decision criteria to drop a leaf [1], [10].

Algebraic Setting

Consider F_{ND} as the set of all elements of the form:

$$F_{ND} = \{F: F \text{ is a } N \times d \text{ matrix}, F_{ij} \in S_j\} \quad (1)$$

called the set of all *fractional factorial designs* (*FFDs*). We define the *groups* G_ρ, G_γ, and G_σ, acting on F_{ND} as $G_\rho = Sym(N)$, the group of all permutations acting on rows; $G_\gamma = Sym(D)$, the group of permutations acting on columns; and $G_\sigma = Sym(S)$, the permutation group acting on symbols. Thus, $\rho \epsilon G_\rho$ defines an action:

$$(F_{i,j}) \rightarrow F_{ND}^{\rho} = (F_{\rho i,j}) \quad (2)$$

similarly, $\gamma \in G_\gamma$ defines an action:

$$\gamma \in \prod_k Sym(J_k) \subseteq Sym(D) \rightarrow F_{ND}^{\gamma} = (F_{i,\gamma j}) \quad (3)$$

and $\sigma \in G_\sigma$ defines an action:

$$\sigma = (\sigma_1, \dots, \sigma) \in \prod_k Sym(J_k) \subseteq Sym(S) \rightarrow F_{ND}^{\sigma} = \left(F_{i,j}^{\sigma_j}\right) \quad (4)$$

Definition 1. Consider the set F_{ND} of $N \times d$ arrays, and G the group of permutations. We define the *action* of the group G on the set F_{ND} as a map $\phi: G \times F_{ND} \rightarrow F_{ND}$ such that:

- $F_e = F, \forall F \in F_{ND}$; e, identity element.
- $(F)(g_1 g_2) = (F g_1) g_2 \; \forall \; g_1, g_2 \in G$.

Corollary 2. Let the map $\emptyset$ define a group homomorphism such that $\emptyset: G_1 \rightarrow G_2$ where G_1 and G_2 are both permutation groups. Then $\emptyset$ is a one-to-one map if and only if $ker(\emptyset) = e$

Proof. Assume the map $\emptyset$ is one-to-one. It holds that $\emptyset(e) = e_2$, the identity element of G_2. Thus, e is the only mapped element into e_2 by $\emptyset$, so $ker(\emptyset) = e$.

Assume now that $ker(\emptyset) = e$. For all $g \in G$ the element mapped into $\emptyset(g)$ are the elements of the right coset $\{eg\} = \{g\}$ showing that $\emptyset$ is one-to-one.

Definition 3. We have the following mappings:

$$\emptyset_\rho : \mathrm{Sym(N)} \rightarrow \mathrm{Sym}(F_{ND}) \quad (5)$$

$$\emptyset_\gamma : \prod_k Sym(J_k) \rightarrow Sym(F_{ND}) \quad (6)$$

$$\emptyset_\sigma : \prod\nolimits_k \mathrm{Sym}(S_j) \rightarrow \mathrm{Sym}(F_{ND}) \quad (7)$$

It follows from definitions 1 and 3,

$$\mathrm{Im}\emptyset_\rho, \mathrm{Im}\emptyset_\gamma, \mathrm{Im}\emptyset_\sigma \leq \mathrm{Sym}(F_{ND}) \quad (8)$$

$$G = < Im\emptyset_\rho, \mathrm{Im}\emptyset_\gamma, \mathrm{Im}\emptyset_\sigma > \quad (9)$$

$$G = G_\rho \times G_\sigma \rtimes G_\gamma \quad (10)$$

where $G_\sigma \rtimes G_\gamma = \prod_{k=1}^{m} \mathrm{Sym}(S_{j,k}) \wr \mathrm{Sym}(J_k)$ or equivalently,

$$G = \emptyset_\rho(\rho) \cdot \emptyset_\sigma(\sigma) \cdot \emptyset_\gamma(\gamma) \leq \mathrm{Sym}(F_{ND}) \quad (11)$$

Definition 4. Let G be a group of permutations acting on a non-empty set F_{ND}; we define the *orbit* of G containing F to the equivalence class given by:

$$\mathrm{Orb_G(F)} = \{Fg \mid g \in G\} \quad (12)$$

we define the *orbit space* as the family of all equivalence classes obtained from G acting on an element F of the set F_{ND}. Let F and T both elements of F_{ND}. We say they are *isomorphic* if there exists a permutation $g \in G$ such that $F = Tg$. The previous expression can also be written as $F = T^g$.

Suppose now that a group G acts on a set F_{ND}; then, for each element $F \in F_{ND}$, we redefine the equivalence class (orbit) containing F as:

$$O_G(F) = \{F^g \mid g \in G\} \quad (14)$$

Lemma 5. Suppose that a group G acts on a set F_{ND}; then, for each $F \in F_{ND}$,

$$|G| = |\mathrm{stab(F)}||O_g(F)| \quad (15)$$

Proof. Suppose that g_1 and g_2 are in the right coset of stab(F) and $g_1 = \pi g_2$ for some $\pi \in \mathrm{stab(F)}$. Thus, $Fg_1 = (F)(\pi g_2) = (F\pi)g_2$. On the other hand, suppose that $Fg_1 = Fg_2$, then $F = Fg_2g_1^{-1}$ implying that $g_2g_1^{-1} \in \mathrm{stab(F)}$; therefore g_1 and g_2 belong to the same right coset of stab(F) if and only if $Fg_1 = Fg_2$. It follows that there is a bijection between the elements in $\mathrm{Orb_G(F)}$ and the right cosets of stab(F), thus

$$|G| = |\mathrm{stab(F)}||\#\text{of right cosets of stab(F)}| = |G| = |\mathrm{stab(F)}||O_g(F)|$$

and the result follows.

Theorem 6. (Burnside's Theorem) Suppose the group G acting on a set F_{ND}; then, the number of orbits in F_{ND}; is given by

$$1/|G| \sum_{F \in F_{ND}} |\mathrm{stab(F)}| \quad (16)$$

Proof. Using lemma 5, we have:

$$1/|G| \sum_{F \in F_{ND}} |\mathrm{stab(F)}| = \sum_{F \in F_{ND}} 1/|O_g(F)| \quad (17)$$

suppose there are O_S orbits in F_{ND}, and F in the orbit O_g; then, $\sum_{F \in F_{ND}} 1/|O_g(F)| = O_S$.

Definition 7. Let G be the group of all row, column, and symbols permutations, and $F \in F_{ND}$. The set of all isomorphisms from F to F is called the *automorphism group* of F and is denoted by Aut(F) The elements of Aut(F) are called *automorphisms of* F.

Using our previous results from Eqs. (15), (16) and (17); the *length* of the G-Orbit of G is the number of distinct objects isomorphic to it. Thus,

$$|\mathrm{Orb_G(F)}| = \frac{|G|}{|\mathrm{Aut(F)}|} \quad (18)$$

ENUMERATION USING GRAPH THEORY

In the previous section, we explained how we mathematically set up the conditions for the construction and enumeration of strength *t* orthogonal arrays. In this section, we formally explain their construction and how we perform the enumeration by mapping the OAs as canonical graphs.

Mapping an OA to its equivalent canonical graph

Let F_{ND} the set of fractional factorial designs with $F \in F_{ND}$. Let F_{ij} be a particular entry in the array F, where i: i^{th} row and j: j^{th} column. We define S_ρ the set of all N-tuples which represent the different rows of the array F. Then, $S_\rho = \{\rho_1, \ldots, \rho_N\}$ and $F_{ij} \in S$; where S is the set containing

the different possible symbols for a particular design *U*.

Definition 8. A *colored graph* is a triple $F_G = (V, E, \Gamma)$, where V is the set of the different vertices, v, of the graph; E is the set of edges, and Γ a map from V to a set of colors C.

Definition 9. We define the *neighbor* of a vertex $v_x \in V$ as $\eta(v_x) = \{v_y \in V \mid \{v_x, v_y\} \in E\}$. An isomorphism $F_G \to F'_G = (V, E, \Gamma)$ is a bijection $\eta: V \to V'$ such that:
$\{v_x, v_y\} \in E \leftrightarrow \{\eta(v_x), \eta(v_y)\} \in E'$ and $\Gamma(v_x) = \Gamma(v_y) \leftrightarrow \Gamma'^{(\eta(v_x))} = \Gamma'^{(\eta(v_{xy}))} \forall\ v_x, v_x \in V$.

Proposition 10. Let $F \in F_{ND}$. We construct a colored graph $F_G = (V, E, \Gamma)$ for the array F as follows:

a) The set of the vertices V, is made on the elements $\rho_i, i: 1,2, \dots, N$; $\gamma_j, j: 1,2, \dots, d$ and $\sigma_{jx}, j: 1, \dots d; x \in S$; corresponding to the rows, columns, and the distinct levels of the array.
b) The set of the edges, E, made on all of the $E_1 = \{\rho_i, \sigma_{jF_{ij}}\}$ and $E_2 = \{\gamma_j, \sigma_{jF_{ij}}\}$ $\forall\ i: 1, \dots, N$ and $j: 1, \dots, d$.
c) The set of the edges, E, made on all of the vertices ρ_i with color C_ρ; all of the vertices γ with color C_γ; and all of the vertices σ_{jx} with color C_{σ_x}.

Thus, F_G has three partitions: rows, columns, and levels. Mathematically, we express this as $V = C_\rho \cup C_\gamma \cup C_{\sigma x}$. Similarly, we write the set of the edges as $E = E_1 \cup E_2 \subseteq (C_\rho \times C_\gamma) \cup (C_{\sigma x} \times C_\gamma)$. It follows that the cardinalities $|V|$ and $|E|$ are given by

$$|V| = N + \sum_I^d k_i + d \tag{19}$$

$$|E| = dN + \sum_I^d k_i \tag{20}$$

To characterize the graph of an OA, we define the *column-color classes* to the disjoint union of color classes C_ρ, C_γ, and $C_{\sigma x}$. The total number of colors of F_G is $2 + m$ and each row-vertex is adjacent to sv symbol-vertices. Moreover, each symbol-vertex is adjacent to exactly one column-vertex, where $sv = \sum_{i=1}^m |C_i|$

Lemma 11. Let S_{FG} the set of all coloured graphs, and the map ∅ defined as $\emptyset: F_{ND} \to S_{FG}$ that takes an array $F \in F_{ND}$ to the corresponding colored graph $F_G \in S_{FG}$; thus, ∅ is an injection.

Proof. The number of vertices of F_G does not depend upon F but only on the design type U and the run size N.

To determine row, symbol, and column vertices, we have the following color partition proposition:

Proposition 12. Let $F \in F_{ND}$ of strength $t \geq 1$ and run-size N. Thus,

a) F_G has a tripartite partition $(C_\rho, C_\gamma, C_{\sigma x})$ with $|C_\rho| = N$, $|C_\gamma| = \sum_{k=1}^m a_k$, and $|C_{\sigma x}| = \sum_{k=1}^m a_k S_k$.
b) Every vertex $v \in V$ has a valence ν denoted by $\nu = V(v)$
c) For the column-vertex set $C_{\sigma x}$, we denote the valency for $c_{\sigma x} \in C_{\sigma x}$ as ν_x, where ν_x is the unique element $\{1, \dots, m\}$.
d) Let $s \in S$, the set of different symbols (levels). Then $\exists\ c_{\sigma x} \in C_{\sigma x}$ such that $\{s, c_{\sigma x}\} \in E$, the set of edges for some k in $\{1, \dots, m\}$.
e) From d), it follows that the valence of a symbol-vertex is given by

$$\nu(v) = \frac{N}{\nu(c_{\sigma x})} + 1 = \frac{N}{\nu_x} + 1 \tag{21}$$

f) Let $\rho \in C_\rho$ and $\gamma \in C_\gamma$; thus, there exists a path of length two from ρ to γ through a vertex in V, and this path is unique.

Definition 13. Let an orthogonal array be of design type U and run size N. Consider also a colored graph which satisfies all of the points given in 12 above. Thus, we call the colored graph as being of the type (U; N), which forms a sub-set of F_G.

Lemma 14. Let F_2 and $F_2 \in F_{ND}$ OAs with designs type *U* and *N*. Let also F_{G1}; $F_{G2} \in S_{FG}$ be their corresponding graphical representations. Thus, F_1 and F_2 are isomorphic arrays if and only if F_{G1} and F_{G2} are isomorphic graphs.

Proof. Suppose F_1 and F_2 are isomorphic arrays $\in F_{ND}$; then $F_1 = F_2^g$; $g \in G$. Because $g \in G$, it follows that g is a product of g_ρ, g_γ, and g_σ permutations; and from c) in proposition (10), we have $F_{G1} = \emptyset(F_1^g) = \emptyset(F_2) = F_{G2}$. Therefore, F_{G1} and F_{G2} are isomorphic graphs. Suppose now that F_{G1} and F_{G2} are isomorphic graphs; thus, $\exists\ g \in G$ such that $F_{G1} = F_{G_2}^g$. Because F_{G1} and F_{G2} satisfy all of the points given in proposition (10), they are tripartite and the permutation g preserves the graph coloring. Therefore, g can be written as the product of g_ρ, g_γ, and g_σ permutations acting on F_1 and the composed map takes F_1 to F_2.

Example. Assume we have an orthogonal array with design type $U(3^1, 2^2)$ and run size $N = 6$ (a fraction of the array shown in Fig. 1); then, the set of

vertices is made up on the elements ρ_i, $i \in \{1,\dots,6\}$; and γ_j, $j \in \{1,\dots,7\}$; and σ_{jx}, $j \in \{1,2,3\}$, $x \in \{1,2\}$ (see proposition (10)). We assign one color to the set of rows C_ρ; one color to the partition $C_{\gamma 1} \subseteq C_\gamma$ corresponding to the level 3; one color to the second partition $C_{\gamma 2} \subseteq C_\gamma$ corresponding to the two levels of the two columns with the same symbol level (0,1); and one color for the set of symbols $C_{\sigma x}$. We have in total $|V| = 6 + \sum_i^3 r_i + 3 = 16$ vertices, and $|E| = 2 \times 6 + 7$ edges. The colored graph of this array is shown in Fig. 2.

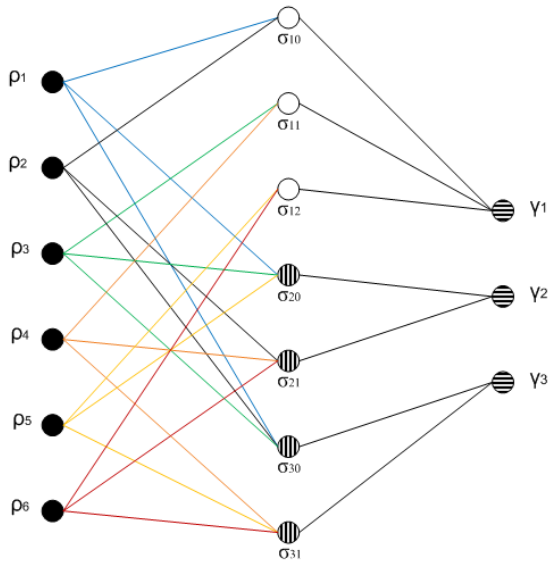

Fig. 2 Canonical graph of the orthogonal array F.

Algorithm Description

The construction process requires an existing orthogonal array with design type U made using simple combinatorial techniques. We then start adding the different symbols according to the specified design. By adding symbols, we create a new column to the existing array until the new required OA is completed.

During the process of adding symbols, our algorithms check that the conditions of strength t and sequence's lexicographical order are being met; otherwise, the entire OA is discarded. The aforementioned process is carried out using *the backtrack* search algorithm [11].

In addition to the previous criteria, we use our permutation group G with the operations g_ρ, g_γ and g_ρ to prune the tree when we find isomorphic graphs downstream of the search tree (this stage help us to save important computational time and memory-usage resources). Furthermore, the recently made array is then mapped to its equivalent canonical graph in order to be compared against the orbit-representative one. If it turns out that the two graphs are isomorphic, the newest array is counted as part of the orbit-representative array and discarded. However, if the graphs are not isomorphic, the newest array is stored and classified as part of the orbit representatives for the particular design U.

The backtrack search algorithm

Mathematically, we consider the idea of finding a $FFd \in F_{ND}$ with a design type U. This design specifies, among other parameters, the strength t of the array, which is the main criterion looked in the search tree to drop a leaf.

Definition 15. We define a *partial image* to the set of distinct entries in a row by $S_{eq\rho} = [F_{i1}, \dots, F_{ir}]$, $0 \le r \le m$. When $r = m$, we call the sequence $S_{eq\rho}$ as *complete*.

The Backtrack Search Algorithm

Algorithm 1.

Input: Design type, U; run size, N; basis design, F, row position index, Λ; an orbit representative, Δ_F

Output: The automorphism size and number.

```
1: Λ := 0; NE := [ ]; extensions := [ ]; Δ := [ ];
2:
   function FillingRows(U,N,V,F,Λ,Δ_F)
3:
      if Λ := (N + 1) then;
4:
         if ∃{< α, β >: α ∈ F, β ∈ Δ| CheckIso(α, β)} then
5:       append(Δ_F, F);
6:
         end if
7:       return Δ, F;
8:
      end if
9:    F[Λ] := F[Λ] + NE;
10:
      if IsStrengtht(F, Δ, U) then
11:     F_NEW, Δ := FillingRows(U, N, V, F, Λ + 1, Δ_F);
12:     extensions := extensions + F_NEW;
13:
      end if
14:   F[Λ, #U] := 1;
15:
      if IsStrenght thenF, Λ, U
16:     F_NEW, Δ := FillingRows(U, N, V, F, Λ + 1, Δ_F);
17:     extensions := extensions + F_NEW;
18:
      end if
19:   Λ := Λ + 1;
20:   return extensions, Δ;
21:
   end function
end
```

Fig. 3 Backtrack Search Algorithm.

According to definition 15, the backtrack search goes through the partial images given by the sequence $S_{eq\rho}$. Within this search, it will use any knowledge of the design to prune the search tree. Note that in constructing a new design we totally

order the sequences $S_{eq\rho}$ so that we induce a *lexicographical order* for the set of partial images. This means that only the first point of each k-orbit has to be considered when extending $S_{eq\rho}$.

Figure 3 shows the algorithm we use to traverse a tree created to search orbits and their representatives. The search will go through some of the elements of the permutation group while skipping some leaves according to the previously discussed criteria.

Isomorphism Classes Enumeration Results

In Table 1, we show some examples of results obtained by Man [1] which were corroborated with our approach. In addition, we introduce new isomorphism classes enumerated using the technique presented in this paper.

The first column of the table represents the run size N for the different designs. The second column corresponds to the actual design type U according to the multiplicity notation for automorphism group orders. The third and fourth columns of the table are the *number* of the automorphism groups and their corresponding *size* respectively. We have indicated with an asterisk the newest designs we have found.

Table 1 Non-isomorphic OAs of strength three

N	Type	#	Size
64	4^5	1	144^1
64	$4^4\,2^1$	3	256^1, 512^1, 1536^1
64	$4^1\,2^5$	12692	
64	$4^1\,2^6$	$\geq 7865^*$	
64	$4^1\,2^7$	$\geq 10661^*$	
64	$4^1\,2^8$	≥ 1189	
72	$6^1\,2^4$	156	256^{36}, 512^{72}, 3072^{32}, 4096^{12}, 110592^4
72	$6^1\,2^5$	64296	
72	$6^1\,2^6$	$\geq 36550^*$	
72	$6^1\,2^7$	$\geq 54834^*$	
80	$4^1\,2^3$	17	
80	$4^1\,2^4$	303	
80	$4^1\,2^5$	$\geq 18653^*$	
80	$4^1\,2^6$	$\geq 15283^*$	

Note: new arrays indicated with an asterisk *.

CONCLUSION

We have presented a mathematical and computational method for constructing and enumerating strength-t orthogonal arrays given a fixed number of experiments. The technique shown provided a feasible generic framework and has been validated through both, the comparison of designs already listed by several different techniques, and the discovery of some new mixed OAs.

ACKNOWLEDGEMENTS

My deepest gratitude to Dr Scott H. Murray for his continuous support throughout the development of this project. Many thanks also to Dr Judith Ascione for her very useful assistance during the early stages of preparing this manuscript.

REFERENCES

[1] Nguyen M, “Computer-algebraic methods for the construction of designs of experiments”. Technische Universiteit. Eindhoven, Eindhoven University Press, 2005.
[2] Blanchard BS and Fabrycky WWJ, “Systems engineering and analysis”, Prentice-Hall international series in industrial and systems engineering, 2011.
[3] Ross PJ, “Taguchi techniques for quality engineering”, McGraw-Hill Education (India), Pvt Limited, 2005.
[4] Tsai JT, “Robust optimal-parameter design approach for tolerance design problems”, Engineering Optimization, 42(12):1079 - 1093, 2010.
[5] Dummit DS and Foote RM, “Abstract Algebra”, Wiley, 2003.
[6] Hedayat AS, Sloane NJA, and Stufken J, “Orthogonal arrays: theory and applications”, Springer series in statistics, Springer-Verlag, 1999.
[7] Montgomery DC, “Design and Analysis of Experiments”, Wiley, 2012.
[8] Lekivetz R and Tang B, “Multi-level orthogonal arrays for estimating main effects and specified interactions”, Journal of Statistical Planning and Inference, 2012.
[9] David G and David B, “Graphs for orthogonal arrays and projective planes of even order”, SIAM Journal on Discrete Mathematics, 26(3):1076-1087, 2012.
[10] Schoen ED and Nguyen M, “Enumeration and classification of orthogonal arrays”. Journal of Algebraic Statistics, 2007.
[11] Hulpke A, “Notes on Computational Group Theory”, Department of Mathematics, Colorado State University, 2010.

First International Conference on Science, Engineering & Environment,
Tsu City, Mie, Japan, Nov.19-21, 2015, ISBN: 978-4-9905958-5-2 C3051

MODEL DEVELOPMENT FOR OUTBREAK OF DENGUE FEVER SURVEILLANCE SYSTEM IN DISTRICT LEVEL

Pongmada Damapong[1], Peerada Damapong[2], Supat Jumparwai[3]
[1,2]College of Allied Health Science, Suan Sunandha Rajabhat University, Thailand
[3]Sirindhorn College of Public Health, Khon Kaen, Thailand

ABSTRACT

There is reportedly confirmed that the number of epidemics of dengue fever has increased. Use of health surveillance system on epidemic of dengue fever at the district level is restricted. A study to develop a suitable Model for Outbreak of Dengue Fever Surveillance System (MODFSS) in district level. The 60 participants, including 3 government officers leaders, 10 local leaders, 3 specialists, and 44 village health volunteer of participating in the development of the model. The present study utilized three sets of a database, reported on a monthly basis. These included dengue fever cases, notification in advance of the mosquito breeding sources, problems and obstacles of the related organization and epidemic of dengue fever by the local community leaders. The five approaches to develop of the MODFSS included situational analysis, prototype system design, system test, system improvement and model dissemination. This study was conducted in 10 communities. The MODFSS model application was created at the district level. The model evaluated and monitored epidemic of dengue fever practices of prevention and control actions in communities. The five important constituents of the MODFSS were 1) organizations of epidemiology networks, 2) indicators of epidemic, 3) data collection tools, 4) data analysis and 5) dissemination of information. The MODFSS consisted of six core activities (detection, registration, confirmation, reporting, analysis and suggestion) and four support activities (communication through meeting and brainstorming, training, supervision and resource-provision). The developed MODFSS is an effective of health surveillance suitable for district level.

Keywords: Model Development, Outbreak, Surveillance System, Dengue Fever

INTRODUCTION

There is reportedly confirmed that the number of epidemics of dengue fever has increased, especially in tropical and subtropical regions distributed globally. Dengue fever(DF) is an acute infectious disease the mosquito Aedes aegypti-borne is responsible for transmitting the dengue virus (DENV) between human [1]. In Thailand, with a population of over 65.12 millions in 2014[2] was around 39,569 cases of dengue fever and morbidity rate was 61.75 for dengue fever per 100,000 in 2014. Of which, they were aged between 5 to 34 years. Their occupations included students (46.1%), pre-school child (19.2%), employed(17.7%) and others (17.0%), respectively[3].

The national policy of Thailand has placed dengue fever on the national strategic since the last decade up to present[4]. However, there were some problems in operation of the policy into real practice the control on dengue fever such as organizations system , authority of local related organizations, local legislation and regulation of dengue fever control[5].

Since there is restricted use of public health surveillance system in dengue fever at the district level in Thailand, this research aimed to study and develop suitable dengue fever surveillance system in district level. Findings will indicate the effective model for bottom up dengue fever surveillance system suitable for communities at the district level. Consequently, reported data, information and message deriving from the surveillance model will aid appropriate solutions in prevention and control of dengue fever, control of major breeding sources of mosquitoes, and people potentially at risk relevant to problems and needs of the district level.

MATERIALS AND METHODS

This research was carried out from June, 2014 to June, 2015 in 10 communities located in Bang Yi Rong Subdistrict, Bang Khonthi District, Samut songkham Province, Central Thailand. It consist 60 participants from all sectors involving with dengue fever in the participating in the model development. These included direct responsible government officers leaders (3), local leaders(10), university specialists(3), and village health volunteer(44). For design, monitoring and evaluation of the developed MODFSS model. The study utilized three sets of database reported on a monthly basis, such as databases included dengue fever cases, notification in advance of the mosquito breeding sources and problems and obstacles of the related organization and epidemic of dengue fever by the local community leaders. The study used five-processual step approach and began with situational

analysis of Step 1 and followed by reforming the existing surveillance system into the developed MODFSS of Step 2 to Step 4. Step 5 involved dissemination of the MODFSS. Each step yielded specific and measurable outputs and outcomes that guide the next steps.

Research step 1: Situation analysis. This step involved assessment of the current community context, environmental condition, status of the dengue fever surveillance system and action by using secondary data sources, survey, observation, interview, and meeting. This step led to finding about the strengths and weaknesses of the existing situation and the current system.

Research step 2: Prototype system design. This step included creation and reformation of the working committee, stakeholders and networks in the dengue fever surveillance system in the district with an assistance of the university specialists. Through the support activities such as meeting and brainstorming using information derived from research step 1.

Research step 3: System test. This step focused on carrying out the process-oriented action steps developed and started the full implementation of the developed MODFSS in the existing condition to achieve goals and objectives of the model. It allowed the working committee and stakeholders/networks to assess effectiveness of the model and to help identifying problematic areas in the processes of model implementation.

Research step 4: System improvement. This step involved modification of the MODFSS and setting guidance for monitoring and evaluation of the overall reform progress of an implementation. Its end result of this step guided to the effectiveness of the MODFSS suitable for local communities at the district level.

Research step 5: Model dissemination. This step involved transferring of the newly developed model (MODFSS) for further implementation in other areas.

Research tools: This research utilized both quantitative and qualitative data collection tools. Quantitative data were collected by using three forms of record sheets of the surveillance system, MODFSS1- MODFSS3 to elicit data on 1) dengue fever cases, 2) Index and to identify the major breeding sources of mosquitoes, House Index(HI), Container Index(CI), Breteau Index (BI), and 3) people potentially at risk. In addition, it also used qualitative data were obtained by using focus group discussion, secondary data review, and participant observation in the meeting and brainstorming sessions of the working committee, networking groups and stakeholders.

Data analysis: Quantitative data on arrested dengue fever cases, index and to identify the major breeding sources of mosquitoes, and reported people potentially at risk, and were analyzed by using descriptive statistics such as frequency, percentage, rate, average and standard deviation. Qualitative data were analyzed by using content analysis.

The study was approved by the Ethics Review Committee for Research Involving Human Subjects, Sirindhorn College of Public Health, Khon Kaen, Thailand (number 050/2557).

RESULTS

Bang Yi Rong Subdistrict, Bang Khonthi District, Samut songkham Province was a comprised 10 communities, based on its total population of 1,978 in 2014, there were 1,184 population aged 5-34 years (59.8%) currently living in the area. Results on situational analysis on community context and existing dengue fever surveillance system, and the developed MODFSS were described as the following.

Situational Analysis

The results of the study reflected community context of Bang Yi Rong Subdistrict, Bang Khonthi District and its existing dengue fever surveillance system.

Community Context: The study found that there were numbers and rate of dengue fever treatment between January to May, 2015 in the areas report to 26 cases (79.5 per 100,000 population). Of which, they were aged between 2 to 72 years(Mean 25.1 years). Their occupations included students (37.4%), employed(33.0%), self-employed (10.5%) and others (19.1%), respectively

Existing dengue fever Surveillance System: The dengue fever surveillance system on epidemic of dengue fever at the district level is limited. As a result, the incomplete data management could impair solutions to help solve the dengue fever problems of the people in responsible areas.

The Developed MODFSS

The development of the MODFSS in this current study grew out from the restricted management of dengue fever data generated among authorities and responsible staffs at district level. Using five-process approach for model development, the attributes of the developed MODFSS, including system structure, delineated as the followings.

The system structure: The structure of the developed MODFSS comprised three important attributes: responsible organizations of epidemiology networks, indicators of epidemic situation, and dissemination of dengue fever information.

1)Responsible organizations of epidemiology networks: The developed MODFSS comprised of staff from both government and private organizations and networks to contributed in the collaborative work. There were five responsible groups: 1) Government official group, including the Public Health Chief Officer, Nurses, and Public Health Officers; 2) Local politician group, including the Mayor, Vice Mayor, and Alderman; 3) Community leader group, comprising heads of the subdistrict and communities; 4) Volunteer group comprising village health volunteer, and 5) Expert group, included the specialists from Suan Sunandha Rajabhat University (College of Allied Health Science) and Sirindhorn College of Public Health, Khon Kaen. Each group had to either carry out dengue fever surveillance tasks, or participate in the monthly meeting, or both. Details of the roles and activities of each responsible organization and network were shown in Table 1.

Table 1 Dengue fever surveillance activities and support activities divided by the responsible organizations and networks.

Organizations/ Networks	**Dengue fever surveillance activities**						**Support activities**			
	Detection	**Registration**	**Data collection**	**Reporting**	**Analyses**	**Feed back**	**Communication**	**Training**	**Supervision**	**Resource provision**
District level										
District Health Center		**x**				**x**	**x**	**x**	**x**	**x**
Subdistrict level										
Health Promotion Hospitals	**x**	**x**	**x**	**x**	**x**	**x**	**x**	**x**		
Subdistrict Administration Organizations	**x**		**x**	**x**			**x**			
Community Leaders	**x**		**x**	**x**			**x**			
Village Health Volunteers	**x**		**x**	**x**						

Note: x = activities and support activities divided by the responsible organizations and networks.

2) Indicators of epidemic situation : Using database on monthly dengue fever cases generated by the Ministry of Public Health , the indicators for determining dengue fever situation in communities had been modified from its original source (Ministry of Public Health). Such modified indicators were then divided into two groups: Index and to identify the major breeding sources of mosquitoes, HI, BI, CI, and people potential at risk.

Group 1-Indicator of dengue fever cases. The indicator for determining morbidity rate of dengue fever cases were divided as the following alarming signs were served as indicators for taking precaution on of dengue fever cases problems in the area: if there were more than 20.0% of the median of morbidity rate of dengue fever over the last 5 years.

Group 2-Indicators of major breeding sources of mosquitoes. The indicators for determining major breeding sources of mosquitoes were divided into three categories. These included indicators for House index (HI), Container index (CI), and Breteau index (BI). The following alarming signs were served as indicators for taking precaution on of dengue fever cases problems in the area: 1) HI: having more than 5.0 % of houses infested with larvae and/or pupae; 2) CI : having more than 2.5% of water-holding containers infested with larvae or pupae; and 3) BI : having more than 2.5 of number of positive containers per 100 houses inspected.

Group 3- Indicators of people potentially at risk. The indicators for determining enabling factors of the people potentially at risk were divided into two categories, including proportion of people potentially at risk and existing dengue fever risk area. The following indicators served as alarming signs for taking precaution on dengue fever problems pertaining to people potentially at risk in the area: 1) having people with dengue fever risk behaviors more than 5 per 1,000 population and 2) having more than 5 of number of positive areas per 100 houses inspected.

The above indicators inter-wovently served as information and guideline leading to appropriate public actions in prevention and control of dengue fever in communities at a district level.

3)Dissemination of dengue fever information: The developed MODFSS recognized the importance of tranferring raw data obtained from the surveillance system into information and message to guide public actions, particularly prevention and control of dengue fever problems in the target communities. Consequently, data dissemination in this newly developed model was done by several means to both public and private sectors. These included communication through meeting and brainstorming among working committee and staff in responsible orgnizations and networks, as well as reporting to local leaders and village health volunteers.

DISCUSSION

At the initiation period, the first application of surveillance system in public health in global was

in disease prevention and control[6],[7]. Application of surveillance in dengue fever in Thailand was recent, started in 1958. However, the surveillance systems previously set up were not consistently and continuously operated[8]. In addition, an existing dengue fever surveillance system does not reach its full coverage. Consequently, there was limited use of dengue fever surveillance system in district level . This current study provided ways to sustainable the dengue fever surveillance system in district level. The newly developed MODFSS in this study was effective for system, findings also indicated the use of information related to dengue fever in several public actions, including prevention and control of dengue fever problems, as well as suppression of such problems.

Dengue fever surveillance system in Thailand basically utilized 2 principal strategies prevention and control such as control of mosquito breeding sources and public health education. Unlike the situation in the Singapore that had implemented the successful dengue fever control by making use of 3 principal strategies, source reduction of Aedes aegypti population, public education, and law enforcement[5]. Consequently, the use of Dengue fever surveillance system in Thailand was more likely to benefit public actions in regards to prevention and control tasks rather than for curative law enforcement. Furthermore, a policy does not focus on developing active surveillance. On the other hand, general surveillance system used in the have focused on passive surveillance[6], [7] ,[9].

The MODFSS in this study is useful for determining magnitude of dengue fever problems for it provides early warning signs of occurrences of emerging problems**.** The data has gathered from hospital registration and records, survey of mosquito breeding sources, and people potentially at risk. In addition, this MODFSS was effective and simple for usage in communities[10]. Finally, the MODFSS developed in communities at Bang Yi Rong Subdistrict, Bang Khonthi District is recommended to be further utilized in other districts elsewhere.

CONCLUSION

The MODFSS developed in this current study was a bottom up and effective form of public health surveillance suitable for communities at a district level. A surveillance system of dengue fever in communities has effectively for monitored a dengue fever problems . A completeness to develop surveillance system has to attention from public sector was a key success factor.

ACKNOWLEDGEMENTS

The researchers are very grateful to all participants for contributing important information to shape the model for dengue fever surveillance system in this current study. Our thanks also go to the public health chief officer, public health officers, nurses, mayor, vice mayor, alderman , community leaders, and village health volunteer of bang yi rong subdistrict, bang khonthi district, samut songkham province for the kind guidance, assistance and cooperation.

Funding : This research was supported by National Research Council of Thailand and Suan Sunandha Rajabhat University, Thailand.

REFERENCES

[1] M. Womack (1993). "The yellow fever mosquito, *Aedes aegypti*". *Wing Beats* 5 (4): 4.

[2] Department of Provincial Administration. Thailand Population Report 2014. The Year 2014 in Review. Available from: http://www.dopa.go.th

[3] Bureau of Epidemiology. Thailand Epidemiology Report 2014. The Year 2014 in Review. Available from:http://www.boe.moph.go.th/files/report/20150106_732528.pdf

[4] Department of Disease Control. National Strategic Plan for Control of Communicable Disease Year 2012 – 2016: Ministry of Public Health, 2012.

[5] Adisak Bhumiratana, Apiradee Intarapuk, Suriyo Chujun, Wuthichai Kaewwaen, Prapa Sorosjinda-Nunthawarasilp & Surachart Koyadun(2014). *Thailand Momentum on Policy and Practice in*
Local Legislation on Dengue Vector Control. Interdisciplinary Perspectives on Infectious Diseases.

[6] Langmuir, Alexander D. 1963. The surveillance of communicable diseases of national importance. New England Journal of Medicine 268 : 182-192.

[7] Last JM. A Dictionary of Epidemiology Second Edition. New York : Oxford University Press 1988.

[8] Department of Disease Control. Guidelines for Operations Surveillance and Prevention of Dengue Fever : Ministry of Public Health, 2014.

[9] Losos J., Z. Rumaloutine and Sentinel Surveillance Methods. Eastern Mediterranean Health Joumal 1996;2:1,46-50.

[10] P. Damapong, N. Kanchanakhan, W. Eungpinichpong, and P. Damapong
"Effectiveness of court-type traditionalThaimassage in patients with chronic tension-type headache: a pilot study," Journal of Health Research, vol. 29, no. 5, 2015.

First International Conference on Science, Engineering & Environment,
Tsu City, Mie, Japan, Nov.19-21, 2015, ISBN: 978-4-9905958-5-2 C3051

DEVELOPMENT OF FISHMEAL PROCESSING FROM CATFISH PROCESSING WASTE

Charun Likitrattanaporn
Faculty of Agricultural Technology, Rajamangala University of Technology Thanyaburi (RMUTT), Thailand

ABSTRACT

Thailand is one of the top fish producing nations in the world not only marine culture but also freshwater aquaculture. Since 1984, the artificially propagated hybrid catfish (clarias gariepinus x c. macrocephalus) has been cultured commercially and increasingly gained popularity among farmers spared throughout the country. At present Catfish processing such as dried fish, pickled fish and fish sausage becomes the important role for the farmer income and household economy. However, the most processing waste transform as organics fertilizer used in their farm is not valued compared to a byproduct as fishmeal. The simple fishmeal processing is developed for Catfish feeds from the Catfish processing waste (CPW). Cooking process is compared between steaming and boiling before squashing and drying process. The qualities of fishmeal were evaluated such as protein, fat, ash and moisture content. The results shows that both cooking processes are not significantly different in term of overall qualities but the boiling process shows slightly lower in term of energy used than the steaming process. All fishmeal samples gain protein content lower than 36% and slightly high fat content about 15% which could be used for Catfish feeds.

Keywords: Catfish, Fishmeal processing, Catfish processing waste

INTRODUCTION

Catfish production in Thailand has increased dramatically after the widespread adoption of hybrid fish and reached about 137,000 ton/year by 2012. [1] Most of the production is sold in domestic markets. The artificially propagated hybrid catfish (*clarias gariepinus* x *clarias macrocephalus*) is easier and quicker to raise than *Clasrias macro-cephalus* and at first, commanded better prices than the previously more widely cultured *Clasrias batrachus*. However, soaring production and a slow growing market have slimmed profit margins and fish farmers have attempted to reduce feed costs and increase unit size.

Since 1960s the marine trash fish has been mainly used for feeding catfish culture, although floating pelleted feeds available in the market for decades. [2] However it has become popular feeds for catfish culture farm since in 1993 [3] but few years later the chicken processing wastes, principally heads, intestines and leg bones have become important catfish feed resources.

Catfish feed, is the major cost for Thai farmers. It can be used so as to alternate feed from chicken or pig manure. To reduce its cost but affect to preferable of customer and deduct the catfish market share of freshwater fish production. Moreover, due to the bird flu (Highly Pathogenic Avian Influenza) disease outbreak in 2003, it caused the negative effect to integrated catfish farming. Catfish feed is commonly major used ingredient composition and nutrient content; protein. Feeds and feeding practices became important technique to overcome the farmer economy.

Simultaneously catfish could be added value by processing, like dried fish, pickled fish, fish sausage etc., estimate double price from raw material. However, catfish processing waste such as fish head, gut and skin were transformed to organics fertilizer which is easy utilized but don't earn any direct income. Estimation of waste maybe more than 50% of total weight that means half of catfish will be thrown out. In marine processing industry their waste will be transformed to fishmeal and fish oil which they can earn a lot of money and it is alternative protein source for cattle and poultry.

Fishmeal processing is carried out in six steps: cooking, pressing, separating, evaporation, drying and grinding. When the fish is heated the protein present in its coagulates and ruptures the fat deposits. The cooked fish will be pressed which removes large amount of liquid from raw material. The liquid is collected to separate the fish oil from water. Then the water which is also known as stick water will be evaporated to a thick syrup containing 30-40% solids. Finally, pressed fish cake is subjected to drying using press cake method to obtain a stable meal. This meal is grinded to the desired particle size. [4]

Catfish production farm needs to apply Sustainable agriculture aims to develop production

especially as self-support on feeds and feed practice, value added by processing and marketing. To reach the goal, first step is to develop on catfish feed by utilize their processing waste to produce fishmeal in order to be the Catfish feed.

MATERIALS AND MATHOD

Catfish Processing Waste (CPW)

The CPW used in this study came from the community enterprise namely "Bueng-Kham-Poi Catfish Processing Centre". This community is situated at Thanyaburi, Pathumthani province. People there produce dried Catfish twice a week at 300kg raw material which gain waste around 40% of raw material. Most of it is heads together with apart of gut. CPW will be collected and cooled down before delivery to laboratory and do experiment.

Fig. 1 The selected Catfish 200-300g each

Fig. 2 The dried Catfish

Fig. 3 The Catfish head, a processing waste (CPW)

Fishmeal Processing Design

Fishmeal processing is carried out in six steps: cooking, pressing, separating, evaporation, drying and grinding as shown in figure 4. Three outputs of this process are fishmeal, fish oil and protein syrup.

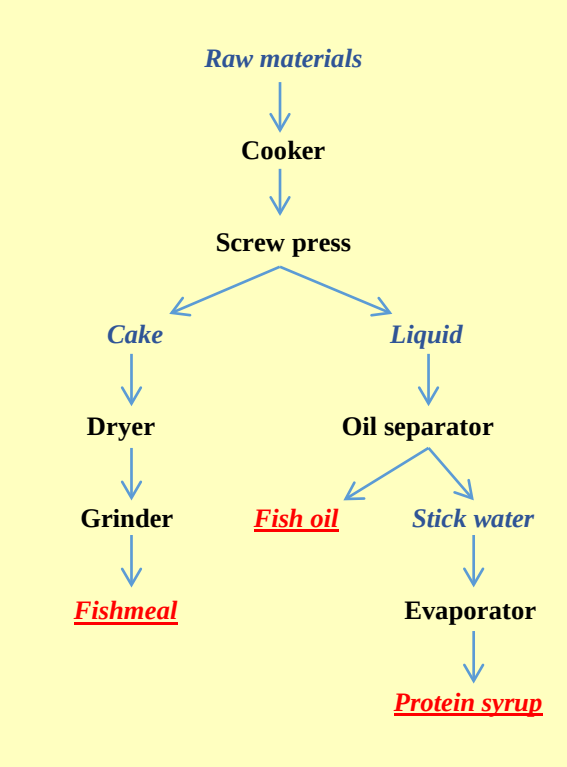

Fig. 4 The fishmeal Processing Flow Diagram (Zhoushan Xinzhou Fishmeal Equipment Factory)

The above flow process diagram shows the industrial fishmeal processing which is commonly used in marine by-product especially Tuna processing waste that contains valuable fish oil and protein extract. While freshwater fish contain different fish oil which may use for other purposes. In this study the processing waste is focused on fishmeal processing in order to add value and may be they can develop their own Catfish feeds in the future. The fishmeal process for sustainable agriculture principle should design a simple process, cheaper, available equipment and low energy requirement.

Therefore, the fishmeal processing consists of 4 processes, start from cooking, after that squashing water with oil from cooked waste. From preliminary test cooked waste is directly dried result shows that high fat content reach 30% of fishmeal. The cake is milled before drying.

Cooking process

The cooking process is the first step to stop enzyme and microorganism in the waste not to deter late and spoilage. Normally boiling and steaming are used for cooking process in this study. To produce fishmeal from the aquatic processing waste should

consider the pathogen transfer which may cause disease problem or contamination [5]. So the cooking process of the Catfish processing waste need to heat at 100ºC for 30 minutes or more. The boiling process, equal weight of CPW and water are used and boiled for 30 minutes with occasional stirring. After that CPW is screened and cooled down before milling. The steaming process, CPW is filled in basket and steamed at atmosphere pressure for 60 minutes, then cool down to room temperature before milling.

Squashing process

The manual compressing equipment, which is a simple squashing process, is used as shown in figure 5. Cooked CPW is filled in the perforated column and then turn the handle clockwise to move the compression plate downward in order to compress the CPW and release the water with oil out of the perforated column.

Fig. 5 the manual compressing equipment

Milling process

The meat grinding equipment is used for cutting CPW into small particles as shown in figure 6. Squashed CPW is fed into a feed tube of equipment continuously and screw inside the grinder pull CPW in and push toward a knight and the holes plate which CPW will cut into small pieces but it is still a wet cake which has to be dried.

Fig. 6 the Milling equipment

Drying process

Two techniques are used in this experiment; the sun drying is applied in order to save power input and a Tray dryer which controls drying temperature at 60ºC**.**

Experimental Design

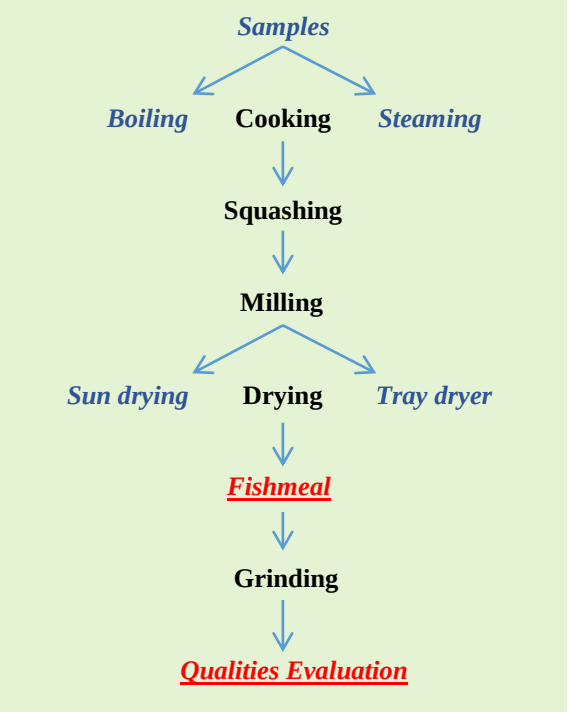

CPW sample was cooked by two different methods; boiling and steaming, after cooking samples were cooled to room temperature and then milling by meat grinding equipment. The sample was dried by the tray dry until the moisture content of sample below 10%. The dried fishmeal will be grind before qualities evaluation; protein, fat, ash, moisture content and Calcium. Three replications are needed and average value are compared and analyzed.

RESULTS

Fishmeal Processing Design

The fishmeal processing design for farmers and community entrepreneur can be a simple process such as normal boiling processing or steaming processing which CPW is cooked or sterilized before milling or drying. Unfortunately, the CPW contains a lot of oil accompany with water during boiling and steaming, it should be squashed the oil and water out before milling and drying. So, cooking process did not require special equipment. The cooking time for boiling process is about 30 min. and steaming process about 1 hour are accepted. Cooking process handling, both boiling and steaming show a little problem on hot material handling during screen boiled CPW and carry steamed CPW after cooking.

Cooked CPW are squashed by the manual compressing equipment which is a simple method to squash water and oil out the CPW. The boiled CPW look like more rot than the steamed CPW may be due to stirring of CPW during cooking.

Compressed CPW may be called a half dried CPW nearly 30% of moisture removal including fish oil. However, this manual compressing equipment needs a man power which is hard to control force steadily. Oil content will affect to its quality and power consumption of drying process.

Drying of CPW under control drying temperature at 60ºC can be sure that heat will not affect to protein content and other vitamins. So both sun drying and tray drying at low temperature will be the same in term of quality but only drying time and power consumption will be different. Tray dry took 72 hours to dry the CPW to 10%MC compared to the sun drying it took 5 days for about 15%MC.

The fishmeal processing from CPW could be developed in simple process which consists of 4 processes continuously; first cooking, then squashing and then milling finally drying. The coarse fishmeal gains from this process and must be grinded again before using as a feed.

CPW →***Cooking*** *- (boiling or steaming)*

→***Squashing*** *– (cylinder compressor)*

→***Milling*** *– (meat grinder)*

→***Drying*** *– (tray dryer or sun drying)*

→***Grinding*** *– (fine fishmeal for feeds mix, option)*

Fig. 7 the simple fishmeal processing for the sustainable agriculture

Fig. 8 Dried CPW fishmeal from boiling process

Fig. 9 Dried CPW fishmeal from steaming process

Qualities evaluation

The dried fishmeal was grinded before qualities evaluation such as protein content, fat content, ash, moisture content and calcium content. The results of fishmeal qualities evaluation from different fishmeal processing are shown in table 1.

Qualities list	Boiling	Steaming
Protein content %	35.68±1.71 [a]	35.91±1.22 [a]
Fat %	15.14±2.24 [a]	14.69±2.53 [a]
Ash %	38.15±0.87 [a]	37.90±1.08 [a]
%MC	8.09±1.52 [a]	6.19±1.33 [b]
Calcium %	12.78±2.63 [b]	15.25±2.17 [a]

Remark: the same letter show non-significantly difference

Table 1. Fishmeal qualities evaluation

The fishmeal qualities from boiling and steaming show non-significantly difference for three major qualities; protein content, fat content and ash. The protein content gains about 36% which slightly below the fishmeal class III (at above 40%) in both samples. While fat content shows quite high compared to the commercial which uses the screw compressor or screw expeller. The manual cylinder compressor may not be met the same level of compression which is a mechanically force. The commercial screw expeller could separate stick water over 50% of moisture removal cause low fat content below 3% in common. To improve this matter the screw compressor should be used instead of the manual cylinder compressor. Percent of ash

shows very high at above 37% in both samples. This may be from soil and clay in the gut. Normally, Catfish live and eat on the ground. The good fishmeal should control at low level ash as much as possible, so the CPW in this process should separate head and gut in order to deduct ash.

For the moisture content in this experiment, the CPW fishmeal shows slightly low percent of moisture content below 10% which is too low for commercial purpose. This occurs only for tray dryer used. For sun drying the CPW fishmeal will dry to 15% in 5 days and shorter if solar dryer is applied.

The calcium content from this experiment shows slightly high level at 12.78 and 15.25% for boiling and steaming respectively. Normally calcium is need for all formula feeds at about 1-3%. In this case the exceed calcium may cause some problems to animals. If it's used it can be applied for specific feed which need high calcium.

Overall qualities of CPW fishmeal both from boiling process and steaming process are non-significantly difference. The CPW fishmeal can be used as the Catfish feeds by mixing the other materials based on feed formula requirement.

Adoption on Feeds Processing

From this experiment the CPW fishmeal shows nutrition value at a certain level and some difficulties on drying process under limitation of using the meat grinder for milling process. The cooked CPW is mixed with other compositions like bran, fine corn etc., to be feeds mixed before milling by the meat grinder or pellet making, and then drying process of feeds. The same process can produce Catfish feeds or others instead of fishmeal.

ACKNOWLEDGEMENTS

The author would like to thank Assitant Professor Dr. Amnart Silawat, Dean of Faculty of Agriculture Technology, Rajamangala University of Technology Thanyaburi (RMUTT) who gave a funding to support this research project and also the staff of community enterprise namely "Bueng-Kham-Poi Catfish Processing Centre", Thanyaburi, Pathumthani province who support the Catfish processing waste (CPW) and lastly thank you Associate professor Wannakarn Likitrattanaporn from SWU who helps edit the paper.

REFERENCES

[1] DOF, Fisheries statics of Thailand 2012. Department of Fisheries, Bangkok, Thailand. 2012.

[2] Edwards, P., K.E. Weber, E.W. McCoy, C. Chantachaeng, C. Pacharakiti, K. Kaewpaitoon and S. Nitsmer. "Small-scale fishery project in Pathumthani province, Central Thailand; A socioeconomic and technological assessment of status and potential". AIT Res. Rep. No.158, Asian Institute of Technology, Bangkok, Thailand. 1983.

[3] Little, D.C., K. Kaewpaitoon, T. Haitook. "The commercial use of chicken processing wastes to raise hybrid Catfish (*clarias gariepinus x clarias macrocephalus*) in Thailand" NAGA, The ICLARM, Aquabyte section, October, 1994.

[4] Thongrod S, "Analysis of feeds and fertilizers for sustainable aquaculture development in thailand", FAO Fisheries Circular No. 497, Vol. 1, Aug. 1987, pp. 23-49.

[5] Tom, A. Gill, "Waste from processing aquatic animal and animal products: implecation on aquatic animal pathogen transfer". FAO Fisheries Circular No. 955. Canadian institute of Fisheries Technology, Dalhousie University, Nova Scotia, Canada. 2000.

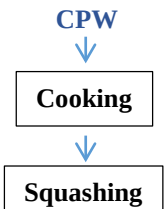

This page has kept blank intentionally

First International Conference on Science, Engineering & Environment,
Tsu City, Mie, Japan, Nov.19-21, 2015, ISBN: 978-4-9905958-5-2 C3051

THE COMPLEX SOLUTION FOR AN INTEGRO- DIFFERENTIAL EQUATION IN ELASTIC MEDIA PROBLEM IN PRESENCE OF HEAT

M. A. Abdou
,[a] Department of Mathematics, Faculty of Education, Alexandria University, Egypt.

Abstract: Complex variables method has been used to derive the solution of the first and second fundamental boundary value problems (**BVPs**) for an infinite elastic plate in presence of a uniform flow heat. The plate is weakened by a curvilinear hole *C. This curvilinear hole is* conformally mapped on the domain outside a unit circle γ using a general rational mapping function. The complex variables method is used to reduce the problem to an integro- differential equation with Cauchy kernel. Then, the two complex potential functions are obtained. Many special cases of the conformal mapping and some applications for different cases are discussed from the work.

Key words and phrases: Boundary value problem, an infinite plate, conformal mapping, integro-differentail equation, complex potential functions.

MSC (2010): 74B10, 30C20.

INTRODUCTION:

Several authors discussed the different solutions of the **BVPs** and its applications in many different sciences; see Gakhov [1], Ciarlet et al. [2], Hairong et.al, [3] Anastasi and Aral [4]. Also, for the contact and mixed problems see Colton and Kress [5], and Abdou [6]. Moreover, for the first and second fundamental problems we see that some authors used Laurent's theorem to express the solution in the series form, see England [7], Pakus [8] and Kalandiya [9]. Others used complex variables method to express the solution of the **BVPs** in the form of two complex potential functions, Gaursat functions, by using many rational mappings, seen Abdou [10, 11], Abdou and Khamis [12] and Abdou and Khar-Eldin [13].

In thermoelastic problems for an elastic media, the first and second **BVPs** are equivalent to finding two analytic functions $\varphi(z)$ and $\psi(z)$ of one complex argument $z = x + iy$. These functions must satisfy the boundary conditions,

$$K\varphi_1(t) - t\overline{\varphi_1'(t)} - \overline{\psi_1(t)} = f(t). \qquad (1)$$

Here, t denotes the affix of a point on the boundary. In terms of $z = c\omega(\zeta), c > 0, \quad \omega'(\zeta) \neq 0, \infty$ for $|\zeta| > 1$, outside a unit circle γ.

For the stress **BVPs**, $K = -1$ and $f(t)$ is a given function of stress. While for $K = k > 1$, $f(t)$ is a given function of displacement which called the thermal conductivity, we have the displacement **BVPs**. The books written by Noda et al. [14], Hetnarski and Ignaczak [15], Parkus [8] and Popov [16] contain many different methods to solve the problems in the theory of elasticity in one, two and three dimensions.

The complex potential functions $\phi_1(t)$ and $\psi_1(t)$ take the following forms see Parkus [8]

$$\varphi_1(\zeta) = -\frac{S_x + iS_y}{2\pi(1+k)}\ln\zeta + c\Gamma\zeta + \varphi(\zeta) \qquad (2)$$

$$\psi_1(\zeta) = k\,\frac{(S_x - iS_y)}{2\pi(1+k)}\,\ln\zeta + c\Gamma^*\zeta + \psi(\zeta) \qquad (3)$$

where, S_x , S_y are the components of the resultant vector of all external forces acting on the boundary and Γ , Γ^* are complex constants. Generally the two complex functions $\varphi(\zeta)$ and $\psi(\zeta)$ are single value analytic functions within the region outside the unit circle γ and $\varphi(\infty) = 0, \psi(\infty) = 0$.

Many authors have used the rational mapping $z = cw(\zeta), c > 0$; $\omega'(\zeta)$ does not vanish or become infinite inside (outside) the unit circle γ , see [11, 13, 17]

In this paper, the rational mapping

$$z = c\omega(\zeta) = c\,\frac{\zeta + m_1\zeta^{-1} + m_2\zeta^{-2}}{(1-n_1\zeta^{-1})(1-n_2\zeta^{-1})}, c > 0\ , n_1 \neq n_2 \qquad (4)$$

where $z'(\zeta)$ does not vanish or become infinite outside the unit circle γ , will be used to map the boundary C of the given region occupied by the middle plane of the plate in the z − plane ($z = x + iy$) onto the unit circle γ in the ζ − plane ($\zeta = \rho e^{i\theta}, 0 \le \theta \le 2\pi$) .

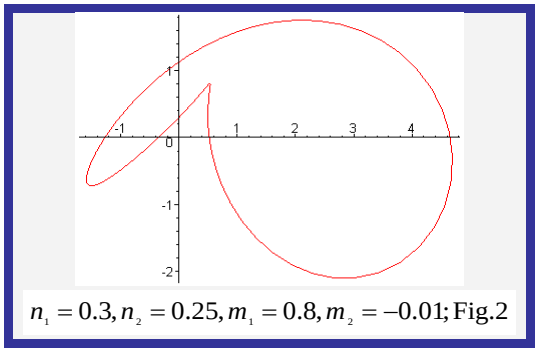

$n_1 = 0.3, n_2 = 0.25, m_1 = 0.8, m_2 = -0.01$; Fig.2

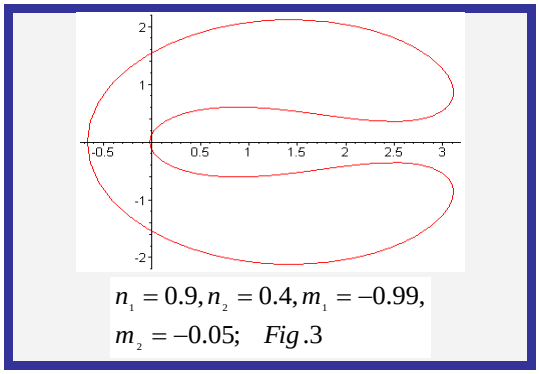

$n_1 = 0.9, n_2 = 0.4, m_1 = -0.99,$
$m_2 = -0.05;$ *Fig*.3

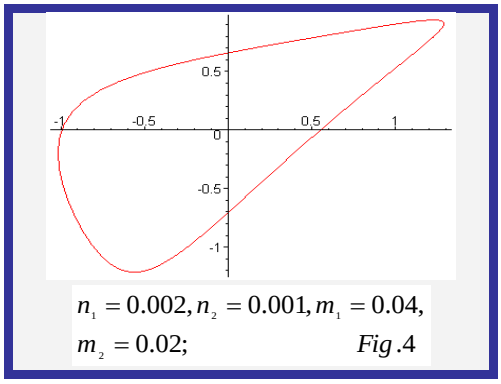

$n_1 = 0.002, n_2 = 0.001, m_1 = 0.04,$
$m_2 = 0.02;$ *Fig*.4

Using the transformation (4), Eq. (1.1) reduce to

$$K\varphi_1(c\omega(\zeta)) - \frac{\omega(\zeta)}{\overline{\omega'(\zeta)}}\overline{\varphi_1(c\omega(\zeta))} - \overline{\psi_1(c\omega(\zeta))} = f(c\omega(\zeta)) \quad (5)$$

The last formula represents the first and second **BVPs** in $\zeta -$ plane. In addition, we consider the **BVP** for an isotropic homogeneous perforated infinite elastic media in presence of uniform flow of heat. Then, we use the more general shape of conformal mapping to obtain the complex potential functions for the problem in the form integro-differential equation with singular kennel. Many special cases when the curvilinear hole takes the circle, ellipse and square shapes with other important and new cases are obtained. Several applications for the first and second **BVPs** are discussed. Moreover, the components of stress, in each application, are computed.

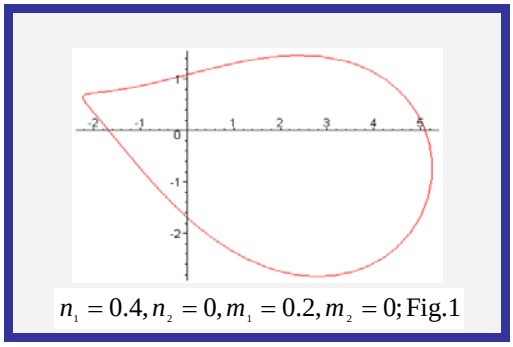

$n_1 = 0.4, n_2 = 0, m_1 = 0.2, m_2 = 0$; Fig.1

FORMULATION OF THE PROBLEM AND THE RATIONAL MAPPING:

Consider a thin infinite plate of thickness h with a curvilinear hole C, where the origin lie inside the hole is conformally mapped on the domain outside a unit circle γ by means of a rational mapping function (4). If a heat $\Theta = qy$ is following uniformly in the direction of the negative $y-$axis, where the increasing temperature Θ is assumed to be constant a cross the thickness of the plate, i.e. $\Theta = \Theta(x, y)$, and q is the constant temperature gradient. The uniform flow of heat is distributed by the presence of an insulated curvilinear hole C. The heat equation satisfies the relation,

$$\nabla^2\Theta = 0, \quad \nabla^2 = \frac{\partial^2}{\partial x^2} + \frac{\partial^2}{\partial y^2} \quad (6)$$

$$\frac{\partial\Theta}{\partial n} = 0, \quad r = r_0 \quad (7)$$

n is the unit vector perpendicular to the surface. The thermoelastic potential Φ, after neglecting the variation of the strain and the stress with respect to the thickness of the plate, satisfies the formula, see Parkus [8]

$$\nabla^2\Phi = (1+\nu)\alpha\Theta. \quad (8)$$

α is scalars which present the coefficient of the thermal expansion and ν is Poisson's ratio. Assume the force of the plate is free of applied loads.

In this case, the formula (1), for the first and second **BVPs** respectively takes the following forms,

$$\varphi_1(t) + t\overline{\varphi_1'(t)} + \overline{\psi_1(t)} = \frac{\partial\Phi}{\partial x} + i\frac{\partial\Phi}{\partial y} + \frac{1}{2G}\int_0^s [iX(s) - Y(s)]ds + c, \quad (9)$$

$$k\varphi_1(t) - t\overline{\varphi_1'(t)} - \overline{\psi_1(t)} = u + iv - \frac{\partial\Phi}{\partial x} - i\frac{\partial\Phi}{\partial y}. \quad (10)$$

Here, the applied stresses $X(s)$ and $Y(s)$ are prescribed on the boundary of the plane, S is the length measured from an arbitrary point. u, v are the displacement components, G is the shear modulus and Φ represents the thermoelastic

potential function. Also, the applied stresses $X(s)$ and $Y(s)$ must satisfy the following, see Parkus [8]

$$X(s)=\sigma_{xx}\frac{dy}{ds}-\sigma_{xy}\frac{dx}{ds},Y(s)=\sigma_{yx}\frac{dy}{ds}-\sigma_{yy}\frac{dx}{ds} \quad (11)$$

Here, σ_{xx}, σ_{xy} and σ_{yy} are the components of stresses given by the following relations,

$$\sigma_{xx}-\sigma_{yy}+2i\sigma_{xy}=2G[\frac{\partial^2\Phi}{\partial y^2}-\frac{\partial^2\Phi}{\partial x^2}+2i\frac{\partial^2\Phi}{\partial x\,\partial y}]$$
$$+4G[\bar{z}\varphi''(z)+\psi''(z)] \quad (12)$$

$$\sigma_{xx}+\sigma_{yy}=4G[\operatorname{Re}\varphi'(z)-\lambda\Theta],(\lambda=\frac{\alpha}{2}(1+\nu)$$
is the coefficient of heat transfer) (13)

the curvilinear hole C in $z-$plane onto the domain of outside unit circle in $\zeta-$plane under the condition $\omega'(\zeta)$ does not vanish or become infinite outside the unit circle γ. The following graphs give the different shapes of the rational mapping (4).

METHOD OF SOLUTION

In this section, we use the complex variable method to obtain the two complex functions, Gaursat functions, $\varphi(\zeta)$, $\psi(\zeta)$. Moreover, the three stress components σ_{xy}, σ_{xx} and σ_{yy} will be complete determined.

The Component of Stresses

The solution of Eq. (2.1) under (2.2) is given by,

$$\Theta=q[R+\frac{r_0^2}{R}],R=\sqrt{x^2+y^2} \quad (14)$$

Substituting Eq. (14) into Eq. (8), after using polar coordinates, we have

$$\Phi=\frac{(1+\nu)\alpha q\,r_0^2}{4}\ln z\quad R^2 \quad (15)$$

In addition, the stresses components, after some algebraic relations, can be adapted in the form,

$$\sigma_{xx}=2G[-\eta(z^2+4z\bar{z}+\bar{z}^2)\operatorname{Im}z+\operatorname{Re}[2\varphi'(z)-M(z,\bar{z})]] \quad (16)$$

$$\sigma_{yy}=2G[\eta(z^2+4z\bar{z}+\bar{z}^2)\operatorname{Im}z+\operatorname{Re}[2\varphi'(z)+M(z,\bar{z})]] \quad (17)$$

$$\sigma_{xy}=2G[\eta(z\bar{z}-2(\operatorname{Im}z)^2\operatorname{Re}z+\operatorname{Im}M(z,\bar{z})] \quad (18)$$

where,

$$\eta=\frac{(1+\nu)r_0^2}{2(z\bar{z})^2};\quad M(z,\bar{z})=\bar{z}\varphi''(z)+\psi'(z), \quad (19)$$

After determine the Gaursat functions the components of stress are completely determined.

Gaursat Functions:

To obtain the two Gaursat functions by using the conformal mapping (4) in the boundary conditions (1), we write the expression $\frac{\omega(\zeta)}{\omega'(\zeta^{-1})}$ in the form,

$$\frac{\omega(\zeta)}{\omega'(\zeta^{-1})}=\alpha(\zeta)+\beta(\zeta^{-1});\quad \alpha(\zeta)=\frac{h_1}{\zeta-n_1}+\frac{h_2}{\zeta-n_2}, \quad (20)$$

$\beta(\zeta^{-1})$ is regular function for $|\zeta|>1$. The expression $\frac{\omega(\zeta)}{\omega'(\zeta^{-1})}$ has two singularities at $\zeta=n_1$ and $\zeta=n_2$.

Using Eqs. (2) and (3) with the aid of (20), the formula (1) yields

$$K\varphi(\sigma)-\alpha(\sigma)\overline{\varphi'(\sigma)}-\overline{\psi_*(\sigma)}=F_*(\sigma), \quad (21)$$

where,

$$\psi_*(\zeta)=\psi(\zeta)+\beta(\zeta)\varphi'(\zeta);\ F(\zeta)=f(c\omega(\zeta))=f(t),$$

$$F_*(\zeta)=F(\zeta)-cK\Gamma\zeta-c\overline{\Gamma^*}\zeta^{-1}+N(\zeta)[\alpha(\zeta)+\overline{\beta(\zeta)}]$$
$$N(\zeta)=c\bar{\Gamma}-\frac{S_x-iS_y}{2\pi(1+k)}\zeta, \quad (22)$$

The function $F(\sigma)$ with its derivatives must satisfy Hölder condition.

Our aim is to determine the functions $\varphi(\zeta)$ and $\psi(\zeta)$ for the various **BVPs**. For this, multiply both side of Eq.(21) by $\frac{d\sigma}{2\pi i(\sigma-\zeta)}$ then integrating over the circle γ, and using (22), we obtain

$$-K\varphi(\zeta)-\frac{1}{2\pi i}\int_\gamma\frac{\alpha(\sigma)\overline{\varphi'(\sigma)}}{(\sigma-\zeta)}d\sigma-\frac{1}{2\pi i}\int_\gamma\frac{N(\sigma)\alpha(\sigma)}{(\sigma-\zeta)}d\sigma$$
$$=A(\zeta)-c\overline{\Gamma^*}\zeta^{-1};\quad A(\zeta)=\frac{1}{2\pi i}\int_\gamma\frac{F(\sigma)}{(\sigma-\zeta)}d\sigma \quad (23).$$

The formula (23) represents the integro differential equation of second kind with Cauchy kernel. The references, Fedotov [18], Hanyga and Seredyńska [19], Bavula [20] and AL-Jawary and Wrobel [21] contain many different methods to solve this kind of the equations analytically and numerically in one, two and three dimensions.

To obtain the integral terms of Eq. (23) we use Eq. (19) and then apply the residue theorem to have,

$$\frac{1}{2\pi i}\int_\gamma\frac{\alpha(\sigma)\overline{\varphi'(\sigma)}}{(\sigma-\zeta)}d\sigma=c\sum_{j=1}^{2}\frac{h_jb_j}{n_j-\zeta}, \quad (24)$$

b_j, $j=1,2$ are complex constants can be determine. In addition, we have

$$\frac{1}{2\pi i}\int_\gamma\frac{N(\sigma)\alpha(\sigma)}{(\sigma-\zeta)}d\sigma=\sum_{j=1}^{2}\frac{N(n_j)h_j}{n_j-\zeta}. \quad (25)$$

Hence, Eq. (23) yields,

$$-K\varphi(\zeta)=A(\zeta)-c\overline{\Gamma^*}\zeta^{-1}+\sum_{j=1}^{2}\frac{h_j}{n_j-\zeta}[N(n_j)+cb_j] \quad (26).$$

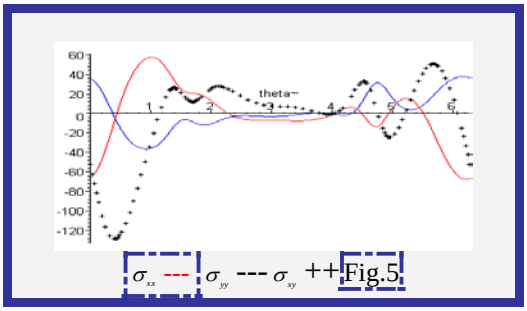

The two constants b_j, after differentiating Eq. (26) and using the result in Eq.(24), are

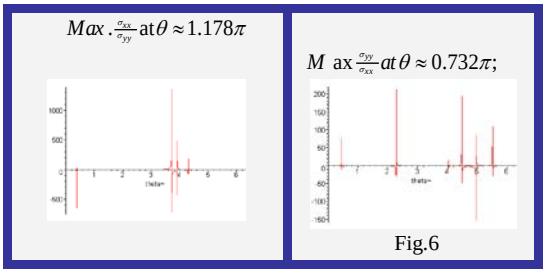

$$b_j=\frac{KE_j-h_jd_j\overline{E}_j}{c(K^2-h_j^2d_j^2)},\quad d_j=\frac{n_j^2}{(1-n_j^2)^2},\quad .$$

$$E_j=-\overline{A'(n_j)}-c\Gamma^*n_j^2-h_jd_j\overline{N(n_j)};\quad j=1,2 \quad (27)$$

The complex functions $\psi(\zeta)$ can be determine directly from (21), after substituting the expression of $\psi_*(\sigma)$ and $F_*(\sigma)$, then taking the complex conjugate of the resulting equation and using the expression of $\overline{\beta(\sigma)}$. After multiplying both sides of the result by $\frac{d\sigma}{2\pi i(\sigma-\zeta)}$ then integrating over the unit circle γ and using the properties of Cauchy integral and calculate sum residue, we obtain

$$\psi(\zeta)=cK\Gamma\zeta^{-1}-\frac{\omega(\zeta^{-1})}{\omega'(\zeta)}\varphi_*(\zeta)+\sum_{j=1}^{2}\frac{h_j\zeta}{1-n_j\zeta}\varphi_*(n_j^{-1}),$$

$$+\frac{1}{2\pi i}\int_\gamma\frac{\overline{F(\sigma)}}{(\sigma-\zeta)}d\sigma-\frac{1}{2\pi i}\int_\gamma\frac{\overline{F(\sigma)}}{\sigma}d\sigma \quad (28)$$

SOME APPLICATIONS

In this section, we assume some different applications for the first and second fundamental **BVPs.** In addition, we compute components of stresses directly.

Application 1: Curvilinear hole for an infinite plate subjected to uniform *tensile stress* and flowing heat:

Assume

$$K=-1,\Gamma=\frac{P}{4};\Gamma^*=\frac{-P}{2}e^{-2i\theta};0\le\theta\le 2\pi,\ S_x=S_y=f=0.$$

Then, the Gaursat functions of Eqs. (26) and (28) become

$$\varphi(\zeta)=\frac{cP}{2}\zeta^{-1}e^{2i\theta}+\sum_{i=1}^{2}\frac{L_j}{n_j-\zeta};\quad ,$$

$$L_j=\frac{cP}{4}h_j\left[\frac{1-2n_j^2\cos 2\theta}{1-h_jd_j}+i\frac{2n_j^2\sin 2\theta}{1+h_jd_j}\right] \quad (29)$$

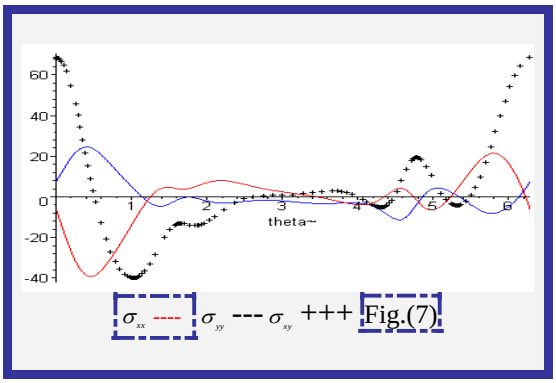

$$\psi(\zeta)=-\frac{cP}{4}\zeta^{-1}-\frac{\omega(\zeta^{-1})}{\omega'(\zeta)}\varphi_*(\zeta)+\sum_{j=1}^{2}\frac{h_j\zeta}{1-n_j\zeta}\varphi_*(n_j^{-1}),$$

$$\varphi_*(\zeta)=\varphi'(\zeta)+\frac{cP}{4}. \quad (30)$$

We have the stress **BVP** of an infinite plate weakened by a curvilinear hole C and stretched at infinity by a uniform tensile stress of intensity P, and heat in the negative direction of $y-$axis.

For $n_1=0.3,\ n_2=0.25$, $m_1=0.8,\ m_2=-0.01,$ $p=0.25$, the stress components σ_{xx} , σ_{yy} and σ_{xy} are obtained in the normal plate see Figs. (5)-(6).

σ_{xx} positive at $0.13\pi\le\theta\le 0.7\pi, 1.27\pi\le\theta\le 1.4\pi$ $1.6\pi\le\theta\le 1.75\pi$. σ_{yy} $0\le\theta\le 0.127\pi, 1.37\pi\le\theta\le$ 2π . σ_{xy} $\frac{\pi}{3}\le\theta\le\frac{3\pi}{2}$, $1.656\pi\le\theta\le 1.94\pi$.

For the thermoelastic plate, after using the substitutions $G=\frac{1}{2}, q=0.1$, $r_0=0.75,\ \alpha=0.7;\ \nu=1,$ we have the following the stress components see Figs.(7) -(8).

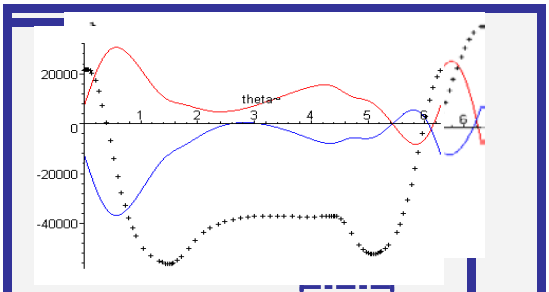

σ_{xx} --- σ_{yy} --- σ_{xy} ++ Fig.(11).

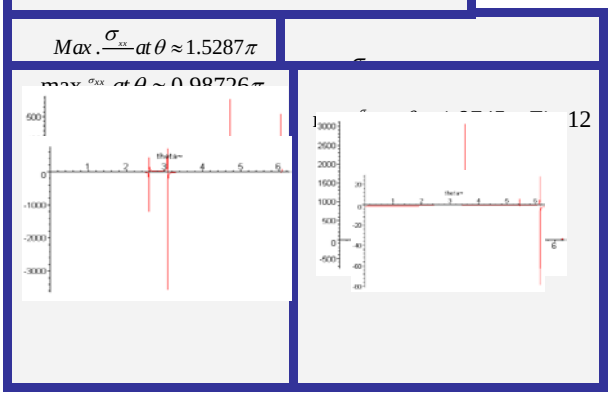

σ_{xx} positive at $0.38\pi \le \theta \le 1.1\pi$, $1.4\pi \le \theta \le 1.53\pi$ and $1.656\pi \le \theta \le 2\pi$. σ_{yy} at $0 \le \theta \le 0.38\pi$; $1.53\pi \le \theta \le 1.72\pi$. σ_{xy} at $0.828\pi \le \theta \le 1.274\pi$; $0 \le \theta \le 0.16\pi$; $1.4\pi \le \theta \le 1.656\pi$ and $1.75\pi \le \theta \le 2\pi$.

Application 2: Curvilinear hole having two poles and the edge is subject to a uniform pressure P :

If $K = -1, S_x = S_y = \Gamma = \Gamma^* = 0, f(t) = Pt; \Theta = qy$.

We have

$$\varphi(\zeta) = cP\sum_{j=1}^{2}\frac{n_j^3 + m_1 n_j + m_2}{(n_j - n_{j\pm1})(n_j - \zeta)} - \sum_{j=1}^{2}\frac{h_j E_j}{(n_j - \zeta)(1 - h_j d_j)} \quad (31)$$

$$\psi(\zeta) = -\frac{\omega(\zeta^{-1})}{\omega'(\zeta)}\varphi'(\zeta) - cP\zeta^{-1} - (n_1 + n_2)cP$$

$$+\sum_{j=1}^{2}\frac{h_j \zeta}{1 - n_j \zeta}\varphi'(n_j^{-1}) \quad (32).$$

We have the solutions of stress **BVP** when the edge of hole is subject to a uniform pressure P .

For $n_1 = 0.3$, $n_2 = 0.25, m_1 = 1, m_2 = -0.01$ $p = 0.25$, the stress components σ_{xx} , σ_{yy} and σ_{xy} are obtained in the normal plate, see Figs. (9), (10).

σ_{xx} *positive at* $0.38\pi \le \theta \le 1.1\pi, 1.4\pi \le \theta \le 1.53\pi$; $1.656\pi \le \theta \le 2\pi$. σ_{yy} *at* $0 \le \theta \le 0.38\pi; 1.53\pi \le \theta \le 1.72\pi$ σ_{xy} *positive at* $0 \le \theta \le 0.16\pi$, $0.828\pi \le \theta \le 1.274\pi$, $1.4\pi \le \theta \le 1.656\pi$ *and* $1.72\pi \le \theta \le 2\pi$. For the thermoelasticity,at $r_0 = 0.75, \alpha = 0.7, \nu = 1$, $G = 0.5, q = 0.1$,.Figs.(11-12)

σ_{xx} *positive at* $0 \le \theta \le 1.7197\pi$. σ_{yy} *at* $0.828\pi \le \theta \le 0.96\pi$ *and* $1.79\pi \le \theta \le 1.91\pi$. σ_{xy} *at* $0 \le \theta \le 0.1274\pi$.

Application 3: The external force acts on the center of the curvilinear.

When, $K = k$, $\Gamma = \Gamma^* = f = 0$. Then, we have

$$-k\,\varphi(\zeta) = \frac{1}{2\pi(1+k)}\sum_{j=1}^{2}\frac{h_j n_j}{(n_j - \zeta)}(Z - 1)$$

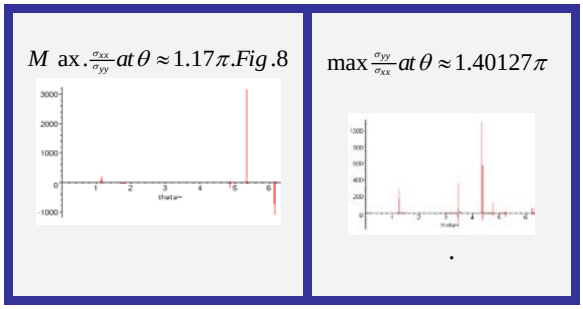

$$Z = \left[\frac{kh_j d_j (S_x + iS_y)}{(k^2 - h_j^2 d_j^2)} - \frac{h_j^2 d_j^2}{(k^2 - h_j^2 d_j^2)}(S_x - iS_y)\right] \quad (33)$$

$$\psi(\zeta) = -\frac{\omega(\zeta^{-1})}{\omega'(\zeta)}\varphi_*(\zeta) + \sum_{j=1}^{2}\frac{h_j \zeta}{1 - n_j \zeta}\varphi_*(n_j^{-1}) \quad (34)$$

Where,

$$\varphi_*(\zeta) = \varphi'(\zeta) - \frac{S_x + iS_y}{2\pi(1+k)}\zeta^{-1}, N(n_j) = -\frac{S_x - iS_y}{2\pi(1+k)}n_j,$$

$$E_j = h_j d_j n_j \frac{S_x + iS_y}{2\pi(1+k)}, \quad b_j = \frac{Z}{2\pi c(1+k)} .$$

We have the solution of the second fundamental **BVP** when the heat is flowing in the negative direction of y – axis and the force acts on the center of the curvilinear hole.

For $n_1 = 0.3$, $n_2 = 0.25$, $m_1 = 1$, $m_2 = -0.01$, $p = 0.25$. the stress components σ_{xx} , σ_{yy} and σ_{xy} are obtained in Figs.(13), (14).

σ_{xx} *positive at* $0 \le \theta \le 1.72\pi$. σ_{yy} *at* $0.83\pi \le \theta \le 0.96\pi$ *and* $1.72\pi \le \theta \le 1.91\pi$. σ_{xy} *at* $0 \le \theta \le 0.13\pi$; $\theta \le 1.91\pi$.

In the thermoelasticity plate, we have the following shapes for the stress components by using the substitutions $G = 1/2$, $q = 0.1$, $r_0 = 0.75$, $\alpha = 0.7$, , $\nu = 1$, see Figs.(15),(16).

σ_{xx} *positive at* $0 \le \theta \le 1.72\pi$. σ_{yy} $0.83\pi \le \theta \le 0.96\pi$ *and* $1.7197\pi \le \theta \le 1.91\pi$. σ_{xy} $0 \le \theta \le 0.1274\pi$.

5 CONCLUCTION

From the previous discussion we have the following result

(i) The conformal mapping $z = c\omega(\zeta), c > 0$ where $\omega'(\zeta) \neq 0, \infty; |\zeta| > 1$, mapped the infinite region to outside a unit circle γ .

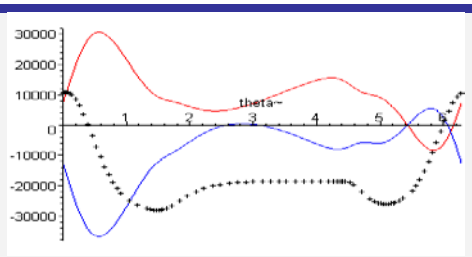

σ_{xx} ____ σ_{yy} ____ σ_{xy} +++Fig.15

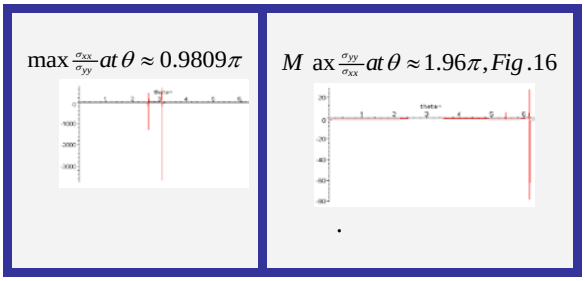

(ii) After applying the mapping, $z = c\omega(\zeta), c > 0$, the boundary value problems reduce to the integro-differential equation with discontinuous kernel.

(iii) Cauchy method is the best method to solving the integro-differential equation with Cauchy kernel and obtaining the two complex functions $\varphi(z)$ and $\psi(z)$ directly.

(iv) The solution of the boundary value problems for isotropic homogeneous infinite elastic media in plane reduces to determine the two complex function called Gaursat functions

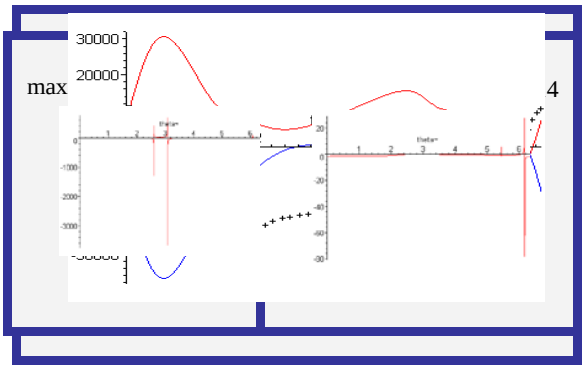

(v) The components of stress σ_{xx}, σ_{yy} and σ_{xy} is completely determine and plotting after obtaining the two complex functions.

(vi) As a main result of inserting the effect of uniform flow of heat in the negative of $y-$direction we have, M ax.$\sigma_{xy}^{N} > M$ ax.σ_{xy}^{H} and $Min.\sigma_{xy}^{N} < Min.\sigma_{xy}^{H}$, where, σ_{xy}^{N} represent the shear components of stress at normal state, while σ_{xy}^{H} represent the shear components of stress after inserting the effect of heating.

(vii) If we denote to the angle that appears the maximum value of $\frac{\sigma_{xx}}{\sigma_{yy}}$ in normal state by θ_1, and the angle that appears the maximum value of $\frac{\sigma_{xx}}{\sigma_{yy}}$ after inserting the effect of heating by θ_2, we note $\theta_1 < \theta_2$

(viii) If we denote to the angle that appears the maximum value of $\frac{\sigma_{yy}}{\sigma_{xx}}$ in normal state by $\hat{\theta}_1$, and the angle that appears the maximum value of $\frac{\sigma_{yy}}{\sigma_{xx}}$ after inserting the effect of heating by $\hat{\theta}_2$, we note $\hat{\theta}_1 < \hat{\theta}_2$

(ix) All of the previous works in this paper is considered as special cases from this study.

REFERENCES

[1] F. D. Gakhov, Boundary Value Problems, Paragon 1966.

[2] P. G. Ciarlet, M. H. Schultz, R. S. Varga, Numerical methods of high-order accuracy for nonlinear boundary value problems I.One dimensional problem, Numer. Math., Vol. 9, 1967.

[3] Hairong Lian1, Dongli Wang1, Zhanbing Bai and Ravi P Agarwal, Periodic and sub harmonic solutions for class of second-order *p*-Laplacian

Hamiltonian systems, j. Boundary Value Problems, 2014, 2014:260pp. 1-15.

[4] G. A. Anastasia, A. Aral, Generalized Picard singular integrals, Compute. Math. Appl. 57 (2009) 821-830.

[5] D. Colton, R. Kress, Integral Equation Methods in Scattering Theory, John Wiley, New York, 1983.

[6] M. A. Abdou, First and second fundamental problems for an elastic infinite plate with a curvilinear hole. Alex. Eng. J. Vol. 33, 1994.

[7] A. H. England, Complex Variable Method in Elasticity, Mc Graw, London, New York, 1971

[8] H. Parkus, Thermo elasticity, Spring-Verlag, Barlen, 1976

[9]A.I. Kalandiya, Mathematical Method of Two Dimensional Elasticity, Moscow,1975

[10] M. A. Abdou, Fundamental problems for infinite plate with a curvilinear hole having infinite poles. Appl. Math. Compute. Vol. 93, 2002.79-91

[11] M. A. Abdou, A.K. Khamis, On a problem of an infinite plate with a curvilinear hole having three poles and arbitrary shape. Bull. Call. Math.Soc, Vol.29, 2000.104-115

[12] M.A. Abdou, E.A. Khar-Eldin, An infinite plate weakened by a hole having arbitrary shape. J. Comp. Appl. Math. Vol. 56, (1994)341-351.

[13] N.I. Muskhelishvili, Some Basic Problems of Mathematical Theory of Elasticity, Holland, 1953.

[14] N. Noda, R.B. Hetnarski, Y. Tanigawa, Thermal Stress, Taylor and Francis, 2003.

[15] R.B. Hetnarski,J. Ignaczak, Mathematical Theory of Elasticity, Taylor and Francis, 2004.

[16] G. Ya. Popov, Contact Problems for a Linearly Deformable Foundation, Kiev, Odessa, 1988.

[17] I. H. El-Sirafy, M.A. Abdou, First and second fundamental problems of infinite plate with a curvilinear hole, J. Math. Phys. Sci.Vol. 18,1984.1-7

[18] A.I. Fedotov, Quadrature-difference methods for solving linear and nonlinear singular integro-differential equations, J. Nonlinear Analysis, Vol. 71, 2009.

[19] A. Hanyga , M. Seredyńska, Positivity of Green's functions for a class of partial integro-differential equations including viscoelasticity, J. Wave Motion, Vol. 47, 2010.

[20] V.V. Bavula, The group of auto morphisms of the algebra of polynomial integro-differential operators, J. Algebra, Vol. 348 , 2011.

[21] M.A. AL-Jawary, L. C. Wrobel, Numerical solution of two-dimensional mixed problems with variable coefficients by the boundary-domain integral and integro-differential equation methods, Engineering Analysis with Boundary Elements, Vol.35, 2011.

First International Conference on Science, Engineering & Environment,
Tsu City, Mie, Japan, Nov.19-21, 2015, ISBN: 978-4-9905958-5-2 C3051

A ROBUST HARMONY SEARCH ALGORITHM BASED NODE DEPLOYMENT FOR HYBRID WIRELESS SENSOR NETWORKS

Abdulqader Mohsen[1], Walid Aljoby[1], Khaled Alenezi[2], and Abdulrahman Alenezi[3]
[1]Faculty of Computing and Information Technology, University of Science and Technology, Yemen
2College of Information and Communication Technology, University Islamic International Malaysia, Malaysia

ABSTRACT

The performance of the wireless sensor networks, composed of static sensor nodes, is significantly influenced by the random deployment. Often, the sensors are scattered incorrectly and hence positioned inaccurately. A frequent criticism of the random deployment of stationary nodes is that it might cause coverage holes in the field being monitored. In this paper, we propose adding mobile sensor nodes after the initial deployment of the stationary nodes to overcome the coverage holes problem. To achieve optimal coverage, a harmony algorithm is employed to find the optimal solution for the added mobile nodes intended for covering of the holes. The proposed algorithm determines the best locations of the mobile nodes that need to be added after the initial deployment of the stationary nodes. The performance of the proposed algorithm was evaluated using several metrics, and the simulation results demonstrated that, compared to similar state-of-the-art algorithms, the proposed algorithm can optimize the network coverage in terms of the overall coverage ratio, coverage degree and the number of additional mobile nodes.

Keywords: *Target Coverage; Mobile Sensor Nodes; Meta Heuristic Algorithms; Coverage Maximization; Stationary Sensor Nodes.*

INTRODUCTION

A Wireless Sensor Network (WSN) is a spatially distributed system consists of collection of autonomous, tiny, low-cost, battery operated sensor nodes that cooperate with each other to monitor and record physical or environmental conditions such as remote environmental monitoring and target tracking [1]. Based on the needed purpose, the sensor nodes achieve the sensing, communication and computation tasks. Usually, each node in WSNs is configured to accomplish sensing task, and thus the sensing attribute is considered as an essential factor in designing the network. Moreover, the coverage of the sensing field and the motion of sensor nodes are the important aspects related to the sensing attribute. Many researchers have studied the coverage problem in WSNs either as target coverage or area coverage [2]. The main objective of the area coverage protocols is to maximize the covered area of the whole sensing field while the main objective of target coverage protocols is to split the sensing field into targets and then maximize the number of targets that could be covered in the sensing field.

The coverage performance is affected by many different factors such as sensing model, sensor mobility, network topology, and deployment strategy and so on. One of the most important factors is the deployment strategy in which the sensor nodes are distributed or dispersed in the field being monitored [3]. Based on the application, the sensor nodes can be scattered either deterministically or randomly. The deterministic deployment is based on a pre-determined design of the sensor locations such as grid deployment. On the other hand, in random deployment the sensor nodes are deployed within the sensing field stochastically and independently such as scattering the nodes from an aircraft randomly. In a hostile environment or remote large scale WSNs, the sensor nodes positions cannot be predetermined and thus the random deployment might be the unique choice. Nevertheless, random deployment of the sensor nodes causes some holes in the field under monitoring; therefore, in most cases, random deployment is not guaranteed to be effective for achieving the required objective in terms of the area coverage [2].

Nevertheless, random deployment of the sensor nodes, in most cases, does not guarantee full coverage, leading to holes formulation problem [23]. Therefore, to overcome this problem and maximizing the covered area or targets, an efficient algorithm should be developed.

According to the application requirements, the nodes might be stationary, mobile, or hybrid [23]. In small-scale WSNs where all nodes are stationary, the coverage can be determined by the initial network configuration and the coverage can be maximized by manually deploying additional nodes

to the initially deployed ones. On the other hand, in large scale WSNs applications, the sensing filed may be hostile or human intervention is not possible and hence, the sensor nodes can deployed only randomly [1].

Typically, two methods can be used to reduce or remove the holes in random deployment after initial deployment based on the motion of the sensor nodes. In the first method, in case all sensor nodes are mobile, an efficient algorithm should be developed to maximize the coverage area and simultaneously minimize the moving cost of the mobile nodes. In this situation, the coverage area is maximized by utilizing the mobility property of the sensor nodes. Therefore an efficient deployment algorithm, such as virtual force algorithm or potential field algorithm can be used to relocate the mobile sensor nodes after the initial deployment these nodes [4], [5].

In the second method, in case the nodes are hybrid in which some of the nodes are stationary and the other are mobile, an efficient algorithm should be employed to get the number and locations of the mobile nodes that should be added after the initial deployment of the stationary nodes. The most efficient optimization algorithms that can be used are the meta-heuristic algorithms, such as genetic algorithm, ant colony optimization, particle swarm optimization, and harmony search algorithm. These algorithms can be used to find an optimal or close to optimal solution for optimization problems in reasonable time [6]. A few researchers in the field of WSNs have proposed heuristic algorithms to find the optimal number of sensor nodes that should be added after the initial deployment to maximize the coverage [15], [18], [19], [22], and [23].

In this paper, we propose a meta-heuristic approach that utilizes the movements of some nodes to remove the holes which would be formulated after the initial deployment. Our approach employed a harmony search algorithm (HSA) to determine the minimum number of mobile nodes that should be used in addition to the previously deployed stationary nodes such that the coverage of the monitored area is maximized. The reason behind usage of HSA is its stochastic components that can explore more regions where the holes could not be covered by the state-of-the-arts solutions such as GA, in an efficient and effective manner.

The rest of this paper is organized as follows. Section II reviews the related work. Section III views the assumptions and the coverage model. Section IV presents the steps of the HSA based coverage optimization. Section V shows simulation experiments and discussion, and Section VI is the conclusion of the paper.

RELATED WORK

An important research problem in WSN is the coverage problem. Many researchers have studied the node deployment problem to attain maximum coverage in WSN extensively. Some researchers have addressed WSNs with mobile sensor nodes [4],[5],[7],[8] where others have addressed WSNs with both static and mobile nodes [9-12].

For mobile sensor networks, several approaches have been proposed. Firstly, Howard proposed a potential field-based approach for deployment. It formed the fields in such a way that allows each node to be repelled by both obstacles and by other nodes, thus forcing the network to distribute the nodes in the field evenly [4]. After that, Zou and Chakrabarty proposed a virtual force algorithm [5] to enhance the coverage by both pulling and pushing force among the nodes. Then, Wang, Cao and Porta used Voronoi diagrams to find the uncovered areas and determine the positions where the nodes can move [7]. Later, Tahiri et al. employed simulated annealing algorithm for nodes placement that maximize the coverage of the area of interest [8]. According to the authors, the algorithm is able to find the near-optimal solution.

In contrast, several works have considered both static and mobile nodes in WSN. Wang et al. designed two bidding protocols to increase the coverage by the movement of mobile sensors. The protocols used Voronoi diagrams with static sensors to discover coverage holes and bid mobile sensors which convene the largest holes by accepting the highest bids [9]. After that, Ahmed, Kanhere and Jha proposed a distributed protocol used the geometric right-hand rule to determine the boundary nodes. Then, the static nodes used a probabilistic coverage algorithm with realistic sensing coverage model to calculate the area coverage and determine coverage holes. Finally, the mobile nodes used the virtual force algorithm to move [10]. In ref [11], Wang and Wang proposed several variants based on particle swarm optimization and virtual force algorithm. These variants used multi-objective function to strike a balance between the coverage and the energy consumption. Their obtained solutions were analyzed to select the variant with best performance for better deployment [11]. Recently, Wang et al. proposed a biogeography-based optimization algorithm to maximize the coverage area of the network with dynamic deployment of static and mobile sensor [12].

In addition to the previous studies, different meta-heuristic algorithms have been proposed to address the problem of node deployment as it is an optimization problem. It is worthy to note that the genetic algorithms is the most popular meta-heuristic used to solve this problem. Most of the proposed genetic algorithms have focused on solving the deterministic node deployment [13-18]. In turn, few researches have addressed the random node deployment [19-22]. In random deployment, genetic algorithms are applied to maximize the coverage by find the near optimal positions for additional mobile. Sahin et al. in [19] proposed a force-based genetic

algorithm in which the mobile nodes utilize the sum of the forces used to choose their direction by the neighbours. After that, Qu and Georgakopoulos developed a multi-objective genetic algorithm which running on a base station to provide maximum sensing coverage area. They claimed that the algorithm can strike a balance between the travelled distance and coverage area by maximizing the coverage and minimizing the travelled distance [20]. Nematy, Rahmani and Yagouti proposed a genetic algorithm to be used in cluster based WSN. The results showed that the algorithm able to increase coverage by finding the best places for the cluster heads with more density of sensor nodes [21]. Rahmani et al. proposed new approach, based on Voronoi diagrams and genetic algorithm, to maximizing coverage. Voronoi diagrams were used to divide the field into cells and then a genetic algorithm was used to determine the best positions for additional mobile nodes maximizing the coverage in every cell [22].

Recently In [23], GA was employed to find the best positions of extra mobile nodes to be added to the network for enhancing the coverage after the initial deployment of stationary nodes.

The harmony search algorithm has not been investigated well to solve the coverage holes problem, especially in hybrid wireless sensor networks. In [24], a simple schema of HSA was employed to find the assignment of sensor nodes in a wireless sensor network that enhance the network coverage. However, it has not considered the coverage degree (i.e., k-coverage), and has not even declared a method for holes removal.

PRELIMINARIES

Network Assumptions

In this paper we assume that the deployment of the sensor nodes is randomly and each node equipped with GPS. Furthermore, the base station node position is stationary and the number of sensor nodes that are initially deployed equals to those that are required to reach the full coverage in case these nodes were deterministically deployed. In addition, extra few mobile nodes are available to be used for repairing the coverage holes after initial deployment of the stationary nodes.

Coverage Model

For the coverage model, it was assumed that every sensor node with a sensing radius r can cover an area of circular shape. Also, sensor S_i can detect a target object O_j if it is inside the sensing range of S_j. Equation (1) shows the binary model of sensor detection:

$$\mathbf{Coverage}\ (\boldsymbol{S}) \leftarrow \begin{cases} \mathbf{1}, & \mathbf{D}(\boldsymbol{S_i}, \boldsymbol{O_j}) \leq \boldsymbol{r} \\ \mathbf{0}, & \mathbf{D}(\boldsymbol{S_i}, \boldsymbol{O_j}) > \boldsymbol{r} \end{cases} \quad (1)$$

where D is the distance between the sensor node S_i and the target object being sensed O_j. When the target object can be covered or sensed, the coverage function (S) equals 1, otherwise 0.

HSA-BASED APPROACH

Harmony search algorithm (HSA) had been very effective in a wide variety of optimization problems, presenting numerous advantages compared to traditional optimization technique [26-28]. The simplicity of implementation and high quality solution of HSA highlight the potential of its usage for the systems that require improvement such as WSN.

HSA is a music-based meta-heuristic optimization algorithm. It requires fewer mathematical requirements and does not require initial value settings of the decision variables [28].
HSA has stimulated by the observation that musician intends to create a piece of music with a suitable state of harmony. This harmony in music is equivalent to find the optimal solution (i.e. global optimum) for a problem under the optimization process. HSA attains the best solution using a determined objective function that is also limited by specific constraints.

The main objective of employing the HSA in this paper is to maximize the coverage by reducing the holes that are formulated as consequence of initial deployment of the stationary nodes.
It is assumed that the base station will run the HSA after gathering the locations of the stationary sensor nodes in order to determine the number and locations of the mobile nodes as follow:

Step 1: *Define the optimization problem and initialize algorithm parameters.*

For the current problem, we have to maximize the coverage ratio of the network and minimize the number of added mobile nodes to the network, which is defined by the objective function as given in (2).

The function is used to estimate the fitness of each solution. The formulation of the fitness depends on the problem determinants. The fitness function is defined to select the best harmony for the purpose of enhancement of the next generated solutions by the HSA. The fitness function in the present problem defines the mutually exclusive coverage ratio of each mobile node. That is, the maximum number of covered targets by each mobile node that have not been uncovered by other mobile or static nodes. Such constraint to the fitness function prevents the overlapping among the

coverage regions of the deployed mobile nodes and forces each mobile node to cover only a distinct region. The fitness function of the mobile sensor node M_{Si} is $\boldsymbol{F(M_{Si})}$, that is given by:

$$\boldsymbol{F(M_{Si})} = \begin{cases} \boldsymbol{F(M_{Si})} + \boldsymbol{1}, \ \boldsymbol{D(M_{S_i}, O_j)} \leq \boldsymbol{r} \\ \quad \textbf{and } \boldsymbol{O_j} \notin \{\boldsymbol{S_C}, \boldsymbol{F(M_{S/i})}\} \\ \boldsymbol{F(M_{Si})}, \qquad\qquad \boldsymbol{Otherwise} \end{cases} \tag{2}$$

$$FR = \left(\frac{\boldsymbol{F(M_{Si})}}{\sum \boldsymbol{O_j}}\right) \% \tag{3}$$

$$\text{Coverage} = \boldsymbol{S_C} + \sum_{i=1}^{m} \boldsymbol{F(M_{Si})} \tag{4}$$

This function calculates the coverage of the $\boldsymbol{M_{Si}}$ as function of the number of covered target locations $\boldsymbol{O_j}$, provided that $\boldsymbol{O_j}$ does not belong to the coverage of any stationary node $\boldsymbol{S_C}$ or mobile node $\boldsymbol{F(M_{S/i})}$. $\boldsymbol{S_C}$ is the coverage of deployed previously stationary sensor nodes , $\boldsymbol{F(M_{S/i})}$ means the coverage of any mobile node except mobile node $\boldsymbol{i}$. In equation (3), the fitness ratio (FR) for each mobile node estimates the percentage coverage of the mobile nodes with respects to other nodes in the network, which is defined as function of its coverage $\boldsymbol{F(M_{Si})}$ and the total number of targets in the network. Furthermore, the whole coverage of the network can be estimated as an accumulation for the coverage of static nodes ($\boldsymbol{S_C}$) and the selected mobile nodes($\boldsymbol{m}$) coverage, as in (4).

The solution of the formulated problem is the (x,y) location of a potential mobile sensor node in the sensing field.

Likewise the population in GA, HSA uses a Harmony Memory Size (HMS) that contains the number of solution vectors in Harmony Memory Matrix. In our case, we initialize the HMS to 50.

In order to use this memory effectively, HSA depends on three variables to improve the solution vector, which are Harmony memory considering rate (HMCR), Pitch Adjusting Rate (PAR), and the maximum number of searches (stopping criterion) [28]. The value of HMCR is assumed to be 0.95. If HMCR rate is too low, only few elite harmonies are selected and it may converge too slowly. Otherwise, the pitches stored in the harmony memory are mostly used, and newer pitches are not explored well. The second variable, PAR, is assumed to be 0.8, which controls the pitch adjustment. Lastly, the maximum number of iterations is considered as 3000.

Step 2: *Initialize the harmony memory (HM)*

The solution of the formulated problem is the (x,y) locations of potential mobile sensor nodes. For the first time, this solution is randomly generated to initialize HM. HM with the size of HMS can be represented by (5).

$$\boldsymbol{HM} = \begin{bmatrix} \boldsymbol{I_1^1} & \boldsymbol{I_2^1} & \cdots & \boldsymbol{I_k^1} \\ \vdots & \vdots & \ddots & \vdots \\ \boldsymbol{I_1^{HMS}} & \boldsymbol{I_2^{HMS}} & \cdots & \boldsymbol{I_k^{HMS}} \end{bmatrix} \rightarrow \begin{bmatrix} \boldsymbol{F^1} \\ \vdots \\ \boldsymbol{F^{HMS}} \end{bmatrix} \tag{5}$$

Each row vector of the first matrix represents a random solution for the optimization problem under consideration, while the value of the objective function given by (4) is computed for each harmony row vector and represented by $\boldsymbol{F^j}$ in the second matrix, respectively.

Step 3: *Improvise a new harmony from the HM*

In this step, the improvisation of randomly generated solutions stored in HM shown in (5) is ensued by generating a new harmony vector $\left[\boldsymbol{I_1^`} \ \ \boldsymbol{I_2^`} \ \cdots \ \boldsymbol{I_k^`}\right]$. Each part of a new harmony vector $\boldsymbol{I_j^`}$ is generated based on the value of HMCR defined in step 1 and according to (6)

$$\boldsymbol{I_j^`} \leftarrow \begin{cases} \boldsymbol{I_j^`} \in \boldsymbol{HM} \textbf{ with probability HMCR} \\ \boldsymbol{I_j^`} \in \boldsymbol{I_j^`} \textbf{ with probability } (\boldsymbol{1 - HMCR}) \end{cases} \tag{6}$$

As in (6), the components of the new harmony vector $\boldsymbol{I_j^`}$ consist of components selected from the HM members with probability of HMCR, and others generated randomly with probability of (1-HMCR). If $\boldsymbol{I_j^`}$ is generated from the HM, then it is further amended according to PAR. The PAR determines the probability of a candidate from the HM to be modified and (1-PAR) is the probability of remaining unchanged. The Pitch adjustment for the selected is $\boldsymbol{I_j^`}$ given by (7)

$$\boldsymbol{I_j^`} \leftarrow \begin{cases} \mathbf{I_j^n} \in \textbf{ HM with probability PAR} \\ \mathbf{I_j^`} \quad \textbf{with probability } (\boldsymbol{1 - PAR}) \end{cases} \tag{7}$$

Step 4: *Update the HM*

The generated vector from step3 and 4 is evaluated based on the objective function value, and compared to the worst harmony vector in the HM. If the objective function value for the new harmony vector is better than the objective function value for the worst harmony in the HM then new Harmony is placed in the HM and the existing worst harmony is excluded from the HM. Otherwise, no changes would happen to the content of HM.

Step 5: *Go to step 3 until termination criterion is reached.*

After the termination criterion is reached, the current best solution is chosen from the HM to

represent the solution for the articulated optimization problem.

SIMULATION RESULT AND DISCUSSION

In this section, the performance of the proposed algorithm is evaluated and compared against genetic algorithm (GA) in [23], in terms of coverage ratio, degree of coverage (k-coverage), and number of additional mobile nodes. Moreover, the effect of the number of randomly deployed static nodes and the sensing ranges on coverage and number of additional mobile nodes were investigated.

In the simulation environment, it was assumed that the sensor nodes were randomly deployed and the targets were uniformly located in a 200 m x 200 m sensor field. Two simulation experiments were conducted for performance evaluation. In the first experiment, the number of deployed static nodes ranged from 100 to 200 to cover 625 targets, whereas the sensing ranges of all nodes are fixed to 12 m. In the second experiment, the number of deployed static nodes is fixed to 100, while the sensing ranges ranged from 10 m to 20 m. In each experiment, the coverage ratio, k-coverage, and number of extra mobile nodes were measured before and after applying both the HSA and the GA in [23].

Effect of Number of Static Nodes

It is most likely that the coverage ratio of the network increases as the number of deployed nodes increases, either these nodes static or mobile nodes. Both GA and HSA schemas propose deploying additional mobile nodes alongside the static nodes to improve the network's coverage. The figure compares the coverage ratio of GA and HSA schemas. Both schemas enhance network coverage as the additional mobile nodes are located into regions where targets are not covered by the static nodes.

However, the achieved coverage ratio of HSA schema outperforms the case of GA schema. For instance, if the number of statically deployed nodes is 160, then the coverage of the network is 79.5%. In such case, GA increases the coverage ratio to 91.8%, whereas HSA schema causes 96.2%, as shown in Fig. 1. According to the numerical results, the percentage improvements on the coverage ratio of HSA schema compared to GA schema reach up to 4.57%. The reason behind that is due to trapping the evolving solutions in GA biased local optima. On the other hand, the stochastic components of HSA lead to tactical exploration for many locations and regions where targets are not covered by the static nodes, as possible in an efficient and effective manner.

Figure 2 shows the number of additional mobile nodes for both schemas. As shown, the number of mobile nodes drops as the number of statically deployed nodes goes up. This is because more targets would be covered as the number of static nodes increases and hence less mobile nodes would be added to increase the coverage ratio.

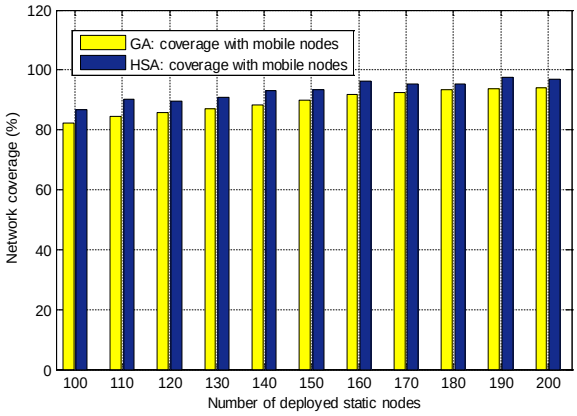

Fig. 1: Comparison of coverage ratio for different number of deployed nodes.

Despite the fact that both GA and HSA schemas ensure to find the minimum number of mobile nodes to be added to the network for improving the coverage, there is a slight increasing in the number of mobile nodes in HSA schema. The petty increasing in the mobile nodes is beneficial for enhancing the part of the coverage that could not be obtained through GA schema. For instance, if the number of statically deployed nodes is 160, the number of added mobile nodes in GA is 28, whereas it is about 30 nodes in HSA schema. The disjoint coverage of the part of increasing is about 1.15%, (i.e., the coverage of surplus two nodes added in HSA), whereas the real percentage of improvement for HSA compared to GA is 4.57%, which means that HSA is more robust and efficient than GA.

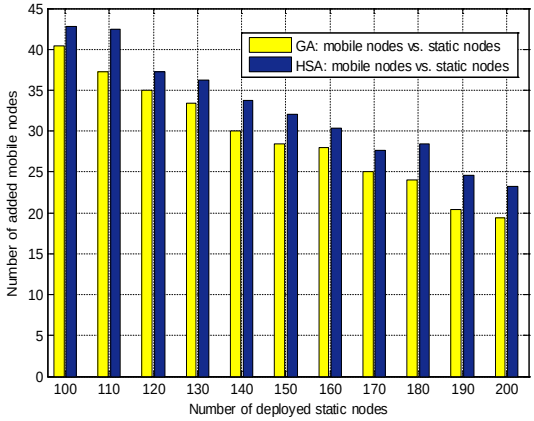

Fig. 2: Number of additional mobile nodes versus number of static nodes

Figure 3 shows the k-coverage after adding the mobile nodes to the randomly deployed static nodes in the network. For both cases, it is shown that as the number of nodes increases, the k-coverage increases. This is because the static nodes in both cases are randomly deployed and it is very likely that the

coverage among these nodes is overlapped, hence the targets would be covered by more sensor nodes as the number of static nodes increases. What is more, the k-coverage for both schemas is close to each other, despite the increasing in mobile nodes for HSA. For instance, if the number of statically deployed nodes is 160, the k-coverage in GA is 2.19, whereas it is about 2.17 in HSA schema. That is a proof that few and extra mobile nodes added by HSA is not arbitrary, but it is intended for covering the holes in the network.

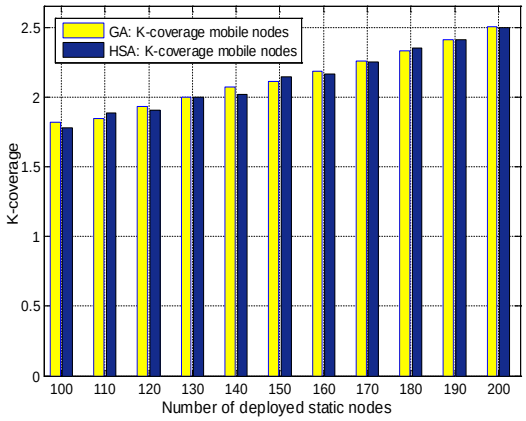

Fig. 3: Comparison of k-coverage for different number of deployed nodes.

Effect of Sensing Range

Figure 4 compares the coverage ratio for GA and HSA schemas in terms of sensing range. Both GA and HSA schemas propose deploying additional mobile nodes alongside the static nodes to improve the network's coverage. The evaluation HSA conducted when the static nodes are randomly deployed and after adding the mobile nodes to the network.

It is shown that the coverage ratio increases as the sensing radii of the deployed nodes increase, since sensor nodes with larger sensing range can cover more targets than that with smaller range. The coverage of the static nodes along with the additional mobile nodes clearly outperforms the case of random deployment of the static nodes as the additional mobile nodes are located into regions where targets are not covered by the static nodes.

However, the achieved coverage ratio of HSA schema outperforms the case of GA schema. For instance, if the sensing radius of the deployed nodes is 15m, then the overall coverage ratio of statically deployed nodes is about 80%. In such case and after adding the mobile nodes, GA increases the coverage ratio to 93.22%, whereas HSA schema causes 97.12%. According to the numerical results, the percentage improvements on the coverage ratio of HSA schema compared to GA schema reach up to 4 %.

Figure 5 shows the number of additional mobile nodes for both schemas as a function of the sensing range. It is shown that the number of mobile nodes drops as the sensing radii of the nodes rise. This is because more targets would be covered as the sensing range of the static nodes goes up and hence less mobile nodes would be added to increase the coverage ratio.

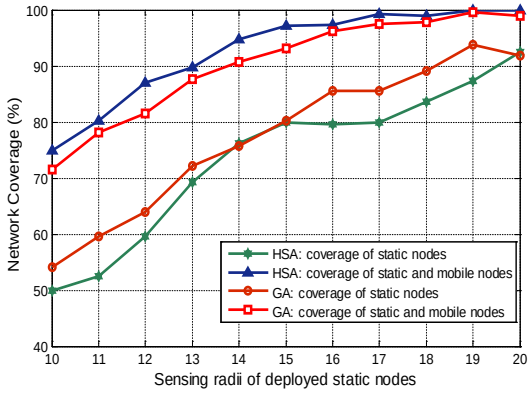

Fig. 4: Comparison of coverage ratio for different sensing ranges.

As stated before in the discussion of Fig. 2, in spite of the slight increasing in the number of mobile nodes in HSA schema, both GA and HSA schemas ensure to find the minimum number of mobile nodes to be added to the network for improving the coverage. However, the minor increasing of the mobile nodes in HSA is advantageous for enhancing the part of the coverage that could not be achieved via GA schema.

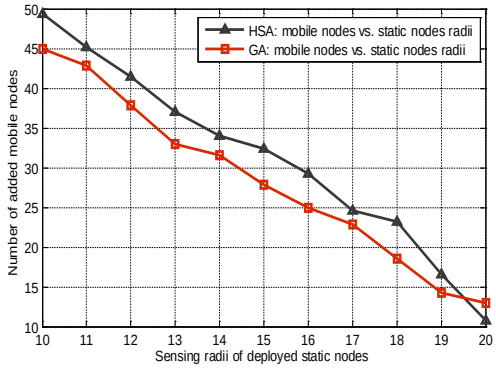

Fig. 5: Number of Additional mobile nodes versus sensing ranges.

Figure 6 shows the k-coverage for GA and HSA when the static nodes are randomly deployed and after adding the mobile nodes as a function of the sensing ranges. As shown, the k-coverage increases as the sensing radii of the deployed nodes increase. This is because the coverage among sensor nodes with large sensing range is very likely to overlap, and hence more targets would be covered by multiple nodes. Furthermore, the k-coverage for

both schemas overlaps to each other, despite the increasing in mobile nodes for HSA. For example, if the sensing radius of the deployed nodes is 15m, the k-coverage in GA is 2.31, whereas it is about 2.28 in HSA schema. The closeness between them is a proof that extra mobile nodes added via HSA is absolutely

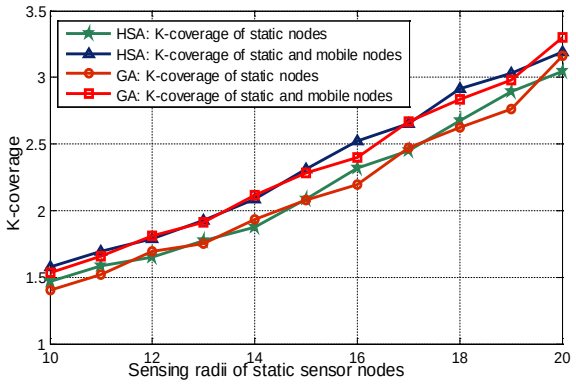

Fig 6: Comparison of k-coverage for different sensing ranges

not arbitrary, but it is intended for covering more holes in the network.

CONCLUSION

In this paper, we present a method that tackles the coverage holes problem in hybrid WSN. This method employs HSA to find an optimal solution to the coverage holes problem caused by random deployment of stationary sensor nodes.

The results of employing HSA have proofed that it explores more regions in an efficient and effective manner where the holes could not be discovered by other solutions. Our simulation results have shown that node deployments based HSA maximize the overall coverage by finding the lowest number of further mobile nodes and their best positions in the sensing field when compared with the state-of-the-art algorithms like GA. Generally, it can be concluded that the HSA simplicity of implementation and high quality solution make it proper for solving complex engineering optimization problems.

REFERENCES

[1] F. Akyildiz, W. Su, Y. Sankarasubramaniam and E. Cayirci, “Wireless Sensor Networks: A Survey,” Computer Networks, Vol. 38, No. 4, 2002, pp. 393-422.

[2] B. Wang, “Coverage Problems in Sensor Networks: A Survey,” ACM Computing Surveys, Vol. 43, No. 4, 2011, 53 p.

[3] M. Younis and K. Akkaya, “Strategies and Techniques for Node Placement in Wireless Sensor Networks: A Survey,” Ad Hoc Networks, Vol. 6, No. 4, 2008, pp. 621-655.

[4] Howard, M. J. Mataric, and G. S. Sukhatme, “Mobile Sensor Network Deployment using Potential Fields: A Distributed, Scalable Solution to the Area Coverage Problem,” Proceedings of 6th International Symposium on Distributed Autonomous Robotics Systems, Fukuoka, 25-27 June 2002, pp. 299-308.

[5] Y. Zou and K. Chakrabarty, “Sensor Deployment and Target Localization in Distributed Sensor Networks,” ACM Transactions on Embedded Computing Systems, Vol. 3, No. 1, 2004, pp. 61-91.

[6] D. E. Goldberg and J. H. Holland. “Genetic Algorithms and Machine Learning,” Machine Learning, Vol. 3, No. 2, 1988, pp. 95-99.

[7] G. Wang, G. Cao and T. Porta, “Movement-Assisted Sensor Deployment,” IEEE Transactions on Mobile Computing, Vol. 5, No. 6, 2006, pp. 640-652.

[8] Tahiri, E. Egea-López, J. Vales-Alonso, J. GarcíaHaro and M. Essaaidi, “A Novel Approach for Optimal Wireless Sensor Network Deployment,” Proceedings of Symposium on Progress in Information & Communication Technology (SPICT’09), Kuala Lumpur, 7-8 December 2009, pp. 40-45.

[9] G. Wang, G. Cao, P. Berman and T. Porta, “Bidding Protocols for Deploying Mobile Sensors,” IEEE Transactions on Mobile Computing, Vol. 6, No. 5, 2007, pp. 515-528.

[10] N. Ahmed, S. Kanhere and S. Jha, “A Pragmatic Approach to Area Coverage in Hybrid Wireless Sensor Networks,” Wireless Communications and Mobile Computing, Vol. 11, No. 1, 2011, pp. 23-45.

[11] X. Wang and S. Wang, “Hierarchical Deployment Optimization for Wireless Sensor Networks,” IEEE Transactions on Mobile Computing, Vol. 10, No. 7, 2011, pp. 354-370.

[12] G. Wang, L. Guo, H. Duan, L. Liu and H. Wang, “Dynamic Deployment of Wireless Sensor Networks by Biogeography Based Optimization Algorithm,” Journal of Sensor and Actuator Networks, Vol. 1, No. 2, 2012, pp. 86-96.

[13] T. Kalayci and A. Ugur, “Genetic Algorithm-Based Sensor Deployment with Area Priority,” Cybernetics and Systems, Vol. 42, No. 8, 2011, pp. 605-620.

[14] X. He, X. Gui and J. An, “A Deterministic Deployment Approach of Nodes in Wireless Sensor Networks for Target Coverage,” Journal of Xi’an Jiaotong University, No. 6, 2010, pp. 6-9.

[15] Y. Xu and X. Yao, “A GA Approach to the Optimal Placement of Sensors in Wireless Sensor Networks with Obstacles and Preferences,” Proceedings of 3rd IEEE Consumer Communications and Networking

Conference, Las Vegas, 8-10 January 2006, pp. 127-131.

[16] J. Seo, Y. Kim, H. Ryou and S. Kang, "A Genetic Algorithm for Sensor Deployment Based on Two-Dimensional Operators," Proceedings of 2008 ACM Symposium on Applied Computing, Fortaleza, 16-20 March 2008, pp. 1812-1813.

[17] Tripathi, P. Gupta, A. Trivedi and R. Kala, "Wireless Sensor Node Placement using Hybrid Genetic Programming and Genetic Algorithms," International Journal of Intelligent Information Technologies, Vol. 7, No. 2, 2011, pp. 63-83.

[18] K. S. Yildirim, T. E. Kalayci and A. Ugur, "Optimizing Coverage in a K-Covered and Connected Sensor Network using Genetic Algorithms," Proceedings of the 9th WSEAS International Conference on Evolutionary Computing (EC'08), Sofia, 2-4 May 2008, pp. 21-26.

[19] C. Sahin, et al., "Design of Genetic Algorithms for Topology Control of Unmanned Vehicles," International Journal of Applied Decision Sciences, Vol. 3, No. 3, 2010, pp. 221-238.

[20] Y. Qu and S. Georgakopoulos, "Relocation of Wireless Sensor Network Nodes using a Genetic Algorithm," Proceedings of 12th Annual IEEE Wireless and Microwave Technology Conference (WAMICON), Clearwater Beach, 18-19 April 2011, pp. 1-5.

[21] F. Nematy, N. Rahmani and R. Yagouti, "An Evolutionary Approach for Relocating Cluster Heads in Wireless Sensor Networks," Proceedings of International Conference on Computational Intelligence and Communication Networks (CICN), Bhopal, 26-28 November 2010, pp. 323-326.

[22] N. Rahmani, F. Nematy, A. Rahmani and M. Hosseinzadeh, "Node Placement for Maximum Coverage Based on Voronoi Diagram using Genetic Algorithm in Wireless Sensor Networks," Australian Journal of Basic and Applied Sciences, Vol. 5, No. 12, 2011, pp. 3221-3232.

[23] O. Banimelhem, M. Mowafi and W. Aljoby, "Genetic Algorithm Based Node Deployment in Hybrid Wireless Sensor Networks," Communications and Network, Vol. 5 No. 4, 2013, pp. 273-279. doi: 10.4236/cn.2013.54034.

[24] Panov, Stojanche, and Saso Koceski. "Area coverage in wireless sensor network by using harmony search algorithm." Embedded Computing (MECO), 2014 3rd Mediterranean Conference on. IEEE, 2014.

[25] Z.W. Geem, J.H. Kim, G.V. Loganathan, "A new heuristic optimization algorithm: harmony search, Simulation Vol. 76 (2), pp. 60-68, 2001.

[26] ZongWoo Geem, Music-Inspired Harmony Search Algorithm", Springer,2008.

[27] K.S. Lee, Z.W. Geem, A new meta-heuristic algorithm for continues engineering optimization: harmony search theory and practice, Comput. Meth. Appl. Mech. Eng. 194, pp. 3902-3933, 2004.

[28] Hoang, D.C.; Yadav, P.; Kumar, R.; Panda, S.K., "A Robust Harmony Search Algorithm Based Clustering Protocol for Wireless Sensor Networks," Communications Workshops (ICC), 2010 IEEE International Conference on , vol., no., pp.1,5, 23-27 May 2010

First International Conference on Science, Engineering & Environment,
Tsu City, Mie, Japan, Nov.19-21, 2015, ISBN: 978-4-9905958-5-2 C3051

THE EFFECT OF FERTILIZER ON GROWTH OF STAGHORN FERN AT SEEDLING STAGE

Sawat Pimsuwan[1], Preeyanat Hongthong[1], Phattraporn Krangpanich[1] and Cholthicha Suwanpinta[1]
[1] Faculty of Agricultural Technology, Rajamangala University of Technology Thanyaburi, Thailand.

ABSTRACT

The effects of two fertilizer types with 3 concentrations on growth of staghorn fern (*Platycerium coronarium*) were studied. This experiment was conducted at the nursery of Division of Crop Production, Faculty of Agricultural Technology, Rajamangala University of Technology Thanyaburi, during October and December 2013. It was laid out in a RCBD with 4 replications and consisted of seven treatments. The treatments were application of: water, a 21-21-21 fertilizer with the concentration of 0.5 g/l, 1.5 g/l, 3g/l, Bio-fertilizer with the concentration of 1 ml/l, 2 ml/l and 3 ml/l of water. Leaf length, leaf width and canopy width of the ferns were measured. The data were subjected to ANOVA, followed by Duncan's Multiple Range Test at 5% level of significance. No significant difference among treatments was found. However, the water showed the best result. It gave 108.79 mm average canopy width, 3.13 mm average leaf length and 89.67 mm average leaf width.

Keywords:fertilizer, fertilizer on Growth of Staghorn fern, Staghorn fern, Platycerium coronarium

1. INTRODUCTION

Ferns are categorized in vascular plants in terms of epiphyte diversity [2], which are important in many aspects, especially in ornamental and gardening purposes. Currently, a trend of popularity for both local and international is moving toward more fern species. Staghorn fern (*P. coronarium)* is one of them. Probably, its rareness and typical form play a role on this matter. Streaky leaf hanging down is very unique to this fern. Moreover, some leaves appear in antler-like form. In the forest, this fern is a good indicator for forest richness. In a garden, by having impressively large leaves, it gives an impression of having a naturally rich forest at home. Moreover, its rareness gives an exotic phenomena and of course, a high price. Due to its price, smuggling this fern from the wild for sale is a major problem [6]. On the other hand, weather may be another factor that causes the decreasing in number of staghorn fern. It may not be suitable for the spore germination and the fern growth for some reasons. Now, the staghorn fern is endangered. To increase the number of staghorn ferns to meet market demand [3] and also reduce the smuggling amount from the forest, any attempt to reproduce this fern would be favorable. To achieve this goal, at least, nursery conditions should mimic the natural condition as much as possible. The key issue is to reduce the mortality of fern seedlings. Currently, many staghorn-fern growers attempt to grow them form the spores, but the survival rate of the seedlings requires some improvement. Also, an appropriate fertilizer for them need to be determined. Therefore, it is important to find out suitable types and rate of fertilizers for staghorn fern in seedling stage.

2. MATERIALS AND METHODS

2.1 Materials

Some 200 staghorn fern (*P. coronarium)* seedlings with a true leaf (sporophyte stage, 1 centimeter) are transplanted onto a peat moss basket for one month. Some of these seedlings were chosen for the experiment when they reached stage 2 or about four months old. Typically, seedlings at this stage pose rounded leaves with the size of 2.5 cm. The selected seedlings were transferred onto individual pots with planting media. The planting media were prepared from roots of *Asplenium nidus* fern and coconut husk chips. Firstly, the fern roots were chopped into small pieces and soaked in water. The two materials were then mixed and after further soaking the mix was filled into pots. Each experimental pot was placed into a clear plastic bag. The bags were tightly tied up and hung on bars (Fig. 8). This procedure was for controlling humidity.

2.2 Experimental design

Experimental design was randomized complete block design (RCBD) with 7 treatments in 4 blocks (replications). The 21-21-21 pellet fertilizer and liquid bio-fertilizer were used as the experimental treatments: 1) water, 2) diluted pellet fertilizer at 0.5 g/a liter of water, 3) diluted pellet fertilizer 1.5 g/a liter of water, 4) diluted pellet fertilizer 3 g/a liter of

water, 5) diluted bio fertilizer at 1 ml/a liter of water, 6) diluted bio fertilizer at 2 ml/a liter of water and 7) diluted bio fertilizer at 3 ml/a liter of water. The fertilizer solution was sprayed onto the plants at a rate of 2 ml/plant once a week.

2.3 **Data analysis**

Statistical analysis was performed using analysis of variance procedure (ANOVA). Duncan's new multiple range test (DMRT) at the significant level of 0.05 was used to compare differences among means.

3. RESULTS

The staghorn ferns grown with water (Trt1) demonstrated the highest growth among treatments. In average, their canopy width was 108.79 mm, leaf width was 89.67 mm, leaf length was 73.13 mm and leaf numbers were 3.33 leaves (Table 1).

Table 1 The growth of staghorn fern (*P. coronarium*) in seedling stage at week 9

Treatment	Average growth of *P. coronarium*			
	canopy width (mm)	leave width (mm)	leave length (mm)	leave number
1	108.79	89.67	73.13	3.33
2	91.94	71.42	61.16	3.42
3	79.23	61.14	51.55	2.83
4	96.29	76.57	64.00	3.08
5	98.76	72.18	62.57	2.67
6	102.61	73.57	61.40	3.08
7	98.21	80.23	67.04	2.58
CV (%)	12.23	14.77	14.55	21.30
F-test	ns	ns	ns	ns

Figures

Figure 1-7 show the growth of *P. coronarium* at the 9th week, from treatments (Trt) 1-7.

Fig.1 Trt1

Fig.2 Trt2

Fig.3 Trt3

Fig.4 Trt4

Fig.5 Trt5

Fig.6 Trt6

Fig.7 Trt7

Fig.8 Hanging of the experimental pots

4. DISCUSSION

All levels of both fertilizers were inferior to water probably due to some toxic effects. One of known toxicity causes by nitrogen so called Biuret. This effect was expected to be the case in this study as it was consistent with a germinating experiment in corn. The corn germination was restrained by NH_3 gas[1]. In another experiment, urea could generate high biuret even only placed nearby. It was suggested that urea gave rise to NH_3 during its degeneration process, and that affected the germination.
In case of seedling plants, the biuret effect may be more serious [4]. Therefore, taking a good consideration on biuret is important for staghorn fern in seedling stage, especially in a closed system. Furthermore, any fertilizer is not recommended.

Timing for removing the staghorn-fern seedlings from the plastic bags is also important. Basically, it may be done when the crown leave reach a diameter of 9.0-10.0 cm. However, in a greenhouse equipped with humidity and sunlight control, the seedlings can removed when the crown leaf has a diameter of 3 cm, approximately [5]. The sporophyte transplanting in the greenhouse has a survival rate of 100% of spores [7].

5. ACKNOWLEDGEMENTS

This research was partially funded by The Faculty of Agricultural Technology, Rajamangala University of Technology Thanyaburi, Thailand.

6. REFERENCES

[1]Chiarawipa R, Rueangkhanab M. and Chantanaorrapint A., Ferns Diversity and Growth Development of Staghorn Fern (*Platycerium coronarium* J.G. Koen.ex. Muell, Desv) Under Oil Palm Plantation, King Mongkut's Agricultural Journal, 30(1) Jan-May. 2555 pp. 32-42[5]

[2]Dubuisson J., Schneider H. and Hennequin S., Epiphytism in ferns: diversity and history. Science Direct. Vol. 332, Issues 2–3, February–March 2009, Pages 120–128[7]

[3]Hunter A. S.and Rosenau W.A., "The Effects of Urea, Biuret, and Ammonia on Germination and Early Growth of Corn (*Zea mays* L.)", Soil Science Society of America. Published: Jan,1966, p. 77-81[1]

[4]Mikkelsen R.L., "Biuret in Urea Fertilizers (North America)", Better Crops with Plant Food, Vol. XCI (91) No. 3, 2007[2]

[5]Sangdanuch P., Platycerium, Bangkok: Amarin printing, 2011, pp.158 [4]

[6]Thongtham C. and Suksathan P., FERNS, Bangkook : Sarakadee Publisher,1997[3]

[7]Wu H. , Liu X, Ji H. and Chen L., Effects of light, macronutrients, and sucrose on germination and development of the endangered fern *Adiantum reniforme* var. *sinense* (Adiantaceae). Scientia Horticulturae . Vol. 125, Issue 3, June 2010, Pages 417–421[6]

First International Conference on Science, Engineering & Environment,
Tsu City, Mie, Japan, Nov.19-21, 2015, ISBN: 978-4-9905958-5-2 C3051

IMMEDIATE EFFECTS OF ONE AND TWO HOURS OF TRADITIONAL THAI MASSAGE ON STRESS, HEART RATE VARIABILITY, AND AUTONOMIC NERVOUS SYSTEM FUNCTION

Thanarat Sripongngam[1,2], Wichai Eungpinichpong[2], Dhavee Sirivongs[3], Jaturat Kanpittaya[4], and Kamonwan Tangvoraphonkchai[5]

[1] Department of Health and Sport Science, Faculty of Education, Mahasarakham University, Thailand;
[2]Research Center in Back, Neck, Other Joint Pain and Human Performance, Khon Kaen University, Thailand;
[3]Department of Medicine, Faculty of Medicine, Khon Kaen University, Khon Kaen, Thailand;
[4]Department of Radiology, Faculty of Medicine, Khon Kaen University, Khon Kaen, Thailand;
[5]Faculty of Medicine, Mahasarakham University, Mahasarakham, Thailand

ABSTRACT

The purpose of this study was to investigate the immediate effects of different duration of treatment by traditional Thai massage (TTM) on stress, heart rate variability (HRV) and autonomic nervous system (ANS) function. Seventeen healthy participants were randomly allocated to receive either 1 hour of TTM (1-TTM) group or 2 hour of TTM (2-TTM) group after which they were swabbed to receive the other one with a 2 - weeks washed out period. Stress, HRV, and ANS function were measured at before and immediately after the TTM treatment. Within-groups comparison demonstrated that stress index was decreased ($p<0.05$) in both groups, stress resistance, the standard deviation of the normal-to-normal intervals (SDNN) and root mean square of successive differences (RMSSD) were increased ($p<0.05$) in both groups, low frequency per high frequency (LF/HF) ratio was decreased ($p<0.05$) in 1-TTM group, HF and ANS activity were increased ($p<0.05$) in 1-TTM group, whereas LF and ANS balance status were not changed in both groups. However, all of them were not significant difference for between groups comparison. We concluded that a single session of either 1 or 2 hours of TTM could decrease stress and increase heart rate variability whereas only the 1-hour TTM could increase ANS function.

Keywords: Massage, Stress, Heart Rate Variability, Autonomic Nervous System

Corresponding author**:**
Wichai Eungpinichpong, Department of Physical Therapy, Faculty of Associated Medical Science, Khon Kaen University, 123 Moo 16 Mittraphap Road, Meuang District, Khon Kaen, 40002, Thailand. Tel. +66 81 7494748, Fax. +66 43 202399, +66 43 347482, E-mail. wiceun@yahoo.com

INTRODUCTION

Massage is an alternative treatment and may provide many benefits on health. Many previous studies found that massage could increase skin temperature and blood flow [1]-[3], decrease anxiety [4]-[7], decrease depression [7], decrease pain, improve sleep quality [5], [8], increase renal blood flow [9], decrease sympathetic nervous activity and increase parasympathetic activity [10]-[11], increase weight gain in infant [12], decrease cortisol levels [10], [13], and decrease stress [14]-[15].

Traditional Thai massage (TTM) is a deep acupressure type of massage that has been commonly used in Thailand because it is simple to practice and suit Thai culture. The previous studies showed that TTM could decrease spasticity, increase functional ability, improve quality of life [16], increase bone formation [17], decrease anxiety, decrease pain [18]-[19], decrease muscle tension [18], increase flexibility, and increase parasympathetic activity [19]. Routine practice of TTM may last 1 - 2 hours depends on available time of clients. Since this is a time consuming method of treatment, we doubt that 1-hour and 2 hours may yield different results in terms of mental stress, heart rate variability (HRV), and autonomic nervous system (ANS) function. Therefore, this study aimed to examine the immediate effects of different duration of treatment by TTM on stress, HRV, and ANS function in healthy subjects.

MATERIAL AND METHOD

This study was a crossover randomized controlled trial, approved by the Ethical Committee of Mahasarakham University, Thailand (272/2557). Twenty participants were recruited in this study but three of them dropped out at the beginning of the study because of illness. The remaining participants

consisted of seventeen healthy participants included 6 males, 11 female, average aged 20.53±1.37 years completed all the procedures. They were randomly allocated into either a 1-hour of TTM (1-TTM) group or a 2-hour of TTM (2-TTM) group after which they were swabbed to the other one with 2 weeks washed out period. Each of them gave written informed consent to participate in this study. The participants were excluded from the study if they had any kind of medication or other medical treatment, moderate to severe muscle or joint pain, impaired skin sensation or hypersensitivity to massage, history of serious disease that must be treated by a doctor. The participants were advised to refrain from eating, drinking alcohol, smoking, and foods containing caffeine, at least 2 hours before participating in this study. Mental stress parameter consisted of stress index and stress resistance, heart rate variability (HRV) consisted of the standard deviation of the normal-to-normal intervals (SDNN), root mean square of successive differences (RMSSD), low frequency per high frequency (LF/HF) ratio, HF, and LF, autonomic nervous system (ANS) function consist of ANS activity and ANS balance status were measured at before and immediately after the TTM treatment.

Procedure and Protocol

The participants received a 1-hr or a 2-hrs session of the TTM which was applied along the Thai meridian lines (Fig. 1) with moderate thumb and palm pressure on each of the body parts including lower limbs, back, neck, head, and upper limbs. The massage was performed in supine, side lying on the left, and on the right positions. Passive stretch for the corresponding muscle groups was performed at the end of massage for each body part.

Mental stress, HRV, and ANS function were measured by SA-3000P (Medicore Co., LTD., Korea) using standard procedure recommended in the SA-3000P operation manual version 2.8. The participants sat on a comfortable chair with a backrest and eyes opened and breathed normally throughout the 5 minutes of data collection.

Stress parameters including stress index and stress resistance were used to assess ANS function. Stress index presents the level of stress in the body. Stress resistance indicates the adaptability of the body against the stress. HRV parameters consisted of the standard deviation of the normal-to-normal intervals (SDNN), root mean square of successive differences (RMSSD) were used to assess ANS activity. High frequency (HF) reflected parasympathetic tone, whereas low frequency (LF) reflected the combination of both sympathetic and parasympathetic tones. LF response to the increase in baroreflex function [20]-[21], which increased baroreflex causing an increase parasympathetic activity and decrease sympathetic activity for maintain homeostasis in the body. Increasing or decreasing HF and LF reflects the ability of the body to maintain ANS balance [22].

The low frequency per high frequency (LF/HF) ratios was used to assess ANS balance. ANS activity and ANS balance status were used to determine ANS function [22]-[23].

Increased stress resistance, SDNN, RMSSD, HF, and ANS activity, decreased stress index, and LF/HF ratio, indicated increased parasympathetic activity. On the other hand, decreased stress resistance, SDNN, RMSSD, HF, and ANS activity, increased stress index, and LF/HF ratio indicated an increased sympathetic activity [22]-[23].

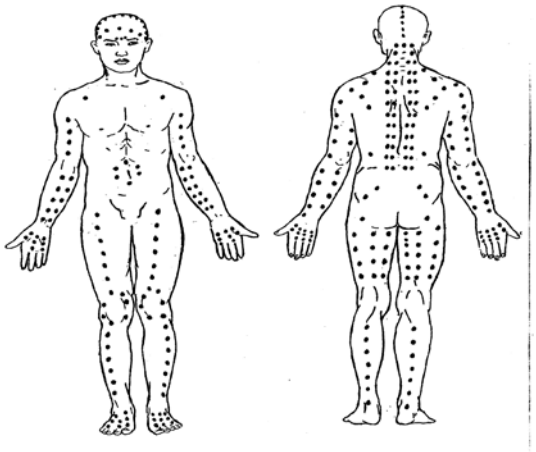

Fig. 1 The massage points on the meridian lines of TTM as depicted by Wichai Eungpinichpong [24]

Statistical analysis

The data were presented as mean ± SD. Shapiro-Wilk Test was used to verify normal distribution. Paired t-test and Wilcoxon Sign Rank-Test were used to compare the outcome variables at before and after TTM treatment within group. Unpaired t-Test and Mann Whitney U-Test were used to compare outcome variables between groups. Statistical significance was set at the $p < 0.05$.

RESULTS

Within-groups comparison of the means between before and after TTM treatment revealed that

stress index was significantly decreased after massage (p = 0.026 and p = 0.019 in 1-TTM and 2-TTM groups, respectively). Stress resistance was significantly increased (p = 0.033 and p = 0.021 in 1-TTM and 2-TTM groups, respectively). SDNN was significantly increased (p = 0.047 and p = 0.006 in 1-TTM and 2-TTM groups, respectively). RMSSD was significantly increased (p = 0.001 and p = 0.001 in 1-TTM and 2-TTM groups, respectively). However, the authors also found significant decrease in LF/HF ratio (p = 0.017), significant increase in HF (p = 0.001), and significant increase in ANS activity (p = 0.03), only in the 1-TTM group. Whereas, the LF and ANS balance status were not changed in both groups (Table 1). All parameters showed no significant differences for between the groups comparison.

Table 1 Comparison on the stress, HRV and ANS function between before and after TTM treatment in 1-TTM group.

outcome	1-TTM group (n = 17)	
	before mean±SD	after mean±SD
Stress index	91.20±13.94	85.53±8.92*
95%CI	83.48, 98.92	80.59, 90.47
Stress resistance	106.33±23.68	113.40±17.86*
95%CI	93.22, 119.45	103.51, 123.29
SDNN	55.65±26.03	69.06±21.96*
95%CI	42.26, 69.03	56.90, 81.23
RMSSD	44.40±19.33	60.78±24.01**
95%CI	34.46, 54.34	48.43, 73.12
LF	6.55±1.04	6.54±0.80
95%CI	5.98, 7.13	6.10, 6.99
HF	5.94±0.75	6.45±0.83**
95%CI	5.55, 6.33	6.02, 6.87
LF/HF ratio	2.28±1.83	1.26±0.88*
95%CI	1.27, 3.30	0.77, 1.75
ANS activity	98.51±13.35	108.75±14.10*
95%CI	91.12, 105.91	100.95, 116.56
ANS balance status	42.49±32.07	43.93±39.86
95%CI	24.73, 60.24	21.85, 66.00

Note: HRV=heart rate variability, ANS=autonomic nervous system, 1-TTM=one hour of traditional Thai massage, SDNN=the standard deviation of the normal-to-normal intervals, RMSSD=root mean square of successive differences, LF=low frequency, HF=high frequency

*Significant difference at *p*-value <0.05

**Significant difference at *p*-value <0.01

Table 2 Comparison on the stress, HRV and ANS function between before and after TTM treatment in 2-TTM group.

outcome	2-TTM group (n = 17)	
	before mean±SD	after mean±SD
Stress index	93.80±9.21	87.47±11.07*
95%CI	88.70, 98.90	81.34, 93.60
Stress resistance	100.20±14.19	110.13±15.64*
95%CI	92.34, 108.06	101.47, 118.80
SDNN	48.61±17.04	64.50±18.74**
95%CI	39.85, 57.37	54.13, 74.88
RMSSD	41.23±18.27	52.26±17.19**
95%CI	31.83, 50.62	43.42, 61.10
LF	6.30±0.96	6.45±0.66
95%CI	5.77, 6.83	6.08, 6.82
HF	5.92±0.67	6.16±0.82
95%CI	5.58, 6.26	5.74, 6.59
LF/HF ratio	1.90±1.23	1.70±1.29
95%CI	1.22, 2.58	0.99, 2.41
ANS activity	99.58±20.08	103.56±18.87
95%CI	88.46, 110.70	93.11, 114.01
ANS balance status	40.74±29.68	45.64±33.01
95%CI	24.30, 57.18	27.36, 63.92

Note: HRV=heart rate variability, ANS=autonomic nervous system, 2-TTM=two hours of traditional Thai massage, SDNN=the standard deviation of the normal-to-normal intervals, RMSSD=root mean square of successive differences, LF=low frequency, HF=high frequency

*Significant difference at *p*-value <0.05

**Significant difference at *p*-value <0.01

DISCUSSION

The present study showed that both one and two hours of TTM could decrease stress index, increase stress resistance, SDNN, and RMSSD. Only one hour of TTM could increase HF and ANS activity and decrease LF/HF ratio. Whereas, LF and ANS balance were not significantly changed in both groups. However, all of these measures were found not significant difference when groups were compared. The finding of the present study demonstrated that TTM could increase parasympathetic activity indicated by increased SDNN, RMSSD, HF, ANS activity, decreased LF/HF ratio, and decreased sympathetic activity indicated by decreased stress index and increased stress resistance. The results of this study were

consistent with the previous studies [4], [10], [11], [19]. They found 20 minutes of light pressure of hand massage, a 30-minutes session of TTM on to the back muscles, 80 min of touch massage (stroking) of the hands and feet, and a 5-minute hand holding could increase parasympathetic activity and decrease sympathetic activity, respectively.

The current study found that HF and ANS activity were increased and LF/HF ratio was decreased in only one hour of TTM but not in two hours of TTM. It could be explained that all of the participants were people who are healthy and a two hours of TTM was long enough for the body to rebalancing the functions of the autonomic nervous system to return to normal. Therefore, it can be seen that one hour of massage provides more effective than two hours of massage.

The LF and ANS balance status were not significantly changed after both TTM treatments for maintaining the balance between sympathetic and parasympathetic activity.

CONCLUSION

The present study demonstrated that a single session of either 1-hr or 2-hrs of TTM could increase parasympathetic activity and decrease sympathetic activity as indicated by decreased stress and increased HRV. However, only 1-hr session of TTM could increase ANS function. We suggest that 1-hr session of TTM is sufficient to provide favorable results on reducing mental stress and increase ANS activity.

ACKNOWLEDGEMENTS

The authors would like to thank the volunteers who participated in the study. Our special thanks to Research Center in Back, Neck, Other Joint Pain and Human Performance, Khon Kaen University for financially supporting this study.

REFERENCES

[1] Zhang W, Takahashi S, Miki T, Fujieda H, Ishida T, “A pilot study exploring the effects of reflexology on cold intolerance”, J Acupunct Meridian Stud, Vol. 3(1), Mar. 2010, pp. 43–48.

[2] Hinds T, McEwan I, Perkes J, Dawson E, Ball D, George K, “Effects of massage on limb and skin blood flow after quadriceps exercise”, Med Sci Sports Exerc, Vol. 36(8), Aug. 2004, 1308–1313.

[3] Mori H, Ohsawa H, Tanaka TH, Taniwaki E, Leisman G, Nishijo K, “Effect of massage on blood flow and muscle fatigue following isometric lumbar exercise”, Med Sci Monit, Vol. 10(5), May 2004, pp. CR173–178.

[4] Kunikata H, Watanabe K, Miyoshi M, Tanioka T, “The effects measurement of hand massage by the autonomic activity and psychological indicators”, J Med Invest, Vol. 59(1-2), 2012, pp. 206–212.

[5] Castro-Sánchez AM, Matarán-Peñarrocha GA, Granero-Molina J, Aguilera-Manrique G, Quesada-Rubio JM, Moreno-Lorenzo C, “Benefits of massage-myofascial release therapy on pain, anxiety, quality of sleep, depression, and quality of life in patients with fibromyalgia”, Evid Based Complement Alternat Med, Vol. 2011, 2011, pp. 1-9.

[6] Field T, “Pregnancy and labor massage”, Expert Rev Obstet Gynecol, Vol. 5(2), Mar. 2010, pp. 177–181.

[7] Sherman KJ, Ludman EJ, Cook AJ, Hawkes RJ, Roy-Byrne PP, Bentley S, Brooks MZ, Cherkin DC, “Effectiveness of therapeutic massage for generalized anxiety disorder: a randomized controlled trial”, Depress Anxiety, Vol. 27(5), May 2010, pp. 441–450.

[8] Nerbass FB, Feltrim MIZ, Souza SA de, Ykeda DS, Lorenzi-Filho G, “Effects of massage therapy on sleep quality after coronary artery bypass graft surgery”, Clinics (Sao Paulo), Vol. 65(11), Nov. 2010, pp. 1105–1110.

[9] Sudmeier I, Bodner G, Egger I, Mur E, Ulmer H, Herold M, “Changes of renal blood flow during organ-associated foot reflexology measured by color Doppler sonography”, Forsch Komplementarmed, Vol. 6(3), Jun. 1999, pp. 129–134.

[10] Lindgren L, Rundgren S, Winsö O, Lehtipalo S, Wiklund U, Karlsson M, Stenlund H, Jacobsson C, Brulin C, “Physiological responses to touch massage in healthy volunteers”, Auton Neurosci, Vol. 158(1-2), Dec. 2010, pp. 105–110.

[11] Pishbin T, Firoozabadi SM, JafarniaDabanlo N, Mohammadi F, Koozehgari S, “Effect of Physical Contact (Hand-Holding) on Heart Rate Variability”, International Journal of Advanced Computer Science, Vol. 2(12), Dec. 2012, pp. 452–456.

[12] Field T, Diego MA, Hernandez-Reif M, Deeds O, Figuereido B, “Moderate versus light pressure massage therapy leads to greater weight gain in preterm infants”, Infant Behav Dev, Vol. 29(4), Dec. 2006, pp. 574–578.

[13] Lee YH, Park BN, Kim SH, “The effects of heat and massage application on autonomic nervous system”, Yonsei Med J, Vol. 52(6), Nov. 2011, pp. 982–989.

[14] Hodgson NA, Lafferty D, “Reflexology versus Swedish Massage to Reduce Physiologic Stress

and Pain and Improve Mood in Nursing Home Residents with Cancer: A Pilot Trial", Evid Based Complement Alternat Med, Vol. 2012, Jul. 2012, pp. 1-5.

[15] Garner B, Phillips LJ, Schmidt HM, Markulev C, O'Connor J, Wood SJ, Berger GE, Burnett P, McGorry PD, "Pilot study evaluating the effect of massage therapy on stress, anxiety and aggression in a young adult psychiatric inpatient unit", Aust N Z J Psychiatry, Vol. 42(5), May 2008, pp. 414-422.

[16] Thanakiatpinyo T, Suwannatrai S, Suwannatrai U, Khumkaew P, Wiwattamongkol D, Vannabhum M, Pianmanakit S, Kuptniratsaikul V, "The efficacy of traditional Thai massage in decreasing spasticity in elderly stroke patients", Clin Interv Aging, Vol. 9, 2014, pp. 1311-1319.

[17] Saetung S, Chailurkit LO, Ongphiphadhanakul B, "Thai traditional massage increases biochemical markers of bone formation in postmenopausal women: a randomized crossover trial", BMC Complement Altern Med, Vol. 25, 2013, pp. 13-69.

[18] Buttagat V, Eungpinichpong W, Chatchawan U, Arayawichanon P, "Therapeutic effects of traditional Thai massage on pain, muscle tension and anxiety in patients with scapulocostal syndrome: a randomized single-blinded pilot study", J Bodyw Mov Ther, Vol. 16(1), Jan. 2012, pp. 57–63.

[19] Buttagat V, Eungpinichpong W, Chatchawan U,Kharmwan S, "The immediate effects of traditional Thai massage on heart rate variability and stress related parameters in patients with back pain associated with myofascial trigger points", J Bodyw Mov Ther, Vol. 15, 2011, pp. 15-23.

[20] Goldstein DS, Bentho O, Park MY, Sharabi Y, "Low frequency power of heart rate variability is not a measure of cardiac sympathetic tone but may be a measure of modulation of cardiac autonomic outflows by baroreflexes" Exp Physiol, Vol. 96, 2011, pp. 1255-1261.

[21] Rahman F, Pechnik S, Gross D, Sewell L, Goldstein DS, "Low frequency power of heart rate variability reflects baroreflex function, not cardiac sympathetic innervation", Clin Auton Res, Vol. 21, 2011, pp. 133-141.

[22] Heart rate variability analysis system clinical information VERSION 3.O. [Internet]. n.d. [cited 2013 Nov 12]. Available from: http://medicore.com/download/HRV_clinical_manual_ver3.0.pdf

[23] Task Force of the European Society of Cardiology and the North American Society of Pacing and Electrophysiology, "Heart rate variability: standards of measurement, physiological interpretation and clinical use", Circulation, Vol. 93, 1996, pp. 1043-1065.

[24] Eungpinichpong W, Therapeutic Thai massage. Bankok: Suweeriyasarn Printing Press, 2008.

First International Conference on Science, Engineering & Environment,
Tsu City, Mie, Japan, Nov.19-21, 2015, ISBN: 978-4-9905958-5-2 C3051

ASSOCIATION OF CHILDHOOD DIARRHEA WITH HOUSEHOLD CONTACTS: OBSERVATION IN URBAN DIARRHEAL DISEASE HOSPITAL IN BANGLADESH

Shahnawaz Ahmed, Farzana Ferdous, Mohammad Abdul Malek, Sumon Kumar Das, Mohammod Jobayer Chisti
Abu Syed Golam Faruque
International Centre for Diarrheal Disease Research, Bangladesh (icddr,b)

ABSTRACT

Although diarrhea is considered as a food and waterborne disease, household transmission is common; however, not well documented in our context. The present study aimed to determine the association of diarrhea among urban under-5 children with household contacts who had diarrhea in recent days. A total of 929 under-5 diarrheal children with family history of diarrhea in past 7 days were enrolled in the Diarrheal Disease Surveillance System (DDSS) of the Dhaka Hospital of icddr,b during 2001–2012. Another 9,908 children constituted comparison group having no family history of diarrhea in last 7 days. In multivariate analysis, children with family history of diarrhea were at 1.69 (95% CI; 1.31- 2.18) times and 1.30 (1.00-1.69) times higher risks for diarrhea due to *Vibrio cholerae* and Enterotoxigenic *E. coli* respectively compared to those with no such family history. Children aged ≥24 months with family history, were at higher risk [aOR-1.55 (95%CI-1.25-1.93)] of diarrhea and prior antibiotic use before coming hospital [1.17 (1.00-1.38)]. Clinical presentation revealed that, children belonging to family with positive history, significantly passed stool >10 times/day [1.39 (1.19- 1.61)], had abdominal pain [1.35 (1.13-1.61)], and stayed longer in the hospital [1.36 (1.16-1.59)]. On the other hand, proportion of children who received vitamin A supplementation [0.85 (0.73-0.99)], were breastfed [0.77 (0.66-0.91)], and drink treated water [0.80 (0.69-0.94)] were lower among children from households with recent diarrhea compared to their counterparts. Recent history of diarrhea among household contacts is directly associated with childhood diarrhea due to *V. cholerae* and ETEC.

Keywords: Childhood, Diarrhea, Household contact, Urban

INTRODUCTION

Globally, 7.6 million children die before completing 5 years of age; among them, 64% die due to infectious disease in which diarrhea is one of the most common diseases [1]. Household transmission of gastroenteritis is common in the United States, particularly in homes with small children [2]. In majority of the developing countries, diarrheal diseases cause significant morbidity and mortality, especially in children [3]. Three quarters of global childhood diarrheal deaths occur within only 15 countries and Bangladesh is in 7th position with 50,800 annual childhood deaths [4]. Although much of the world faces cholera risk during pandemics, due to aquatic reservoirs, cholera has been endemic in Bangladesh for centuries and is hyperendemic in rural Bangladesh [5, 6]. From the environment more than 200 different serogroups have been isolated; serogroups O1 and O139 are major causes of cholera. *V. cholerae* O1 biotype El Tor is currently the predominant cause of cholera globally and in Bangladesh [5, 6]. In two large prospective cohorts of contacts of cholera patients in Bangladesh, rectal swab positive infections occurred in 78 of 506 (17%) household contacts of patients with cholera caused by *V. cholerae* O1 biotype classical [5, 6].

Diarrhea reporting patients received oral rehydration solution (ORS).If dehydration was present, intravenous fluids were used to treat patients with severe dehydration and those with moderate dehydration who could not take fluids by mouth. Antibiotics are important adjuncts in the treatment of symptomatic *V. cholerae* infection; adults received single dose doxycycline (300 mg) until resistance became widespread in Bangladesh in 2005 [5, 6]. Subsequently, single dose ciprofloxacin (1 gram) or azithromycin (1 gram) were used; children under the age of 18 years were treated with erythromycin (30–50 mg /kg/day for three days) or single dose azithromycin (20 mg/kg) [5, 6]. In developing countries, like Bangladesh diarrhea is often inadequately managed at home, which may result in poor outcomes. Timely medical attention for diarrhea is important for reducing deaths from diarrhea [7].

Individual contact has been recognized as being accountable not only for small-scale transmission among household contacts and communities, but

also for the spread over a much wider geographical area [8]. Intra-familial transmission of diarrhea is much common in children and family members and playmates perform important role in such transmission [8]. Spreading of diarrheal disease by sharing sources of contaminated food and water or fecal-oral transmission within household has been reported by several studies [5-7]. A household contact may acquire the disease by contact with the household cases of cholera or indivuals may get *V. cholerae* infections by attending a gathering in the week preceding the disease [5]. Similarly, the use of reservoir water has been observed to be a risk factor for the infections caused by *V. cholerae* [6]. Previous studies have identified risk factors for developing invasive diarrhea such as age, high fly counts, food, and a recent overnight trip [8-11] . Children living in overcrowded areas with inadequate sanitation reported illness of diarrhea with known etiology [7]. Exposure to an infected household member with vomiting was associated with a 6-fold greater risk for new infection, whereas exposure to diarrhea elevated, but not significantly, the risk for new infection [13]. Moreover, a recent study in rural Bangladesh observed that 40% of the tube well sample had detectable *Shigella* (10%), *Vibrio* (10%), *and* pathogenic *E.coli* (8%) suggesting water to be a potential risk factor for bacterial pathogens [14].

However, very little research has been conducted to find out the association of childhood diarrhea with family members who had diarrhea in recent past (7 days). Thus we intended to determine the association of diarrhea among urban under-5 children with household contacts who had diarrhea in recent days.

METHODS AND MATERIALS

Study Site

The study was conducted among under-five children visiting urban Dhaka Hospital of the International Centre for Diarrhoeal Disease Research, Bangladesh (icddr,b). Established in 1963, the Dhaka Hospital located in urban Dhaka, currently provides free care and treatment to around 140,000 diarrheal patients each year. The hospital has been maintaining a Diarrheal Disease Surveillance System (DDSS) since 1979, and systematically enrolls patients attending the facility (2% since 1996), irrespective of age and sex. The DDSS provides valuable information to hospital clinicians in their decision-making process and enables to detect the emergence of new pathogens and in early identification of outbreaks and their locations, thereby alerts the host Government to take appropriate preventive and control measures. Extensive microbiological assessments of fecal samples (culture, ELISA, and microscopy) are performed to identify diarrheal pathogens.

Definition:

Diarrhea was defined as three or more loose stools in a 24-hour period and dysentery was defined as invasive diarrhea with visible blood in one or more stools [16]. Dehydration was defined according to icddr,b criteria; some dehydration if the patient had any two of the following criteria present: irritability, sunken eyes, dry mucosa, thirst, or reduced skin turgor and severe dehydration was defined as some dehydration with inability to drink, lethargy, unconsciousness, or absence/imperceptible radial pulse [6]. Household contact was defined as persons sharing the same cooking pot at least for previous three days [6]. Maternal illiteracy, monthly income of the family (>100$), Non sanitary toilet, Treatment of drinking water, consider as a socio-demographic indicator; duration of diarrhea (>3 days), dehydration status (severe), Number of stool (>10 times/24 hrs), abdominal pain, vomiting, fever, cough, and *Vibrio cholerae*, *Shigella*, rotavirus and ETEC, *Giardia lamblia*, Entamoeba hystolytica consider as etiologic indicator .

Study Participants

From 2001 to 2012, 14,491 under-5 children reported to DDSS in icddr,b's Dhaka Hospital; among them, 929 under-5 diarrheal children with family history of diarrhea in past 7 days were enrolled and another 9,908 children constituted the comparison group having no family history of diarrhea within the same period.

Specimen Collection and Laboratory Procedure

Single, fresh, whole stool specimen (at least 3 ml or grams, ideally 10 ml or grams) was collected from patients at enrollment. Stool specimens were labeled with the subject's identification number, date and time of collection and sent to the laboratory soon after collection for isolation of etiologic agents including rotavirus [17], *Shigella* [18] and *Vibrio cholerae* [18, 19] and ETEC [18].

Ethical Statement

The Diarrheal Disease Surveillance System (DDSS) of icddr,b is a routine ongoing activity of the Dhaka Hospital which has been approved by the Research Review Committee (RRC) and Ethical Review Committee (ERC) of icddr,b and verbal consent was obtained from the caretakers/legal guardians before enrollment.

Data Analysis

Statistical analyses were performed using Statistical Package for Social Science (SPSS, Chicago, IL version 15.5) and Epi Info (Version 6.0, USD, Stone Mountain, GA). For categorical variables, differences in the proportion were compared by Chi-square test and strengths of associations were estimated by calculating the odds ratio (OR) with 95% confidence intervals (CI). A probability of less than 0.05 was considered to be statistically significant. Finally, logistic regression analysis was performed to determine the factors those were associated with family members who had diarrhea. In the present analysis, variables of interest were those variables that were found significantly associated with dependent variable in univariate analysis.

RESULTS

In urban Bangladesh; Older children (24-59 months) were more often affected whose family members had diarrhea compared to non diarrhea families (25% vs. 14%; p<0.001). Female diarrhea sick children were more common among diarrhea families compared to non-diarrhea families (43% vs. 38%, p=0.002). Families who reported diarrhea had more illiterate mothers, treated drinking water more commonly, had breastfed child often, less frequently used antimicrobials at home before coming to the hospital, less commonly used non sanitary toilet as well as their children received vitamin A (Table 1). Diarrhea children whose family had diarrhea; they were suffering from longer duration of diarrhea, presented with severe dehydration more often, and had higher stool frequency (Table 1).Rotavirus was less common (p<0.001) among children whose family had diarrhea, however, these children were often infected with *V. cholerae* (p<0.001) and ETEC (p<0.006) (Table 2).

In multivariate analysis, children with family history of diarrhea were at 1.69 (95% CI; 1.31- 2.18) times and 1.30 (1.00-1.69) times higher risk for diarrhea due to *Vibrio cholerae* and Enterotoxigenic *E. coli* respectively compared to those families without any diarrheal illnesses. Children aged ≥24 months with family history, were at higher risk [aOR-1.55 (95%CI-1.25-1.93)] of diarrhea and prior antibiotic use before coming to hospital [1.17 (1.00-1.38)]. Clinical presentation revealed that, children belonging to families with diarrhea history, significantly passed frequent stool (>10 times/day) [1.39 (1.19- 1.61)], had abdominal pain [1.35 (1.13-1.61)], and longer duration of diarrhea (>3 days) [1.36 (1.16-1.59)]. On the other hand, they less frequently received vitamin A supplementation [0.85 (0.73-0.99)], breastfed [0.77 (0.66-0.91)], and drank treated water [0.80 (0.69-0.94)] (Table 3).

DISCUSSION

Cholera is often spread by ingestion of contaminated food and water; person-to-person spread of cholera is infrequent because of the large infectious dose (10^3-10^6 cells if contaminated water is the source and 10^2-10^4 cells if contaminated food) [21]. During the first 2–3 years of life, much of the diarrheal disease burden is attributed to infection with rotavirus, ETEC, EPEC, *Shigella* and many other bacterial, viral, and protozoal organisms [20]. However; in the present study, under-five children were also commonly infected with *V.cholera*e which is less frequently observed in this age group. Previous studies indicated that cholera is transmitted within the household by other members of the affected households [22]. It seems likely that food contaminated within a household and use of the water reservoir is the most likely transmission routes for cholera. Intra-familial transmission of *shigella* carries a risk of diarrhoea, nine-fold higher among children with intra-familial transmission than among children of households without intra-familial transmission [23]. In our study, ETEC was also isolated among the children whose family members had diarrhea. The insufficient epidemiologic facts available suggests that Enterotoxigenic *Escherichia coli* (ETEC) are usually spread by contaminated food and water vehicles; little is known about the risk of secondary spread by direct contact transmission [21].

Older children were more often affected whose family members had diarrhea compared to non diarrhea families which are one of the interesting findings of this study. Environmental contamination often plays important role in case of person-to-person secondary transmission [4]. Children aged 24-59 months are playful and much more independent to stay in touch with dirt, mud, water source compared to younger children. It might also be reflecting changes in the population, such as in baseline levels of immunity or population density, or changes in organism virulence.

Personal contact has been documented as being responsible not only for small-scale transmission among household contacts and communities, but also for the spread over a much wider geographical area [23]. In urban Bangladesh the burden of diarrheal sickness in household contacts of cholera patients is higher than as earlier estimated. Considering etiology, most of the studies documented rotavirus as most frequently causing childhood diarrhea and *Vibrio cholerae* infection is less common among under-5 children in Bangladesh [24, 25].

Table I. Socio-demographic and nutritional status of family member had diarrhea and family member had no diarrhea among under-5 children

Variable	Family member had diarrhea; n= 929 (%)	Family member had no diarrhea; n= 9908 (%)	OR; (95% CI) p value
Age			
24-59 months	233 (25)	1348 (14)	2.13 (1.81, 2.50) <0.001
Female sex	400 (43)	3764 (38)	1.23(1.07, 1.42) <0.002
Maternal Illiteracy	271 (29)	2550 (26)	1.19 (1.02, 1.38) <0.023
Non sanitary toilet	261 (28)	3116 (31)	0.85 (0.73, 0.99) 0.038
Treatment of drinking water	385 (42)	3783 (38)	1.15 (1.00, 1.32) 0.052
Monthly income of the family (>100$)	349 (38)	3928 (40)	0.92 (0.80, 1.06) 0.237
Vitamin A capsule supplementation	474 (51)	5505 (56)	0.83 (0.73, 0.96) 0.008
Breastfed Practice	273 (33)	2484 (26)	1.35 (1.16, 1.58) <0.001
Use of antibiotic prior to hospital visit	608 (65)	6926 (70)	0.82 (0.71, 0.94) <0.005
Use of ORS before hospital visit	882 (95)	9529 (96)	0.75 (0.54, 1.03) 0.080
Diarrhea duration (>3 days)	321 (35)	2966 (30)	1.42 (1.07, 1.43) 0.003
Dehydration status			
Severe	64 (7)	496 (5)	1.41 (1.06, 1.86) <0.015
Number of stool (>10 times/24 hrs)	435 (47)	4002 (40)	1.30 (1.13, 1.49) <0.001
Abdominal pain	242 (26)	1747 (18)	1.65 (1.40, 1.93) <0.001
Vomiting	700 (75)	7531 (76)	0.96 (0.82, 1.13) 0.862
Fever	60 (7)	653 (7)	0.98 (0.74, 1.30) 0.932
Cough	400 (43)	4006 (40)	1.11 (0.97, 1.28) 0.127
Stunting	268 (30)	2924 (30)	0.99 (0.85, 1.15) 0.899
Wasting	231 (26)	2397 (25)	1.06 (0.90, 1.24) 0.495
Under-weight	341 (38)	3570(37)	1.05 (0.91, 1.22) 0.492

Table II: Isolation of pathogen among under-5 children whose family member had diarrhea and non-diarrhea

Variable	Family member had diarrhea; n= 929 (%)	Family member had no diarrhea; n= 9908 (%)	OR; (95% CI) p value
Rotavirus	296 (33)	4319 (44)	0.61 (0.53, 0.71) <0.001
V.cholerae 01	129 (14)	762 (8)	1.94 (1.58, 2.38) <0.001
Shigella	43 (5)	441 (5)	1.04 (0.75, 1.45) 0.866
ETEC	81 (9)	630 (6)	1.41 (1.01, 1.81) 0.006
Giardia lamblia	05 (1)	61 (1)	0.90 (0.32, 2.35) 0.995
Entamoeba hystolytica	3 (0.4)	18 (0.2)	1.82 (0.43, 6.61) 0.251

Use of antimicrobials against infection is essential for treating infectious diseases [26]. Although, childhood diarrhea is a self limiting disease and an emerging public health burden in Bangladesh due to etiology specific high use of irrational antimicrobials. This might be due to family member being inexperienced enough regarding diarrhea treatment and can be explained in several ways: easy access to drug stores with availability of frequently used low cost antimicrobials and irrational prescribing practices by the non professionals such as salesman of drug stores as well as better socio-economic status of the families who can afford for the antimicrobials. Other than that, due to lack of legislation that prohibits sales or prescribing of antimicrobials by the nonprofessionals [26].

Clinical manifestation raises concern regarding abdominal pain, passage of frequent stool (>10 times/24hours) and longer diarrhea duration (>3 days) significantly more in children from families with diarrheah. More frequent purging as well as large voluminous stool are the common clinical features of cholera [6]. Family members first initiate oral fluid therapy at household level to treat their children which is followed by visiting local pharmacy in some cases, such attempt in many cases can cause unnecessary delay in reporting to the

facilities. Our observations also correlate with these findings. Receipt of vitamin A supplementation was less in children from diarrhea families; but breast feeding and boiled water drink was more frequent; however, such findings contradict with our observations. There is no readily explanation but likely explanation may be that boiling of water or breast feeding practice was not up to the mark to influence any protection against childhood diarrheal illnesses. Transmission within family is more common in case of severely malnourished children who are also at higher risk of death [16]. But, present study showed no significant difference in any indicators of nutritional status among the groups.

CONCLUSION

The present study documented several socio-demographic and clinical features and etiology that may have influence in household spread of diarrheal disease of under-5 children. Etiologic evidence of recent days indicated that family history of diarrhea among household contacts is directly associated with childhood diarrhea due to *V. Cholerae* and ETEC which are emerging public health burdens in Bangladesh. Knowledge of the epidemiology and mode of transmission of *V. cholerae, ETEC* as well as other enteric pathogens is important to prevent its spread and may be useful in identifying high-risk populations.

LIMITATION OF THE STUDY

Unbiased systemic sampling methods to enroll patients into surveillance system irrespective of age, sex, nutritional status, socio-economic background; and the large dataset with standard laboratory facility were strengths of the present study. However, lack of detailed information about family members who had diarrhea and non detection of pathogens from family member were the main limitations of our study.

COMPETING INTEREST

There is no potent conflict of interest to declare. All authors confirm that there is no professional affiliation, financial agreement or other involvement with any company whose product figures prominently in the submitted manuscript.

ACKNOWLEDGEMENTS

Hospital surveillance was funded by icddr,b and the Government of the People's Republic of Bangladesh through IHP-HNPRP. ICDDR,B acknowledges with gratitude the commitment of the Government of the People's Republic of Bangladesh to icddr,b's research efforts. icddr,b also gratefully acknowledges the following donors which provide unrestricted support : Government of the People's Republic of Bangladesh; the Department of Foreign Affairs, Trade and Development (DFATD), Canada; Swedish International Development Cooperation Agency (Sida) and the Department for International Development (UK Aid).

Table III. Factors associated with Family member had diarrhea and family member had no diarrhea among under-5 children (Dependent variable: Family member had diarrhea =1, family member had no diarrhea =0)

Indicator	Adjusted OR (95% CI) p value
Age 24-59 months	1.55 (1.25, 1.93) <0.001
Treatment of drinking water (1= yes, no=0)	0.80 (0.69, 0.94) < 0.006
Received vitamin A supplementation (1= yes,	0.85 (0.73, 0.99) 0.043
Breastfeeding practice (1= yes, no=0)	0.77 (0.66, 0.911) 0.002
Antibiotic prior to hospital visit (1= yes, no=0)	1.17 (1.00, 1.38) <0.001
Diarrhea duration >3 days (1= yes, no=0)	1.36 (1.16, 1.59) <0.001
Number of stool >10 times/24hrs (1= yes, no=0)	1.39 (1.19, 1.61) <0.001
Abdominal pain (1= yes, no=0)	1.35 (1.13, 1.61) <0.001
Rotavirus (1=yes, no=0)	0.74 (0.64, 0.87) <0.001
V.cholerae (1=yes, no=0)	1.69 (1.31, 2.18) <0.001
ETEC (1= yes, no=0)	1.30 (1.00, 1.69) 0.045

REFERENCES

[1] Liu, L. Global, regional, and national causes of child mortality: an updated systematic analysis for 2010 with time trends since 2000. Lancet, 2012. 379(9832): p. 2151-61.

[2] Perry, S. Household transmission of gastroenteritis. Emerg Infect Dis, 2005. 11(7): p. 1093-6.

[3] Kotloff, K.L. Burden and aetiology of diarrhoeal disease in infants and young children in developing countries (the Global Enteric Multicenter Study, GEMS): a prospective, case-control study. Lancet, 2013. 382(9888): p. 209-22.

[4] Das SK, Ahmed S. Disease Severity and Common Etiology of Diarrhea among Children Under-five in Mirzapur, Rural Bangladesh. International Journal of TROPICAL DISEASE & Health, 3 (2) : 82-93, 2013.[5] Weil, A.A. Bacterial shedding in household contacts of

cholera patients in Dhaka, Bangladesh. Am J Trop Med Hyg, 2014. 91(4): p. 738-42.
[6] Weil, A.A. Clinical outcomes in household contacts of patients with cholera in Bangladesh. Clin Infect Dis, 2009. 49(10): p. 1473-9.
[7] Chowdhury F, Khan IA.Diarrheal Illness and Healthcare Seeking Behavior among a Population at High Risk for Diarrhea in Dhaka, Bangladesh. 2015 Jun29;10(6):e0130105.doi: 10.1371/journal.pone.0130105
[8] Khan, A.I. Detection of intra-familial transmission of shigella infection using conventional serotyping and pulsed-field gel electrophoresis. Epidemiol Infect, 2006. 134(3): p. 605-11.
[9] Boyce, J.M. Patterns of Shigella infection in families in rural Bangladesh. Am J Trop Med Hyg, 1982. 31(5): p. 1015-20.
[10] Wilson, R. Family illness associated with Shigella infection: the interrelationship of age of the index patient and the age of household members in acquisition of illness. J Infect Dis, 1981. 143(1): p. 130-2.
[11] Cohen, D. Reduction of transmission of shigellosis by control of houseflies (Musca domestica). Lancet, 1991. 337(8748): p. 993-7.
[12] Levine, O.S. and M.M. Levine, Houseflies (Musca domestica) as mechanical vectors of shigellosis. Rev Infect Dis, 1991. 13(4): p. 688-96.
[13] Martin, D.L. Contaminated produce--a common source for two outbreaks of Shigella gastroenteritis. Am J Epidemiol, 1986. 124(2): p. 299-305.
[14] Sin, M.A. Carrier prevalence, secondary household transmission, and long-term shedding in 2 districts during the Escherichia coli O104:H4 outbreak in Germany, 2011. J Infect Dis, 2013. 207(3): p. 432-8.
[15] Ferguson, A.S. Comparison of fecal indicators with pathogenic bacteria and rotavirus in groundwater. Sci Total Environ, 2012. 431: p. 314-22.
[16] Ferdous, F. Severity of diarrhea and malnutrition among under five-year-old children in rural Bangladesh. Am J Trop Med Hyg, 2013. 89(2): p. 223-8.
[17] Rahman, M. Genetic characterization of a novel, naturally occurring recombinant human G6P[6] rotavirus. J Clin Microbiol, 2003. 41(5): p. 2088-95.
[18] WHO. Manual for laboratory investigations of acute enteric infections. Geneva: Programme for control of diarrhoeal disease: World Health Organization;. 1987.
[19] Qadri,F. Production, characterization, and application of monoclonal antibodies to Vibrio cholerae O139 synonym Bengal. Clin Diagn Lab Immunol, 1994. 1(1): p. 51-4.
[20] Qadri, F. Enterotoxigenic Escherichia coli and Vibrio cholerae diarrhea, Bangladesh, 2004. Emerg Infect Dis, 2005. 11(7): p. 1104-7.
[21] Sugimotol.Household Transmission of Vibrio cholerae in Bangladesh. PLoS Negl Trop Dis, 2014. 8(11): p. e3314.
[22] Albert.Pathogenesis of Providencia alcalifaciens-induced diarrhea. Infect Immun, 1992. 60(12): p. 5017-24.
[23] Ahmed, F. Family latrines and paediatric shigellosis in rural Bangladesh: benefit or risk? Int J Epidemiol, 1994. 23(4): p. 856-62.
[24] Kanungo. Clinical, epidemiological, and spatial characteristics of Vibrio parahaemolyticus diarrhea and cholera in the urban slums of Kolkata, India. BMC Public Health, 2012. 12: p. 830.
[25] Pastore G. Treatment of cholera in the adult. Studies during recent epidemics in Apulia. Ann Sclavo, 1975. 17(3): p. 399-418.
[26] Ahmed S. Urban-Rural Differentials in Using Antimicrobials at Home among Under-5 Children with Diarrhea. Science Journal of Clinical Medicine. Vol. 2, No. 3, 2013, pp. 81-86. doi: 10.11648/j.sjcm.20130203.14

First International Conference on Science, Engineering & Environment,
Tsu City, Mie, Japan, Nov.19-21, 2015, ISBN: 978-4-9905958-5-2 C3051

EFFICACY OF HORMONES ON PROLONGEVITY OF BANANA FRUITS

H.N.P. Singh, Sunita Kumari and M.M. Prasad
Post Graduate Department of Biotechnology
T.M. Bhagalpur University, Bhagalpur-812007 (India)

ABSTRACT

Banana fruits are extensively cultivated in the Gangetic belt of Bihar (India). Cultivation of banana serves as staple food of common people of Bihar. But these fruits are lost every year due to faulty methods of storage. The various concentrations i.e., 10^{-2}M, 10^{-3}M, 10^{-4}M, 10^{-5}M and 10^{-6}M molar solutions of two growth regulators like *Indole Acetic Acid* (IAA) and *Gibberellic Acid* (GA) were selected subsequently and these solutions were tried on mature healthy fruits of *Chinia variety*. Out of five concentrations, 10^{-3}M molar solution of indole acetic acid and 10^{-2}M solution of gibberellic acid were found to be most effective in retaining total chlorophyll, chlorophyll 'a' and chlorophyll 'b' contents of banana fruits on 2nd day of storage. While minimum retention of total chlorophyll, chlorophyll 'a' and chlorophyll 'b' was observed by the treatment of 10^{-6}M, molar solution of IAA and GA at the end of the incubation period. However, result also exhibited that in controlled fruits, concentrations of total chlorophyll, chlorophyll 'a' and chlorophyll 'b' was reduced to a considerable extent with increase in storage period.

Keywords: Efficacy, hormones, prolongivity.

INTRODUCTION

Application of modern technology has considerably enhanced the yield of banana fruits and vegetables. However, a sizeable quantity is lost during storage and marketing before it reaches to the consumers. Faulty keeping quality of the fruits has also caused deterioration in the nutritive contents which ultimately lowers the market value to a considerable extent [7]. As such, it appears worthwhile to establish such methods which may delay fruit ripening and senescence till they are consumed. Keeping this in view the present investigation has been aimed to increase the longevity of banana fruits by the application/use of two plant hormones like Indole Acetic Acid (IAA) and Gibberellic Acid (GA).

Material Methods

In order to study the longevity of the fruits in term of chlorophyll content, auxin, IAA and gibberellic acid (GA) were tested under laboratory conditions. To evaluate the effect of growth regulators on chlorophyll content , molar solution of auxin and gibberellic acid was diluted to desired concentrations i.e., 10^{-2}M, 10^{-3}M, 10^{-4}M, 10^{-5}M and 10^{-6}M. Mature healthy looking fruit, approximately of same age were sprayed with different concentrations of growth regulators and were kept in polyethylene bags separately. They were incubated along with control for ten days. Total chlorophyll, chlorophyll 'a'and chlorophyll 'b'of both treated and controlled fruits were estimated at the regular interval of 2,4,6,8 & 10 days [10].

1 gm of fruit skin was taken and homogenized with excess of acetone in a glass homogenizer. The supernatant was decanted and filtered using whatman's filter paper no. 42. Subsequently the absorbancy of the processed solution was taken at 645 and 663 nm. The values were put into the formulae and amount of total chlorophyll, chlorophyll 'a' and chlorophyll 'b' was calculated

Table 1: Effect of Indole Acetic Acid & Gibberellic Acid on total chlorophyll (mg/g) contents of banana fruits

Concentration	0 Day	2 Days	4 Days	6Days	8 Days	10 Days
Control	0.483	0.313	0.192	0.187	0.168	0.145
Indole Acetic Acid						
10^{-2}M		0.366	0.334	0.327	0.327	0.309
10^{-3}M		0.463	0.431	0.418	0.391	0.372
10^{-4}M		0.414	0.382	0.388	0.356	0.347
10^{-5}M		0.394	0.366	0.371	0.317	0.309
10^{-6}M		0.370	0.342	0.339	0.283	0.263
Gibberellic Acid						
10^{-2}M		0.439	0.324	0.301	0.213	0.154
10^{-3}M		0.434	0.230	0.213	0.192	0.128
10^{-4}M		0.418	0.296	0.230	0.143	0.114
10^{-5}M		0.397	0.328	0.175	0.149	0.118
10^{-6}M		0.327	0.291	0.171	0.181	0.126

Table 2 : Effect of Indole Acetic Acid & Gibberellic Acid on chlorophyll 'a' (mg/g) contents of banana fruits

Concentration	0 Day	2 Days	4 Days	6 Days	8 Days	10 Days
Control	0.176	0.152	0.076	0.071	0.074	0.062
Indole Acetic Acid						
10^{-2}M		0.199	0.182	0.182	0.169	0.165
10^{-3}M		0.248	0.231	0.225	0.221	0.216
10^{-4}M		0.240	0.224	0.259	0.217	0.213
10^{-5}M		0.243	0.233	0.239	0.227	0.211
10^{-6}M		0.244	0.229	0.236	0.231	0.203
Gibberellic Acid						
10^{-2}M		0.173	0.188	0.185	0.150	0.095
10^{-3}M		0.181	0.094	0.127	0.127	0.089
10^{-4}M		0.197	0.167	0.148	0.072	0.066
10^{-5}M		0.192	0.194	0.102	0.072	0.090
10^{-6}M		0.162	0.193	0.083	0.138	0.067

Table 3 : Effect of Indole Acetic Acid & Gibberellic Acid on chlorophyll 'b' (mg/g) contents of banana fruits

Concentration	0 Day	2 Days	4 Days	6 Days	8 Days	10 Days
Control	0.307	0.161	0.116	0.115	0.094	0.083
Indole Acetic Acid						
10^{-2}M		0.167	0.151	0.145	0.157	0.143
10^{-3}M		0.215	0.199	0.192	0.169	0.155
10^{-4}M		0.174	0.158	0.157	0.247	0.133
10^{-5}M		0.151	0.133	0.132	0.120	0.098
10^{-6}M		0.130	0.112	0.103	0.084	0.059
Gibberellic Acid						
10^{-2}M		0.265	0.135	0.115	0.062	0.054
10^{-3}M		0.253	0.135	0.081	0.064	0.039
10^{-4}M		0.220	0.128	0.082	0.076	0.047
10^{-5}M		0.205	0.132	0.074	0.062	0.027
10^{-6}M		0.157	0.092	0.087	0.043	0.058

RESULT

Total Chlorophyll: It is evident from the Table.1 that the total chlorophyll content (0.483 mg/g) of controlled fruits gradually declined with the increase in the storage period and was recorded 0.145 mg/g on 10^{th} day. The treatment of fruits with various molar concentrations of IAA and GA gave variable retention of total chlorophyll. 10^{-3}M of IAA and 10^{-2} M of GA showed most satisfactory results.

Chlorophyll 'a': Table.2 shows that application of different molar concentrations of IAA and GA had variable effect on retention of chlorophyll 'a'. Maximum retention was noticed by 10^{-3} M solution of IAA and 10^{-2} M solution of GA. On tenth day 0.216 mg/g and 0.095 mg/g of chlorophyll 'a' was noticed.

Chlorophyll 'b': The amount of chlorophyll 'b' in treated fruits variably declined with increase in days of incubation. Comparatively 10^{-3} M concentration of IAA and 10^{-2} M of GA were recorded most effective in retaining the faster fall in the level of chlorophyll 'b'.

CONCLUSION

A comparative review of the results (table 1, 2 & 3) showed that in controlled fruits concentration of total chlorophyll, chlorophyll 'a' and chlorophyll 'b' was reduced to a considerable extent with increase in the storage period of all the five concentrations of IAA and GA, 10^{-3}M solution of IAA and 10^{-2} M solution of GA were most effective in retaining the total chlorophyll, chlorophyll 'a' and chlorophyll 'b' in banana fruits.

Change in skin colour during ripening and senescence of fruits involved either in chlorophyll degradation or qualitative &

quantitative alteration of the green pigments into other pigments [2]. Marked alteration in the pigmentation in the peels of banana fruits under controlled condition supports the above findings [9]. The delayed ripening and senescence of banana fruits in present experiment under treatment of the two growth hormones supports the results [1], [3], [4], [5], [6], [8], [9], [11].

ACKNOWLEDGEMENT

The authors are grateful to Prof. A.K Singh, Head University Dept. of Botany & course co-coordinator, P.G. Dept. of Biotechnology, TMBU, Bhagalpur University for providing lab as well as library facility. UGC, New Delhi is also thankful for providing all the required financial support.

REFERENCE

[1] Bevington, K.B (1973). Effect of Gibberellic acid on rind quality and storage of coastal naval orange. Aust *Jounral. Exptl Agric Animal. Flus 30:196*
[2] Beevers, L (1976). "plant Biochemistry" 3rd Edn. (Ed.J.Banner and J.E Varner) Academic Press, New York San Francisco, London 775p
[3] Gutter, Y(1956). Influnce of growth regulators on the keeping quality of stored ementines, Ktavia 6:119.
[4] Hatton, T.T (1958). Effect of waxes and 2,4,5-trichlorophenoxy acetic acid as post-harvest treatment of Persian limes. Proc. Pla. State Hort. Soc., 17:312.
[5] Stewart, W.S. (1948). Effect of plant growth regulators on stored Citrous fruits. Calif.Citogr., 34:80-84.
[6] Stewart, W.S., J.E. Palmer and H.Z. Hield (1952). Packaging house experiment on use of 2,4,-dichloroacetic acid to increase storage life of lemons, Proc. Amer. Soc. Hort. Sci., 59:327-334.
[7] Singh, H.N.P (1992). Studies on diseases of Banana: A pathological and bio-chemical approach. Ph.D. Thesis, T.M. Bhagalpur University, Bhagalpur.
[8] Prasad, A.K. (1986). Pathological investigation on some varities of Pointed Gourd fruits common in Bihar. Ph.D Thesis, T.M. Bhagalpur University, Bhagalpur.
[9] Prasad, M.M and H.N.P. Singh (1993). Effect of Hormones on longevity of banana fruits. Nat. Acad. Sci. Letter 16, 2:59-62.
[10] Maclachan, S. and Zalik, S. (1963). Cand. J. Bot. 41:1053.
[11] Tosh,S., M.A Choudhary and E.E. Chatterjee (1977). Hormonal regulation of senescence in fruits of Trichosanthes dioica Robx. Indian. J. Exp. Biol. 15:12-34.

First International Conference on Science, Engineering & Environment,
Tsu City, Mie, Japan, Nov.19-21, 2015, ISBN: 978-4-9905958-5-2 C3051

AEROBIC DANCE WITH FLEXIBLE STICK EXERCISE COULD INCREASE MUSCLE STRENGTH, MUSCLE ENDURANCE, AND FLEXIBILITY IN HEALTHY SUBJECTS

Suchira Nongaudom[1], Napatsawan Thanaphonganan[2], Thanarat Sripongngam[2]

[1]Department of Sport and Health Science, Faculty of Education, Mahasarakham University, Thailand;
[2]Department of Sport and Health Science, Faculty of Education, Mahasarakham University, Thailand

ABSTRACT

The aim of this study was to examine the effects of aerobic dance with flexible stick on muscle strength, muscle endurance, and flexibility in healthy subjects. Twenty-five subjects (20.5 ± 1.1 years; BMI: 21.4 ± 4.1 kg/m2) were included in this study and they performed moderate of an aerobic dance with resistance training exercise by using flexible stick 40 minutes per time included a 5-minute of warm up, a 30-minute of exercise, and a 5-minute of cool down, 3 times per weeks, for 4 weeks. Weight, back muscle strength, abdominal muscle endurance, and flexibility were measured before and after exercise. This study found that significantly increased in back muscle strength (p=0.33), abdominal muscle endurance (p=0.001), and flexibility (p=0.0001) after exercise. However, 4 weeks of exercise did not affected on body weight. We conclude that 4 weeks of aerobic exercise with flexible stick could increase back muscle strength, abdominal muscle endurance, and flexibility in healthy subjects.

Keywords: Aerobic Dance, Exercise, Muscle Strength, Muscle Endurance, Flexibility

Corresponding author**:**
Napatsawan Thanaphonganan**,** Department of Sport and Health Science, Faculty of Education, Mahasarakham University, 269/2 Nakhon Sawan Road, Meuang District, Mahasarakham, 44000, Thailand. Tel. +66 43754440, Fax. +66 43754440, E-mail. nut4993@gmail.com

INTRODUCTION

Aerobic and resistance exercise are usually use for improve physical performance. The previous study found that aerobic and/or resistance exercises were useful for improving body composition and physical fitness [1]-[4]. Aerobic dance is a kind of aerobic exercise that can perform easiest and a flexible exercise, that is, the people can decide the way to dance matching with the chosen melody and rhythm. Moreover, we can create variety of ways to dance. Aerobic dance focuses on cardiorespiratory endurance, muscle strength, flexibility, muscle endurance, and agility. However, exercising can become more benefits if more loads are added to increase intensity in exercises [5].

The flexible stick, which was adapted from Daroonwan Suksom' flexible stick [6], was used for the exercise to increased resistance. It's made of a rubber that is, readily available and inexpensive. The property of flexible stick is reflexing reaction or pulling back force after being stretched out. That is called stretch reflex. Every time the elastic straps are stretched out, proprioception will be stimulated by the property of the elastic straps to be aware and react to the stretched straps. A study on the effects of resistance exercise by using elastic band found that increased muscle strength [7]-[8] and increased physical performance included balance, speed, and muscle endurance [8]-[9].

From the previous study showed that both aerobic and resistance exercise provides many benefits on health. Thus, this study was to investigate the effects of aerobic exercise by using aerobic dance combined with resistance exercise by using flexible stick on muscle strength, muscle endurance, and flexibility in healthy subjects.

MATERIAL AND METHOD

This study was a pre-experimental one-group pretest-posttest study, approved by the Ethical committee of Mahasarakham University, Thailand (241/2557). Twenty-five volunteers signed and gave consent to participation in this study. The volunteers were at the age of 20.5 ± 1.1 years, and had BMI of 21.4 ± 4.1 kg/m^2. The volunteers were excluded from the study if they had muscle or joint pain, a history of chronic systemic or musculoskeletal diseases, use of medications with known effects on musculoskeletal system. The aerobic exercise with flexible stick program consisted of a 40 minutes a

day, 3 days a week for 4 weeks consecutively. The exercise started with warming up for 5 minutes, aerobic dance with flexible stick exercise (32 postures) for 30 minutes, and cooling down for 5 minutes. Body weight, back muscle strength, abdominal muscle endurance, and flexibility were measured at before and after the exercise.

Poses for exercise	description
	Grip the sticks with both hands. Stretch out to the front and then spread your arms by using both hands at a time.
Poses for exercise	description
	Step on a sticks. Grip the other, extend your arms forward, and stretch the flexible stick up and down.

Fig.1 The example posture of aerobic dance with flexible stick exercise

Research instrument and measurement

The flexible sticks consisted of a pair of 20-centimeter tubes and were connected by flexible sticks in the form of continuous small loops, which about 30 centimeters long. Each connecting loop consisted of 3 elastic bands (Fig. 2)

Back muscle strength was measured by using leg dynamometer. The volunteers were instructed to set their feet six inches apart in the parallel position, the hands catch the handheld of the instrument and they held their head, back, as well as legs in a straight line. Then bent the body forward 45 degree after that they pull the handheld by keep the body to a straight. Back muscle strength was measured in kilogram [10].

Abdominal muscle endurance was measured by sit-ups test. The volunteers were instructed to lie down with tuning face up on mattresses, bent their knees in right angle, and separated their feet a little. Then joined their hands on their chests and had other volunteers, who are kneeling down, grabbed and pressed the ankles of the volunteers who are lying down. After the signal had been given, the lying volunteers had to do sit-up in 30 seconds as many times as possible and counted how many times they could do [10].

Flexibility was measured by using flexibility meter. The volunteers were instructed to sit on the ground, extended their legs forward, and used their feet in dosiflexion position, which touch the flexibility meter. Then bent their bodies forward with arms extending straight, and used their fingers to touch the scale, written on a material, for 2 seconds. The unit of scale was in centimeter [10].

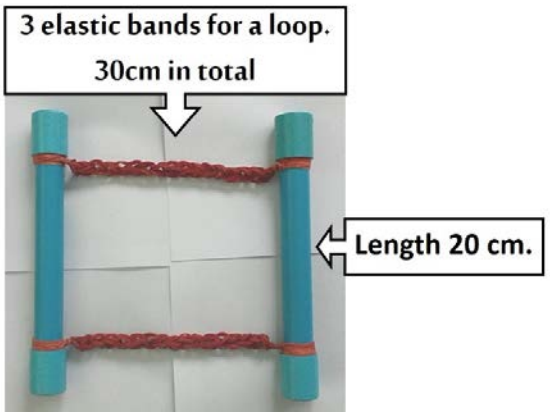

Fig. 2 Flexible stick (adapted from Daroonwan Suksom' flexible stick [6])

Statistical analysis

The data were presented as mean ± SD. Kolmogorov-Smirnov was used to verify normal distribution. Paired t-test and Wilcoxon Sign Rank-Test were used to compare the outcome variables at before and after TTM treatment within group. Statistical significance was set at the $p < 0.05$.

RESULTS

This study demonstrated that back muscle strength was significantly increased ($p = 0.033$), abdominal muscle endurance was significantly increased ($p = 0.001$), and flexibility was significantly increased ($p = 0.0001$) after aerobic dance with flexible stick exercise. However, weight showed no significant differences within-groups comparison (Table 1).

DISCUSSION

The aim of this research is to study about the effects of aerobic dance with flexible stick exercise on back muscle strength, abdominal muscle endurance, and flexibility. From this study, it is found that aerobic dance with flexible stick exercise can improve back muscle strength, abdominal muscle endurance, and flexibility. The results of this

study were corresponded with Larsson et al. [1], Sanal et al. [3], and Rhyu et al. [7] found that a 15-week and a 12-week resistance exercise, and a six-week elastic band exercise could increase muscle strength, respectively. Moreover, Jin et al. [8] showed that a 12-week and a 5-month elastic band resistance exercise could increase muscle endurance. The present study demonstrated that just a 4-week aerobic dance with flexible stick exercise could improve physical fitness as indicated by increased muscle strength, muscle endurance, and flexibility in healthy volunteers.

Body weight was not significantly changed after exercise. The result of this study was consistent with Nassis et al. [11], they found that 12 weeks of aerobic exercise training could not change body weight in overweight and obese girls. Whereas, Taghian et al. [12] found that aerobic exercise, which a maximal heart rate percentage of 60-65 and 80-85 and duration of 15-20 and 45-50 minutes, at the beginning and the end of exercise could decrease body weight in obese women.

Table 1 Comparison on the body weight, back muscle strength, abdominal muscle endurance, and flexibility between before and after aerobic dance with flexible stick exercise.

outcome	aerobic exercise with flexible stick (n = 25)	
	before	after
	mean±SD	mean±SD
Body weight	57.89±10.57	57.62±10.11
95%CI	53.53, 62.25	53.45, 61.80
Back muscle strength	65.16±38.11	72.77±29.78*
95%CI	49.43, 80.90	60.50, 85.06
Abdominal muscle endurance	18.60±4.83	22.08±4.12**
95%CI	16.61, 20.60	20.38, 23.79
Flexibility	9.36±7.51	11.96±7.43**
95%CI	6.26,12.46	8.90,15.03

*Significant difference at p-value <0.05
**Significant difference at p-value <0.01

CONCLUSION

The present study showed that aerobic dance with flexible stick exercise for 40 minutes a day, 3 days a week, and 4 weeks could increase back muscle strength, abdominal muscle endurance and flexibility. However, a four-week exercise had no effect on body weight changed.

ACKNOWLEDGEMENTS

We are grateful to thank the volunteers, who dedicated their precious time to this study, and Sport Department of Mahasarakham University, who lent us equipment for the test and allowed us to use the place for collecting data until the study has been completed.

REFERENCES

[1] Larsson A, Palstam A, Löfgren M, Ernberg M, Bjersing J, Bileviciute-Ljungar I, Gerdle B, Kosek E, Mannerkorpi K, “Resistance exercise improves muscle strength, health status and pain intensity in fibromyalgia-a randomized controlled trial”, Arthritis Res Ther, Vol. 17, Jun. 2015, pp. 161-1175.

[2] Shultz SP, Dahiya R, Leong GM, Rowlands DS, Hills AP, Byrne NM, “Muscular strength, aerobic capacity, and adipocytokines in obese youth after resistance training: A pilot study”, Australas Med J, Vol. 8(4), Apr. 2015, pp. 113-120.

[3] Sanal E, Ardic F, Kirac S, “Effects of aerobic or combined aerobic resistance exercise on body composition in overweight and obese adults: gender differences. A randomized intervention study”, Eur J Phys Rehabil Med, Vol. 49(1), Feb. 2013, 1-11.

[4] Sarsan A, Ardiç F, Ozgen M, Topuz O, Sermez Y, “The effects of aerobic and resistance exercises in obese women”, Clin Rehabil, Vol. 20(9), Sep. 2006, pp. 733-782.

[5] American College of Sports Medicine, “ACSM’s guidelines for exercise testing and Prescription”, 7th ed. Baltimor: Lippincott Willian & Wilkins, 2006.

[6] Suksom D, Siripatt A, “Flexible Stick Exercise: the Alternative Kinds of Exercise for Thai People”, Thai Health Promotion Foundation (THPF), 2007.

[7] Rhyu HS, Kim SH, Park HS, “The effects of band exercise using proprioceptive neuromuscular facilitation on muscular strength in lower extremity”, J Exerc Rehabil, Vol. 11(1), Feb. 2015, pp. 36-40.

[8] Jin EH, Park S, So JM, “The effect of muscle power training with elastic band on blood glucose, cytokine, and physical function in elderly women with hyperglycemia”, J Exerc Nutrition Biochem, Vol. 19(1), Mar. 2015, pp. 19-24.

[9] Ahn N, Kim K, “Effects of an elastic band resistance exercise program on lower extremity muscle strength and gait ability in patients with Alzheimer's disease”, J Phys Ther Sci, Vol. 27(6), Jun. 2015, pp. 1953-1955.

[10] Faculty of Sports and Health science, Institute of Physical Education, Chumphon. The physical fitness test [online] 2015 [cited 2015 July 20]. Available from: http://www.ipecp.ac.th/ ipecp/ cgi-binn/vni/Program/unit5/index.html

[11] Nassis GP, Papantakou K, Skenderi K, Triandafillopoulou M, Kavouras SA, Yannakoulia M, Chrousos GP, Sidossis LS, "Aerobic exercise training improve insulin sensitivity without changes in body weight, body fat, adiponectin, and inflammatory markers in overweight and obese girls", Metabolism, Vol. 54(11), Nov. 2005, pp. 1472-1479.

[12] Taghian F, Zolfaghari M, Hedayati M, "Effects of Aerobic Exercise on Serum Retinol Binding Protein4, Insulin Resistance and Blood Lipids in Obese Women", Iran J Public Health, Vol. 43(5), May. 2014, pp. 658-665.

First International Conference on Science, Engineering & Environment,
Tsu City, Mie, Japan, Nov.19-21, 2015, ISBN: 978-4-9905958-5-2 C3051

IMMEDIATE EFFECTS OF TRADITIONAL THAI MASSAGE ON HEART RATE, BLOOD PRESSURE, AND ANXIETY IN DEPRESSION PATIENTS: A PILOTSTUDY

Warangkana Chompoopan[1,2], Wichai Eungpinichpong[1,2] and Wilai Eungpinichpong[3]

[1]Faculty of Associated Medical Sciences, KhonKaen University, KhonKaen, Thailand
[2]Research Center in Back, Neck, Other Joint Pain and Human Performance, KhonKaen University,Thailand
[3]Graduate School, Northeastern University, KhonKaen, Thailand

ABSTRACT

Major Depressive Disorder has been predicted, the second leading cause of death and disability by the year 2020. Massage has been the most popular complementary and alternative medical treatment for depression. Massage is likely to effectively reduce anxiety. This study aimed to preliminarily examine the immediate effects of Traditional Thai Massage (TTM) on heart rate, blood pressure, and anxiety on patients with depression. The study was conducted at a district hospital, and 5 Local Health Promoting Hospitals in KhonKaen province, Thailand. A single group pre-post design was applied. Fifteen patients diagnosed with depression participated in the study. Before and immediately after the intervention, blood pressure, heart rate, and anxiety state (using the state trait anxiety inventory; STAI) were measured. The results demonstrated a significant reduction on heart rate (mean different 5.57±4.80 bpm: $p=0.001$), and STAI after receiving TTM (mean score 38.47±5.51: $p < 0.001$). However, no significant difference has been found in blood pressure ($p=0.12$). TTM seems to have some beneficial immediate effects on patients with depression concerning reducing heart rate, and anxiety. A further study using randomized controlled trial with larger sample size and long-term follow-up is suggested to verify the effects.
Keywords: Traditional Thai Massage, Depression, Heart rate, Anxiety

INTRODUCTION

Depression is a worldwide common mental illness, estimated 350 million people affected [1], and recognized a risk factor for coronary artery disease. Some previous studies have found elevated heart rate and lower heart rate variability in patients with depression than non-depression patients [2], [3].Coronary heart disease has been found associated with coexisting level of anxiety than depression [4].Interestingly, the onset of anxiety generally precedes depression, whereas anxiety disorders were strongly related to major depressive disorder (MDD) regardless of the time frame [5]. However, recent studied evidence has suggested that the pattern generalized anxiety has usually developed into depression or vice versa [6].

Massage has shown some evidence of increasing parasympathetic activities, reducing heart rate, and blood pressure in patients with musculoskeletal disorders [7]. If massage could reduce heart rate and anxiety state of patients with depression, it could be beneficial as an alternative therapy. However, no study has yet reported its effect on the patient population with depression regarding the heart rate and anxiety. The purpose of this study was to preliminarily examine the effects of Traditional Thai Massage (TTM) on heart rate, blood pressure, and anxiety of patients with depression.

METHODS

1. Design and setting

A single group pre-post experimental design was applied. This was done by having the patients exposed to a session of 90 minutes TTM. All the outcome measures were assessed before and immediately after the TTM treatment. The study was conducted at TTM room of a district hospital, and 5 Local Health Promoting Hospitals, in KhonKaen province, Thailand.

2. Participants

15 patients, aged 15-59 years, were recruited from the psychiatric clinic at the hospital. All patients were classified accordingly to the inclusive criteria to participate in the study through Patient Health Questionnaire Screening by answering the

first 2 set of questions (PHQ-2 and PHQ-9), 9-questions were answered if they fell into the criteria. Patient Health Questionnaires were verified by clinicians. Patients with any history of contraindication consisted of either diabetes mellitus, hypertension, multiple sclerosis or heart disease were excluded.

3. Intervention of Traditional Thai Massage (TTM)

The technique of TTM used in this study based on a standard whole body Thai massage known as Sen Sib Nuad Thai. The TTM protocol consisted of the following steps. Initially, having the patients lay on his/her back the massage therapist applied gentle but firm palm pressure on the patient's medial aspect of upper arm aiming to temporally occlude the brachial artery for 20-30 seconds after which releasing the pressure to let blood flow to the arm and hand. This technique was also done for the lower limb using the palm pressure on the femoral artery. This technique is called opening the wind gate which aims to stimulate blood flow to all the tissues of the limbs. Then the therapist applied gentle but deep thumb pressure massage along the ten meridian lines of TTM that covered major muscles of limbs, back, neck, and head consequently. Thumb pressure massage along each of the line was repeated 5 rounds. The amount of thumb pressure on each of the body parts was adjusted by the therapist according to but not exceeds the pressure pain threshold of the patient. At the end of the massage session, the therapist applied gentle stretch for those muscles including calf, hamstring, quadriceps, pectorals, back, neck, shoulder, arm, forearm, and finger muscles. The TTM session covered one and a half hour.

4. Procedure

Every session of the study took place at the same time of each day. Each patient arrived at 8.30 a.m.for the STAI interview, heart rate recording and measuring the blood pressure. After that the patient rested in a TTM room for a few minutes, a qualified female massage therapist who, passed the training by the Department of Alternative Medicine, Ministry of Public Health gave a session of 90 minutes of standard TTM procedure while the patient lying on the supine, and prone position. TTM was performed on the patient in the morning. Conversation was minimized during the massage procedure, only few questions were allowed. The massage session was always ended with stretching. Immediately, after receiving TTM, STAI, heart rate and blood pressure were reassessed.

5. Measurement equipment

Blood pressure and heart rate were measured at rest in sitting position using a digital sphygmomanometer (Omron, Japan). A standard STAI was used to evaluate the state trait anxiety.

Table 1. Demographic data

Characteristic	n(%)
Age	
20-40	2(13.33)
>40	13(86.67)
(Mean ± S.D.)	48.67±8.63
Menopause	
yes	3(20.00)
No	13(80.00)
Education	
primary	14(93.33)
secondary	1(6.67)
Occupational	
workers	9(60.00)
Farmer	4(26.76)
housewives	2(13.33)
Income	
<5000 Baht/month	13(86.67)
>5000 Baht/month	2(13.33)

STATISTICAL ANALYSES

Shapiro-Wilk test was used to verify the normal distribution of continuous variables. Data were analyzed using STATA Version 10. Demographic data and descriptive statistics were also applied. Paired t-test and Wilcoxon Sign Rank-Test were used to compare the outcome variables between the pre-and the post-treatment procedure. A difference at the level of $p<0.05$ was considered statistically significant.

RESULTS

Demographic data showed that 86.67% of the patients were more than 40 years of age. Three patients (20%) were at the stage of menopause. 60% was labored workers. Most of them had only primary school background. Their incomes ranged from less than 5000 baht/month (86.67%) to more than 5000 baht/month (13.33%) (in Table 1).

A Comparison on HR within the group before and after TTM treatment showed that TTM could significantly reduce heart rate (p=0.001) (Fig. 1).

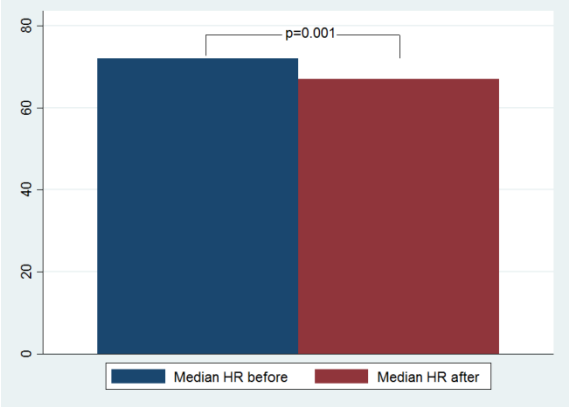

Fig.1 Comparison of resting HR before and after TTM treatment.

Table 2 Comparison of blood pressure, heart rate, and STAI within the group before and after TTM treatment.

outcome	TTM group (n = 15)	
	before	after
	Mean ± SD	Mean ± SD
Blood pressure		
SBP	123.12±4.35	117.56±3.93
DBP	72.00±2.50	75.16±2.45
STAI	40.20±1.39	48.93±0.84*

Note: SBP=systolic blood pressure, DBP=diastolic blood pressure, STAI=state trait anxiety inventory
*Significant difference at *p*-value <0.001

DISCUSSION

The result of this study has suggested that TTM may have calming effect for this patient population since it had reduced heart rate, blood pressure, and anxiety. The findings of this study are in line with the previous two studies [6], [7]. Although the psychiatric symptoms vary from patient to patient depend upon the severity and complexity of the disease, the anxiety level of all the patients with depression has been reduced immediately after having TTM. This may be due to feeling of comfort and confident during the massage. These psychological effects are very important for the patients with depressive disorders since they always have feeling of discomfort, agitate, and anxiety. Although biological mechanism of massage on depression has not been understood, massage has been known as one of the ways to convey love and care to the patients. The massage therapist and the patients are not family members or relatives; nevertheless, all the patients still could feel the touch and care that any medicine could not provide. Consequently, the heart rate was reduced probably because of relaxation and the increasing of parasympathetic activities of the autonomic nervous system [8]. Both systolic and diastolic blood pressures were not significantly changed after the massage in this study. These may be due to the complex control mechanism of both sympathetic and parasympathetic nervous systems, renal and endocrine systems [9]. In addition, the blood pressures of the patients were within normal limit initially. Therefore, a single session of TTM may not be able to affect them.

The limitation of the study consisted of small sample size since it was a pilot study, and the only immediate effects were investigated. Further study should be conducted on a sufficient sample size and extended to a long-term treatment with follow-up. TTM may be an alternative therapy for this type of patient population. More importantly, the side effect of TTM is relatively minimal.

CONCLUSION

Based on the results of this pilot study, we conclude that a single session of TTM may reduce heart rate and anxiety state of patients with depression. We suggest that further research with randomized controlled trial and follow-up study should be applied to verify the effects of Traditional Thai Massage for this patient population.

ACKNOWLEDGEMENTS

This study would not have been possible without the kind cooperation of Sum Soong hospital, 5 Local Health Promoting Hospitals (HuaiTuey, Kam Mad, Kranuan, Kukam, Bannoonand the 15 patients. More importantly, the Research Center in Back, Neck, Other Joint Pain and Human Performance, KhonKaen University as well as Sirindhorn College of Public Health where have funded this study.

REFERENCES

[1] World Health Organization, Sixty-fifth world Healthassrmbly2012.http://www.who.int/mediac entre/factsheets/fs369/en/

[2] Delaney JPA, Leong KS, Watkins A, Brodie D, "The short-term effects of myofascial trigger point massage therapy on cardiac autonomic tone in healthy subjects", Journal of advanced nursing, Vol.37, Feb. 2002, pp. 364-71.

[3] Carney RM, Freedland KE, & Veith RC, "Depression, the Autonomic Nervous Systeand Coronary Heart Disease", Psychosomatic Medicine , Vol. 67, May-June. 2005, pp. 29-33.

[4] Lechin F, van der Dijs B, Orozco B, Lechin ME, Báez S, Lechin AE, et al, " Plasma neurotransmitters, blood pressure, and heart rate during supine-resting, orthostasis, and moderate exercise conditions in major depressed patients", Biological Psychiatry, Vol. 38, Aug. 1995, pp.166-73.

[5] Hasin DS, Goodwin RD, Stinson FS, Grant BF, "Epidemiology of major depressive disorder: Resultsfrom the national epidemiologic survey on alcoholism and related conditions", Archives of general psychiatry, vol. 62, Oct. 2005, pp. 1097-106.

[6] Moffitt TE, Harrington H, Caspi A, Kim-Cohen J, Goldberg D, Gregory AM, & Poulton R, "Depression and Generalized Anxiety Disorder", Arch Gen Psychiatry, Vol.64, Jun. 2007, pp. 651- 60.

[7] Delaney JPA, Leong KS, Watkins A, Brodie D, "The short-term effects of myofascial trigger point massage therapy on cardiac autonomic tone in healthy subjects", Journal of advanced nursing, Vol. 37, Feb. 2002, pp. 364-71.

[8] Buttagat V, Eungpinichpong W, Chatchawan U, Arayawichanon P, "Therapeutic effects of traditional Thai massage on pain, muscle tension and anxiety in patients with scapulocostal syndrome: a randomized single-blinded pilot study", J Bodyw Mov Ther, Vol.16, Jan. 2012, pp. 57–63.

[9]Chopra S, Baby C, Jacob JJ, "Neuro-endocrine regulation of blood pressure", Indian Journal of Endocrinology and Metabolism, Vol.15, Oct. 2011, pp. 281-288.

First International Conference on Science, Engineering & Environment,
Tsu City, Mie, Japan, Nov.19-21, 2015, ISBN: 978-4-9905958-5-2 C3051

ATOMIC FORCE MICROSCOPIC AND ELECTROCHEMICAL CHARACTERIZATION OF THE MODIFIED SCREEN PRINTED CARBON ELECTRODE BY SELF ASSEMBLED DEPOSITION OF CHITOSAN AND ACTIVATED CARBON

Porntip Wongkaew[1,2] and Suta Poosittisak[1,3]
[1]Biosensing Technology for Sustainable Development Research Group, Khon Kaen University, Khon Kaen 40002, Thailand; [2]Department of Plant Science and Agricultural Resources, Faculty of Agriculture, Khon Kaen University, Khon Kaen 40002, Thailand;
[3]Department of Chemistry, Faculty of Science, Khon Kaen University, Khon Kaen 40002, Thailand.

ABSTRACT

The surface topographic characteristics generated after a modification of screen printed carbon electrode (SPCE) with either chitosan or activated carbon blending chitosan were closely investigated by atomic force microscopy and a complementary electrochemical techniques. Eighty five percent deacetylation degree chitosan was used at 1% in 1% acetic acid while the activated carbon blending ratio used was 1:1 in chitosan solution. The modification was performed via self assembled deposition directly onto the working electrode surface area. Growth feature of each modified surface was obviously differentiated by all roughness parameters such as an average roughness, root mean square, height different, grain and fractal. The highest roughness value with the least grain was from chitosan modified SPCE. A good correlation result was obtained with electrochemical cyclic voltammetry that a great change in current response was also appeared. Both the modified SPCE by chitosan and activated carbon blending chitosan could produce comparable higher current sensitivity with up to around 0.5 slope value following by their regression coefficient of 0.99. Thus affordable and efficient platforms for a fabrication of desirable pesticide biosensor could be achieved with these modifications as expected.

Keywords: Atomic force microscopy, cyclic voltammetry, Modified SPCE, Chitosan, Activated carbon

INTRODUCTION

In the development of electrochemical appliances including sensors, catalytic implements and electronic devices, there are several types of materials introduced for active electrode fabrication such as metal oxides, clays, conducting polymers and carbon based elements [1]. Among these, however in our viewpoint, a natural biopolymer as chitosan and a high surface area activated carbon have attracted much attention by their excellent attributions which are not only a prompt availability and productivity but also environmental friendly and cheap. Chitosan, the second most abundant polymer in nature, is derived by deacetylation process from chitin which is the main exoskeleton component of crustaceans and cell wall of fungi. It has a broadening of being researched for applications in many fields because of many interesting properties related to both biological activity and electrochemical affinity [2]. It is indeed a natural cationic biopolymer and behaves as a polycation by its protonated amine function at multiple sites of the molecule chains. Another interesting category, the activated carbon, has been considered due to its impressive properties concerning a high magnitude in surface area, chemical stability and conductivity. Activated carbon is well known for its superfine nanoporous structure which provides superb simultaneous adsorptive activity that allows more chemical catalytic reaction and electrical charge built up. This material also enables superior energy storage performance and a processing for supercapacitors [3]. Recently it has become in use as a predominant electrode material for commercial electrochemical double-layer capacitance [4]. As the porous activated carbon can be coated or blended with a biocompatible polymer to give a smooth and permeable film without blocking the pores and its properties [5]. A homogenously dispersing of activated carbon in chitosan biopolymer is thus expected for the preparation of electroactive material in our modification of the basal screen printed electrode.

In this study, modified screen printed electrodes were formulated by surface incorporating with either chitosan or activated carbon blending chitosan to get an effective and affordable implement for electrochemical application. Their morphological characteristics were closely investigated using by atomic force microscopic techniques in comparison to their original SPCE surface. Coexisting complementary electrochemical behaviour of them were also determined by the use of voltammetric analysis.

MATERIALS AND METHODS

Materials

Screen printed carbon electrode DRP-150 that consisted of 4 mm spot carbon as working electrode surrounded with platinum line as counter electrode and silver line as reference electrode was provided by DropSens, S.L. Llanera (Asturias) Spain. Chitosan (85% degree of deacetylation) was obtained from Bioline Lab, Co., Thailand. An analytical grade of activated carbon (DARCO®) and other chemicals for reagent preparation were purchased from Sigma-Aldrich Co. LLC, USA and Ajax Finechem Pty, Ltd., Australia. High purity deionized water of 18.2 MΩ from Milli-Q RG system (Millipore Corporation, MA, USA) was used in all solutions.

Electrode modification

The Screen printed carbon electrode DRP-150 provided by DropSens, S.L. Llanera (Asturias) Spain was used as basal electrode for further modification. The working 4 mm spot surface area of SPCE was cleaned by 3 times rinsing with deionized water. The self assembled chitosan modified electrode was subsequently prepared by applying a 3.0 µl drop of 1% chitosan in 1% acetic acid solution onto this working carbon electrode surface area and naturally dried up. Then it was covered with a 5 µl drop of 0.1 M NaOH for 30 min to fix the film forming and let it dried again. In case of the activated carbon blending chitosan modified electrode, an activated carbon powder was added to 1% chitosan in 1% acetic acid solution at 1:1 ratio by weight and thoroughly mixed and degassed prior to use. Similarly, a 3 µl drop of this blending solution was applied to the working electrode surface spot area, dried up, and fixed by 5 µl drop of 0.1 M NaOH for 30 min. These modified electrodes were then ready after since a natural air dried process was finished.

AFM investigation

The working surface of each electrode was observed by a XE-120 Atomic force microscope (Park Systems Corp., Suwon, Korea) controlled with XEP software for data acquisition and XEI software for image processing and analysis. AFM images were obtained by 2×2 µm area of the sample surface (x-y accessible area) at 0.5 Hz scan rate. Measurements were based on true non contact mode with a PPP-NCHR silicon cantilever consisting of a < 10 nm tip radius and 42 N/m force constant (Nanosensors TM, Neuchâtel, Switzerland). Surface topography parameters such as average roughness *Ra* (nm), root mean square or standard deviation of the height value *Rq* (nm), height different or peak-to-valley (*Rpv*), ten point height (*Rz*), mean spacing average (*Rsm*), skewness (*Rsk*) and kurtosis (*Sku*) as well as fractal and grain analysis, all were inspected by the XEI software.

Electrochemical analysis

Electrochemical experiments were performed at room temperature using ECoChemie Autolab PGSTAT 302N controlled with the Autolab Nova software (Metrohm Autolab B.V., Utrecht, The Netherlands). Cyclic voltammetry (CV) was the principal method of electrochemical analyses in this observation. Configuration of the self assembled layer of chitosan and activated carbon blending chitosan on SPCE working area surface was testified by their CV performance in a 0.05 M phosphate buffer saline (pH 6.5) containing 0.05 M EDTA plus 0.1 M KCl and 1.0 mM K3Fe(CN)6 at a scan rate of 25, 50, 100, 150 and 200 m·Vs−1 with a scan from −0.6 to + 0.6 V.

RESULTS AND DISCUSSION

Morphological characterization by AFM

Surface roughness characteristics

Characterization of the investigated working electrode surfaces was achieved by measuring the roughness parameters extracted from AFM topography using instrument's XEI software. Quantitative morphological characteristics such as average roughness (*Ra*), root mean square roughness (*Rq*), peak-to-valley (*Rpv*), ten point height (*Rz*), mean spacing average (*Rsm*), skewness (*Rsk*), kurtosis (*Sku*) and fractal were obviously perceived as compiled in Table 1. Different nanoscaled surface features were visualized as shown by 3D AFM images in Fig.1. An average and root mean square roughness of the chitosan modified SPCE were 1.2 fold higher but about 1.5 lesser in height and spacing parameter than the basal SPCE surface. These assessments provided a rougher but lower peak spacing and spike planar surface after chitosan covering on to basal SPCE, thus indicated a thick layer topping. While a covering with activated carbon blending chitosan yielded smoother surface with 1.6 to 2 fold smaller in roughness and height parameters. The fractal or self similarity value of this modified surface was increased up to 2.35 suggesting a thoroughly dispersion of activated carbon along the surface film layer.

Surface grain profile

The nanostructural differences among basal SPCE and its modifying surface were also defined by their grain profile determination by XEI software. Average grain size measured by area, volume, perimeter and peak-to-valley as well as an estimated grain numbers could be revealed as displayed in Table 2, notwithstanding their irregularity in shape and size. Chitosan modified SPCE yielded fewest amount of grain with 106.5 unit/μm^2 in their surface area while the highest amount of 307.5 unit/μm^2 were from activated carbon blending chitosan modified SPCE. The grain profile of basal SPCE was displayed as sizable and voluminous granule with reference to its predicated parameters. After a covering with chitosan, the surface became lessen in grain number in coupling a different form of its grain size and shape. These grains of chitosan modified surface were the largest in area and perimeter but very small peak-to-valley value and looked rather slightly wrinkle taper smear on top of basal SPCE. In case of a modification with activated carbon blending chitosan, the amount of the grain was increased to about 3 times more than the covering with chitosan only. The size and shape of the grains in this case was much smaller than both the basal SPCE and chitosan modified SPCE. Investigation on a distribution of different grain sizes along the 2×2 μm scanning surface layer of each inspected electrode was also done and its results are as illustrated in Fig. 2.

Table 1 Surface profile parameters before and after modification of the screen printed carbon electrode with chitosan and activated carbon blending chitosan

Parameters	Bare SPCE	SPCE-Chi	SPCE-Chi-ActC
Ra (nm)	18.693	21.780	11.388
Rq (nm)	24.494	25.193	13.505
Rpv (nm)	157.231	109.762	77.546
Rz (nm)	155.236	107.966	76.862
Rsm (μm)	0.8303	0.4353	0.2398
Rsk	-0.191	-0.180	-0.521
Rku	3.316	1.950	2.623
Fractal	2.2095	2.213	2.348

Note: SPCE = screen printed carbon electrode, SPCE-Chi = chitosan modified screen printed carbon electrode, SPCE-Chi-ActC = activated carbon blending chitosan modified screen printed carbon electrode, *Ra* = roughness average, *Rq* = standard deviation of the height value, *Rpv* = peak-to-valley, *Rz* = ten point height, *Rsm* = mean spacing average, *Rsk* = skewness, *Rku* = kurtosis

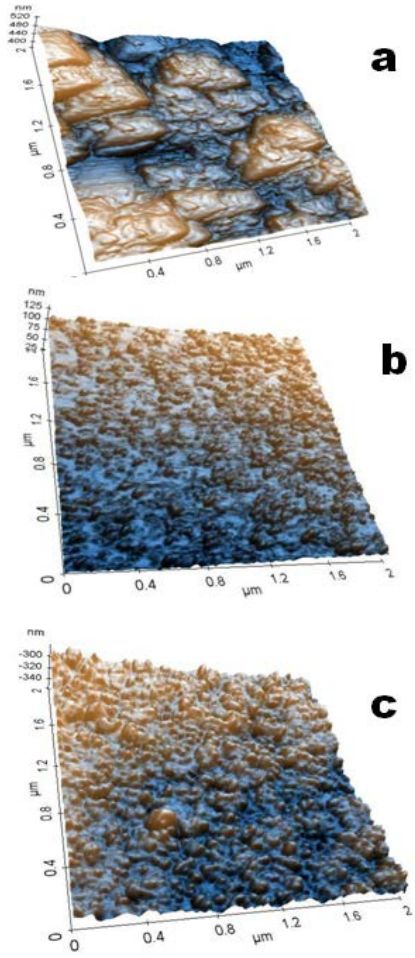

Fig. 1 Three-dimensional AFM images of (a) bare screen printed carbon electrode, (b) chitosan modified screen printed carbon electrode and (c) activated carbon blending chitosan modified screen printed carbon electrode.

Table 2 Grain parameters of electrode surface measured before and after modification of the screen printed carbon electrode with chitosan and activated carbon blending chitosan

Parameters	Bare SPCE	SPCE-Chi	SPCE-Chi-ActC
Area (μm^2)	0.0073	0.0177	0.0057
Volume (μm^3)	0.0031	0.0013	0.0019
Perimeter (μm)	0.378	0.493	0.328
Rpv(nm)	13.471	9. 365	9.759
Total Number/μm^2	143	106.5	307.5

Note: SPCE = screen printed carbon electrode, SPCE-Chi = chitosan modified screen printed carbon electrode, SPCE-Chi-ActC = activated carbon blending chitosan modified screen printed carbon electrode, *Rpv* = peak-to-valley

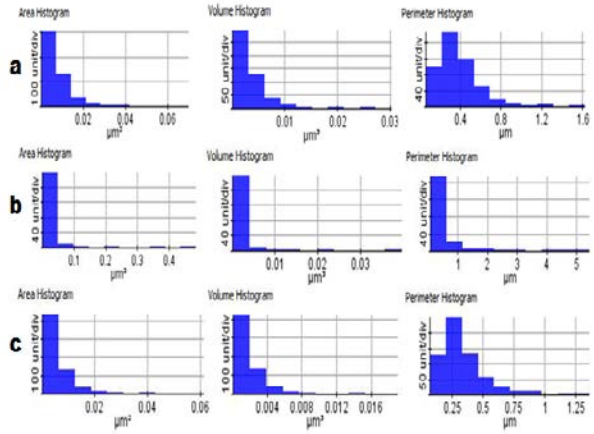

Fig. 2 Grain size distribution histogram of electrode surface by AFM analysis: (a) bare screen printed carbon electrode, (b) chitosan modified screen printed carbon electrode and (c) activated carbon blending chitosan modified screen printed carbon electrode.

Electrochemical characterization

Electrochemical characterization of both modified electrodes in comparison with the original SPCE was defined by cyclic votammetry using the ferri-ferro cyanide ($Fe(CN)6^{3-}/Fe(CN)6^{4-}$) response system indicator. As this performance usually involves a single electron transfer and produce an ideal quasi-reversible outer sphere kinetic behaviour at the electrode surface that can be used toward a quantitative analysis [6]. Comparison among voltammograms obtained from bare SPCE, chitosan modified SPCE and activated carbon blending chitosan modified electrode in 0.05 M phosphate buffer saline (pH 6.5) containing 0.05 M EDTA plus 0.1 M KCl and 1.0 mM $K_3Fe(CN)_6$ at 100 mVs-1 scan rate was as shown in Fig. 3. The voltammetric response could be detected in the potential ranged from −0.6 to + 0.6 V. A reversible process was appeared regarding a redox couple voltammogram with the peak current (I_p) of each at initial positive potential. The current signal responses of $K_3Fe(CN)_6$ were significantly enhanced at both modified electrode and hence indicated a prominent redox peak and peak current magnitude. The anodic (I_{pa}) and cathodic (I_{pc}) peak current of chitosan modified SPCE was seen about +5e-5 A and -5e-5 A at the anodic (E_{pa}) and cathodic (E_{pc}) peak potential about 0.19 V and 0.07 V, respectively. Similar peak current pattern was also formed by the activated carbon blending chitosan modified electrode with the I_{pa} and I_{pc} about +4e-5 A and -4e-5 A at the E_{pa} and E_{pc} about 0.17 V and 0.07 V. These I_p values were almost 2-3 times higher with approximately 2 times lower in their corresponding E_p than that was yielded from the bare SPCE. The evaluated peak current and potential magnitude has indicated the consequent changes at the surface of basal SPCE after covering with the investigated materials. A higher peak current and a lower peak potential of the two modified electrodes could provided better flow of electron transfer and oxidative reaction that implied a more sensitivity and reactivity. Thus a significant electrochemical behaviour improvement could be achieved in the modification of SPCE with chitosan and activated carbon blending components.

The scan rate effect from cyclic voltammetric performance of each electrode type was as demonstrated in Fig.3. Table 3 was allocated to represent the results concluded from this experiment on scan rate effect. Linear regression relationship could be constructed from the peak current versus square root of the scan rate variants. A proper linearity was produced and the slope magnitudes of both modified SPCE were approached to 0.5 with the regression coefficient around 0.99. The electrochemical property of these evidences is therefore belonged to diffusion controlled current and could be used for further study in quantitative determination.

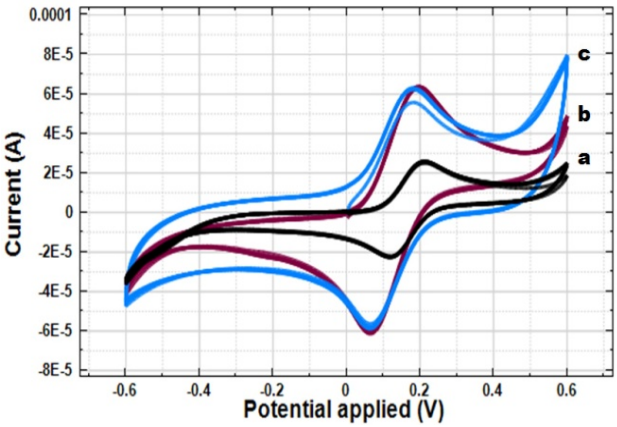

Fig. 2 Cyclic voltammograms of (a) bare screen printed carbon electrode, (b) chitosan-modified screen printed carbon electrode and (c) activated carbon blending chitosan-modified screen printed carbon electrode in 0.1 M PBE (pH 6.5) containing 1.0 mM $[K_3Fe(CN)_6]^{3-}/^{4-}$ at 100 m·Vs−1 scan rate.

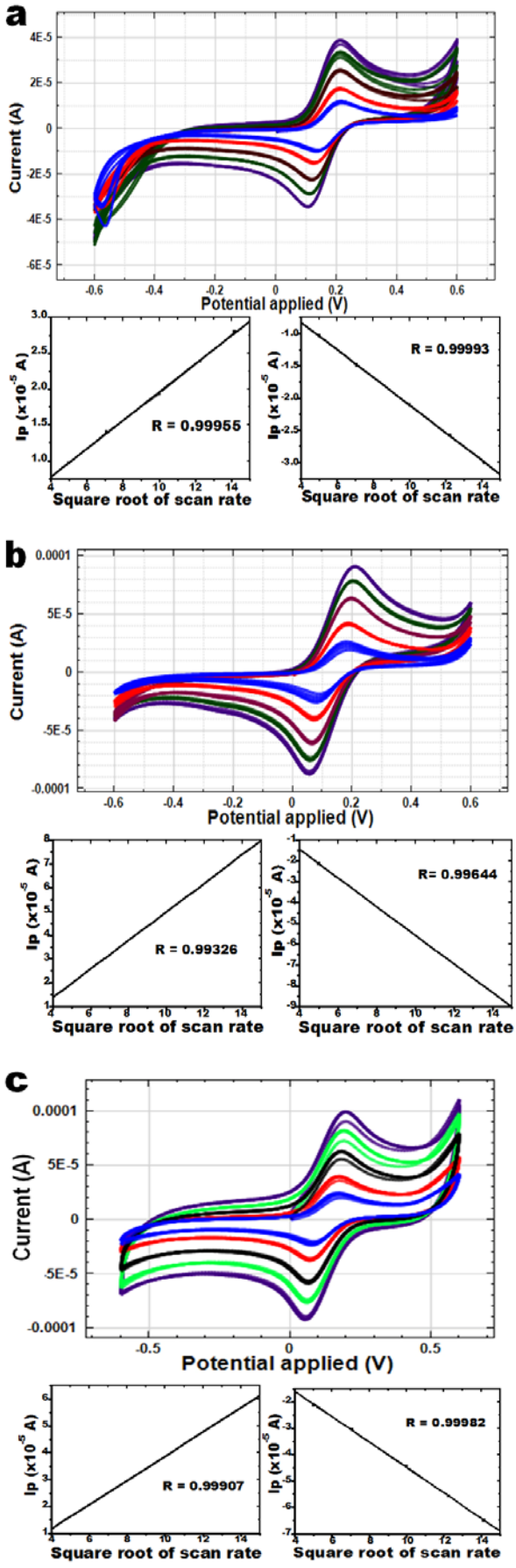

Fig. 3 Cyclic voltammograms of (a) bare screen printed carbon electrode, (b) chitosan-modified screen printed carbon electrode and (c) activated carbon blending chitosan-modified screen printed carbon electrode in 0.1 M PBE (pH 6.5) containing 1.0 mM [K3Fe(CN)6]3−/4− accounted by curves from inner to outer corresponding to 25, 50, 100, 150 and 200 m·Vs−1 scan rates, respectively. Plots located at the bottom of each CV show their corresponding linear relationship of anodic and cathodic peak current vs. square root of the scan rate.

Table 3 Linear relationship of anodic(*Ipa*) and cathodic (*Ipc*) cyclic voltammetric peak current vs. square root of the corresponding scan rate at 25, 50, 100, 150 and 200 m·Vs−1 among the investigated electrodes.

Linear regression relationship of	Equation (y = a+bx)	R^2
Bare SPCE		
Ipa	y = (-0.0217±0.0353) + (0.1981±0.0034)x	0.9988
Ipc	y = (0.0436±0.0889) + (-0.2202±0.0087)x	0.9938
SPCE-Chi		
Ipa	y = (-1.0207±0.4154) + (0.6016±0.0405)x	0.9933
Ipc	y = (1.2995±0.3442) + (-0.6879±0.0336)x	0.9964
SPCE-Chi-ActC		
Ipa	y = (-0.6349±0.1154) + (0.451±0.0113)x	0.9991
Ipc	y = (0.3236±0.0547) + (-0.4811±0.0053)x	0.9998

Note: R^2 = regression coefficient value

CONCLUSION

In this investigation, modification of screen printed carbon electrode (SPCE) with chitosan and activated carbon blending chitosan at the working carbon area surface was performed. Each modified SPCE and also its basal bare SPCE was intensely observed by atomic force microscope (AFM) to evaluate the consequent surface morphological developing. The surface roughness was found increasing but with much lower peak height and spacing in the chitosan modified SPCE. In case of the modification using activated carbon blending chitosan, however, the surface layer became

smoother altogether with a higher fractal value which indicated an evenly dispersion of activated carbon particle in this surface layer. Similar assumption was noted from the grain profile analysis. The grain number per area was lesser in chitosan modified one and their size and shape tend to be tapering form in average. While more grain amount was obtained with the modification by activated carbon blending chitosan and the average grain was irregular nodule shape and much smaller in size than those of basal chitosan only. A good correlation between AFM and electrochemical determination could be achieved in this study. These topographic modifications of SPCE were strongly responded to electrochemistry surface as the voltammetric response was obviously improved. Remarkable better peak potential and peak current magnitude from the ferri-ferro cyanide redox activity was gained in both modified SPCE. The test in scan rate effect was also showed a diffusion controlled behavior with considerable high stability and sensitivity which capable for desirable quantitative inspection. Thus, an easy, simple and inexpensive fabrication of modified electrode can be presented for convenient applications in various fields of physicochemical and biological analysis.

ACKNOWLEDGEMENTS

The research work was carried out under the Biosensor Technology for Sustainable Development Research Group of Khon Kaen University. The authors acknowledge the University's Division of Research and Technology Transfer Affair for partial funding through this program.

REFERENCES

[1] Ramachandran R , Mani V , Chen S-M, Gnana kumar G , Govindasamy M, "Recent Developments in Electrode materials and Methods for Pesticide Analysis - An overview", Int. J. Of Electrochemical Sciences, Vol. 10, Dec. 2015, pp. 859 – 869.

[2] Liu Y, Gaskell KJ, Chen Z, Yu LL, Pay GF, "Chitosan-coated electrodes for bimodal sensing: selective post-electrode film reaction for spectroelectrochemical analysis", Langmuir, Vol. 24, Jun. 2008, pp. 7223-7231.

[3] Wei L, Marta Sevilla M, Fuertes AB, Mokaya R, Yushin G," Polypyrrole-Derived Activated Carbons for High-Performance Electrical Double-Layer Capacitors with Ionic Liquid Electrolyte", Advanced Functional Materials, Vol. 22, Feb.2012, pp. 827–834.

[4] Salinas-Torres D, Lozano-Castelló D, Magdalena-Titirici M, Zhao L, Yu L, Morallón E, Cazorla-Amoros D, "Electrochemical behaviour of activated carbons obtained *via* hydrothermal carbonization", J. Of Material Chemistry. A, Vol.3, Jun. 2015, pp. 15558-15567.

[5] Chang TM, "Coated charcoal haemoperfusion", Life Support System", Vol. 2, Apr-Jun 1984, pp. 99-106.

[6] Nicholson RS, "Theory and Application of Cyclic Voltammetry for Measurement of Electrode Reaction Kinetics", Analytical Chemistry, Vol. 37, Apr. 1965, pp. 1351-1355.

First International Conference on Science, Engineering & Environment,
Tsu City, Mie, Japan, Nov.19-21, 2015, ISBN: 978-4-9905958-5-2 C3051

EFFECT OF DIETARY PROTEIN INGREDIENTS FROM NON-TOXICAGRICULTURAL FIELD ON MEAT QUALITY OF NILE TILAPIA (*OREOCHROMIS NILOTICUS*)

Boontarika Thongdonphum[1], Kittima Vanichkul[1] and Lalita Siriwattananon[1]
[1]Faculty of Agricultural technology, Rajamangala University of Technology Thanyaburi, Thailand

ABSTRACT

Nile Tilapia (*Oreochromis niloticus*) is one of freshwater fish of economically important in Thailand. This study was thus aimed to assess the effect of dietary protein ingredients from non-toxic agricultural field on production quality of *O. niloticus*. The experiments were set of three treatments including (1) 100 percentage of rice bran from non-toxic agricultural field, (2) mixing feed (fish meal, rice bran and dried corn grains from non-toxic agricultural field), and (3) commercial feed. Growth rate, survival rate, and Quality parameters of tilapia meat; including color (L*, a* and b*), texture, and sensorial preference were determined within 120 days after starting of the experiment. Results indicated that weight growth rate were significantly different ($p \leq 0.05$) and showed the best in mixing feed treatment group (75.36±25.99 g) while average daily growth **(**ADG) and Feed conversion ratio (FCR) of tilapia showed the best in treatment 2 with average 1.27±0.12 g/day **(**$p \leq 0.05$) and 1.74±0.42 **(**$p > 0.05$), respectively. Quality parameters of tilapia meat showed significant different in color and texture, while sensorial preference tended to be better on treatment 3. The overall results suggested that dietary protein ingredients from non-toxic agricultural field had effects on meat quality of *O. niloticus*.

Keywords: Dietary protein ingredients, Non-toxic agricultural field, Meat quality, Nile Tilapia

INTRODUCTION

Nile tilapia or tilapia (*Oreochromis niloticus*) is one of the most important herbivorous fish species in world aquaculture [1]. They are widely cultured in about 100 countries in the tropical and subtropical region [2]. Tilapia culture is widely distributed and be the one of economically important fish in Thailand. Production and consumption of tilapia are increasing at a rapidly rate globally [3] because they are easily cultured on the high tolerance to adverse environmental condition as well as wide variety of nutrient source from pond algae and bacteria to high quality feedstuffs such as grain, oilseeds and fishmeal [4],[5].

Currently, fish farmers adapt to complete commercial diets based on plant and animal protein sources that are expensive for most fish farmers [3],[6]. Then, varieties of feed ingredients are used in the tilapia dietary including plant protein source such as rice polish [1], Spirulina flakes [5], and soybean product [7]. However, fish production is expected to increase quality in terms of the growth performance and meat quality. Therefore, the effect of diets from planting organic agriculture as the one approach to chemical reduction in the culture should be consideration for non-toxic aquaculture feed production because of the alternative source of protein was developed on basis of their agro-by-product.

This study was thus aimed to assess the effect of plant protein ingredients from non-toxic agricultural field on the growth and meat quality of tilapia using three different diets.

METERIALS AND METHODS

Fish Source

The fingerlings of Nile Tilapia (*Oreochromis niloticus*) were obtained from the Pathumthani Aquaculture Genetic Research Institute and transported to the hatchery at Division of Fisheries, Rajamangala University of Technology Thanyaburi, Pathum Thani. Similar size (3-5 cm.) of fishes were acclimatized in plastic tank for two weeks using clean water.

Experimental Design

The experiment were designed by completely randomized design (CRD) that comprised of three treatments including 100 percentage of rice bran from non-toxic agricultural field (T1), mixing feed (rice bran, dried corn grains and fish meal from non-toxic agricultural field), and commercial feed (T3). Then, fish were counted and stocked at density of 20 fishes per cage for 120 days study period. The fingerlings in nine cages were fed on different diets according to the treatment (08:30 and 16:00 h) at a

rate of 3-4% of their body weight per day. After one hour of each feeding, uneaten diet and fecal matter were siphoned out of the tanks.

The proximate chemical composition (protein, lipid, fiber, ash, moisture, and dry matter) in the experimental diets and tilapia meat were analyzed using Association of Analytical Chemists [8]. Number of death fish were recorded after start the experiment. Weight and length data were recorded in two weeks intervals throughout the experiment for growth assessment. Average daily growth (ADG), survival rate (SR), and food conversion ratio (FCR) were calculated by;

$ADG = (W_e-W_s)/t$, where W_e is the weight at the end of the experiment; W_s is the weight at the start of the experiment, and t is the number of days.

$SR = ((N_e-N_s)/N_s)x100$, where N_e is the number of fish at the end of the experiment; N_s is the number of fish at the start of the experiment.

$FCR = W_f/W_t$, where W_f is feed intake, and W_t is the total weight of fish at the end of the experiment.

Based on the work of Pomeranz and Meloan (1994) [9], color value analysis (L*, a* and b*) was applied to analyzed for measuring color and light using Konica minolta sensing inc, WF 120). Hardness value was determined according to texture profile analysis [10]. Sensory analysis, such as color, texture, taste and odor was evaluated using nine point grading hedonic scale (dislike extremely = 1, dislike very much = 2, dislike moderately = 3, dislike slightly = 4, neither like nor dislike = 5, like slightly = 6, like moderately = 7, like very much = 8, and like extremely = 9) [11]

Data Analysis

Analysis of variance (ANOVA) was used to consider growth factor and sensory data in each treatment, significance between the means were compared with the Duncan's new multiple range test (DMRT) at a probability level 0.05 ($p\leq0.05$)

RESULTS AND DISCUSSIONS

The composition of experimental diets are shown in Table 1. Protein and lipid were used to mainly assess in the results. The highest percentage of protein (20.0%) was found in the mixing feed (T2), while protein value of the commercial feed (T3) was 18.2% that lower than mark (should be 35%). Moreover, ash content in T3 was high when compared between diet groups. Lipid levels showed highest (10.0%) in 100% of rice bran from non-toxic agricultural field (T1).

Table 1 Proximate composition (%) of the experimental diets

Parameters	Experimental diets		
	T1	T2	T3
Protein	12.8	20.0	18.2
Lipid	10.0	7.5	4.0
Fiber	5.3	7.8	8.0
Ash	8.0	8.7	11.8
Moisture	10.5	6.4	9.3
Dry matter	89.5	93.6	90.7

Growth performance of tilapia reared in each treatment are summarized in Table 2. Average weight and length of tilapia at the end of the experiment were significantly different ($p\leq0.05$). The highest average weight and length were on the mixing feed treatment (T2). Different diets also had significant ($p\leq0.05$) that affected on average daily growth (ADG), the highest ADG were recorded on the mixing feed (T2) and the lowest one in those fed on commercial feed (T3). No significant differences in survival rate (SR) and food conversion ratio (FCR) were observed between treatments. However, low food conversion ratio (FCR) value is an indicator of feed utilization efficiency [1], which tended to be better on the mixing feed (T2), as shown in Table 2.

Table 1 Growth parameter (mean±SD) of the Nile Tilapia fed on the three diet treatments

Parameters	Experimental diets		
	T1	T2	T3
W_s (g)	1.47 ± 0.30^a	1.52 ± 0.44^a	1.62 ± 0.51^a
W_e (g)	47.28 ± 17.10^a	75.36 ± 25.99^b	41.08 ± 12.04^a
L_s (cm)	4.54 ± 0.26^a	4.53 ± 0.34^a	4.51 ± 0.42^a
L_e (cm)	13.69 ± 1.80^a	15.94 ± 1.76^b	12.77 ± 1.31^c
ADG (g/day)	0.81 ± 0.14^a	1.27 ± 0.12^b	0.69 ± 0.04^a
SR (%)	65.0 ± 20.0^a	70.0 ± 15.0^a	78.3 ± 16.1^a
FCR	2.07 ± 0.25^a	1.74 ± 0.42^a	2.01 ± 0.28^a

Note: weight at the start (W_s) and the end (W_e) of the experiment, length at the start (L_s) and the end (L_e) of the experiment, average daily growth (ADG), survival rate (SR), and food conversion ratio (FR). The mean values in the same row followed by the same letter superscripts are significantly different ($p>0.05$).

The results revealed that protein ingredients from non-toxic agricultural field had effected on *O. niloticus* growth. The present study showed that the protein and lipid levels were close to of other supplemented diets used to feed tilapia fingerlings [5]. Dietary protein plays an important role in tilapia growth [12]. The protein requirement for tilapia growth had been estimated to be between 25 and 40% depending on species, age/size of fish, ingredient digestibility, and extent on foraging natural ingredients [3],[4].

Proximate composition in tilapia meat as shown

in Table 3. Protein percentage content in tilapia meat was high in commercial feed (T3) followed by mixing feed (T2) and 100% of rice bran from non-toxic agricultural field (T1), respectively. Feed intake of each experimental diets could be attributed to different the chemical composition levels in tilapia meat due to chemical composition such as protein, lipid, and fiber content in rice bran, dried corn grains, as well as fish meal used in feed production are different [1]. Then, the silage composition of both quality and quantity is directly related to its source material [13].

Table 3 Proximate composition (%) of the Nile Tilapia fed on the three diet treatments

Parameters	Experimental diets			
	Initial	T1	T2	T3
Protein	58.86[a]	60.09[a]	60.83[a]	67.46[b]
Lipid	6.29[a]	27.26[b]	28.86[c]	15.35[d]
Ash	26.04[a]	11.62[b]	14.46[c]	19.82[d]
Moisture	2.95[a]	2.33[b]	4.49[c]	2.78[d]
Dry matter	97.05[a]	97.67[b]	95.51[c]	97.22[d]

Note: mean values in the same row followed by the different letter superscripts are significantly different ($p \leq 0.05$).

Quality parameter in term of color value; light value (L*), red value (a*) and yellow value (b*) are shown in Table 4. Results implied that the effect experimental feeds had not significantly different ($p > 0.05$) on L* of both raw and boiled meat. a* of outer boiled meat had different between dietary treatments ($p \leq 0.05$), while b* of both raw and boiled meat showed significantly different among groups ($p \leq 0.05$).

Table 4 Color values (L* lightness, a* redness and b* yellowness) of Nile tilapia meat affected by tilapia raw and boiled meat

Tilapia meat	Color value	Experimental Diets		
		T1	T2	T3
Raw meat				
Outer	L*	33.3±4.0[a]	37.5±5.9[a]	35.1±6.4[a]
	a*	-0.5±0.4[a]	-1.5±0.6[a]	-1.3±0.5[a]
	b*	1.3±1.6[a]	7.5±2.0[b]	3.0±1.2[a]
Inner	L*	45.9±0.8[b]	38.2±2.7[a]	39.7±0.7[a]
	a*	-2.3±1.1[a]	1.6±2.7[b]	-1.6±1.1[ab]
	b*	1.9±1.5[a]	2.4±1.9[a]	3.9±0.9[a]
Boiled meat				
Outer	L*	28.4±7.8[a]	28.6±5.5[a]	30.8±8.8[a]
	a*	-0.5±0.4[a]	-0.7±0.9[b]	1.2±0.2[b]
	b*	-0.4±0.7[a]	1.6±1.3[ab]	2.4±1.2[b]
Inner	L*	67.5±6.8[a]	66.2±6.6[a]	58.5±5.2[a]
	a*	1.7±0.7[a]	1.7±1.1[a]	3.9±1.7[a]
	b*	15.1±2.3[a]	14.4±1.7[a]	18.5±0.6[b]

Note: mean values in the same row followed by the different letter superscripts are significantly different ($p \leq 0.05$).

Table 5 showed the quality of tilapia meat texture. Results revealed that hardness values had not significant difference ($p > 0.05$) of both raw and boiled meat among diet groups.

Table 5 Hardness values (kg force) of the Nile Tilapia meat affected by tilapia raw and boiled meat

Tilapia meat	Experimental diets		
	T1	T2	T3
Raw meat			
Outer	0.7±0.1[a]	0.6±0.1[a]	0.6±0.0[a]
Inner	0.5±0.1[b]	0.4±0.0[a]	0.4±0.0[a]
Boiled meat			
Inner	0.3±0.1[a]	0.3±0.0[a]	0.3±0.0[a]

Note: mean values in the same row followed by the different letter superscripts are significantly different ($p \leq 0.05$).

Sensorial preference of tilapia meat quality showed high score in the commercial feed (T3) followed by the mixing feed (T2) and 100% of rice bran from non-toxic agricultural field (T1), respectively. However, the results implied that plant protein ingredients from non-toxic agricultural field could be replaced in tilapia feed production due to had not significant difference ($p > 0.05$) among diet treatments. Khan [1] reported that partial replacement of fish meal by rice polish (up to 20%) and mustard oil cake (up to 22%) would be economically efficient by reducing on feed formulation cost about 24% without changing the nutritional quality. Therefore, plant protein ingredients from non-toxic agricultural field replacement of fish meal could be changed feed cost for fish farmers and had not effected on the fish consumers.

Table 6 Sensorial preference scores of fish boiled meat of the three diet treatments

Sensorial preference	Experimental diets		
	T1	T2	T3
Texture	6.2±1.4[a]	6.9±1.2[b]	8.2±0.7[c]
Color	5.2±1.4[a]	6.8±1.4[b]	7.3±1.8[b]
Odor	3.4±1.8[a]	4.4±2.3[a]	6.3±1.9[b]
Taste	7.1±1.4[a]	7.3±1.5[a]	7.1±2.5[a]
Over all acceptability	6.4±1.4[a]	7.4±1.0[b]	8.1±0.9[c]

Note: mean values in the same row followed by the different letter superscripts are significantly different ($p \leq 0.05$).

CONCLUSION

The best growth performance was observed in the mixing feed in terms of weight, length, ADG, and FCR. Meat quality parameters implied that plant protein ingredients from non-toxic agricultural field could be alternative dietary protein sources in the formulation for tilapia feed production.

ACKNOWLEDGEMENTS

The authors would like to express deep gratitude to Institute of Research and Development, Rajamangala University of Technology Thanyaburi for the financial support of the culture development of dietary protein ingredients from non-toxic agricultural field for Nile tilapia (*Oreochromis niloticus*) project.

REFERENCES

[1] Khan MSK, Siddique MAM & Zamal M, "Replacement of fish meal by plant protein sources in Nile tilapia (*Oreochromis niloticus*) diet: growth performance and utilization", Iranian J. of Fisheries Sciences, Vol.12(4), May 2013, pp. 864-872.

[2] El-Sayed AFM, "Protein nutrition of farmed tilapia: searching for unconventional sources", Oceanography Department, Faculty of Science, University of Alexandria, Egypt, accessed : http://ag.arizona.edu/oip/ista6/ista6web/pdf/364.pdf (Aug 16, 2015)

[3] Swick RA, "Feed based tilapia culture", ASA Technical Bulletin, Vol. AQ49, 2001, pp. 1-10.

[4] Mjoun K, Rosentrater KA & Brown ML, "Tilapia: environmental biology and nutritional requirements", South Dakota Cooperative Extension Service, South Dakota State University, Oct. 2010, pp. 1-7. accessed : http://pubstorage.sdstate.edu/AgBio_Publications/articles/fs963-02.pdf (Aug 16, 2015)

[5] Sultana N, Noor P, Abdullah ATM, Hasan MR, Ahmed KM & Naser MN, "Growth performance and nutrient composition of juvenile Nile tilapia (*Oreochromis niloticus*) fed Spirulina flakes, rice bran and mustard oil cake", Mal J Nutr, Vol. 18(2), Oct. 2012, pp. 275-282.

[6] Workagegn KB, Ababboa ED, Yimer GT & Amare TA, "Growth perfomance of Nile tilapia (*Oreochromis niloticus* L.) fed different types of diets formulated from varieties of feed ingredients", J. Aquac Res Development, Vol. 5(3), 2014, pp. 1-4.

[7] Furuya WM, Pezzato LE, Barros MM, Pezzato AC, Furuya VRB & Miranda EC, "Use of ideal protein concept for precision formulation of amino acid levels in fish-meal-free diets for juvenile Nile tilapia (*Oreochromis niloticus* L.)" Aquaculture Research, Vol. 35, 2004, pp. 1110-1116.

[8] AOAC. "Official methods of analysis", 15th ed. Wilson Boulevard Arlington, Verginia, USA, 2000. 1298 p.

[9] Pomeranz Y & Meloan CE, "Food analysis: Theory and practice"3rd ed. Chapman and Hall, New York. 1994.

[10] Garcia ML, Domingoez R, Galvez MD & Selgas MD, "Utilization of cereal and fruit fibers in low fat dry fermented sausage", Meat Science, Vol. 60, pp. 227-236.

[11] Chamber E, "The 9-point hedonic scale", Peryam & Kroll Research Corperation, Illinois,70 p. accessed : http://www.pk-research.com/services/media/paperandpublications/theninepointhedonicscale-papers.pdf (Aug 17, 2015)

[12] Thongdonphum B, Vanichkul K & Siriwattananon L, " Growth effect of dietary protein ingredients from non-toxic agricultural fields on Nile tilapia (*Oreochromis niloticus*)", in Proc. 3rd Academic Science and Technology Conference, 2015, pp. 382-385.

[13] Arruda LFD, Borghesi R, Brum A, D'arce MR & Oetterer M, "Nutritional aspects of Nile tilapia (*Oreochromis niloticus*) silage", Ciênc. Tecnol. Aliment., Campinas, Vol. 26(4), 2006, pp. 749-753.

First International Conference on Science, Engineering & Environment,
Tsu City, Mie, Japan, Nov.19-21, 2015, ISBN: 978-4-9905958-5-2 C3051

ELECTROCHEMICAL STUDY OF ALOE GEL AND EMODIN ON A SCREEN PRINTED CARBON ELECTRODE

Suta Poosittisak[1,2] and Porntip Wongkaew[1,3]
[1]Biosensing Technology for Sustainable Development Research Group, Khon Kaen University, Khon Kaen 40002, Thailand; [2]Department of Chemistry, Faculty of Science, Khon Kaen University, Khon Kaen 40002, Thailand, [3]Department of Plant Science and Agricultural Resources, Faculty of Agriculture, Khon Kaen University, Khon Kaen 40002, Thailand.

ABSTRACT

The most useful part of natural aloe vera is aloe-gel(AG) and aloe-emodin(AE). AE comprises various pharmacological effects including, antiviral, antimicrobial and laxative activities, while AG has mainly used as anti- inflammable agent. Some medical activity of these are related to their redox activity. This paper has presented a simple strategy to carry out direct and sensitive determination of AG and AE based on screen printed carbon electrode (SPCE).The electrochemistry of AG and AE was investigated at pH 7.0 by cyclic voltammetry and differential pulse voltammetry. A redox mechanism is comprehensively discussed.

Keywords: Aloe gel, emodin, screen printed electrode, electrochemical redox mechanism

INTRODUCTION

Aloe vera is a medicinal plant of the members of the Liliaceae family and a significant source of 'aloin' (4.5 to 25 per cent)[1]. It has been widely used in food products, beverages and pharmaceuticals as well as cosmetics because of its pharmacological properties such as anti-oxidant, anti-inflammatory and anti-cancer activities [2–8]. The two basic products of this plant are aloe gel and latex. Aloe latex (or aloe juice) is the bitter yellow exudate from the pericyclic tubules in the outer skin of the leaves. The major and active constituents of aloe latex are hydroxyanthracene derivatives (15–40%) such as the anthraquinone glycosides aloin A and B [9]. Aloe latex is known for its laxative properties. Aloe gel is the colourless gel contained in the inner part of the fresh leaves [10]. The gel consists primarily of water (>98%) and polysaccharides (pectins, cellulose, hemicellulose, glucomannan, acemannan and mannose derivatives). Acemannan is considered the main functional component of aloe vera and is composed of a long chain of acetylated mannose [11-13]

Aloe-emodin (Fig.1), one of the main bioactive constituents in aloe vera leaves, has a specific in vitro and in vivo antineuroectodermal tumor activity (8) because of the hydroxyanthraquinone presence. In the measurement of the anti-oxidant activity of aloe-emodin, it was found that the interaction between aloe-emodin and DNA was concentration dependent [10].

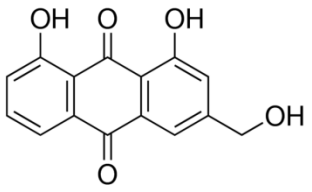

Fig. 1 The structure of aloe-emodin

Because of chemical composition of aloe emodin classified as anthraquinone derivertive with electro-activity , current investigations of emodin include spectroscopic method [14], oscillopolarography [15], micellar electrokinetic capillary chromatography [16]. It was discovered that multi-wall carbon nanotube modified glassy carbon electrode had better electrocatalytic effect for the redox of emodin than that of bare glassy carbon electrode [17]. Among these analytical techniques, the eletrochemical techniques have the advantage of celerity, simplicity and high sensitivity. To support these requirements, screen printed carbon electrode (SPCE) was used to investigate the electrochemical behavior of extracted aloe emodin and fresh aloe gel. Therefore a new possible way was provided for the investigation of fresh and extracted aloe emodin .

EXPERIMENTALS AND APPARATUS EADINGS

The three electrodes in one single strip: a carbon working electrode, a carbon counter electrode and a silver pseudo-reference electrode from Dropsens—available from Palm Instruments, was used in this experiment as a screen-printed electrochemical cell. A computer-controlled Autolab PGSTAT (302N-

High performance) with general-purposes electrochemical software operating system (NOVA version 10.1.1) from Eco Chemie B.V., The Netherlands, was used for the electrochemical measurements. The integrated three electrode strips were connected to the Autolab PGSTAT-302N with a specially adapted electrical connector. The pH values were determined with a Radiometer pH meter.

Experimental conditions

The measurements were performed by dropping a 50ul of a known sample from a dry weight of methanol extracted aloe emodin and a fresh aloe vera sample on the surface of the SPCE. The electrochemical characterization of solution samples were investigated by cyclic voltammetric and differential pulse voltammetric technique.

Sample preparation

The fresh leaves of aloe vera were washed with distilled water and were cut into 2″ – 3″ pieces. The upper green skin of leaves was scratched with a sterilized knife. These scratched pieces were cut into the small pieces were extracted with a known volume of methanol. Hydroxyanthracene derivatives were extracted with methanol. Samples were sonicated in an ultrasonic bath for 10 min, filtered through 0.2 µm membrane filters. The filtrate was dried by freezing drying process. The aloe emodin dry sample was used to prepare the known concentration for analysis. For the fresh aloe gel samples were filtered via a 0.2 µm membrane filter and mixed with a PBS buffer solution before electrochemical measurement.

RESULTS AND DISCUSSION

Response characteristics

In cyclic voltammetric measurement, two potential ranges (0,60 V to -1.00V and 0.60 V to -0.40 V) were assigned to probe electrochemical processes at the screen printed carbon electrode(SPCE). A representative CV recorded in a PBS buffer solution at pH 7.05 is shown in Fig. 1. Because of electochemical activity of a bare carbon electrode itself in the negative potential region from -0.40 V to -1.00 V . The available working potential range for the study was the potential window between 0.60 V to -0.40 V.

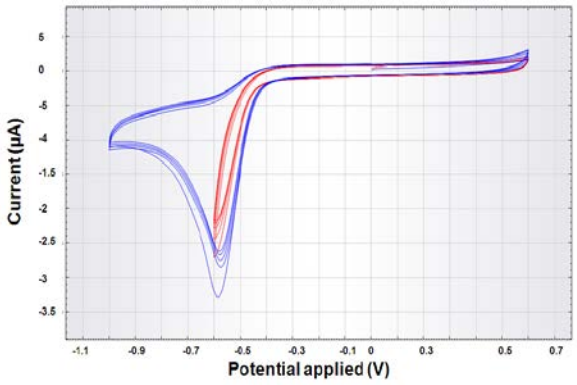

Fig.1 The CV comparisons of a bare SPCE in a PBS buffer solution at pH 7.05 running from 0.60 v to -1.00 V and 0.60 V to 0.40 V at scan rate 25 mVs^{-1} and 5 cycle.

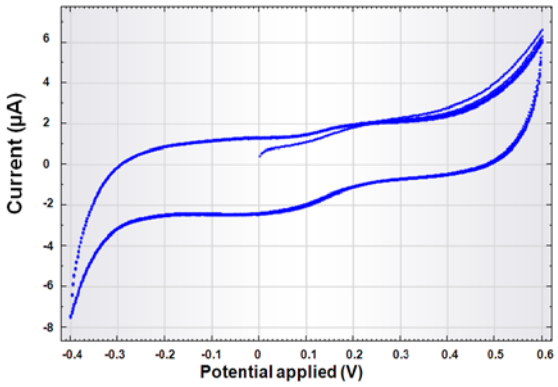

Fig. 2. CV of a bare SPCE in fresh aloe gel solution in PBS buffer solution at pH 7.05 at a scan rate 25 mVs^{-1} and 5 cycles.

After potential range was given between 0.60 V and -0.40 V for the voltammetric measurement, CV behaviors of fresh aloe vera gel in a PBS buffer solution of pH 7.05 at bare SPCE was studied, the result is shown in Fig. 2. An anodic peak can be seen at 0.185V with the peak current of 1.10×10^{-6} A. A cathodic peak can be seen at 0.068 V with the peak current of 1.80×10^{-6} A at bare SPCE. It was also found that the peak currents of the cathodic peak increase linearly with the square root of scan rate in the range of 9 to 36 mVs^{-1} , and the linear regression could be represented as $y = (-0.74 \pm 0.121) + (0.295 \pm 0.026)x$, which indicated that it was a diffusion controlled process (Fig.3b).

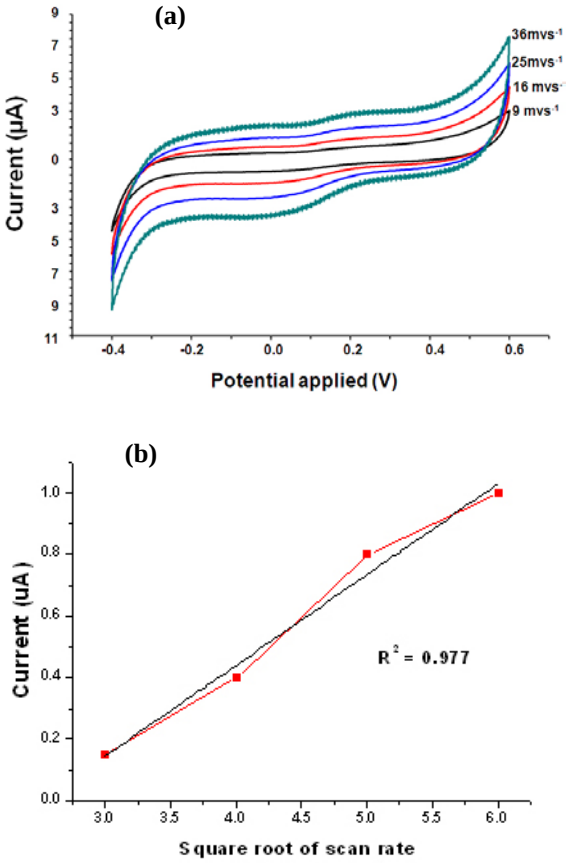

Fig. 3 The effect of the scan rate on CV of the extracted aloe emodin solution in PBS buffer solution at pH 7.05 at different scan rate 9, 16, 25 and 36 mVs^{-1}.

Electrochemical behavior of extracted aloe emodin in buffer solution at different pH values

Due to the main bioactive compound of aloe vera was aloe emodin which consisted of anthraquinone derivative s and the redox process of anthraquinone derivatives was frequently related to proton participation [17]. Therefore the electrochemical behavior of extracted aloe emodin in buffer solutions at different pH values were studied. The relationship between the cathodic and anodic peak currents of the extracted aloe emodin at SPCE and pH values were shown in Fig. 4. It can be seen that the peak potentials of the cathodic peaks shifted negatively as pH increased from 3.05 to 9.07 (Fig. 4), indicating that this electrochemical process involving proton.[17]

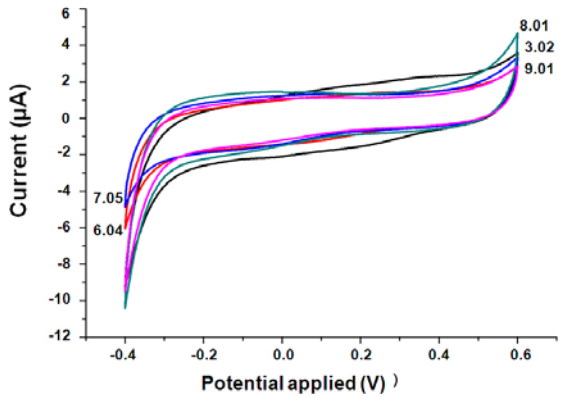

Fig. 4. The effect of different PBS pH 3.05 ,6.04 7.05 8.01 and 9.07 on CV of the same concentration 1056 extracted aloe emodin ppm at scan rate 16 mV/s^{-1}

Electrochemical behavior of extracted aloe emodin and fresh aloe gel

In differential pulse voltammetric study of the methanol extracted aloe vera sample and fresh aloe gel in a PBS buffer solution at pH 7.05 were investigated both cathodic and anodic direction from 0.60V to -0.40V. The results showed only one cathodic peak in methanol extracted sample at -0.290V (Fig. 5) while three cathodic peak of fresh aloe gel respectively showed at -0.312V, -0.014V and 0.087V (Fig.6a). The cathodic peak of aloe emodin should observed at -0.312V which the reduction potential was different from using bare glassy carbon electrode and multi-wall carbon nanotube modified glassy carbon electrode [17]. The anodic peaks of aloe emodin and other oxidative species were also observed in Fig.6b. The appearance of other cathodic and anodic peak in fresh aloe vera sample indicated that fresh aloe vera consisted of several redox species.

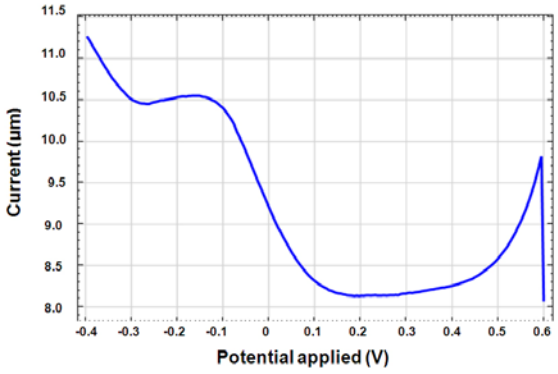

Fig.5. DPV of a 1056 ppm of extracted aloe gel in a PBS buffer solution at pH 7.05.

(a)

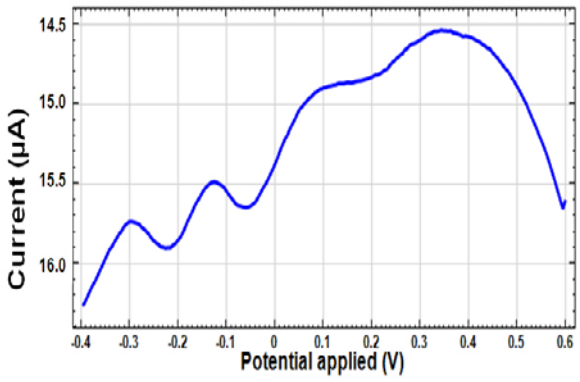

(b)

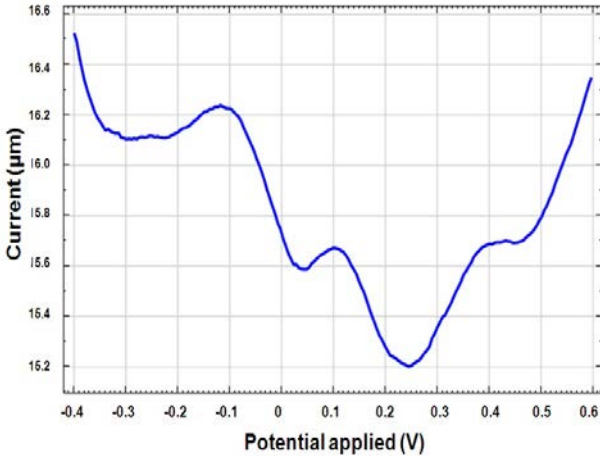

Fig.6 Cathodic differential pulse voltammograme (a) and anodic differential voltammograme (b) of fresh aloe vera gel in a PBS buffer solution at pH 7.05 .

CONCLUSION

In this paper, the electrochemical behavior of aloe emodin extracts was investigated using SPCE as an active electrode. It could be assumed that the aloe emodin was presented in the extract as well as in the fresh aloe gel according to an electrochemical behavior performance at SPCE. Therefore a low cost, easy and convenient detection of aloe emodin was successfully achieved with this electrochemical system.

ACKNOWLEDGEMENTS

The research work was carried out under the Biosensor Technology for Sustainable Development Research Group of Khon Kaen University. The authors acknowledge the University's Division of Research and Technology Transfer Affair for partial funding through this program.

REFERENCES

[1] Rajendran A, Narayanan V, Gnanavel I, Photochemical and Electrochemical Stabilities of Aloe Vera Sap Journal of Applied Sciences Research, Vol.3, 2007, pp. 1871-1878.

[2] Yen GC, Duh PD, Chuang DY, Antioxidant activity of anthraquinones and anthrone. *Food Chem*, Vol 70, 2000, pp.437–441.

[3] Bozzi A, Perrin C, Austin S, Vera FA. Quality and authenticity of commercial aloe vera gel powders. Food Chem, Vol.103, 2007, pp. 22–30.

[4] Tian B, Hua YJ, Concentration-dependence of peroxidant and antioxidant effects of aloin and aloe- emodin on DNA. Food Chem, Vol.91, 2005, pp. 413–418.

[5] Yun Hu, Juan XUu and Qiuhuihu , Evaluation of Antioxidant Potential of Aloe vera(Aloe barbadensis Miller) Extracts J. Agric. Food Chem. Vol.51, 2003, pp. 7788-7791

[6] Park MY, Kwon HJ, Sung MK, Evaluation of aloin and aloe-emodin as anti-inflammatory agents in aloe by using murine macrophages. Biosci Biotechnol Biochem, Vol.73, 2009, pp. 828–832.

[7] Pecere T, Gazzola MV, Mucignat C, Parolin C, Vecchia FD, Cavaggioni A, Basso G, Diaspro A, Salvato B, Carli M, Palù G, Aloe-emodin is a new type of anticancer agent with selective activity against neuroectodermal tumors. Cancer Res. 2000, Jun,Vol.60 (11), pp.2800-4.

[8] Saccu D, Bogoni P, Procida G, Aloe exudate: characterization by reversed phase HPLC and headspace GC–MS, J. of Agricultural and Food Chemistry, Vol.49 (10), 2001 , pp. 4526– 4530.

[9] Reynolds T and Dweck A. C, Aloe vera leaf gel: a review Update, J.of Ethnopharmacology, Vol.68 (1-3), 1999, pp. 3–37.

[10] Djeraba A and Quere P, In vivo macrophage activation in Chickens with Acemannan, a complex carbohydrate extracted from aloe vera.International Journal of Immunopharmacology, Vol. 22 (5), 2000, pp. 365–372.

[11] Femenia, A., Sanchez, E. S., Simal, S., and Rossello, C. Compositional features of polysaccharides from aloe vera (Aloe barbadensis Miller) plant tissues. Carbohydrate Polymers, 1999, Vol. 39(2), pp.109–117.

[12] Lee, J. K., Lee, M. K., Yun, Y. P., Kim, Y., Kim, J. S., Kim, Y. S., et al. Acemannan purified from aloe vera induces phenotypic and functional maturation of immature dendritic

cells. International Immunopharmacology, Vol.1 (7), 2001, pp.1275–1284.

[13] X.M Sun, C. Ma, S.J. Wu, X.Y. Wang, D.M. Cha, Spectrophotometric determination of Rheum emodin and its application, J. South-Cent. Univ. Natl. (Nat. Sci.) Vol.20, 2001, pp. 13–16.

[14] H. Zou, Z.B. Yuan, Investigation on electrochemical behavior of emodin and its application, Acta Pharm. Sinica Vol.32, 1997, pp. 310–313.

[15] Y.Y. Zong, M.T. Yu, Z.Q. Zhu, C.T. Che, Micellar electrokinetic capillary chromatography separation and determination of Chinese traditional medicine-several rheum species, Acta Pharm. Sinica , Vol.30, 1995, pp. 594–598

[16] Zhao-Hui Yin 1, Qiao Xu 1, Yi Tu, Qiu-Ju Zou, Jiu-Hong Yu, and Yuan-Di Zhao Electrocatalysis of emodin at multi-wall nanotubes Bioelectrochemistry, Vol. 72 ,2008, pp. 155–160.

First International Conference on Science, Engineering & Environment,
Tsu City, Mie, Japan, Nov.19-21, 2015, ISBN: 978-4-9905958-5-2 C3051

TOTAL PHENOLIC CONTENTS AND ANTIOXIDANT ACTIVITY OF FRESH THAI CURRY

Nuanchai Kotsaeng[1] and Muntana Nakornriab[2]

[1]Faculty of Liberal Arts and Science, Kalasin Rajabhat University, Somdech, 46230, Thailand

[2]Faculty of Science, Mahasarakham University, Maha Sarakham, 44150, Thailand

ABSTRACT

The objectives of this work were to study the total phenolic contents (TPC) and antioxidant activity of methanolic extracts of six fresh Thai curries. The TPC of the fresh Thai curries were found to be in the range of 0.989-1.1132 mg GAE/mg of the extract. Among the curries, the red curry presented the highest amount of TPC. Antioxidant activity of the extracts was measured by DPPH-radical-scavenging assay, lipid peroxidation inhibition and metal ion chelating assay. The Thai red curry extract exhibited the highest inhibition of lipid peroxidation of linoleic acid emulsion (81.41±0.55%) and radical-scavenging activity (IC_{50} = 0.0476 mg/mL). In addition, the fresh Thai red curry had the highest metal chelating activity (76.58±0.72%). However, all of the fresh Thai curries showed similar metal chelating potential activities and there were no significant statistical differences. These results suggest that the fresh Thai curries had interesting antioxidant activities and should be proposed as potential sources of safe natural antioxidants and preservatives by the curry industry.

Keywords: Antioxidant, Chelating, Fresh Thai curry, Phenolic

INTRODUCTION

Thai food has gained popularity, and Thai curries, such as tom-yum, red curry and green curry, are important ethnic foods consumed worldwide due to their tastes, colors and health effects. The major ingredients of Thai curry include garlic, chili and shallot (red onion). Garlic and onion have generally been found to be sources of antibacterial [1], antidiabetic, hypocholesterolemic and cancer preventive agents [2]. Allicin, one of the active components of freshly crushed or homogenated garlic, has a variety of antimicrobial, antifungal, antiparasitic and antiviral activities [3]. Spices have a lot of carotenoids, which have antimutagenic or anticarcinogenic properties [4]. Essential oil and flavonoids from shallot are used as flavoring or seasoning agents. Therapeutic properties include antioxidant activity, alleviation of stomach pain and as antiheimintic, antidiarrhoeal, expectorant, antitussive, diuretic and antiflu agents. In addition, other ingredients of Thai curries include galagal root, lemon grass, kaffir lime leaves, shrimp paste, and *Kaempferia pandurata*, which are effective in inhibiting tumors in the digestive tract [5]-[8]. The essential oil of lemon grass is mainly comprised of citral, which exhibited a broad antifungal spectrum [9], [10]. While galangal root can be purchased fresh or dried, and it resembles a ginger root and is known as the "defisher" as it reduces the fishy smell of foods. Kaffir lime leaves have antioxidant properties and contain volatile oil. A digestive aid, Kaffir leaves cleanse the blood while helping maintain healthy teeth and gums. Kaffir can be applied to the hair and scalp, and even prevents hair loss. It is also used as a deodorant. The fresh lime fruits can also be used if available. Therefore, the objectives of this work were to study the total phenolic contents (TPC) and antioxidant activity of methanolic extracts of six fresh Thai curries.

METHODOLOGY

Fresh Thai curry, 6 types: green curry, tom-yum, kaeng-sum, tom-kha, pa-naeng and red curry, were obtained in 2012 from a department store in Mahasarakham Province, Thailand. All chemical reagents used were analytical grade.

Crude Extraction

The Thai curries (25g) were extracted with 80% ethanol (3×100 mL) and 0.5% TFA-80% ethanol (3×80 mL) for 30 min with intermittent shaking at room temperature. The extracts were combined and filtered through a 0.45 µm nylon membrane filter. The extracts were then slowly concentrated under reduced pressure, below 40 °C, on a rotary evaporator to yield the crude antioxidants. The crude samples were used for the determination of antioxidant activities.

Antioxidant Activities

Total phenolic compounds

The TCP of the crude Thai curry extracts were determined by a spectrophotometric method using Folin–Ciocalteu's phenol reagent (24). The crude extract in ethanol (0.5 mL) was placed in a test tube and diluted to 5 mL with a glass of distilled water. Folin–Ciocalteu's phenol reagent (5 mL) was added, and the contents of the test tube were mixed thoroughly. After 3 min, 5 mL of 10% sodium carbonate solution was added, and the mixture was allowed to stand for 1 h with intermittent shaking. The absorbance of the blue color was measured in a DU-7500 Spectrophotometer (Beckman Instruments Inc., Fullerton, CA, USA) at 750 nm. The concentration of TPC was determined using the gallic acid equation (mg/g extract) obtained from a standard gallic acid calibration curve. This experiment was carried out three times, and the results were averaged for the different fractions in the Thai curries.

Thiocyanate method

Antioxidative activity was determined using the linoleic acid system (24). In a well-stopped Erlenmeyer flask containing linoleic acid (0.13 mL) in a 0.2 M NaOH-phosphate buffer (10 mL, pH 7), the crude antioxidants in ethanol (1 mg) from the different fractions of the Thai curries were added, and the volume increased to 25 mL with a glass of distilled water. The flasks were incubated at 40 °C for a two-week period, and the degree of oxidative activity was measured according to the thiocyanate method (25). The incubation mixture (0.2 mL) was reacted with NH_4SCN (30%, 0.2 mL), 9.4 mL of 75% EtOH, and 0.2 mL of $FeCl_2$ (2.53×10^{-2} g/ 10 mL 3.5 % HCl) solution. The absorbance of the blue color (peroxide value) was measured in a DU-7500 Spectrophotometer (Beckman Instruments Inc., Fullerton, CA, USA) at 500 nm. The control solution was prepared in a similar manner without the addition of any antioxidant, while α-tocopherol and butylated hydroxyanisole (BHA) at 200 µg per flask were used as a standard for comparison. This experiment was performed three times, and the results were averaged for the different fractions in the Thai curries. The percentage of inhibition of lipid peroxidation was calculated using the following equation:

$$\text{Inhibition (\%)} = [(A_c - A_s)/A_c] \times 100,$$

Where A_c is the absorbance of the control solution and A_s is the absorbance in the presence of the curry extracts.

DPPH free radical-scavenging activity

The radical scavenging activity of the crude extracts was measured using the method of Yamaguchi et al. [11]. The crude extract and α-tocopherol (5-40 mg/mL) were added to 1.5 mL of 0.1 mM DPPH (2,2-diphenyl-1-picrylhydrazyl) in ethanol. The mixture was shaken vigorously and was left to stand for 20 min at room temperature in the dark. The absorbance was measured in a DU 7400 Spectrophotometer (Beckman Instruments Inc., CA, USA) at 517 nm. The control reaction contained all reagents except for the crude samples.
The radical scavenging effect was calculated by the following equation:

$$\text{Scavenging effect (\%)} = [(A_c - A_s)/A_c] \times 100,$$

Where A_c is the absorbance of the control at 517 nm and A_s is the absorbance of the extract/standard at 517nm. This experiment was repeated thrice, and the results were averaged for the different fractions in the Thai curries.

Metal ion chelating activity

The chelating of ferrous ions was measured using the method of Dinis et al. [12]. The extracts (5-25 mg/mL) were reacted with 0.05 mL of 2 mM $FeCl_2$. The mixture was then added to 0.2 mL of 5 mM ferrozine. The control did not contain $FeCl_2$ and ferrozine. After which, the reaction was shaken and incubated at room temperature for 10 min. The absorbance of the red color was measured in a DU-7500 Spectrophotometer (Beckman Instruments Inc., CA, USA) at 562 nm. This experiment was carried out three times, and the results were averaged for the different fractions in the Thai curries. The percentage of metal chelating activity was calculated by the following equation:

$$\text{\% Metal chelating activity} = [(A_c - A_s)/A_c] \times 100,$$

Where A_c is the absorbance of the control at 562 nm and A_s is the absorbance of the extract/standard at 562nm. This method was performed three times, and the results were averaged for the different fractions in Thai curries. Na_2EDTA was used as a positive control.

RESULTS AND DISCUSSION

Total Phenolic Compounds

TPC was measured by the Folin-Ciocalteu reagent method using gallic acid as the standard. A linear calibration curve of gallic acid resulted with a correlation coefficient of R^2 = 0.9990 over the concentration range 20-120 µg/mL. This linear equation was used to determine the total phenolic compounds in the Thai curry extracts. The average amount of the TPC found in the Thai curry extracts is shown in Table 1. TPCs of fresh Thai curries were in the range of 0.989 – 1.1132 mg GAE/mg of the

extract. Among the curries, red curry presented the highest amount of TPC.

Antioxidant Activities

The antioxidant activity of the extracts was measured by lipid peroxidation inhibition, DPPH-radical-scavenging assay and metal ion chelating assay. The Thai red curry extract exhibited the highest inhibition of lipid peroxidation of linoleic acid emulsion (81.41±0.55%) and the tom-kha extract showed the lowest lipid peroxidation. It is suggested that the antioxidant activity in Thai curry comes from free radicals that promote chain reactions during the linoleic acid peroxidation system.

The radical-scavenging activity of each crude Thai curry extract was measured by using the DPPH assay. When the DPPH radical was scavenged by an antioxidant through the donation of H• to form the reduced DPPH-H, the color changed from purple to yellow. In this study, the scavenging activity was amplified with the increased concentration of all the rice antioxidants in the range of 0-40 mg/mL, and it was constant at a concentration above 15 mg/mL. In the DPPH radical-scavenging assay, the red curry extract of fresh Thai curry showed the highest activity (IC_{50} = 0.0476 mg/mL). The average amounts of the DPPH assays for the Thai curry extracts were shown in Table 1. In addition, the fresh Thai red curry had the highest metal chelating activity (76.58±0.72%), and the tom-kha extract showed the lowest (IC_{50} = 0.5553 mg/mL). The lower the IC_{50} value means the higher the antioxidant activity. In this analysis, the possible mechanisms suggest that the radical-scavenging effects of curry extracts might be due to the hydroxyl groups in the antioxidants of the extracts.

Table 1 Total phenolic compounds and radical-scavenging activity in Thai curry extracts determined using the DPPH assay.

Thai curry paste	Total phenolic content (mg GAE/mg)	IC_{50} (mg/mL)
Green curry	0.989	0.104
Tom-yum	1.092	0.067
Kaeng-sum	1.024	0.068
Tom-kha	0.936	1.749
Pa-naeng	1.111	0.053
Red-curry	1.132	0.048

The metal chelating activity of the Thai curry extracts was estimated by the ferrozine assay [12]. Ferrozine is a quantitative formation of a complex with Fe^{2+} ions. The results indicated that the chelating ability increased with an increased concentration of all the Thai curry antioxidants in the range of 0-15 mg/mL. [Fig. 2]. EDTA was used as a reference chelating agent. At a concentration of 5µg/mL, the fresh red curry variety showed the highest percentage of metal chelating, which was much lower than that of EDTA at the same concentration. The metal chelating activity was significant since it reduced the concentration of the catalyzing transition metal in the lipid peroxidation. The chelating agents, which form σ-bonds with a metal, are effective as secondary antioxidants because they reduce the redox potential.

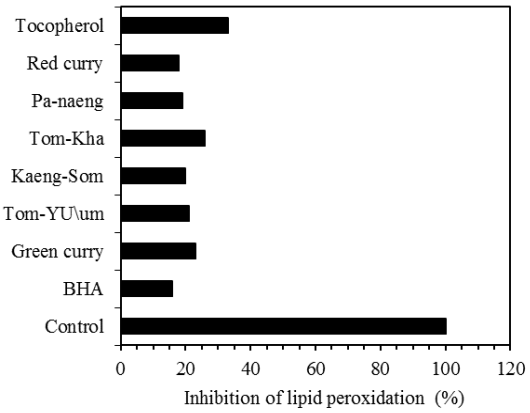

Fig 1. Thiocyanate method compared with α-tocopherol and BHA.

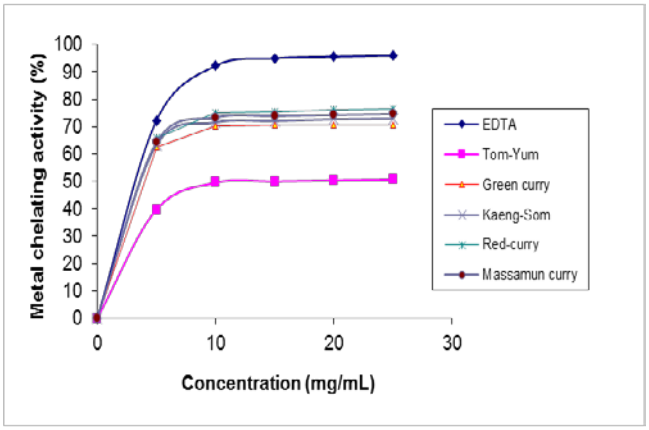

Fig 2. Metal chelating activity of Thai curries extracts estimated by the ferrozine assay.

CONCLUSION

The results presented in this study showed that Thai curries possess a relatively strong antioxidant activity as assessed by all the methods used. There is also a correlation between the capacities of total and specific antioxidant and total phenolic contents of the Thai curry samples, which indicates that the antioxidant activities of the fresh Thai curries are largely due to the phenolic group of compounds. Therefore, the Thai curries are a potential source of antioxidative phytochemicals and a useful ingredient for nutraceutical or functional food products.

ACKNOWLEDGEMENTS

The authors wish to thank the Department of Chemistry, Faculty of Science, Mahasarakham University for partial support for some chemicals. Financial support from the Faculty of Science and Mahasarakham University is acknowledged.

REFERENCES

[1] Nishimura H, Takahashi T, Wijaya CH, Satoh A, Ariga T, "Themochemical transformation of sulfur compounds in Japanese domestic *Allum*, *Allum*, *victoralis*, *L*," BioFactors, Vol. 13, 2000, pp. 257-263.

[2] Shelef LA, "Antimicrobial effects of spices," J. Food Safety, Vol. 6, 1983, pp 29-44.

[3] Siripongvutikorn S, Thummaratwasik P, Huang YW, "Antimicrobial and antioxidation effects of Thai seasoning, *Tom-Yum*," Lebensm. Wiss. Technol, Vol. 38, 2005, pp. 347-352.

[4] Monsereenusorn Y, Kongsamut S, Pezalla PD, "Capsaicin in literature survey," CRC Crit. Rev. Toxicol, Vol. 10, 1982, pp. 321-339.

[5] Murakami A, .Kondo A, Nakamura Y, Ohigashi H, Koshimizu K, "Possible anti-tumor promoting properties of edible plants from Thailand and identification of an active constituent cardomonin (2',4' dihydroxy-6' methoxychalcon) of *Boesenbergia pundurata*," Biosci. Biotechnol. Biochem. Vol. 57, 1993, pp. 1971-1973.

[6] Murakami A, .Kondo A, Nakamura Y, Ohigashi H, Koshimizu K, "Glyceroglycolipids from *Citrus hystrix*, a traditional herb in Thailand, potenly inhibit the tumor promoting activity of 12-O-tetradecanoylphorbol 13-actate in mouse skin," J. Agri. Food Chem, Vol. 43, 1995, pp. 2779-2783.

[7] Murakami A, Ohigashi H, Koshimizu K, "Possible antitumor promoting properties of edible Thai food items and some of their active constituents," Asia Pacific J. Clinic Nut, Vol. 3, 1994, pp. 185-191.

[8] Trakoontivakorn G, Nakahara K, Shinmoto H, Takenaka M, Onishi-Kameyama M, Ono H, Yoshida M, Nagata T, Tsushida T, "Structure analysis of a novel antimutagenic compound, 4-hydroxypanduratin A and antimutagenic activity of flavonoids in a Thai apice,fingerrot (*Boesenbegia pandurata* Schult) againt mutagenic heterocyclic amines," J. Agri. Food Chem, Vol. 49, 2001, pp. 3046-3050.

[9] Adegoke, GO, Odesola BA, "Storage of maize and cowpea and inhibitory of microbial agents of biodeterioration using the powder and essential oil of lemon grass (*Cymbepogon citralis*)," Int. Biodeter. Biodegrad. Vol. 178, 1996, pp. 81-84.

[10] Schaneber BT, Khan IA, "Comparison of extraction method for marker compounds in essential oil of lemon grass by GC," J. Agri. Food Chem, Vol. 50, 2002, pp. 1345-1349..

[11] Yamaguchi T, Takamura H, Matobe T, Terao J, "HPLC method for evaluation of the free radical-scavenging activity of food by using 1,1-diphenyl-2-picrylhydrazyl," Biosci. Biotechnol. Biochem. Vol. 62, 1998, pp. 1201-1204.

[12] Dinis TCP, Madeira VMC, Almeida LM, "Action of phenolic derivates (acetoamino phen, salycilate and s-aminosalycilate) as inhibitors of membrane lipid peroxidation and as peroxyl radical scavengers," Arch. Biochem. Biophys. Vol. 315, 1994, pp. 161-169.

First International Conference on Science, Engineering & Environment,
Tsu City, Mie, Japan, Nov.19-21, 2015, ISBN: 978-4-9905958-5-2 C3051

COMPARATIVE STUDY OF MORPHO-HISTOLOGY OF OVARIES OF WT (HDRR) AND P53 (-/-) OF MEDAKA (*ORYZIAS LATIPES*)

Alaa El-Din H. Sayed[a] and Hiroshi Mitani[b]

b Zoology department, Faculty of Science, Assiut University, 71516Assiut, Egypt.
[a] Department of Integrated Biosciences, Graduate School of Frontier Sciences, The University of Tokyo, Kashiwa, Chiba 277-8562.

ABSTRACT

In the present paper comparative study of morpho-histology of ovaries of both WT (HdrR) and P53 (-/-) of medaka (*Oryzias latipes*) has been done. The ovaries of adult are paired and oval-rounded in shape and are situated ventrolaterally. Histologically the ovaries consist of follicles with various stages of development, such as primodial follicle, large follicle and growing follicle. Also, the ovaries can be differentiated into outer functional regions and inner non-functional regions. The histological structure of the ovary in both strains fishes represents the generalized teleostean structure with some differences in follicles count and distribution. We conclude that, the difference recorded in the present study has an impact on the maturation inside and eggs release from the ovaries.

Keywords: Compartive, Ovary, HdrR, P53 (-/-), Oryzias latipes

1−INTRODUCTION:-

Although, medaka is an important fish in japan and recently used as animal model in research, little is known about the histology structure of the different strains. From this start point, we begins to do an investigation for all of the body organs in details with highlights on the difference between the two main strains HdrR and P53 (-/-) of *Oryzias latipes*. Shima and Mitani (2004) have been reported that many reports attest to the power and promise of the medaka for embryological studies. It is exciting that the medaka has also come of age as a fully developed model system for evolutionary studies, combining rapidly increasing genomic information with valuable inbred lines and highly divergent wild populations (Shima and Mitani, 2004).

Recently, many published articles were focused on medaka as a developmental and genetic model system (Ishikawa, 2000; Wittbrodt et al., 2002);). Also, Shima et al., (2003) has been described the current state of medaka genomic analysis (Shima et al., 2003) and medaka genetic mapping was studied (Naruse et al., 2004). The popularity of medaka among developmental biologists has led to important insights into vertebrate development (Wittbrodt et al., 2002).

It has been well established that inbred medaka strains display differences in numerous quantitative traits, such as body shape, brain morphology, behavior, reproductive rate, life span and susceptibility to chemical or radiation-induced tumorigenesis (Hyodo-Taguchi and Etoh, 1985; Hyodo-Taguchi and Matsudaira, 1987; Ishikawa, 2000). Therefore, inbred strains provide a powerful tool for genomic analyses since haplotype polymorphisms underlying complex polygenic traits can be identified that would be impossible to recognize in non-inbred wild populations (Shima and Mitani, 2004).

Histology offers a powerful tool in the study of reproductive health of fishes. It is routinely used for sex verification, identifying stage of development, documenting presence of intersex, tumors, parasites and other abnormalities and quantifying atresia. One important way histology is commonly used in fisheries is the study of fish reproductive tissue. Although macroscopic evaluation of gonads can provide important information, the ability to examine reproductive tissue at the microscopic, or cellular, level gives biologists a powerful tool to understand the details of fish reproduction. Histology of ovarian tissue is commonly used to better understand: (1) size/age at maturity; (2) daily and seasonal pattern of spawning; (3) spawning location; and, (4) fecundity. On the other hand, gonadal histology, in conjunction with hormone and vitellogenin measurements, morphological and fecundity studies, can provide insights into the effects of various environmental stressors on reproductive health. However, much research, both field and laboratory, is needed to understand cause and effect for observed changes and to understand the meaning of many of the histological observations made in field studies, in terms of reproductive success of fish populations (Blazer, 2002). The usefulness and importance of histological techniques in reproductive studies have been widely discussed for gonochoristic fish species (Alonso-Fernández et al., 2011).

The medaka (*Oryzias latipes*), a small aquarium fish that is used widely in ecotoxicological studies, is a unique vertebrate model for investigating the effects of IR but there is a few articles about the structure and description of the different stages of the ovary in

both WT and P53, so that, we will investigates and examine the structure and different developmental stages in comparative study.

2–MATERIALS AND METHODS:-

2.1. Fish:-

Sexually mature WT (Hd-rR) and p53 (-/-) adult female (3-4 cm) medaka (*O. letipes*) were studied during October 2011. The fish were kept at 20 -21 º C under 14 h light: 10 h dark cycle. They were fed a powdered diet (Tetra-min, Tetra Werke Co., Mells, Germany) and brine shrimp (*Artemia franciscana*) three times a day.

2.2. Specimen collection:-

Since most fishes used in this study are sexually mature, they are often large and hence have large gonads. One aspect of reproductive studies that needs standardization is the number, size and location of the pieces fixed for histology. The fish (6 fish per strain) were dissected and the whole ovary was isolated and used in following process for histological sections preparations.

2.3. Fixation:-

Ovaries were fixed in Davidson's solution overnight then the fixed gonads were extracted, dehydrated, embedded in paraffin, serial sectioned at 7 µm from anterior to posterior direction (Oviduct connection) as shown in fig (1), and stained with hematoxylin and eosin for microscopic analysis with a digital camera on digital microscope (Olympus, Japan).

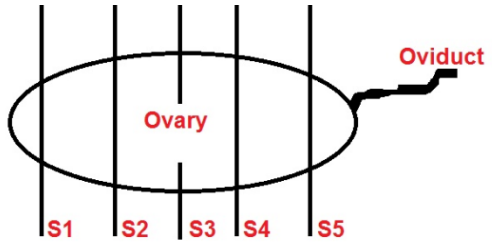

Fig 1:- Digram of the ovary showing the sectioning direction.

2.4. Developmental stages counting:-

Slides were selected on the basis of staining quality, coded, randomized and scored blindly. In each specimen, serial sections were used for counting under a 40 x objective and 10 × eyepiece to identify different developmental stages in separate slides. The established criteria for identifying of follicles (oocyte developmental stages) were according to (Kurokawa et al., 2007) to ensure authentic scoring.

2.5. Statistical analysis

The means, standard divisions and ranges were estimated. One-way analysis of variance was used to analyze the data using SPSS software (SPSS, 1998) at the 0.05 significance level.

2.6. Ethics statement

All experiments were performed in accordance with the Japanese laws and university guidelines for the care of experimental animals according to The University of Tokyo Animal Experiment Enforcement Rule.

3- RESULTS

3.1. Morphology of the Ovary:-

The histological structure of the ovary in the examined fishes represents the generalized teleostean structure. The morpho-histology of the ovary of *Oryzias latipes* as described before (Kurokawa et al., 2007; Srivastava, 1966) is a median and unpaired sac-like organ and fills up most of the body cavity behind the posterior edges of the liver. It contains a large number of egg follicles in different developmental stages during October 2011 when these experiments were carried out. The follicles are attached to the thin but strong muscular ovarian wall (epithelium). The developing oocytes are similar to those of teleostean fishes (Marza et al., 1937; Sayed et al., 2012) except in size. A small oocyte (primodial follicle) becomes transformed into a large egg containing a mass of yolk (growing follicle). During development the ova are surrounded by a thick chorion and follicular epithelium which form a protective covering. The oocytes at the youngest stage are characterized by a round nucleus which contains several deeply staining nucleoli (Fig.2). At this stage the oocyte has a large nucleus and a small amount of cytoplasm which is deeply basophilic. In the outer surface of the cytoplasm there is found Balbiani's vitelline body (Raven, 1961), in the form of a deeply staining oval body (Fig.2). With the growth of the oocytes the cytoplasm increases in relative volume and nucleus enlarges. As the oocyte grows, yolk vesicles appear, the as the formation of the yolk-vesicle proceeds, the oocytes become markedly enlarged and are provided with a thick follicular layer (large follicle). In subsequent development, the nucleus shifts to one side and the fully ripened egg is completely filled with yolk (growing follicle). Atretie oocytes have been observed quite frequently between the developing oocytes (Fig.2).

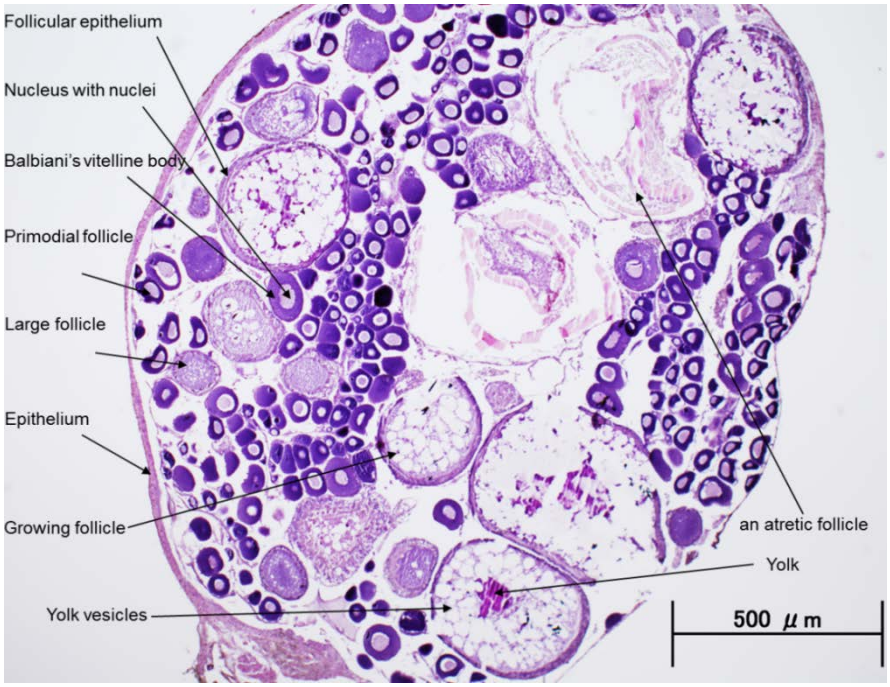

Fig. 2: T.S. of the ovary of *Oryzias latipes* showing the moropho-histology. H&E stain.

3.2. Difference between the Wt (Hd-rR) and p53 (-/-) mutant of the ovary:-

3.2.1. Ovary color, size and shape:-

The color and the size of the ovary is differs as it appears white and small in Wt while yellow-white in P53t. The size was indicated by number of sections obtained at 7 µ, where the ovary of Wt give about 17-18 sections while 22-34 Sections from P53t ovary. The shape of both strains was rounded and the P53 (-/-) ovary showed less thick ovary wall (ovary epithelium) in comparison with Wt ovary (**Fig. 3).** Also, the interstial tissue in P53t between follicles is more than that of Wt (**Fig. 3)**. No ova-testis in both Wt and P53t was observed.

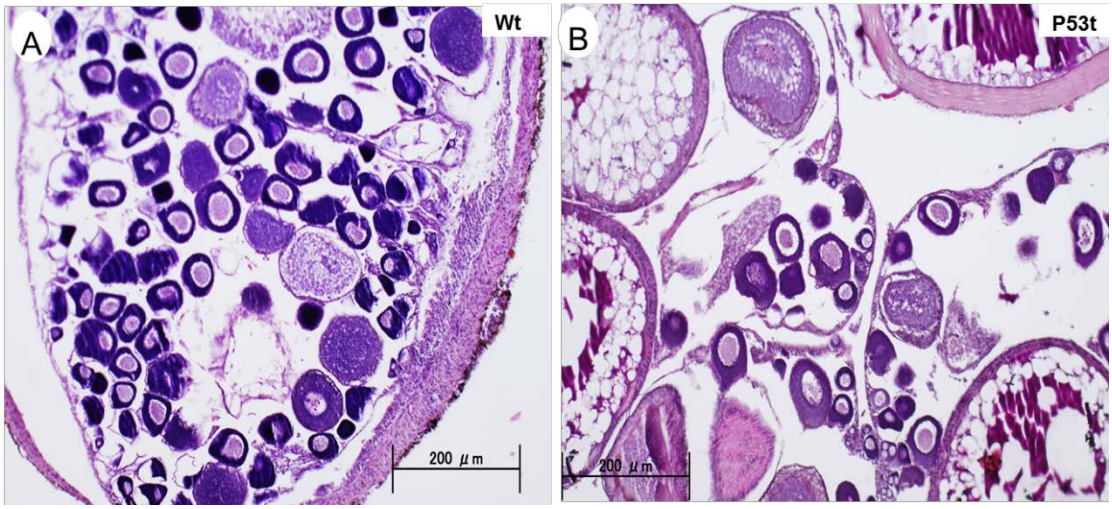

Fig. 3: T.S. of the ovary of *Oryzias latipes* showing large number of primary (primodial) follicles in (A) Wt (Hd-rR) compared with (B) p53 (-/-) mutant. H&E stain.

3.2.2. Average number and frequency of oogonial stages:-

Chart 1 and Fig (4 &5) summarizes the frequency of ovarian follicles in both Wt and P53. The percentages of total follicles in P53 was little than in Wt (Chart 1 & Fig. 2). Statistical analysis showed small number of the primodial follicles in P53 (-/-) compared with the number in Wt (Fig. 3).The

distribution of the follicles in P53t is regular distributed in whole the cavity of the ovary while in case of Wt, it is look like aggregations of follicles (Fig. 4). Although the results showed large total number of follicles in Wt, the growing follicles and large follicles recoreded high number in P53 (-/-) than Wt (Chart 2& Fig. 5).

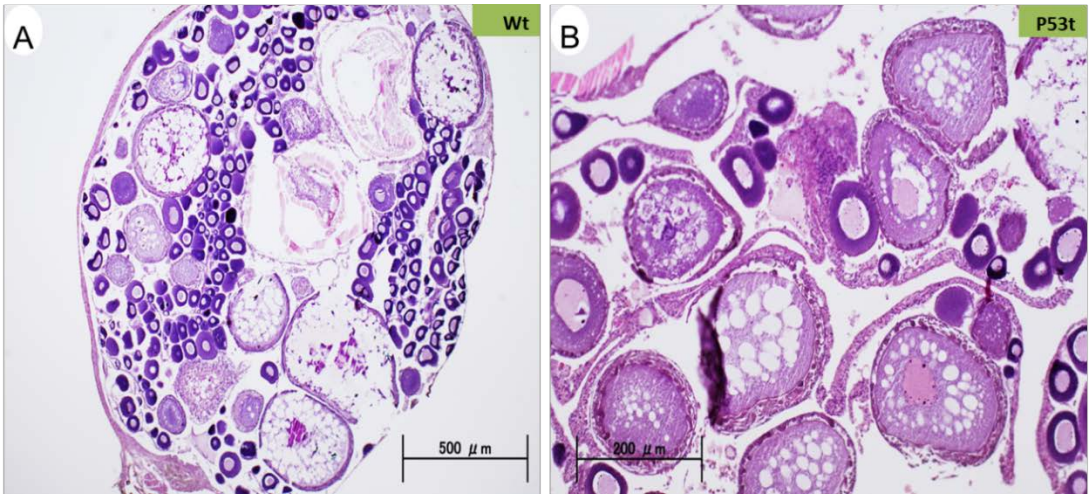

Fig. 4: T.S. of the ovary of *Oryzias latipes* showing clumps distribution of follicles in (A) Wt (Hd-rR) compared with regular distribution in (B) p53 (-/-) mutant. H&E stain.

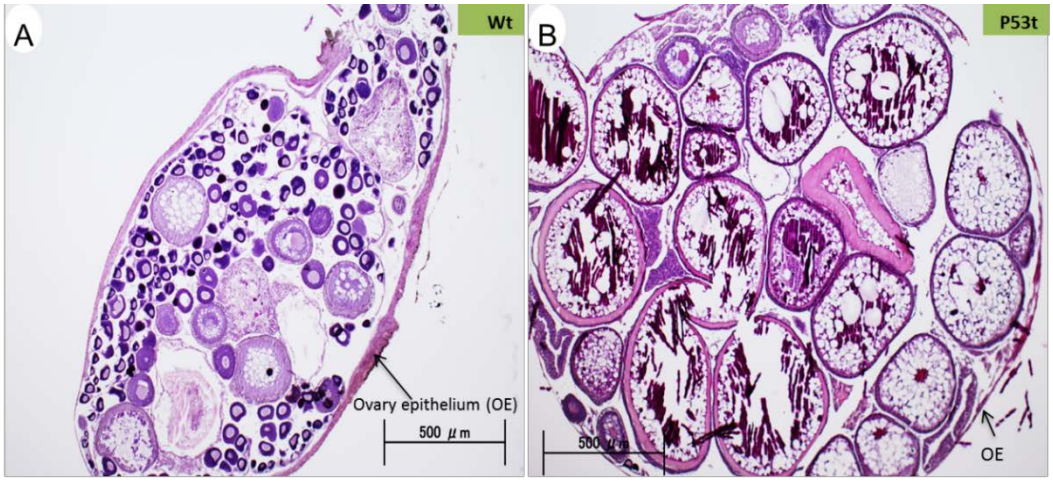

Fig. 5: T.S. of the ovary of *Oryzias latipes* showing small number of growing follicles in (A) Wt (Hd-rR) compared with (B) p53 (-/-) mutant. H&E stain.

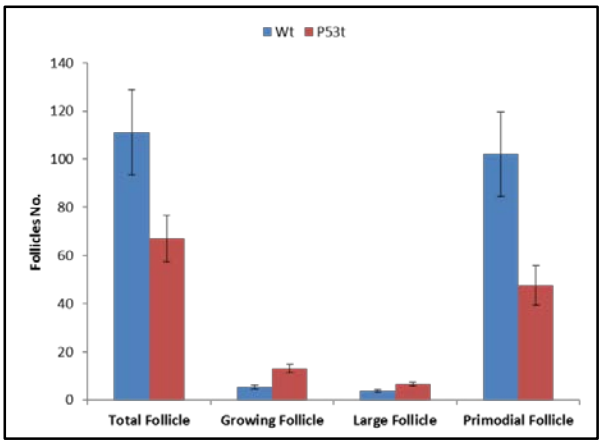

Chart 1: Quantification of ovarian follicles frequency of the ovary of *Oryzias latipes* showing the difference between Wt (Hd-rR) compared with p53 (-/-) mutant.

4- DISCUSSION AND CONCLUSION

The purpose of this present study was to use a histological approach to establish the difference between two strains from WT (HdrR) and P53 (-/-) of medaka (*Oryzias latipes*) in the organization of the gonad histology. Wide studies about structural changes in ovarian morphology in fish tissue have done by different researchers (Alonso-Fernández et al., 2011; Blazer, 2002; Kopiejewska and Kozłowski, 2007). Those studies including seasonal changes can be the study ovarian tissue red mullet *Mulets surmuletus* southern coast of the UK (N'Da and Deniel, 1993), reproductive cycle and time of the annual reproductive Sea bass on ovarian morphology and histology (Guiguen et al., 1993), Histology study and development stages fish ovarian bester sturgeon (Amiri et al., 1996), macroscopic and microscopic stages of ovarian development in white sturgeon *Acipenser transmuntanus* (Doroshov et al., 1997), effects of ionizing radiation on the ovaries of Japanese medaka (Srivastava, 1966), comparative study on ovarian structures in scorpaenids (Koya and Muñoz, 2007) ovarian cycles of Hungarian riverine fish species (Lefler et al., 2008), and on *sparus aurata* ovary (El -Sayyad et al., 2013), ovarian development and sexual maturity of kutum (Saeed et al., 2010) and ovarian development of female white bream (Kopiejewska and Kozłowski, 2007), study the reproductive biology of hermaphrodite fishes (Alonso-Fernández et al., 2011) and for assessment of gonadal tissue in wild fishes (Blazer, 2002). Historically, much less attention has been focused on gonadal histology of fishes (Blazer, 2002). In the present study, differences in the ovaries structure in of ovaries of Wt (HdrR) and P53 (-/-) of medaka (*O. latipes*) were reported.

The present study results of histological observation of the ovarian structure and developmental stages quantification are summarized in (Fig. 2-5 & chart 1). The histological structure of the ovary in medaka has been described before morphologically but not numerically, although a lot of studies have been done as comparative study for different fish species with different reproductive mode indicated many changes inside the ovary (Koya and Muñoz, 2007). On the other hand, El -Sayyad et al., (2013) reported variations between sea fishes and farm in different points, including pattern of sex inversion, gonadosomatic indices and oogenesis by assessment either histological structure or by scanning and transmission electron microscope.

Our results showed normal development of the ovarian structure and stages of medaka in both WT (HdrR) and P53 (-/-) of medaka (*O. latipes*) compared with other teloests fishes. The histological structure of ovarian follicles in WT (HdrR) obtained in this investigation, similar to P53 (-/-) fish. During ovarian development of teleosts, oocyte undergoes vitellogenisis which induced by estradiol in the liver, then transported vitellogenin via blood to the ovary for starting another process called oogenesis (El -Sayyad et al., 2013; Wallace and Selman, 1980).

Previous studies have been reported seasonal variations in gonadosomatic indices in fishes (El -Sayyad et al., 2013), While other studies recorded histological structure changes due to different reproductive modes of the scorpaenidae (Koya and Muñoz, 2007). From the present study, histological variations of female in the medaka fish, *Oryzias latipes* inhabiting both WT (HdrR) and P53 (-/-) revealed high developmental stage frequency changes. There was a considerable change in the oocyte maturation stages. It has been reported changes in the building level morphology and structure of ovarian oocyte referrals can be index and good in different stages of maturity in fish species and other valuable fish species (Tyler and Sumpter, 1996).

Oogenesis and development as indicated from the histological investigations and assessment of frequency of different developmental stages appeared being much more in number in WT (HdrR) than in P53 (-/-). The developmental structure of ovaries in female white bream has been studies indicated the different developmental stages inside the ovary (Kopiejewska and Kozłowski, 2007).

Our findings can be concluded as follows (1) The histological structure of the ovary in the examined fishes represents the generalized teleostean structure (2) The color and the size of the ovary is differs in both WT strains and p53 -mutants (3) No ova-testis in both Wt and P53t was observed (4) Total follicles in P53 was little than in Wt while small number of the primodial follicles in P53 (-/-) compared with the number in Wt (5) The distribution of the follicles in P53t is regular distributed in whole the cavity of the ovary while in case of Wt, it is look like aggregations of follicles (6) Although the results showed large total number of follicles in Wt, the growing follicles and large follicles recorded high number in P53 (-/-) than Wt.

Acknowledgments

This research was supported partly by a Grant-in-Aid for Scientific Research to H.M. (21221003) from the Ministry of Education, Culture, Sports, Science and Technology of Japan

5- REFERENCES

Alonso-Fernández, A., Alós, J., Grau, A., Domínguez-Petit, R., Saborido-Rey, F., 2011. The Use of Histological Techniques to Study the Reproductive Biology of the Hermaphroditic Mediterranean Fishes Coris julis, Serranus scriba, and Diplodus annularis. Marine and Coastal Fisheries: Dynamics, Management, and Ecosystem Science 3, 145–159.

Amiri, M., Maebayashi, M., Hara, A., Adachi, S., Yamauchi, K., 1996. Ovarian development and

serum sex steroid and vitellogenin profiles in the female cultured sturgeon hybrid the Bester. J. Fish Biol. 48, 1164-1178.

Blazer, V.S., 2002. Histopathological assessment of gonadal tissue in wild fishes. Fish Physiology and Biochemistry 26, 85–101.

Doroshov, S.I., Moberg, G.P., Venennam, J.P., 1997. .Observation on the reproduction cycle of culturedwhite sturgeon, *Acipenser transmuntanus*. Envir. Biol. of Fishes 48, 265-278.

El -Sayyad, H.I., Elsayyad, F.I., El -Shershaby, E.M., Amer, M.A., El -Gammal, I.M.M., 2013. Comparative studies on sparus aurata ovary from fish farm and sea. Egyptian Society of Experimental Biology (Zoology) 9, 181 – 188.

Guiguen, Y., Cauty, C., Fostier, A., Fuchs, J., Jalabert, B., 1993 Reproductive cycle and sex inversion of the Sea Bass, Lates calcalifer, reared in sea cage French Polynesia, histological and morphometric description. Envir. Biol. Of Fishes 39, 231-247.

Hyodo-Taguchi, Y., Etoh, H., 1985. Tritium effects on the gonads of the aquarium fish, Oryzias latipes. 1. Fecundity and fertility, in: Matsudaira, H., Yamaguchi, T., Etoh, H. (Eds.), Tritium Radiobiology and Health Phys. National Institute of Radiological Sciences, Chiba, pp. 207–220.

Hyodo-Taguchi, Y., Matsudaira, H., 1987. Higher susceptibility to N-methyl-N'-nitro-N-nitrosoguanidine-induced tumorigenesis in an interstrain hybrid of the fish, *Oryzias latipes* (medaka). Jpn J Cancer Res. 78(5), 487-493.

Ishikawa, Y., 2000. Medakafish as a model system for vertebrate developmental genetics. Bioessays 22, 487-495.

Kopiejewska, W., Kozłowski, J., 2007. Development structure of ovaries in female white bream, Abramis bjoerkna from Lake Kortowskie in North-Eastern Poland. Folia Zool. 56, 90–96.

Koya, Y., Muñoz, M., 2007. Comparative study on ovarian structures in scorpaenids: Possible evolutional process of reproductive mode. Ichthyological research 54, 221–230.

Kurokawa, H., Saito, D., Nakamura, S., Katoh-Fukui, Y., Ohta, K., Baba, T., Morohashi, K., Tanaka, M., 2007. Germ cells are essential for sexual dimorphism in the medaka gonad. Proceedings of the National Academy of Sciences of the United States of America 104, 16958–16963.

Lefler, K.K., Hegyi, Á., Baska, F., Gál, J., Horváth, Á., Urbányi, B., Szabó, T., 2008. Comparison of ovarian cycles of Hungarian riverine fish species representing different spawning strategies. Czech J. Anim. Sci. 53, 441–452.

Marza, V.D., Marza, E.V., Guthrie, M.J., 1937. Histochemistry of the ovary of Fundulus heteroclitus with special reference to the differentiating oocytes. Biol. Bull. 73, 67-92.

N'Da, K., Deniel, C., 1993. Sexual cycle and seasonal changes in the ovary of the red mullet, *Mullus surmuletus*, from the southern coast of Brittany. J. Fish Biol. 43, 229-244.

Naruse, K., Tanaka, M., Mita, K., Shima, A., Postlethwait, J., Mitani, H., 2004. A medaka gene map: the trace of ancestral vertebrate proto-chromosomes revealed by comparative gene mapping. Genome Res. 14, 820-828.

Raven, C.P., 1961. Oogenesis: the storage of developmental information. Pergamon Press, New York.

Saeed, S.S., Reza, I.M., Bagher, A.F., Saeed, G., 2010. Histological Study of Ovarian Development and Sexual Maturity of Kutum (Rutilus frisii kutum Kamenskii, 1901). World Applied Sciences Journal 8, 1343-1350.

Sayed, A.E., Mekkawy, I.A., Mahmoud, U.M., 2012. Histopathological Alterations in some Body Organs of Adult Clarias gariepinus (Burchell, 1822) Exposed to 4-Nonylphenol, in: Garcia, M. (Ed.), Zoology. Janeza Trdine 9, 51000 Rijeka, Croatia, pp. 163-184.

Shima, A., Himmelbauer, H., Mitani, H., Furutani-Seiki, M., Wittbrodt, J., Schartl, M., 2003. Fish genomes flying. Symposium on Medaka Genomics. EMBO Rep. 4, 121-125.

Shima, A., Mitani, H., 2004. Medaka as a research organism: past, present and future. Mech Dev 121, 599–604.

SPSS, 1998. SPSS for Windows. SPSS Inc, Headquarters, Chicago.

Srivastava, P.N., 1966. Effect of ionizing radiation on the ovaries of Japanese medaka, Oryzias latipes (t. et s.). Acta Anat (Basel) 63, 434-444.

Tyler, C.R., Sumpter, J.P., 1996. Oocyte growth and development in teleost. Rev Fish Biol Fisheries 6, 287–318.

Wallace, R.A., Selman, K., 1980. Oogenesis in Fundulus heteroclitus II. The transition from vitellogenesis into maturation. Gen.Comp. Endocrinol. 42, 345–354.

Wittbrodt, J., Shima, A., Schartl, M., 2002. Medaka—a model organism from the far East. Nat Rev Genet 3, 53–64.

First International Conference on Science, Engineering & Environment,
Tsu City, Mie, Japan, Nov.19-21, 2015, ISBN: 978-4-9905958-5-2 C3051

EFFECTS OF TRADITIONAL THAI MASSAGE ON STANDING BALANCE, MUSCLE FATIGUE, CONCENTRATION, AND FREE THROW ACCURACY IN BASKETBALL ATHLETES

Krittachai Sarakul[1], Wichai Eungpinichpong[2], Thanarat Sripongngam[3]

[1]PhD candidate, Graduate School, KhonKaen University, Thailand;
[2]Research Center in Back, Neck, Other Joint Pain and Human Performance, KhonKaen University, Thailand;
[3]Department of Health and Sport Science, Faculty of Education, Mahasarakham University, Thailand

ABSTRACT

The free throw is the single most important shot in the game of basketball. Factors influencing the ability of the basketball free throw accuracy consisted of skill, standing balance, muscle fatigue, and concentration. Massage has been used for reducing muscle fatigue in sports that may affect standing balance, concentration, and free throw accuracy. However, no research available on these regards. The aim of this study was to determine the effects of traditional Thai massage (TTM) on standing balance, muscle fatigue, concentration, and basketball free throw accuracy. Thirty male basketball athletes were randomly allocated into either traditional Thai massage (TTM) group or Control (C) group after which they were swabbed to receive the other one with a 2-week washed out period. Standing balance, perceived muscle fatigue, concentration, and basketball free throw accuracy were measured at before and in the next day after receiving either 1-hour session of TTM or rest. The study found that balance and concentration were significantly increased ($p<0.05$) only in the TTM group. Fatigue was significantly decreased ($p<0.05$) in TTM group while there was significantly increased ($p<0.05$) in C group. Between-group comparison revealed that standing balance and fatigue were significantly different ($p<0.05$). However, free throw accuracy was not changed in both within- and between- groups comparison. We conclude that a 1-hour session TTM could increase standing balance, decrease muscle fatigue, and increase concentration but could not affect free throw accuracy in basketball athletes.

Keywords: Massage, Balance, Fatigue, Concentration, Accuracy

INTRODUCTION

Basketball is a very popular sport competing in both national and international competitions included SEA Games, Asian Games and Olympic Games.

The free throw in the basketball game is very important. It may contribute 20 percent of the total score [1**]**. The free throw in basketball games is probably the easiest task because the player can shoot alone without protection from the opponents. The free throw area is only about 15 feet from the loop, and sophisticated skills are not needed. The steps of shooting include as follows. Firstly, holding the ball in the position of "lock and load". That is holding the ball with the fingertips and using another hand to hold it and direct the ball and bend the knee by holding the ball lower than the head. Secondly, eyes targeting and focusing at the loop and using another hand to reinforce the direction of ball. Normally, the player is suggested not to shoot with both hands because if one hand is far away from the ball, it is difficult to shoot accurately. Thirdly, throwing the ball directly to the loop at arm's length with elbow stretching and flicking of the wrist. The elbow of the hand shooting must be in the same line with the body so the arm straights up and makes shooting more accuracy. Fourthly, when releasing the ball with the fingertips, the ball should roll back and the middle finger will release the ball. At the end, the ball should follow through the fingertips, not with the palm. More than 80 percent of the free throw is a missed. So, the most important thing while shooting free throw is the concentration of the basketball player, the balance of the body, and movement control without muscle fatigue.

Sport massage is currently receiving attention and commonly used because it may help athletes to improve in many aspects including facilitate recovery from fatigue, and reduce muscle tightness and pain resulting from the competition. Recent studies found that massage may help athletes reduce lactic acid in the muscles [2**]-**[3**]** and fatigue in the muscles **(**DOMS) [4]-[5]. Massage for athletes also helps muscles to return to normal condition quickly [3], [6]. Massage for athletes, according to the reports, has also helped reduce psychology [7], tension [8], depression [9], enhance better mood [10], and quality of life [11]. Moreover, massage also improves the flexibility of the body, and reduces injuries from hard-working muscles [12].

Traditional Thai massage (TTM) is a deep-pressure type of massage that the therapist apply thumb or palm pressure along meridian lines on the

body. It always affects deep the soft tissues (muscles, tendons, and ligaments) of limbs, neck, and back. It has been used for hundreds years to treat patients with chronic soft tissue injuries [13]. TTM has beneficial effects for both body and mind, for it can reduce pain in muscles and joints as well as anxiety. According to a study using TTM in patients with low back pain, it was found that TTM could reduce back pain perception and substance P in the subject's saliva [14]. Udompittayason (2003) [15] found that TTM can reduce the symptoms of stress and headaches. In addition, at the end of beta wave of electroencephalography: (EEG) is reduced which reflect that TTM may induce mental relaxation as well as significantly reduces pain in patients with scapula - thoracic pain [16]. Leelayuwat et al. (2001) [17] found TTM can increase endurance of back muscles and significantly reduce back pain in patients with chronic back pain. Considering the effects of Thai traditional massage in soccer players, it was revealed that Thai traditional massage can relax muscles and decrease pulse rate significantly after practicing soccer. It was also noted that the players receiving massage can recover from fatigue effectively. It has been known that Thai traditional massage provides relaxation, recovery from the fatigue after practicing sports and increase of the durability of the muscles. Therefore, the researchers believe that Thai traditional massage is useful for improving the basketball free throw accuracy by reducing muscle fatigue and increasing efficiency during the race. Therefore, the objective of the study was to explore the effects of TTM on standing balance, muscle fatigue, concentration, and basketball free throw accuracy in basketball athletes.

MATERIAL AND METHOD

The current study was a crossover randomized controlled trial, which was approved by the Ethical Committee of Khon Kaen University, Thailand (HE582041). Thirty male basketball athletes whose average aged 19.83±0.80 year old, average weight 67.13±2.92 km, and average height 178.73±3.32 cm. They were randomly allocated into either traditional Thai massage (TTM) group or Control (C) group after which they were swabbed to receive the other one with a 2-week washed out period. Each of them signed an informed consent form to participate in this study. Exclusion criteria consisted of the participants receive psychotropic drug, analgesic and anti-inflammatory drugs, moderate to severe of muscle or joint pain, impair skin or hypersensitivity to massage, and the participants who slept at less than 6 hours the night before participating. Standing balance, muscle fatigue, concentration, and basketball free throw accuracy were measured at before and in the next day after received a 1-hour session of TTM or rest.

Procedure and Protocol

The TTM group received moderate pressure massage on both side of arms, legs, and the body along the points of massage for 1 hour (Fig. 1). The massage was performed in supine, side lying on the left, and on the right positions. The participants rest in C group.

Flamingo balance test was used to test the standing balance of the body. The participants had to stand with one foot on a test stand (3 cm wide, 30 cm long and 5 cm high wood, and the stable area is 15 cm long and 2 cm wide on either side). Another leg must be bent with one hand holding the heel. One arm stretched out to balance the body. The test checker stood in front of the participant and the participant held the test checker's arm. After receiving the signal, the participants released the test checker's arm and maintained the balance as long as possible. The time was stopped when the participant lose his or her balance.

The muscle fatigue test was tested by visual analogue scale.

Concentration test was done by using the program in the mobile phone. The test was done by allowing the participants to identify whether the name of the color matched the color of the alphabets or not. For example, if the black color was shown with yellow alphabets, the participant had to choose the wrong mark (the cross mark), but if blue color was presented in blue alphabets, the participant had to choose the correct mark (check mark). There were 100 questions. If the participants answer incorrectly, the program will immediately stop. The record of time was used as the measurement of the concentration and the response of reaction.

The participants were tested with basketball free throw of 5 sets: and 10 balls per set. So, the total was 50 balls. This was used to assess basketball free throw accuracy.

Statistical analysis

The data were presented as mean ± SD. Shapiro-Wilk test was used to assess normal distribution. Paired t-test and Wilcoxon Sign Rank-Test were used to compare the outcome variables between before and after intervention within-group. Unpaired t-Test and Mann Whitney U-Test were used to compare outcome variables between-groups.

Statistical significance was set at the $p < 0.05$.

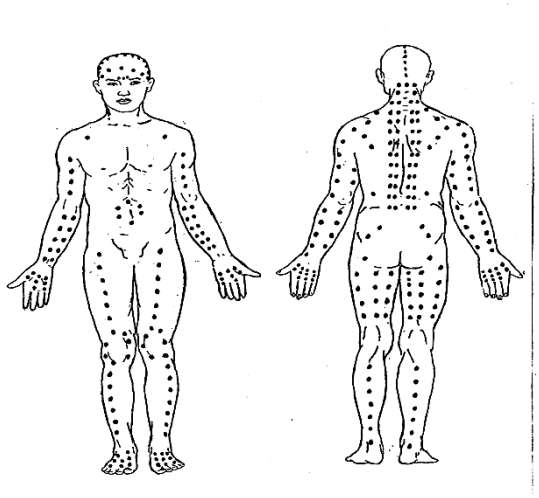

Fig. 1 The massage point or line is established by Eungpinichpong [18]

RESULTS

The present study demonstrated that standing balance was significantly increased only in TTM group (d = -1.20±1.03, 95 % CI = -1.58, -0.51, P = 0.001), the time of concentration was significantly decreased only in TTM group (d = 3.13±4.24, 95 % CI= 1.54, 4.71, P = 0.001), muscle fatigue was significantly decreased in TTM group (P = 0.001) (Table 1), and there was significantly increased in C group (P = 0.001) (Table 2). Basketball free throw accuracy was not significantly changed in both groups (Table 1, 2).

When compared the outcomes between TTM and C groups, we found that standing balance and muscle fatigue were significantly difference (P = 0.017). Basketball free throw accuracy and concentration showed no differences between the groups comparison (Table 3).

DISCUSSION

The finding of the present study revealed that TTM could increase standing balance, decrease muscle fatigue, and increase concentration. Standing balance was significantly increased only in TTM group. This was consistent with Sefton et al. (2004) [19] found that a 60-minute massage therapy could improve both static and dynamic balance in 35 older persons. Ploypailin (2011) [20] study found that foot massage could improve the functional mobility and balance performance in 29 healthy elderly female.

We suggested that Flamingo balance test method may not be suitable because this test cause tired of standing rather than sustained loss of balance. Future studies should use other methods, such as the path of COP by using Force plate or a Wii Fit.

This study demonstrated that TTM could decrease muscle fatigue which corresponding to Mori et al. (2004) [21]. They studied the effect of massage on blood flow and muscle fatigue following isometric exercise in 29 healthy male subjects. The subjects lay prone on the table and extend their trunks for 90 seconds (Load I) after that the subjects received either massage on lumbar region or rest for 5 minutes, then repeated the same load (Load II). They found that muscle blood volume was higher after massage than after rest ($p < 0.05$), skin blood flow was greater after massage than after rest ($p < 0.05$), and fatigue was lower with massage than with rest ($p < 0.01$). Leelayuwat et al. (2003) [17] found that the subject has longer isometric endurance time after a 2-hour Thai massage than after a 2-hour lie down due to increasing resistance to fatigue of back muscles.

The current study showed that TTM could increase concentration may be due to massage produced mechanical pressure which increased parasympathetic and decreased sympathetic activity [22]-[24] leading to increase concentration. Moreover, concentration was associated with delta activity and previous study found that massage could increase delta activity. Buttagat et al. (2012) [16] studied a 30-min session of TTM in 40 patients with scapulocostal syndrome. They found a significantly increased in relaxation as indicated by increased in delta activity ($p < 0.05$) and decreased in theta, alpha, and beta activity ($p < 0.01$).

Although, TTM could increase standing balance, decrease muscle fatigue and increase concentration which that is the factors influencing the ability of the basketball free throw accuracy but such changes could not affect this accuracy. The accuracy is not changed much may depend on the skill of the athlete. The present study focused on the short-term effects of massage, however we did not know whether long-term or cumulative effects of TTM would affect these variables or not. Thus, Future studies should determine whether long-term effects of TTM on standing balance, muscle fatigue, concentration, and basketball free throw accuracy.

CONCLUSION

The present study showed that TTM could increase standing balance, decrease muscle fatigue, and increase concentration. However, basketball free throw accuracy was not changed after a single session of TTM.

ACKNOWLEDGEMENTS

The authors would like to express my special thanks to the basketball athletes who participated in the study.

Table 1 Comparison between before and after on the standing balance, muscle fatigue, concentration, and basketball free throw accuracy in TTM group.

outcome	TTM group (n = 30)	
	before mean±SD	after mean±SD
Standing balance (min)	31.23±3.20	32.43±3.34**
95%CI	30.04, 32.43	31.19, 33.68
Muscle fatigue	4.80±0.81	3.73±0.83**
95%CI	4.50, 5.10	3.42, 4.04
Concentration (ms)	209.07±39.53	205.53±38.49**
95%CI	194.31, 223.83	191.56, 220.31
Accuracy (times)	28.30±3.54	28.5±3.74
95%CI	26.98, 29.62	27.10, 29.90

Note: TTM= traditional Thai massage
**Significant difference at p-value <0.01

Table 2 Comparison between before and after on the standing balance, muscle fatigue, concentration, and basketball free throw accuracy in control group.

outcome	C group (n = 30)	
	before mean±SD	after mean±SD
Standing balance (min)	30.60±2.88	29.97±2.33
95%CI	29.52, 31.68	29.10, 30.84
Muscle fatigue	4.83±0.70	5.73±0.94**
95%CI	4.57, 5.09	5.38, 6.09
Concentration (ms)	209.40±39.46	210.33±39.41
95%CI	194.67, 224.14	195.62, 225.05
Accuracy (times)	28.53±3.66	28.40±3.42
95%CI	27.16, 29.90	27.12, 29.68

Note: C = Control
**Significant difference at p-value <0.01

Table 3 Comparison between-groups on the standing balance, muscle fatigue, concentration, and basketball free throw accuracy.

outcome	After intervention	
	TTM group mean±SD	C group mean±SD
Standing balance (min)	32.43±3.34	29.97±2.33*
95%CI	31.19, 33.68	29.10, 30.84
Muscle fatigue	3.73±0.83	5.73±0.94**
95%CI	3.42, 4.04	5.38, 6.09
Concentration (ms)	205.53±38.49	210.33±39.41
95%CI	191.56, 220.31	195.62, 225.05
Accuracy (times)	28.5±3.74	28.40±3.42
95%CI	27.10, 29.90	27.12, 29.68

Note: TTM = traditional Thai massage, C = Control
*Significant difference at p-value <0.05
**Significant difference at p-value <0.01

REFERENCES

[1] Kozar B, Vaughn RE, Lord RH, Whitfield KE, Dve B, “Importance of free throw at various stages of basketball game”, Perceptual and Motor Skill, Vol. 78(1), 1994, pp. 243-248.

[2] Robertson A, Walt JM, Galloway SD, “Effect of leg massage on recovery from high intensity cycling exercise”, Br J Sport Med, Vol. 38, 2004, pp. 173-176.

[3] Monedero J, Donne B, “Effect of recovery interventions on lactate removal and subsequent performance”, Int J Sport Med, Vol. 21, 2004, pp. 593-597.

[4] Hilbert JE, Sforzo GA, Swensen T, “The effect of massage on delayed onset muscle soreness”, Br J Sport Med, Vol. 37, 2003, pp. 72-75.

[5] Farr T, Nottle C, Nosaka K, Sacco P, “The effects of therapeutic massage on delayed onset muscle soreness and muscle function following downhill walking”, J Sci Med Sport , Vol. 5, 2002, 297-306.

[6] Hemming B, Smith M, Graydon J, Dyson R, “Effect of massage on physiological restoration, perceived recovery, and repeated sports performance”, Br J Sports Med, Vol. 34, 2000, 109-114.

[7] Moyer CA, Round J, Hannum JW, “A meta-analysis of massage therapy research”, Psychol Bull, Vol. 130, 2004, pp. 3-8.

[8] Weinberg R, Jackson A, Kolodny K, “The relationship of massage and exercise to mood enhancement”, The Sport Psychologist, Vol. 2, 1988, pp. 202-211.

[9] Jones NA, Field T, "Massage and music therapies attenuate frontal EEG asymmetry in depressed adolescents", Adolescence, Vol. 34, 1999, pp. 529-534.
[10] Hemandez – Reif M, Field T, Hart S, "Smoking cravings are reduced by self-massage", Prev Med, Vol. 28, 1999, pp. 28-32.
[11] Birke TJ, Mcgrady A, Mac Arthur RD, Khuder S, "The effects of massage therapy alone and in combination with other complementary therapies on immune system measures and quality of life in human immune deficiency virus", J Altern complement Med, Vol. 6(5), 2000, pp. 405-414.
[12] Maclaren DP, Gibson H, Parry-Billings M, Edwards RH, "A review of metabolic and physiological factors in fatigue", Exerc Sport Sci Rev, Vol. 17, 1989, pp. 29-66.
[13] The Institute of Thai Traditional Medicine, Thai massage. Bangkok: Thai veteran organization, 2001.
[14] Mackawan S, Eungpinichpong W, Pantumethakul R, Chatchawan U, Hunsawong T, Arayawichanon P, "Effects of traditional Thai massage versus jointmobilization on substance P and pain perceptionin patients with non-specific low back pain", Journal of Bodywork and Movement Therapies, Vol. 11, 2007, pp. 9–16.
[15] Udompittayason W, "Effects of Thai Massage on Reduction of Tension - Type Headache", Prince of Songkla University, 1999.
[16] Buttagat V, Eungpinichpong W, Chatchawan U, Arayawichanon P, "Therapeutic effects of traditional Thai massage on pain, muscle tension, and anxiety in patients with scapulocostal syndrome: A randomized single-blinded pilot study", Journal of Bodywork and Movement Therapies, Vol. 16(1), 2012, pp. 57-63.
[17] Leelayuwat N, Eungpinichpong W, Manimmanakorn A, "The effects of Thai massage on resistance to fatigue of back muscles in chronic low back pain patients", J Med Tech Phy Ther, Vol. 13, 2001, pp. 13-19.
[18] Eungpinichpong W, Therapeutic Thai massage. Bankok: Suweeriyasarn Printing Press, 2008.
[19] Sefton JM, Yarar C, Berry JW, "Massage Therapy Produces Short-term Improvements in Balance, Neurological, and Cardiovascular Measures in Older Persons", Int J Ther Massage Bodywork, Vol. 5(3), 2012, pp. 16-27.
[20] Ploypailin N, "Immediate effect of foot massage on functional mobility and balance performance in the elderly", Khon Kaen University, 2014.
[21] Mori H, Ohsawa H, Tanaka TH, Taniwaki E, Leisman G, Nishijo K, "Effect of massage on blood flow and muscle fatigue following isometric lumbar exercise", Med Sci Monit, Vol. 10, 2004, pp. CR173-178.
[22] Buttagat V, Eungpinichpong W, Chatchawan U,Kharmwan S, "The immediate effects of traditional Thai massage on heart rate variability and stress related parameters in patients with back pain associated with myofascial trigger points", J Bodyw Mov Ther, Vol. 15, 2011, pp. 15-23.
[23] Lindgren L, Rundgren S, Winsö O, Lehtipalo S, Wiklund U, Karlsson M, Stenlund H, Jacobsson C, Brulin C, "Physiological responses to touch massage in healthy volunteers", Auton Neurosci, Vol. 158(1-2), Dec. 2010, pp. 105–110.
[24] Pishbin T, Firoozabadi SM, JafarniaDabanlo N, Mohammadi F, Koozehgari S, "Effect of Physical Contact (Hand-Holding) on Heart Rate Variability", International Journal of Advanced Computer Science, Vol. 2(12), Dec. 2012, pp. 452–456.

Engineering

First International Conference on Science, Engineering & Environment,
Tsu City, Mie, Japan, Nov.19-21, 2015, ISBN: 978-4-9905958-5-2 C3051

APPLICATIONS OF CORRELATION RELATED FUNCTIONS IN SIGNAL AND IMAGE PROCESSING AND PATTERN IDENTIFICATION

Humera Rafique[1], Samina Rafique[2]
[1]Faculty (Department of Mechatronic Engineering), SZAB Institute of Science and Technology, Karachi, Pakistan;
[2]PhD Scholar and Faculty (Department of Electrical Engineering), Bahria University, Islamabad, Pakistan

ABSTRACT

This paper presents applications of Correlation functions in pattern identification and signal separation, specifically and image processing in general. The main focus is on images, specially those carry information in the form of alphabetic characters. The purpose of this paper is to describe what correlation function is, how this function can perform discrimination among several signals, images and objects within them, and at last a comparison of various techniques will be presented. This work is an intermediate stage work of pattern matching of Urdu handwritten broken characters with correlation and finally with curve fitting techniques.

Keywords: Alphabetic character identification, Auto correlation function (ACF), Correlation, Cross correlation function (CCF), Correlation coefficient, Image analysis, Pattern identification, Feature extraction.

INTRODUCTION

For a period of four decades, pattern identification has been used for the classification of objects into categories, seen by a computing machine [1]. This sub-field of Image and Signal processing has several applications in medicine, weather forecasting, forensics, industrial inspection, communication, geology, agriculture and security. There are a number of techniques and algorithms to teach a computing machine by which these are able to identify objects within images and videos even in real time. There are several advanced and growing techniques for this purpose, while this paper represents a simple, easy and strong thus widely used technique that can serve the described purpose independently, as well as can be a part of many advanced and robust pattern identification algorithms and techniques, namely Correlation, its variants and related algorithms.

Correlation, or Discrete Time Correlation is a mathematical operation that is similar to Discrete Time Convolution apparently. This operation compares two signals, at a time, by measuring the degree of similarity of these signals. On the basis of this measure, further application dependent information can be obtained. Good, but advanced examples of applications are radar communication, under water sound navigation systems (SONAR), general communication systems, and medical imaging [2].

The mathematical definition of correlation has two versions, as the correlation itself has two forms: Autocorrelation and Crosscorelation. Autocorrelation, primarily a comparison of a signal with its own, while the Crosscorrelation compares a signal with some other signal. The connection between signals is often used to determine system characteristics, these signals are related to. [8]. Defining two signals $x_1(n)$ and $x_2(n)$, $\forall\ x_1(n) = x_2(n)$, then the corresponding sequence is defined as

$$\mathbb{C}_{12}(\ell) = x_1(n) \otimes x_2(n) = \sum_{n=0}^{N-1} x_1(n)\, x_2(n-\ell) \qquad (1)$$

where, index $\boldsymbol{\ell} = \cdots, -\mathbf{2}, -\mathbf{1}, \mathbf{0}, \mathbf{1}, \mathbf{2}, \ldots$ and defined as the time shift or lag, and subscript '12' represents the order of correlation, or the direction of shift of one signal. Reversing that order will not change the resultant, as correlation is a 'Commutative process'.

Now, defining two signals $x_1(n)$ and $x_2(n)$, $\forall\ x_1(n) \neq x_2(n)$, then the corresponding sequence is defined as

$$\mathbb{C}_{12}(\ell) = x_1(n) \otimes x_2(n) = \sum_{n=0}^{N-1} x_1(n)\, x_2(n-\ell) \qquad (2)$$

where, index $\boldsymbol{\ell} = \cdots, -\mathbf{2}, -\mathbf{1}, \mathbf{0}, \mathbf{1}, \mathbf{2}, \ldots$ and defined as the time shift or lag, and subscript '12' represents the order of correlation, or the direction of shift of one signal. Again, 'commutative property' is valid here. Both equations look same, but results will be different because of similarities and dissimilarities of two signals being compared.

Process of Correlation

The *Correlation* is a process that intently seems like the process of *Convolution;* a process in which one of the signals to be convolved (in fact any one of them), will be *folded*, than *shifted*, and then *multiplied* with the other signal. All products (depends how many samples or elements of one

signal in range of the other one, (i.e, one to many) will be added to deliver elements of the output signal respectively. This three step process is repeated multiple times, (as folding is perfumed once throughout the process), until the whole signal is covered. The *Correlation* applies the same process onto the signals, without *folding*. i.e. *Shifting*, *multiplication* and *Summation*. Due to this similarity of process, many computer programs use alternate commands for both operations by providing the folded version of the signal. i.e., $x_1(-n)$.

APPLICATIONS OF CORRELATION FUNCTIONS IN SIGNAL AND AUDIO PROCESSING

This section will describe a few synthetic signal, and audio signal processing applications mainly focusing on signals' characteristic detection and identification:

1. Detection and Estimation of Periodic Signals Concealed in Random Noise

Many signals on communication lines suffer transmission impairments and noise interruption problems. A periodic signal e.g., has been received at a receiver as noise corrupted signal, can be identified in random noise by characterizing ACF of both signals. Fig.1-1 shows signals and their respective ACF plots. As a broad band signal (random noise) possesses narrower correlation peaks, thus easy to identify [9]. Fig. 1-2. Conclusively, the received signal is not 'just' noise, but it carries usable information too, to be extracted.

Pseudo Code flow:

- *Sampling frequency (fs), signal's frequency (f), time sweep (t),*
- *Sinusoid x(n), Random noise rn(n)*
- *acf(x), acf(rn), acf(x+rn)*
- *Plots*

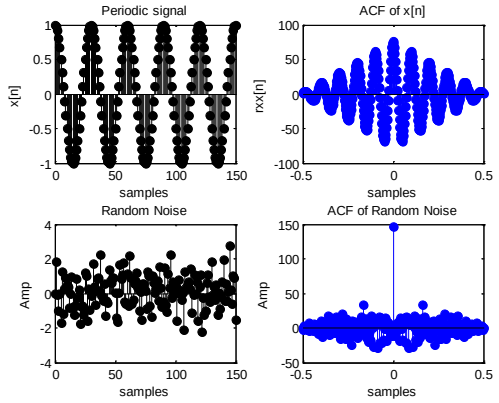

Fig. 1-1 Separate periodic cosine wave and random noise, and their respective ACF plots

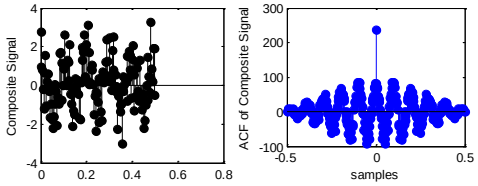

Fig. 1-2 Periodic signal embedded in random noise and their composite ACF

2. Estimation of Power Spectral Density of a Signal via Autocorrelation

The power spectral density (PSD) is an estimate of amplitude variations of a signal over a range of frequency. 'The Fourier transform of the autocorrelation function of an energy signal is equal to the energy spectral density of that signal' [5].

$$\mathcal{F}[\mathbb{C}_{xx}(\ell)] = \mathcal{P}_{xx}(\omega) \qquad (3)$$

The test signal is a sinusoid with three harmonic components. One power spectral density (PSD) has been computed by fast Fourier transform (FFT); the right hand side of Eq. (3). The ACF of the signal then brought to frequency domain via FFT.
Both PSDs of Eq. (3) are found comparable.

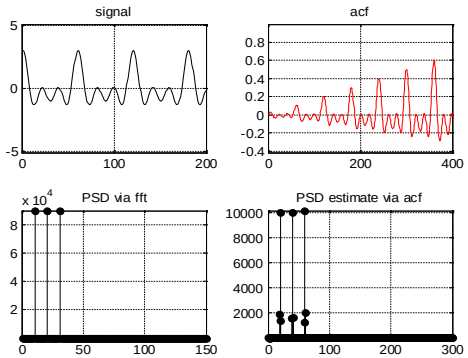

Fig. 2-1 Multi frequency sinusoid, its ACF and their respective PSDs

The Fourier transform relationship of the ACF and the power spectrum describes their mathematical equivalency, as they possess the same information. Though, the power spectrum is more accustomed and generally easily interpretable. The ACF is powerful for theoretical work, for determining the non-whiteness of data or residuals, for detecting periodic components in data, and for identifying the dominant power law noise type [6].

Pseudo Code flow:

- *fs, f1, f2=2f2, f3=3f1, t,*
- *Three Sinusoids x1, x2, x3, y = x1+x2+x3*
- *(magni(fft(acf(y)))^2, (magni(fft(y)))^2, plots*

3. The ACF of a Real Valued Signal is An Even Function, while CCF is An Odd Function. [2].

These properties of both functions have been implemented using a few periodic and aperiodic signals. *Plots in Fig 3-1 and Fig 3-2 can be plotted using built in commands of any computing software.*

i. The ACF is symmetric about the central lag i.e., an even function:

$$\mathbb{C}_{11}(-\ell) = \mathbb{C}_{11}(\ell) \qquad (4)$$

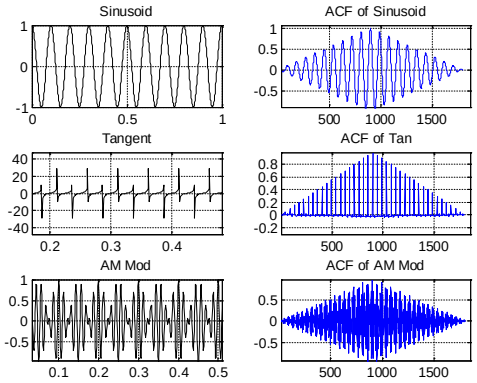

Fig. 3-1 Periodic signals and their respective ACF (even function symmetry)

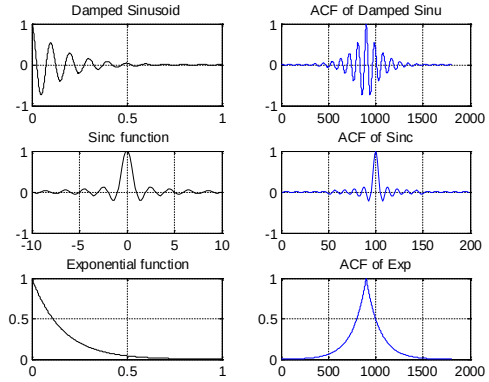

Fig 3-2 Aperiodic signals and their respective ACF (even function symmetry)

As signals in Fig. 3-1 and Fig.3-2 are of low frequencies, their ACF plots show a border range over entire lag sweep.

ii. The CCF is symmetric with amplitude reversal about the central lag i.e., an odd function:

$$\mathbb{C}_{12}(-\ell) = -\mathbb{C}_{21}(\ell) \qquad (5)$$

Note, that possessing even or odd symmetries in corresponding correlation functions, depend on the degree of similarity between the two signals.

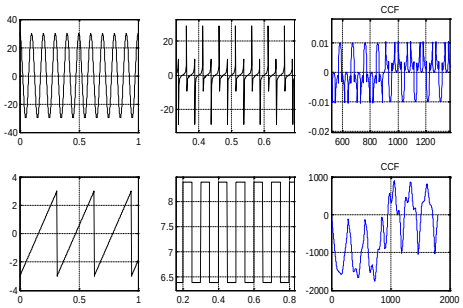

Fig. 3-3 Couple of CCF of two (different[☼]) signals (odd function symmetry)

4. Frequency Detection

A highly variant ACF time domain plot describes how fast the signal itself changes w.r.t time and vice versa. Fig 4-1.

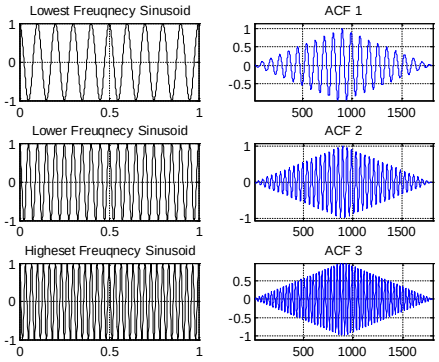

Fig. 4-1 Three signals (harmonics) and their respective ACFs, showing faster time changes as the signals go faster (increasing frequency)

5. Identifying Information Carrying Signal from Random Noise, with Occurrence in Time Domain

In addition to the identification of noise buried signal, Correlation can identify the exact localization of signal in time domain. Two wave audio signals 'car horn' and 'train whistle' are test signals. Fig. 5-1.

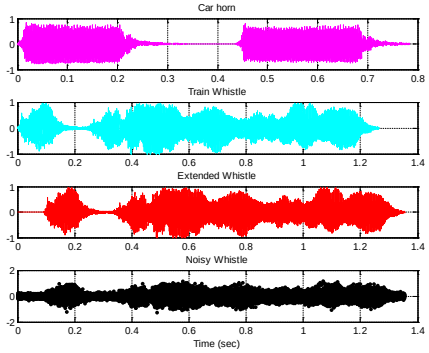

Fig. 5-1 Time series plots of wave files, and train sound buried in random noise

Getting their 'Welch Spectra' will not reveal the required information easily regarding (a) if noisy signal contains information (Train whistle) sound, and (b) when the information signal joins the random noise.

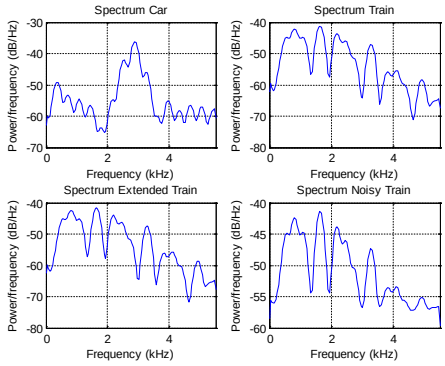

Fig. 5-2 Welch Spectra of separate and noisy signals

In Fig. 5-1 and 5-2 it is very difficult to get answers of (a) and (b), specially (b). While computing Cross correlation of two signals with the noisy signal will answer both. In Fig 5-3, CCF of car horn sound shows minor amplitudes (notice the difference of amplitude scales, at same scale this plot will show almost a straight line). The larger values show the presence (matching) of train whistle sound in noisy signal, while the position of largest peak from zeroth lag (i.e., 90.7 ms) describes the time when the train sound joins the random noise. Third plot of Fig. 5-1 shows this time delay clearly.

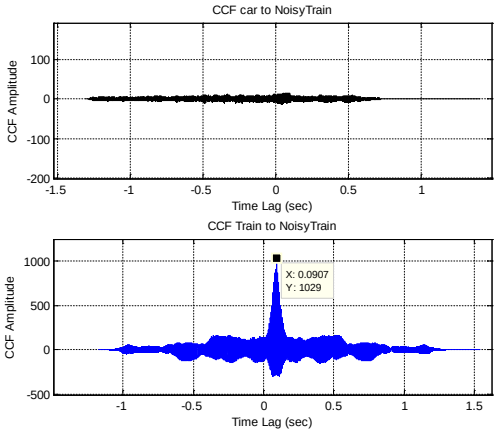

Fig. 5-3 CCF of both sounds with Noisy sound

Pseudo Code flow:

- *x = audioread(car.wav), get fs*
- *y = audioread(train.wav),*
- *y1 = zeropad(y,10ms)*
- *rn = random, z = addmix(rn,y1), plots*
- *welchspectrum(x,y,y1,z), plots*
- *c1 = ccf(x,z), c2 = ccf(y,z), plots*
- *timedelay = maxi(c2)/fs*

(Note: fs for the whole system should be the same)

APPLICATIONS OF CORRELATION FUNCTIONS IN IMAGE AND VIDEO PROCESSING

This section will describe a few image processing and alphabetic character identification applications:

6. Alphabetic Character Identification using Cross-Correlation Maxima

To demonstrate the above the system will follow the algorithm shown in Fig. 6-1.

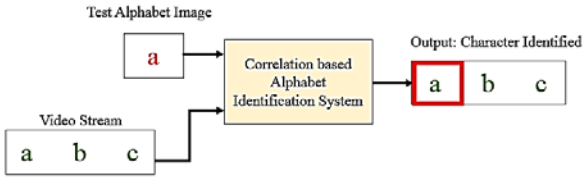

Fig. 6-1 Basic Block Diagram of Alphabetic Identification System

To implement the above block diagram, a series of .png images has been created. Fig. 6-2. These images have been converted into an avi file, each image as frame [10]. The created video file run these images one by one with an adjustable time delay.

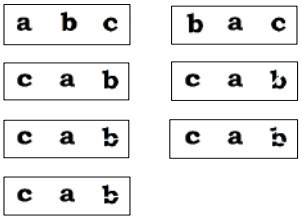

Fig. 6-2 Individual images of three alphabets in different order, standard and broken forms

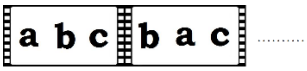

Fig. 6-3 Individual images run as avi file

Correlation Based Alphabet Identification System Block Algorithm [3]

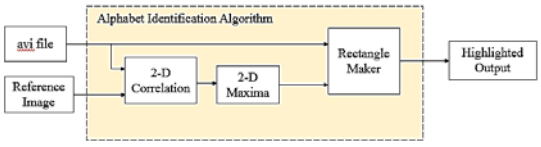

Fig. 6-4 Simplified Block Diagram of Algorithm

Each frame of video contains three alphabets and reference of target image contains a specific

alphabet. The target image is compared frame by frame, alphabet by alphabet by computing the 2D correlation and then its maxima.

The alphabet with highest maxima is then encircled with a rectangle box as output per frame. The system has been tested with different fonts. The system is even able to identify broken characters.

Table 1 Results of 2D Correlation Maxima Algorithm for letter 'b'

Frame	Font 1	Output	Comments
1	a b c	a b c	Recognized
2	a c b	a c b	Recognized
3	c a b*	c a b*	Recognized

* Broken alphabet

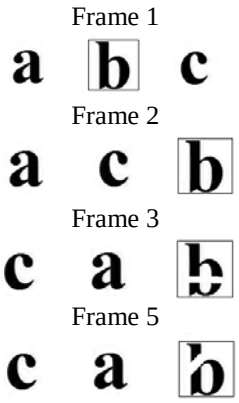

Fig. 6-5 Results of 2D Correlation Maxima Algorithm for letter 'b' in '*Times New Roman*'. Frame 3 and 5 show broken alphabets recognition*

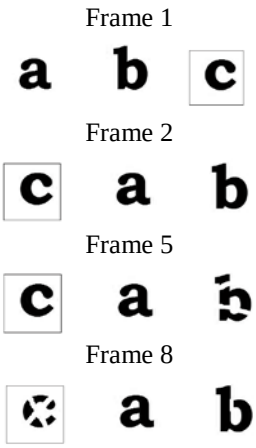

Fig. 6-6 Results of 2D Correlation Maxima Algorithm for letter 'c' in 'Bookman Old Style'. Frame 8 shows badly broken alphabet recognition

Pseudo Code flow:

- *x1 … x7 = images with 3 alphabets each*
- *abc.avi = videomake(x1,x2,…x7)*
- *mov1 = readvideio(abc.avi)*
- *y =2dcorr(frame1,tartgetimage1)*
- *ym = 2dmaxi(y)*
- *rect-shape = compare(frame1,ym), output*

Table 2 Correlation Maxima Factors of Alphabets

Alphabet	Matching Alphabet	Correlation maxima Factor (Ratios)
a	a	247
b	b	201
c	c	201

7. Sharpening of Colored Image using Luminance Processing with 2D Correlation Filter

A high pass image filter can make transitions of an image more critical making the image sharper interns. A colored RGB image if converted into Y'CbCr image so that its luma intensity should be filtered in the described manner. Fig. 7-1.

Algorithm [3]

A 'Y'CbCr' version of an 'RGB' image (bird.jpg) has been made intentionally blurred using averaging correlation filter of mask size 15×15. The intensity layer of image has been processing by a high pass correlation filter and then converted back to its RGB form. The output images show two levels of sharpening.

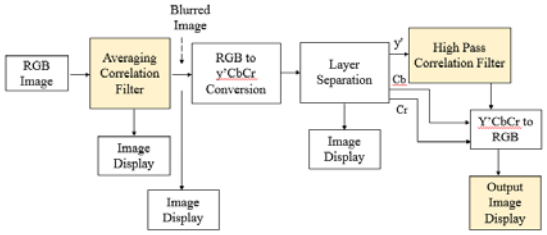

Fig. 7-1 Block Diagram of Luminance Processing Algorithm

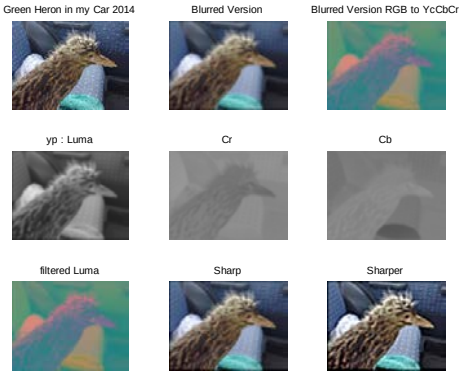

Fig. 7-2 Results of high pass filtering of luminance intensity of a colored image

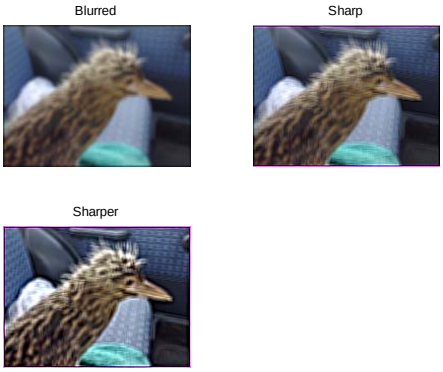

Fig. 7-3 A closer look of results for better comparison

CONCLUSION

This study has successfully described the Correlation and its related functions along with several applications in signal, audio and image processing. Selected algorithms and implementation methodologies in the form of pseudo code have described to facilitate the reader for better understanding.

REFERENCES

[1] Gose Earl, J. Richard, Steve Jost "Pattern Recognition and Image Analysis" 2008.

[2] Proakis John G., Manolakis, D. G. "Digital Signal Processing, principles, Algorithms, and Applications" 2009.

[3] Mathworks Inc. Online Manuals.

[4] Gonzalez Rafael C., Woods, Richard E. "Digital Image Processing" 2012.

[5] Corinthios Michael, "Signals, Systems, Transforms and Digital Signal Processing with MATLAB" 2009.

[6] Riley W. J., "Use of the Autocorrelation Function for Frequency Stability Analysis" 2003.

[7] Irvin Tom, "The Autocorrelation - Revision A" 2012.

[8] Roberts M. J., "Fundamentals of Signals and Systems" 2012.

[9] Adrian-Martinez S., Ardid M., "Acoustic Signal detection Through the Cross-correlation Methods in Experiments with Different Signal to Noise Ratio and Reverberation Conditions", Journal of Instrumentation and Detectors, ArVix Database, 2015

[10] Credit: Roberson Walter, 'png to avi conversion'

First International Conference on Science, Engineering & Environment,
Tsu City, Mie, Japan, Nov.19-21, 2015, ISBN: 978-4-9905958-5-2 C3051

DEVELOPMENT OF METHYL, ESTER AND CARBONYL TERMINATED N-SI(111) ELECTRODE FOR PHOTO-ELECTROCHEMICAL CELL

Toshihito Ohtake and Ken-ichiro Iijima
Faculty of Engineering, Aichi University of Technology, Japan

ABSTRACT

We have remarked photovoltaic power generation, and have produced higher efficiency solar cells by proceeding to the influential investigation. However, those include great problems which take high costs to produce them by semiconductor fabrication processes as p-n junction and use of transparent conductive indium oxide etc. Previously, higher open circuit voltage was discovered with n-Si photo-electrochemical cell (PEC) comparing with familiar p-n junction solar cell, and was able to fabricate them with low costs and ease. But, the cell has a point that the n-Si surface is gradually oxidized by exposing to an electrolyte solution, and then SiO_2 is slowly formed as an insulation layer on the surface. Hence, we investigated alkyl terminated n-Si surface by ATR-FTIR and XPS. Consequently, we confirmed the methyl termination with measuring the Si(111) surface on the surface by the UV irradiation in PCl_5/chlorobenzene solution and immersing them in CH_3Li/diethyl ether. The coverage was estimated at about 63.7 %, and the re-termination of hydrogen was not obtained. Furthermore, we attempted an immobilization which was applied by hydrosilylation terminated with ester (hydrophobic) or carbonyl (hydrophilic) group. The hydrosilylation on the hydrogen-terminated Si reacted as the ester termination in the propiolate/hexan solution. Similarly, the carbonyl group termination was also performed and estimated in the propiolic-acid/hexan solution, and the Si surface was immobilized by the hydrophobic or hydrophilic functional groups. The Si surface was hardly oxidized by XPS measurement.

Keywords: Silicon electrode, Alkyl termination, Photo energy conversion, Photo electrochemistry

INTRODUCTION

We are faced with problems about energy and global environment, and solar energy has been noticed to solve them. However, there are high costs to be complicated manufacturing processes or the use of expensive materials for transparent conductive oxide including indium etc, the application of the solar energy is studied in activity, which the solar energy conversion developments of high efficiently and low costs are required to spread them largely [1], [2]. For example, it is known that a hydrogen generation by a solar water splitting cell with using n-Si electrode, which is interested with low costs, but the stability of Si electrode in electrolytic solution is not so good to form SiO_2 layer on the surface by oxidation of Si. Some researchers have been carried out to solve the problem by immobilizing the surface with alkyl base etc. [3]–[11]. For example, the alkyl termination on the Si surface is investigated toward developments of bio sensors for DNA and protein detection by giving functionalize on the surface [12], furthermore, the termination is known to make the surface stable for the oxidation in the solution [13], [14]. In addition, controls of electrode properties are expected for the termination by the functional groups on Si surface.

In this study, termination with ester or carboxy group was carried out by a hydrosilylation on hydrogen-terminated Si surface. The termination was estimated by ATR- FTIR and XPS measurement, simultaneously with evaluation of Si surface oxidation.

EXPERIMENTAL

We carried out the methyl termination with a method reported by Bansal et al, which was immobilization on the surface by two steps alkyl termination via a chlorination in Scheme 1 [15]. The n-Si(111) surface was exposed by so-called RCA washing process as HF, H_2O, NH_3 + H_2O_2 solution, H_2O, HCl + H_2O_2 solution and H_2O_2 and then the surface was terminated hydrogen.

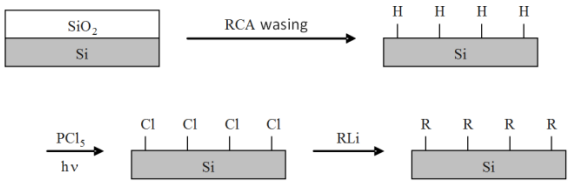

Scheme 1 Hydrogen, chlorine and alkyl base termination process.

Methyl Termination

After the surface was washed by diethyl ether, the chlorine termination was performed by immersing the Si(111) to sat. PCl_5/chlorobenzene solution under heating at 100 °C for 1 h irradiating UV light in flowing Ar gas. Next immersing them in CH_3Li/diethyle ether in Ar, and refluxing at 50 °C for 3 h, and the methyl termination was completed on the surface. Before the surface was measured by ART-FTIR, they are washed by diethyl ether, 2-propanol and pure water.

Ester Termination

The ester termination directly was made use of the hydrosilylation on the hydrogen-terminated Si in Scheme 2. The Si was immersed in 0.1 M methyl propiolate/hexan solution for 24 h at room temperature under Ar atmosphere in schlenk flask, after washed with diethyl ether. Furthermore, the immersed time was changed from 2 h to 15 h in methyl propiolate/hexan solution. Carbonyl group termination on the hydrogen-terminated Si was performed by the hydrosilylation with an unsaturated carboxylic acid. Similarly, the Si was immersed in 0.1 M propiolic acid/hexan solution for 24 h. The Si surface was measured by ATR-FTIR and XPS, and cumulative number was 256 and 64 respectively.

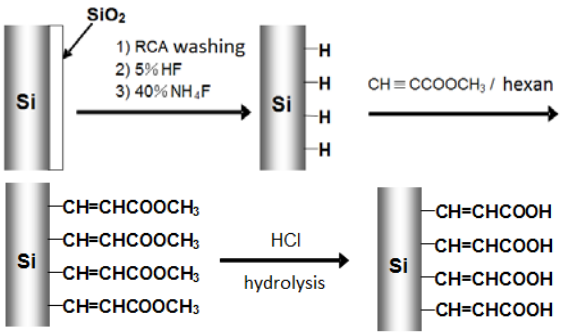

Scheme 2 Ester termination process by methyl propiolate/hexan solution and carbonyl termination by hydrolysis.

RESULTS & DISCUSSION

ATR-FTIR spectrum is shown about the hydrogen and methyl terminated n-Si(111) surface in Fig. 1 (A). Since we were able to observe peaks of C-H stretching vibrations based on the methyl base at 2975 cm^{-1} (asymmetry) at line (b), the methyl termination would be performed. Other peaks were also obtained by detecting the methylene base identified C-H stretching vibration at 2930 cm^{-1} (asymmetry) and 2855 cm^{-1} (symmetry). Furthermore, try of hydrogen re-termination results in not obtaining the spectra based on hydrogen termination on the n-Si(111) surface. This result would show that the surface was covered sufficiently with the methyl bases by this processes, hence the re-termination by hydrogen will not happen.

The rough coverage of the methyl termination was calculated from the peak areas. The result gave ca. 63.7 %, and it would suppose that the methyl termination was completed adequately. A coverage have been reported at about 50 % by alkene (1-octene, 1-octadecene, 1-octyne and styrene etc.) on the n-Si(111) surface [16], hence this coverage of methyl termination will be enough. The Si surface was estimated by the XPS spectrum of Si_{2p} in Fig. 1 (B), which showed peak for no oxidation at about 103 eV except a main peak at about 100 eV [17].

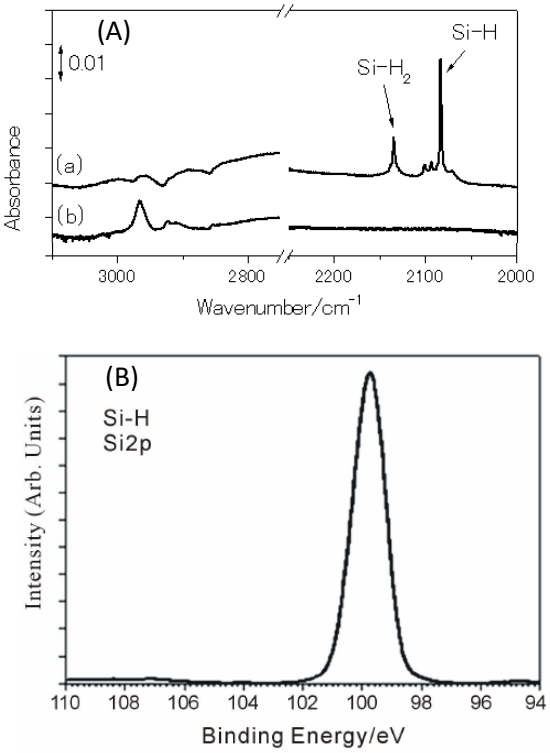

Fig. 1 (A) is ATR-FTIR spectra of (a); hydrogen termination and (b): methyl termination on the Si surface. (B) is XPS spectrum of Si_{2p} for the hydrogen termination.

The ester termination on Si surface was estimated about C=C, C=O and Si-H stretching vibration. Fig. 2 (A) shows ATR-FTIR spectra of the n-Si(111) surface terminated with methyl propiolate by 24 h immersing time in line (a) and terminated with hydrogen by RCA washing in line (b). This result would show the ester termination by applying methyl propiolate because peaks of C=O at 1728 and C=C at 1588 stretching vibration based on the ester was appeared, and Si-H stretching vibration at 2083 cm^{-1} was disappeared simultaneously. These results

would conclude that the ester termination by the hydrosilylation progressed instead of the hydrogen termination on Si surface.

Fig. 2 (B) shows XPS spectra of C_{1s} about the ester termination which indicated three peaks of C-H, C-O and O=C-O [18]. These results would confirm the termination by the ester followed by the ATR-FTIR measurements in the same way. Although a XPS spectrum of Si_{2p} indicated a peak barely at about 103 eV in Fig. 2 (C), the surface would not be effected by the oxidation.

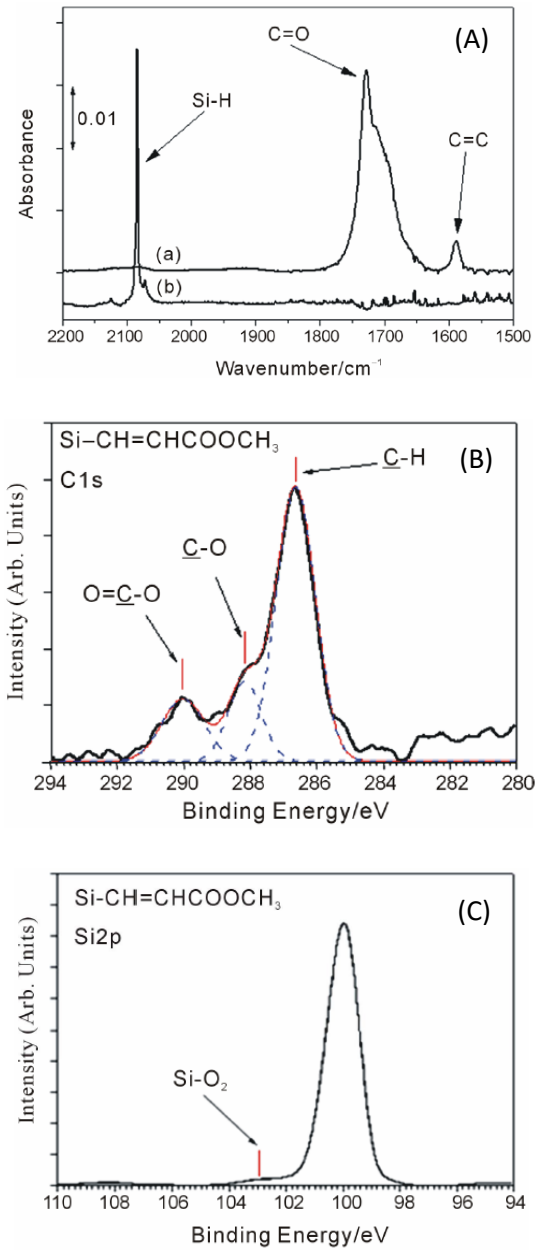

Fig. 2 (A) is ATR-FTIR spectra of (a); methyl propiolate termination and (b); hydrogen termination on the Si surface. (B) is XPS spectrum of C_{1s} and (C) is Si_{2p} for the ester.

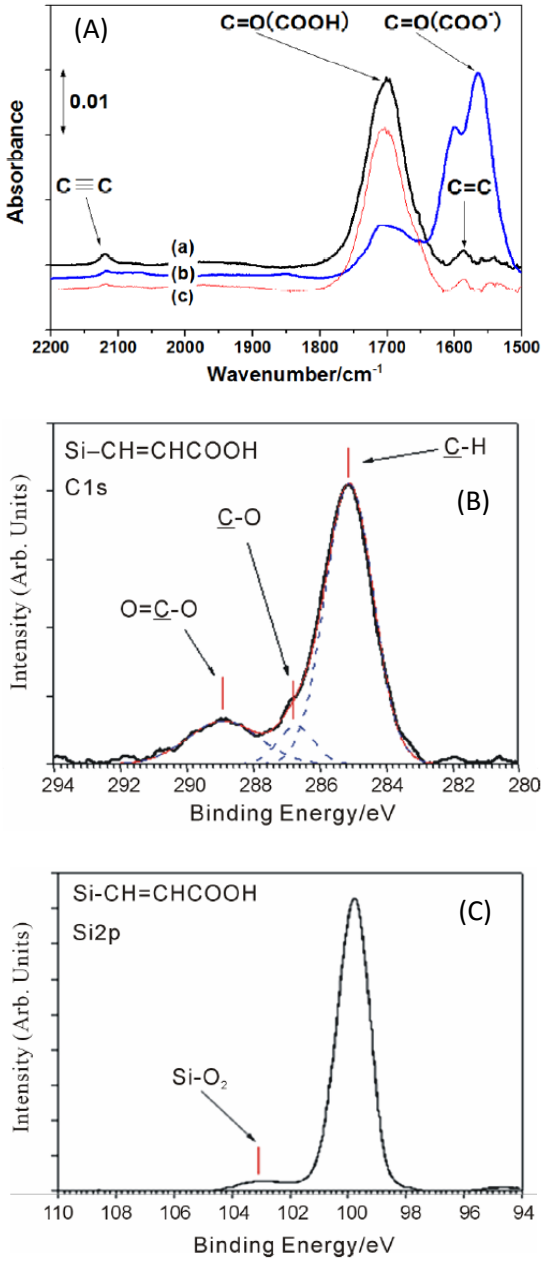

Fig. 3 (A) is ATR-FTIR spectra of (a); carboxy group termination on the Si surface and (b); after immersing in 0.01 M NaOH and (c); immersing in 2.0 M HCl subsequently. (B) is XPS spectrum of C_{1s} and (C) is Si_{2p} for the carbonyl group termination.

The carbonyl group termination on Si surface was similarly evaluated at line (a) in Fig. 3 (A). The ATR-FTIR spectra showed peaks of C=O at 1709 cm^{-1} and C=C at 1586 stretching vibration based on the carbonyl group, hence the Si surface would be immobilized by the carbonyl group. Moreover, spectra of the sample applied in 0.01 M NaOH solution obtained a peak of C=O based on $–COO^–$ at about 1550 cm^{-1} instead of decrease in the peak of C=O based on –COOH at 1709 cm^{-1} showed in line (b). Subsequently, spectra of the sample applied in

2.0 M HCl aq. showed the peak of C=O based on –COOH at 1709 cm^{-1} instead of disappear at the peak based on $–COO^-$ at about 1550 cm^{-1} in line (c). Hence, the carbonyl group terminated on the Si surface will cause acid-base reaction with the NaOH or HCl solution. Then, a peak of C≡C stretching vibration at 2119 cm^{-1} disappeared by the acid-base reaction. However the peak is not clear yet, dimers formed between the immobilized carbonyl group and an unreacted propiolic acid might exist on the Si surface in Scheme 2. Consequently, the peak based on C≡C at 2119 cm^{-1} might be appeared by the termination, and disappeared by acid-base reactions.

XPS spectrum of C_{1s} indicated three peaks of C-H, C-O and O=C-O in Fig. 3 (B) [18]. These results would confirm the termination by carbonyl group followed by the ATR-FTIR measurements. A spectrum was obtained slightly at about 103 eV in Fig. 3 (C), which will be caused by immersing in the propiolic acid/hexan solution. The peak for the carbonyl group termination was larger than that of the ester termination. This result might show a difference of hydrophobic or hydrophilic functional groups. These terminated Si would be applied as the functional electrodes.

CONCLUSION

By measuring the Si(111) surface by ATR-FTIR, we confirmed the methyl termination on the surface by the UV irradiation in PCl_5/chlorobenzene solution and immersing them in CH_3Li/diethyl ether in Ar, and refluxing at 50 °C for 3 h. Furthermore the coverage was estimated at about 63.7 %. Similarly, the carbonyl group termination was also performed and estimated in the propiolic acid/hexan solution, and the Si surface was immobilized by the hydrophobic or hydrophilic functional groups. It will be necessary to form more pure Si surface since the Si surface was hardly oxidized by XPS measurement.

ACKNOWLEDGEMENT

This work was supported by JSPS KAKENHI Grant Number 15K05602.

REFERENCES

[1] Chopra K. L., Paulson P. D. and Dutta V., “Thin-film solar cells: an overview”, Prog. Photovolt. Vol. 12, March 2004, pp. 69-92.

[2] Goetzberger A., Hebling C. and Schock H. W., “Photovoltaic materials, history, status and outlook”, Mater. Sci. Eng. R, Vol. 40, Jan. 2003, pp. 1-46.

[3] Linford M. R. and Chidsey C. E. D., “Alkyl monolayers covalently bonded to silicon surfaces”, J. Am. Chem. Soc., Vol. 115, Dec. 1993, pp. 12631-12632.

[4] Inford M. R., Fenter P., Eisenberger P. M. and Chidsey C. E. D., “Alkyl Monolayers on Silicon Prepared from 1-Alkenes and Hydrogen-Terminated Silicon”, J. Am. Chem. Soc., Vol. 117, March 1995, pp. 3145-3155.

[5] Bansal A., Li X. L., Lauermann I., Lewis N. S., Yi S. I. and Weinberg W. H., “Alkylation of Si Surfaces Using a Two-Step Halogenation/Grignard Route”, J. Am. Chem. Soc., Vol. 118, July 1996, pp. 7225-7226.

[6] Buriak J. M., “Organometallic chemistry on silicon surfaces: formation of functional monolayers bound through Si–C bonds”, Chem. Commun. 1999 Issue 12, pp. 1051-1060.

[7] Buriak J. M., “Organometallic Chemistry on Silicon and Germanium Surfaces”, Chem. Rev., Vol. 102, March 2002, pp. 1271-1308.

[8] Wayner D. D. M. and Wolkow R. A., “Organic modification of hydrogen terminated silicon surfaces”, J. Chem. Soc., Perkin Trans. 2, Nov. 2002, pp. 23-24.

[9] Inford M. R., Fenter P., Eisenberger P. M. and Chidsey C. E. D., “Alkyl Monolayers on Silicon Prepared from 1-Alkenes and Hydrogen-Terminated Silicon”, J. Am. Chem. Soc., Vol. 117 March 1995, pp. 3145-3155.

[10] Buriak J. M., “Organometallic chemistry on silicon surfaces: formation of functional monolayers bound through Si–C bonds”, Chem. Commun., Issue 12 1999, pp. 1051-1060.

[11] Buriak J. M. “Organometallic Chemistry on Silicon and Germanium Surfaces”, Chem. Rev., Vol. 102, May 2002, pp. 1271-1308.

[12] Strother T., Cai W., Zhao X. S., Hamers R. J. and Smith L. M., “Synthesis and Characterization of DNA-Modified Silicon (111) Surfaces”, J. Am. Chem. Soc., Vol. 122, Jan. 2000, pp. 1205-1209.

[13] Bansal A. and Lewis N. S., “Stabilization of Si Photoanodes in Aqueous Electrolytes through Surface Alkylation”, J. Phys. Chem. B, Vol. 102, May 1998, pp. 4058-4060.

[14] Royea W. J., Juang A. and Lewis N. S., “Preparation of air-stable, low recombination velocity Si(111) surfaces through alkyl termination”, Appl. Phys. Lett., Vol. 77, No. 13 2000, pp. 1988-1990.

[15] Okubo T., Tsuchiya H., Sadakata M., Yasuda T. and Tanaka K., “An organic functional group introduced to Si(111) via silicon-carbon bond: a liquid-phase approach”, Appl. Surf. Sci., Vol 171, No. 3-4, 2001, pp. 252-256.

[16] Cicero R. L., Linford M. R. and Chidsey C. E. D., “Photoreactivity of Unsaturated Compounds with Hydrogen-Terminated Sillicon(111)”, Langmuir, Vol. 16, Feb. 2000, pp. 5688-5695.

[17] Danner J. B. and Vohs, J. M., “Surface Reactions during the Growth of SiO_2 Thin

Films on Si(100) Using Tetraethoxysilane", Langmuir, Vol. 10, Sep. 1994, pp. 3116-3121.

[18] Vallant T., Brunner H., Kattner J., Mayer U., Hoffmann H., Leitner T., Friedbacher G., Schügerl G., Svagera R. and Ebel M., "Monolayer-Controlled Deposition of Silicon Oxide Films on Gold, Silicon, and Mica Substrates by Room-Temperature Adsorption and Oxidation of Alkylsiloxane Monolayers", J. Phys. Chem. B, Vol. 104, May 2000, pp. 5309-5317.

First International Conference on Science, Engineering & Environment,
Tsu City, Mie, Japan, Nov.19-21, 2015, ISBN: 978-4-9905958-5-2 C3051

EFFECT OF ADSORPTION CONDITION ON THERMAL STABILITY OF PROTEINS ADSORBED ONTO BIOMASS CHARCOAL POWDER

Hidetaka Noritomi[1], Shunichi Kurihara[1], Nobuyuki Endo[2], Satoru Kato[1] and Katsumi Uchiyama[1]
[1]Department of Applied Chemistry, Tokyo Metropolitan University, Japan; [2] EEN Co., Ltd., Japan

ABSTRACT

Authors have found out that bamboo charcoal powder (BCP), which is prepared from bamboo wastes by pyrolysis at low temperatures, is very useful as a carrier for the thermal stabilization of proteins. Hen egg white lysozyme (HEWL) and α-chymotrypsin (CT) were effectively adsorbed onto BCP. The thermal stability of BCP-adsorbed HEWL was strongly dependent upon the adsorption conditions such as solution pH, ionic strength, and temperature. Moreover, Writers have revealed the heat-resistant mechanism on the basis of the structure of HEWL. Likewise, the thermal stability of BCP-adsorbed CT could be enhanced by selecting the adsorption condition.

Keywords: Biomass Charcoal Powder, Protein, Adsorption, Thermal Stability, Hen Egg White Lysozyme, α-Chymotrypsin

INTRODUCTION

The utilization of biomass to energies and functional materials is one of the most important challenges to establish a recycling society [1]-[4]. However, plant biomass wastes have not sufficiently been recycled yet, although a large number of plant biomass wastes have been discharged in the world. Moreover, the development in the high value-added function of plant biomass wastes has been desired.

On the other hand, proteins are biomolecules of great importance in the fields of biotechnology, fine chemistry, pharmacy, biosensor, and biofuel cell, since they exhibit their outstanding biological activities under mild conditions [5]-[7]. However, most of proteins are immediately denatured and inactivated by heat due to the disruption of weak interactions including ionic bonds, hydrogen bonds, and hydrophobic interactions, which are prime determinants of protein tertiary structures [8]. Adsorption of proteins onto various water-insoluble carriers has attracted continuous attention as the simplest and most economical method of stabilizing proteins [9], [10]. Moreover, the performances of adsorbed proteins such as activity, specificity, and stability are markedly dependent upon the physical and chemical surface properties of carriers. Accordingly, it is possible to derive the desired performances of proteins by selecting a suitable carrier. However, there have been few reports about the relation between the performances of adsorbed proteins and the adsorption conditions.

In order to investigate the valuable function of plant biomass wastes, authors have so far studied the interaction of proteins with biomass charcoal powders derived from plant biomass wastes by pyrolysis at low temperatures. Writers have found out that proteins are effectively adsorbed onto biomass charcoal powders, and adsorbed proteins exhibit the enhanced storage stability and the excellent thermal stability, compared to those of free proteins [11]-[15].

In the present work, researches have investigated the thermal stability and structure of proteins adsorbed onto bamboo charcoal powder (BCP) under various adsorption conditions such as ionic strength, solution pH, and temperature in order to address how the adsorption conditions affect the thermal stability of BCP-adsorbed proteins.

MATERIALS AND METHODS

Materials

Lysozyme from hen egg white (EC 3.2.1.17, 46400 units/mg solid, MW=14300, pI=11), α-chymotrypsin from bovine pancreas (EC 3.4.21.1, 52 units/mg solid, MW=25000), and *Micrococcus lysodeikticus* (ATCC No. 4698) were purchased from Sigma-Aldrich Co. (St. Louis, USA). *p*-Nitrophenyl acetate was obtained from Wako Pure Chemical Industries, Ltd. (Osaka, Japan).

Preparation of BCP

Under nitrogen atmosphere, bamboo wastes were dried at 180 ℃ for 2 hr, were pyrolyzed at 450 ℃ for 2 hr, were carbonized at 350 ℃ for 3 hr, and then were cooled at 100 ℃ for 1 hr by pyrolyzer (EE21 Pyrolyzer, EEN Co. Ltd., Japan). Bamboo charcoal powder (BCP) was obtained by grinding the resultant bamboo charcoal with jet mill (100AS, Fuji Sangyo Co. Ltd., Japan).

Adsorption of Proteins onto BCP

As a typical procedure, 0.01 M phosphate buffer solution at pH 7 containing 500 μM hen egg white lysozyme (HEWL) and 3 g/L BCP was incubated at 25 ℃ and 120 rpm for 24 hr [11]. After adsorption, the mixture was filtrated with a membrane filter (pore size: 0.1 μm, Millipore Co. Ltd., USA). The amount of HEWL adsorbed on BCP was calculated by subtracting the amount of HEWL included in the supernatant liquid after adsorption from the amount of HEWL in its aqueous solution before adsorption. The amount of HEWL was measured at 280 nm by UV/vis spectrophotometer (UV-1800, Shimadzu Co. Ltd., Japan).

Similarly, the adsorption of α-chymotrypsin (CT) onto BCP was carried out by using 300 μM CT instead of 500 μM HEWL [12].

Measurement of Activity of BCP-Adsorbed Proteins

The activity of HEWL was determined using *Micrococcus lysodeikticus* as a substrate [13]. Three hundred and fifty μL of 0.01 M phosphate buffer solution at pH 7.0 of BCP-adsorbed HEWL was added to 21 mL of 0.01 M phosphate buffer solution at pH 7.0 containing 200 mg/L *Micrococcus lysodeikticus*, and the mixture was incubated by stirring at 25 ℃. The absorbance of the mixture was periodically measured at 450 nm by UV/vis spectrophotometer (UV-1800, Shimadzu Co. Ltd.).

The activity of CT was determined using *p*-nitrophenyl acetate as a substrate [15]. Four mL of 0.01 M phosphate buffer solution at pH 7.5 of BCP-adsorbed CT was added to 16 mL of 0.01 M phosphate buffer solution at pH 7.5 containing 750 μM *p*-nitrophenyl acetate, and the mixture was incubated at 25 ℃ and 120 rpm. The absorbance of the mixture was periodically measured at 400 nm by UV/vis spectrophotometer.

Heat Treatment of BCP-Adsorbed Proteins

A requisite amount of BCP-adsorbed HEWL was dispersed in 0.01 M phosphate buffer solution at pH 7.0, the mixture was incubated in thermostated silicone oil bath at 90 ℃ for 30 min, and then was cooled at 25 ℃ for 30 min. On the other hand, a requisite amount of BCP-adsorbed CT was dispersed in 0.01 M phosphate buffer solution at pH 7.5, the mixture was incubated in thermostated water bath at 45 ℃ for 10 min, and then was cooled at 25 ℃ for 60 min.

In order to assess the thermal stability of BCP-adsorbed proteins, the activities of BCP-adsorbed proteins were measured before and after heat treatment. The remaining activity was obtained by Eq. (1).

$$\text{Remaining activity (\%)} = \frac{\text{Activity after heat treatment}}{\text{Activity before heat treatment}} \text{X } 100 \qquad (1)$$

Measurements of Circular Dichroism (CD), Fourier Transform Infrared (FTIR) Spectroscopies, and ζ -Potential

CD measurements of HEWL were carried out using a Jasco spectropolarimeter model J-820. The CD spectra were run on the HEWL solutions of 0.1 mg/mL in a quartz cell with 1.0 cm path length at an appropriate temperature.

FTIR measurements of native and BCP-adsorbed HEWL were carried out using a Jasco FT/IR spectrometer model FT/IR-4100. A KBr pellet containing 0.5 mg of native or BCP-adsorbed HEWL powder per 100 mg of KBr was prepared, and the measurements were performed using 512 scans under 4.0 cm^{-1} resolution.

The ζ potentials for HEWL were measured by massively parallel-phase analysis light scattering (Möbiu ζ , WYATT Technology Co. Ltd.), while those for BCP were measured by electrophoretic light scattering (ELS-Z2, OTSUKA Electronics Co. Ltd.).

RESULTS AND DISCUSSION

Effect of Ionic Strength of Adsorption Medium on Thermal Stability of BCP-Adsorbed HEWL

In order to investigate the relation between the thermal stability of BCP-adsorbed proteins and the adsorption condition, researches employed hen egg white lysozyme (HEWL) as a model protein, since it is well investigated regarding its structure, functions, and properties [16].

Researches have previously reported that the amount of proteins adsorbed onto BCP is strongly dependent upon the ionic strength of adsorption medium [11], [12]. So as to estimate the influence of ionic strength of adsorption medium on the thermal stability of BCP-adsorbed HEWL, authors have carried out the adsorption of HEWL onto BCP at pH 7 and different KCl concentrations. Figure 1 shows the relationship between the KCl concentration of adsorption medium and the remaining activity of BCP-adsorbed HEWL. The remaining activity of BCP-adsorbed HEWL decreased with an increase in KCl concentration. From the results of CP/MAS ^{13}C-NMR and X-ray photoelectron spectroscopy (XPS), acidic functional groups such as phenols, carbonyl groups, and carboxyl groups were detected in BCP [11]. On the other hand, Figure 2 shows the ζ potentials of BCP and HEWL against the solution

pH. As shown in Fig. 2, the ζ potential of BCP exhibited a negative value at pH 7, while the ζ potential of HEWL exhibited a positive value at pH 7. Accordingly, it is suggested that at higher ionic strength, the electrostatic attraction between HEWL and BCP decreases with a concomitant increase in the electrostatic screening effect when HEWL is adsorbed onto BCP.

Writers have measured the FTIR spectra of native and BCP-adsorbed HEWL to elucidate the influence of adsorption on the secondary structure of HEWL. Figure 3 shows the FTIR spectra of native HEWL and HEWL adsorbed onto BCP with or without KCl of adsorption medium. The most sensitive spectral region to protein secondary structural components is amide I (1700 – 1600 cm^{-1}), which is due almost entirely to the C=O stretch vibrations of the peptide linkages [17]. As seen in Fig. 3, the spectral pattern of BCP-adsorbed HEWL exhibited a specific shape of secondary structures, similar to native HEWL. Thus, the secondary

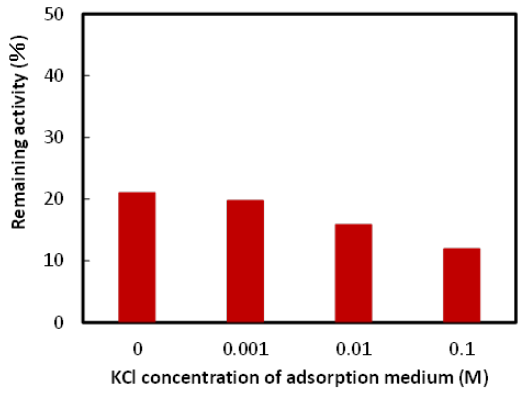

Fig. 1 Effect of KCl concentration of adsorption medium on the remaining activity of BCP-adsorbed HEWL after the heat treatment at 90 ℃ for 30 min.

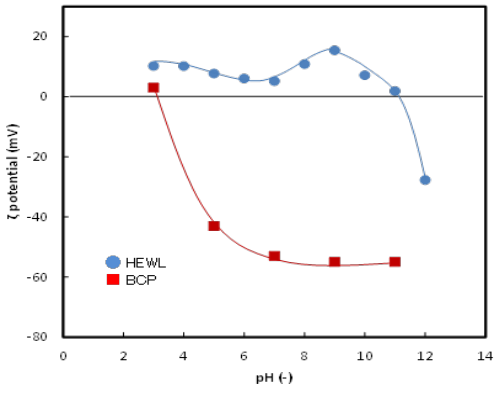

Fig. 2 Relationship of ζ-potentials of HEWL and BCP with solution pH.

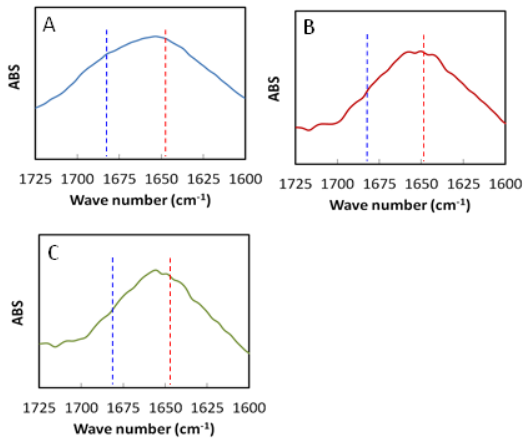

Fig. 3 (A) FTIR spectrum of free HEWL. (B) FTIR spectrum of HEWL adsorbed onto BCP without KCl. (C) FTIR spectrum of HEWL adsorbed onto BCP at 0.1 M KCl.

structure of HEWL was kept to some extent after the adsorption with or without KBr. In order to evaluate the change in the secondary structure of BCP-adsorbed HEWL, authors have assessed the ratio of the absorbance at 1681 cm^{-1} to the absorbance at 1647 cm^{-1} (ABS_{1681}/ABS_{1647}), since the band located at ca. 1681cm^{-1} is assigned to intramolecular β-sheet, and the band located at ca. 1647 cm^{-1} is assigned to α-helix [17]. The ABS_{1681}/ABS_{1647} ratio at 0.1 M KCl (0.66) was similar to that without KCl (0.69) although the ABS_{1681}/ABS_{1647} ratio of BCP-adsorbed HEWL was different from that of native HEWL (0.88). These results indicate that the change in the remaining activity of BCP-adsorbed HEWL results not from the structural change of BCP-adsorbed HEWL but from the change in the electrostatic attraction between BCP and HEWL due to the electrostatic screening effect. In other words, when the structures of HEWL adsorbed onto BCP under different conditions are similar, the thermal stability of BCP-adsorbed HEWL is more efficiently enhanced by the stronger electrostatic attraction between HEWL and BCP.

Effect of pH of Adsorption Medium on Thermal Stability of BCP-adsorbed HEWL

In general, the activity and stability of proteins in an aqueous solution are influenced by the solution pH [5]. Figure 4 shows the relation between the solution pH of adsorption medium and the remaining activity of HEWL adsorbed onto BCP. The remaining activity of BCP-adsorbed HEWL was markedly dependent upon the pH of adsorption medium, and exhibited the maximum at pH 5. The electrostatic force between HEWL and BCP at pH 5 is smaller than that in the range from pH 7 to 9 due to ζ potentials of BCP and HEWL, as shown in Fig.

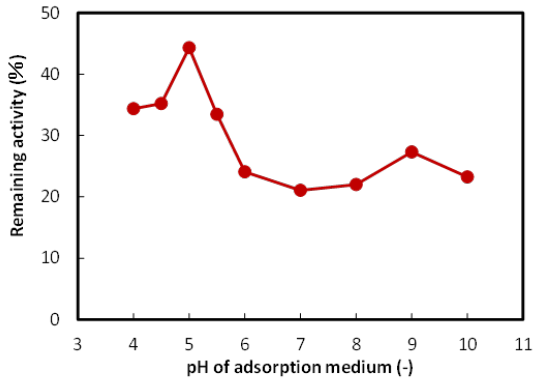

Fig. 4 Effect of pH of adsorption medium on the remaining activity of BCP-adsorbed HEWL after the heat treatment at 90 ℃ for 30 min.

2. In this case, the remaining activity of BCP-adsorbed HEWL was not correlated with the electrostatic force between HEWL and BCP.

Writers have measured the CD spectra of HEWL at different pH to investigate the influence of solution pH on the conformation of HEWL, since a protein is a polyelectrolyte. Figure 5 shows the CD spectra of free HEWL in the far- and near-UV regions dissolved in aqueous solutions at different pH. In the far-UV region, the CD spectrum of HEWL was independent upon the solution pH. The CD spectra in the far-UV (200-250 nm) correspond

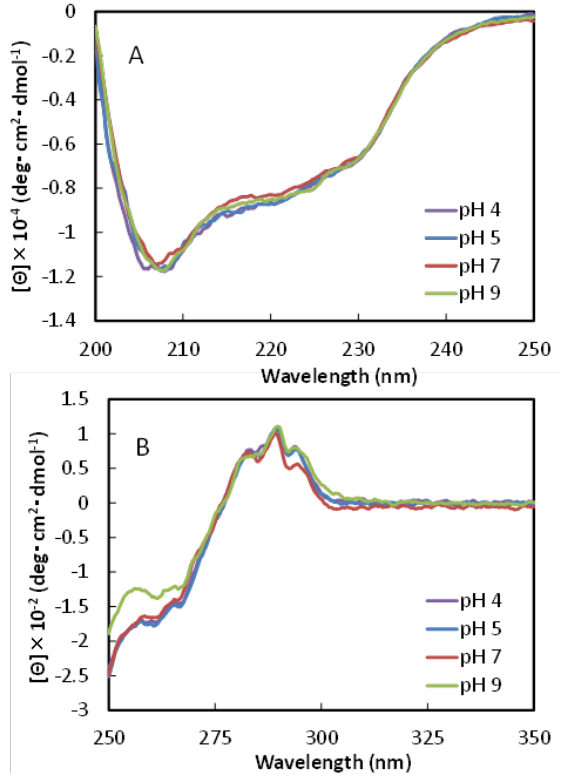

Fig. 5 (A) CD spectra of HEWL dissolved in buffer solutions at different pH in far-UV region. (B) CD spectra of HEWL dissolved in buffer solutions at different pH in near-UV region.

upon the secondary structure of proteins [18], [19]. Especially, the mean residue ellipticity at 215 nm is assigned to β-sheet, and the mean residue ellipticity at 222 nm is assigned to α-helix. The constancy in the mean residue ellipticities at 215 and 222 nm at different pH indicates that the β-sheet and α-helix contents of HEWL are kept constant at different pH. Likewise, the CD spectrum of HEWL in the near-UV region did not almost change with the solution pH. The CD spectra in the near-UV (250-350 nm) correspond upon the local asymmetric environment of aromatic amino acid residues [20], [21]. The mean residue ellipticities at 283 and 289 nm are assigned to tryptophan and tyrosine residues, and the mean residue ellipticity at 294 nm is assigned to tryptophan. Accordingly, the result of CD spectra in the near-UV suggests that the tertiary structure of HEWL is not influenced by the solution pH in the present work.

Figure 6 shows the FTIR spectra of native HEWL and HEWL adsorbed onto BCP at different pH. The spectral pattern of BCP-adsorbed HEWL was influenced by the pH of adsorption medium. The ABS_{1681}/ABS_{1647} ratio at pH 5 (0.86), where the remaining activity showed the maximum value, was similar to that of native HEWL (0.88). Likewise, the ABS_{1681}/ABS_{1647} ratio at pH 4 (0.92) was near that

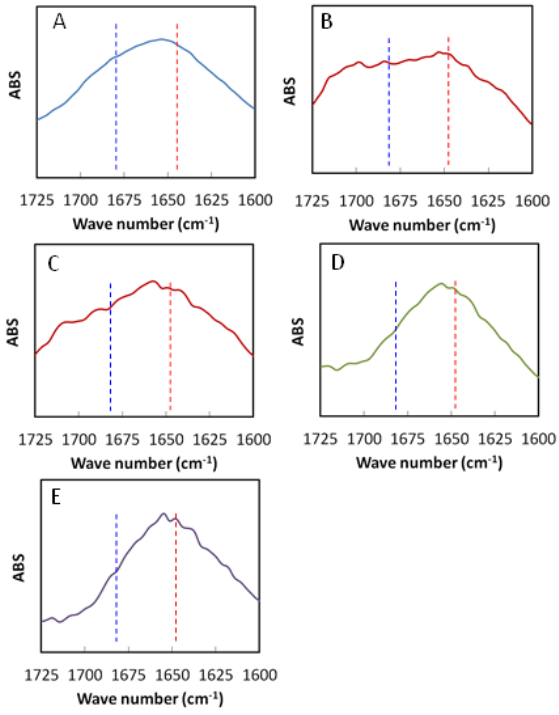

Fig. 6 (A) FTIR spectrum of free HEWL. (B) FTIR spectrum of HEWL adsorbed onto BCP at pH 4. (C) FTIR spectrum of HEWL adsorbed onto BCP at pH 5. (D) FTIR spectrum of HEWL adsorbed onto BCP at pH 7. (E) FTIR spectrum of HEWL adsorbed onto BCP at pH 9.

of native HEWL. On the other hand, the ABS_{1681}/ABS_{1647} ratios at pH 7 (0.69) and 9 (0.61), where the electrostatic force between HEWL and BCP was high due to ζ potentials of BCP and HEWL, were different from that of native HEWL. From these results, authors have summarized about the effect of solution pH of adsorption medium on the thermal stability of BCP-adsorbed HEWL as follows. When HEWL was adsorbed onto BCP at pH 4, the structure of BCP-adsorbed HEWL was nearly the native structure of HEWL, but the electrostatic force between HEWL and BCP was not sufficient for the thermal stability. When HEWL was adsorbed onto BCP at pH 5, the native structure of HEWL was kept, and the electrostatic force between HEWL and BCP was strong enough to help retain the structure of HEWL at high temperatures. When HEWL was adsorbed onto BCP at pH 7 and 9, the structure of HEWL was partially destroyed since the electrostatic force was too strong to keep the native structure of HEWL, and the thermal stability of BCP-adsorbed HEWL dropped.

Effect of Temperature of Adsorption Medium on Thermal Stability of BCP-Adsorbed HEWL

The activity and stability of proteins tend to depend upon the temperature [5]. Furthermore, the writers have found out that the temperature markedly affects the amount of proteins adsorbed onto BCP [11], [12].

In order to estimate the dependence of the thermal stability of BCP-adsorbed HEWL on the temperature of adsorption medium, the researches have examined the adsorption of HEWL onto BCP at pH 7 and different temperatures. Figure 7 shows the relationship between the temperature of adsorption medium and the remaining activity of BCP-adsorbed HEWL. The remaining activity of BCP-adsorbed HEWL decreased with increasing the temperature of adsorption medium. On the other hand, the CD spectrum of HEWL remained almost unchanged with the temperature both in the far- and near-UV regions, indicating that the conformation of HEWL is not influenced by heat in the present temperature range. Moreover, the FTIR spectral patterns and the ABS_{1681}/ABS_{1647} ratios of BCP-adsorbed HEWL at 5, 25, and 50 ℃ were similar, indicating that the secondary structure of BCP-adsorbed HEWL is not dependent upon the temperature of adsorption medium. It has been reported that the orientation of protein molecules onto the solid surface is influenced by the temperature [22]. It is suggested that the orientation of HEWL adsorbed onto BCP at lower temperature is more beneficial to the thermal stability of BCP-adsorbed HEWL.

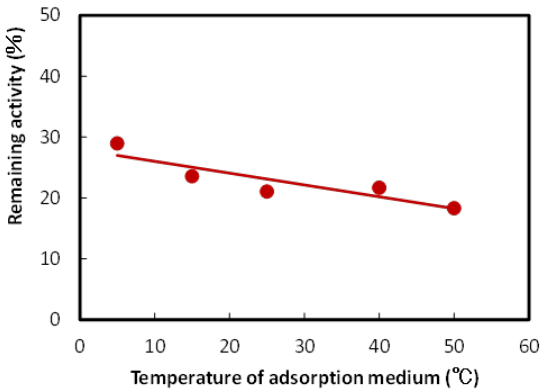

Fig. 7 Effect of temperature of adsorption medium on the remaining activity of BCP-adsorbed HEWL after the heat treatment at 90 ℃ for 30 min.

Effect of Adsorption Condition on Thermal Stability of BCP-Adsorbed CT

In order to assess the generality on the effect of adsorption condition on the thermal stability of BCP-adsorbed proteins, the researches employed bovine pancreas α-chymotrypsin (CT) as another model protein, since it is well investigated regarding its structure, functions, and properties [23].

The remaining activity of CT adsorbed onto BCP at pH 5 and 15 ℃ (65%) was 1.2 times greater than that at pH 7 and 25 ℃ (55%). The result indicates that the selection of adsorption condition is remarkably effective in enhancing the thermal stability of BCP-adsorbed CT, similar to the case of BCP-adsorbed HEWL.

CONCLUSION

The authors have demonstrated that the thermal stability of BCP-adsorbed proteins varies accordingly to the history of adsorption. The thermal stability of BCP-adsorbed HEWL increased with a decrease in the ionic strength of adsorption medium. The thermal stability and structure of BCP-adsorbed HEWL were strongly dependent upon the pH of adsorption medium, and the maximum remaining activity was obtained at pH 5, where the structure of BCP-adsorbed HEWL was kept native. The thermal stability of BCP-adsorbed HEWL increased with decreasing the temperature of adsorption medium. Likewise, the thermal stability of BCP-adsorbed CT was enhanced by selecting the adsorption condition. These results indicate that BCP-adsorbed proteins exhibit the excellent thermal stability when the native structure of proteins is kept after the adsorption, and the adsorption force is strong enough to help retain its structure against the heat stress. Accordingly, the enhancement in the thermal stabilization of proteins by selecting the adsorption

condition would be encouraging for the preparation of immobilized enzyme, biosensor, and biofuel cell.

ACKNOWLEDGEMENTS

This work was supported by a Grant-in-Aid for Scientific Research from Japan Society for the Promotion of Science (C) (No. 24561013).

REFERENCES

[1] Ho YC, Show KY, "A perspective in renewable energy production from biomass pyrolysis-challenges and prospects", Current Organic Chem., Vol. 19, 2015, pp. 423-436.

[2] Straathof AJ, "Transformation of biomass into commodity chemicals using enzymes or cells", Chem. Rev., Vol. 114, 2014, pp. 1871-1908.

[3] Peterson SC, Jackson MA, Appell M, "Biochar: Sustainable and versatile", ACS Symposium Series, Vol. 1143, 2013, pp. 193-205.

[4] Manya JJ, "Pyrolysis for biochar purposes: A review to establish current knowledge gaps and research needs", Environmental Sci. Technol., Vol. 46, 2012, pp. 7939-7954.

[5] Buchholz K, Kasche V, Bornscheuer UT, Biocatalyst and Enzyme Technology 2nd ed. Wiley-Blackwell, 2012.

[6] Silwana B, Horst CVD, Iwuoha E, "Amperometric determination of cadmium, lead, and mercury metal ions using a novel polymer immobilized horseradish peroxidase biosensor system", J. Environmental Sci. Health Part A, Vol. 49, 2014, pp.1501-1511.

[7] Leech D, Kavanagh P, Schuhmann W, "Enzymatic fuel cells: Recent progress", Electrochimica Acta, Vol. 84, 2012, pp. 223-234.

[8] Volkin DB, Klibanov AM, "Minimizing protein inactivation", Protein Function: Practical Approach, Creighton Ed. IRL Press, 1989, pp. 1-24.

[9] Elnashar MMM, "Review article: Immobilized molecules using biomaterials and nanobiotechnology", J. Biomaterials Nanobiotechnol., Vol. 1, 2010, pp. 61-77.

[10] [Mateo C, Palomo JM, Fernandez-Lorente G, Guisan JM, Fernandez-Lorente R, "Improvement of enzyme activity, stability and selectivity via immobilization techniques", Enzyme Microbial Technol., Vol. 40, 2007, pp. 1451-1463.

[11] Noritomi H, Iwai D, Kai R, Tanaka M, Kato S, "Adsorption of lysozyme on biomass charcoal powder prepared from plant biomass wastes", J. Chem. Eng. Jpn., Vol.v46, 2013, pp. 196-200.

[12] Noritomi H, Hishinuma K, Kurihara S, Nishigami J, Takemoto T, Endo N, Kato S, "Adsorption of α-chymotrypsin on plant biomass charcoal", J. Surface Eng. Materials Adv. Technol., Vol. 3, 2013, pp. 269-274.

[13] Noritomi H, Kai R, Iwai D, Tanaka H, Kamiya R, Tanaka M, Muneki K, Kato S, "Increase in thermal stability of proteins adsorbed on biomass charcoal powder prepared from plant biomass wastes", J. Biomedical Sci. Eng., Vol. 4, 2011, pp. 692-698.

[14] Noritomi H, Ishiyama R, Kai R, Iwai D, Tanaka M, Kato S, "Immobilization of lysozyme on biomass charcoal powder derived from plant biomass wastes", J. Biomaterials Nanobiotechnol., Vol 3, 2012, pp. 446-451.

[15] Noritomi H, Kurihara S, Endo N, Kato S, "Heat-resistant properties of α-chymotrypsin adsorbed onto biomass charcoal powder", J. Biomaterials Nanobiotechnol., Vol. 5, 2014, pp. 179-185.

[16] Jollès P, Lysozymes: Model Enzymes in Biochemistry and Biology 1st ed. Birkhäuser Verlag, 1996.

[17] Surewicz WK, Mantsch HH, "New insight into protein secondary structure from resolution-enhanced infrared spectra", Biochim. Biophys. Acta, Vol. 952, 1988, pp. 115-130.

[18] Chen YH, Yang JT, Martinez HM, "Determination of the secondary structures of proteins by circular dichroism and optical rotatory dispersion", Biochemistry, Vol. 11, 1972, pp. 4120-4131.

[19] Venyaminov SY, Yang JT, "Determination of protein secondary structure", Circular Dichroism and the Conformational Analysis of Biomolecules, Fasman Ed. Plenum Press, 1996, pp. 69-107.

[20] Ikeda K, Hamaguchi K, "The binding of *N*-acetylglucosamine to lysozyme: Studies on circular dichroism", J. Biochem., Vol. 66, 1969, pp. 513-520.

[21] Woody RW, Dunker AK, "Aromatic and cysteine side-chain circular dichroism in proteins", Circular Dichroism and the Conformational Analysis of Biomolecules, Fasman Ed. Plenum Press, 1996, pp. 109-157.

[22] Cheng X, Canavan HE, Graham DJ, Castner DG, Ratner BD, "Temperature dependent activity and structure of adsorbed proteins on plasma polymerized *N*-isopropyl acrylamide", Biointerphases, Vol. 1, 2006, pp.61-72.

[23] Kumar A, Venkatesu P, "Overview of the stability of α-chymotrypsin in different solvent media, Chem. Rev., Vol. 112, 2012, pp.4283-4307.

First International Conference on Science, Engineering & Environment,
Tsu City, Mie, Japan, Nov.19-21, 2015, ISBN: 978-4-9905958-5-2 C3051

CONSTRUCTION OF RAINFALL AND WATER-STAGE REALTIONSHIP FOR INUNDATION FORECAST AND EARLY WARNING IN TYPHOON EVENT

Huei-Tau Ouyang [1] and Yi-Chun Chen[2]
[1]Associate Professor, National Yilan University, Taiwan; [2] First River Management Office, WRA, Taiwan

ABSTRACT

In Taiwan, people often suffer severe typhoon attacks during summer time each year. Heavy rainfalls accompanied with these typhoons often cause serious inundation disasters in some areas. In order to effectively monitor the inundation situation during typhoon attacks, water-stage gauges were set up in a flood prone area in Yilan County. The surveillance data is transmitted back in real time basis during the period of typhoon attack. The system has proven to be very effective in acquiring the real time on-site inundation situation during typhoon attacks. Furthermore, in order to effectively carry out in-advanced disaster prevention actions, it is essential for the system to be able to predict future inundation situation on-site for the next few hours. For that, models based on ARX and ARMAX that are capable of simulating the rainfall and water-level relationships for the target area were constructed, using data of typhoon events collected in the past few years. The incorporation of these models into the system has shown great benefits in disaster prevention and rescue works during typhoon attacks.

Keywords: Typhoon, Inundation, ARX, ARMAX, model prediction

INTRODUCTION

Yilan County, located in northeastern Taiwan with classical subtropical monsoon weather, is notorious for its rainy climate. The area has in average over 200 rainy days each year with annual rainfall higher than 2500mm [1]. In spring it is always having little rains which sometimes lasts for over months. The situation is worse in typhoon season during July through September. Statistic data shows that more than 80% of typhoons attacking Taiwan each year hits eastern coast first [2], and Yilan is often within the list of typhoon attacking areas. During the period of typhoon attacks, the rainfall intensities pouring down to some areas can reach more than hundreds of millimeters per hour and last for several hours. Heavy rainfall in the surrounding mountains soon gathers into floods hammering down to the downstream area, where the elevation is almost at sea level. The flood in the area is difficult to catharsis due to the low-lying elevation. Plus, the drainage system of the area is heavily subjected to tidal influence of the sea. As a result, these downstream areas often suffer severe inundations which not only cause serious damages in properties but also threaten the life of the local residence. Among which, the Xinnan area (Fig. 1) is the worst one, where the averaged elevation of the terrain is under 2 meters while the high tide can sometimes reach around 1.8m [3].

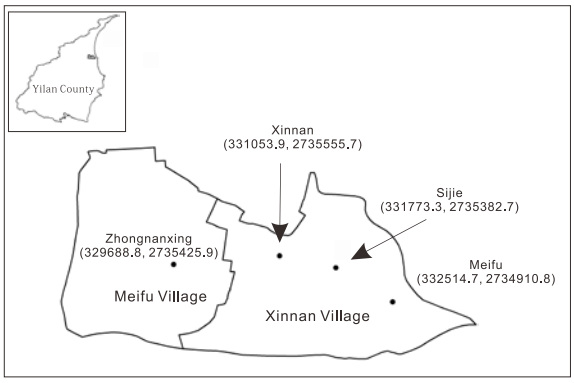

Fig. 1 Xinnan area in Yilan County

To mitigate the situation, the Early Warning System for Typhoon Inundation (EWSTI) in Xinnan area was structured in 2011 [3]. The system consists of four water-stage gauges consistently transmitting on-site water level data in a 10-minute frequency during the period of typhoon attack. The spatial distribution of these water-stage gauges is as shown in Fig. **1**. These data is fed into EWSTI which is based on a Geographic Information System (GIS). The extent of the flooding area and the depth distribution of the inundation are then estimated by utilizing the local digital elevation model (DEM). These data provides valuable information for the authorities to acquire the on-site inundation situation in the area during typhoon attack in real time basis. In order to take actions prior to the emerging of severe inundation to prevent any devastating disaster from happening, an import function of the system is

being capable of forecasting the future variation of the on-site water-stages for the next few hours, such that precautions and actions can be made in advance to mitigate damages of any kind that might occur. For that, data records consist of event-based rainfall and water-stages collected after the operation of the system from 2011 were analyzed [4]. The goal is to find suitable models that can properly represent the relationship between the rainfall and the water-stage distribution in the area.

Theory of System Identification [5] was employed to construct models for each of the gauges in the system. By incorporating the rainfall forecast data of the QPESUMS (Quantitative Precipitation Estimation and Segregation Using Multiple Sensor) transmitted from the Central Weather Bureau in Taiwan, the system is able to predict the variation of the water-stages at each of the sites with 3 hours of lead time. The results are reported in this paper.

The paper is arranged as follows. Following a brief description of the Early Warning System for Typhoon Inundation in Xinnan area, construction of the models representing the rainfall and water-stage relationships for each of the gauge stations based on theory of System Identification were detailed. The performance of the models were evaluated based on a number of indexes. In the end, the optimal model for each of the water-stage stations were identified by examining the performance indices.

THE EARLY WARNING SYSTEM FOR TYPHOON INUNDATION (EWSTI)

In Xinnan area, the EWSTI has been constructed and functioning since 2011 to provide on-site inundation information during typhoon attacks. EWSTI comprising four radio-transmitted water-stage gauges located as shown in Fig. **1**, and a data-interface to receive rainfall observation and forecast data transmitted from QPESUMS provided by the Central Weather Bureau. Fig. **2** shows the photo view of the Sijie water-stage gauge in the system. After construction, EWSTI has collected five typhoon events over the years. Table 1 lists the details of these typhoon events. The water-stage hydrographs recorded by the system and the rainfall hyetograph transmitted from the QPESUMS collected during typhoon Saola are as shown in Fig. **3**.

Table 1 Typhoon data collected by EWSTI

Typhoon	Attacking date	Duration (hrs)	Total rainfall (mm)
Nanmadol	2011/8/27	91	227
Songda	2011/5/27	83	353
Saola	2012/7/31	63	429
Trami	2013/820	45	55
Usagi	2013/9/19	69	59

Fig. 2 Sijie water-stage gauge

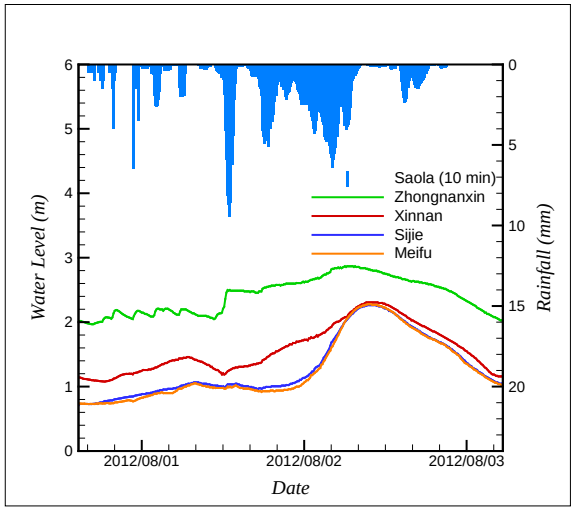

Fig. 3 Water-stage hydrographs and rainfall hyetograph for typhoon Saola

These data not only provides valuable on-site information to monitor the inundation situation in Xinnan area but also can be used as a data base in constructing models for the relationship between rainfall and water-stages.

THE RAINFALL WATER-STAGE MODELS

An essential function of EWSTI is the ability to forecast the future inundation situation in the area for the next few hours, so that precautions and actions can be taken before the emerging of severe inundations to mitigate the possible damages. This inundation forecasting function relies on a number of models that can simulate the relationship between the rainfall and the water-stages of the area in event basis. On considerations in the requirement of fast actions and responses for disaster mitigation, it is crucial for the system to provide reasonable forecast as fast as possible. For that, black box types of

models were employed into the system due to their ability to provide fast predictions [6]. As a first stage of model development, the ARX (Auto-Regressive eXogenous) and ARMAX (Auto-Regressive Moving Average eXogenous) models which are types of linear black box models were incorporated into the system.

The ARX model was originated from the Auto-Regressive Model (AR) in time series analysis proposed by Yule [7] which using the past data to predict the future value. The AR model was extended to ARX model during 1970s with other variables incorporated into the model which has the following form (namely "model structure" in theory of system identification).

$$\boldsymbol{y(t) + a_1 y(t-1) + \cdots + a_{n_a} y(t-n_a) = b_1 u(t-n_k) + \cdots + b_{n_b} u(t-n_b-n_k+1) + e(t)} \quad (1)$$

where $\boldsymbol{n_a}$ is the order of past data; $\boldsymbol{n_b}$ is the order of the exogenous inputs $\boldsymbol{u(t)}$; $\boldsymbol{b_1}$ through $\boldsymbol{b_{n_b}}$ are adjustable parameters for $\boldsymbol{u(t)}$; and $\boldsymbol{n_k}$ is the delay of $\boldsymbol{u(t)}$ which represents the number of samples before $\boldsymbol{u(t)}$ affects the output $\boldsymbol{y(t)}$.

ARMAX model is another types of linear black box model which is an extension of the Auto-Regressive Moving Average (ARMA) model. ARMA model was first proposed by Box and Jenkins in 1970 which is a combination of the AR model and the MA (Moving Average) model proposed by Slutsky [8]. By incorporating exogenous inputs $\boldsymbol{u(t)}$ into the model, the model structure of ARMAX is as follows.

$$\boldsymbol{y(t) + a_1 y(t-1) + \cdots + a_{n_a} y(t-n_a) = b_1 u(t-n_k) + \cdots + b_{n_b} u(t-n_b-n_k+1) + c_1 e(t-1) + \cdots + c_{n_c} e(t-n_c) + e(t)} \quad (2)$$

where $\boldsymbol{n_a}$, $\boldsymbol{n_b}$, and $\boldsymbol{n_c}$ are orders of $\boldsymbol{y(t)}$, $\boldsymbol{u(t)}$, and $\boldsymbol{e(t)}$, respectively; and $\boldsymbol{a_1}$ through $\boldsymbol{a_{n_a}}$, $\boldsymbol{b_1}$ through $\boldsymbol{b_{n_b}}$, and $\boldsymbol{c_1}$ through $\boldsymbol{c_{n_c}}$ are adjustable parameters for $\boldsymbol{y(t)}$, $\boldsymbol{u(t)}$, and $\boldsymbol{e(t)}$, respectively.

After preliminary studies, several models based on the ARX and ARMAX for each of the water-stage gauges were proposed to simulate the rainfall and water-stage relationship. In these models, the rainfall data provided by QPESUMS was used as the exogenous input $\boldsymbol{u(t)}$, and the water-stage for each of the gauges is $\boldsymbol{y(t)}$. Table 2 lists the model structures examined for each of water-stage gauges, where arx and amx denote the ARX and ARMAX models, respectively. In ARX models, the first figure denotes the order of water-stage $\boldsymbol{y(t)}$, the second figure is the order of rainfall $\boldsymbol{u(t)}$, and the third figure indicates the response delay of rainfall. In ARMAX models, the first, second, and fourth figures represent the orders of $\boldsymbol{y(t)}$, $\boldsymbol{u(t)}$, and response delay of $\boldsymbol{u(t)}$, respectively, and the third figure denotes the order of $\boldsymbol{e(t)}$.

Table 2 Model structures for the rainfall and water-stage relationship

Site	Xinnan	Zhong-nanxin	Sijie	Meifu
Model structure	amx3290	arx110	arx440	amx1240
	amx5790	arx120	amx4790	amx1340
	amx8380	arx130	amx4890	amx1350
	amx9290	arx140	amx4990	amx1440
	amx9770	arx170	amx7790	amx1450

MODEL PERFORMANCE EVALUATION

The performance of each of the models were revaluated by using four indices described in the following.

(1) Efficiency Coefficient (CE)

CE was proposed by Nash and Sutcliffe [9] to assess the predictive ability of a hydrological model, which is defined as:

$$\mathbf{CE} = \mathbf{1} - \frac{\sum_{t=1}^{n}[y_{obs}(t) - y_{est}(t)]^2}{\sum_{t=1}^{n}[y_{obs}(t) - \bar{y}_{obs}]^2} \quad (3)$$

where $\boldsymbol{y_{obs}}$ and $\boldsymbol{y_{est}}$ represent the observed and estimated water-stages, respectively; $\boldsymbol{\bar{y}_{obs}}$ is averaged water-stage observation; $\boldsymbol{n}$ is the number of data. CE quantifies the goodness of fit between the observed and estimated hydrographs of the water-stages. Value of CE closer to 1 indicates a better fit of the model.

(2) Root Mean Square Error (RMSE), which reads:

$$\mathbf{RMSE} = \sqrt{\frac{\sum_{t=1}^{nt}(y_{obs}(t) - y_{est}(t))^2}{n}} \quad (4)$$

RMSE represents the mean error between the observed and estimated hydrographs. A better model is indicated by a smaller value of RMSE.

(3) Error of peak water-stage (ESP), which is as follows.

$$\mathbf{ESP} = \frac{y_{p,est} - y_{p,obs}}{y_{p,obs}} \times \mathbf{100}\% \quad (5)$$

where $\boldsymbol{y_{p,obs}}$ and $\boldsymbol{y_{p,est}}$ denote the observed and estimated peak water-stages, respectively. ESP quantifies the error between the observed peak

water-stage and the model estimation. Positive ESP indicates an over estimate of the model, while negative ESP means under estimation. A better fit is indicated by a smaller absolute value of ESP.

(4) Error of the time for the peak to arrive (ETP), which is defined as

$$\mathbf{ETP} = \boldsymbol{T_{p,est} - T_{p,obs}} \quad (6)$$

where $\boldsymbol{T_{H_{P,est}}}$ and $\boldsymbol{T_{H_{P,obs}}}$ denote the time at which the observed and estimated peak water-stages emerge. A positive ETP indicates an early prediction of the peak stage which is, in the early warming point of view, much welcome than a negative ETP signifying a late prediction.

RESULTS AND DISCUSSION

The typhoon data of Songda and Usagi were employed to calibrate the rainfall water-stage models listed in Table 2, and the other three events in Table 1 were utilized for model verifications. Table 3 through Table 6 lists the averaged performance of the four stations. As seen, the averaged CE of the proposed models are all higher than 0.9, signifying good prediction abilities.

For Xinnan station, Table 3 shows that there are three models having the highest CE of 0.978, which are amx8380, amx9290, and amx9770. Upon which, amx9770 has slightly lower RMSE of 0.047 than the other two. Hence, in terms of overall simulation performance for typhoon event, amx9770 is the optimal one for Xinnan station. However, in disaster mitigation point of view, the peak of water-stage and the time of arriving of the peak would be the major concern. In observing ESP and ETP, it is seen that amx 5790 has the lowest values and is the optimal model in terms of peak water-stage predictions.

Examinations in Table 4 shows that model arx130, arx140, and arx170 perform equally well in terms of overall event simulations for Zhongnanxin station, as indicated by the equal values on CE and RMSE. Upon which, arx170 also has the lowest ESP among all the models and is therefore the optimal model for peak water-stage predictions. Although arx170 has ETP higher than the other models, however, positive value of ETP represents early prediction on peak arrival which is somehow favored in our early warning system.

For Sijie station, Table 5 shows that model arx440 has the highest CE and the lowest RMSE than the others, indicating its superiority in overall event simulations. The model also has the lowest ESP showing good performance in peak water-stage prediction. Although its ETP is little higher than the others, which however is favored in EWSTI.

For Meifu station, it is seen in Table 6 that, with all the models having the same CE, amx1350 exhibits the lowest RMSE and ESP indicating the models has good performance in both the overall event simulations and peak water-stage predictions.

Figure 4 shows the predicted water-stage hydrograph for 3 hours of lead time simulated by model arx440 and the measured data at Sijie station for typhoon Saola. As shown in the figure, the agreement between the prediction and the data is favorable. The model prediction not only presents close fit to the measure data throughout the event, but also shows good predictions both on the peak water-stage and the arriving time.

Table 3 Averaged performance of the models for Xinnan station

	CE	RMSE (m)	ESP (%)	ETP (hr)
amx3290	0.977	0.048	2.196	1.1
amx5790	0.953	0.065	1.979	1
amx8380	0.978	0.048	2.324	1
amx9290	0.978	0.048	2.283	1.1
amx9770	0.978	0.047	2.34	1

Table 4 Averaged performance of the models for Zhongnanxin station

	CE	RMSE (m)	ESP (%)	ETP (hr)
arx110	0.922	0.051	1.838	1
arx120	0.925	0.05	1.425	0.9
arx130	0.926	0.049	1.197	1.1
arx140	0.926	0.049	1.034	1.4
arx170	0.926	0.049	0.983	1.4

Table 5 Averaged performance of the models for Sijie station

	CE	RMSE (m)	ESP (%)	ETP (hr)
arx440	0.965	0.042	0.733	0.4
amx4790	0.95	0.053	1.357	0.3
amx4890	0.95	0.053	1.385	0.3
amx4990	0.95	0.053	1.376	0.3
amx7790	0.95	0.053	1.328	0.3

Table 6 Averaged performance of the models for Meifu station

	CE	RMSE (m)	ESP (%)	ETP (hr)

amx1240	0.964	0.057	2.476	1.8
amx1340	0.964	0.056	2.461	1.9
amx1350	0.964	0.049	2.417	1.9
amx1440	0.964	0.056	2.494	1.9
amx1450	0.964	0.056	2.467	1.9

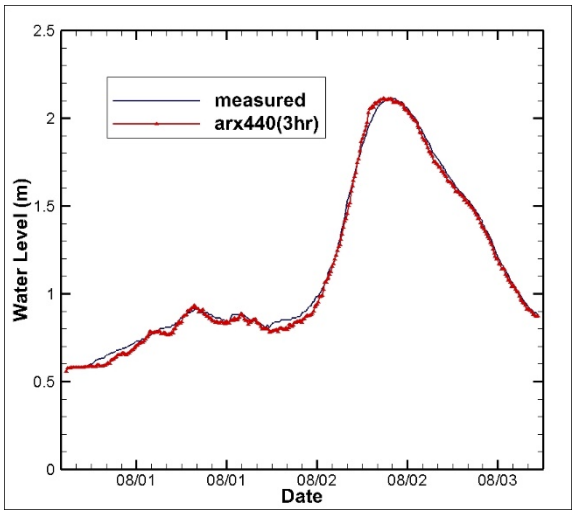

Figure 4 Comparison of predicted water-stage hydrograph with 3-hr leads and measured data for typhoon Saola (Sijie station)

CONCLUSION

A number of models based on ARX and ARMAX capable of representing the relationship between rainfall and water-stages of typhoon events were examined and tested. These models were specifically designed for the Early Warning System of Typhoon Inundation (EWSTI) for the Xinnan area in Taiwan, with the purpose of damage control and mitigation prior to the emerge of any disaster. The results show good performance of their abilities both in overall typhoon event simulations and peak water-stage predictions. The comparison of the model prediction with three-hours of lead time to the measured data presents promising fit throughout the event and good predictions on both the peak water-stage and the arriving time. By incorporating these models into EWSTI, the system can now not only provide real time on-site inundation situation during typhoon attack, but also issue warnings in advance on severe catastrophes such that corresponding actions can be taken in prior.

ACKNOWLEDGEMENTS

This research is supported by the Ministry of Science and Technology in Taiwan under grant No. 104-2625-M-197-001. Support from the Water Resources Agency in Taiwan is also acknowledged.

REFERENCES

[1] Website of Central Weather Bureau, Taiwan, http://www.cwb.gov.tw
[2] Website of Water Resources Agency, Taiwan, http://www.wra.gov.tw
[3] Ouyang HT, Hsu HM, Construction of self-recording water level monitoring stations and flood damage assessment system, Project report of First River Management Office, WRA, 2011.
[4] Ouyang HT, Hsu HM, Chen SJ, Early Warning System for Typhoon Inundation System (EWSTI) for Xinnan area in Yilan County, Project report of First River Management Office, WRA, 2014.
[5] Lennart Ljung L, System Identification — Theory For the User, 2nd ed, PTR Prentice Hall, Upper Saddle River, N.J., 1999.
[6] Karlsson M, Yakowitz B, "Rainfall-runoff forecasting methods, old and new", Stochastic Hydrology and Hydraulics, Vol. 1(4), 1987, pp 303-318.
[7] Yule GU "On a Method of Investigating Periodicities in Disturbed Series, with Special Reference to Wolfer's Sunspot Numbers", Philosophical Transactions of the Royal Society of London, Ser. A, Vol. 226, 1927, pp. 267–298.
[8] Slutsky, E. "The summation of random causes as the source of cyclic processes", Voprosy Koniunktury, Vol. 3, 1927, pp. 34-64. (English translation in Econometrika Vol. 5, pp. 105-146.)

First International Conference on Science, Engineering & Environment,
Tsu City, Mie, Japan, Nov.19-21, 2015, ISBN: 978-4-9905958-5-2 C3051

FLOOD ANALYSIS IN LANGAT RIVER BASIN USING STOCHATIC MODEL

Yuk Feng Huang[1], Majid Mirzaei [2]
[1] Universiti Tunku Abdul Rahman, Faculty of Engineering and Science, Malaysia
[2] Universiti Tunku Abdul Rahman, Faculty of Engineering and Science, Malaysia

ABSTRACT

This study analyzed the annual maximum stage readings of four rivers in Langat River Basin for flood forecasting using Autoregressive Integrated Moving-average (ARIMA) model. Model identification was done by visual inspection on the Autocorrelation Function (ACF) and Partial Autocorrelation Function (PACF). The model parameters were computed using the Maximum Likelihood (ML) method. In model verification, the chosen criterion for model parsimony was the Akaike Information Criteria Corrected (AICC) and the diagnostic checks include residuals' independence, homoscedasticity and normal distribution. The best ARIMA models for the Dengkil, Kg. Lui and Kg. Rinching series were (1,1,0), (1,1,0) and (1,1,1) respectively, with their AICC values of 133.736, 55.348 and 42.292. Homoscedasticity was confirmed with the Breusch-Pagan test giving p-values of 0.145, 0.195 and 0.747 for the Dengkil, Kg. Lui and Kg. Rinching models respectively. Forecast series up to a lead time of eight years were generated using the accepted ARIMA models. Model accuracy was checked by comparing the synthetic series with the original series. Results show that the ARIMA models for the rivers and the forecast series were adequate. In conclusion, the Box-Jenkins approach to ARIMA modelling was found to be appropriate and adequate for the rivers. The flood forecast up to a lead time of eight years for the three models exhibit a straight line with near constant streamflow values showing that the forecast values were similar to the last recorded observation.

Keywords: Flood Analysis, ARIMA, Box-Jenkins Approach, Langat River Basin

INTRODUCTION

Floods have huge environmental and economic impact. According to a study conducted by KTA Tenaga in 2002, the total flood affected area in Malaysia in 2000 was about 9.04% of the total land area in Malaysia. The population in flood affected areas in 2000 was 22% of the total population at that time and the Annual Average Damage estimated was RM 915 million. On the other hand, the design of hydraulic structures such as dams and reservoirs also depends on the design flood of the particular river. An inaccurate design flood can lead to inefficiency of those hydraulic structures.

The study area is the Langat River Basin which spans two states in Malaysia, namely Selangor and Negeri Sembilan. The Langat River Basin is shown in Fig. 1. It has a catchment area of approximately 2,348 km^2. The Langat River is the main stream while other major tributaries include the Semenyih River, the Labu River and the Beranang River. Two dams are located at the upper region of the river basin; the Semenyih dam and the Langat dam. The Semenyih dam has a catchment area of 56.7 km^2 while the Langat dam has a catchment area of 41.1km^2.

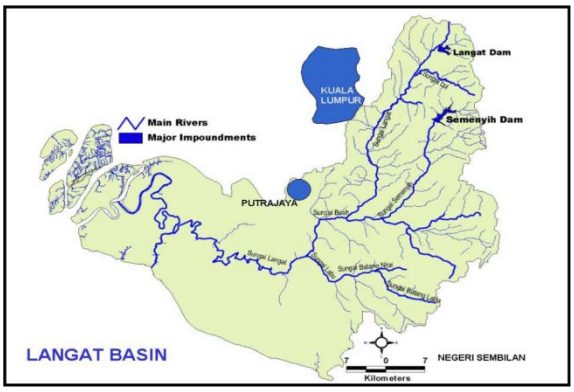

Fig. 1: The Langat River Basin

The objectives of this study are to develop stochastic ARIMA models for the study rivers using Box-Jenkins approach and to forecast future annual maximum streamflow values in the study rivers using the developed ARIMA models.

ARIMA MODEL

The ARIMA modelling is actually an approach that has the flexibility to fit a model which is adapted from the data structure itself. With the help of the computed autocorrelation function and partial autocorrelation function, the time series' stochastic

nature can be modelled and vital information such as trend, periodic components, random components and serial correlation can be obtained. The Box-Jenkins approach to ARIMA modelling is an iterative model building process where the best models have to be determined through trial and error. However, with the advent of computers and statistical software packages, this iterative process can be simplified. Commonly used software packages include Statgraphics, Minitab and Statistica.

The ARIMA model has three main components, namely Autoregressive (AR), Integrated (I) and Moving-Average (MA). The AR component represents the autocorrelation between current and past observations while the MA component describes the autocorrelation structure of error. The integrated component represents the level of differencing required to transform a non-stationary series into a stationary series [1]. A non-seasonal ARIMA model is usually denoted by (*p*,*d*,*q*).The order of the AR component is denoted by *p*, the order of differencing is denoted by *d*and *q* is the order of the MA component.

Throughout the years researchers have used the ARIMA model for different scientific and technical applications. [2] described the random component of streamflow time series by examining the stochastic structure of the flow data for the Upper Delaware River. Forecasting monthly rainfall data using various ARIMA models was done by [3], whereas [4] carried out streamflow prediction on a medium sized basin in Mississippi. The ARIMA model was applied to monthly data from Kelkit Stream watershed by [5]. [6] reviewed the performance of two stochastic models (Thomas-Fiering and ARIMA) on Yesilirmak River, Turkey.

There have been a lot of reviews on the performance of the ARIMA model. [7] argued that the ARIMA model is only suitable for short term forecasting. The ARIMA model needs a long input series to produce forecasts that are more accurate. Therefore, the ARIMA model may not work well for short input series. [8] showed that the performance of ARIMA is satisfactory in forecasting either a linear or non-linear interval series. It is also a good forecasting alternative to inter-valued time series.

Stationarity

The Box-Jenkins approach is a stationary time series approach. If a time series is non-stationary, differencing is required to make it stationary before the Box-Jenkins approach can be carried out. There are many ways to determine non-stationarity. The common tests used include unit root and trend tests.

ADF Test

The testing for unit root's presence in a time series is a normal starting point of applied work in macroeconomics. One of the popular tests for unit root is the Augmented Dickey-Fuller (ADF) test. This test is based on estimates from an augmented autoregression. One of the main issues in the ADF test is the choice of lag length *k*.

KPSS Test

Another well known test for stationarity in econometrics is the Kwiatkowski-Phillips-Schmidt-Shin (KPSS) test. It tests for the null hypothesis of stationarity as opposed to the ADF test which tests for the null hypothesis of non-stationarity. One of the important arguments against the use of tests withstationarity as the null hypothesis is that it is very difficult to control their size when the process is stationary andextremely autoregressive [9].

Mann-Kendall Trend Test

The Mann-Kendall trend test is commonly used to test the presence of trend in a time series. It is not a parametric test so the data do not have to be normally distributed and it has low sensitivity to sudden changes due to non-homogeneous time series. The Mann-Kendall S Statistic shows the behaviour of a trend. A positive S indicates an upward trend while a downward trend is indicated by a negative S. Another statistic obtained from the test is the Kendall's tau, which measures the strength of the dependence between two variables. A positive value of Kendall's tau shows that the variables' ranks increase together while a negative value shows that as one variable's rank increases, the other variable's rank decrease.

Independence

The basic assumption is that the residuals of an ARIMA model are white noise. A white noise series have uncorrelated random shock with zero mean and constant variance. If the residuals are independent, it means that there is no more information that could be extracted from the series. One of the ways to determine the independence is to visually inspect the correlogram of the residuals. If the correlogram shows values that are close to zero, the residuals are uncorrelated and independent.

Homoscedasticity

Homoscedasticity is the term used to define that the variance of the disturbance term in each observation is constant. If the residuals are homoscedastic, their variances are stable. The probability of the disturbance terms reaching a given positive or negative value will be the same in all observations, which means that they have the same dispersion.

Forecasting

Forecasting can be categorized into short-term forecasting and long-term forecasting. Short-term forecasting can predict values that are a few time periods (a few years) into the future. Long-term forecasting on the other hand, can predict values for time periods that extend far beyond that. In terms of applications, long-term forecasts are used for strategic planning while short-term forecasts are used for project developments as well as operation management. Statistical methods are good for short-term forecasting because the historical data normally exhibit inertia and do not show drastic changes. Short-term forecasting is based on identifying, modelling and extrapolating the patterns found in the data.

METHODOLOGY

The general ARIMA (*p*,*d*,*q*) model is:

$$U_t = \phi_1 U_{t-1} + \phi_2 U_{t-2} + \ldots + \phi_p U_{t-p} + \varepsilon_t - \theta_1 \varepsilon_{t-1} - \theta_2 \varepsilon_{t-2} - \ldots - \theta_q \varepsilon_{t-q} \quad (1)$$

$$U_t = X_t - X_{t-d} \quad (2)$$

ϕ_p = autoregressive parameter
ε_t = residual
θ_q = moving-average parameter
X = dependent variable
U = d-th difference of the dependent variable.

Plotting the Series and Its ACF and PACF

The main tools used for identification of model were the visual displays of the series, which included the autocorrelation function (ACF) and the partial correlation function (PACF).Using the annual maximum stage readings as the input time series, the autocovariancefunction (c_k), the autocorrelation coefficients (r_k) and the partial correlation coefficients ($\phi_k(k)$) were calculated and the series with its ACF and PACF were plotted using XLSTAT. The number of lags*k* should fall between *N*/4 and *N*, therefore the chosen number of lags in this study was sufficient.

$$c_k = \frac{1}{N}\sum_{t=1}^{N-k}(x_t - \bar{x})\,(x_{t+k} - \bar{x}), \qquad 0 \le k \le N \quad (3)$$

$$r_k = \frac{c_k}{c_0} = \frac{\sum_{t=1}^{N-k}(x_t - \bar{x})\,(x_{t+k} - \bar{x})}{\sum_{t=1}^{N}(x_t - \bar{x})^2} \quad (4)$$

$$\hat{\phi}_{k+1}(k+1) = \left[r_{k+1} - \sum_{j=1}^{k}\hat{\phi}_k(j) r_{k+1-j}\right] \Big/ \left[1 - \sum_{j=1}^{k}\hat{\phi}_k(j) r_j\right] \quad (5a)$$

$$\hat{\phi}_{k+1}(j) = \hat{\phi}_k(j) - \hat{\phi}_{k+1}(k+1)\hat{\phi}_k(k-j+1) \quad (5b)$$

The ACF and PACF were then analysed to determine behaviour and stationarity of the series. If all the ACF and PACF values are insignificant and fall within the confidence band, it indicates that the observations are independent. In such a case the time series is a white noise process and no modelling could be performed.

Stationarity Tests

Unit root tests such as the Augmented Dickey-Fuller (ADF) test and the Kwiatkowski-Phillips-Schmidt-Shin (KPSS) test were carried out to test the presence of a unit root while the Mann-Kendall trend test was performed to check for the presence of a trend.The presence of a unit root or a trend should indicate non-stationarity of the series. The significance level used was 5%. If the series is non-stationary, differencing is required to transform it into a stationary series. On the other hand, if the series is stationary, the series is modelled as an ARMA process instead, which requires no differencing.

Differencing

The series was initially differenced once (d = 1) and the ACF and PACF of the differenced series were plotted and analysed. If the ACF and PACF decay rapidly then it indicates stationarity is achieved. Another indicator is the standard deviation of the differenced series. The optimum differenced series should have the lowest standard deviation. The differenced series was then differenced again (d = 2) to check for under-differencing or over-differencing. Similarly, the ACF and PACF were plotted and analysed. The lag 1 ACF and PACF of an over-differenced series will be lower than negative 0.5. If the standard deviation of the current series is lower than that of the previous series, then the current series has the optimum order of differencing. It is noteworthy that some researchers argue that the effect of over-differencing is much less serious than the effect of under-differencing.

Identifying *p* and *q*

Having identified the optimum order of differencing (d), the next step was to identify the order of the autoregressive and moving-average parameters. The ACF (symbolized as ρ_k) and the PACF for the optimum differenced series were analysed to determine the *p* and *q*.

Choosing the Best ARIMA Model

The previous step gave an indication of the order of *p* and *q* that should be fitted in the model. However, it was recommended to try a few different

values of *p* and *q* to get the best model while preserving the parsimony of the parameters. To test for the parsimony of parameters, the corrected Akaike Information Criteria (AICC) was used. The model with the minimum AICC was selected as the best model. The XLSTAT software can find the best model based on the AICC values calculated for a range of *p* and *q*. In this study the maximum *p* selected was 3 and the maximum *q* selected was also 3. The model with the minimum AICC was then subjected to diagnostic checks.

Diagnostic Checks

After the best initial model was determined, the next step was running the diagnostic checks. Its purpose was to verify the proposed model's validity. Before any checking was done onto the residuals, the values of the estimated ARIMA parameters first have to be in an interval computed using the Hessian standard errors. If the values are out of that interval, then they are not significant and the ARIMA model should not be used.

Series Comparison and Forecasting

The best model that passed the diagnostic checking will then have its synthetic series compared to the original data series. This determined the degree of resemblance between the synthetic series and the original data series. If the pattern of the synthetic series appears similar to the pattern of the original series, then the fitted model is a good model. The final step was to generate a forecast of future values. The ARIMA model can predict future values as well as its confidence interval using the calculated model parameters. In this study the chosen number of forecasted values was eight, which means that the values were forecasted for the next eight years after the last observation.

RESULTS AND DISCUSSION

The ACF and PACF for the Dengkil station are presented in Fig. 2 and Fig. 3, respectively.

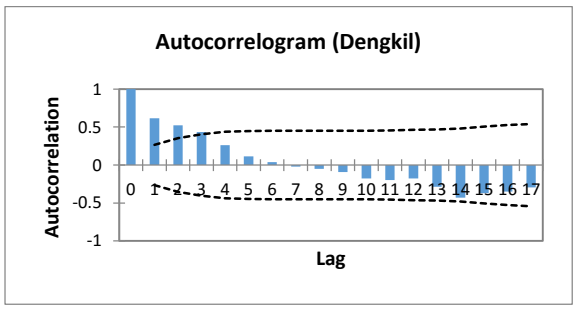

Fig. 2: ACF of Dengkil Series

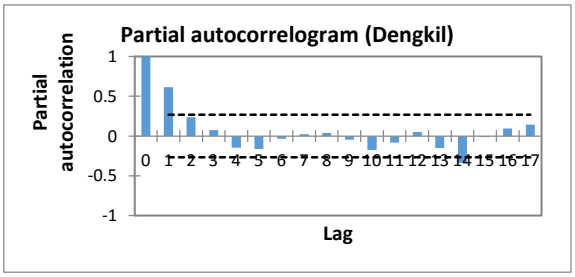

Fig. 3: PACF of Dengkil Series

The ACF plots for the Dengkil series, the Kg. Lui series and the Kg. Rinching series exhibited slow decay, indicating the possibility of non-stationarity. The ACF plot for the Kajang series indicated that the series may be white noise because its values were not significant. Further white noise tests (Box-Pierce test and Ljung-Box test) were applied to the Kajang series and they showed that the series was indeed a white noise series. Table 1 shows the results of the white noise tests. Therefore, no further modelling was done onto the Kajang series.

Table 1: Results of White Noise Tests

Test	Value	p-value	Remarks
Box-Pierce	12.477	0.408	White noise
Ljung-Box	15.525	0.214	White noise
McLeod-Li	15.445	0.218	White noise

Stationarity Tests

Stationarity tests were carried out for the remaining three series to confirm the initial presumption that they were non-stationary. The results for the ADF test, KPSS test and Mann-Kendall trend test are presented in Table 2.

Table 2: Results of Stationarity Tests

Station	ADF test	KPSS test	Mann-Kendall trend test	Remarks
	p-value	p-value	p-value	
Dengkil	0.350	0.001	0.438	Non-stationary
Kg. Lui	0.138	0.005	0.072	Non-stationary
Kg. Rinching	0.411	0.030	<0.0001	Non-stationary

The tests confirmed that all the data series were non-stationary. The Augmented Dickey-Fuller test and the KPSS test showed that all three series had unit roots. The Mann-Kendall test also detected a trend in the Kg. Rinching series. A series that has either a unit root or a trend was considered as non-stationary and therefore required differencing.

Differencing the Series

The series were differenced once and twice to obtain the optimum *d*. The standard deviations of the original and differenced series are shown in Table 3.

Table 3: Standard Deviations of Original Series and Differenced Series

Order, *d*	Dengkil	Kg. Lui	Kg. Rinching
0	1.035	0.597	0.658
1	0.903	0.490	0.481
2	1.521	0.858	0.829

The ACF and PACF of the once differenced (*d* = 1) series decayed rapidly compared to the ACF and PACF of the original series. Comparing the standard deviations of the series, the minimum standard deviations were obtained from the series with *d* = 1. The results also showed that the first lags of the twice differenced (*d* = 2) series were lower than -0.5, indicating over-differencing. Therefore, the optimum level of differencing for the three series was one and the *d* value used in the ARIMA model would be one.

ARIMA Modelling and Diagnostic Checking

The AICC for ARIMA models were computed with *p* starting from one to three and *q* starting from zero to three. The models tested were (1,1,0), (1,1,1), (1,1,2), (1,1,3), (2,1,0), (2,1,1), (2,1,2), (2,1,3), (3,1,0), (3,1,1), (3,1,2) and (3,1,3). For each station, the model having the minimum AICC was chosen as the best model. The best models along with their estimated parameter values are tabulated in Table 4. The results showed that the preliminary models determined from the ACF and PACF of the differenced series were indeed the best models

Table 4: Best ARIMA Models

	Dengkil	Kg. Lui	Kg. Rinching
Best model	(1,1,0)	(1,1,0)	(1,1,1)
AICC	133.736	55.348	42.292
MSE	0.672	0.169	0.137
AR(1)	-0.395	-0.532	0.241
MA(1)	-	-	-1.000
Constant	-0.023	0.044	-0.047

The Hessian standard errors were calculated and all the estimated parameters successfully fell within the significance interval. The RACF and RPACF for the best ARIMA models were plotted. The RACF and RPACF for all the three series fell within the confidence interval. They were not significant and this showed that the residuals were independent, therefore satisfying the first residual criterion. The next requirement was residuals' homoscedasticity and Table 5 shows the results of Breusch-Pagan test. Fig. 4 shows the distribution of the standardized residuals for the Dengkil series.

Table 5: Results of Breusch-Pagan Test

Station	p-value	Remarks
Dengkil	0.145	Homoscedastic
Kg. Lui	0.195	Homoscedastic
Kg. Rinching	0.747	Homoscedastic

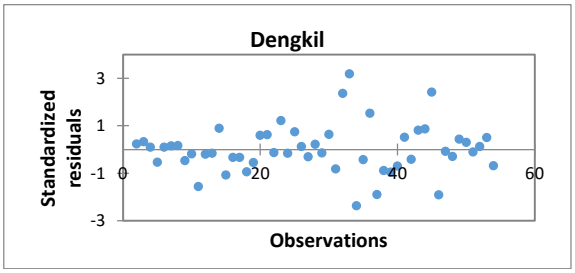

Fig. 4: Distribution of Standardized Residuals

The residuals were homoscedastic which mean tthat they had constant variances. It was important for the residuals to be homoscedastic because it determined whether the model's ability to predict variable values was consistent. A model with heteroscedastic residuals cannot give results that are trustworthy andtransformation of the data is required. The third criterion for diagnostic checking was the distribution of the residuals. The residuals were subjected to normality tests and histograms were also plotted to give a visual representation of their distributions. The results of normality tests are presented in Table 6, while the histograms are shown in Fig. 5.

Table 6: Results of Normality Tests

Station	Shapiro-Wilk test	Anderson-Darling test	Jarque-Bera test
	p-value	p-value	p-value
Dengkil	0.017	0.012	0.007
Kg. Lui	0.140	0.066	0.064
Kg. Rinching	0.315	0.223	0.331

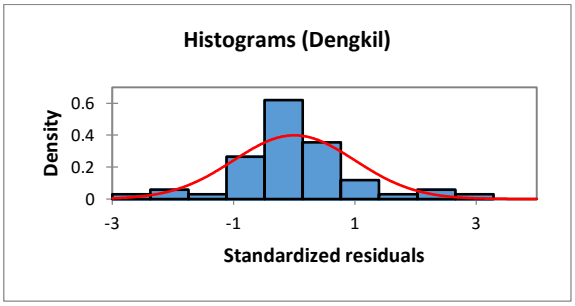

Fig. 5: Histograms of Residuals

Both the normality tests and histograms showed that the Kg. Lui series and the Kg. Rinching series had normally distributed residuals. The Dengkil series however, failed the normality tests but its histograms showed that it was very close to a normal distribution, which was good enough. The normality of residuals' distribution was important to produce a satisfactory confidence interval for the forecast.

Comparison of Series and Forecasting

The synthetic series generated by the ARIMA models were compared to the original series to

check for model accuracy. Forecast series were also generated for a lead time of eight years with 95% confidence intervals. Fig. 6 shows the original series, the synthetic series and the forecast series for the three stations.

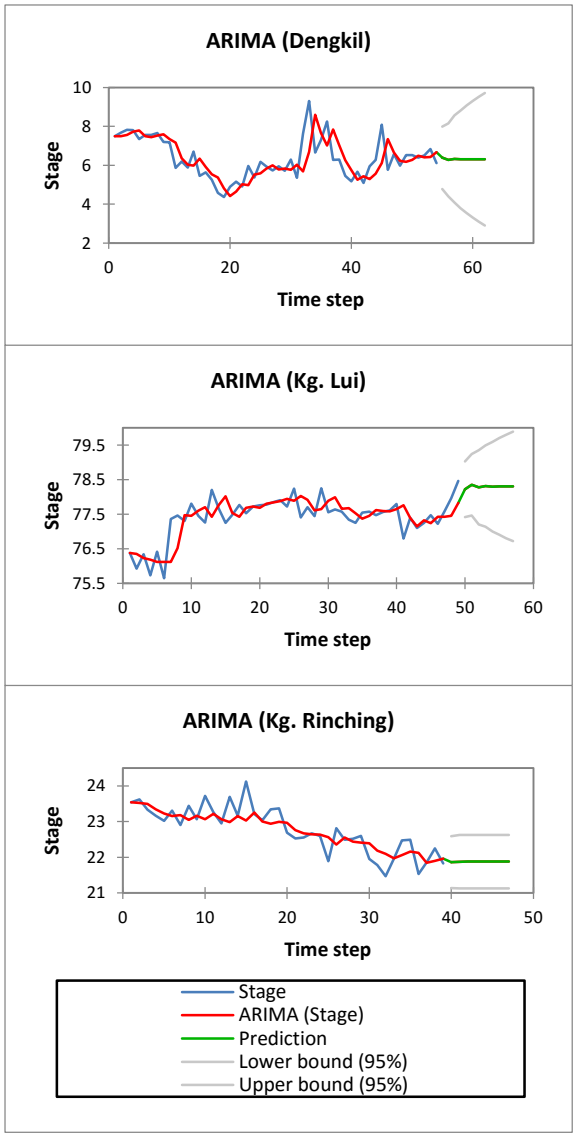

Fig. 6: Original, Synthetic and Forecast Series

CONCLUSION

Statistical modelling was successfully performed onto the study rivers using the autoregressive integrated moving-average (ARIMA) method. Forecast series were also generated by the models to give sequences of future stage and streamflow values. One of the series, the Kajang series, could not be modelled because it was a white noise series and no dependence existed between its successive streamflow values. The best ARIMA models for the other three series, Dengkil, Kg. Lui and Kg. Rinching series were (1,1,0), (1,1,0) and (1,1,1) respectively. The ARIMA model is suitable for short term forecasting because the ARMA family models can model short term persistence very well.

In conclusion, the Box-Jenkins approach for ARIMA modelling was found to be appropriate and adequate for the rivers under study in Langat River Basin. The flood forecast up to a lead time of eight years for the three models exhibited a straight line with near constant streamflow values showing that the forecast values were similar to the last recorded observation.

REFERENCES

[1] Hasmida, H., 2009. *Water quality trend at the upper part of Johor River in relationto rainfall and runoff pattern*.UniversitiTeknologi Malaysia.

[2] Ahlert, R.C. and Mehta, B.M., 1981.Stochastic analysis and transfer functions for flows of the Upper Delaware River.*Ecological Modeling*, 14, pp. 59 − 78

[3] Fernando, D.A.K. and Jayawardena, A.W., 1994.Generation and forecasting ofmonsoon rainfall data.*Proceeedings on the20th WEDC Conference on Affordable Water Supply and Sanitation*.Colombo, Sri Lanka, pp. 310 − 313

[4] Hsu, K.L., Gupta, H.V. and Sorooshian, S., 1995.Artificial neural network modeling of the rainfall-runoff process, *Water Resources Research*, 31, pp. 2517 − 2530

[5] Yurekli, K., Kurunc, A. and Ozturk, F., 2005.Application of linear stochastic models to monthly flow data of KelkitStream.*Ecological Modelling*, 183, pp. 67 − 75

[6] Kurunc, A., Yurekli, K. and Cevik, O., 2005. Performance of two stochastic approaches for forecasting water quality and streamflow data from Yeşilırmak River, Turkey.*Environmental Modelling & Software*, 20, pp. 1195 − 1200

[7] Tang, Z., de Almeida, C. and Fishwick, P.A., 1991. Time series forecasting using neural networks vs. Box-Jenkins methodology.*Simulation*, 57 (5), pp. 303 − 310

[8] Maia, A.L.S., de Carvalho, F.D.A.T. and Ludermir, T.B., 2008. Forecasting models for interval-valued time series.*Neurocomputing*, 71, pp. 3344 − 3352

[9] Hobijn, B. and Franses, P.H.B.F., 1997. Asymptotically perfect and relativeconvergence of productivity.*Econometric Institute Report no. 9725/A*. ErasmusUniversity Rotterdam

First International Conference on Science, Engineering & Environment,
Tsu City, Mie, Japan, Nov.19-21, 2015, ISBN: 978-4-9905958-5-2 C3051

SHEAR STRENGTHENING WITH CFRP SHEETS APPLIED IN REINFORCED CONCRETE FLAT PLATES WITH OPENINGS

Nazar K. Oukaili[1], and Thaar S. Al-Gasham[2]
[1]College of Engineering, University of Baghdad, Iraq; [2]College of Engineering, University of Wasit, Iraq

ABSTRACT

Experimental and analytical investigations were undertaken to evaluate the punching shear capacity of interior slab-column connections for panels with openings, strengthened using (CFRP) sheets. Sixteen simply supported reinforced concrete flat plates with (1000×1000×70) mm dimensions loaded through a central column where fifteen of them had various arrangements of the openings around the column. These specimens were divided into five groups using two different CFRP strengthening schemes. In scheme I, the CFRP sheets were applied around the column and opening in one layer of width equal to the opening width. In scheme II, the CFRP sheets were applied in two layers with widths equal to half of the opening width considering the same cross sectional area used in scheme I. Due to the presence of the openings, the unstrengthen specimens showed a decrease in punching shear capacity between 11.43% and 29.25% with respect to the control solid slab. Test results clearly demonstrated that using CFRP leads to significant improvements of the stiffness and shear capacity of slab-column connections. Depending on the CFRP strengthening scheme used, the punching shear capacity was increased by 5.1% to 60.6%.
Using ANSYS program, an analytical model was developed to predict the punching shear capacity of the specimens strengthened with CFRP sheets. It is found that, the analytical results are satisfactorily correlated with experimental data where the maximum difference in ultimate load was around (16%).

Keywords: Flat Plate, Opening, Punching, Shear Strengthening, CFRP Sheets

INTRODUCTION

In a particular situation, it is often necessary to create openings in existing slabs to allow electrical, water or air conditioning duct to go through floors. These openings, located next to column for practical and aesthetic reasons, reduce the punching shear capacity of the connection. In such case, the slab must be strengthened.

FRP sheets are used to repair and strengthen reinforced concrete members especially beams and columns. Many reinforced concrete beams have been tested and have demonstrated the feasibility and efficiency of this technology to improve the flexural stiffness and strength as well as seismic response [1]. On the other hand, experimental studies of the effectiveness of FRP sheets in increasing the shear capacity of flat plates are very limited, especially for reinforced concrete flat plates with openings. The tests reported in this work partially fill this void.

TEST SPECIMENS

The slab specimens have dimensions of (1000×1000×70mm) with top column stub (150×150mm) extending out (200mm) from the center of the slab. Fifteen specimens were designed to have opening with different sizes and positions. All specimens were simply supported on the (900×900mm) perimeter on the bottom of the slab. All specimens were reinforced by one bottom layer of (6mm) diameter steel bars, with average yield strength of 598 MPa, spaced (75mm) c/c in each direction and arranged to give an average effective depth (dav) of (54mm). All column stubs were reinforced with four (12mm) diameter longitudinal steel bars of 648 MPa yield strength and two (6mm) diameter transverse steel ties.

The openings were not bordered with reinforcement as is used and requested by code design specifications. This condition was imposed in order to find out which is the quantum when bordering is passed over and the cut in slab is made on site without accounting the possible loss of strength in the control perimeter. The reinforcement details of the specimens are shown in Figure (1).

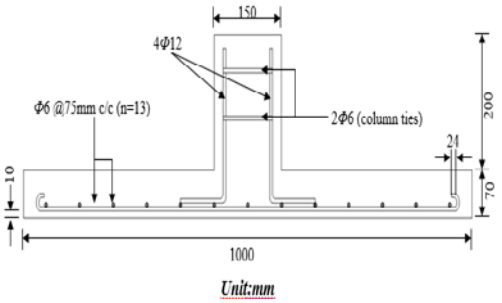

Fig. 1 Test specimen dimensions and reinforcement layout.

The test specimens are divided into three series. Series I includes six unstrengthened control specimens, five of them having openings whereas the remaining specimen is without opening. Series II includes five specimens having openings and strengthened with CFRP using scheme I, Figure (2). Series III includes five specimens having openings and strengthened with CFRP using scheme II, Figure (3). All openings are with square configuration with the sides, of length l, parallel to the sides of the column. Three sizes of openings were used: (100×100mm) with l/c= 0.67; (150×150mm) with l/c=1; and (225×225) with l/c=1.5, where c is the length of the side of the column. The amount of CFRP used in both schemes was approximately the same in order to evaluate the effect of the arrangement of CFRP strips on strengthening efficiency of the concrete slab-column connection against punching shear failure.

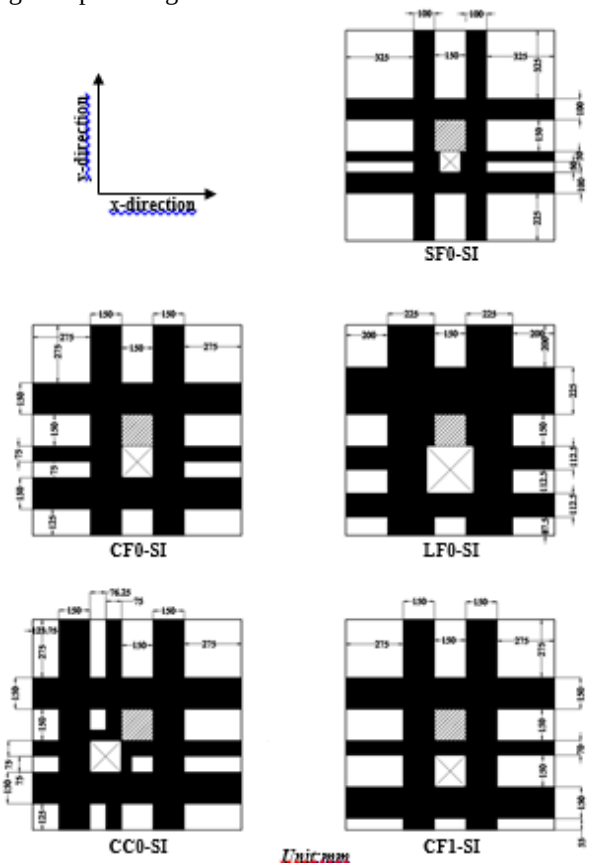

Fig. 2 Specimens of scheme I

In scheme I, the CFRP flexible unidirectional sheets were cut into strips with width equal to the opening size l. The strips were applied in one layer to the tension face of the slab around the opening and the column in two orthogonal directions, parallel to the directions of internal reinforcement. Same procedure of scheme I was followed in scheme II but the CFRP strips were applied in two layers with width equal to the half size (0.5 l) of the opening.

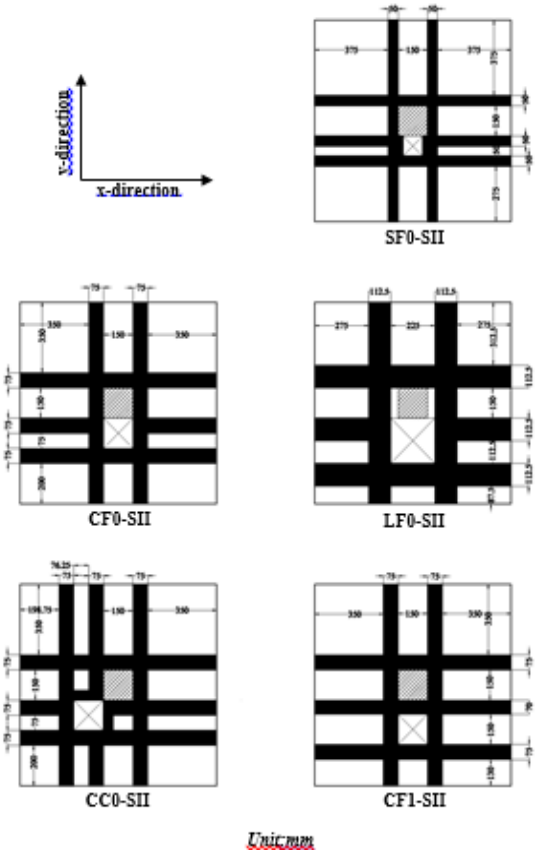

Fig. 3 Specimens of scheme II

To avoid bond failure of the CFRP sheets, in both schemes, the sheets were extended along the full dimensions of the slab and additional strips of CFRP sheets were applied in one layer with width equal to the half size of the opening. The additional strips located as close as possible to the column face and either warped around the openings, in case of the openings located directly next to the column, or extended along the full dimensions of the slab in case of the openings located at a distance of (70mm) from the column face. To resist the vertical inclined shear cracks that may develop in some of the sides of the opening (nearest sides to the column face), additional CFRP sheets with one layer and length of (170mm) were warped around sides of the opening.

The CFRP consisted of Sika Wrap Hex-230C flexible sheets. The manufacturer's data sheet stated that the design thickness of the fabric is 0.13 mm, the modulus of elasticity is 238 GPa, the tensile strength is 4300 MPa, and the ultimate tensile strain is 1.8%.

The concrete mixes were designed to achieve a target concrete compression strength fc' of 30 MPa. Ordinary Portland cement was used along with washed sand and graded crushed gravel having aggregates of 10 mm. The proportions by weight of cement: sand: gravel were 1.00:1.77:2.22 with water/cement ratio of 0.55.

The specimen designation can be explained as follows. The first letter indicates the size of the opening, where C equals to the column stub size (150×150mm), S smaller than the column stub size (100×100mm), and L larger than the column stub size (225×225mm). The second letter indicates the position of the opening around the column, where F indicates that the opening positioned in front of the column stub and C indicates that the opening positioned at the corner of the column stub. The third letter indicates the ratio of the distance of the opening from the column face D divided by the slab thickness h, where D/h equals either 0 or 1. The last letters denote to strengthening scheme of CFRP sheets, where SI indicated that the specimen strengthened using scheme I and SII mean that the strengthening performed using scheme II. In case of a solid slab (without opening and CFRP strengthening), the designation (XXX) is used.

TEST PROCEDURE AND RESULTS

Flat plate specimens were placed inside the testing frame and loaded centrally through the column stub with monotonically increasing load until failure. The load was applied slowly with increment of (3.5 kN) using a hydraulic jack of (1000 kN) capacity. At each loading stage, the magnitude of the applied load, deflection of the slab at five locations, and first crack width were measured. At the end of each test, the angle at which the shear cracks propagated away from the column face was measured and the crack pattern and mode of failure for each specimen were carefully examined.

General Behavior and Crack Patterns

The six unstrengthened specimens failed in a brittle sudden punching mode. Under loading, the first cracks (flexural) occurred at a load range of about (21.1% to 28.6%) of the ultimate punching capacity of the specimens. The cracks first started with diagonal cracks running from the corners of the column stub toward the slab edges on the tension side. As the load was increased, circumferential cracks occurred at a location farther away from the column stub and developed gradually over the entire slab. At load of (54.9% to 63%) of the specimens failure load, the flexural cracks reached all the way out to the edges of the slabs. The formation of inclined shear cracks was visible inside the openings during testing of interior slab-column connections. These cracks developed at approximately (40-80%) of the failure load at an angle of approximately (26-53) degrees. The inclined shear cracks usually continued from flexural cracks. Very often these flexural cracks first developed at the corner of the opening. On average, the shear failure cone ranged from 154 to 191mm from the face of the column which corresponds 2.86 to 3.54 d, where d is the effective depth of the slab.

Initiation of flexural cracks on the tension face of the specimens strengthened with CFRP started at a load range of about (23.3% to 40%) of the ultimate punching capacity of the specimens. Due to the presence of CFRP sheets, cracking directly adjacent to the column could not be observed during the test. However, diagonal cracks were observed in between the CFRP sheets. As the load increased, more diagonal cracks developed and extended toward the slab edges and corners. Finally, the diagonal cracks were linked together and the slab failed in punching shear failure mode which was sudden and brittle. Fine cracks were also seen around the column on the compression side of the slab after failure.

The distance at which the shear cracks propagated away from the face of the column was generally the same as that of the control specimens and was not influenced by the area of CFRP sheets used. Also, it is clear that the extent and width of diagonal cracks were more pronounced for specimens strengthened using scheme II in comparison with those strengthened using scheme I.

It is worth mentioning that, none of the CFRP specimens experienced bond failure between the CFRP sheets and the concrete surface on the tension side of the slab. However, CFRP sheets at failure load detached transversally near the shear crack as a result of the transverse movement of concrete on either side of the crack when punching failure occurred and because the sheets have virtually little resistance in the transverse, out-of plane, direction. Figures (4 and 5) show typical crack patterns for specimens CF0, CF0-SI, and CF0-SII, respectively.

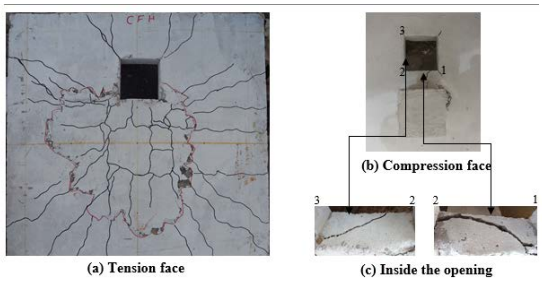

Fig. 4 Cracks pattern of CF0

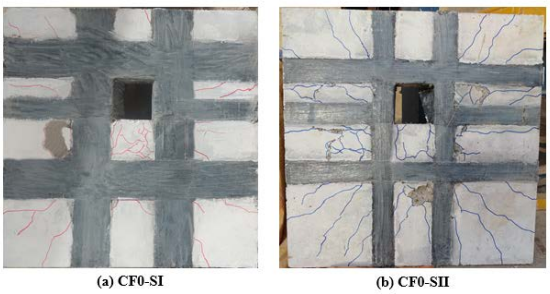

Fig. 5 Cracks pattern of CF0-SI and CF0-SII

First Cracking and Ultimate Loads Results

In order to compare the test results of specimens with different compressive strength, the measured load of each specimen is normalized to the concrete compressive strength of the control Specimen XXX, (35.69 MPa). The normalized load is obtained by multiplying the measured load by (35.69/fc')1/2, where fc' is the cylinder concrete compressive strength of the individual specimen in (MPa). A summary of test results showing the normalized cracking and ultimate loads of the specimens is presented in Table (1).

The test results clearly show that providing CFRP strips increase the cracking strength and results in considerable improvement in the ultimate strength capacity. The corresponding increases depend on the arrangement of CFRP sheets around the opening and column.

Since it was not possible to visually observe first cracking on the underside of the strengthened specimens, the point where the load-deflection response deviated from the initial elastic response could be accepted as the point of first cracking. In general, it can be seen that the increase of the first cracking loads for specimens strengthened using scheme I are greater than those for specimens strengthened using scheme II. With regard to the normalized ultimate loads, slabs SF0-SI and SF0-SII, with 100×100mm openings directly adjacent to the column face, have 19.5% and 5.1% increase in the punching load over the control slab SF0, respectively. Specimens CF0-SI and CF0-SII which have 150×150mm openings just adjacent to the column stub edge, achieve the greatest increases in the normalized ultimate load, these are 60.6% and 42.1% over the control slab, respectively. In specimens with the largest front face openings, significant increases in the normalized ultimate load carrying capacity are observed as 59.3% and 34.5% for specimens LF0-SI and LF0-SII, respectively, in comparison with specimen LF0. In slabs CC0-SI and CC0-SII with corner face openings, the normalized ultimate loads are 21.9% and 30.2% larger than that of specimen CC0, respectively. Specimens CF1-SI and CF1-SII, with the openings located at 70mm away from the column stub, show increase in the normalized punching shear load which are 18.8% and 41.9% over the control specimen, respectively.

Table 1 Cracking and ultimate loads of test specimens

Group	Specimen designation	Experimental load, (kN)		Normalized load, (kN)		Increase of first cracking load, %	Increase of ultimate load, %
		First cracking load, P_{cr}	Ultimate loads, P_u	First cracking load, P_{ncr}	Ultimate loads, P_{nu}		
	SF0	25.41	90.76	24.93	89.02	0.0	0.0
I	SF0-SI	36.31	116.18	33.24	106.36	33.3	19.5
	SF0-SII	25.41	87.13	27.30	93.60	9.5	5.1
	CF0	21.78	79.87	22.28	81.68	0.0	0.0
II	CF0-SI	39.94	127.07	41.23	131.19	85.1	60.6
	CF0-SII	32.67	112.55	33.71	116.10	51.3	42.1
	LF0	14.52	68.98	15.14	71.92	0.0	0.0
III	LF0-SI	43.57	108.92	45.82	114.56	202.6	59.3
	LF0-SII	32.67	90.76	34.83	96.75	130.0	34.5
	CCO	25.41	90.76	25.21	90.03	0.0	0.0
IV	CCO-SI	36.31	112.55	35.42	109.80	40.5	21.9
	CCO-SII	25.41	108.92	27.35	117.22	8.5	30.2
	CF1	25.41	88.95	25.13	87.95	0.0	0.0
V	CF1-SI	39.94	105.28	39.64	104.50	57.8	18.8
	CF1-SII	36.31	116.18	39.00	124.80	55.2	41.9

Load-defection response

Figure (6) shows the applied normalized load versus central deflection responses of the various specimens in test groups I to V, respectively. The load-deflection response of the specimens consisted of a stiff pre-cracking stage, followed by a nonlinearly elastic stage until punching shear failure occurred in a sudden manner, leading to a sharp drop in load resistance. The load-deflection responses of identical specimens for each group are convergent in the pre-cracking stage, while the post-cracking responses appear to be different. From these figures, it can be seen that the overall post-cracking stiffness of the CFRP strengthened specimens are considerably greater than the control specimens. These increases in the stiffness may be due to absorbing the stresses by existence of CFRP sheets near the column edges.

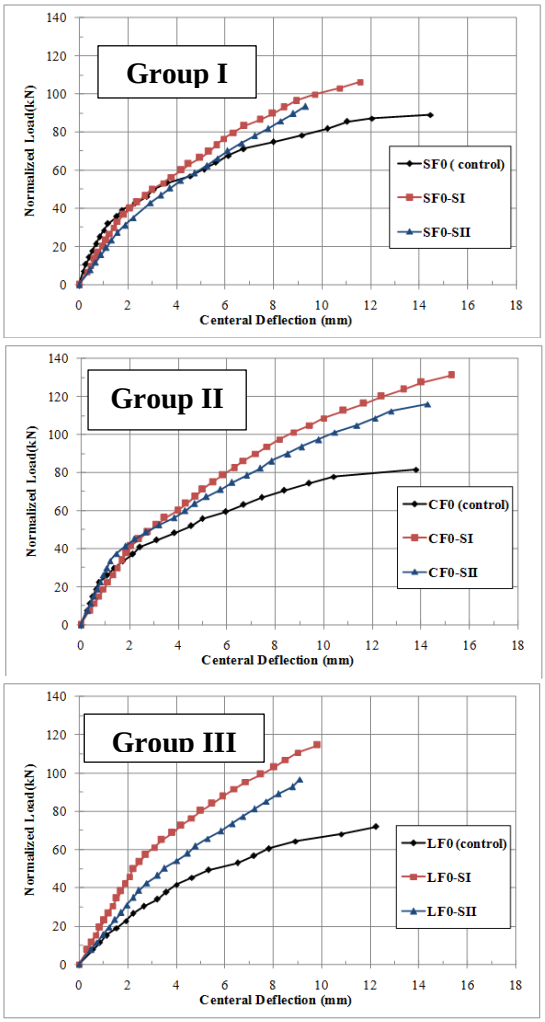

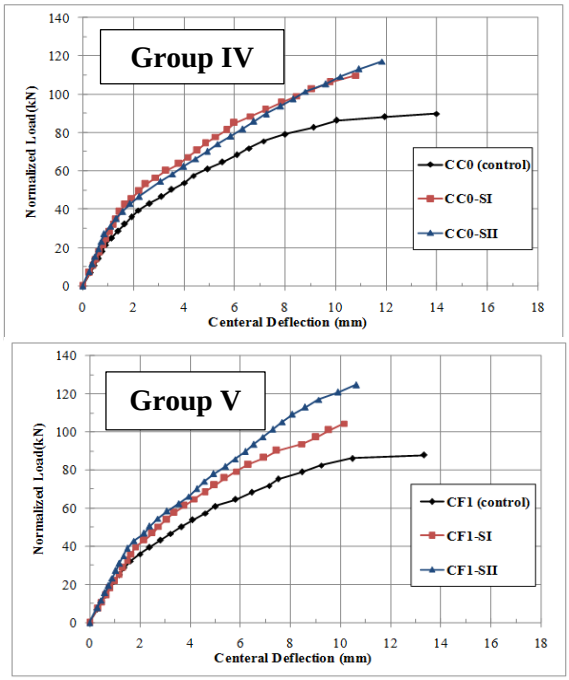

Fig. 6 Load deflection responses for experimental specimens

FINITE ELEMENT IDEALIZATION OF TEST FLAT PLATES

The flat plates have been modelled using different element types. In order to place the reinforcement mesh in its real location as in the experimental case, the 70 mm thickness of the specimens was divided into four layers, the three upper layers had an equal thickness (18mm), and the lowest layer was 16mm thick. Each layer was subdivided into square SOLID65 elements with a 25 mm side length. The column stub was divided into 288 cubic SOLID65 elements with a 25mm side length. The mesh of the concrete and steel plate for the solid specimen is shown Figure (7).

LINK8 elements were used to model the slab and column reinforcement. For specimens strengthened with CFRP, SHELL41 elements were used to model the CFRP sheets. Concrete and CFRP sheets elements are sharing the same nodes along the surface of interaction in between both materials. Perfect bond is assumed to occur between CFRP sheets and concrete. Displacement boundary conditions were used for modeling end supports of slabs. To ensure that the model behave in the same way as the experimental slabs, boundary conditions need to be applied at points that are used to support specimens in experimental tests. Since the flat plates were simply supported along all four edges, all nodes along the supporting line of the slab were fixed against translation in y-direction. Finally, the

central force applied through the column stub was converted to uniformly distributed load on the projection area of the steel plate elements to prevent stress concentration problems.

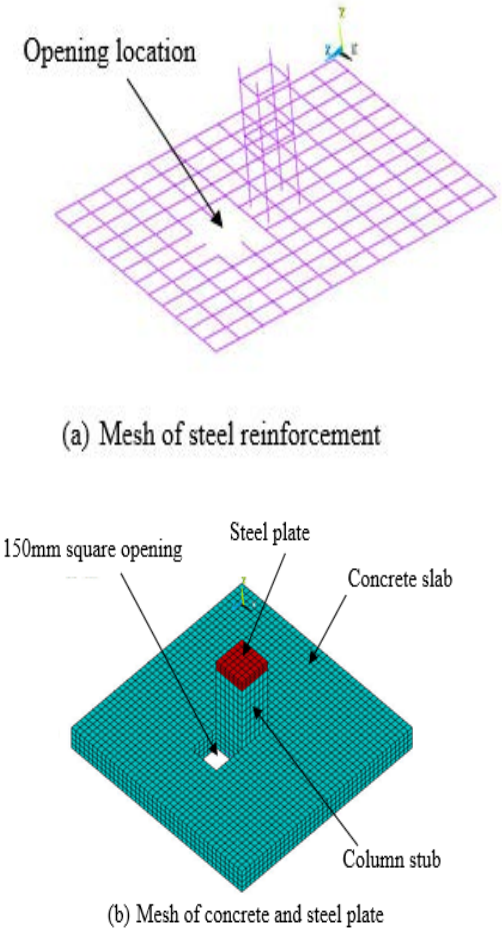

Fig. 7 Finite elements modelling

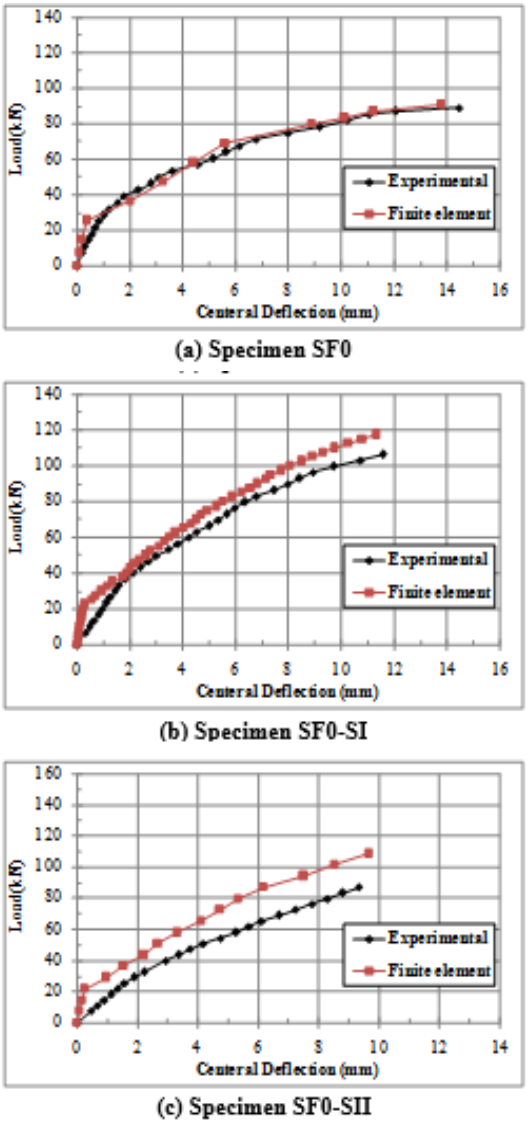

Fig. 8 Comparison of predicted and experimental load-deflection curves for specimens of group I

Figure (8) shows load-deflection curves of the flat plates of the present finite element analysis and experimental data for group I. According to this figure, it can be observed that the present finite element model performs satisfactorily and it predicts the real behavior of the flat plates.

The results of the finite element analysis of the investigated slabs in terms of ultimate load are compared against the experimental measurement and listed in Table (2). It should be mentioned that, the ratio of the predicted to the experimental ultimate load ranges from 0.86 to 1.16 with an average and a standard deviation of 0.99 and 0.09, respectively.

Table 2 Comparison between the experimental and predicted ultimate load

Group	Specimen	Pexp, kN	Pansys, kN	Pansys/Pexp
	XXX	101.65	108.30	1.07
	SF0	89.02	90.75	1.02
I	SF0-SI	106.36	117.66	1.11
	SF0-SII	93.60	108.90	1.16
	CF0	81.68	88.44	1.08
II	CF0-SI	131.19	112.53	0.86
	CF0-SII	116.10	112.53	0.97
	LF0	71.92	67.02	0.93
III	LF0-SI	114.56	98.92	0.86
	LF0-SII	96.75	84.06	0.87
	CC0	90.03	83.49	0.93
IV	CC0-SI	109.80	112.53	1.02
	CC0-SII	117.22	108.90	0.93
	CF1	87.95	87.12	0.99
V	CF1-SI	104.50	112.53	1.08
	CF1-SII	124.80	127.05	1.02
Average value (Pansys/Pexp)				0.99
Standard deviation				0.09

CONCLUSIONS

The conclusions, based on the experimental results and finite elements analysis, are summarized as follows:-

1. The presence of CFRP strips increased the flexural stiffness of slabs, delayed the initiation of cracks, restricted the extensive crack opening, and hence, increased the punching shear capacity. Depending on opening size and location as well as the CFRP strengthening scheme used, the increase in two-way shear resistance varied between 5.1% and 60.6%. Accordingly, all strengthened specimens failed in punching shear mode. No de-bonding of the CFRP sheets was observed.
2. The strengthened specimens exhibited much stiffer responses and lower deflections than the corresponding control specimens.
3. For specimens with front face openings, the CFRP strengthening scheme I was more effective in increasing the punching shear strength than CFRP strengthening scheme II. This situation inverted for other specimens where the openings were constructed either away from column or adjacent to its corner.
4. The general behavior of the finite element models represented by the load-deflection curves at the center of the slabs showed good agreement with the experimental data. However, the finite element models showed slightly stiffer than the test results in both the linear and nonlinear ranges. The effects of bond-slip, (between the concrete and steel reinforcing), and micro-cracks occurring in the actual flat plates were excluded in the finite element models, contributing to the higher stiffness of the finite element models. The maximum difference in ultimate load between the experimental and analytical data was only 16%.

REFERNCES

[1] Soudki K., “Rehabilitation of bridges and structures by FRP laminates-Canadian perspective”. ICCRI workshop, 1999.

[2] Tan K., and Zhao H., “Strengthening of openings in one-way reinforced-concrete slabs using carbon fiber-reinforced polymer systems", Journal of Composites for construction ,ASCE, 2004,Vol. 8, No. 5, pp. 393-402.

[3] K. Soudki, A. El-Sayed and T. Vanzwol. Strengthening of concrete slab-column connections using cfrp strips, Journal of King Saud University-Engineering Sciences, 2012, Vol.24, Issue 1, January, pp. 25-33.

First International Conference on Science, Engineering & Environment,
Tsu City, Mie, Japan, Nov.19-21, 2015, ISBN: 978-4-9905958-5-2 C3051

A TIME-INDEPENDENT FINITE DIFFERENCE ANALYSIS OF FLOW INDUCED CYLINDER VIBRATION

Chih-Chun Chu and Bang-Fuh Chen
Department of Marine Environment and Engineering, National Sun Yat-sen University, Kaohsiung, Taiwan.

ABSTRACT

The flow induced cylinder vibration or earthquake-induced cylinder motion are moving in an arbitrary direction with time. The phenomenon of flow across cylinder is highly nonlinear and a linear-superposition of flow pattern across separated oscillating direction of cylinder motion is not valid to obtain the flow pattern across a cylinder oscillating in multiple directions. A time-independent finite difference scheme is developed to simulate the viscous flow across an arbitrary moving circular cylinder and we call this a complete two-dimensional flow-cylinder interaction. That is, the cylinder is simultaneously oscillating in x- and y- directions. The time-dependent domain and meshes associated with the moving cylinder are mapped to a fixed computational domain and meshes which are time independent. The numerical results are validated by several bench mark studies. Several examples are introduced including flow across steam-wise, transverse oscillating cylinder and flow across rotating cylinder and flow across arbitrary moving cylinder. The forces acting on cylinder are compared with those predicted by Morison's formula and the Morison's formula can not describe the complex interaction phenomenon between cross flow and oscillating circular cylinder. And the completed 2D computational fluid dynamic analysis should be made to obtain the correct hydrodynamic force acting on the cylinder.

Keywords: viscous flow, 2D cylinder interaction, finite-difference method

INTRODUCTION

In marine engineering, offshore structures often encounter waves, currents and earthquake excitations. The fluid-structure interaction is a topic of primary interest in research and design. One of the basic studies is flow across a moving cylinder. During earthquake excitations, the relative velocity between the cross flow (current) and a moving cylinder (induced by ground motion) could be very large and the flow might be turbulent.

In the 20th century, the earliest study of flow around circular cylinder was reported by Blasius in 1908 with a boundary layer theory for a second order time series solution. The first experimental study was made by Prandtl in 1925. Viscous flows across a circular cylinder have drawn significant attention during the last several decades. Collins & Dennis (1973a & b) obtained a higher order boundary layer solution. These two studies provided a good description for the development of vorticity and flow patterns with the drag force. Bouard and Coutanceau (1980) reported a much more detailed flow visualization for various Reynolds numbers, (Re = $2aV_o/\eta$, in which V_o = the velocity of the cross flow, η the kinematic viscosity of fluid and a the radius of the cylinder) and discussed the mechanism of the so-called phenomena α and β. These numerical results and experiments have provided valuable benchmark data sets for validations of computational fluid dynamics (CFD) algorithms as well as theoretical models. The numerical simulation of flow with simple circular geometry is still a very big challenge because its flow separation, abruptly varied velocity and vorticity development along the impulsive oscillating cylinder.

Extensive numerical simulations have been reported in the literature. As early as 1958, Payne reported a numerical method to study the flow past a circular cylinder for Re = 40 to 100. After then, various numerical methods were developed to solve the problems for higher Reynolds number. A brief review of numerical methods was made by Li et al. (2004). In both numerical and theoretical studies, the flow is commonly described by the incompressible Navier–Stokes equations.

In the present study, a novel finite difference scheme is developed to simulate the viscous flow across an arbitrary moving circular cylinder and we call this a complete 2D (two-dimensional) flow-cylinder interaction. The time-dependent flow region is mapped onto a fixed domain, and the boundary conditions are transformed, as the forcing functions, in the Navier-Stokes equations (Hung 1981). Also, refined meshes near the moving cylinder are required; they are stretched to regular meshes in the computational domain. The implicit finite difference approximation and higher order upwind scheme are used in solving stream function and vorticity transport equation and corresponding diffusive terms. The numerical scheme is firstly validated by many comparisons with existing numerical studies and flow

visualizations reported by Phuoc Loc & Bouard (1985) for Re = 3000 and 9500 for a simpler case of a stationary cylinder (KC = 0). For cross flow with oscillating cylinder, the flow is controlled by the Keulegan-Carpenter number. The flow around the cylinder is analyzed along with vortices, and the generation, transport and decay of the vorticity. Several examples are introduced including flow across steam-wise oscillating cylinder, flow across transverse oscillating cylinder, flow across rotating cylinder and flow across arbitrary moving cylinder.

BASIC EQUATIONS

In this study, the cross flow is moving with a constant speed V_0 and the cylinder is stream-wise oscillating. The two-dimensional flow can be described by the vorticity ($\tilde{\omega}$) transport equation and the Poisson equation of the stream function, ψ , in the polar coordinate $(\tilde{r},\theta)$ system:

$$\frac{\partial\tilde{\omega}}{\partial t}-\frac{1}{\tilde{r}}\left(\frac{\partial}{\partial\theta}\frac{\partial\tilde{\omega}}{\partial\tilde{r}}-\frac{\partial\tilde{\omega}}{\partial\theta}\frac{\partial\psi}{\partial\tilde{r}}\right)=\eta\nabla^2\tilde{\omega} \tag{1}$$

$$\nabla^2\psi=\left[\frac{1}{\tilde{r}}\frac{\partial}{\partial\tilde{r}}\left(\tilde{r}\frac{\partial\psi}{\partial\tilde{r}}\right)+\frac{1}{\tilde{r}^2}\frac{\partial^2\psi}{\partial\theta^2}\right]=-\tilde{\omega} \tag{2}$$

The definition sketch of the problem is shown in Fig. 1, where a is the radius of the cylinder, a_r is the distance between the outer boundary and the origin of the polar coordinate system. According to the results of Ta Phuoc Loc & Bouar (1985), a_r greater then 2.5a is appropriate for Re =3000 to 9500, if the cylinder is fixed. However, as Re increases and the cylinder is in motion, the larger a_r would be needed. $\vec{r}'$ is the radial distance measured from the instant center of moving cylinder and ϕ is the angle between $\vec{r}'$ and horizontal direction. The corresponding flow velocity in $\vec{r}'$ and θ directions are defined as u and v and can be calculated through the definitions of velocity and stream function;

$$u=\frac{1}{\tilde{r}}\frac{\partial\psi}{\partial\theta},\quad v=-\frac{\partial\psi}{\partial\tilde{r}} \tag{3}$$

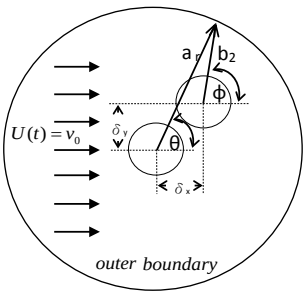

Fig. 1 The definition of sketch of the problem (please re-plot these figures)

COORDINATE TRANSFORMATION AND GOVERNING EQUATIONS

Since the oscillating cylinder surface is varying with time, the first of the following equations is used to remove the dependence of b_2 on time (Hung 1981).

$$\begin{cases} r^* = (r'-a)/[b_2(\phi,t)-a] \\ \Phi=\phi/\pi \end{cases} \tag{4}$$

Also shown in the definition sketch, b_2 is the distance between outer boundary and the instant center of the moving circular cylinder and can be shown and expressed as

$$b_2(\phi,t)=-\delta_x\cos\phi+\{a_r^2-[\delta_x(t)\sin\phi^2]^2\}^{1/2} \tag{5}$$

in which $\delta_x(t)$ is displacement of the oscillating cylinder and a_r is distance between the outer boundary and the fixed origin. The cylinder face is mapped onto $r^* = 0$ and the outer boundary onto $r^* = 1$. And the second transformation would map ϕ onto a region $\Phi = 0$ and 2. Thus, the time-dependent boundary of the moving cylinder is transformed to a fixed computational domain of a rectangular region. Because of the transient boundary layer development, fine grids in the radial direction are required around the cylinder. The coordinates r^* is further transformed so that the layer nears the cylinder will be stretched to produce finer grid meshes Δr^* near the cylinder face. This requirement is accomplished by using the following transformation:

$$R=\beta_1+(r^*-\gamma_1)e^{k_1r^*(r^*-1)} \tag{6}$$

where γ_1 and k_1 are the coefficients used to control the radial grid sizes. When $k_1 = 0$, the grid is not stretched. The grid size will be more stretched as k_1 increases. The grid size will is only stretched in single side with $\gamma_1 = 1$ and fine meshes are on the cylinder face. Among those parameters, the following relationship can be given

$$\tilde{r}\cos\theta=\delta_x+r'\cos\varphi \tag{7}$$

in which δ_x is the corresponding horizontal displacements of the cylinder in stream-wise direction. The relationship between θ and ϕ can be shown and written as

$$\varphi=\sin^{-1}\frac{\tilde{r}\sin\theta}{r'}(if\ \ \tilde{r}\cos\theta-\delta_x\ge 0)$$
$$\varphi=\pi-\sin^{-1}\frac{\tilde{r}\sin\theta}{r'}(if\ \ \tilde{r}\cos\theta-\delta_x<0) \tag{8}$$

The dimensionless variables are defined as

$$U=\frac{v_r}{v_0},\ V=\frac{v_\theta}{v_0},\ r=\frac{\tilde{r}}{a},\ T=\frac{t\cdot v_0}{a},$$
$$\Psi=\frac{\psi}{v_0\cdot a},\omega=\frac{\tilde{\omega}\cdot a}{v_0},\ P=\frac{p-p_o}{\rho\cdot v_0^{\ 2}} \tag{9}$$

where p_o is the pressure of the outer boundary.

NUMERICAL METHOD

The onset potential flow is obtained by solving Eq. (2) for irrotational flow ($\omega = 0$). The results are used to compute the vorticities on the boundary, which lead to the calculation of vorticity on the cylinder when the non-slipping boundary condition is considered. Its values result in the simulation of vorticity transport by Eq. (1) or its finite-difference expression in the computational domain, i.e., Eq. (18). In the two-dimensional analysis, the fluid flow is solved in a rectangular mesh network in the transformed domain (R-Φ). The finite difference method is used in the analysis and central difference is used in both space and time derivatives. The original mesh network and corresponding transformed (R-Φ) domain are shown in Fig. 2.

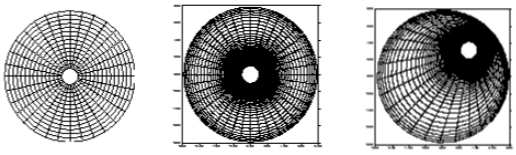

Fig. 2 The concept of coordinate transformation and grid stretching

The numerical procedures are based on the Crank-Nicolson method. Since two equations are coupled, iteration is needed to achieve acceptable convergence condition. Secondly, calculate velocity fields and integrate the momentum equation to obtain the pressure on the cylinder surface. Then, the drag and lift forces can be calculated by integrating the pressure along the cylinder surface. The staggered grid C-type system, which is used in the present analysis.

As mentioned earlier, all the time derivative terms are approximated by central time-difference expression. However, for each time step, the explicit method is used at the first iteration to obtain a pre-condition. The Crank-Nicolson method is, thereafter, used to solve the time dependent terms at each time step and the Gauss-Seidel method is used to solve the systems of linear equations.

RESULTS AND DISCUSSIONS

Before presenting the numerical results obtained by the developed numerical model, a bench mark test is performed to validate the accuracy of the numerical scheme used in this study.

5.1 Bench mark tests (flow past a fixed circular cylinder, Re = 3000 and 9500)

In this section, the developed finite difference scheme is firstly applied to study the flow across a fixed circular cylinder and the calculated results are compared with the reported numerical results and experimental measurements. Fig. 3 compares the phenomenon α (Re = 3000) obtained by the present numerical study with those reported by Phuoc Loc & Bouard (1985) and Fig. 5 compares the corresponding results of phenomenon β (Re = 9500) of both studies. As shown in those two figures, a good accordance is found between experimental and present numerical results. The good agreements of the comparison demonstrate the accuracy of the proposed novel numerical scheme.

(a)

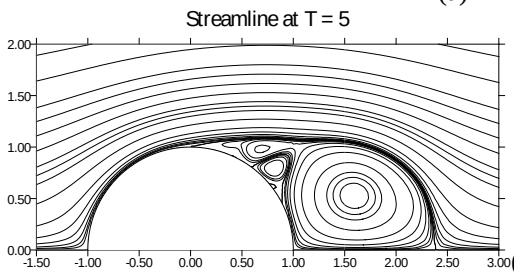

(b)

Fig. 3 The comparison of streamline pattern, Re = 3000, at T = 5: (a) visualization by Phuoc Loc & Bouard (1985) (b) present numerical results

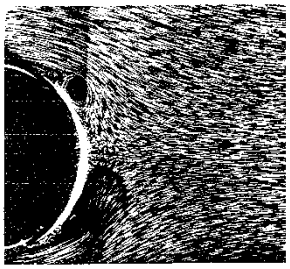

(a)

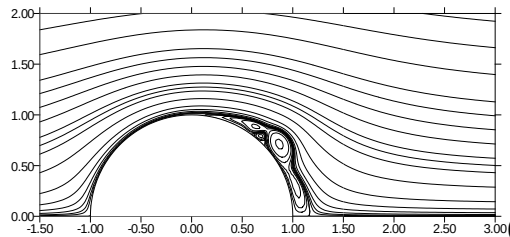

(b)

Fig. 4 The comparison of streamline pattern, Re = 9500, at T = 2: (a) visualization by Phuoc Loc & Bouard (1985) (b) present numerical results

5.2 Flow around oscillating circular cylinder (Re = 100, KC = 5)

The flow induced by an oscillating cylinder is complex and the corresponding vortex development is varied with different conditions of cylinder motion. In 1999, Tatsuno and Bearman (1990) proposed a flows regimes based on various combination of Re and KC numbers. In this section, the present numerical model is used to simulate a flow condition corresponding to regime A. The cylinder is forced to move in east-west (stream-wise) direction in a rest fluid field and the results are examined for Re = 100 and KC = 5. Fig. 5 plots the vorticity isolines at different stages of a typical oscillating cycle. The stable and symmetric vortex shedding are found and stagnation points at the front and back of the cylinder are invariant.

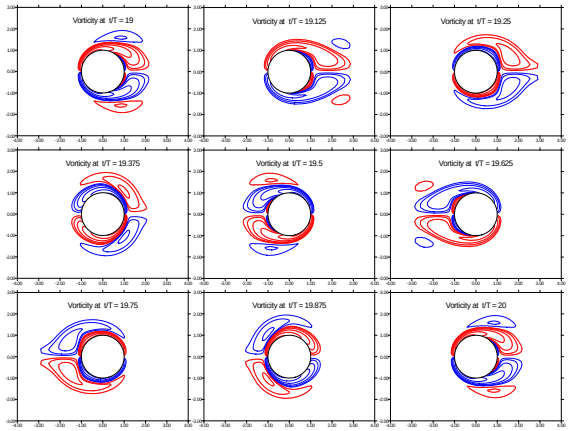

Fig. 5 The vorticity isolines of flow around a stream-wise oscillating cylinder (Re = 100, KC = 5)

Fig. 6 depicts the inline force acting on the cylinder and the dominant contribution to the total force is pressure force. Also shown in the figure are the calculated results (symbols) of Dutch (1998) and the agreements are very good.

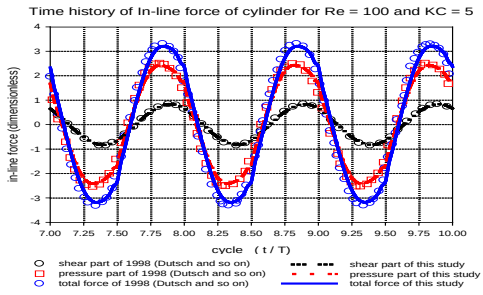

Fig. 6 The comparison of the inline force acting on cylinder for Re = 100 and KC = 5; line: present numerical results, symbol: the results of Dutsch et al. (1998)

5.3 Flow past a stream-wise oscillating circular cylinder (Re = 100, KC = 5)

In the previous section, the flow mechanism is generated by a stream-wise oscillating circular cylinder and the fluid is initially at rest. In the present section, a uniform flow past a stream-wise oscillating circular cylinder is studied. That is, the interaction between cross flow and the oscillating cylinder is studied. Fig. 7 displays the vorticity isolines of uniform flow past a stream-wise oscillating cylinder (named case A). At the beginning of each cycle, the cylinder is moving in westward direction with the same speed of the uniform cross flow and the cylinder is experienced with a Reynolds number = 200. At this instant, the positive vorticity occurs at the right upper part of the cylinder, from $\theta = 0$ to 65^{o}. For the case of oscillating cylinder in a rest fluid (case B), the vortex shape around the cylinder face is about the same as that of the case A but the positive vortex occurs from $\theta = 0$ to 55^{o}. At 0.25 cycles later, the cylinder moves to its most westward point and the Re reduces to 100, the uniform flow prevent the development of positive vortex whereas, at the same time, the positive vortex covers the entire upper part of the cylinder. After then, the cylinder switches moving direction to eastward direction, the cross flow restricts the evolution of the positive vortex and the shape and strength of the positive vortex of case A are, therefore, smaller than those of case B. At the mid of the cycle, the cylinder moves back to its starting point and the Re becomes 0, the positive vortex still constrained by the uniform flow and a clear kink can be seen in Fig. 7(c). After then, a strong negative vortex occurs and force positive vortex leave the cylinder surface and it will shed away by the aid of the uniform cross flow in the later cycles.

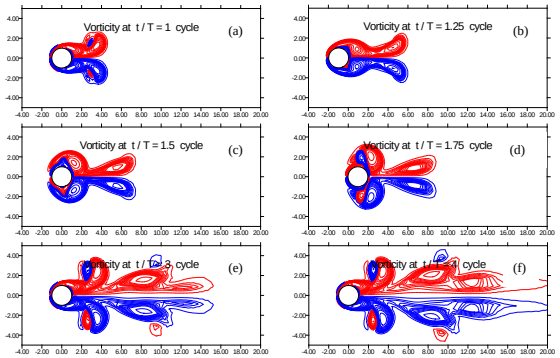

Fig. 7 The vorticity isolines of flow around a stream-wise oscillating cylinder in an uniform flow field. (Re = 100, KC = 5)

Fig. 8 plots the drag forces of cases A and B acting on the cylinder versus time. The equivalent Reynolds number of case A is from Re = 200 to 0 and that of case B is from 100 to -100. The vortex distributions at the leeward side of the cylinder of both cases are about the same. Since the uniform cross flow restricts the evolution of vorticity at the windward side of the cylinder and the positive drag forces of both cases are about the same but the negative forces of case A is smaller than those of case B. Also shown in the figure are the results evaluated by an empirical formula

given by Morrison's equation. As depicted in the figure, the Morrison's equation can accurately predict the drag force acting on the cylinder face of the case B, whereas it underestimates the drag force of the case A during the first and fourth stages of each cycle.

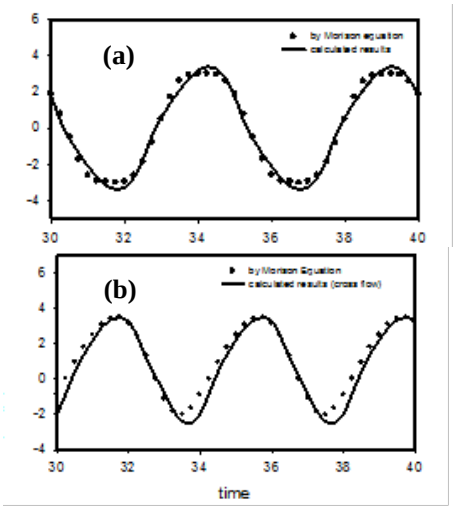

Fig. 8 The comparison of the calculated results with those predicted by Morison equation; (a) Re = 100, KC = 5 without cross flow; (b) with cross flow

5.4 Flow past a transverse oscillating circular cylinder (Re = 500, ymax / D = 0.25)

In this section, the uniform flow passing a transverse oscillating circular cylinder is studied and the results are simulated for Re = 500 and y_{max} / D = 0.25, the frequency ratio F = 0.89, where F = f_o / f_V (f_o = forced oscillating frequency and f_V = natural shedding frequency). Different numerical models generate different natural shedding frequencies. The natural shedding frequency used in Blackburn and Henderson (1999) is f_V = 0.228, whereas, the natural shedding frequency obtained by our model is f_V = 0.22 (close to Lu and Sato (1996)). The natural shedding frequency f_V = 0.22 is, therefore, used in this study. Fig. 9 shows the vorticity contours around cylinder and a clear Kármán-street shedding is obtained in this study. The comparison of the results obtained by present numerical model with those of Blackburn and Henderson (1999) is also shown in the figure and only minor disagreement is found and it might be due to the different natural shedding frequencies used in both studies. Fig. 10 depicts the time-series of C_d and C_l and the comparison between present results and those of Blackburn and Henderson, 1999 and the agreement is also very good. The good agreements of the numerical comparison imply the accuracy of the proposed numerical model.

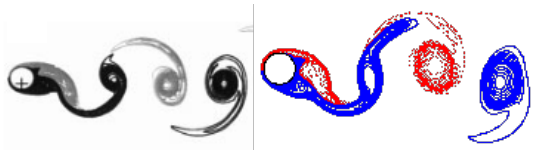

Fig. 9 The comparison of streamline patterns; Re = 500, F = 0.89 and y_{max}/D = 0.25; left: the results of Blackburn and Henderson (1999) and right: the present study

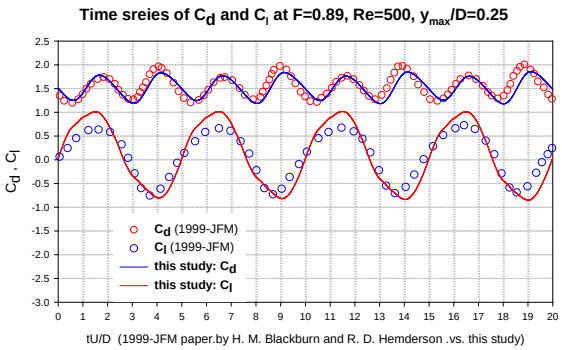

Fig. 10 The comparison of the drag and lift forces acting on cylinder for Re = 500, F = 0.89 and y_{max}/D = 0.25; line: present numerical results, symbol: the results of Blackburn and Henderson (1999)

CONCLUSIONS

A time-independent finite difference method is developed to solve for uniform cross flow past a moving circular cylinder. The numerical simulations presented in this study include (1) oscillating flow past a motionless circular cylinder; and uniform flow (2) past a motionless circular cylinder; (3) past a stream-wise oscillating circular cylinder; (4) past a transversal oscillating circular cylinder; (5) past a rotating circular cylinder and (6) past a moving cylinder in simultaneously stream-wise and transverse directions. We have reached the following conclusions:

(i) The developed numerical model is validated by extensive numerical comparisons of the results obtained by this study with those reported in the literatures and the agreement of the numerical comparison is very good.

(ii) In the study of oscillating flow past a motionless circular cylinder with Re = 100 and KC = 5, the cylinder is experienced with a various Reynolds number from +100 to -100 and the positive and negative vorticity with equal strength are always periodically occurred in the upper and lower part of the cylinder. Besides, the wake structure at both sides of the cylinder is also periodically presented. In this case, the Morison's equation can correctly predict the C_D and C_L acting on cylinder.

(iii) In the case of uniform flow past a stream-wise oscillating circular cylinder, the cylinder is

experienced with a various Reynolds number from +200 to 0. The uniform flow constraint the evolution of the wake structure at the windward side whereas the size and strength of the wake at the leeward side of the cylinder notably increases and the positive vortex will shed away at the end of each cycle. In this case, the Morison's equation underestimates the C_D and C_L acting on cylinder.

(iv) In the case of uniform flow past a rotating circular cylinder, the combined effects of the uniform flow and rotating cylinder will help the shedding of the vortex from the cylinder.

(v) In the case of completed 2D fluid-structure interaction, the uniform flow past a simultaneous stream-wise and transversal oscillating cylinder is studied. The complicated vortex formation is found and the combined effects of uniform flow, movement of the cylinder and the rotating vortices determine the evolution of the wake at both leeside and windward sides of the cylinder. The wake structures are periodically repeated every two cycles.

(vi) The Morison's formula can not describe the complex interaction phenomenon between cross flow and oscillating circular cylinder. And the completed 2D computational fluid dynamic analysis should be made to obtain the correct hydrodynamic force acting on the cylinder.

ACKNOWLEDGEMENTS

The study is supported by National Science Council under a grant NSC 97-2221-E-110-087.

REFERENCES

[1] Blackburn, HM & Henderson, RD, "A study of two –dimensional flow past an oscillating cylinder", J. Fluid Mech, Vol. 385, 1999, pp. 255-286.

[2] Bouard, R & Coutanceau, M, "The early stage of development of the wake behind an impulsively started cylinder for $40<Re<10^4$", J. Fluid Mech, Vol. 101, 1980, pp. 583-607.

[3] Collins, WM & Dennis, SCR, "The initial flow past an impulsively started circular cylinder", Q. J. Mech. Appl. Math., Vol. 26, 1973a, pp. 53-75.

[4] Collins, WM & Dennis, SCR., "Flow past an impulsively started circular cylinder", J. Fluid Mech., Vol. 60, 1973b, pp. 105-127.

[5] Dutsch, H, Durst, F, Becker, S & Lienhart, H, "Low-Reynolds-number flow around an oscillating circular cylinder at low Keulegan-Carpenter numbers", J. Fluid Mech., Vol. 360, 1998, pp. 249-271.

[6] Hung, T.K, "Forcing Functions in Navier-Stokes Equations", Eng. Mech. Div., Vol. 107, No. EM3, 1981, pp. 643-648.

[7] Lu, XY & Sato, J, "A numerical study of flow past a rotationally oscillating circular cylinder", J. Fluid Struct., Vol. 10, 1996, pp. 829-849.

[8] Prandtl, W, "The magnus effect and windpowered ships", Naturwissenschaften, Vol. 13, 1925, pp. 93-108.

[9] Ta Phuoc Loc & Bouard, R, "Numerical solution of the early stage of the unsteady viscous flow around a circular cylinder : a comparison with experimental visualization and measurement", J. Fluid Mech., Vol. 160, 1985, pp. 93-117.

[10] Tatsuno, M & Bearman, PW, "A visual study of the flow around an oscillating circular cylinder at low Keulegan-Carpenter numbers and low Stokes numbers", J. Fluid Mech., Vol. 211, 1990, pp. 157-182.

[11] Li, Y, Shock, R, Zhang, R & Chen, H, "Numerical study past an impulsively started cylinder by the lattice-Boltzmann method", J. Fluid Mech., Vol. 519, 2004, pp. 273-300.

First International Conference on Science, Engineering & Environment,
Tsu City, Mie, Japan, Nov.19-21, 2015, ISBN: 978-4-9905958-5-2 C3051

RELATIONSHIP BETWEEN BORDERLAND AND THE PEDESTRIAN IMAGE

Tetsuya YANOBE[1], Kazunari TANAKA[2] and Shin YOSHIKAWA[3]
[1] Engineering, Osaka Institute of Technology, Japan; [2,3] Osaka Institute of Technology, Japan

ABSTRACT

The boundary of the internal space and outside space is clearly classified in many Japanese cities, however, the space such as the borderland existing in a boundary area is ambiguous. This research's object is to understand the relationship between the ambiguous space and the outside space. As a result, I will be able to analyze spatial image and understand the possibility that a new borderland exists.

Keywords: Inside space, Public Space, Borderland, Pedestrian

INTRODUCTION

Japanese historical streets and European and American streets catch internal space and outside space as something homogeneous, The relationship between the outside space and the internal space is fixed, and the design is made. There is a sense of security in the internal space compared with the outside space, A boundary is on the other side of the internal space and outside space clearly. There is also a boundary in the outside space in the respective area around buildings and blocks in many Japanese cities. Therefore a unified town isn't formed.

On the other hand, because the internal space and outside space are being separated, it's confronted with each space, and there is a way of thinking which can work on a problem. How should you design a Japanese city today to grow as a unified town? I can think the ambiguous space where the reach such as the borderland and the role aren't also clear exists in a boundary part of the internal space and outside space. The Japanese find a boundary such as a like a veranda to be beautiful, and prefers ambiguous space and so to make such ambiguous space intervene between a city, must have a good influence on the city.

Fig.1 Public Space

PURPOSE OF RESEARCH

In this study, I will clarify the existence of the domain that it is hard to catch in the city space. And it is intended to find a clue to bring it up as a town with the unities. Therefore, in the space where it is thought that some domains exist, I will clarify the domain that it is had to arrest by clarifying the relationship between the pedestrian image, psychological structure and the space component.

METHOD OF RESEARCH

The method of research I used is a Semantic Differential Method. And I identified what kind of influence a borderland has on a pedestrian. Furthermore, I identified the overall structure of the public space by measuring the space component. Using this data, I weigh the physical quantity against quantity of psychology.

TARGET AREA

There are components such as a sidewalk, pillars, colors and trees for example. The characteristic varies regarding the space component for each target area. Therefore, in consideration of various space elements, it is necessary to choose the target area. Thus, I chose the a former settlement of Kobe-shi, Hyogo and examined the characteristics of this area.

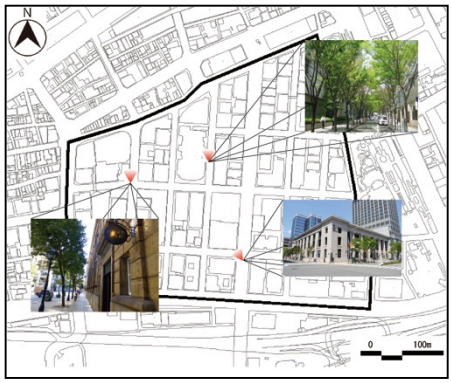

Fig.2 The Former Foreign Settlement of Kobe

ANALYSIS

I divide between a quantity of psychology analysis and physical quantity analysis in this study. I performed preliminary investigation and this investigation by the SD method. Using a correlation analysis, I confirmed the relationship with the variable interval and performed a factor analysis. And I established the influence that a borderland gives to people based on this results. Then, I confirmed the space component in the target area, I understood a chief ingredient analysis for understanding the space characteristic. Moreover, I confirmed the relationship of the quantity of psychology and physical quantity and planed the creation of new space using three dimensional CG.

Finally, I examined a walkers action, to inspect the relationship of the quantity of psychology and the physical quantity.

QUANTITY OF PSYCHOLOGY ANALYSIS

I understood to confirm the psychological structure in the different spaces by the quantity of psychology analysis. I obtained answers using an evaluation with five phases of things that a subject felt for plural photographs by the SD method. After that I made profiles as a result of the SD method. Fig.5 is the profile result of Kobe Daimaru.

Fig.3 Outside walk

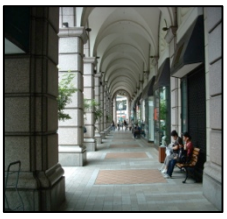

Fig.4 Borderland

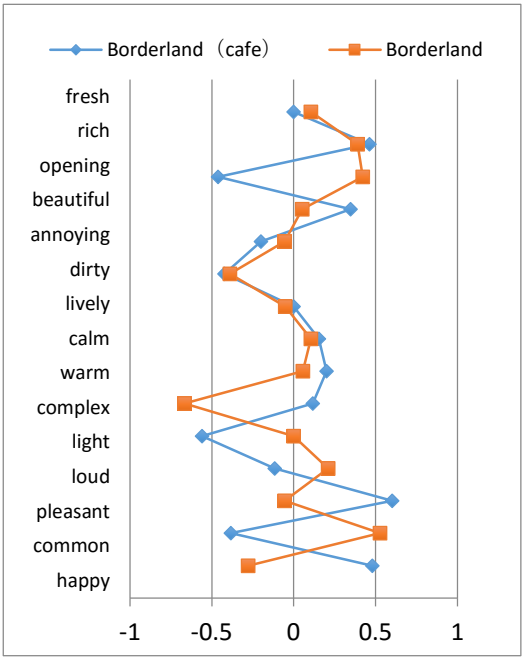

Fig.5 Profile

As a result of the SD method, of each target space, I was able to confirm a remarkable characteristic. In Kobe Daimaru, as for the In particularly, Hommachi garden city has fewer components than other target areas, and an influence on the is result that the colors are unified for the tiles on the ground. I understood that borderland and outside space are strong in a connection of the space. As a result, I understood that the connection of the space is influence by the physical element.

I performed a correlation analysis, and a factor analysis using the data of the SD method. As a result of the factor analysis, I was able to extract three common factors in the preliminary investigation（Comfort factor, Activity factor, Daily life factor）. And I was able to extract three common factors in the main research（Comfort factor, Activity factor, Refreshing factor）. Furthermore, I calculated a factor score to confirm how a subject felt heaviness for each factor from the result of the factor analysis. Fig.6 is the factor score graph in the main research.

The subjects was felt to be strong in activity in the pilotis, and it followed that it was felt to be strong in comfort on the sidewalk as a result of the investigation.

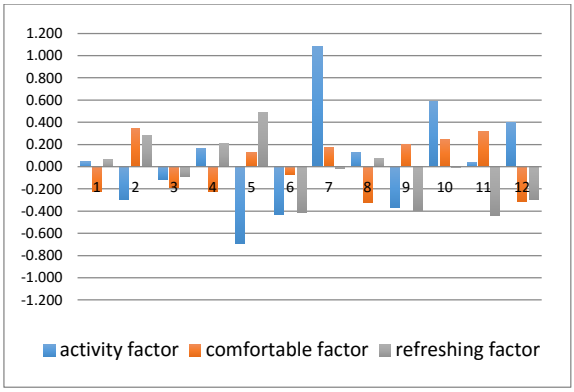

Fig.6 Factor Score Graph

Furthermore, I established whether a causal model fits for real data. Using a covariance structure analysis, I made a causal model and confirmed a conformity degree. As a result of the covariance structure analysis, I was able to confirm that the conformity degree of the causal model was good.

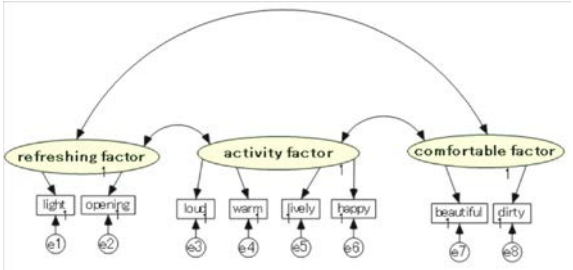

Fig.7 Causal Model

QUANTITY OF PHYSICAL ANALYSIS

I was able to hypothesize that the feeling about space depended on the components as a result of quantity of psychology analysis. Thus, in comparison with the result provided by this investigation, I examined a component of each target space to inspect the hypothesis. Furthermore, I found the new index of the component by performing chief ingredient analysis.

I identified 13 space components （sidewalk width, car width, pilotis width, the height of the pillar, building height, width between the pillar, building width, floor level, number of roadside trees, emission decrement value, the number of the street lights and billboards）. After that I performed a correlation analysis and chief ingredient analysis. As a result, I was able to extract three factors.

Fig.8 Building Maturity Degree

Fig.9 Natural Light Relationship

Fig.10 Traffic Buffering

COMPARATIVE REVIEW

I extracted a comfort factor, an activity factor, a daily life factor as a result of the preliminary investigation. In addition, I extracted the activity factor, the refreshing factor, and the comfort factor as a result of this investigation. The factor properties of the refresh factor resembles the daily life factor. I found that the possible nature of the refresh factor （daily factor）captured the impression of the place of the street.

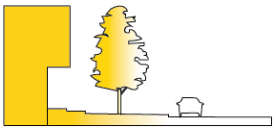

Fig.11 Activity

Fig.12 Comfort

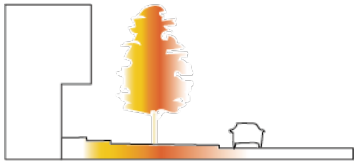

Fig.13 Refreshing

In addition, I found that I could explain space components by 3axes in which are the building maturity degree, a natural light relationship, and traffic buffering as a result of the physical quantity analysis.

I performed a multiple regression analysis to confirm these relationships. As a results, I found that the refresh factor is strongly related with a buildings maturity degree, a natural light relationship, and traffic buffering. Therefore, it is important to extract a borderland without distinguishing pilotis which it is easy to consider as a borderland and sidewalk. Regardless of the kind of the space, it is the 3axes provided by the physical quantity analysis that affect the refresh factor.

Figure-14 expresses the borderland of the city using the score of refresh factor.

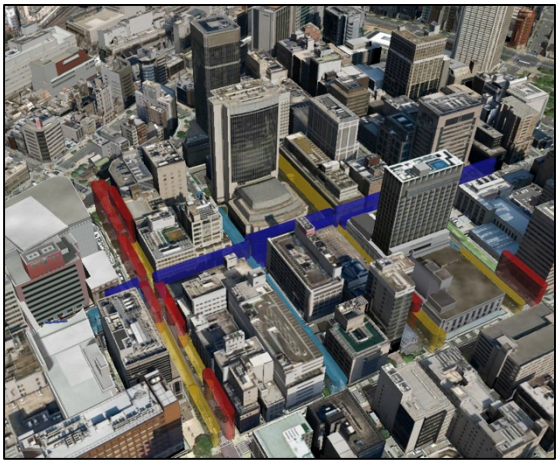

Fig.14 Modeling Of The Factor Score Graph

INSPECTION

As a conventional results, I found that a refreshing factor is strongly related with a building maturity degree, a natural light relationship, a traffic buffering. In particular, the refreshing factor are related with a natural light relationship. I paid my attention to a pedestrian action to inspect this result. I investigated target space in Kobe Daimaru which was the highest in the refreshing factor score. I shot movie with a video camera about the investigation method horizontally from two spots that I showed on the map.

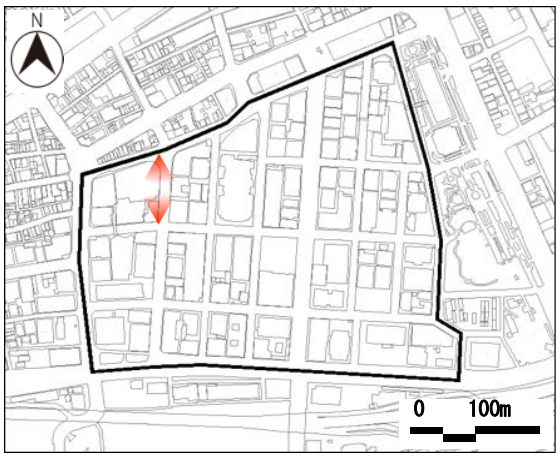

Fig.15 Photography Position

I plotted a point from the result of the animation every one second and made a pedestrian trace. Fig.16 expresses the pedestrian trace of twenty person walking towards the north side.

The roadside tree was located in the center of the sidewalk, and walked with the roadside tree as a border.

I established the characteristic of the pedestrian action using this trace. The indexes of the pedestrian action include speed, density and a progress angle.

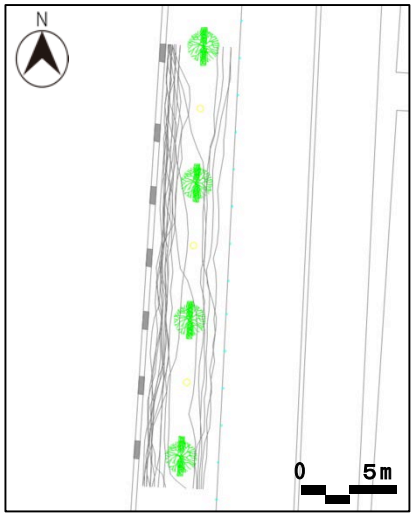

Fig.16 Pedestrian Trace

Therefore I paid my attention to pedestrian speed. At first I established pedestrian speed at the position of the interval for one second. I gave information of the pedestrian speed to a point and performed a kernel density estimate. Fig17 expresses the density value of point. Fig.18 expresses pedestrian speed.

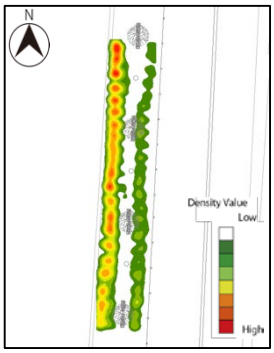

Fig.17 Density value

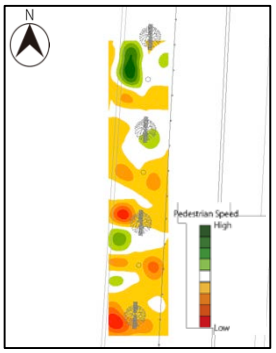

Fig.18Pedestrian Speed

It followed that I knew the space that Pedestrian walked at low speed or high speed from a result of Fig.18 clearly on the sidewalk of Kobe Daimaru. I think that it is caused by the shadow and trees. I confirmed that the speed of the pedestrian tends to change in tree neighborhood.

As a result, on the sidewalk of Kobe Daimaru, I established that pedestrian speed changed under the influence of a tree.

CONCLUSION

I established what refresh factor strongly influenced together in the sidewalk and the pilotis in conclusion. Therefore, I found that the refresh factor is strongly related with a buildings maturity degree, a natural light relationship, and traffic buffering. In particular, the refreshing factor are related with a natural light relationship. Moreover, as a result of having paid its attention to pedestrian speed in inspection, pedestrian speed changed near a roadside tree. Because a natural light relationship was a variable about the trees, I was able to inspect that the refresh factor and a natural light relationship were close.

I define the new borderland by thinking about a pedestrian action as future development deeply.

REFERENCES

[1] Ashihara Y, “Aesthetics of the cityscape”.
[2] Kurokawa K, “Thought and technique of the city planning”.
[3] Space study subcommittee, “Space education celebration for a building, city planning” Inoueshoin, pp.145-155.
[4] Space study subcommittee, “Investigation, analysis method for a building, city planning” Inoueshoin,pp.65-70

First International Conference on Science, Engineering & Environment,
Tsu City, Mie, Japan, Nov.19-21, 2015, ISBN: 978-4-9905958-5-2 C3051

DEVELOPMENT OF ACOUSTICAL SIMULATION MODEL FOR MUFFLER

Wei-Hong Tan[1], T.S. Khor[2], N.H. Zunaidi[3]
[1,2,3]Mechanical Engineering Programme, School of Mechatronic Engineering, Universiti Malaysia Perlis Malaysia.

ABSTRACT

Mufflers have been widely used to reduce the noise level emitted from various vehicles. The simple and high accuracy simulation model for muffler is highly requested by designers in evaluation stage of preliminary design. In this paper, the simulation model was developed by using SysNoise application in LMS Virtual Lab. The basic geometry of simple expansion chamber muffler was proposed for simulation and evaluation in terms of transmission loss (TL). The developed model via simulation had been verified by comparing the predicted TL of simple expansion chamber muffler with the experimental data in literature. It can be observed that simulation results have good agreement with the experimental data from literature. In addition, simulation-based muffler analysis also was conducted for parametrical studies in order to enhance the TL of muffler. As a conclusion, the computational acoustic model based on Finite Element Method (FEM) was successfully developed for prediction of TL on mufflers.

Keywords: Muffler, Transmission Loss (TL), Acoustical Simulation, Finite Element Method (FEM)

INTRODUCTION

Muffler is one of the components used to reduce the noise from a system containing a noise source connecting to a tube. For example, combustion engines, compressors, and air-conditioning system. For modern vehicles, generally it is installed in the tail section of the exhaust pipe part, to suppress the noise generated by engine exhaust emissions in reducing the exhaust and intake system noise. A lot of researches were done on designing these muffling systems. The traditional "build & test" procedure is considered time consuming and expensive, and it can be assisted by acoustical simulation models at the preliminary stage. By this, the initial performance of the designed muffling system can be predicted. In general, muffler can be defined by two types, which are reactive and dissipative [1].

Reactive muffler is composed by several chambers with different volumes and shapes connected together with tubes, and it can reflect the sound energy back to the source, they are virtually sound filters and very useful for the noise either there is a hot, dirty or high-speed gas flow. Reactive muffler also can be made inexpensively and maintenance free. However, dissipative muffler uses acoustic absorbing material to absorb the acoustic energy and turn it into heat. These type mufflers suitable for the source produces noise in a broad frequency band and effective for high frequencies [2,3]. Selection this type muffler will depend upon the noise source and environmental factors.

Transmission loss (TL) of muffler is considered an important parameter for the designing works. In the past few decades, a lot of research works have been conducted to present this work. Normally, the TL of muffler obtained by using two-load method, three-point method [4], and four-pole method [5]. TL is considered the discrepancy in the sound power between the incident wave entering and the transmitted wave exiting the muffler when the muffler termination is anechoic [6].

In this study, acoustic performance of the muffler is simulated and analyzed. Normally, a muffler or a silencer is used to reduce the noise emitted by the exhaust due to the internal combustion engine. By having the acoustical simulation modeling of the muffler, it will help to identify the TL of muffler in the early stage of design. The acoustical simulation result of the muffler will allow manufacturers to understand the function and the traits of a muffler before manufacturing it.

THEORETICAL DEVELOPMENT

Two-load Method

Two-load method is one of the popular approaches to be used for calculating the transmission loss (TL) of muffler. For the two-load method [7], when the loads are very similar, the TL result will become unstable. Normally, two loads situation can be achieved by two different length tubes or a single tube with and without absorbing material as shown in Fig. 1.

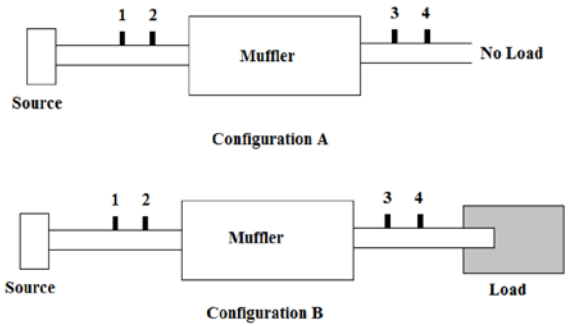

Fig. 1 Two-load method [6,8]

The two load method is based on the transfer matrix approach [8]. This method is used four-pole equation to obtain the TL of muffler, so the formulae almost similar with four-pole method and it easier to be used compare with four-pole method.

$$\begin{bmatrix} \boldsymbol{p_1} \\ \boldsymbol{v_1} \end{bmatrix} = \begin{bmatrix} \boldsymbol{A} & \boldsymbol{B} \\ \boldsymbol{C} & \boldsymbol{D} \end{bmatrix} \begin{bmatrix} \boldsymbol{p_2} \\ \boldsymbol{v_2} \end{bmatrix} \quad (1)$$

Where: p_1= sound pressure at the inlet, p_2= sound pressure at the outlet, v_1= particle velocities at the inlet, v_2= particle velocities at the outlet.

$$A=(p_1/p_2)|\ v_2=0,\ v_1=1 \quad (2)$$

$$B=(p_1/v_2)|\ p_2=0,\ v_1=1 \quad (3)$$

$$C=(v_1/p_2)|\ v_2=0,\ v_1=1 \quad (4)$$

$$D=(v_1/v_2)|\ p_2=0,\ v_1=1 \quad (5)$$

Finally, the transmission loss can be obtained as the formula below [9],

$$TL = 20\left(\frac{1}{2}\left|\boldsymbol{A}+\frac{\boldsymbol{B}}{\boldsymbol{\rho c}}+\boldsymbol{C\rho c}+\boldsymbol{D}\right|\right) \quad (6)$$

ρ = air density, c = speed of sound

For a simple expansion chamber muffler, the theoretical TL can be calculated by Eq. 7 [10, 11] using the 1-dimensional plane-wave approach,

$$\boldsymbol{TL = 10\ \log_{10}\left[1+\frac{1}{4}\left(m-\frac{1}{m}\right)^2 \sin^2 kl\right]} \quad (7)$$

where $m = \frac{S_c}{S_i}$, S_c is the area of cross-section central chamber, and S_i is the area of cross-section inlet pipe, k is wave number and l is the length of central chamber.

METHODOLOGY

LMS Virtual.Lab Acoustic

In this study, the software of LMS Virtual.Lab Acoustic will be used to build the FEM model of muffler, acoustical simulation, and the calculation of muffler TL. The software is considered user friendly as the simulation model easy to be built or designed. By using this software, the acoustical simulation model of muffler was developed and the performance of muffler can be analyzed before carrying out the prototyping

Acoustical Simulation Procedures

In LMS Virtual.Lab software, the CAD model of muffler is drawn and meshed. Then the meshed muffler model is imported into the acoustic harmonic FEM module of the software for simulation. For the acoustical simulation, the acoustic properties were defined. In this simulation, 340m/s is speed of sound and 1.225kg/m^3 for mass density.

There are two boundary conditions are applied on the model. The boundary conditions are imposed at the inlet and outlet. The normal velocity with the harmonic amplitude 1 m/s is applied to the inlet, and acoustic impedance, ρc=416.5 kg/m^{2}s is defined to the outlet for creating the anechoic termination. In order to determine the TL of simulated muffler, input and output point (I/O point) are defined at the inlet and outlet.

RESULT AND DISCUSSION

There are five muffler configurations were analyzed using the acoustical simulation method. The configurations include simple expansion chamber muffler, double expansion chamber muffler, simple elliptic expansion chamber, simple elliptic expansion chamber with extended tube at the inlet or outlet muffler, and expansion chamber with perforated tube muffler. The acoustical simulation results and discussions were presented in the following section.

Simple Expansion Chamber Muffler

Figure 2 shows the geometry of the modeled muffler and isometric view for the simulation analysis.

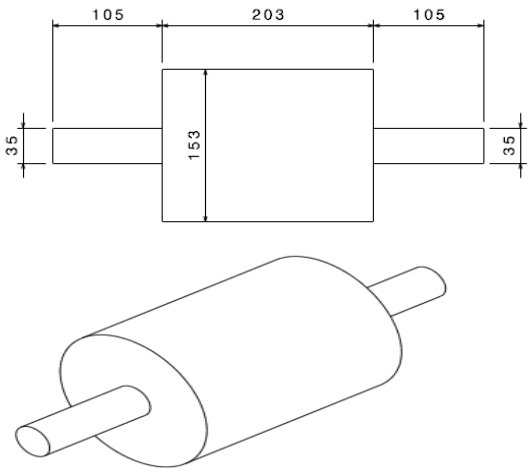

Fig. 2 All dimensions in millimeter (mm) and isometric view

Figure 3 shows finite element method (FEM) result compared with analytical result and experimental measurement of Z. Tao et al., 2003 [6]. 50-3000 Hz frequency range was chose in the simulation. In the comparison, it is apparent that the analytical result deviates from the experimental measurement and FEM result for the frequency range 500-3000 Hz. On the other hand, FEM results show good agreement with experimental result for the frequency range 0-2500 Hz. Frequency 2500 Hz and above, the result deviates from each other, it is most probably caused by insufficient anechoic termination [6]. Based on the observation in Fig. 3, the FEM is considered more accurate than analytical method compared with experimental measurement of Z. Tao et al., 2003 [6] as the correlation coefficient is 0.94.

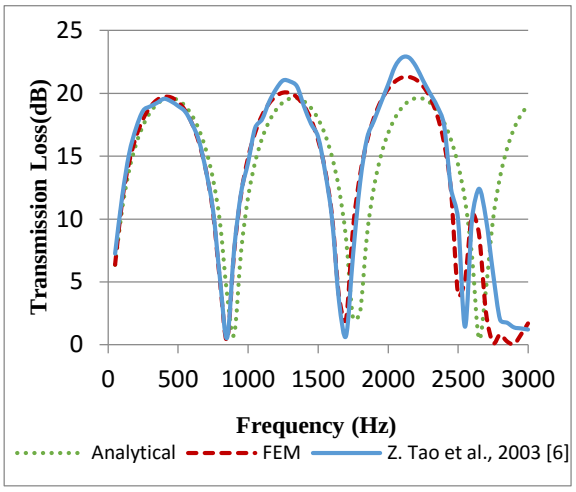

Fig. 3 Transmission loss of simple expansion muffler obtained by analytical, FEM and experimental measurement of Z. Tao et al., 2003 [6]

Double Expansion Chamber Muffler

The dimension and isometric view of double expansion chamber muffler for the acoustical simulation analysis are shown in Fig. 4.

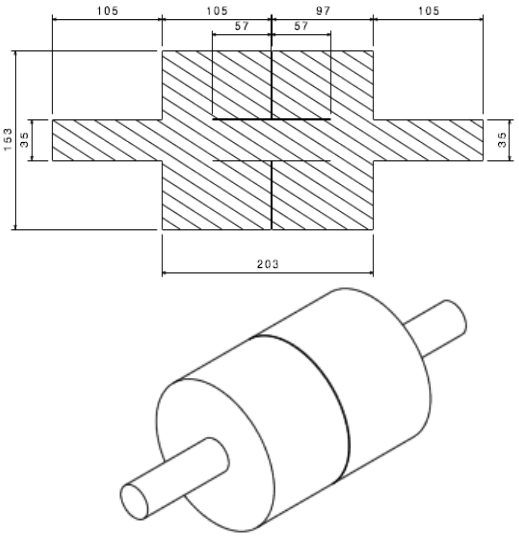

Fig. 4 All dimension in millimeter (mm) and isometric view

Figure 5 shows FEM result compared with BEM and experimental measurement result obtained in the study of Z. Tao et al., 2003 [6]. Based on Fig. 5, FEM analysis shows the similar TL trend with the experimental measurement for the frequency range 50-950 Hz. Frequency range 950-1200 Hz and 1800-2150 Hz, the TL curve of FEM and BEM deviate from each other's. Although the FEM results are different with the experimental measurements, the data still can be accepted since the correlation coefficient is 0.86.

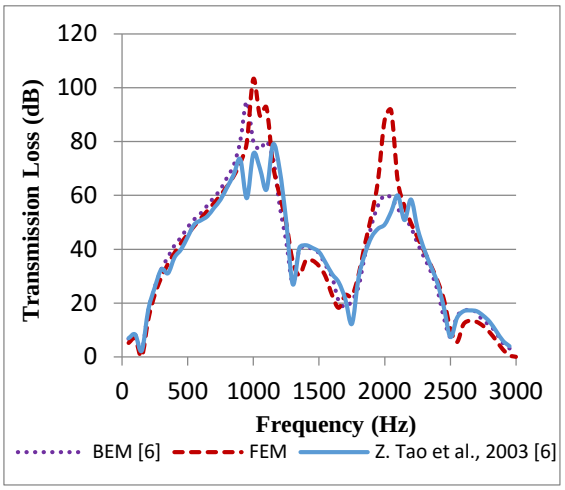

Fig. 5 Transmission loss of double expansion muffler obtained by BEM [6], FEM and Experimental measurement of Z. Tao et al., 2003 [6]

Simple Elliptic Expansion Chamber Muffler

Figure 6 shows the geometry of a simple elliptic expansion chamber and isometric view. The dimension unit for the geometry is in millimeter (mm).

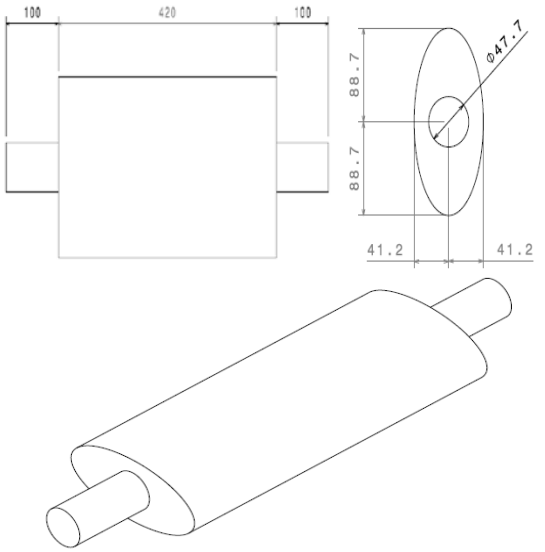

Fig. 6 Geometry of a simple elliptic expansion chamber muffler and isometric view

Figure 7 shows the comparison between the experimental measurements [12] and the FEM numerical TL results. There is 50-3000 Hz frequency range was selected for the simulation analysis. Based on Fig. 7, it is showed that the TL curve is good agreement with each other's for the first loop to last loop, where the maximum differences of 5 dB only. The highest peak TL for FEM drops at 2400 Hz with TL of 28 dB. However, the highest peak of experimental measurement drops at 2600 Hz, which the TL is 32 dB. The correction coefficient between FEM results and experimental measurement for the frequency range 50-2000 Hz is 0.68.

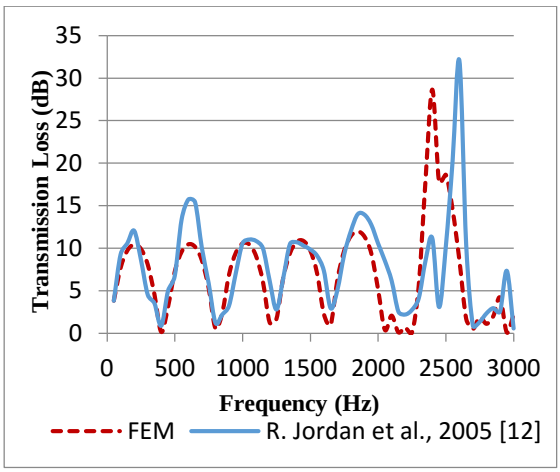

Fig. 7 Transmission loss of simple elliptic expansion chamber obtained by FEM and experimental measurement of R. Jordan et al., 2005 [12]

Simple Elliptic Expansion Chamber with Extended Tube

Figure 8 is another type of simple elliptic expansion chamber muffler attached with the extended tube at the inlet. The unit for the dimension of the chamber is in millimeter (mm).

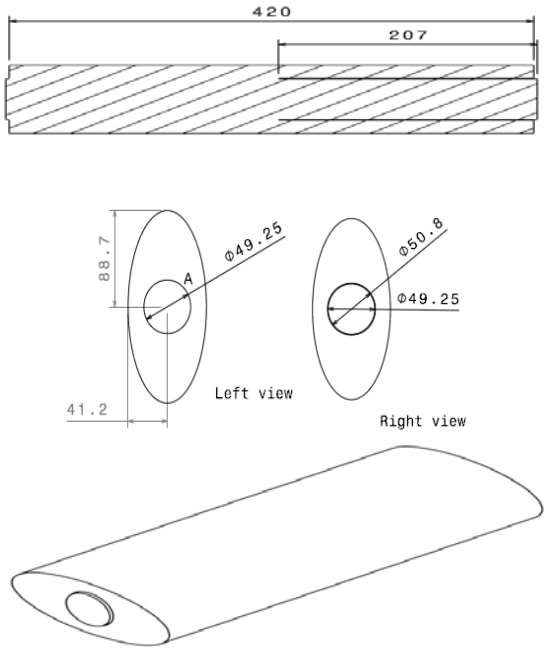

Fig. 8 Muffler attached with the extended tube at the inlet and isometric view

The comparisons between the values of TL obtained from experimental measurement [12] and FEM are shown in Fig. 9. There is 50-3000 Hz frequency range was selected for the simulation analysis. Based on Fig. 9, the first three peaks of the TL are very similar with each other for the frequency range 50-2000 Hz. The highest peak TL for FEM and experimental measurement drop at 1200 Hz with TL 71 dB and 40 dB respectively. The frequency 2000 Hz and above, no significant TL was observed. There is 0.76 of correlation coefficient between FEM results and experimental measurements for the frequency range 50-2000 Hz.

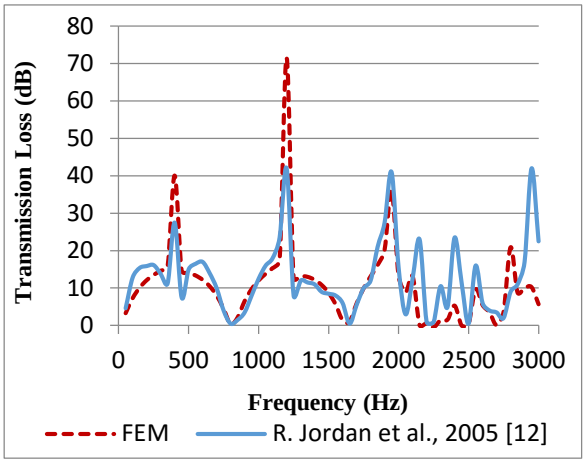

Fig. 9 Transmission loss of chambers with extended tube obtained by FEM and Experimental measurement of R. Jordan et al., 2005 [12]

Muffler with Perforated Wall

Figure 10 shows the model dimension was selected for acoustical simulation analysis and the results will be compared with the experimental result of Sullivan and Crocker [13]. The diameter perforations on the perforated wall are 0.00249m and 0.00081m for the wall thickness. The porosity of the perforated wall is 3.8%.

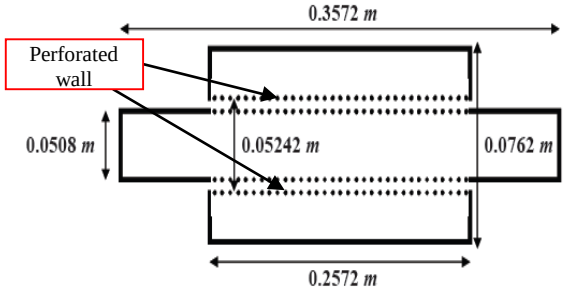

Fig. 10 Model dimension [14]

Figure 11 shows the FEM results compared with experimental results [13]. There is 10-3600 Hz frequency range was selected for this simulation. By referring to Fig. 11, the TL of muffler with perforated wall has a good agreement with Sullivan and Croker's results [13]. The relatively high correction coefficient of 0.89 in this comparison.

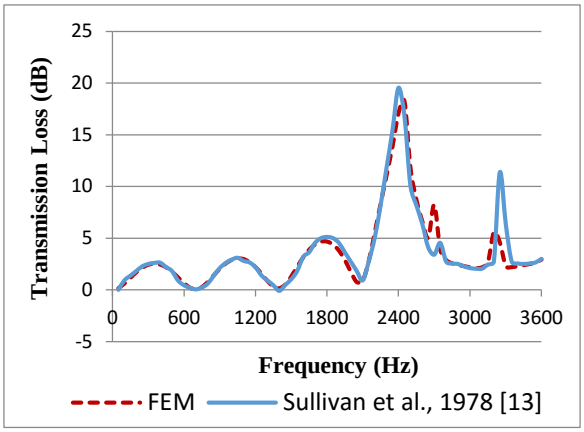

Fig. 11 FEM result compare with experimental result of Sullivan and Crocker [13]

Parametric Study on Simple Expansion Chamber Muffler

In this section, the basic design simple expansion chamber muffler was selected and used for parametric study. Fig. 12 depicts the geometrical parameters of the muffler and Table 1 lists 4 geometrical dimensions for 4 designs of muffler. The diameter, length of inlet and outlet tubes are remain constant for the parametric study. For the chamber, the length is unchanged and the diameter is changed to 75 mm, 125 mm, 175 mm and 225 mm accordingly.

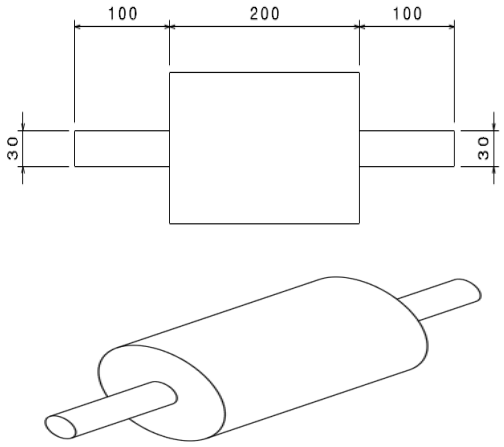

Fig. 12 Dimension and isometric view

Table 1 Length and Diameter for different design type of muffler

Design Type	1	2	3	4
Length (mm)	200	200	200	200
Diameter (mm)	75	125	175	225

Figure 13 shows the simulation result by using the built model FEM. 0-3000 Hz frequency range was chose in this simulation. Based on Fig. 13, it is observed that the bigger diameter of the chamber will produce higher TL for the frequency range 0-1750 Hz. For the frequency 1750 Hz and above, the TL curve obtained from design type 3 and design type 4 are deviating with each other. However, the TL curve of design type 1 and 2 are similar for the frequency range 0-3000Hz.

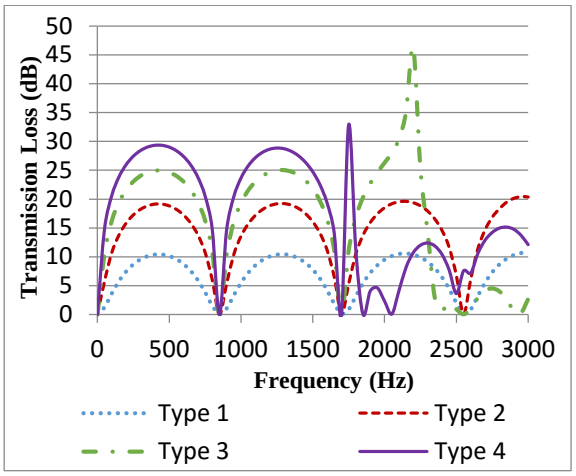

Fig. 13 Transmission loss of different design of the muffler

CONCLUSION

In this study, the results of FEM simulation for each of the muffler are good agreement with the experimental measurement results. Especially, the results of TL for simple expansion chamber muffler, double expansion chamber muffler and chamber with perforated tube muffler almost similar compared with the experimental measurement results, which give the correlation coefficient in between 0.76 to 0.94. This proves the FEM acoustical simulation model of muffler is developed successfully and validated, and the FEM model analysis on the muffler can be used to predict the TL of muffler in the early stage of design before prototyping.

ACKNOWLEDGMENT

This paper is done with the financial support from Universiti Malaysia Perlis (UniMAP) Incentive Grant (No Project: 9007-00252). Technical Support from USM TheVibration Lab also is greatly acknowledged.

REFERENCES

[1] Kumar. S, "Linear Acoustic Modeling and Testing of Exhaust Mufflers", M.S. thesis, Royal Institute of Technology, Stockholm, Sweden, 2007.

[2] Beraek L.L, Noise and vibration control. New York: McGraw-Hill, 1971.

[3] F. Cui, Y. Wang, R. C. Cai, "Improving muffler performance using simulation-based design", in INTER-NOISE and NOISE-CON Congress and Conference Proceedings, 2014, pp. 1190-1194.

[4] T.W. Wu and G. C. Wan, "Muffler Performance Studies Using a Direct Mixed-Body Boundary Element Method and a Three-Point Method for Evaluating Transmission Loss", J. of Vibration and Acoustics, Vol. 118, Jul.1996, pp. 479-484.

[5] T.W. Wu and P. Zhang, "Boundary Element Analysis of Mufflers With an Imposed Method for Deriving the Four-Pole Parameters", J. of Sound and Vibration, Vol. 217, June. 1998, pp.767-779.

[6] Z. Tao and A.F. Seybert, "A review of current techniques for measuring muffler transmission loss",SAE International, in Noise & Vibration Conference & Exhibition, Traverse City, 2003.

[7] Lung, T.Y, Doige, A.G, "A Time-Averaging Transient Testing Method for Acoustic Properties of Piping Systems and Mufflers", J. of Acoustical Society of America, Vol. 73, Mach. 1983, pp. 867-876.

[8] M.B. Jadhav and A. P. Bhattu, "Validation of the Experimental Setup for the Determination of Transmission Loss of Known Reactive Muffler Model by Using Finite Element Method", International J. of Engineering and Innovative Technology , Vol. 2, July. 2012.

[9] S. Bilawchuk, K.R. Fyfe, "Comparison and implementation of the various numerical methods used for calculating transmission loss in silencer systems", Applied Acoustics, Vol. 64, Feb. 2003, pp. 903-916.

[10] Bell LH, Industrial noise control. New York: Marcel Dekker, 1994.

[11] Bhattacharya. P, Panua. R, Bose P. K, Ghosh B, "Design of Reactive Muffler for Study on the Noise Level and Performance of a Two Cylinder Four Stroke 16 H.P Diesel Engine", Noise Worldwide, Vol. 39, Sept. 2008, pp 24-27.

[12] S. N.Y. Gerges, R. Jordan, F. A. Thieme, J. L. Bento Coelho, J. P. Arenas. "Muffler Modeling by Transfer Matrix Method and Experimental Verification", J. of the Brazilian Society of Mechanical Sciences and Engineering, Vol. 27, Apr. 2005.

[13] Sullivan, J.W. and Crocker, M.J, "Analysis of Concentric-Tube Resonator Having Unpartitioned Cavities", J. of the Acoustical Society of America, Vol. 64, 1978, pp. 207-215.

[14] S. Jeon, D. Kim, C. Hong, W. Jeong, " Acoustic Performance of Industrial Muffler with CAE Modeling and Simulation", International J. of Naval Architecture and Ocean Egineering, Vol.6, Dec. 2014, pp. 935-946.

First International Conference on Science, Engineering & Environment,
Tsu City, Mie, Japan, Nov.19-21, 2015, ISBN: 978-4-9905958-5-2 C3051

EXPERIENCES WITH GEOCELL REINFORCED EARTHWORK IN TERMS OF DEFORMATION RESISTANCE

Vlastimil Chebeň[1], Ľubomír Pepucha[2]
[1,2] Faculty of Civil Engineering, University of Žilina, Slovakia

ABSTRACT

Over past 30 years, production, use, research and development of geosynthetics turned to a leading segment of world´s construction materials industry. Increase of its popularity can be linked to its main advantages: versatility, natural material reduction and recovered plastics substance resulting in lower CO_2 footprint. A specific category of geosynthetics are geocells, the three-dimensional honeycombed cellular structures, used for soil improvement and reinforcement. Practical study of solving foundation engineering problem is presented using geocell reinforced subbase. Deposits of highly compressible soft soil consisting of clay were present at subgrade of pavement and floor area of newly built production facility. Improvement techniques such as soil replacement, lime stabilization and other could be an option if high ground water table did not occur. Geocell reinforced earthwork of 600 mm thickness has to meet project´s ULS and SLS requirements. A full scale PLT field tests on staged earthwork were carried out to research deformation characteristics and its performance on soft subgrade with E≈5 MPa. After construction, series of control measurements were collected to verify concept of hardening effect of geocell reinforced structure over 3 year period, that confirmed more than 30 % increase in earthwork´s deformation resistance. Please use this document as a template.

Keywords: Geocells, Earthwork, Plate Load test, Deformation Modulus

INTRODUCTION

Over the past three decades geosynthetic products has been utilized in geotechnical engineering to improve building methods, design and costs of construction. At present, in Slovakia from variety of geosynthetic materials were adopted predominantly geogrids and geotextiles used in highway, railroad engineering and embankment construction. These two dimensional reinforcement elements are challenged with three dimensional geosynthetic products known as geocell. The geocell is a geosynthetic product with a three dimensional cellular network in honeycomb configuration made from thin polymeric strips. Despite the extensive research and successful field applications over past ten years, geocell applications are still not widely used in comparison with traditional methods like piling, soil replacement, lime stabilization or geogrid/ geotextile reinforcement. It is probably due to the lack of design procedures and dominant market position of traditional producers of geosynthetics. Therefore, in summer 2012 was carried out full-scale field tests on a site where testing was performed on geocell reinforced and unreinforced gravel mattress. Investigation was focused on reinforcing effect expressed by increase of deformation modulus of subgrade and its change over time.

In many ways efficient geotechnical design cannot be carried out without reliable in situ testing [3], especially in areas of artificial deposits, organic deposits or soft soil in place of foundation, or in the place of old mining activity, or underground movements. There is another important design strategy that should be taken into account by geotechnical engineers – design limits and appropriate use of new calculation methodology.

PRINCIPLE OF GEOCELL REINFORCEMENT MECHANISM

Numerous field trials and full-scale laboratory investigations have illustrated that geosynthetics used to reinforce unpaved roads on soft subgrade facilitate compaction, improve the bearing capacity extend the service life, reduce the necessary fill thickness, diminish deformations. The combination of geosynthetic reinforcement and fill help to spread the concentrated vertical loads and to inhibit large deformations and local failures. Three modes of action can be distinguished [10], [11].

Lateral confinement effect

As shown on Figure 1, due to the three-dimensional structure the geocell can provide lateral confinement to soil particles within cells. The concept of lateral confinement by cellular structures dates back to 1970s. The United States Army Corps of Engineers developed this idea for providing lateral confinement to improve the bearing capacity of poorly-graded sand. It was observed that the soil developed cohesive strength resulting from the confinement by the geocell, and the magnitude of the cohesive strength varied with the properties of the geocell. In [7] is suggested a simple methodology for estimating the magnitude of the apparent cohesive strength. A geocell consists of three-dimensional cells that contain, confine and reinforce a variety of filled materials within its cells that completely arrest the lateral spreading and increase the shear strength of filled materials. Moreover, interfacial resistance, which result from the interaction between the geocell reinforcement and the soil below and above the reinforcement, as shown in Figure 1, increase the lateral confinement and lower lateral strain, that result in an increase in the modulus of the mattress and improving vertical stress distribution on the subgrade which is called "vertical stress dispersion effect" below, and reducing the vertical pressure on the top of the subgrade correspondingly.

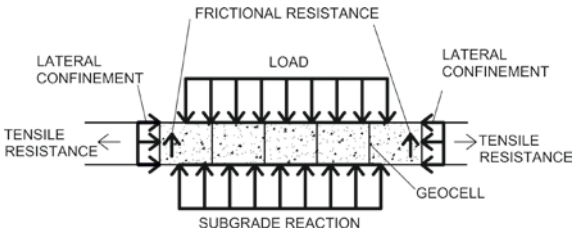

Fig. 1 Concept of geocell lateral confinement

Vertical confinement – stress dispersion effect

The geocell provides the vertical confinement in two ways: the friction between the infill material and the geocell wall and the geocell-reinforced base acts as a mattress to restrain the soil from moving upward outside the loading area. As mentioned above, the horizontal geocell-reinforced mattress behaves as an immediate working platform that redistributes the footing load per unit area over a wider area, as shown on Figure 2. This refers to herein as "stress dispersion effect". As a result, the soil-pressure onto the soft subgrade soil surface is smaller than that onto the subgrade soil in the absence of geocell.

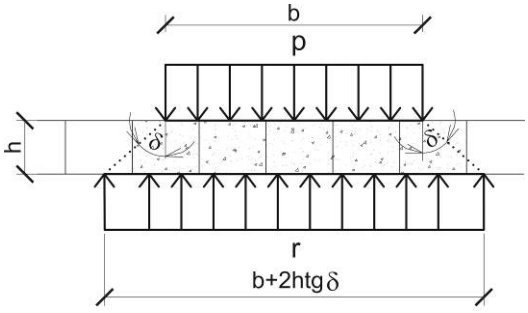

Fig. 2 Concept of geocell lateral confinement

Membrane effect

Regarding the membrane effect, it is inevitable to describe the concept of membrane, that is two dimensional flexible element different from surrounding environment in which it is embedded while not separating it in two distinct layers. Since the membrane bears primarily tension component from imposed loads that result in wider planar stress distribution, the term tension membrane effect is adopted and is referred to the tension developed in the curved geocell-reinforced mattress resisting the vertical load [5]. The loads from the embankment deform the geocell reinforcement thus generate a further tension force (Figure 3). The vertical component of the tension force in the reinforcement is helpful to reduce the pressure on the subgrade soil. Then the vertical deformation of the soft subgrade is reduced and the bearing capacity of the subgrade soil is enhanced as well. As the depth of the ruts increases the deformed shape of the geocell reinforcement, the reinforcement can provide a further tension force due to this membrane effect. Another approach state, that due to the thickness of the geocell, the geocell-reinforced mattress more likely provides a beam or plate effect rather than a membrane effect. The confinement of the geocell increases the stiffness of the reinforced base thus having a wider area of stress distribution.

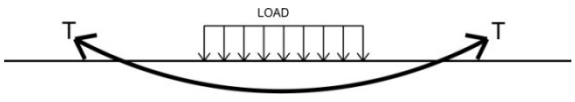

Fig. 3 Concept of membrane effect

FULL SCALE FIELD TESTING

Field testing was carried out in two stages: a series of testing during construction process and after construction, during operation. First tests were performed in 2012, when a new production and warehouse shop for growing industrial company were built near Ružomberok, Slovakia. The other in 2014 and 2015, to explore the influence of

consolidation on hardening effect of geocell reinforced earthwork originating in properties of polymeric materials that often have nonlinear and time-dependent stress-strain relationships [10]. Tests were conducted with circular plate load tester (PLT) of 357 mm diameter, revealing the deformation modulus of subgrade $E_{v,2}$ from second loading-unloading loop. In 2015 testing series, besides PLT, a light weight deflectometer LWD based on falling weight inducing very short dynamic impuls on the base plate was employed to enrich the data set.

Site geology

Geological survey of the proposed area resulted difficult foundation conditions comprising high water table and compressible high plastic subgrade soils. This fact would have led to dramatic rise of construction costs in very beginning of the project. It was required to employ value engineering with reasonable options. Several methods were taken into account, e.g. lime stabilization, soil replacement, reinforced soil and considered all pros and cons. High water table and possibly even higher than expected and lack of suitable soil discarded lime stabilization and soil replacement. Finally, competition of reinforced soil techniques succeeded geocell method due to guaranteed overall performance based on possibility of use a fair quality infill material from nearby quarry and possibility of decreasing the thickness of embankment what resulted in reasonable costs.

Construction stage field tests and material properties

Because of lack of trustworthy calculation methods and required saving literally every inch of construction, two testing fields were built at the site. Test field 1 (Figure 4a) was unreinforced made up from granular material, test field 2 (Figure 4b) was reinforced with geocell system at the base. Subgrade soil was formed by soft-stiff high plastic clay of Young modulus 4 MPa resulting $E_{v,2}$=7MPa. Clay layer was underlain by sand-gravel soil with slight pressure water table stable in depth of 1,2 m below ground level, thus 0,5 m from foundation base level.

Tests were conducted by following methodology: embankments of 750 mm final height were built as staged construction by 200 – 300 mm compaction steps.

Quality of compaction was controlled by PLT using a 357 mm diameter circle plate to determine the deformability and load-bearing capacity resulting in deformation modulus $E_{v,2}$. Initial plate load test was performed on subgrade soil and every construction step thereafter. The value of $E_{v,2}$ that was taken into account was at the top of embankment.

Fig. 4a Test field 1 – Unreinforced embankment

Fig. 4b Test field 2 – Geocell reinforced embankment

Material of geocells was HDPE formed in strips of height 200 mm with wall perforation and cell dimension 210x260 mm. Material properties should conform [8], [9] shown in Table 1. Infill material was poorly graded gravel of maximum particle size 63 mm.

Table 1 Geocell material properties

Tensile stress [kN]	Tensile stress of joints and seams [kN]	Tensile strength for joints by wide-width strip method [kN]	Ductility [%]
15	22	21	60

It must be noted that infill material was considerably inhomogeneous, without smooth soil grading curve predominantly containing sand (0,06-2 mm) over gravel particles (2-63 mm) probably caused by its calcareous origin.

Initial mean $E_{v,2}$ of original subsoil was 8,5 MPa what yields 4,5 MPa Young´s module with maximum plate settlement 16,49 mm as shown in tables 2 and 3. This corresponds to soft-stiff consistency. Designed $E_{v,2}$ value for floor subgrade was 80 MPa that was comfortably achieved with 750 mm high embankment.

Table 2 Settlement in mm at various embankment height/loading steps on field 1 - unreinforced

Plate loading (kPa) / Height (mm)	0	50	100	200	300
0	0	1,65	3,68	8,19	15,65
200	0	0,81	2,15	5,6	9,88
450	0	0,29	0,85	2,29	3,93

Table 3 Settlement in mm at various embankment height/loading steps on field 2 - reinforced

Plate loading (kPa) Height (mm)	0	50	100	200	300
0	0	0,91	2,46	8,08	16,49
450	0	0,25	0,63	1,46	2,36
700	0	0,15	0,35	0,96	1,54

Testing the geocell reinforced embankment succeeded and was found reasonable as soil improvement technique.

Concerning unreinforced gravel mattress, it is evident that $E_{v,2}$ increase is not that persuasive. Quality of infill material strongly correlates with its deformation properties therefore the fact that grain size, shape, diagenesis, porosity etc. should be taken into account.

If the embankment was made solely with gravel, the required value of $E_{v,2}$ would have been reached at least by 1000 mm height, that was practically impossible to build and measure with given instrumentation.

Other set of tests were performed during major construction works as compaction control followed by stage of operation, when additional tests were performed on existing unpaved surface to reveal almost 3 years period. These testing places were selected carefully meeting condition of never imposed loading over the time.

RESULTS

The main advantage of geocell reinforced earthwork is due to the soil being confined by the walls of membranes. Tension in the membranes of the geocells gives rise to a compression stress in the soil that is resulting in an increased strength and stiffness behaviour of the composite. Another advantage is increasing stiffness of the composite due to properties of polymeric materials what will be later discussed.

Presented results were measured at building and operation (after construction) stage. Data for 750 mm high embankment come from building stage of embankment in 2012, whereas control measurements were taken in 2014 and 2015 on 600 mm high embankment. This was possible due to unpaved road as can be seen on Fig. 5.

Fig.5 View on the unpaved area, where measurements were taken

Despite this fact, collected data are of the same origin and structure.

Effect of time shows Figure 6, where rise of deformation modulus $E_{v,2}$ by 25% can be observed between years 2012 and 2014 and another 5% from 2014 till 2015. It must be noted that test points had never been loaded by traffic or any other loads.

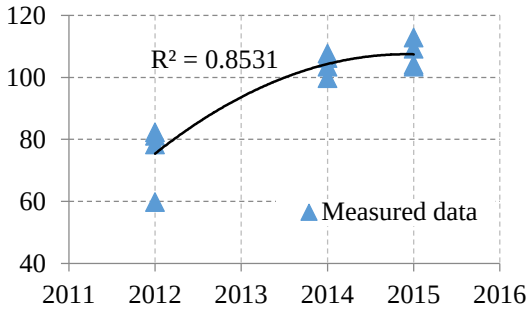

Fig.6 Increase of deformation modulus $E_{v,2}$ from loading tests over 3 year time period

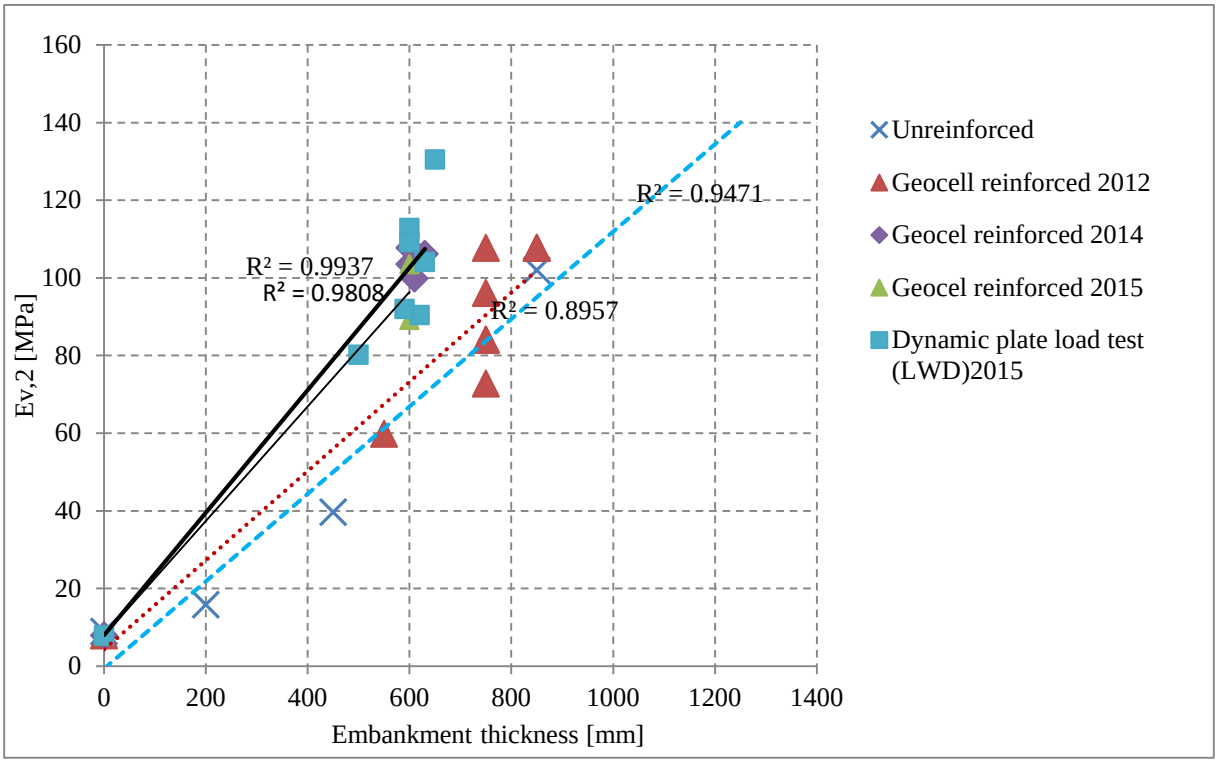

Fig. 7 Improvement effect using geocell reinforcement

Figure 7 shows deformation modulus $E_{v,2}$ during construction and operation stage after 3 year time period. Enhancement of earthwork with geocell mattress can be seen evidently in increase of structure stiffness expressed by $E_{v,2}$ with simultaneous decrease of its height.

Important fact is that embankment had been exposed for a certain time to climate and geological factors that should deteriorate deformation properties as a result of gradual degradation process. One of the climate factors that have substantial influence on earthwork condition is frost depth which in the discussed region of Northern Slovakia is about 800 – 1000 mm. As structure height is 600 mm with fine soils in subgrade, there should fail prevention of subgrade freezing and clay soil must got frozen over 3 winter periods. Nevertheless, none of this reflected in quality of earthwork.

CONCLUSION

Using geocell reinforcement in the base of earthwork in form of mattress confirmed the benefit of reinforcement and improved both bearing capacity and deformation resistance, thus reduction in settlement of the construction. Performed field tests showed about 30-40% increase in deformation modulus $E_{v,2}$ over gravel-built structure what yields an advantage of geocells. It is also in good agreement with some latest researches on the topic that suggest geocells distribute the load laterally and to a relatively shallow depth as compared to unreinforced and the geogrid reinforced soils. This conclusion is based both on numerical model and experimental studies [3].

Employing geocell give effect primarily in the embankment height reduction and limiting the excavation volumes resulting in saving of granular materials and the amount of unsuitable material for removal and deposition. This results in cost effective and ecological profit, whereas use of geotechnically inappropriate material e.g. tailings, poor quality granular soil etc. can find its application in geocell fill. Additional benefits come from hardening effect of geocells over the time, that proved testing in 3 year time span on 600 mm thick embankment resulting in adding 30 % to original deformation modulus $E_{v,2}$.

ACKNOWLEDGEMENTS

The research is supported by European regional development fund and Slovak state budget by the project “Research centre of University of Zilina”, ITMS 26220220183.

REFERENCES

[1] Adam CH., Adam D., Kopf F., Paulmichl I., “Computational validation of static and dynamic plate load testing”, Acta Geotechnica, Volume 4, Berlin, 2009.

[2] Decký, M. - Drusa, M. - Pepucha, Ľ. - Zgútová, K., “Earth Structures of Transport Constructions”, Pearson Education Limited 2013,

Edinburg Gate, Harlow, Essex CM20 2JE. Edited by Martin Decký, p. 180, ISBN 978-1-78399-925-5

[3] Hegde A., Sitharam T.G., "3-Dimensional numerical modelling of geocell reinforced sand beds", Geotextiles and Geomembranes, Volume 43, pp 171-181, 2015.

[4] Mužík M., "Meshless solution of the slope stability", SGEM 2013 Conference Proceedings, ISBN 978-954-91818-8-3 / ISSN 1314-2704, June 16-22, 2013, Vol. 2, 249 - 256 pp. DOI: 10.5593/SGEM2013/BA1.V2/S02.033.

[5] Nelson D.R., Tsvi P. "Statistical mechanics of membranes and surfaces", World Scientific Publishing, Singapore, 2004, ISBN 981- 238-760

[6] Pokharel S.K., Han J., Leshchinsky D., Parsons R.L., Halahmi I., "Investigation of factors influencing behavior of single geocell-reinforced bases under static loading", Geotextiles and Geomembranes, Volume 28, Issue 6, December 2010.

[7] Rajagopal K., Krishnaswamy N.R., Latha G., "Behavior of sand confined with single and multiple geocells" Geotextiles and Geomembranes, Volume 17, Issue 3, pp 171-184 June, 1999.

[8] STN EN ISO 10319 Geosyntetika. Ťahová skúška pevnosti širokej vzorky.

[9] STN EN ISO 10321 Geosyntetika. Ťahová skúška pevnosti spojov/švov metódou Strip na širokých vzorkách.

[10] Wesseloo J., "The Strength and Stiffness of Geocell Support Packs", Doctoral thesis, University of Pretoria, August 2004

[11] Zhang L., Zhao M., Zou X., Zhao H., "Deformation analysis of geocell reinforcement using Winkler model", Geotextiles and Geomembranes, Volume 36, Issue 6, July 2009.

[12] Zhang L., Zhao M., Shi C., Zhao H., " Bearing capacity of geocell reinforcement in embankment engineering", Geotextiles and Geomembranes, Volume 28, Issue 5, October 2010.

First International Conference on Science, Engineering & Environment,
Tsu City, Mie, Japan, Nov.19-21, 2015, ISBN: 978-4-9905958-5-2 C3051

EFFECT OF REINFORCEMENT ON IMPROVE SURFACE PAVEMENT FOR WEAK SUBGRADE CONDITIONS

Saad F. Ibrahim, Namir G. Ahmed and Dhuha E. Mohammed
Dep. of Highway & Transp. Eng. / University of Al- Mustansiriya

ABSTRACT

A pavement structure consists of several layers for the primary purpose of transmitting and distributing traffic loads to the subgrade. Rutting is one form of pavement distresses that may influence the performance of road pavements. Soft subgrade soils are distinguished by their low undrianed shear strength and high compressibility. The effect of geogrid and steel mesh to improve the performance pavement is experimentally investigated and evaluated. To compare the experimental and analytical outputs, three dimensions finite element throughout models using ABAQUS ver.6.12.3 software are developed to simulate and analyze the relations between the cycling load and deformation of the suggested pavement modes. Based on the results and the limitation of this study it is concluded that, using geogrid and steel mesh in pavement layers leads to increases in load carrying capacity and decrease the permanent deformation in surface pavement for (1000) cycles load by (27.3%) and (18.3%) respectively, as compared with unreinforced model. The results of ABAQUS program are very close to results of laboratory tests.

Keywords: Soft subgrade, Geogrid, Steel mesh, Abaqus models

INTRODUCTION

In recent years, the reinforcement of road pavements has increased quickly for improvement construction and performance. In pavement systems, the term reinforcement refers to the ability of an interlayer to better distribute the applied load over a larger area and to compensate for the lack of tensile strength within structural materials. As with any reinforcement applications, the interlayer should be stiffer than the material to be strengthened [1]. In such pavement applications, reinforcements involving either (1) subgrade and granular layers or (2) HMA layers and overlays have achieved particular success. Fig. 1 illustrates a number of potential geosynthetic applications in a layered pavement system to improve its performance [2]. Subgrade stabilization refers to situations where geosynthetics are placed on weak subgrade prior to the placement of an aggregate layer. Reinforcement placed within asphalt layers are used to reduce fatigue, thermal and reflective cracking, control rutting.

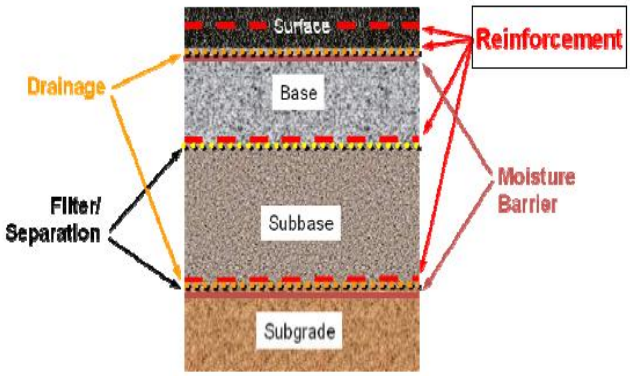

Fig. 1 Potential applications of geosynthetics in a layered pavement system.

STUDY OBJECTIVE

1. Investigating, evaluating experimentally the effect of geosynthetics to improve the performance of pavement.

2. Developing a three dimensions finite element throughout using ABAQUS ver.6.12.3 software to simulate and analyze the relations between the cycling load and deformation of the proposed pavement modes; raw material model, geosynthetics model.

EXPERIMENTAL WORK

Materials Properties

Soil

A brown lean clayey soil is brought from a depth of 5m from the site of abridge in the sport city within Al-Basrah city. Standard tests are performed to determine the physical and chemical properties of the soil, details are given in Table 1.

Table 1 Physical and Chemical Properties of Natural Clayey Soil Used

Property	Value	Standard
Liquid limit %(LL)	47	ASTM D4318
Plastic limit %(PL)	23	ASTM D4318
Plasticity index %(PI)	24	
Liquidity index %(LI)	0.48	
Specific gravity (Gs)	2.7	ASTM D854
Total soluble salt%	6.13	
SO3 content%	0.6	B.S.1377:1990
Organic matter O.M%	1.09	
Gypsum content%	1.17	
pH	8.34	
Classification (USCS)	CL	

Subbase

The subbase is brought from Al_Nibaee/ quarry, north of Baghdad, this type of subbase is commonly used as a granular layer in flexible pavement section.

Base

Base layer consists of weighting aggregate and filler according to the State Corporation for Roads & Bridges in Iraq [3].

Asphalt cement

The asphalt cement used in this study is of (40-50) penetration grade, and brought from Daurah Refinery. Table 2 shows the physical properties of Asphalt Cement.

Table 2 Physical Properties of Asphalt Cement

Test	Result	Unit	SCRB Specifications
Penetration (25°C,100g,5sec) ASTM D 5	48	1/10mm	40 – 50
Ductility (25°C, 5 cm/min). ASTM D 113	166	Cm	≥ 100
Flash point (cleave land open cup) ASTM D 92	252	°C	≥ 232
Ductility of residue	151	Cm	> 25

Aggregate

The (crushed) aggregate used in this work is brought from Al-Nibaee quarry. The physical properties of the aggregate (coarse and fine) are shown in Table 3.

Table 3 Physical Properties of Nibaee Aggregates

Property	Coarse Aggregate	Fine aggregate
Bulk Specific Gravity (ASTM C127 and C128)	2.672	2.633
Apparent specific Gravity (ASTM C127 and C128).	2.601	2.431
Percent water absorption (ASTM C127 and C128)	0.45	0.531
Percent wear (Los- Angeles Abrasion) (ASTM C131)	20.10	-

Geogrid reinforcement

The geogrid material used in this study is Pars Mesh Polymer (PMP) Type SQ12 manufactured by the Iranian company Pars Mesh Polymer.

Steel wire netting

Steel wire reinforcement consists of a double twist, hexagonal shape, galvanized wire netting.

Preparation of Model Test

Natural subgrade soil is mixed with quantity of water to get the desired consistency. After that, the soil is placed in a steel container (600*600*700) mm in five layer. After that, the geogrid layer is placed on the surface of the subgrade soft soil (in case of the subbase reinforced model) and folded in 90° against the long side of the steel container to obtain necessary anchorage and slight pre-tensioning, as well as to prevent shifting of the geogrids out of position, [4]. Then, the construction of the subbase and base layers begins.

Preparation of asphalt layer consists of mixing aggregate, filler and asphalt according to the gradation of [3]. To prepare the slab reinforcement asphalt pavement, the same procedure to prepare of the ordinary slab asphalt pavement is followed and the reinforcement is embedded at the bottom of the binder layer which matches what was recommended by [5].

Experimental Setup

To study and investigate the optimal way to improve the strength of pavement layers over weak subgrade; an experimental setup is designed and assembled to achieve this goal as shown in Fig. 2.

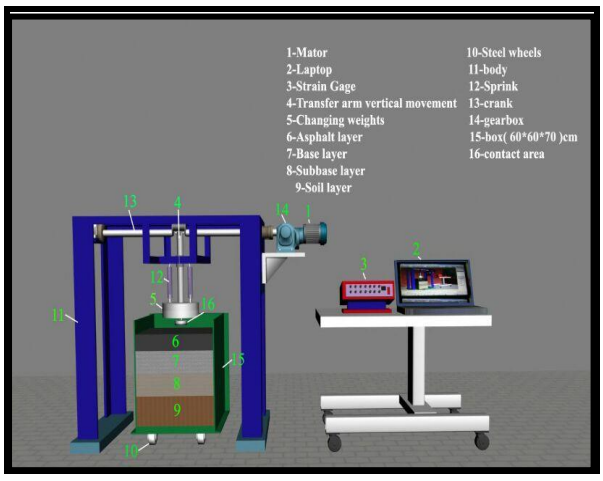

Fig. 2 Experimental Test Container and Loading System

Results of Experimental Work

The data obtained from the experimental work is permanent deformation as shown in following figures.

Fig. 3 show the relation between permanent deformation and loading cycles for the asphalt surface layer. It is clearly noticed that, the permanent deformation increases with the increase in the number of cycle load.

The permanent deformation is recorded at 1600 cycle load and compared with the raw material model. The geogrid and steel mesh decreases the permanent deformation in surface pavement for (1000) cycles load by (27.3%) and (18.3%) respectively.

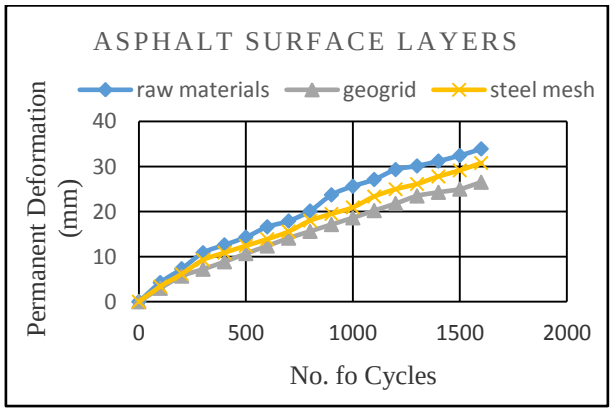

Fig. 3 Permanent Deformations versus the Number of Cycle for Asphalt Concrete Layers

FINITE ELEMENT MODELING

Pavement Layers Modeling based on ABAQUS

Model geometry

Three-dimensional continuum solid elements are often selected to simulate the problem in consideration. The model consists of a 130 mm of asphalt surface layer (wearing and binder) placed on 150 mm of subbase and 150 mm base over 200 mm of sub-grade soil.

Material Characteristics

The most important aspect of Finite Element Analyses is the simulation of the material characteristics. The material properties for pavement layers are summarized in Table 4.

Table 4 Material Properties (Input Data)

Layer	Density (Kg/m³)	Young's Modulus (MPa)	Poisson's Ratio (**ν**)
Wearing	1922	2413	0.35

layer			
Binder layer	1734	2375	0.35
Base layer	2141	241	0.4
Subbase layer	2200	110	0.4
Subgrade layer	982	8	0.45

Element type and mesh size

The pavement structure is meshed using an 8-node continuum linear brick reduced integration element (C3D8R element). The total number of element is 12096 and the mesh convergence study is executed to find this optimum number of element. All layers are simulated with the same shape to preserve the continuity of nodes between consecutive layers. Fig. 4 shows meshing of total model.

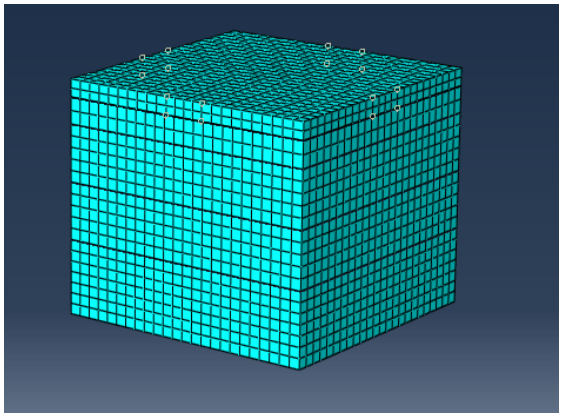

Fig. 4 3D Finite Element Mesh Model

Loading and boundary condition

The F.E is then run simulating a dynamic load, modeled as a pressure load applying at the same location of the pavement, as shown in Fig. 5 . The load applied in the ABAQUS is 280 Kg (2.8 KN).

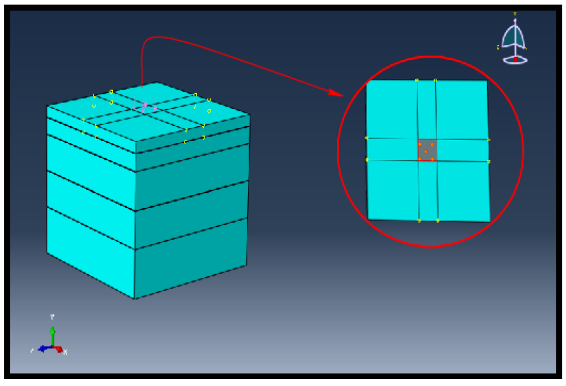

Fig. 5 Loading Applied in ABAQUS Program

The boundary conditions have a significant influence in predicting the response of the model, the bottom surface of the subgrade and sides of layers is assumed to be fixed, Fig. 6 shows the boundary conditions used in the analysis

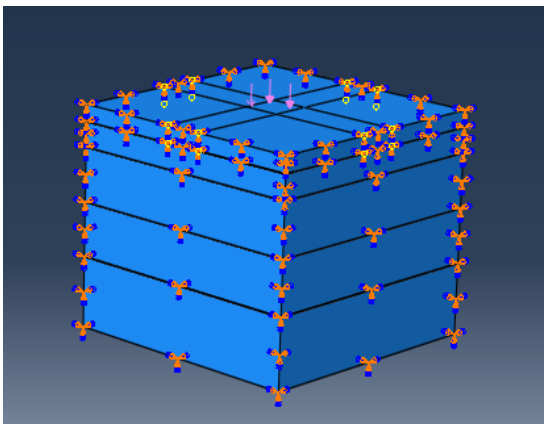

Fig. 6 Boundary Conditions for Model

ABAQUS Program's Output

Rutting is simulated as a vertical displacement in the ABAQUS model analysis. The magnitude of the displacement U beneath the center of the load at 1000 cycles load is shown in Fig. 7, 8 and 9.

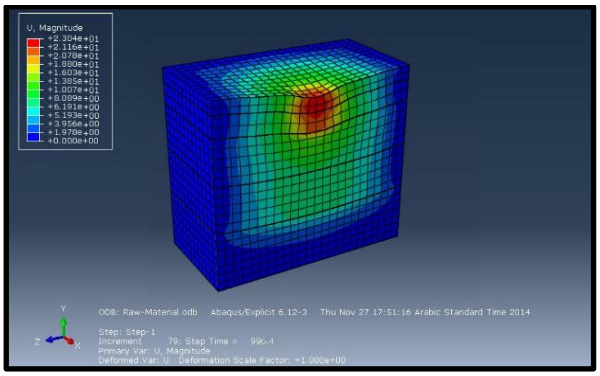

Fig. 7 Vertical Displacement for the Model with Raw Materials

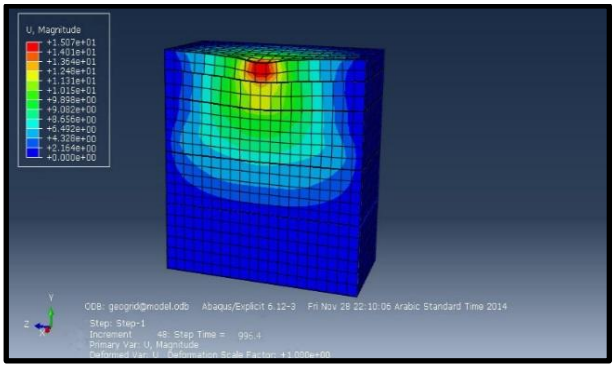

Fig. 8 Vertical Displacement for the Model with Geogrid

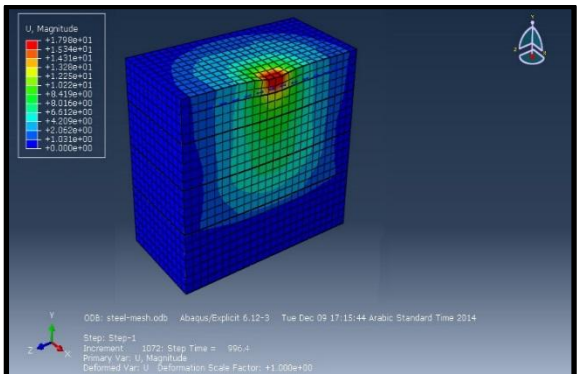

Fig. 9 Vertical Displacement for the Model with Steel Mesh

Fig. 10, 11 and 12 show the comparison between vertical displacements (rutting) obtained by experimental work and ABAQUS results at different number of cycle load. It can be seen that there is no significant difference appears between experimental and ABAQUS results.

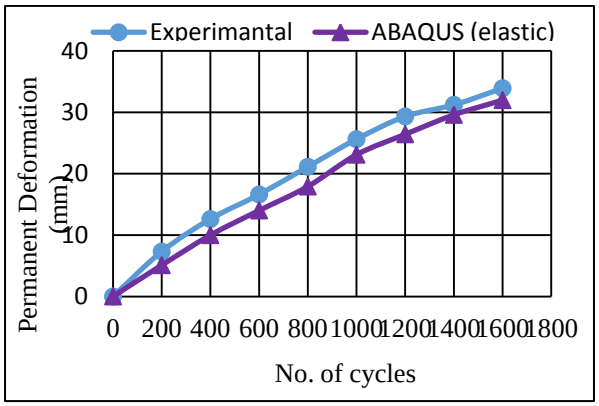

Fig. 10 Comparison between Experimental Result and ABAQUS for Raw Materials Model

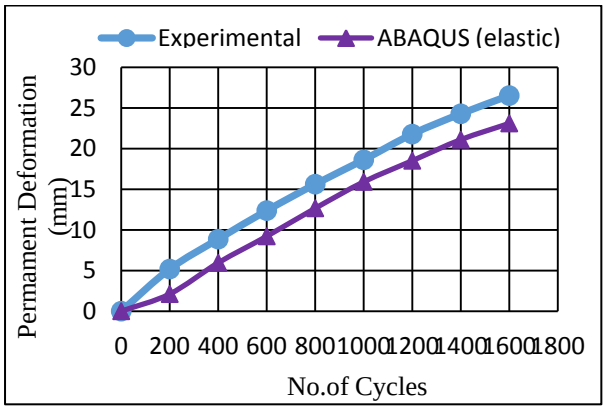

Fig. 11 Comparison between Experimental Results and ABAQUS for Geogrid Model

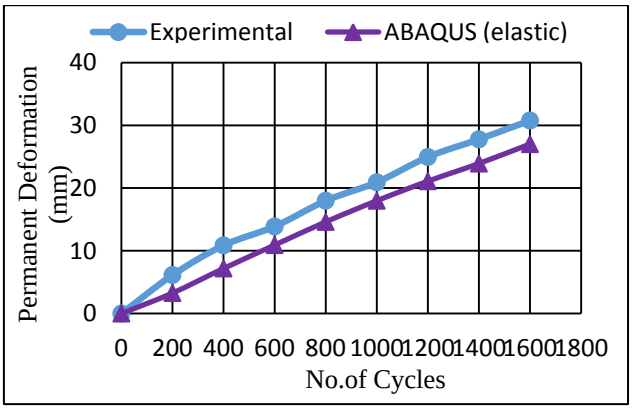

Fig. 12 Comparison between Experimental Results and ABAQUS for Steel Mesh Model

CONCLUSIONS

1. It is found that, using geogrid, is more practical and suitable to improve weak subgrade against permanent deformation as compare with steel mesh mode. It shows a typical increase in the ability to support repeated and dynamic loads transmitted from the pavement structure.
2. ABAQUSE program was successful in simulation pavement structure models, so ABAQUS program can use in analysis of paved road.

REFERENCES

[1]. Rigo, J. M. (1993). "General introduction, main conclusions of 1989 conference on reflective cracking in pavements, and future prospects." Proc., 2nd International RILEM Conference – Reflective Cracking in Pavements, E & FN Spon, Liege, Belgium, 3-20

[2]. Christopher, B.R. (2010) "Geogrids in Roadway and Pavement Systems"

[3]. Iraqi General Specification for Roads and Bridges, (2003): "Standard Specification for Roads and Bridges", the state Corporation for Road and Bridges, Revised Edition.

[4]. Tang X., Chehab G.R. and Palomino A.M. (2008)."Accelerated Testing of Geogrid-Reinforced Subgrade in Flexible Pavements." ASCE, Conference Proceeding Paper, pp. 1049-1055.

[5]. Jassem, N.H. (2012), "Experimental Investigation and Analytical Modeling of Reinforced Flexible Pavement" AL-Mustansiriya University College of Engineering Highway and Transportation Engineering Department MSc Thesis.

First International Conference on Science, Engineering & Environment,
Tsu City, Mie, Japan, Nov.19-21, 2015, ISBN: 978-4-9905958-5-2 C3051

TREATMENT OF SLUDGE FROM A WASTEWATER TREATMENT

Catherine N. Mulligan[1], Mehdi Sharifi-Nistanak[1]
[1]Dept. Bldg, Civil and Environ. Eng., Concordia University, Montreal, Quebec , Canada

ABSTRACT

Preventing wastage of resources is an important priority for sustainability. Sludge from a wastewater treatment plant (WWTP) is such a resource that it often wasted. It is a source of nutrients and organic materials that can be used as a fertilizer. At a waste water treatment plant in Montreal, the sludge is currently incinerated and sent for disposal. Alternatives to the practice are thus desirable. Elevated concentrations of cadmium, copper, cobalt and selenium are found in the sludge and therefore a treatment process is required before use as a fertilizer according to the Province of Quebec regulations. Leaching was selected as there is potential for heavy metal removal. However, nutrient loss must be minimized to preserve its use as a fertilizer. To meet these goals, a new leaching agent (K_2HPO_4) is proposed, and investigated for heavy metal removal efficiency on the sludge. A correlation of heavy metal removal and preserved nutrient concentration with time and pH was found. Removal efficiencies of cadmium, copper, cobalt and selenium of 80%, 44%, 70% and 93%, respectively were determined. In addition, concentrations of nitrogen, phosphorus and potassium of 17%, 17% and 25%, respectively, resulted in the treated sludge. In conclusion, the use of dipotassium phosphate is an effective leaching method to remove heavy metals and simultaneously increase the primary macro nutrients at an acceptable cost.

Keywords: Heavy metals, Nutrients, WWTP, Sludge, Leaching

INTRODUCTION

Sludge is produced as the results of the wastewater treatment process, dewatered and disposed of in landfills. Disposal of sludge has many disadvantages but is utilized due to its simplicity. However sustainability concerns, resource depletion and increased sludge production due to population growth, require better solutions to this problem.

New cost effective methods for treating and recycling of sludge must be employed to prevent resources wastage and damaging the environment. High concentrations of different nutrients and organic materials enable use of sludge as a fertilizer in agriculture fields. Chemical fertilizers can easily leach through the soil where they are no longer available for plant usage. This problem can be solved by humus in the soil which is stable organic matter in the soil that can preserve nutrients for plants. Using sludge as a fertilizer can increase organic matter. In comparison to chemical fertilizers, using sludge as fertilizer can add various nutrients to the soil, and enhance soil fertility, while preserving nutrients in the root area.

One of the largest wastewater treatment plant (WWTP) in the world is located in Montreal (Jean-R. Marcotte). This WWTP produces a large volume of sludge daily, sending their sludge to landfill for disposal. To decrease the volume of sludge and to control biological pollution, incineration facilities were built at the plant and its bottom and fly ashes are disposed of instead of the raw sludge.

As heavy metals are found in the influent flow to the Montreal WWTP, the resulting ashes contain heavy metals. Therefore disposing of the ash can have harmful effects on the Montreal environment. Also the useful resources of the nutrient content of the sludge have been wasted up to now. An alternative solution must be proposed for this problem to remedy the existing procedures. Instead of disposing of the ashes in the landfill, it is possible to use the sludge as a fertilizer in an agriculture field. However, heavy metal removal is a necessity prior to use as a fertilizer while the nutrient content must be conserved.

High concentrations of pathogens and chemicals in the sludge can be harmful for environment and living organisms so that reducing the dangerous contents to below acceptable levels before returning the sludge contents to the environment or reuse is necessary. Common methods for sludge treatment are aerobic or anaerobic digestion, alkaline stabilization, composting, and incineration [1]. Each method produces different products.

Among the various treatment methods, leaching was selected for evaluation. This method is simple and does not require any expensive or complex facilities. The leaching method is usually effective for heavy metals but nutrients can also be removed. In this research an attempt is made to remove this disadvantage and convert the sludge of Montreal WWTP to a fertilizer by a leaching method.

The general objective of this research was to develop a method for conversion of the sludge to a

high quality fertilizer. The specific objectives were to evaluate the effects of the proposed leachant on the sludge, and determine the correlation between pH and reaction time with treated sludge concentrations of heavy metals and nutrients.

MATERIALS AND METHODS

Materials

Chemicals

Dipotassium phosphate, 70% (K_2HPO_4), nitric acid (70%, trace metal), hydrogen peroxide (30%): and hydrochloric acid (70%, trace metal)) were purchased from Fisher Scientific Co.

Sludge samples

The samples were obtained from Montreal Jean.R.Marcotte WWTP. After pumping the water, the pre-treatment is started with screening units to remove large solids and continued with grit removal to be sure that nothing can disturb the treatment process. The main treatment unit in this WWTP is primary treatment, a coagulant, ferric chloride or alum, is added before the screening units. Also an additional flocculation aid, a long string polymer, is added after grit chamber units. Coagulation and flocculation occur in the primary clarifiers. The total solid in the primary sludge is around 3%. This sludge is sent to be homogenized, conditioned and dewatered. Also there are mechanical traversing bridges to remove the scum from the surface of the water. The treated water is discharged to the regional river. There are four reservoirs after the primary clarifier to help managing the sludge treatment. Sludge is pumped from these reservoirs to a homogenization unit. Polymer is added before dewatering to increase efficiency of filter presses. After producing cake, it is sent to incineration and the ash is sent for disposal.

Samplings were done in August and November 2012 and February and May 2013. The samples were obtained from the primary sludge after dewatering and before sending the cake to the incinerator. Also the samples were kept in plastic containers inside the refrigerator at 4 ^oC .

Experimental Methods

The experiments were divided into two parts, one for determining initial concentrations of elements, and the other one for leaching experiments to determine final concentrations at different pHs and reaction times.

Leaching solutions (pH 1, 2 and 3) were prepared with 1 M di-potassium phosphate (K_2HPO_4) solution, deionized water and HNO_3 (for pH adjustment). The adjusted pH was 1, 2 or 3. One gram of dewatered sludge was added to 50 ml leachate in a 50 ml tube. The samples were shaken at 150 rpm. Different reaction times on the shaker on a horizontal shaker were used for the various experiments (1, 2 or 4 hours). At the end of the experiment, the samples were centrifuged at 3000 RPM for 15 minutes. The leachate was then decanted from the sludge and then analyzed. The leaching experiments were performed in triplicate. The final result was the average of these three experiments.

Heavy Metal Analysis

All heavy metal analysis was done by ICP-MS (Agilent Technology 7700 X ICP-MS). All samples were digested by the EPA 3050B method. For digestion, 1 gram of dewatered sludge (cake) was separated, 10 ml of 1:1 HNO_3 and water were added, and then heated to 95^o C by a hot plate for 15 min. After cooling the sample, 5 ml HNO_3 were added and heated for 2 hours. After cooling the sample, 2 ml of deionized (DI) water and 3 ml H_2O_2 were added. The solution was heated while adding 1 ml H_2O_2 until the general appearance of sample is unchanged. The final step of the digestion was to heat the sample with a hotplate for two hours. After cooling and diluting with DI water 100 times, the sample was filtered with a 0.7 micrometer filter paper. All the samples were diluted 500 times by 2% HNO_3 and 1% HCl. To obtain a final concentration should be less than 200 ppb. The concentrations of all analyzed samples were calculated based on the calibration curve. In this case, five calibration samples with 0.1, 1, 10, 100 and 300µg/L were prepared.

Nutrient Analysis

Persulfate digestion was used before nitrogen analysis based on the Hach instructions It has been developed for soil and fresh water [2]. The sample and persulfate powder were added to the HR total nitrogen hydroxide digestion vial and after 30 seconds of mixing it was heated to 105^{o}C for 30 minutes by the Hach Digital Reactor Block 200. Nitrogen concentrations in the samples were read by the DR2800 product of Hach Company, a portable spectrophotometer. The digested sample was cooled before nitrogen analysis.

The nitrogen analysis was also followed based on the Hach instructions. It included adding two different powders (A and B) to the digested sample and taking 2 ml from the produced solution for mixing with a new solution called C. At the end nitrogen analysis results were shown by the DR 2800 Hach device.

Analysis for all nutrients except for nitrogen was done by ICP-MS. As the nutrient concentration range was higher than the heavy metals, more dilution was required with the same dilution solution. A 50000 times dilution was used for calcium, magnesium and iron and 1000000 times dilution for potassium and phosphorus.

RESULTS AND DISCUSSION

Initial Content of Heavy Metals in Sludge

The initial concentrations of heavy metals of the untreated sludge were determined based on an average of 28 samples. Seven samples were taken each three month period over seven consecutive days. The samplings were done in February, May, August and November. The average concentrations were compared to the C1 and C2 levels according to the Guide for Recycling of Residual Materials for Fertilizers [3].

As it can be seen in Table 1, by comparison between Quebec regulations and the average concentrations in 2014, heavy metals can be divided into two groups. The first group includes As, Cr, Ni, Pb, Zn, Co, and Cu and Se can pass both regulations without any treatment. The second group includes Hg, Mo and Cd that can pass C2 so and thus the prepared sludge is acceptable but improving the quality of sludge is needed to decrease their concentration to the C1 limit.

The concentrations of the various heavy metals in historical data were provided by the WWTP and therefore a comparison was made between those values in 2007, 2011 and 2014. The concentration of Cd increased from 9 in 2007 to 16.7 in 2011 and now has decreased to 3.9. Therefore at one time it could not even pass C2 guidelines. Cobalt levels increased from 19 in 2007 to 72 mg/kg in 2011 where it could not pass the C1 level but now it can. Selenium on the other hand has decreased from 2007 (9 mg/kg) to 8.1 mg/kg in 2011 to current levels. Therefore it seems to be no longer problematic. Copper has also decreased over the years (from 477 to 468 to 146 mg/kg in 2007, 2011 and 2014, respectively).

Therefore Cd can be defined as the major problem for use of the sludge as a fertilizer. As currently copper and cobalt are below C1 levels, they can be classified as non-problems currently. Se is currently very close to C1 levels so it can be classified as potential problematic. However all four heavy metals were followed during the leaching tests

Table 1 Comparison of metal sludge contents (mg/kg dry basis) to Quebec guidelines [3]

Elements	Concentration	C1	C2
Co	15.7	64	150
Cu	145.9	400	1000
Se	1.25	2	14
Cd	3.9	3	10

Leaching Test Results for Heavy Metals

To decrease metal concentrations in the sludge, leaching tests were performed to ensure the produced sludge will reach an acceptable cadmium removal for passing C1 Quebec regulations. In addition a decrease in copper, cobalt and selenium contents were desirable while preserving or increasing the nutrient concentrations of the sludge. pH and time were the two important factors evaluated.

Figure 1 shows the average removal percentage for cadmium at different pHs over a 4 hour time period. Only a short time period is required as most of the removal occurred in the first hour. Also there is an indirect correlation between removal percentage and pH as decreasing the pH increased the removal percentage. Moreover the removal percentage by this method for cadmium reached its maximum removal percentage, around 80%, Also the difference between using a salt and using only acid is shown in Fig. 1. The salt and acid combination is much more effective than the salt alone. The experiments also show that an acceptable removal at pH 3 is possible to pass the C1 regulation after four hours reaction at pH 1.

Similar trends were obtained for all three other metals (graphs not shown). pH 1 with the salt gave maximal results. Only copper showed a less significant difference between the results at pH 1 and pH 3. Table 2 shows the final content for all metals after leaching with the salt and pH 1. It can be seen that substantial removal is obtained for all 4 metals.

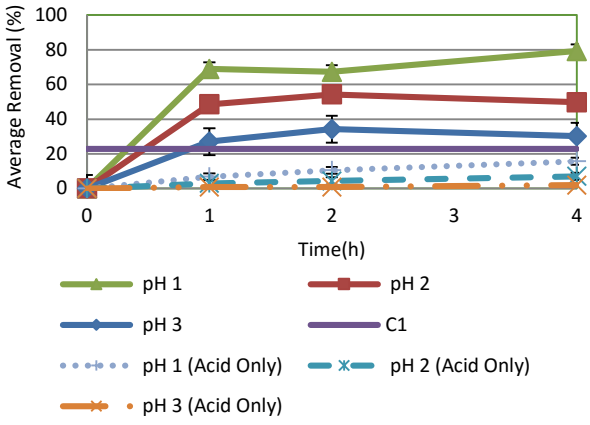

Fig. 1 Cadmium removal under various conditions

Table 2 Heavy metal removal from sludge after treatment (pH 1 & time of 4 h)

Heavy Metal	Final content after leaching (mg/kg)	% Removal
Cd	0.8	79.5
Co	4.9	69.9
Cu	81.4	44.2
Se	0.02	98.4

Nutrient Content of the Sludge

In addition to removing harmful heavy metals from the sludge, it is important to preserve or increase the existing nutrients. As the most important nutrients are nitrogen, phosphorus and potassium, these were chosen for monitoring during the treatment method. The selected acid and salt were also chosen because three of these elements are present in their composition. The effect of this leaching method on the concentration of six different nutrients was this investigated.

From Table 3, it can be seen that there is a large difference between primary macro nutrients in the initial and final macro nutrient contents. Potassium exchange is the main mechanism for heavy metal removal and the increase of potassium in the final product.

Table 3 Comparison of primary macronutrients before and after treatment

Primary Macro Nutrients	Initial sludge 2014 (mg/kg)	Treated sludge (pH 1 & Time = 4 h) (mg/kg)
N	1.36	17.07
P	0.00	17.57
K	0.63	25.20

Figure 3 shows the effect of pH during the leaching test on the nitrogen content the method increases the nitrogen concentration in the sludge. The increae in nitrogen is due to the use of nitric acid for adjusting pH during the experiments. Also it is seen that the initial amount of nitrogen is 1.36% and the highest amount is reached at pH 1 and pH 2 which is more than 17%. Also at these pH, after one hour there was no significant increase in the nitrogen content. However at pH 3, the maximum content was reached at four hours.

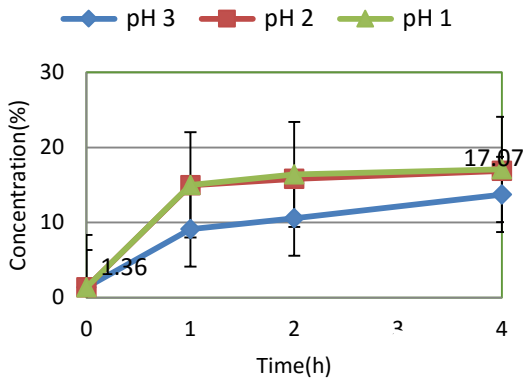

Fig. 3 Nitrogen contents after leaching at various pH

Although phosphorus had the lowest concentration of the nutrients, a significant enhancement was obtained by this method. A 17% concentration after 2 hours was achieved at pH 1 or 2. Therefore decreasing the pH to less than two was not necessary. The same trends as for nitrogen were obtained. A pH of 3 gave inferior results.

The increase of phosphorus during the experiment is likely the result of producing salts with low solubility salts such as magnesium phosphate, calcium phosphate and sodium phosphate Corresponding solubilities of these salts are 0.002, 0.02 and 121 g/L respectively [4].

Other nutrients including magnesium, calcium and iron were also monitored. All three showed a decrease in contents. Magnesium showed the smallest decrease. A pH of 3 showed the lowest decrease (data not shown). Decreasing the pH to 1 further increased the leaching of magnesium. It takes more time for higher pH solutions to reach the maximum. For example it takes one hour when pH 1 and two hours when pH 2 and more than two hours at pH 3. The maximum loss of magnesium is also around 52% which occurs at pH 1 after four hours reaction time.

Although calcium loss (78%) was more significant than magnesium, the same trends were found. For pH 1, the maximum occurred at 1 hour for pH 2 it was 2 hours (35%) and for pH 3, 4 hours. Therefore decreasing the reaction time and decreasing the pH can help to retain more calcium in the produced sludge.

Figure 4-1: Remains Phosphorus Concentration in Sludge after Leac

Maximum iron removal was 68% at pH 1 and 1 hour. Slightly less removal was achieved after 2 hours at pH 2 (50%). At pH 3, 4 hours was necessary to achieve the same level of removal. It is important to mention that iron is a micro nutrient and plants use this element in very low

concentration. Higher iron concentrations in the soil can be toxic for plants although this limit is dependent on the type of plant.

Overall, the treated sludge with acid and salt is lower in heavy metal contents with enhanced nutrient contents. Optimization of the pH and leaching can lead to an optimized product.

Table 4 Comparison of the other nutrients in the initial and treated sludge

Nutrients	Initial sludge (%)	Treated sludge (pH 1 & Time = 4 h (%)
Mg	0.23	0.11
Ca	0.23	0.05
Fe	1.58	0.51

Mechanism of Leaching

The main mechanism in this method is using a potassium leaching solution for removing heavy metals from the sludge by ion exchange of potassium with the heavy metal ions into the leachate solution. Therefore the treated sludge has potassium instead of heavy metals. The existence of the ion exchange process between potassium and several heavy metals cations was studied and shown by Sparks [5] in soil previously and this research shows a new application for that.

Potassium is an important nutrient for plant too during the removal of heavy metals the fertility of sludge is increased by adding potassium to it. On other hand the quality of sludge is increased by two ways at the same time, first by removal of harmful heavy metals and second, by adding a useful nutrient.

CONCLUSIONS

The objective of the research was to develop an alternative treatment for WWTP sludge to enable its use as a fertilizer due to its nutrient. The produced sludge needs to pass Quebec regulations for approval for agricultural usage. The removal of heavy metals with concentrations higher than the C1 regulation was required from the sludge in addition to preservation of nutrient concentration was an additional objective for high quality sludge.

Cadmium, copper, cobalt and selenium levels were higher than the C1 regulation. Three of these heavy metals passed the C2 regulations which are less strict than C1. As cadmium cannot pass the C2 level, it is in the major problem group while the others only cannot pass C1 so they are in the minor problem group.

The primary macro nutrients (nitrogen, phosphorus and potassium) and two secondary macro nutrients (magnesium and calcium) and one micro nutrient with high concentration in sludge (iron) were studied.

The most frequent leachant for heavy metal removal is usually acid or base alone. Here a dissolved salt at low pH was proposed as the leachant. The main factor for removal was found to be the salt instead of the acid or base as the main mechanism is ion exchange not acid extraction.

The leaching experiment for the sludge was performed with dipotassium phosphate (K_2HPO_4) and nitric acid (HNO_3) as leachant. The effect of pH and reaction time on removal efficiency was evaluated.

The maximal metal removal was at pH 1 with 4 hours of leaching (93% selenium, 80% cadmium, 70% cobalt and 44% copper). Although copper did not show any correlation with pH but all heavy metals of them have direct correlation with reaction time. Most of the removal occurred in the first hour. In contrast to other reviewed papers which show removal at very low pHs. An acceptable removal could be achieved at pH 3 in this study. Therefore this method is effective and fast for heavy metal removal and safer for employees because of less acid usage.

As all three primary macro nutrients (nitrogen, phosphorus and potassium) are involved in removal process the concentrations of these three are higher than expected after the experiments. Although there is loss of the other nutrients during this method but as they will be used in low concentration by plants, still the results are acceptable.

Macroprimary nutrient concentration has direct and indirect correlations with time and pH but there is a maximum capacity for sludge which can be reached after 2 hours and with pH 2. Therefore increasing the time or decreasing pH is not effective after that point.

Non primary macro nutrient concentrations decreased with this method. But it can be seen that they are highly dependent on pH. Leachate with higher pH needs more time to decrease the concentration. Also it shows that after four hours in any pHs there are approximately the same results which means the maximum available amount of these elements in all pHs are equal but different times were required to reach that point at different pHs.

ACKNOWLEDGEMENTS

The authors would like to acknowledge the financial support of Concordia University and the assistance of the employees at the WWTP during sampling.

REFERENCES

[1] EPA, 2004. *Primer for Municipal Wastewater Treatment System.* [Online] Available at: http://water.epa.gov/aboutow/owm/upload/2005_08_19_primer.pdf [Accessed 04 03 2014].

[2] Cabrera ML. & Beare MH "Alkaline persulfate oxidation for determining total nitrogen in microbial biomass extracts". Soil Science Society, Vol. 57, 1993, pp. 1007-1012.

[3] MINISTÈRE DU DÉVELOPPEMENT DURABLE, DE L'ENVIRONNEMENT ET DES PARCS (MDDEP), Guide sur le recyclage des matères résiduelles fertilisantes : Critères de référence et normes réglementaires , Québec, ministère du Développement durable, de l'Environnement et des Parcs, 2012. ISBN 978-2-550-64355-5, 170 p.

[4] Zumdahl SS. & Zumdahl SA, Chemistry. 6th ed. Boston: Houghton Mifflin, 2003.

[5] Sparks, D. L, Kinetics of Soil Chemical Processes. New York: Academic Sparks, 1989.

First International Conference on Science, Engineering & Environment,
Tsu City, Mie, Japan, Nov.19-21, 2015, ISBN: 978-4-9905958-5-2 C3051

ANALYZING THE STRUCTURE OF MONTMORILLONITE CAUSED BY CALCINATION USING SYNCHROTRON X-RAY POWDER DIFFRACTION (SR-XRD) AND CHANGES IN ADSORPTION OF CAFFEINE

Kenichiro Yamamoto[1], Takashi Shiono[1], Yasuto Matsui[2] and Minoru Yoneda[2]
[1]Research Laboratories for Beverage Technologies, Kirin Company, Limited, Japan; [2]Department of Environmental Engineering, Kyoto University Graduate School of Engineering, Japan

ABSTRACT

Montmorillonite is widely used as a natural adsorbent. It is generally considered that the adsorption properties of montmorillonite are largely due to its characteristic layer structure. The structure of montmorillonite changes under different temperature conditions. In this study, changes in the structure of montmorillonite with temperature are analyzed using Synchrotron X-Ray Powder Diffraction (SR-XRD). Observations are made on how montmorillonite with a modified structure is affected by the adsorption of nonionic organic compounds in a water system. The object of this study is to elucidate the mechanism by which montmorillonite adsorbs nonionic organic compounds. It is confirmed that, without calcination treatment, adsorption of caffeine on montmorillonite changes its layer structure. Calcination treatment at above 573 K causes irreversible dehydration in the structure of montmorillonite. Samples of montmorillonite calcined at 673 K and 873 K show a reduction in the amount of caffeine adsorbed. In addition, calcination treatment of montmorillonite at 673 K and 873 K causes less intercalation into the layers. These results show that adsorption of caffeine on montmorillonite without calcination treatment occurs with the intercalation of caffeine between layers of montmorillonite. On the other hand, montmorillonite calcined at 873 K is confirmed to adsorb approximately 20 % of caffeine compared to untreated montmorillonite. It suggested the possibility of the adsorption of caffeine even on the surfaces and end faces of layers of montmorillonite.

Keywords: Montmorillonite, Synchrotron X-Ray Powder Diffraction (SR-XRD), Calcination, Adsorption, Caffeine,

INTRODUCTION

Montmorillonite is a clay mineral and is a principal component of bentonite, which is mined naturally. This material is low cost and highly stable, and has been used in a wide range of fields. Due to the swelling property, plasticity, and adsorption function of the material, it is used as a soil amendment and a binder for agricultural chemicals in the agricultural sector. In the civil engineering field, it is used, for example, as a wall-building agent and lubricity agent, and as a water impermeable material for waste disposal. It also has practical applications in various areas other than agriculture and civil engineering, such as a solidification material for animal excrement [1].

Montmorillonite is a plate crystal with a thickness of about 1 nm, and it consists of tetrahedral silicate and octahedral alumina [2]. Several plate crystals are stacked to form a layer structure. The plate crystal has a three-layer structure consisting of the central layer of $Al(OH)_6$ and both outer layers of $Si_4O_6(OH)_4$. Partial isomorphous substitution of Al by Mg and Fe takes place in the central layer. Isomorphous substitution causes each layer to take on a negative charge. To cover for the negative charge, cations are retained between the layers. In water, the adsorption of water molecules between the layers causes the material to swell, and the interlayer distance varies [3], [4]. Montmorillonite that is swollen in water readily exchanges cations that are present in the solution with those ones retained between the layers [5]. For this reason, the material is often used as a cation exchanger in a water system. On the one hand, nonionic organic compounds are thought to be adsorbed at different sites depending on factors such as the polarity of the chemical compound [6], [7]. A chemical compound that can get into the layers is believed to be adsorbed by its intercalation between the layers [8], [9]. Because of the very large surface area between the layers, the adsorption capacity is extremely high. On the other hand, a chemical compound that cannot get into the layers is thought to react with and be adsorbed on the surfaces and end faces of the layers [10].

In this study, montmorillonite is calcined to remove water molecules from its structure and change the distance between layers. The structural change caused by calcination is determined and

analyzed with Synchrotron X-Ray Powder Diffraction (SR-XRD). In addition, calcined montmorillonite is suspended in caffeine solutions to quantify variations in the adsorption of caffeine. To examine the hypothesis that the layer structure of montmorillonite may play a key role in the adsorption of caffeine, changes caused by calcination in the structure and the adsorption of caffeine are observed.

MATERIALS AND METHODS

Calcination Treatment of Montmorillonite and Adsorption Test of Caffeine

Samples of commercially available montmorillonite (from Mizusawa Industrial Chemicals, Ltd.) of 20 g each were placed in a heat-resistant crucible and calcined at 373 K, 473 K, 573 K, 673 K, or 873 K for two hours. Then, the samples of calcined montmorillonite were cooled at room temperature for one hour.

Caffeine (from Wako Pure Chemical Industries, Ltd.) was dissolved in ultrapure water and the concentration was adjusted to 400 mg/L to prepare a caffeine solution. Montmorillonite of 4.0 g was added to the caffeine solution of 400 mL and was suspended. The montmorillonite kept in contact with the caffeine solution for 60 minutes. The suspension was centrifuged (3000 rpm, 10 minutes) and the precipitated clay mineral was dried in an oven (EYELA) at 378 K overnight. The dried clay mineral was ground into a powder with a mortar to prepare a sample for analysis.

Adsorption of caffeine was tested using caffeine solutions with concentrations adjusted from 10 to 5000 mg/L. Montmorillonite of 4.0 g was added to the caffeine solution of 400 mL and was suspended. The montmorillonite kept in contact with the caffeine solution for 60 minutes. The suspension was centrifuged (3000 rpm, 10 minutes) to obtain the supernatant solution. The supernatant solution was filtered through a membrane filter (0.45 um, PTFE). The concentration of caffeine in the filtrate was measured using HPLC-UV/Vis. The measurement conditions of HPLC are shown in Table 1. Adsorption of caffeine per unit weight was calculated.

Based on the results of the caffeine adsorption test, Langmuir adsorption isotherm was obtained. The concentration of caffeine in the filtrate was used as an equilibrium concentration Q_{eq}. Based on the concentration of caffeine in a supernatant solution, adsorption per weight of montmorillonite C_{eq} was calculated. In addition, using the Langmuir adsorption isotherm equation as in Eq. (1), the maximum adsorption capacities (Q_{max}) and the equilibrium constants (K_{Lang}) were calculated.

$$Q_{eq} = \frac{K_{Lamg} \cdot Q_{\max} \cdot C_{eq}}{1 + K_{Lang} \cdot C_{eq}} \quad (1)$$

Table 1 HPLC-UV/Vis condition for analysis of caffeine.

Column	Shodex Asahipak ODP-50 2D (2.0mmI.D. x 150mm)
Mobile phase	A: 0.1% formic acid B: 100%MeOH/Acetonitrile = 50/50
Step gradient	A/B = 0 to 10min : 90/10, 10 to 15min : 10/90, after 10min : 90/10
Flow rate	1 mL/min
Detector	UV (275nm)
Column temp.	40 ºC

Synchrotron X-Ray Powder Diffraction (SR-XRD)

The diffraction patterns of calcined montmorillonite were obtained using a large synchrotron radiation facility (SPring-8 BL19B2, Japan Synchrotron Radiation Research Institute: JASRI). A large Debye-Scherrer camera (286.48 mm in diameter, Rigaku Corporation) was mounted on the rear hatch and an imaging plate (0.01 °, BAS2500, FUJIFILM Corporation) was used for detection. The X-ray source was derived from the synchrotron radiation and a monochromatic X-ray beam with a wavelength of about 1 Å is used. The beam size was 0.3 (H) mm x 3 (W) mm. A measurement samples were filled in a glass capillary with a diameter of 0.3 mm. The exposure time for measurement was 5 minutes for each sample.

Quantitative Analysis of Exchangeable Cation

Ammonium chloride (from Wako Pure Chemical Industries, Ltd.) was dissolved in ultrapure water and the concentration was adjusted to 1.0 mol/L to prepare an ionic solution. Calcined montmorillonite was added to the ionic solution to prepare a 1 wt% solution, and then was suspended. The solution and montmorillonite were kept in contact with each other for 60 minutes. The suspension was centrifuged (3000 rpm, 10 minutes) to obtain the supernatant solution. The supernatant solution was filtered through a membrane filter (0.45 um, PTFE). The filtrate was analyzed for Na, K, Ca, and Mg ions by ICP-AES.

RESULTS AND DISCUSSION

The SR-XRD patterns of montmorillonite after calcination treatment are shown in Fig. 1. The

samples of montmorillonite with calcination treatment at 373 K and 473 K show no change in diffraction peaks, which indicates their basal distances. The change of basal distance indicates the change of interlayer distance in the layer structure. Samples of montmorillonite with calcination treatment at 373 K and 473 K show no change of interlayer distance. These results suggest that, during calcination, water such as adsorbed water and interlayer water was partially removed. Then, water molecules in the atmosphere rehydrated when cooled to normal temperature after calcination. Rehydration during the cooling process is considered to have led to the same interlayer distance as that of the montmorillonite before calcination. Montmorillonite with calcination treatment at 573 K showed no diffraction peak indicating the basal distance. This result indicates that dehydration within the structure of montmorillonite with calcination treatment at 573 K was to be an irreversible change. It is considered that montmorillonite calcined at 573 K was dehydrated within the structure, and it is considered to be an irreversible change. In other words, the structure of montmorillonite calcined at 573 K, after dehydration during calcination, cannot return to the structure before calcination. For montmorillonite samples calcined at 673 K and 873 K, a diffraction peak, which had not been present with the montmorillonite before calcination, was identified at about 6.1 º. These results mean that calcination treatment at 673 K and 873 K appreciably changed the structure of montmorillonite compared to that before calcination.

Basal distances were calculated based on the diffraction peaks shown in Fig. 1 (Table 2). For Ca-type montmorillonite, three basal distances (two water phases: 1.5 nm, one water phase: 1.17 nm, no water phase: 1.03 nm) depending on water absorption condition were reported [11]. Basal distances of montmorillonite samples calcined at 373 K and 473 K were similar to the reported values of two water phases. This is because, after calcination and subsequent cooling, montmorillonite adsorbed atmospheric water molecules, which rehydrated to the level of two water phases. In addition, samples of montmorillonite calcined at 673 K and 873 K had basal distances approaching 1.03 nm. The calcination treatment at 673 K and 873 K caused irreversible structural changes, which does not allow rehydration and results in a montmorillonite structure with no water phase. For montmorillonite calcined at 573 K, no diffraction peak indicating a basal distance was identified.

There are several reports on the calcination of montmorillonite. First, for montmorillonite after calcination treatment, water molecules that are not involved in the montmorillonite structure, such as adsorbed water and interlayer water, are removed. It is reported that this dehydration is reversible, and

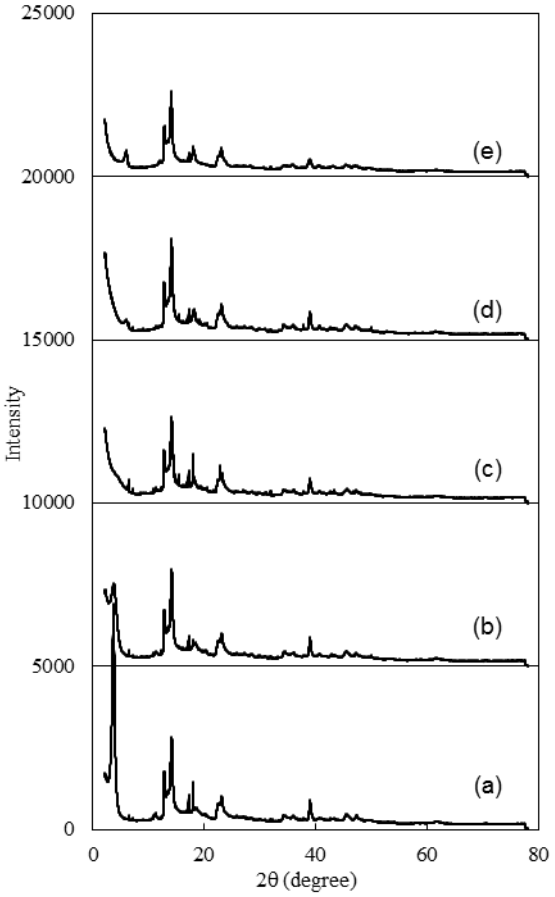

Fig. 1 SR-XRD pattern of montmorillonite calcined at (a) 373 K, (b) 473 K, (c) 573 K, (d) 673 K, and (e) 873 K.

Table 2 Basal distances with montmorillonite after calcination treatment.

	basal distance (nm)
373 K	1.54
473 K	1.51
573 K	n.d.
673 K	0.94
873 K	0.95

rehydration takes place with calcined smectite when it is cooled after calcination [12]. Besides, it is reported that montmorillonite calcined at a high temperature above 773 K results in the removal of water molecules involved in the montmorillonite structure, and dehydration due to calcination above 773 K is irreversible [13]. We observed an irreversible structural change caused by calcination treatment above 573 K. Based on the results shown in Fig. 1, montmorillonite calcined below 473 K showed rehydration when cooled after calcination treatment, while montmorillonite calcined above 573 K showed no rehydration after being cooled.

Fig. 2 and Table 3 show the cation exchange capacity of calcined montmorillonite samples. The cation exchange capacity (CEC) is calculated by summing the products of the amounts of exchangeable cations multiplied by the electric charge for each ion. The amounts of Ca and Mg ions, which are exchangeable cations, decreased with montmorillonite calcined above 573 K compared to that calcined at 373 K. Ca ions decreased by 70 % with calcination at 573 K, 78 % at 673 K, and 84 % at 873 K compared to montmorillonite calcined at 373 K. Cation exchange is less likely to occur in montmorillonite samples with calcination treatment at 573 K, 673 K, and 873 K. This is because less rehydration tends to occur with treatment. The cation exchange with montmorillonite in a water system occurs when cations such as Ca or Mg ion retained between the layers of montmorillonite are exchanged with water molecules, or other cations present in the solution [5]. Therefore, it is considered that montmorillonite samples calcined at 573 K, 673 K, and 873 K had no exchange of water molecules for cations between the layers and did not take in water molecules between the layers. This result shows, based on Fig. 1, that rehydration within the structure of calcined montmorillonite at 573 K, 673 K, and 873 K were prevented.

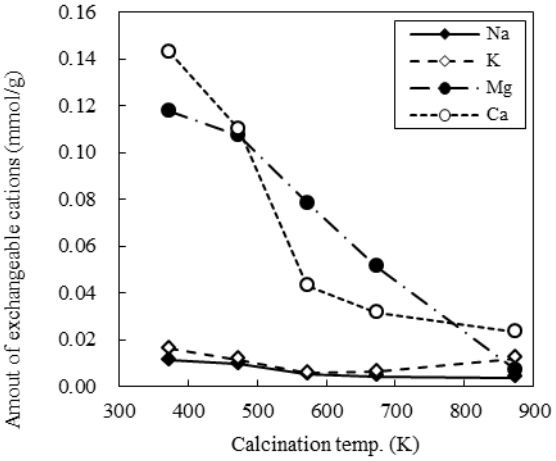

Fig. 2 The amount of cations eluted from montmorillonite after calcination treatment.

Table 3 Cation exchange capacity of montmorillonite after calcination treatment.

temperature of calcination treatment (K)	cation exchange capacity (meq/100 g)
373	54.9
473	45.6
573	25.4
673	17.7
873	7.8

The SR-XRD patterns of montmorillonite after a caffeine adsorption test are shown in Fig. 3. The region from about 2 to 10 ° where diffraction peaks, indicating reflection corresponding to the basal distance in the structure (basal reflection), is magnified. Montmorillonite without adsorbed caffeine was confirmed to have a diffraction peak at 3.69 ° indicating its basal distance. On the other hand, a diffraction peak at 3.75 ° was identified with its strength decreased to 85 % for montmorillonite having adsorbed caffeine. According to the change of diffraction peak, it is probable that caffeine molecules are intercalated between the layers of montmorillonite.

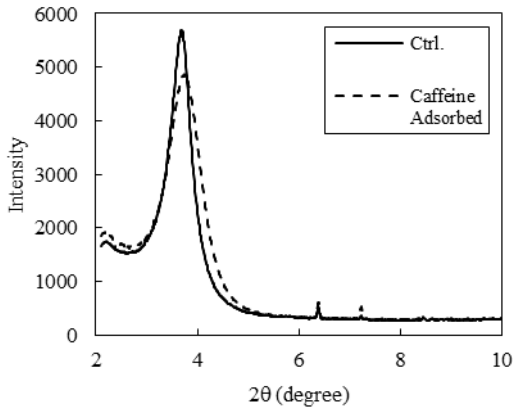

Fig. 3 The SR-XRD pattern of montmorillonite after caffeine adsorption treatment.

Fig. 4 shows the results when measuring the amount of adsorbed caffeine on montmorillonite with calcination treatment. Fig. 4 plots test results for the adsorption of caffeine on montmorillonite. The horizontal axis shows the equilibrium concentration (mmol/L) after adsorption equilibrium is reached, and the vertical axis shows the amount of adsorbed caffeine (mmol/g) at adsorption equilibrium. The maximum adsorption capacities (Q_{max}) were also determined from the adsorption isotherm equation (Eq. 2) based on the adsorption test of caffeine. The maximum adsorption capacities are shown in Fig. 5. The maximum adsorption capacity was 0.51 mmol/g for the samples of montmorillonite calcined at 473 K and 573 K. It is 1.08 times higher than the adsorption capacity of montmorillonite calcined at 373 K. The maximum adsorption capacity of montmorillonite calcined at 673 K was 0.33 mmol/g, and that of montmorillonite calcined at 873 K was 0.09 mmol/g. These reduced maximum adsorption capacities occur because the intercalation of caffeine between the layers of montmorillonite is less likely due to the structural changes in montmorillonite as shown in Fig. 1. It is considered that the montmorillonite samples

calcined at 673 K and 873 K had a reduced adsorption capacity for caffeine because caffeine molecules are no longer intercalated between the layers. It is indicated that the adsorption of caffeine on the samples of montmorillonite calcined at 673 K and 873 K were occurred on the surfaces and end faces of adsorbent. In addition, according to the results shown in Table 3 and Fig. 5, no correlation was found between cation exchange capacity (CEC) and amount of adsorbed caffeine at all calcination temperatures (R=0.54). Based on this result, it is probable that the adsorption of caffeine on montmorillonite does not involve electrostatic adsorption to which cation exchange capacity makes a contribution.

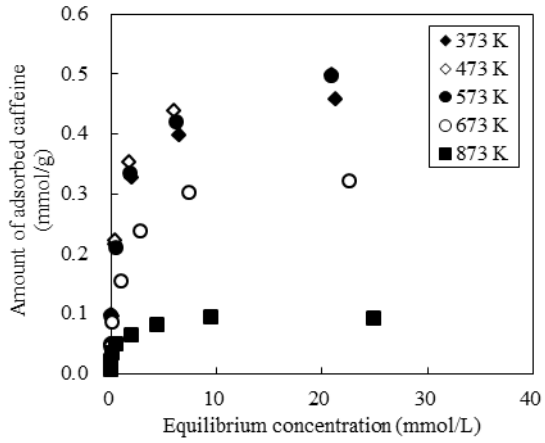

Fig. 4 Adsorption isotherms of caffeine on montmorillonite with calcination treatment.

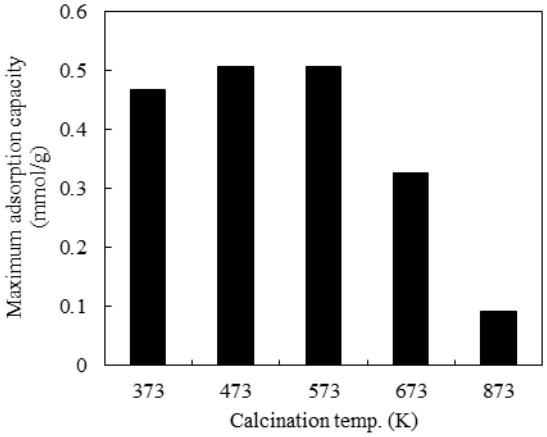

Fig. 5 Maximum adsorption capacity determined from the adsorption isotherm.

In the future, the effects of water molecules on structural changes of montmorillonite during calcination treatment need to be observed. The structure of montmorillonite in water and in a wet state should be analyzed accurately, and the reversibility/irreversibility of its dehydration and rehydration should be observed and quantified.

CONCLUSION

The measurement results show the following:

1. Montmorillonite with calcination treatment above 573 K shows irreversible dehydration in its structure. Two types of analysis—structure analysis with SR-XRD and quantitative evaluation of exchangeable cations—were performed, and both support this conclusion.
2. Because the montmorillonite samples that had been calcined at 673 K and 873 K indicated a reduction in the amount of caffeine adsorbed, adsorption of caffeine on montmorillonite without a calcination treatment is shown to involve intercalation between the layers of montmorillonite.
3. Montmorillonite calcined at 673 K and 873 K is confirmed to adsorb caffeine. Therefore, regarding the adsorption phenomenon of caffeine on montmorillonite, the possibility of adsorption even on the surfaces and end faces of layers of montmorillonite is suggested, as well as intercalation into the layers.

ACKNOWLEDGEMENTS

We are gratefully acknowledged to Mr. Shiota (Kyoto University), and Mr. Deuchi (Kirin Co., Ltd.) for their great deal of discussions and suggestions. We would like to thank the many staffs of the SPring-8. Technical assistance of JASRI stuff working at BL19B2 is also acknowledged.

REFERENCES

[1] Handbook of Clays and Clay Minerals, The Clay Science Society of Japan, Japan (2009) p. 11-20
[2] F. Bergaya, B.K.G. Theng, G. Lagaly ed., Handbook of Clay Science, Elsevier Science, Amsterdam (2006).
[3] I. Ravina and P. F. Low, Clays and Clay Minerals (1977) 25, p. 201-204
[4] J. W. Odom and P. F. Low, Clays and Clay Minerals (1978) 26, p. 345-351
[5] D. L. Sparks, Environmental Soil Chemistry (2nd ed.), Academic Press, Amsterdam (2003) p. 352
[6] B.K.G. Theng, The Chemistry of Clay-Organic Reactions, John Wiley & Sons, New York (1974)
[7] T. Okada, J. Oguchi, K. Yamamoto, T. Shiono, M. Fujita, and T. Iiyama, Langmuir (2015) 31 (1), p. 180-187
[8] G. Lagaly, Solid State Ionics (1986) 22, p. 43-51
[9] G. W. Brindley, Clay Minerals (1965) 5, p. 91

[10] T. Okada, M. Ogawa, Bull. Chem. Soc. Jpn. (2004) 77, p. 1165-1170
[11] H. J. Bray, S. A. T. Redfern, and S. M. Clark, Mineralogical Magazine (1998) 62, p. 647-656
[12] D. M. C. MacEwan and M. J. Wilson, Crystal Structures of Clay Minerals and their X-ray Identification (G. W. Brindley and G. Brown, eds), Mineralogical Soc., London (1980) p. 249-303
[13] M. Kawano and K. Tomita, Clays and Clay Minerals (1991) 39, p. 174-183

First International Conference on Science, Engineering & Environment,
Tsu City, Mie, Japan, Nov.19-21, 2015, ISBN: 978-4-9905958-5-2 C3051

EVALUATION OF THE LONG-TERM POLLUTION REMOVAL PERFORMANCE OF ESTABLISHED BIORETENTION CELLS

Terry Lucke[1] and Peter Nichols[1]
[1]Stormwater Research Group, University of the Sunshine Coast, Queensland, Australia

ABSTRACT

Over the last two decades bioretention (biofiltration) systems have been commonly constructed in urban areas to manage stormwater runoff by moderating peak flows and reducing downstream pollution loads. Bioretention systems are generally soil-plant based systems which typically include a filter medium above a drainage layer. They are often either lined with a geofabric to support infiltration, or with an impermeable membrane to prevent infiltration and/or to allow stormwater harvesting and reuse. Bioretention systems are known to treat a range of stormwater pollutants through physical, chemical and biological processes such as mechanical filtering, sedimentation, adsorption, and plant and microbial uptake. However, the long-term pollution removal performance, particularly of heavy metals, remains largely unknown. It is generally accepted that the filter media used in bioretention systems has a finite life span, after which time it should be replaced. However, there is only very limited information available on when this should occur, or how to assess this. It is also recognised that contaminated filter media may require regulated disposal. This study presents results from a series of controlled field experiments conducted over two years which evaluated the pollution removal performance of a series of 10 year old bioretention systems located in an industrial estate in Australia.

Keywords: Stormwater Pollution, Bioretention Systems, Heavy Metals, Filter Media

INTRODUCTION

The increase of impervious surfaces that comes with urban development has caused both the volume of stormwater runoff, and the amount of pollution flowing downstream to rise, often causing environmental harm [1], [2]. Consequently, stormwater management in urban areas has become a priority for those responsible for planning and construction of new developments, and maintenance of existing stormwater infrastructure [3].

Bioretention (biofiltration) systems have been used widely over the past 20 years to manage stormwater in urban areas, they reducing peak flows and downstream pollution loads [4] – [6]. The flexibility in their design helps with easy retrofitting into existing urban areas [7] raising their popularity. They also contribute to a range of other benefits beyond stormwater quality and quality functions, including aesthetic and social benefits [8], [9]. Small bioretention systems are often incorporated into existing roadways in place of a traditional grass street verge [3].

Bioretention systems are generally soil-plant based systems that typically consist of a filter medium (usually sandy), underlain by a gravel drainage layer [1], [8]. Bioretention systems may be lined with geofabric to allow infiltration, or include an impermeable liner to assist in stormwater capture and reuse [10]. Bioretention systems treat stormwater via a range of chemical, physical, and biological processes. These include sedimentation, filtration, adsorption, and plant and microbial uptake [8]. Despite a number of previous studies on the performance of bioretention systems, the mechanisms through which pollutants are removed or treated are yet to be fully understood [8]. There have also been few studies on the long-term performance of bioretention systems regarding heavy metals [11].

Clogging of bioretention systems over time and depth and sizing of the filter media [11] have been seen as the cause of heavy metal accumulation or breakthrough [6], [12]. Heavy metal breakthrough may occur even faster in sub-tropical locations (such as Brisbane) that experience higher rainfall intensities. It has also been suggested that if the filter media needs replacement during regular maintenance of these systems, it may need to be classified as contaminated waste due to the build-up of pollutants over time and necessitating special disposal procedures [11].

Laboratory scale studies have been the predominant form of analysis of many previous studies investigating the performance of bioretention systems [6] - [8], [11], [12]. Field-based studies have reported varied results, particularly regarding soluble forms of nitrogen and phosphorous, and areas subject to high contaminant loading such as fuel stations or waste recycling sites [1].

This paper presents the pollution removal performance results of a series of field-based

experiments undertaken on five, 10-year old street-side bioretention systems. The bioretention basins, located on the Sunshine Coast in Australia, were subjected to a series of simulated rainfall events using synthetic stormwater. Four different synthetic stormwater pollutant concentrations were used in the study. Tests were undertaken to determine the levels of contaminant and heavy metals build-up that occurred in the filter media over the 10 year operational life of the bioretention systems.

METHODOLOGY

Site Description

The bioretention systems evaluated in this study were installed in 2005 to treat stormwater road runoff from a mixed commercial and industrial catchment of approximately 0.6 ha in area. There are five individual bioretention basins located directly adjacent to the roadway, which runs centrally through the catchment (Figure 1). The bioretention basins were designed to have an operational hydraulic conductivity of 180 mm/h and achieve the recommended regulatory pollution reduction objectives of 80% of Total Suspended Solids (TSS), 60% of Total Phosphorous (TP), and 45% of Total Nitrogen (TN) [13] (ANZECC, 2000).

Fig. 1 One of the bioretention basins evaluated in the study.

Figures 2 and 3 show the design and construction plans of the bioretention basins. The design comprised an impermeable plastic liner, a 200 mm gravel drainage layer base surrounding a 100 mm diameter, perforated drainage pipe. A 100 mm thick sand transition layer was laid above the gravel base and a 900 mm sandy-loam filter media was included above the sand (Figure 3). An indigenous plant species *Lomandra longifolia* (Matt Rush) was planted into the filter media at a typical spacing of one plant per square metre. Outflow pipes from the bioretention systems were diverted through the nearest downstream drainage gulley within the standard underground stormwater drainage system. A purpose built metal spout was attached to the wall of the pit to collect outflows and direct them through the measurement equipment installed in the pits.

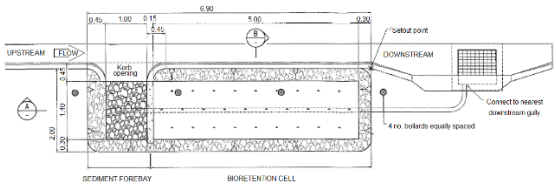

Fig. 2 Plans of the bioretention basins evaluated in the study.

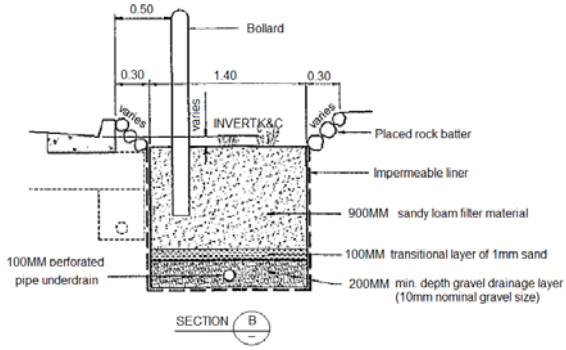

Fig. 3 Section "B" view of bioretention system.

Sampling Equipment and Testing

Owing to the different existing pit locations, it was only possible to effectively evaluate three of the five bioretention basins. The three identically-sized basins were fitted with flow monitoring and water sampling equipment including 50 mm diameter flow meters (Octave Ultrasonic Water Meter DN50) to measure flowrates. An ISCO GLS auto-sampler was used to collect outflow samples in each pit. Sampling equipment also included a Datataker (DT80) datalogger, battery pack and battery charger.

In order to reduce the potential variability and difficulty in monitoring pollution removal performance during natural rainfall events, simulated rainfall runoff techniques were used in this study. Using a purpose-built stormwater simulation test rig (Figure 4), each bioretention basin was subjected to the equivalent runoff inflow rate that would be generated from a 54.8 m^2 roadway catchment emanating from a 30 minute duration, two year average recurrence interval (ARI) rainfall intensity event (Figure 5) at the test location based on procedures outlined in Australian Rainfall and Runoff [14]. Two 1,000 litre tanks with adjustable outlet control were used to simulate the inflow volumes (total inflow volume = 2,000 L). In order to replicate typical stormwater pollution loads found in urban runoff, the synthetic stormwater was dosed with contaminants using a similar methodology to that used by [15] and [16].

Fig. 4 Stormwater supply rig used to simulate test inflow rates used in the study

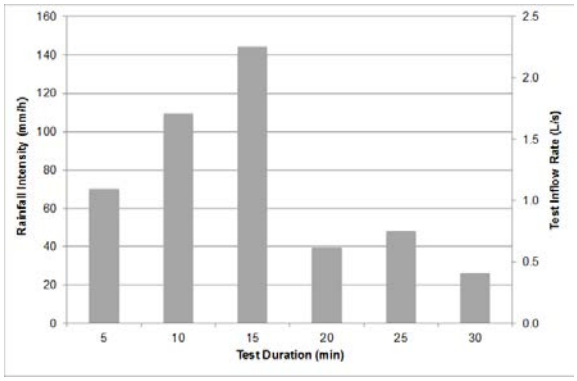

Fig. 5 Rainfall intensities and equivalent test inflow rates used in the study to simulate the roadway runoff volumes from a two year, 30 minute storm event.

Four different pollution concentrations were tested on each of the three bioretention basins (Table 1). The four concentrations tested were: A) no pollution; B) typical Australian urban pollutant loads (TSS 150 mg/L; N 2.6 mg/L, and; P 0.35 mg/L) [17] - [19]; C) double the typical pollution loads, and; D) five times the typical pollution loads. The higher pollution loads were included to help identify any trends that may otherwise be difficult to measure. Silica sediment (Sibelco 60G, Table 2), phosphorus (KH_2PO_4) and nitrogen (KNO_3) was added to 2,000L of municipal water to produce the simulated pollutant concentrations [20], [21].

Table 1 Pollution concentrations used in study (A - Nil pollution; B - typical Australian pollutant loads; C – 2 X typical loads; D – 5 X typical loads).

Test	TSS	TP	TN	Stormwater
A	0	0	0	2,000 L
B	300 g	8.79 g	14.4 g	2,000 L
C	600 g	17.6 g	28.8 g	2,000 L
D	1,500 g	44.0 g	72.2 g	2,000 L

Note: Synthetic additives include: TSS- 60G Silica; TP- KH_2PO_4; TN- KNO_3

Table 2 Particle size distribution (PSD) of Sibelco 60G synthetic sediment used during testing

Particle size (µm)	% finer
<250	99
<150	94.1
<106	86.2
<75	65
<45	60
<20	33.7
<10	19.1
<2	5.9
<1	5.1

Concentration Reduction Efficiency (CRE) was calculated for each simulated event as the percentage reduction in concentration with respect to inflow concentration for each pollutant (TSS, TN, and TP). Average CRE was calculated as shown in Eq. (1) below. Total pollutant loads and Event Mean Concentrations (EMCs) were determined for each test flow event, and efficiency ratios (ER) calculated using Eq. (2).

$$\text{Avg.CRE} = \frac{\sum\left[\frac{(EMC_{\text{inf low}} - EMC_{outflow})}{EMC_{\text{inf low}}}\right]}{numberofevents} \quad (1)$$

$$\text{ER} = \frac{EMC_{\text{inf low}} - EMC_{outflow}}{EMC_{\text{inf low}}} \quad (2)$$

Soil Testing

The study site land use was classified as commercial/industrial, and subject to high traffic volumes over the last decade. It was therefore anticipated that the bioretention filter media would contain significant heavy metal and hydrocarbon pollution loads. In order to evaluate the pollution build-up in the filter media, soil core samples of 500 mm depth were taken at three different locations in all five bioretention basins (Figure 6). Each of the core samples was separated into three distinctive sub-sample depths (0 – 50 mm, 50 – 100 mm and 100 – 500 mm) and these were sent to a soil testing laboratory for pollutant analysis. The sub-samples were analysed to determine their concentration levels across the entire range of measurable heavy metal and hydrocarbon pollutants.

Fig. 6 Soil core sampling

Sub-sample pollutant concentrations were compared with health investigation levels (HIL) for soil contaminants contained within the Australian Government regulation National Environment Protection Measure [22]. Levels specified under Recreational Land Classification (C) were applicable as the basins were located on public open space as defined by this legislation, and exceedances have been noted.

Sample collection and testing was undertaken in accordance with test methods specified in Standard Methods for the Examination of water and Wastewater (APHA, 2005) [23]. Sample collection, storage and transport complied with AS/NZS 5667.1:1998 [24]. Heavy metals and hydrocarbons were extracted using standards methods (Table 3). The results presented in this study focused on the four main heavy metals recognised as being particularly harmful to aquatic ecosystems, namely: chromium (Cr), lead (Pb), copper (Cu), and zinc (Zn) [25].

Table 3 Test descriptions and methods used during laboratory analysis of soil

Test	Method
Total Recoverable Hydrocarbons (1999 NEPM Fractions)	TRH C6-C36 - LTM-ORG-2010
Total Recoverable Hydrocarbons - 2013 NEPM Fractions	TRH C6-C40 - LTM-ORG-2010
BTEX (Benzene, Toluene, and Xylenes)	TRH C6-C40 - LTM-ORG-2010
Polycyclic Aromatic Hydrocarbons	USEPA 8270 PAH
Metals	USEPA 6010/6020 Heavy Metals & USEPA 7470/71 Mercury
Percentage Moisture	LTM-GEN-7080 Moisture

RESULTS

Nutrient Pollution Removal Performance

Pollution removal performance as measured by event mean concentrations (EMC) for the three regulated pollutants varied significantly between inflow and outflow for TSS (p<0.03*) and TP (p<0.01*) but not for TN (p<0.18) across pollution dosage concentration treatments (Table 4).

Table 4 Student t-test results of bioretention basin nutrient pollution removal performance across basins

Pollution concentration dose	TSS (p)	TN (p)	TP (p)
Nil	<0.05*	<0.11	0.43
Single	<0.72	<0.75	<0.17
Double	<0.03*	<0.73	<0.001*
X 5	<0.001*	<0.01*	<0.05*

Note: * significant

Bioretention basin pollution removal results for Tests A-C were highly variable (Figure 7). Tests D, with five times the standard pollution concentrations, were the only tests that demonstrated significant pollution reduction performance by the bioretention basins for all three pollutants (Figure 7). During test A (Nil concentrations) results showed that the basins exported both TSS and TN, while TP was found to show a modest pollution removal performance (26.8%). This was not anticipated and may have been due to possible equipment contamination from previous tests. Although every effort was made to wash remnant contaminants from the supply tanks between tests, we found it practically impossible to achieve in the field. Therefore, it was accepted that some of the inflow samples may have contained trace amounts of pollutants from previous tests. The measured trace contaminant concentrations however, were found to be very small for all pollutants measured. Similar issues have been found in previous studies involving synthetic stormwater (particularly involving sediment), where delivery of the polluted water is difficult during testing [11].

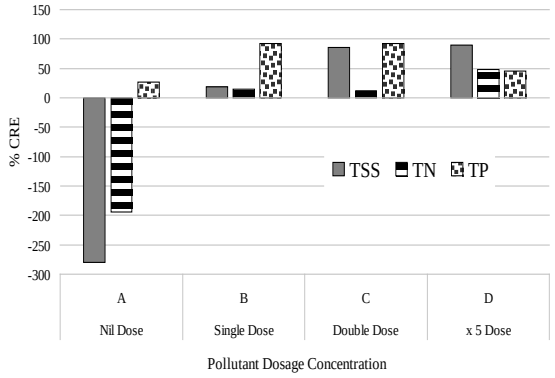

Fig. 7 Bioretention pollution removal performance (CRE).

Heavy Metal and Hydrocarbon Pollution Removal Performance

Heavy metal and polycyclic aromatic hydrocarbon (PAH) pollution concentration levels in the soil core samples were found to be within acceptable limits for all pollutants analysed. Heavy metal pollution levels were found to be highest in the upper 0-50 mm soil layers of the basins. Although trace amounts of several heavy metals (most prominently Mn and Zn) were found in most of the basins, all heavy metal levels found in the soil were either below detectable limits, or within acceptable limits based on legislated health-based investigation levels (Table 5).

Table 5 Comparison of Bioretention Basin PAH soil content with typical global levels

Location	Typical Concentration Range (mg/kg)	Description	Ref.
Worldwide	0.01-0.1	Rural soil	[26]
	0.05-0.1	Forest soil	[26]
	0.6-3.0	Urban soil	[26]
	14.6-99.6	UK roadside soil	[26]
Europe	2.02	UK urban soil	[27]
Australia	1.2-4.8	Bioretention basins	This study

While remaining within acceptable limits in four of the bioretention basins, the carcinogenic BaP (Benzo(a)pyrene) was found to be higher (4.8 mg/kg) in the upper layer (0-50 mm) of the fifth basin. However, these BaP levels are comparable with similar urban and roadside locations throughout the world (Table 5). To place the relative risk into context, the highest risk to human health from BaPs is through inhalation of contaminated air, and food consumption. Although, soil and drinking water can be sources of BaPs during normal daily activities [27]. The risks to human health from PaHs contained within the bioretention basin soil are very low. The risk may be higher during activities that involve soil disturbance, including maintenance (weeding etc.), or soil filter media replacement.

DISCUSSION AND CONCLUSION

Although highly variable between basins and tests, as the pollution concentrations of the simulated stormwater tests were increased, the ER performance of the bioretention basins was also found to increase. Basins were also found to export pollutants during tests where no pollutants were added to the simulated inflow water. Depending on the precise filter media used in the basin design, bioretention basins have previously been known to be occasional exporters of pollution, particularly particulate-bound phosphorous [18]. This study found that bioretention basins reduced TP loads in all tests, although the removal performance was found to be most effective during the higher pollution concentration tests, C and D.

Because the land was commercial/industrial, and subjected to large numbers of daily vehicle and truck movements over the last ten years, it was anticipated that the bioretention filter media would contain significant hydrocarbon and heavy metal pollution loads [12], [28]. However, results from soil core samples in this study found only minimal quantities of these pollutants in the filter media. This was not anticipated. One possible explanation may be that hydrocarbons and heavy metals were not captured by the bioretention basins during high intensity rainfall events (high flow bypass), and diverted directly to the conventional piped network. Although the basins were originally designed with a hydraulic conductivity of 180 mm/h, this may have reduced over time due to clogging leading to regular bypass conditions in the basins. If so, a higher level of maintenance may be required to ensure effective hydrologic design performance over the longer term to maintain effective overall pollution removal performance. Further research would be required to confirm this.

Another possible reason for the absence of accumulated pollutants in the filter media may be that pollutants trapped during one storm event are then washed through the filter media during subsequent rainfall events. This has been reported as a possible explanation during previous studies [18]. The study results clearly demonstrated that

pollutants were exported during pollutant-free tests (A) and this may add support to this hypothesis. Further work is required to examine this in more detail.

Analysis of the filter media used in the bioretention systems found that all pollutants were either below detectable limits, or within acceptable limits based on legislated health-based investigation levels after 10 years in operation. The filter media was not be classified as contaminated and would not require special disposal at this stage.

The results show the large degree of variability in the performance of individual bioretention basins. The authors suggest this variability may be due to a number of reasons, including the slightly different construction techniques used for each basin, and the variability of pollution loads and stormwater inflow volumes experienced between basins due to different environmental conditions.

While this study has added to the existing knowledge about the long-term pollution removal and stormwater reduction performance of street-side bioretention basins, more work is required in order to fully understand the potential stormwater management benefits of these systems.

ACKNOWLEDGEMENTS

The project was jointly funded by the Sunshine Coast Council, the University of the Sunshine Coast and the Australian Research Council (Linkage Project Grant-LP120200678). The authors would like to thank Liam Owen, Tim Stabler and Matthew Johnson, and the technical staff and the University of the Sunshine Coast for their assistance during the study.

REFERENCES

[1] Dietz, M.E., "Low Impact Development Practices: A Review of Current 17 Research and Recommendations for Future Directions." Water Air Soil Pollution, 2007, 186: 351-363.

[2] Lucke, T., & Beecham, S. "Field investigation of clogging in a permeable pavement system." J. Build. Res. Inf. 2011, 39(6): 603–615.

[3] Nichols, P.W.B., White, R., & Lucke, T. "Do sediment type and test durations affect results of laboratory-based, accelerated testing studies of permeable pavement clogging?" Sci.Tot.Env. 2015, (511): 786-791.

[4] Davis, A. "Field Performance of Bioretention: Hydrology Impacts." Journal of Hydrologic Engineering 2008, 13(2), 90-95. DOI: 10.1061/(ASCE)1084-0699(2008)13:2(90)

[5] Hunt, W., Smith, J., Jadlocki, S., Hathaway, J., & Eubanks, P. "Pollutant Removal and Peak Flow Mitigation by a Bioretention Cell in Urban Charlotte, N.C." J. of Env. Eng. 2008, 134(5): 403-408. DOI:10.1061/(ASCE)0733-9372(2008)134:5(403)

[6] Le Coustumer, S., Fletcher, T.D., Deletic, A., Barraud, S., & Poelsma, P. "The influence of design parameters on clogging of stormwater biofilters: a large-scale column study." Water Research, 2012, 46(20): 6743-6752.

[7] Bratieres, K., Fletcher, T.D., Deletic, A., & Zinger, Y. "Nutrient and sediment removal by stormwater biofilters: A large-scale design optimisation study." Water Research. 2008, 42, 3930-3940. DOI: 10.1016/j.watres.2008.06.009

[8] Deletic, A., McCarthy, D., Chandresena, G., Li, Y., Hatt, B., Payne, E., Zhang, K., Henry, R., Kolotelo, P., Randjelovic, A., Meng, Z., Glaister, B., Pham, P., & Ellerton, J. "Biofilters and wetlands for stormwater treatment and harvesting". Melbourne: Cooperative Research Centre for Water Sensitive Cities, Monash University, October, 2014, pp. 67.

[9] Mullaney, J., Lucke, T., & Trueman, S.J. "A review of benefits and challenges in growing street trees in paved urban environments." Landscape and Urban Planning, 2015, 134: 157-166.

[10] FAWB "Adoption Guidelines for Stormwater Bioretention Systems. Faculty for Advancing Water Biofiltration." Monash University. June 2009.

[11] Hatt, B.E., Steinel, A., Deletic, A., & Fletcher, T.D. "Retention of heavy metals by stormwater filtration systems: Breakthrough analysis. Water Science & Technology, 2011, 64: 1913-1919.

[12] Hatt, B.E., Fletcher, T.D., & Deletic, A. "Pollutant removal performance of field-scale stormwater bioretention systems. Water Science & Technology, 2009, 59(8): 1567-1576. DOI: 10.2166/wst.2009.173

[13] ANZECC and ARMCANZ "Australian and New Zealand guidelines for fresh and marine waters. National Water Quality Management Strategy Paper No 4", Australian and New Zealand Environment and Conservation Council & Agriculture Resource Management Council of Australia and New Zealand, Canberra, 2000.

[14] Pilgrim, D.H., (Ed). "Australian Rainfall & Runoff – A Guide to Flood Estimation", Institution of Engineers, Australia, Barton, ACT, 1987.

[15] Lloyd, S.D. "Water Sensitive Urban Design in the Australian Context. Synthesis of a Conference held 30–31 August 2000, Melbourne", Australia (Technical Report No. 01/7 Cooperative Research Centre for Catchment Hydrology, Melbourne, Australia (2001)

[16] Deletic, A. & Fletcher, T.D. "Performance of grass filters used for stormwater treatment—a field and modelling study." Journal of

Hydrology 2006, 317(3): 261-275.
[17] Duncan, H. "Urban stormwater quality: a statistical overview" Clayton Victoria: CRC for Catchment Hydrology, 1999.
[18] Hatt, B.E., Fletcher, T.D., Deletic, A. "Hydraulic and pollutant removal performance of stormwater filters under variable wetting and drying regimes." Water Science & Technology, 2007, 56(12): 11-19.
[19] Liu, J., Sample, D., Bell, C., & Guan, Y. "Review and Research Needs of Bioretention Used for the Treatment of Urban Stormwater." Water, 2014, 6(4): 1069-1099.
[20] Ansaf, K.M.M., Lucke, T., & Boogaard, F. "Preliminary investigation into the pollution reduction performance of swales used in a stormwater treatment train. Water Sci. & Tech., 2014, 69 (5): 1014-1020.
[21] Lucke, T., Mohamed, M.A.K., Tindale, N. "Pollutant Removal and Hydraulic Reduction Performance of Field Grassed Swales during Runoff Simulation Experiments." Water, 2014, (6): 1887-1904.
[22] Australian Government "National Environmental Protection (Assessment of Site Contamination) Measure" (AG NEPC). National Environmental Protection Council, Adelaide, Australia, 1999. https://www.comlaw.gov.au/. Accessed 30 June 2015.
[23] American Public Health Association (APHA) "Standard methods for the examination of water & wastewater." 21st edition, 2005, Eaton, A.D., Clesceri, L.S., Rice, E.W., Greenberg, A.E., Franson, M.A.H. APHA, Washington.
[24] Standards Australia/New Zealand. "Water quality - Sampling - Guidance on the design of sampling programs, sampling techniques and the preservation and handling of samples." (AS/NZS 5667.1:1998). Retrieved from http://www.saiglobal.com 30 June 2015.
[25] Feng, W.J., Hatt, B.E., McCarthy, D.T., Fletcher, T.D., & Deletic, A. "Biofilters for Stormwater Harvesting: Understanding the Treatment Performance of Key Metals That Pose a Risk for Water Use." Environmental Science & Technology, 2012, 46(9), 5100-5108.
[26] Menzie, C.A., Potocki, B.B., & Santodonato, J. "Exposure to carcinogenic PAHs in the environment." Environmental science & technology, 1992, 26(7): 1278-1284.
[27] Harrison, R.M., Smith, D.J.T., Piou, C.A., & Castro, L. M. "Comparative receptor modelling study of airborne particulate pollutants in Birmingham (United Kingdom)," Coimbra (Portugal) and Lahore (Pakistan). Atmospheric Environment, 1997, 31(20), 3309-3321.
[28] Davis, A.P., Shokouhian, M., Sharma, H., Minami, C., Winogradoff, D. "Water quality improvement through bioretention: lead, copper, and zinc removal. Water Environment Research. 2003, 75(1): 73–82.

First International Conference on Science, Engineering & Environment,
Tsu City, Mie, Japan, Nov.19-21, 2015, ISBN: 978-4-9905958-5-2 C3051

THE DETERMINATION OF IRRIGATION WATER STORAGE FOR CORN IN THE DRY SEASONS IN CHAU PHU DISTRICT, AN GIANG PROVINCE, VIETNAM

N.V. Tuyen[1], P.V.Toan[1], N.H.Chiem[1], L.A.Tuan[2], V.P.D.Tri[1]
[1]College of Environment and Natural Resources, Can Tho University, Viet Nam; [2]Delta Research and Global Observation Network **(**DRAGON) Institute, Can Tho University

ABSTRACT

Drought is one of considerable issues for agriculture cultivation in the Vietnamese Mekong Delta during the annual dry seasons. Aiming to ensure water requirement for corn cultivation, a study on water storage during annual flooding seasons for irrigation in semi-dyke area the dry season was carried out in Chau Phu District, An Giang Province, Viet Nam. In this study, field experiments were conducted to: (1) determine designed parameters of water storage pond by a water balance model and the AquaCrop model; (2) propose a suitable model for storing irrigation water to Spring-Winter corn cropping. Results showed that with the 0.24 m^3 per day average precipitation, 1.87 m^3 per day surface water evaporation, 4.12 m^3 per day seepage from pond, water demand for corn was 8.30 m^3 per day. Simulated AquaCrop model has gained 5.10 ton per hectare on corn yield as similar to the actual yield.

Keywords: Water Storage in Pond, Water Balance Equation, AquaCrop Model, Irrigation Demand.

INTRODUCTION

In the upstream provinces of Vietnamese Mekong Delta (VMD), natural land is deeply submerged in the flood season, but the land becomes dry and local residents suffer water shortage during the dry season [5]. The hydropower dam contruction in the upstream countries having affected to water regime of the Mekong River downstream countries [7]. Laos and Cambodia are seeking to increase the 31.000 km^2 irrigated area for crop production [4] that may lead to reduce water supply in the dry season result negative impacts to agriculture production of the VMD [11]. Many countries have plans on water storage to remain cultivation and adapt to water shortage which are affected by the decreasing of water flow from upstream and the saline intrusion in the coastal of the delta in term of time and space [6]. In Cambodia, farmers live in the back swamps around the Tonle Sap. These farmers retained floodwater in bunded areas and then used it to supply paddies cultivated on the swamps during the dry season [3]. In the Northest of Rajasthan in India, approximately 10.000 constructions were built to store ground water for irrigation of 14.000 ha gains and vegetables [8]. In the semi-arid regions in Africa, a reservoir system was built to harvest rainwater to supply water for cultivation [12]. In Viet Nam, there were difference studies about water-storage to supply water for different purposes such as: agriculture, industry and others, but almost of the studies based on natural land feature such as lakes, swamps and forests to store water [10].

Corn is the third important plant in the world after wheat and rice. All parts of corn plants including seed, the stems and leaves can be used as food for human, livestock or for producing ethanol, source of materials for biofuel processing [13]. In agricultural production in the study area (Chau Phu district, An Giang province, Viet Nam), corn is the second cereal product after rice [1], contributing partly to people's livelihoods and food security. In this study, corn was selected to determine the volume of water storage in pond and on-farm in dry season.

MATAERIALS AND METHODS

The study was implemented at a semi-dyke protected field in the Vinh Thanh Trung Commune, Chau Phu Distrist, An Giang Province (Fig.1) during the period of January, 2012 to December, 2014.

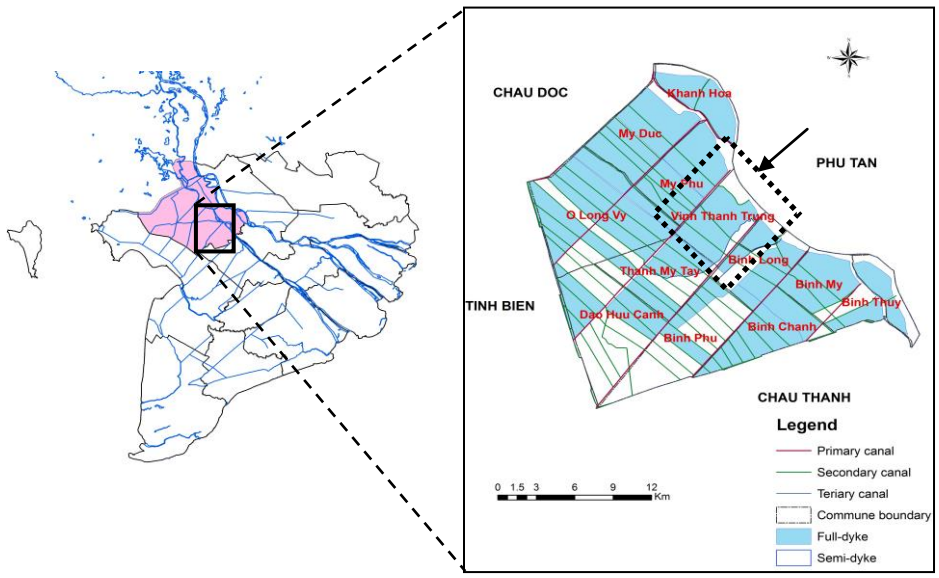

Fig. 1 Location map of the study site

The total of study area was 0.4 hectare, where the water pond area was 0.1 hectare, over 0.3 hectare of remainning area was used for corn cultivation as presented in Fig.2. Corn variety of NK7328 was selected for research. Life-cycle of the crop was 90 – 95 days and the planting density was 9 plants per m^2. The designed size of the pond was 2m x 20m x 50m (depth x width x length).

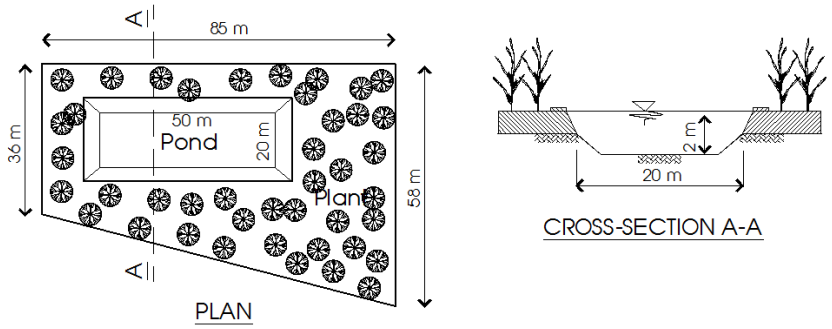

Fig. 2 Diagram for setting up experiement

Application of Water Balance Model in Pond

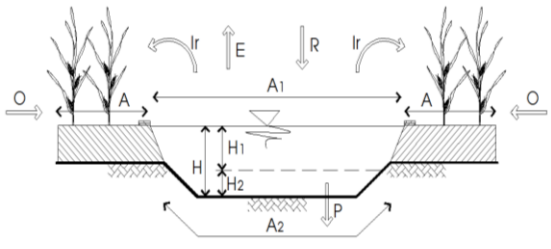

Fig. 3 Survey diagram for water balance

The altitude of the pond edge built was at the altitude of the semi-dyke so that the pond could stored water from run-off due to flooding and rain (R). Water in the pond was determined by the water balance equation to irrigate (Ir) corn per day after deducting the amount of evaporation (E) and percolation (P). These are shown on the Fig. 3.

Water balance equation for the system as follows:

$H = H_1 + H_2$ (m) Eq. (1)

$O = H_1.A_1 = E.A_1 + Ir.A + P.A_2 - R.A_1$ (m^3) Eq. (2)

Where:

- O: Overflowing water, m^3.
- H: height of water column in the pond after the flood measured by data-logger, m.
- H_1: height of storage water column for irrigation, m
- H_2: height of remaining water in the pond after crop, m
- A: corn cultivation area, m^2
- A_1: pond surface area, m^2
- A_2: area of bottom and surrounding pond, m^2

- R: rainfall measured by automatic rain gauge, m
- E: evaporation directly measured by A evaporation pan, m
- Ir: water irrigation measured through the flow meter, m
- P: percolation caculated from Eq. (3):

$$P.A_2 = H_1.A_1 + R.A_1 - Ir.A - E.A_1 \ (m^3) \quad \text{Eq. (3)}$$

- $W = H_1.A_1$ (m^3): volume of water for irrigation.

The Aquacrop Model

The inputs of the model included soil data (texture, wilting point, field capacity, saturated moisture, permeability coefficient) was collected and analyzed from Laboratory of Soil Science Department, Can Tho University, Viet Nam. Climate data consisting of air temperature, precipitation, evaporation were collected by equipments located near pond. Other climate data such as wind speed, sunshine hours, the concentration of CO_2 were collected at The Hydro-Meteorological station in Chau Doc (20km far from the study site), the bio-physiscal characteristics plant data consisting of canopy cover, depth of roots, yield, crop production schedule were directly collected in the field. The output consisted of water demand and yield generated by AquaCrop software version 3.1$^+$. The model was operated at a daily time step.

RESULTS AND DISCUSSIONS

Design Parameters of a Water Storage Pond

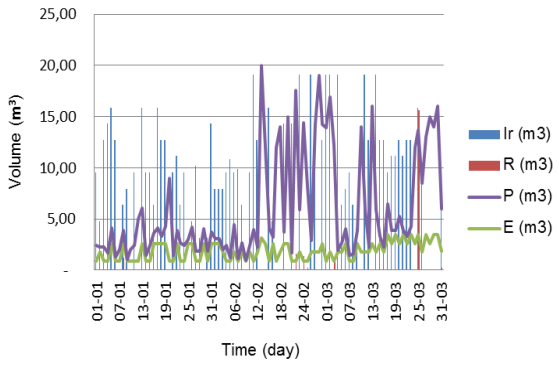

Fig. 4 Variation of evaporation, irrigation, rainfall and percolation during the experiments

Corn was cultivated in dry season, so rainfall was recorded as little as 15.6 mm per day at the end of crop. The average evaporation (E) from pond was 1.87 m^3 per day. The average value of percolation (P) was 4.12 m^3 per day. The average irrigation (Ir) volume was 8.30 m^3 per day (Fig. 4).

Simulation of Water Storage Ablity for Corn

Weather data

Weather data at study area during the study period (from 1st January, 2013 to 31st March, 2013) are shown in Fig. 5, including highest and lowest air temperature T_{max} ($^{\circ}$C), T_{min} ($^{\circ}$C), reference evapotranspiration (ET_O) and rainfall (R).

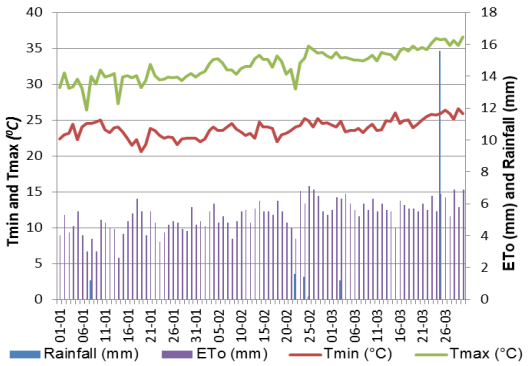

Fig. 5 Air temerature, rainfall and reference evaportranspiration (ETo)

Air temperature at the study area ranged from 20.6°C to 36.6°C. The average sunshine hours was 2,279 hours per year. The average wind speed was with 4.9 ± 1.42 m/s. The average humidity was 76.1% [1]. Fig. 6 shows the parameters of humidity, sunshine hours and wind speed.

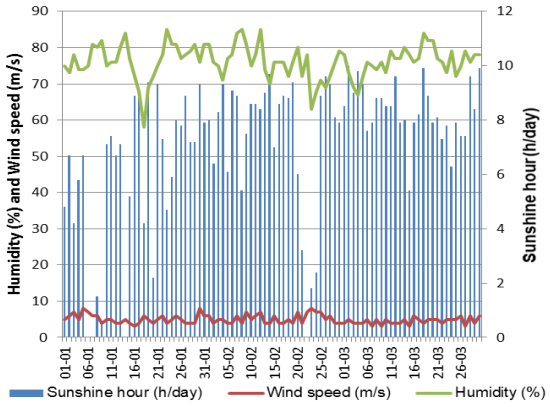

Fig. 6 Average humidity, wind speed and sunshine hours

Soil data at study site

The soil at the study site was characterized with heavy clay, low organic matter, good water retention and slow saturation. Its physical characteristics are shown in Table 1.

Simulated yield for corn in the Spring –Winter cropping season in the year 2013

Beside soil physical characteristics in Table 1 used as inputs of model, parameters of the corn showed in Table 2 were combined for calibration so that there was a similar yield between reality and simulated results. The parameters were calibrated based on the reference value range for corn, other parameters were fixed with default values proposed in the model [9].

Table 1 Physical soil characteristics at the study site in year 2013

Layer	Depth (cm)	Clay (%)	Silty (%)	Sand (%)	Texture	OM (%)	EC (ms/ cm)	PWP (%)	FC (%)	SAT (%)
1	0-10	39.10	55.20	5.70	Silty clay loam	1.31	1.40	24.22	40.82	48.70
2	10-20	44.10	49.20	6.70	Silty clay	1.10	2.00	24.60	38.06	43.22
3	20-30	43.20	50.20	6.60	Silty clay	0.95	2.40	19.19	29.66	36.26

Notes: OM: Organic matter; PWP: Permanent wilting point; FC: Field capacity; SAT: Saturation.

Table 2 Calibrated parameters of corn

Parameters	Unit	Reference value	Calibrated
WP	g/m^3	33.7	33.7
HIo	%	48-52	48
CCo	Plant/ha	50.000-100.000	90.000
CCx	%	65-99%	80%

(Source: [2])

The calibrated parameters in Table 2 were high sensitive and they directly impacted on the simulated results. Real water demand of corn used as the input of model was shown in Fig. 7.

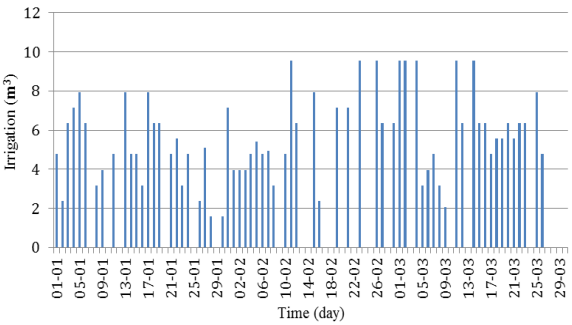

Fig. 7 Reality irrigation of corn in the Spring – Winter cropping season in the year 2013.

Simulated yield of corn in the Spring-Winter cropping season in the year 2013 with irrigation water presented in Fig. 7 was 5.10 ton per hectare. This simulated yield was similar to the actual harvesting yield (5.23 ton per hectare).

Simulated water demand of Corn in the Spring-Winter cropping season in the year 2014.

In order to operate the model for simulating water demand of corn in the Spring – Winter cropping season in the year 2014, the input parameters of the AquaCrop model were determined as follows:

- Climate data: air temperature, rainfall, wind speed, evaporation, sunshine hour, and CO_2 concentration were fixed as 2013.
- Soil data: a new soil sampling batch was conducted in the first season of year 2014 . Results of physical soil characteristics were shown in Table 3.
- Crop data: cultivation time of corn was from January to March 2014.
- Calibrated parameters of model: the basic parameters (WP, HI_O, CC_O, CC_X) were values used for the model in the year 2013. Irrigation water was adjusted so as to corn yield gained 6.2 ton per

hectare. The simulated results of water demand were shown in Fig. 8.

Table 3 Physical soil characteristics at study site in the year 2014

Layer	Depth (cm)	Clay (%)	Silty (%)	Sand (%)	Texture	OM (%)	EC (ms/ cm)	PWP (%)	FC (%)	SAT (%)
1	0-10	39.46	57.11	3.44	Silty clay loam	1.58	1.58	28.61	49.36	48.87
2	10-20	46.84	49.80	3.37	Silty clay	1.51	1.61	30.72	47.70	49.93
3	20-30	44.79	51.68	3.53	Silty clay	1.46	1.62	30.72	46.47	52.10

Notes: OM: Organic matter; PWP: Permanent wilting point; FC: Field capacity; SAT: Saturation

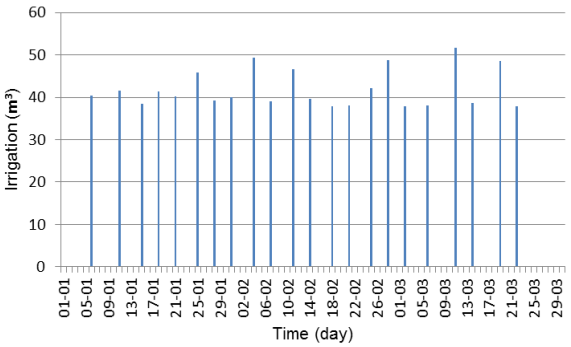

Fig. 8 Simulation results of irrigation demand for corn in the Spring-Winter cropping season in the year 2014.

CONCLUSIONS

Designed parameters of the reservoir were determined by a proper combination between water balance equation and the AquaCrop model. The AquaCrop model simulated crop yield and water demand of corn in different irrigation conditions. In addition, the study recommended a water storage physical model for irrigating corn in Spring -Winter cropping season in the year 2014. The study results also contributed data for finding water demand of corn. In this study, the experiment time was relative short (03 months), only one crops and one kind of corn. Further experiment should be conducted for other plants such as: seasame, chilli and green soy... and longer crop as well. Such experiments could be scientific background for proposing suitable water saving plants and high crop yields under climate change.

ACKNOWLEDGEMENTS

The authors highly appriciate to colleagues for their help and contribution in this study. Besides, the authors thank the JIRCAS organization for their financial support during research time . The research is one of the component of project on technical development for agriculture in the Mekong delta adapting to climate change.

REFERENCES

[1] An Giang Statistical Office. Statistical yearbook of An Giang. At HCM City statistical printing company limited. 2013.

[2] FAO. Aquacrop. Rome, Italy. 2011.

[3] Fox J, and Ledgerwood J. Dry-season flood-recession rice in the Mekong Delta: Two thousand years of sustainable agriculture. Asian Perspect. 38, 1999, pp. 37–50.

[4] ICEM. MRC SEA for hydropower on the Mekong mainstream. Fisheries baseline assessment working paper. (International center environmental managemaent, HaNoi). 2010.

[5] Khem S, Goto A, and Mizutani M. Determination of the potential land for securing double-rice cropping in the Cambodian Mekong Delta, based on a sub-area based modeling of flood inundation. Paddy Water Environ. 6 (3), 2008: pp. 285–298.

[6] Lu XX, and Siew RY. Water discharge and sediment flux changes over the past decades in the Lower Mekong River: possible impacts of the Chinese dams. Hydrol. Earth Syst. Sci. 10(2), 2006, pp. 181–195.

[7] Osborn M. The MeKong river under threat. Lowy institute for international policy 2009.

[8] Panigrahi B, Panda S, and Mull R. Simulation of water harvesting potential in rainfed ricelands using water balance model. Agric. Sci. 6, 2011, pp. 165–182.

[9] Saadati Z, Pirmoradian N, and Rezaei M. Calibration and valuation of aquacrop model in rice growth simulation under different irrigation managements. CID 21st Int. Congr. Irrig. Drainage. 2011, pp. 589 – 600.

[10]Son NT. Water balance for Kien Giang river basis by IQQM model. J. Nat. Sci. Tech. . Ha Noi Natl. Univ. 25 (3), 2009, pp. 499–507.

[11]Sunada K. Study on Asian River Basin. CREST Asian River Basins Water policy study team. 2009.

[12]Traore S and Wang YM. On-farm rainwater reservoir system optimal sizing for increasing rainfed production in the semiarid region of Africa. African J. Agric. Res. 6(20), 2011, pp. 4711–4720.

[13]Wagger MG and Cassel DK. Corn yield and water use effiency as affected by tillage and Irrigation. Soil Sci. Soc. Ameriacan 5, 1993, pp. 229–234.

First International Conference on Science, Engineering & Environment,
Tsu City, Mie, Japan, Nov.19-21, 2015, ISBN: 978-4-9905958-5-2 C3051

NUMERICAL SOLUTION OF SOIL - FOUNDATION INTERACTION

Radim Cajka[1], Jana Labudkova[2], Petr Mynarcik[3]
[1,2,3] Faculty of Civil Engineering, VSB - Technical University Ostrava, Department of Structures, Ludvika Podeste 1875/17, 708 33 Ostrava – Poruba, Czech Republic

ABSTRACT

Several experimental measurements of reinforced concrete slab – subsoil interaction are compared with numerical analysis of shallow foundation by means of FEM. At the Faculty of Civil Engineering VSB – Technical University of Ostrava testing device was constructed so that the phenomena of soil – foundation interaction could be experimentally investigated and compared with numerical models. Results of experimental loading test are compared with soil – foundation interaction analysis based on finite element method (FEM). The purpose of this paper is to compare resulting deformation of the slab, subsidence of the subsoil, bending moments and contact stress calculated by different software based on FEM. Currently there are several software that, can deal with the interaction of foundations and subsoil.

Keywords: Foundation Structure, Experimental Measurement, Soil – Structure Interaction, Interaction Models, FEM Calculation.

INTRODUCTION

Analysis of the subsoil-structure interaction is influenced by physical and non-linear behaviour of the structure, by the interaction of the upper structure and foundation structure and by selecting of interaction model. Insufficient theoretical basics of the investigated issue and the absence of an appropriate calculation tools still hinder to unambiguous solution of subsoil-structure interaction. Analysis of this interaction task is also made more difficult by lower accuracy of input data. Lower accuracy of input data is associated with a description of the subsoil properties and subsoil behaviour. Subsoil is made up of heterogeneous particles. Uncertainties of description of subsoil behaviour are also associated with the complexity to describe the geological profile in detail. Using a combination of experimental measurements, laboratory tests and testing in-situ, modelling and numerical methods is optimal to obtain reliable results of interaction tasks. Such experimental measurements are performed in the Czech Republic and in the world, in past and also in present.

THE SPATIAL NUMERICAL MODEL

Interaction model of prestressed concrete foundation slab with the subsoil was solved using 3D numerical modelling in ANSYS 15.0. Input data of solved task were taken from experimental measurements ongoing during the loading test carried out with the experimental equipment. The experimental equipment is described in [15]. Another experimental loading tests and their results are also described in [2, 3, 6, 7, 8, 11, 19].

The test sample of experimental loading test was post-tensioned concrete slab [5]. Post-tensioned concrete slab had the dimensions 2000x2000x150mm. Concrete class C35/45 was used. Slab was post-tensioned by six threaded prestressing bars. The bars were from steel Y 1050 and their diameter was 18 mm. Each rod was tensioned by force of 100kN.

These are simple foundation conditions from a geological point of view. The 300 mm layer of clay soil was removed before loading test of post-tensioned concrete slab. The footing bottom was filled with gravel fraction 0-4 mm to the edge of the surrounding terrain. The original subsoil composed of loess loam with consistency class F4 and with layer 5m remained under a new gravel bed. Deformation characteristics thus composed subsoil were determined by geotechnical testing. Subsoil has been described by following characteristics - Poisson coefficient $\mu = 0.35$, modulus of deformability $E_{def\,2} = 33.86$MPa.

Post-tensioned concrete slab model was loaded in the middle of the slab by pressure exerted by the hydraulic press during the experimental loading test. The dimensions of the loaded area were 200x200mm. Loading was carried out in parts, 75kN / 30min. The slab failed during the 7th cycle during this method of loading. The maximum level of load was 525 kN. The first significant cracks were detected after the 4th loading cycle. These cracks were located in the vicinity of the middle anchors of prestressing bars. The model of post-tensioned concrete foundation slab was violated by punching shear. Punching shear of slabs is discussed in detail [1].

THE SPATIAL NUMERICAL MODEL OF INHOMOGENEOUS HALF-SPACE

3D subsoil model can be created as a half-space, ie. body bounded from above by plane. Half-space can be modelled discretely or as a continuum. The simplest idealization of the elastic half-space is homogeneous and isotropic body. Soil is heterogeneous material and its properties are different from idealization linear elastic, isotropic and homogeneous substance. Therefore, the calculated values of the settlement do not correspond with the real values - measured in real buildings or during the experiments [9, 10, 17, 18, 20]. Inhomogeneous half-space was used for the analysis of the interaction of loaded post-tensioned concrete slab with the subsoil. In inhomogeneous half-space the concentration of vertical stress is different than in homogeneous half-space. Modulus of deformability varies continuously with depth. Using of inhomogeneous half-space is also described in papers [12, 13, 14]. The author of paper [14] establishes an equation for shifts in inhomogeneous half-space outside the loaded area in the context of shifts within the loaded area.

The computational model was created using the element SHELL 181 (2D) for slab and using the element SOLID 45 (3D) for the subsoil model. The slab thickness, which was 150 mm, was added to the 2D element SHELL 181. Assignment of specified material properties to the modelled slab and subsoil followed. Material No. 1 was marked concrete with modulus of elasticity E = 34.0GPa and the Poisson coefficient μ = 0.2. The subsoil model was divided into 30 layers. Inhomogeneity of the subsoil was taken into consideration with an increasing modulus of deformability $E_{def,2}$. Material No. 2-31 was marked soil with the changing modulus of deformability $E_{def,2}$ and the Poisson coefficient μ = 0.35. Self weight of soil massif and concrete slab was neglected. Thickness of one layer in subsoil model was 0.2 m. The value of modulus of deformability began on the surface of the subsoil model $E_{def,2}$ = 33.86MPa and its value gradually increased with the deeper layers (Fig. 1) of the formula (1):

$$E_{def} = E_0 z^m \quad Fig.1 \tag{1}$$

$$m = \frac{1}{\mu} - 2 = \frac{1}{0.35} - 2 = \underline{\underline{0.857}} \tag{2}$$

where

E_0 - modulus of deformability on the upper surface of subsoil model

z - z - coordinate (depth)

m - coefficient addicted on Poisson ratio μ

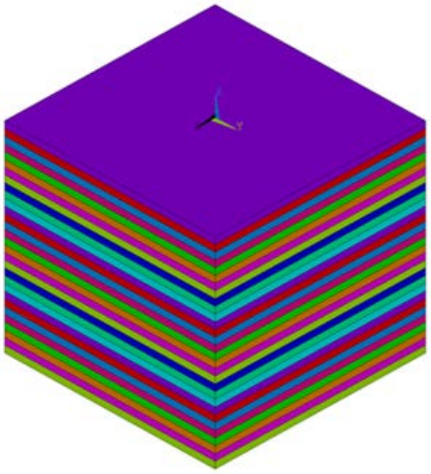

z [m]	E_{def} [MPa]	z [m]	E_{def} [MPa]
0,0	33,86	3,0	111,11
0,2	39,59	3,2	115,85
0,4	45,18	3,4	120,56
0,6	50,66	3,6	125,25
0,8	56,04	3,8	129,90
1,0	61,34	4,0	134,53
1,2	66,56	4,2	139,12
1,4	71,71	4,4	143,70
1,6	76,80	4,6	148,25
1,8	81,84	4,8	152,78
2,0	86,83	5,0	157,28
2,2	91,76	5,2	161,76
2,4	96,66	5,4	166,23
2,6	101,51	5,6	170,67
2,8	106,33	5,8	175,09
3,0	111,11	6,0	179,50

Fig. 1 Inhomogeneous half-space, modulus of deformability increases with depth

Volumes of the individual layers had different properties according to the table in Fig. 1. 3D finite elements of mesh of subsoil model had dimensions 0.2x0.2x0.2m. 2D finite elements of mesh of slab model had dimensions 0.1x0.1m. Both finite-element meshes were regular.

The load was applied to the nodes in the loaded area with size 200x200mm. The load value was approximately 525kN at the moment of sample failure. This value was also implemented in the numerical model. Prestressing was placed in quarters of all sides of slab model. Force in prestressed reinforcement was 100kN as well as during the experiment (Fig. 2).

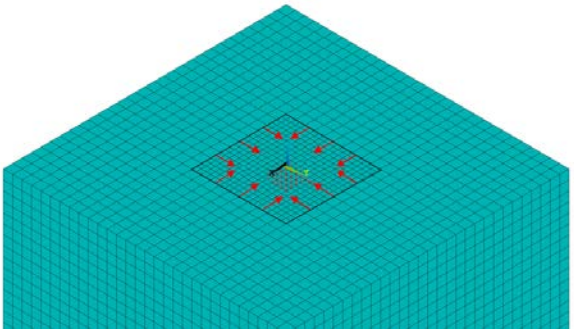

Fig. 2 Prestressing forces introduced into the slab model

Creation of mutual contact and definition of the contact area is necessary for the transmission of load effects from the foundation slab to the subsoil. Contact was made using a contact pair TARGE170 and CONTA173. The influence of friction between the slab and the subsoil on the contact area was neglected. Friction coefficient equalled zero. After creating a contact, it is necessary to verify that the normals of both contact surfaces directed against each other (Fig. 3).

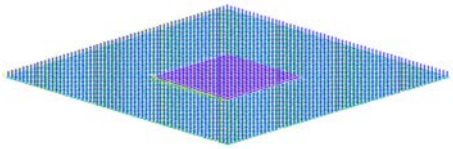

Fig. 3 Contact area made using contact pair TARGE170 and CONTA173

Horizontal nodes shifts in external walls of the subsoil model (No. 2, 3, 4, 5 in Fig. 4) and vertical nodes shifts in the lower base of the subsoil model (No. 6 in Fig. 4) were hindered by boundary conditions. No boundary conditions hindered the nodes shifts in the upper level of the subsoil model, which represented the terrain (Fig. 4 marked no. 1).

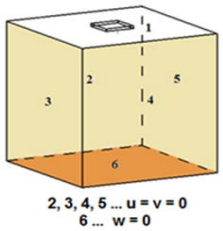

Fig. 4 Boundary conditions in the walls of the subsoil model

Subsoil model with dimensions 6.0x6.0x6.0m and with the aforementioned boundary conditions was made on the basis of parametric study [9, 17, 18], and on the basis of the influence mentioned parameters of the 3D model to the total deformation. Numerical modelling of the subsoil-structure interaction is also described in [4, 16].

The resulting stress and deformations of the post-tensioned concrete slab

The resulting deformations of the post-tensioned concrete slab model

Fig. 5 shows the total vertical deformations of the subsoil model. As expected, the maximum vertical deformation is in the centre of the slab and its value is 4.24 mm. Course and shape of the deformed model is symmetric, thus can also check the accuracy of insertion of symmetrical load, and especially of symmetric prestressing of the slab.

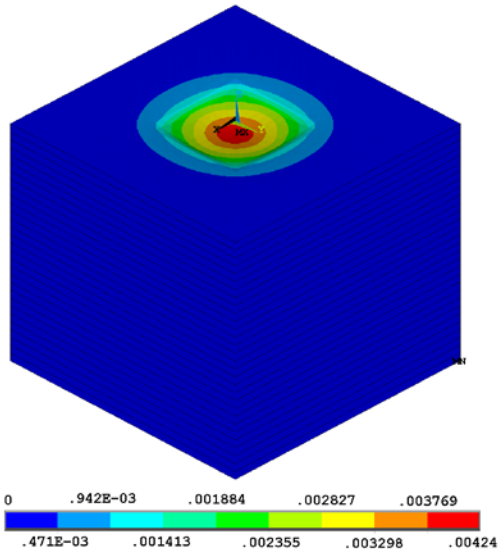

Fig. 5 The resulting vertical deformations [m]

Fig. 6 shows the horizontal deformations of the subsoil model. The course and shape of the deformed model is symmetric (in direction of the coordinate axes x and y) and for presentation of results was chosen only the state of horizontal deformations in direction of the y-axis, the deformation *v*. Horizontal deformations in direction of the x-axis have the same course, but rotated about 90^0. Deformations in the y-direction are totally symmetrical to the beginning of coordinate system situated in the centre of the slab. Horizontal deformations in y-direction toward the slab centre have the same value but the opposite sign, which is evident in Fig. 6. The deformation in the horizontal direction, x and also y, are affected by the inserted prestress. This is modelled in the level of the prestressed slab model. Fig. 6 shows the locations of the prestressed reinforcement, for clarity in direction of the y-axis. These locations are marked by cross sections A-A, B-B and C-C.

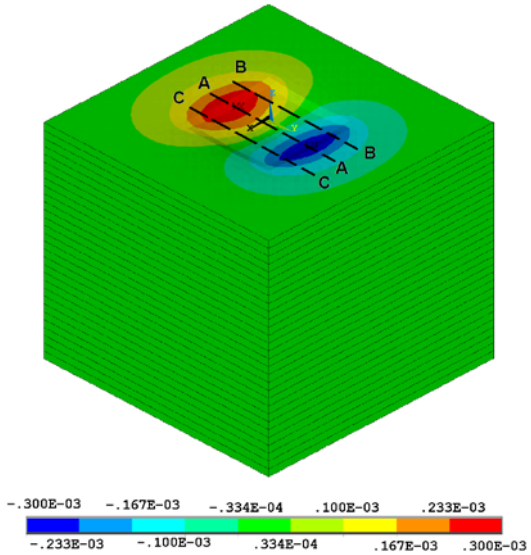

Fig. 6 The resulting horizontal deformations [m]

Horizontal deformations are depicted on the following Fig. 7 in sectional views A-A, B-B, C-C. Influence of the introduced prestressing force to the deformation in the mid-plane of the slab is shown in Fig. 7. Sections shown in the Fig. 7 are conducted in the placement of the prestressing reinforcement. This influence is the greatest under the prestressing reinforcement anchors and gradually fades towards the centre of the slab. Deformations in the y-direction are totally symmetrical to the beginning of the coordinate system, which is situated in the centre of the slab. Horizontal deformations in y-direction lead to the slab centre and they have the same value but the opposite sign, which is also visible in Fig. 7.

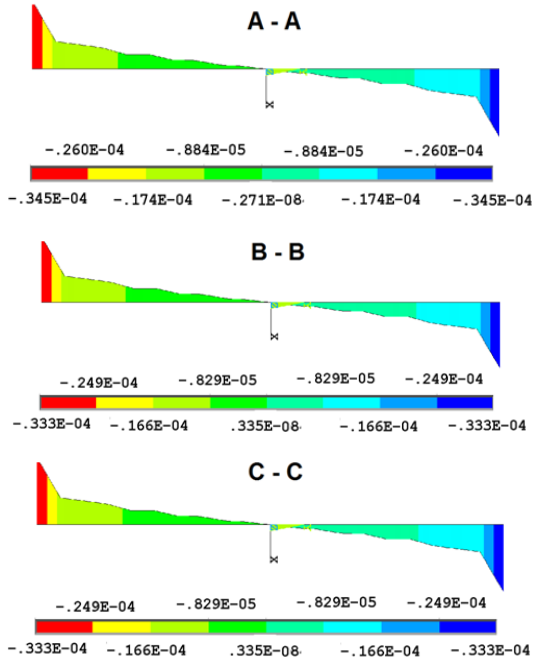

Fig. 7 Horizontal deformations in sectional views A-A, B-B, C-C, [m]

Horizontal deformations in direction of y-axis in the section A-A are larger than horizontal deformations in sections B-B and C-C. Thereby the assumption was confirmed that a horizontal deformation caused by introduced prestressing forces along the y-axis in the sectional view A-A conducted through the centre of the slab is influenced by forces introduced in the quarter of sides of the slab in sections B-B and C-C. According to the same assumption the horizontal deformations in the sections B-B and C-C are smaller and also symmetrical, which corresponds to the symmetric load and symmetric geometry of the task.

Horizontal deformations in the task without the inserted horizontal prestressing forces were also observed. This observation served mainly to the check of the numerical model and to the monitoring of the influence of introduced prestressing forces. Comparison of horizontal deformations in the y-axis direction in the section A-A with inserted horizontal prestressing forces is shown in the Fig. 8 (above) and without inserted horizontal prestressing forces is shown in the Fig. 8 (below) - this is almost zero.

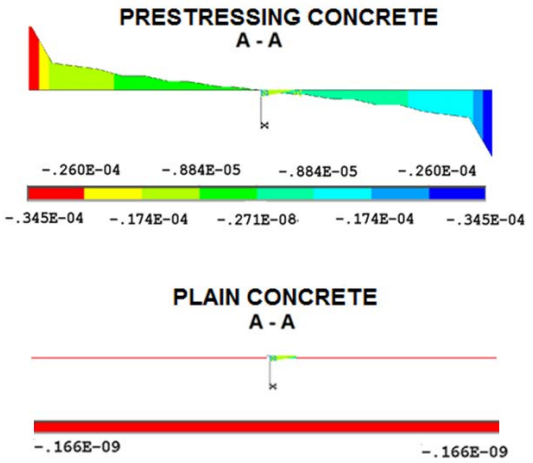

Fig. 8 Comparison of horizontal deformations of prestressing concrete slab and plain concrete slab [m]

The resulting stress of the post-tensioned concrete slab

The vertical component of stress σ_z in the subsoil is plotted in Fig. 9. Red areas show the greatest tensile stress in the location of the settlement trough of the subsoil, with values from 650 to 7817.73Pa. Yellow areas show smaller tensile stresses in the subsoil, with values of 0 to 650Pa.

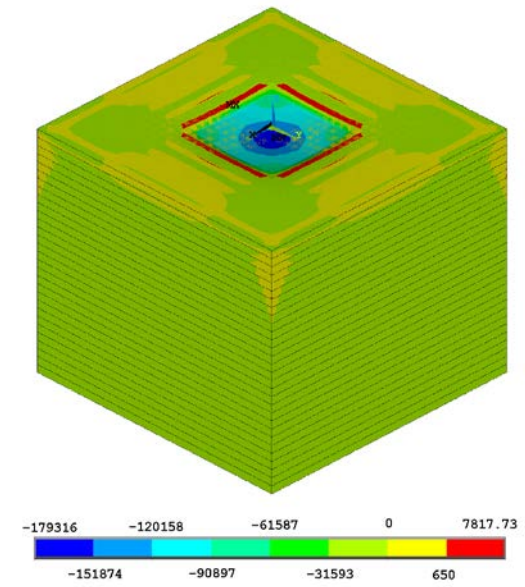

Fig. 9 The vertical component of stress σ_z [Pa]

Horizontal component of stress σ_y is depicted on the following Fig. 10 in sectional views A-A, B-B,

C-C. Influence of the introduced prestressing force to the stress σ_y in the mid-plane of the slab is shown in Fig. 10. Sections shown in the Fig. 10 are conducted in the placement of the prestressing reinforcement. Stress σ_y gradually increases toward the centre of the slab model due to vertical load applied at the centre of the slab. Introduced forces in the y-axis direction (and the x-axis direction) lead to the middle of the slab. They have the same value of 50kN and the influence under anchor also evident from Fig. 10. Course of stress σ_y depicted in Fig. 10 is the result of vertical loads and also introduced horizontal forces acting simultaneously.

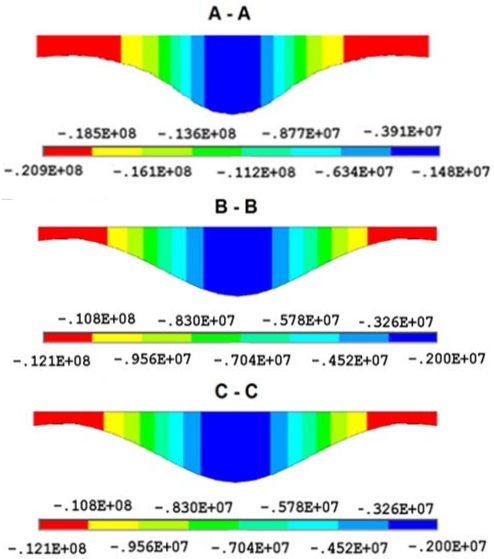

Fig. 10 Horizontal component of stress σ_y in sectional views A-A, B-B, C-C, [Pa]

Horizontal component of stress σ_y in direction of y-axis in the section A-A is larger than horizontal stress σ_y in sections B-B and C-C. Thereby the assumption was confirmed that σ_y caused by introduced prestressing forces along the y-axis in the sectional view A-A conducted through the centre of the slab is influenced by forces introduced in the quarter of sides of the slab in sections B-B and C-C. According to the same assumption the horizontal component of stress σ_y in the sections B-B and C-C are smaller and also symmetrical, which corresponds to the symmetric load and symmetric geometry of the task.

As already mentioned, stress σ_y plotted in Fig. 10 is influenced by a vertical load applied perpendicularly to the mid-plane of the slab (caused by hydraulic press) and horizontal loads in a level of the mid-plane of the slab (caused introduced forces characterizing the prestressing).

Fig. 11 shows course of the stress σ_y for both load cases. Course of the stress σ_y is plotted in the section A-A. Nevertheless, the principle of the influence of horizontal and vertical acting forces is the same even in the case of sections B-B and C-C, only values are different in comparison with the section A-A. The course of total horizontal component of stress σ_y is the sum of two partial load cases of forces acting in the direction of y-axis (ΣF_y) and the z-axis (ΣF_z).

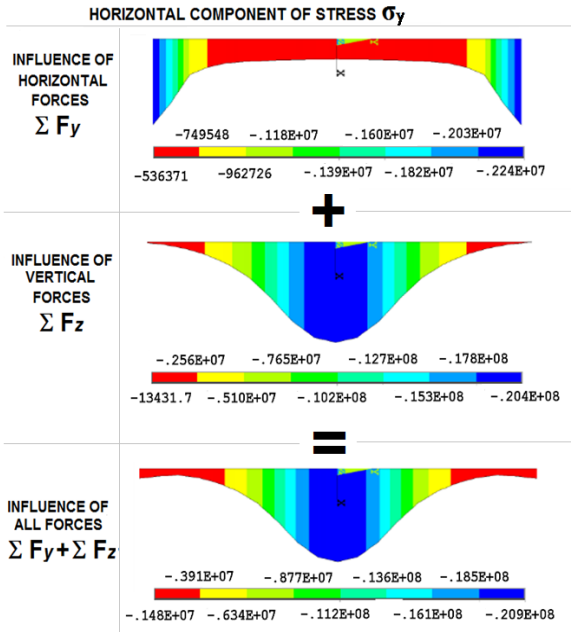

Fig. 11 Horizontal component of stress σ_y in the section A-A

CONCLUSION

Numerical analysis of the interaction of prestressed concrete slab and subsoil was carried out using an inhomogeneous half-space in which the value of the modulus of deformability increases with depth, and can be relatively well capture soil behavior. Modulus of deformability increases with subsoil depth. Experimental value of deflection in the middle of slab measured during test was 17.8mm. Result from numerical model was 4.24mm. Nevertheless value 17.8mm was determined for cracked concrete. Deflection in the middle of concrete slab was about 5mm during the first crack initiation. It is only 18% difference between numerical and tested values. The numerical model also reflected the effects of prestressing and the influence of prestressing on deformation and stress. While monitoring the effect of prestressing and its consideration in the numerical model, the emphasis was mainly on components of stress and strain in the plane of the modelled slab. However, the prestressing increases the rigidity of the element and thus has an influence during the transfer of the vertical load components. In consequence of the increase of rigidity due to the prestressing, smaller vertical deflections of the slab than in the case of prestressed slabs were calculated.

ACKNOWLEDGEMENTS

The works were supported from sources for the conceptual development of research, development and innovations for 2015 at the VSB-Technical University of Ostrava.

REFERENCES

[1] R. Halvonik, J., Fillo, "The Maximum Punching Shear Resistance of Flat Slabs, Procedia Engineering", vol.: 65, 2013, pp 376-381, ISSN 1877 - 7058,

[2] M. Aboutalebi, A. Alani, J. Rizzuto, D. Beckett, "Structural behaviour and deformation patterns in loaded plain concrete ground-supported slabs". Structural Concrete. 2014, vol. 15, issue. 1, pp. 81-93. ISSN 1464-4177.

[3] T. Clément, A.P. Ramos, M.F. Ruiz, A. Muttoni, "Influence of prestressing on the punching strength of post-tensioned slabs", Engineering Structure, vol. 72, pp. 56-69 (14 p), ISSN: 0141-0296, 2014

[4] K. Frydrysek, R. Janco, H. Gondek, "Solutions of Beams, Frames and 3D Structures on Elastic Foundation Using FEM", International Journal of Mechanics, Issue 4, Vol. 7, p. 362-369, 2013.

[5] P. Mynarcik, "The Subsidence Analysis of Experimental Post-tensioned Concrete Slab Model in the Course of the Static Load Test", Applied Mechanics and Materials, vol. 744 – 746, pp. 1556-1559 (4 p), Trans Tech Publications, Switzerland, 2015.

[6] A. Alani, M. Aboutalebi, "Analysis of the subgrade stiffness effect on the behaviour of ground-supported concrete slabs" Structural Concrete, Issue 13, Volume 2, pages 102-108, DOI: 10.1002/suco.201100043, 2012.

[7] R. Cajka, R. Fojtik, "Development of Temperature and Stress during Foundation Slab Concreting of National Supercomputer Centre IT4", Procedia Engineering, vol. 65, 2013, pp. 230-235 (6 p), ISSN 1877-7058,

[8] R. Cajka, K. Burkovic, V. Buchta, "Foundation Slab in Interaction with Subsoil", Advanced Materials Research, Vols. 838-841, pp. 375-380, Trans Tech Publications, Switzerland, 2014.

[9] R. Cajka, J. Labudkova, „Influence of parameters of a 3D numerical model on deformation arising in interaction of a foundation structure and subsoil", 1st International Conference on High-Performance Concrete Structures and Materials (COSTMA '13), Budapest, Hungary, 2013.

[10] R. Cajka, P. Mateckova, "Comparison of calculating methods and consequent carrying capacities of pre-stressed precast concrete roof purlin", in proceedings of First International Workshop "Design of Concrete Structures using EN 1992-1-1, Prague, 15 March 2010, ISBN 978-80-01-04581-7, WOS: 000324078100017.

[11] M. Janulikova, R. Cajka, P. Mateckova, V. Buchta, "Laboratory Testing of Asphalt Belts Rheological Properties Exposed to Shear Loads", Transactions of the VŠB - Technical University of Ostrava, Civil Engineering Series, vol. XII, iss. 2, pp. 59–66 (8 p), ISSN (Online) 1804-4824, ISSN (Print) 1213-1962.

[12] K. Zhou , W. W. Chen, L. M. Keer, X. Ai, K. Sawamiphakdi, P. Glaws, Q. J. Wang, "Multiple 3D inhomogeneous inclusions in a half space under contact loading", Mechanics of Materials, Vol. 43, Issue 8, Pages 444–457, 2011.

[13] V. I. Fabrikant, T. S. Sankar, „On contact problems in an inhomogeneous half-space", International Journal of Solids and Structures, Volume 20, Issue 2, Pages 159–166, 1984.

[14] K. Zhou, W. W. Chen, L. M. Keer, X. Ai, K. Sawamiphakdi, P. Glaws, Q. J. Wang, „Multiple 3D inhomogeneous inclusions in a half space under contact loading", Mechanics of Materials, Vol- 43, Issue 8, pp.444–457, 2011.

[15] R. Cajka, V. Krivy, D. Sekanina, "Design and Development of a Testing Device for Experimental Measurements of Foundation Slabs on the Subsoil", Transactions of the VŠB – Technical University of Ostrava, Civil Engineering Series, vol. XI, iss. 1, pp. 1-6, ISSN 1804-4824, ISBN 978-80-248-2332-4.

[16] R. Cajka, "Analytical derivation of friction parameters for FEM calculation of the state of stress in foundation structures on undermined territories", Acta Montanistica Slovaca, vol. 18, iss. 4, pp. 254-261 (8 p), ISSN: 13351788, 2013.

[17] R. Cajka, J. Labudkova, „Dependence of deformation of a plate on the subsoil in relation to the parameters of the 3D model", International Journal of Mechanics, Volume 8, Pages 208-215, 2014, ISSN: 1998-4448.

[18] J. Labudkova, R. Cajka, "Comparsion of Measured Displacement of the Plate in Interaction with the Subsoil and the Results of 3D Numerical Model", Advanced Material Research, vol. 1020, pp. 204-209 (6 p), Trans Tech Publications, Switzerland, ISSN (Online) 1662-8985, ISSN (Print) 1022-6680, 2014.

[19] Cajka, K. Burkovic, V. Buchta, R. Fojtik, "Experimental soil - Concrete plate interaction test and numerical models", Key Engineering Materials, vol. 577-578, pp. 33-36 (4 p), Trans Tech Publications, Switzerland, 2014.

[20] Bin Tian, Rui Li, Yang Zhong, "Integral transform solutions to the bending problems of moderately thick rectangular plates with all edges free resting on elastic foundations", Applied Mathematical Modelling, Vol. 39, Issue 1, 2015, pp. 128–136.

First International Conference on Science, Engineering & Environment,
Tsu City, Mie, Japan, Nov.19-21, 2015, ISBN: 978-4-9905958-5-2 C3051

ALTERNATIVE AGGREGATES FOR CONCRETE

Daniela Ionescu[1], Joe Petrolito[1] Bandita Mainali[1], Jemily Sweet[1] and David Robinson[1]
[1]Engineering Department, La Trobe University, Bendigo, Australia

ABSTRACT

The construction industry uses large quantities of raw materials, such as aggregates and crushed rocks, and this significantly depletes the sources of natural aggregates. Due to the environmental impacts associated with opening new quarries, the use of secondary materials, such as recycled aggregate, is being considered more often by the building industry. Also, preliminary tests on recycled aggregates have shown that recycled masonry has a similar specific gravity as scoria and relatively good strength, therefore crushed masonry can be used to replace natural aggregates for concrete production. This paper reports on continuing research at La Trobe University on the use of recycled aggregates in the production of low weight concrete. The effects of partial or total replacement of normal-weight aggregates with recycled low weight aggregates on the strength and elastic properties of concrete, and the partial replacement of water with superplasticisers were investigated. The apparent volume of permeable voids was also determined to provide an indication of the durability of the concrete. It was found that concrete mixes produced with recycled aggregates generated comparable results to mixes produced with scoria with lower production cost.

Keywords: Construction and demolition waste, Crushed brick, Recycled Aggregates, Recycled Masonry, Superplasticiser.

INTRODUCTION

Concrete forms the basis of modern life and it will continue to be a preferred construction material due to its versatility, mechanical properties and economic feasibility. Concrete can be designed for specific purposes by altering the proportions and materials of its constituents [1]. In the last decade or so, the use of recycled aggregates has become common practice to conserve natural resources, reduce solid waste to landfills and minimize environmental impacts [2]-[4].

However, the production of concrete is an energy-intensive process [3], and it accounts for 5% of man-made carbon dioxide emissions worldwide [5]. This is due to the use of cement, which consumes approximately 4 GJ of energy for each tonne produced, and the extraction of raw materials (sand, gravel, crushed rock), of which 10 to 11 billion tonnes per year are used globally [6]. New techniques are being investigated to reduce the energy needed to produce concrete as a result of these environmental concerns. The use of recycled materials in place of natural aggregates is a simple and effective way to make concrete a more sustainable construction option [3, 7].

Although not a recycled material, but rather a naturally occurring one, scoria presents itself as another ideal alternative aggregate for concrete. Scoria is a crimson, versicular igneous rock with visible air pockets that produces a lightweight material [8]. Additionally, it has a high strength to weight ratio that makes it a useful constituent in lightweight structural concrete. However, scoria has not been widely studied for this use as it is mainly used for landscaping.

Using alternative aggregates, such as recycled masonry and scoria, in concrete can somewhat compromise the durability of concrete and may also produce a low strength, unworkable concrete. Recycled aggregates have a higher water absorption than natural aggregates due to a larger amount of fines, which in turn reduces the overall strength of concrete. Additionally, it has been reported by many researchers that the workability of recycled aggregate concrete is lower than traditional concrete, especially when the replacement is greater than fifty percent [4, 6, 7, 9]. A common technique to improve the workability and mechanical properties of concrete is to incorporate a water-reducing admixture to the mix. The effects of high-range water reducers or superplasticisers on concrete has been widely researched [10]. Superplasticisers can achieve a 20% reduction in water content by dispersing cement grains through the modification of the electrical charges on the cement surface [10]. The reduction of the water content due to the use of superplasticisers with the same cement content results in a workable and strong concrete.

This paper discusses the results of a continuing study at La Trobe University into the use of crushed bricks from a local supplier (All Stone Quarry) as a partial or total aggregate replacement for the production of concrete. The effects of partial replacement of water with superplasticiser are also reported in the paper. All Stone Quarries (ASQ) is

located in Eaglehawk, Central Victoria. Each year, ASQ receives approximately 37,000 tonnes of masonry debris from local demolition operations, of which brick rubble is about 17,000 tonne, with the remainder being concrete debris. From the brick rubble received, ASQ produces about 40 % coarse (20 mm) crushed brick aggregates and 60% fine crushed brick (finer that 14 mm). Coarse aggregates are currently used for drainage purposes, whereas broader gradation aggregates are mainly used for driveways. ASQ is considering using crushed bricks for concrete production to increase its efficiency.

MATERIALS REQUIREMENTS

Aggregates play a vital role in the properties of concrete since they occupy about 75% of the concrete volume. Neville [11] reviewed the properties of aggregates that highly affect the behaviour of both fresh and hard concrete, namely strength, hardness, toughness, durability, porosity, volume change, grains shape and texture, chemical reactivity and relative density. Past research into the possible uses of crushed masonry has suggested that crushed brick has most of the required properties, and hence it may be used as a partial or total replacement for naturally occurring aggregates to produce low weight concrete [12].

Equal amounts of pull-out failure and fracturing of the coarse aggregates on the shear surface indicate a good concrete mix [11]. Hence, aggregates that have angular grains with a rough surface texture and a broad gradation produce a minimum void space in the concrete matrix. Proportions of flaky and elongated particles should be limited to avoid potential fracture planes in the concrete. Furthermore, aggregates with high water absorption should be avoided to ensure a quality concrete [11, 13].

EXPERIMENTAL PROGRAMME

The physical characteristics of the supplied materials were determined in accordance with relevant Australian Standards (primarily [14-16]) to provide a reasonable indication of their mechanical properties. The governing factors were the compliance with current specifications and the economic feasibility of obtaining the optimum material.

Concrete Aggregate

Considering the economic aspects, it was decided that the recycled crushed brick aggregates would be used as supplied with no additional crushing, sieving or washing. ASQ supplied coarse aggregates in separated fractions and fine aggregates in a blended state.

The particle size distribution (PSD) curves of the supplied materials were compared with the grading specifications and the ideal gradations for aggregates for concrete production [16, 17]. The supplied materials were also compared with the local materials currently used for concrete production. It was observed that the coarse and fine fractions combine best if Gradation 2 is used as the target gradation.

Hymix Quarry in Axedale (HQA) is one the principal suppliers of coarse and fine aggregate for the production of concrete in Bendigo. Crushed basalt (B-CA) and blended washed river sand (BWRS-FA) were used to produce the control normal-weight concrete specimens. The PSD of BWRS-FA fits closely to the coarser boundary of the specifications for natural sands (see Figure 1(a)). The gradation of the combined aggregates (coarse and fine) is shown in Figure 1(b).

Low weight concrete was produced by replacing normal-weight aggregates with light-weight natural (scoria) and recycled (brick) aggregates supplied by ASQ. Recycled brick was available in two representative samples. One sample was coarse-grained brick with a maximum nominal size of 20 mm (Br-CA) and containing few particles smaller than 6.7 mm. The second sample was classified as a fine aggregate with a maximum nominal size of 14 mm (Br-FA) as shown in Figure 1(a). When fractions coarser than 4.75 mm were separated, the PSD of fine brick fits within the boundaries set for manufactured sand and the dust (grains < 0.075 mm) content was less than 4%. The PSD of the combined coarse and fine brick aggregates is shown in Figure 1(b).

Scoria was supplied as separated coarse fractions with maximum nominal sizes of 28 mm and 14 mm, respectively. Scoria fractions were blended to obtain the coarser aggregate mix (Sc-CA), which in turn was mixed with blended washed river sand (BWRS-FA) as shown in Figure 1(b). Furthermore, to provide comparisons, coarse brick was used as a replacement for crushed basalt and was combined with blended washed sand (Br-CA + BWRS-FA in Figure 1(b). Crushed basalt was combined with recycled fine brick (B-CA + Br-FA in Figure 1(b)). Figure 1(b) shows that the PSD of the combined coarse and fine aggregates fits relatively close to the target Gradation 2 for 20 mm used in the mix design. Fines (grains < 0.425 mm) in finer aggregates from the two sources were tested for any clay content. The summary of the consistency tests [15] and clay and silt contend [18] is presented in Table 1. It was found that the finer fractions classify as non-plastic/low plasticity silts [12]. In addition, the physical properties of both coarse and fine aggregates were determined and they are summarized in Table 2. As expected, both scoria and recycled brick showed significantly higher water

absorption when compared with the currently-used aggregates. The water absorption for scoria is more than seven times that of basalt.

The water absorption for coarse recycled brick is more than four times that of basalt. In addition, the fine recycled brick has a water absorption that is more than seven times that of blended washed river sand. Scoria and recycled brick are 20% to 30% lighter than basalt and blended washed river sand, resulting in a reduced dead load for a concrete structure.

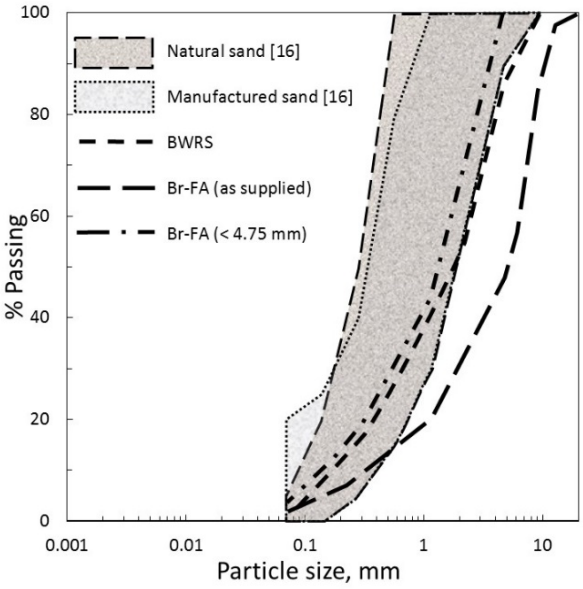

(a)

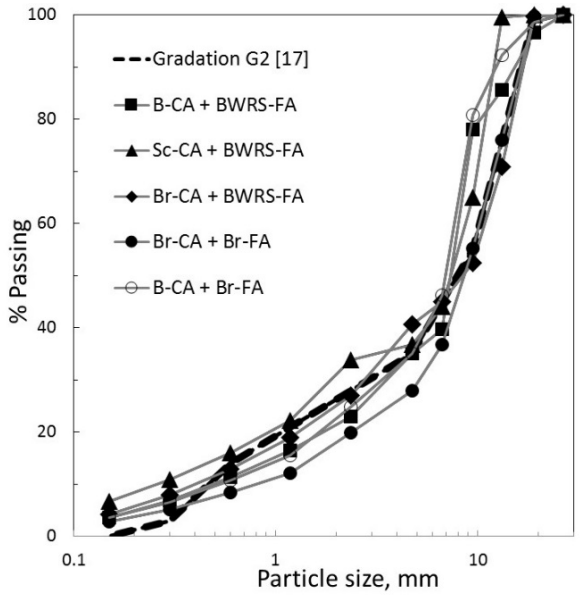

(b)

Figure 1: Particle size distribution of aggregates used to prepare the concrete specimens: (a) fine aggregates; (b) combined gradations (CA + FA) for nominal size 20 mm.

Table 1 Consistency characteristics and silt content in fine aggregates

Material	w_L (%)	w_P (%)	PI (%)	LS (%)	SC (%)
BWRS-FA	18	14	4	2	6
Br-FA	19	16	3	1	7

Note: w_L = liquid limit, w_P = plastic limit, PI = plasticity index, LS = linear shrinkage, SC = silt content.

Table 2 Physical properties of aggregates used

Material	MC (%)	WA (%)	$\rho_{p\text{-}SSD}$ (t/m^3)
B-CA	1.2	2.23	2.72
Sc-CA	6.7	17.7	1.85
Br-CA	2.2	7.0	2.20
BWRS-FA	0.1	0.6	2.61
Br-FA	2.4	4.6	2.44

Note: MC = moisture content, WA = water absorption, $\rho_{p\text{-}SSD}$ = particle density in saturated surface dry condition.

Concrete Strength

Five concrete mixes were produced with the supplied materials as follows:

- HQA coarse basalt and blended washed river sand (B-CA + BWRS-FA)
- ASQ coarse scoria and HQA blended washed river sand (Sc-CA + BWRS-FA)
- ASQ coarse recycled brick and HQA blended washed river sand (Br-CA + BWRS-FA)
- ASQ coarse and fine recycled brick (Br-CA + Br-FA)
- HSQ coarse basalt and ASQ fine recycled brick (B-CA + Br-FA).

The quantities for the concrete mixes were based on a nominal characteristic compressive strength of 32 MPa. A 50-mm slump was use [19] and the aggregates were used in the air-dried condition. Table 3 presents the quantities of materials used for each mix designed in accordance with Australian Standards [14]. It should be mentioned that the addition of 2 L/m^3 of superplasticiser enabled a reduction of water content by 9-28% depending on the mix prepared. Tables 4 and 5 summarize the average strength of concrete and density of concrete at seven and 28 days. Prior to testing concrete specimens were water cured to enable proper growth of calcium silicate hydrate crystals. As expected the density of concrete increased with age and concrete produced with the alternate aggregates had a lower density independent of the age of the concrete. Concrete produced with scoria (CA) and blended washed river sand (FA) exhibited the largest reduction in density (more than 10%), whereas

concrete produced with basalt (CA) and crushed brick (FA) showed an insignificant density change. As expected, the strength of concrete increased with age. However, the increase in strength varied significantly

Table 3 Mix design proportions used

Mix type	c (kg)	w (kg)	FA (kg)	CA (kg)
B-CA+BWRS-FA	370	166	620	1090
Sc-CA+BWRS-FA	370	180	620	680
Br-CA+BWRS-FA	370	188	620	950
Br-CA+Br-FA	370	216	530	950
B-CA+Br-FA	370	196	530	1090

Note: c = cement, w = water, FA = fine aggregates and CA = coarse aggregates.

Table 4 Average properties for 7 days old concrete

Mix type	f_{cm} (MPa)	$f_{ct.sp}$ (MPa)	$f_{ct.f}$ (MPa)	$\rho_{p\text{-}SSD}$ (kg/m^3)
B-CA+BWRS-FA	62.5	4.9	6.6	2420
Sc-CA+BWRS-FA	43.0	3.8	6.1	2100
Br-CA+BWRS-FA	48.5	4.1	5.7	2260
Br-CA+Br-FA	38.0	3.0	5.0	2190
B-CA+Br-FA	67.5	4.1	6.1	2400

Note: f_c' = characteristic compressive (cylinder) strength of concrete at 7 days, $f_{ct.sp}$ = measured splitting tensile strength of concrete, $f_{ct.f}$ = measured flexural tensile strength of concrete.

Table 5 Average properties for 28 days old concrete

Mix type	f_c' (MPa)	$f_{ct.sp}$ (MPa)	$f_{ct.f}$ (MPa)	$\rho_{p\text{-}SSD}$ (kg/m^3)
B-CA+BWRS-FA	81.5	5.2	7.4	2440
Sc-CA+BWRS-FA	45.5	3.9	6.3	2120
Br-CA+BWRS-FA	59.0	4.2	5.8	2280
Br-CA+Br-FA	52.0	3.5	5.4	2200
B-CA+Br-FA	73.0	4.3	6.9	2420

Note: f_c' = characteristic compressive (cylinder) strength of concrete at 28 days, $f_{ct.sp}$ and $f_{ct.f}$ as defined above.

for the mixes used. At seven days, the strength of concrete produced with alternate aggregates was 60-78% of that of the control batch. It is worth noting that the strength of concrete produced with masonry was 8% higher than that of the control batch. At 28 days, the strength reduction of concrete produced with the alternate aggregates was even larger, from 10% for basalt (CA) and crushed brick (FA) to 44% for scoria (CA) and blended washed river sand (FA). Similarly, the indirect tensile strength of concrete produced with the alternate aggregates was 16-33% lower than that of the control batch, whereas the flexural strength was 7-27% below that of concrete with normal aggregates. In most cases, concrete produced with recycled brick (CA+FA) showed the largest reduction in strength, perhaps due to a slightly higher clay content in FA. The strength reduction was higher for the 28-day concrete, and this can possibly affect the concrete durability.

Elastic Properties of Concrete

Tables 6 and 7 summarize modulus of elasticity and Poisson's ratio values obtained from the elasticity tests performed in accordance with Australian Standards [14]. The computed values of the modulus of elasticity used the empirical relationship recommended by the Australian Standard [20], namely

$$E_{cj} = \rho^{1.5} \times \left(0.024 \times \sqrt{f_{cmi}} + 0.12\right) \qquad (1)$$

where E_{cj} is the mean value of the modulus of elasticity of concrete at a certain age, ρ is the density of concrete measured in accordance with the relevant specifications [14] and f_{cmi} is the mean value of the compressive strength of concrete at the relevant age.

The computed and the measured values of the modulus of elasticity compare quite well, with the former being higher (2-16%). In addition, it should be noted that the trends observed from the strength tests were replicated by the elastic properties. A higher strength is correlated with a higher modulus of elasticity and a lower Poisson's ratio.

Concrete mix prepared with both FA and CA recycled brick displayed the highest reduction (41-47%) in the modulus of elasticity, followed by the mix produced with scoria (CA) and blended washed river sand (FA) with a reduction of 31-32%. The concrete produced with recycled brick (CA) and blended washed river sand (FA) showed a 28-29% reduction in the modulus of elasticity, whereas the concrete mix produced with basalt (CA) and crushed brick (FA) showed only a 13-16% reduction in the modulus of elasticity. As expected, the reductions in the modulus of elasticity for the mixes produced with alternate aggregates were higher at seven days. As the concrete strength increases with age, it is expected that some of the negative effects of the alternate aggregates on the modulus of elasticity will diminish with time. However, a lower modulus of elasticity is expected to be associated with more creep deformation and possibly higher shrinkage.

Durability of Concrete

There is general agreement that there is an indirect correlation between the water-permeable voids present in the hardened concrete and the durability

of concrete. Hence, the water absorption and the apparent volume of permeable voids were determined from tests performed in accordance with Australian Standards [14] and the results are presented in Table 8. As expected, the use of porous aggregates resulted in an increase in the apparent volume of permeable voids (AVPV). Concrete produced with

Table 6. Elastic properties for seven days old concrete

Mix type	E (MPa)		ν
	Measured	Empirical	
B-CA+BWRS-FA	38000	39000	0.19
Sc-CA+BWRS-FA	26000	26000	0.15
Br-CA+BWRS-FA	27000	31000	0.17
Br-CA+Br-FA	20000	23000	0.15
B-CA+Br-FA	32000	37000	0.16

Note: E = modulus of elasticity, ν = Poisson's ratio.

Table 7 Elastic properties for 28 days old concrete

Mix type	E (MPa)		ν
	Measured	Empirical	
B-CA+BWRS-FA	39000	39000	0.17
Sc-CA+BWRS-FA	27000	27000	0.12
Br-CA+BWRS-FA	28000	32000	0.16
Br-CA+Br-FA	23000	25000	0.15
B-CA+Br-FA	34000	38000	0.15

Table 8 Apparent volume of permeable voids for 28 days old concrete (with superplasticiser)

Mix type	Immersed absorption (%)	Boiled absorption (%)	Apparent volume permeable voids (%)
B-CA+BWRS-FA	5.6	5.8	13.5
Sc-CA+BWRS-FA	8.1	8.7	18.5
Br-CA+BWRS-FA	7.2	7.3	15.5
Br-CA+Br-FA	9.6	9.9	16.2
B-CA+Br-FA	6.6	6.2	14.0

scoria showed the highest AVPV followed closely by the concrete prepared with recycled brick aggregates. It is interesting to note that the Br-CA + Br-FA batch showed the highest water absorption in 24 hours. This indicates that this concrete is not suitable for wet areas. Table 9 summarizes the AVPV for all the concrete mixes without superplasticizers. The addition of superplasticizer enabled the production of a more compact concrete, which resulted in a lower (15-24%) apparent volume of permeable voids and this produces a more durable concrete.

CONCLUSIONS

The effects of light aggregates (scoria and recycled brick) used for low weight concrete production were discussed in this paper and the following conclusions can be drawn.

The use of scoria as a CA resulted in the lowest density concrete of the five batches, and the strength, elastic properties and durability of the concrete were

Table 9 Apparent volume of permeable voids for 28 days old concrete (without superplasticiser) [12]

Mix type	Immersed absorption (%)	Boiled absorption (%)	Apparent volume permeable voids (%)
B-CA+BWRS-FA	6.8	7.0	16.1
Sc-CA+BWRS-FA	9.8	11.7	22.2
Br-CA+BWRS-FA	8.5	9.0	18.3
Br-CA+Br-FA	10.6	10.9	21.3
B-CA+Br-FA	8.1	8.3	18.0

reduced as well.

Similar outcomes were obtained when the concrete was produced with coarse and fine recycled brick aggregates. The only advantage of these aggregates is the lower cost of production in comparison with scoria.

Partial replacement of natural aggregates (that is, replacing B-CA with Br-CA or replacing BWRS-FA with Br-FA) appears to be a suitable solution for low weight concrete. Br-CA + BWRS-FA and B-CA + Br-FA mixes produced concrete with acceptable strength and elastic properties, although slightly lower than the currently-used mixes, B-CA+ BWRS-FA. Hence, their use may result in a less durable concrete due to a higher volume of permeable voids. The use of superplasticizer improved the properties of the concrete, resulting in a higher strength and a lower volume of permeable voids. The durability of concrete may possibly be further improved if water-repellent admixtures are added to the mix. Overall, the cost of production of concrete with recycled brick aggregates is lower than that of normal-weight concrete, while providing environmental benefits.

ACKNOWLEDGEMENTS

The authors gratefully acknowledge the help provided by All Stone Quarry, Bendigo with the supply of materials. The assistance with preparation and testing provided by Mr David Osborne is also recognized.

REFERENCES

[1] Kosmataka SH and Willson ML, "Design and control of concrete mixtures: The guide to applications, methods and materials", Portland Cement Association, 2011.
[2] Tam VWY and Tam CM, "A review of the viable technology for construction waste recycling resources", Conservation and Recycling, Elsevier, Vol. 47, Jan. 2006, pp. 209-221.
[3] Del Rio Merino M, Gracia PI and Azevedo IS, "Sustainable construction: construction and demolition waste considered", J. of Waste Management and Research, Vol. 28, 2010, pp. 118-129.
[4] Cavalline TL and Weggel DC, "Recycled brick masonry aggregate concrete", Structural Survey, Vol. 31, Mar. 2013, pp. 160-180.
[5] Sabnis GM, "Future sustainable city: The case of Masdar city", Green Building with Concrete: Sustainable Design and Construction, 2nd Ed. Sabnis GM (ed), Boca Raton: CRC Press, 2015.
[6] Mehta KP, "Reducing the environmental impact of concrete", Concrete International, Vol. 23, No. 10, 2001, pp. 61-66.
[7] Ionescu D, "Sustainable civil engineering materials", Incorporating Sustainable Practice in Mechanics of Structures and Materials, Fragomeni, Venkatesan, Lam and Setunge (eds), CRC Press: Taylor and Francis Group, 2010, pp. 833-838.
[8] Estes MB, Ritterbush LW and Nicolaysen K, "Clinker, pumic, scoria, or paralave? Vesicular artifacts of the Lower Misouri Basin", Plains Anthropologist, Vol. 55, No. 213, 2010, pp. 67-81.
[9] Rao A, Jha KN and Misra S, "Use of aggregates from recycled construction and demolition waste in concrete", J. of Resources, Conservation and Recycling, Vol. 50, 2007, pp. 71-81.
[10] Hover KC, "Concrete mixture proportioning with water-reducing admixtures to enhance durability: A quantitative model", J. of Cement and Concrete Composites, Vol. 20, 1998, pp. 113-119.
[11] Neville AM, Properties of Concrete, 4th Ed., Harlow: Pearson Prentice Hall, 2005.
[12] Ionescu D, Mainali B, Petrolito J, Al Abadi H, Davies S and Dickens B, "Construction potential of recycled masonry for concrete", Sustainable Solutions in Structural Engineering and Construction, Saha, Lloyd, Yazdani, and Singh (Eds), ISEC Press, accepted, 2015.
[13] Gani MSJ Cement and concrete, London: Chapman and Hall, 2000.
[14] Standards Australia, Methods of Testing Concrete, AS 1012, Sydney: Standards Australia, 2000.
[15] Standards Australia, Methods of Testing Soils for Engineering Purposes, AS 1289, Sydney: Standards Australia, 2005.
[16] Standards Australia, Aggregates and Rock for Engineering Purposes - Concrete Aggregates, AS 2758.1, Sydney: Standards Australia, 2014.
[17] Cement & Concrete Association of Australia (C&CAA), Design, Control and Characteristic of Concrete, UDC 620.1, Sydney: C&CAA, 1976.
[18] Standards Australia, Methods of Sampling and Testing Aggregates – Method 33: Clay and Fine Silt (Settling Method), AS 1141.33, Sydney: Standards Australia, 1997.
[19] Cement & Concrete Association of Australia (C&CAA), Guide to Concrete Construction, C&CAA T41, Sydney: Standards Australia, 2002.
[20] Standards Australia, Concrete Structures, AS 3600, Sydney: Standards Australia, 2009.

First International Conference on Science, Engineering & Environment,
Tsu City, Mie, Japan, Nov.19-21, 2015, ISBN: 978-4-9905958-5-2 C3051

GENERALIZED STRENGTH DEVELOPMENT MODEL OF SOLIDIFIED FINE-GRAINED DREDGED MARINE SOILS

Chee-Ming Chan[1] and Amira Azhar[2]
[1]Faculty of Engineering and Technology, Universiti Tun Hussein Onn Malaysia, Malaysia
[2]Faculty of Civil and Environmental Engineering, Universiti Tun Hussein Onn Malaysia, Malaysia

ABSTRACT

Dredged marine soils (DMS) are the sediment and debris removed in the dredging process. Large amount of DMS is generated from the dredging operations yearly, especially from the maintenance of existing shipping channels and the development of various coastal infrastructures. In practice, DMS are generally disposed of at designated offshore dump sites. Inadvertently, these discarded DMS would in time be deposited back near shore due to tidal dynamics, necessitating dredging works again. Considering that DMS are essentially soils with poor engineering properties, particularly low shear strength, there could be potential for the materials' reuse as acceptable or good geomaterials if the original conditions can be improved. Pre-treatment for enhancement of the soil's strength, such as solidification, is a feasible option. In the present study, the solidification of 3 DMS samples was examined with the admixing of cement and/or bottom ash, where cement acts as a binder while the bottom ash functions a filler material to lend structure to the weak soil. The strength improvement of the solidified DMS was monitored with the unconfined compression tests. The key factors that influence strength development in solidified soils were investigated, i.e. curing period, water-binder ratio and binder-filler mix ratio. The curing period was prefixed at 3, 7, 14, 28 and 56 days, while the water-binder ratio examined were 1, 3 and 5. The test results indicated that strength increased with curing time and higher water-binder ratio. The optimal binder-filler mix ratio determined was 75 % cement to 25 % bottom ash. The bottom ash was found to contribute to strength gain too, albeit in a minor way compared to the highly reactive cement. For the generalized strength development plots, the unconfined compressive strength of a particular day (q) was divided with the strength on day 28 (q_{28}). The resulting q/q_{28} vs. curing period plots were linear with varying gradients dependent on the water-binder ratio, though it was apparent that the gradient of the plot decreased with increased water-binder ratio. In summary, solidification with cement-bottom ash is expedient in improving the original low strength of the DMS, and the generalized strength development model is useful for modeling, design and prediction on site.

Keywords: Dredged marine soils; solidification; water-binder ratio, cement, bottom ash, strength development

INTRODUCTION

Dredging is defined as underwater excavation of soils and rock that generates large volume of dredged marine soils [1]. Dredged marine soils (DMS) are the sediments and debris were removed during the dredging process [2]. Every year, hundreds of million cubic meters of DMS are generated from the dredging operations. For instance, the volume of DMS removed in the maintenance dredging works at Kuala Perlis alone was reported to be 300,000 m^3 within 2-3 years [3].

In Malaysia, DMS are considered a geowaste and are therefore not being considered for recycling or reuse. In general, the DMS are disposed off in open waters at designated locations [4]. Unfortunately, after a certain time, these DMS would be re-deposited near shore with the wave dynamics and tidal effects, and dredging would be required again.

The disposal of DMS is mainly due to economic, logistical, legislative and environmental constraints, as well as a lack of understanding of the materials' reuse potential. DMS can be a valuable resource and a reusable material for construction purposes, unless the dredged material is found to be excessively affected by industrial contaminants. For example, if the dredged material consists of coarse particles, it can be reused in backfills, while the finer particles can be used for landscaping or improving agricultural land [1]. Indeed, the reuse of DMS can make major contribution towards sustainable development, simultaneously reducing the quantities of primary resources needed for construction and habitat creation activities [5].

The fine-grained DMS is usually grey in colour with high plasticity, and contains predominantly clay and silt fractions. The plastic limit and plasticity index were often found to be significantly high and that the optimum moisture content upon compaction was generally below the plastic limit [6 & 7]. These inherent physical properties indicate the poor engineering properties of the material, especially in terms of load resistance. For reuse, DMS need to undergo some form of pre-treatment to enhance the

strength. An alternative is to admix binding additives like cement with the DMS to both reduce the initially high moisture content and to subsequently improve the engineering properties via cementation [1].

The components of solidification include soils and binders. As mentioned above, the binders used are normally cementitious materials [8]. Coarse particles can also be admixed with the soil as filler materials to lend structure for the bonding process, i.e. enhance the resulting strength improvement. 3 DMS samples were used in the present study, with cement used as the binder and bottom ash added as a filler material respectively.

MATERIALS AND METHODS

Test Materials

3 types of fine-grained dredged marine soils (DMS) were used in this study, and they were all sourced from the Malaysian waters. The first DMS sample was retrieved from Marina Melaka, Melaka (sample MM). According to the Unified Soil Classification System (USCS) [9], the sample was classified as a high plasticity clay (CH). The second and third samples were collected from Tok Bali, Kelantan, samples TBA and TBB. These samples were classified as high plasticity (MH) and low plasticity silt (ML) respectively. The binder used in this study was ordinary Portland cement (C) while the filler added was bottom ash (BA). The bottom ash was collected from Tanjung Bin coal power plant in the locality. The properties of the DMS, OPC and BA are shown in Table 1, while Table 2 summarizes the chemical compositions of the DMS, cement (C) and filler, i.e. bottom ash (BA).

Table 1: Properties of dredged marine soil samples

Properties	DMS samples			C	BA
	MM	TBA	TBB		
Moisture content (%)	142.97	137.60	92.23	-	-
Liquid limit (%)	65.00	51.80	36.90	-	-
Plastic limit (%)	50.46	35.30	25.83	-	-
Plasticity index (%)	14.54	16.50	11.07	-	-
Specific gravity	2.56	2.43	2.41	3.10	2.30
Loss on ignition (%)	9.49	1.38	4.78	-	-
pH	8.32	8.53	8.51	12.35	9.17
Soil classification	CH	MH	ML	-	-

Table 2: Chemical compositions of DMS, C and BA (%)

Chemical composition	DMS samples (soil type)			C	BA
	CH	ML	MH		
Al_2O_3	21.60	21.10	24.40	9.52	26.60
CaO	1.93	4.04	4.04	54.10	8.73
Fe_2O_3	7.33	7.05	7.87	5.32	8.51
K_2O	2.97	2.64	2.66	0.88	1.05
MgO	2.18	2.24	1.91	1.20	1.76
SiO_2	57.00	57.00	54.40	24.50	48.80
TiO_2	1.03	0.85	0.87	0.69	1.95
Others	5.96	3.67	4.95	3.79	2.6

Specimen Preparation and Test Methods

The DMS were mixed with the additives based on predetermined water-binder (w/b) ratio as well as C:BA portions. Calculations for the amount of cement and bottom ash for each mixture was made based on dry mass and moisture content of the soil. The w/b ratios were fixed at 1, 3 and 5. Elaborations on the mix ratio derivation can be referred to in Azhar *et al.* [10].

The mixing procedure began with remoulding of the DMS which was left standing overnight to ensure uniform pore water distribution in the soil mass. The measured dry cement and bottom ash were then added to the remoulded soil. The mixture was initially hand-mixed with a spatula prior to more vigorous mixing with a kitchen mixer. The mechanical mixing process was paused every 3 minutes, so that materials adhering to the sides of the mixing bowl and mixing paddle can be scraped off and returned to the bowl. The steps were repeated 2-3 times till all cement and bottom ashes were thoroughly mixed with DMS.

The mixture was next transferred to a cylindrical split mould to form specimens of 38 mm in diameter and 76 mm in height. In 3 equal layers, the mixture was flattened and lightly compressed and kneaded using a miniature compaction tool. Upon removal of the mould' collar, the excess mixture was trimmed off and the cylindrical specimen was slid out of the mould. Wrapped in cling film and stored on raised platforms in a tight-lid bucket with mild bleach solution to prevent fungal growth, the specimens were left to cure for 3, 7, 14, 28 and 56 days prior to the unconfined compression tests.

The unconfined compression tests were conducted according to BS 1377:1990, Part 7 [11]. Load was applied at a rate of 1.5 mm per minute and the data were recorded in a stress-strain plot for determination of the maximum stress, i.e. unconfined compressive strength, q. Duplicate samples were tested to verify reliability of the measurements.

Table 3: Mix portions of cement and bottom ash

Specimen	Portion of cement, C (%)	Portion of bottom ash, BA (%)
100C	100	0
75C25BA	75	25
50C50BA	50	50
25C75BA	25	75

RESULTS AND DISCUSSIONS

As mentioned earlier, without any solidification process or treatment, the natural dredged soil has limited undrained shear strength for load-bearing. The undrained shear strength of natural DMS is often no more than 50 kPa [12]. Therefore the solidification process was aimed at improving the strength of the naturally weak material for possible reuse as good soils. Results from the unconfined compression tests are compiled and discussed below.

Fig. 1 shows the unconfined compressive strength (q) of the solidified CH, MH and ML samples plotted against the water-binder ratio (w/b). It is immediately apparent that higher w/b resulted in lower strength gain, irrespective of the soil type. Compiled with data from past studies of similarly treated fine-grained marine soils from Bangladesh and Singapore [13, 14 & 15], the trend was found to be similar as that of the present study. Note that all 3 samples were not admixed with binders at w/b less than 2, with resulting strengths of no more than 2 MPa. While the data points at w/b greater than 5 appears to confirm the expected diminishing trend of the q-w/b plot, the strengths recorded in the present study do seem to be higher in the w/b range of 3 to 5. Some factors that can account for the discrepancies are the type of binders used, curing time and pore water chemistry.

The increased strength with lower w/b can be attributed to the amount of cement and bottom ash used in the solidification. Inversely related, lower w/b corresponds with higher cement dosages at the same water content. Hence as w/b decreased, the amount of cement in the DMS increased, producing more effective solidification and strength gain. At approximately w/b=3, the q-w/b relationship appeared to level off, as depicted by the rather drastic change in gradient of the plot in Fig. 1 to a plateau. It is indicative that beyond a certain w/b, i.e. 10 in this case, strength improvement was no longer significant with almost unchanged q with higher w/b.

When too much water is present in the soil-additive mixture, flocculation tends to occur with the cemented aggregates of soil-BA dispersed in a porous matrix [16]. Without good contact between the cemented aggregates, load resistance would be limited as the voids are filled with semi-solidified fine particles. Also, the amount of cement available for reaction with the excess water was disproportionate, causing the mixture to harden but not strengthened. This can be observed in the greater deformation recorded of the weaker specimens in the unconfined compression test. Radial deformation accompanied by vertical displacement resulted in apparent bulging of these specimens prior to failure.

Fig. 2 illustrates the strength (q) recorded for all specimens at different curing time (D). Immediately noticeable is the remarkable strength improvement charted by CH compared to MH and ML, particularly at w/b=1. This could be explained by the greater specific area of the finer grained CH soil available for reaction with the cement and eventual soil-BA bonding. Note that clay particles are smaller than 2 μm, whereas silt particles range between 2 and 75 μm [9]. Comparing the q-D plots at w/b=3 for MH and ML, there appeared to be a continuous rise in strength for ML while MH demonstrated a decline in strength gain rate beyond 28 days of curing. Nonetheless at the final measurement age, i.e. 56 days old, both MH and ML showed very similar q attained for all C-BA mix ratios.

It is also apparent that the unconfined compressive strength attained by the solidified soil is very much dependent on the w/b ratio, with increased w/b resulting in lower strengths. This is in line with earlier discussions referring to Fig. 1, where q declined with increased w/b. The seeming banding of the q-D plots according to w/b for all soil samples also suggests the dominant influence of w/b on the resulting strength of the solidified soil. In general, the steep rise in q with time was sustained up to 14 days of curing, after which the gradual turn in the plots of Fig. 2 indicates less remarkable strength gain even with prolonged curing. The initial high water content apparently impeded further strength improvement of the soil.

To examine the influence of curing on the solidified strength, q/q28 is plotted against curing time (D) in Fig. 3. For w/b=1, the rate of strength improvement from day 3 to day 28 is higher compared to the subsequent days. This indicates that the cementation process which includes hydration and pozzolanic reactions were most active in the first 4 weeks. There was almost no increment at all in strength after day 28 as shown in the w/b=1 plots in Fig. 3. For w/b=3 and w/b=5, the strength increased steadily from day 3 till day 56, though the strength increment rate in w/b=3 was clearly higher. This could be due to the less excessive water present in the soil-additives mixtures. However, in both cases of w/b=3 and w/b=5, the strength is expected to keep rising with prolonged curing.

In the same plots in Fig. 3, comparison was made with results of treated Bangkok clay as derived by Horpibulsuk *et al.* [17], which is similar to the

materials used in the present study (w/b = 3, 5 and 10). Gradient of the q/q_{28}-D plot can be seen to reduce with prolonged curing, pointing to the reduced strength gain as well as diminishing influence of w/b on the solidified strength of different C-BA mix ratios. Nevertheless the best sustained strength improvement ratio is observed in specimens with w/b=3, with q/q_{28} at 56 days clustered according to the soil type, i.e. CH, MH and ML in ascending order. This is an indicator of soil type dependency of strength gain with solidification, though at a certain w/b ratio. More detailed work is required to validate this postulation though. In addition, the best fit line for Bangkok clay [17] was found to line up best with that of w/b=5. This is suggestive of a common q/q_{28}-D correlation for solidified soils pre-dominated by the w/b ratio.

CONCLUSIONS

The strength development of solidified DMS is influenced by w/b and curing period. It was observed that as w/b decreases, the strength (q) would increase regardless of the soil type. The q-w/b plot shows significant drop of strength with increased w/b up to approximately w/b=5, beyond which q appeared to be rather insensitive towards the change in cement dosage with excessive water in the mixture. On the other hand, the normalized strength of the solidified DMS (q_u/q_{28}) – curing time relationship at w/b=5 was found to be compatible with reports by Horpibulsuk *et al.* [17]. This suggests a universal correlation of q-D irrespective of the origin of the fine-grained soils. It is however uncertain if the agreement between different soils types would persist at w/b ratio more than 5. Further work could be directed at identifying the extent of the compatibility with increased w/b.

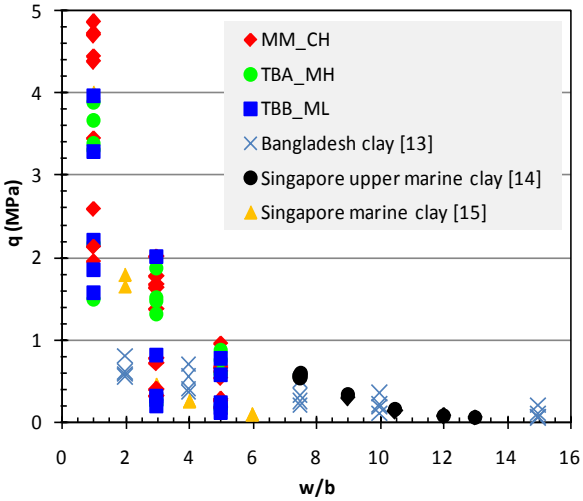

Fig. 1: q - w/b plot

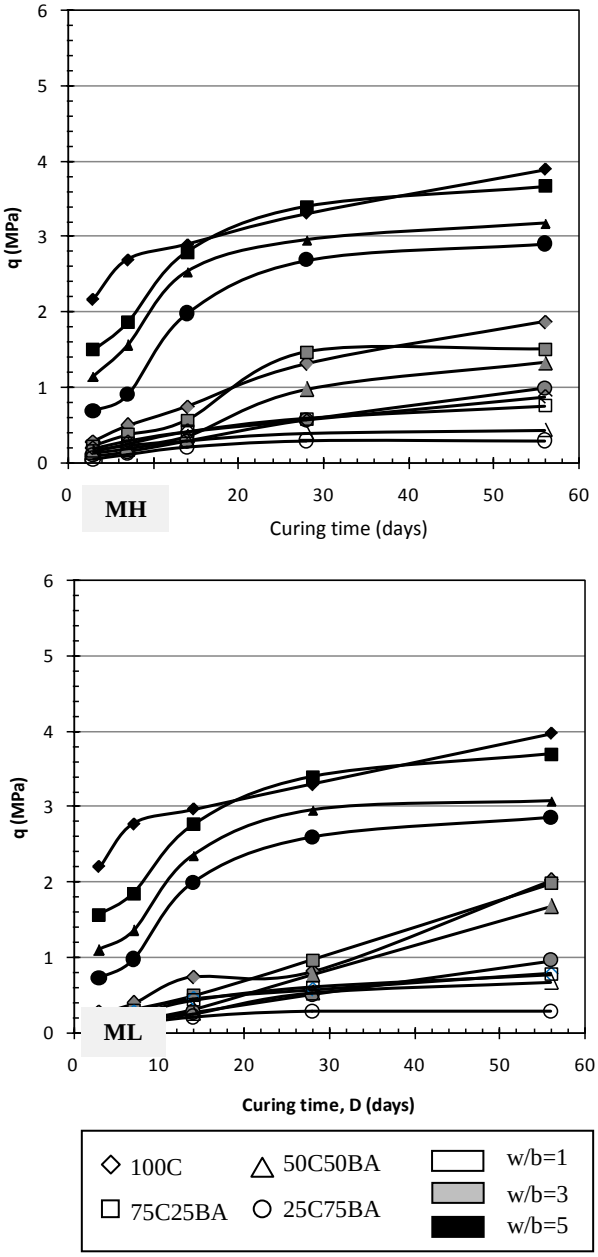

Fig. 2: q - curing time plots

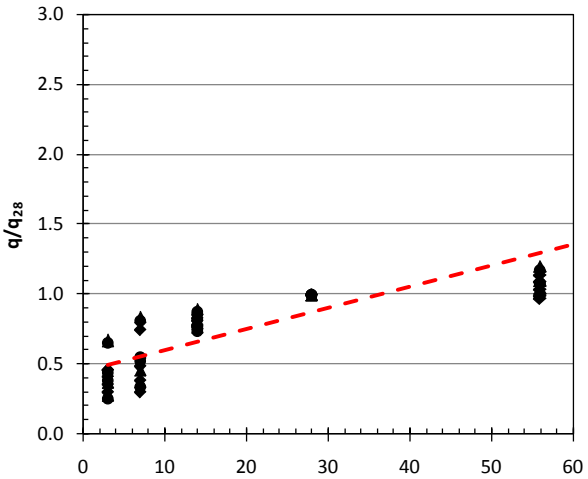

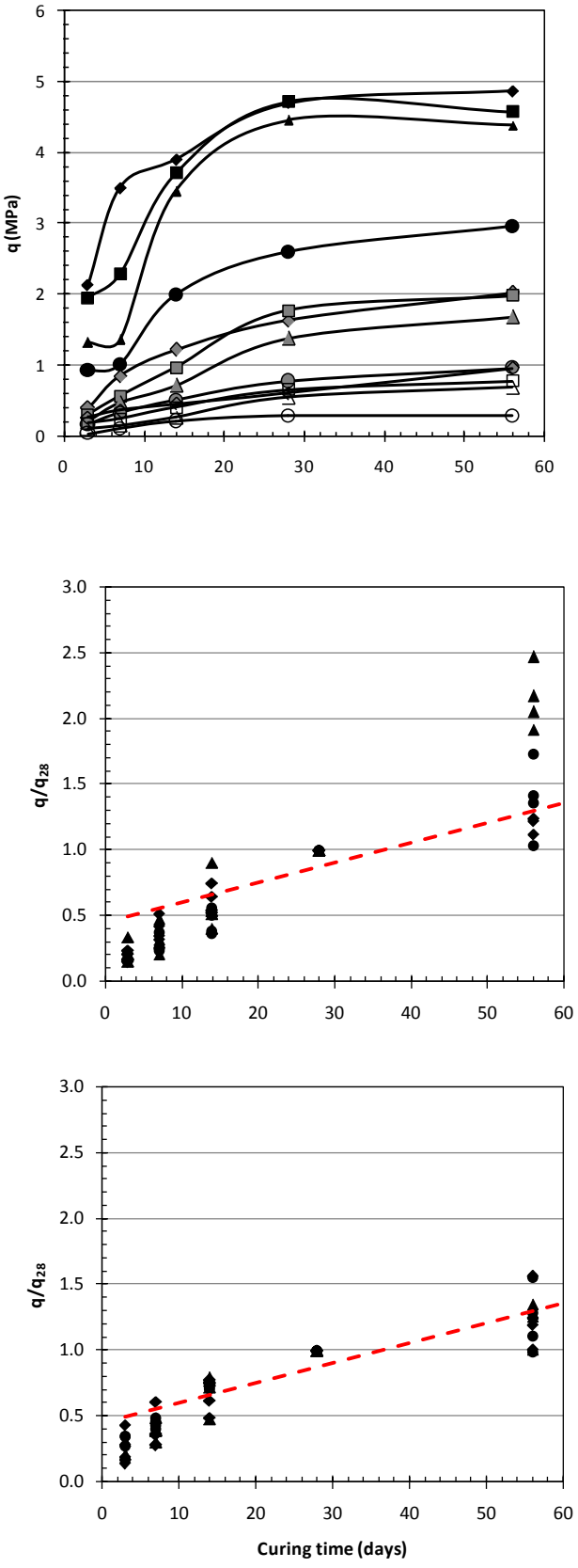

ACKNOWLEDGEMENT

The technical support from the RECESS laboratory is duly acknowledged. Funds for the study were provided by Research Grant ScienceFund S025, MOSTI and ORICC, UTHM.

REFERENCES

[1] Bray N & Cohen M, Dredging for Development: A Joint Publication, 6th ed. Netherlands & Japan: IADC & IAPH, 2010.

[2] Maher A, Douglas WS, Jafari F & Pecchioli J, The Processing and Beneficial Use of Fine-grained Dredged Material: A Manual for Engineers. New Jersey, Washington: RUTGERS Centre for Advanced Infrastructure and Transportation, 2013.

[3] Wan Salim WS, Mohd Noor NA, Sadikon SF, Arshad MF, Wahid N & Mohd S, "The preliminary investigation on the dredged marine sediment of Kuala Perlis as a potential brick material", in Proc. 2nd Int. Conf. on Biotechnology and Environment Management (IPCBEE), 2012, pp. 25-29.

[4] Rekik B & Boutouil M, "Geotechnical properties of dredged marine sediments treated at high water/cement ratio", Geo-Marine Letters, Vol. 29(3), 2009, pp. 171-179.

[5] CEDA, Dredging and the Environment: Moving Sediments in Natural Systems. CEDA Information Paper, 2009.

[6] Rao DK, Raju RP, Sowjanya C & Rao P, "Laboratory studies on the properties of stabilized marine clay from Kakinada sea coast, India", Int. J. of Engineering Science and Technology (IJEST), Vol. 3(1), 2009, pp. 421-428.

[7] Basack S & Purkayastha RD, "Engineering properties of marine clays from the eastern coast of India", J. of Engineering and Technology Research, Vol. 1(6), 2009, pp. 109-114.

[8] Makusa GP, Soil Stabilisation Methods and Materials in Engineering Practice. Sweden: Luleå University of Technology, 2012.

[9] ASTM D-2487-11, Standard Practice for Classification of Soils for Engineering Purposes: Unified Soil Classification System, ASTM, 2006.

[10] Azhar A, Chan C-M & Abd Karim AT, "Solification potential of fine-grained dredged marine soils: water-binder ratio effects", J. of Civil Engineering Research, Vol. 4 (3A), 2014, pp. 48-53.

[11] BS1377, Methods of Test for Civil Engineering Purposes, BSI, 1990.

[12] Chiu CF, Zhu W & Zhang CL, "Yielding and shear behaviour of cement-treated dredged

materials", J. of Engineering Geology, Vol. 103(1-2), 2009, pp. 1-12.

[13] Rahman MM, Siddique A, & Uddin MK, "Clay-water / Cement ratio as the prime parameter for fine grained soil improvement at high water content", J. of Dhaka University of Engineering & Technology (DUET), Vol. 1(3), 2012, pp. 1-11.

[14] Lu YT, Tan T S, & Phoon KK, "Accelerated testing of cement treated Singapore marine clay cured under elevated temperature", in Proc. GeoCongress2012, 2012, pp. 3199-3208.

[15] Lee F, Lee Y, Chew S & Yong K, "Strength and Modulus of Marine Clay-Cement Mixes", ASCE J. of Geotechnical & Geoenvironmental Engineering, Vol. 131(2), 2005, pp. 178-186.

[16] Chan C-M, "Influence of mix uniformity on the induced solidification of dredged marine clay", Environmental Earth Sciences, Vol. 71(3), 2014, pp. 1061-1071.

[17] Horpibulsuk S, Phojan W, Suddeepong A, Chinkulkijniwat A, & Liu MD, "Strength development in blended cement admixed saline clay", Applied Clay Science, 2011, Vol. 104, pp. 318-323.

First International Conference on Science, Engineering & Environment,
Tsu City, Mie, Japan, Nov.19-21, 2015, ISBN: 978-4-9905958-5-2 C3051

THE BEHAVIOR OF COUPLING BEAMS FOR MASONRY STRUCTURES IN SEISMIC REGIONS

Barnaure Mircea[1], Stoica Daniel[2]
[1,2] Technical University of Civil Engineering Bucharest, Romania

ABSTRACT

A force based approach is considered for the seismic design of masonry structures in Europe. Practicing engineers generally use simplified numerical models, in which the walls are modeled as equivalent frames. These simplified models can lead to reasonably accurate results, but caution should be given to the simplifying assumptions. If the behavior of the masonry piers has been extensively studied in the past, the influence of the spandrel elements that act as coupling beams between them is less known. An analysis of how various parameters considered in the numerical model influence the seismic behavior of confined masonry walls is made.

Keywords: Coupling Beam, Masonry, Earthquake Modeling

INTRODUCTION

Masonry is one of the most used structural systems for low and mid rise buildings. In Europe, the seismic design of this type of structures is done in accordance with the in-force regulations [1], [2] and generally requires the use of numerical models.

As the structural behavior of masonry structures submitted to earthquake loads is influenced by many parameters [3], a very accurate numerical model involves complicated tools [4]. The latter would be too sophisticated for addressing the necessities of common structural design and, as a result, practicing engineers tend to rely on simplified models.

The use of commercially available structural design software that is simple enough to be used by professional engineers can lead to accurate nonlinear modeling [5].

The European seismic design of the buildings is a force-based design, using force-reduction factors for earthquake loads, while the distribution of lateral forces between the structural elements is based on elastic estimates of stiffness. A single ductility value for a structural type is considered, regardless of the geometry of the buildings. This may lead to underestimating the distribution of forces in the structural elements, with a risk of brittle failure [6].

Simple equivalent frame models can often be used for design purposes while requiring very low computational time [7].

For the masonry buildings modeled using an equivalent frame model, the strength of the piers and spandrels need to be estimated based on mechanical or empirical models. If there are many such models that have been extensively tested in the case of piers, there are few such models for spandrels [8].

The present work investigates the influence of various spandrel related parameters on the structural behavior of confined masonry structures. As spandrels are very stiff, assuring a consistent coupling between piers of modern masonry structures, we will refer to them as coupling beams.

A numerical simulation on several plane models of a structural shear wall is carried out using the ETABS software. The parameters considered involve the pier and coupling beam dimensions, the reinforcement of beams and columns and the coupling beam type. Conclusions are drawn on the behavior of the structure as well as on the influence of simplified procedures on the results.

COUPLING BEAM CONFIGURATIONS

For historical buildings, the spandrel elements are generally weak, with lintels being made or masonry arches, wood or steel profiles (Fig. 1).

Masonry arch over door/window openings

Steel profiles over door/window openings

Fig. 1 Coupling beam solutions for historic buildings

Because of this, old masonry structures are often analyzed with a simplified weak spandrel - strong pier approach. In this model, the hypothesis of both null strength and null stiffness of spandrels is often adopted and the piers are assumed as uncoupled [9].

On the contrary, for modern confined masonry buildings, the analysis is often based on a simplified weak pier-strong spandrel model. In new buildings, the masonry spandrels are connected to the lintels, tie-beams and slabs made of reinforced concrete.

The coupling beams of the new buildings have high strength capacity, meaning that the assumption that failure occurs in the masonry piers is generally valid. The hypothesis corresponds to experimental results showing that modern spandrels display a much higher strength when compared to traditional solutions [10].

On a given facade wall, an architect may choose to have multiple door and window types. As the position and shape of openings vary, the dimension of the coupling beams between the piers will also differ (Fig. 2). These possible configurations could influence the seismic response of the building.

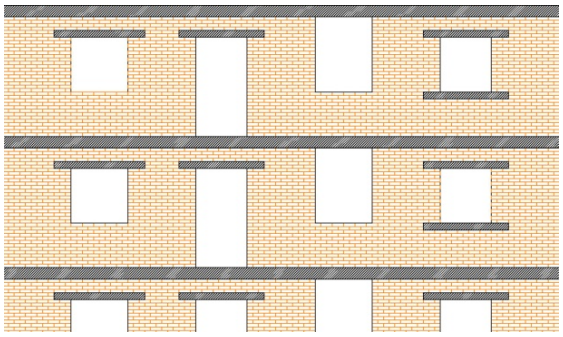

Fig. 2 Coupling beam solutions for new buildings

NUMERICAL MODEL

A 5 storey building with a 3 m floor height is considered. The analysis of an outer wall with 4 spans (Fig. 3) is conducted. A 500 cm spacing between the walls axes is chosen. The wall is modeled as a grid of linear elements (posts and beams).

For the masonry piers, three lengths are considered - 2 m, 3m and 4 m. A value of 25 cm is chosen for the width of the walls. Square concrete columns 25 x 25 cm, reinforced with 4 D14 longitudinal bars are defined at both ends of the walls. The geometry of the elements is defined using the section design feature of the software.

The chosen materials in the model are as follows: solid brick masonry f_k=6 N/mm^2, C20/25 concrete and PC52 (f_{yd} = 300N/mm^2) reinforcement.

Nonlinear hinges are assigned to the column and beam ends. For the intersections, perfectly rigid zones are specified based on element geometry.

Two load definition patterns for the gravitational loads are considered. The first pattern consists in applying distributed loads on the beams, while the second refers to applying loads only at the nodes.

For the in-plane seismic action, push-over analyses are carried out, as described in [11]. A maximum displacement of 600 mm is imposed for the analysis.

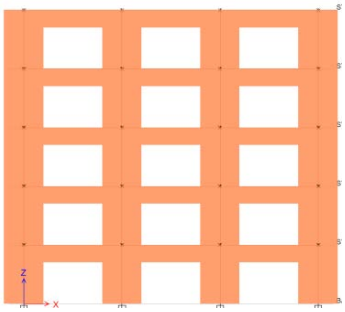

Fig. 3 Geometry of the wall in the model

Six different specifications for the coupling beam geometry are considered (Fig. 4). R1 corresponds to a RC tie beam 15 cm height, while for R2 a 25 cm tie beam is imposed. The R3 specification has a parapet over the tie beam. R4 consists of a 15 cm lintel, masonry and a 25 cm tie beam. R5 is similar to R3, but with a 15 cm tie beam at the top of the parapet. Lastly, R6 corresponds to a mixture of the R4 and R5 coupling beams.

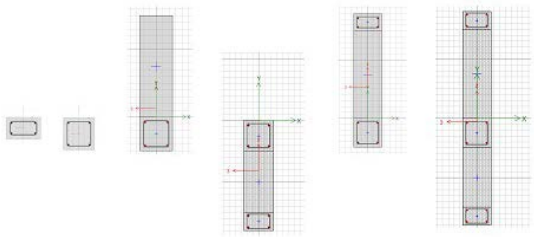

Fig. 4 Types of coupling beams considered

The coupling beams are analyzed for 3 cases of reinforcement in their RC members - 4Φ12, 4Φ14 and 4Φ16 bars.

RESULTS

Influence of the loading pattern

The load definition pattern has an influence only on the 2 m wall 3 m model for the R1 and R2 coupling beams. For this scenario, a difference in behavior appears between the loaded and unloaded

beam models. This can be explained by the fact that in the loaded model the R1 and R2 beams reach their bending capacity due to gravitational loads, while the seismic load causes a faster collapse than in the case of the unloaded beam models. For the other types of beams, the choice between applying loads only at the nodes or fully loading the beams brings no significant difference in the results.

Influence of the coupling beam geometry

The force-displacement diagrams for the 3 m long beams models are presented in Fig. 5. For this scenario, a lower stiffness can be observed for R1 and R2 beams.

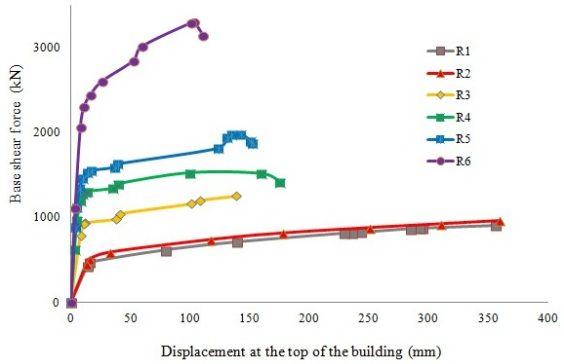

Fig. 5 Force-displacement curve for various beam types (3 m beams with 4 D12 rebar)

For the 2 m (Fig. 6) and 1 m long coupling beams, using type R1 or R2 coupling leads not only to high displacement capacity of the building, but also to high values for maximum base shear.

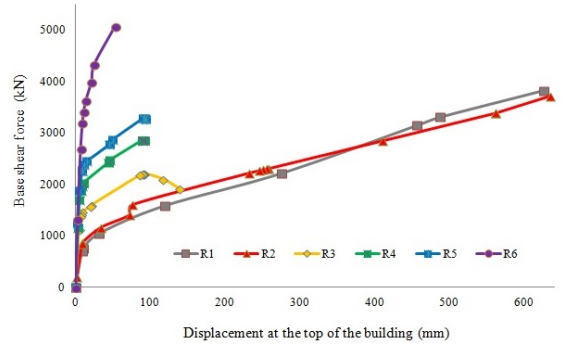

Fig. 6 Force-displacement curve for various beam types (2 m beams with 4 D12 rebar)

For the R3 to R6 beam specifications, a lower beam length leads to a higher maximum base shear (Fig. 7) while the maximum displacement is decreased (Fig. 8). In the case of the R1 and R2 beams, there is a very high increase in the maximum base shear as well as in displacement if the beam length is low. The difference can be explained by the high rotation capacity of the R1 and R2 beams as compared to remaining specifications, where the beams considered are relatively rigid. A much favorable structural behavior is obtained, given that more plastic hinges are developed before reaching collapse.

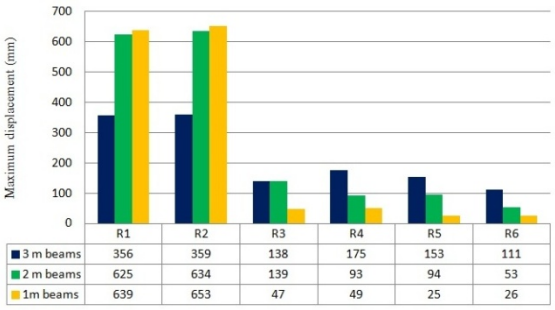

	R1	R2	R3	R4	R5	R6
3 m beams	356	359	138	175	153	111
2 m beams	625	634	139	93	94	53
1m beams	639	653	47	49	25	26

Fig. 7 Influence of the coupling beam length on the maximum displacement

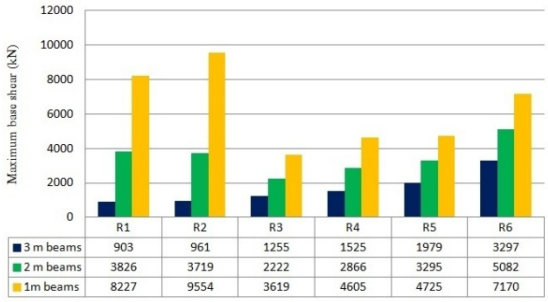

	R1	R2	R3	R4	R5	R6
3 m beams	903	961	1255	1525	1979	3297
2 m beams	3826	3719	2222	2866	3295	5082
1m beams	8227	9554	3619	4605	4725	7170

Fig. 8 Influence of the coupling beam length on the maximum base shear

Influence of the coupling beam reinforcement

The influence of the rebar diameter on the maximum top displacement and the base shear is analyzed in what follows. For the 3 m beams, no clear influence of maximum displacement can be established (Fig. 9). For the R1 and R2 beams, the reinforcement has little to no influence on the maximum base shear (Fig. 10).

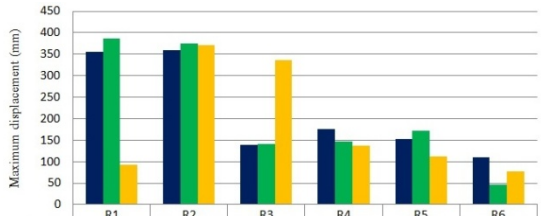

	R1	R2	R3	R4	R5	R6
D12 rebar	356	359	138	175	153	111
D14 rebar	385	375	141	146	171	46
D16 rebar	93	370	337	137	113	78

Fig. 9 Influence of the beam reinforcement on the maximum displacement (3 m beams)

When considering the R3 to R6 beams, higher

reinforcement leads to higher base shear (up to 44% base shear increase for R5 between D16 and D12 rebar). A similar behavior is observed for the 1 m and 2 m beam models.

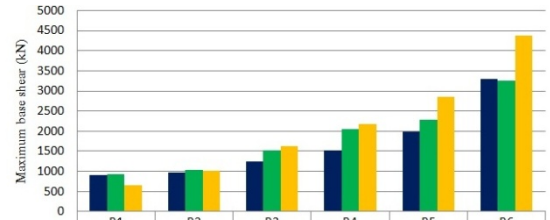

	R1	R2	R3	R4	R5	R6
D12 rebar	903	961	1255	1525	1979	3297
D14 rebar	922	1029	1519	2052	2281	3248
D16 rebar	663	1019	1627	2179	2846	4368

Fig. 10 Influence of the beam reinforcement on the maximum base shear (3 m beams)

CONCLUSIONS

A numerical simulation on plane models of a confined masonry wall was carried out. Several parameters were considered: the way of defining loads, the wall and coupling beams dimensions, the coupling beam types and the reinforcement of beams.

Similar results were obtained on the models with loads only applied at nodes and on models with loads applied both on beams and at nodes.

Low height coupling beams (R1 and R2) showed a very high post elastic rotation capacity, which leads to a relatively high displacement capacity of the building.

When the behavior of the high coupling beams was analyzed, a lower displacement capacity of the building was observed if the beam length was lower. Still, for the 3 m, 2 m and 1 m long beams, a linear increase of the maximum base shear was observed.

The beam reinforcement had no clear impact on the maximum displacement of the building. For low height beams, the reinforcement had little influence on the maximum base shear. In the case of high coupling beams, higher reinforcement ratios led to higher base shear.

REFERENCES

[1] CEN (2004) Eurocode 8: Design of structures for earthquake resistance - Part 1: General rules, seismic actions and rules for buildings. EN 1998-1:2004, Brussels

[2] CEN (2005) Eurocode 6: Design of masonry structures - Part 1-1: General rules for buildings - Rules for reinforced and unreinforced masonry EN 1996-1-1:2005, Brussels

[3] Nucera, F., et al. "Influence of geometrical and mechanical parameters on the seismic vulnerability assessment of confined masonry buildings by macro-element modeling", in Proceedings of 15th World Conference on Earthquake Engineering, 2012. pp. 24-28.

[4] Marques, R., & Lourenço, P. B.. Unreinforced and confined masonry buildings in seismic regions: Validation of macro-element models and cost analysis. Engineering Structures, 64, 2014, pp. 52-67.

[5] Pasticier, L., Amadio, C., & Fragiacomo, M. "Non-linear seismic analysis and vulnerability evaluation of a masonry building by means of the SAP2000 V. 10 code" Earthquake Engineering & Structural Dynamics, 37(3), 2008, pp. 467-485.

[6] Priestley, M. J. N., Calvi, G. M., & Kowalsky, M. J. "Direct displacement-based seismic design of structures", in 2007 NZSEE Conference.

[7] Kappos, A. J., Penelis, G. G., & Drakopoulos, C. G., "Evaluation of simplified models for lateral load analysis of unreinforced masonry buildings", Journal of structural Engineering, 128(7), 2002, pp. 890-897.

[8] Beyer, K., & Mangalathu, S. "Review of strength models for masonry spandrels", Bulletin of Earthquake Engineering, 11(2), 2013, pp. 521-542.

[9] Cattari, S., & Lagomarsino, S. "A strength criterion for the flexural behaviour of spandrel in un-reinforced masonry walls", in Proc. of 14th WCEE, 2008.

[10] Parisi, F., Augenti, N., & Prota, A. "Implications of the spandrel type on the lateral behavior of unreinforced masonry walls", Earthquake Engineering & Structural Dynamics, 43(12), 2014, pp. 1867-1887.

[11] Barnaure, M., Stoica D., "On the numerical modeling of confined masonry structures for in-plane earthquake loads", accepted in Analele Universitatii Eftimie Murgu, 2015

First International Conference on Science, Engineering & Environment,
Tsu City, Mie, Japan, Nov.19-21, 2015, ISBN: 978-4-9905958-5-2 C3051

A NOVEL PRODUCTION PROCESS MODELING FOR ANALYTICS

Rich Lee[12]
[1]National Taipei University of Technology, Taiwan; [2] IBM, Taiwan

ABSTRACT

The nowadays manufacturing is facing the critical challenges from various aspects including the trend of moving towards the new era of Industrial 4.0 [1]—an analytical and predictive driven production thinking, the Smart Factory. To effectively embed the necessary processes for analytics, a new way of modeling the process flows is essential to realize the goal of the predictive lean production. To reach these objectives, this paper presents a novel process modeling approach for analytics to the practitioners and the industries. The analysis of the smart factory theme includes the statistics, the data mining, and the operation research approaches [2] based on the various management improvement or the prediction objectives. The proposed process modeling for analytics extends the XML (e**X**tensible **M**arkup **L**anguage), which is also commonly used in software engineering [3]. The purpose of using this is to streamline the latter integration with the analytical processes among the software systems and will play a key part of the factory knowledge management for continuous improvement.

Keywords: Smart Factory, Operation Management, Business Analytics, Production Modeling

INTRODUCTION

Nowadays, the business environment is volatile and harsh, making-decision intuitively cannot answer this complexity with confidence; many organizations are evolving their operations and decision-making processes to be more analytical and predictive driven. In manufacturing, these enterprises commence their Industry 4.0 initiatives and experience their journeys toward a smarter factory. Using the analytical approach to enhance the quality and the precision of operational activities is not a new thing to the enterprises, for instances, Engineering Data Analysis (EDA), Manufacturing Execution System (MES) and Management Accounting have been a part of daily operations for decades in a factory. These discontinuous analytical processes have limited synergistic influence on the enterprise efficiency improvement. On the other hand, these processes are a part of intellectual capital of an enterprise, which is unique and not easily to mimic from the competitors [4]. The essence of smart factory is not just looking for the factory automation—deploying the robotic equipment to replace the labors, nor limited in pursuing the efficiency of processes. In rather, the smart factory is an attitude of an enterprise to take the analytical perspective as the tool in exploring the potential causes of and the feasible approaches in resolving the problems.

Such an attitude requires a systematic scheme to reposit and adopt these analytical processes in a synergetic way. The Knowledge Management (KM) is to capture, classify, store, transform, analyze, implicate, disseminate, and adopt the information synergistically. During this knowledge generation process, the taxonomy of the information plays a significant role in extracting and adopting the information from the repository effectively. Intensifying the positive externality [5] from these analytical processes requires more capabilities from the general knowledge management, including the execution orders and sequences among these processes. These process execution orders and sequences are parts of operation activities that are under the enterprise business process management. Therefore, the smart factory demands these analytical processes to be governed by both knowledge and the Business Process Management (BPM) at the same time [6].

This paper presents a novel way to incorporate the knowledge and the business process management to intensify the outcome from the synergy of analytical processes, and to evolving the factory towards the smarter organization.

SMART FACTORY THEME

The lean production—to illuminate all possible wastes including the tangible and the intangible ones including the labor, the resources, and the time—has governed the factory management for years. The concept of Industry 4.0 supports the lean production objectives in a predictive way. One major reason causes the unpredictable volatility is the variance of the coming customer orders. This paper conducted the literature review by looking up the Google Scholar using the keywords of “Smart factory” or

"Industrie 4.0" —which is the original idea of smart factory from—respectively contained in their titles from the year of 2014—after the Industry 4.0 was brought up with clear pictures—to the present. There were 17 articles titled with the keyword of "Smart factory", 12 in English, 4 in German, and 1 in Russian language; while there were 81 articles titled with the keyword of "Industrie 4.0" which means "Industry 4.0" in English, 9 in English and 11 in German language of the first 20 articles appeared in the search.

Two word-cloud diagrams were generated against the term frequencies appearing in different sizes accordingly, one was derived from the titles; the other was derived from the abstracts, total 6,216 terms were processed, the most significant ones of the abstracts were: "production" (318 times), "systems" (277 times), "processes" (259 times), "technology" (212 times), "information" (187 times), "integration" (150 times), "models" (124 times), "networks" (119), "technical" (114 times), "revolution" (109 times), "approach" (105 times), "structures" (101 times), "engineering" (97 times), "organization" (94 times), and "change" (91 times) .

Fig. 1 The Word-Cloud Diagram Derived from the Article Titles

Fig. 2 The Word-Cloud Diagram Derived from the Abstracts

From the word-cloud diagram illustrated in **Fig. 1**, it gives an idea of what smart factory is; it is about innovation, technology, solution, algorithm, computing, and systems; it faces the opportunities and challenges; and it focuses on sustainable, environment, and management. Therefore, this paper examines the current lean production processes where the smart factory theme can facilitate the production in pursuing better responsive, quality objectives.

The smart factory theme in predictive perspective, illustrated in **Fig. 2**, contains three major kinds of analyses commonly applied in the manufacturing: (1) the statistical, (2) the data mining, and (3) the operation research approaches. In the lean production processes, the proposed minimal analyses are: (1) Purchase Order, (2) Production Scheduling, (3) Inventory Management, (4) Quality Assurance and Control, (5) Production Management, (6) Logistics Management, and (7) Management Accounting; show in **Table 1**.

Table 1 The Proposed Minimal Analyses for the Lean Production

Category	Analytic Model	
	Statistical or/and Data Mining	Operation Research
Purchase Order	Purchase Order Analysis and Prediction	Order Contribution and Sequencing Analysis
Production Scheduling	Production Scheduling Variance Analysis	Production Resources Allocation Optimization
Inventory Management	Aging Analysis and Prediction	Safety Stock Estimation and Cost Prediction
Quality Assurance and Control	Quality Risk Measurement and Analysis	Inspection Measurement and Analysis
Production Management	Production Process Variances Analysis	Outsourcing Contribution Analysis and Optimization
Logistics Management	Logistics Variances Analysis	Logistics Cost Optimization
Management Accounting	Operation Risk Measurement and Analysis	Investment Return Analysis and Optimization

Modeling Analytical Process

In the holistic view of an analytical process, it involves the participants and the components including: (1) the actor—who initiates the process; (2) the process—which consumes the input information and generates the results; (3) the actant—who takes the actions accordingly; (4) the dispatch—which usually kicks another series of processes sequentially or simultaneously. The **Fig. 3**

illustrates the basic pattern of an analytic process; the dispatch can be another analytical process, a computational script task, or a manual task to take managerial actions. In many occasions, the actor is actually time-driven; the dispatch can send messages to an electronic kanban device, to kick a persistent service task, or to reposit information into the knowledge management system through a receive task.

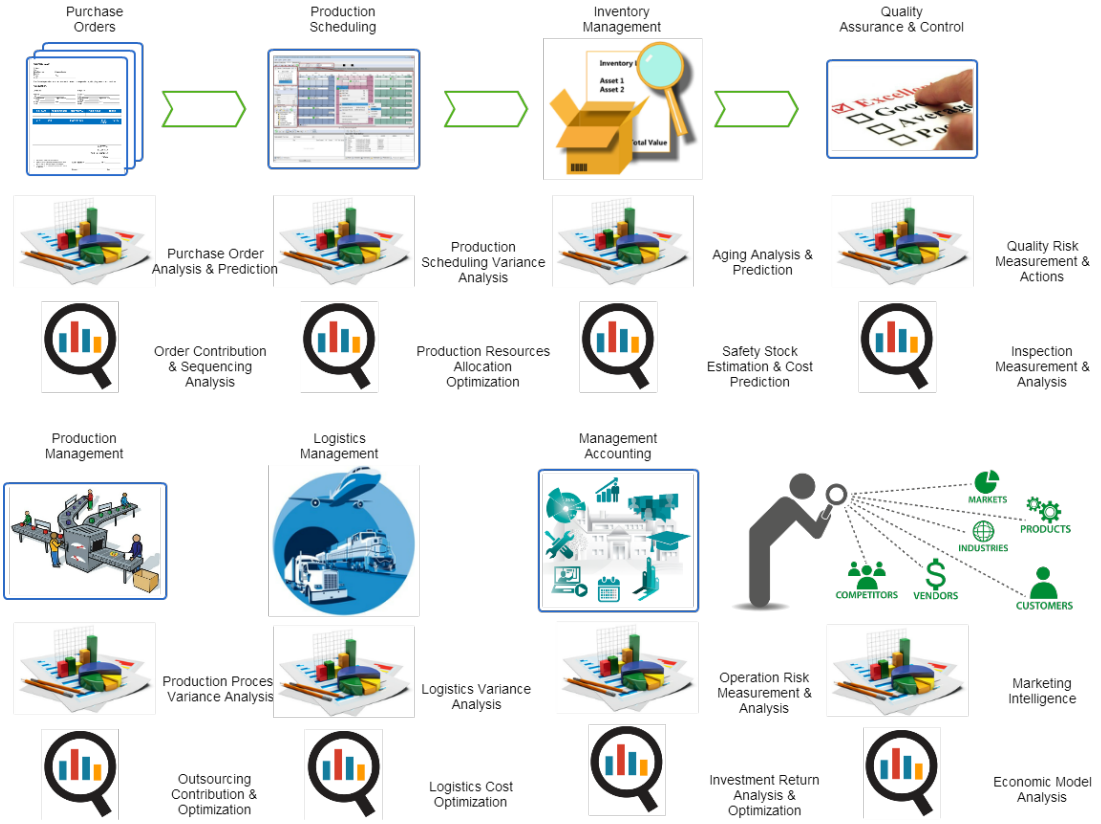

Fig. 3 The Smart Factory Theme

Each analytical process has a unique identifier so do the participants and the components. This paper proposes 5 types of participants and the components, shown in **Table 2**, including: (1) actor/actant, (2) analytical process, (3) manual task, (4) script tasks, and (5) mail task. Among the information column, each array contains nothing means no following task or a list of consecutive tasks. The script task is the actual activity applying analytic methods such as descriptive statistics, multi-variable regression, or k-mean classification. **Fig. 4** illustrates the basic pattern of a generic analytical process; while **Fig. 5** shows a specific pattern of a time-driven analytical process.

Table 2 Analytical Process Participants and Components

Participants/Components	Information (at least inclusive)
Actor/Actant	• Unique Identifier • Role Description • Name of Role • Message Sent/Received
Analytical Process	• Unique Identifier • Purpose of Analysis • Result Implication • Script Identifier (Script Array) • Dispatch (Task Array)
Manual Task	• Unique Identifier • Purpose of Task • Actor (Array) • Message Sent/Received • Dispatch (Task Array)
Script Task	• Unique Identifier • Purpose of Script • Data Source • Script Language • Major Methods of Analysis • Result Data
Receive Task	• Unique Identifier • Purpose of Task • Message Received • Taxonomy

Service Task	• Unique Identifier • Purpose of Task • Message Received • Trigger Time • Script Identifier (Script Array)
Mail Task	• Unique Identifier • Purpose of Task • Message Received • Device Identifier (Device Array)

The participants of the business processes, a combination of series of tasks often use a process modeling tool—BPM systems—to describe how these tasks, collaborate together to accomplish the business objectives; in many occasions, the process flows are implicitly embedded within the IT systems and no modeling required; such systems the ERP, MES, and EDA are the examples of them. The conventional BPM are development-driven focusing on the automation of the predefined process flows. The positive externality of synergistic effect can be also expected within a boundary. The KM is kind of Open Innovation Model—stimulating the participants willing to share their creativity and the solutions of the raised questions [7]; for simplicity, the proposed analytical process is a BPM element in the KM.

Both BPM and KM can be facilitated by the BPMN—a form of XML. Two aforementioned analytical process patterns described in XML form, the first part in grey color is the common header of the XML; the second part is the detail of analytical process description.

There are XML tags for the details: (1) *targetNamespace*—used for the stages of a lean production; (2) process—used for describing the whole analytical process; (3) *userTask*—used for identifying the participants; (4) *analyticalProcess*—used as the main body of analysis; (5) *eventBasedGateway*—used as the dispatch; (6) *manualTask*—used for manual operation; (7) *scriptTask*—used for a analytical program such as Python, R, or designed in other computing language; (8) *messageEventDefinition*—used for describing the message content as the input or the result; (9) *timerEventDefinition*—used as a time trigger to kick the analytical process; and (10) *sequenceFlow*—used as the link between connected tasks.

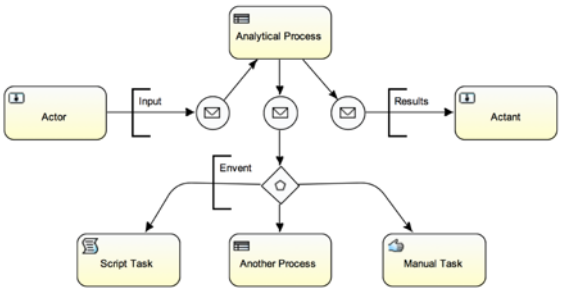

Fig. 4 Basic Pattern of an Analytical Process

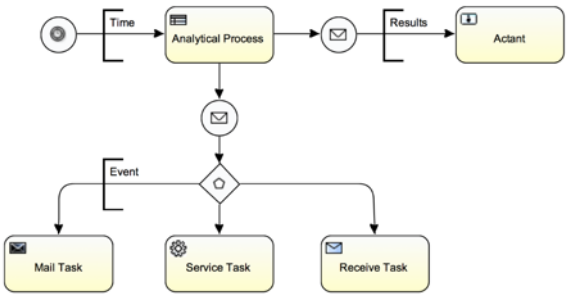

Fig. 5 A Pattern of a Time-driven Analytical Process

Analytical Process Knowledge Management

The ultimate purpose of the analytical processes is to improve the business agility—toward a smart factory—through the synergy of the Open Innovation Model. To accomplish this mission, setting the Knowledge Goal in phases is essential. Some factories commence their smart factory journeys without a clear goal, usually over-invested the automation equipment and realigned their business strategy less. In fact, the smart factory is not just pursuing the factory automation but transforming their enterprises toward a learning organization—the employees applying a system thinking to resolve the business obstacles [8].

The knowledge initiator (as a participant) addresses a need of a piece of knowledge based on the business situation and reality; using an analytical modeler to form and develop the knowledge generating scheme, an analytical process, and then reposit this knowledge—qualitative or/and quantitative—into the analytical KM. Another source of knowledge development is through predefined big data processes, collecting raw data, transforming the data into information, and giving the business implication to derive the quantitative knowledge.

Disseminating the knowledge, in which the conventional KM already has rich features, to other participants, including external partners will speed

up the decision-making cycle and enhance the quality of the decisions. The knowledge consumer (as a participant) using the information retrieval features of the KM to extract and reuse the required knowledge to resolve their business issues retains the knowledge with scenarios and the associated data; during this process, the consumer assesses the usefulness, the applicable situations, and the request-for-improvement about the knowledge and feedbacks to the initiator. This whole iterative process refines the quality and the usefulness of the knowledge; through reusing the retained knowledge, consequently, a learning organization is seamlessly formed. The **Fig. 6** illustrates how analytic knowledge management process, setting the goal, identifying, developing, disseminating, utilizing, retaining, and assessing the knowledge, can benefit the business agility—such as improving the quality of delivery, illuminating the wastes by taking advantage of the outcomes from the analytics—through the synergy among the participants.

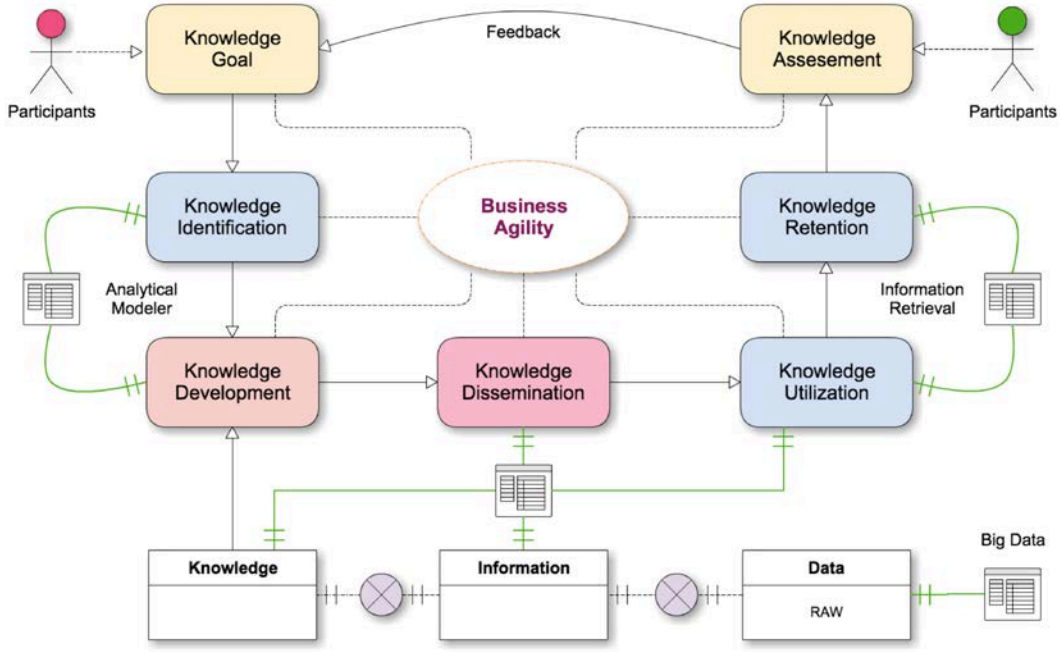

Fig. 6 The Analytical Process Knowledge Management

CONCLUSION

The Smart Factory is the next level of lean production; not just deals with the present wastes, but also foresees the potential coming wastes and take actions proactively. This paper identifies there is a strong need of analytical process modeling notation for Smart Factory from the recent literatures. To avoid the reinvestment on IT systems, this paper applies the KM and BMP that have been already deployed in many factories to derive the special process models for the needs of Smart Factory. Finally, this paper emphasizes that transforming the factory into a learning organization—accumulating the intellectual capital—is equally important as the factory automation. No matter what, modeling the analytical process to form the knowledge is the uncontroversial starting point of the journey toward the Smart Factory.

REFERENCES

[1] Matthias Ackermann, *Reporting and Big Data. Big Data as One Megatrend of Industry 4.0 and the Impacts on Controlling*. Munich: GRIN Verlag, 2015.

[2] Alexey Goryachev et al., "“Smart Factory”: Intelligent System for Workshop Resource Allocation, Scheduling, Optimization and Controlling in Real Time," *Advanced Materials Research*, vol. 6, no. 30, pp. 508-513., Dec. 2012, DOI:10.4028/www.scientific.net/AMR.630.508.

[3] Thomas Stahl and Markus Völter, *Model-Driven Software Development-Technology, Engineering*,

Management. Chichester, England: John Wiley & Sons Ltd, 2006.

[4] Kai Wright, *Drivers for Corporate Competitiveness. Intellectual Capital and Related Intangible Assets and Intellectual Property*. Munich: GRIN Verlag, 2014, Business economics - Business Management, Corporate Governance.

[5] Joan Torrent-Sellens, "Knowledge Products and Network Externalities: Implications for the Business Strategy," *Journal of the Knowledge Economy*, vol. 6, no. 1, pp. 138-156, 2015.

[6] Christian Stary, "Non-disruptive Knowledge and Business Processing in Knowledge Life Cycles–Aligning Value Network Analysis to Process Management," *Journal of Knowledge Management*, vol. 18, no. 4, pp. 651-686, 2014.

[7] Henry Chesbrough, "Open Innovation: A New Paradigm for Understanding Industrial Innovation," in *Dynamics of Industry and Innovation: Organizations, Networks and Systems*, Copenhagen, Denmark, 2015.

[8] Peter M. Senge and George Roth, *The Dance of Change: The Challenges to Sustaining Momentum in a Learning Organization*.: Crown Business, 1999.

First International Conference on Science, Engineering & Environment,
Tsu City, Mie, Japan, Nov.19-21, 2015, ISBN: 978-4-9905958-5-2 C3051

ENERGY EFFICIENT FOR HEAT EXCHANGER, REFRIGERATION AND AIR CONDITIONING

Abdeen Omer[1]
[1]Energy Research Institute (ERI), United Kingdom

ABSTRACT

Over the years, all parts of a commercial refrigerator, such as the compressor, heat exchangers, refrigerant, and packaging, have been improved considerably due to the extensive research and development efforts carried out by academia and industry. However, the achieved and anticipated improvement in conventional refrigeration technology are incremental since this technology is already nearing its fundamentals limit of energy efficiency is described is 'magnetic refrigeration' which is an evolving cooling technology. The word 'green' designates more than a colour. It is a way of life, one that is becoming more and more common throughout the world. An interesting topic on 'sustainable technologies for a greener world' details about what each technology is and how it achieves green goals. Recently, conventional chillers using absorption technology consume energy for hot water generator but absorption chillers carry no energy saving. With the aim of providing a single point solution for this dual purpose application, a product is launched but can provide simultaneous chilling and heating using its vapour absorption technology with 40% saving in heating energy. Using energy efficiency and managing customer energy use has become an integral and valuable exercise. The reason for this is green technology helps to sustain life on earth. This not only applies to humans but to plants, animals and the rest of the ecosystem. Energy prices and consumption will always be on an upward trajectory. In fact, energy costs have steadily risen over last decade and are expected to carry on doing so as consumption grows.

Keywords: Energy Saving; Energy Efficiency, Sustainable Technologies; Heat Exchangers; Refrigerant; Future Prospective

INTRODUCTION

This section describes the different methods and techniques for providing energy for heating and cooling systems. It also, covers the optimisation and improvement of the operation conditions of the heat cycles and the performance of the ground source heat pump systems (GSHPs).

With the improvement of people's living standards and the development of economies, heat pumps have become widely used for air conditioning. The driver to this was that environmental problems associated with the use of refrigeration equipment, the ozone layer depletion and global warming are increasingly becoming the main concerns in developed and developing countries alike. With development and enlargement of the cities in cold regions, the conventional heating methods can severely pollute the environment. In order to clean the cities, the governments drew many measures to restrict citizen heating by burning coal and oil and encourage them to use electric or gas-burning heating. New approaches are being studied and solar-assisted reversible absorption heat pump for small power applications using water-ammonia is under development [1].

An air-source heat pump is convenient to use and so it is a better method for electric heating. The ambient temperature in winter is comparatively high in most regions, so heat pumps with high efficiency can satisfy their heating requirement. On the other hand, a conventional heat pump is unable to meet the heating requirement in severely cold regions anyway, because it's heating capacity decreases rapidly when ambient temperature is below -10^{o}C. According to the weather data in cold regions, the air-source heat pump for heating applications must operate for long times with high efficiency and reliability when ambient temperature is as low as -15^{o}C. Hence, much researches and developments have been conducted to enable heat pumps to operate steadily with high efficiency and reliability in low temperature environments [2]. For example, the burner of a room air conditioner, which uses kerosene, was developed to improve the performance in low outside temperature [3]. Similarly, the packaged heat pump with variable frequency scroll compressor was developed to realise high temperature air supply and high capacity even under the low ambient temperature of –10 to –20^{o}C [4]. Such a heat pump systems can be conveniently used for heating in cold regions. However, the importance of targeting the low

capacity range is clear if one has in mind that the air conditioning units below 10 kW cooling account for more than 90% of the total number of units installed in the EU [5].

Conventional heating or cooling systems require energy from limited resources, e.g., electricity and natural gas, which have become increasingly more expensive and are at times subjects to shortages. Much attention has been given to sources subject to sources of energy that exist as natural phenomena. Such energy includes geothermal energy, solar energy, tidal energy, and wind generated energy. While all of these energy sources have advantages and disadvantages, geothermal energy, i.e., energy derived from the earth or ground, has been considered by many as the most reliable, readily available, and most easily tapped of the natural phenomena.

Ground source based geothermal systems have been used with heat pumps or air handling units to satisfy building HVAC (heating, ventilation, and air conditioning) loads. These systems are favoured because geothermal systems are environmentally friendly and have low greenhouse emissions.

The installation and operation of a geothermal system of the present invention may be affected by various factors. These factors include, but are not limited to, the field size, the hydrology of the site the thermal conductivity and thermal diffusivity of the rock formation, the number of wells, the distribution pattern of the wells, the drilled depth of each well, and the building load profiles. Undersized field installations require higher duty cycles, which may result in more extreme water temperatures and lower HVAC performance in certain cases. Oversized field designs, on the other hand, require more wells, pumps and field plumbing and therefore will be more expensive, albeit adequate to handle almost any load circumstances. The detailed knowledge of the field rock (e.g., porosity, permeability, thermal diffusivity, heat capacity, or other aquifer parameters) may facilitate the determination of the appropriate drilling depth for each well, as well as the number and position of such wells needed at that site. Some of this information may be obtained during the drilling operation.

EARTH-ENERGY SYSTEMS (EESS)

The earth-energy systems, EESs, have two parts; a circuit of underground piping outside the house, and a heat pump unit inside the house. And unlike the air-source heat pump, where one heat exchanger (and frequently the compressor) is located outside, the entire GSHP unit for the EES is located inside the house.

Hot water heating is easy with EESs because the compressor is located inside. Because EESs have relatively constant heating capacity, they generally have many more hours of surplus heating capacity than required for space heating. In fact, there are sources of energy all around in the form of stored solar energy, which even if they have a low temperature, can provide the surroundings with enough energy to heat the soil, bedrock and ground water as a heat source for domestic dwellings as shown in Fig. 1, for example. Some emphasis has recently been put on the utilisation of the ambient energy from ground source and other renewable energy sources in order to stimulate alternative energy sources for heating and cooling of buildings. Exploitation of renewable energy sources and particularly ground heat in buildings can significantly contribute towards reducing dependency on fossil fuels.

FUNCTION OF THE GSHP CIRCUIT

The collector liquid (cooling medium) is pumped up from the borehole in tubing and passed to the heat pump. Another fluid, a refrigerant, circulates in the heat pump in a closed system with the most important characteristic of having a low boiling point. When the refrigerant reaches the evaporator, which has received energy from the borehole, and the refrigerant evaporates. The vapour is fed to a compressor where it is compressed. This results in a high increase in temperature. The warm refrigerant is fed to the condenser, which is positioned in the boiler water. Here the refrigerant gives off its energy to the boiler water, so that its temperature drops and the refrigerant changes state from gas to liquid. The refrigerant then goes via filters to an expansion valve, where the pressure and temperature are further reduced. The refrigerant has now completed its circuit and is once more fed into the evaporator where it is evaporated yet again due to the effect of the energy that the collector has carried from the energy source (Fig. 2).

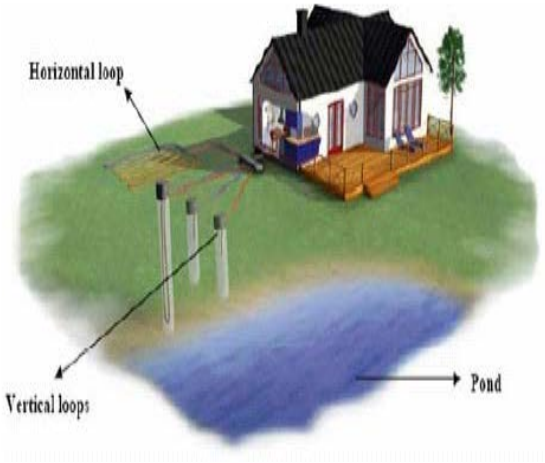

Fig. 1 Using the soil, bedrock or groundwater as the heat source.

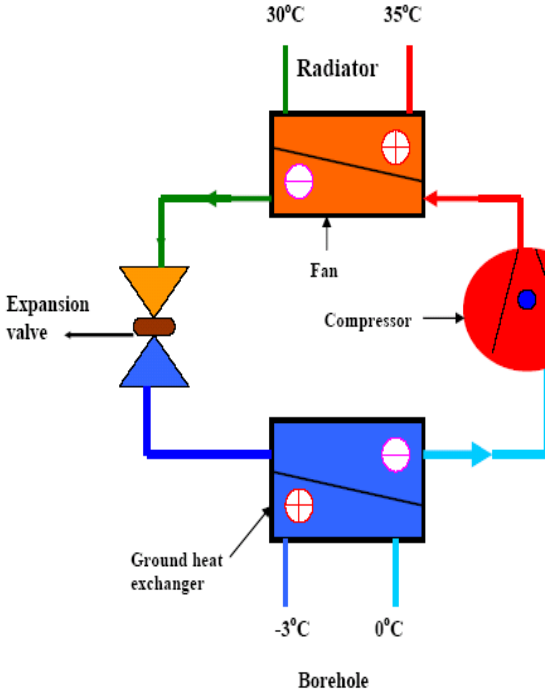

Fig. 2 Detail of the GSHP circuit.

Naturally, it would be preferred, for comfort reasons that this index would be small, preferably nil. It may be seen that the variable is directly related to temperature discomfort: the larger the value of the index, the farthest will inside conditions be from expected wellbeing. Also, the use of electricity operated air conditioning systems will be more expensive the higher this variable is. Hence, energy expenditure to offset discomfort will be higher when comparing two index values; the ratio of them is proportional to the expected energy savings [6]. When the external shade blocks the windowpane completely, the excessive heat gains belong to the lowest values in the set, and the dimensionless index will be constant with orientation. For the climate conditions of the locality, it can be seen that a naked window can produce undesirable heat gains if the orientation is especially unfavourable, when the index can have an increase of up to 0.3 with respect to the totally shaded window.

CONCLUSION

With increasing worldwide awareness of the serious environmental problems due to fossil fuel consumption, efforts are being made to develop energy efficient and environmentally friendly systems by utilisation of non-polluting renewable energy sources, such as solar energy, industrial waste heat or geothermal water. The GSHPs are suitable for heating and cooling of buildings and so could play a significant role in reducing CO_2 emissions. Ground source or geothermal heat pumps are a highly efficient, renewable energy technology for space heating and cooling. This technology relies on the fact that, at depth, the Earth has a relatively constant temperature, warmer than the air in winter and cooler than the air in summer.

A geothermal heat pump can transfer heat stored in the earth into a building during the winter, and transfer heat out of the building during the summer. Furthermore, special geological conditions, such as hot springs, are not needed for successful application of geothermal heat pumps. The GSHPs are receiving increasing interest because of their potential to reduce primary energy consumption and thus reduce emissions of the GHGs. The GSHP is generally recognised to be one of the most outstanding technologies of heating and cooling in both residential and commercial buildings, because it provides high coefficient of performance (COP), up to 3-4 for an indirect heating system and 3.5-5 for a direct heating system.

The main benefit of using the GSHPs is that the temperature of the subsurface is not subject to large variations experienced by air. It is currently the most common thermal energy source for the heat pumps, and so would allow construction of more efficient systems with superior performance. The GSHPs do not need large cooling towers and their running costs are lower than conventional heating and air conditioning systems. As a result, the GSHPs have increasingly been used for building heating and cooling with annual rate of increase of 10% in recent years.

ACKNOWLEDGMENT

The financial support for this research work is from the Energy Research Institute (ERI). Thanks to my wife Kawthar Abdelhai Ali for her warmth and love. Her unwavering faith in me, her intelligence, humour, spontaneity, curiosity and wisdom added to this article and to my life.

REFERENCES

[1] Luo, L.; Tondeur, D.; Le Gall, H.; and Corbel, S. Constructal approach and multi- scale components. *Applied Thermal Engineering*, 2007, 27, 1708-1714.

[2] Luo, L.; Fan, Y.; and Tondeur, D. Heat exchanger: from micro to multi- scale design optimisation. *International Journal of Energy Research*, 2007, 31, 1266-1274.

[3] Philappacopoulus, A.J.; and Berndt, M.L. Influence of de-bonding in ground heat exchangers used with geothermal heat pumps. *Geothermics*, 2001, 30, 5, 527-545.

[4] Jo, H.Y.; Katsumi, T.; Benson, C.H.; and Edil, T.B. Hydraulic conductivity and swelling of non-prehydrated GCLs permeated with single-species salt solutions. *Journal of Geotechnical and Geo-environmental Engineering*, 2001, 127, 7, 557-567.

[5] Anandarajah, A. Mechanism controlling permeability changes in clays due to changes in pore fluids. *Journal of Geotechnical and Geo-environmental Engineering*, 2003, 129, 2, 163-172.

[6] Abdeen M. Omer, Low energy building design: Heating, ventilation and air conditioning, Scientific Journal of Review, Vol.4, No.2, England, 2015, pp. 30-46.

NOMENCLATURES

ACH	Air changes per hour
GSHP	Ground source heat pump
HRV	Heat recovery ventilator
HSPF	Heating season performance factor
SEER	Seasonal energy efficiency ratio
COP	Coefficient of performance (%)

First International Conference on Science, Engineering & Environment,
Tsu City, Mie, Japan, Nov.19-21, 2015, ISBN: 978-4-9905958-5-2 C3051

REMOVAL OF REACTIVE DYES FROM AN AQUEOUS SOLUTION USING PLANT-BASED SURFACTANT VIA MICELLAR-ENHANCED MICROFILTRATION

Puasa S.W[1], Ruzitah M.S[2] and Sharifah A.S.A.K[3]
[1,2,3]Faculty of Chemical Engineering, Universiti Teknologi MARA, Shah Alam, 40450 Selangor, Malaysia

ABSTRACT

The removal of C.I Reactive Black 5 (RB5) and C.I Reactive Orange 16 (RO16) using plant based esterquat (PBE) surfactant by micellar-enhanced microfiltration (MEMF) was investigated. The critical micelle concentration (CMC) of PBE surfactant was obtained at 93.5 mg/L via conductivity method. The diameter of micelles formed was at size range from 140 to 1500 nm. The MEMF process was performed using hydrophilic mixed cellulose esters microfiltration membrane (MCE) with pore size of 0.45 µm and the surfactant concentration was varied from 1.5CMC to 2.5CMC at operating pressure of 100 kPa. Results obtained in MEMF study shows almost complete decolourization of RB5 and RO16. The highest dye rejection obtained were 99.98% and 99.81% for RB5 and RO16, respectively at PBE concentration of 2.25CMC. This finding proved that MEMF using biodegradable plant based esterquat has a great potential to be utilised as a new green technology for removing reactive dyes from textile wastewater.

Keywords: Micellar-enhanced Ultrafiltration, Reactive Dye, Esterquat, Critical Micelle Concentration; Micelle

INTRODUCTION

Textile industry is one of the largest and most global industries in the world. Reactive dye was used extensively by the textile industries. It is a water soluble anionic dye that contain one or more reactive groups which are designed to bond covalently with hydroxyl group in cellulosic fibres [1]. These dyes have extensive selection of colour, high wet fastness profiles which ease the application where it require minimal energy consumption for dyeing process [2].

Textile industries nowadays are facing problems due to large volumes of wastewater polluted with dyes produced in dyeing and finishing process [3]-[4]. The existence of even little amount of dye in water is noticeable which affects the water clearness and aquatic life by blocking the penetration of sunlight through the water [5]. According to Lazaridis, et al. [6], the concentration of dyes present in textile effluent are commonly between 10 to 50 mg/L and noticeable at dye concentration of 1 mg/L.

The treatment of wastewater from cotton textile processing industry has been widely explored in the literature, especially for the wastewater from dyeing operations. The removal of dyes depends on the chemical structure of dyes which lead to the selection of the suitable method use for wastewater treatment. Most of the compound structure of dyes can be very complex hence effect on the degree of biodegradability. Generally, dye with low solubility can be easily removed by physical means such as flocculation and coagulation. However, water soluble dyes such as reactive dyes cannot be removed efficiently by coagulation or adsorption process. The conventional biological treatment processes also unable to achieve adequate colour removal [7]. Each of the method used for treatment of textile dyeing effluent has its own capability on dyes removal. These methods have some limitation and disadvantages on the treatment processes.

Membrane filtration process is recognized as one of the treatment method used in the textile wastewater treatment [8]. Nanofiltration (NF) membrane has confirmed its capability in decolorization of reactive dyes from textile effluent. However, major limitation of membrane-based separation processes is the decline in permeate flux due to concentration polarization over the membrane surface and membrane fouling [9]. Due to this limitation, it is a challenge for researchers to discover new or enhanced method for membrane separation process which is able to decolorize reactive dyes (noticeable at concentration above 1 mg/L) and at the same time produce high permeate flux at low operating pressure.

Surfactant-enhanced membrane separation technology is found as one of the attractive method for membrane separation process. This process involves the addition of surfactant to textile effluent, and the process is namely as Micellar-enhanced ultrafiltration (MEUF) or Micellar-enhanced microfiltration process (MEMF) depending on the pore size of the membrane. MEUF use ultrafiltration membrane while MEMF use microfiltration

membrane for the required separation. MEUF and MEMF are known as viable alternative techniques as they have proved their ability to remove contaminants from wastewater [10]-[12].

In MEUF and MEMF processes, surfactant is added into the aqueous stream containing contaminants or solute (e.g metal ion, organic materials, low molecular weight solute) above its critical micelle concentration (CMC) [13]. When the surfactant concentration exceeding the CMC value, the surfactant monomers will assemble [14] and aggregate to form large amphiphilic transparent micelles [15] having hydrodynamic diameter significantly larger than the pore diameter of ultrafiltration or microfiltration membrane [14], [16]-[17]. The contaminants or solute will entrap in the micelles if they are attracted strongly by micelle surface and will solubilize in the micelle interior [9]. Micelles containing solubilized contaminants with larger diameter than membrane pore size will be rejected by the membrane during filtration process leaving only water, unsolubilized contaminants and surfactant monomers in permeate stream [9], [17].

The MEUF processes on dyes removal have been explored by many researchers [9]-[10], [18]-[21]. Their works show that MEUF is a promising technique for dye removal. However, the chemical surfactants used in the MEUF process exist in the permeate solution at concentration less than its CMC. Consequently, further treatment on recovery of surfactant from permeate solution is required to ensure the process is clean from hazardous materials. The limitation on the loss of surfactant monomers and submicellar aggregates through the membrane also limits the use of MEUF technique [11]. Furthermore, in actual situation the real textile wastewater contains several mixtures of reactive dyes. Based on these studies, there is a need to investigate the competitive removal of reactive dyes mixture using biodegradable plant-based surfactant in surfactant – based separation process to ensure the technology is safe and environmental friendly.

The objective of this study is to remove the C.I Reactive Black 5 (RB5) and C.I Reactive Orange 16 (RO16) from aqueous solution using Micellar-enhanced Microfiltration (MEMF). The surfactant was characterized based on its functional group, critical micelle concentration (CMC) and micelle particle size. The study on MEMF was conducted at a constant feed dye concentration of 50 mg/L. A cationic biodegradable surfactant, plant based esterquat (PBE) was used in MEMF process and its effectiveness was investigated. A Mixed Cellulose Ester (MCE) microfiltration membrane with pore size of 0.45 μm was used under unstirred dead-end filtration. The investigation on the effect of feed surfactant concentration on MEMF of RB5 and RO16 dye is based on the percentage of dye removal and permeate flux of the separation.

EXPERIMENTAL

Materials

Reactive dyes; Reactive Black 5 (RB5) (MW 991.82) and Reactive Orange 16 (RO16) (MW 617.54) were purchased from Sigma Aldrich (M) Sdn. Bhd. The plant based esterquat (PBE) and mixed cellulose esters (MCE) membrane with pore size of 0.45 μm were obtained from Malaysian Palm Oil Board (MPOB) and Merck-Milipore respectively.

Critical Micelle Concentration

The critical micelle concentration (CMC) was determined from the concentration depending on the specific conductivity measurement of the aqueous solution at 27°C via WTW 3420 Multimeter. The conductivity measurements were conducted by placing a known volume of micellar surfactant solution into a beaker, and successive injection of deionized water was added respective to the selected surfactant concentration [22]. The solution was stirred via MR Hei-Tech Digital Hotplate stirrer whereby EKT Hei-Con temperature control was used to maintain the temperature of surfactant solution and the conductivity was measured. The final reading of conductivity value was obtained after 5 minutes of injection to ensure the attainment of equilibrium in the system.

Micellar-enhanced microfiltration (MEMF) process

All experiments were carried out at room temperature (27°C) using batch unstirred dead end filtration (model Sterlitech™ HP4750, USA). The dyes and PBE surfactant were mixed for 10 minutes with stirring speed of 300 rpm before it was loaded in the stirred cell. The operating pressure was controlled at 100 kPa (14.5 psig). The membrane was sonicated in deionized water (DI) water for 10 minutes at the end of each experiment and it will be reused if the water flux through the membrane deviated within ±5% of its initial value.

The dye concentration were kept constant at 50 mg/L throughout the experiment and the PBE concentration was varied at 1.5CMC, 1.75CMC, 2CMC, 2.25CMC, 2.5CMC

Analysis of the particle size and dyes concentration

Particle size analysis of PBE micelle formation was performed by Dynamic Light Scattering method using Zetananosizer ZS90. The analysis was performed at 100, 175 and 250 mg/L of PBE concentrations. Concentration of dyes in the feed and permeate were measured by Lambda UV-Vis

Spectrophotometer. The wavelength at which maximum absorption occur was 598 nm for RB5 and 493 nm for RO16.

RESULTS AND DISCUSSION

Critical micelle concentration

The critical micelle concentration (CMC) is considered as an indication of micellar stability form of surfactant relative to its monomeric form [23]. Determination of PBE's CMC measurement via conductivity method is shown in Fig. 1. From this figure, it is clearly shown that the conductivity values increase rapidly at the beginning, but then the increment gradually decreases with increased of PBE concentration. This observation indicates the formation of micelles in the surfactant solution. The break in slope of the curve at certain surfactant concentration identify the critical micelle concentration (CMC) [24]. The same observation also has been reported by other researchers in their study on determination of surfactant's CMC in aqueous solution [22], [25]-[27]. The CMC of PBE obtained from this study is 93.5 mg/L

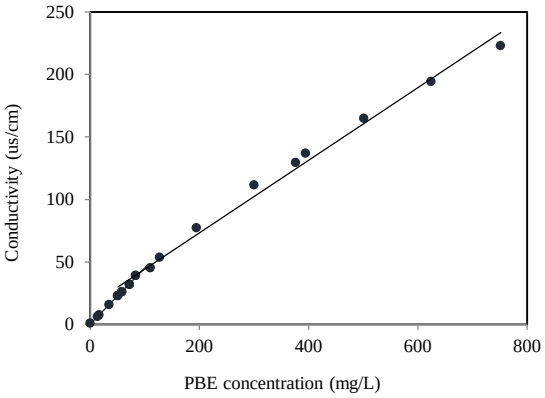

Fig. 1 Determination of PBE's CMC via conductivity method

Particle Size Analysis

The size distribution for PBE surfactant in aqueous solution was investigated by Dynamic Light Scattering (DLS) method. The PBE concentration was selected above its critical micelle concentration. Fig. 2 shows intensity-weighted particle size distribution of PBE micelles. It was found that a unimodal distribution was obtained for 100 and 175 mg/L of PBE surfactant. The highest intensity-weight percentage obtained at this concentration is 64% at 190 nm diameter (D). The diameter of micelles increased to 342 nm as the concentration of PBE surfactant increased to 175 mg/L, however there was a slight decreased of highest intensity-weighted percentage to 44%. The increase in particle diameter is due to the aggregation of micelles in solution. Further increment of PBE concentration to 250 mg/L resulted in bimodal distribution. The intensity-weight obtained were 6% (D=141 nm) and 16% (D=825 nm) represented by the first and second peak, respectively. Even though there was a sharp increment in micelles size, micelles with smaller diameter was also noticeable in the solution. Therefore, the bimodal distribution may indicates that some of the micelles formed are unstable at high concentration. As a result, some of the micelles formed disaggregate to monomer which can be observed as first peak of the bimodal distribution.

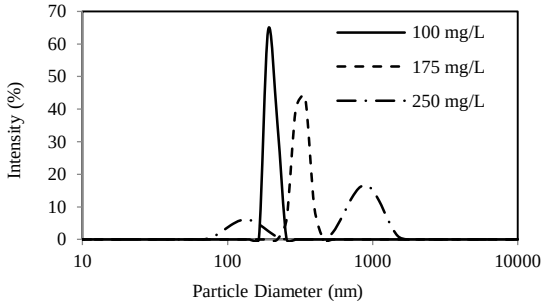

Fig. 2 Particle size distributions of aqueous dispersion of micelles at various PBE concentrations

Micellar-enhanced microfiltration (MEMF)

Fig. 3 presents the percentage of dye removal for MEMF of RB5 and RO16 dye using PBE surfactant For MEMF of RB5 and RO16 dye, it was observed that the percentage of dye removal for RB5 is higher than RO16 for all PBE concentrations. This finding is contradict with the study reported by Ahmad and Puasa [10] and Puasa, et al. [28] where the dye rejection of RO16 is higher as compared to RB5 using cetylpyridinium chloride (CPC) as surfactant via micellar-enhanced ultrafiltration (MEUF). The difference between these findings is due to the different type of surfactant used in the separation process. The CPC and PBE esterquat surfactants have different chemical structure although both are cationic surfactant. PBE esterquat consists of two hydrophobic tails while CPC consists only one hydrophobic tail and this lead to formation of different micelle shape for PBE esterquat and CPC. The CPC surfactant formed spherical micelle in aqueous solution [29], while PBE esterquat surfactant with double hydrophobic tail is unable to organize into classical spherical micelles but preferentially form vesicles and flexible bilayer micelles [23], [30]-[32]. During MEMF process, the micelle array on membrane surface for esterquat is more compact than CPC, hence increase the resistance of dye to pass through the membrane surface to the permeate side. Since RB5 has higher molecular weight (MW 991.82) than RO16 (MW 617.54), the possibilities of free-RB5 dye to retain

on membrane surface is higher as compared to RO16, thus increase the RB5 rejection.

For MEMF of single RB5 and RO16 dye, it was observed that as the concentration of PBE increased from 1.5CMC to 2.25CMC, there is a gradual increased of RO16 removal as compared to RB5 then slightly reduced at 2.5CMC. As discussed earlier, the elevated PBE concentration enhanced the number of micelles, consequently increase the RO16 solubilization in micelles [10], [21], [33]-[34]. As a result, more micelle will be retained on the membrane surface hence lead to sharp increment of RO16 dye rejection. The percentage of dye removal for MEMF of single RB5 dye initially increase slightly from 1.5CMC to 1.75CMC then it became almost invariant at PBE concentration exceed 1.75CMC. The highest dye removal obtained at PBE concentration of 2.25CMC were 99.98% and 99.81% for RB5 and RO16, respectively.

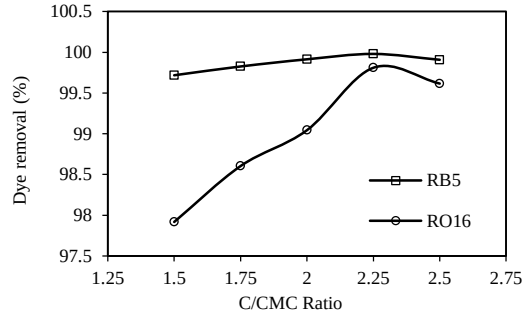

Fig. 3 Percentage of dye removal for MEMF of single RB5 and single RO16 dye for PBE surfactant

It is clearly shown in Fig. 4 that the permeate flux decreases with increase in PBE concentration. This indicates that the concentration of micelles increases with ascending of surfactant concentration. Thus, more micelles are retained on the membrane surface, forming a thicker layer of micelles known as gel layer, thereby offer more resistance against the solvent flux, consequently lowering the permeate flux. The same observation was also reported in the literature using MEUF [18], [35].

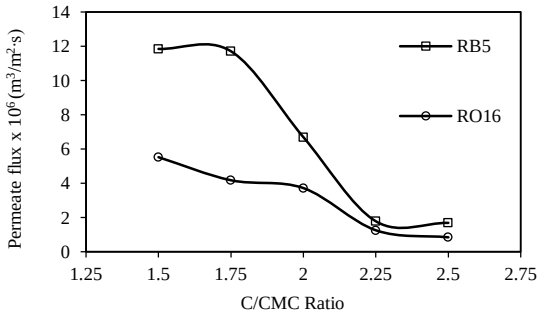

Fig. 4 Permeate flux for MEMF of RB5 and RO16 dye using PBE surfactant

The MEMF of RB5 dye obtained the highest permeate flux appears to be contradict with the finding reported by Puasa, et al. [28]. They reported the permeate flux for MEUF of RB5 is lower than RO16. The contradict results between these two findings may due to the different of surfactant used in separation process. Both RB5 and RO16 have good solubilization ability in CPC micelles although it is noted that RO16 more solubilize than RB5. However for PBE surfactant, the potential of RB5 to produce sparingly soluble precipitate with surfactant is high, hence reducing the chances of RB5 to get solubilized in PBE micelles. As a result, the micelles are less compacted with RB5 and subsequently reduce the volume of RB5-PBE micelles. Therefore, high permeate flux was obtained for MEMF of single RB5 as compared to other MEMF process.

In addition, it is noticeable that lowest permeate flux was obtained for MEMF of RO16 at 2.25CMC and 2.5CMC. This finding reveals that the solubilization of RO16 increase rapidly as the PBE concentration increased to 2.5CMC, thus increasing the amount of RO16 solubilized in surfactant micelles. Micelles are compacted with RO16 which increase the volume of RO16-PBE micelles, hence increasing the gel layer thickness and creating more resistance to the feed.

CONCLUSION

The Critical Micelle Concentration of PBE surfactant obtained was at the range of 93.5 mg/L via conductivity method. Since the CMC value of esterquat is less than 100 mg/L, therefore less amount of PBE surfactant is required in MEMF process. Based on particle size analysis, the diameter of micelles formed ranges from 140 to 1500 nm which facilitates the application of microfiltration membrane in separation process. The highest dye removal of RB5 and RO16 were 99.98% and 99.81%, respectively. From these observations, it is proven that MEMF using PBE as surfactant is possible to remove reactive dyes from aqueous solution. Results obtained in MEMF study using PBE surfactant shows almost complete decolourization of RB5 and RO16 where the permeate concentration is less than 1 mg/L. Therefore, MEMF using biodegradable plant based esterquat has a great potential to become a new green technology for removing reactive dyes from textile wastewater.

ACKNOWLEDGEMENTS

This work was financially supported by the Fundamental of Research Grant Scheme, from Ministry of Higher Education, Malaysia and Universiti Teknologi MARA, Malaysia. The authors would like to thank the Malaysian Palm Oil Board

(MPOB) for providing the plant-based esterquat for this project.

REFERENCES

[1] A. Latif, S. Noor, Q. M. Sharif, and M. Najeebullah, "Different Techniques Recently Used For the Treatment of Textile Dyeing Effluents: A Review," J. Chem. Sok. Pak, Vol. 32, 2010, pp. 115 - 124.

[2] Y. H. Lee and S. G. Pavlostathis, "Decolorization and toxicity of reactive anthraquinone textile dyes under methanogenic conditions," Water Research, Vol. 38, 2004, pp. 1838-1852.

[3] M. Grekova-Vasileva and Y. Topalova, "Biological Algorithms for textile wastewater management," Biotechnology & Biotechnological Equipment, Vol. 23 (2), May2009, pp. 442-447.

[4] S. Šostar-Turk, M. Simonič, and I. Petrinić, "Wastewater treatment after reactive printing," Dyes and Pigments, Vol. 64, 2005, pp. 147-152.

[5] D. Rajkumar and J. G. Kim, "Oxidation of various reactive dyes with in situ electro-generated active chlorine for textile dyeing industry wastewater treatment," Journal of Hazardous Materials, Vol. 136, 2006, pp. 203-212.

[6] N. K. Lazaridis, T. D. Karapantsios, and D. Georgantas, "Kinetic analysis for the removal of a reactive dye from aqueous solution onto hydrotalcite by adsorption," Water Research, Vol. 37, 2003, pp. 3023-3033.

[7] T.-H. Kim, C. Park, and S. Kim, "Water recycling from desalination and purification process of reactive dye manufacturing industry by combined membrane filtration," Journal of Cleaner Production, Vol. 13, 2005, pp. 779-786.

[8] C. Tang and V. Chen, "Nanofiltration of textile wastewater for water reuse," Desalination, Vol. 143, 2002, pp. 11-20.

[9] N. Zaghbani, A. Hafiane, and M. Dhahbi, "Removal of Direct Blue 71 from wastewater using micellar enhanced ultrafiltration," Desalination and Water Treatment, Vol. 6, Jun2009, pp. 204-210.

[10] A. L. Ahmad and S. W. Puasa, "Reactive dyes decolourization from an aqueous solution by combined coagulation/micellar-enhanced ultrafiltration process," Chemical Engineering Journal, Vol. 132, 2007, pp. 257-265.

[11] K. Exall, V. K. Balakrishnan, J. Toito, and R. McFadyen, "Impact of selected wastewater constituents on the removal of sulfonamide antibiotics via ultrafiltration and micellar enhanced ultrafiltration," Science of The Total Environment, Vol. 461–462, 2013, pp. 371-376.

[12] Ü. Danis and B. Keskinler, "Chromate removal from wastewater using micellar enhanced crossflow filtration: Effect of transmembrane pressure and crossflow velocity," Desalination, Vol. 249, 2009, pp. 1356-1364.

[13] J. Landaburu-Aguirre, V. García, E. Pongrácz, and R. L. Keiski, "The removal of zinc from synthetic wastewaters by micellar-enhanced ultrafiltration: statistical design of experiments," Desalination, Vol. 240, 2009, pp. 262-269.

[14] Y. S. Chung, S. H. Yoo, and C. K. Kim, "Effects of membrane hydrophilicity on the removal of a trihalomethane via micellar-enhanced ultrafiltration process," Journal of Membrane Science, Vol. 326, 2009, pp. 714-720.

[15] F. Luo, G.-M. Zeng, J.-H. Huang, C. Zhang, Y.-Y. Fang, Y.-H. Qu, *et al.*, "Effect of groups difference in surfactant on solubilization of aqueous phenol using MEUF," Journal of Hazardous Materials, Vol. 173, 2010, pp. 455-461.

[16] P. Yenphan, A. Chanachai, and R. Jiraratananon, "Experimental study on micellar-enhanced ultrafiltration (MEUF) of aqueous solution and wastewater containing lead ion with mixed surfactants," Desalination, Vol. 253, 2010, pp. 30-37.

[17] S. K. Misra, A. K. Mahatele, S. C. Tripathi, and A. Dakshinamoorthy, "Studies on the simultaneous removal of dissolved DBP and TBP as well as uranyl ions from aqueous solutions by using Micellar-Enhanced Ultrafiltration Technique," Hydrometallurgy, Vol. 96, 2009, pp. 47-51.

[18] N. Zaghbani, A. Hafiane, and M. Dhahbi, "Removal of Eriochrome Blue Black R from wastewater using micellar-enhanced ultrafiltration," Journal of Hazardous Materials, Vol. 168, 2009, pp. 1417-1421.

[19] M. Bielska and K. Prochaska, "Dyes separation by means of cross-flow ultrafiltration of micellar solutions," Dyes and Pigments, Vol. 74, 2007, pp. 410-415.

[20] G.-M. Zeng, X. Li, J.-H. Huang, C. Zhang, C.-F. Zhou, J. Niu, *et al.*, "Micellar-enhanced ultrafiltration of cadmium and methylene blue in synthetic wastewater using SDS," Journal of Hazardous Materials, Vol. 185, 2011, pp. 1304-1310.

[21] J.-H. Huang, C.-F. Zhou, G.-M. Zeng, X. Li, H.-J. Huang, J. Niu, *et al.*, "Studies on the

solubilization of aqueous methylene blue in surfactant using MEUF," Separation and Purification Technology, Vol. 98, 2012, pp. 497-502.

[22] S. K. Mehta, K. K. Bhasin, R. Chauhan, and S. Dham, "Effect of temperature on critical micelle concentration and thermodynamic behavior of dodecyldimethylethylammonium bromide and dodecyltrimethylammonium chloride in aqueous media," Colloids and Surfaces A: Physicochemical and Engineering Aspects, Vol. 255, 2005, pp. 153-157.

[23] M. Achouri, S. Alehyen, A. Assioui, R. Chami, F. Bensajjay, L. Pérez, *et al.*, "Synthesis and Physico-Chemical Studies of Ester-Quat Surfactants in the Series of (Dodecanoyloxy)propyl n-Alkyl Dimethyl Ammonium Bromide," Journal of Surfactants and Detergents, Vol. 16, 2013/07/012013, pp. 473-485.

[24] A. Di Michele, L. Brinchi, P. Di Profio, R. Germani, G. Savelli, and G. Onori, "Effect of head group size, temperature and counterion specificity on cationic micelles," Journal of Colloid and Interface Science, Vol. 358, 2011, pp. 160-166.

[25] N. Kumaraguru, K. Santhakumar, S. Arunachalam, and M. N. Arumugham, "Synthesis, characterization and micellization behaviour of some surface active mixed-ligand complexes of cobalt(III)," Polyhedron, Vol. 25, 2006, pp. 3253-3260.

[26] E. Samper, M. Rodríguez, M. A. De la Rubia, and D. Prats, "Removal of metal ions at low concentration by micellar-enhanced ultrafiltration (MEUF) using sodium dodecyl sulfate (SDS) and linear alkylbenzene sulfonate (LAS)," Separation and Purification Technology, Vol. 65, 2009, pp. 337-342.

[27] T. Farías, L. C. de Ménorval, J. Zajac, and A. Rivera, "Solubilization of drugs by cationic surfactants micelles: Conductivity and 1H NMR experiments," Colloids and Surfaces A: Physicochemical and Engineering Aspects, Vol. 345, 2009, pp. 51-57.

[28] S. W. Puasa, M. S. Ruzitah, and A. S. A. K. Sharifah, "Competitive removal of Reactive Black 5/Reactive Orange 16 from aqueous solution via Micellar-enhanced ultrafiltration," International Journal of Chemical Engineering and Applications, Vol. 3, October 20122012, pp. 354-358.

[29] M. Syamal, S. De, and P. K. Bhattacharya, "Phenol solubilization by cetyl pyridinium chloride micelles in micellar enhanced ultrafiltration," Journal of Membrane Science, Vol. 137, 12/24/1997, pp. 99-107.

[30] D. Myers, "Surfactant Science and Technology", Third Edition ed. New Jersey: John Wiley & Sons. Inc, 2006.

[31] S. Tunç, O. Duman, and B. Kancı, "Spectrophotometric investigation of the interactions between cationic dye (C.I. Basic Yellow 2) and anionic surfactant (sodium dioctylsulfosuccinate) in the premicellar and micellar region," Dyes and Pigments, Vol. 94, 2012, pp. 233-238.

[32] F. Abdel-Salam and A. El-Said, "Synthesis and Surface Active Properties of Gemini Cationic Surfactants and Interaction with Anionic Azo Dye (AR52)," Journal of Surfactants and Detergents, Vol. 14, 2011/07/012011, pp. 371-379.

[33] W. Zhang, G. Huang, J. Wei, H. Li, R. Zheng, and Y. Zhou, "Removal of phenol from synthetic waste water using Gemini micellar-enhanced ultrafiltration (GMEUF)," Journal of Hazardous Materials, Vol. 235–236, 2012, pp. 128-137.

[34] M. K. Purkait, S. DasGupta, and S. De, "Removal of dye from wastewater using micellar-enhanced ultrafiltration and recovery of surfactant," Separation and Purification Technology, Vol. 37, 2004, pp. 81-92.

[35] W. Zhang, G. Huang, J. Wei, and D. Yan, "Gemini micellar enhanced ultrafiltration (GMEUF) process for the treatment of phenol wastewater," Desalination, Vol. 311, 2013, pp. 31-36.

First International Conference on Science, Engineering & Environment,
Tsu City, Mie, Japan, Nov.19-21, 2015, ISBN: 978-4-9905958-5-2 C3051

MESSAGE PASSING ALGORITHM BASED ON CUT NODE TREE

Zhang Huanming, Xian Kaiyi, Feng Lijun, Hu Chaokang
Electronics and Information Engineering Institute
Foshan University, Foshan, Guangdong, China, 528000

ABSTRACT

An LDPC code can be described by a bipartite graph called Tanner graph[1]. Loops, especially short loops in tanner graph, degrade the performance of LDPC decoder, because they affect the independence of the extrinsic information exchanged in the iterative decoding. This paper, based on message passing in trees in Graph, proposes new decoding schemes for LDPC codes to suppress repeated iteration of information in SPA.

Keywords—LDPC; belief propagation (BP); graph; iterative decoding; loop; cycle

1. BACKGROUD

In coding theory, Tanner graph, named after Michael Tanner, is a bipartite graph used to state constraints or equations which specify error correcting codes[2]. See Figure 1. They are used to construct longer codes from smaller ones. Both encoders and decoders employ these graphs extensively[3][4].

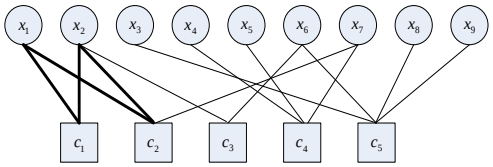

Figure 1. Tanner graph of an LDPC code

In communication system, the transmitted random vector $x=\{x_1,\cdots,x_N\}$ is not observed; instead received noisy vector $y=\{y_1,\cdots,y_N\}$.

N is the length of codeword，Parity check equation vector is $c=\{c_1,c_2,\cdots,c_M\}$, *M* is the number of equations. $f=\{f_1^{\,a},\cdots,f_N^{\,a}\}$ represents initial information about transmitted codeword.

Where v_i is the *i*th variable node, and c_j is the *j*th check equation.

The belief propagation(BP) of LDPC code states as follows[5-7]：

R_{ji}^a is check information from check node c_j to variable node v_i, and Q_{ij}^a variable information from v_i to check node c_j .See Figure 2.

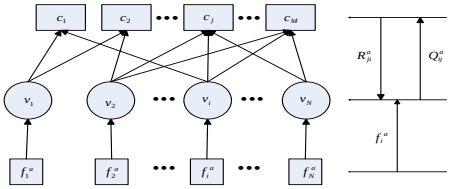

Figure 2. Iterative Decoding Algorithm

$$R_{ji}^0(t+1)=\frac{1}{2}\left(1+\prod_{j'\in N(i)\setminus j}\left(1-2Q_{ij'}^1(t)\right)\right) \quad (1)$$

$$R_{ji}^1(t+1)=1-R_{ji}^0(t+1) \quad (2)$$

$$Q_{ij}^0(t+1)=\alpha_{ij}(1-P_i)\prod_{i'\in M(j)\setminus i}R_{ji}^0(t+1) \quad (3)$$

$$Q_{ij}^1(t+1)=\alpha_{ij}P_i\prod_{i'\in M(j)\setminus i}R_{ji}^1(t+1) \quad (4)$$

where α_{ij} denotes a normalization constant, $Q_{ij}^0(t+1)+Q_{ij}^1(t+1)=1$. See Figure 3[8].

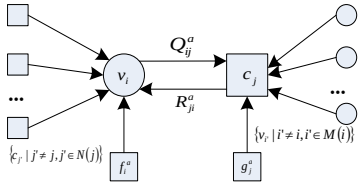

Figure 3. Updating rule for message passing

2. PRINCIPLE OF CUT-NODE TREE

In order to solute loops of LDPC code, avoiding repeated information iteration. Tanner graph is re-drew as following principle: Choosing an element '1' in *H*, its variable(or check) node considered root node, check (or variable)nodes connected to the variable(or check) node as 1st order child-nodes, a current node, once appearance in ancestor node or sibling node, will be cut and forbid to grow and become an end node like a leaf, but not a leaf actually. And so forth, at last a cut-node tree can be get. If all nodes are connected, a single cut-node tree can be got, otherwise it is forest. Repeating this process until all end nodes are either cut-node or leaf node. See Figure 4.

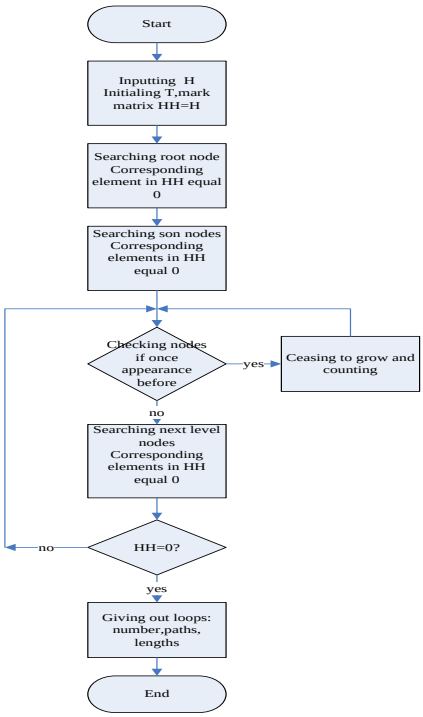

Figure 4. Flow process chart of algorithm

HH is mark matrix, when a node appears in graph, the element in HH changes to zero, every element is zero in HH represents end of algorithm.

3. IMPLEMENT OF PRINCIPLE AND RESULTS

First, a node (variable node or check node), for instance, variable node $v_i, h_{ij}=1$, should be chose as root node, its son nodes are those which connect to it, according to this principle, all child-nodes can be obtained. This process can be implemented by computer simulation in matlab's celluar array, and express H by means of cut-node tree[6].

An example: for

$$H=\begin{bmatrix}1&0&1&0&1&0&1&0\\1&0&0&1&0&1&0&1\\0&1&1&0&0&1&1&0\\0&1&0&1&1&0&0&1\end{bmatrix} \quad (5)$$

has following cut-node tree graph(See Figure 5.)

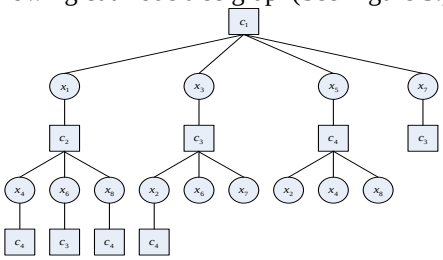

Figure 5. Tree Graph of LDPC codes

Another example: For instance, an LDPC code with check matrix H:

$$H=\begin{bmatrix}1&1&1&1&0&0&0&0&0&0\\1&0&0&0&1&1&1&0&0&0\\0&1&0&0&1&0&0&1&1&0\\0&0&1&0&0&1&0&1&0&1\\0&0&0&1&0&0&1&1&0&1\end{bmatrix} \quad (6)$$

Following tree matrix expressed by matlab can be get, In fact, tree matrix matches along with Tree of Graph, [i j k l m], [i j] states current node, [k l] states father node, m states times being cut.

So，searched by a computer, all loops and features can be get by this algorithm, see Table 1.

Table 1: Features of loops about above example:

Sparsity	loops	Total length of loops	Average length	girth	Maximum length	Loop relativity
0.4	16	108	6.75	6	10	3.18

Here, H is just a situation of single tree, with 15 cut-nodes, no leaf node and 16 loops. Further, Message-passing form for cut-node tree has following rule:

In a tree, Message-passing fellows a two-pass form, first sweeping upwards from leaves to a node designated as the root, and then downwards from the root to leaves.

In a graph with cycle，Cut-node tree graph can be get by cutting all loops, See Figure 6.

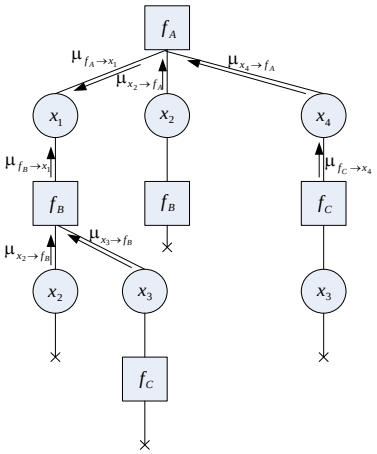

Figure 6. Message passing over cut-node tree graph

Cut node tree has all same characters with Tanner graph.

4. CONLUSION

This paper provides a new method to describe graph of LDPC codes, it aims to solute loops of LDPC codes and message passing over cut node tree. For a large matrix H, it is difficult to solute loops, because loops convolve each other. Features of loops have certain relationship with performances. In this paper, A cut node tree can be expressed by a certain matrix. By computer simulation, cut-node tree can get right answer

and gives out method to calculate loops of LDPC codes and cut node tree graph, its results assist to further research on this relationship.

REFERENCE

[1] R. G. Gallager, Low-Density Parity Check Codes, MIT Press, Cambridge, MA, 1963.

[2] D. J. C. Mackay, "Good Error-Correcting Codes Based on Very Sparse Matrices", IEEE Trans. Inform. Theory, vol. 45, 399-431,Mar. 1999.

[3] R. M. Tanner, "A recursive approach to low complexity codes," IEEE Trans. Inf Theory, pp. 533-547, Sept. 1981

[4]R.Kschischang, B.J.Frey, and H.A.Loeliger, “Factor graphs and the sum-product algorithm” IEEE Trans. Inform. Theory, vol.47, no.2, pp.498–519, Feb 2001.

[5] N.Wiberg, Codes and decoding on general graphs, Linkoping Studies in Science and Technology, Ph.D. dissertation No. 440, Univ. Link oping, Sweden, 1996.

[6] Reinhard D, Graph Theory[M]. New York: Springer-Verlag, 1997

[7] Martin J. Wainwright, Sparse Graph Codes for Side Information and Binning, IEEE SIGNAL PROCESSING MAGAZINE [47],47-57, SEPTEMBER 2007

[8] Martin Wainwright, Tommi Jaakkola, and Alan Willsky, Tree-based reparameterization analysis of belief propagation and related algorithms for approximate inference on graphs with cycles, ISIT2002, Lausanne, Switzerland, June 30-July 5, 2002

First International Conference on Science, Engineering & Environment,
Tsu City, Mie, Japan, Nov.19-21, 2015, ISBN: 978-4-9905958-5-2 C3051

ON THE TURBULENT BOUNDARY LAYER OF A RAPID-FLOWING DRY GRANULAR MATTER DOWN AN INCLINE: THEORY AND NUMERICAL SIMULATIONS

Chung Fang
Department of Civil Engineering, National Cheng Kung University, Taiwan

ABSTRACT

Rheological characteristics of the turbulent boundary layer of an isothermal dry granular avalanche down an incline are investigated by using the proposed zero-order turbulent closure model. The first and second laws of thermodynamics are used to derive the equilibrium closure relations satisfying turbulence realizability conditions, with their dynamic responses postulated within a nonlinear theory. While the mean volume fraction and velocity increase from the solid plane toward the free surface exponentially, the turbulent kinetic energy and dissipation evolve in a reverse manner. Most turbulent kinetic energy and dissipation are confined within the thin turbulent boundary layer immediately above the plane, with nearly vanishing turbulent kinetic energy and finite turbulent dissipation in the relatively thick layer (the passive layer) above the turbulent boundary layer. These features demonstrate a similarity with those of conventional Newtonian fluids in turbulent boundary layer flows. The turbulent boundary and passive layers are preferable verified by the distributions of the turbulent kinetic energy and dissipation

Keywords: Closure model, Dry granular avalanche, Thermodynamics, Turbulent boundary layer

INTRODUCTION

Dry granular avalanches are dry granular flows in collisional state, in which the grain-grain interactions result mainly from the short-term instantaneous inelastic collision, with minor contribution from the long-term enduring frictional contact and sliding [1-4]. Field observations suggest that a dry granular avalanche consists of two layers: immediately above the base there exists a very thin layer, called the turbulent boundary layer, in which the grains collide vigorously with one another, resulting in reduced base friction so that an avalanche can travel unexpected long distance. Above the turbulent boundary layer these exists a relatively thick layer, called the passive layer. In the passive layer, the grains are dominated by the long-term grain-grain interaction. They interlock with one another to form a kind of inelastic network and behave as a lump solid [5-8].

Although the two-layer conjecture of a granular avalanche can to some extent be verified by using the laminar flow formulations through the solid content and velocity distributions, e.g. [9-15], it will be preferably verified by studying the distributions of the turbulent kinetic energy and dissipation, for two-fold grain-grain interaction induce fluctuations on the macroscopic properties, a phenomenon similar to turbulent flows on conventional Newtonian fluids [16,17].

Thus, the goal of the study is to propose a zero-order turbulent closure model for isothermal, dry granular avalanches with incompressible solid grains. To this end, the first and second laws of thermodynamics, in the context of Mueller-Liu entropy principle, will be used to derive the equilibrium closure relations satisfying turbulence realizability conditions, with the non-equilibrium responses postulated within a nonlinear theory. The obtained closure model is used to analyses of a gravity-driven stationary flow down an incline to illustrate the distributions of the turbulent kinetic energy and dissipation with their influence on the mean flow characteristics, and to verify the rheological characteristics of the turbulent boundary and passive layers with their similarities to those of Newtonian fluids.

MEAN BALANCE EQUATIONS

Following previous works [18-20], the balance equations are given by

$$0 = \dot{\bar{\gamma}}\bar{\nu} + \bar{\gamma}\dot{\bar{\nu}} + \bar{\gamma}\bar{\nu}\nabla\cdot\bar{\boldsymbol{v}}, \tag{1}$$

$$\boldsymbol{0} = \bar{\gamma}\bar{\nu}\dot{\bar{\boldsymbol{v}}} - \nabla\cdot(\bar{\boldsymbol{t}} + \boldsymbol{R}) - \bar{\gamma}\bar{\nu}\bar{\boldsymbol{b}}, \tag{2}$$

$$\boldsymbol{0} = \bar{\boldsymbol{t}} - \bar{\boldsymbol{t}}^{\mathrm{t}}, \tag{3}$$

$$0 = \bar{\gamma}\bar{\nu}\dot{\bar{e}} - \bar{\boldsymbol{t}}\cdot\bar{\boldsymbol{D}} + \nabla\cdot(\bar{\boldsymbol{q}} + \boldsymbol{Q}) - \bar{\gamma}\bar{\nu}\varepsilon - \bar{\gamma}\bar{\nu}\bar{r} - \ell\bar{\boldsymbol{h}}\cdot\nabla\dot{\bar{\nu}} + \bar{\gamma}\bar{\nu}\bar{f}\ell\dot{\bar{\nu}} - \bar{\gamma}\bar{\nu}H, \tag{4}$$

$$0 = \bar{\gamma}\bar{\nu}\dot{\bar{\eta}} + \nabla\cdot(\bar{\phi} + \phi') - \bar{\gamma}\bar{\nu}\bar{\sigma} - \bar{\pi}, \tag{5}$$

$$0 = \bar{\gamma}\bar{\nu}\ell\ddot{\bar{\nu}} - \nabla\cdot(\bar{\boldsymbol{h}} + \boldsymbol{H}) - \bar{\gamma}\bar{\nu}\bar{f}, \tag{6}$$

$$\boldsymbol{0} = \mathring{\bar{\boldsymbol{Z}}} - \bar{\boldsymbol{\Phi}},\ (\mathring{\bar{\boldsymbol{Z}}} \equiv \dot{\bar{\boldsymbol{Z}}} - [\bar{\boldsymbol{\Omega}}, \bar{\boldsymbol{Z}}]), \tag{7}$$

$$0 = \bar{\gamma}\bar{\nu}\dot{\bar{k}} - \boldsymbol{R}\cdot\bar{\boldsymbol{D}} - \nabla\cdot\boldsymbol{K} + \bar{\gamma}\bar{\nu}\varepsilon, \tag{8}$$

$$0 = \bar{\gamma}\bar{\nu}\dot{s} - \ell\boldsymbol{H}\cdot\nabla\dot{\bar{\nu}} - \nabla\cdot\boldsymbol{L} + \bar{\gamma}\bar{\nu}H, \tag{9}$$

with the ergodic terms,

$$0 = R_{ij} + \bar{\gamma}\bar{\nu}\overline{v_i' v_j'}, \qquad 0 = H_j - \ell R_{ij}\frac{\partial \bar{\nu}}{\partial x_i}, \tag{10}$$

$$0 = \phi_j' - \bar{\gamma}\bar{\nu}\overline{\eta' v_j'}, \qquad 0 = Q_j - \bar{\gamma}\bar{\nu}\overline{e' v_j'}, \tag{11}$$

$$0 = \bar{\gamma}\bar{\nu}\varepsilon - \overline{t_{ij}'\frac{\partial v_i'}{\partial x_j}}, \qquad 0 = M_{ij} - \ell\overline{h_i' v_j'}, \tag{12}$$

$$0 = \bar{\gamma}\bar{\nu}k - \frac{1}{2}\bar{\gamma}\bar{\nu}\overline{v_i' v_j'}, \quad 0 = K_j - \overline{t_{ij}' v_i'} - \frac{1}{2}R_{iij}, \tag{13}$$

$$0 = \bar{\gamma}\bar{\nu}s + \frac{1}{2}\ell^2 R_{ij}\frac{\partial \bar{\nu}}{\partial x_i}\frac{\partial \bar{\nu}}{\partial x_j}, \tag{14}$$

$$0 = \bar{\gamma}\bar{\nu}H - M_{ij}\frac{\partial^2 \bar{\nu}}{\partial x_i x_j} - \bar{\gamma}\bar{\nu}d, \tag{15}$$

$$0 = \bar{\gamma}\bar{\nu}d - \ell\left(\overline{h_i'\frac{\partial v_j'}{\partial x_i}} - \bar{\gamma}\bar{\nu}\overline{f' v_j'}\right)\frac{\partial \bar{\nu}}{\partial x_j}, \tag{16}$$

$$0 = R_{ijk} + \bar{\gamma}\bar{\nu}\overline{v_i' v_j' v_k'}, \tag{17}$$

$$0 = L_j - M_{ji}\frac{\partial \bar{\nu}}{\partial x_i} - \frac{1}{2}\ell^2 R_{ijk}\frac{\partial \bar{\nu}}{\partial x_i}\frac{\partial \bar{\nu}}{\partial x_k}, \tag{18}$$

with the physical interpretations of the variables and equations (1)-(18) summarized in [21]. The ergodic terms needs be prescribed as functions of the primitive mean fields, as will be discussed in the following.

With these, the quantities

$$\begin{aligned}\mathcal{P} &= \{\bar{\gamma}, \bar{\nu}, \bar{\boldsymbol{v}}, \bar{\boldsymbol{Z}}, \vartheta^M, \vartheta^T, \vartheta^G\},\\ \mathcal{C} &= \{\bar{\boldsymbol{t}}, \boldsymbol{R}, \bar{e}, \bar{\boldsymbol{q}}, \boldsymbol{Q}, \bar{\eta}, \boldsymbol{\phi}^T, \bar{\boldsymbol{h}}, \boldsymbol{H}, \bar{f}, \bar{\boldsymbol{\Phi}}, k, s, \boldsymbol{K}, \boldsymbol{L}, \varepsilon, H\},\end{aligned} \tag{19}$$

are introduced respectively as the primitive mean fields and closure relations, by which C should be constructed based on the turbulent state space given by

$$\begin{aligned}\mathcal{Q} &= \{\nu_0, \bar{\nu}, \dot{\bar{\nu}}, \boldsymbol{g}_1, \bar{\gamma}, \boldsymbol{g}_2, \vartheta^M, \boldsymbol{g}_3, \vartheta^T, \boldsymbol{g}_4, \vartheta^G, \boldsymbol{g}_5, \bar{\boldsymbol{D}}, \bar{\boldsymbol{Z}}\},\\ \mathcal{C} &= \hat{\mathcal{C}}(\mathcal{Q}),\end{aligned} \tag{20}$$

with the definitions and interpretations summarized again in [21].

THERMODYNAMIC ANALYSIS

The turbulence realizability conditions require that, during a physically admissible process, the second law of thermodynamics with a local form of a non-negative entropy production, and all balance equations should be fulfilled simultaneously. This can be achieved by considering the mean balance equations as the constraints of the inequality (5) via the method of Lagrange multiplier viz.,

$$\begin{aligned}\bar{\pi} = {} & \bar{\gamma}\bar{\nu}\dot{\bar{\eta}} + \nabla\cdot\boldsymbol{\phi}^T - \bar{\gamma}\bar{\nu}\bar{\sigma}\\ & -\lambda^{\bar{\gamma}}\left(\dot{\bar{\gamma}}\bar{\nu} + \bar{\gamma}\dot{\bar{\nu}} + \bar{\gamma}\bar{\nu}\nabla\cdot\bar{\boldsymbol{v}}\right)\\ & -\boldsymbol{\lambda}^{\bar{\boldsymbol{v}}}\cdot\left(\bar{\gamma}\bar{\nu}\dot{\bar{\boldsymbol{v}}} - \nabla\cdot(\bar{\boldsymbol{t}} + \boldsymbol{R}) - \bar{\gamma}\bar{\nu}\bar{\boldsymbol{b}}\right)\\ & -\lambda^{\bar{e}}\big(\bar{\gamma}\bar{\nu}\dot{\bar{e}} - \bar{\boldsymbol{t}}\cdot\bar{\boldsymbol{D}} + \nabla\cdot(\bar{\boldsymbol{q}} + \boldsymbol{Q}) - \bar{\gamma}\bar{\nu}\varepsilon - \bar{\gamma}\bar{\nu}\bar{r}\\ & \qquad -\ell\bar{\boldsymbol{h}}\cdot\nabla\dot{\bar{\nu}} + \bar{\gamma}\bar{\nu}\bar{f}\ell\dot{\bar{\nu}} - \bar{\gamma}\bar{\nu}H\big)\\ & -\lambda^{\bar{\nu}}\left(\bar{\gamma}\bar{\nu}\ell\ddot{\bar{\nu}} - \nabla\cdot(\bar{\boldsymbol{h}} + \boldsymbol{H}) - \bar{\gamma}\bar{\nu}\bar{f}\right)\\ & -\boldsymbol{\lambda}^{\bar{\boldsymbol{Z}}}\cdot\left(\dot{\bar{\boldsymbol{Z}}} - [\boldsymbol{\Omega}, \bar{\boldsymbol{Z}}] - \bar{\boldsymbol{\Phi}}\right)\\ & -\lambda^{k}\left(\bar{\gamma}\bar{\nu}\dot{k} - \boldsymbol{R}\cdot\bar{\boldsymbol{D}} - \nabla\cdot\boldsymbol{K} + \bar{\gamma}\bar{\nu}\varepsilon\right)\\ & -\lambda^{s}\left(\bar{\gamma}\bar{\nu}\dot{s} - \ell\boldsymbol{H}\cdot\nabla\dot{\bar{\nu}} - \nabla\cdot\boldsymbol{L} + \bar{\gamma}\bar{\nu}H\right) \geq 0,\end{aligned} \tag{21}$$

which can be further exploited by using (19) with the chain rule of differentiation. In doing so, the Liu identities and residual entropy inequality can be deduced. While the former can be applied to identify the functionals of the physical properties, in particular the turbulent Helmholtz free energy, the latter is used to derive the equilibrium closure relations. Please refer to [21] for detailed information.

With these, the derived thermodynamically consistent equilibrium closure relations are given by

$$\begin{aligned}0 = {} & (\vartheta^M - \vartheta^T)\bar{\gamma}\bar{\nu}\varepsilon|_{\mathrm{E}} + (\vartheta^M - \vartheta^G)\bar{\gamma}\bar{\nu}H|_{\mathrm{E}}\\ & -\bar{\gamma}\bar{\nu}\vartheta^M\psi^T_{,\bar{\boldsymbol{Z}}}\cdot\bar{\boldsymbol{\Phi}}|_{\mathrm{E}},\end{aligned} \tag{22}$$

$$\begin{aligned}0 = {} & \vartheta^M(\bar{p} - \bar{\beta} - \bar{\gamma}\bar{\nu}\bar{f}|_{\mathrm{E}}\ell) + (\vartheta^M - \vartheta^T)\bar{\gamma}\bar{\nu}\varepsilon_{,\dot{\bar{\nu}}}|_{\mathrm{E}}\\ & +(\vartheta^M - \vartheta^G)\bar{\gamma}\bar{\nu}H_{,\dot{\bar{\nu}}}|_{\mathrm{E}} - \bar{\gamma}\bar{\nu}\vartheta^M\psi^T_{,\bar{\boldsymbol{Z}}}\cdot\bar{\boldsymbol{\Phi}}_{,\dot{\bar{\nu}}}|_{\mathrm{E}},\end{aligned} \tag{23}$$

$$\begin{aligned}\boldsymbol{0} = {} & (\bar{\boldsymbol{q}} + \boldsymbol{Q})|_{\mathrm{E}} + (\vartheta^M - \vartheta^T)\bar{\gamma}\bar{\nu}\varepsilon_{,\boldsymbol{g}_3}|_{\mathrm{E}}\\ & +(\vartheta^M - \vartheta^G)\bar{\gamma}\bar{\nu}H_{,\boldsymbol{g}_3}|_{\mathrm{E}} - \bar{\gamma}\bar{\nu}\vartheta^M\psi^T_{,\bar{\boldsymbol{Z}}}\cdot\bar{\boldsymbol{\Phi}}_{,\boldsymbol{g}_3}|_{\mathrm{E}},\end{aligned} \tag{24}$$

$$\begin{aligned}\boldsymbol{0} = {} & -\boldsymbol{K}|_{\mathrm{E}} + (\vartheta^M - \vartheta^T)\bar{\gamma}\bar{\nu}\varepsilon_{,\boldsymbol{g}_4}|_{\mathrm{E}}\\ & +(\vartheta^M - \vartheta^G)\bar{\gamma}\bar{\nu}H_{,\boldsymbol{g}_4}|_{\mathrm{E}} - \bar{\gamma}\bar{\nu}\vartheta^M\psi^T_{,\bar{\boldsymbol{Z}}}\cdot\bar{\boldsymbol{\Phi}}_{,\boldsymbol{g}_4}|_{\mathrm{E}},\end{aligned} \tag{25}$$

$$\begin{aligned}\boldsymbol{0} = {} & -\boldsymbol{L}|_{\mathrm{E}} + (\vartheta^M - \vartheta^T)\bar{\gamma}\bar{\nu}\varepsilon_{,\boldsymbol{g}_5}|_{\mathrm{E}}\\ & +(\vartheta^M - \vartheta^G)\bar{\gamma}\bar{\nu}H_{,\boldsymbol{g}_5}|_{\mathrm{E}} - \bar{\gamma}\bar{\nu}\vartheta^M\psi^T_{,\bar{\boldsymbol{Z}}}\cdot\bar{\boldsymbol{\Phi}}_{,\boldsymbol{g}_5}|_{\mathrm{E}},\end{aligned} \tag{26}$$

$$\begin{aligned}\boldsymbol{0} = {} & \vartheta^M\bar{\boldsymbol{t}}|_{\mathrm{E}} + \vartheta^T\boldsymbol{R}|_{\mathrm{E}} + \bar{\nu}\vartheta^M\bar{p}\boldsymbol{I} + \bar{\gamma}\bar{\nu}\vartheta^M\psi^T_{,\boldsymbol{g}_1}\otimes\boldsymbol{g}_1\\ & +(\vartheta^M - \vartheta^T)\bar{\gamma}\bar{\nu}\varepsilon_{,\bar{\boldsymbol{D}}}|_{\mathrm{E}} + (\vartheta^M - \vartheta^G)\bar{\gamma}\bar{\nu}H_{,\bar{\boldsymbol{D}}}|_{\mathrm{E}}\\ & -\bar{\gamma}\bar{\nu}\vartheta^M\psi^T_{,\bar{\boldsymbol{Z}}}\cdot\bar{\boldsymbol{\Phi}}_{,\bar{\boldsymbol{D}}}|_{\mathrm{E}}.\end{aligned} \tag{27}$$

CLOSURE MODEL

For isothermal flows with incompressible grains, the specific forms of the dynamic responses of the closure relations are postulated by

$$\begin{aligned}\boldsymbol{0} &= \bar{\boldsymbol{t}}^D - \epsilon^M\dot{\bar{\nu}}\boldsymbol{I} - \lambda^M(tr\bar{\boldsymbol{D}})\boldsymbol{I} - 2\mu^M\bar{\boldsymbol{D}},\\ \boldsymbol{0} &= \boldsymbol{R}^D - \epsilon^T\dot{\bar{\nu}}\boldsymbol{I} - \lambda^T(tr\bar{\boldsymbol{D}})\boldsymbol{I} - 2\mu^T\bar{\boldsymbol{D}},\\ 0 &= f^D + \zeta\dot{\bar{\nu}} + \delta(tr\bar{\boldsymbol{D}}),\\ 0 &= \bar{\gamma}\bar{\nu}\varepsilon^D - f_1\dot{\bar{\nu}} - f_2(tr\bar{\boldsymbol{D}}) - f_3(\boldsymbol{g}_4\cdot\boldsymbol{g}_4),\\ 0 &= \bar{\gamma}\bar{\nu}H^D - f_4\dot{\bar{\nu}} - f_5(tr\bar{\boldsymbol{D}}) - f_6(\boldsymbol{g}_5\cdot\boldsymbol{g}_5),\\ \boldsymbol{0} &= \boldsymbol{K}^D + f_7\boldsymbol{g}_4, \qquad \boldsymbol{0} = \boldsymbol{L}^D + f_8\boldsymbol{g}_5,\end{aligned} \tag{28}$$

with the physical parameters defined in [22]. These quasi-static expressions of the dynamic closure relations are justified as a first approximation in the turbulent formulation of dry granular avalanche.

By prescribing the specific forms of the turbulent Helmholtz free energy, material and turbulent viscosities, and a hypoplastic model for the rate-independent characteristics, the complete closure relations are established viz.,

$$0 = \bar{\gamma}\bar{\nu}k - \bar{\gamma}\bar{\nu}\left(\alpha_0(\bar{\nu}-\bar{\nu}_m)^2 + \beta_0\left(\frac{\bar{\nu}_m}{\bar{\nu}_\infty-\bar{\nu}}\right)^2\cdot (\boldsymbol{g}_1\cdot\boldsymbol{g}_1)\right)\left(1+\frac{\vartheta^T}{\vartheta^M}\right), \tag{29}$$

$$0 = \bar{\gamma}\bar{\nu}\varepsilon - f_1\dot{\bar{\nu}} - f_2(tr\bar{\boldsymbol{D}}) - f_3(\boldsymbol{g}_4\cdot\boldsymbol{g}_4), \tag{30}$$

$$0 = \bar{\gamma}\bar{\nu}s - \bar{\gamma}\bar{\nu}\left(\alpha_0(\bar{\nu}-\bar{\nu}_m)^2 + \beta_0\left(\frac{\bar{\nu}_m}{\bar{\nu}_\infty-\bar{\nu}}\right)^2\cdot (\boldsymbol{g}_1\cdot\boldsymbol{g}_1)\right)\left(1+\frac{\vartheta^G}{\vartheta^M}\right), \tag{31}$$

$$0 = \bar{\gamma}\bar{\nu}H - f_4\dot{\bar{\nu}} - f_5(tr\bar{\boldsymbol{D}}) - f_6(\boldsymbol{g}_5\cdot\boldsymbol{g}_5), \tag{32}$$

$$\boldsymbol{0} = \ell(\vartheta^M\bar{\boldsymbol{h}} + \vartheta^G\boldsymbol{H}) - 2\beta_0\bar{\gamma}\bar{\nu}\vartheta^M\mathcal{F}_c\left(\frac{\bar{\nu}_m}{\bar{\nu}_\infty-\bar{\nu}}\right)^2\boldsymbol{g}_1 \tag{33}$$

$$\boldsymbol{0} = \boldsymbol{H} - \ell\boldsymbol{R}\boldsymbol{g}_1, \quad \boldsymbol{0} = \boldsymbol{K} + f_7\boldsymbol{g}_4, \quad \boldsymbol{0} = \boldsymbol{L} + f_8\boldsymbol{g}_5 \tag{34}$$

$$0 = \bar{f} - \frac{\bar{p}}{\bar{\gamma}\bar{\nu}\ell} + \frac{2}{\ell}\left(\alpha_0(\bar{\nu}-\bar{\nu}_m) + \frac{\beta_0\bar{\nu}_m^2}{(\bar{\nu}_\infty-\bar{\nu})^3}\cdot(\boldsymbol{g}_1\cdot\boldsymbol{g}_1)\right)\mathcal{F}_c - \left(1-\frac{\vartheta^T}{\vartheta^M}\right)\frac{f_1}{\bar{\gamma}\bar{\nu}\ell} - \left(1-\frac{\vartheta^G}{\vartheta^M}\right)\frac{f_4}{\bar{\gamma}\bar{\nu}\ell} + \zeta\dot{\bar{\nu}} + \delta(tr\bar{\boldsymbol{D}}), \tag{35}$$

$$\boldsymbol{0} = \bar{\boldsymbol{t}} - \left(-\bar{\nu}p + \epsilon^M\dot{\bar{\nu}} + \lambda^M tr\bar{\boldsymbol{D}}\right)\boldsymbol{I} - f_s(\zeta_1\boldsymbol{I} + \zeta_2\bar{\boldsymbol{Z}} + \zeta_3\bar{\boldsymbol{Z}}^2) + 2\beta_0\bar{\gamma}\bar{\nu}\mathcal{F}_c\left(\frac{\bar{\nu}_m}{\bar{\nu}_\infty-\bar{\nu}}\right)^2\boldsymbol{g}_1\otimes\boldsymbol{g}_1 - 2\mu_0\bar{\gamma}^2\left(\frac{\bar{\nu}_m}{\bar{\nu}_\infty-\bar{\nu}}\right)^8\sqrt{|I_{\bar{\boldsymbol{D}}}^2|}\bar{\boldsymbol{D}}, \tag{36}$$

$$\boldsymbol{0} = \boldsymbol{R} - \left\{-\left(\frac{\vartheta^M}{\vartheta^T}-1\right)f_2 - \left(\frac{\vartheta^M}{\vartheta^T}-\frac{\vartheta^G}{\vartheta^T}\right)f_5 + \epsilon + \lambda^T tr\bar{\boldsymbol{D}}\right\}\boldsymbol{I} - 2\mu_0\bar{\gamma}^2(\mathcal{F}_c-1)\left(\frac{\bar{\nu}_m}{\bar{\nu}_\infty-\bar{\nu}}\right)^8\cdot\sqrt{|I_{\bar{\boldsymbol{D}}}^2|}\bar{\boldsymbol{D}}, \tag{37}$$

where Cayley-Hamilton theorem and some abbreviations, defined in [22], have been used.

GRAVITY-DRIVEN FLOW

Consider a fully developed, isochoric, two-dimensional stationary avalanche down an incline, as shown in Fig. 1. It is assumed that

$$\begin{aligned} &\bar{\boldsymbol{v}} = [\bar{u}(y), \bar{v}(y), 0], \quad \bar{\nu} = \bar{\nu}(y), \quad \bar{p} = \bar{p}(y), \\ &\vartheta^T = \vartheta^T(y), \quad \vartheta^G = \vartheta^G(y), \quad \bar{Z}_{ij} = \bar{Z}_{ij}(y), \end{aligned} \tag{38}$$

with the fluctuating velocities in the x- and y-directions much smaller than the averaged values.

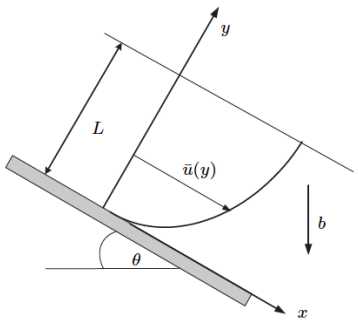

Fig. 1 Gravity-driven stationary avalanche down an incline and the coordinate.

The flow corresponds to the critical state in geophysical circumstances. With this, one can conclude that the balance equation of the mean internal friction is decoupled from other mane balance equations. Thus, the simplified field equations are given by

$$0 = \frac{\mathrm{d}}{\mathrm{d}y}\left\{\frac{1-\bar{\nu}_s}{1-\bar{\nu}}\left(\zeta_2\bar{Z}_{xy} + \zeta_3\bar{Z}_{xy}^2\right) + \mu_0\bar{\gamma}^2\mathcal{F}_c\left(\frac{\bar{\nu}_m}{\bar{\nu}_\infty-\bar{\nu}}\right)^8\left(\frac{\mathrm{d}\bar{u}}{\mathrm{d}y}\right)^2\right\} + \bar{\gamma}\bar{\nu}bsin\theta, \tag{39}$$

$$0 = \frac{\mathrm{d}\bar{t}_{yy}}{\mathrm{d}y} - \bar{\gamma}\bar{\nu}cos\theta, \tag{40}$$

$$0 = \frac{\mathrm{d}}{\mathrm{d}y}\left\{\frac{2\beta_0\bar{\gamma}\bar{\nu}\mathcal{F}_c}{\ell}\left(\frac{\bar{\nu}_m}{\bar{\nu}_\infty-\bar{\nu}}\right)^2\frac{\mathrm{d}\bar{\nu}}{\mathrm{d}y}\right\} + \frac{1}{\bar{\nu}\ell}\left\{-\bar{t}_{yy} + \frac{1-\bar{\nu}_s}{1-\bar{\nu}}\left(\zeta_1 + \zeta_2\bar{Z}_{yy} + \zeta_3\bar{Z}_{yy}^2\right) - 2\alpha_0\bar{\gamma}\bar{\nu}^2(\bar{\nu}-\bar{\nu}_m)\mathcal{F}_c - 2\beta_0\bar{\gamma}\bar{\nu}\left(\frac{\bar{\nu}_m}{\bar{\nu}_\infty-\bar{\nu}}\right)^2\left(\frac{\mathrm{d}\bar{\nu}}{\mathrm{d}y}\right)^2\frac{\bar{\nu}_\infty\mathcal{F}_c}{\bar{\nu}_\infty-\bar{\nu}}\right\}, \tag{41}$$

$$0 = \mu_0\bar{\gamma}^2(\mathcal{F}_c-1)\left(\frac{\bar{\nu}_m}{\bar{\nu}_\infty-\bar{\nu}}\right)^8\left(\frac{\mathrm{d}\bar{u}}{\mathrm{d}y}\right)^3 - f_7\frac{\mathrm{d}^2\vartheta^T}{\mathrm{d}y^2} - f_3\left(\frac{\mathrm{d}\vartheta^T}{\mathrm{d}y}\right)^2, \tag{42}$$

$$0 = -f_8\frac{\mathrm{d}^2\vartheta^G}{\mathrm{d}y^2} - f_6\left(\frac{\mathrm{d}\vartheta^G}{\mathrm{d}y}\right)^2, \tag{43}$$

for the five primitive mean fields: velocity component in the x-direction, mean volume fraction, normal stress component, and two granular coldnesses. The coupled nonlinear ODE are subject to the boundary conditions given by

$$y=0:\ \bar{u}=0,\ \bar{\nu}=\bar{\nu}_b,\ \vartheta^T=\vartheta^T_b,\ \vartheta^G=\vartheta^G_b;$$
$$y=L:\ \frac{\mathrm{d}\bar{u}}{\mathrm{d}y}=\frac{\mathrm{d}\bar{\nu}}{\mathrm{d}y}=0,\ \frac{\mathrm{d}\vartheta^T}{\mathrm{d}y}=a_T,\ \frac{\mathrm{d}\vartheta^G}{\mathrm{d}y}=a_G,\ \bar{t}_{yy}=\bar{t}_b; \quad (44)$$

with the physical interpretations given in [22].

The two-point nonlinear BVP (39)-(44) are solved numerically to obtain the distributions of the mean volume fraction, velocity and turbulent kinetic energy and dissipation across the flow layer. To this end, the BVP (39)-(44) should be non-dimensionalized, followed by the iterative method with under-relaxation scheme. Typical calculated results are summarized in Fig. 2.

Fig. 2 illustrates the normalized profiles of the dimensionless mean volume fraction, velocity, two-fold turbulent kinetic energies and dissipations , in which the values of the parameters are prescribed and displayed in the figure. Solid lines are the results by using the proposed zero-order closure model; dashed lines are the laminar flow solutions quoted from [23]; with dotted line denoting Newtonian fluid characteristic in laminar motion. Increasing the flow thickness tends to enlarge the difference in the mean volume fractions between the free surface and solid plane, as shown in Fig. 2(a). This results from the weight of the granular body: when the flow is thicker, larger compressive stress is applied on the grains in the thin layer immediately above the solid plane, where the shearing is maximum, causing the grains to collide intensively with one another, resulting in smaller values of the mean volume fraction. Above this thin layer there exists a relatively thick layer, in which the grains form a kind of inelastic network and behaves as a lump solid with nearly uniform mean volume fraction and velocity, as displayed in the velocity profiles in Fig. 2(b).

The thin and relatively thick layers are respectively referred to as the turbulent boundary layer and passive layer, a significant non-Newtonian characteristic. As $\tilde{L}$ increases, the turbulent boundary layer becomes thinner with larger velocity gradients at the interface between two layers. When compared with laminar flow solutions, the mean volume fraction and velocity profiles are more convex, with larger amplitudes in the passive layer. These are due to the influence of turbulent fluctuation, turbulent kinetic energy and dissipation, to be discussed later.

The profiles of two-fold turbulent kinetic energies are illustrated in Figs. 2(c) and 2(d). They both decrease from their maximum values on the solid plane, where the shearing is maximum, toward the *nearly vanishing* values on the free surface with an “exponential-like" tendency. This tendency is equally manifest for the profiles of two-fold turbulent dissipations displayed in Figs. 2(e) and 2(f), except that their f*inite* values on the free surface are obtained. As the flow thickness increases, the decreasing tendencies of two-fold turbulent kinetic energies and two-fold turbulent dissipations become more obvious. These findings correspond not only to those found in turbulent boundary layer flows of Newtonian fluids, but also are justified, for turbulent kinetic energy and dissipation should assume maximum values in the regions where shearing is maximum, and larger turbulent kinetic energy induces larger turbulent dissipation [16,17].

However, the turbulent boundary layers in a Newtonian fluid and a dry granular avalanche are not exactly the same. Although in both cases the turbulent kinetic energies and dissipations evolve in a similar manner, vanishing turbulent kinetic energy and dissipation of a Newtonian fluid are identified on the free surface, while it is not so for a dry granular avalanche. These reflect the discrete nature of dry granular system and its distinguish turbulent feature in comparison with Newtonian fluids.

Although the turbulent boundary and passive layers of an avalanche can be identified by the profiles of the volume fraction and velocity in previous laminar formulations e.g. [23], they are preferable verified from the perspective of the turbulent kinetic energy and dissipation distributions, as shown in Figs 2(c)-2(f). In the passive layer, the dominant grain-grain interaction is the long-term one, causing the grains to form a kind of inelastic network to yield nearly vanishing two-fold turbulent kinetic energies and finite two-fold turbulent dissipations. On the other hand, the grains in the turbulent boundary layer are dominated by the short-term grain-grain interaction, giving rise to intensive turbulent fluctuation with significant two-fold turbulent kinetic energies and dissipations. The intensive turbulent fluctuation in the turbulent boundary layer reduces the base friction significantly, resulting in larger mean volume fraction and velocity in the passive layer, when compared with laminar flow solutions. These findings correspond to field observations [5-8].

CONCLUSION

Turbulence realizability conditions, in the context of Mueller-Liu entropy principle, were investigated to derive the equilibrium closure relations, with the dynamic responses postulated by a quasi-static theory. The established zero-order closure model was applied to analyses of a gravity-driven, isothermal, isochoric, dry granular avalanche with incompressible grains down an incline.

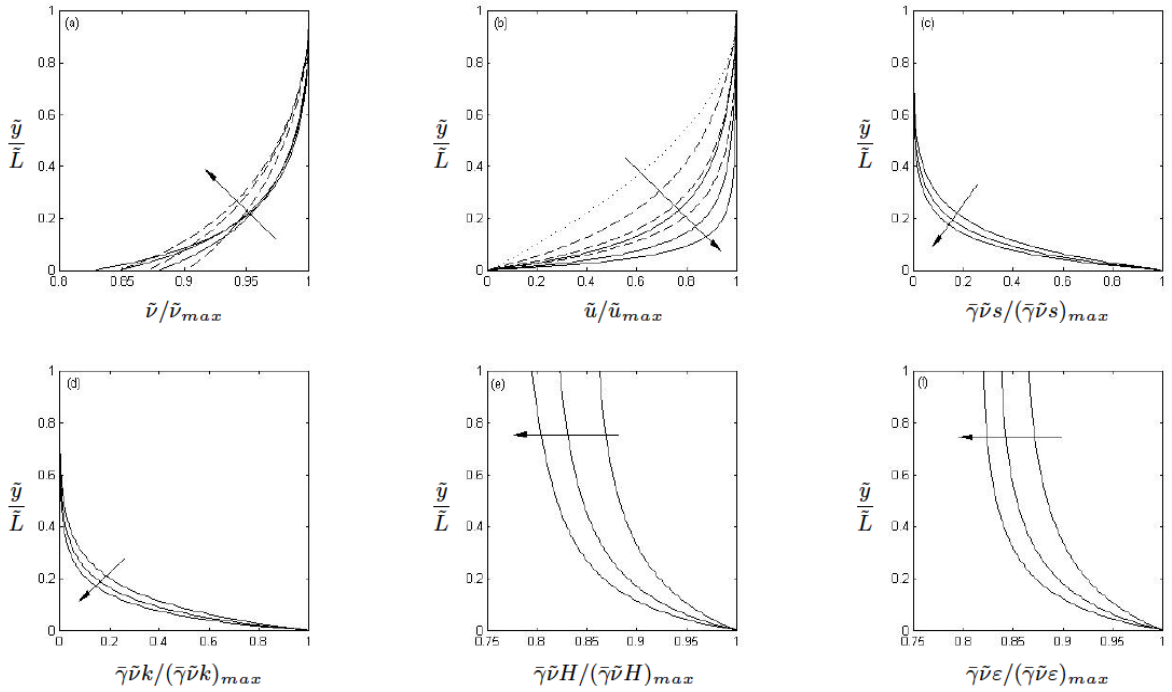

Fig. 2 Normalized profiles of $\tilde{\nu}$, $\tilde{u}$, $\bar{\gamma}\tilde{\nu}s$, $\bar{\gamma}\tilde{\nu}k$, $\bar{\gamma}\tilde{\nu}H$ and $\bar{\gamma}\tilde{\nu}\varepsilon$, in which $\tilde{a}_T = \tilde{a}_G = 0.1$, $\Xi_1 = \Xi_2 = 0.01$, $\tilde{\pi}_b = 0.01$, $S_2 = 0.02$ and $\tilde{L} = [10, 15, 20]$ indicated by the arrows. (a), (b): Mean volume fraction and velocity profiles; (c), (d): turbulent configurational kinetic energy and turbulent kinetic energy profiles; (e), (f): turbulent configurational dissipation and turbulent dissipation profiles. Dashed lines: laminar flow solutions; dotted line: Newtonian fluid characteristic in laminar motion.

While the mean volume fraction and velocity evolve from their minimum values on the inclined plane toward the maximum values on the free surface, corresponding to the field observations and laboratory experiments, two-fold turbulent kinetic energies and dissipations distribute in a reverse manner, with the characteristics that most of them are confined within a thin layer immediately above the base (the turbulent boundary layer). Above the thin layer, the grains behave as a lump solid with nearly uniform mean volume fraction and velocity (the passive layer). These result from different microstructural grain-grain interactions in two layers. In the turbulent boundary layer, the grains are dominated by the short-term grain-grain interaction, giving rise to intensive turbulent fluctuation with significant kinetic energy and dissipation, while the grains in the passive layer are dominated by the long-term grain-grain interaction to interlock with one another, and form a kind of inelastic network. Thus, these two layers are preferable verified from the turbulent kinetic energy and dissipation profiles, in contrast to those based on the volume fraction and velocity profiles in purely laminar flow consideration.

The turbulent boundary and passive layers of a dry granular avalanche are similar to those of Newtonian fluids in turbulent boundary layer flows. However, they are not exactly the same. Although the turbulent kinetic energy and dissipation of these two matters evolve in a similar manner from the solid plane toward the free surface, their vanishing values on the free surface are found for conventional Newtonian fluids, while nearly vanishing two-fold turbulent kinetic energies and finite two-fold turbulent dissipations are obtained for granular avalanches. This results from the discrete nature of dry granular system and different dominant grain-grain interactions in the turbulent boundary and passive layers. Significant discrepancies in the estimated mean volume fraction and velocity profiles from the laminar flow solutions suggest that the energy cascade induced by the turbulent fluctuation needs be taken into account for better estimation of the characteristics of dry granular avalanche.

ACKNOWLEDGEMENTS

The author is indebted to the Ministry of Science and Technology, Taiwan, for the financial support through the project MOST 103-2221-E-006-116-.

REFERENCES

[1] Aranson IS, Tsimring LS (2009) Granular Patterns. Oxford University Press, Oxford New York

[2] Ausloos M, Lambiotte R, Trojan K, Koza Z, Pekala M (2005) Granular matter: A wonderful

world of clusters in far-from-equilibrium systems. Physica A 357:337—349
[3] Poeschel T, Brilliantov NV (2013) Granular Gas Dynamics. In: Lecture Notes in Physics (Book 624), Springer-Verlag, New York
[4] Rao KK, Nott PR (2008) Introduction to Granular Flows. Cambridge University Press, London New York
[5] Jakob M, Hungr O (2005) Debris-flow Hazards and Related Phenomena. Springer, Berlin Heidelberg
[6] Pudasaini S, Hutter K (2007) Avalanche Dynamics. Springer Verlag, Berlin Heidelberg
[7] Takahashi T (2007) Debris Flow: Mechanics, Prediction and Countermeasures. Taylor \& Francis, London
[8] Vescovi D, di Prisco C, Berzi D (2013) From solid to granular gases: the steady state for granular materials. Int J Numer Anal Meth Geomech 37:2937--2951
[9] Campbell CS (2005) Stress-controlled elastic granular shear flows. J Fluid Mech 539:273--297
[10] Daniel RC, Poloski AP, S\'{a}ez AE (2007) A continuum constitutive model for cohesionless granular flows. Chem Eng Sci 62:1343--1350
[11] Faccanoni G, Mangeney A (2013) Exact solution for granular flows. Int J Numer Anal Meth Geomech 37:1408--1433
[12] Fang C (2010) Rheological characteristics of solid-fluid transition in dry granular dense flows: a thermodynamically consistent constitutive model with a pressure-ratio order parameter. Int J Numer Anal Meth Geomech 34:881--905
[13] Jop P (2008) Hydrodynamic modeling of granular flows in a modified Couette Cell. Phys Rev E 77:032301
[14] Kirchner N (2002) Thermodynamically consistent modeling of abrasive granular materials. I: Non-equilibrium theory. Proc R Soc Lond A 458:2153--2176
[15] Wang Y, Hutter K (1999) A constitutive theory of fluid-saturated granular materials and its application in gravitational flows. Rheol Acta 38:214--223
[16] Hinze JO (1975) Turbulence. McGraw-Hill, New York
[17] Tsinober A (2009) An Informal Conceptual Introduction to Turbulence. Springer, Heidelberg
[18] Fang C, Wu W (2014) On the weak turbulent motions of an isothermal dry granular dense flow with incompressible grains, part I. Equilibrium turbulent closure models. Acta Geotech (in press, DOI: 10.1007/s11440-014-0313-4)
[19] Fang C, Wu W (2014) On the weak turbulent motions of an isothermal dry granular dense flow with incompressible grains, part II. Complete closure models and numerical simulations. Acta Geotech (in press, DOI: 10.1007/s11440-014-0314-3)
[20] Fang C (2014) A variational analysis of the equilibrium turbulent closure models of a dry granular densified motion with weak turbulent intensity. Arch Mech (in press)
[21] Fang C (2014) On the turbulent boundary layer of a dry granular avalanche down an incline. Part I. Thermodynamic analysis. Rheol Acta (in review)
[22] Fang C (2014) On the turbulent boundary layer of a dry granular avalanche down an incline. Part II. Closure model with numerical simulations. Rheol Acta (in review)
[23] Fang C (2009) Gravity-driven dry granular slow flows down an inclined moving plane: a comparative study between two concepts of the evolution of porosity. Rheol Acta 48:971—992

First International Conference on Science, Engineering & Environment,
Tsu City, Mie, Japan, Nov.19-21, 2015, ISBN: 978-4-9905958-5-2 C3051

POST-CYCLIC BEHAVIOR OF GRANULAR SOIL- STRUCTURE INTERFACE DIRECT SHEAR TESTS

Suriyavut Pra-ai[1], Marc Boulon[2]
[1]Automotive and Transportation Technology Development Center (ATTDC), School of Engineering, University of Phayao, Phayao, Thailand;
[2]Laboratoire 3S-R, Université de Grenoble, Grenoble, France

ABSTRACT

The purpose of this paper is to present one of the most important phases of a series of cyclic direct shear tests on granular soil and rough material interface under constant normal stiffness (CNS) condition. These cyclic interface tests were performed in order to simulate the situation along the pile shaft subjected to a large number of cycles due to environmental or anthropic loadings. This post-cyclic phase can be performed by one single large cycle after the cyclic phase in order to characterize the change of interface resistance. The principal characteristic of interface subjected to cyclic loading is the progressive contraction. This phenomenon leads to the degradation in normal stress acting on the pile shaft and consequently the shear resistance decreases. The influence of relative density of granular soil, initial normal stress, level of stress ratio, cyclic amplitude and imposed normal stiffness on the post-cyclic responses is discussed.

.

Keywords: Post-Cyclic Loading, Interface Resistance, Constant Normal Stiffness, a Large Number of Cycles

INTRODUCTION

When civil engineering structures have to undergo cyclic loading condition, the bearing capacity of structures is often reductive. Designers often have to consider the cyclic bearing capacity and stiffness, as well as the permanent displacements due to cycling and potentially changing patterns of soil. Especially, many offshore oil rig works have to undergo cyclic loading conditions (wind, wave, machine operations, etc.) for a long life. This reductive phenomenon can also be found in the serviceability of railways and bridges due to traffic loadings. Even though the magnitude of traffic loadings is rather small, a large number of cycles would be crucial. The most recent studies which concern a large number of cycles carried out by Wichtmann [17] can be found. Moreover, the recent developments of renewable installations on shore as well as off shore of energy sources bring the professionals and the researchers to be interested in the effect of very large number of cycles on the soil-structure interactions. Therefore, understanding the interface behavior subjected to cyclic loading is of significant importance. Indeed at the present time, there are not enough methods of reliable calculation of the structure foundations subjected to this stress type and most of the experts adopt the proposed safety factors to take into account the degradations of bearing capacity due to the cycles.

The studies of interface behavior have been specified on the conventional interface experiments with the constant normal load (CNL). In this case, the normal load applied on the interface is kept constant during the process of shearing. Interestingly, when interfaces subjected to cyclic loading, numerous experimental investigations have been reported that the interface responses turn into a progressive densification with increasing number of cycles. This leads to the mobilization of shear strength ([1], [5], [9]).

Boulon and Foray [3] reported that the skin friction of granular soil-pile shaft decreased as a function of number of cycles. This can be attributed that cyclic loadings bring on the contraction of sand adjacent to pile. A decrease in volume of sand leads to a progressive decrease in lateral stress, and consequently a decrease of shear resistance.

A laboratory test of soil-pile interface can simply be interpreted as an interface under constant normal stiffness (CNS) condition (see Fig.1). Considering a pile with radius R_0, embedded in soil with a pressuremetric modulus (E_p), and the thickness of the interface layer (e) mobilized during the large localized shear ($e << R_0$). The normal stiffness imposed to the interface (k) according to Boulon and Foray [3] resulting from the definition of the pressuremetric modulus (E_p) can be expressed as:

$$E_p = \frac{\Delta\sigma_n}{-2\Delta V / V_0} \cong \frac{\Delta\sigma_n}{-2\Delta[u]}(R_0 + e) \cong \frac{\Delta\sigma_n}{-2\Delta[u]} R_0 \quad (1)$$

where $\Delta V/V_0$ is the relative volume change and consequently:

$$k = \frac{2E_p}{R_0} = \frac{\Delta\sigma_n}{-\Delta[u]} \quad (2)$$

where $\Delta\sigma_n$ is the variation of normal stress acting on the interface and $\Delta[u]$ is the variation of normal displacement.

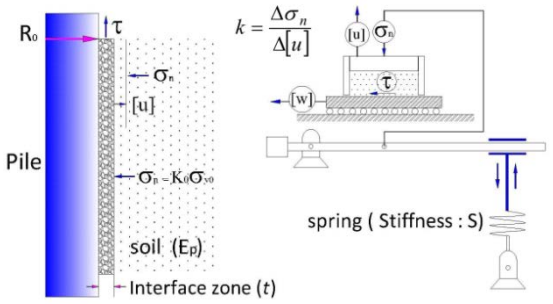

Fig. 1 Localized shear zone along pile and a direct shear test with an imposed normal stiffness after Boulon and Foray [3].

Under CNS condition, the behavior of soil-structure interface exhibits a mobilization of stress state acting on the interface. During shear loading phase, for example, dense sample commonly shows the dilative behavior which leads to an increase in normal stress associated with shear stress. Contrarily, a significant reduction in normal stress as well as shear stress can be found on loose sample. This phenomenon is due to the significant contraction.

The effect of imposed normal stiffness (k) on cyclic interface behavior becomes crucial. The main characteristic of cyclic interfaces under CNS condition performed by either direct shear or simple shear tests is the significant degradation in normal stress acting on the interface as a result of the gradual contraction. Consequently, the degradation of shear stress can be found ([1], [4], [5], [8], [9], [14]). In case of shear stress-controlled tests, the significant degradation of normal stress as a result of the progressive contraction accompanied with N brought the mean cyclic stress ratio (η_{cm}) defined as the ratio between mean cyclic shear stress (τ_{cm}) and mean cyclic normal stress ($\sigma_{n\,cm}$), ($\eta_{cm} = \tau_{cm}/\sigma_{n\,cm}$), to the critical state line ([10]-[12]).

This paper presents some of experimental observations carried out from a series of direct shear tests of sand and rough surface structure under constant normal stiffness (CNS) condition with a large number of small cycles in terms of shear stress. The responses of post-cyclic phase will be discussed. This work was supported by the SOLCYP (French acronym for National Project in Piles under Cyclic Solicitations) research project.

DEVICE AND MATERIALS

With less difficulty in performing the interface test campaigns, the modified direct shear is used in this study as shown in Fig.2. The upper shear box has a diameter of 60 mm containing the specimen with the height of approximately 20 mm. This enables the preparation of sample in various conditions. The lower shear box is replaced by the steel plate on which the surface roughness is made by gluing a mixture of epoxy and Fontainebleau sand.

The surface roughness of structural materials were quantified as the modified roughness in term of a maximum height R_{max}, which is the relative height between the highest peak and the lowest valley along a surface profile over the gauge length L = 0.20 mm ([15]).The value of roughness (R_{max}) can effectively be quantified by morphology method ([6]) which provides R_{max}= 0.20 mm. When normalizing R_{max} with mean particle diameter D_{50} (i.e., $R_n = R_{max}/D_{50}$ [15], [16]), the structural plate used in this study can then represent the rough surface ($R_n \geq 0.10$ would be able to stand for rough surface [7], [15], [16]).

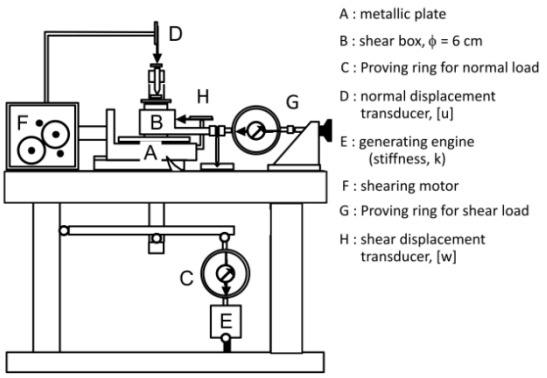

Fig. 2 Experimental device.

On this device, the normal stress (σ_n) is applied vertically via a piston (top cap) by a generating engine in two directions (ensuring loading or unloading of the samples). The operation of this generating engine which is controlled by a computer enables the application of a constant normal stress (k

= 0, CNL) and constant normal stiffness ($k \neq 0$, CNS) conditions in accordance with the control set:

$$C = \Delta\sigma - k[\Delta u] = 0 \quad (3)$$

Again, $\Delta\sigma$ is the variation of normal stress acting on the interface and $\Delta[u]$ is the variation of normal displacement.

The tangential displacement of the structural surface which can directly be controlled by the computer provides the shear loading. It can be assumed that there is no influence of shear rate on test results by using the shear rate with low range. In this study, the compatible maximum of shear rate of 0.5 mm/min is then used with a sufficient data acquisition. In case of cyclic (shear stress-controlled) tests, two thresholds (high and low, adjustable) of shear stress are prescribed, causing a reversal of shear direction when they are reached.

In this study, the measured and recorded variables are the stress vector applied on the interface (normal, σ_n and shear, τ components) and the relative displacement vector on soil-structure (normal, $[u]$ and tangential, $[w]$ components). The normal stress and normal relative displacement can be defined as $\sigma_n > 0$ in compression and $[u] > 0$ in dilation.

Two sands were tested in this study, Loon-Plage (post-glacial Flandrian) and Fontainebleau sands. The first one was tested with saturated specific weight (γ_{sat}) of 18.64 kN/m^3 and water content (w) of 18%. This initial density can be considered as dense ($I_D \approx 75\%$, [2]) condition. This sand was tested to combine the in situ axial pile tests in order to complement and extend the existing data set ([13]). The second one was tested in dry condition with relative density of approximately 90% (dense condition). To achieve the desired samples, two techniques of pouring and tamping were commonly used. In this study, all tests were carried out as completely drained tests.

In addition, to prepare the sample, a spacing of 0.3 mm between the rough plate and the upper shear box was set by a pair of brass foils. This technique is used in order to prevent the direct friction between the shear box and the rough plate. However, this gap would inevitably provide the leakage of fine particle which would take place during shear loading, especially when cyclic tests were performed. A simple inclusive correction can then be performed by considering the loss of sand as the fictitious contraction.

TEST RESULTS

The cyclic tests were performed in order to investigate some of factor influencing the interface behavior under CNS condition. Prior to performing those tests, monotonic tests were performed in order to evaluate the main variables (Table 1), e.g., the three values of stress ratio defined as $\eta = \tau/\sigma_n$ [11] ;

- peak stress ratio (η_p),
- critical stress ratio (η_{cr})
- characteristic stress ratio (η_{ch}, separating the dilative and contractive domains, where $\eta_{ch} < \eta_{cr} < \eta_p$)

The responses of monotonic tests then provided a series of cyclic tests (e.g., the level of mean cyclic stress ratio, η_{cm} and the amplitude of cycles, $\Delta\tau$). The cyclic tests examined in the present work are summarized on Table 2.

The cyclic test procedure in this study consists of 5 consecutive phases:

- 1st Phase: the application of normal stress since the neutral state until mean cyclic normal stress ($\sigma_{n\,cm}$)
- 2nd Phase: the application of shear loading until mean cyclic shear stress (τ_{cm})
- 3rd Phase: the application of N cycles of small amplitude of controlled-shear stress ($\Delta\tau$)
- 4th Phase: one great cycle of shear (after N cycles were reached) to failure
- 5th Phase: discharge in shear stress (τ) and then the normal stress until $\sigma_n = 0$, respectively.

Table 1 Main variables from monotonic interface direct shear tests

Variables	Loon-Plage sand	Fontainebleau sand
η_p	0.90	0.79
η_{cr}	0.64	0.566
η_{ch}	0.59	0.555

Table 2 CNS cyclic test program

Sands	$\sigma_{n\,cm0}$ (kPa)	η_{cm0} (-)	$\Delta\eta$ (kPa)	k (kPa/mm)
Loon-Plage	100	$1/2\,\eta_p$	44	143
Fontainebleau	310	$1/2\,\eta_p$	10	1000

One of the most important phases of the cyclic tests is the post-cyclic phase. This phase can generally be carried out by one single large cycle after the cyclic phase (4th phase) in order to characterize the change of interface resistance (δ_p) due to cyclic loading. However, under CNS condition this post-cyclic phase could not be carried out when performing the initial mean cyclic stress ratio (η_{cm0}) close to the critical stress ratio (η_{cr}) due to the early termination (i.e., the stress state move towards the critical state line [10], [12]). As can be deduced from experimental observations, within the range of $\eta_{cm0} < \eta_{ch}$ the principal characteristic of

interface subjected to cyclic loading was the progressive contraction. Considering the stress plane in Fig.3, during the interface subjected to cyclic loading under CNS condition, the shear stress was kept constant while the normal stress decreased as a function of N then the mean cyclic stress ratio η_{cm} which started from the beginning (η_{cm0}) increased and then moved to the critical state line.

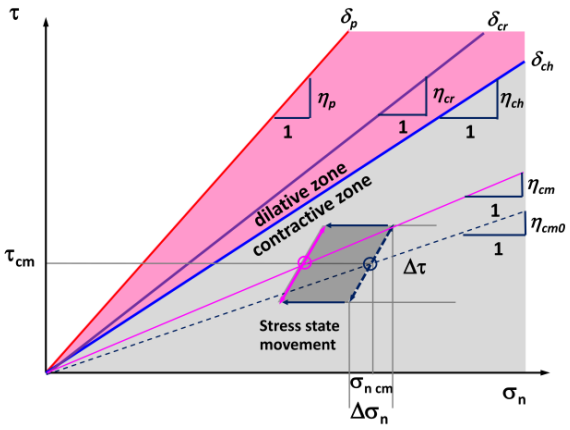

Fig. 3 Typical cyclic CNS paths of soil-structure interface.

Fig. 4 shows the post-cyclic behavior for σ_{n0} = 100 kPa on Loon-Plage sand with k = 143 kPa/mm, η_{cm0} = 0.44 (22 < τ < 66 kPa) in comparison with CNS monotonic test. As can be observed in Fig. 4a, the degradation of normal stress as a function of N increased very slowly. This was due to the low value of imposed normal stiffness (k = 143 kPa/mm). The values of peak stress ratio (η_p) after cyclic phase was slightly higher than that of CNS monotonic test (Fig. 4b, 4d). Considering the volumetric behavior, [u]−[w] diagram in Fig. 4c, the interface response provided more densification (contraction) during cyclic phase. However, the dilation rate at post-cyclic phase was not different from that of CNS monotonic test.

Indeed, dense sand has high tendency of grain breakage within the localized shear zone. The change in particle size could be attributed to I_{D0}, σ_{n0}, η_{cm} and $\Delta\tau$. The abrasion between the grains and the surface roughness of plate on dense sand therefore provided an increase in crushing and wear of grains. The finer grains resulting from crushing grains during cyclic loading then replaced the void within the interface zone. Uesugi and Kishida [15] concluded that during cyclic loading an increase of crushing particles due to the high intensity of stress state increasing the normalized the surface roughness (R_n) of the soil-structure interface then led to the higher coefficient of friction interface.

In case of dense Fontainebleau sand with σ_{n0} = 310 kPa, η_{cm0} = 0.35 (105 < τ < 115 kPa), this test was performed until N = 32669 while the stress state (η_{cm} = 0.43) was still so far from the critical line, subsequently the post-cyclic phase was performed instead (Fig. 5). In this case, the degradation of normal stress as a function of N increased very slowly. This can be described that with high value of σ_{n0} and low level of η_{cm0} the initial stress state was so far from the critical state line, then the stress state was able to evolve further. In this case, a large number of cycles were required to reach the critical state.

Considering the post-cyclic phase, this phase started at $\sigma_n \approx$ 230-240 kPa (as shown in Fig. 5a, 5d), the peak shear stress ratio (η_p) at post-cyclic phase was obviously lower than that of monotonic CNS test. Although the cyclic loading induced more densification of interface, there was not a large difference in dilation between the post-cyclic phase and CNS monotonic test (see [u] − [w] diagram in Fig. 5c). This phenomenon might be attributed to the crushing and wear of the grains resulting from an increase of inter-granular particles in the localized shear zone between sand and rough plate during cyclic phase ([1], [14]). Tabucanon et al. [14] reported that there was a lower stress recovery during post-cyclic response and the loss of strength increased with increasing the number of cycles due to the smaller volume change accompanying shear loading of the interface. Fakharian and Evgin [5] also explained that the shear stress which mobilized to the peak value decreased to a residual stress with a sufficient increase in sliding displacement or slip at interface.

CONCLUSION

Based on the post-cyclic phase of interface direct shear tests, the main results presented in this paper can be summarized as follows:

- At post-cyclic phase, the interface exhibited dilative behavior as a result of gradual densification.
- The peak stress ratio at post-cyclic phase could be attributed to the evolution of grain breakage within interface shear zone. With low value of initial normal stress, an increase of crushing particles during cyclic loading increased the normalized the surface roughness (R_n) of the soil-structure interface then led to the higher coefficient of friction interface.
- In case of high value of initial normal stress, a lower stress recovery during post-cyclic response can be found and the loss of strength increased with increasing the number of cycles due to the smaller volume

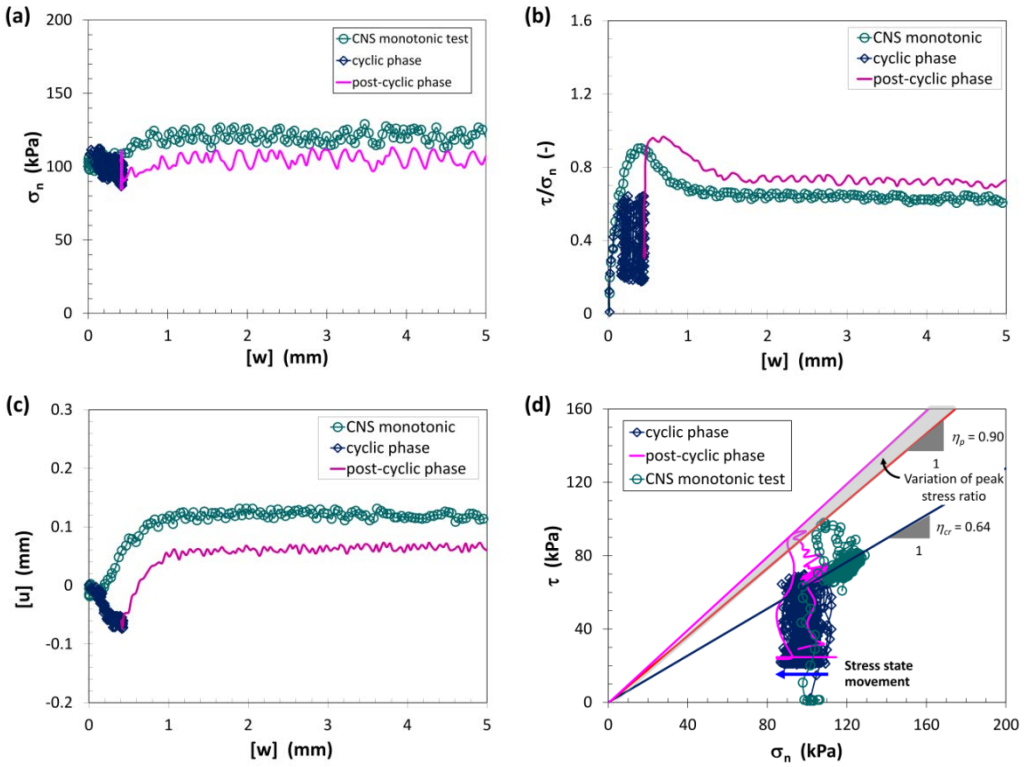

Fig. 4 Post-cyclic phase for σ_{n0} = 100 kPa on dense Loon-Plage sand with k = 143 kPa/mm, η_{cm0} = 0.44 (22 < τ < 66 kPa) in comparison with CNS monotonic test.

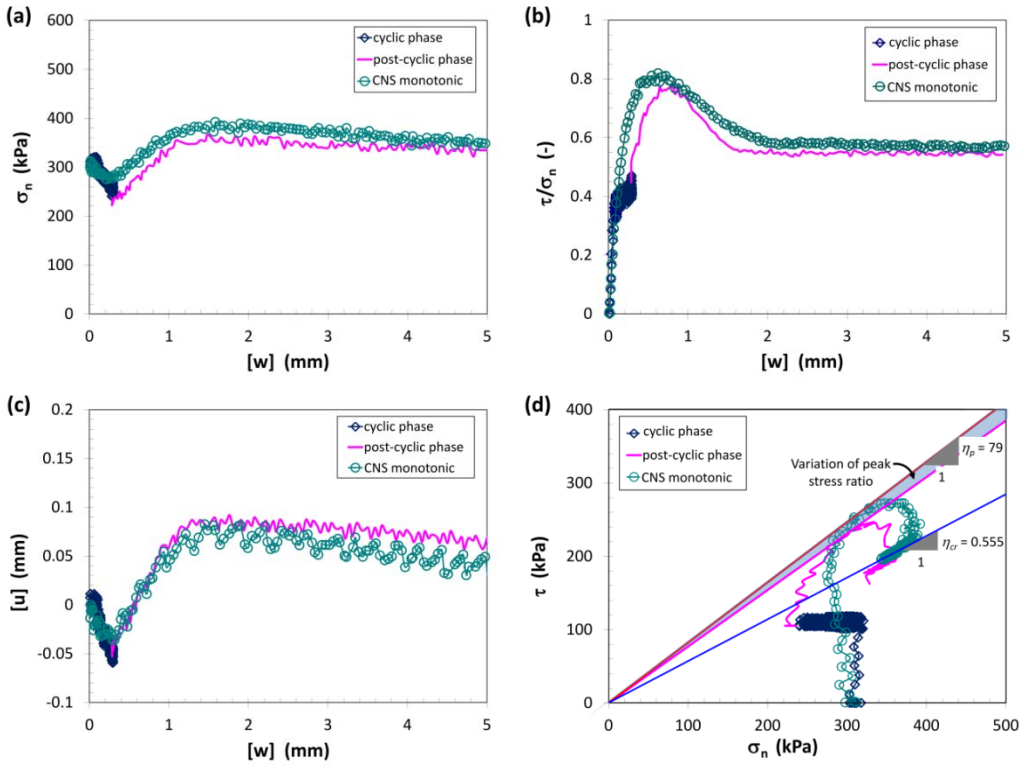

Fig. 5 Post-cyclic phase for σ_{n0} = 310 kPa on dense Fontainebleau sand with k = 1000 kPa/mm, η_{cm0} = 0.35 (105 < τ < 115kPa) in comparison with CNS monotonic test.

change accompanying shear loading of the interface.

ACKNOWLEDGEMENTS

The author cordially thanks the ANR-SOLCYP French program and 3S-R Laboratory, particularly Prof. Piere Foray for all his supports.

REFERENCES

[1] Al-Douri R, Poulos H, "Static and cyclic shear tests on carbonate sands", ASTM Geotechnical Journal testing 15(2), 1992, pp. 138-158.

[2] Benzaria O, Puech A, Le Kouby A, "Cyclic axial load tests on bored piles in dense sands", in Proc. TC 209 Workshop 18th ICSMGE, A. Puech (eds), Paris, 2013, pp.77-80.

[3] Boulon M, Foray P, "Physical and numerical simulations of lateral shaft friction along offshore piles in sand", in Proc. 3rd Int. Conf. on Numerical Methods in offshore piling, Nante, 1986, pp. 127-147.

[4] Dejong J, Randolph M, White M, "Interface load transfer degradation during cyclic loading: a micro scale investigation", Soils and Foundations, 43(4), 2003, pp. 81-93.

[5] Fakharian K, Evgin E, "Cyclic simple shear behaviour of sand-steel interface under constant normal stiffness condition", ASCE J. Geotech. Geoenviron. Eng., 123(12), 1997, pp. 1096-1105.

[6] Hans J, Boulon M, "A new device for investigating the hydro-mechanical properties of rock joints", Int. J. Numer. Anal. Meth. Geomech., 27, 2003, pp. 513-548.

[7] Hu L, Pu J, "Testing and modeling of soil-structure interface", ASCE J. Geotech. Geoenviron. Eng., 130(8), 2003, pp. 851-860.

[8] Mortara G, Mangiola A, Ghionna V, "Cyclic shear stress degradation and post-cyclic behavior from sand-steel interface direct shear tests", Can. Geotech. J., 44, 2007, pp. 739-752.

[9] Oumarou T, Evgin E, "Cyclic behavior of sand-steel plate interface", Can. Geotech. J., 42, 2005, pp. 1695-1704.

[10] Pra-ai S, "Essais et modélisation du cisaillement cyclique sol-structure à grand nombre de cycles: Application aux pieux". Thèse de Doctorat, Université de Grenoble, France, 2013.

[11] Pra-ai S, Boulon M, "Cyclic direct shear tests on sand-structure interface under constant normal stiffness (CNL) condition", in Proc. 20th NCCE, 2015.

[12] Pra-ai S, Boulon M, "Cyclic direct shear tests on sand-structure interface under constant normal load (CNS) condition", in Proc. 20th NCCE, 2015.

[13] Puech A, "Advances in axial cyclic pile design: contribution of the SOLCYP project", in Proc. 18th ICSMGE, 2013, pp. 1071-1096.

[14] T.J. Tabucanon, D.W. Airey, H.G. Poulos. "Pile skin friction in sands from constant normal stiffness tests". Geotechnical Testing Journal, 18(3), pp. 350-364, 1995.

[15] Uesugi M, Kishida K, "Influential factors of friction between steel and dry sands", Soils and Foundations, 6(2), 1986, pp. 33-46.

[16] Uesugi M, Kishida K, Yasunori T, "Friction between sand and steel under repeated loading", Soils and Foundations, 29(3), 1989, pp. 127-137.

[17] Wichtmann T, Niemunis A, Triantafyllidis T, "Strain accumulation in sand due to cyclic loading: drained triaxial tets", Soil Dynamics and Earthquake Engineering, 25, 2005, pp. 967-979.

First International Conference on Science, Engineering & Environment,
Tsu City, Mie, Japan, Nov.19-21, 2015, ISBN: 978-4-9905958-5-2 C3051

INDICATORS TO MEASURE DESIGN QUALITY OF BUILDINGS

Azeanita Suratkon[1] and Safuan Jusoh[2]
[1]Jamilus Research Centre, Faculty of Civil and Environmental Engineering, Universiti Tun Hussein Onn Malaysia, Malaysia
[2]Faculty of Civil and Environmental Engineering, Universiti Tun Hussein Onn Malaysia, Malaysia

ABSTRACT

Design quality is an important component in measuring satisfaction towards total product quality (TPQ) of buildings, the product of construction projects. Design Quality Indicator (DQI), developed by the Construction Industry Council (CIC) in the UK looking at three quality fields, i.e. functionality, build quality, and impact of building in measuring the quality of design embodied in the buildings through feedback and perceptions of all stakeholders involved in the production and use of buildings. Design quality is always a major concern in the Malaysian construction industry. With inspiration from this DQI, this study was carried out to identify indicators for measuring the satisfaction towards design quality of buildings and to evaluate the suitability of the indicators for application in the context of Malaysian construction industry. Through literature survey, 34 indicators of design quality were identified and grouped into the three design quality fields. A questionnaire survey was carried out among Malaysian construction professionals (architects, engineers, quantity surveyors, contractors and developers) to assess the identified design quality indicators in terms of their significance or relevance in the context of construction industry in Malaysia. The survey reveals that access, natural lighting, structure elements, landscape and location are among the design quality indicators that were perceived as the most important to be looked at. In overall, all the indicators are relevance for adoption in the Malaysian construction industry to measure the satisfaction towards design quality of buildings.

Keywords: Design quality indicators, Satisfaction measurement, Stakeholders' perception, Malaysian construction industry,

INTRODUCTION

Quality is one of the triple constraints or forces for every construction project besides the other two parameters i.e. time and cost. Adopting the definitions by Webster, Oxford and Cambridge dictionaries, quality can be defined as any character or characteristics that determine whether an object good or bad after measuring the character or characteristics against a standard. The standard refers to specification of the object to be designed [1]. Buildings are design object, the product of the design. The actual result related to the design quality of the building will be only known after several years of building is occupied [2]. During the occupancy stage, measurement and feedback such post-occupancy evaluation (POE) can be carried out to acquire the relevant data to determine the level of design quality in satisfying the needs and requirements of building client/customer/occupants. This approach also can be categorized under satisfaction measurement (SM) which is used to measure the level of project performance [3]. Satisfaction is a measure of the difference between actual and expected performance of a product or service to meet the needs and requirements of users and current perspective [4]. Satisfaction is a sense of excitement or disappointment after comparing the effects or results received with the expected [5]. Design quality will determine the suitability of buildings and the quality of compliance that shows how the building in accordance with the specifications required by the design [6]. The quality of the design can produce more efficient intermediation services and will improve the work environment for all those who use it [7].

Over the past decades, measuring and valuing the quality of design draws the attention clients, designers, and other construction practitioners as well as many researchers [8] and [9]. Design quality is always a major concern in the Malaysian construction industry. Construction Industry Development Board (CIDB) Malaysia, a government agency and an important player in Malaysian construction industry emphasizes the issues of quality in Construction Industry Master Plan (CIMP) 2006-2015 under Strategic Thrust 3; strive for the highest standard of quality, occupational safety and health, and environmental practices [10] Despite this emphasize from the CIDB, the Malaysian construction industry still suffers with many quality-related problems [11], such as quality below expectation [12], low quality finishes on buildings [13], and there is no benchmark to measure the standard of quality of houses constructed by developers [14]. It is apparent that

appropriate mechanism should take place in Malaysian construction industry to resolve quality-related issues especially on design quality.

Design Quality Indicator (DQI), developed by the Construction Industry Council (CIC) in the UK has successfully used in the UK's construction industry since it was launched in 2002. Design quality is a combination of functionality (how useful the facility is in achieving its purpose); impact (how well the facility creates a sense of place); and build quality (performance of the completed facility) [15]. The indicators and evaluation approach can be adopted in Malaysian construction industry with some modification. Therefore, with inspiration from this DQI, the objectives of this paper are to identify indicators to measure satisfaction towards design quality of buildings and to assess the suitability of the indicators in the context of the construction industry in Malaysia.

INDICATORS OF DESIGN QUALITY

Design Quality Indicators (DQI) of UK

The DQI was developed to measure the quality of design embodied in the product, the buildings themselves through feedback and perceptions of individuals who have interest or connection with the product [16]. It is applicable for new or refurbished buildings. It is in the form of a questionnaire which contains a set of statements that collect the views or perceptions of all stakeholders by looking at three quality indicators, i.e. Functionality, build quality, and impact of buildings [17].

The functionality of buildings is emphasized on the arrangement, quality and inter-relationship of spaces, and how the building is designed to be useful. It looks into three following aspects:

a. Use - how well the building caters for the functions it may accommodate originally and in the future.
b. Size - the size and interrelationship of the building's, rooms or component spaces.
c. Access - how easy it is for all people to get to, and around the building.

The built quality of buildings is evaluated on how well the building is constructed: its structure, fabric, finishes and fittings, its engineering systems, and the coordination of all these and how well they perform. The evaluation is on the following aspects:

a. Performance - the building's mechanical, environmental and safety systems.
b. Engineering - the quality of the building's components.
c. Construction - how well the building is put together.

The impact of buildings highlights building's ability to delight, to intrigue, to create a sense of place, and uplift the local community and environment, and also the design's contribution to the arts and science of building and architecture. The evaluation includes the following items:

a. Character and innovation - what people think of the overall building?
b. Form and materials - the building's physical composition, scale and configuration within its boundaries.
c. Internal environment - the quality inside the building's envelope.
d. Urban and social integration - the relationship, of the building with its surroundings.

Indicators of Design Quality from Previous Studies

Thirty-four (34) indicators that relevant for measuring design quality from previous studies (from year 1996 to 2014) were identified and tabulated in Table 1. The thirty-four indicators are regrouped into the three quality fields as listed and explained in Table 2, 3 and 4.

METHODOLOGY

Questionnaire Development and Sampling Frame

Quantitative approach using questionnaire surveys has been used to collect data. The purpose of the questionnaire survey was intended for feedback on the suitability or significance of the design quality indicators which are grouped under three categories i.e. functionality, build quality and impact in the context of Malaysian construction industry. A pilot test was conducted before distributing the questionnaire to respondents for actual survey. Questionnaires were distributed to 70 established construction companies in Malaysia to elicit feedback from 300 samples. This phase involves postal surveys via ordinary mail.

Data Analysis

A five-point Likert-scale with options ranging from "1 = Not Significant" to "5 = Very Significant" has been adopted to elicit feedback on the indicators. In order to determine the level of significance of the indicators, average index (AI) analysis was carried out. The interpretation of the AI value (adopted and modified based on [18] is shown in Table 5.

RESULT AND DISCUSSION

Background of Respondents

Eighty-eight (88) respondents completed and returned the questionnaires; make up the valid response rate at 29%. This is close to the 25-30% normal response rate for construction research that

was suggested by [19]. Most of the respondents are engineers (33%), contractors (23%) and developer (17%). The remaining respondents are quantity surveyors (11%), architect (3%) and other construction project personnel such as project manager and landscape architect (13%). The majority (64%) of the respondents have bachelor degree. 23% of respondents have diploma degree. Respondents with higher degree level (master and PhD) accounted for 11%, and the remaining 2 % have qualification below diploma level. For their working experience, most of the respondents (52%) have worked in the construction industry less than 6 years.

Table 1 Indicators for measuring design quality of buildings

Items	[20]	[21]	[22]	[16]	[23]	[24]	[25]	[7]	[26]	[27]	[28]	[29]	[30]	[31]	[32]
Layout	√	√				√									
Design	√	√	√	√	√		√		√	√		√	√	√	√
Access			√	√	√	√	√			√	√	√		√	
Space			√	√	√		√			√	√	√		√	√
Lighting						√			√	√	√	√			
Open space						√									
Service						√									
Natural Lighting									√						
Natural ventilation									√						
Use			√	√	√		√							√	
Engineering system			√	√	√	√	√							√	
Landscape						√			√				√		
Security system										√		√			
Energy						√									
Green energy and sustainability						√									
Finishes									√	√	√	√			√
Structure element		√											√		
Road width													√		
Infrastructure													√		
Building stability		√													
Pedestrian walkway													√		
Building maintenance	√	√									√			√	
Colour									√	√	√	√			
Building stability		√													
Pedestrian walkway													√		
Building maintenance	√	√									√				
Colour									√	√	√	√			
Form and materials	√	√	√	√	√		√		√	√		√	√		
Comfort									√	√	√				
Internal environment		√	√	√	√		√		√		√				
External environment															√
Character and innovation			√	√	√		√								
Urban and social integration			√	√	√		√								
Location		√				√									
Visual Effect						√					√				
Security		√							√						
Natural disaster									√						
Noise												√			

Table 2 Functionality aspect and quality indicators

Indicators	Descriptions
Layout	The building layout is easily understood by its users to find their way round the building
Design	The design of building is attractive
Access	The building provides good and safe access for everyone (users and visitors including those with disabilities)
Space	The spaces in building are the right size for their functions
Lighting	The lighting is efficient and allows for different user requirements
Service	The building provides essential services to the user
Natural lighting	Position of windows and doors are suitable for natural lighting
Natural ventilation	Position of windows and doors are suitable for natural ventilation

Table 3 Build quality aspect and quality indicators

Indicators	Descriptions
Use	The building easily accommodates the users' needs
Engineering system	Mechanical and electrical systems in building functioning properly
Landscape	Building landscape is attractive
Security system	Security system of the building is function properly
Energy	The building is efficient in its use of energy
Green energy & sustainability	Building using green energy sources and sustainability system
Finishing	Finishes of the building is attractive
Structure element	The building's structure is efficient
Road width	The road width of the building is suitable
Infrastructure	Building infrastructure is sufficient
Stability	Building is stable from natural elements e.g. wind, rain and earthquake
Pedestrian walkway	Building walkway is suitable and pedestrian- friendly
Building maintenance	Building is maintained properly

The involvements of these respondents were reasonably balanced by those who have worked for more than 6 years up to 20 years or more (48%). This provides a substantially reliable data for this study as their feedbacks represent the perspective of the key construction players in Malaysian construction industry.

Table 4 Impact aspect and quality indicators

Indicators	Descriptions
Colour	Building colour is suitable for the building
Form & Material	The building has the shape and materials in accordance with the functions
Comfort	Buildings provide comfort to the user
Internal environment	Atmosphere in building, relation between light and space and working climate at workplaces provide comfort
External environment	External surrounding is good quality for users
Character & innovation	The impact of buildings on the character, thinking and human appearance
Urban & integration social	Interaction with private and public areas and the impact of buildings on the city and community
Location	Positioning of the building in good location
Visual effect	The scene of the building is attractive
Security	The building provides a sense of security
Natural disaster	Location of buildings survived from natural disaster like floods or others
Noise	Surrounding noise of the building is not intrusive and affect human health

Table 5 Average index (AI) range value and interpretation

AI range value	Interpretation
$4.50 \leq$ AI < 5.00	Very Significant
$3.50 \leq$ AI < 4.50	Significant
$2.50 \leq$ AI < 3.50	Moderately Significant
$1.50 \leq$ AI < 2.50	Less Significant
$1.00 \leq$ AI < 1.50	Not Significant

Perception on Indicators of Design Quality

As shown in Fig. 1, 2 and 3, the AI value of all the indicators under functionality, build quality and impact aspects are within the range of $3.50 <$ AI < 4.50, suggesting that all the indicators are significant to be considered in evaluating the design quality of buildings in Malaysia. Under functionality aspect, natural lighting and access scored the highest AI values. This finding indicates that buildings in Malaysia should be designed to efficiently utilise the

natural lighting to light up the indoor considering Malaysia is a tropical country with abundance of natural-light. A building with good access to its users especially users with disabilities is perceived as a significant indicator to measure design quality. In Malaysia, there is a growing awareness, efforts and commitment of key building stakeholders to improve the accessibility of buildings especially for users with disabilities.

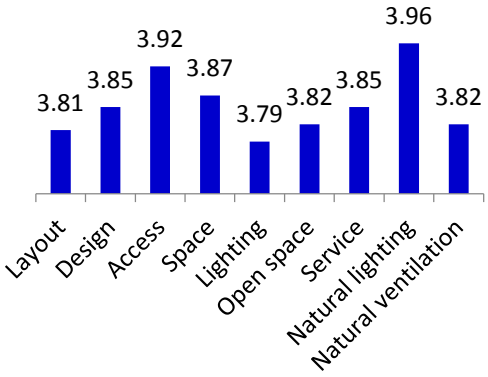

Fig. 1 Average index of indicators - functionality

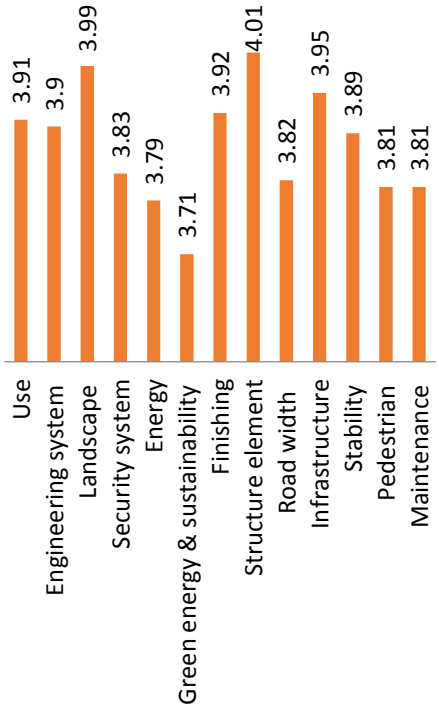

Fig. 2 Average index of indicators - build quality

Structure element of buildings such as beams, columns and floors which are efficient is considered as significant build quality indicators with the highest AI value (4.01). The efficiency of the structure elements can accommodate challenging and creative architectural designs and will lead to buildings that are of high build quality. Landscape scored the second highest AI value. Building landscape should be designed not only to be attractive but at the same time it can strengthen the identity and character of the building.

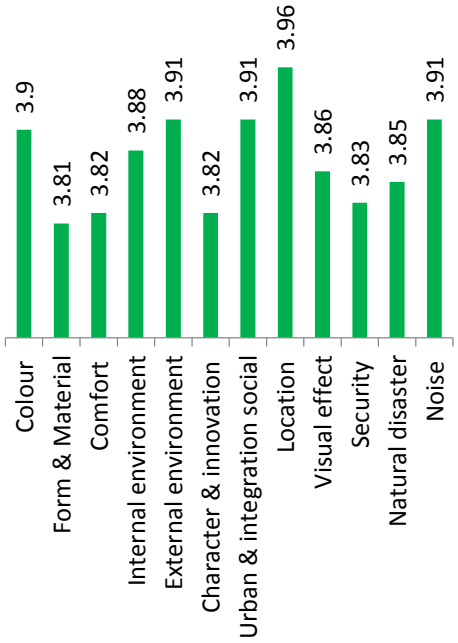

Fig. 3 Average index of indicators – impact

Among the impact indicators, location scored the highest AI value. Positioning of building in appropriate location or local environment will help the building to create a sense of place. The other three impact indicators i.e. external environment, urban and social integration and noise scored same 3.91 AI value.

CONCLUSION

Indicators to measure design quality that has been adopted in the DQI of the UK can be adopted in Malaysian construction industry with some modification. This study was carried out to identify indicators to measure satisfaction towards design quality of buildings and to assess the suitability of the indicators in the context of the construction industry in Malaysia. The survey revealed that all the indicators are significant in measuring the design quality of buildings in the context of construction industry in Malaysia. The identified design quality indicators are likely to be useful to all building stakeholders especially owner, user, contractor and designer who have direct participation in producing or utilising the building. The work is also expected to support the existing green building assessment system particularly on eliciting stakeholders' perception on the actual design quality of buildings.

REFERENCES

[1] Aas, EJ., "Design quality and design efficiency: definitions, metrics and relevant design experiences",

in 1st International Symposium on Quality of Electronic Design (ISQED), 2000, pp. 389-394.

[2] Giddings, B, Sharma, M, Jones, P and Jensen, P, "An evaluation tool for design quality: PFI sheltered housing", Building Research & Information, 2013, Vol. 41: 6, pp. 690–705.

[3] Masrom, MA, Skitmore, M and Bridge, A, "The identification of Malaysian contractor satisfaction dimensions: a strategy for continuous improvement", in Proc. 4th Int. Conf. on Construction Eng. and Proj. Mgmt., 2011, accessed through http://eprints.quit.edu.au/.

[4] Ibem, EO, Opoko, AP, Adeboye, AB, & Amole, D, "Performance evaluation of residential buildings in public housing estates in Ogun State, Nigeria: Users' satisfaction perspective", Frontiers of Architectural Research, 2013, 2(2), pp. 178–190.

[5] Xiaozhong, Y and Haishuang, L,"The fuzzy comprehensive evaluation of stakeholder's satisfaction in construction project", in Proc. Int. Conf. on Computers and Industrial Eng., Jul. 2009, pp. 1137–1142.

[6] Wu, L, "Managing design quality and conformance quality: models and insights", Total Quality Management, 2010, Vol. 21:4, pp. 383–389.

[7] Farooqui, RU, & Ahmed, SM, "Designing for quality : an empirical study of design quality indicator (DQI) tool", Building Research & Information, 2009, pp. 1–7.

[8] Gann, D and Whyte, J, "Design quality, its measurement and management in the built environment", Building Research & Information, 2003, pp. 314-317.

[9] Deewuf, G, and Van Meel, J, "Sense and nonsense of measuring design quality", Building Research & Information, 2004, pp. 247–250.

[10] CIDB, "Malaysian Construction Industry Master Plan 2006 – 2015". Kuala Lumpur, CIDB.

[11] Kamal, EM, Haron, SH, Md Ulang, N and Baharum, F, "The Critical Review on the Malaysian Construction Industry", Journal of Economics and Sustainable Development, Vol.3:13, 2012, pp. 81-87.

[12] Ibrahim, AR, Roy, MH, Ahmed, Z and Imtiaz, G, "An Investigation of the Status of the Malaysian Construction Industry", Benchmarking: An International Journal, Vol. 17:2, 2010, pp. 294-308.

[13] Hamid, ZA and Kamar, KAM, "Modernising the Malaysian Construction Industry", W089-Special Track 18th CIB World Building Congress. pp.267-280.

[14] Sufian, A & Rahman, RA, "Quality housing: Regulatory and administrative framework in Malaysia", International Journal of Economic and Management. Vol. 2:1, 2008, pp. 141-156.

[15] Office of Government Commerce (OGC), "Design quality: Achieving excellence in construction procurement guide", 2007, UK.Commerce

[16] Gann, DM, Salter, AJ & Whyte, JK, "Design Quality Indicator as a tool for thinking. Building Research & Information, Vol. 31:5, 2003, pp. 318–333.

[17] Construction Industry Council (CIC), Design Quality Indicator Online, www.dqi.org.uk, accessed on 6th December 2010.

[18] Abd Majid, MZ & McCaffer, R, "Assessment of work performance of maintenance contractors in Saudi Arabia", Journal of Management in Engineering, 1997, pp. 91-91.

[19] Fellows, R & Liu, A, "Research methods for construction", Blackwell Science, 1997.

[20] Low, SP & Willie, CKT, "The influence of workload instability on quality in the construction industry", International Journal of Quality & Reliability Management, Vol. 13:3, 1996, pp.42 – 56.

[21] Abdul-Rahman, H, Kwan, CL & Woods, PC, "Quality function deployment in construction design: application in low-cost housing design", International Journal of Quality & Reliability Management, 1999, pp. 591-605.

[22] Whyte, JK & Gann, DM, "Design Quality Indicators: work in progress", Building Research & Information", Vol. 31:5, 2003, pp. 387–398.

[23] Thomson, DS, Austin, SA, Devine-Wright, H, & Mills, GR, "Managing value and quality in design. Building Research & Information", Vol. 31: 5, 2003, pp.334–345.

[24] Eley, J, "Design quality in buildings", Building Research & Information, Vol. 32:3, 2004, pp. 255–260.

[25] Volker, L, Lauche, K, Heintz, JL, & De Jonge, H, "Deciding about design quality: design perception during a European tendering procedure", Design Studies, Vol. 29, 2008, pp. 387-409.

[26] Yongqiang, S, & Qiangli, L, "Evaluation method of building engineering design quality", 2nd IEEE Int. Conf. on Information Management and Engineering, 2010, pp. 634–637.

[27] Abu Samah, Z, Ibrahim, N, Othman, S & Abd Wahab, MH, "Assessing quality design of interiors: a case study of a hospital outpatient unit in Malaysia", Procedia - Social and Behavioral Sciences, Vol. 35, 2012, pp. 245–252.

[28] Stringer, A, Dunne, J, & Boussabaine, H, "Schools design quality : a user perspective", Architectural Engineering and Design Management, Vol. 8:4, pp. 257–272.

[29] Abu Samah, Z, Ibrahim, N, & Amir, JS, "Translating quality care factors to quality space: design criteria for outpatient facility", Procedia - Social and Behavioral Sciences, Vol. 105, 2013, pp. 265–272.

[30] Cook, JA, Bose, M, Marshall, WE, & Main, DS (2009). How Does Design Quality Add to our Understanding of Walkable Communities ?", Landscape Journal, Vol. 32:2, 2013, pp. 151-162.

[31] Amer Hatem, W, "Comparing Design Quality for School Buildings in Iraq (Directorate General of Education in Diyala Case Study)", http://fte.edu.iq /upload/upfile/ar/12165.pdf., accessed on Jan. 2014.

[32] John, R, Smith, A, Chotipanich, S and Pitt, M, "Awareness and effectiveness of quality function deployment (QFD) in design and build projects in Nigeria", Journal of Facilities Management, Vol. 12:1, Jan. 2014, pp.72 – 88.

First International Conference on Science, Engineering & Environment,
Tsu City, Mie, Japan, Nov.19-21, 2015, ISBN: 978-4-9905958-5-2 C3051

A GENETIC ALGORITHM–BASED APPROACH TO PREDICT PAVEMENT MAINTENANCE STRATEGIES: IRAQI EXPRESSWAY NO.1 CASE STUDY

Namir G. Ahmed Alkawaaz, PhD
A. Prof., M.ASCE, M.ASTM
College of Engineering/ University of Almustansiriyah, Iraq

ABSTRACT

The present paper articulates the applicability of genetic algorithms (GAs) as an optimization tool capable of supporting decision-makers (DMs) to make the right decisions throughout the selection of an optimal pavement maintenance strategy and to predict future pavement condition. GAs efficiently take advantage of historical information to locate search points with improved performance.
In this regard, pavement condition index (PCI) for the in-service pavement of the selected case study (Expressway No.1 (R4/A) in Iraq) is estimated based on ASTM D6433-11 and using MicroPAVER 6.5.2 software. Moreover, the related field measurements of the in-service pavement distresses are carried out and classified.

To predict the optimal maintenance strategy for the pavement segments within the selected pavement portion case study, a GA optimization technique is implemented as an application of stochastic approach using EVOLVER 6.3.1 software to evaluate the pavement performance based on PCI.

For the required validation process of the predicted PCI results obtained by the GA technique, predicted PCI results obtained by experts' opinions based on the design questionnaire were estimated and applied. The statistical validation analyses showed that the predicted PCI values obtained via EVOLVER 6 Genetic Algorithm software seem to be close to those obtained via the analyses of the experts' questionnaires.
Based on the research outcomes, it is concluded that one can recognize using the presented procedure throughout the implementation of stochastic approach in the form of GA to predict the optimal pavement maintenance strategy for in-service pavement.

Keywords: Pavement Maintenance Strategies, Genetic Algorithm, Optimization, Pavement Condition Index.

INTRODUCTION

Pavement management requires a large investment and much effort. Accordingly, the related agencies need to maintain and manage the required process effectively. Effective pavement management would yield a safe environment for public users.

The decision-makers (DMs) who have to make these types of choices often do so based on a number of criteria. Such criteria include an application of a proper optimization technique to predict the limited budget for capital and recurrent expenditure and the need to keep the transportation facilities operation at an acceptable level of service.

In many real-life problems, objectives under consideration conflict with one another, and optimizing a particular solution with respect to a single objective can result in unacceptable results with respect to other objectives. A reasonable solution to a multi-objective problem is to investigate a set of solutions, each of which satisfies the objectives at an acceptable level without being dominated by any other solution [1].

There has been a tremendous research effort to solve the complex problems by applying techniques to produce sufficiently precise results given the scope of the problem. These techniques are generally known as soft computing methods, which mainly include computing methods based on artificial neural network (ANN), genetic algorithm (GA), and others. All of these methods have a wide range of applications in engineering problems [2]. GAs are a class of computational models working based on the evolutionary process in nature. GAs use the adaptation-based random directed search techniques inspired by natural selection to obtain robust and computationally efficient solutions for engineering problems. They have been very popular in the last three decades due to their attractive features, such as the fact that they do not require a previous knowledge of the problem domain, so their robustness has been well established. There are numerous successful implementations in the

literature for search and optimization problems as well as machine learning [3].

Purpose Statement

Rating of the pavement maintenance alternative for selecting the optimal alternative is the largest problem facing pavement management agencies; this procedure is costly and causes delay. DMs are required to select a maintenance alternative that closely meets their criteria. Decision-making in pavement management is a complex process due to budget constraints and multiple criteria. For this reason and to assist the local agencies, it is proposed that agencies use an optimization process throughout the application of a stochastic approach based on GA to simplify selecting an optimal maintenance alternative and predict the future condition of pavement.

Research Goals

The main goal of the present paper is to predict pavement maintenance alternatives using a stochastic technique to evaluate and estimate in-service pavement performance and to predict an optimal maintenance strategy for the future based on a GA technique using EVOLVER 6 software to predict the pavement condition index (PCI). Accordingly, the goal is to predict the optimal maintenance alternative for the pavement segments within the selected case study: Expressway No.1 (R/4A) in Iraq**.**

PAVEMENT CONDITION ASSESSMENT

Fig. 1 presents a simulation between the standard PCI rating scale and the custom rating scale. Accordingly, it is recommended to consider reconstruction pavement maintenance for the PCI range of 0 to 55, and rehabilitation and reconstruction for the PCI values of 56 to 70 and 71 to 100, respectively.

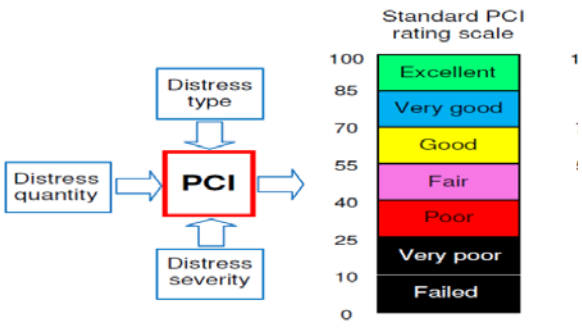

Fig. 1 Simulation between the Standard PCI Rating Scale and the Custom Rating Scale [4].

ESTIMATED PCI VALUES OF THE IN-SERVICE PAVEMENT CASE STUDY

PCI is analyzed using MicroPAVER 6.5.2 software. The related pavement distresses, such as alligator cracks, lane/shoulder drop-off, longitudinal and transverse cracking, polished aggregate, potholes, rutting, slippage cracking, raveling, and weathering are measured based on ASTM D6433-11. This index can be used to identify when treatments are needed, to define the condition state, for ranking or prioritization, and as the number used to forecast pavement condition and the average PCI of the selected fifteen segments within the pavement selected case study. The estimated PCI values can be seen in Table 1.

Table 1 The estimated PCIs (MicroPAVER 6.5.2 software output)

Pavement Segment	PCI Estimate	Pavement Segment	PCI Estimated
1	54	9	63
2	76	10	34
3	53	11	41
4	64	12	58
5	80	13	52
6	76	14	47
7	37	15	58
8	63	---	---

PAVEMENT MAINTENANCE DECISIONS USING GENETIC ALGORTHIMS

GA is an optimization method based on biological principles of evolution to provide an interesting alternative. This method is related to the stochastic approach, which is particularly useful for highly nonlinear problems and models, when computation time is not a primary concern.

The search process of GAs for solutions that best satisfy the objective function involves generating an initial random pool of feasible solutions to form a parent solution pool, followed by obtaining new solutions and forming new parent pools through an iterative process.

The fitness value of each solution is used to determine its probable contribution in the generation of new solutions, known as offspring. The next parent pool is then formed by selecting the fittest

offspring based on their objective function values. The entire process is repeated until a predetermined stopping criterion is reached [5].

OPTIMAL SOLUTION CONCEPT

In objective optimization, to measure the fitness of a solution in a given iteration, the process continues until the entire population is ranked, as illustrated in Fig.2. A solution with a lower numbered rank is assigned a higher fitness than that for a solution with a higher numbered rank.

The main goal of the objective optimization process is to achieve a balance between obtaining a well-converged and well-distributed set of optimal solutions. The more diverse the solution is, the better informed the DM is about the range and the spectrum of the possible solutions.

Solution Representation

Application of the GA technique for any problem requires setting the solution representation by the mean of chromosomes. Chromosome structure is made of a string of values associated with the problem variables. Figure 2 presents the general structure, the solution, and the chromosome production of the GAs. For the problem at hand, each of the chromosome elements has a value from 0 to 100, corresponding to one of the maintenance strategies (70–100 = preventive maintenance, 56–70 = rehabilitation maintenance, and 0–55 = reconstruction).

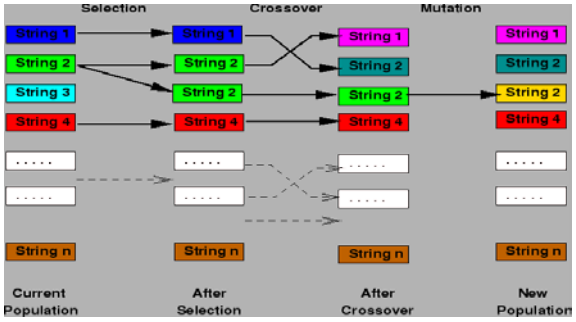

Fig.2 GA Mutation Operation and Chromosome Production [6].

Objective Function

In the present paper, an objective function optimization model is proposed to maximize the pavement condition. The optimization model outcome is adopted to estimate the values of the objective function. The objective function aims to maximize the condition of the pavement performance, as follows:

Max Average Condition = $\sum_i^n (\boldsymbol{PCI})\boldsymbol{i}/\boldsymbol{n}$,
Where (PCI)i = the pavement condition index of section i and n = the number of pavement segment.

CASE STUDY AND GA IMPLEMETATION

The case study represents fifteen pavement segments of 300 m length each, from the Iraqi Expressway No.1 – (R/4A). Expressway No.1 is the major arterial expressway in Iraq and extends from the Syrian and Jordanian borders to the Kuwaiti border. Section R4 is the segment of Expressway No.1 composed of the contracts R/4A and was constructed in the period of 1979–1989. Section R/4A starts at station 32+000 km and ends at 36+500 km, which is located at AL-Mahmudiya city and serves traffic from Baghdad to Hilla. The pavement section has six lanes, three in each direction, with a standing lane; each direction is separated by an island.

Data include pavement section number and the status of the pavement case study, which is expressed in the form of PCI for each segment based on the field inspections in the current year (2014) and the outputs of MicroPAVER 6.5.2 software. These numbers were used as a base to implement the GA technique, as precisely described in the following subsections. Moreover, the criteria mentioned in section 4 are considered a guide to classify the pavement maintenance strategy for each segment based on its own PCI values.

Genetic Algorithm Optimization

A GA is a method for solving both constrained and unconstrained optimization problems based on a natural selection process that mimics biological evolution. Therefore, it seems like a good idea to mimic the processes of reproduction and survival of the fittest to try to evolve answers to problems. At each step, the GA randomly selects individuals from the current population and uses them as parents to produce the children for the next generation. The following steps describe the optimization process based on the GA:

- Generate a population of possible answers to the problem at hand.
- Choose the best individuals from the population (using methods inspired by survival of the fittest).
- Produce a new generation by combining these best individuals (using techniques inspired by reproduction).
- Stop when the best individual of a generation is good enough (or you run out of time).

Implementation of Genetic Algorithm

EVOLVER 6 GA software is proposed to be used in this research. Based on the selection of design variables and constraints, this program allows the user to take an Excel spreadsheet with any type of calculation data (no matter how complex) and optimize a calculation outcome. Moreover, the optimization can be performed as a maximization, minimization, or the attempt to reach a target value.

GA Computation and Results Representation

The predicted PCI values for the proposed maintenance presented in Table 1 are used as input data for the EVOLVER 6 GA software. The results to maximize PCI value depending on the software output can be seen in Table 2.

Table 2 GA Computation–Predicted PCI Values after Proposed Maintenance Strategy for the Case Study Iraqi Expressway (No.1 – R/4A) In-Service Pavement Portion

Pavement Segment	a	b	c	d
1	54	_	_	84
2	76	78	_	_
3	53		_	91
4	64	_	68	_
5	80	83	_	_
6	76	81	_	_
7	37	_	_	76
8	63	_	70	_
9	63	_	71	_
10	34	_	_	63
11	41	_	_	77
12	58	_	65	_
13	52	_	_	83
14	47	_	68	_
15	58	_	65	_
Average	53	81	68	79

a: In-service pavement's estimated (PCI), b, c, and d : (PCI)'s values if Preventive, Rehabilitation and Reconstruction maintenance is implemented.

STATISTICAL EVALUATION

The following subsections describe the estimation of PCI values and pavement maintenance alternatives based on expert opinions and statistical analysis to evaluate the PCI results predicted via GA computation.

Estimating PCI Values and Pavement Maintenance Alternatives Based on Expert Opinions

Based on the previously mentioned criteria (Pavement Condition Assessment), the average opinion regarding the PCI values and the maintenance strategy for the selected pavement segments of twenty-eight experts in pavement maintenance, such as academic specialist staff and professional maintenance engineers, through a designed questionnaire were gathered and can be seen in Table 3.

Table 3 Expert Opinions of Predicted PCI Values after Proposed Maintenance Strategy for the Case Study Iraqi Expressway (No.1 – R/4A) In-Service Pavement Portion

Pavement Segment	a	b	c	d
1	54	_	_	88
2	76	81	_	_
3	53	_	_	86
4	64	_	71	_
5	80	83	_	_
6	76	80	_	_
7	37	_	_	75
8	63	_	70	_
9	63	_	70	_
10	34	_	_	73
11	41	_	_	75
12	58	_	68	_
13	52	_	_	86
14	47	_	_	84
15	58	_	69	_
Average	53.7	81.3	69.6	81

a: In-service pavement's estimated (PCI), b, c, and d : (PCI)'s values if Preventive, Rehabilitation and Reconstruction maintenance is implemented.

Figures 3 and 4 present the comparison between the PCI values from the experts' opinions and GA computation results. It clearly shows that the PCI results seem to be close enough to conclude that the PCI–GA computation results can be considered to predict pavement maintenance strategies.

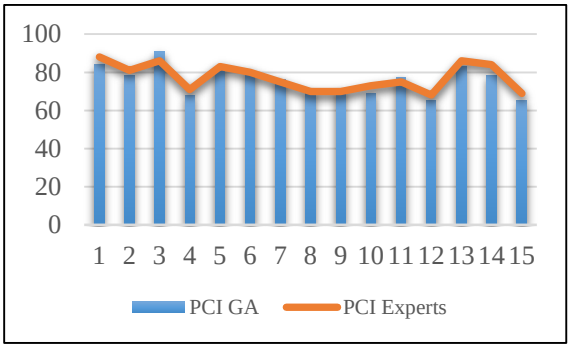

Fig. 3 Comparison between PCI Values of Expert Opinions and GA results for the fifteen pavement segments.

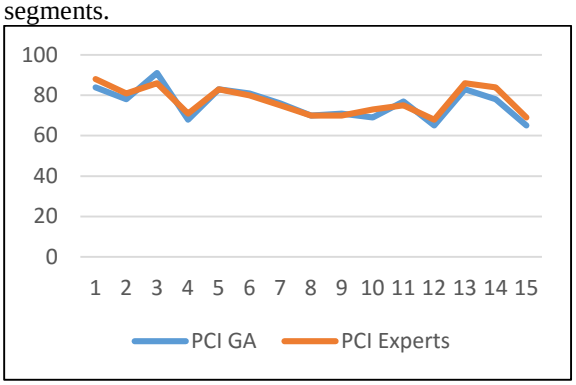

Fig.4 PCI's GA Computation vs. Average Opinion of Experts for Pavement Maintenance Strategy of the fifteen pavement segments,

The average PCI values obtained via expert opinion and GA computation are presented in Table 4. The average PCI results seem to be close to those in Fig. 5. A good fit can be seen in this figure that reflects a strong relationship between the values of PCI, which were estimated by GA computation and obtained from the average opinion of experts.

Table 4 Average PCI Values Obtained via Expert Opinions and GA Computation

PCI Experts	81.3	69.6	81
PCI GA	80.7	67.8	79

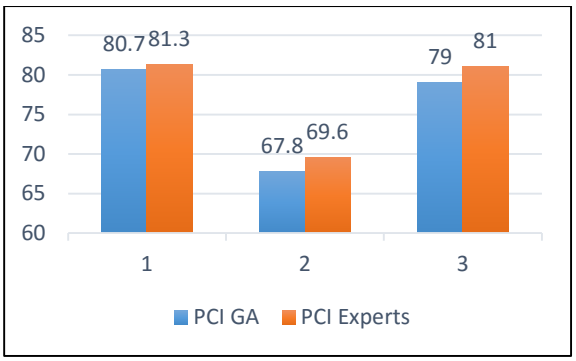

Fig.5 Average PCI from GA Computation vs. Average Opinion of Experts for Pavement Maintenance Strategy

To compare results of PCI obtained by GA computation with those obtained from experts' opinions in the questionnaires, statistical technique is followed through the following two steps: calculating relative error (RE) and graphical techniques.

Relative Error

To calculate the error between the output results of PCI, the RE technique is proposed. RE is computed as follows [7]:

RE= $|(\mathbf{PCI\ Expert} - \mathbf{PCI\ GA})/(\mathbf{PCI\ Expert})|$ …. (1),

Where: RE = relative error percent,

PCI Expert = estimated PCI based on expert opinion, and, PCI GA = calculated PCI based on GA computation.

Results of RE analysis are shown in Table 5 and Fig. 6.

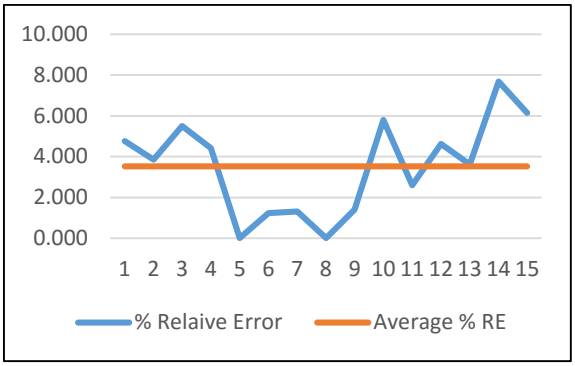

Fig.6 RE Computations for PCI $_{GA}$ and PCI $_{Experts}$

Table 5 RE Computations for PCI$_{GA}$ and PCI $_{Experts}$

No. of	PCI GA	PCI	Relative
1	84	88	4.762
2	78	81	3.846
3	91	86	5.495
4	68	71	4.412
5	83	83	0.000
6	81	80	1.235
7	76	75	1.316

8	70	70	0.000
9	71	70	1.408
10	69	73	5.797
11	77	75	2.597
12	65	68	4.615
13	83	86	3.614
14	78	84	7.692
15	65	69	6.154

The percentage of average RE is found to be 3.53, which is accepted as a prediction error if a confidence level of 95% is adopted.

CONCLUSION AND RECOMMENDATIONS

On the basis of the research findings, the following conclusions are appropriate:

1. Optimal maintenance alternatives for the in-service pavement segments within the selected case study (Expressway No.1- (R4/A)) were predicted based on the application of GA optimization technique.
2. Depending on the statistical analyses, it is concluded that the predicted PCI values obtained by expert opinions seem to be in good agreement with these obtained via GA software. Accordingly, it is concluded that using a stochastic GA technique is recommended as a desired optimization approach to predict the optimal maintenance alternative for pavement section.

Based on the study findings, it is recommended to use the presented procedure using a stochastic approach based on GA to estimate the optimal pavement alternatives for in-service pavement and to predict the best maintenance strategy. Furthermore, this approach can assist DMs and local engineers of pavement management systems and highway administration agencies to make the proper decisions during the selection of the proper pavement maintenance alternatives and schedule maintenance allocations for the next years.

ACKNOWLEDGMENT

The author wishes to thanks the State Corporation of Road and Bridges in Iraq, represented by Mr. Nihad Kassim, the head of Planning and Design Department, for his valuable support during the field measurement part of the study and for providing related pavement historical data.

REFERENCES

[1] Konak, A. W. David, and E. Smith. “Multi-Objective Optimization using genetic algorithms,” *Reliab. Eng. Syst. Saf.* (2006): 992–1007.

[2] Tutumluer, E., O. Pekcan, and J. Ghaboussi, J. “Nondestructive Pavement Evaluation Using Finite Element Analysis Based Soft Computing Models,” 2009, NEXTRANS Project No 010IY01.

[3] Goldberg, D. E., *Genetic Algorithms in Search, Optimization and Machine Learning* (Boston, MA: Addison-Wesley Publication, 1989).

[4] Hammond, Lindsi “Pavement Rating 101: PAVER,” NWPMA Conference, October 29, 2014, Seattle, WA.

[5] Fwa, T. F., and W. T. Chan. “Multiobjective optimization for pavement maintenance programming,” *J. Transp. Eng., ASEC* 126 (2000): 367–373.

[6] Mathew, T., V., *Genetic Algorithms.* Indian Institute of Technology Bombay, Mumbai-400076. Retrieved from: http://www.civil.iitb.ac.in/tvm/2701_dga/2701-ga-notes/gadoc/gadoc.html

[7] Wang, L., and E. Masad, E., *Analysis of Asphalt Pavement Materials and Systems, Engineering Methods* (American Society of Civil Engineers, Virginia, 2009).

First International Conference on Science, Engineering & Environment,
Tsu City, Mie, Japan, Nov.19-21, 2015, ISBN: 978-4-9905958-5-2 C3051

EXTRACTION OF SILICA GEL FROM AGRICULTURAL WASTE FOR POZZOLANIC APPLICATION: A REVIEW

Rahimah Embong[1, 2], Nasir Shafiq[1], and Andri Kusbiantoro[2]
[1]Civil and Environmental Engineering Department, Universiti Teknologi PETRONAS, Malaysia;
[2]Faculty of Engineering Technology, Universiti Malaysia Pahang, Malaysia

ABSTRACT

Conventional production of Portland cement and biomass-waste generated from agricultural based industry are both producing negative impact to the environment quality in which they are situated. However, there is a prospective potential to recycle agricultural waste and convert it into cement replacements material with consideration of several processing methods to activate its pozzolanic reactivity. Role of a pozzolan in improving the properties of cementitious product relies on the additional reaction in cementitious system to form Calcium Silicate Hydrate (C-S-H) structure. Generally, this by-product is converted into reactive ash by incinerating it in high temperature. The conversion of silica ash into gel forms results in further investigation of novel processing method to prepare silica gel that would result in the better control of micro-porous structure, thermal performance, and adsorption level of this pozzolanic product. This article reviews on the recent progress of synthesis of silica gel that encompassing its material background, production processes, applications, and gelification procedure. The article also discusses the integration of several main by products, e.g. oil shale ash, geothermal sludge, and rice husk ash (RHA) into the production of silica gel. Considering its effect to the environment quality, application of silica ash in a gel form as pozzolanic materials in concrete is capable to constitute a new material recycling and sustainability effort.

Keywords: Agricultural waste, Pozzolanic, Gelification, Silica gel

INTRODUCTION

Silica gel ($SiO_2.NH_2O$) in its physical state is a granular, vitreous, porous form of silicon dioxide that is made from the gelification of sodium silicate solution. Gelification methods may vary and depend on the specific application of each related industry; hence the process may formulate various types of silica gels with different pore structures. Silica gel can also be a naturally available mineral that is purified and processed into granular or beaded form.

Silica gel has micro porous structure with interlocking cavities, which produces a very high surface area (~800m^2/g) and make it capable as high capacity desiccant. It absorbs water readily which act as drying agent and at the same time reduce the relative humidity in a closed space almost 40%. Its unique chemical composition and physical structure contribute to the specific characteristics such as stable thermal performance, high adsorption feature, and stable physical property.

APPLICATIONS OF SILICA GEL

Silica gel has been applied in various industries because of the high adsorptivity and easy to be furnished into wide range of mesh sizes. Characteristics of silica gel, i.e. inert, non-toxic, and non-corrosive have increased its popularity since it does not require any chemical reaction in the adsorption process and does not form any by-products.

In the area of dyes and pigments research, investigation on the anchoring of silica gel on aluminium pigments surface has been initiated. Silica gel was expected to provide corrosion resistance based on the basis of oxidation process of aluminium by hydrogen peroxide [1]. Successful encapsulation of media concentration at 5.1 x 10-5 mol/m^2 produced the highest anchorage efficiency with a dense coating was formed, had a smooth surface and free from crack. This coating layer exhibited the best corrosion resistance on the aluminium flake surfaces. Thermal conductivity and contact resistance of mesoporous silica gel have also been studied in the cooling systems applications [2]. Measurement on thermal conductivity and thermal contact resistance by using guarded-hot plate apparatus under vacuum pressure has indicated the invention of new composite with a promising adsorption rate for cooling systems after the bonding of silica gel with polyvinyl pyrrolidone (PVP). Other utilizations of silica gel commonly found in industries are summarized in Table 1.

In concrete, silica gel has been used in the immobilization of bacteria for self-healing concrete [4]. It could enhance the immobilizing of bacteria and exhibit higher activity than polyurethane-

immobilized bacteria, which was a readily used agent

Table 1. Applications in industries associated by Fuji Silvia Chemical Product [3]

Industries	Areas	Applications
Dessicant & Dehumidifier	Storage containers, Computer, Instruments, Photos, Batteries, Circuit boards, Pet foods	Drying and cleaning of air and gases, analytical samples, solvents, and synthesis product Desiccant in gas industry, dehydration and purification in Oxygen, Hydrogen and Chlorine
Paints & Coating	Decorative Paint, Wood & Floors, Protective, Roof, Gel-Coats, Paper Coatings, Adhesives, Sealants	Matting, Anti-Corrosion, Water, Resistant Aid, Water Scavenger, Hydrophobic Properties, Filler, Viscosity Control, Mold Release Aid
Inks & Printing	Gravure, Flexo, Silk Screen Laser Printing, Thermal Transfer, Ink Receptivity, Over Print Varnish	Matting, Anti-Block/Tact Control, Color Bleed Control, Dot Gain, Control, Adhesion, Anti-Static, Fast Ink Dry, Clarity
Plastics	Films, Non-Films, Color Dispersions, Production Aid	Matting, Anti-Block, Superior Clarity, Filler, Texturizing, Viscosity Control, Purging Compound, Plate Out, Kinetic CoF
Food Pharmaceutical Personal Care	Food & Spices, Cosmetics, Personal Care, Dentifrice, Beers & Wine, Pharmaceuticals, Neutraceuticals	Free Flow Aid, Liquid Powderizing, Ingredient Carrier, Smooth Texturing, Matting, Stability/Emulsion Aid, Scrub Additive, Sebum Control, Chill, Proofing Agent, Filtering Aid, Compounding Agent, Drug Delivery System

in self- healing study [5-8]. Based on thermogravimetric analysis, $CaCO_3$ precipitated in silica gel (25% by mass) more than in polyurethane, which was only 11% (by mass). Silica gel is also known as a good carrier for microorganisms such as bacterial cells, yeast and algae due to its good mechanical, thermal and photochemical stability properties. The microstructural matrix of silica gel is also efficient for transmission of molecules and ions [9, 10].

In 2011, Samantha et al [11] studied the effects of silica gel from the residue of rice husk as a cement replacement material. In this study, silica gel replaced the portion of cement in the mixture from 0% to 5%. Based on pozzolanic reactivity test, silica gel could consume calcium hydroxide at higher rate (787 mg/g) than the minimum value attributed for conventional pozzolanic materials (330 mg/g). Substitution of cement with silica gel also corresponded to the strength increment as early as 3 days (control = 35 MPa; 2.5% silica gel = 52 MPa; 5% silica gel = 56 MPa). A consistent strength improvement was also presented by silica gel concrete after 28 days of curing. The researchers claimed that pozzolanic reactivity of silica gel was similar to silica fume and nano-silica produced by other amorphous pozzolans reported in numerous studies [12-16].

EXTRACTION AND GELIFICATION OF SILICA GEL

Investigation on the synthesis of ultrafine silica powder from oil shale ash (OSA) using fluidized bed drying of wet-gel slurry has also been studied [17]. Fluidization technique was employed in the drying process of wet-gel slurry at ambient temperature. The experiment was performed by dissolving 5 g/g (liquid/solid) with 20-40 wt.% of sodium hydroxide (NaOH) in distilled water under constant stirring to produce sodium metasilicate solutions. It was heated at 80-100 °C for 3, 4 and 5 hours. Gelification procedure was initiated by adding 0.5 mol/L H_2SO_4 solution into the prepared sodium metasilicate solution until it reached pH 4. Silica gel produced was then aged for 24 hours and washed

before proceed to make wet-gel slurry.

In 2014, investigation on the production of silica gels was expanded to the geothermal sludge based system [18]. Geothermal sludge ash was dissolved in NaOH solution to produce sodium silicate, which then diluted with various concentrations of HCl or tartaric acid to produce silica gels. In this study, the effects of silica concentration and pH to the silica gel properties were investigated with the introduction of two steps of aging process. In the first step of aging, the process was purposed to increase the size and uniformity of primary silica gel particles, while the second step of aging was conducted to strengthen the gel network of silica.

Muljani et al [18] conducted the extraction process by dispersing 10 g of geothermal sludge (GS) with particle size ranging from 147 µm - 175 µm in 100 ml of NaOH solution (0.5-2M) and boiled for 1 hour under reflux and constant stirring in order to dissolved the silica and produced a sodium silicate solution. The solution was then cooled down to room temperature and filtered to extract the sodium silicate solution for the subsequent gelification process. Two steps in the gelification process referred to the two consecutive aging process that involved the titration using difference acids, namely hydrochloric acid (inorganic acid) and tartaric acid (organic acid).

MATERIAL CHARACTERIZATION OF SILICA GEL

Characterization of silica gel conducted by Samantha et al [11] provided a valuable insight on the potential feature of agricultural based silica gel, particularly for the cementitious system. In the first analytical stage, Chapelle test was conducted to measure the pozzolanic reactivity of siliceous gel with reference to the French Norm FN P 18-513, Annexe A. It measured the quantity of calcium hydroxide fixed by siliceous materials from pozzolans. Chapelle test indicated the rapid consumption of calcium hydroxide by siliceous gel, which would be prominently beneficial to densify the microstructure of cementitious system via the formation of secondary calcium-silicate-hydrate gels.

X-ray fluorescence (XRF) analysis was employed to provide additional information on the chemical composition and loss of ignition of the silica gel. The escalating level of silica content in the silica gel illustrated the effectiveness of extraction method and gelification process, which was closely related to the measured pozzolanic reactivity. About 82% of SiO_2 content was detected in rice husk ash after pre-treatment process using HCl solution; however it showed an increasing value up to 91% SiO_2 content after gelification,

Based on the result of Brunaeur–Emmett-Teller (BET) analysis that provided a detailed specific surface area from the nitrogen adsorption process [19, 20], silica gel was reported to have finer particle size with higher surface area than rice husk ash and Portland cement [11]. Amorphous pattern of silica particles was observed with x-ray diffraction (XRD) analysis and it was entirely free from sodium chloride. It justified the effectiveness of gelification process in producing siliceous gel with high purity. Additional analysis using infrared spectroscopy showed the presence of ethanol in silica gel specimen, which was originated from humidity-reduction ethanol. Characteristics bands patterns observed in the infrared spectrum of alcohols was believed to be influenced by hydrogen bonds and the position of the group in the molecule. The decreasing FTIR pattern at 300 cm^{-1} to 1815 cm^{-1} was presumed to correspond with the nil presence of NaCl precursors after complete washing of the gel [11]. Observation on the microstructural images displays the existence of silica group in the form of irregular, cohesive surface, and spherical clusters [11].

CONCLUSION

This study reviews the possible approach to extract high purity pozzolanic silica from agricultural or industrial by products. Conversion of white silica ash into siliceous gel provides a positive outcomes, particularly related to the escalation of pozzolanic reactivity and its effect to the mechanical strength performance of cementitious system. Gelification as the subsequent process to conventional incineration practice gives an encouraging insight to the whole procedure, which will provide a basis for the future research. Nevertheless, new methods in this area could be further explored and in-depth information on the material characteristic are essentially required.

ACKNOWLEDGEMENTS

The authors would like to thank the financial support from Ministry of Education Malaysia. Universiti Teknologi PETRONAS (UTP) and Universiti Malaysia Pahang (UMP) under research grant 0153AB-K04 (UTP) and RDU130614 (UMP).

REFERENCES

[1] Z.-L. Ma, et al., "Silica sol–gel anchoring on aluminum pigments surface for corrosion resistance based on aluminum oxidized by hydrogen peroxide," Dyes and Pigments, vol. 114, pp. 253-258, 2015.

[2] A. Sharafian, et al., "Thermal conductivity and contact resistance of mesoporous silica gel adsorbents bound with polyvinylpyrrolidone in contact with a metallic substrate for adsorption

cooling system applications," International Journal of Heat and Mass Transfer, vol. 79, pp. 64-71, 2014.
[3] F. Silysia, Silica-gel uses in industries and applications. 2013.
[4] J.Wang, "Use of silica gel or polyurethane immobilized bacteria for self-healing concrete," Construction and Building Materials, vol. 26, pp. 532-540, 2012.
[5] V. R. J.L.Day, S.S Bang, "Microbiologically induced sealant for concrete crack remediation," presented at the 16th Engineering Mechanics Conference, Seattle, Washington, 2003.
[6] N. D. B. K.Van Tittelboom, W.De Muynuck, W.Verstraete, "Use of bacteria to repair craks in concrete," Cement and Concrete research, vol. 40, pp. 157-166, 2010.
[7] S. K. R. K.Santosh, V.Ramakrishnan, S.S.Bang, "Remediation of concrete using microorganisms," American concrete institute materials journal, vol. 98, pp. 3-9, 2001.
[8] J. K. G. S.S.Bang, V.Ramakrishnan, "Calcite precipitation induced by polyurethane-immobilized Bacillus pasteurii, enzyme and microbial technology", vol. 28, pp. 404-409, 2001.
[9] J. R. U. Soltman, S.Selenska Pobell, "Biosoprtion of heavy metals by sol-gel immobilized Bacillus sphaericus cell, spores and s-layers," Journal of sol-gel Sci Technology, vol. 26, pp. 1209-1212, 2003.
[10] H. B. U. Soltman, "Utilization of sol-gel ceramics for the immobilization of living microorganisms," Journal of sol-gel Sci Technology, vol. 48, pp. 66-72, 2008.
[11] R. P. Samantha Pinheiro, Guilherme Chagas Cordeiro, Marcia Rodrigues, Romildo Dias, "Production of silica gel from residual rice husk ash," Journal of Quimica Nova, vol. 34, pp. 71-75, 2011.
[12] H. Tanyildizi, "Variance analysis of crack characteristics of structural lightweight concrete containing silica fume exposed to high temperature," Construction and Building Materials, vol. 47, pp. 1154-1159, 2013.
[13] Ö. Çakır and Ö. Ö. Sofyanlı, "Influence of silica fume on mechanical and physical properties of recycled aggregate concrete," HBRC Journal.
[14] R. Siddique, "Utilization of silica fume in concrete: Review of hardened properties," Resources, Conservation and Recycling, vol. 55, pp. 923-932, 2011.
[15] P. Van den Heede, et al., "Influence of active crack width control on the chloride penetration resistance and global warming potential of slabs made with fly ash & silica fume concrete," Construction and Building Materials, vol. 67, Part A, pp. 74-80, 2014.
[16] A. F. Bingöl and İ. Tohumcu, "Effects of different curing regimes on the compressive strength properties of self compacting concrete incorporating fly ash and silica fume," Materials & Design, vol. 51, pp. 12-18, 2013.
[17] G.-M. Gao, et al., "Synthesis of ultrafine silica powders based on oil shale ash by fluidized bed drying of wet-gel slurry," Fuel, vol. 88, pp. 1223-1227, 2009.
[18] H. S. Srie Muljani, Gede Wibawa, Ali Altway, "A facile method for the production of high-surface-area mesoporous silica gels from geothermal sludge," Advanced Powder Technology, vol. 25, pp. 1593-1599, 2014.
[19] Q. Zeng, et al., "Characterizing pore structure of cement blend pastes using water vapor sorption analysis," Materials Characterization, vol. 95, pp. 72-84, 2014.
[20] W. Bao, et al., "Synthesis of hydrophobic alumina aerogel with surface modification from oil shale ash," Powder Technology, vol. 249, pp. 220-224, 2013.

First International Conference on Science, Engineering & Environment,
Tsu City, Mie, Japan, Nov.19-21, 2015, ISBN: 978-4-9905958-5-2 C3051

VALORISATION OF NATURAL POZZOLAN OF "DJOUNGO" (CAMEROON) AS LIGHTWEIGHT AGGREGATE FOR LIGHTWEIGHT CONCRETE

Willy JUIMO[1,2], Toufik CHERRADI[1] and Larbi ABIDI[1]
[1]Mohammadia School of Engineering, Mohammed V University of Rabat, Morocco
[2] Higher Institute of the Sahel, University of Maroua, Cameroon

ABSTRACT

Cameroon has an appreciable quantity of volcanic pozzolanic materials, but a very low proportion is used as cement additives. These materials are abundant but are rarely or very little used because of the lack or limited of studies to develop, promote and popularize its use naturally as an adjuvant or as aggregates in the production lightweights aggregates concretes . The main objective of this study is to promote these sources of low environmental impact construction materials. Its aim is to characterize and value the natural pozzolan source "Djoungo" as lightweight aggregate for lightweight concrete. Analyzes and tests conducted in this study were performed on aggregates produced from this resource. They concern the chemical and mineralogical analysis, the production of aggregates (Crushing and Sieving), physical properties (appearance and shape, natural water content, porosity, density and water absorption) and mechanical (Compressive strength, tensile strength and elastic modulus) to optimize the mechanical properties and durability of lightweight aggregate concrete obtained from this resource.

Keywords: Valorisation, Natural Pozzolan, Lightweight Aggregate and Concrete.

INTRODUCTION

Natural pozzolans, when they are used as constituents of Portland cements, such as additives or as aggregates in concrete, can improve its performance. Therefore, some technical advantages the use of pozzolan in concrete cannot be obtained when ordinary Porland Cement is used alone. Those advantages include: the high workability, reducing hydration heat as well as improved resistance to sulfates and alkali-aggregate expansion. Moreover, in many cases, the use of pozzolan in concrete proves Economic and allows for important energy savings [1]–[4].

Cameroon has an appreciable amount of volcanic pozzolan materials with a very small proportion (the "Djoungo" of lowland of Tombel, one source among many existing) used as a cement addition (6-35% of according Cameroonian Standard NC 234: 2009-06 on cement production) by local cement factories for portland cement (CEM II / A, CEM II / B, and CPJ 35) and pozzolanic cement (CEM IV / A and CEM IV / B), as base coat of pavement, strengthening of unpaved roads and very rarely as aggregates into the formulation of lightweight concrete [4]–[8]. These natural pozzolan are abundant but rarely or very little used because of the inadequacy or lack of studies to develop, promote and popularize its use as a lightweight aggregate.

VOLCANISM IN CAMEROON

Cameroon has been affected by a gigantic tectonic accident linking the Sao Tome and would continue until the Tibesti. This accident is observed by the alignment of forty massifs lie amidst over 500 km, from the Atlantic Ocean to Lake Chad which is the "Cameroon Volcanic Line".

Cameroon Volcanic Line (CVL)

The CVL is a suite of volcanic and sub volcanic devices, that are aligned in the direction North 30 ° East. 1600 km long, it is dotted with volcanic massifs of the Southwest to Northeast, It comprises Gulf of Guinea islands, mostly volcanic: Bioko Pagalu, Sao Tome, Principe and also some sea-mounts; the region of West Cameroon, with alternating mountains: Mount Cameroon (Altitude: 4100 m), the Manengouba Mountains (shield volcano of 20 km in diameter, with no known historic activity presents some Strombolian cones Bamboutou, Mbam and Oku and grabens (Kumba, Tombel, Mamfe, Mbos, Ndop) and end the Tikar lowland (Foumban in Banyo). These massifs located in the western part of the countryat the border with Nigeria are dotted with their shallow by many slag deposits. Especially on the slopes of Mount Cameroon (Fig. 1), the slopes of Mount Manengouba, Mount Galim, the plains of Tombel around Djoungo, Kumba plain, the plain of Noun around Foumbot, Lake Nyos area and the plateau of the Adamaroua [8].

Tombel Plain: Site of "Djoungo"

Volcanic scoria of locality of Djoungo on the plain of Tombel (Longitude: 9°37'32" East Latitude: 4°35'16" North) are the pozzolan which has been of the greatest number of studies. The slag Djoungo, purplish black and brick red, clean, without clay, are exploited because of their privileged geographical location (near the railway and seaport). These are fragments of vesicular magma of low density (<1), internal structure constituted by cells and more or less tight pore (Fig. 1). The ability to use these materials in manufacture of lightweight concrete can be an important economic asset [4]–[6].

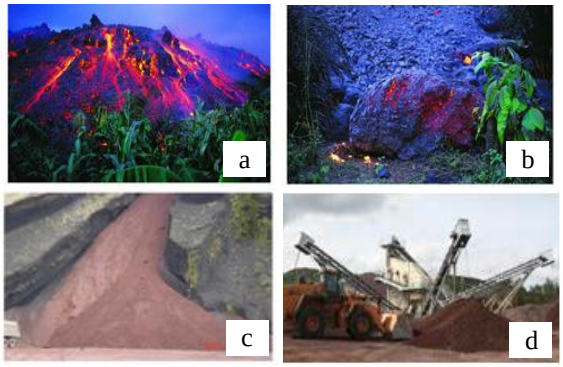

Fig. 1 Mount Cameroon (a) active larva (b) larva casting Front of the eruption of 1999 (Picture: Patrick Barois); Pozzolan Djoungo (c) Part of the site, (d) Operating Career [5].

MATERIALS AND PRODUCTS

Laboratories materials used for the valorization are presented as well as the collected scoria and aggregates obtained.

Volcanic scoria

Fig. 2 Packaging of specimens.

Specimens pozzolanic aggregates are obtained according to different techniques of preparation rock Specimens. The extraction of the natural pozzolan at the site of "Djoungo" in Cameroon took place on January 27, 2015.

Packaging and transport of specimens

Samples have been kept in plastic bags and then packed in cartons and sent to Rabat (Morocco) by flight (Fig. 2).

Selection and reduction of specimens

The reduction of specimens is performed initially sieving in order to separate the small volcanic scoria and large ones. Volcanic scorias are reduced by crushing (Fig. 3).

Fig. 3 Scoria (e) before and (f) after crushing.

Materials used

Getting the aggregates was carried out in one or two operations as appropriate. By sieving only or by crushing and sieving according to the size of volcanic scoria. The materials used are those of "Laboratoire Traitement des Minerais of Département des mines of Ecole Nationale Supérieure des Mines de Rabat (ENSMR) ".

Fig. 4 Crushers : (g) Roll crusher (h) Jaw crusher.

Screening or sieving

The sieving is performed directly on the small size scoria or after crushing for the considerable size scoria. The compounds undergo a sieving 20, 10, 5, 2.5 and 1.25 mm using stainless steel sieve of diameter 20 cm. Each sieving operation is carried out for 2 minutes using a sieve. Specimens undergo

the whole of the elaboration process follows: Drying in the open air for 24 hours for the removal of moisture in the rocks, crushing, sieving and Characterization.

Crushing

For crushing, we used a cylinder (Roll) crusher for of scoria size less than 80 mm and a jaw crusher to those of size greater than 80 mm (Fig. 4). The product obtained after the crushing is sieved on.

Products obtained

Lightweight aggregates obtained were classified into two categories: those derived by simply sieving and those obtained after crushing. Eight types of aggregates, which differ in the method of production and their size, were studied (Fig. 5).

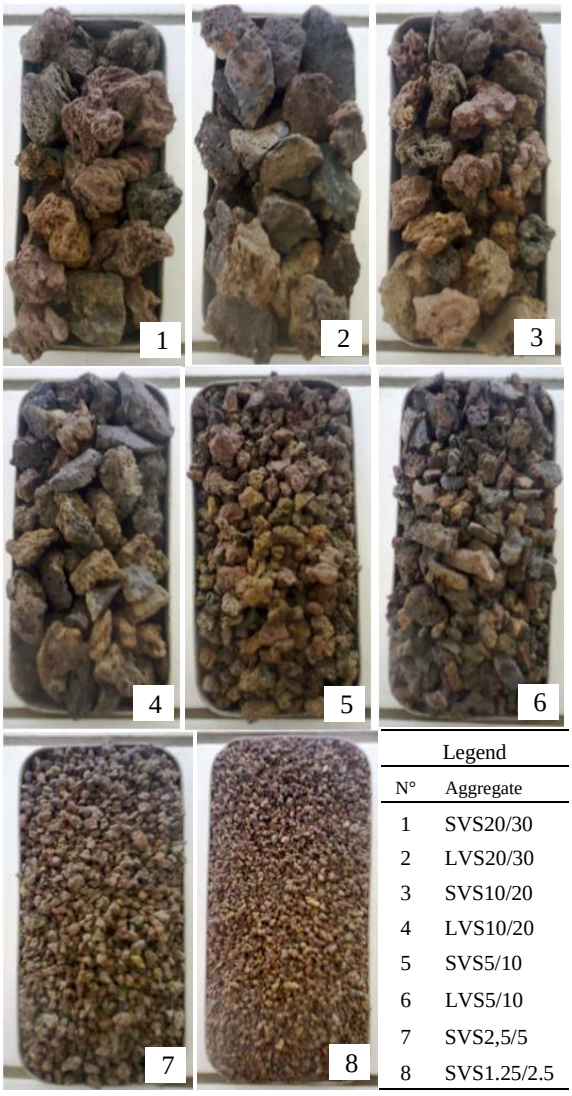

Legend	
N°	Aggregate
1	SVS20/30
2	LVS20/30
3	SVS10/20
4	LVS10/20
5	SVS5/10
6	LVS5/10
7	SVS2,5/5
8	SVS1.25/2.5

Fig. 5 Macroscopic view of different aggregates.

These aggregates are subsequently appointed by the terminology introduced (Tab. 1). The first two letters are references to the origin of derived from aggregate: small volcanic scoria (SVS) and large volcanic scoria or volcanic tuffs (LVS). Numerical values indicate the size range of d/D where d (mm) is the minimum diameter D (mm) the maximum diameter of aggregates.

An observation with the naked eye of the various aggregates (Fig. 5) shows the macroscopic geometry of the aggregates, namely more angular shape for crushed aggregates LVS5/10, LVS10/20 and LVS20/30 and more or less rolled for aggregates SVS1.25/2.5, SVS2.5/5, SVS5/10, SVS10/20 and SVS20/30.

ANALYSES AND CHARACTERIZATIONS

Chemical and mineralogical composition, texture, size and shape affect the physical and mechanical proprieties of aggregates. For this purpose we conducted analyzes to identify the influence of these parameters on the proprieties of the aggregates obtained.

Chemical and mineralogical properties

The chemical and mineralogical characterization of "Djoungo" were realized through overall chemical analysis and X-ray diffractometric analysis (XRD) on obtained by crushing powders (grain size 63-80μm) by several authors [4]–[6].

To perform the study of the chemical composition, the aggregates are first crushed. Then, these specimens were prepared in pellet form after fusion. The analyzed volume is of the order of several μm^3. The results of some tests conducted by some authors are presented (Tab. 1).

Chemical compositions

Table 1 Chemical analyzes of "Djoungo".

Ref.	[6]	[5]	[4]	[3], [9]
	DVS	ZD	DB1	ACI
SiO_2	45.57	44.04	45.79	43–72
Al_2O_3	15.94	15.26	15.68	9–20
Fe_2O_3	12.81	12.77	12.83	1–12
CaO	8.97	9.29	9.60	1–15
MgO	5.76	7.00	6.26	0.5–7
MnO	-	0.17	0.17	/
Na_2O	3.28	5.64	3.54	0.5–11
K_2O	1.03	1.35	1.39	0.2–8
SO_3	-	0.01	-	0–1.4
TiO_2	2.11	2.87	2.84	/
P_2O_5	-	0.53	0.60	/
L.O.I.	0.20	1.1	0.31	0.2–19

Natural pozzolan of "Djoungo" is composed of SiO_2, Fe_2O_3 and Al_2O_3 as main elements (% by

weight more than 10%), CaO, MgO, MnO, Na_2O, K_2O, TiO_2 and P_2O_5 as minor elements (less than 10%) and the loss on ignition (L.O.I.) is less than 2% (Tab. 2). This composition is according with ACI (American Concrete Institute) standard on natural pozzolans [9].

Mineralogical compositions

The X-ray diffractogram of scoria show more crystalline phases, the presence of a dome that extends between 20 and 40°(2s). This dome expresses the existence of the amorphous phase [5]. In summary, volcanic scoria contains amorphous phases. These materials, due to the presence of amorphous phases within them are therefore well suited as raw materials for the production of aggregates (Fig. 6).

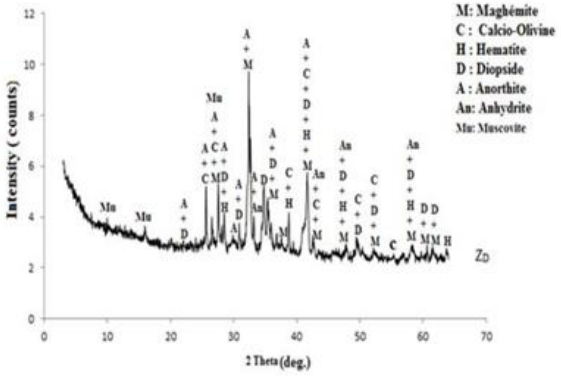

Fig. 6 Diffractogram of "Djoungo" [6].

Physical properties

Geometrical characteristics

The particle size is one of the most important parameters to consider in establishing a formulation of concrete. His knowledge allows for the precise dosage of aggregates to optimize the granular composition. Analyses are conducted according to NF EN 933-1, 1997 standard (Fig. 7).

Curves of particle size analyzes express only average grain size. We subsequently specify the different form scoria naturally and aggregates obtained after crushing.

By using of NF EN 933-4 standard, we establish a study protocol to measure by a vernier caliper: the length (L) which corresponds to the greatest distance of a pair of parallel tangent planes; the width (l) and thickness (e) which are respectively the largest and the smallest gap of a couple taking tangent parallel.

Scoria is sieved to the sieve 20, 25, 28, 31.5, 35.5, 40, 50 and 63 mm. For aggregates obtained after crushing, they are sieved to sieves of 5, 6.30, 8, 9, 10, 12.5, 14, 16 and 18 mm. A test specimen of 20 aggregates is taken from each sieve. The flattening coefficient (p=e/l) and the elongation coefficient (l/L) used to get an idea about the shape of the removed scoria and aggregates obtained (Fig. 8).

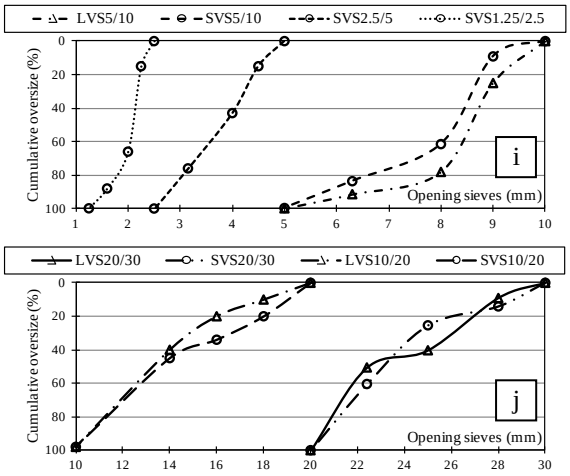

Fig. 7 Granulometry (i) SVS1.25/2.5, SVS2.5/5, SVS5/10 et LVS5/10; (j) SVS10/20, LVS10/20, SVS20/30 et LVC20/30.

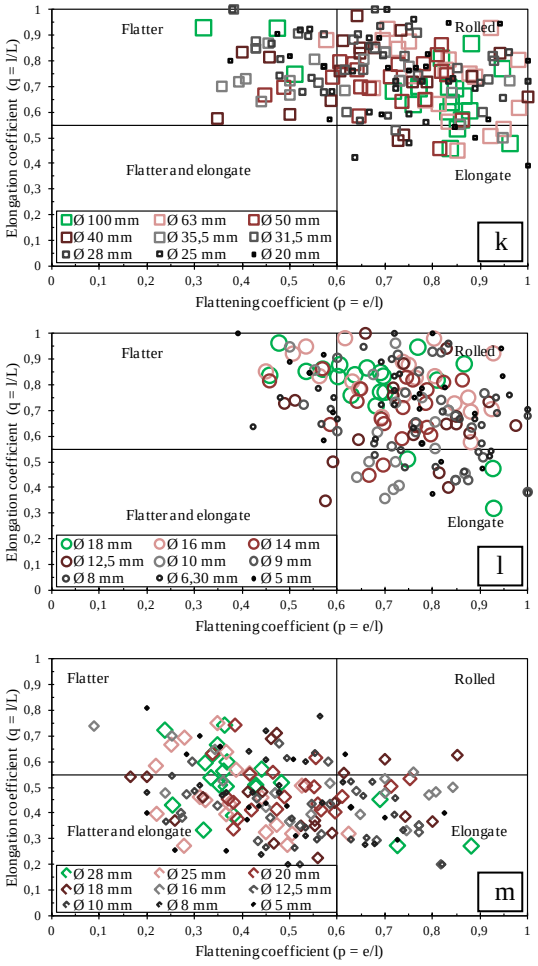

Fig. 8 Form of scoria in the natural state (k) and (l), Aggregates obtained by crushing (m).

The shape of aggregates varies according to

their method of production and size. Composition forms aggregates (Flatter and elongate, flatter, elongate or rolled) have been presented. The collected scoria has a more or less rolled. Aggregates obtained by sieving have a rolled shape and those obtained after crushing are flatter and elongate (Tab. 3).

Table 3 The composition form.

Aggregate	Flatter and elongate	Flatter	Elongate	Rolled
Scoria "Djoungo"	0%	21%	12%	67%
SVS20/30	0%	11%	4%	85%
LVS20/30	87%	9%	4%	0%
SVS10/20	1%	8%	9%	82%
LVS10/20	91%	3%	4%	2%
SVS5/10	0%	8%	6%	86%
LVS5/10	84%	7%	8%	1%
SVS2.5/5	x	x	x	✓
SVS1.5/2.5	x	x	x	✓

Water content, densities and porosity

The water content, bulk density, specific density and porosities are defined for aggregates according to the procedure used in the laboratory, accordance with NF EN 1097, 2006 standard (Tab. 4).

Table 4 Water content, densities and porosity.

Aggregate	Water content	Bulk density	Specific density	Porosity e (%)
Scoria "Djoungo"	2.56	0.56	1.58	51
LVS20/30	1.25	0.67	2.24	48
LVS10/20	1.04	0.79	2.52	51
LVS5/10	1.88	0.82	2.73	54

Water absorption

Knowledge of the water absorption coefficient of aggregates used to adjust the mixing water content in the composition of the concrete. Measurements of the absorption of water by the aggregates were therefore carried out following the procedure of NF EN 1097-6, 2001 standard (Fig. 9). The water absorption coefficient is defined as the ratio of the absorption coefficient is defined by:

$$\mathbf{W_a} = \frac{\mathbf{M_e}}{\mathbf{M_s}}.\mathbf{100}\% \quad (1)$$

Where $\mathbf{M_e}$ is the mass of water absorbed and $\mathbf{M_s}$the dry mass of the specimen after drying oven at 105°C.

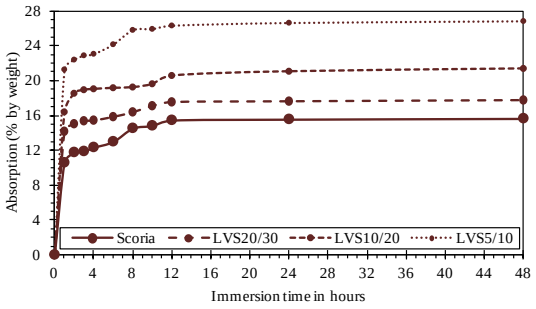

Fig. 9 Water absorption evolution with the time.

Mechanical properties

The realization of mechanical testing requires the manufacture of rock specimens large enough to ensure the homogeneity of the material in the specimen and its representation relative to the site of the aggregate. It is not possible to obtain carrots from the scoria to allow changing mechanical performance. We will use the empirical formulas and literature data to approximate the mechanical properties (Compressive strength, tensile strength and elastic modulus) of scoria and aggregates obtained (Tab. 5).

Table 5 Mechanical properties of aggregates according to their bulk densities.

Ref.	European Standard EN 13055-1, [10]			
	Scoria	LVS20/30	LVS10/20	LVS5/10
$\mathbf{d_V}$	0.56	0.67	0.79	0.82
$\mathbf{f_{gpot}\ 1}$	7.37	14.74	22.78	-
$\mathbf{f_{gpot}\ 2}$	9.43	13.94	-	-
$\mathbf{f_{eg}\ 1}$	15.09	26.95	39.89	43.12
$\mathbf{f_{eg}\ 2}$	52.52	74.74	98.98	105.04
$\mathbf{f_{tg}}$	2.41	3.19	4.05	4.26
$\mathbf{E_g}$	2508.8	3591.2	4992.8	5379.2

$\mathbf{d_V}$: Bulk density ; $\mathbf{f_{gpot}\ 1}$ and $\mathbf{f_{gpot}\ 2}$: Compressive strength in pot ($\mathbf{f_{gpot}1 = 67(d_V - 0,45)}$ with $\mathbf{0,45 < d_V < 0,82}$), ($\mathbf{f_{gpot}\ 2 = 41(d_V - 0,33)}$ with $\mathbf{0,38 < d_V < 0,73}$) ; $\mathbf{f_{eg}\ 1}$: Hydrostatic compression strength of individual aggregate ($\mathbf{f_{eg}\ 1 = 107,8(d_V - 0,42)}$); $\mathbf{f_{eg}\ 2}$: Hydrostatic compressive strength of aggregates taken in batches ($\mathbf{f_{eg}\ 2 = 202(d_V - 0,30)}$) ; $\mathbf{f_{tg}}$: Wire tensile strength ($\mathbf{f_{tg} = 3,9(1,82d_V - 0,40)}$) in MPa ; Elastic modulus : $\mathbf{E_g = 8000\ \rho_g^2}$ where $\mathbf{E_g}$ is expressed in Mpa and $\boldsymbol{\rho_g}$ in t/m^3.

DISCUSSIONS

Many studies have focused on the use of volcanic scoria as lightweight aggregate. Different sources of materials have been explored (Tab. 6).

Table 6 Data of some natural pozzolan lightweight aggregates studies by different authors.

Aggregate	Origin	Class	Ref.
LWCA1	Béni-Saf, Algeria	2-8	[1]
LWCA2		8-16	
CVPA	Papua New Guinea	1.18-20	[2]
FVPA		0.15-9.5	
DB1	Djoungo, Cameroon	5-10	
FB1	Djimbouot, Mfesset, Fosset (Foumbot), Cameroon	5-10	[4]
FB2		5-10	
FB3		5-10	
FB4		5-10	
G3/8	Béni-Saf, Algeria	3-8	[7]
G8/15		8-15	
Scoria	Iceland	0-100	Euro LightCon

We have presented the data diagrams to enable comparison with the results obtained with those of the literature (Fig. 10). The properties of lightweight aggregates obtained in this work, are more or less close to the results obtained with other natural pozzolan lightweight aggregates already studied.

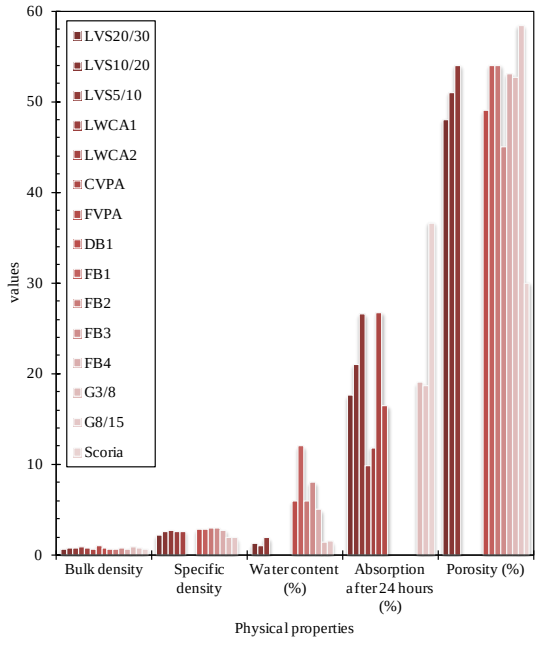

Fig. 10 Diagram of some physical properties.

CONCLUSION

Based on the results of experimental work, "Djoungo" scoria lightweight aggregate can be used in the production of lightweight concrete. It will reduce the coast and environmental pollution. Knowledge about physical, chemical and mechanical properties can be heft to control castings, mechanical properties and durability for lightweight aggregate concrete production.

ACKNOWLEDGEMENTS

The Authors thank staff of Ecole Nationale Supérieure des Mines de Rabat (ENSMR) for the permission to use their laboratory instruments.

REFERENCES

[1] Mouli M and Khelafi H, "Performance characteristics of lightweight aggregate concrete containing natural pozzolan", Building and Environment 43 (2008), 2006, pp. 31–36.

[2] Hossain K M A, Ahmed S and Lachemi M, "Lightweight concrete incorporating pumice based blended cement and aggregate: Mechanical and durability characteristics", Const and Build Mater 25, 2011, pp.1186-1195.

[3] Kaid N, Cyr M, Julien S and Khelafi H, "Durability of concrete containing a natural pozzolan as defined by a performance based approach", Const and Building Materials, 23, 2009, pp. 3457-3467.

[4] Bidjocka C, "Conception de bétons légers isolants porteurs. Applications aux pouzzolanes naturelles du Cameroun", Thèse de doctorat, INSA de Lyon, 1990, 167p.

[5] Billong N, Melo U C, Njopwouo D, Louvet F and Bonnet J P, "Physicochemical characteristics of some Cameroonian pozzolans for use in sustainable cement like materials", Materials Sc. and App. , 4, 2013, pp. 14-21.

[6] Tchakouté K H, "Elaboration et caractérisation de ciments géopolymères à base de scories volcaniques", PhD Thesis, UY I, 2013, 170 p.

[7] Ferhat A, Goual SM, Goual I et Khelafi H, "Valorisation de la pouzzolane de Beni-Saf (Algérie) par transformation en granulats de bétons légers", Actes Séminaire International Innovation et Valorisation dans le genie civil, Hammamet, Tunisie, 5-7 fév 2009, pp. 447-455.

[8] Tsafack J P F, Wandji P, Bardintzeff J-M, Bellon H and Guillou, "The Mount Cameroon stratavolano (Cameroon Volcanic Line, Central Africa) : Petrology geochemistry, isotope and age data", Geochemistry, Mineralogy and Petrology, Sofia, 47, 2009, pp. 65-78.

[9] ACI, "Use of Raw or Processed Natural Pozzolans in Concrete", ACI Committee 232, Manual of Concrete Pratice ACI 232.1, 2000.

[10] Ke Y, "Caractérisation du comportement mécanique des bétons de granulats légers: expérience et modélisation", Thèse de doctorat , Université de Cergy Pontoise, 2008, 316 p.

First International Conference on Science, Engineering & Environment,
Tsu City, Mie, Japan, Nov.19-21, 2015, ISBN: 978-4-9905958-5-2 C3051

NUMERICAL SOLUTION APPROACH TO THE DYNAMIC RESPONSE OF SIMULATED UNDERGROUND STRUCTURES DUE TO VARIOUS ACCIDENTAL EXPLOSIONS

Akinola Johnson OLAREWAJU
Civil Engineering Department, School of Engineering, The Federal Polytechnic Ilaro, Ogun State, Nigeria.

ABSTRACT

Solution to the complex phenomenon involving accidental explosion could not be easily and accurately achieved except through the use of numerical tool. Various accidental explosion scenarios involving underground structures will require the interaction of quite a number of parameters such as the structures, blast loads, blast duration, ground media, contact definition between the components under consideration, material definition, boundary condition, etc. The numerical tool that is capable of analyzing all these variables to yield the required observed parameters should be examined. This tool should be able to incorporate one or more numerical methods of analysis in its program formulation with a view to simplifying and widening research horizon as well as expanding the application of the numerical tool to other field of research. In the case of modeled underground structures, the required observed parameters after analysis are displacement, pressure, stress and strain which could still be subjected to further analysis.

Keywords: Analysis, Dynamic, Numerical, Tool, Structures, Underground

INTRODUCTION

There are many methods available to determine the dynamic responses of underground structures due to loads from accidental explosions. These are the analytical methods and the numerical methods. The analytic method is deterministic such as empirical phenomenological and computational fluid mechanics models which are used for explosion load prediction. They are used for elastic response or limited plastic response, and it does not allow for large deflection and unstable responses [6]. There are several numerical methods for assessing the response of underground structures due to dynamic loadings. These are iteration, series methods, weighted residuals, finite increment techniques usually referred to as finite difference, Newmark, Wilson, Newton, Houbolt, Eular, Runge-Kuta and Theta methods. The finite difference is popularly used to solve ordinary and partial differential equations, in particular, dynamic problems [8]; [4].

BACKGROUND STUDY

The ground media that could be considered in the study of the dynamic response of underground structures due to loads arising from accidental explosions are loose sand, dense sand and undrained clay. The geotechnical properties of these ground media as revealed by several researchers could be used. For accidental explosions to have taken place outside the vicinity of the underground structures, elastic scenario could be considered. Since the two elastic constants are enough to study the mechanics of such scenarios. These constants are the modulus of elasticity, E, Poisson's ratio and density [8]. Peradventure the blast (i. e. accidental explosion) takes place within the nearby region or proximity of the underground structures, then, more constitutive relations and parameters are required. Therefore, detailed soil test results are required for the study [7].

Load parameters from accidental explosions are also determined experimentally or by means of technical manuals. [15] which supersede other technical manuals like TM 5-1300 (1990) could be used to predict positive phase at various stand-off points. Pressure is the determining factor in the design and dynamic response of underground structures due to surface accidental explosions. In order to evaluate ground shock parameters due to underground accidental explosions, parameters such as peak particle displacement, peak particle velocity, loading wave velocity etc. could be determined. Soil test results are required in the final design to accurately determine the density and loading wave velocity of the particular soil at the exact site location [12].

PROBLEM DEFINITION

Underground structures are basically structures constructed below the ground surface consisting of many different elements and various forms as the case may be depending on the functions cost as well as the applications as detailed in Figure 1.

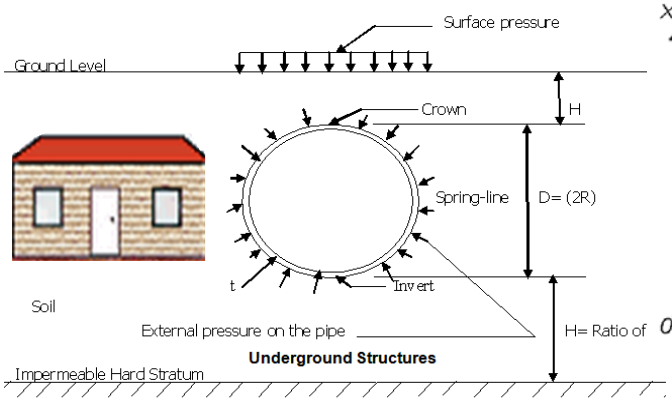

Figure 1: Cross-section of buried/underground structures [10]; [12]; [16]

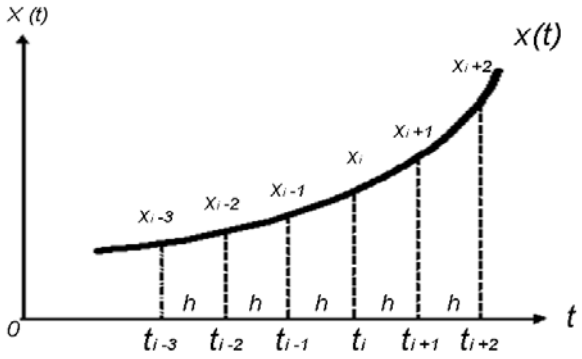

Figure 2: Finite difference discretization

ANALYSIS OF THE CONSTITUENTS OF ACCIDENTAL EXPLOSIONS

In this study, the numerical approach for studying the dynamic response of modeled underground structures due to loads from accidental explosions will be examined. This is with a view to examining its application and incorporation into available numerical tool(s) or code(s).

Finite Difference Method

Finite Difference Method is the former name for Finite Element Method, which allows the incorporation of certain features that makes it possible to be used in the ABAQUS software package for studying the response of underground structures due to various accidental explosions. Finite difference methods can be implicit method where the partial differential equation could be solved indirectly by solving a system of simultaneous linear equations. In this case, convergence is always assured. In other words, it could be explicit method where the partial differential equation could be solved directly using the appropriate boundary conditions and proceeding backward in time through small intervals until the determination of optimal path. In this case, convergence is assured for specific size of increment length of interval. The main principal reason for using implicit solution method is to allow for large time-step size, though it is more complex to program and require more computational effort in each solution step.

Mathematically, finite-difference methods are numerical methods for approximating the solutions to differential equations using finite difference equations to approximate derivatives. In this method, there is always a difference in the approximation and the exact solution known as error. The two main sources of error in finite difference methods are round-off error and truncation error or discretization error, that is, the difference between the exact solution of the finite difference equation and the exact quantity assuming perfect arithmetic [4]; [9]; [13].

Looking at the function x (t) shown in Figure 2 having grid points of *i* to be 1, 2, ... n along the coordinates t equally spaced with interval of h. Taylor's series could be used to express in terms of xi as shown below

$$f(x)=f(h_i)+(h-h_i)f'(h_i)+\frac{(h-h_i)^2}{2!}f''(h_i)+\cdots+\frac{(h-h_i)^n}{n!}f^{(n)}(h_i)+\cdots \qquad 1$$

Evaluating at point t_{i+1}, we have

$$f(x_{i+1})=f(h_i)+(h_{i+1}-h_i)f'(h_i)+\frac{(h_{i+1}-h_i)^2}{2!}f''(h_i)+\cdots+\frac{(h_{i+1}-h_i)^n}{n!}f^{(n)}(h_i)+\cdots \qquad 2$$

Truncating the series after the first derivative (f' = dy/dx) term, we have,

$$f(x_{i+1})\approx f(h_i)+(h_{i+1}-h_i)f'(h_i) \qquad 3$$

Solving for the first derivative, i. e. $f'=\frac{dy}{dx}$ = the rate of change of a dependent variable, such as *y*, with respect to an independent variable, such as *x* gives the forward difference approximation of the first derivative

$$f'(x_i)\approx\frac{f(x_{i+1})-f(x_i)}{x_{i+1}-x_i} \text{ or better still } f'(x_i)\approx\frac{f(x_{i+1})-f(x_i)}{h} \qquad 4$$

Backward difference approximation of the first derivative gives

$f'(x_i) \approx \frac{f(x_i) - f(x_{i-1})}{x_i - x_{i-1}}$ or better still $f'(x_i) \approx \frac{f(x_i) - f(x_{i-1})}{h}$ 5

While the central difference of the first derivative gives

$$f'(x_i) \approx \frac{f(x_{i+1}) - f(x_{i-1})}{2h} \quad 6$$

Solving for the second derivative (i. e. $f'' = \frac{d^2y}{dx^2} = \frac{d}{dx}\left(\frac{dy}{dx}\right)$) gives the forward difference approximation of the second derivative

$$f''(x_i) \approx \frac{f(x_{i+2}) - 2f(x_{i+1}) + f(x_i)}{h^2} \quad 7$$

Backward difference approximation of the second derivative gives

$$f''(x_i) \approx \frac{f(x_i) - 2f(x_{i-1}) + f(x_{i-2})}{h^2} \quad 8$$

While central difference approximation gives

$$f''(x_i) \approx \frac{f(x_{i+1}) - 2f(x_i) + f(x_{i-1})}{h^2} \quad 9$$

The truncation error in the centered difference approximation is of the order of h^2 while the truncation error in the forward and backward difference approximation is of the order of *h*. Central difference approximation is more accurate than the forward or backward difference approximation and as a result of this, it could be used in the study of the response of modelled underground structures due to loads from accidental explosions to solve the equation of motion using explicit integration scheme in any available numerical code. Most of the numerical methods in the analysis of dynamic problems are based on the finite difference approach [8]; [12]. Direct-integration dynamics of time integration in the explicit integration scheme of central difference method of numerical method could be used to solve the equations of motion (Eqs 10, 11 or 12) of the system. This is integrated through time. That is,

$$[m][\dot{U}] + [c'][\dot{U}] + [k][U] = [P] \quad 10$$

This could be rewritten as

$$[m]\frac{d^2x}{dt^2} + [c']\frac{dx}{dt} + [k][x] = F(t) \quad 11$$

This could also be rewritten as

$$[m]f'' + [c']f' + [k]f = F(t) \quad 12$$

for $U_{(t=0)} = U_0$ and $\dot{U}_{(t=0)} = \dot{U} = V_0$ 13

$$P = m\frac{x_{(1+1)} - 2x_i + x_{(i-1)}}{(\Delta t)^2} + c\frac{x_{(1+1)} - x_{(1-1)}}{2\Delta t}kx_i = Pi \quad 14$$

where $Ui = U(t)$ and U_{+1} can be written as

$$U_{(i+1)} = \frac{1}{\frac{m}{h^2} + \frac{c'}{2h}}[\{\frac{2m}{h^2} - k\}Ui + \{\frac{c'}{2h} - \frac{m}{h^2}\}U_{(i-1)} + Pi \quad 15$$

where *m*, *c*, and *k* are element mass, damping and stiffness matrices and *t* is the time. *U* and *P* are displacement and load vectors while dot indicate their time derivatives. $\ddot{U}_o$ is known from the given initial conditions while *i* is the increment number of an explicit dynamic step. The terms $_{i+1}$ and $_{i-1}$ refers to mid-increment values. The time duration (period) for the numerical solution could be divided into intervals of time Δt (h). It should be noted that with no damping

$$\Delta t \le \frac{2}{\omega \max} \quad 16$$

for stable and satisfactory solution or with damping

$$\Delta t \le \frac{2}{\omega \max}(\sqrt{1 + \xi \max^2} - \xi \max) \quad 17$$

$$\ddot{U}_o = (m)^{-1}(Po - c\dot{U}_o - kUo) \quad 18$$

$$U_{-1} = Uo - h\ddot{U}_o + \frac{h^2}{2}\ddot{U}_o \quad 19$$

$\omega \max$ is the maximum natural frequency, $\xi \max$ is the critical damping factor. Stability limit is the largest time increment that can be taken without the method generating large rapid growing errors. The accuracy of the solution depends on the time step Δt = h. However, there are some conditionally stable methods where any time step can be chosen on consideration of accuracy only and need not consider stability aspect [2]; [8]; [10].

Bulk Viscosity

Bulk viscosity introduces damping associated with the volumetric straining. Its purpose is to improve the modeling of high-speed dynamic events like accidental explosions, crash, etc. Basically there are two forms of viscosity in explicit that could be

used in the study. The first is found in all elements and is introduced to damp the oscillation in the highest element frequency. This damping is sometimes referred to as truncation frequency damping. It generates a bulk viscosity pressure, which is linear in the volumetric strain. The second form of bulk viscosity is found only in solid continuum element. This form is quadratic in the volumetric strain rate. The bulk viscosity pressure is not included in the material point stresses in the simulation because it is intended as a numerical effect only; it is not considered to be part of the material's constitutive response. Linear bulk viscosity is always included in explicit with default values of 0.06 and 1.2 for linear and quadratic viscosity respectively to control oscillations in the model during analysis failure of which would result to termination of the analysis [2].

Using the explicit integration scheme in ABAQUS CAE (Complete ABAQUS Environment) to solve equation of motion (i. e. eq. 10, 11, or 12) makes it unnecessary for the formation and inversion of the global mass and stiffness matrices [M], [K]. It also simplifies the treatment of contact illustrated in Figures 3 (a, b & c) between the constituents of blast and requires no iteration. This means that each increment is relatively inexpensive compared to the increments in an implicit integration scheme. It also performs a large number of small increments efficiently. Explicit integration scheme are used for the analysis of large models with relative short dynamic response times and extremely discontinuous events or processes. This makes it relevant and justifiable to be used for the analysis of the study of the response of underground structures due to loads arising from accidental explosions because blast is a short discontinuous event, or better still, it is an artificial earthquake [14].

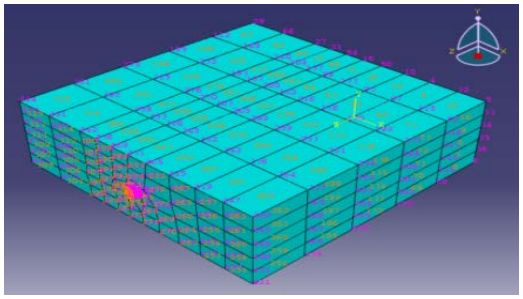

a

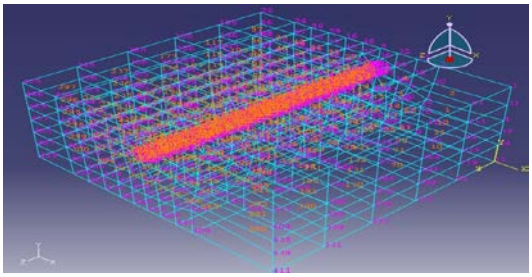

b

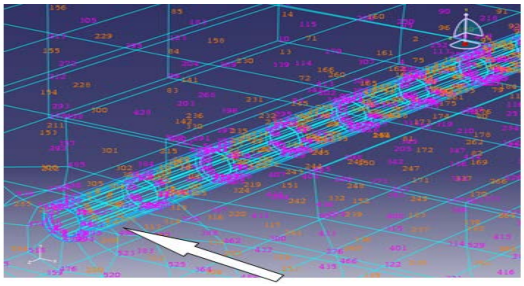

c

Figure 3: (a) Finite element model (a) Soil model and (c) Pipe model

Hourglassing

The reduced-integration scheme has a disadvantage such that it can lead to mesh instability during analysis. This instability is known as hourglassing. This consequence does not cause any strain, consequently it does not contribute to energy integral. It only behaves in a manner that is similar to that of a rigid body mode. The common causes of this consequence if excessive are the concentrated of forces at a single node and in the study of the response of underground structures due to blast loads, the forces could be distributed among several nodes by applying a distributed load; hence, hourglasing would be avoided and secondly, boundary condition at a single node which could be rectified in the study by distributing the boundary constraint among several nodes [1]; [10].

Contact Definition

In the study of the dynamic response of underground structures due to accidental explosions, there are soil-structure interactions from the various parameters that are involved in the analysis. As a result of these, there is need for the definition of these interactions between the constituents of blast. The explicit integration method efficiently solves extremely discontinuous events. Contact is an extremely discontinuous form of nonlinearity. It is possible to solve complicated, very general, three-dimensional contact problems with deformable bodies in ABAQUS/Explicit numerical tool. It provides two algorithms for modeling contact: (a)

General contact, which allows the definition of contact between many or all regions of constituents of blast in a model with a single contact; (b) Contact pair, which describes contact between two surfaces and it requires more careful definition of contact. In this case, every possible contact pair interaction must be defined and it has restrictions on the types of surfaces involved. The pair algorithms could be used for two-dimensional models. Contacts between the constituents of blast could be defined for various coefficients of friction and parametric studies using this algorithm [1]; [2]; [11].

Factors to be considered in the selection of Numerical Tools

In other to select a numerical tool to the study of the response of underground structures due to various accidental explosions, the various constituents and their interactions must be taken into consideration. This interactions involves the contact between the constituents. ABAQUS/Explicit numerical tool provides the capability to analyze high-speed dynamics like drop test and crash analyses of structural members as well as large, nonlinear, quasi-static analyses like deep drawing, blow molding, and assembly simulations. It can also analyze high discontinuous post buckling and collapsing simulations as well as extreme deformations like bulk metal forming, impact and crushing, coupled temperature-displacement (dynamic) and structural acoustics. Other challenging problems which ABAQUS/Explicit can handle efficiently and effectively are: rubber door seal, wire crimping, gas tank impact, column impact, metal forming, wiper blade, etc.

The advantages of ABAQUS/Explicit over other modules in the numerical code are; it has been designed to solve highly discontinuous, high-speed dynamic problem efficiently and it has a very robust contact algorithm that does not add additional degrees of freedom to the model. In addition to these, it does not require as much disc space as ABAQUS/Standard for large problems and it often provides a more efficient solution for very large problems. It also contains many capabilities that make it easy to simulate quasi-static problems, among others. Finally the impact analysis (including all deformable components) uses elastic materials and the constitutive models available for all materials commonly found in impact analysis are: Elastic/plastic models for metals, soil, etc; Pressure-dependent plasticity models for thermoplastics; Hyper-elastic models for solid rubbers; Hyper foam models for foam rubbers; Failure models for vulnerability analysis and solder joint; etc. Most materials can be made strain-rate and direction dependent. The limiting factor is generally the availability of material data [1], [17], [18], [19].

CONCLUSION

The various numerical methods were highlighted and constituents of blast were equally discussed. The numerical method that could be used for the study of the dynamic response of underground structures due to various blast scenarios was discussed. The numerical tool that could be used was also mentioned with focuses on finite difference incorporating finite element in the analysis, bulk viscosity, hourglassing, contact definition, impact analysis, deciding factors, etc. Finally, various applications of ABAQUS numerical tool with emphasis on ABAQUS/Explicit were extensively discussed.

ACKNOWLEDGEMENT

The financial supports provided by Ministry of Science Technology and Innovation, MOSTI, Malaysia under e-Science Grant no. 03-01-10-SF0042 (Universiti Malaysia Sabah, UMS, Kota Kinabalu, Sabah, Malaysia) is gratefully appreciated.

REFERENCES

[1] ABAQUS Inc. 2009. ABAQUS/Explicit: Advanced Topics, Dassault Systemes Simulia, Providence, Rhode Island, USA,

[2] ABAQUS Inc. 2009. ABAQUS Analysis User's Manuals - Documentation, Dassault Systemes Simulia, Providence, Rhode Island, USA,

[3] ABAQUS Inc. 2009. Geotechnical Modelling and Analysis with ABAQUS, Dassault Systemes Simulia, Providence, Rhode Island, USA.

[4] Autar Kaw and Eric Kalu, E. 2008. Numerical Methods with Applications

[5] Bowles, J. E. 1981. Engineering Properties of Soils and their Measurement (2nd edition), McGraw-Hill Intl., London, 79-92.

[6] George, P. K., George, D. B. and Charis, J. G. 2007. Analytical calculation of blast induced strains to buried pipelines. International Journal of Impact Engineering, 34, 1683-1704.

[7] Kameswara Rao, N. S. V. 2000. Dynamic Soil Tests and Applications (1st edition), Wheeler Publishing Co. Ltd., New Delhi, India, 6-30, 84-134, 164-177.

[8] Kameswara Rao, N.S.V. 1998. Vibration Analysis and Foundation Dynamics (1st edition), Wheeler Publishing Co. Ltd., New Delhi, India.

[9] Morton, K. W. and Mayers, D. F. 2005. Numerical Solution of Partial Differential Equations, An Introduction. Cambridge University Press.

[10] Olarewaju, A. J., 2015. Chapter 13: A Study on the Dynamic Dimensionless Behaviours of Underground Pipes Due to Blast Loads Using Finite Element Method, Book Title: "Earthquake Engineering – From Engineering Seismology to Optimal Seismic Design of Engineering Structures'' Abbas Moustafa (Ed.), ISBN: 978-953-51-2039-1, Geology and Geophysics, InTech Publisher, University Campus STeP Ri, Slavka Krautzeka 83/A 51000 Rijeka, Croatia, Europe, Published May 20, under CC BY 3.0 license, http://dx.doi.org/10.5772/59490, pp 331 - 356.

[11] Olarewaju, A.J. 2014. Estimation of Blast Loads for Studying the Dynamic Effects of Coefficient of Friction on Buried Pipes by Simulation, International Journal of GEOMATE, Scientific International Journal on Geotechnique, Construction Materials and Environment, Tsu city, Mie, Japan, ISSN 2186-2982 (P), 2186-2990 (O), September, (received on April 17), Vol. 7, No. 1 (SI No. 13), pp 1017-1024.

[12] Olarewaju, A.J. 2013. A Study on the Response of Underground Pipes Due to Blast Loads. Ph.D Thesis, School of Engineering and Information Technology, SKTM, Universiti Malaysia Sabah, Malaysia.

[13] Oliver Rübenkönig, 2006. The Finite Difference Method - An Introduction, Albert Ludwigs University of Freiburg.

[14] Robert, W.D. 2002. Geotechnical Earthquake Engineering Handbook, McGraw Hill, New York, pp 5-120.

[15] Unified Facilities Criteria. 2008. Structures to Resist the Effects of Accidental Explosions, UFC 3-340-02, Department of Defense, US Army Corps of Engineers, Naval Facilities Engineering Command, Air Force Civil Engineer Support Agency, United States of America.

[16] http://www.vibroflotation.com/Vibro/vibroflotation_fr.nsf/site/Design-and-Quality.The-Design

[17] Olarewaju, A. J. 2014. Investigation on the Effects of Ground Media on the Behaviour of Buried Pipes due to Blast Loads by Simulation, Advanced Materials Research (AMR), ISSN: 1662-8985, Advances in Applied Materials and Electronics Engineering III, Trans Tech Publications, Switzerland,doi:10.4028/www.scientific.net/AMR.905.273, Volume 905, pp 273 – 276.

[18] Olarewaju, A. J. 2012. Study on the Impact of Varying Degrees of Underground Accidental Explosions on Underground Pipes by Simulation, Earth Science Research (ESR) Journal, July 6, ISSN 1927-0542 (Print), ISSN 1927-0550 (Online), Volume 1, Number 2, Canadian Center of Science and Education, Canada, doi:10.5539/esr.v1n2p189 URL: http://dx.doi.org/10.5539/esr.v1n2p189, pp 189 -199.

[19] Olarewaju, A. J., Kameswara Rao, N.S.V and Mannan, M.A. 2012. Chapter 20: Response of Underground Pipes to Blast Loads, Book Title: " Earthquake-Resistant Structures - Design, Assessment and Rehabilitation", Abbas Moustafa (Ed.), ISBN: 978-953-51-0123-9, Geology and Geophysics, InTech Publisher, University Campus STeP Ri, Slavka Krautzeka 83/A 51000 Rijeka, Croatia, Europe, February, DOI: 10.5772/29101, pp 507 - 524,

First International Conference on Science, Engineering & Environment,
Tsu City, Mie, Japan, Nov.19-21, 2015, ISBN: 978-4-9905958-5-2 C3051

OPTIMIZATION OF LOCAL PARALLEL INDEX (LPI) IN PARALLEL/DISTRIBUTED DATABASE SYSTEMS

Mohamed CHAKRAOUI, Abderrafiaa ELKALAY
Faculty of Sciences and Techniques Gueliz, Cadi Ayyad University, Marrakech, Morocco.

ABSTRACT

The widespread growth of data has created many problems for businesses, such as delay requests; in this paper, we propose several methods of partitioning an index B*Tree in multi-processor machines in parallel/distributed database systems and collaboration between processors when executing multi-queries. Indexing a large database is an essential task; when optimizing, indexing automatically comes to mind; we distinguish two types of indexing: B*Tree and Bitmap. Since the advent of multicore computers (multi processors) parallelism becomes an indispensable part of optimization. Our work will focus on partitioning each table on three parts following indexing key partitioning; each processor will host a partition of the index, and the first processor that will finish will immediately take another partition of the index pending according to the priority.

The parallelism will reduce the CPU cost and execution time, and then collaboration between processors will further reduce these costs.

*Keywords: tuning; index; collaboration between processors; optimization; B*Tree; partitioning*

INTRODUCTION

Tuning databases is an essential task since the design phase to the maintenance phase of parallel/distributed database systems. When a request is sent to the RDBMS, it will be parsed and translated into RDBMS language, and then the RDBMS establishes several execution plans possible, then the DBMS optimizer chooses the most suitable one, and finally it runs the execution plan chosen. All RDBMS provide two types of optimizers: Rules Based Optimizer (RBO) and Cost Based Optimizer (CBO), all of actual RDBMS use the CBO[1]. The CBO is an optimizer that is based on the estimated costs of performing the operations execution plans. For a given query, the RDBMS creates several possible execution plans, and the RDBMS optimizer estimates for each one the cost performance and chooses the lowest.

Many solicited issues in this research field are about the efficiency, speed and reliability of database systems. Many papers have discussed optimization of databases; however, they still remain insufficient and could not get a top requested by the researcher community. Our paper comes in this context to a progressive thread, and provides a complete theme in parallel databases indexing, and supports it by yielded experimental results never been established. Asking specialists in this interesting discussion and provides a solid idea to RDBMS designers, and asking CPU designers to take into consideration the collaboration between processors when accessing the parallel databases with this method since the results are there.

To estimate the cost of an execution plan the RDBMS evaluates the cost of resources used to implement the plan following the priority:

CPU time.

The number of input / output (I/O) disk storage.

The amount of memory (Random Access Memory) required.

This cost depends not only on the query itself, but also on the data that it bears, for example. Given a table of 100 records, a single query can be rapid, but for a request of 1.000.000 records a simple query can be so slow and expensive (input/output disk and CPU utilization), so the cost depends on the data of the query and not only on the query itself; it's the reason why we resort to indexing.

Retrieval of data does cause serious problems when schemas and indexes are not created properly. However, inserting data can often causes serious performance issues as well[2].

With the arriving of big data and the development of automation technology, the data access increases exponentially, the primordial constraint is the time, response time increases too. To understand and decrease the real response time of our database system we have to sample in real time such equipment[3].

Our contribution in this manuscript can be listed as:

Parallelism is an excellent technique to reduce the execution time and optimize databases.

Multiple query execution time, partitioning every

query to three parts, and make a waiting line to every processor to accessing to each part.

Collaboration between processors is a new technique based on the parallelism and benefits from sleeping time of each processor.

Table 1 A part of the running table CLIENTS

NCLIENT	NAME	CITY	COUNTRY
1	Mohamed	Marrakech	Maroc
3	Hamid	Casa	Maroc
25	Khalid	Fes	Maroc
32	Salah	Casa	Maroc
39	Karim	Safi	Maroc
43	Houdi	Essaouira	Maroc
46	Jalal	Sfaqes	Tunisie
50	Charif	Casa	Maroc
55	Jamali	Agadir	Maroc
66	Gill	Doncaster	United
67	Will	Arizona	USA
70	Bernar	Munichen	Germany
76	Mak	Curitiba	Brazil
78	Bridge	PointeClaire	Canada
80	Fransis	Yamagata	Japan
81	Brolin	Rockford	USA
83	Clark	Linz	Australia
85	Favreau	Zagreb	Croatia
87	Phillippe	Lyon	France
88	Nakai	New Delhi	India
…	…	…	…

Index B*Tree:

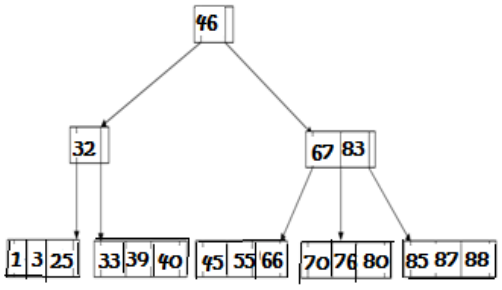

Fig. 1 Part of index B*Tree for the Table CLIENTS

RELATED WORK

The indexes in databases are like indexes in books; it addresses directly the desired information, without going through the whole book. Indexes are divided into two major types, Bitmap index and B*Tree index.

Several researches on different indexes and optimization of relational distributed databases are discussed before; DAVID Taniar[4] discussed B+Tree, SERGEY Bereg and all[5] discussed K-Tree, FM-Index[6], AR-Tree[7], R-Tree[8], and others. In addition, many studies have been optimized complex queries in distributed databases, and cloud computing using partitioned databases[9]. Following our investigations there is no approach like our, making the collaboration between processors in partitioned databases on multi-core and multiprocessors machine[10]. New database architecture based on batching queries and shared computation across many concurrent queries in a shared disk[10].

In B*Tree, internal nodes (non-leaf) can have a variable number of child nodes within some pre-defined ranges. When data are inserted or removed from a node, its number of child nodes changes. In order to maintain the pre-defined range, internal nodes may joined or split. Because a range of child nodes is permitted, B*Trees do not need re-balancing as frequently as other self-balancing search trees, but may waste some space, since nodes are not entirely full[11].

Each internal node of a B*Tree will contain a number of keys. Keys act as separation values, which divide its node. For example, if an internal node has three child nodes, then it must have two keys: a and b. All values in the leftmost node will be less than a; all values in the middle node will be between a and b; and all values in the rightmost node will be greater than b. usually, the number of pages is the fixed size capable of holding up to 2*k keys, but pages need only be partially replete.

These trees grow and contract; the nodes can split into brothers, or two brothers can merge or "concatenate" into a single node. The splitting and concatenation processes are initiated at the leaves only, and propagates them to the root. When the root node splits, a new root must be introduced, and this is the way in which the height of the tree can increase[12].

The opposite process occurs if the tree contracts.

Definition: We suppose h >= 0 an integer, k is a natural number. A directed tree T is in the class Z(k,h) of B*Trees if T is either empty (h=0) or has the following properties:

i) Each path from the root to any leaf has the same length h, also called the height of T, i.e., h = number of nodes in path.

ii) Each node except the root and the leaves have at least k + 1 son. The root is a leaf or has at least two sons.

iii) Each node has at most 2*k + 1 daughters[13].

OPTIMIZING INDEX

Our contribution in this paper is within the scope of parallel/distributed databases indexing, as this subject is not discussed since 2004[4]. Following an investigation into the business and technology services, we saw a dire

need in terms of tuning the search and update data. Several specialists in the design of database systems, fails index usages, strong reasons that push us to propose two strong methods about database optimization, and report to researchers that there are still things to do in the optimization of parallel/distributed database systems.

Indexes consist of one column or more, but store the data in a logically sorted manner to improve search performance. The same principle for a telephone book (a printed one). They are usually sorted by last_name, first_name or other criteria. This sorting makes it possible to find all entries for a specific last name quickly. If you know the first name too, you can even find the entries for the combination last name/first name very quickly…

For a large database, indexing in any RDBMS helps to retrieving and updating data records faster and more efficiently. For example, a simple SQL statement using indexing that helps to retrieve and sort data faster is shown below.

```
SELECT AVG (AGE) FROM CLIENTS
        GROUP BY CITY;
```

In the fact that the columns AGE and CITY are not indexed, the RDBMS will have to scan all rows for AGE, then, it do a full scan for the table CLIENTS to perform sorting GROUP BY CITY. If we have more than 1.000.000 records, it makes the selecting and sorting processes very slow. Since the index is always sorted, the DBMS does not need to search the entire table. Therefore, an index on AGE and CITY will speed up the process.

An index improves a lot of performances of queries, but it is associated with two types of costs: it takes up disk space, and takes time to maintain when the underlying data changes[1]. Space requirement for index is larger than the space needed to store the data.

With the advent of multi-core computers, it is essential to take advantage of these cores, so we appeal to the parallelism. This paper presents different database optimization techniques that can be employed for parallel/distributed processing. Our motivation to optimize parallel database/distributed systems is its importance on rapidity and reliability of information retrieval. Rapidity has become an important thing everywhere, so slow database applications become known as inefficient and inacceptable.

In the first time, we partition our table by range (attribute NoClient) into three parts, then we create and partition a local parallel index (attribute NoClient) into three parts too, then we attribute each part to one processor, and so on for each table that participate to related queries, then we collaborate between processors.

In the second time, we partition our tables by list into three parts and, then we create and partition our local parallel index into three parts by list too, and subsequently we always attribute each part to one processor, then we collaborate between processors.
The table 1 illustrates a simple table with four attributes client (noclient, name, city, country) like a testing example.

Finally, we compare between the results obtained by the two methods.
I would like to note that David Taniar discussed the Global Parallel index GPI[4]. However, our proposed method is a combination of new and old methods and technologies, our contribution improves the results already obtained, by changing these principles by ours, and GPI by local parallel index (LPI), and then we add a great optimizing method that consists on the collaboration between processors.

We use java 1.7 to programming our test application,

We use MySQL 5 and Oracle database 11g release 2 to execute our methods.

We use the MPJ (Message Passing Interface for java) to communicate between processors.

GLOBAL PARALLEL INDEX

Global Index is a tree structure that can be made in an attribute or more of number or varchar type and not lob or bfile. We can be partition it by range, by hash or by list, and it can be based on a partitioned or non-partitioned table.

Global Parallel Index (GPI)[14] can be partitioned indifferently with the underlying table; but the problem is harder to maintain when the based table is partitioned.

Our work focuses principally on the Local Parallel Index (LPI), and we take GPI as reference and we demonstrate improved results.

LOCAL PARALLEL INDEX

To discuss the parallel databases automatically we discuss table partitioning. Local Parallel Index (LPI) has the advantage that the index and the underlying table partition identically. In this paper, we propose two types of table partitioning. The first time is to partition our running tables as CLIENTS (NOCLIENT, NAME, CITY, COUNTRY) by RANGE into three parts and we suggest that we have a multiprocessors computer (3 processors or more). Then we create and partition our local index by range into 3 parts too, then we assign each partition to one processor to benefit from the

parallelization, and finally our processors have to work together I.e. The processor that finish its work gives help to the next and so on.

Global indexes may not be efficient for this type of query processing, because it causes correlations between the index and table partitioning, so accessing a specific value in a table may involve access to several or all of the index partitions; the same for the index involvement. Nevertheless, sometimes, we need a unique index, which does not include the partitioning key of the table; then we have no choice other than global index. Another reason why global index can be expensive is that when the data in an underlying table partition is moved or removed using a partition maintenance operation, all partitions of a global index are affected, and the index must be completely rebuilt. The shortcomings of a global index are addressed by local indexes.

Local indexes are the preferred indexes to use when a table is partitioned. A local index inherits its partitioning criteria from the underlying table. It has the same number of partitions, sub partitions; and the same partitions and sub partitions bounds as the underlying table, because the index is partitioned identically to the underlying table partitioning. Thus, when partitions are added, dropped, split, or merged in the underlying table, the corresponding index partitions are automatically modified by the RDBMS as part of the same statement. This makes maintenance of the local index extremely efficient, since the entire index does not need to be rebuilt, unlike a global index.

When partitioning the table by Hash, the hash table index uses the same hash function to arrange the RowIDs on different segments in ascendant order. The optimizer sends the value of each data to the hash function to build segments of data elements[15]. The following section presents our proposed methods briefly.

The figure 2 shows distributed partitioning queries, and how allowing every part to one processor, following the algorithm of allowing distributed queries to processors.

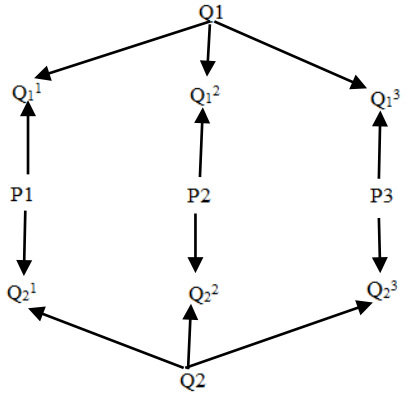

Fig. 2 Distributed partitioned queries

We partition Q1 to Q_1^1 Q_1^2 Q_1^3. P1, P2 and P3 are successively processor number one, processor number two and processor number three. The number n of distributed queries is Qn.

Algorithm1: allowing distributed queries to processors:

```
Sorting (Q1^n); // n =1, 2, 3
For i=1 until i=k; // k is the number of queries
    If (Qi^n is given); // n=1, 2, 3
    Then free Pn;
    Allow (Pn) to Qm; //m!=n and m=1, 2, 3
    When Qi^m is given;
Allow (Pn and Pm to Pl); // l !=m and l !=n and // l =1, 2, 3
When Qi^l is given
Return (Q1)
Free P1, P2 and P3
END
```

For multiple distributed join queries, we use the one-to-many algorithm, to assign each processor to one table (generally, we have at most a join of three tables).

Algorithm2: One-to-many

```
1 n: denote the number of tables
2 Ti: denotes the table number i
3 Pi: denotes the processor number i
4 If (n < 3) then
5    We assign each processor to one table
6 Else
7    Assign T1 to P1, T2 to P2, T3 to P3, then T4  8 to P1, T5 to P2 and T6 to P6 and so on.
9 END
```

First Partitioned Method

In this proposed method we will use all the last algorithms, partition our table into 3 parts by range and the index into 3 parts by range too; the attribute of index partitioning is the same of table partitioning attribute like GPI 1 [4]. In this case, the attribute of index is NoClient. Then we assign each part to one processor, following the availability; the range of NoClient(attribute partitioning) the sets from 1 to 40 is assigned to the processor number one following the availability, from 41 to 80 are assigned to processor two, more than 80 are assigned to processor three. The figure 3 illustrates the processors allocation following the first method. The processor has finished its part giving a helping hand to the next who has not yet finished.

To implement an LPI we must be careful. However, it is not difficult as the global parallel index (GPI); this is one of the strength points of the LPI. We explain that the root node is replicated to the processor 2 and not to all processors; the child node 32 and their children are not replicated to processor 2 but to the processor 1.

The child node 67, 70, 76 and 50, 55, 66 and 80, 81, 83 are replicated to the processor 2; the child node 80, 81, 83 is replicated to processor 3 too, because 81, 83 are replicated to processor 3 and 80 is replicated to both processor 2 and 3.

The node 85, 87, 88 is replicated to the processor number 3.

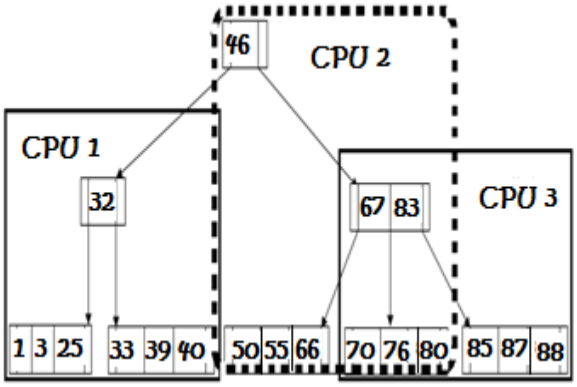

Fig. 3 LPI first method

Second Method

In this method we will use the same running table example called CLIENTS for simplicity and we will partition it into 3 parts by list (attribute country) like GPI 2[14]. The first partition takes Morocco and Tunisia following the table 2. The second takes United Kingdom, Germany, France, and Croatia as described on table 3. And the third partition takes the rest, the table 4 shows the n-uplets components of this part; we index and partition our table following the same attribute of table partitioning, then we assign each partition to one processor following the availability, and finally the processor that finish its work gives help to the next.

The LPI 2 is based on a Varchar2 attribute (NAME Varchar2 (30)), so this is different from the first method; the three lists partitioning (Morocco, Tunisia) and (United Kingdom, Germany, France, Croatia) and (USA, Brazil, Canada, Japan, Australia, India and others) gives the following results:

- The root node 46 is replicated to processor 1
- The Childs node (32) and (1,3,25) and (32, 39, 40) are replicated to processor 1
- The child node (50, 55, 66) is replicated to both of processor 1 and 2, because 50 and 60 are replicated to processor 1 and 66 is replicates to processor 2
- The child node (67, 70, 76) is replicated to both of processor 2 and 3, because 67 and 76 are replicated to 3 and 70 is replicated to processor 2
- The child node (85, 87, 88) is replicated to both of processor 2 and 3, because 85 and 87 are replicated to processor 2 and 88 is replicated to processor 3
- The child node (80, 81, 83) is replicated to processor 3

Table 2 Lines attributed to CPU1 on the second method

CPU1			
1	Mohamed	Marrakech	Morocco
3	Ali	Casa	Morocco
25	Khaled	Fas	Morocco
32	Salah	B. Mellal	Morocco
39	Karim	Safi	Morocco
43	Houdi	Essaouira	Morocco
46	Omar	Sfaqes	Tunisia
50	Charif	Tetouan	Morocco
55	Adam	Agadir	Morocco

Table 3 Lines attributed to CPU2 on the second method

CPU2			
66	Gill	Doncaster	U. Kingdom
70	Bernar	Munichen	Germany
85	Favreau	Zagreb	Croatia
87	Phillippe	Lyon	France

Table 4 Lines attributed to CPU3 on the second method

CPU3			
67	Will	Arizona	USA
76	Mak	Curitiba	Brazil
78	Bridge	Pointe	Canada
80	Fransis	Yamagata	Japan
81	Brolin	Rockford	USA
83	Clark	Linz	Australia
88	Nakai	New Delhi	India

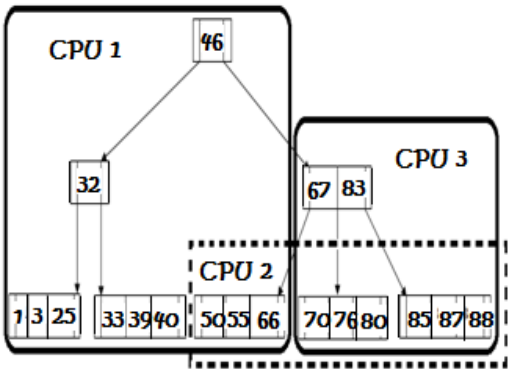

Fig. 4 Local parallel Index (LPI) schema Second method

competitor access

Concurrent access is among the real problems in the parallelization index, so we think of introducing this algorithm to arrange access to nodes replicated to two processors

Algorithm1: Node-Concurrent-Access

```
1  if (node is replicated to two processors: p1and p2)
2
3     prohibit (p2)
4     allow (p1)
5     if the operation is update
6        lock (node)
7        if (p1 has finished)
8           unlock (node)
9        end if
10    end if
11 end if
```

1. Maintenance Algorithm of Parallel B*Tree

Many methods of concurrent operations on B*Tree and B+Tree have been discussed by Bayer and Schkolnick, David Taniar and others. The solution given in the current paper has the advantage that we use B*Tree and we benefit of parallelism and **collaboration between processors**. In addition, no search through the tree is ever prevented from reading any node (locks only prevent multiple update access). These characteristics do not apply to the previous solution.

Node Insertion

Node insertion is one of the frequent operations applied to the B*Tree. Inserting an element can merge the node if it is full down, or collapsing it if it is full up. The figure 5, figure 6 and figure 7 bellow illustrate the steps for one case of node insertion:

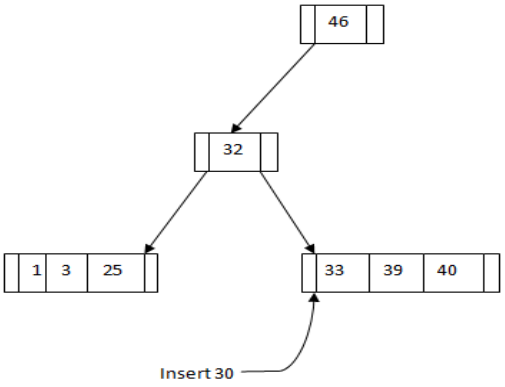

Fig. 5 Node insertion step 1

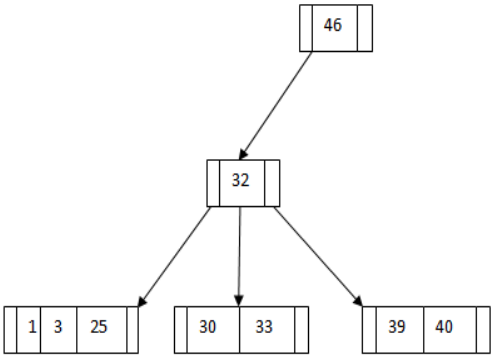

Fig. 6 Node insertion step 2

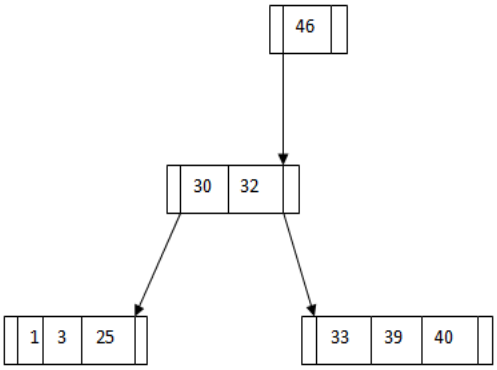

Fig. 7 Node insertion step 3

Node deletion

Node deletion also usually called.
The following schemas: figure 8, figure 9 and figure 10 describe the steps for one case of node deletion:

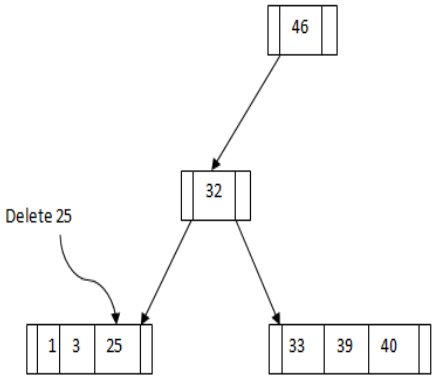

Fig. 8 Node deletion step 1

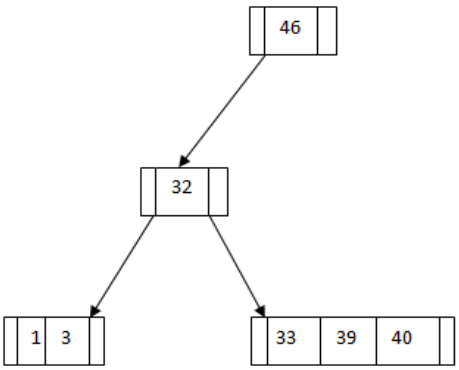

Fig. 9 Node deletion step 2

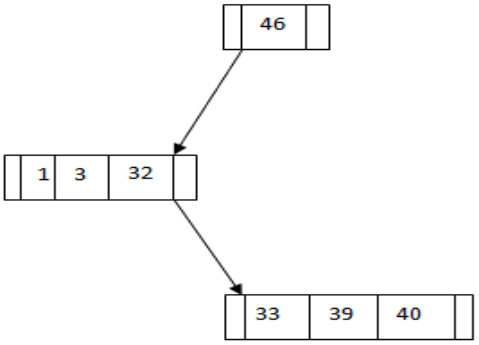

Fig. 10 Node deletion step 3

The following algorithm describes how processors work together:

Algorithm 2: collaboration between processors

1 (range varray)
2 Find the available processor or processors
3 Establish an array of number of size 3: the
4 numbers of the processors, and order it
5 following the availability of each one
6 Assign each range of index to one processor
7 following the order of array making in last step
8 If the processor that key i is finishing its work,
9 gives help to processor i+1 and so 10 on.

EXPERIMENTAL RESULTS AND ANALYSIS

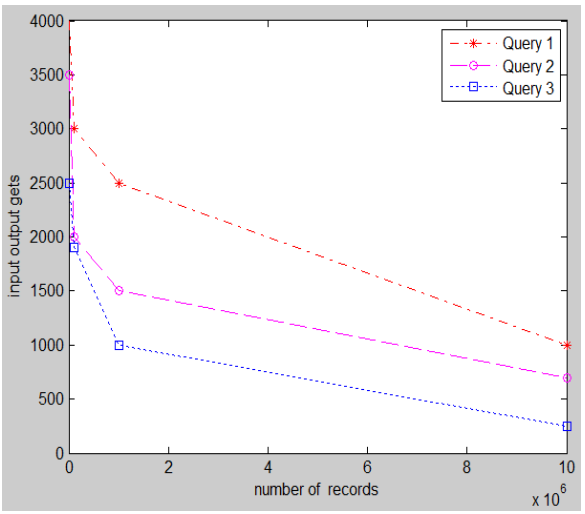

Fig. 11 Costs of different distributed queries for the first method

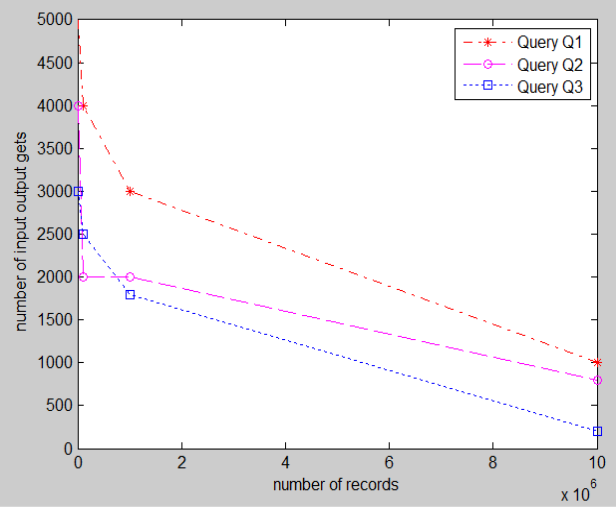

Fig. 12 Costs of different distributed queries for the second method

There are various methods of partitioning an index in parallel database systems, but in this paper, we discuss and improve two most powerful methods for the reason of avoiding redundancy in this current.

Existing analysis:

In shared-memory and shared-disk systems, the major problem for multi-processors machines is the interference between processors in both memory and disk. To reduce network traffic and to minimize latency, each processor is given a large private cache[16]. Parallelism increases performance, but shared resources increase interferences and limit performances. Multi-processor computers often use many processes to reduce interferences. Partitioning a shared-memory system creates many interferences and problems; we find that the performance of shared memory machines is not cost-effective with some processors when running database systems. The shared-disk architecture is not very effective for database systems. the processor that want to update the data must declare its intention to update the data, once this declaration has been honored and acknowledged by all the other processors, the declared processor can read the shared data from disk and update it. This creates interferences between processors, and then creates delays.

Multiple query analysis:

When we launch a multiple query in parallel search processing, generally it proceeds three steps: processors involvement, index scan, and record (data) loading[4] for everyone. In the first step, the RDBMS finds the processor or processors selected by the algorithm of collaboration between processors. In tree traversal, we can localize the record in each processor following the range of the tree or list of name and of course the method used.

The three major methods of access to tables are as following. The first is Full Table Scan, when the table is parsed entirely following the order of blocs in the tablespaces. Secondly, the PARTITION methods made when the query is performed on a partition of table and not on the table entirely, in this case the table must be partitioned. Moreover, if the optimizer does not accept the PARTITION method, we can force it through the HINT. Finally, the third method is the Table Access by RowID, this method allows the access directly of the RowID in this case the query is based on an index.

Then let us analyze the three major index access methods, UNIQUE SCAN, RANGE SCAN and PARTITION SCAN. Regarding UNIQUE SCAN, the optimizer chooses to parse the tree to find a unique record, generally used for the type of query whose the clause where is an equal like NoClient= 234. For RANGE SCAN, the optimizer parses a part of the tree that host the range searched often used for the type of query of the clause where is an interval like NoClient between 2.000 and 3.000;. And thirdly, the PARTITION SCAN is used by index accessing if the index is partitioned, this method allows the optimizer to parse just the partition of index that host the key or the range of keys on the clause where of the query.

Finally, we cite the three major methods of performing the join operations. The first is NESTED LOOP; we suggest that we have two tables. CLIENTS table and COMMANDES table. CLIENTS is 10 times bigger than COMMANDES. The NESTED LOOP parses COMMANDES entirely for each data of the table CIENTS, generally used for the sub-query. MERGE JOIN, in this case we use the same tables but we suggest that the sizes of them are approximately close, then we sort both of them following the same criteria for simplify the data search. The third method is the HASH JOIN that we construct a hash table following the index key, and then we parse the second table for each value of column join in the hash table.

Algorithms analysis:

Based on Table 1, Figure 3 and Figure 4, the first method is more accepted as an optimized method than the second method. Following the Figure 4 that illustrates the second method, we find more correlation between processors, since only selected processors are used, and tree traversal and record loading are locally done. In parallel searching, we search single values (for exact match) or several values (for range search). In this type of query, both of the local parallel index first method and second method are efficient but the most optimized is the local parallel index first method, because there are no correlation between processors.

Which means only selected processors by the algorithm are used (implicated), and data loading are locally done.

When we launch a query in parallel one-index join processing, we search on the indexed table by the attribute of the index, and the record loading is pointed by the RowID. The problem in this processing (one-index join) is that we search each record on the non-indexed attribute (on non-indexed table) this takes a lot of input/output on blocs, which takes a lot of memory. These constraints increase the execution time. In parallel one-index join, we search single values (for exact match) or several values (for range search) from the indexed table and we search for all values of join attribute from the non-indexed table. This processing is not efficient for big tables (table that contains more than 10.000 tuples, but not indexed). In this processing, both parts of the local parallel index are not efficient, but the most wished one is the local parallel index used at the first method, because it bears on the same attribute that uses the join operation in the indexed table.

About parallel two-index join processing, we search single values (for exact match) or several values (for range search) from the first table then the same processing from the second table, and finally we compare the results done according to the predicate of join operation. If the tables involved in the join operation contain more than 10.000 n-uplets, this processing is preferred; else, if one of them is small, this processing is not efficient. In this case the local parallel index first method is the most suitable because the parallel index is based on the same attribute of the index join attribute[4].

CONCLUSION AND FUTURE WORK

In this paper, we have presented in first time two algorithms of tuning parallel databases. The first is based on partitioning our table and create and partitioning a local parallel index by range. Moreover, the second method is based on partitioning both of them by list. In both of these methods, we assign each part of one processor. The first part is assigned for the processor number one. The second part is assigned for the processor number two, and the third part is assigned for the processor number three. Finally, the processor that finished its work giving a helping hand to the processor that not yet finished (collaboration between processors). Following the figures 11 and 12, we are in favor of the first method (partitioning by range) and their algorithms as the most optimized algorithm.

In a second time, we have discussed (presented) three of major methods of query optimization. No-replicated-index, partially-replicated-index and fully-replicated-index [14]; all of them are used with the parallelization and collaboration between processors. We used each of these three methods separately with our proposed methods, for eventually find the most optimal result, according to the results obtained is the third method (fully replicated index). Throughout this paper, we discuss the local parallel index, thanks to these advantages like the absence of correlations between the index and table partitioning, contrariwise the global parallel index.

For our future work, we will plan to implement the collaboration between procesors in the background of a DBMS like postgreSQL.

REFERENCES

1. Navarro, L., *Optimisation des Bases de Donnees.* Pearson, 2010.
2. Flora S. Tsai, A.T.K., *Database optimization for novelty mining of business blogs.* Expert Systems with Applications, 2011.
3. Xianhui Li, C.R., Menglong Yue, *A Distributed Real-time Database Index Algorithm Based on B+ Tree and Consistent Hashing.* ELSEVIER, 2011.
4. David Taniar, J.W.R., *Global parallel index for multi-processors database systems.* elsevier, 2004.
5. Sergey Berega, H., *Wiener indices of balanced binary trees.* Discrete Applied Mathematics, 2007.
6. Alejandro Chacon, J.C.M., Antonio Espinosa, Porfidio Hernandez, *n-step FM-Index for faster pattern matching.* Procedia Computer Science, 2013.
7. HaRim Jung, Y.S.K., Yon Dohn Chung, *QR-tree: An efficient and scalable method for evaluation of continuous range queries.* Information Sciences, 2014.
8. Yunjun Gao, Q.L., Baihua Zheng, Gang Chen, *On efficient reverse skyline query processing.* Expert Systems with Applications, 2014.
9. Tansel Dokeroglu, M.A.B., Ahmet Cosar, *Robust heuristic algorithms for exploiting the common tasks ofrelational cloud database queries.* Applied Soft Computing, 2015.
10. G. Giannikis, G.A., D.Kossmann, SharedDB, *SharedDB: killing one thousand queries with one stone,.* Proc. VLDB, 2012. **Vol. 5, no. 6**.
11. R. Bayer, M.S., *Concurrency of Operations on B-Trees.* Acta Informatica, 1977.
12. Lilian Hobbs, S.H., Shilpa Lawande, Pete Smith, *Oracle_10g_Data_Warehousing.* Elsevier Digital Press, 2005.
13. R. Bayer, E.M., *Organization and Maintenance of Large Ordered Indexes.* Acta Informatica, 1972.

14. DAVID TANIAR, J.W.R., *A Taxonomy of Indexing Schemes for Parallel Database Systems.* Distributed and Parallel Databases, 2002.
15. Xiaoqing Niu , X.J., Jing Han, Haihong E, and Xiaosu Zhan, *A Cache-Sensitive Hash Indexing Structure for Main Memory Database.* Springer, 2013.
16. David J. DeWitt, J.G., *Parallel Database Systems: The Future of Database Processing or a Passing Fad?* 1991.

First International Conference on Science, Engineering & Environment,
Tsu City, Mie, Japan, Nov.19-21, 2015, ISBN: 978-4-9905958-5-2 C3051

THE TECHNIQUE OF OPTIMAL LEASING DURATION ESTIMATION FOR THE CITY BUS USING THECHNICAL AND ECONOMICAL PARAMETERS

Nikita Pozhivilov [1], Ilya Kavalchuk[2], Victor Maksimov[1], Lev Zimanov[1]

[1]State Technical University -MADI, Moscow, Russian Federation
[2]School of Engineering, Deakin University, Australia

ABSTRACT

A transit agency has a lot of ways to get buses. The most convenient is lease. There is no need to pay a whole price once, a company has to pay every month fix amount of money and use buses at the same time. But a manager of a transit agency should decide for a period of time, when they will need to use the busses.

This paper presents the technique for determining duration of the city bus lease, taking into account the influence of technical and economical parameters. The bus must bring maximum profit and bus garage must make a transportation work full and with good quality for passenger satisfaction.

The technique is applied to a real-world case study of transit agency in Moscow, Russian Federation which operates Iveco Daily, also detailed analysis of the results is presented.

This study can be used for the impact of the fleet management program of the subsequent years for the replacement of aging fleet by transit agency, can help to manage fleet of a transit agency to improve transportation service and clients satisfaction.

Keywords: Bus, Engineering Management, Lease Duration, Passenger Traffic, Transit Agency.

INTRODUCTION

Transportation by the public bus system is one of the biggest forms of passenger traffic in cities throughout the world. Russian transportation market studies showed that vehicle transportation has 59.0% of the share [1], [2]. In terms of the types of passenger transportation, in 2013 regular buses had a transportation market share of 58.4% for intra-urban, 75.1% for suburban and 63.3% for intercity transportation [1]. High demand initiate business competition among the transit agencies for costumer attention and route allocation.

From an economical point of view the main aim of transit fleet management is to maximal profit. The quality of their services is another challenge as it has influence on the customer satisfaction rates. The most flexible way to start using buses for a company is by getting their fleet through a lease scheme [2], [3]. A lease is a contractual arrangement calling for the lessee (user) to pay the lessor (owner) for use of an asset [3]. There is no need to pay the full price outright, because lessee pays a fixed price per month over time duration according to the leasing contract agreement.

The determination of an optimal lease period for a bus needs to be analysed using both technical and economical groups of parameters for the whole period of the lease.

The proposed optimization model was targeted on maximizing the net present profit with the constraint of the minimization of the average remaining life of buses in a transit agency. It has a direct influence on the servicing costs and customer satisfaction.

A number of studies explored these questions. The advantages and disadvantages of bus lease as a purchasing method have been covered in [4], [5]. The main advantage is that leasing allows companies to make renovations of the fleet in a shorter period of time. However, payments are made on a monthly bases, reduces the financial load on the company. Another advantage is the wide range of available lease programs. Some of them are based on the time duration, as a payment factor, and called fixed-term tenancy. Such schemes have defined beginning date and defined ending date. Others programs are based on the operating duration in years or kilometres. The later leasing programs are beneficial for companies with seasonal or small workload.

Leasing with fixed-term tenancy was applied in the methodology. A fixed term tenancy comes to an end automatically when the fixed term runs out. At the end of the lease duration busses goes back to the lessor. [6]

Lifetime of the vehicles affects the average age of the fleet. [7] The average age of the fleet affects the performance indicators and resource requirements, such as servicing cost, demand for the labour and spare parts [8]. As costs have direct input

on the profitability of the company, its minimization can be a problem for the managers.

THEORETICAL INVESTIGATION

There are two sets of parameters which have influence on the optimal leasing period selection. One set is Economical parameters. Such parameters cover financial aspects such as income and costs. The second group of parameters are the technical parameters.

Influence of Economical Parameters

During its lifetime, a bus fleet should show continuous profitability. Several parameters have influence on the profit of a company. Dependency can be determine using (1) [11]:

$$C = I - (C_{fuel} + C_{leas.} + C_{parts} + C_{salar.} + C_{plandef.} + C_{rent} + C_{outsour.} + C_{issue} + C_{fail.} + C_{other}) \quad (1)$$

Where I - income; C_{fuel} - fuel costs; C_{lease} –lease payments costs; C_{parts}. – spare parts costs; $C_{salar.}$– salary costs; C_{rent} - rental payment; $C_{plandef.}$– plan default; $C_{outsour.}$ – outsourcing costs; C_{idle} – amount of income loss because of the idle; $C_{fail.}$– technical failure costs; C_{other}– others costs.

Formula for the general profit calculation:

$$C=I - (TFC+TVC) \quad (2)$$

I – income from the unit of the fleet for exact age/mileage; TFC - time-fixed costs (not depends on bus age); TVC - time-variable costs (depends on bus age).

The typical structure of income from unit at exact age/mileage in a transit agency is showed on Fig. 1. [12].

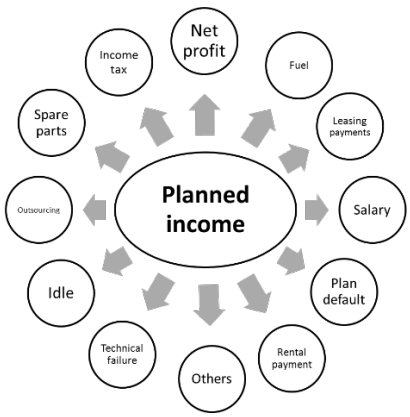

Fig. 1 Structure of the planned income from a fleet unit of a certain age/mileage.

When bus economical parameters are analysed, it is possible to construct a bus economical parameters graph Fig. 2. [12]. If statistic data is not enough to construct full graph, then it is necessary to predict the rest of graph using various mathematical modelling methods.

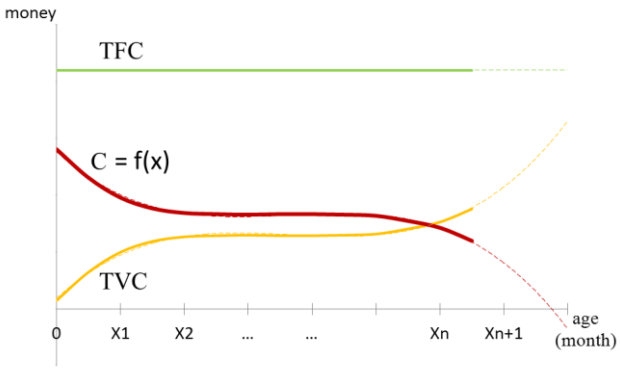

Fig. 2 Example of the dynamic of bus economical parameters

Influence of Technical Parameters

Changes of technical parameters according to increasing age and mileage of buses create a negative effect on the bus operational characteristics, which reduce the transportation service quality [8], [12].

The technique implies to analyse the changes of technical parameters for the full fleet or for a group of buses from the specific transportation route with the average fleet age.

Several technical factors can be identified for the leased fleet technical analysis. Factor X_1 takes into account the percentage of buses on the route. Factor X_2 takes into account a number of extraordinary returns to the garage or service station. Factor X_3 takes into account a number road accidents. Factor X_4 takes into account a number of working posts in a service zone of the bus garage. Factor X_5 takes into account total maintenance and repair downtime.

In this article one parameter was selected. It shows the influence of the fleet medium age on coefficient of buses on the routes. It can be calculated using (3) [12]:

$$\boldsymbol{X_1} = \frac{\alpha_{br}^{F}}{\alpha_{br}^{P}} \quad (3)$$

Where α_{br}^{F} is an actual percentage of buses on the route; α_{br}^{P} is planned percentage of buses on the route. Factor X_1 has to be not less 1 for any period of bus lease duration to provide maximum income and quality.

Planned percentage of buses on the route is

calculated based on the schedule of the passenger's traffic. Actual percentage of the buses on a given route is evaluated using (4):

$$\alpha_{br} = \alpha_{\mathrm{T}} - \alpha_r \quad (4)$$

Where α_{T} is a coefficient of the fleet technical readiness; α_r is the percentage of buses in reserve.

The coefficient of technical readiness can be calculated with formula (5) [12]:

$$\alpha_T = \frac{1}{1+l_d \cdot \frac{D_{main}}{1000} \cdot K_2} \quad (5)$$

Where l_d is an average daily mileage of the bus in a transit agency; D_{main} is the time needed for bus repair and maintenance in a service zone measured in days/1000 kilometres; K_2 is a coefficient of vehicle type and modification. For buses K_2 is equal to 1.

The time needed for bus repair and maintenance in a service zone can be evaluated by (6) [9]:

$$\boldsymbol{D_{main} = D_{main}^{norm} \cdot K'_4} \quad (6)$$

D_{main}^{norm} is a normative parameter for repairs and maintenance time in a service zone (days/1000 kilometres), see Table 1. K_4` is a correction coefficient of repairs and maintenance time in bus garage. It depends on mileage, see Table 1.

Table 1 Normative parameter for repairs and maintenance time in a service zone

Buses types	Spending time at repairs and maintenance (days/1000 kilometres), D_{main}^{norm}
Extra small, small and middle	0.30-0.50
Large and extra large	0.50-0.55

Table 2 Correction coefficient values of repairs and maintenance time in bus garage

Mileage from the beginning of operation in fractions of a normative resource mileage	**K'$_4$**
from 0,25	0,7
from 0,25 to 0,50	0,7
» 0,50 » 0,75	1,0
» 0,75 » 1,00	1,3
» 1,00 » 1,25	1,4
» 1,25 » 1,50	1,4
» 1,50 » 1,75	1,4
» 1,75 » 2,00	1,4
from 2,00	1,4

Coefficient of the percentage of reserved buses is evaluated according to results of a transit agency works and can be calculated by the (7) [12]:

$$\alpha_r = \alpha_{br} \cdot P_C, \quad (7)$$

Where P_C is an average percentage of buses which cannot finish work on a given route and come back to bus garage.

The Determination of Bus Lease Optimum Period

The company should choose the strategy of purchase, relationship with lessor and predict the economic situation of the market before determining the optimum duration of the lease [4].

There are two main strategies to determine the optimum duration of bus lease and can be identified as:

- Maximization of the accumulated profit;
- Maximization of the average profit per bus.

The result is limited by the main technical parameters that can be controlled through the changes of the fleet's technical characteristics.

Maximization of the accumulated profit

This strategy is suited to a lease contract with the maximum economical profit accumulation that is to say to make settlements the duration of leasing, which bring maximum profits from whole vehicle service life.

To do that we should calculate the profit accumulation for a buses lifetime.

The objective function for this method is Z_x (profit). It can be calculated using (8):

$$Z_x = \int_{x_0}^{x_l} [I(x) - TFC(x) - TVC(x)]dx \rightarrow max \quad (8)$$

Where x_0 is the age of buses which were selected for the leasing contract; x_l is the age when bus goes back to lessor.

The meanings of x_0 and x_l are the points of time frames for the bus lease period. In (9) they can be submitted as number of months, mileage of a bus or interval numbers. It is easier to get statistical data of a bus and agency work for interval which contains months or mileage. Intervals are more convenient

because collection of statistical data is easier and more demonstrative.

Maximization of the average profit per bus

This strategy can be used when a transit agency and lessor have good, reliable relationships or they are parts of the same company. In this case transit agency can sign flexible contracts every year or month.

The technique proposes to calculate the average profit per whole life of a bus for different life times of it.

The objective function is Z_x(profit), which can be calculated using (9).

$$Z_x = \frac{\int_{x_0}^{x_l}[I(x)-TFC(x)-TVC(x)]dx}{x} \to max \quad (9)$$

All technical limitations has to be taken into consideration, which allow to improve quality, safety and convenience of the transportation. Technical constraints can be selected as (10)-(14):

$$\begin{cases} X_1 = \frac{a_{br}^F}{a_{br}^P} \geq 1 & (10) \\ X_2 = \frac{a_{returns}^F}{a_{returns}^P} \leq 1 & (11) \\ X_3 = \frac{a_{accident}^F}{a_{accident}^P} \leq 1 & (12) \\ X_4 = \frac{a_{post}^F}{a_{post}^P} \geq 1 & (13) \\ X_5 = \frac{a_{downtime}^F}{a_{downtime}^P} \leq 1 & (14) \end{cases}$$

CASE STUDY

Information about a Transit Agency

Proposed technique was examined on a company which provides regular passenger transportation in Moscow, The Company has its own technical department and obtains buses on lease. The Company's staff have fixed salary rates. Some aspects of the technical work (maintenance, repair etc.) are being done by outsourcing companies. All buses work according to a time schedule.

Some information about the transit agency:

The number of company working days: 365;

The average daily mileage of one bus: 260 km;

The average annual mileage of bus: 94000 km;

The average specific planned income from 1 working hour of one bus: 650 Rubles;

The fare for passengers – 30 Rubles.

Total number of fleet – 92 Iveco Daily;

Average bus mileage in the agency – 420000 km;

The total planned percentage of buses on the route of the whole transit agency is 79.0%.

Leasing conditions are highlighted in Table 3. Rates for the down payment are 0.

Table 3 Lease rates according to lease duration of bus Iveco Daily by lessor

№	Lease duration (months)	Lease rates per month (th. dollars)	The total amount for the whole duration (th. dollars)
1	33	1.33	43.89
2	36	1.24	44.64
3	39	1.21	47.19
4	42	1.18	49.56
5	45	1.14	51.30
6	48	1.10	52.80
7	52	1.05	54.60
8	56	1.04	58.24

The structure of planned income from Iveco Daily in the selected transit agency is represented on the Fig. 3.

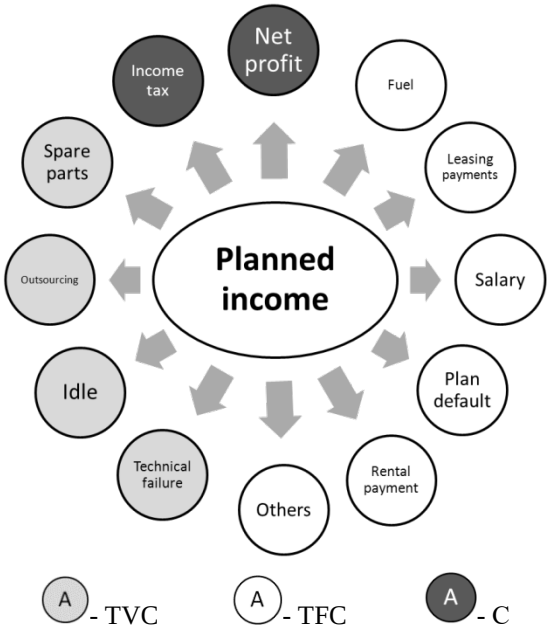

Fig. 3 The structure of planned income from Iveco Daily in the transit agency

Initial conditions are: the transit agency is going to get 20 buses Iveco Daily. In this paper we will choose the best lease duration from the next periods: 33, 36, 39, 42, 45, 48, 52 or 56 months.

The economical, technical and operational data were obtained from the transit agency and statistical

data were collected as a result of the experiment with 10 buses Iveco Daily. These 10 buses were operated in the transit agency for 3 years.

Application of Method

The objective function

Two functions were selected for analysis and calculated in (15) and (16).

Maximization of the accumulated profit:

$$Z_x = \int_{x_0}^{x_l}[I(x) - (TFC + TVC(x))]dx = \int_{x_0}^{x_l}\big[I - (C_{fuel} + C_{leas.} + C_{parts}(x) + C_{salar.} + C_{plandef.} + C_{rent} + C_{outsour.}(x) + C_{issue}(x) + C_{fail.}(x) + C_{other})\big]dx \rightarrow max \quad (15)$$

Maximization of the average profit per bus:

$$Z_x = \frac{\int_{x_0}^{x_l}[I(x) - (TFC(x) + TVC(x))]dx}{x} = \Big(\int_{x_0}^{x_1}\big[I - (C_{fuel} + C_{leas.} + C_{parts}(x) + C_{salar.} + C_{plandef.} + C_{rent} + C_{outsour.}(x) + C_{issue}(x) + C_{fail.}(x) + C_{other})\big]dx\Big)/x \rightarrow max \quad (16)$$

Constraints

In the article one constraint X_1 was examined. Results of the X_1 calculations are shown in Table 4. The total profits per period/months are showed in Table 4 as well.

Table 4 Result of different lease duration of bus in the transit agency

№	Lease duration, months	Profits, th. dollars		Constraints	
		Maximization of the accumulated profit	Maximization of the average profit per bus	a^F_{issue}, %	$X_1 \geq 1$
1	33	27.44	0.83	**79.1**	+
2	36	32.08	0.89	**79.1**	+
3	39	35.12	0.90	**79.1**	+
4	42	38.04	0.91	**79.1**	+
5	45	41.12	**0.91**	78.5	-
6	48	43.90	**0.91**	78.5	-
7	52	**46.70**	0.90	78.5	-
8	56	46.36	0.83	78.5	-

The best lease duration is 52 months for maximization of the accumulated profit and 45 or 48 months for maximization of the average profit per bus. But factor X_1 is admissible for lease duration of 42 month or less, because the total planned percentage of buses on the route should be more than 79.0 %.

42 month is the best duration to take a bus or group of buses on lease for the transit agency to satisfy both technical and economic factors. The technical analysis showed that technical factor X_1 is in the acceptable interval, so the company will be able to make service in full volume.

CONCLUSION

Using buses start from purchasing or signing of the leasing contract. Leasing is the most convenient way for business today. In this study a new model to address long-term planning was proposed. The technique proposed in this paper is the result of continuing research on the topic of optimization of transit fleet management over a planning period.

The methodology allows us to solve important problems for an optimum leasing duration of buses in a transit agency. It allows for an increase in company profits, revenue, return of investments, and internal rate of return, cost effectiveness; makes a forecast of the short and long-term future of the company, improvement of service quality, makes the management of a fleet easier and more predictable. All this can not only save current costumers, but also increase the number of customers. Minimization of costs allows to evaluate the level of service, planned budget allocation, significant resource savings, and more effective age management.

The technique was applied for the medium duty buses which operates in Moscow. However, the methodology can be applied to other agencies with different fleet types, budget size or structure of planned income.

ACKNOWLEDGEMENTS

Publication was sponsored by Deakin University, Australia. The research was partially supported by State Technical University - MADI. The authors would like to express their sincere appreciation to rector MADI, Doctor of Science, Vjacheslav Prikhodko; Associate Professor MADI Victor Egorov; coordinator learning, Mercedes-Benz Russia Maria Zhelyabina, Master Vasilisa Pozhivilova.

REFERENCES

[1] Rosstat, «Transport and communications in Russia 2014,» Federalnaya slujba gosudarstvennoi statistiki, Moscow, 2014 (rus).

[2] V. Dobrovolskii, "Leasing as a mechanism for updating the bus fleet," Transport Rossiiskoi Federacii, no. №2(33), pp. 30-31, 2011 (rus).

[3] Stickney and Weil (Glossary of Financial Accounting: An Intro. to Concepts, Methods, and Use 12e), 2007, p. 791.
[4] F. Wegmann and T. Newsom, "Accomplishments of an innovative statewide van lease and purchase program," in Proceedings of the 2003 Mid-Continent Transportation Research Symposium, Iowa, Iowa State University, 2003.
[5] C. Wolski, "Making the Decision: Owning or Leasing," May 2011. [Online]. Available: http://www.fleetfinancials.com/article/story/2013/07/making-the-decision-owning-or-leasing/page/2.aspx. [Accessed 27 April 2015].
[6] "Accounting for leases," 17 November 2014. [Online].Available:http://www.accaglobal.com/sg/en/student/acca-qual-student-journey/qual-resource/acca-qualification/f7/technical-articles/accounting-for-leases.html. [Accessed 20 April 2015].
[7] U. Dutta and T. Maze, "Model for Comparing Performance of Various Transit Maintenance Repair Policies," Journal of Transportation Engineering, no. 115(4), pp. 450-456, 1989.
[8] E. Kuznetsov, A. Boldin, V. Vlasov and et al., Vehicle technical maintenance: textbook for high schools, 4th ed., Moscow: Science, 2004, p. 535(rus).
[9] Regulations on the maintenance and repair of rolling stock automobile transport, Moscow: Ministry of automobile transport Russian Federation, Transport, 1988, p. 72 (rus).
[10] S. Mishra, S. Sharma, S. Khasnabis and T. Mathew, "Preserving an aging transit fleet: an optimal resource allocation perspective based on service life and constrained budget," 5. Mishra S., Sharma S., Khasnabis S., Mathew T.V. 2013 Preserving an aging Transportation research part A, no. 47, pp. 111-123, 2013.
[11] N. Pozhivilov and L. Zimanov, "Determine the optimal strategy of the lease term bus very small class with the technical and economic performance of the transit agency," in Problemi tehnicheskoi ekspluatacii i avtoservisa podvijnogo sostava avtomobilnogo transporta_ sb. nauch. tr., Moscow, 2015 (rus).
[12] N. Pozhivilov, "Influence of technical and economic parameters for service life of the city bus very small class which purchase on lease," Avtotransportnoe predpriyatie, no. №11, pp. 52-55, November 2014 (rus).

First International Conference on Science, Engineering & Environment,
Tsu City, Mie, Japan, Nov.19-21, 2015, ISBN: 978-4-9905958-5-2 C3051

SETTLEMENT OF STRIP FOOTING ON SANDY SOIL DUE TO ECCENTRICTY

Kraker Saber Braim[1], Syarifah Nur Atiqah Syed Ahmad[2], Ahmad Safuan A Rashid[3], Hisham Mohamad[4]
[1,2,3,4] Department of Geotechnics and Transportation, Faculty of Civil Engineering, Universiti Teknologi Malaysia

ABSTRACT

This study investigates the effect of eccentricity on settlement of shallow foundation rested on sandy soil. A series of small-scale 1*g* physical modeling tests was carried out by preparing a model of medium dry sand with 50% of relative density on a rigid testing chamber. A rigid plate was used to replicate a strip footing foundation. Close range photogrammetry and particle image velocimetry (PIV) methods were used to examine the failure mechanisms under the eccentricity design load. In this study, the ultimate, allowable bearing capacity and bearing capacity factor (N_γ) under the eccentricity loading were investigated. It was found that with the increasing of footing eccentricity, the bearing capacity decreased with increasing settlement

Keywords: *shallow foundation, settlement, eccentricity, particle image velocimetry (PIV).*

INTRODUCTION

The function of a shallow foundation is to transmit load from the superstructure to the supporting soils. In some cases, the footing carry eccentric or moment load subjected from the eccentricity of vertical load from the column or by horizontal load acting at some distance above the foundation base. These loads may be permanent (retaining wall) or temporary (wind or seismic load). Many studies have been conducted to investigate the performance of a shallow foundation on sandy soils [1-9].

However, most of the studies were carried to investigate the geometry shape of shallow foundation rested on a sandy soil. Limited study was conducted to examine the influence of the eccentricity load on this particular soil [10-11]. Although El Sawwaf, [11] performed a study on the effect of eccentricity on the bearing capacity of sandy soil, however he intended to investigate the used of the geogrid layer as an improvement method to enhance the stability of the sandy soil under the eccentricity load. He found that the footing performance could be significantly improved by the used of layers of geogrid leading to an economic design of the footing.

Thus, this study attempts to investigate the effect of eccentricity on settlement of shallow foundation rested on sandy soil. A series of small scale physical modeling was carried out to study settlement behavior. The deformation was observed using a close range photogrammetry and Particle Image Velocimetry techniques [12].

EXPERIMENTAL SYSTEM

A 200 mm height of sand model was prepared in a rigid aluminum testing chamber with a dimension of 320 mm in height x 150 mm in width x 430 mm in depth. The front side of the box was fitted with a removable transparent Perspex panel to allow a real time observation on soil movements during the loading test as shown in Fig. 1. Sand model with 50% of relative density index was prepared to represent a medium dense sandy soil by using a compaction method. A rigid plate of 60 mm in width, B and 150 mm in length, L was used to replicate a strip foundation. 3 holes with a diameter of 3 mm were fabricated at the top of the rigid plate. Each of the holes were located at the centre, 0.05 B and 0.1 B from the centre with respect to the width of the footing. Due to the sand has a uniform white colour, an additive black colour was used to colour the ¼ of the total weight of soil by using dyed black solution. The technique was used in order to enhance the difference of brightness intensity during the image analysis using the PIV.

A strain control system with a variable speed AC motor and worm gear configuration was used to provide strain loading system during the testing. The used of the strain loading system is to determine the ultimate bearing capacity of the sandy soil. A dead loading system was used to investigate the settlement of the strip footing by applying an equivalent stress of the ultimate and allowable bearing capacities for both centric and eccentric cases as shown in Fig. 2. The stresses and displacements were recorded using a load cell and Linear Variable Differential Transformer (LVDT) transducers. A digital camera was employed and mounted in front of the Perspex panel to capture the soil movements in continuous shooting mode during the testing so that the failure pattern could be observed with the aid of the Matlab software. A set of target markers was used to calibrate the camera movement during the shooting period.

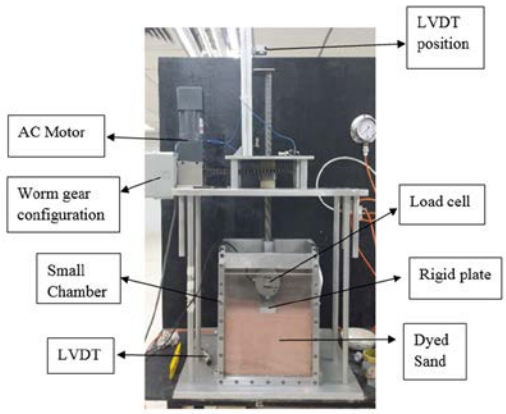

Fig. 1: Experimental setup using a strain control system

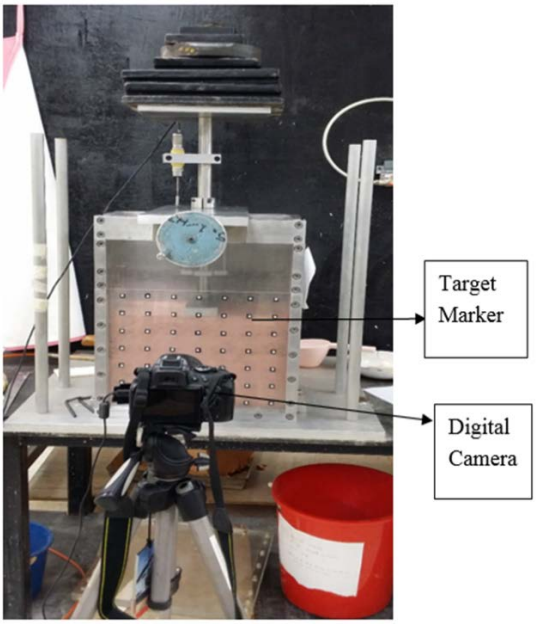

Figure 2: Dead loading system

TESTING MATERIAL

The result of physical property of sand is listed in Table 1. The particle size distribution test was determined by using a dry sieving method and the result is shown in Fig. 3. The sample was classified as Well Graded sand (SW). Relative density test was carried out and the 50% of density of sand was determined at 16.53 kN/m^3. The angle of internal friction and the modulus of elasticity of sand were determined from the Shear box test.

Table 1: Physical property of sandy soil

Property	Value
Specific gravity, G_s	2.65
Maximum dry unit weight, $\gamma_{dry\ (max)}$, kN/m^3	18.39
Minimum dry unit weight, $\gamma_{dry\ (min)}$, kN/m^3	15.01
Relative Index, I_D	50%
Effective size, D_{10} (mm)	0.22
D_{30} (mm)	0.57
D_{60} (mm)	1.45
Coefficient of uniformity, C_u	6.55
Coefficient of gradation or curvature, C_c or C_r	1.01
Angle of Internal friction, $Ø_{direct\ shear}$ (degree)	35.89
Modulus of elasticity, E (kPa)	2887.9

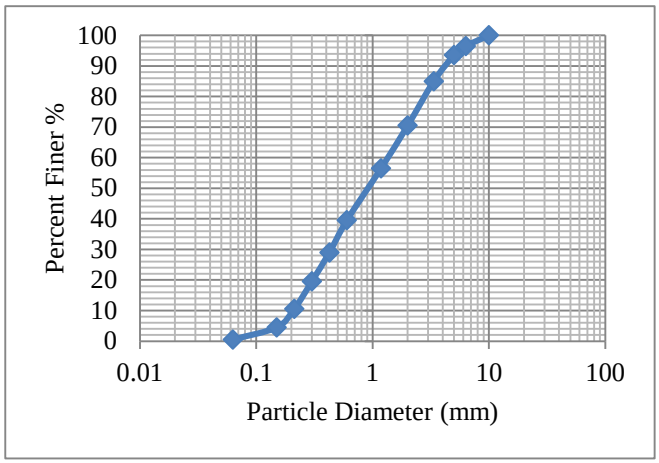

Fig. 3: Particle size distribution of sand

RESULTS AND DISCUSSIONS

Bearing Capacity and Bearing Capacity Factor N_γ

Three different tests were conducted for centrically and eccentrically loaded with 0.0B, 0.05B, and 0.1B eccentricities for Tests 1, 2, and 3 respectively. For each test, the rigid plate which represents strip footing was loaded until reach 20 mm penetration to meet the failure state. Fig. 4 shows the stress- displacement/ footing width curve. It was found that the ultimate bearing capacity values, q_{ult} for Tests 1, 2, and 3 are 43.66 kPa, 35.38 kPa, and 29.85 kPa respectively. It can be seen that the value of q_{ult} decreases when the eccentricity increases.

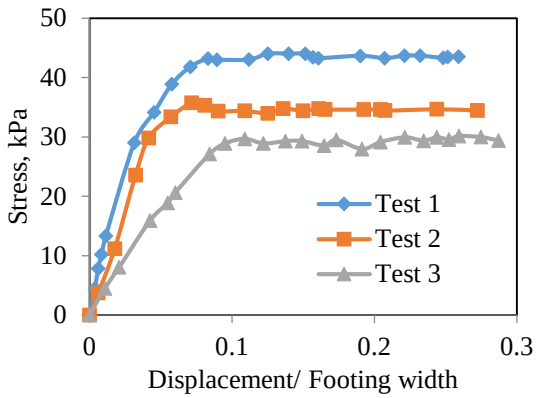

Fig. 4: Stress- Displacement/footing width curve

Equation 1 was used to calculate the bearing capacity factor, N_γ for each test based on the q_{ult} results [1]. The values of N_γ were found as 104.81, 102.89, and 107.85 for Tests 1, 2, and 3 respectively. The angle of internal friction of sand model was determined as 43.56 based on the N_γ results. It was noticed that the discrepancies between the angle of internal friction of sand obtained from the small scale physical model and shear box test was approximately 17.6%. The difference might be contributed from a difference confining pressure mechanism between both tests.

$$q_{ult} = \frac{1}{2}\,\gamma\,(B - 2e)N_\gamma s_\gamma d_\gamma i_\gamma \qquad (1)$$

where, γ is the unit weight of soil, s_γ,d_γ and i_γ are the shape, depth and inclination factors respectively.

Settlement Measurement

Six tests were conducted under 3 differences to determine the settlement as presented in Table 3. Each case consists of two tests under fully and two third of ultimate bearing capacities. It can be observed that by increasing the eccentricity values, the settlement for each test was increases. Figure 5 shows the effect of eccentricity on footing settlement. The results show that the settlement increases with the increasing of the eccentricity. The settlement over footing width ratio (S/B) and the applied stress was plotted as shown in Figure 6. It can be seen that when the applied stress decreased due to increasing of eccentricity, the settlements increased.

Tests	Stress condition		Applied Stress value (kPa)	settlement (mm)
1	centric (e=0.0B)	two third q_{ult}	29.11	0.94
2		full load q_{ult}	43.66	1.58
3	eccentric (e=0.05B)	two third q_{ult}	23.59	1.57
4		full load q_{ult}	35.38	2.3
5	eccentric (e=0.1B)	two third q_{ult}	19.2	2.43
6		full load q_{ult}	29.85	3.19

Table 3: Settlement test results

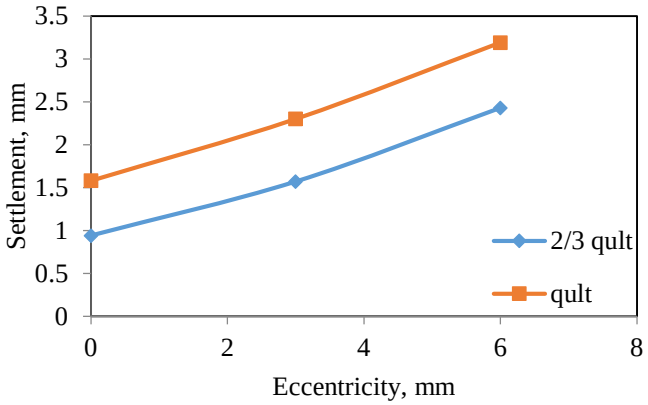

Fig. 5 Effect of eccentricity on the soil settlement

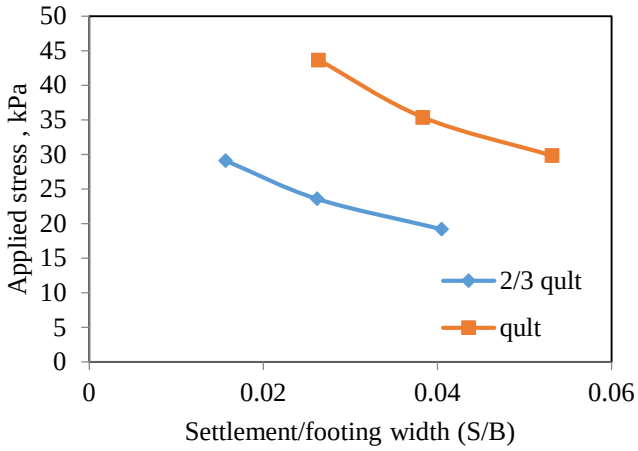

Fig. 6: Relationship between settlement/footing width and applied stress

The main parameters of footing settlement due to eccentricity load which may act on the sand parameters are those due to footing width,

eccentricity, dry unit weight, γ and applied stress, q. Based on the Buckingham π theory, two dimensionless equation were chosen to investigate the effect of the those parameters. The proposed dimensionless equations are $\gamma e/q$ and S/B. Fig. 7 shows the plot of $\gamma e/q$ and S/B. It was found that the normalized settlement increased with the increasing of $\gamma e/q$ value.

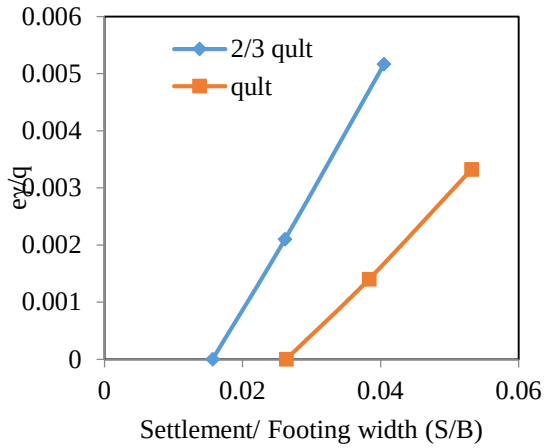

Fig. 7: Relationship between $\gamma e/q$ and S/B

Soil Deformation

The images taken during the ultimate bearing capacity tests were analyzed using the Particle Image Velocimetry analyses. Figs. 8 to 10 show the soil deformation obtained from the PIV analyses for Tests 2, 4 and 6. Fig. 8 shows a clear Prandtl failure mechanism with the soil beneath and adjacent the footing deformed approximately the same size of the footing width. Based on the Figs. 9 to 10, a clear soil movement toward the right side of the footing was observed due to the footing eccentricity. The footing experienced a larger rotation on the eccentricity side when the eccentric was increased as shown in Figure 10.

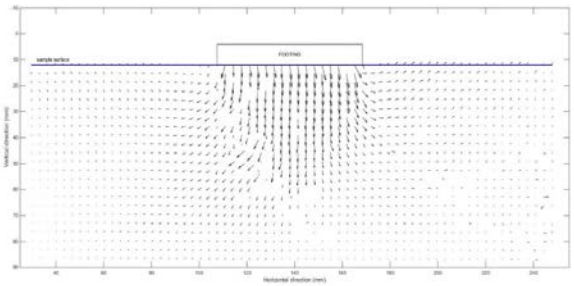

Fig. 8: Vector of soil deformation for Test 2

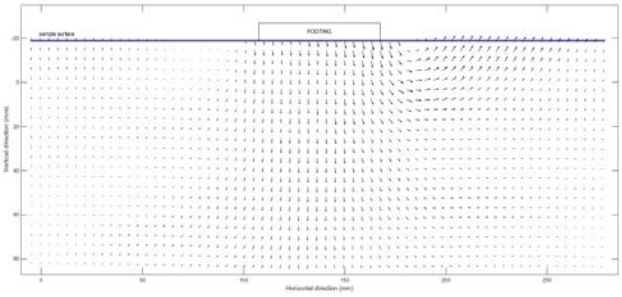

Fig. 9: Vector of soil deformation for Test 4

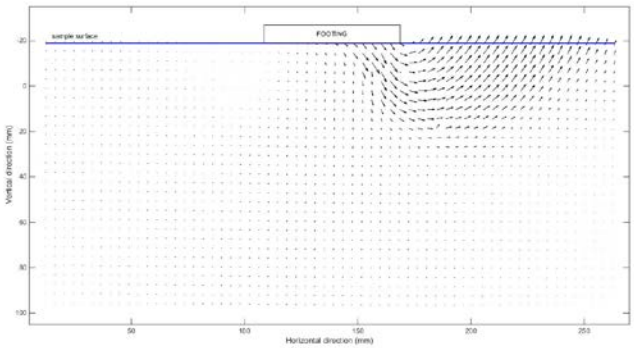

Fig. 10: Vector of soil deformation for Test 6

CONCLUSION

The bearing capacity factor, settlement, and ground deformation of sand was investigated based on small physical modelling and PIV method. The conclusions that can be made from this research are listed as follows:

1. The bearing capacity decreased while the settlement increased with the increasing of eccentricity to footing width ratio.
2. The discrepancies between the angle of internal friction of sand back-calculated from the small scale physical model and shear box test was approximately 17.6% due to the difference confining pressure mechanism.
3. A clear soil movement toward the right side of the footing was observed due to the footing eccentricity with the largest rotation happened on the largest eccentricity side as shown in Figure 10.

ACKNOWLEDGEMENTS

The research was supported by Fundamental Research Grant Scheme (FRGS) – 4F658 (Relationship Between Shear Wave Velocity and Compressibility Indices of Cohesive Soil Using Constant Rate Strain Equipped With Bender Element Devices) from Ministry of Education of Malaysia and Universiti Teknologi Malaysia

REFERENCES

[1] Meyerhof G.G. (1953). Bearing capacity of foundation under eccentric and inclined loads. Proceeding of the 3rd international conference on soil mechanic and foundation engineering, Zurich, vol. 1, 440-445.

[2] Fellenius, B. H. and Altaee, A. (1994). Stress and settlement of footings in sand. Proceedings of the American Society of Civil Engineers, ASCE, Conference on Vertical and Horizontal Deformations for Foundations and Embankments, Geotechnical Special Publication, GSP, No. 40, College Station, TX, June 16 - 18, 1994, Vol. 2 pp. 1760 - 1773

[3] Montrasio, L. and Nova, R. (1997). Settlement of Shallow Foundation on Sand. *Geotechnique* 47(1), 49-60.

[4] Zhu, F., Clark, J. I. and Phillips, R. (2001). Scale Effect of Strip and Circular Footings Resting on Dense Sand. *Journal of Geotechnical and Geoenvironmental Engineering, ASCE* **127**(7), 613-621.

[5] Awad, M. A. and El-Mezaini, N. S. (2001). Effect of Footings Interaction on Bearing Capacity and Settlement of Sandy Soil. *Journal of the Islamic University of Gaza* **9**(1), pp. 43 - 55.

[6] Cerato, A. B. and Lutenegger, A. J. (2007), "Scale Effects of Shallow Foundation Bearing Capacity on Granular Material", *Journal of Geotechnical and Geoenvironmental Engineering, ASCE* **133**(10), 1192-1202.

[7] Kumar, J. and Khatri, V. N. (2008). Effect of Footing Width on Bearing Capacity Factor, Nγ. *Journal of Geotechnical and Environmental Engineering, ASCE* **134**(9), 1299-1310.

[8] Loukidis D., T. Chakraborty and R. Salgado. (2008). Bearing capacity of strip footing on purely frictional soil under eccentric and inclined loads. Canadian Journal of Geotech, 45: 768-787.

[9] Al-Khuzaei, H. M. (2011). Verification of Scale Effect of Shallow Foundation in Determination of Bearing Capacity of Sand. *Al-Rafidain Engineering* **2**(2), 1-11.

[10] Patra, C. R., Das, B. M., Bhoi, M., and Shin, E. C. (2006). Eccentrically loaded strip foundation on geogrid-reinforced sand. Geotext. Geomembr. 24 (4) 254–259.

[11] El Sawwaf, M. (2009). Experimental and Numerical Study of Eccentrically Loaded Strip Footings Resting on Reinforced Sand. *J. Geotech. Geoenviron. Eng.*, 135(10), 1509–1518.

[12] White, D. J., & Take, W. A. (2002). GeoPIV: Particle Image Velocimetry (PIV) software for use in geotechnical testing.

FifthInternational Conference on Geotechnique, Construction Materials and Environment, Osaka, Japan,Nov. 16-18, 2015, ISBN: 978-4-9905958-4-5 C3051

WATER PURIFICATION IN INLAND FRESH WATER LAKE BY TIDAL ENERGY USING UTSURO

R.-T. Jung[1], K. Akai[2], and H. Isshiki[3]

[1]University of Ulsan, Republic of Korea; [2]NGO, "UTSURO" Research group, Japan; [3 1]at the time of study, now, Institute of Mathematical Analysis, Japan

ABSTRACT

Recently, the deterioration of water quality in the artificial lake after the reclamation of an intertidal flat at the mouth of a river has become serious problems in Japan as in the cases of Isahaya bay and Ago bay. We propose a novel method of water purification using tidal potential energy by installing an enclosed permeable embankment, or Utsuro proposed by Akai in 1990, in the lake and bay. Two new UTSURO systems are proposed: One is using an inflatable bag on the seabed within Utsuro while the other is using a moored floating barge out of dyke. In short, equalization of water level between Utsuro and sea out of dyke or between UTSURO and the barge changes water level in UTSURO and make water flow through the permeable embankment of Utsuro. The flow through the void between stones and rocks in the embankment of UTSURO reduces the water pollution by utilizing biological effect. Some numerical calculations were conducted both for a method using inflatable bag and a method using a float.

Keywords:Contaminated Water, Water Purification, Fresh Water Lake, Reclamation, UTSURO

INTRODUCTION

Water purification in reclamation area is an important milestone because the artificially changed costal environments are suffered to adapt to the surroundings over many years. The change easily makes the marine environment worse, if it is not carefully controlled. The disaster on the water quality in reclamation area can be found find in many places: Isahaya Bay[1] in Japan, Shiwa lake[2] in Korea, Haringvliet dam[3] in Netherland, Tuckombil waterway[4] in Australia and etc. The first target value to make the environmentally-friendly surroundings settled down in plan-stage is extremely difficult to keep it.

Nature-friendly reclamation should be accompanied by water quality management. The prevention and/or reduction of water pollution and eutrophication due to contamination by large pollutant effluent from the land should be considered as the surrounding marine environmental matters. As a self-purification system, a rockfill-type enclosed embankment in the dyke can be introduced. This rubble seawall, named "UTSURO"[5], functions like a rubble mound breakwater introduced by Palmer[6] to protect a coastal area from excessive waves. The Japanese word UTSURO means a calm space enclosed by permeable embankment, and it is known that the water is purified making water passing through the UTSURO embankment. An additional part is a system to generate water current across the dyke using tidal potential energy. Consideration of water level management is important because the water in the reclamation area dramatically changes from running to stagnant water before and after construction of the dyke, respectively. Since the water current in the lake is significantly reduced after construction of the dyke. This can result in degradation of water quality, because nutrient concentration in stagnant water increases continuously by external pollution such as supply via streams, rivers, and wastewater discharge.

We propose two types of new engineering purification systems for water in the reclamation area. In both, tidal potential energy is utilized in order to force water circulation in the region. These two methods may reduce the stagnant places in the reclamation area.

TWO PURIFICATION METHOD

Inflatable bag method

The first suggested system consists of an impermeable submerged inflatable bag located at the bottom of the UTSURO, as shown in Figure 1(a). A pipe connects the sea to the bag. Tide flows into the pipe, and the bag is swelled by sea water at high tide. As the level of water in the UTSURO increases, the water level inside the UTSURO becomes higher than the water level outside. This causes the flow outward through the embankment of the UTSURO

(and vice versa) over the course of two tides per day. Sea water and fresh water remain separated because the inflatable bag swells up and down via the incoming and outgoing sea water in the pipe, that is, the sea water passes two ways in it. “F” and “S” refer to fresh water and salt water, respectively. Figures 1(b), (c) and (d) show the managed water level W.L. is 0, positive, and negative, respectively according to the tide. Higher tidal difference results in larger flow exchange through the rubble so that we may expect good purification by an UTSURO placed inside lake.

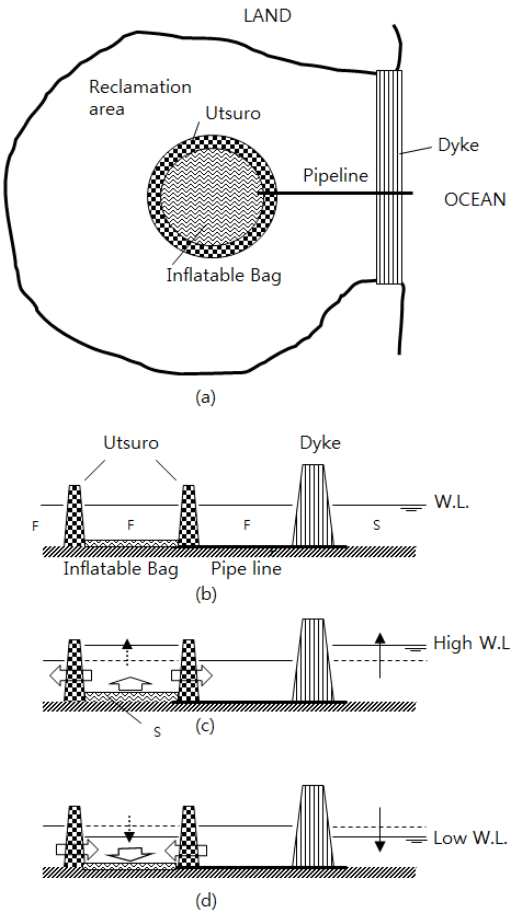

Fig. 1 A suggested schematic plan using an inflatable bag surrounded by UTSURO(F: fresh water, S: Sea water). The inflatable bag contains much and less sea water at the high and low tide, respectively.

Floating body method

The second suggestion to use the tidal difference is shown in Figure 2(a), which provides a plan view of the system. In this option, we place a float at sea connected to the UTSURO in the lake with a pipe. The water in the float is the fresh water. There is no inflatable bag here, as was suggested in the previous section. So, we may consider that the level of the surface in the UTSURO and that in the float would be equal, as in Figure 2(b). Furthermore, the level of the surface inside and outside the UTSURO would also be equal in Figures 2(c) and (d). Once the float goes up due to the tide, the water flows from the float to the UTSURO via the pipe because the water level inside the float tends to equal the level in the UTSURO. The transferred water within the UTSURO moves toward the outside of the UTSURO through the embankment of the UTSURO, as shown in Figure 2(c). When the float goes down, the water flows from the UTSURO to the float, and the water outside the UTSURO moves inside the UTSURO through the embankment, as shown in Figure 2(d). The water having with potential energy in the pipe transfers two ways between the float and the UTSURO.

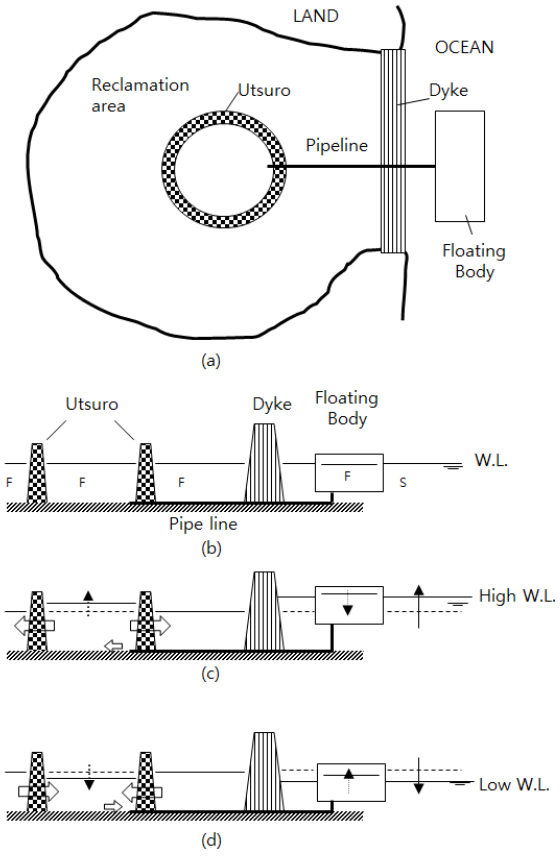

Fig. 2 A suggested schematic plan using a floating body placed outside of dyke(F: fresh water, S: Sea water). Arrows show flow direction.

NUMERICAL EQUATIONS

We think there are many solutions to obtain the high water quality in the reclamation area. We studied a solution on how to make the huge amount

of water in the reclamation area cleaner. We denote the governing equations of each method for the UTSURO simulation.

Inflatable bag method

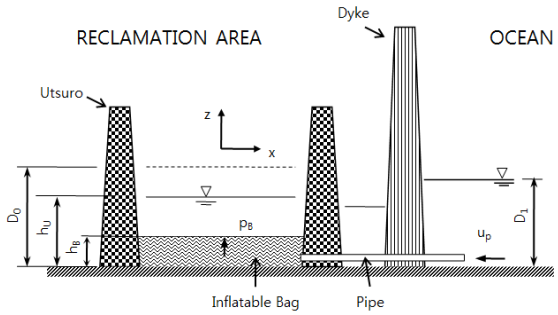

Fig.3 A schematic view using an Inflatable bag

In order to have a flow simulation, we studied the inflatable bag method first. For the simulation, a tide is assumed to change sinusoidally. D_1 is the instantaneous depth of the sea water with mean depth D_0 . The pressure is also needed for the assumption at the upper surface of the inflatable bag and given as

$$p_B = \rho_F g(h_U - h_B) + f(h_B) \tag{1}$$

where g , ρ_F , h_U , h_B , and f are the gravitational acceleration, density of fresh water, height of the water surface in the UTSURO, expansion height of the inflatable bag, and restoring force of inflatable bag, respectively. The restoring force f acting on the upper moving part of the inflatable bag is given by [7]

$$f(h_B) = \begin{cases} 0 & \text{when } h_B < W \\ k(h_B - W) & \text{otherwise} \end{cases} \tag{2}$$

or

$$f(h_B) = kh_B^{\chi} \tag{3}$$

The force f consists of two coefficients k, χ and an assumed height of the bag W .

In order to set up the governing equations, we defined the two cases of the hydrodynamic relations for convenience: ~~as~~

$$\rho_S g D_1 > \left[\rho_F g(h_U - h_B) + f\right] + \rho_S g h_B \tag{4}$$

and

$$\rho_S g D_1 < \left[\rho_F g(h_U - h_B) + f\right] + \rho_S g h_B \tag{5}$$

then, applying Bernoulli's equation, we can get flow velocity in pipe and governing equations

$$u_p = \mathrm{sgn}\left(D_1 - \frac{\rho_F}{\rho_S}h_U - \frac{f(h_B)}{\rho_S g}\right)\sqrt{\frac{2g}{1+\mu}\left|D_1 - \frac{\rho_F}{\rho_S}h_U - \frac{f(h_B)}{\rho_S g}\right|} \tag{6}$$

$$S_U \frac{dh_U}{dt} = u_p S_P - \alpha\,\mathrm{sgn}(h_U - D_0)\sqrt{g\,|h_U - D_0|}\,l_U \begin{cases} h_U - h_B & \text{when } h_U \geq D_0 \\ D_0 - h_B & \text{when } h_U < D_0 \end{cases} \tag{7}$$

$$S_U \frac{dh_B}{dt} = u_p S_P \tag{8}$$

where ρ_S , S_U , S_P , l_U , and α are the density of sea water, water surface area of the UTSURO, cross sectional area of the connecting pipe, circumferential length of S_U and permeability coefficient of the UTSURO, respectively. Equations (7) and (8) are the mass balance of the UTSURO and that of the inflatable bag, respectively.

In order to solve Eqs. (7) and (8), we obtain ordinary differential equations for h_U and h_B . The unknowns h_U and h_B are obtained numerically by a Runge-Kutta method. The restoring force f can be applied by the Equation (2) or (3). Table 1 is a value set of the parameters used in equations and an example of the inflatable bag case.

Table 1 Parameters used in a numerical example of an inflatable bag

Items	value	Items	Value
g	$9.8 m/s^2$	S_U	$8{,}000 m^2$
ρ_F	$1000 kg/m^3$	S_p	$1.0 m^2$
ρ_S	$1040 kg/m^3$	D_m	$10 m$
μ	0.2	h_U	$10 m$
α	0.000001	h_B	$4 m$
D_0	$10 m$	A	$1 m$
T	$12 h$	k	$1000 Nm^{-2}$
χ	3	dt	$1 s$

Floating body method

In order to establish a set of governing equation in case of the floating body method, it is convenient to classify the free surface level relations in two cases given by Eqs. (9) and (10):

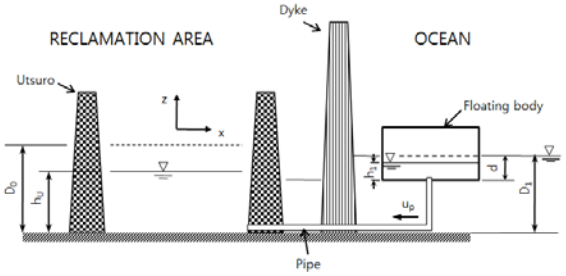

Fig.4 A schematic view using a Floating body method.

$$D_1 - d + h_1 > h_U \tag{9}$$

or

$$D_1 - d + h_1 < h_U \tag{10}$$

where, D_1 is given by the tide, d is draft of the floating body, h_1 is a water surface level in the floating body, h_U is a free surface level in the UTSURO.

Applying Bernoulli's equation, we obtain the flow velocity in pipe and governing equations such as

$$u_p = \mathrm{sgn}((D_1 - d + h_1) - h_U)\sqrt{\frac{2g}{1+\mu}|(D_1 - d + h_1) - h_U|} \tag{11}$$

$$S_U \frac{dh_U}{dt} = u_p S_P - \alpha\,\mathrm{sgn}(h_U - D_0)\sqrt{g\,|h_U - D_0|}\,l_U \begin{cases} h_U & \text{when } h_U \geq D_0 \\ D_0 & \text{when } h_U < D_0 \end{cases} \tag{12}$$

$$S_1 \frac{dh_1}{dt} = -u_p S_P \tag{13}$$

$$\ddot{d} + \frac{\rho_S g d}{M_1 + \rho_F h_1 S_1}\left(S_1 + b(1+0.5\gamma d)l_1\right) = -\left(\frac{2\pi}{T}\right)^2 A\sin\left(\frac{2\pi}{T}t\right) + g \tag{14}$$

where M_1, S_1, $b(1+0.5\gamma d)$, l_1, ρ_S, S_U, S_P, l_U and α are the mass of the float, the surface area of fresh water in the float, the thickness of the wall of the float at draft d, the circumferential length of S_1, the density of sea water, the water surface area of the UTSURO, the cross sectional area of the connecting pipe, the circumferential length of S_U, and the permeability coefficient of the UTSURO, respectively. Eqs(12),(13) are mass balance of water in UTSURO and floating body, and Eq(14) is a vertical motion equation of the floating body where the added mass of the float and wave and viscous damping are neglected because of long period in tide.[7]

The floating draft d, the water depth h_1 and h_U are determined by Runge-Kutta method numerically using the Eq. (11)~(14). Table 2 is a value set of the parameters used in the numerical calculations.

Table 2 Parameters used in a numerical example of a floating body

Items	value	Items	value
g	$9.8\,m/s^2$	S_U	$8{,}000m^2$
ρ_F	$1000\,kg/m^3$	S_p	$1.0m^2$
ρ_S	$1040\,kg/m^3$	D_m	$10m$
μ	0.2	h_U	$10m$
α	0.000001	h_1	$5m$
D_0	$10m$	A	$1m$
T	$12h$	M_1	$4{,}000{,}000kg$
S_1	$8{,}000m^2$	dt	$1s$
b	$4m$	l_1	$400m$

SIMULATION RESULTS

Simulations based on the governing equation had been carried out how the two suggested methods such as the inflatable bag method and the floating body method work in the direction to the large water level difference between inside and outside of the UTSURO because the difference causes a driving force for the circulation around the UTSURO.

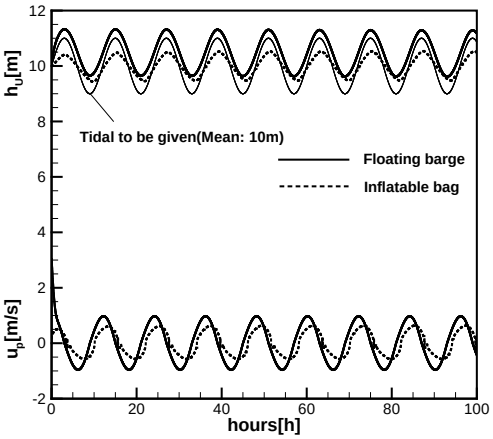

Fig.5 Simulation results on the water level in UTSURO and flow velocity in pipe(dotted for the inflatable bag method and solid line for the floating barge method)

As shown in Fig.5 which is simulated based on the Table 1 and 2, the amplitude of the water level in the floating barge method follows the tidal level while that in the inflatable bag method is only half. It means the flow velocity in pipe in the floating

barge method has also wider amplitude(+/- 1.0m/s) than the inflatable bag method. The amplitude of the water level maintains even though the barge mass changes. The mass of the barge in the simulation in Fig5 was 4,000ton.

Permeability coefficient α is one of the major parameter for this simulation because it makes the water level difference between inside and outside of the UTSURO. Fig 6 shows the characteristics of the simulated value h_U and. The α is depicted in a log-plot from 10^{-6} to 10^{-3}. In both cases of the inflatable bag method and floating barge method, the amplitude of h_U becomes zero as α value is large. However, the value of h_U at $\alpha = 10^{-6}$ in case of floating barge is bigger than that of the inflatable bag. It is sustained until 10^{-4} of α . The flow velocity in pipe with the different permeability coefficient is also simulated. The higher velocity in pipe is shown in the case of the floating barge because of higher potential energy than the inflatable bag. The velocity is about 50% greater than that of the inflatable bag case. The Fig.6 also shows that the floating barge is more practical than the inflatable bag. The permeability coefficient α should be from 10^{-5} to 10^{-4}.

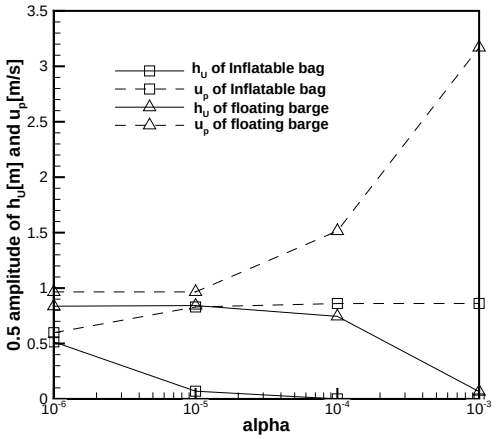

Fig.6 Permeability α vs. both h_U and u_p in case of the inflatable bag and floating barge method respectably

The difference of water level decides how much water exchange occurs. In case of the floating barge method, this method can be applied as much as the difference is high. In Fig.7, three different cases of the barge mass are shown when the permeability coefficient α is the same value of 0.000001. Each mean value of the h_U approaches to the mean depth of 10m as the value of mass becomes large. Light mass barge can contain much more water in it resulting the high level of h_U .

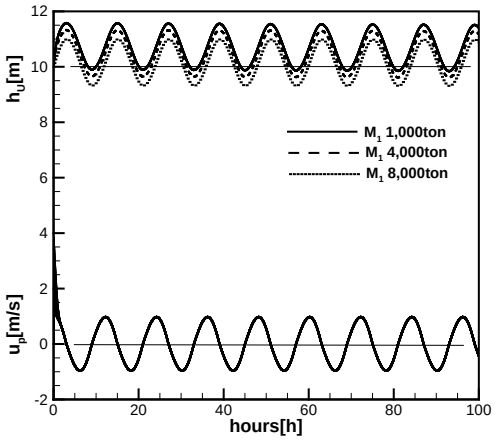

Fig.7 UTSURO height h_U in case of three different barge mass 1,000ton, 4,000ton, and 8,000ton. The flow velocity u_p is also shown for the three cases.

CONCLUSION

We focused on reducing the pollution of a freshwater lake after closing the breakwater at the region of a large tidal current after the completion of the reclamation and suggested two new types of purification systems to cope with it.

One uses an inflatable bag on the seabed within the UTSURO. The seawater is charged into an impermeable bag and discharged from the bag through the connecting pipe by the reciprocal motion due to the tidal difference.

Another simulation on the floating body case shows there is an increased possibility of purification effects because the motion of the water surface in the UTSURO is 1.5-times larger than that of the bag case. According to the permeability parameter α , the h_U values have about ± 0.8m differences from the simulations. The more enhancement of water exchange through the UTSURO, the more purification effects take place.

The two suggested ideas using the ocean tidal energy are in effective for the purification around UTSURO because it makes a circulation of water. Through the simulation, it shows the floating body type has bigger amplitude of the water surface which enhances the circulation than the inflatable bag

REFERENCES

[1] Yokoyama, T. and Kyozuka, Y., 2003, "Experimental study on flow and tidal exchange of a reservoir through dike gates in Isahaya Bay", Proceedings of the 13th International Offshore and Polar Engineering Conference, Hawaii, USA, pp. 331-337.

[2] Park, Y.C., Park, J.K., Han, M.W., Son, S.K., Kim, M.K. and Huh, S.H., 1997, "Biogeochemical study of dissolved organic and inorganic compounds under oxic/anoxic environment in reservoir shihwa", J. Kor. Soc. Ocean., Vol. 2, No. 2, pp. 53-68

[3] Stuyfzand, P.J., De Lange, W.J. and Zindler, J.A., 2004, "Recognition, dating and genesis of fresh and brackish groundwaters in the Hollandsch Diep estuary in the compound Rhine-Meuse delta", the 18th Salt Water Intrusion Meeting (SWIM), Cartagena, Spain, pp. 665-678.

[4] Richmond River County Council, 2007, "Final report for Tuckombil Canal management structure review of gate alternative", GHD Pty Ltd. No. 21-15892-128245, Sydney, Australia.

[5] K. Akai, S. Ueda, Y. Wada and R. Tuda, The water quality purification system for the enclosed sea area, Marine Pollution Bulletin, 1990, vol 23, 683-685.

[6] G.N. Palmer, C.D. Christian. Design and construction of rubble mound breakwaters, IPENZ Transactions, Vol.25, No.1, 1998, 19-33.

[7] R.-T. Jung and H. Isshiki, "Application of tidal energy for purification in fresh water lake", Int. J. Nav. Archit. Ocean Eng. 2015 7:212-225

First International Conference on Science, Engineering & Environment,
Tsu City, Mie, Japan, Nov.19-21, 2015, ISBN: 978-4-9905958-5-2 C3051

IMAGE-BASED AS-BUILT 3D MODELING FOR DEFORMATION ASSESSMENT OF HISTORICAL BUILDINGS

Bhakapong Bhadrakom[1]and Krisada Chaiyasarn[1]
[1]Department of Civil Engineering, Thammasat University, Thailand

ABSTRACT

Assessing the state of historical buildings is non-trivial tasks as limited information is available and only non-invasive assessment can be performed on these buildings. Image-based 3D reconstruction is a recent technique, which can construct an as-built model of a historical building to be used for damage and deformation assessment. The technique is based on Structure from Motion, which can automatically create a 3D model from uncalibrated images. In this paper, VisualSFM, automated image-based 3D modeling software, is applied to construct a 3D model of a historical building. The model is compared with a model obtained from a laser scan (LIDAR). To perform a deformation assessment on the building, a series of horizontal plane is sliced through the 3D model, and then a centre of each 3D slice is joined to form a line representing an incline angle of the building. This technique is performed against a laboratory dataset to determine its accuracy. It was found that for a small incline angle (less than 4^o), the technique contains the inaccuracy of 2.75% with increasing inaccuracy as inclined angles become larger. When applying the technique to a real temple dataset, it was found that the angle of inclination is less than 3^o, which is in an acceptable range for the proposed technique. Additionally, it was found that the inclined angles obtained from VisualSFM and LIDAR are almost identical. It was recommended that VisualSFM can be used instead of LIDAR when performing damage assessment in historical buildings.

Keywords: Structure From Motion, As-built Modeling, Damage Assessment, Laser Scan, Historical Buildings

INTRODUCTION

Historical buildings are sensitive to damages due to ageing and nearby activities. To assess the damage on historical buildings, only non-invasive inspection method is possible, and visual inspection is a preferred method. As-built 3D models are now commonly used in archiving historical buildings, as users can use the models to explore and study the buildings more closely off-line. The as-built models can also be used for inspection as demonstrated in this paper.

As shown in Fig. 1, many temples from Ayutthaya have been tilting possibly due to nearby road activities or ground subsidence. The city was founded by King Ramathibodi I in 1350, and in 1969, the Fine Arts department began with renovations of the ruins, which became more serious after it was declared a historical park in 1976. The park was declared a UNESCO World heritage site in 1991. The scale of conservation and preservation is so large, and many temples have been neglected and deteriorated for many years.

This paper provides further improvement to the study by Bhadakom et al. (2012), who have conducted a study on some Ayutthaya temples to measure tilt angles using traditional photogrammetry techniques. The techniques require control points to be manually identified, and a full 3D model of entire buildings can only be constructed from multiple 3D sub-models. The techniques require 3D registration which is troublesome and induces inaccuracy.

The paper proposed methods to assess damage in historical buildings by estimating how much the buildings are tilted using fully automated software that can create a 3D model from uncalibrated images. The proposed method utilized the 3D model from the software to estimate a tilt angle of a historical building. The methods were tested against laboratory dataset to estimate inaccuracy that can occur from the proposed method of obtaining tilt angles. The 3D model obtained from the software is also compared against the model obtained from a laser scan (LIDAR). It was found that the 3D models from the software and a laser scan provide identical result when estimating tilt angles and they can be used interchangeably for the purpose of damage assessment and inspection.

Fig. 1 The picture of the temple used in the study.

The subsequent section, Literature Review, summarises previous work in applying 3D modeling in damage assessment. Then, the overview of the method is outlined in Method Outline. In Implementation and Experiment, the proposed method is explained in detail and the results obtained from a laboratory dataset are shown. The result from a real dataset is explained in the section Field Trial, and the paper ends with the discussion of the proposed method and conclusion.

LITERATURE REVIEW

Non-invasive inspection is required when assessing damage in vulnerable historical buildings to prevent further damage that can occur from the inspection process themselves [8]. Close range photogrammetry has been used to reconstruct 3D models of historical sites for archiving and for damage assessment purposes [9]. Traditional photogrammetry data collection process requires procedures to identify control points manually, which can become impractical in real sites [4]. Recently, free automatic photogrammetry software packages with computer vision algorithms have been used to create 3D models of historical buildings [3]. The software relies on automatic control point detection algorithms and Structure from Motion, which allow 3D models to be created with ease as images can be taken with arbitrary motions.

Many techniques have been applied in assessing damage in historical buildings using 3D models. The followings are some recent examples. Fregonese et. al. (2013) applied Terrestrial Laser Scanner (TLS) to monitor out-of-plane displacement of an ancient building by registering two sets of laser scan data to several geo-referenced control points. It was concluded that TLS could be used for structural monitoring. El-Tokhey et. al. (2013) transformed control points from a laser scan data to a total station data using a series of transformation to find discrepancy between two sets of data and displacements. Tapete et. al. (2013) integrated Ground-Based Synthetic Aperture Radar Interferometry (GBInSAR), which can detect deformation of objects between two SAR images, to TSL data. Armesto et. al. (2009) applied TLS to a masonry bridge and the bridge deformation was estimated by an algorithm based on an arch symmetry. Armesto-Gonzalez et. al. (2010) analysed damage in buildings by classification algorithms onto 2D images that were constructed from laser scanner as they can provide other material properties. Bhakapong et. al. (2012) applied photogrammetry technique to compare the cross-sectional profile of temples in order to assess the amount of building inclination.

It can be seen that many recent studies have utilised 3D point cloud to detect damage or changes in historical sites. Most studies use 3D point cloud from a laser scan data, which is believe to be more accurate. However, it is demonstrated in this paper that for some applications, 3D point cloud from images can provide equally good results.

METHOD OUTLINE

Figure 2 shows the outline of the methods proposed in this paper. The first module is 3D modelling. This module is achieved by free open-source software called VisualSFM, which can create a 3D point cloud model together with camera poses from uncalibrated images. The second module is 3D Registration. The 3D point clouds are registered together so that they are in the same global coordinate frame. The third module is Deformation Assessment, which are achieved by estimating a tilt angle of a 3D model. The detail of each step is explained in Implementation and Experiment.

There are two datasets presented in this paper: (1) a laboratory dataset and (2) a field dataset. The laboratory dataset is used to verify the accuracy of the proposed method, and the field dataset is an actual data obtained from a real site from Ayutthaya. The laboratory dataset is a set of cylinder images taken at 5 angle elevations. The field dataset contains a set of images of the temple and a 3D model of the temple obtained from a laser scan; this is explained in Field Trial.

Fig. 2 The outline of the proposed method.

IMPLEMENTATION AND EXPERIMENT

Modelling

Five sets of images of a concrete cylinder are collected for use in verifying the method in this study. An example image is shown in Figure 3. The cylinder has a diameter of 15 cm and the height of 30 cm, and is placed on a wooden base, in which angles can be adjusted. Sixteen 2x2cm checkerboard pattern are used as control points, which are placed on the cylinder surface. Three 10x10x10 cm concrete cubes are placed on a wooden base; these cubes are used as reference for registration, explained in the next section.

The five image datasets are taken at different angle elevations, i.e. at 0^o, 2^o, 4^o, 10^o and 14^o degrees, respectively. For each set of images, photos are taken at different viewpoints to cover an entire object using a Canon 550D with a Sigma lens and settings set as Auto. There are no strict rules in how to take images for VisualSFM, although the rule of thumb is to ensure that an overlap between two consecutive images is at least 50%.

A 3D model for each set is created by VisualSFM. This software provides a 3D model and camera poses. The software is based on Structure from Motion (SfM), and interested readers can refer to Snavely et. al. (2006) for more detail of the theory and technology. Figure 4 shows actual 3D models for each angle elevation. The models are 3D dense point clouds, in which their texture is obtained from image pixels. Table 1 provides a summary of the dataset including the number of pictures taken and the number of 3D points created by VisualSFM for each angle of elevation.

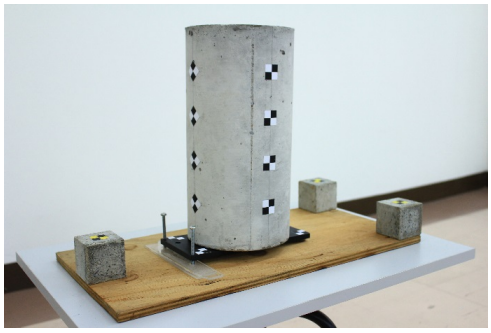

Fig. 3 An example picture of a cylinder

Fig. 4 3D models of the cylinder at 5 angles of inclination

Table 1 A summary table of the cylinder dataset

Elevation	#images	VisualSFM #points
0^o	61	342,975
2^o	81	317,737
4^o	79	308,511
10^o	73	350,205
14^o	77	350,972

Registration

To measure tile angles between different models, the models must be registered so that they are in the same global coordinate frame. The 3D models are registered in the software called CloudCompare [11] using an iterative closest point (ICP) algorithm. To ensure that registration process is accurate, three 10x10x10 cm concrete cubes are used as reference for registration. As shown in Figure 5, coordinates on the cubes are used for registration, i.e. R_0 is registered with A_0, R_1 with A_1 and R_2 with A_2, and the errors of these points are minimized. Figure 5(b) shows an example of registration between two models using CloudCompare. The model with the elevation angle 0^o is used as a reference model, from which models from other angles are registered and measured the tilt angles. The cylinder is tilted by adjusting a metal base place and real elevations are recorded for comparison explained in the next section.

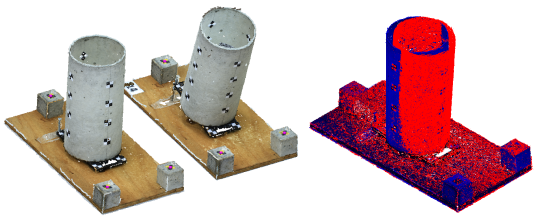

(a) (b)

Fig. 5 (a) Examples of the model with different tilt angles; (b) the models are registered.

Deformation Assessment

To find an angle of inclination, a 3D centre line of an object is required. To achieve this for an object that cannot be represented by primitives, such as historical buildings as presented in this study, the following methods are applied. Firstly, the model is sliced horizontally at different heights using slicer in CloudCompare as shown in Figure 6. Figure 6(a) shows an example of a boundary of a slicer box in CloudCompare and Figure 6(b) shows horizontal planes that sliced through the cylindrical 3D model. The thickness of each slice is approximately 1 cm so that the sliced point cloud can be assumed as a plane. The planar slicers are re-used for all other 3D models to ensure that a 3D model are cut by the same planes. Then, the point cloud from each slice is input into a least square solution for an eclipse. In this study, the shape of a point cloud in a slice is assumed to be an eclipse since the centre can be found easily and the point cloud is not a perfect circle. The algorithm to find the best fit for an eclipse is as follows. An eclipse can be written as

$$\frac{(x-x_0)^2}{a^2}+\frac{(y-y_0)^2}{b^2}=1 \qquad (1)$$

which can be re-arranged to be a form of linear quadratic equations as

$$2b'xy+c'y^2+2d'x+2f'y+g'=-x^2 \qquad (2)$$

For the best fit problem, m data points provides m linear equations, hence the equation (2) for m equations can be written in matrix form as

$$X\beta=y \qquad (3)$$

where $X=\begin{bmatrix} 2x_1y_1 & y_1^2 & 2x_1 & 2y_1 & 1 \\ \vdots & \vdots & \vdots & \vdots & \vdots \\ 2x_my_m & y_m^2 & 2x_m & 2y_m & 1 \end{bmatrix}$, $\beta=\begin{bmatrix} b' \\ c' \\ d' \\ f' \\ g' \end{bmatrix}$ and $y=\begin{bmatrix} -x_1^2 \\ \vdots \\ -x_m^2 \end{bmatrix}$. For the least square problem, the objective function or the residual, min $\|y-X\beta\|^2$, is minimized. The solution to the equation 3 can be found as $\beta=X^{+}y$, where X^{+} is a peudo-inverse of the matrix X. Once the parameters in the vector β are found, they can be converted to major and minor axes, x_0 and y_0 to describe the properties of an eclipse. The centre of an eclipse (x_0,y_0) for each slicer is used to estimate a centre line of a cylinder. The angle of elevation is obtained by estimating the slope of a best fit line (constrained at the base) that passes through (x_0,y_0) for all slices.

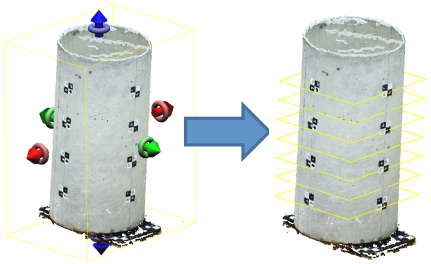

Fig. 6 Examples of horizontal slices used to cut a 3D model

Results

Figure 7 shows the results for all elevations. The slope of each line is converted to angles. The subscripts and the legend indicate the real angles of elevation. The deviation from the real angle is the largest at 11% when the angle is 14°. For angle of 4°, the difference is smallest, less than 0.11° or approximately 3%. Therefore, when an angle of elevation is around 3°- 4°, the proposed method can provide reasonable results.

FIELD TRIAL

In this section, similar methods are applied on a dataset obtained from a real site, which is a temple from Ayutthaya historical park.

Modeling

In this section, two sets of data were collected, an image dataset for VisualSFM and data from a laser scan. The point clouds from these models are used for comparison as explained in later subsection. The image dataset is used with VisualSFM and the camera used and how the images are obtained identical to the cylinder dataset. There are no strict rules in taking pictures; the rule of thumb is consecutive images must have an overlap of at least 50%.

In the temple dataset, pictures were taken at a distance where an entire building was visible, and then the subsequent image was taken at approximate 3-4 meters from the previous image and the procedure was repeated to obtain images for an entire building. As shown in Fig. 8, the output from VisualSFM shows a sparse point cloud and the locations of where each image was taken. It can also give a dense 3D surface model, in which the point cloud is denser and provides more realistic visualization for a building as depicted in Figure 9(a).

A 3D point cloud from laser scanner was collected for a temple as shown in Fig. 9(b). The 3D laser scanner used in this work is FARO Focus3D. This system requires at least 3 physical control points, where these points must be visible for the laser scan, which can be troublesome to find suitable locations for these control points. Once the locations of control points were setup, the laser scan can then collect the data. The data were collected from 8 locations for each temple in order to obtain point clouds that cover entire buildings. Then the software Faro Scene was applied to register the point clouds from each location to form a single point cloud for the entire temple.

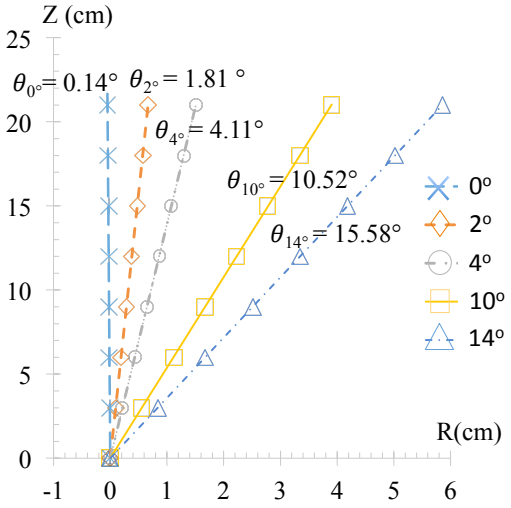

Fig. 7 An example picture of a cylinder

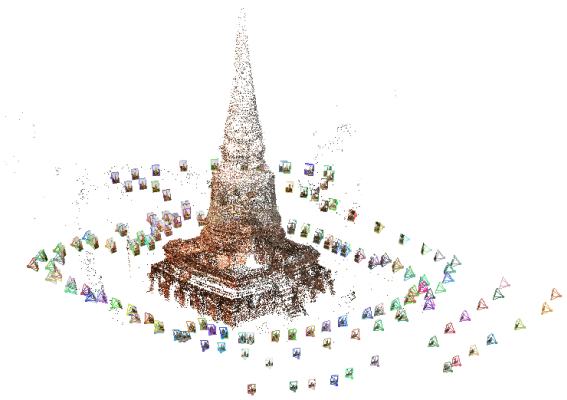

Fig. 8 A 3D model of the temple created from VisualSFM with camera positions.

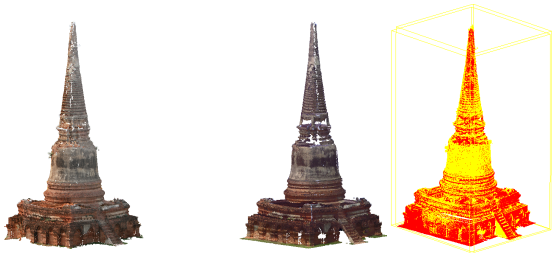

(a) (b) (c)

Fig. 9 (a) 3D model from VisualSFM (b) 3D model from LIDAR (c) the results of registration between the model from VisualSFM and LIDAR.

Registration

In this section, the comparison is made between models from VisualSFM and LIDAR. The 3D models from VisualSFM and LIDAR are registered in CloudCompare using an iterative closest point (ICP) algorithm, which is applied iteratively until RMS errors between the models are constant taken as the final RMS error. Initial alignment between two models must be specified as a reference in order to register the models accurately. In this study, the base of the temple was used as the initial alignment. Fig. 9(c) and Tab. 2 shows the results from registration of the two 3D models.

Table 2 A summary table of the registration result between the VisualSFM and LIDAR models.

Data	Small Stupa
RMS	0.0902
LIDAR #points	1,000,000
VisualSFM #points	1,122,143
#points Ratio	0.8911

Deformation Assessment

As shown from Fig. 10(a), the centre line of the temple starts from the centre of the temple base, which was found by an intersection of the diagonal of the base. In this study, it was assumed that the whole temple does not tilt together as a single rigid object. The temple is split into an upper part with the height between 11 to 22 meters and a lower part with the height from 0 to 11 meters. This is based on the assumption that the top of temple can move more than the lower part and also the point cloud is more complete at the lower part than the upper part. As shown in Fig. 10(b), the temple will have two tilt angles, θ_{top} for the upper section and θ_{bottom} for the lower section. Simlar to the cylinder dataset, the tilt angle is found by a slope of a best fit line to data. Figure 11 shows the results of tilt angles of the temple. The orange line is the LIDAR data and the blue line is the VisualSFM data. Figure 11(a) is the cross section using x-z plane and Fig. 11(b) is the cross section on y-z plane. On Fig. 11, it can be seen that the tilt angles on the x-z plane are different on upper and lower part for both datasets, whereas the angles are almost identical for the y-z plane. The tilt angles are almost identical for both datasets, which suggests that the accuracy of the model from VisualSFM is similar to the model from LIDAR. The angle of inclination is between 1^{o} – 3^{o}, and the laboratory results suggest these angles of inclination are within the range of accuracy tolerance that the proposed method can provide sufficiently accurate results.

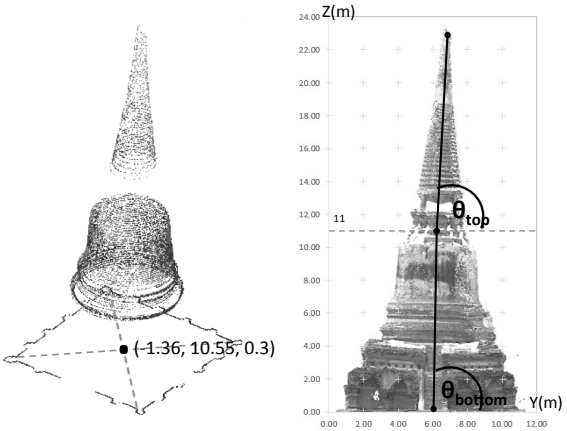

(a) (b)

Fig. 10 (a) Show the location of the centre of the temple; (b) show angles of inclination of the top and bottom parts of the temple.

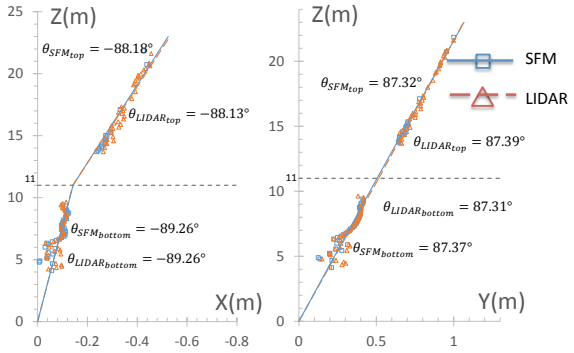

(a) (b)

Fig. 11 Shows the results of inclined angles on the (a) x-z plane and (b) y-z plane, respectively.

DISCUSSION AND CONCLUSION

It can be seen that the angles of inclination obtained from both LIDAR and VisualSFM are almost identical; this suggests that VisualSFM can be used instead of LIDAR. However, inaccuracy is observed by the proposed method. It can be seen that, from the cylinder dataset, the centres of slices lie well on the best fit line, unlike in the temple dataset. A 3D point cloud model is not water tight, hence holes can be observed in many locations. Therefore, some slices may not contain sufficient data points, and the estimation of the centres can be skewed. This problem will be seen in both the models from VisualSFM and LIDAR. Inaccuracy can also arise due to registration between 3D models, this problem is not trivial and further work is required.

Conclusion

To perform damage assessment on historical buildings, non-invasive inspection method is preferred. This paper presents a method to assess damage on historical buildings by measuring angles of inclination from 3D models. The proposed method provides sufficient accuracy in estimating a tile angle for a small angle as observed in the cylinder dataset. The angles of inclination are identical for both models from VisualSFM and LIDAR, which can be suggested that the model from VisualSFM can be used instead of LIDAR as it provides the same accuracy for this task, and the technology is easier and cheaper to use. The proposed method still poses some inaccuracy in estimating the centre lines due to inaccuracy in a point cloud model. This can be improved by making the point cloud model denser or by converting the point cloud to a watertight surface model. This is planned for further study.

REFERENCES

[1] B.Bhadrakom, N. Poovarodom, U. Weesakul, Y. Fujii, K. Watanabe and S Kawano. Application of Photogrammetry for Conservation of Historical Remains. NCCE 18, 2012

[2] D. Tapete, N. Casagli, G.. Luzi, R. Fanti,, G.. Gigli,, and D. Leva, (2013). Integrating radar and laser-based remote sensing techniques for monitoring structural deformation of archaeological monuments. *Journal of Archaeological Science*, *40*(1), 176-189.

[3] F. Remondino, S.D. Pizzo, Th. P. Kersten, Salvatore Troisi. "Low- Cost and Open-Source Solutions for Automated Image Orientation – A Critical Overview". Progress in Cultural Heritage Preservation 4th International Conference, EuroMed 2012 Limassol, Cyprus

[4] H.M. Yilmaz, M. Yakar, S.A. Gulec, O.N. Dulgerler. Importance of digital close-range photogrammetry in documentation of cultural heritage. Journal of Cultural Heritage, pp.428-433, 2008.

[5] J. Armesto, J. Roca-Pardiñas, H. Lorenzo, P. Arias. (2010). Modelling masonry arches shape using terrestrial laser scanning data and nonparametric methods. *Engineering Structures*, *32*(2), 607-615.

[6] J. Armesto-González, B. Riveiro-Rodríguez, D. González-Aguilera, and M.T.Rivas-Brea. (2010). Terrestrial laser scanning intensity data applied to damage detection for historical buildings. *Journal of Archaeological Science*, *37*(12), 3037-3047.

[7] L. Fregonese, G. Barbieri, L. Biolzi, M. Bocciarelli, A. Frigeri, and L. Taffurelli. (2013). Surveying and monitoring for vulnerability assessment of an ancient building. *Sensors*, *13*(8), 9747-9773.

[8] M.E. El-Tokhey, Abdel-Gawad, A. K., Mogahed, Y. M., & El-Maghraby, A. M. (2013). Accuracy Assessment of Laser Scanner in Measuring and Monitoring Deformations of Structures. *World Applied Sciences Journal*, *26*(2), 144-151.

[9] N. Snavely, S. Seitz, and R. Szeliski. Photo tourism: exploring photo collections in 3d. ACM Transactions on Graphics, 2006, 25(3), 835–846.

[10] Y.Alshawabkeh and M. El-Khalili, Detection and Quantification of Material Displacements at Historical Structures Using Photogrammetry and Laser Scanning Techniques, Mediterranean Archaeology and Archaeometry, Vol. 13, No 2, pp. 57-67, 2013

[11] CloudCompare, http://www.danielgm.net/cc/, accessed 07/2015

First International Conference on Science, Engineering & Environment,
Tsu City, Mie, Japan, Nov.19-21, 2015, ISBN: 978-4-9905958-5-2 C3051

PRICING ANALYSIS OF ELECTRICAL SYSTEM AND BRAZILIAN ENERGY MATRIX DIVERSIFICATION

Vitor Hugo Eiti Moritsugu, Miguel Morales Udaeta, André Luiz Veiga Gimenes, Paulo Helio Kanayama

Energy Group of Electric Energy and Automation Engineering Department / Polytechnic School / University of São Paulo (GEPEA/EPUSP).
São Paulo, Brazil.

ABSTRACT

The objective of this work is to analyze the economics aspects of the poewr sector in Brazil. First one historical analysis is made considering the sector evolution in Brazil, beginning with a free market approach, to an interventionist state until a more regulated environment. During this process, we can verify the disparity between the growing demand and the lack of investment resulting in energy shortages.

The energy sector restructuring created entities such as; EPE (Company for Energy Research), ONS (National System Operator), CCEE (Electrical Energy Commercializing Chamber). Each entity has a role that is detailed in the work. The sector reform resulted in division; Generation, Transmission and distribution. In this division there are two markets the free market and the captive market. In the free market, there are commercializing entities that buy and sell energy (without producing) to independent consumers.

For the captive market, the relation between the generation sector and the distribution is explained. Based in this relation, the customer rate composition is detailed. The government program for energy matrix diversification is presented (named “Proinfa”). This program focus in the wind, biomass and small hydro plants. This program guarantee that the generated energy will be contracted using funds from regular energy fare.

Keywords: Power Sector, Energy Pricing, Energy Planning, IRP

INTRODUCTION

The available infrastructure for a country is extremely important to determine country development. The energy is one of the basis of a country infrastructure. In the present work, we will study the power sector with economic focus related to energy pricing. Considering that the energy sector is a sector that demands great resources for its development an analysis from an economic point of view is extremely relevant.

Based in a historical analysis of the sector we can verify the gap between energy planning and investment attraction. These two factors among others have been responsible for rationing energy in various periods of the history of Brazil.

HISTORICAL ANALYSIS

The first experience in the electricity sector in Brazil was in 1879 for lightning of the central station of the railway. The pioneer was Light (Brazilian Traction Light and Power Company), dominating the consumer market in the electricity sector. Smaller companies were active in the same market but supplying a lower demand.

Initially there was almost no regulation and interference by the government. The companies in this market were free to apply the rate without any government intervention. The first attempt of regulation was the "gold clause" which linked the tariff increase to 50% in the gold price.

The Law 1145 and the Decree No 5704 of Rodrigues Alves government (1903-1904) imposed new conditions. This law defines that hydraulic energy from rivers is responsibility of the federal government.

The action was not effective considering that the agreements between the companies and the states / municipalities were not affected.

In the 20s the Amforp company emerged by purchasing a number of smaller companies in the sector. The companies from the sector were active in the generation, transmission and distribution of energy. This period was characterized by purchases of domestic companies by foreign capital and the increase in the number of companies in the sector.

The public institutions were weak, the regulation was based in contracts for services in the area of power generation. This expansion took place in an

uncoordinated way without interconnections, this created isolated energy islands.

With policy and institutional changes in the country and the change in economic thought propagated by John Maynard Keynes, a new economic scenario was created with liberalism. This scenario indicated a greater state intervention in the economy, different from free trade thought.

In 1934 with the code of Waters the responsibility of the hydroelectric potential use became dependent authorization or concession by the Union. The rates considered operating costs and investments history. Given that rates did not take into account inflation, the sector was severely affected.

Table 1 Average annual growth of electrical energy installed capacity. **Error! Reference source not found.**

Period	**1883-1900**	**1900 -10**	**1910 -20**	**1920 -30**	**1930-40**	**1940 -45**
% a.a	35.7	30.7	8.8	7.8	4.8	1.5

Since the companies did not reinvested in system expansion blackouts occurred. With this scenario the Hydro-Electric Company of San Francisco was created in 1945 to build and operate the Paulo Afonso Power Plant that was inaugurated in 1955. Each state in Brazil created their own electric companies in order to meet the growing demand.

In the 60s the Ministry of Mines and Energy and Eletrobrás were created. To support Eletrobras the Federal Electrification Fund and the Electricity tax were created.

Eletrobrás would be the administrator of the Federal Electrification Fund as a financial agent and could act directly in power generation projects. In the 70s and 80s the basic structure of Eletrobrás was consolidated based in the companies states companies such as, Eletronorte, Eletrosul, Furnas and Chesf.

During this period the investment was provided by a system which had three sources: taxes, income and bank loans from developments.

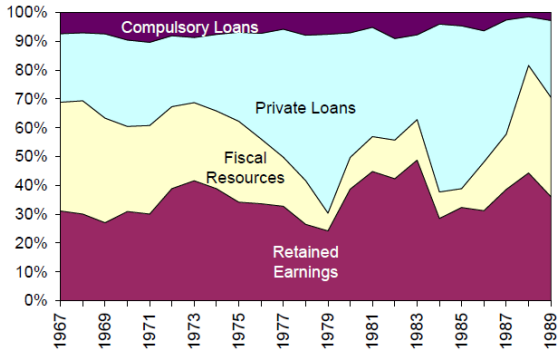

Fig. 1 Financial sources electric sector investments **Error! Reference source not found.**.

In the 70s there was an increase in international interest rates, reducing forms of financing. Thus the investments reduced and debt costs increase.

The financing strategy was based primarily on Eletrobras that from 1974 to 1983 had to increased the investment in the sector from 32.6% to 60.7%. In 1977 a single energy tariff was implemented in the whole country in order to reduce regional disparities. This initiative presented a major challenge given the disparity of the states systems. There were states with higher costs (north and northeast) and states with lower cost (South and Southeast). Thus the states with lower cost were forced to transfer the excess revenues to a fund (Warranty General Reserve - RGG) controlled by Eletrobrás.

During the 90's the companies passed by a process of privatization, this process pretend to increase government income and improve the sector efficiency.

RE-SEB PROJECT - BRAZILIAN POWER SECTOR RESTRUCTURING

In 1998 it was created a New Industry Model. The complete vertical companies composed the old model. In this new model activities were segregated in generation, transmission, distribution and commercialization. In addition to this segregation there was restriction in co-participation of the same agent in two activities. A third agent was created, the commercial, this agent could buy and sell energy without having a plant, acting as a representative of others.

Without the monopoly, private companies could invest in projects and compete in the energy generation and commercialization.

For the operation of this model transmission companies should allow free access to their networks to consumers and generators. They receive the "toll" for the use of the network.

The generation agents use the networks to supply energy to consumers. One example of generation agents are companies that are allowed by the government to explore the hydro resources to

generate electricity. The agents can be divided into generators, independent producers and auto producers. The activity of these agents is open to competition and they have free access to the transmission system.

On the other side of the network are the distribution companies. They are responsible for the distribution system in its concession area. They use the basic network transmission to receive power from the generators.

Another agent is the independent consumer, this agent operate in the free market and have the requirement that the contracted demand is greater than 0.5MW. For demands between 0.5MW and 0.3 MW hiring must be made from encouraged energy sources. The captive customers (regular residential and small consumers) the tariffs are regulated, in contrast to the free market that rates are freely negotiated.

The commercial agent was introduced. They are agents that act on the purchase and sale of energy neither produce nor distribute energy. The classes in this category are traders and Importers / Exporters.

ANEEL is responsible for the regulation and supervision of the electricity sector activities. ANEEL is responsible for; the concessions, authorizations and permissions of new plants, the tariff affordability and competition stimulus.

CCEE is the environment where the purchase and sale of electricity in the National System is done an registered. Also CCEE accounts the "spot" market rate.

In this new model the National System Operator (ONS) is responsible for scheduling, dispatching and operating generation in the National Integrated System (SIN) and the management of the core network.

To minimize impacts made by the ONS, economic mechanisms of power allocation were created. The mechanism is called energy reallocation mechanism (MRE).

The Expansion Planning Coordinating Committee (CCPE) was responsible for the expansion of the Brazilian electricity sector but currently this activity is carried out by the Energy Research Company (EPE).

POWER RATIONING

A number of factors contributed to the electricity rationing, but the fact that the generating and transmission companies were controlled by the federal government ended up damaging the sector. The companies were used as instruments of government policy. The use of these companies prioritized politics over the operation, this kind of administration resulted in lower resources for electric system expansion. Thus when the demand came close to supply the power rationing started.

The government failed to attract private sector investment in the sector and did not have resources to carry out the necessary works.

Due to the lack of resources the expansion has not occurred, resulting in system overload. An attempt to avoid rationing was the Thermoelectric Priority Program - PPT in 2000, this program included the construction of 49 power plants. But the lack transparency in the natural gas price, lack of natural gas transport infrastructure, delays in environmental permits imposed challenges to the program. Only 10 plants were put into operation of 49 planned.

An unfavorable hydrological period, together with the factors already mentioned complemented the energy crisis.

ELECTRICITY MARKET ENVIRONMENT

The market is divided in two environments. The regulated and the free environment.

Generation agents can act in the two. The hiring in the regulated environment is conducted through auctions and in the free market where trading is free.

The demand from the distribution agent is only negotiated in the regulated. The free environment presents the demand from the independent consumer and the commercial agents. The free environment corresponds to 20% of the sector.

GENERATORS AGENTS AUCTIONS

The generators participate in auctions. In the auctions the demand is the object of hiring, there the generators dispute possibility of attending the future demand.

Existent energy auction (A-1)

This auction is characterized by using energy from plants already built. In this case the cost of tariff is transferred to consumers in integral respecting the 1% limit of the hiring volume, above that the transfer is 70% of the price. In this case there is a hiring limitation, each distributor can hire 105% of the contracts that are due in the year of the auction.

New energy auction (A-5)

These auctions consists in the hiring of energy that will be available in 5 years.

New energy auction (A-3)

The A-3 auctions have the planned supply in three years from the date of the auction. These auctions are regular and are predominantly thermoelectric companies. The cost related to the

acquisition is transferred to the tariff according to; in the first three years of the contract the transfer is limited to the Reference Value after three years the transfer is integral.

Adjust auction (A-3)

Adjusts auctions are used to meet short-term market fluctuations with the output or special consumer input. The tariff transfer in this case is limited by the reference value.

END CUSTOMERS TARIFF/PRICING

The distribution sector is a monopoly and it is highly regulated. The monopoly occurs because the competition would not be beneficial for consumers due to high infrastructure cost.

The Distributors revenue is divided between part A and part B.

The part A is composed by the costs that are not manageable by the concessionaire, examples of these costs are, the acquired electricity, transmission charges and industry charges.

The portion B has costs under distributor's responsibility such as operating costs, maintenance and return on capital.

The cost increases in part A are fully repassed. In part B the adjustment is performed by the national price index.

The portion A is composed of: Global Reversion Reserve Quota - RGR, Fuel Consumption Account, Electric Energy Services Inspection Fee, purchase of electricity charges for access and the use of the transmission and distribution systems.

The Fuel Consumption Account - CCC, is a rate of based on thermoelectric generation costs, they are required for regions outside of the interconnected system. This cost involves energy prices, the import of energy and cost of transmission. The refund will be the difference between the cost of energy in isolated regions and the average cost of power and energy traded in the regulated market.

The Global Reversion Reserve is intended to provide funds for expansion and improvement of public services, alternative sources financing and subsidizing low-income class. It is 2.5% of investments limited to 3% of annual revenue.

The Electric Energy Services Inspection Fee is 0.4% of the benefit earned by the energy concessionaire. Before the law n12.783 / 2013 this share was 0.5%.

The dealers also pay a value for the cost of the ONS, the cost of basic network facilities, the cost of Connections facilities and the cost of transport of electricity from Itaipu Binacional.

The Energy Development Quota aims to provide resources, competitiveness of wind power, small hydro, biomass, natural gas and coal, provide the universal service, subsidize the low-income group tariff.

Charges for System Services represents the cost incurred to maintain the system reliability and stability. This charge consists of the payment of the generators that receive dispatch of ONS order to meet transmission constraints.

Research and Development - R & D, requires that distributors must apply 0.5% of operating revenue in research and development and 0.5% in energy efficiency programs.

The portion B consists of; Return on capital cost, operation and maintenance costs and Reintegration Regulatory Quotas.

The capital remuneration rate is calculated using the Weighted Average Cost of Capital. In this context the technical notes ANEEL such as the Technical Note No 184/2007-SER / ANEEL, aim to reward investors with capital compatible with comparable risk applications.

The regulatory reintegration quota consists of depreciation and amortization investment values, to compensate the long life assets depreciation.

The calculation of operating and maintenance costs analyze the results consistency obtained by the company compared with a "reference company".

Rates are adjusted annually by the tariff adjustment index, this index is composed of two portions: economic portion and the financial portion.

To transfer the purchase costs the reference value has been created, this reference value is formed by the weighted average acquisition costs of "new energy".

PROINFA

Proinfa is the Incentive Program for Alternative Sources of Energy, this program was created in 2004 to diversify the Brazilian energy matrix through increased generation from wind farms, biomass, and small hydroelectric plants.

This incentive focuses on the figure of an autonomous independent producer. The producer is characterized by not being controlled or related to a generation concessionaire, transmission or distribution of electricity. These restrictions differ from the independent producer, in this case the independent producer can be hired if the contract value does not exceed 25% of the annual program.

The first stage of the program aimed to implement 3.300MW equally distributed between biomass, wind and PCH. According to Law 10.438 power purchasing is performed according to the technology employed, the lowest level is 80% of the national average price. It was later determined that the value should enable a standard medium project.

The calculation of each economic value will be made by the following criteria.

i) for a period of thirty years considering

hydroelectric plants and twenty years in the case of other technologies;

ii) capital return rate compatible with risks from contractual warranty and price;

iii) efficiency levels compatible with technological development stage and the national energy potential;

iv) average unit costs for determining the amount to be invested in the project;

v) estimated residual value;

vi) forecast of operating expenses, including losses, average costs of connection and use of electrical systems and taxes;

vii) any special conditions of financing;

viii) appropriate relationship between equity and debt capital;

ix) specific discounts provided by law for the use of transmission and distribution network;

x) average levels of sector defaults.

Eletrobras define the amounts paid by electricity and they are defined by the economic value of each source.

Table 1 Electricity Consumption and generation by natural gas.

Source	Type	Amazon and Northest Area BRL /MWh	Other areas BRL /MWh
Biomass	Biogas	166.31	170.12
	Rice Sector	108.17	126.67
	Lumber Sector	116.05	121.85
	Etanol Sector	119.61	89.59
Wind	Gross Factor Capacity ≤ 34%	221.81	213.68
	34 < Gross Factor Capacity < 44%	between 181.46 and 221.81	between 181.46 and 221.81
	44 ≥ Gross Factor Capacity	181.46	191.7
Small Hydroplants	-	114.74	125.09

The second phase of the program aims to increased generation from these sources until they meet 10% of the annual electricity consumption of the country. The compensation will follow the competitive power generation value (VEC) defined as weighted average cost of hydro generation and central thermoelectric natural gas. The contract will have a term of 15 years considering an increase of 15% in energy supply.

CONCLUSION

Brazil went through several periods with different tariff characteristics and government directives.

Initially the foreign-funded companies operated in a deregulated environment. The tariffs were defined by these companies and the government could not direct and integrate investments in the sector. This created energy isles in the country.

By the entry of state companies in market the government could influence and direct investments in order to coordinate the sector to an integrated operation. Eletrobras managed the funds for the sector implementing government policies.

The government imposed a universal tariff that was independent of the region. Thus southern and southeastern companies that had lower costs were required to pass part of their profits to a government reserve. This has made companies inefficient with growing costs.

With greater government control even during macroeconomic crises the tariff was maintained low to reduce the inflation, in addition the financial costs have increased, therefore the electricity sector has not expanded to meet rising demand. We can see that historically the government interfere in the electricity tariff. Interventionist policies in the past have generated negative effects on the sector, resulting in the reduction of investments and creation of large structures difficult to manage.

With the reformulation of the electricity sector RESEB occurred the sector segmentation in order to allow the participation of more agents. By segregating the activities in generation, transmission and distribution, more agents participated in the sector, reducing the state's responsibility as well as the necessary financial support. By assuring the open access to the transmission infrastructure, the generation companies can compete in the free or regulated market.

The tariff system was divided into various formats. For independent consumers buying energy was negotiated in the electricity trading chamber. This body is responsible for registering the agreements between independent generators and independent consumers.

For captive consumers the energy acquisition is by auctions. The demand from distributors is the auction object. The auctions favor the generation of companies that have a lower cost which have the energy supply hired.

The tariff for captive consumers was divided into two components. Component A and Component B.

Component A is relative to costs that are not of the distributor responsibility as example taxes, transmission costs and cost of generated power.

The B component relates to the costs that the company has control. To accomplish this analysis is used a company model. The company efficiency is evaluated by comparison with the company "model".

One way that the government found to direct investments is through programs that use the funds raised by taxes. An example of this action is the initiative of called Proinfa. This initiative aims to diversify the Brazilian energy matrix, in order to stimulate the development of wind power, natural gas and small hydro plants. The stimulus is based on contracts of hiring future generation. These hires are made through funds collected in rates such as energy development quota.

CITATION AND REFERENCE LIST

[1] GOMES, A. C. S.; ABARCA, C. D. G.; FARIA, E. A. S. T.; FERNANDES, H. H. de O. BNDES 50 anos – Histórias Setoriais: Setor elétrico. Rio de Janeiro: BNDES, 2002. 21p. (Publicações BNDES). Disponível em <http://www.bndes.gov.br/conhecimento/livro_setorial/setorial14.pdf> Access in: 18 dez. 2007.

[2] OLIVEIRA R.G. The political economy of the Brazilian power industry reform. Stanford: Program on Energy and Sustainable Development, 2004, 58p. (Working Paper n. 2)

First International Conference on Science, Engineering & Environment,
Tsu City, Mie, Japan, Nov.19-21, 2015, ISBN: 978-4-9905958-5-2 C3051

EFFECT OF DRYING METHODS ON DIETARY FIBER CONTENT IN DRIED FRUIT AND VEGETABLE FROM NON-TOXIC AGRICULTURAL FIELD

Lalita Siriwattananon[1] and Jiradech Maneerate[2]
[1,2]Faculty of Agricultural technology, Rajamangala University of Technology Thanyaburi, Thailand

ABSTRACT

Fruits and vegetables are rich in vitamins, minerals and dietary fiber. However, they are getting spoil easily and their shelf-life is very short after harvest. Especially, fruits and vegetables from organic or non-toxic agricultural field have not contained any preservation reagent. Converted into dried powder form is easy to preserve and use as ingredients. Drying methods may affect to the quality of dried fruits or vegetables. Drying with higher temperature resulted in losing of nutrients but little studies have showed the change in dietary fiber. So, the objective of this study was to compare the effect of drying methods on dietary fiber contents in pumpkin, yardlong bean, tomato, red cabbage and guava. Natural sun drying, hot air oven drying and freeze drying were used to dry those fruit and vegetables. Then, dried fruit and vegetables were grained into a powder and analyze the dietary fiber contents. The results shown that dietary fiber contents in dried pumpkin, yardlong bean, red cabbage and guava were the same tendency, which having higher amounts of dietary fiber from natural sun dry, hot air oven dry and freeze dry, respectively. While, in tomato showed higher content in hot air oven, freeze dry and natural sun dry, respectively. According to the results, it was concluded that the condition of natural sun drying may works efficiently to get higher dietary fiber content in fruit or vegetables.

Keywords: Fruits, Vegetables, Powders, Drying, Dietary fiber

INTRODUCTION

Fruits and vegetables are highly seasonal, rich in vitamins, minerals, dietary fiber, and available in various certain times of the year. In the high season, high productivity makes the selling price decreases and remains a lot of products. Due to an oversupply in the market may result in the spoilage of large quantities. Especially, fruits and vegetables from organic or non-toxic agricultural field are easily to be spoiled as it has not contained any preservation reagent. In an areas having high productivity of non-toxic fruits and vegetables, it is necessary to consider how to make values of an oversupply products.

Various processing techniques were applied to produce new products or preserve it for a long use, while one of the most used technique for preserving fruits and vegetables is to dehydrate and keep it as a dried products or powder, which are the key ingredients in dairy product, cereals, dietetic foods formulated, etc. Dehydration is a preservation technique, in which the moisture content is reduced to a level at which the product is physically or chemically stable [1]. The major function of converting fruits and vegetables into powder form is to maintain the stability and the functionality of the ingredients until they are utilized [2].Various drying methods have been studied and applied by many researchers [3]-[5] to produce dried fruit and vegetable [6], in addition to improve products' qualities. In tropical countries dehydration of fruits and vegetables by sun drying method is a popular practice due to its low cost. However, the quality of those products such as color, texture or dying period may resulted in different quality in different dying methods [7].

Recently, people are concerned more to their consumption quality and food nutrition. Especially, dietary fiber consists of non-digestible carbohydrates and lignin, which is intrinsic and intact in plants that have beneficial physiological effects in humans [8]. Additionally, dietary fiber intake has been linked to the prevention and management of many diseases [9].

It's challenging to preserver fruits and vegetables using dehydration techniques, while remaining its nutrition value. Recently in Thailand, the common used methods by farmers or communities for drying agricultural products are sun drying because of its low cost and there is a sunshine throughout the year. The day time temperature may rise up to 45-55^{o}C or to 60^{o}C in the closed container. A part from sun drying, the hot air oven drying also wildly used in a small enterprises or factory as its advantage in a quality control. Moreover, a freeze drying is became popularly use to product a health products as it is remains higher nutrients comparing to other drying methods. So, to evaluate the effectiveness of drying methods on nutritional value in fruit and vegetables,

three methods of sun drying, hot air oven drying, and freeze drying were employed to make dried of fruit and vegetable, and objective to compare the dietary fiber contents in those fruit and vegetable. The results from this study are expected to be benefited to farmers, commercials or anyone who may use to produce a dried fruit or vegetable.

MATERIALS AND METHODS

Materials

Fruit and vegetables used in this study were planted and harvested as a non-toxic fruit and vegetable from the fields in Nongsue district, Pathum Thani province, Thailand. A fruit of guava (*Psidium guajava* Linn.) and four vegetables of pumpkin (*Cucurbita moschata* Decne.), yardlong bean (*Vigna unguiculata* sub sp. *Sesquipedalis*), tomato (*Lycopersicon esculentum* Mill.) and red cabbage (*Brassica oleraceae* var. *rubra*) were selected for this study as it widely growth in this area.

Methods

All fruit and vegetables were cleaned an outside skin using a dry towel and then sliced into a small piece, having a size of 5 x 10 x 5 mm^3. Sliced guava, pumpkin, yardlong bean, tomato and red cabbage were divided into four groups.

The first group was used for analyze as a fresh product.

The second group was put on the tray and dry under the natural sun dry until the moisture content is significant stable.

The third group was dried using hot air oven at 70^oC until the moisture content is significant stable.

The fourth group was dried using freeze drying method. The materials of fourth group were put into a freezer (temperature -45^oC) for 24 hours, and then moved to vacuum chamber for removing ice crystals as sublimation. Dried materials from the three methods were also used to analyze its physical, chemical, and nutritional properties as well as a fresh material.

Analyses

The fresh fruit and vegetables of guava, pumpkin, yardlong bean, tomato and red cabbage were analyzed moisture content, ash, protein, and dietary fiber were analyzed [10].

Moisture content was measured by drying in an oven at 105^oC for 24 h. Ash was measured by burning in a muffle furnace at about 550^oC for 18 h. Protein was measured by using a Kjeldahl methods and dietary fiber was measured by McCleary Method (AOAC 2009.01)

Statistical Analysis

The experiments were done for 3 repetitions, and the results were analyzed using SPSS program at the significant different at 95% confident level.

RESULTS AND DISCUSSION

1. Moisture content and nutrients in dried fruit and vegetables

A fruit of guava and four vegetables of pumpkin, yardlong bean, tomato and red cabbage were cut and dried under different drying methods of sun drying, hot air oven drying, and freeze drying. As shown in Table 1, the moisture contents of fruit and vegetables after the 36 hours of sun dried, the 24 hours of oven dried, and the 15 hours of freeze dried. The results showed that the three methods of drying were effectively decreased the moisture content in fruit and vegetables, however drying times and moisture contents were different.

Table 1 Moisture content of fruit and vegetables

Fruit/ Vegetable	Moisture Content (%)			
	Fresh	Sun dried	Oven dried	Freeze dried
Guava	87.92^a	9.60^b	6.27^c	4.73^d
Pumpkin	84.57^a	8.62^b	6.72^c	6.72^c
Yardlong Bean	88.74^a	7.41^b	5.58^d	6.82^c
Tomato	90.61^a	14.15^b	8.85^c	8.55^d
Red Cabbage	92.09^a	9.80^c	9.93^b	9.54^d

Note: a-d shown significant different ($p \leq 0.05$) in roll

According to the experimental results, freeze drying method was significantly ($p \leq 0.05$) decreased the moisture contents in most of fruit and vegetables, compared to those of sun drying or oven drying method. This effectiveness may cause due to the process of freeze dying method, which the molecule of water in fruit or vegetable will be freeze and then removed.

Additionally, the amount of ash, protein, and dietary fiber in fresh fruit and vegetables were shown in Fig. 1. In fresh pumpkin has contained the amount of ash, protein, and dietary fiber of 0.78%, 0.37% and 3.50%, respectively. While in a fresh yardlong bean has contained 0.69% ash, 0.60% protein and 1.88% dietary fiber. Guava having ash, protein and dietary fiber of 0.69%, 0.19% and 2.03%, respectively. Red cabbage has contained 0.89% ash, 0.25% protein and 2.96% dietary fiber. In addition to fresh tomato has contained higher ash of 1.16%, but lower in protein of 0.03% and dietary fiber of 1.77.

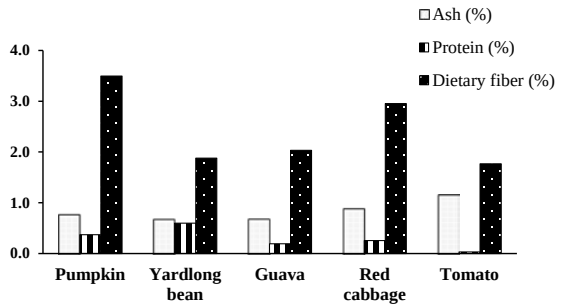

Fig. 1 the amount of ash, protein, and dietary fiber in fresh fruit and vegetables

2. Changing of nutritional contents in dried fruit and vegetables

The experimental results showed that the average nutritional contents of ash, protein and dietary fiber in sun dried guava were 15.66%, 1.17% and 21.86%, respectively. Dried guava (Fig. 2) by hot air oven remained 19.34% ash, 1.17% protein and 24.39% dietary fiber. While, dried guava from the freeze dry having ash, protein and dietary fiber of 12.68%, 1.18% and 18.01%, respectively. Figure 3 shown the differences of nutritional contents in dried guava from three different drying methods, sun drying was significantly different ($p \leq 0.05$) in higher protein and dietary fiber compared with hot air oven or freeze drying.

Fig. 2 Dried guava

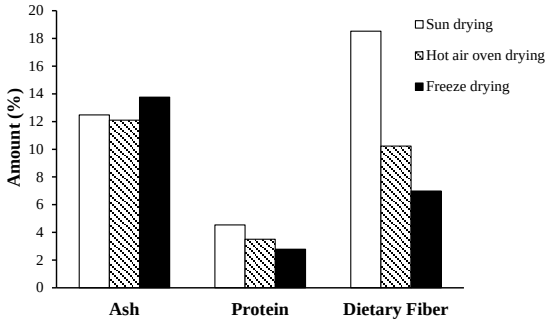

Fig. 3 Nutritional contents in dried guava

Drying pumpkin by different drying methods (Fig. 4) of sun dry, oven dry and freeze dry were measured the amount of ash, protein and dietary fiber as shown in Fig.5. The differences of nutritional contents in dried pumpkin from sun drying was significantly different ($p \leq 0.05$) in higher protein and dietary fiber compared with hot air oven or freeze drying.

Fig. 4 Dried pumpkin

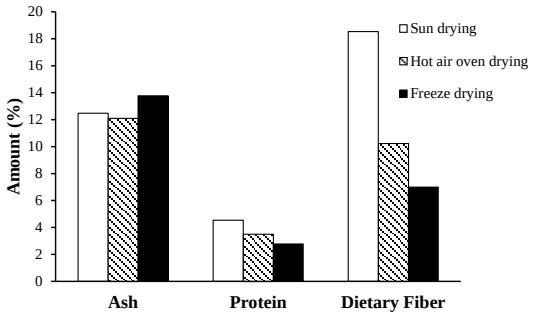

Fig. 5 Nutritional contents in dried pumpkin

Figures 6 and 7 shown the experimental results for dried yardlong bean, which having ash, protein and dietary fiber in sun dried yardlong bean of 12.48%, 4.54% and 18.53%, respectively. Dried yardlong bean by hot air oven remained 12.10% ash, 3.51% protein and 10.23% dietary fiber. While, dried yardlong bean from the freeze dry having ash, protein and dietary fiber of 13.77%, 2.78% and 6.99%, respectively. Additionally, the differences of nutritional contents in dried yardlong bean from three different drying methods, freeze drying was significantly different ($p \leq 0.05$) in higher protein, while hot air oven drying showed higher in dietary fiber.

Fig. 6 Dried yardlong bean

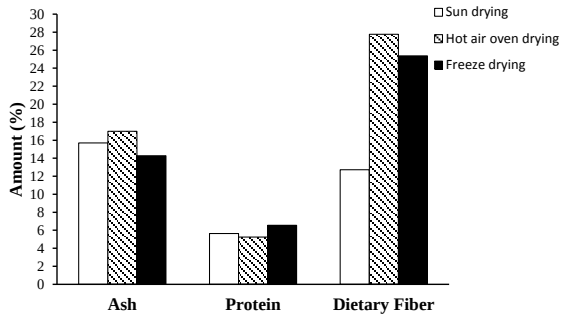

Fig. 7 Nutritional contents in dried yardlong bean

As shown in Figs. 8 and 9, dried tomato by sun drying was significantly ($p \leq 0.05$) higher in the amount of protein (2.47%), while the amount of ash (19.85%) and dietary fiber (13.40%) were higher in hot air oven drying method.

Fig. 8 Dried tomato

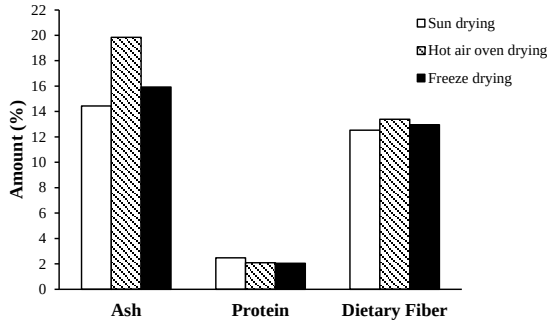

Fig. 9 Nutritional contents in dried tomato

Nutritional contents of dried red cabbage (Fig. 10) by the three different drying methods were shown in Fig. 11, the amount of ash (14.68%) and dietary fiber (59.99%) in red cabbage using sun drying method were significantly ($p \leq 0.05$) higher than that using hot air oven or freeze drying. However, the amount of protein (5.61%) was higher in red cabbage using hot air oven drying method.

Fig. 10 Dried red cabbage

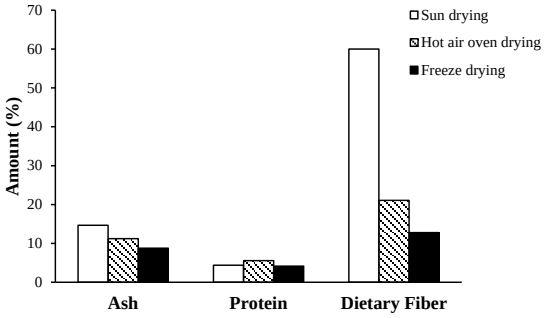

Fig. 11 Nutritional contents in dried red cabbage

Different drying methods have resulted in different quality of fruits and vegetables such as texture, color, moisture, nutritional contents, etc. Changing in quality of dried fruit or vegetable may due to the high temperatures and long drying time [11]. Higher temperature may affected in the dark color, however it does not matter on the nutritional contents. Time of drying is more affected to the changing of nutrients.

CONCLUSION

It was clearly shown that the quality of the dried samples was greatly affected by the method used for drying, especially the prior of drying. The results shown that dietary fiber contents in dried pumpkin, yardlong bean, red cabbage and guava were the same tendency, which having higher amounts of dietary fiber from natural sun dry, hot air oven dry and freeze dry, respectively. While, in tomato showed higher content in hot air oven, freeze dry and natural sun dry, respectively. According to the results, it was concluded that the condition of natural sun drying may works efficiently to get higher dietary fiber content in fruit or vegetables. Sun drying is expected to be an important method of preservation, especially when taking into consideration for economic and ecological aspects.

ACKNOWLEDGEMENTS

This study was granted and supported by Rajamangala University of Technology Thanyaburi (RMUTT), Thailand.

REFERENCES

[1] Jangam, S.V., Law, C.L. and Mujumdar, A.S. "Drying of foods, vegetables and fruits", Vol. 1, 2010, ISBN: 978-981-08-6759-1.

[2] Fitzpatrick, J. J. and Lilia, A. "Food powder handling and processing: Industry problems, knowledge barriers and research opportunities". Chem Eng Process, 2005, 44, 209–214.

[3] Sagar, V. R. and Kumar, S. P. "Recent advances in drying and dehydration of fruits and vegetables: A review". J. Food Sci. Technol., 2010, 47(1): 15-26.

[4] Jayaraman, K. S. and Das Gupta, D. K. "Dehydration of fruits and vegetables-recent development in principles and teniques". Drying Technol., 1992, 10 (1), 1.

[5] Daimante, L. M. Ihns, R., Savage, G. P., and Leo Vanhanen, L. "A new mathematical model for thin layer drying of fruits". International Journal of Food Science and Technology, 2010, 45, pp. 1956-1962.

[6] Que, F., Mao, L., Fang, Y., and Wu, T. "Comparison of hot air drting and freeze drying on the physiochemical properties and antioxidant activities of pumpkin". International Journal of Food Science and Technology, 2008, 2, pp. 1195-1201.

[7] Derya, A., and Mehmet, M. Ö. "Study the effect of sun, oven and microwave drying on quality of onion slices". Journal of Food Science and Technology, 2010. 43 (7).

[8] Institute of Medicine (IOM). "Crossing the Quality Chasm. Crossing the Quality Chasm: A New Health System for the 21st Century". Washington, D.C: National Academy Press. 2001.

[9] Weinstein, J.S., Vogt, T.M., and Gerrior, S.A. "Healthy eating index scores are associated with blood nutrient concentrations in the third National Health and Nutrition Examination Survey". Journal of the American Dietetic Association, 2004, 104, pp. 576–584.

[10] AOAC. "Official Methods of the Association of Official Analytical Chemists. 17thed". Association Official Analytical Chemists., Washington D.C. 2000.

[11] Sumnu, G., Turabi, E. and Öztop, M. "Drying of carrots in microwave and halogen lamp-microwave combination ovens". Lebensmittel Wissenschaft und Technologie, 2005, 38: pp. 549–553.

First International Conference on Science, Engineering & Environment,
Tsu City, Mie, Japan, Nov.19-21, 2015, ISBN: 978-4-9905958-5-2 C3051

TUNING DIFFERENT TYPES OF COMPLEX QUERIES USING THE APPROPRIATE INDEXES IN PARALLEL/DISTRIBUTED DATABASE SYSTEMS

Mohamed CHAKRAOUI, Abderrafiaa ELKALAY, Naoual MOUHNI
Laboratory of applied Mathematics and Computer Science, Faculty of Sciences and Techniques Gueliz Cadi Ayyad University, B.P 549, Av.Abdelkarim Elkhattabi, Guéliz Marrakech, Morocco.

ABSTRACT

in this paper, we discuss the most powerful techniques of tuning parallel/distributed databases. As in engineering, database tuning becomes an inescapable part of big projects since the conception phase of research projects. The needs of companies including big data have increased to databases optimization. Systems that not take into account the optimization rules become heavy after five years of their production; these reasons were of a paramount of importance to prepare this paper. Indexing is the most suitable way to optimize database systems, further one of the top ways of optimizing index is the application of parallelization. In this paper, we will discuss parallelization, and we will practice it with different complex queries and sub-queries using different types of indexes; then we will compare the results gotten from each index. To top it all, the most suitable interference between the major types of index: B*Tree index, Bitmap index, composite parallel index, local parallel index and global parallel index.

*Keywords: tuning, parallelization, sub-query, optimization, interference between indexes, b*tree, bitmap, local index, data partitioning, sub-query.*

INTRODUCTION

To satisfy the needs of data processing speed and decrease the response time of complex queries, optimizing a large database remains essentially to good query writing. A poorly written query can increase the input output gets, which leads to the increasing of the execution time. The most companies' needs have increased to store and analyze the ever-growing data transparently, such as search logs, crawled web content and click streams. Such analysis becomes crucial for businesses in different ways; such as to improve service quality and support novel features, to detect changes in patterns over time and to detect fraudulent activities[1] . As actual computers have powerful processors and very speed RAM, then applications require much higher data operation speed, the traditional RDBMS. Difference between memory and disk in terms of writing and reading speed is very large, so since 1980s, researchers try to move the whole database from disk into main memory to improve the execution time. From the one hand to optimize the latency time, because main memory is faster than disk, and from the other hand, to minimize the interference between different processes when accessing to the data; this type of databases is called Main Memory Databases[2]. Our ultimate topic in this paper is not to discuss main memory databases, but to discuss and analyze different types of indexes and their interferences on a given query.

The most researches and practices focus on two types of indexes, BTree and Bitmap. BTree is three types, local index, global index and composite index. The same for Bitmap index is also three types, bitmap local index, bitmap global index and bitmap composite index. We will make a join query between two or more tables, each one is indexed by a distinct type of index; we analyze every method, and compare between them.

The list-based, view-based, and disk-based methods are other optimization's methods. First, the list-based methods construct a set of lists by sorting all tuples based on their values in each attribute. It then finds the tuples by merging as many lists as needed. Second, the view-based methods pre-compute the results of multiple queries, and store these results as a view. Third, disk-based methods build an index using disk[3].

Commercial optimizers classify query optimization techniques into two dimensions, optimization time and optimization granularity. Optimization time is when optimization decisions are made. However, optimization granularity defines if the optimization decisions are based upon dynamic sampling. In terms of optimization time, some database systems determine query plans in advance at compile time. While others forego pre-computed plans and "route" tuples on the fly at runtime. [4].

Our contribution in this paper is to propose a set of index interference structures and algorithms, which allow us to decrease efficiently the costs of different complex queries in parallel/distributed database systems. These costs are real-time querying or real execution time and CPU cost or input output gets.

The following table describes a part of the table CLIENTS. Is due to flexibility of the document, we cannot specify the full table.

NOCLIENT	NAME	CITY	COUNTRY
1	Moha	Marra	Maroc
3	Hami	Casa	Maroc
25	Khali	Fes	Maroc
32	Salah	Casa	Maroc
39	Karim	Safi	Maroc
43	Houdi	Essao	Maroc

46	Jalal	Sfaqes	Tunisie
50	Charif	Casa	Maroc
55	Jamali	Agadir	Maroc
66	Gill	Donca	United
67	Will	Arizon	USA
70	Berna	Munic	Germany
76	Mak	Curiti	Brazil
78	Bridg	Pointe	Canada
80	Fransi	Yama	Japan
81	Brolin	Rockf	USA
83	Clark	Linz	Australia
85	Favre	Zagre	Croatia
87	Philli	Lyon	France
88	Nakai	New	India

TAB. 1 – A part of the running table CLIENTS

RELATED WORKS

Types of indexes:

the Structured Query Language (SQL) is the most used language in the existing database applications by database researchers as a standard language of querying[5]. SQL was designed for managing data in a Relational or Object Database Management Systems (RDBMS or ODBMS). SQL makes it possible to create, read, update and/or delete records. Actually SQL has many dialects that can well-establishes different query languages, it is widely applied in industrial context. SQL is specified around a set of operations on data stored in tables. Working with object concepts, requires traditional Object-Relational Mapping (ORM). Furthermore, the complexity of such queries would quickly increase beyond levels of feasibility. Even though the creation of nested, recursive queries using standard SQL is available through some implementations and extension modules. Even if there is, no standardized support that would be necessary to match the requirements formulated earlier [6] .

Btree Index:

BTree is a well-organized structure as a tree , so the information retrieval will be easier; a BTree index is based on either one column or more (composite BTree index).

The BTree contains many nodes, the highest node called root node, the descendent node called child node. Each node that have a child called internal node, and the node that has no child called leaf node. Each node have k keys; we suppose that the root node has two keys n and m, the right child keys must be lower than n, the left child keys must be higher than m, and the middle child node keys must be between n and m.

We distinguish between two major types of BTree, B+Tree discussed by David Taniar[7] and B*Tree discussed by Chakraoui Mohamed[8] The Figure 1. Describes a part of tree structure.

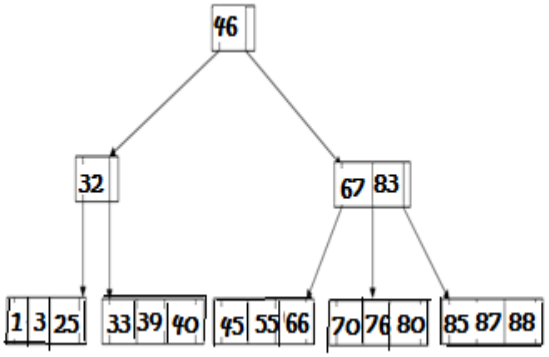

Fig. 1. A part of our B*Tree index structure

Bitmap Index:

The bitmap index is also based on one or more columns; it is based on the bit masks for the separate values on the indexed column or columns.

This type of index is useful when the column of index contains many distinct values, and when the predicate in the query is an equal operation[9].

PARALLELISM

Resources such as memory space or CPU time used for buffering messages or temporal data can be released once a given query has consumed its quantum, being necessary to keep only the partial results calculated until that moment and the query state data used to enable its next quantum in the next super step. Thus processing a given query completely can take one or more super steps. In the case of asynchronous mode of parallel computing, the round-robin principle is emulated by performing proper thread scheduling at each processor to grant each active query its respective quantum of execution[10] .

With the arriving of big data, the classical index takes an important portion of the main memory and execution time; it is not match reduced on a given query. Then researchers have migrate to parallelism as a good way to reduce this execution time, following the number of processors available on a given machine. Parallelism allow executing one query by more than one processor.

We take the following tables as a running example:

CLIENTS (noclient number not null, name varchar2(50) not null, city varchar2(50), country varchar2(25)).

CMD (nocmd number not null, noclient# number, datecmd date, etatcmd char(1)).

LINECMD (noline number not nul, nocmd# number not null, productId number not nul, quantity number not null, amount number not null).

Partitioning by Range

We divide the table CLIENTS by range into three partitions. We give to the first partition the range [0, 40], to

the second partition the range] 40, 80] and to the third partition the rest] 80, +1000].

The Figure 2, describes the partitioning bounds of the underlying table by range.

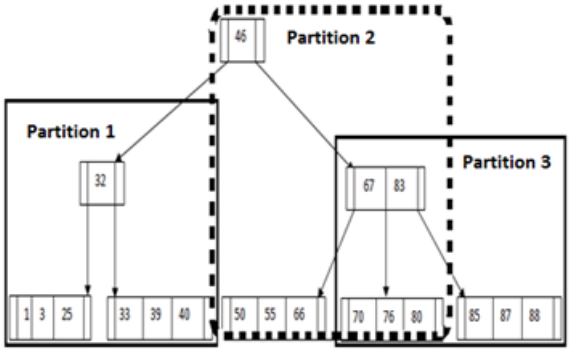

Fig. 2. A part of partitioning B*Tree index by range

Partitioning by List

In this case, the index is based on a varchar column, and then the partitioning can perform as follows: if the second letter of name (partitioning column) is a consonant, we place the record in the first partition. If the second letter of name is a vowel of a letter a or e, the record go to partition two, and finally if the second letter of the name is a vowel of letter i, o or u the record went to the third partition[7].

The following tables illustrate the partitioning of our running example of index B*Tree.

Partition 1	
NOCLIENT	NAME
25	Khalid
50	Charif
78	Bridge
80	Fransis
81	Brolin
83	Clark
87	Phillipp

TAB. 2 – Part 1of index partitioning by list

Partition 2	
NOCLIENT	NAME
3	Hamid
32	Salah
39	Karim
46	Jalal
55	Jamali
70	Bernar
76	Mak
85	Favrea
88	Nakai

TAB. 3 – Part 2 of index partitioning by list

Partition 3	
NOCLIENT	NAME
1	Mohamed
43	Houdi
66	Gill
67	Will

TAB. 4 – Part 3 of index partitioning by list

Global Parallel Index

Global parallel index (GPI) is a BTree structure made on the underlying table globally, GPI do not like to partition the underlying table. However, it could do so; but partitioning methods and intervals on global index and partitioning methods and intervals on the underlying table could differ. One of the disadvantages of global index is when a data on the underlying table is moved or removed, all partitions of a global index are affected, and the index must be completely rebuilt[11].

Local Parallel Index

Local index is a BTree structure that can be partitioned. The partition methods, intervals and bounds must be respectively the same of the partition methods, intervals and bounds on the underlying table. One of the most useful indexes is the local index, among their advantages, the simplicity and the fact that the bounds of their partitions are the same of table partitions[9], and it is very dependent to the underlying table.

Composite Parallel Index (CPI)

Composite parallel index is a BTree index, it can be a global or local parallel index; it is based on two or more columns. Composite index can be useful when the predicate on the query is a logical and between two values on two columns. Parallelism can be exploited by partitioning one or more underlying attributes at the underlying table.

INTERFERENCE BETWEEN LOCAL AND GLOBAL PARALLEL INDEXES

For an efficient execution of the continuous location-dependent queries, incremental search algorithms are required, thus avoiding solving each search problem independently from scratch[12]. Incremental search implies reusing information from previous researches for each query, to obtain the current result without having to recomputing everything each time[13].

Simple Select Query (SSQ)

For search queries, the RDBMS cannot lock any partition, because the select query does not change any underlying data. We take the following query as a running example:

SELECT city FROM CLIENTS where noclient = 39 and name = ‘jack’;

The execution time is described in the Figure 3.

Select Join Query (SJQ)

The same reasoning for the previous section, initially, we partition the table CLIENTS by list following the column ‘name’ as described before; then we create a local parallel index based on the same column ‘name’, and we partition it too following the underlying table partitioning. Secondly, we create a global index based on the table CMD, we take the following query as a testing example.

SELECT datecommande FROM CMD, CLIENTS WHERE CLIENTS.noclient = CMD.noclient AND CLIENTS.name in ‘mohamed’;

The execution time for this interference example is described in Figure 3.

Simple Update Query (SUQ)

Optimizing update query based on a single table is simple; we analyze the index interferences in this type of query by taking two predicates on the same running query each one is based on an index; then compare between obtained results; the following query is as a running example:

UPDATE CLIENTS SET name = ‘ALI’ WHERE noclient = 30;

Following the partitioning methods, if three processors try to send requests to the current table, three cases are possible. The first is when the range of the clause where belongs to one partition, the partition one for example, it will be locked by the first request; but others partitions remain unlocked, and accessible for others processors. Secondly, if the clause where of our update query is extended to two ranges (partitions), for example the partition [0, 40] and the partition] 80, 1000], these ranges will be locked, but the range] 40, 80] remains unlocked; then it behaves like two tables. Nevertheless, if the clause where is based on three ranges, we proceeds like three tables. The following query illustrates this case treatment:

UPDATE CLIENTS SET city = ‘paris’ WHERE noclient = 45 or noclient = 10 or noclient = 120;

Taking x in milliseconds (ms) the execution time cost; the table CLIENTS behavior seems heavy, but when we partition it as described in this section the execution time becomes: x/3 (ms) + interference (ms); with an interference $\approx$ x/9 and x $\in \mathbb{R}$. Due to the parallelism, the SGBD can handle more than one request in the same time, following the number of processors that we have.

Join Update Query on Local and Global Index

Join Update Query (JUQ) throws many problems, as concurrent access when the query is based on more than one partition.

We take the following query as testing example:

UPDATE CLIENTS SET name = ‘thomas’ WHERE CLIENTS.noclient IN (select noclient from CMD where CLIENTS.noclient = CMD.noclient);

We create an index LPI on CLIENTS and an index GPI on CMD. Local parallel index allows the same partitioning rules as the CLIENTS table; then LPI partition the table CLIENTS. However, global parallel index did not partition the underlying table; then the table CMD remains non-partitioned. The execution time is described in the Figure 3.

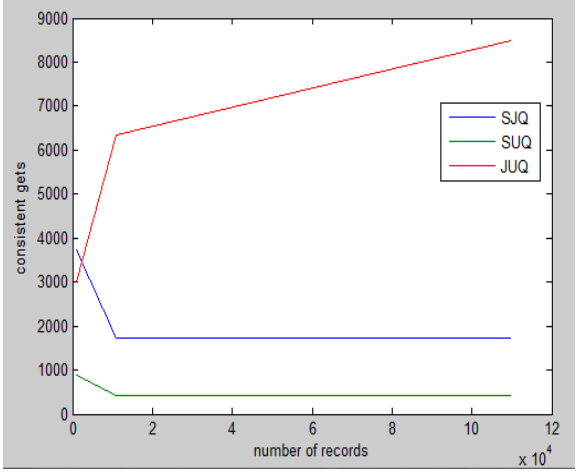

Fig. 3. Number of consistent gets for different query interferences between LPI and GPI

INTERFERENCE BETWEEN COMPOSITE PARALLEL INDEX AND OTHER PARALLEL INDEX ON COMPLEX QUERIES

Interference between composite parallel index and local parallel index

This type of query interference is rarely used, the execution time following the number of operations have to be performed by the RDBMS in the clause where:

UPDATE CLIENTS SET nom = 'simon' where ville = 'paris' AND pays= 'france';

The execution time is described in the Figure 4.

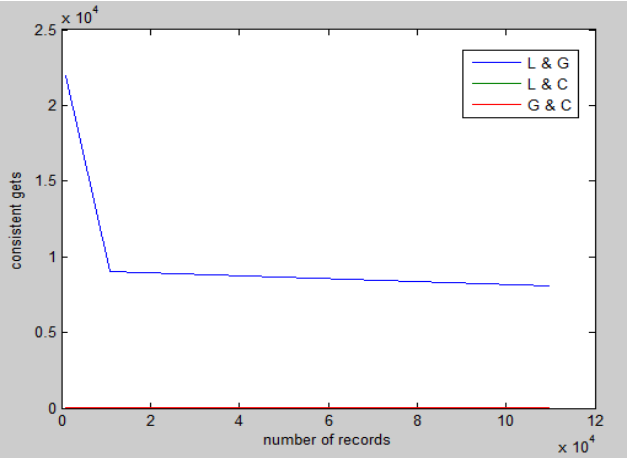

Fig. 4. Number of consistent gets of different index interferences

Interference between global parallel index and composite index

This type of query is slightly close to the last cited interference on term of syntax, but different on term of execution time, following the number of operations have to be performed by the RDBMS in the clause where.

UPDATE CMD SET nocmd = 1234567890 WHERE datecmd = to_date('08-10-2013', 'dd-mm-yyyy') AND etatcmd = 'C';

The execution time is described in the Figure 5.

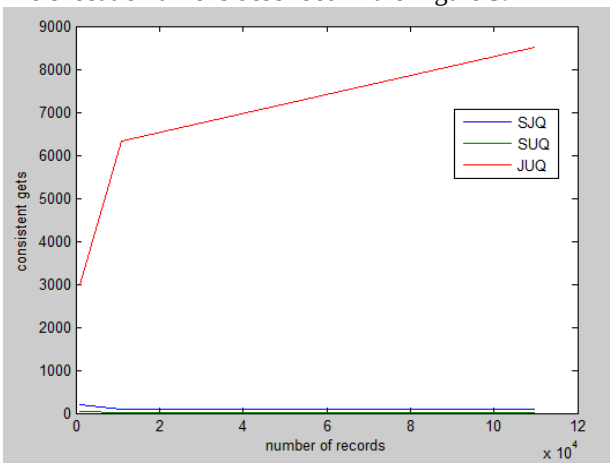

Fig. 5. Number of consistent gets of different type of queries between GPI and CPI

Interference between complex aggregate queries with LPI and with GPI

Complex aggregate query is a query with several query blocks (views or sub-queries) correlated together with a multiple joins[14].

To compare the performance of complex aggregate queries between LPI, GPI and CPI, we use the following two views attended by one query with our running example:

CREATE VIEW V1_AGG as SELECT noline, average = AVG (amount)
FROM LINECMD GROUP BY noline;

CREATE VIEW V2_AGG AS SELECT noline, maximum = MAX (average)
FROM V1_AGG GROUP BY noline;

SELECT V1_AGG.noline, V2_AGG.maximum
FROM V1_AGG, V1_AGG
WHERE V1_AGG.noline = V2_AGG.noline AND V2_1GG.maximum = V1_AGG.average;

The results obtained using this query with our running examples are presented in the Figure 8.

INTERFERENCE BETWEEN BITMAP LOCAL PARALLEL INDEX AND BITMAP GLOBAL PARALLEL INDEX

The bitmap index is the bit masks for distinct values of indexed columns: the binary AND and OR can make the equality tests.

For bitmap index, we do not prefer the global index because it cannot partition the table, but we use the bitmap local parallel index. We take the following as running query:

SELECT name FROM CLIENTS WHERE city = ‘paris’ AND country = ‘france’;

The column city is indexed by bitmap local parallel index; however, the column country is indexed by bitmap global parallel index. The local index has partition the underlying table, but global bitmap index did not partition it, then the local bitmap parallel index is most suitable in this case.

Sub-Query and Index Partitioning

Sub-query is a select query embedded in a clause of another SQL statement. We distinguish between two statements, the outer query or outer statement and the inner query or inner statement. Then we say that the sub-query is nested within the outer query; there are two strategies to executing sub-queries: serial and parallel execution scheduling strategies. When a sub-query is being processed, parallelization techniques must be applied[15]. One of the highlights of sub-queries is via query parallelization, and data partitioning, a query can be segmented to multiple sub-queries; each of them, which contains joins on partitioned data sets and pre-aggregation. The final results are obtained by applying a final aggregation over the results of sub-queries [16].

[17] presents four other optimization methods for indexes that we use its interferences with sub-queries in this paper. Continuous index tuning, periodic index tuning, triggered index tuning and hybrid index tuning. The sub-query reconstruction mechanism consists of reconstructing the set of original queries before dispatching them to the data sources and computing the answers to the original queries based on answers to the reconstructed queries [16].

Sub-query and global parallel index

In this section, we take the same global index used above with the following sub-query:

SELECT datecmd FROM CMD WHERE noclient IN (SELECT noclient FROM CLIENTS WHERE name = 'alain');

The results obtained are showed in Figure 6.

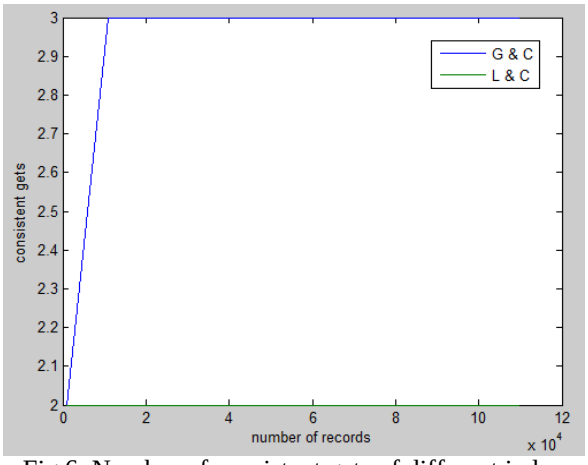

Fig.6. Number of consistent gets of different index interferences

Sub-query and local index

In this case, we use the same sub-query used in section A, with our local parallel index; then we get the results of Figure 7.

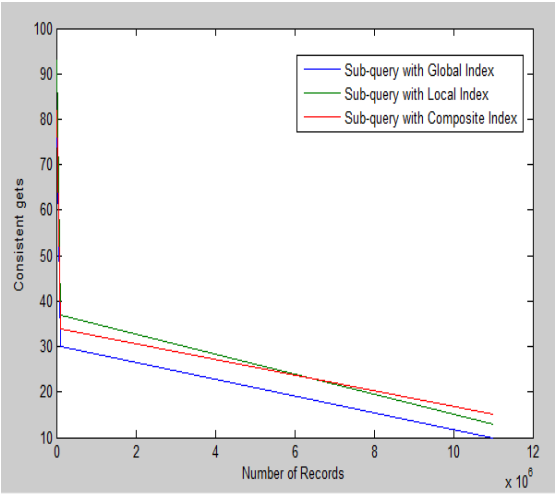

Fig.7. Number of consistent gets in sub-query with different indexes

Sub-query and composite index

With the last sub-query used in section A, indexed by composite parallel index, we get the results of Figure 8.

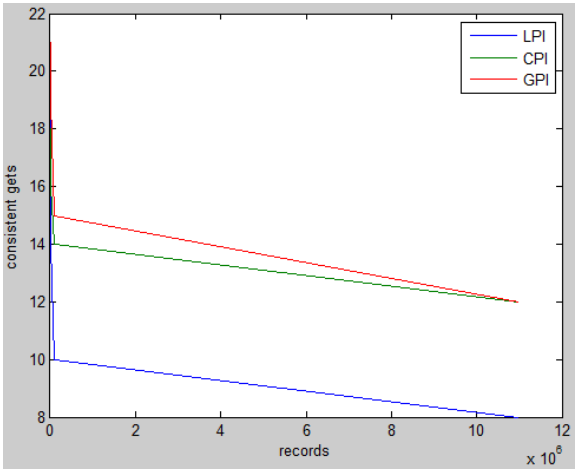

Fig.8. Number of consistent gets in complex aggregate queries with different indexes

Complex sub-query with many types of index

Tables can reference the same table under a different correlation names. Adding two attributes to our table CLIENTS and considering a query to find all the clients who are younger than the oldest client of their gender[18]:

SELECT S1.noclient, S1.name, S1.sex, S1. age
FROM CLIENTS AS S1 WHERE age < (SELECT MAX(age)
FROM CLIENTS AS S2 WHERE S1.sex = S2.sex);

We can also demonstrate the efficiency of the inline views with the following sub-query:

SELECT C.noclient, M.name, CMD.datecmd FROM CLIENTS C, (SELECT LC.amount, CMD.noclient, MCD.nocmd FROM CMD, (SELECT LC.nocmd, amount, quantity FROM linecmd) LC WHERE CMD.nocmd = LC.nocmd) M WHERE M. noclient = G. noclient;

The results of the two last queries are described in Figure 9 and Figure 10.

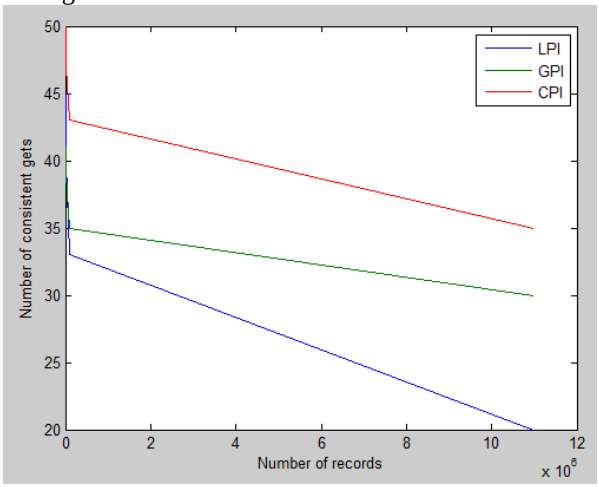

Fig.9. Number of consistent gets in complex sub-queries with different indexes

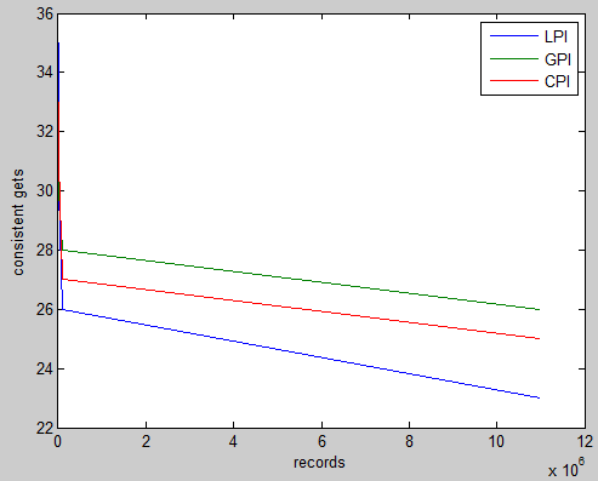

Fig.10. Number of consistent gets in complex sub-queries written on inline views with different indexes

RESULTS AND ANALYSIS

Our experiments are performed on Intel (R) Pentium(R) Dual CPU T3200 @2.00 GHz machine with 3 GB of main memory running a Windows 7 Integral Edition operating system. All queries are performed on an oracle 11g release 2.

The total cost of a parallel synchronous query program is the cumulative sum of the costs of its super steps, and the cost of each superstep is the sum of the following three quantities, the maximum of the computations performed by each processor (CPU cost), the maximum of the messages sent/received by each processor (I/O CPU)[10]. Then we can minimize the cost of a query by minimizing the CPU cost and the number of I/O disk, these costs are the subject of this paper. Analyzing the results obtained, we can get the following explanations:

- SJQ: Following the Figure 3, the interference between local and global index, the number of input output decreases when the number of records increases, once the number of records on the underlying tables outgrew, the number of input output becomes stable and less than 2000.
- SUQ: Following the Figure 3, initially the number of consistent gets was around 2000; then it starts to decrease slightly and then stabilizes when the number of data in the underlying tables becomes too big. SUQ consumes less input output than SJQ.
- L & G: Following the Figure 4, this interference causes many inputs outputs bloc.
- L & C: Following the Figure 4, interference between local and composite allows many and stable input output gets.
- G & C: Following the Figure 6, interference between global and composite index is slightly close to the L & C.
- JUQ: Following Figure 3, and Figure 5, interference between local and global index, join update query increases the number of input-output gets with the increase of the data of the underlying tables.
- Sub-query and different indexes: following the Figure 7, for the small table, the global index and the composite index are the most suitable with sub-query; however when the underlying table is so big, the most suitable index is local parallel index followed by global index with sub-query.
- Complex query and complex sub-query, with different indexes: the results obtained in Figures 9, and Figure 10, by executing complex query, and complex sub-query successively, demonstrate that all time the LPI causes less consistent gets followed by CPI, itself followed by GPI.

Comparative analysis:

As there are different kinds of interferences between different indexes, it is important to analyze the efficiency of each case of interference scheme discussed above.

When it is a join query, is not recommended to use both of local parallel index and global parallel index, each one on a table; but in this case it is advisable to use either a global parallel index or a local parallel index and not both of them.

In the case of a single table, we can use either local parallel index, or global parallel index, or both of them following the type of query; but the number of consistent gets remains close for each case. The use of global or local parallel index on join query with composite index is useful, according to the scheme. Generally, the use of different indexes is useful when the number of data in tables is big.

We can explain the efficiency of LPI by the consistency, between the partitioning of attribute, and the underlying table partitioning; the same reasoning of CPI, thing is not realized for GPI. In many past researches, GPI was the most whished index, but these researches partition just the index, but not both of index and underling table. Finally, we are in favor on our proposed partitioning method for the LPI as the most efficient and optimized index, followed by CPI, and finally GPI.

Using sub-query also prefers the local parallel index as best optimization result.

CONCLUSION AND FUTURE WORK

On the first part of this paper, we introduce different parallel indexes, and a taxonomy of various parallel indexes, and their interferences.

Interferences between different parallel indexes mean that we can use more than one type of parallel index in the same query. Different queries are made in the current paper to conclude the most desirable combinations of indexes.

Following different queries and analysis, we can conclude that the most useful interference is the local

parallel index with the composite parallel index, and the global parallel index with the composite parallel index. These interferences between different indexes and data structures, allows us to propose the optimized model for the use of both multiple indexes.

The second part of this paper studies the uses of sub-queries with different indexes used in the first part, the results obtained are in favor of the uses of the sub-queries with the LPI.

For our future works, we plan to incorporate these methods in the backgrounds of a noncommercial RDBMS like PostgreSQL.

REFERENCES

1. Jingren Zhou, N.B., Ming-ChuanWu, Per-Ake Larson, Ronnie Chaiken, Darren Shakib, *SCOPE: parallel databases meet MapReduce.* Springer, 2012.
2. Xiaoqing Niu , X.J., Jing Han, Haihong E, and Xiaosu Zhan, *A Cache-Sensitive Hash Indexing Structure for Main Memory Database.* Springer, 2013.
3. Ihm, S.-Y., *A partitioned layer-based index for efficient processing top-k queries.* ELSEVIER, 2014.
4. Rimma V. Nehme , K.W., Chuan Lei, Elke A. Rundensteiner, Elisa Bertino, *Multi-route query processing and optimization.* Journal of Computer and System Sciences, 2013.
5. Codd, E.F., *A relational model of data for large shared data banks,*. 1970.
6. Wiet Mazairac, J.B., *BIMQL – An open query language for building information models.* Advanced Engineering Informatics, 2013.
7. Taniar, D. and J. Wenny Rahayu, *Global parallel index for multi-processors database systems.* Information Sciences, 2004. **165**(1-2): p. 103-127.
8. Mohamed CHAKRAOUI, A.E.K., Naoual MOUHNI, *Local Parallel Index in Databases System.* The 4th International Conference on Multimedia computing and systems (ICMCS'14), 2014.
9. Navarro, L., *Optimisation des Bases de Donnees.* Pearson, 2010.
10. Veronica Gil-Costa, M.M., Nora Reyes, *Parallel query processing on distributed clustering indexes.* Journal of Discrete Algorithms, 2009.
11. Lilian Hobbs, S.H., Shilpa Lawande, Pete Smith, *Oracle_10g_Data_Warehousing.* Elsevier Digital Press, 2005.
12. Sun X , Y.W., Koenig S, *Efficient incremental search for moving target search.* IJCAI International Joint Conference on Artificial Intelligence, 2009.
13. Imad Afyouni, C.R., Sergio Ilarri, Christophe Claramunt, *A PostgreSQL extension for continuous path and range queries in indoor mobile environments.* Pervasive and Mobile Computing, 2013.
14. Damianos Chatziantoniou, K.A.R., *Partitioned optimization of complex queries.* Information Systems, 2005.
15. David Taniar, C.H.C.L., *Query execution scheduling in parallel object-oriented databases.* Information and Software Technology, 1999.
16. Feng Chen, R.L., Xiaodong Zhang, *Essential Roles of Exploiting Internal Parallelism of Flash Memory based Solid State Drives in High-Speed Data Processing.* IEEE, 2011.
17. Karen Works, E.A.R., Emmanuel Agu, *Optimizing adaptive multi-route query processing via time-partitioned indices.* Journal of Computer and System Sciences, 2013.
18. Celko, J., *Advanced SQL Programming.* ScienceDirect, 2011.

First International Conference on Science, Engineering & Environment,
Tsu City, Mie, Japan, Nov.19-21, 2015, ISBN: 978-4-9905958-5-2 C3051

THE DEVELOPMENT OF A LOW COST MOTION ANALYSIS SYSTEM: CEKAK VISUAL 3D V1.0

Ghazirah Mustapha[1,3], Mohd Firdaus Abd Razak[2,3], Mohd Salzahrin Mohd Hamzah[3], Nur Hayati Mohd Yahya[1] and Jamaluddin Mahmud[1]
[1]Faculty of Mechanical Engineering, Universiti Teknologi MARA, Malaysia,
[2]School of Civil Engineering, Universiti Sains Malaysia, Malaysia,
[3]Persatuan Seni Silat Cekak Malaysia

ABSTRACT

To date, there is lack of biomechanical characterisation on defensive technique (martial arts) due to the unavailability of appropriate motion tracking system that can be used to characterise the technique in quasi-training environment. Therefore, this paper presents the development of a novel low cost motion analysis system, Cekak Visual 3D v1.0 which is capable to track dual martial art practitioner's skeleton motion in a single frame using integration of Matlab GUIs and Microsoft Kinect. The accuracy and precision of the coordinate data recorded by the system was tested to ensure the quality of the system. The systems perform the tracking motion with a single Kinect which is a combination of various sensors (RGB and depth sensor) thus makes it capable in providing three dimensional coordinate data. The analysis reveals that Visual Cekak 1.0 v1.0 resulted lower percentage error with high internal consistency (Cronbach Alpha, $\alpha = 0.904$). The proposed marker-less system is capable to track and store dual skeleton data in a single session tracking. This capability makes the systems suitable in providing quasi-training and natural setting environment for any martial arts biomechanics investigation. Therefore, we believe that the system provide new concept development for basic research in martial arts biomechanics.

Keywords: Cekak Visual 3D v1.0, Low Cost, Martial Arts, Motion Analysis System, Seni Silat Cekak Malaysia

INTRODUCTION

Motion capture is a process where a movement can be recorded digitally and most commonly used in Martial Arts Biomechanics [1]–[3]. Analysis on trends of publications each year reveals that motion capture technology as a research tools is currently attracting more attention from the martial arts biomechanics community [4]. Shinagawa and Nakajima (1997) for instance, have used this method to analyse human stability by capturing body movement by using a few camera video [5]. The system was then used to analyse Shorinji Kempo, a technique in Chinese Martial Art in order to verify the three dimensional analysis system. The motion capture activities was also observed in Wong and Fok (2007) work on stance position effectiveness study in providing striking force in aspects of Tai Chi Chuan (side kick, roundhouse kick, rising kick, straight punch) with the aid of the smart motion capture system. Recently, Motion Capture (MoCap) Systems like the Vicon (U.K) and Eva Real Time (U.S.A) is available to serve the need in biomechanics study and was observed has been used to characterize pushing and kicking technique [6], [7]. The capability to rapidly track (multiple points) small and high speed movement in three dimensional space [8], [9] maybe the reason on why Motion Capture technology are more popular compared to others available research tools.

Despite its popularity, motion capture technique possesses several limitations. Existing motion capture system requires multiple expensive high performance cameras structured and calibrated within a controlled environment system (dedicated room, tracking suit and lighting capacity) [6], [9], [11], [12]. Due to that, this technology must undergo complicated set up for the advanced hardware that makes the process complex resulting difficulties for the system to be used in quasi-training environment such as sport field and training studio [13]. The cameras restrictions also create another drawback which is the markers placement. The marker attached will probably affect the subject's movement and its placement is time consuming [14].

Factors mentioned encourage the exploration towards low cost and portable solution [10], [15]. There are several potential devices that can replace the role of expensive high performances cameras such as web cam, depth cameras and RGB sensor [16]–[18]. The availability of Kinect™ sensor released by Microsoft Corporation in 2010 offers a great potential to be used as an alternative low-cost motion tracking tool. This cost effective, light and portable devices [14] is capable to substitute the role of digital high speed camera with the ability to

provide an array of three dimensional coordinate data. Thus, this features contributed in a large number of applications such as 3D measurements, angle measurements, gait tracking, postural control observation, motion assessment, rehabilitations, ergonomics, coaching, metrological evaluation as well as the martial arts biomechanics [19]–[22]. Virtual Sensei Lite is an example of Kinect application in martial arts biomechanics study. This system helps the karate practitioners in their training session to characterize their motion as well as to enhance their capacity [10], [21].

Martial art is an affiliation of systematic techniques designed to response towards an attack (defensive technique - evade, fend off, grab, block) and to incapacitate the attacker (offensive technique - kick, punch, strike, punch) [4]. The difficulty on preparing the quasi-fighting environment may contribute to the imbalance research patterns (offensive vs defensive) in martial arts biomechanics study [4]. A systematic defensive technique in Seni Silat Cekak (a traditional Malay Martial Style) for instance can be explored extensively. Doubts on defensive technique capability and effectiveness in deflecting the incoming force (attacking force) [23] may be answered scientifically. The feasibility of Virtual Sensei Lite to characterise offensive technique inspired the development of a system which is compatible to characterise the defensive technique and consider the quasi-training environment for more realistic data (tracking dual skeleton).

In this paper, we describe / proposed a novel low cost motion analysis system to address the problem of preparing the quasi-training environment to obtain the kinematics in the upper and lower extremities of Seni Silat Cekak practitioner during the defensive technique execution. The proposed system was compared with Virtual Sensei Lite system and the accuracy and consistency of the data acquired was observed.

SYSTEM DESCRIPTION

The schematic diagram (Figure 1) simplifies the principle of motion analysis system operation on how the system provides the kinematic of the motion with the help of inverse kinematic approach. In order to develop an alternative system, the proposed system must be able to provide the coordinate / position data that were digitized at equal time increments throughout the movement sequence. The chosen device to substitute the role of high performance cameras for the proposed system is Microsoft Kinect Sensor.

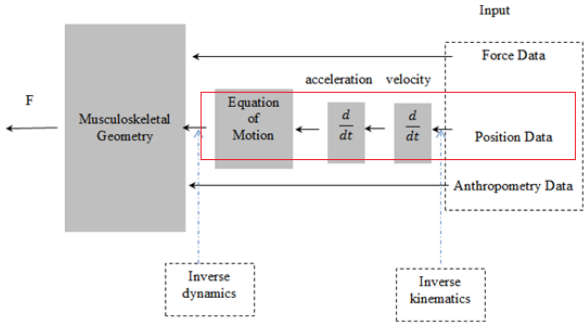

Fig. 1 Principles of Motion Analysis System Operation (Inverse Kinematic Approach)

Kinect Sensor

Microsoft released the Microsoft Kinect Sensor and refer it as a Natural User Interface Device [24]. This device core application is to control the Xbox console via gestures, movements and spoken commands [20]. As such the Kinect capable to drive software as well as manipulate and interact with virtual worlds through whole body movements [24]. Kinect sensor comprising of RGB camera, an infrared (IR) emitter and IR depth sensor [25] Those sensors make it capable to captures depth and color images at 30 frames per second to generate three dimensional (3D) points from an infrared pattern projected on the subject [8]. Researchers have discovered that the depth sensing technology of Kinect could be extended far beyond the gaming application as this technology offers much lower cost than traditional 3D cameras. Moreover, it is easy to operate and may offer a portable 3-D motion analysis system to overcome the limitation of the existing systems that require the laboratory experimental set up [25]. The Kinect sensor has found itself in the mainstream of development of a low cost alternative for measurement and motion of human kinematics analysis [10].

Graphical User Interface: Cekak Visual 3D v1.0

This system able to track and store dual skeleton data in a single session (Figure 2). Cekak Visual 3D will process data in three steps which is position data acquisition of each point, calculate the kinematic data and visualize the kinematic data for each skeletal point. The skeletal data captured / tracked, consisted of three dimensional coordinate data of 20 skeletal joints. The marker-less based system tracked the skeletal joints by software developed using Matlab.

Fig. 2 User interface of proposed system (Main & Sub Window)

The following flowchart (Figure 3) simplifies the steps on how the Graphical User Interface (GUI) of the system was used. It can be seen that the workflow process involved three main processes. The Kinect sensor tracks the movement and the GUI will view the dual skeleton joints in RGB image. (Figure 2). The coordinate data will be recorded and saved in excel file format. The position data recorded was then displayed / playback in order to trim the data for the best frame selection. This information was then will be imported / passed to the tracking and analysis process which applies the numerical approach (central difference method) to compute the time derivation of displacement (velocity and acceleration) for the analysis and data visualization

$$v_i = \frac{s_{i+1} - s_{i-1}}{2(\Delta t)} \quad (1)$$

$$a_i = \frac{v_{i+1} - v_{i-1}}{2(\Delta t)} = \frac{s_{i+2} - 2s_i + s_{i-2}}{4(\Delta t)^2} \quad (2)$$

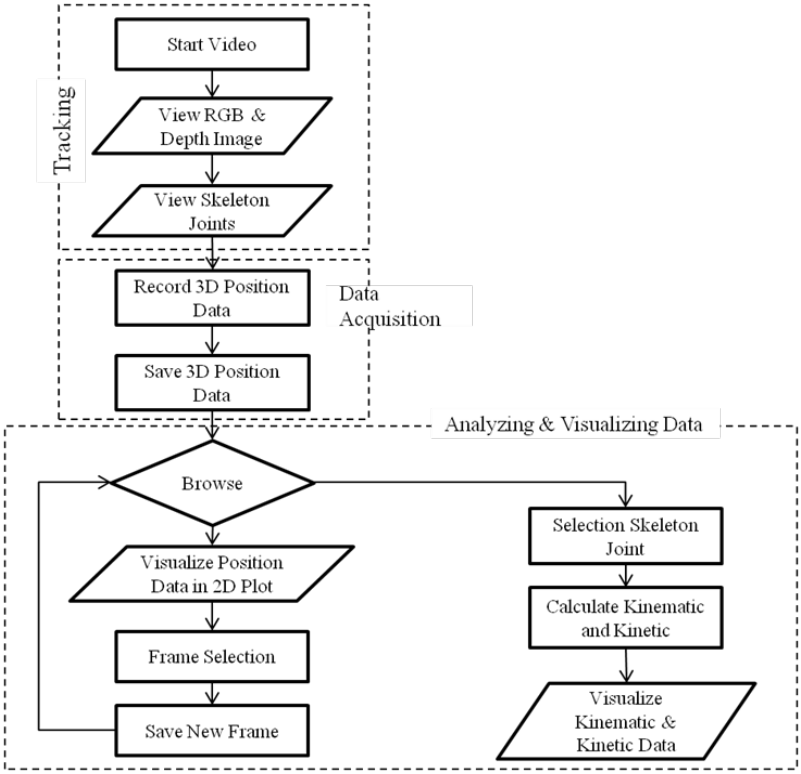

Fig. 3 Workflow of the Cekak Visual 3D v1.0

PRELIMINARY EVALUATION

In order to further the development of Cekak Visual 3D v1.0 an accuracy and consistency test were carried out. The accuracy of a measurement system rely on the degree of closeness of measurement to its true value while precision is the degree which repeated measurements shows the same results [20]. In order to observe accuracy, the differences between the data measured by Cekak Visual 3D and the actual values (manually measured by range finder) were calculated. Finally, the SD and Cronbach Alpha value calculated measure the precision of the system.

Accuracy and Precision

Figure 4 shows the comparison of the accuracy and precision between Cekak Visual 3D and Virtual Sensei Lite based on percentage error, standard deviation and Cronbach Alpha's value. The data from each system were averaged in order to be compared with the manual measurement value. The graphs reveal that Cekak Visual 3D observed lower percentage error which is below 5% and consistent standard deviation, SD. The analysis reveals that Visual Cekak 3D resulted lower percentage error with high internal consistency (consistent Standard Deviation and Cronbach Alpha, $\alpha = 0.904$).

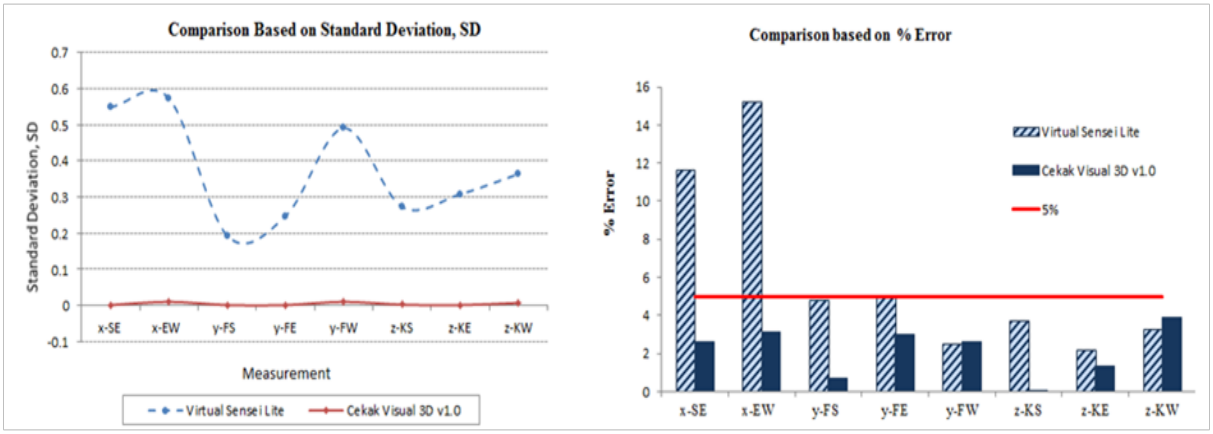

Fig. 4 Accuracy and consistency comparison

CONCLUSION

This paper has proposed a low cost motion analysis system for martial arts purposes. A preliminary evaluation on system capabilities was reported to observe the accuracy and precision of the substitute device proposed. Future research will work on refining the reliability test and enhancement of the system capability to determine the kinetics of martial arts motion.

ACKNOWLEDGEMENTS

The authors would gratefully acknowledge Persatuan Seni Silat Cekak Malaysia for providing research fund to facilitate the study and Ministry of Education Malaysia for sponsoring the research via Universiti Teknologi MARA (grant no. 600-RMI/FRGS5/3(76/2013)).

REFERENCES

[1] W. J. Cynarski and M. Kudlacz, "Injuries in martial arts and combat sports - a comparative study," *Arch. Budo*, vol. 4, pp. 91–97, 2008.

[2] I. Estevan, O. Alvarez, and C. Falco, "Impact Force and Time Analysis Influenced by Execution Distance in a Roundhouse Kick to the Head in Taekwondo," vol. 25, no. 10, pp. 2851–2856, 2011.

[3] I. Estevan, D. Jandacka, and C. Falco, "Effect of stance position on kick performance in taekwondo," *J. Sports Sci.*, vol. 31, no. 16, p. 1815, 2013.

[4] G. Mustapha, J. Mahmud, M. Zakaria, Sulaiman, and W. R. Wan, "Biomechanics research on martial arts – the importance of defensive study," *Arch. Budo*, vol. 11, pp. 187–195, 2015.

[5] Y. Shinagawa and J. Nakajima, "Capturing and analyzing stability of human body motions using video cameras," *Comput. Animat.*, 1997.

[6] F. Quinzi, P. Sbriccoli, J. Alderson, A. Di Mario, and V. Camomilla, "Intra-limb coordination in karate kicking: Effect of impacting or not impacting a target.," *Hum. Mov. Sci.*, vol. 33, pp. 108–119, Sep. 2013.

[7] Y.-T. Chang and J.-H. Chang, "Biomechanical analysis of Tai Chi Chuan Fixed-Step Push-Hand.," *Int. Symp. Biomech. Sport.*, 2010.

[8] K. Yamaoka, M. Uehara, T. Shima, and Y. Tamura, "Feedback of Flying Disc Throw with

Kinect and its Evaluation," *Procedia Comput. Sci.*, vol. 22, pp. 912–920, Jan. 2013.

[9] S. Corazza, L. Mundermann, A. M. Chaudari, T. Demattio, C. Cobelli, and T. P. Aandriachi, "A Markerless Motion Capture System to Study Musculoskeletal Biomechanics: Visual Hull and Simulated Annealing Approach," *Ann. Biomed. Eng.*, vol. 34, no. 6, pp. 1019–1029, 2006.

[10] G. Mustapha, M. S. Aizat, N. H. M. Yahaya, and J. Mahmud, "Measurement System Analysis of VS Lite," *Appl. Mech. Mater.*, vol. 680, pp. 447–450, 2014.

[11] S. M. Machado, R. A. L. Osório, N. S. Silva, and M. Magini, "Biomechanical analysis of the muscular power of martial arts athletes," *Med. Biol. Eng. Comput.*, vol. 48, no. 6, pp. 573–577, Jun. 2010.

[12] T. S.-H. T. Wong and A. S.-L. A. Fok, "Biomechanical Analysis On Some Martial Art Aspects Of Tai Chi Chuan," *J. Biomech.*, vol. 40, p. S453, Jan. 2007.

[13] A. Schmitz, M. Ye, R. Shapiro, R. Yang, and B. Noehren, "Accuracy and repeatability of joint angles measured using a single camera markerless motion capture system," *J. Biomech.*, 2014.

[14] B. Bonnechère, B. Jansen, P. Salvia, H. Bouzahouene, L. Omelina, F. Moiseev, V. Sholukha, J. Cornelis, M. Rooze, and S. Van Sint Jan, "Validity and reliability of the Kinect within functional assessment activities: comparison with standard stereophotogrammetry.," *Gait Posture*, vol. 39, no. 1, pp. 593–8, Jan. 2014.

[15] K. Khoshelham and S. Elberink, "Accuracy and resolution of kinect depth data for indoor mapping applications," *Sensors*, 2012.

[16] C. Krishnan, E. P. Washabaugh, and Y. Seetharaman, "A low cost real-time motion tracking approach using webcam technology.," *J. Biomech.*, vol. 48, no. 3, pp. 544–8, Feb. 2015.

[17] Z. Liu, H. Qin, S. Bu, M. Yan, J. Huang, X. Tang, and J. Han, "3D real human reconstruction via multiple low-cost depth cameras," *Signal Processing*, vol. 112, pp. 162–179, Jul. 2015.

[18] M. Pesce, L. M. Galantucci, G. Percoco, and F. Lavecchia, "A Low-cost Multi Camera 3D Scanning System for Quality Measurement of Non-static Subjects," *Procedia CIRP*, vol. 28, pp. 88–93, 2015.

[19] B. Molnár, C. K. Toth, and A. Detrekői, "Accuracy Test Of Microsoft Kinect For Human Morphologic Measurements," in *International Archives of the Photogrammetry, Remote Sensing and Spatial Information Sciences*, 2012, vol. XXXIX–B3, pp. 544–547.

[20] M. Bueno, L. Díaz-Vilariño, J. Martínez-Sánchez, H. González-Jorge, H. Lorenzo, and P. Arias, "Metrological evaluation of KinectFusion and its comparison with Microsoft Kinect sensor," *Measurement*, vol. 73, pp. 137–145, May 2015.

[21] Alessandro Timmi, "Virtual Sensei Lite," 2011. [Online]. Available: http://www.virtualsensei.it/lite/.

[22] R. A. Clark, Y.-H. Pua, C. C. Oliveira, K. J. Bower, S. Thilarajah, R. McGaw, K. Hasanki, and B. F. Mentiplay, "Reliability and concurrent validity of the Microsoft Kinect V2 for assessment of standing balance and postural control," *Gait Posture*, Apr. 2015.

[23] J. Wąsik, "Chosen aspects of physics in martial arts," *Arch. Budo*, 2009.

[24] J. S. Wheat, S. Choppin, and A. Goyal, "Development and assessment of a Microsoft Kinect based system for imaging the breast in three dimensions.," *Med. Eng. Phys.*, vol. 36, no. 6, pp. 732–8, Jun. 2014.

[25] T. Dutta, "Evaluation of The kinect sensor for 3D Kinematic Measurement in The work place," *Appl. Ergon.*, vol. 43, pp. 645–649, 2012.

Environment

First International Conference on Science, Engineering & Environment,
Tsu City, Mie, Japan, Nov.19-21, 2015, ISBN: 978-4-9905958-5-2 C3051

EVALUATION OF AERMOD AND CALPUFF DISPERSION MODEL PERFORMANCE IN PREDICTING SULFUR DIOXIDE CONCENTRATION FROM PETROLEUM REFINERY COMPLEX IN THAILAND

Sarawut Thepanondh[1,2], Pantitcha Outapa[1], and Suwadi Saikomol[1]
[1,2]Department of Sanitary Engineering, Faculty of Public Health, Mahidol University, Bangkok, Thailand
[1,2]Center of Excellence on Environmental Health and Toxicology (EHT), Bangkok, Thailand.

ABSTRACT

The AERMOD and CALPUFF air dispersion models are tested for their performance in predicting ground level concentration of sulfur dioxide in Thailand. Emission data used in this study are obtained from petroleum refinery complex. Predicted results are compared with those measured data using the year 2012 as a reference year. A set of statistical parameters are employed to evaluate model performance. Overall results indicated that both AERMOD and CALPUFF can provide good results. However, AERMOD can perform better in predicting of extreme end of the concentration distribution at the receptor sites. The maximum ground level concentrations of sulfur dioxide within the modeling domain are about 359 and 456 $\mu g/m^3$ for AERMOD and CALPUFF simulations, respectively. This result indicates that CALPUFF provides more conservative of maximum result than predicted data from AERMOD. The decision to select an appropriate dispersion model in the study is accomplish by using the Multi-Criteria Attribute (MCA) analysis. Result from MCA supports that AERMOD is more appropriate to be applied for study of air dispersion in this area than CALPUFF system.

Keywords: AERMOD, CALPUFF, Sulfur Dioxide, Multi Criteria Attribute, Thailand

INTRODUCTION

Sulfur dioxide (SO_2) is one of a group of highly reactive gasses known as "oxides of sulfur." The largest sources of SO_2 emissions are from fossil fuel combustion at power plants and other industrial facilities. Smaller sources of SO_2 emissions include industrial processes such as extracting metal from ore, and the burning of high sulfur containing fuels by locomotives, large ships, and road equipment. SO_2 is also linked with a number of adverse effects on the respiratory system [1].

The steady-state model AERMOD and Lagrangian puff model CALPUFF are the U.S. Environmental Protection Agency preferred models for demonstrating regulatory compliance in the near field (less than 50 km) and far field (more than 50 km), respectively [2]. However, CALPUFF also be recommended to use for the analysis of air pollution dispersion in the vicinity of emission source in case of complex terrain and wind characteristics. AERMOD assumes that a plume disperses in the horizontal and vertical directions resulting in Gaussian concentration distributions. It does not track the contribution or carry-over of plume from previous hours. Consequently, each hour a plume is dispersed in the direction of that hour's meteorology in a straight-line trajectory [3]. AERMOD's concentration algorithm considers the effects of vertical variation of wind, temperature and turbulence profiles. These profiles are represented by equivalent values constructed by averaging these values over the planetary boundary layer (PBL) through which plume material travel directly from the source to the receptor [4]. CALPUFF is a multi-layer, multi-species, non-steady state puff dispersion model. Dispersion is simulated for discrete "puffs" of species emitted from modeled sources. The puffs are tracked until they have left the modeling domain while calculating dispersion, transformation and removal along the way [5]. It is an atmospheric source-receptor model recommended by the U.S. Environmental Protection Agency for use on a case-by-case basis in complex terrain and wind conditions [6]. In Thailand, both models are regulated as preferred model for an environmental impact assessment (EIA) process. In this study, performances of these models are evaluated for sulfur dioxide dispersion as resulted from emission of petroleum refinery complex in the Eastern seaboard area of Thailand. This study is aimed to evaluate performance of AERMOD and CALPUFF air dispersion models by comparing model predictions with field measurements. Finally, decision of model selection, based on its appropriateness is analyzed by multi-criteria attribute (MCA) analysis using results from statistical analysis of model performance evaluation.

METHODOLOGY

In this study, measured data of ambient sulfur dioxide concentration, obtained from 3 monitoring stations, located in the surrounding area of petroleum refinery complex are used in the analysis. These data are available on an hourly basis. Measured data in the year 2012 and 2013 are used to compare with those modeled data. Emission data are obtained from 13 stack emission sources. Total emission rate of sulfur dioxide is about 120.7 g/s. Emission rate is calculated using amount of sulfur containing in fuel oil and fuel gas on a daily basis. Meteorological data, used for both models are obtained from simulation of MM5 meteorological modeling (the fifth-generation NCAR / Penn State mesoscale model). The gridded data needed by both models are selected from Digital Elevation Model (DEM) data and the terrain data are collected from the Shuttle Radar Topography Mission (SRTM3/SRTM1) database.

Model Configuration

AERMOD (version 8.7) and CALPUFF (version 5.8) of Lakes Environment are used in this study. AERMOD modeling domain is designed for radius of 20 km with the finest grid spacing of 90 m. A 30-km × 30–km model domain having grid spacing of 100 m is established for CALPUFF. Both models are centered approximately on the stack which having highest emission rate. The regulatory modeling options in this research use the default mode of operation for the urban options of dispersion coefficient. Sulfur dioxide ambient concentrations are calculated in 1 hour period on elevated terrain height option. The maximum one-hour concentration for the year 2012 and 2013 at each of the receptor sites are calculated together with the maximum group level concentration within modeling domain to evaluate ability in predicting high concentration of the model

Model performance evaluation

Numerous steps have been taken to ensure that the best model is properly used for each regulatory application and that the model is not arbitrarily imposed. Two types of performance measures are identified: 1) measures of difference and 2) measures of correlation.

Measures of difference represent a quantitative estimate of the size of the differences between predicted and observed values. Measures of correlation indicate quantitative measures of the association between predicted and observed values [7]. In this study, performance of AERMOD was examined for each case using the following statistical parameters: Observed Mean (O_{mean}), Predicted/modeled Mean (P_{mean}), Observed Standard Deviation/sigma (O_{std}), Predicted/modeled Standard Deviation/sigma (P_{std}), Pearson Correlation Coefficient (r^2), Root Mean Square Error (RMSE), Index Of Agreement (IOA), Fraction Bias (Fb), Fraction Variance (Fs) and Robust Highest Concentration (RHC).

The performances of model are tested by comparing the predicted pollutant concentrations of SO_2 with those measured actual values (hourly mean concentrations) at three ambient air quality stations. Comparisons are performed by characterizing the bias. For this purpose, three metrics relating to the bias, the mean bias (e.g., the mean difference between the modeled and the observed data), the root mean square error (RMSE), and fractional bias (Fb) are chosen. The mean bias is easily understood and preserved the sign of bias. The RMSE is a measure of the deviations from the 1:1 relationship and preserves the scale of the original measurements. It is derived from the mean square error which comprised of bias (the extent of over or under estimation) and variance (precision) [8]. The fractional bias is presented because it is the statistic recommended by U.S.EPA. Fractional bias is symmetrical and bounded with values ranging between +2 (extreme under prediction) and -2 (extreme over-prediction). The U.S.EPA guidance for selecting the best performing air dispersion model stated that although a completely objective basis for choosing a minimum level of performance was lacking, accumulating results from a number of model evaluation studies suggested that a factor of two is a reasonable performance target a model should achieve before it is used for refined regulatory analysis [9]. The guidance goes on to recommend the fractional bias as a screening tool for evaluating whether a model should be eliminated from consideration. The fractional variance (Fs) is also presented in the model evaluation in this study.

RESULTS AND DISCUSSION

For the paired ensemble means performance objective, the dataset was based on the union of the predicted and observed concentrations [10]. In this study, only predicted and observed concentration pairs greater than zero were considered. Missing data of measured concentrations were replaced by average values of the hour before and after that missing time. Results of statistical analysis are summarized in Table 1 and Table 2. Results from statistical evaluation indicated that there were differences between the model and observed values. However, these differences were much lower than their respective predicted standard deviations (RMSE < Pstd), indicating that accurate results were being shown by the model. Generally, both models performed well for the prediction of average

concentration at every monitoring site; at least to within the accuracy of the observations (standard deviation). In general, it is found that AERMOD is more accurate than CALPUFF (as determined by fraction bias and root mean square error). AERMOD also provides better result than CALPUFF in determining of robust highest concentration (RHC). The RHC is preferred to the actual peak value and represents a rounded estimate of the highest concentrations, based on a tail exponential fit to the upper end of the distribution. With this procedure, the effect of extreme values on model comparison is reduced [11]. Results from robust highest concentration indicated that AERMOD provided slightly better result in predicting extreme end of SO_2 concentration than CALPUFF (percentage of overall difference in RHC from AERMOD was about 33 % while this value from CALPUFF prediction was about 35%). However, both models do not perform well in predicting the extreme concentration at station "A". These results can be explained by the fact that station "A" is located very close to emission sources in the model simulations. This assumption is supported by the conceptual framework of a Lagrangian puff model which is better suited for long range transport where winds vary spatially across the model domain. Hence, Lagrangian puff models may be preferable for dose reconstruction where model domains can be large and where the assessment question is an unbiased estimate of concentration in time and space [10].

It was found that the values of Fb calculated from predicted data from both model were positive values indicating under-prediction of the simulated results. Good performance was identified with value close to zero. The maximum Fb were found for simulated data at station "A" while the best model performances were found at station "B" (Fb = 0.21 and 0.35 for AERMOD and CALPUFF simulations, respectively) as shown in Fig 1.

The maximum ground level concentrations of sulfur dioxide within the modeling domain in the year 2012 are 359 and 456 µg/m^3 for AERMOD and CALPUFF simulations, respectively. CALPUFF also provides higher predicted maximum concentration than AERMOD in the simulation year of 2013 (AERMOD = 339 µg/m^3, CALPUFF = 365 µg/m^3). Results of the maximum concentration in each grid cell from simulation of both models are illustrated in Fig 2 and Fig 3. This finding indicates that the predicted maximum ground level concentrations within modeling domain computed from AERMOD are slightly lower than those obtained from CALPUFF simulations.

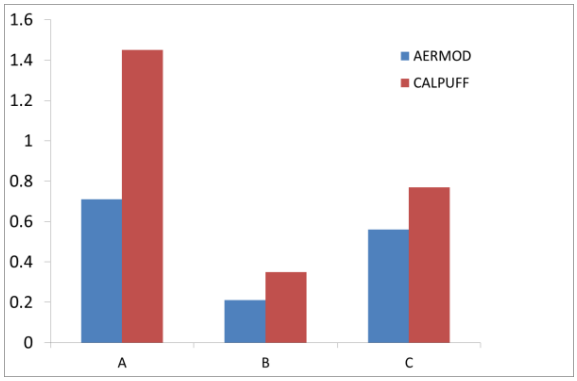

Fig 1 Model performance evaluation using Fb

Table 1 Comparisons of model performance in predicting high concentration (unit :µg/m^3)

Model	Monitoring site	RHC	
		measured	predicted
AERMOD	A	129.94	151.55
	B	91.54	38.4
	C	24.47	17.76
CALPUFF	A	129.94	46.64
	B	91.54	94.63
	C	24.47	33.68

Table 2 Comparisons of overall performance of the models using statistical analysis

Model	Monitoring site	Omean (µg/m^3)	Pmean (µg/m^3)	Ostd	Pstd	r^2	RMSE	IOA	Fb	Fs
AERMOD	A	4.05	5.77	4.17	10.45	0.81	9.76	0.82	0.71	0.19
	B	2.92	9.25	1.2	7.55	0.91	4.3	0.93	0.21	0.16
	C	4.43	3.52	6.08	2.47	0.88	3.47	0.77	0.56	0.48
CALPUFF	A	4.05	4.23	4.17	4.72	0.87	28.38	0.48	1.45	1.28
	B	2.92	13.39	1.2	16.84	0.96	9.3	0.89	0.35	-1.34
	C	4.43	4.93	6.08	4.99	0.86	6.71	0.66	0.77	-0.15

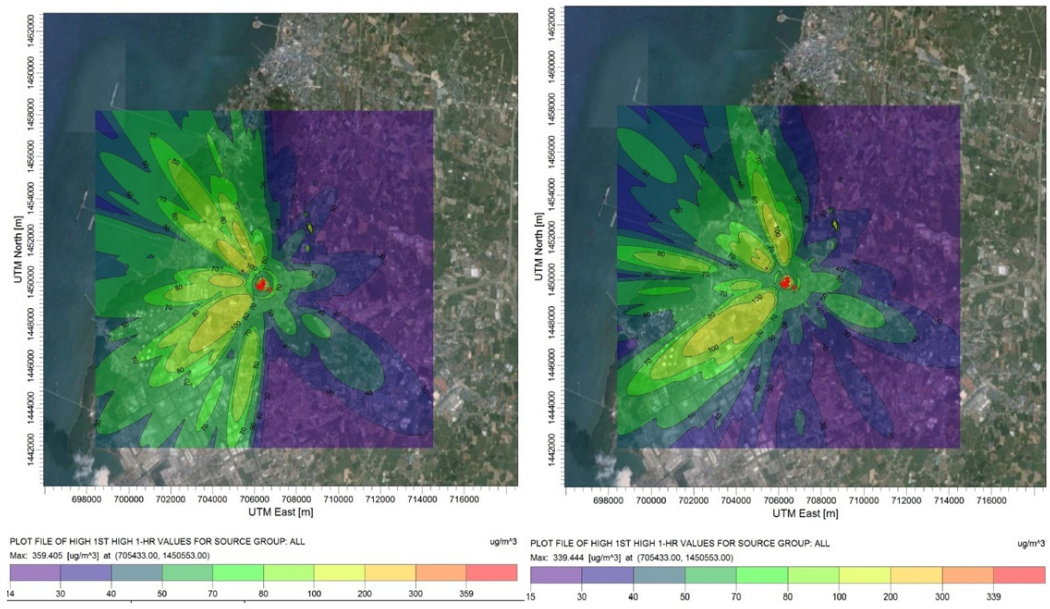

(2012) (2013)

Fig 2 Plot file of the highest 1-hr concentration of SO_2 in µg/m^3 (AERMOD result)

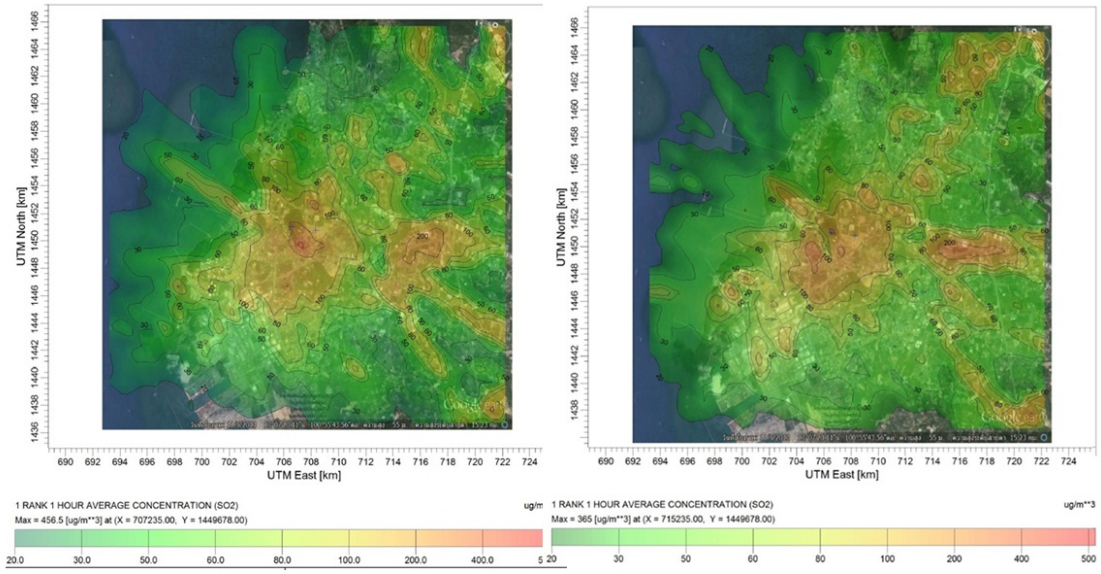

(2012) (2013)

Fig 3 Plot file of the highest 1-hr concentration of SO_2 in µg/m^3 (CALPUFF result)

The decision to select an appropriate dispersion model in the study is accomplish by using the Multi-Criteria Attribute (MCA) analysis. MCA approach is a tool to calculate overall scores and rankings based on the scores given for each individual option [12]. This assessment method does not try to monetize everything, but to supply and unrefined view on the many different dimensions of the multiple effects of a certain policy/project option. In this study, 4 criteria are set for selection of the most appropriate model. They are 1) availability of meteorological data; 2) percentage of difference of measured and predicted RHC; 3) index of agreement and 4) factional bias. Each criterion is weighted as 25% of the total score. Details of score given to each criterion are as described in Table 3. Availability of meteorological data for using in CALPUFF model was given as 50% while the meteorological data for AERMOD was rated as 75%. In Thailand, the number and spatial distribution of meteorological

monitoring stations may be limited. Therefore, data of observed wind characteristics varied spatially across the model domain are insufficient for CALPUFF simulation. Result of the MCA analysis indicates that AERMOD is more appropriate choice for model selection in this study as shown in Table 4. It should be noted that even though the availability of meteorological data were weighted as the same score for AERMOD and CALPUFF, total score of MCA of AERMOD was still slightly higher than the total score of CALPUFF.

Table 3 Criteria and indicators for scoring

Score	% difference in RHC	IOA	Fractional bias
100	0 - 20	0.8 - 1.0	< 0.2
75	20 - 50	0.6 - 0.8	0.2 - 0.5
60	-	-	0.5 - 0.75
50	50 -75	0.5 - 0.6	0.75 -1.0
25	75 - 100	-	-
10	>100	< 0.5	> 1.0

Table 4 MCA analysis for the selection of appropriate model

Criteria	Score	AERMOD	CALPUFF
Data availability (Meteorological data)	25	18.75	12.5
% Difference of RHC	25	18.75	18.75
IOA	25	18.75	18.75
Fractional bias	25	15	12.5
Total	100	71.25	62.5

CONCLUSIONS

The AERMOD and CALPUFF air dispersion models are tested for their performance in predicting ground level concentration of sulfur dioxide (SO_2) in Thailand. Emission data used in this study are obtained from petroleum refinery complex. Predicted results are compared with those measured data using the year 2012 as a reference year. In this study, measured data of ambient air concentration, obtained from 3 monitoring stations on an hourly basis were used for model validation.

A set of statistical parameters are employed to evaluate model performance. Overall results indicated that both AERMOD and CALPUFF can provide good results. However, AERMOD can perform better in predicting of extreme end of the concentration distribution at the receptor sites. Overall predicted results obtained from AERMOD simulations were shown to have less bias with those measured results as compared with predicted data from CALPUFF and may be considered as the appropriate calculation for prediction of annual average concentration. As for selection of appropriate model, the multi criteria attribute (MCA) analysis is applied here to assist as a decision tool for evaluation. Result from MCA also supports that AERMOD is more appropriate to be applied for study of air dispersion in this area than CALPUFF system.

ACKNOWLEDGEMENTS

The authors sincerely thank the Pollution Control Department for providing observed data used for model performance evaluation in this study. This study was partially supported for publication by the China Medical Board (CMB), Faculty of Public Health, Mahidol University, Thailand. We also would like to thank the Faculty of Graduate Studies, Mahidol University in providing us travel grant for the presentation of this work.

REFERENCES

[1] U.S. EPA (United States Environmental Protection Agency), 2014. Sulfur Dioxide. http://www.epa.gov/airquality/sulfurdioxide /index.html. Accessed 30 January 2015

[2] Rood A, Performance evaluation of AERMOD, CALPUFF, and legacy air dispersion models using the Winter Validation Tracer Study dataset. Atmospheric Environment, 89, 2014, pp. 707–720.

[3] EPA., User's guide for the AMS/EPA regulatory model-AERMOD. USA, 2004.

[4] Cimorelli, A.J., Perry, S.G., Venkatram. A., Weil, J.C., Paine, R.J., Wilson, R.B., Lee, R.F., Peters, W.D., Paumier, J.O., AERMOD: description of model formulation. U.S. Environmental Protection Agency Report. EPA 454/R-03-002d, North Carolina, 2003, 85 pages.

[5] Scire J., Strmaitis D., and Yamartino R, A user's guide for CALPUFF dispersion model (ver.5). Earth Tech Inc.USA. 2000.

[6] Macintosh, D., Stewart, J., Myatt, T., Use of CALPUFF for exposure assessment in a near-field, complex terrain setting. Atmospheric Environment. Vol 44, 2010,pp. 262-270.

[7] Kuma, A., Dixit, S., Varadarajan, C., Vijayan, A., Masuraha, A., Evaluation of the AERMOD dispersion model as a function of atmospheric stability for an urban area. Environmental Progress 25(2), 2006, pp.141 – 151

[8] Pratt, G.C., Wu, C.Y., Bock., Adgate. J.L., Ramachandran, G., Stock, T.H., Morandi, M., Sexton, K., Comparing air dispersion model predictions with measured concentrations of

VOCs in urban communities. Environmental Science and Technology 38, 2004, pp. 1949-1959.

[9] US.EPA (United States Environmental Protection Agency), 1992. Protocol for determining the best performing model. USA.

[10] Rood, A.S., Performance evaluation of AERMOD, CALPUFF, and legacy air dispersion models using the Winter Validation Tracer Study dataset. Atmospheric Environment 89, 2014, pp.707-720.

[11] Chusai C, Manomaiphiboon K, Saiyasitpanich P, Thepanondh S. NO_2 and SO_2 dispersion modeling and relative roles of emission sources over Map Ta Phut industrial area, Thailand. J Air and Waste Management Association 62(8), 2012, pp. 932-945

[12] Stockholm Environment Institute. Greenhouse gas mitigation screening exercise for LEAP and excel, 2012.

First International Conference on Science, Engineering & Environment,
Tsu City, Mie, Japan, Nov.19-21, 2015, ISBN: 978-4-9905958-5-2 C3051

ON THE LONG-TERM VARIATIONS OF THE SURFACE HYDROGRAPHIC ANOMALIES IN THE NORTHERN HEMISPHERE

Ibrahim A. Maiyza, Tarek M. El-Geziry, Hussein I. Maiyza and Mohamed S. Kamel
National Institute of Oceanography & Fisheries, Alexandria, Egypt

ABSTRACT

Many researchers worldwide have spotted light on and concluded the cyclic nature of long-term marine climatology variations rather than continuous increasing trends. The authors of the present study initially investigated these variations in the South-eastern Mediterranean Sea. Their results determined cyclic behaviour and expanded the focal point of interest from local to regional scale depending on the cyclic occurrence of the Nile drought and agreed with the detected 70-year cycle determined by other researchers. Using the linear and quadratic regression approaches, the present work aims at modelling the general long-term trend in the monthly surface hydrographic anomalies (MSTA & MSSA), for 63 years (1948-2010), within the North Atlantic and Pacific Oceans. The paper also compares the present results with that obtained by the same techniques and period at the same latitudes in the South-eastern Mediterranean Sea.The MSTA variations in the two oceans reflect general linear increases (opposite to that in South-eastern Mediterranean Sea) and two quadratic concave-up (cyclic) forms with different magnitudes. The years of minimum occurrence in the two oceans precede that in the South-eastern Mediterranean basin. The linear trends of MSSA are in contrast. While the North Atlantic examined a general trend of increase (as in the South-eastern Mediterranean Sea), the North Pacific had a rate of decrease. The MSSA quadratic regression model of the former (as in the South-eastern Mediterranean basin) reflected a concave-up (cyclic) form, with same minimum occurrence in 1980, while the later did not show any cyclic trend.

Keywords: North Atlantic Ocean; North Pacific Ocean; Surface Temperature; Surface Salinity; Anomalies

INTRODUCTION

The long-term variation in the climatology of marine environment is one of the important issues addressed by many researchers worldwide. This involves studies on inter-annual, decadal and longer time scales of the hydrographic and meteorological parameters, in relation to air-sea interaction processes and fish catch. Examples of such research include [1]-[18] and others. Many have spotted the light on and concluded the cyclic nature in the long-term variations of the investigated phenomena rather than the widely known concept of continuous increasing trends.

On local scale, the authors of the present study initially investigated the long-term variations in the hydrography [10],[11]; the climate [19]; the wind pattern [14] and fish catch [20] in the South-eastern Mediterranean Sea. Their results determined cyclic behaviour in the changes of the studied parameters, and expanded the focal point of interest from local to regional scale [6] depending on the cyclic occurrence of the phenomenon of the Nile drought. Moreover, their results came in agreement with the detected 70-year cycle determined by other researchers worldwide, *e.g.* [21]-[25].

The present work aims at modelling the general long-term trend of changes in the surface hydrographic anomalies of the Northern Hemisphere within the Atlantic and the Pacific Oceans. This is carried out by applying the same techniques of linear and quadratic regression approaches, which were applied by the authors in their previous research. The paper also attempts to compare the results of the present study within both North Atlantic and North Pacific Oceans with those at the same latitudinal area in the South-eastern Mediterranean Sea; in order to declare a more comprehensive relationship between the three areas, considering that the Mediterranean is an important marginal sea to the Atlantic Ocean and the Pacific is a vital water body being the largest ocean in the world.

DATA AND METHODS OF ANALYSIS

Northern Hemisphere is represented and examined in the present work through two water bodies within the North Atlantic and Pacific Oceans.

Figure 1 shows the areas of investigation in the present work. Four grids of the size 5°x3° were constructed in the North Atlantic Ocean to cover the geographical area extending between latitudes 30° 00’ and 33° 00’ N and longitudes 20° 00’ and 40°

00' W. Meanwhile, four grids of the size 10°x3° were constructed in the North Pacific Ocean covering the same latitudinal area but extend longitudinally from 140° 00' to 180° 00' W.

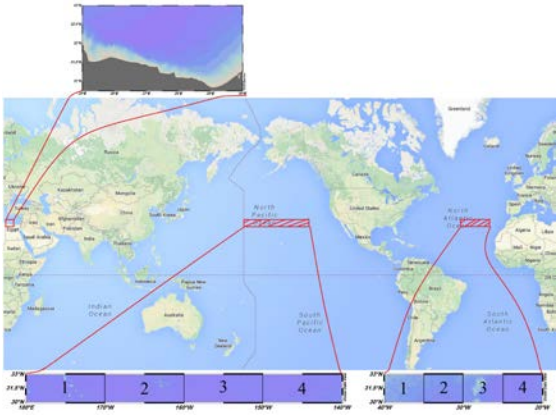

Fig. 1 Grids within the North Atlantic and the North Pacific Oceans and the previous investigated (same latitudinal zone) South-eastern Mediterranean Sea region.

Surface hydrographic data (temperature and salinity) were collected for 61 years (1948-2008) of surface temperature and for 63 years (1948-2010) of surface salinity; in order to examine the long-term variations in the surface hydrographic anomalies in the specified areas within the two oceans. The data have been selected, to cover the same period of the South-eastern Mediterranean file, from [26] data bank and from [27] archive (2005-2010).

In the present work the surface layer is taken as the mean for the upper 20 m layer [15],[28],[29]; in order to compensate the diurnal variation.

The monthly anomalies of surface temperature and of surface salinity have been calculated, for every grid, in the two specified oceanic areas using the same approach, described hereunder:

The mean monthly surface temperature over the period of 61 years and the monthly mean surface temperature for every month in the whole data set are calculated. This is essential in order to secure a full elimination of any daily or annual cycles' effects on the final calculations and results.

The deviation from the monthly mean is computed on monthly basis to express the Monthly Surface Temperature Anomaly (MSTA), using the following equation:

$$\Delta T = T - T_m \quad (1)$$

where,

ΔT is the MSTA (°C),

T is the mean monthly surface temperature (°C, mean for specific month every year) and

T_m is the monthly mean surface temperature (°C, mean for specific month of all years)

The same calculation has been performed for the 63-year data set of the surface salinity. The Monthly Surface Salinity Anomaly (MSSA) is, therefore, mathematically expressed as:

$$\Delta S = S - S_m \quad (2)$$

where,

ΔS is the MSSA (°C),

S is the mean monthly surface salinity (mean for specific month every year) and

S_m is the monthly mean surface salinity (mean for specific month of all years).

The general trends of the variations in the MSTA and in the MSSA within the two oceans, representing the Northern Hemisphere in the present study, are examined using both linear and quadratic regression approaches. The representative equations for each regression model are generated and the trends of variations are drawn. This technique was previously applied by the authors to examine the long-term variations in the same surface hydrographic anomalies in the South-eastern Mediterranean Sea at the same latitudinal zone.

RESULTS

Trends of Variations in the North Atlantic MSTA:

Figure 2 shows the variations in the North Atlantic MSTA over the period 1948-2008. The general linear trend of variation reflects an increasing trend with a rate of 0.011°C/month, *i.e.* 0.13°C/year. This is mathematically expressed by the following Equation:

$$y = 0.0112\,x - 22.324 \quad (3)$$

On the other hand, the quadratic trend of the North Atlantic MSTA variations shows a parabolic curvature, the minimum of which occurs in 1966. The quadratic regression is expressed by the following Equation:

$$y = 0.0003\,x^2 - 1.3663\,x + 1342.3 \quad (4)$$

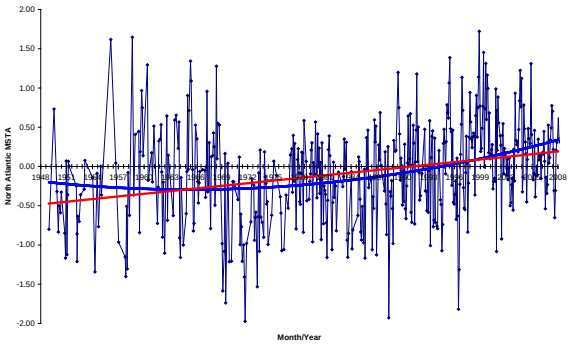

Fig. 2 Trends of variations in the North Atlantic MSTA during the period (1948-2008).

Trends of Variations in the North Atlantic MSSA:

The regression models, which describe the variations in the North Atlantic MSSA, are graphically shown in Fig. 3. The linear trend reflects a general increase in the surface salinity with a rate of 0.0037/month, *i.e.* 0.045/year. The linear trend of variations over the 63 years of investigation is mathematically expressed by the following Equation:

$$y = 0.0038\ x - 7.5134 \quad (5)$$

On the other hand, the quadratic trend of the long-term variations in the North Atlantic MSSA is graphically represented by a concave up parabola, the minimum of which occurs in 1980. This is mathematically expressed by the following Equation:

$$y = 0.0002\ x2 - 0.5973\ x + 589.59 \quad (6)$$

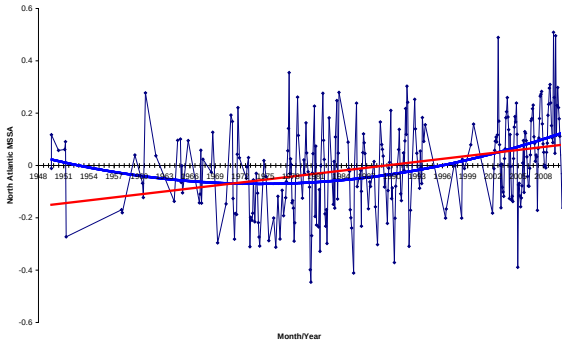

Fig. 3 The regression models of the North Atlantic MSSA during the period (1948-2010).

Trends of Variations in the North Pacific MSTA:

Figure 4 represents the monthly variations in the North Pacific MSTA over the period 1948-2008. The linear trend of variations reflects a very weak increase in the MSTA over the period of investigation with a rate of 0.004°C/month, *i.e.* 0.048°C/year. This is mathematically expressed by the following Equation:

$$y = 0.004\ x - 8.1455 \quad (7)$$

On the other hand, the quadratic regression model of the North Pacific MSTA reflects a parabolic trend of variations, which can be expressed by the following Equation:

$$y = 0.0009\ x^2 - 3.3719\ x + 3341.1 \quad (8)$$

The minimum occurrence of the North Pacific MSTA was in 1982.

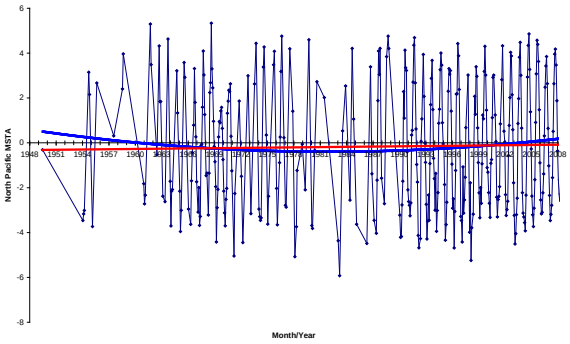

Fig. 4 The trends of variations in the North Pacific MSTA during the period (1948-2008).

Trends of Variations in the North Pacific MSSA:

The linear trend of variations (Fig. 5) in the North Pacific MSSA reflects a general decrease over the study period (1948-2010) with a rate of -0.0013/month, *i.e.* -0.0156/year. The linear trend of variations of the North Pacific MSSA is expressed by the following Equation:

$$y = -0.0013\ x + 2.4815 \quad (9)$$

Lastly, the quadratic regression of the North Pacific MSSA variations is represented by the following Equation:

$$y = -2E\text{-}07\ x2 - 0.0003\ x + 1.5506 \quad (10)$$

No cyclic behaviour can be detected for the MSSA variations as shown in Figure (8). The quadratic trend (Solid blue) tends to be almost superimposable with the linear trend (Dashed red) over the period of investigation.

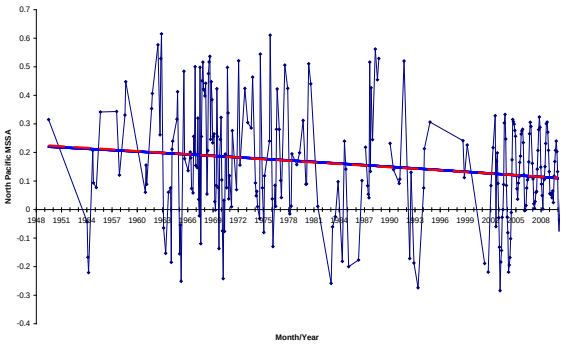

Fig. 5 The regression models of the North Pacific MSSA during the period (1948-2010).

DISCUSSION AND CONCLUSION

The present work aims at drawing the possible long-term trends in the surface hydrographic parameters, namely: temperature and salinity in the Northern Hemisphere, taking two areas in the North Atlantic and North Pacific Oceans as case studies. This is carried out by investigating the variations in the MSTA & MSSA on monthly basis and by using the linear and quadratic regression model approaches. This technique was previously applied

by the authors to examine the long-term variations in the South-eastern Mediterranean Sea in the same latitudinal area.

The linear trends of variations of MSTA in the two oceans reflect general increases over the period of investigation. However, the rate of increase in the North Pacific is weak (0.004°C/month) in comparison to that in the North Atlantic (0.011°C/month). Moreover, the two quadratic trends of MSTA in the two oceans reflect parabolic forms, *i.e.* cyclic variations. The minimum occurrence of MSTA varied between the two water bodies being in 1966 for the North Atlantic and in 1982 for the North Pacific.

The linear trends of MSSA are in contrast between the two oceans. While the North Atlantic examined a general trend of increase over the study period (1948-2010) with a rate of 0.0037/month, the North Pacific had a decreasing rate of 0.0013/month over the same period. This trend difference might refer to the interannual variability of ice melting, evaporation and rainfall process on the Pacific than on the Atlantic.

From a quadratic point of view, the long-term variations in the North Atlantic MSSA reflect a parabolic form, the minimum of which occurred in 1980. On the other hand, the quadratic regression model of the monthly North Pacific MSSA did not show any cyclic trend. Results reveal that the quadratic trend tends to be almost superimposable with the linear one, which might reflect the absence of cyclic variations or a very large cycle of variations, a tiny part of it, appeared in the present research over the investigated period.

Looking at the same investigation approaches, which were carried out in the South-eastern Mediterranean basin for the MSTA [10] and MSSA [11] in the same geographical (Latitudinal) zone, it can be easily deduced that the linear variations in the surface temperature anomalies have opposite trends. While in the Northern Oceans there is a general rate of increase in the MSTA, the trend in the South-eastern Mediterranean Sea [10] is a decreasing one. This may be attributed to the general closed basin morphometry of the Mediterranean Sea. On the other hand, the rate of variations in the MSSA is positive in both the North Atlantic and South-eastern Mediterranean basin and negative in the North Pacific Ocean.

The Quadratic trends reveal that, the years of minimum occurrence of MSTA in the two oceans precede that in the South-eastern Mediterranean basin. Moreover, while the quadratic trends of the MSSA in both the North Atlantic and the South-eastern Mediterranean basin reflect cyclic behaviour with minimum occurrence in the year 1980, no apparent cyclic trend, during the present period of investigation, can be detected within the Pacific Ocean (Table 1).

Table 1 Comparison between linear rates of changes in the North Atlantic and Pacific Oceans and the South-eastern Mediterranean Sea and the years of minimum MSTA & MSSA occurrence for the quadratic trends

	North Atlantic Ocean	North Pacific Ocean	SE-Mediterranean Basin
MSTA	0.011°C	0.004°C	-0.06°C
MSSA	0.0037	-0.0013	0.031
Year of minimum MSTA	1966	1982	1985
Year of minimum MSSA	1980	----	1980

REFERENCES

[1] Maiyza IA, Long-term variation of water temperature in the eastern part of the Mediterranean Sea, Ph.D. thesis, Moscow University, Russia, 1984.

[2] Fedrouich, LA, Regular formation of large scale temperature anomalies of the surface layer in the northern Pacific Ocean. Ph.D. thesis, Moscow University, Russia, 1985.

[3] Miller AJ, Cayan DR, Barnett TP, Graham NE and Oberhuber JB, "Interdecadal variability of the Pacific Ocean: model response to observed heat flux and wind stress anomalies", *Clim. Dyn.*, Vol. 9, 1994, pp. 287-302.

[4] Levitus S, Interannual to decadal scale variability of the world Ocean at *IAPSO XXI General Assembly*, Honolulu, Hawaii, USA, 1995.

[5] Maiyza IA, Mohamed EE, Saad NN and Sharaf El-Din SH, "Sea surface temperature anomalies in the western Mediterranean" at *IAPSO XXI General Assembly*, Honolulu, Hawaii, USA, 1995.

[6] Hurrell JW and van Loon H, "Decadal variations in climate associated with the North Atlantic Oscillation", *Clim. Chan.*, Vol. 36, 1997, pp. 301-326.

[7] Maiyza IA, El-Geziry TM, Maiyza HI and Kamel MS, "Climatological trend of air temperature anomalies in the South-eastern Mediterranean Sea", *JKAU: Mar. Sci.*, Vol. 22 (2), 2011, pp. 55-65.

[8] Brunel T and Boucher J, "Long-term trends in fish recruitment in the north-east Atlantic related to climate change", *Fish. Oceanogr.*, Vol. 16 (4), 2007, pp. 336-349.

[9] Sundby S and Drinkwater K, "On the mechanisms behind salinity anomaly signal of the northern North Atlantic", *Prog. Oceanogr.* Vol. 73, 2007, pp. 190–202.

[10] Maiyza IA and Kamel MS, "Climatological Trend of Sea Surface Temperature Anomalies in the South Eastern Mediterranean Sea", *JKAU: Mar. Sci.*, Vol. 20, 2009, pp. 59-66.
[11] Maiyza IA and Kamel MS, "Climatological trend of Sea surface salinity anomalies in the South Eastern Mediterranean Sea", *JKAU: Mar. Sci.* Vol. 21 (2), 2010, pp. 63-72.
[12] Deser, C, Alexander MA, Xie Sh-P and Phillips AS, "Sea surface temperature variability: Patterns and mechanisms", *Ann. Rev. Mar. Sci.*, Vol. 2, 2010, pp. 115-143.
[13] Eastman R and Warren SG, "Variations in cloud cover and cloud types over the ocean from surface observations 1954-2008", *J. Clim.*, Vol. 24, 2011, pp. 5914-5933.
[14] El-Geziry TM, Maiyza IA, Abdel-Hafez S, Maiyza ShI and Kamel MS, "Interannual variability of the South-eastern Mediterranean catch and its relation to hydrographical and air-temperature anomalies", *JKAU: Mar. Sci.*, Vol. 24 (1), 2013, pp. 43-54.
[15] Güçlü Y., "Sea surface temperature anomalies along the Black Sea region coast of Turkey (1971-2010 period)", *Int. J. Hum. Sci.*, Vol. 10 (1), 2013, pp. 863-896.
[16] Kozar ME, Mann ME, Emanuel KA and Evans JL, "Long-term variations of North Atlantic tropical cyclone activity downscaled from a coupled model simulation of the last millennium", *J. Geophys. Res.: Atmos.*, Vol. 118 (13), 2013, pp. 383-392.
[17] El-Geziry TM, Maiyza IA and Maiyza HI, "General trend of wind anomalies in the South-eastern Mediterranean Sea", *JKAU: Mar. Sci.*, Vol. 24 (2), 2013, pp. 85-97.
[18] El-Geziry TM, On the Long-term Behaviour of Wind-Wave Climatology over the West Region of Scotland, Submitted to the *Journal of Operational Oceanography*, 2014.
[19] Güçlü Y, "Sea surface temperature anomalies at the Mediterranean coast of Turkey (Period of 1968-2010)", *Proc. Soc. Behav. Sci.*, Vol. 120, 2014, pp. 476-486.
[20] Hylen A, Fluctuations in abundance of Northeast Arctic cod during the 20th century in: *ICES Marine Science Symposia*, 2002, pp. 534-550.
[21] Kawasaki T, "A decade of the regime shift of small pelagics". *Bul. Japan Soci. Fisher. Oceanogr*., Vol. 58, 1994, pp. 321-333.
[22] Klyashtorin, LB and Lyubushin AA, Cyclic climate changes and fish reproductivity. ISBN 978-5-85382-339-6, 2007 pp. 226.
[23] Maiyza IA, Continuous global warming or progressive part of long-term temperature cycle: Personal history with the problem, in: Environmental Pollution and its Relation to Climate Change (Nova Publishers) 2011, Chapter 20.
[24] Minobe S, "A 50-70 year climatic oscillation over the North Pacific and North America", *Geophys. Res. Let.*, Vol. 24, 1997, pp. 683-686.
[25] Schlesinger ME and Ramankutty N, "An oscillation in the global climate system of period 65-70 years", Nature, Vol. 367, 1994, pp. 723-726.
[26] http://odv.awi.de/en/data/ocean/
[27] http://apdrc.soest.hawaii.edu/projects/Argo/data/gridded/On_standard_levels/Monthly_mean/1x1/2013/m12/index_grd-bin.html
[28] Soloviev A and Lukas R, The near-surface layer of the ocean: Structure, dynamics and applications, (Springer, The Netherlands), 2006, pp. 572.
[29] Maiyza IA, Said MA and Kamel MS, "Sea Surface Temperature Anomalies in the South Eastern Mediterranean Sea", *JKAU: Mar. Sci.* Vol. 21(1), 2010, pp. 151-159.

First International Conference on Science, Engineering & Environment,
Tsu City, Mie, Japan, Nov.19-21, 2015, ISBN: 978-4-9905958-5-2 C3051

ANAEROBIC DIGESTION OF COMMON (INVASIVE) WEED SPECIES (CO-DIGESTION WITH MANURE): A LITERATURE REVIEW

Author Name, Jamal Algraeo
School of Biosciences, University of Nottingham, United Kingdom

ABSTRACT

Anaerobic digestion, biogas and biomass have been defined in this literature review, the historic background of AD is presented and conditions and variables that influence AD are investigated. These include solid content, retention time and temperature. In addition to the standard practice of using manure for biogas production, other sources of biomass may be utilized such as aquatic and terrestrial plants. Aquatic weeds are classed as two kinds, which are marine weeds and freshwater weeds, while terrestrial weeds are divided into several sections: wastewater crops, leaves and grasses. Over 100 types of biomass have been tested as sources of biogas and results reported in many studies. Some examples have been highlighted in this paper. Generally, the methane concentration within the biogas produced ranged from 50% to 70% and the carbon dioxide from 30% to 50%. Anaerobic digestion has several benefits such as biogas production which can be used for electricity generation, heating and cooking or as fuel for vehicles. A byproduct of AD is digestate, a nutrient rich slurry that can be used as a high quality fertilizer. The EU has set a fixed aim that about 20% of European energy needs to come from renewable energy systems (RES) provided from farming and forestry by 2020. At least 25% of bioenergy in future will be produced from wet organic material such as cattle dung, waste crops, waste food and weeds.

Keywords: Anaerobic Digestion, Biogas, Biomass, Digestate, Co-digestion.

1. INTRODUCTION

Biogas is defined as “gas rich in methane, which is produced by the fermentation of animal dung, human sewage or crop residues in an air-tight container” [1]. Biogas is produced in practically all landfills containing biomass and by anaerobic digesters that treat organic wastes. Biomass is defined as “contemporary plant matter formed by photosynthetic capture of solar energy and stored as chemical energy” [2]. Biogas is the gas resulting from fermentation of biodegradables such as animal manure, sewage, weeds and energy crops. This type of biofuel is primarily composed of methane and carbon dioxide; in addition it contains a small percentage of other gases. Methane gas has many purposes, for instance heating, cooking and electricity. Also, biogas can be compressed, compared to natural gas, and is used in vehicles to provide mechanical energy. Interest in renewable energy sources has been growing due to the decrease in oil production and rising oil prices. Therefore, biogas will be one of the most significant renewable sources over the coming decades [3].

The purpose of this paper is to show what anaerobic digestion (AD) is, how biogas is produced, what the biogas production stages are, the types of biomass used in the production process of this gas and attempt to find out whether it is possible to produce economically feasible biogas from varieties of plants that have not been tried before. This literature review is outlined as follows: introduction, conception of AD, history and background of AD, common biomass types and conclusion. Manure can be the most important material for biogas generation either as a single substrate or when co-digested with other material because of the presence of decomposer and methanogenic bacteria.

2. HISTORY OF ANAEROBIC DIGESTION

Historical information indicates that the AD process is one of the oldest technologies known. By 1859 industrialization of AD had started in India with the first digestion process and biogas was produced from wastewater for the first time by Mouras from France, who invented a septic tank in 1860 named the ‘automatic scavenger’. In 1895 biogas was generated from wastewater in England by Cameron, who constructed a tank similar to the automatic scavenger; however, it resulted in better

treatment and Cameron named it the 'septic tank'. As a result of the success achieved in using these tanks, the local government in Exeter (England) approved the treatment of the entire city's wastewater by these septic tanks [4]. Therefore, Exeter used this biogas for electricity production for streetlamps. Although the bacteria and conditions promoting methane production were identified in the 1930 [5], production of methane gas from plant species by AD has only been known about since the 1970s. This in general, gave great hope for generating clean, methane-rich energy on a large scale and to also remove harmful herbs, waste and biodegradable municipal solid wastes (MSW) that cause environmental pollution [6].

Anaerobic digestion (AD) is now the main producer of biogas in all countries of the world. AD consists of using a tank into which is put biodegradable organic materials (weeds, food scraps, manure, crops, etc.). The organic materials degrade through bacterial decomposition in the absence of oxygen and a result of this process is a biogas that can ultimately be fed to a CHP unit to produce electricity and heat, while organic material is transformed into high-quality compost (Fig. 1). Resulting from this process is a mixture of methane and carbon dioxide. In addition, a natural fertilizer in slurry form is produced. The output gas is collected in a tank, the volume of which is estimated at between 1.5 and 2.5 times the digester size. For example, if we assume that the size of the digester is a thousand litres, the output volume of gas is about 1,500 to 2,500 litres. However, the proportion of methane varies depending on the feedstock used, but the ratio generally ranges from 50% to 70% methane and 30% to 50% carbon dioxide; in addition, a small concentration of other gases such as hydrogen sulphide may be present. Various appliances can be fueled by biogas, with stoves offering an application appropriate for deployment in developing countries. Now, there are about four and 27 million biogas plants in India and China respectively [7].

3. CONDITIONS AND VARIABLES INFLUENCING AD

Many steps and conditions must be followed when using AD to complete the biogas production process successfully; the main conditions are discussed in the following sections.

3.1. Solid content

Three ranges of solid content are selected: low solids (LS), medium solids (MS) and high solids (HS). In the LS case the AD systems contain less than 10% total solids, while in the MS case, AD contains between 15-20% and for HS, it contains from 22-40%.

3.2. Temperature

In the majority of AD processes temperature should be maintained relatively constant to sustain the rate of gas production. However, the temperature optimum depends on the type of organic material and composition of the digester. AD can work at two temperature ranges: (1) thermophilic conditions, which are from 50°C and 65°C (averaging 55°C) and (2) mesophilic conditions, between 20°C to 45°C, usually 35°C. Mesophilic digesters need less heat input and are less sensitive to operating and environmental changes; however, they are less efficient in terms of retention time, loading rate and nominal gas production than thermophilic ones [5].

3.3. Retention time

Retention time is the time that is needed to complete the degradation processes of the raw material. The retention time varies between thermophilic and mesophilic digesters, with the latter ranging between 15 and 30 days, and thermophilic digesters from 12 to 14 days [5].

3.4. Rate of acidity (pH)

pH affects the methanogenesis and acidogenesis stages and it is different for both stages. The pH rate decreases when acetic, lactic and propionic acids are formed during the acidogenesis stage; a declining pH is usually buffered by the systems, but if it falls below 6.4 methanogenesis is inhibited and methane will not be produced. Therefore, the optimal pH range for methanogenesis is between 6.6 and 7.0 [8].

3.5. Ratio of carbon to nitrogen (C:N)

The ratio of carbon to nitrogen present in biomass is expressed as C:N; the optimum ratio of C:N in the process of biogas production is from 20 to 30. Increasing C:N will result in a rapid consumption of nitrogen and leads to lower gas production; while a decreased C:N leads to an accumulation of ammonium and increasing pH, which limits methanogenic bacteria. Avoiding all these problems should be achieved by mixing wastes of low and high C:N; for instance, mixing organic solid waste with cattle dung or wastewater [5].

3.6. Mixing

Mixing improves connections between micro-organisms and organic waste; in addition, it improves the nutrient availability to the microbial community. Mixing also prevents scum emergence and temperature development in AD. However, over-mixing can impede and/or disrupt the micro-organisms.

3.7 Organic loading rate (OLR)/volatile solids (VS)

Organic loading rate (OLR) is related to the AD feeding system; it is a measure of the biological conversion ability in the digester, therefore a high OLR results in system failure and is expressed in kilograms of chemical oxygen demand (COD) or volatile solids (VS) per cubic metre of the reactor. OLR has a relationship with retention time and volume of AD. The value for VS is obtained from complete combustion of organic waste, therefore VS represents organic material in the sample that is measured as solid content minus ash content. So, VS includes biodegradable volatile solids (BVS) and refractory volatile solids (RVS). Therefore, a high VS content with low RVS should be suitable for AD.

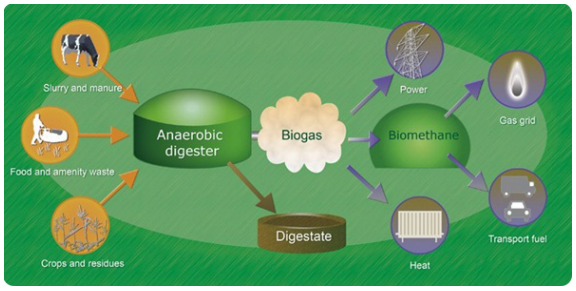

Fig. 1. The key inputs and outputs of anaerobic digestion. Source: LeoGroup Ltd. recycling company web page.

4. ANAEROBIC CO-DIGESTION

Anaerobic co-digestion occurs when different organic wastes are combined to produce a feedstock that is more balanced, degradable and assorted in terms of nutrients [9]. The co-digestion process has several benefits such as: mitigation of potentially toxic compounds, providing a buffer capacity to the mixture, expanding the range of bacterial strains taking part in the process, modifying humidity and pH and increasing the degradable material content [9]. Co-digestion should be passed through four stages: pre-treatment, digestion, gas upgrading and digestate treatment [5].

Many experiments and studies prove that biogas yields by anaerobic co-digestion are higher than for AD utilizing a single-feedstock. For example, wastewater sludge was digested by Luostarinen et al. [10] along with grease trap waste taken from a meat-processing plant; reactor experiments were conducted at 35°C. Addition of grease to sewage sludge resulted in higher methane production (918 m^3/t VS added) than from the sewage sludge alone. However, at high grease trap waste additions (55% and 71% of VS feed) methane production either remained the same or decreased [10].

4.1. Pre-treatment

Lignocellulosic material in particular, which would otherwise take up unnecessary space in the digester and decrease the digestion efficiency may need to be pre-treated prior to digestion. Pre-treatment is an old and important process for making recalcitrant materials easier to degrade. Additionally, pre-treatment provides a uniform feedstock of small particle size resulting in efficient digestion and protecting the downstream plant from material that may cause physical damage. Organic solids can be more accessible and degradable to microorganisms following pre-treatment [9]. For instance, if weeds and other plant materials are shredded a more homogeneous feed stock is produced. Many weed species need pre-treatment because they contain significant amounts of woody lignin which is difficult to degrade. However, this difficulty does not necessarily reduce the value of the digestate produced, although a pre-treatment step may increase the cost of methane production [5].

5. COMMON BIOMASS TYPES

Attention given to biogas production from organic material has recently increased. About 100 types of plants as valid sources of biogas have been explored, such as aquatic and terrestrial weeds, wood, crops, leaves and grasses. All these types have been tested by AD for methane potential and the experiments emphasized that many species of plants have good digestion properties either before or after pre-treatment. Many studies also emphasize the urgent need to evaluate unexplored genera of plants as sources of methane production [2].

5.1. Manure

The increase and intensification of animal production is one of the most significant aims for Europe and developed countries. Increasing livestock production is always accompanied by plenty of cattle dung and a surplus represents a serious threat to the environment. Therefore, large quantities of dung need to be effectively and appropriately managed.

Arguably the best method for manure management and disposal of surplus animal manure is to treat it by AD, to produce biogas and the finest types of compost. The EU has set a fixed aim that about 20% of European energy needs to come from renewable energy systems (RES) provided from farming and forestry by 2020. At least 25% of bioenergy in future will be produced from wet organic material such as cattle dung, waste crops, waste food and weeds [11].

5.2. Aquatic weeds

In a two-stage rumen-derived AD process carried out by Kivaisi and Mtila [12], biogas was generated from water hyacinth shoots and from a mixture of

shoots and cow dung in a ratio of 7:3 respectively. The degradation efficiency for the shoots alone was 38% and 43% for the shoot/dung mixture. Overall, a 10% increase in digestibility of the water hyacinth was observed in the mixture. Increasing the loading rate to 15.4 g VS/l/d from 11.6 g VS/l/d enhanced degradation of the feedstock. The authors suggested that the increased degradation of water hyacinth in mixture was due to solubilization of low molecular weight lignin rather than lignin degradation per se. The average biogas yield was 0.44 l/g VS digested across the experimental treatments and the authors concluded that the high loading rate and relatively short retention time required (90 h) is indicative that a small volume reactor is suitable for the feedstock studied [12].

5.3. Marine biomass

Although marine plants and algae are an important source of biomass, reports of their use for biogas generation are limited [13], yet generating biogas from marine plants is economically feasible. Marine algae, *Macrocystis pyrifera* and *Durvillea antarctica* and their blend, 1:1 (w/w), were anaerobically digested at laboratory scale by Vergara-Fernandez et al. using a two-phase AD system, an anaerobic sequencing batch reactor (ASBR) and an upflow anaerobic filter (UAF). Each algal species and the blend of both produced similar biogas volumes (average of 180.4±1.5 ml/day/g dry wt.), which consisted of 60-70% methane. The similarities between the species were attributed to their comparable elemental concentrations [13].

5.4. Crops

In India, nine types of crop waste and common weeds were experimented with to produce biogas (banana stem, maize stover, rice straw, wheat straw, sugarcane bagasse, water hyacinth, *Cannabis sativa*, *Croton sparsiflorus* and *Parthenium hysterophorus*). The plant waste from each species was incubated independently, but each with 200 ml of cow dung slurry. The bottle tops had closed gas outlets and they were incubated at room temperature (30-35°C) for eight weeks. After 60 days of digestion there appeared a decline in the carbon content, which varied from 17% to 13%. Production of methane and carbon dioxide led to the organic carbon loss. The highest amount of methane was produced from banana stem (118.65 l/kg total solids (TS)). The other crop wastes and weeds produced between 90.26 and 100.07 l/kg TS [14].

Three crops, maize, hemp and faba bean were tested by Pakarinen et al. [15]. Methane production was 379±16 l/kg VS from maize, 387±20 l/kg VS from faba bean and 239±9 l/kg VS from hemp. However, when accounting for the crop yield per hectare, maize is the best productive raw material source for methane production [15].

Hassan Dar and Tandon [16] evaluated biogas production and quality from pre-treated wheat straw, *Lantana* residues, apple and peach leaf litter with livestock manure (1:1, w/w at 10% slurry level). Crop residues produced methane as follows: *Lantana*, 63.6%; apple leaf litter, 59.6%; wheat straw, 58%; peach leaf litter, 57.7% and cattle dung, 56.6%. The digestion efficiency (biogas/g dry matter) was 31-42% higher than that of the cattle dung [16]. Pre-treatment was done by addition of 1% NaOH for seven days and it improved microbial digestibility and biodegradability during anaerobic fermentation at ambient temperature (28-31◦C). Twofold increases in organic matter degradability and biogas production were achieved as a result.

Parawira et al. [17] batch digested potato waste either alone or with sugar beet leaves at the laboratory scale using anaerobically digested sewage sludge as an inoculum. During their experiments, the total solids were maintained at 40% which gave the highest methane yield when potato waste was digested on its own. The mixtures were obtained by reducing potato waste from 40% TS to 0% TS and simultaneously increasing the sugar beet leaves from 0% to 40% TS. Co-digestion of the two wastes resulted in higher methane yields. Methane production increased by 31-62% compared to potato waste alone and by 6-31% relative to sugar beet leaves alone. The authors interpreted this improvement as a result of additional nutrients being present in the mixture compared with each species alone. They suggested that a high inoculum-to-substrate ratio was necessary for maximum methane production.

5.5. Tree leaves

Trees produce a large amount of leaf material which could be utilized for biogas production. Many types of tree leaves have been tested as a substrate for biogas production in several countries. *Gliricidia* is a tree grown in India and is used as a green-leaf manure. Gunaseelan [18] digested *Gliricidia* leaves at 32±3°C in laboratory digesters using anaerobically digested cattle manure as the inoculum. The feedstock produced a methane yield of 165-180 ml/g VS added with a VS reduction during the process of 37-39%. Increases in N, P and K of 32%, 8% and 28% respectively (averaged across treatments) were reported in the anaerobic digestate relative to the undigested green-manure.

5.6. Grasses

Grasses are some of the more widespread natural plants, because they grow in each region that offers natural climatic conditions without any effort provided by humans. Grass is generally underutilized with the exception of livestock

farming and is therefore a potentially sustainable source of biogas. Tests to date have demonstrated that grasses can efficiently be used for the production of biogas. Fernandes et al. [19] pre-treated three plant species, two of which were grasses (hay and straw) in addition to bracken, for 40 days with calcium hydroxide, ammonium carbonate and maleic acid. The pre-treatments (apart from calcium hydroxide) generally increased the ammonium and phosphate concentrations of the substrates due to hydrolysis. Whilst the pre-treatments of straw and bracken enhanced biodegradability during subsequent anaerobic digestion, no effect was observed for hay. Therefore hay (dried grass) can be satisfactorily anaerobically digested without the need for pre-treatments [19].

6.3. Potential for use of other species

One note of caution when digesting plant species is to ensure that none is toxic, either to the AD process or as residues within the resulting digestate. Saini et al. [20] anaerobically digested fresh and pre-treated (aerobically decomposed) *Lantana camara* leaves with cattle dung at 35ºC for 50 days. Treatments containing fresh leaves did not produce any biogas, but when mixtures consisted of 25% pre-treated leaves and 75% cattle dung, or 50:50 pre-treated leaves and dung, biogas production was 8.37% and 60.7% higher respectively than for dung alone. The treatment containing 75:25 pre-treated *Lantana*:dung did not yield any biogas.

There is much untapped biomass that has potential for use in AD systems, for example, *Posidonia oceanica* which is an endemic seagrass covering vast areas of the sea bottom between seawater surface and 35m depth [28]. It grows in tufts and has green leaves reaching up to 1.50 m in length. A great amount of *P. oceanica* residue is thrown annually onto the shore and is a particular problem along the Mediterranean coast [21] where it causes environmental, social and health problems which also affect tourism and the economics of the region. These problems can be solved by using *P. oceanica* as a substrate in AD. A biodegradability analysis confirmed that *P. oceanica* is efficiently biodegraded and can be recommended as a feedstock for co-digestion [22]. Libya which is located on the Mediterranean Sea and has about 2000 km of beaches that suffers from *P. oceanica* encroachment; using the material for biogas production will be the solution for these problems [22].

There are many other potential sources of biomass that are worth of consideration. For example, the flesh of olives derived from the solid waste of olive mills, which is a mass of dough consisting of olive peel and crushed seeds after olive pressing. Olive flesh has a content of about 65% of olive weight [23] and is an appropriate material for co-digestion. According to 2007 statistics, Libya has approximately 280,000 hectares of olive planted area, and produces about 157,500 tonnes of olives.

6. CONCLUSION

Anaerobic digestion, biogas and biomass have been defined in this literature review, the historic background of AD was presented and conditions and variables that influence AD were investigated. These include solids content, retention time and temperature. In addition, types of biomass used for biogas production by AD were considered such as manure, crop residues, tree leaves, aquatic and terrestrial weeds and grasses. Over 100 types of biomass have been tested as sources of biogas and therefore only a sample can be discussed here. Generally, the concentration of methane within the biogas ranged from 50-70% and carbon dioxide from 30-50%. It is evident that there is great potential for using a range of different plant species as co-digestants within AD systems.

7. REFERENCES

[1] Hilkiah Igoni, A., Ayotamuno, M., Eze, C., Ogaji, S. and Probert, S. (2008). Designs of Anaerobic Digesters for Producing Biogas from Municipal Solid-Waste. Applied Energy 85 (6), 430-438.

[2] Gunaseelan, VN. (1997). Anaerobic digestion of biomass for methane production: A review. Biomass and Bioenergy, 13(1-2), 83-114.

[3] Appels, L., Lauwers, J., Degrève, J., Helsen, L., Lievens, B., Willems, K., Van Impe, J. and Dewil, R. (2011). Anaerobic Digestion in Global Bio-Energy Production: Potential and Research Challenges. Renewable and Sustainable Energy Reviews 15 (9), 4295-4301.

[4] Abbasi, T., Tauseef, S. and Abbasi, S. (2012) Biogas Energy. New York, NY: Springer.

[5] Monnet, F. (2003). An Introduction to Anaerobic Digestion of Organic Wastes. In: Remade Scotland, Biogasmax, Final Report.

[6] Abbasi, T. and Abbasi, S. (2010). Production of Clean Energy by Anaerobic Digestion of Phytomass - New Prospects for a Global Warming Amelioration Technology. Renewable and Sustainable Energy Reviews 14 (6), 1653-1659.

[7] Bond, T. and Templeton, M. (2011). History and Future of Domestic Biogas Plants in the Developing World. Energy for Sustainable Development 15 (4), 347-354.

[8] Appels, L., Baeyens, J., Degrève, J. and Dewil, R. (2008) Principles and Potential of the Anaerobic Digestion of Waste-Activated

Sludge. Progress in Energy and Combustion Science 34 (6), 755-781.

[9] Esposito, G., Frunzo, L., Giordano, A., Liotta, F., Panico, A. and Pirozzi, F. (2012) Anaerobic Co-Digestion of Organic Wastes. Reviews in Environmental Science and Bio/Technology 11 (4), 325-341.

[10] Luostarinen, S., Luste, S. and Sillanpää, M. 2009. Increased Biogas Production at Wastewater Treatment Plants through Co-digestion of Sewage Sludge with Grease Trap Sludge from a Meat Processing Plant. Bioresource Technology 100(1), 79-85.

[11] Holm-Nielsen, J., Al Seadi, T. and Oleskowicz-Popiel, P. 2009. The Future of Anaerobic Digestion and Biogas Utilization. Bioresource Technology 100(22), 5478-5484.

[12] Kivaisi, A. and Mtila, M. (1997). Production of Biogas from Water Hyacinth (*Eichhornia crassipes*) (Mart) (Solms) in a Two-stage Bioreactor. World Journal of Microbiology and Biotechnology, 14 (1), 125-131.

[13] Vergara-Fernandez, A., Vargas, G., Alarcon, N. and Velasco, A. (2008). Evaluation of Marine Algae as a Source of Biogas in a Two-Stage Anaerobic Reactor System. Biomass and Bioenergy, 32 (4), 338-344.

[14] Thakur, S. and Singh, K. (2003). Anaerobic Digestion of Agricultural Wastes and Weeds for Biogas Production. Annals of Biology 19, 245-249.

[15] Pakarinen, A., Maijala, P., Stoddard, F., Santanen, A., Tuomainen, P., Kymäläinen, M. and Viikari, L. (2011). Evaluation of Annual Bioenergy Crops in the Boreal Zone for Biogas and Ethanol Production. Biomass and Bioenergy 35 (7), 3071-3078.

[16] Hassan Dar, G. and Tandon, S. (1987). Biogas Production from Pretreated Wheat Straw, *Lantana* Residue, Apple and Peach Leaf Litter With Cattle Dung. Biological Wastes, 21 (2), 75-83.

[17] Parawira, W., Murto, M., Zvauya, R. and Mattiasson, B. (2004). Anaerobic Batch Digestion of Solid Potato Waste Alone and in Combination with Sugar Beet Leaves. Renewable Energy, 29 (11), 1811-1823.

[18] Gunaseelan, VN. (1988) Anaerobic Digestion of *Gliricidia* Leaves for Biogas and Organic Manure. Biomass, 17 (1), 1-11

[19] Fernandes, T., Klaasse Bos, G., Zeeman, G., Sanders, J. and van Lier, J. (2009). Effects of Thermo-Chemical Pre-Treatment on Anaerobic Biodegradability and Hydrolysis of Lignocellulosic Biomass. Bioresource Technology 100 (9), 2575-2579.

[20] Saini, R., Kanwar, S., Sharma, O. and Gupta, M. (2003) Biomethanation of *Lantana* Weed and Biotransformation of its Toxins. World Journal of Microbiology and Biotechnology, 19 (2), 209–213.

[21] Gacia, E., Invers, O., Manzanera, M., Ballesteros, E. and Romero, J. (2007) Impact of the Brine from a Desalination Plant on a Shallow Seagrass (*Posidonia oceanica*) Meadow. Estuarine, Coastal and Shelf Science 72 (4), 579-590

[22] Plis, A., Lasek, J., Skawińska, A. and Kopczyński, M. (2014). Thermo-Chemical Properties of Biomass from *Posidonia oceanica*. Chemical Papers 68 (7), 879-889.

First International Conference on Science, Engineering & Environment,
Tsu City, Mie, Japan, Nov.19-21, 2015, ISBN: 978-4-9905958-5-2 C3051

WATERPLANT PURIFICATION OF EUTROPHICATED WATER IN EXPERIMENTAL MESOCOSM SYSTEM WITH LONG-TERM OBSERVATION

Kazuhito Murakami[1] and Akiko Inoue-Kohama[2]
[1]Department of Life and Environmental Sciences, Chiba Institute of Technology, Japan; [2]Department of Environmental Energy, Tohoku Institute of Technology, Japan

ABSTRACT

To compare the ability of water purification as N, P, COD and Chl.a removal, 8 mesocosm systems were established and observation was conducted for 4 years. Results obtained were as follows; 1) In all treated mesocosm system, Aoko (*Microcystis aeruginosa* and *Anabaena spiroides*) did not appear, 2) CaO sprinkling treatment showed the most effect for water purification with P-elution controlling in long-term observation, but bio-diversity for phytoplankton and zooplankton became poor because of its too purificated water body, 3) MgO sprinkling treatment showed long-term effective P-elution control, and phytoplankton flora was not so poor as that in CaO sprinkling treatment, 4) Large size zooplankton such as *Philodina erythrophthalma* and *Brachionus angularis*, were observed in case of water glass purification system, because of the structure of water plant roots for rich niche construction, 5) The diversity index (Shannon Index; H') for phytoplankton flora was higher under complicated community structure such as phytoplankton, zooplankton and water plants, 6) Water plant purification system was disturbed by birds as predator, that is, immigration birds such as *Anas platyrhynchos* ate water plants and supply their excrement to water, so positive maintenance is important to keep this system in order, and 7) Hybrid treatment system did not show the hybrid effect on water purification, so it considered important that environmental improvement level should be optimized.

Keywords: Chemical remediation materials, Mesocosm, Phytoplankton, Waterbloom, Waterplant

INTRODUCTION

The Hasunuma seaside park, is locating in Kujyukurihama Coastal Line in Chiba prefecture, Japan, where is the very famous long beach crowded with many attendance person/tourists, especially in summer season. However, as an eutrophication has been progressed in recent years in this park pond, Aoko, the water bloom of harmful cyanophyceae, such as *Microcystis aeruginosa* and *Anabaena spiroides*, became observed in every summer. It is important that the basic information about the succession of phytoplankton community for prevention the eutrophication of water environment [1][2]. In this study, water quality improvement by waterplant was investigated using experimental mesocosm system. Waterplant purification technology is expected as one of the most efficient method from the viewpoint of cost and the impact to natural ecosystem [3]. Four years experiment and observation was conducted to compare the waterplant purification and chemical remediation materials for their ability of water purification.

MATERIALS AND METHODS

Outline of Kujyukurihama Coastal Line

Kujyukurihama coastal line (about 55km length) is one of the most famous beach resort zone in Japan, facing to the Pacific ocean. The climate is calm through a year, and it's cool in summer and warm in winter. Fishery and farming is prosperous. Thousands of people visit to this beach resort especially in summer, because of its closeness from Tokyo metropolitan and Narita International Airport.

Outline of Hasunuma Seaside Park Pond

Outline of Hasunuma seaside park pond is shown in Fig.1. The surface area of this pond is about 10,380m^2, and the pond capacity is about 7,000m^3. Hasunuma village is so influenced on the Kuroshio current (the Japanese current) that the climate is warm and much rain with an average air temperature is about 14.7℃ and a rainfall is about 1,224mm. The park area is 38.3ha, pond volume is 6,747m^3, and water depth is 0.65m in average. As for in the water of this boat pond excessive the collection water and the phosphor acid from the surroundings/the spring water from the Pacific Ocean that contains 1.0-1.5 mg/l of PO_4-P, the eco-balance which can be indicated as N/P mass ratio in this pond is under P surplus condition [4]. Phytoplankton requires N and P as their nutrient salts for its growth, and it is enough for water bloom forming cyanophyceae, that is Aoko, to grow massive in this pond.

Design of Experimental Mesocosm

To investigate waterplant purification possibility to eutrophicated water bodies, experimental mesocosm system (2m×2m×0.5m) were set up in eutrophicated brackish park pond locating Kujyukuruhama coastal line, Japan. The outline of mesocosm system was shown in Fig.2. This park pond is so much eutrophicated that massive Aoko formed by *Microcystis aeruginosa* and *Anabaena spiroides* appear every summer. This phenomena leads many problems to citizen as water use [5]. To compare the ability of water purification as N, P, COD and Chl.a removal, eight mesocosm systems were established. Those are; Run 1: control (water only), Run 2: control (water and sediment), Run 3: chemical remediation materials (MgO) sprinkled, Run 4: chemical remediation materials (CaO) sprinkled, Run5: waterplant treatment (*Eichhornia crassipes*), Run6: waterplant treatment (*Nasturium officinale*), Run7: hybrid treatment (MgO + *Eichhornia crassipes*), and Run8: hybrid treatment (MgO + *Nasturium officinale*). These experimental series were shown in Table 1. Experimental culture was started in Aug.2003, and continued to 2007 (4 years long). Sampling was conducted once a month, and water quality analysis was conducted in laboratory as soon as possible. Parameters for analysis were pH, DO, Cl^-, T-N, NO_3-N, NO_2-N, NH_4-N, T-P, PO_4-P, COD, Chl.a, phytoplankton flora and zooplankton fauna.

Restraint Mechanism

Waterplant purification

Waterplant purification technology is considered as one of the bio-environmental engineering technology [3]. There has been much experiment and discussion about this technology, and the characteristics for water purification of waterplant species were made clear [6]. *Eichhornia crassipes* is widely known as one of the harmful waterplant as its irregular growth in eutrophicated water bodies against navigation of fishery and so on. On the other hand, its ability for adsorption of nutrient salts is very high, and it expected to be very essential for water purification under optimum treatment. *Nasturium officinale* is known as one of the famous plant for food. It is also utilized in biotope (for example, Lake Kasumigaura, Japan) to purify lake water. These two waterplant are shown in Fig.3. The mechanism for water purification of these waterplant is considered as i) adsorption of nutrient salts, ii) shade of sun light and iii) allelopathy effect.

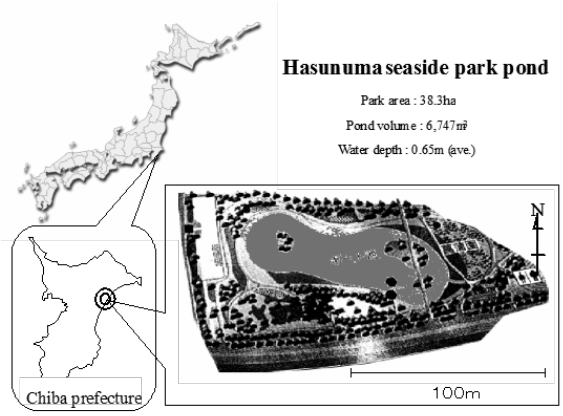

Fig.1 Outline and location of Hasunuma seaside park pond

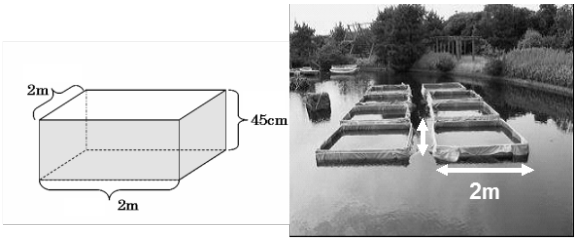

Fig.2 Outline of experimental mesocosm system

Table 1 Experimental series in this study

Run 1	control (water only)
Run 2	control (water + sediment)
Run 3	chemical treatment (MgO)
Run 4	chemical treatment (CaO)
Run 5	waterplant treatment (*Eichhornia crassipes*)
Run 6	waterplant treatment (*Nasturium officinale*)
Run 7	hybrid treatment (MgO + *Eichhornia crassipes*)
Run 8	hybrid treatment (MgO + *Nasturium officinale*)

a) *Eichhornia crassipes* b) *Nasturium officinale*

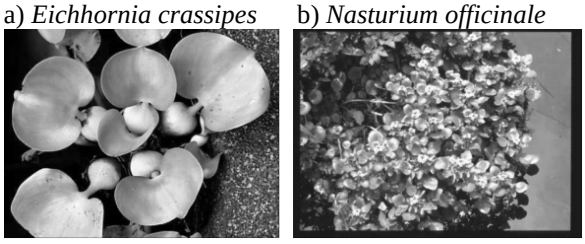

Fig.3 Waterplant applied to water purification

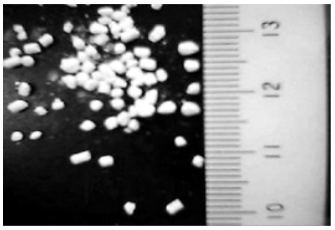

Fig.4 Chemical remediation material

The quantity of waterplant was adjusted as 0.25kg/m^2 of *Eichhornia crassipes* and 0.5kg/m^2 of *Nasturium officinale*, respectively.

Chemical remediation materials

Chemical remediation means the purification technology for eutrophicated sediment using some chemicals such as MgO, CaO and so on [7]. The most efficient merit of this technology is in maintenance-free and low cost. On the other hand, this method has demerit as large impact to ecosystem. For example, CaO fixes PO_4-P effectively, but washes out NH_4-N from sediment layer at the same time. In addition, it makes pH higher, and not only microorganisms but also fish, waterplant, macrobenthos and so on are damaged. The optimum pH for MgO and CaO reaction is 7 and 9, respectively. The quantity of chemical remediation materials in this study was adjusted as 1kg/m^2 of MgO and 0.5kg/m^2 of CaO, respectively. The quantity of these chemicals was determined with consideration of the optimum quantity to obtain most effective restraint of nutrient elution from sediment layer. The chemical remediation materials were shown in Fig.4. The chemical reaction of these chemical remediation materials are described below.

$$Mg^{2+} + HPO_4^{2-} + 3H_2O \Leftrightarrow MgHPO_4 \cdot 3H_2O \downarrow \quad (pH\ 7)$$

$$Mg^{2+} + NH_4^{+} + PO_4^{3-} + 6H_2O \Leftrightarrow MgNH_4PO_4 \cdot 6H_2O\ (MAP) \downarrow \quad (pH\ 7)$$

$$Ca^{2+} + HPO_4^{2-} \Leftrightarrow CaHPO_4 \downarrow \quad (pH\ 9)$$

RESULTS AND DISCUSSION

Restraint Rate of Nitrogen and Phosphorus

The restraint rate (%) of T-N and T-P as results of mesocosm experiment was shown in Fig.5 and Fig.6, respectively. Run 5, Run 6, Run 7 and Run 8 were planted waterplant in the initial stage, but after the first year passed, waterplant was dead except for Run 4. From this fact, it was made clear that the waterplant purification technology requires proper and delicate management. From these figures, Run 3, Run 4, Run 7 and Run 8 showed effective restraint of nutrient salts.

Restraint Rate of COD and Chl.a

The restraint rate (%) of COD and Chl.a as results of mesocosm experiment was shown in Fig.7 and Fig.8, respectively. From these figures, Run 8 showed negative-effective restraint of COD in the initial period. Chl.a restraint rate was negative in all mesocosms in the middle period. Both COD and Chl.a restraint rate recovered in the last period in all mesocosms. This phenomena is due to the eutrophication of water quality in Run 2, that is, control. Though the restraint of COD and that of Chl.a showed almost same succession pattern, this means COD is depending on Chl.a which indicates phytoplankton quantity. That is, the organic matter existing in water in mesocosm system is considered to be mainly phytoplankton.

Succession of Biota in Mesocosm

In all treated mesocosm system, Aoko (*Microcystis aeruginosa* and *Anabaena spiroides*) did not appear, the other hand, non-treated mesocosm system (Run 1 and Run 2) was dominated by cyanophyceae, that is, *Microcystis aeruginosa* and *Anabaena spiroides*. In other words, every treatment technology in this study indicated the restraint effect against the irregular growth of phytoplankton. CaO sprinkling treatment (Run 4) showed the most effect for water purification with P-elution controlling in long-term observation, but bio-diversity for phytoplankton and zooplankton became poor because of its too purificated water body. MgO sprinkling treatment (Run 3) showed long-term effective P-elution control, and phytoplankton flora was not so poor as that in CaO sprinkling treatment. Large size zooplankton such as *Philodina erythrophthalma* and *Brachionus angularis*, were observed in case of water glass purification system (Run 5, Run 6, Run 7 and Run 8), because of the structure of waterplant roots for rich niche construction. The diversity index (Shannon Index; H') for phytoplankton flora was higher under complicated community structure such as phytoplankton, zooplankton and waterplants. Hybrid treatment system (Run7 and Run 8) did not show the hybrid effect on water purification effect, so it considered important that environmental improvement level should be optimized. Actual restraint mechanism of each purification technology in each mesocosm is shown in Fig.9.

Environmental Factors

Waterplant purification system (Run 5, Run 6, Run 7 and Run 8) was disturbed by birds as predator, that is, immigration birds such as *Anas platyrhynchos* ate waterplants and supply their excrement to water, so positive maintenance is important to keep this system in order. Furthermore, pine tree as prevent-sand wall is generally planted around seaside park pond. This tree, *Pinus thunbergii*, releases much pollen into the air in spring season, and these pollen are poured into the lake water to supply nutrient salts such as nitrogen and phosphorus. In fact, water surface of every mesocosm were covered by pollen and colored in yellow. So, to keep the experimental system in order,

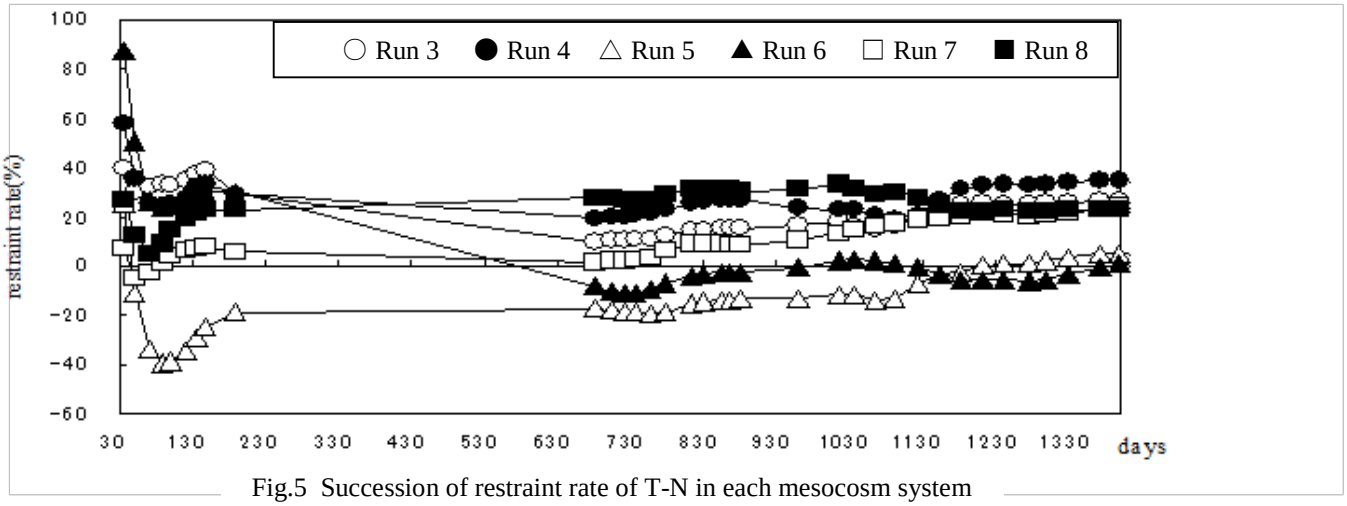

Fig.5 Succession of restraint rate of T-N in each mesocosm system

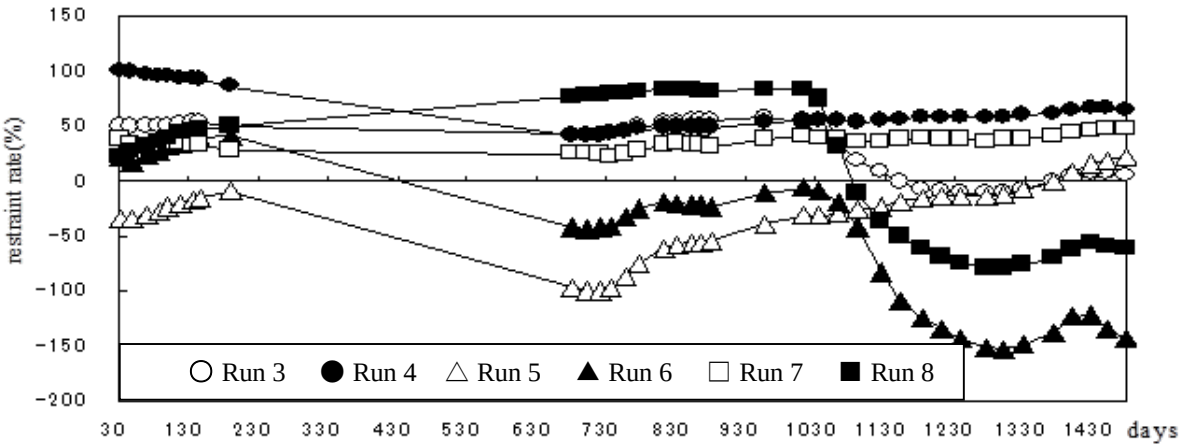

Fig.6 Succession of restraint rate of T-P in each mesocosm system

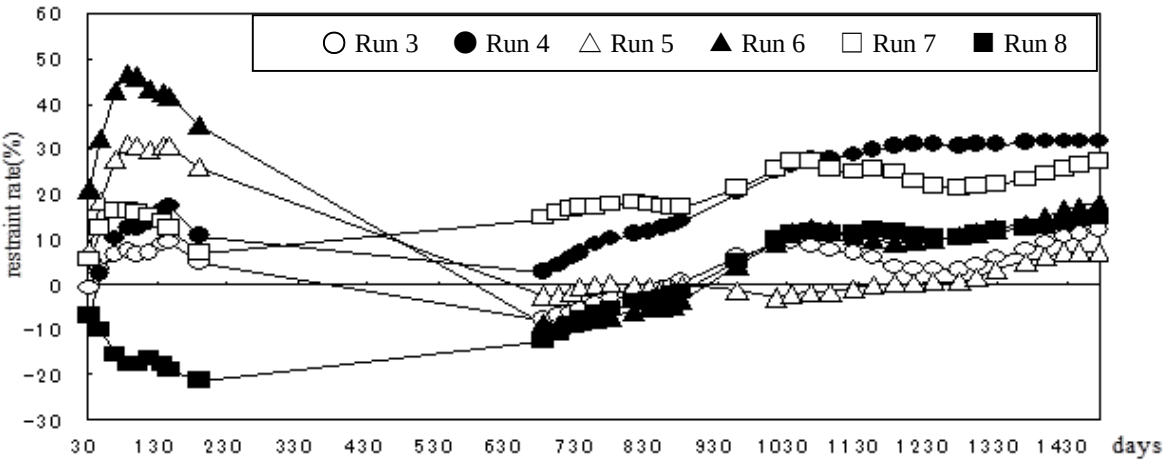

Fig.7 Succession of restraint rate of COD in each mesocosm system

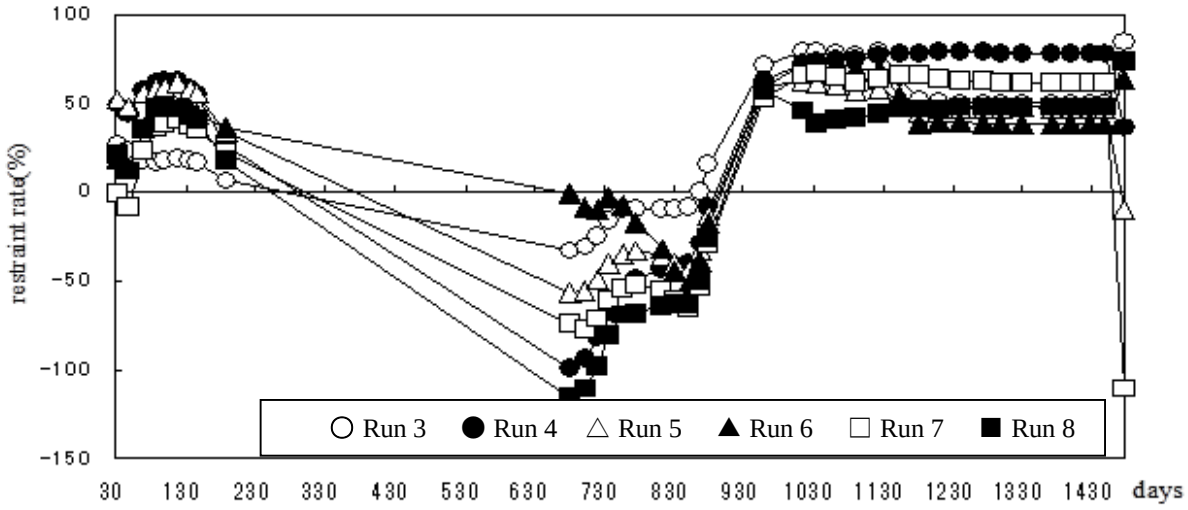

Fig.8 Succession of restraint rate of Chl.a in each mesocosm system

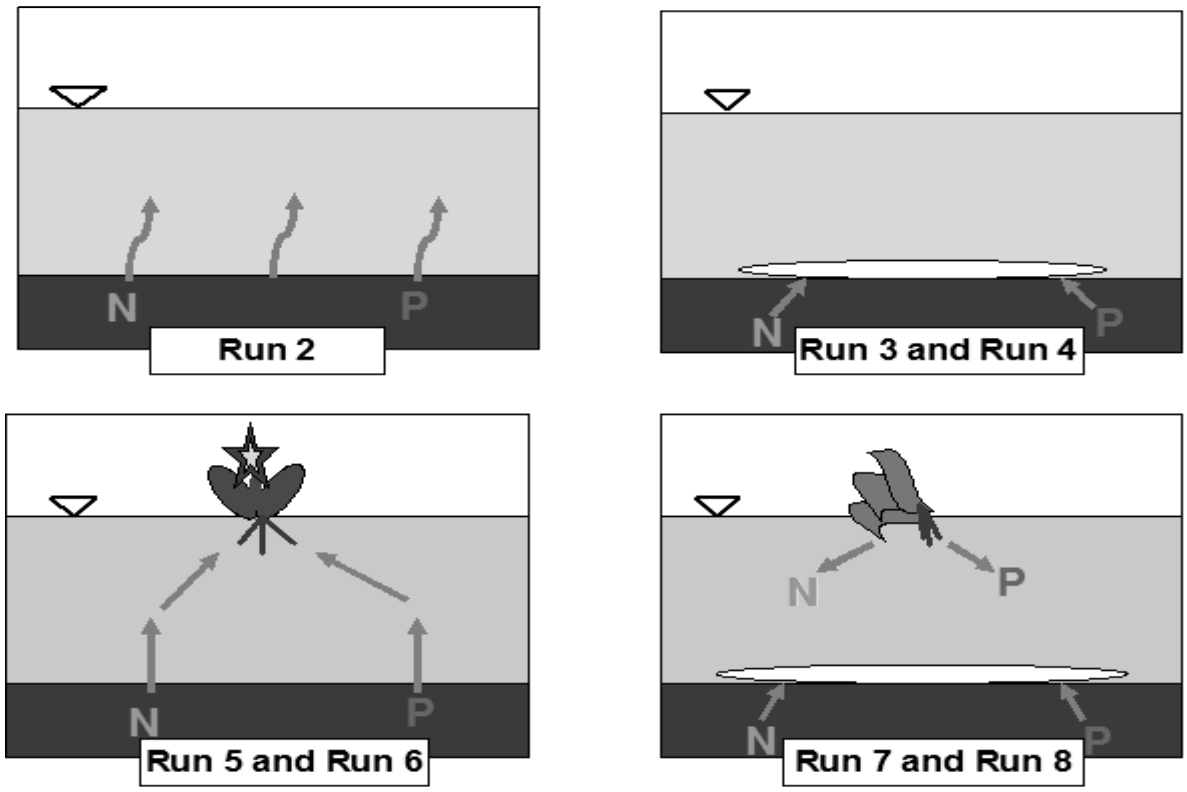

Fig.9 Actual restraint mechanism of each purification technology in each mesocosm

the environmental factor such as pollen of *Pinus thunbergii* should be considered.

CONCLUSION

Four years experimental mesocosm experiment and observation was conducted to compare the waterplant purification and chemical remediation materials for their ability of water purification in this study. Results obtained can be concluded as follows;

1) In all treated mesocosm system, Aoko (*Microcystis aeruginosa* and *Anabaena spiroides*) did not appear.

2) CaO sprinkling treatment (Run 4) showed the most effect for water purification with P-elution controlling in long-term observation, but bio-diversity for phytoplankton and zooplankton became poor because of its too purificated water body.

3) MgO sprinkling treatment (Run 3) showed long-term effective P-elution control, and phytoplankton flora was not so poor as that in CaO sprinkling treatment.

4) Large size zooplankton such as *Philodina erythrophthalma* and *Brachionus angularis*, were observed in case of water glass purification system (Run 5, Run 6, Run 7 and Run 8), because of the structure of waterplant roots for rich niche construction.

5) The diversity index (Shannon Index; H') for phytoplankton flora was higher under complicated community structure such as phytoplankton, zooplankton and waterplants.

6) Water plant purification system (Run 5, Run 6, Run 7 and Run 8) was disturbed by birds as predator, that is, immigration birds such as *Anas platyrhynchos* ate water plants and supply their excrement to water, so positive maintenance is important to keep this system in order.

7) Hybrid treatment system (Run7 and Run 8) did not show the hybrid effect on water purification effect, so it considered important that environmental improvement level should be optimized.

ACKNOWLEDGEMENT

Greatly thanks to Sanmu Reagional Center of Chiba Prefecture, Japan for their cooperation to conduct this study.

REFERENCES

[1] Odum E.P., "Ecology", Holt Rinehart & Winston, Inc., Massachusetts, 1963.

[2] Kurihara Y., "Ecology and ecotechnology in estuarine-coastal area", Tokai University Publishers (in Japanese), 1988.

[3] Fujita M. and Ike M., "Bio-environmental engineering", CMC Publishing, Tokyo (in Japanese). 2006.

[4] Murakami K., Narawa S., Ishii T., Taki K. and Matsushima,H., "Ecocycle management for on-site purification of eutrophicated lakes", Proc. of 3rd IWA World Water Congress (enviro 2002), CD-ROM, 2002.

[5] Murakami K., Ishii T., Taki K. and Matsushima H., "Effect of environmental factors on waterbloom in seaside park pond", Ann. J. Civil Eng.Ocean, JSCE, Vol.23, 2007, pp.627-632.(in Japanese).

[6] Moshir G.A., "Constructed wetland for water quality improvement", CRC Press, 1993.

[7] Amano Y., Taki K., Murakami K., Ishii T. and Matsushima H., "Sediment remediation for ecosystem in eutrophicated lakes", The Scientific World, Vol.2, 2002, pp.885-891.

First International Conference on Science, Engineering & Environment,
Tsu City, Mie, Japan, Nov.19-21, 2015, ISBN: 978-4-9905958-5-2 C3051

DEVELOPMENT OF FUEL CONSUMPTION MODEL IN ESTIMATING ENERGY DEMAND AND CO_2 EMISSIONS FOR INTER-REGIONAL ROAD TRANSPORT USING ROAD SEGMENTS AND O-D DATA

Marloe Sundo[1], Karl Vergel[2], and Ricardo G. Sigua[3]
[1]Faculty, Department of Civil Engineering, University of the Philippines Los Baños, Philippines; [2,3]Faculty, Institute of Civil Engineering, University of the Philippines Diliman, Philippines

ABSTRACT

Given the increasing scientific understanding on the threat of global warming and depleting oil supply to meet the demand, many countries are now finding ways to make energy consumption more efficient to reduce greenhouse gas emissions. Transport engineers and planners nowadays focused more on the development of a new approach or tool that provides fast and reliable means of assessing different transportation strategies to achieve low-carbon transportation system. In this study, a new mathematical Origin-Destination (O-D) approach of estimating energy demand and CO2 emissions is presented using inter-regional passenger and freight flow data. The lengths of three major road segments were used as independent variables to model fuel consumption using full tank method. The estimated energy demand under BAU scenario was compared to four different low-carbon policy scenarios. Study shows that the energy demand from inter-regional public buses and freight road transport under BAU scenario substantially increased from 0.48 million TJ in 2015 to 2.77 million TJ in 2050. These findings equates to 35.20 Megatons and 205.60 Megatons of CO2 emissions in 2015 and 2050, respectively. Results show that shifting to low-carbon alternative fuel such as CNG for buses and trucks provide the highest reduction in overall inter-regional CO2 emissions as compared to other policy measures. Simultaneous implementation of the three selected policy measures would substantially reduce the CO2 emissions by half (50.17%) in 2050.

Keywords:Energy Demand, CO_2 Emission, Origin-Destination, Passenger Trips, Vehicle-Kilometer Travel

INTRODUCTION

One major concern pertaining transportation planning and development is the implications to the overall energy demand and emissions produced during implementation and operation. Specifically, land transport from motor vehicles is considered one of the leading consumer of energy and a major contributor of greenhouse gas emission to the atmosphere not only in the country but also around the globe.

Given the increasing scientific understanding of the threat of global climate change and the decline of oil production to meet the demand, many countries are now finding ways to make energy consumption more efficient to reduce greenhouse gas emissions. Carbon dioxide (CO2) from the transport sector is by far considered as the major contributor of GHG emission into the atmosphere accounting 38% of the total fuel consumed in 2000 [1].

IEA estimates that the global transport sector is responsible for 23% of all energy-related carbon dioxide (CO2) emissions since majority (94%) of the transport sector is still oil-based. Although nearly half (47%) of the total transport energy consumption is in light vehicles mostly passenger cars, but trucks and buses account for a significant share of 27% worldwide [2].

In the Philippines, land-based transport is the most dominant mode of transport representing 98% and 58% of passenger and cargo travel, respectively. However, for land-based inter-regional travel, 95.88% of public mode of transport used buses and 95.06% of freight transport used trucks. From 2000-2012, the country's total number of registered motor vehicles has doubled from around 3.7 million to 7.5 million. The total number continues to rise as registration of new MVs increased by an annual average of 6% from 2004 to 2013 [3].

The Philippine Government created several policy measures to efficiently utilize its energy supply and resources from the transport sector. Administrative Order No. 126 Series of 2005 was issued directing all sectors in the government to enhance the implementation of its energy conservation program launched in August of 2004. The primary objective is to make energy conservation a way of life for every Filipino.

The government also launched the Natural Gas Vehicle Program for Public Transport (NGVPPT) designed to promote the utilization of compressed natural gas (CNG) in the transport sector in consonance with the goal of ensuring fuel supply

diversification and supply security and help improve urban air quality through the reduction of harmful vehicular emissions [4].

To be able to assess effectively the impact of different plans and programs of the government in its effort to fight against global warming, appropriate methods or technique of estimating energy demand and emissions must be readily available to the public. The Philippine government currently used the top-down method in estimating energy demand as mandated under Memorandum Circular No. 93-03-05 Series of 1993. However, the top-down approach is considered not reliable in capturing the impact of different transport policy measures particularly geared towards the reduction of energy demand and vehicle emissions from road transport at the regional level.

While, a limited number of studies in the Philippines with emphasis on national energy demand and CO_2 emissions from the transport sector, attempt to develop a new technique of estimating energy demand and CO_2 emissions using inter-regional passenger and freight flow O-D data is considered very valuable to provide efficient methods of evaluating low-carbon measures[5],[6].

In order to address this gap, availability of practical approach in estimating inter-regional energy demand and CO_2 emission must be sought to provide fast and reliable result in the assessment of strategies to realize low-carbon transport in the country.

OBJECTIVES OF THE STUDY

The general objectives of this study is to develop a fuel consumption model for buses and trucks and present a new approach of estimating and forecasting energy demand and CO_2 emissions for the Philippine inter-regional road transport using available origin-destination data. The study will also develop a fuel efficiency model for buses and trucks in relation to road segment classifications such as urban road, rural highway, and expressway, to be used in estimating energy demand.

The study will also assess the potential implications of selected policies in the overall reduction of CO_2 emissions from the Philippine road transport sector.

STUDY METHODOLOGY

The general approach of this study is to estimate inter-regional energy demand and CO2 emissions Origin-Destination data. Parameters used for the analysis are average vehicle kilometer traveled per vehicle trip, annual passenger trips, occupancy factor, load factor, and the distribution of vehicle and fuel types.

In developing a generalized fuel consumption models for buses and trucks, data from the result of the fuel consumption validation surveys were used. A regression analysis is then carried out using lengths of road segments and average speed as independent variables and total fuel consumption per trip as dependent variables.

The study consider only buses and trucks in modeling and estimating energy demand and CO2 emissions as these two modes of transport dominated the share for all land-based public and freight inter-regional travel with an average of 95.88% and 95.06%, respectively.

Traffic growth rates by region found in Volume 1 of the DPWH Manual were used to forecast passenger trips to future scenario [7]. The conceptual approach in developing energy demand and CO_2 estimation model is shown in Fig.1.

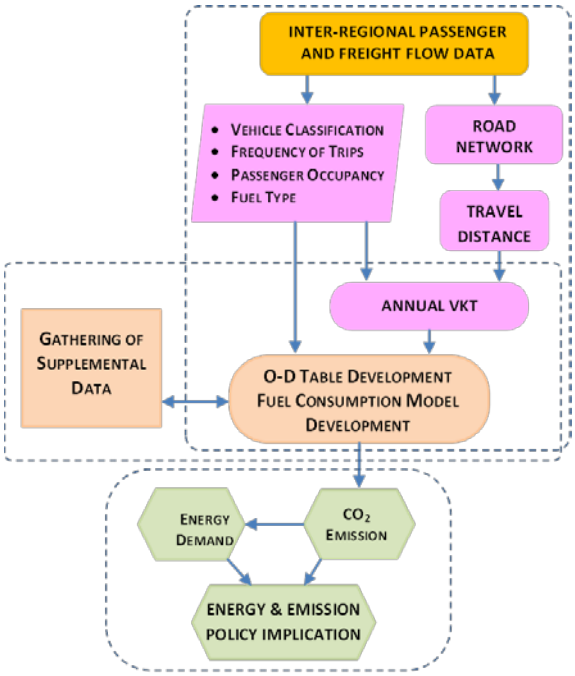

Fig. 1 Conceptual framework of the study

DEVELOPMENT OF FUEL CONSUMPTION MODEL (FCM) FOR BUSES AND TRUCKS

Fuel Consumption Model for Large Bus

Eighteen data samples from the fuel validation surveys were used to model fuel consumption for large buses using regression analysis. The first model considers the different lengths of road segment, that is, urban road (*UR*), rural road (*RR*), expressway (*E*), and average speed of the entire travel ($\overline{V}$) as independent variables and fuel consumption as dependent variable. The result of the regression analysis for large bus yield high r-square of 0.97 and t-statistics greater than 2.0 as shown in

Table 6.1. To evaluate if the first model can still be improved, the length of urban and rural road segments was combined. The result of the regression analysis for the second model shows significant improvements on the r-square, t-statistics, and p-value as shown in Table 1, thus accepted as the final model to be used in estimating fuel consumption for large buses.

Table 1 Result of first fuel consumption model for large buses, *n*=18

Variables	*Coeff*	*t-Stat*	*P-value*	R^2
Intercept	44.455	4.400	0.0007	
UR	0.323	2.533	0.0250	
RR	0.326	32.718	0.0000	0.97
E	0.305	4.730	0.0004	
$\bar{V}$	-1.123	-4.208	0.0010	

Table 2 Result of second fuel consumption model for large buses

Variables	*Coeff*	*t-Stat*	*P-value*	R^2
Intercept	53.909	7.019	0.0000	
UR+RR	0.318	32.522	0.0000	0.98
E	0.329	5.760	0.0000	
$\bar{V}$	-1.285	-5.857	0.0000	

To check whether the actual or observed sample frequencies are consistent from expected or predicted frequencies derived from the proposed model (i.e., the observed fuel consumption data is close to the predicted value), a chi-square test was performed. Since the sum of the chi-square of the predicted values of fuel consumption is 6.3326 and is less than the critical value of 27.587 at 0.05 level of significance and 17 degree of freedom, it is safe to conclude that the model can predict actual fuel consumption for inter-regional travel.

Therefore, the proposed model for estimating fuel consumption for large buses is shown in Eq. (1).

$$FCM_{LB} = 53.909 + 0.318(UR+RR) + 0.329(E) - 1.285(\bar{V}) \quad (1)$$

Where:

FC_{LB} : estimated fuel consumption for large bus per trip in liters
UR : length of urban road segment, km
RR : length of rural road segment, km
E : length of expressway segment, km
$\bar{V}$: average speed of road, kph

The development of the fuel consumption model for small buses, large trucks with 3 or more axles, and small trucks with only two axles were also performed using the same criteria above and the summary of the resulting models are shown in Eq. (2) to Eq. (4) below.

Proposed Fuel Consumption Model for Small Bus

$$\boldsymbol{FCM_{SB} = 112.5409 + 0.1823(UR + RR) - 0.2790(EXPWY) - 0.8222(AVSPEED)} \quad (2)$$

R^2=0.95, *n=12*, Sum of Chi-Square of 2.8537<Critical value of 19.675 at 0.05 level of significance and 11 degree of freedom.

Proposed Fuel Consumption Model for Large Trucks

$$\boldsymbol{FCM_{LT} = 39.832 + 0.275(UR) + 0.472(RR) + 0.442(E) - 1.006(\bar{V})} \quad (3)$$

R^2=0.96, *n=20*, Sum of Chi-Square of 8.1142< critical value of 31.144 at 0.05 level of significance and 19 degree of freedom.

Proposed Fuel Consumption Model for Small Trucks

$$\boldsymbol{FCM_{ST} = 33.409 + 0.192(UR + RR) + 0.119(E) - 0.719(\bar{V})} \quad (4)$$

R^2=0.96, *n=30*, Sum of Chi-Square of 39.94682<Critical value of 42.557 at 0.05 level of significance and 29 degree of freedom.

APPROACH OF ESTIMATING ENERGY DEMAND AND CO2 EMISSION

In estimating inter-regional energy demand and CO2 emission from the road transport sector, the study follows the ASIF theory in a more elaborate approach. The modified formulas in estimating energy demand from the public and freight transport sectors are shown in Eq. (5) and Eq. (6), where $E_m(PT)$ is the estimated total inter-regional energy consumption for public transport (buses) in TJoules, while $E_m(Freight)$ is for freight transport (trucks) in TJoules.

$$E_m(PT) = \frac{P_m}{\hat{O}_m} x\,(D_m)(FCM_{i,j})(A_{i,m})(Bi_{i,m,j})(C_j) \quad (5)$$

$$E_m(Freight) = \frac{W_m}{\bar{Z}_m} x\,(D_m)(FCM_{i,j})(A_{i,m})(B_{i,m,j})(C_j) \quad (6)$$

P_m is the constructed O-D table of annual passenger trips under vehicle category *m;* $\hat{\boldsymbol{O}}_m$ is the constructed O-D table of average occupancy of all vehicles; $\hat{\boldsymbol{D}}_m$ is the constructed O-D table of average annual distance travelled in km; $A_{i,m}$ is the modal share for each vehicle type *i* and category *m;* W_m is

the constructed O-D table of annual gross tonnage of all commodity; $\hat{\boldsymbol{Z}}_m$ is constructed O-D table of average carrying tonnage per freight trip; $B_{i,m,j}$ is the fuel composition factor; C_j is the energy conversion factor; $FCM_{i,j}$ is the formulated fuel consumption model; *m is the* vehicle category (i.e., public & freight transport); *i* is vehicle type (small bus, large bus, small truck, & large truck); and *j* is the fuel type.

In general, P_m and W_m are the expanded annual passenger trips and commodity flows for public and freight transport, respectively as a result of expanding 10-hour sample data to 24-hour population data.

Having estimated the energy demand for each category *m* and fuel type *j*, it is now possible to estimate the total energy demand as the sum of all categories as shown in Eq. (7).

$$E_{TJ}(Total) = \sum_j E_m(PT)_j + \sum_j E_m(Freight)_j \qquad (7)$$

Likewise, the total CO_2 emissions for each fuel type j, in tones can also be computed by applying the corresponding emission factor where EF_j is the emission factor of fuel type *j* as shown in Eq. (8).

$$CO2_{Tons}(Total) = \sum_j E_m(PT)_j(EF)_j + \sum_j E_m(Freight)_j(EF)_j \qquad (8)$$

RESULTS AND ANALYSIS

Integrating fuel consumption models into Eq. (5) and Eq. (6), the inter-regional energy demand and CO2 emissions for buses and trucks can now be estimated. Results of the estimation shows that energy demand from inter-regional public buses and freight road transport under BAU scenario substantially increased from 475,029.52TJ in 2015 to 2,774,695.28TJ in 2050. Consequently, the estimated CO2 emissions from inter-regional public buses and freight road transport under BAU scenario is 35.20 Megatons in 2015 and 205.60 Megatons in 2050.

Results of the study shows that inter-regional travel from NCR to CAR registered the highest energy demand for buses followed by Region V to NCR as shown in Fig 2.

The highest inter-regional energy demand for freight trucks is from NCR to Region IV, followed by region I to NCR as indicated in Fig. 3.

Likewise, the computed 2015 inter-regional CO_2 emissions for buses and trucks from the seven regions in Luzon are shown in Fig.4 and Fig.5. Results show that inter-regional travel from NCR to CAR generates the highest CO_2 emissions for buses followed by Region V to NCR as shown in Fig.4, while inter-regional travel from Region II to NCR generates the highest CO_2 emissions for freight trucks followed by Region II to Region III as shown in Fig.5.

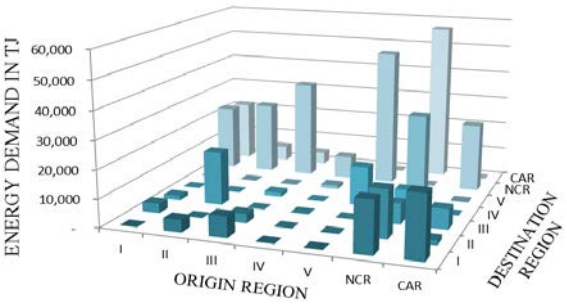

Fig. 2 Computed inter-regional energy demand for buses in 2015

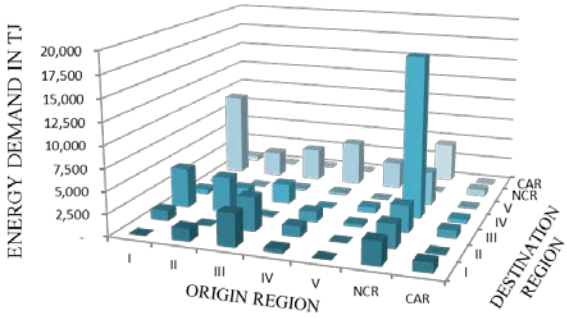

Fig 3 Computed inter-regional energy demand for inter-regional for freight trucks in 2015

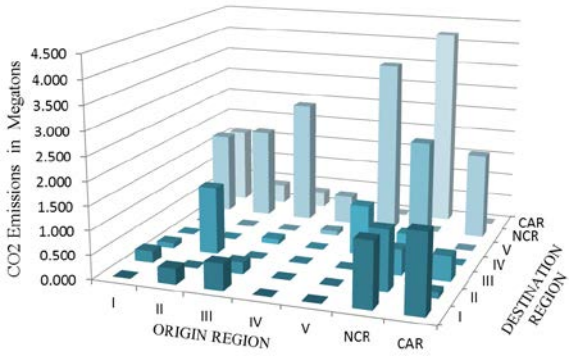

Fig. 4 Computed inter-regional CO_2 emissions for buses in 2015

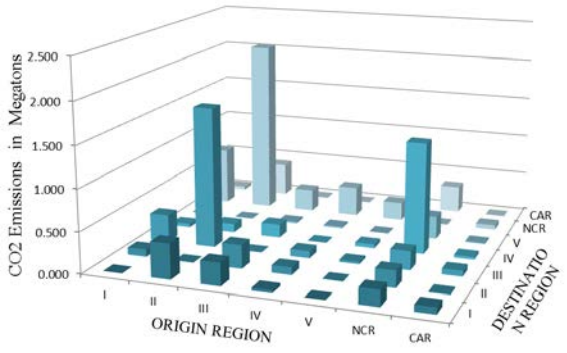

Fig. 5 Computed inter-regional CO_2 emissions for freight trucks in 2015

Implications of Selected Policy Scenarios on Inter-Regional CO_2 Emission

There were four selected policy scenarios to be simulated and compared to the BAU scenario (S1). These are the promotion of alternative fuel program (S2), revitalize the Philippine National Railway (S3), promote better logistic management for freight transport (S4), and the combination of all three scenarios (S5).

Under the promotion of alternative fuel program (S2), the goal is to have a gradual shift from conventional fuel to CNG for trucks and buses by 20% and 35% by 2030 and 2050, respectively.

The revitalized Philippine National Railway (S3) is projected to attract road-based public and freight transport to switch to railway in 2030 by 25% and 20%, respectively. Then continue to increase by 40% and 35% in 2050, respectively.

The study also assumed that through systematic and efficient logistic management, frequency of travel can be reduced by at least 1 in every 5-6 trips, thus resulting to at least 20% reduction in annual vehicle kilometer travel (VKT).

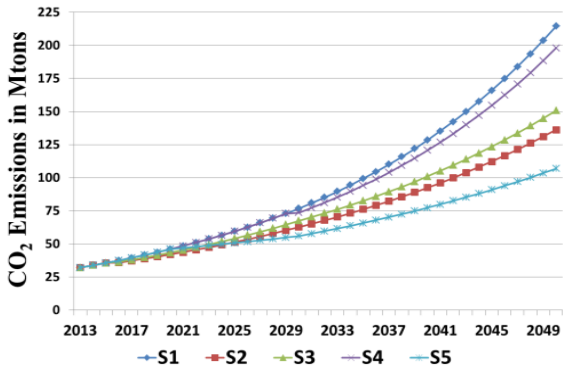

Figure 6 Comparison of selected scenarios for inter-regional CO_2 emissions

Comparisons of different scenarios show that promotion to alternative fuel program provides a more significant reduction in CO_2 emissions from the BAU scenario followed by the revitalized Philippine National Railway system. The least reduction of CO2 emissions can be seen from the better logistic management scenario as this only involve freight vehicle populations. Results also show that simultaneous implementations of all the selected scenarios substantially reduce the BAU CO2 emissions in 2050 by half (50.17%).

SUMMARY AND CONCLUSION

The study presented a new technique and methodology of estimating energy demand and CO_2 emissions for public and freight transport using inter-regional passenger and freight flow data.

A fuel consumption model was developed using regressions analysis and was used to estimate the CO_2 emissions from the different policy measures being selected. The estimated CO_2 emissions from the selected policy scenarios were compared to the reference "BAU" scenario. The study shows that the shift to better fuel such as CNG for buses and trucks provide a very substantial reduction of the estimated inter-regional CO_2 emission in Luzon compared the other selected scenarios.

Findings of this study will further strengthen the government's existing policies to promote the utilization of compressed natural gas (CNG) in the transport sector under the Natural Gas Vehicle Program for Public Transport (NGVPPT).

ACKNOWLEDGEMENTS

The author would like to thanks the Department of Science and Technology for funding this research through the Engineering Research and Development Technology Grant.

REFERENCES

[1] Fabian H, Gota S. CO_2 emissions from the land transport sector in the Philippines: estimates and policy implications, Paper presented at the 17th Annual Conference of the Transportation Science Society of the Philippines, September 4, 2009

[2] Whyte K, Daly H, Gallachóir B. Modelling HGV freight transport energy demand in Ireland and the impacts of the property construction bubble. *Energy* (50), 2013, 245-251.

[3] 2013 Annual Report of the Philippine Land Transportation Office, 2013, 17pp

[4] Department of Energy (DOE). Alternative fuels program. Available at : http://www.doe.gov.ph/ programs-projects-alternative-fuels/293-auto-lpg, 2011

[5] Bayot G, Majarucon C, Sigua R. Analysis and update of the Philippine transport Energy demand, Proceedings of Symposium on Infrastructure Development and the Environment, University of the Philippines, Diliman, Quezon City, December 7-8, 2006, 12pp

[6] Asian Development Bank. Reducing carbon emissions from transport projects. Evaluation Study. Reference Number EKB, REG 2010-16, 107pp.

[7] Department of Public Works and Highways (DPWH). Highway planning manual, Volume 1, 2004, 104pp

[8] Guidelines for National Greenhouse Gas Inventories.3.1-3.78.

First International Conference on Science, Engineering & Environment,
Tsu City, Mie, Japan, Nov.19-21, 2015, ISBN: 978-4-9905958-5-2 C3051

INVESTIGATING THE LINKS BETWEEN LAND USE AND WATER QUALITY FOR FRESHWATER PEARL MUSSEL, MARGARITIFERA MARGARITIFERA, IN THE RIVER SOUTH ESK, SCOTLAND

Le Ma[12]
[1]School of Geographical and Earth Science, University of Glasgow, United Kingdom; [2]School of Veterinary and Life Science, Murdoch University, Australia

ABSTRACT

The Freshwater Pearl Mussel, *Margaritifera margaritifera*, is an endangered species and its population has decreased rapidly over the last century. Scotland is the home to half of the known populations of *M. margaritifera*. Land use is a significant factor affecting water quality as well as the distribution of freshwater pearl mussels. Thirty eight sites in River South Esk were selected to investigate the impact of land use on water conductivity, pH and the concentration of nitrate and phosphorus on the distribution of mussels. *M. margaritifera* was more abundant in habitats in woodland with low and stable water nutrient level. Water chemical analysis indicates that pollutant concentration is related to the vegetation of river catchment. River water passing woodland has a relatively better quality. Overhanging boughs of trees create shadows which attract mussels. Catchment of livestock pasture seems to have less significant chemical effects, but animal activities may disturb the living of mussels and increase water turbidity. Water pollution in irrigated crops land is relatively higher. Heather moorland is less concerned because of its inappropriate channel type for mussels. Housing, roads and bridges seem to be avoided by the mussels. *Margaritifera margaritifera* did not show any preference on the type of shadows. Living mussels has been discovered at the sites which have the shadows created by overhanging branches or high riverbanks.

Keywords: Margaritifera margaritifera, Land use, Water quality, Unionoida, Woodland

INTRODUCTION

Land use surrounding a stream has a significant influence on the abiotic and biotic conditions of the stream [1]. Land clearing will affect the water quality of rivers [2], [3]. Consequently, the biota within waterways also can be impacted [4]-[6]. Nowadays, human activity plays a major role in disturbing river catchments all over the world. Thus, a large number of aquatic species are under threat due to human influences.

Freshwater mussels (Mollusca: Bivalvia: Unionoida) are important for both local ecosystems and humans. Firstly, mussels act as "ecological generalists" and are able to benefit the biodiversity and productivity of a freshwater community [7], [8]. The filter feeding function of freshwater mussels directly improves water clarity and quality [7], [9], [10]. Furthermore, freshwater mussels help to enhance the nutrient transportation connecting the benthic and pelagic layers of water body [11]-[13]. Moreover, shells of mussels also become shelters of many benthic species [14], [15]. Economically, freshwater pearl mussels have been harvested as a source of pearls and mother-of pearls from pre-history [16]-[18]. And mussel meat has been taken as a food source by people as well [16], [19]. Environmentalists have used freshwater mussels as bio-indictors for determining the health of a water body [20], [21].

Unfortunately, despite their importance, the freshwater mussels are also endangered throughout the world. The Freshwater Pearl Mussel, *Margaritifera margaritifera* was abundant and widely distributed in Europe for thousands of years [22], [23]. However, populations of *M. margaritifera* have decreased dramatically in recent years [24], [25]. An earlier estimation has claimed that *M. margaritifera* will be extinct by 2025 as a result of overfishing and habitat degeneration [23], [26], [27]. Recent research has confirmed the potential impact of land use on the recruitment of juvenile *M. margaritifera* [28].

This investigation attempted to discover the relationship between riparian land use and the presence of mussels in River South Esk, Scotland. Additionally, selected parameters for water chemistry were analyzed since the catchment land use is also able to affect water quality.

MATERIALS AND METHODS

Thirty eight sites were selected for visual survey. Land use information was obtained from DigiMap® and confirmed in fieldwork. A buffer zone up to 50m width and the vegetation within 5m from the

riparian was investigated in the survey. Main land uses of River South Esk catchment were categorized as four types: health moorland, livestock pasture, woodland and irrigated crops land [29]-[31]. Channel and bank features were assessed during fieldwork in spring-summer by using the method employed by the Scottish Environment Protection Agency (SEPA) [32]. The vegetation types within the 5m width buffer zone were categorized as either trees or grass.

Abundance of mussels was classified based on the visible number of mussels [33]. Searching started from the access point of river and continued for up to 50 meters upstream unless the channel condition was inadequate. Mussels were counted by visual inspection to avoid disturbance. No mussels were killed or taken out of the river in the fieldwork.

General water quality information was obtained from [32]. Conductivity, Dissolved Oxygen (DO) and pH were measured at the site. Nitrate and phosphate levels were examined within 24 hours after sampling. Water samples were collected at one occasion.

All data analyses were conducted with R software. The difference of mussel population, as well as water chemical parameters, in the four types of land use categories was analyzed by one-way ANOVA. The linear relationships of the mussel population, water chemistry and landscape categories were analyzed by general linear regression.

RESULTS

The abundance of mussels was significantly influenced by land use in the catchment, with more mussels found in woodland than in pasture or crops land and no mussels found in heath moorland (ANOVA: df=3, F=8.63, P<0.001, Fig. 1). Linear regression model suggested that woodland in 50m width buffer zone could be the most significant predictor for the distribution of mussels and a positive relationship might exit (general linear regression: estimate coefficient=1.234 t-test t=1.959 P=0.06). Pasture, irrigated crops land and health moorland seemed to be in a negative relation to the abundance of mussels but did not show a statistical significance (general linear regression: all t-test |t|<1 P>0.4). Statistical result did not illustrate a clear relationship between vegetation type within the 5 m buffer zone and the population of freshwater pearl mussels, yet (ANOVA analysis: P=0.15, general linear regression P=0.19). Additionally, habitat assessment recorded that shading of either overhanging boughs or river bank higher than 5m was presenting in the sites where living mussels were discovered.

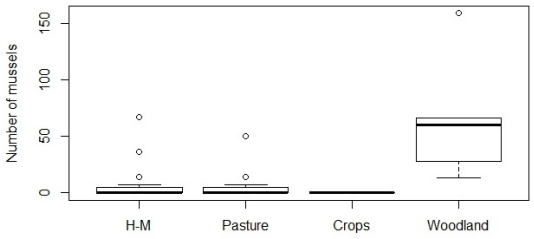

Fig. 1 Population of *Margaritifera margaritifera* with 50m buffer zone land use: Heather moorland (H-M), livestock pasture (Pasture), irrigated crops land (Crops) & Woodland (Woodland).

Water chemistry analysis also demonstrated that the pollution in woodland is relatively lower than other types of land use (Fig. 2). Water nitrate, dissolved oxygen and conductivity performed to be negatively affected by woodland (estimate coefficient: N=-1.27, DO=-0.17, Conductivity=-0.57; t-test t: N=-2.13, DO=-2.49, Conductivity=-2.57; t-test P: N=0.04, DO=0.02, Conductivity=0.015). Difference of DO and conductivity in four strata of land use was also statistically significant (ANVOA DO: df=3, F=3.37, P=0.03; Conductivity: df=3, F=5.65, P=0.003). Furthermore, trees in 5m buffer zone was advised to have positive impacts on dissolved oxygen (estimate coefficient=0.18, t-test t=2.64, t-test P=0.01, Fig. 3). Moreover, conductivity level in the 5m buffer zone with trees was higher than the buffer zone with grass (ANOVA: df=1, F=6, P=0.0187, Fig. 4). Unfortunately, the rest statistical results concerning the relationship between landscape and water quality were out of the confidence interval.

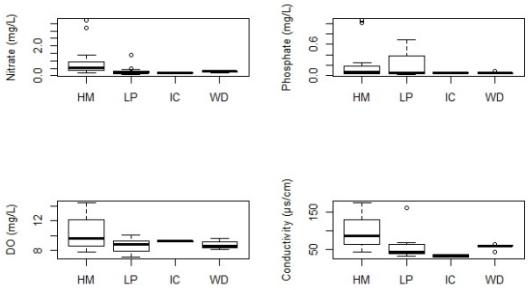

Fig.2 Pollutant concentration in heather moorland (HM), livestock pasture (LP), irrigated crops land (IC) and woodland (WD).

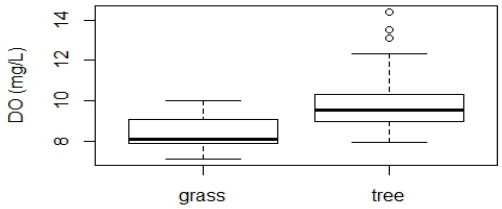

Fig. 3 Dissolved Oxygen of river water coinciding with the landscape of 5m width buffer zone.

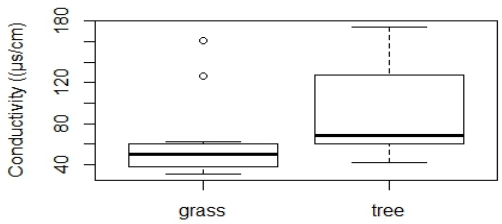

Fig.4 Water conductivity coinciding with the vegetation type of 5m buffer zone.

General linear regression only illustrated a clear negative relationship between the mussel abundance and water dissolved oxygen (estimate coefficient=-0.63 t-test t=-2.258 P=0.03, Fig. 5). Other water quality indicators demonstrated a range in the habitat of freshwater pearl mussels but did not have any confident linear relation (Fig. 6). The variation range of selected water chemicals indicators was recorded in Table 1.

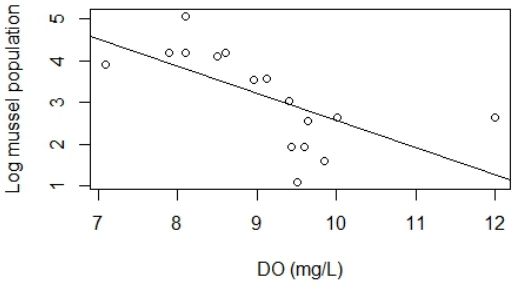

Fig. 5 Linear regression of the abundance of *Margaritifera margaritifera* and DO level of river water.

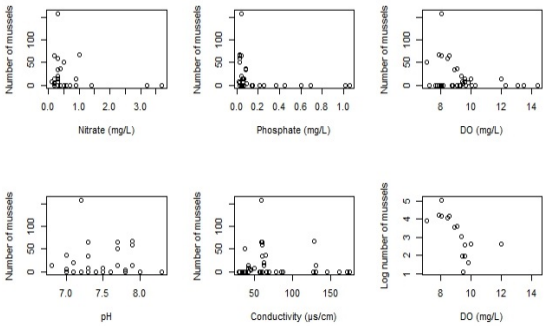

Fig. 6 Abundance of *Margaritifera margaritifera* and water quality.

Table 1: Water quality ranges in the surveyed mussel habitat

Chemical Indicator	Range
$N(NO_3^-)$ (mg/L)	0.1~1.0
$P(PO_4^-)$ (mg/L)	0.02~0.09
DO (mg/L)	7.1~12
pH	6.8~7.9
Conductivity (µ s/cm)	37.30~130.70

DISCUSSION

Woodland may be able to positively affect the population density of *Margaritifera margaritifera*. The concentrations of nitrates and phosphates were lower in the forested areas of the river which is same as the conclusion in [34]. The largest population of freshwater pearl mussels were discovered in the channel within woodland in this research. Besides, water salinity, a crucial factor affecting freshwater mussels, was less variable when flowing through woodland. Furthermore, the DO level in woodland was relatively stable while was not extremely high. Other studies also have shown that organic and inorganic carbon nutrients were relatively lower in forested streams, possibly because of a reduction in water turbidity [34], [35].

Other positive effects of woodland are associated with the shadows created by overhanging boughs and exposed roots [36]. Algal blooms may be toxic to freshwater pearl mussels, and shady areas from trees, as well as lower dissolved oxygen in this region, can limit their occurrence [27], [36]. In this and previous studies, no mussels were found in sections of the river that flowed through heather moorland and density of mussels was reduced in river reaches in livestock pasture and crops land [30], [31]. Furthermore, all discovered mussels were in the shade of trees or high bank in this project as in [30]. Thus, clearing of woodland can be detrimental

for the conservation of freshwater pearl mussels [37], [38].

In addition to the importance of water quality and shading on mussel density, roads, bridges and houses may have several negative impacts on mussels [39]. Mussels were also observed to avoid these type of catchment in this survey. For instance, runoff, sedimentation and disturbing can become a problem although no such event was observed in this research. However, these were reasons in the past for large mortality in mussel populations and should therefore be re-considered as an ongoing threat [40].

The water quality requirements of *M. margaritifera* also may vary among populations as indicated in [30]. Although it is suspected that *M. margaritifera* is sensitive to water quality changes [26], [27], there are freshwater pearl mussels inhabiting reaches which are classified as having poor water quality by SEPA [41]. The water quality results of this survey also did not strictly follow the conclusions proposed in previous studies (Table 2) [26], [42]. While the average nitrate concentration of water stayed within suggested levels, the average level of phosphate exceeded the recommended range. Moreover, DO level had a negative relationship with the number of mussels. Mussels are able to adapt to environmental changes, especially when change is gradual [39], so this variation is not unexpected.

Table 2: Nitrate and phosphate concentration in mussel habitat and target

	$N(NO_3^-)$(mg/L)	$P(PO_4^-)$(mg/L)
Mean	0.3562	0.0487
Range	0.1~1.0	0.02~0.09
Target[26]	< 0.5	<0.03
Target[42]	<1.0	<0.03

CONCLUSION

This research has demonstrated that woodland has positive effects on *Margaritifera margaritifera*. Therefore, the protection of riparian woodland might be important for the conservation and management of freshwater pearl mussels. Land clearance in such areas needs to be reconsidered with care. The combination of large scale land use information and small scale microhabitat investigation is helpful for research concerning species conservation [43].

Questions remain for further studies. This research selected 50m as the buffer zone, which may not be applicable for other research purposes. Furthermore, the conservation of freshwater pearl mussel requires the protection of both: the mussels and the host fishes, trout and salmon. Moreover, the model for protecting freshwater system is complex [40], so the proposal for universal protection may be better than focusing on several selected species.

ACKNOWLEDGEMENTS

This project is supported by University of Glasgow, Scottish Natural Heritage (SNH) and Murdoch University. Lots of thanks are to Dr. Rhian Thomas, Ms. Julia Hobson and Prof. Alan Lymbery for the comments and drafting. Many thanks are to Dr. Iain Sime for the record of mussels in previous investigations. Thanks to Dr. A. McGowan, Mr. K. Roberts and Miss R. Mitchell for the valuable assistance in fieldwork. Appreciation to all landlords who gave me permission to investigate the river channel located in their territories.

REFERENCES

[1] Allan J, “Landscapes and riverscapes: the influence of land use on stream ecosystems”, Annu. Rev. Ecol. Evol. S., Vol. 35, 2004, pp. 257-284.

[2] Mattikalli NM. & Richards KS, "Estimation of surface water Quality Changes in Response to Land Use Change: Application of the Export Coefficient Model Using Remote Sensing and Geographical Information System", J. Environ. Manage., Vol. 48, 1996, pp. 263-282.

[3] Johnes PJ & Heathwaite AL, "Modelling the Impact of Land use Change on Water Quality in Agricultural Catchments", Hydrol. Process, Vol. 11, 1997, pp. 269-286.

[4] Richards C & Host G, “Examining land-use influences on stream habitats and macroinvertebrates – a GIS approach.”, Water Resour. Bull., Vol. 30, 1994, pp. 729-738.

[5] Hutchens JJ, Schuldt JA, Richards C, Johnson LB, Host GE & Breneman DH, “Multi-scale mechanistic indicators of Midwestern USA stream macroinvertebrates”, Ecol. Indic., Vol. 9, 2009, pp. 1138-1150.

[6] Agren A & Lofgren S, “pH sensitivity of Swedish forest streams related to catchment characteristics and geographical location – implications for forest bioenergy harvest and ash return”, For. Ecol. Manag.. Vol. 276, 2012, pp. 10-23

[7] Mackie GL, & Claudi R, Monitoring and Control of Macrofouling Mollusks in Fresh Water Systems, 2nd ed, Canada, CRC Press, 2009 Ch. 6, pp. 265-286.

[8] Walker KF, Jones HA, & Klunzinger MW, “Bivalves in a bottleneck: taxonomy, phylogeography and conservation of frehswater mussels (Bivalvia: Unionoida), Australia”, Hydrobiologia, Vol. 735, 2014, pp. 61-79.

[9] Caraco NF, Cole JJ, & Strayer DL, “Top-down control from the bottom: Regulation of

eutrophication in a large river by benthic grazing", Limnol. Oceanogr., Vol. 51, 2006, pp. 664-670.

[10] Howard JK, & Cuffey KM, "The functional role of native freshwater mussels in the fluvial benthic environment", Freshwater Biol., Vol 51:3, 2006, pp. 460-474.

[11] Greenwood KS, Thorp JH, Summers RB, & Guelda DL, "Effects of an exotic bivalve mollusc on benthic invertebrates and food quality in the Ohio River", Hydrobiologia, Vol. 462, 2001, pp. 169-172.

[12] Vanni MJ, "Nutrient cycling by animals in freshwater ecosystems", Annu. Rev. Ecol. Evol. S., Vol. 33, 2002, pp. 341-370.

[13] Strayer DL, "Understanding how nutrient cycles and freshwater mussels (Unionoida) affect one another", Hydrobiologia, Vol. 735:1, 2014, pp. 277-292.

[14] Jaramillo PQE, & Pino M, "Macroinfaunal assemblages associated with mussel and clam beds in an estuary of southern Chile", Estuaries, Vol. 19, 1996, pp. 62-74.

[15] Seed R, "Patterns of biodiversity in the macroinvertebrate fauna associated with mussel patches on rocky shores.", J. Mar. Biol. Assoc. UK, Vol. 76, 1996, pp. 203-210.

[16] Claassen C, "Washboards, pigtoes, and muckets: historic musseling in the Mississippi watershed", Historical Archeology, Vol. 28, 1994, pp. 1-145.

[17] Ziuganov V, Zotin A, Nezlin L, & Tretiakov V, The freshwater pearl mussels and their relationships with salmonid fish. Moscow: VNIRO Publishing House, 1994.

[18] Ray S, Ray M, Chakraborty S, & Mukherjee S, "Immunotoxicity of environmental chemicals in the pearl forming mussel of India - a review", Mussels: Anatomy, Habitat and Environmental Impact, McGevin Ed, New York: Nova Science Publishers Inc., 2011, pp. 429-440.

[19] Anthony JL, & Downing JA, "Exploitation trajectory of a declining fauna: A century of freshwater mussel fisheries in North America", Can. J. Fish. Aquat. Sci., Vol. 58, 2001, pp. 2071-2090.

[20] Dame RF, Ecology of Marine Bivalves: An Ecosystem Approach, Boca Raton: CRC Press, 1996

[21] Machado AA, Wood CM, Bianchini A, & Gillis PL, "Responses of biomarkers in wild freshwater mussels chronically exposed to complex contaminant mixtures", Ecotoxicology, Vol. 23(7), 2014, pp. 1345-1358.

[22] Bauer G, "Variation in the life span and size of the freshwater pearl mussel", in J. Anim. Ecol., Vol. 61, 1992, pp. 425-436.

[23] Skinner A, Young MR, & Hastie LC, Ecology of Freshwater Pearl Mussel, Peterborough, Gnhlish Nature, 2003, 16 pp.

[24] Beasley CR, & Roberts D, "The current distribution and status of the freshwater pearl mussel *Margaritifera margaritifera* L. in northwest Ireland", Aquat. Conserv., Vol. 6, 1996, pp. 169-177.

[25] Cosgrove PJ, & Young MR, The Status of The Freshwater Pearl Mussel *Margaritifera margaritifera* in Scotland. Edinburgh: Scottish Natural Heritage, 1998.

[26] Bauer G, "Threats to the freshwater pearl mussel in Central Europe", Biol. Conserv., Vol. 45, 1988, pp. 239-253.

[27] Young MR, Cosgrove PF, & Hastie LC, "The extent of, and causes for, the decline of a highly threatened naiad: *Margaritifera margaritifera*", Ecological Studies, Vol. 145, 2001, pp. 337-357.

[28] Österling M, & Högberg JO, "The impact of land use on the mussel *Margaritifera margaritifera* and its host fish *Salmo trutta*", in Hydrobiologia, Vol. 735, 2014, pp. 213-220.

[29] The River South Esk Catchment Partnership, The South Esk Catchment Management Plan, Forfar: Angus Council Economic Development, 2009, 65 pp.

[30] Young Associate, Freshwater Pearl Mussel and River Habitat Survey of A Candidate Special Area of Conservation: River South Esk. Scottish Natural Heritage Research Report F02PA04b (Unpublished report). Inverness: Scottish Natural Heritage, 2003

[31] Hastie LC, Site Condition Monitoring of Freshwater Pearl Mussels in the River South Esk Special Area of Conservation. Scottish Natural Heritage Commissioned Report No. XXX (ROAME No. F0XXX). Inverness: Scottish Natural Heritage, 2009.

[32] Raven PJ, Holmes TH, Dawson FH, Fox PJA, Everard M, Fozzard IR, & Rouen KJ, River Habitat Quality: The Physical Character of Rivers and Streams in the UK and Isle of Man, River Habitat Survey Report No. 2, Edinburgh: Scottish Environment Protection Agency (SEPA), 1998, 96 pp.

[33] Cosgrove PJ, Hastie LC, & Young MR, "Freshwater pearl mussels in peril", British Wildlife, Vol. 11, 2000, pp. 340-347.

[34] Hastie LC, Boon PJ, &Young MR, "Physical microhabitat requirements of freshwater pearl mussel *Margaritifera margaritifera* (L.)", Hydrobiologia, Vol. 429, 2000, pp. 59-71.

[35] Quinn JM, Cooper AB, Davies-Colley RJ, Rutherford JC & Williamson RB, "Land use effects on habitat, water quality, periphyton, and benthic invertebrates in Waikato, New Zealand, hill-country streams", New Zeal. J. Mar. Fresh., Vol. 31:5, 1997, pp. 579-597.

[36] Österling M, Bergman E, Greenberg L, Baldwin BS & Mills EL, "Turbidity-mediated interactions between invasive filer-feeding

mussels and native bioturbating mayflies", Freshwater Biol., Vol. 52, 2007, pp. 1602-1610.

[37] Österling ME, Arvidsson BL, & Greenberg AL, "Habitat degradation and the decline of the threatened mussel *Margaritifera margaritifera*: influence of turbidity and sedimentation on the mussel and its host.", J. Appl. Ecol., Vol. 47, 2010, pp. 759–768.

[38] Dale V, Brown S, Haeuber R, Hobbs N, Huntly N., Naiman R, Riebsame W, Turner M, and Valone T, "Ecological principles and guidelines for managing the use of land.", Ecol. Appl., Vol. 10, 2000, pp. 639–670.

[39] Jones JA, Swanson FJ, Wemple BC & Snyder KU, "Effects of roads on hydrology, geomorphology, and disturbance patches in stream networks", Conserv. Biol., Vol. 14:1, 2000, pp. 76-85.

[40] Strayer DL, Freshwater Mussel Ecology: A Multifactor Approach to Distribution and Abundance, Berkley, CA, USA: University of California Press, 2008, ch. 2 & 8, pp. 9-24, pp. 113-120.

[41] Hastie LC, "Determination of Mortality in exploited freshwater pearl mussel (*Margaritifera margaritifera*) Population", Fish. Res., Vol. 99, 2006, pp. 305-311.

[42] Oliver G, Conservation Objectives for the Freshwater Pearl Mussel (*Margaritifera margaritifera*)., Peterborough, English Nature, 2000.

[43] Li F, Chung N, Bar M, Kwon Y & Park Y, "Relationships between stream marcoinvertebrates and environmental variables at multiple spatial scales", Freshwater Biol., 2012, Vol. 54, pp. 321-330.

First Intern ational Conference on Science, Engineering & Environment, Tsu City, Mie, Japan, Nov.19-21, 2015, ISBN: 978-4-9905958-5-2 C3051

USE OF SI-PHYTOLITHS IN DEPOLLUTION OF MINING INFLUENCED AREAS IN SEMI-DESERT TO DESERT REGIONS OF THE CERRADO-CAATINGA, MINAS GERAIS, BRAZIL. A LOW COST PROCESS.

Adolf Heinrich Horn[1], Regynaldo Arruda Sampaio[2], Heloiza Márcia Fernandes-Horn[2], Ely Sandra Alves de Oliveira[2], Igo Fernando Lepsch[3] & Essaid Bilal[4]

[1]Federal University of Minas Gerais, IGC, 31.270-901 Belo Horizonte - MG, Av. Antônio Carlos, 6627, Brazil,
[2]Federal University of Minas Gerais, ICA, 31630-900 Montes Claros - MG, A. Universitária, 1000, Brazil,
[3]Federal University of Minas Gerais ICA, Montes Claros – MG, Brazil,
[4]Ecole des Mines de St. Etienne, 42023 St. Etienne, Cedex 2158, cours Fauriel

ABSTRACT

Treating of metal contaminated areas became a very important problem with increasing industrial and agricultural activities. Many of the used methods are very expensive, need intensive human interaction or have a very negative influence on the cleaned regions. The use of Si-Phytoliths is a simple, low cost and a very effective way to obtain good results in low contaminated or as the final process in highly contaminated places. The method is based on the fact that plants produce Si-Phytoliths and trap significant quantities of heavy metals in these amorphous to microcrystalline structures. The solubility of the Si-Phytoliths under tropical soil conditions is lower than that of the heavy elements brought directly in the soil by wash-fall out, or by degrading of organic parts of the plants on the surface. In this way, it is possible to retain liberation to the environment from short to long periods and attend environmental laws and norms. Initial tests with different plants like ***Ricinus comunis* L., *Andropogon arundinaceus* Willd., *Zea Mays* L.**, ***Brachiaria sp.* L.** and ***Saccharum officinarum* L.** planted on substrates with metal concentrations (Al, Fe, Mn, Ti, Zn, Cu, Pb, Cd, Ba, Hg, S) have shown that the plants absorbed elements and quantities in the different parts like leaves, roots, stems, flowers and fruits. This allows a selective use due to contamination varieties and a possible economic use of parts of the plants and an effective planning of the decontamination conditions.

Keywords: *Si-Phytoliths, Soil contamination, Heavy metals, Decontamination, Mitigation,*

INTRODUCTION

Contamination process

With the increasing population, the necessity for more raw materials and manufacturing products increases significantly. With this increasing activities also the intensity and the amount of introduction of polluents increases. During the history a lot of environment disasters were described and also an increase of health problems due to the changes of environmental quality. Mining, metallurgy or industrial process produces waste material which is able to contaminate surface areas and need to be disposed. The areas around these sites often suffer with high metal contents.

Decontamination processes

A lot of decontamination methods are known. A lot of them are very expensive, other are very aggressive or need a longtime accompaniment (table 1). The conservative methods are very aggressive, very expensive or need a big amount of human intervention and monitoring. The effects are changes in soil structure and composition, the introduction of strange compounds or plants. Often it is necessary to take of the biological material and deposit it on special places.

The use of Si-Phytoliths seems to be one of the less aggressive, low-cost and independent methods (table 2).

Different to the classic methods, the use of Si-Phytoliths does not interfere in soils and it is possible to use local plants.

Table 1: Used decontamination methods and their properties

Method	Impact	time	Contam. type
Removing of soil	Very strong	short	Inorg./org., high
Use of biomass	low	intermediate	Inorg./org.
Using of additives	Strong to very strong	Short to long	Inorg./org.
Use of phytoliths	Very low	Intermediate to long	Inorg./org. Medium to low

After seeding no more intervention is necessary only the heavy metal content of the soil needs to be verified time in time.

Table 2: Medium quantities of phytoliths in the used plants

Part of plant	Localization	Quantity
Leaves	Surface, inside /between cells	500 ppm
Stem/trunk	Inside/ between cells	300 ppm
Fruits	Inside/ between cells	200 ppm
Roots	Inside and between cells	250 ppm
External	surface of roots, leaves and trunk	800 ppm

Phytoliths

Phytoliths are inorganic material like SiO_2, $CaCO_3$, $(CaMg)CO_3$ or other which are formed in some plants by precipitation of these materials in amorphous ore microcrystalline structures. These organelles are formed in and between plant cells that give them their peculiar form. This form can be used for plant determination.

These particles are formed for different purposes like to enhance structure, to create sharp and hard tissue alimentation and probably also to trap dangerous compounds. Figure 1 show there different forms and where they are localized.

The relative high heavy metal content in the Si-Phytoliths and their low solubility is the basic concept of the use in long-term decontamination of polluted areas like deposits, well regions, mining and industrial sites.

Figure 2 show the possibilities of metal trapping in the organic amorphous SiO_2-structures.

Biomass and Phytolith production

All plants produce biomass and distribute them to the different parts. The production of biomass depends on soil, weather and other physical-chemical factor and therefore differs very between

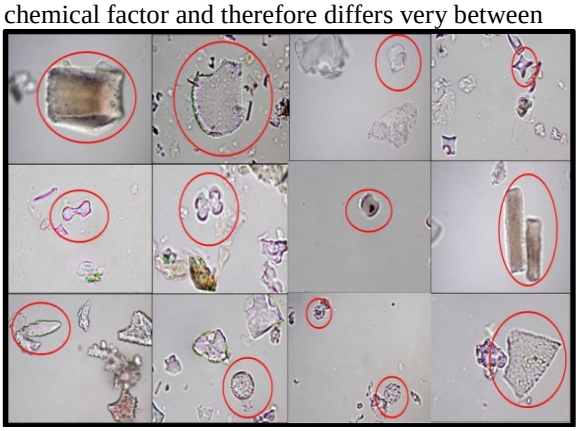

Figure 1: Phytolith forms of plants from Cerrado-Caatinga [14], [11] Left up to right down:
1st row: bulliform; parallelepipedal; cuneiform; blocky; rondell;
2nd row: bilobate; cross; saddle; elongate;
3rd row: acicular; globular granulate; globular echinate; cone shape;

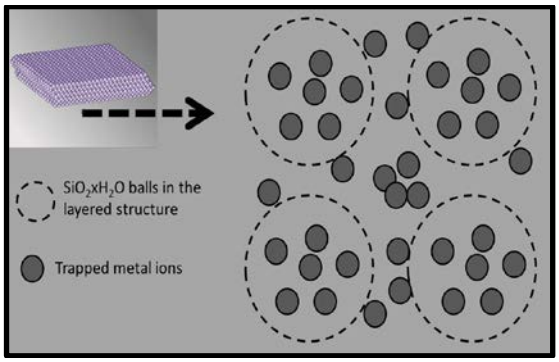

Figure 2: SiO_2-Structure and possible sites of metal ions [1], [7];

authors [5] and [17]. The biomass for millet (*Pennisetum sp.* Schum.) is informed between 9000 and 15.000 $kgha^{-1}y^{-1}$ [13], [15], for *Amaranthus spp.* L. 2500 to 3000 $kgha^{-1}y^{-1}$ [2] and for some grasses from 4000 to 6000 $kgha^{-1}y^{-1}$ [8]. All plants contain significant quantities of some heavy elements. The problem is that after decomposition these quantities return to the soil.

The phytolith concentration varies from plant to plant. The grass used herehave around 9-30 $kgha^{-1}y^{-1}$ and the other plants around 35-65 $kgha^{-1}y^{-1}$.

This phytoliths can trap from 1 ppm (Hg) up to 0,05 % (Fe). This is an important amount for yearly plants. Due to the solubility of SiO_2 (figure 3) this amount returns very slowly to the soil, reducing in this way its heavy metal concentration [4], [6], [9].

The next table 3 shows the heavy metal maximum trapping in SiO_2-modifications. The biological opal due to its structural features, his high content of water and OH^- and it open organization can capture up to 200 g kg^{-1} of metal ions like Al, Ca, Fe, K, Na, Cu, Zn, Ti, Zn and Hg.

These elements are fixed in the structure and closed between the SiO_2 structures.

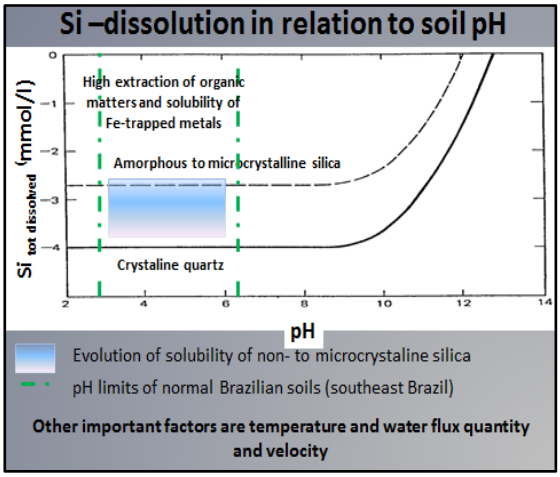

Figure 3: Solubility of the different SiO_2-modifications in relation to the pH.

Table 3: Principal properties and trapping capacities of crystalline quartz, geological- and biological opal [11], [10].* for Cerrado plants; ** analyses of fifty opal specimen.

Mineral	Density	Hardness	Impurities g kg^{-1}	H_2O g kg^{-1}
Quartz	2,65	7,0	traces	0
Plant opal	1,5-2,3	5,5-6,5	50-150*	40-90
Geol. opal	1,2-2,9	5,5-6,5	$\leq$ 200**	2-10

Biomass and Phytolith cycles

During growing all plant produce biomass distributed between its part and also different amounts of phytoliths. During the decomposition this material returns to soil were the biological part is reintegrated by decomposition, liberating the extracted metals. The phytoliths stay without alteration for some thousand years and therefore liberate metals very slowly (figure 4);

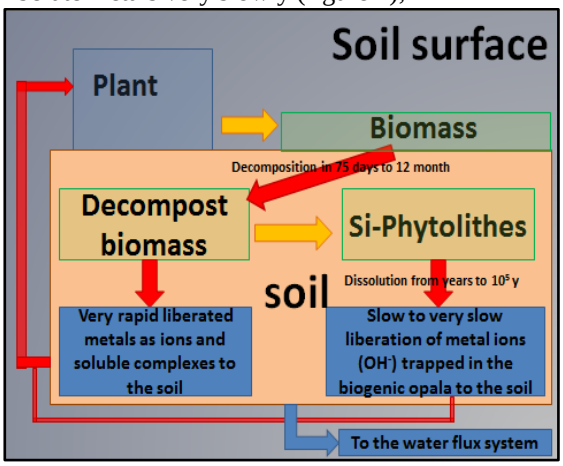

Figure 4: Scheme of principle remediation circulation of phytoliths, biomass and elements in the biogenic and geological cycle.

The next table 3 shows the heavy metal maximum trapping in SiO_2-modifications. The biological opal due to its structural features, his high content of water and OH^- and it open organization can capture up to 200 g kg^{-1} of metal ions like Al, Ca, Fe, K, Na, Cu, Zn, Ti, Zn and Hg.

These elements are fixed in the structure and closed between the SiO_2 structures.

MATERIALS AND METHODS

Soil

We used collected soil from northern part of Minas Gerais. This soil was mixtured with different concentrations of heavy metals and put in 10l bags (table 4).

Table 4: Physical-chemical properties of the used soil. (Laboratory of ICA-UFMG after EMPRAPA methodology)

N	**P**	**K**	**Na**	**Ca**
%	%	%	%	%
3,24	0,75	3,36	0,02	2,21
Mg	**S**	**Fe**	**Mn**	**Al**
%	S	ppm	ppm	$Cmolc/dm^3$
0,26	1,93	44,8	195	0,2
Cu	**Cd**	**Pb**	**Cr**	**Ni**
ppm	ppm	ppm	ppm	ppm
147,5	1,27	36,53	50	24,7

Used plants

For this initial tests to obtain information of heavy metal uptakes several one year plants like ***Ricinus comunis* L., *Andropogon arundinaceus* Willd., *Zea Mays* L., *Brachiaria sp.* L.** and ***Saccharum officinarum* L.** were used (figure 5).

Figure 5: Example of planted corn like used in the remediation tests.

Field tests

Table 5: Element concentration used in the experiments with the different plants

Compound	$g_{element}$/pot	$g_{element}$/kg_{soil}
$BaCl_2$	1	0,2
HgO	0,11	0,022
$Pb(CH_2COO)_2$	0,2	0,04
$Zn(CH_2COO)_2$	3,5	0,7
MnO_2	0,4	0,08
$Cu(CH_2COO)_2$	1,0	0,2
$FeCl_3$	0,7	0,14

Preparation of the samples

The plant samples were separated in its, leaves, roots, fruits and stems and then send to laboratory for drying.

Laboratory

In the laboratory the phytolith preparation and separation were done using process described by [16]. The separated phytoliths were opened by dissolving with mixtures of HNO_3/HF/HCl and the metal concentrations in the filtered solutions determined by analyses with ICP-OES and ICP-MS. Semiquantitave determinations in single phytolith were carried out by using a microprobe with ed-analyzer. The analyses were done in comparison with national and international metal standards.

RESULTS

All analyses indicate the presence of significant quantities of Al, Fe, Mn, Cu up to 10^3 ppm, S, K, Ca, Cr, Zn and Pb (>10 ppm) and a lot of other trace elements near the detection limits of the employed methodologies.

Concentration of elements in phytoliths from ***Brachiaria decumbens*** and ***Andropogon arundinaceus*** (falso massanbará) grown on substrate with or without sewage sludge addition. The analyses were done with ICP-OES and ICP-MS equipment. The results show significant enrichment of some interest trace elements like Cu and Zn.

Andropogon arundinaceus (*Poacea*) shows a significant presence of Si, de S, K, Ca, Cr e Fe (>10mgkg^{-1}). Zn e Cu was found in concentration near detection limits.

Ricinus communis show high Al, Fe, Ti and K (<500 mgkg^{-1}). Only slightly differences in element concentrations between the plants from pots with and without sewage sludge were observed.

Table 6: Analytical results of *Brachiaria decumbens* from substrates with element addition. (Analyses done by ICC-OES at NGqA-UFMG)

Treatment	Fe	Mn	Cu	Zn	Ba
	%	ppm	ppm	ppm	ppm
Soil/Fe	0,05	9	35	11	13
Soil/Mn	0,04	**12**	33	12	14
Soil/Zn	0,03	8	29	**3**	12
Soil/Cu	0,02	10	**453**	13	12
Soil/Ba	0,03	10	28	12	**26**
Soil/Hg	0,03	10	28	11	11
Soil/sludge	0,03	8	**119**	**3**	17
Pure soil	0,03	11	29	12	12

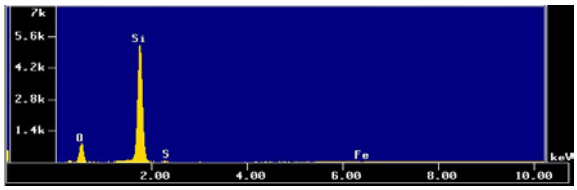

Figure 7: Element trapping of Al in Andropogon arundinaceus.

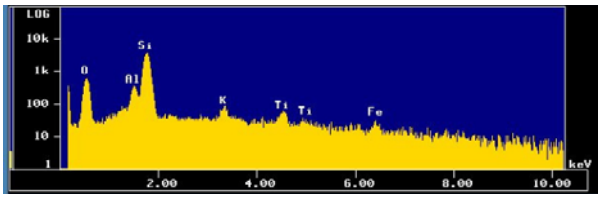

Figure 8 Element trapping shown for Phytoliths of *Ricinus comunis*.

DISCUSSION

The obtained results show that a significant amount of metal ions can be trapped in Si-Phytoliths of a variety of specific plants.

This concentration related to the biomass production show that it is possible to clean areas with considerable soluble metal contamination by using this method of planting selected species of local plants.

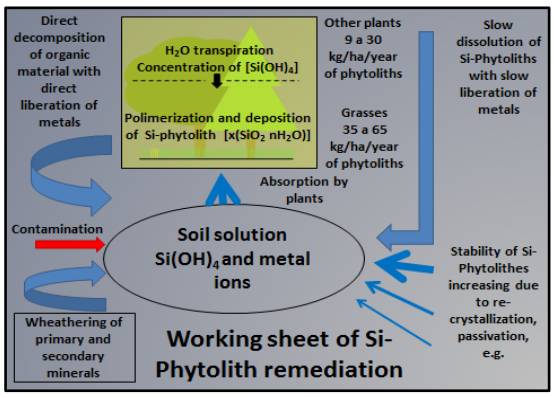

Figure 9: Suggested remediation process using phytolith rich local plants.

The relative simplicity of application and use, the employment of local plants and the long time process predestinate this method for cleaning of sensitive biotopes in endangered environments.

ACKNOWLEDGEMENTS

We thank CNPq, CAPES, IGC-UFMG and ICA-UFMG for financial and logistic support.

BIBLIOGRAPHIC REFERENCES

[1] ALEXANDRE, A.; MEUNIER J.D.; COLIN, F. & KOUD, J.M. Plant impact on the biogeochemical cycle of silicon and related weathering processes. Geochim. et Cosmochim. Acta, 1997, Vol. 61. No. 3: 677-682.

[2] AZEVEDO, D.M.P. & NASCIMENTO H.T.S. Potencial forrageiro de espécies para cultivo no período de safrinha em solos de tabuleiros costeiros. Teresina, Embrapa, 2002. 4p. (Com. Téc. 148).

[3] COSTA, L. M. DA; SANTOS, R. F. DOS; SCHAEFER, E. G. R.; MOREAU, A. M. S. DOS S. & MOREAU, M. S. Ocorrência de corpos siliciosos em horizontes superficiais de solos de diferentes ecossistemas. Rev. Bras. Ciênc. Solo. 2010, Vol. 34, No. 3: 3-7.

[4] DANDURAND, J.L. & SCHOTT, J. New data on the Solubility of Amorphous Silica in Organic Compound-Water Solutions and a New Model for the thermodynamic Behavior of Aqueous Silica in Aqueous Complex Solutions . J. of Sol. Chem., 1987, Vol. 16, No. 3: 237-256.

[5] BOER, C.A.; ASSIS, R.L.DE; SILVA, G.P.; BRAZ, A.J.B.P.; BARROSO, A.L.DE, L.;. FILHO, A.C. & PIRES, F.R. Biomassa, decomposição e cobertura do solo ocasionado por resíduos culturais de três espécies vegetais na região Centro-Oeste do Brasil. Ver. Bras. Ci. Solo, 2008, 32: 843-851.

[6] DOVE, P.; HAN, N.; WALLACE, A.F. & YOREO, J. J. DE Kinetics of amorphous silica dissolution and the paradox of silica polymorphs. Proceed. of the Nat. Acad. Sci. 2008, Vol. 105, No. 29: 9903-9908. www.pnas.org

[7] FELIPE, P.L.L.; CECCHET, F.A.; BRUSTOLINE, L.; CALEGARI, M.R. & PESSENDA, L.C.R. Coleção de referência de fitólitos da floresta ombrófila densa (Linhares; ES): Subsídios para reconstrução palaeoambiental. Reference collection of phytoliths from Ombrophilous Dense Forrest (Linhares, ES): Support for palaeo-environmental reconstruction. CENA-USP: 1971, 33p.

[8] FRANSCISCO, E.A.B.; CÂMARA, G.M.S. & SEGATELLI, C.R. Estado nutricional e produção do capim-pé-de-galinha e da soja cultivada em sucessão em sistema antecipado de adubação. Bragantia, 2007, 66:259-266.

[9] GUNNARSON, I. & ARNÓRSSON, S. Amorphous sílica solubility and the thermodynamic properties of H_4SiO_4 in the range of 0^o to 340^oC at P_{sat}. Geochim. et Cosmochim. Acta, 2000, Vol. 64, Issue 13: 2295-2307.

[10] HORN, A.H.; LEPSCH, I.F.; SAMPAIO, R.A.; RODRIGUES, M.N.; ALVARENGA, A.C. & OLIVEIRA, E.S.A. Heavy metals and aluminum content inside silica phytoliths from *Ricinus comunis*, *Andropogon arundinaceus* Willd, *Ricinus communis* and *Brachiaria decumbens* grown on soils added with sewage sludge and heavy metal salts. 2014, 2p.

[11] LEPSCH, I.F.; RIBEIRO, J.M.; HORN, A.H.; CAVALCANTI, T.F.M.; RODRIGUES, M.N. & COE, H.H.G. Morfologia, quantidade e análise elementar de sílico-fitólitos em tecidos de *Andropogon arundinaceus* Willd crescida em solo com e sem adição de lodo de esgoto. XXXIV. Cong. Bras. Solo. Florianopolis, SC. 2013, 2p.

[12] Element - Issue 3 - The new CT 200h speaker is crafted from bamboo. http://www.lexus-int.com/magazine/issue3/element/; Accessed at 25.3.2015

[13] MORAES, R.M. de. Decomposição das palhadas de sorgo e milheto, mineralização de nutrientes e seus efeitos no solo e na cultura do milho em plantio direto. Lavras, UFL, Master Thesis, 2001, 90p.

[14] MULHOLLAND, S.C. & RAPP G.JR. A Morphological Classification of Grass Silica-Bodies In: Rapp Gré. & Mulholland, S.C. (eds.) 1992. Phytolith Systematics; Emerging Studies. Advances in Archaeol. and Mus. Sci., 1992, Vol. 1, p 65-89.

[15] OLIVEIRA, T.K.; CARVALHO, G.J. & MORAES, R.N.S. Plantas de cobertura e seus efeitos sobre o feijoeiro em plantio direto. Pesq. Agropec. Bras., 2002, 37:1079-1087.

[16] PARR, J.F.; LENTFER, C.J. & BOYD, W.E. A Comparative analyses of wet and dry ashing techniques for the extractions of phytoliths from plant material. J. of Archaeol. Sci., 2001, 28: 875-886.

[17] USP-LCN Dinâmica de Ecossistemas-Cerrado. http://www.ib.usp.br/~delitti/mestres.html; Accessed at 15.3.2015

First International Conference on Science, Engineering & Environment,
Tsu City, Mie, Japan, Nov.19-21, 2015, ISBN: 978-4-9905958-5-2 C3051

EFFECT OF SPEED ON EMISSIONS OF CONVENTIONAL AIR POLLUTANTS IN URBAN ENVIRONMENT: CASE STUDY OF TRUCK EMISSIONS

Pantitcha Outapa[1,2], Akira Kondo[3], Sarawut Thepanondh[1,2]

[1]Faculty of Public Health, Mahidol University, Thailand,
[2]Center of Excellence on Environmental Health and Toxicology (EHT), Bangkok, Thailand,
[3]Graduate school of Engineering, Osaka University, Japan

ABSTRACT

Dynamic emission factors and emission inventories of CO, VOC, $VOC_{evap.}$, NO_x, SO_x and PM of truck in Bangkok, Thailand were developed using IVE (International vehicle emission) model for the year 2012 to 2024. The year 2012 was chosen as base year since fuel quality had been improved from Euro II to Euro IV standard from that year. Speed of truck driven in study area was chosen as variable parameter for sensitivity analysis of its influence to the emissions of air pollutants because there are no further plans in upgrading or improvement of fuel quality during this period. Truck's Bangkok driving cycle was used as input data in the IVE model. Average speeds used in the model simulation were varied from existing condition (15 km/hr) to the maximum of 80 km/hr. It was found that an average speed of 40 km/hr was the optimal speed in reducing of air pollutants emitted from truck. At this speed, reduction of emission factors of air pollutants as compared with current average velocity of 15 km/hr were about 46%, 54%, 16%, 51%, 53% and 27% for CO, VOC, $VOC_{evap.}$, NO_x, SO_x and PM, respectively. Therefore, efforts in increasing average speed of at least to about 40 km/hr can be used as a measure to achieve the sustainable transport particularly in the green logistic businesses.

Keywords: Emission factors, Emission inventory, Conventional air pollutants, Speed, IVE model

INTRODUCTION

Demanding of energy in the transport sector is increased since Thailand started to transform its economy to an industrialized country. The transport sector has been the largest energy consuming sector since 1995 [1]. In Thailand, manufacturing and mining sector and transport sector are about 70 percent of total energy use. Almost all energy used by the transport sector comes from petroleum products which represent 72 percent of the total consumption of petroleum products and 76 percent of transport energy are consumed in the road sector. Truck transport is a dominant of Thailand's freight of the logistics industry that was carrying over 95 percent of ton/km of freight [2]. In addition, consumption of the fuel in the transport sector is also produced an extremely large amount of pollutants emissions. Almost all of the carbon monoxide (CO), 75% of the hydrocarbon (HC) and volatile organic compound (VOC), and 65% of the nitrogen oxide (NO_x) are emitted from vehicles [3]. Pollutant emissions from vehicles are determined by the vehicle's engine type and the fuel it uses that are the two most common engines including spark-ignition (gasoline engines) and diesel engines [4]. Emission control technologies and the age of emission control equipments are one of the factors that effected of pollutants emissions [5].

Moreover pollutant emissions from vehicles are also affected by the driving patterns which depend on traffic conditions. Therefore, driving cycles have been developed to represent behavior and characteristics of driving patterns to support estimation of mobile source emissions in many studies.

There are two major alternatives to develop driving cycle. Firstly, it can be computed from various driving modes of constant acceleration, deceleration and speed such as the New European Driving Cycle (NEDC) and the Urban Driving Cycle (ECE-15). Secondly, it can be derived from actual driving data and is referred as real world cycle. The real world cycles are more dynamic, reflecting the more rapid acceleration and deceleration patterns experienced during on road conditions [3].

Defining the speed limits based on the concept of optimal speed of road transport systems has a significant part in the speed management of vehicles [6], [7]. In the logistic business, trucks are important vehicle type used for transporting of goods. There are high variability with regard to trucks characteristics, types and possible uses [8]. Trucks potentially emit air pollutants such as carbon monoxide (CO), nitrogen oxide (NO_x), particulate matter (PM) and volatile organic compound (VOC). These emissions generally relate to speed of the truck. Generally, emissions of air pollutants from mobile sources are higher at lower average speeds, less sensitive for mid-range speeds, and higher as

speeds increased depend on the type of pollutants [7]. Results from a study of the US.EPA showed that VOC and CO emissions rates normally drop as speed increases. In addition, NO_x emissions rates turn up at higher speeds. However the emissions rates at all speeds have been falling over time as newer and more controlled vehicles enter the fleet [9].

This paper proposes the optimal speed in reducing of air pollutants emitted from trucks in Bangkok, Thailand. The dynamic emission factors and emission inventories of conventional air pollutants namely CO, VOC, $VOC_{evap.}$, NO_x, SO_x and PM of trucks were developed using the IVE model for the year 2012 to 2024. The year 2012 was selected as base year in this study since it was the start year which fuel quality in Thailand had been improved from Euro II to Euro IV standard. Bangkok driving cycle developed for truck was used to represent driving pattern and characteristics in this analysis. Average speeds used in the model simulation were varied from 15, 20, 30, 40, 50, 60, 70 and 80 km/hr.

METHODOLOGY

In this study, average speed of truck driven in Bangkok was chosen as variable parameter for sensitivity analysis of its influence to the emissions of air pollutants. We assumed that there are no further plans in upgrading or improvement of fuel quality which may affect to truck's emissions. Estimations of emissions were carried out from the year 2012 to 2024 (12 years). Numbers of trucks in the inventory period were forecasted using data of average annual growth rate of truck in Bangkok. This value of 4 % increasing from previous year was derived from average of statistical data from the year 2000 – 2010. Moreover fleet characteristics of each predicted year were used taking into accounts the existing regulated emission controls and fuel standards in that year. A truck in this study is defined by weight of more than 12 tons and was named as heavy duty diesel truck. An average speed of 15 km/hr was used as BAU (Business as Usual) case. This study assumed that vehicular growth will be estimated, with all new vehicles based on current policies. The BAU case also assumed there will be no considerable changes in environmental or transport policies [10].

The IVE input data consist of a Location file and a Fleet file. Input data of the Location file include truck's Bangkok driving cycle, soak time, number of start up, fuel characteristics, and average velocity. The Bangkok driving cycle of truck used in this study was as shown in Fig. 1. This driving cycle was converted to vehicle specific power (VSP) bin prior be used in IVE model. The Fleet files in each year were created from secondary data collection. An information on average kilometer traveled, vehicle models, fuel types and age of trucks were collected as the secondary data and were used as input data in Location file. Parameters which affect to the hot stabilized emissions of trucks are trucks technology distribution, VSP and engine stress distribution, inspection and maintenance (I/M) scheme, fuel quality, altitude and meteorological condition (humidity and temperature).These parameters were placed in the model by using actual characteristic of truck and study area. Warm-start and cold-start emissions were separately calculated in the IVE model. These data were computed to obtain an average emission rate expressed in the unit of g/km of trucks.

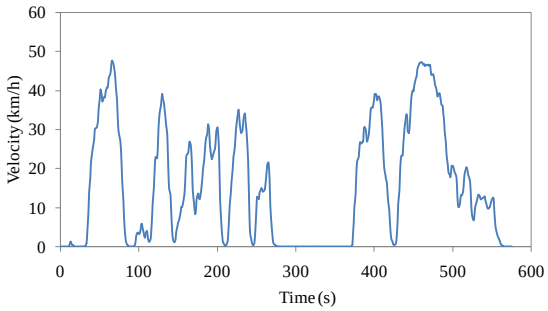

Fig. 1 The truck's Bangkok driving cycle, Thailand.

In BAU scenario, there were about 4% and 96% of trucks in Bangkok driven by CNG (Compress Natural Gas) and diesel (Euro IV standard) fuels, respectively. Fleet technologies of trucks and their index number code used in IVE model in this study were listed in Table 1. The IVE model has a total of 1372 established technologies, and 45 non-defined technologies [11]. All technologies are set as index; each index has an engine/vehicle description including type of vehicle, fuel type, weight, air/fuel control system, exhaust control system, evaporation control system and vehicle age; depends on vehicle kilometer travel. Conceptual diagram of emission calculation process was as presented in Fig. 2.

RESULTS AND DISCUSSIONS

Number of trucks and speed limited

Criterion used in this study, which the truck age doesn't exceed more than 15 years was assumed in this inventory. Average annual growth rate of trucks of 4% is used to estimate total number of truck in each inventory year. Results are as shown in Fig. 3. Number of trucks is slightly decreased from 2013 to 2024. Speeds of truck are varied from its existing value (15 km/hr) to the maximum of 80 km/hr.

Truck dynamic emission factors

Dynamic emission factors of air pollutants of truck calculated from the BAU scenario (average speed of 15 km/hr) were shown in Fig. 4. It was found that NO_x was the dominant pollutant having the highest emission factor from truck as compared with other pollutants followed by CO, PM, VOC, $VOC_{evap.}$ and SO_x, respectively. Emission factors of these pollutants in the base year (2012) were 17.32, 5.19, 2.82, 1.01, 0.08 and 0.01 g/km for NO_x, CO, PM, VOC, $VOC_{evap.}$ and SO_x, respectively.

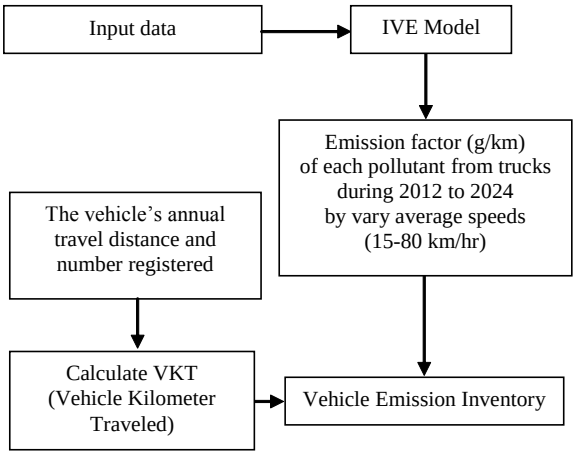

Fig. 2 Calculation process.

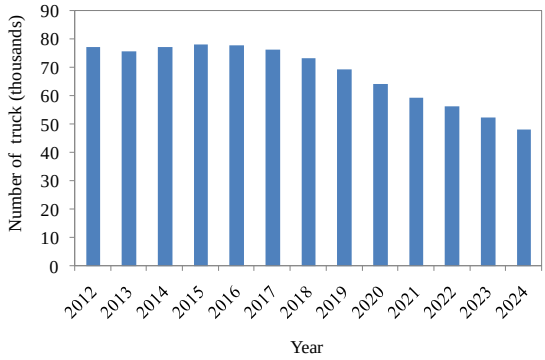

Fig. 3 Number of trucks from 2012 to 2024.

Average speeds used in the model simulation were varied from its existing condition/BAU (15 km/hr) to the maximum of 80 km/hr. Temporal variations of dynamic emission factors of each pollutant at each average speed were shown in Fig. 5. Generally, it was found that the lower average speed of the trucks is the higher of emission factor of air pollutant, they emitted. In order to evaluate the difference of emission factor obtained from calculation using each average speed with the BAU scenario, percentage of reduction of emission factors of each air pollutants as compared with current average velocity of 15 km/hr in BAU case were shown in Fig. 6.

Fig. 6 clearly illustrated that emission factors of NO_x was the most sensitive to changing of average speed of truck. Almost 60% of NO_x emission factor was decreased from its BAU scenario when average speed of 40 km/hr was applied in the calculation. At higher speed (50-80 km/hr), emission factors were still slightly decreased. CO and VOC emissions were also greatly affected by the alteration of average speed. However, SO_x emission factor was less sensitive to the changing of average speed of truck. Maximum reduction rate of SO_x emission was about 25% from its BAU scenario when average speed of truck was increased to about 80 km/hr. These could be explained by the fact that mostly of sulfur dioxide emissions were emitted as result of conversion from sulfur contained in fuel. Unlike with SO_2 emissions, oxides of nitrogen were mostly emitted as results of combustion activities (thermal NO_x).

Table 1 Fleet technology of trucks

Index	Meaning
996 **997** **998**	Heavy duty fuel injected natural gas vehicle with 3 way catalyst and Exhaust Gas Recirculation (EGR). Vehicles >33,001 lbs Gross Vehicle Weight Rating (GVWR) and typically >60,000 lbs.
1132 **1133**	Heavy duty fuel injected diesel vehicle certified to Euro II standards. Vehicles >33,001 lbs GVWR and typically >60,000 lbs.
1140 **1141** **1142**	Heavy duty fuel injected diesel vehicle certified to Euro III standards. Vehicles >33,001 lbs GVWR and typically >60,000 lbs.

US.EPA reported the average in use emissions from diesel heavy duty truck by using MOBILE 6 emission model [12]. Emission rates of NO_x and CO at the average speed of 64 km/hr (40 miles/hour) were reported as about 13.78 and 3.70 g/km, respectively. These values were higher than emission rates obtained from calculation at the same speed using IVE model in this study. These differences can be explained by difference of driving cycle, fleet characteristics and fuel quality in each area.

The optimal speed in this study was determined based on decreasing rate of emission factor. This speed was also used as reference value to maintain speed limits at higher than or on average equal to the optimal speed [6].

In this study, an average speed of 40 km/hr was selected as the optimal speed in reducing of air pollutants emitted from truck. This selected value was based on two major criteria.

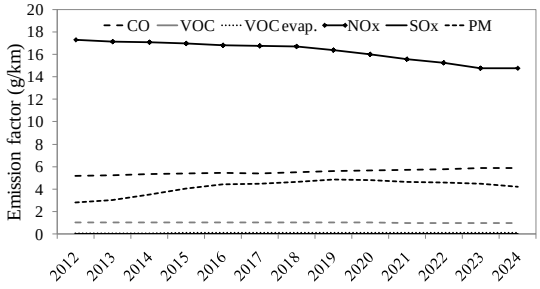

Fig. 4 Dynamic emission factor of each pollutant as BAU case.

The first criteria was obtained from results of this study which indicated that an average speed of 40 km/hr could yield significantly decreased of air pollutants emitted from truck, though emission factors were still slightly decreased at higher speed than this level.

The second factor of selection of optimal speed was speed limit of truck of not more than 60 km/hr regulated in Thailand. Therefore, with the current policy, trucks are not allowed to drive faster than this level. However, by considering existing speed of 15 km/hr, and characteristics of Bangkok which is a mega-city, we proposed that in practical, the optimal average speed of truck in Bangkok can be raised up to level of 40 km/hr and no driving over than 60 km/hr.

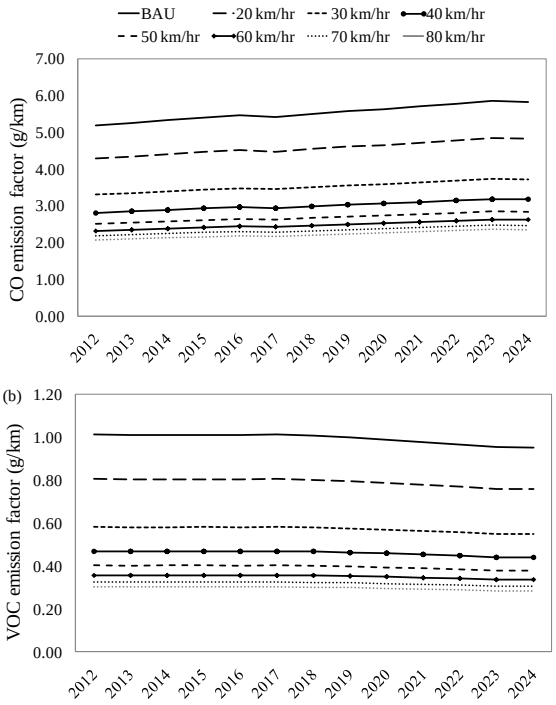

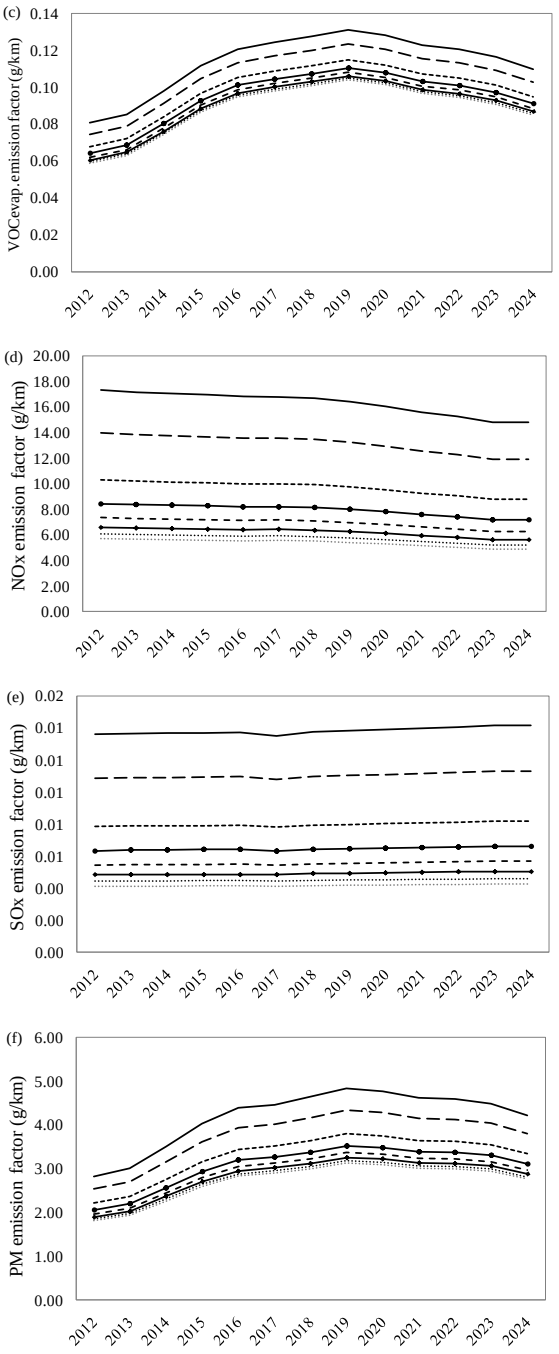

Fig. 5 Trucks emission factors of each pollutant from 2012 to 2024 are affected by average speed.

Truck dynamic emission inventories

Other objective of this study is to assess and elaborate total amount of emission in order to identify factor influenced to emission inventory of air pollutants. Dynamic emission inventories indicate that factors influencing emission amounts of air pollutants from trucks in Bangkok are Vehicle Kilometer Travel (VKT), number of vehicles and emission factor [10]. The VKT of trucks in Bangkok were estimated base on the VKT studied in urban

area by [13]. Emission inventories of CO, VOC, $VOC_{evap.}$, NO_x, SO_x and PM were calculated for the year 2012 to 2024. Results were as shown in Fig. 7. Emission inventory of VOC, NO_x were slightly increased from 2012 to 2015, and were significantly decreased from 2015 to 2024. CO, SO_x and PM were slightly increased from 2012 to 2016, and were significantly decreased from 2016 to 2024. Moreover, VOC_{evap} was slightly increased from 2012 to 2017, and was significantly decreased from 2017 to 2024. These trends were relevant to number of truck driven and their fleet technologies in each year. Results clearly indicated that NO_x was the major pollutant emitted from truck. Comparison of emission inventory from proposed optimal speed (average speed of 40 km/hr), calculated results showed that emission amount of CO, VOC, $VOC_{evap.}$, NO_x, SO_x and PM were about 46%, 54%, 17%, 51%, 53% and 27% decreased from BAU scenario (average speed of 15 km/hr), respectively.

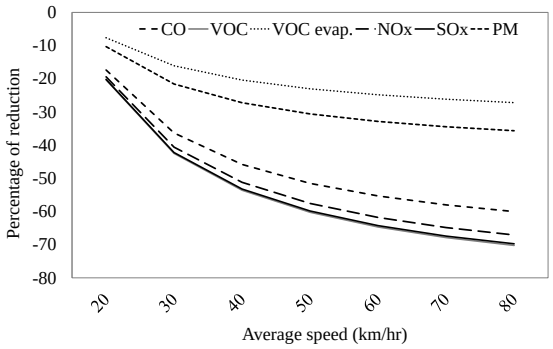

Fig. 6 Percentage of reduction of trucks emission factors comparing with BAU case are affected by average speed.

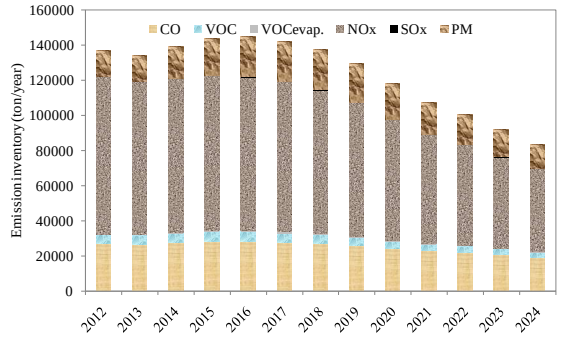

Fig. 7 Trucks emission inventory from 2012-2024 as BAU case.

CONCLUSION

Emission factors of air pollutants from truck driven in Bangkok, Thailand were developed using the IVE model. It was found that NO_x was the major type of pollutant emitted from truck. Speed of truck in Bangkok driving cycle was used as variable parameter for testing its influenced to values of emission factor. Results indicated that the higher of average speed, the lower of emission factors of air pollutants emitted from truck. Temporal analysis during the year 2012 to 2024 clearly indicated that dynamic emission factors of air pollutants had decreasing tendency. Emission factor of NO_x was successfully decreased as a result of higher speed of truck which could be explained by better control of thermal NO_x from increasing of combustion efficiency. Average speed of 40 km/hr was proposed as optimal speed for truck in this study. Two major criteria were used to support this selection. Firstly, at this proposed speed, there were dramatically decreased of emission factors of air pollutants as compared with current fleet characteristics of truck in Bangkok (average speed of 15 km/hr). At higher speed than this level (>40 km/hr), emission factors were still slightly decreased. Secondly, speed limit of truck in Thailand is regulated as not higher than 60 km/hr. By considering that Bangkok is a mega-city, this regulated speed limit may not appropriate to use, practically. Other supporting of this proposed was the maximum speed of truck from the survey of truck driving cycle in Bangkok was 48 km/hr. Therefore, average speed of 40 km/hr was selected as optimal speed of truck in this urban area. Emission inventory of air pollutants emitted from truck were also calculated using derived emission factors obtain from this study. Results indicated that amount of air pollutants emitted from trucks had decreasing tendency. These reductions were resulted by decreasing of emission factors which mostly due to termination of old truck as well as replacing by the new one with higher technology. By increasing average speed from its current level (15 km/hr) to the proposed optimal average speed of 40 km/hr, emission amount of air pollutants were decreased. Particularly, NO_x emissions were decreased more than 50% from their BAU scenario. However there are many factors that affect to emission factors including engine technology, vehicle age, level of maintenance, fuel quality and emission standard in each area. These factors should be considered when estimating emission rate from mobile sources.

The proposed optimal speed at 40 km/hr can be reached by improvement of highway system as well as designated specific time period to allow commuting of truck during the on-road off peak period (from 22.00 – 05.00) when traveling in urban and sub-urban areas should be strictly implemented.

ACKNOWLEDGEMENTS

The authors greatly appreciate the support with data from the Pollution Control Department and the Land Transport Department of Thailand. Financial support of this research was granted by Research and Researcher for Industrial, the Thailand Research

Fund. These studies were partially supported for publication by the China Medical Board (CMB), Faculty of Public Health, Mahidol University, Thailand.

REFERENCES

[1] Pongthanaisawan J, Sorapipatana C, and Limmeechokchai B, "Road Transport Energy Demand Analysis and Energy Saving Potentials in Thailand", Asian J. Energy Environ., vol. 8, 2007, pp. 49–72.

[2] Thailand-World Bank Country Development Partnership for Infrastructure, "THAILAND : MAKING TRANSPORT MORE ENERGY EFFICIENT" retrieved Jan. 2014 from, http://siteresources.worldbank.org/THAILANDEXTN/Resources/333295-1253072771677/TH_MakingTransportMoreEnergyEfficient_fullreport.pdf

[3] Tzirakis E, Pitsas K, Zannikos F, and Stournas S, "Vehicle Emissions and Driving Cycles : Comparison of the Athens Driving Cycle (ADC) With Ece-15 and European Driving Cycle (EDC)", Glob. NEST J., vol. 8, 2006, pp. 282–290.

[4] Faiz A, Weaver CHS, and Walsh MP, "Air pollution from motor vehicles", retrieved Jan. 2015 from http://www.un.org/esa/gite/iandm/faizpaper.pdf

[5] Takigawa A, Mieda A, andPeng Y, "REACTION BEHAVIOR OF C_6H_6 IN THE THREE-WAY CATALYTICCONVERTER EQUIPPED A GASOLINE ENGINE",Int. J. of GEOMATE, vol. 6, June. 2014, pp. 2–6.

[6] Hosseinlou HM, Kheyrabadi AH, and Zolfaghari A, "Determining optimal speed limits in traffic networks" retrieved April. 2015 from http://dx.doi.org/10.1016/j.iatssr.2014.08.003

[7] Center for Transportation Research and Education (CTRE), "Role of Passenger Vehicle and Heavy Truck Speed Differences in Emissions Modeling" retrieved April. 2015 from, http://www.researchgate.net/profile/Shauna_Hallmark/publication/242273295_Role_of_Passenger_Vehicle_and_Heavy_Truck_Speed_Differences_in_Emissions_Modeling_tech_transfer_summary/links/0f31752f24ed565333000000.pdf

[8] Fontaras G, Martini G, Manfredi U, Marotta A, Krasenbrink A, Maffioletti F, Terenghi R, and Colombo M, "Assessment of on-road emissions of four Euro V diesel and CNG waste collection trucks for supporting air-quality improvement initiatives in the city of Milan". J. of Science of the Total Environment, Vol. 426, April 2012, pp.65-72.

[9] U.S. Department of transportation, "Transportation Air Quality Facts and Figures January 2006" retrieved April. 2015 from http://www.fhwa.dot.gov/environment/air_quality/publications/fact_book/page15.cfm

[10] Outapa P and Thepanondh S, "Development of Air toxic emission Factor and inventory of On-road Mobile Sources". J. of Air, Soil and Water Research, 2014, Vol.7, pp. 1–10.

[11] International Sustainable Systems Research Center, "IVE model users manual version 2.0" retrieved Sep. 2014 from, http://www.issrc.org/ive/

[12] United States Environment Protection Agency (USEPA), "Emission Facts: Average In-Use Emissions from Heavy-Duty Trucks" retrieved May. 2015 from, http://www.epa.gov/otaq/consumer/420f08027.pdf

[13] Limanond Th, Pongthanaisawan J, Watthanaklang D, and Sangphong O, "An Analysis of Vehicle Kilometers of Travel of Major Cities in Thailand" retrieved Jan. 2014 from, http://www.atransociety.com/2015/pdf/pdfSymposium2010/download/ppt_day_1/(1)Dr.%20Thirayoot%20Limanond.pdf

First International Conference on Science, Engineering & Environment,
Tsu City, Mie, Japan, Nov.19-21, 2015, ISBN: 978-4-9905958-5-2 C3051

ZOOPLANKTON AND PHYTOPLANKTON IN ALL ANOXIC LAYERS OF LAKE FUKAMI-IKE

Hiromi Suda [1], Masaaki Tanaka [2], Megumi Nobori [1] and Akihiko Yagi [1]
[1] Faculty of Civil Engineering Department of Urban Environment, Aichi Institute of Technology, Japan
[2] Faculty of Environmental and Information Sciences, Yokkaichi University, Japan

ABSTRACT

Lake Fukami-ike is a small monomictic and eutrophic lake, located in southern Nagano Prefecture in Central Japan. An uncommon phenomenon of dissolved oxygen 0-1 mgL^{-1} from the surface to the bottom layer occurred on 16 November, 2013. On November 2 (before all layers under the anoxic condition), *Trichocerca similis* (Rotatoria) etc. dominantly distributed from the surface layer to 5 m depth depending on distribution dissolved oxygen. *Tintinnopsis lacustris* (Protozoa) was found in the bottom layer under the anoxic condition. The number of cells (*Synedra rumpens* (Bacillariophyceae) and *Crucigenia tetrapedia* (Chlorophyceae)) abounded from the surface to 5 m layer. On November 16 (all layers under the anoxic condition), *Tintinnopsis lacustris* (Protozoa) distributed from the surface to the bottom layer. Phytoplankton were few in any layer at that time. Then, *Tintinnopsis lacustris* continued to distribute from the surface to the bottom layer, and the genus *Synedra* (Bacillariophyceae) was found to have distributed uniformly from the surface to 6 m depth in the next investigation on 21 December, when the dissolved oxygen concentration was about 10 mgL^{-1} from the surface to the bottom layer. The changes in vertical distribution of *Tintinnopsis lacustris* from 2 to 16 November, seemed to indicate that lake water was lifted from the bottom layer (*Tintinnopsis lacustris* living) when shift stagnation periods to circulation periods.

Keywords: All layers, Anoxic condition, Zooplankton, Phytoplankton

INTRODUCTION

Lake Fukami-ike is a small monomictic and eutrophic lake. The studies in this lake were begun from 1978, and it is continuing now mainly about water quality roughly once a month. An uncommon phenomenon occurred due to dissolved oxygen 0 - 1 mgL^{-1} from the surface to bottom layer on 16 November, 2013.

This paper describes the results of zooplankton and phytoplankton distribution, nutrients, and chlorophyll-*a* in all layers in the anoxic condition, compared with the previous investigation (on 2 November) and the following investigation (on 21 December).

METHODS

Sampling analysis

Lake water samples were collected at the deepest point with a hand−operation water pump connected to a polyvinylchloride tube from every 0.25 m depth during the period of water stratification from April to October or from every 50 cm-1 m depth in other months.

A part of the water samples was filtered through a glass fiber filter (Whatman, GF/F, 47 mm) immediately after the sampling. The samples were stored at -20 ℃ until chemical analysis in the laboratory. The filtrate was used for the determination of ammonium, nitrate, nitrite and phosphorous. Inorganic nitrogen (ammonium, nitrate, and nitrite) was measured by ion chromatography analysis (DKK-TOA CORPORATION, PCI-311S). Total dissolved phosphorus was measured by the molybdenum blue colorimetric method (Murphy and Riley, 1962).

Chlorophyll-*a* was measured by the fluorometric method (Holm-Hansen et al., 1965). Water temperature was measured with a thermistor thermometer, and dissolved oxygen was determined with a DO meter.

Plankton samples were taken with a Van Dorn water sampler (10L, Rigo Co., Ltd., Tokyo Japan) every 1 m from the upper layer to the bottom layer. When the water sampling in 7 m layer, take a slight mud of bottom layer. All samples were preserved in 1% formalin in the field immediately, then counted and identified by optical microscope (BX51, OLYMPUS Optical Co., Ltd., Tokyo, Japan) in the laboratory. The cells of phytoplankton and individual zooplankton were counted using a ruled line glass slide. Dominance was shown by the numbers of cells and individuals.

Study site description

Lake Fukami-ike is a small monomictic and eutrophic lake, located in southern Nagano Prefecture in Central Japan; north latitude 35° 32′ 55″ 77, east longitude 137° 81′ 93″ 56, with a small diameter: 150 m, 300 m, area 2.1 ha, volume 1.0 × 105 m^3 and a maximum depth of 7.75 m (Fig. 1) (Yagi, 2009, 2010).

Circulation periods were in November to March, and stagnation periods in April to October; the dissolved oxygen concentration was zero in about the 4 m to 5 m deeper layer in mid-summer (Yagi et al., 2009).

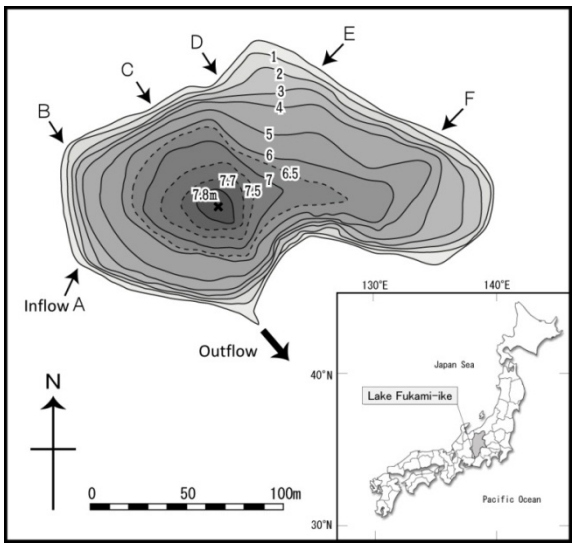

Fig. 1 Bathymetrical map of Lake Fukami-ike.

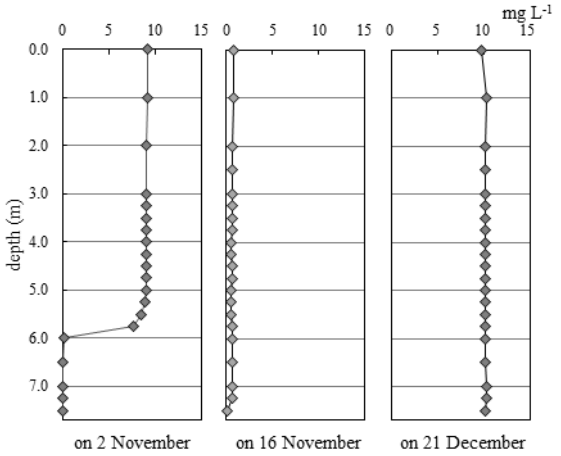

Fig. 2 Vertical distribution of dissolved oxygen on 2 and 16 November, and 21 December.

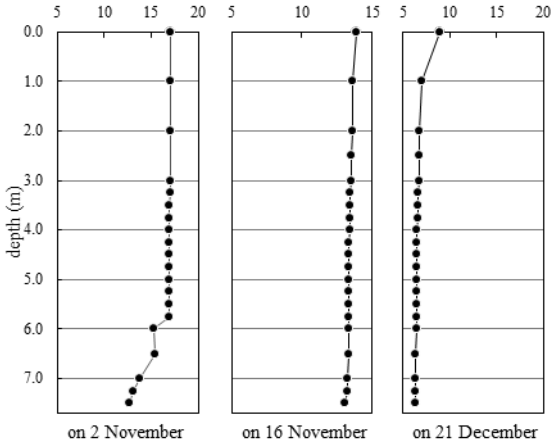

Fig. 3 Vertical distribution of water temperature on 2 and 16 November, and 21 December.

RESULTS

Water temperature and dissolved oxygen

Vertical distributions of dissolved oxygen on 2 and 16 November, and 21 December were shown in Fig. 2. Vertical distribution of water temperature was shown in Fig. 3.

Dissolved oxygen decreased to about zero about 6 m deeper, water temperature decrease (<15.5 ℃) 6 m deeper on 2 November; meaning in stagnation periods.

On 16 November, the value were shown at nearly zero in all layer, water temperature were constantly at about 14 ℃ in all layers.

On 21 December, the value were constantly at about 10 mgL^{-1} in all layers, water temperature was constantly about 7 ℃ 1 m; meaning in circulation periods.

Zooplankton

Vertical distribution of zooplankton on 2 and 16 November and 21 December was shown in Fig. 4.

Trichocerca similis (Rotatoria) and *Bosmina longirostris* (Crustaceae) dominantly distributed from the surface layer to 5 m depth. They distributed depending on the sufficiently dissolved oxygen concentration layer. *Tintinnopsis lacustris* (Protozoa) distributed in the bottom layer (anoxic condition), on 2 November.

On 16 November, *Tintinnopsis lacustris* (Protozoa), which distributed only in the bottom layer on 6 November, distributed from the surface to the bottom layer. *Epistylis* sp. (Protozoa) was found in all layers the secondly.

On 21 December, *Tintinnopsis lacustris* continued to distribute from the surface to the bottom layer; density (ind. L^{-1}) was much the same while dissolved oxygen was zero on 2 November.

Epistylis sp. (Protozoa) and *Bosmina longirostris* (Crustaceae) etc. were found.

From 16 November to 21 December, for about one month, *Tintinnopsis lacustris* continued distribution in all layers. At the next investigation (on 18 January, after about one month), *Tintinnopsis lacustris* was not found.

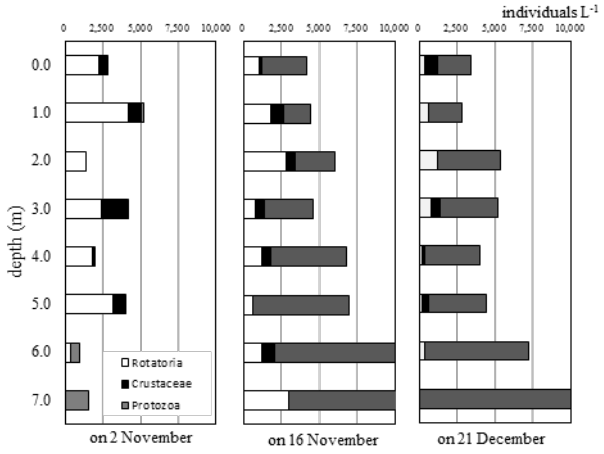

Fig. 4 Vertical distribution of phytoplankton on 2 and 16 November, and 21 December.

Nutrients

Ammonium (NH_4-N), nitrate (NO_2-N), nitrite (NO_3-N) and phosphorus phosphate (PO_4-P) were shown in Table 1-3.

On 2 November (during stagnation periods), NH_4-N and PO_4-P concentrations were high (6 m deeper layer), and the NO_3-N concentration was 0 in 6 m deeper layer. On 16 November, NH_4-N, NO_3-N, NO_2-N and PO_4-P concentrations were constant from 0 m to 7.5 m, except for NO_3-N and PO_4-P in 7.5 m.

On 21 December (during circulation periods), NH_4-N, NO_3-N, NO_2-N and PO_4-P concentration were constant from 0 m to 7.5 m.

The concentrations were highest on 16 November in the range 0 m from 6.5 m, on 2 and 16 November, and 21 December, except for release from bottom layer (in 6.5 m deeper layer) on 2 November (during stagnation periods).

Table 1 Vertical distribution of NH_4-N, NO_2-N, NO_3-N and PO_4-P on 2 November.

(mg l^{-1})

depth (m)	NH_4-N	NO_2-N	NO_3-N	PO_4-P
0	0.04	0.00	0.31	0.02
1	0.03	0.00	0.34	0.02
2	0.02	0.00	0.42	0.01
3	0.02	0.00	0.33	0.02
4	0.02	0.00	0.37	0.01
5	0.01	0.00	0.37	0.01
6	0.07	0.00	0.00	0.12
7	0.08	0.00	0.00	0.79
7.5	0.06	0.00	0.00	0.91

Table 2 Vertical distribution of NH_4-N, NO_2-N, NO_3-N and PO_4-P on 16 November.

(mg l^{-1})

depth (m)	NH_4-N	NO_2-N	NO_3-N	PO_4-P
0	0.90	0.00	0.30	0.01
1	0.19	0.00	0.26	0.02
2	1.00	0.00	0.29	0.01
3	1.05	0.00	0.28	0.00
4	0.95	0.00	0.27	0.03
5	-	0.00	0.28	0.05
6	0.75	0.00	0.30	0.01
7	1.10	0.00	0.43	0.02
7.5	-	0.01	0.07	0.19

Table 3 Vertical distribution of NH_4-N, NO_2-N, NO_3-N and PO_4-P on 21 December.

(mg l^{-1})

depth (m)	NH_4-N	NO_2-N	NO_3-N	PO_4-P
0	0.18	0.02	0.59	0.02
1	0.23	0.01	0.48	0.01
2	0.24	0.03	0.42	0.01
3	0.19	0.03	0.33	0.01
4	0.19	0.02	0.42	0.00
5	0.19	0.03	0.55	0.01
6	0.19	0.00	0.33	0.01
7	0.19	0.00	0.23	0.01
7.5	0.20	0.05	0.50	0.00

Chlorophyll-a

Vertical distributions of chlorophyll-*a* on 2 and 16 November, and 21 December were shown in Fig. 5.

The values were about 60 mg L^{-1} at 0 m to 5 m, about 200 to 400 mg L^{-1} (as bacterio chlorophyll-*c*) in 5 m deeper on 2 November. The values constantly ranged from about 10 to 20, except for about 200 mg L^{-1} in 7.5 m on 16 November. The values constantly

ranged from about 40 to 60 in all layers. The values of 16 November were low in the three investigations.

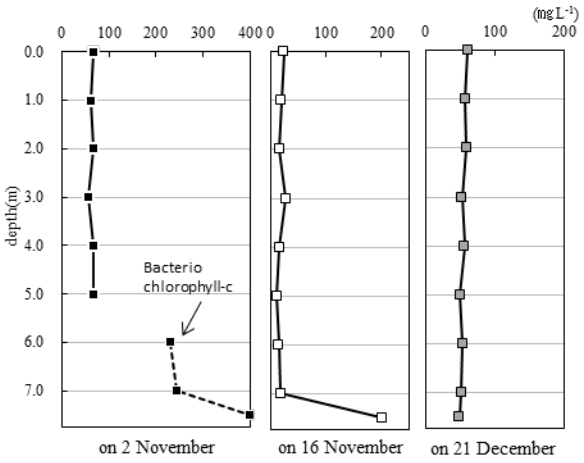

Fig. 5 Vertical distribution of Chlorophyll-*a* concentration on 2 and 16 November, and 21 December.

Phytoplankton

Vertical distribution of phytoplankton on 2 November, 16 November and 21 December were shown in Fig. 6.

The number of cells abounded from the surface to 5 m layer; *Synedra rumpens* (Bacillariophyceae) and *Crucigenia tetrapedia* (Chlorophyceae) were dominant. It was the same as the vertical distribution of dissolved oxygen in the water column on 2 November. The peak in 7 m seemed to reflect sinking from the layer above and precipitated in the bottom layer. On 16 November, phytoplankton were few in all layers. (The peak in 7 m seemed to constitute sinking from the layer above and precipitated in the bottom layer). On 21 December, phytoplankton with genus *Synedra* (Bacillariophyceae) distributed uniformly from the surface to 6 m depth (The peak in 7 m seemed to constitute sinking from the layer above and precipitated in the bottom layer).

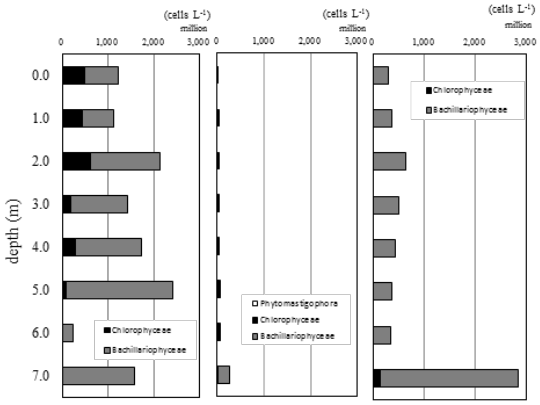

Fig. 6 Vertical distribution of phytoplankton on 2 and 16 November, and 21 December.

CONCLUSION

Phytoplankton were few in any layer under anoxic condition on 16 November. It seemed that phytoplankton cannot grow by exhaustion of nutrients in the water column because their concentration was highest under the anoxic condition. Dissolved oxygen in the water column was not enough to live and use for growth.

Tintinnopsis lacustris was found in all layers under anoxic condition. It seemed to have poor tolerance of dissolved oxygen because they were found the bottom layer on 2 November. The reason that individuals increased on 16 November, and continued on 21 December is not well understood.

The changes in their vertical distribution from 2 to 16 November, seemed due to the lake water lifting from the bottom layer (*Tintinnopsis lacustris* living) on November to all layers when shift stagnation periods to circulate on periods. There is little research on the vertical distribution of plankton, nutrient, and chlorophyll-*a*, in the anoxic condition. This paper is thus a valuable description of an uncommon phenomenon

.

ACKNOWLEDGEMENTS

We are grateful to the Anan-cho authorities in Shimoina-gun, Nagano Prefecture, who generously provided research facilities. We especially thank Sohey Hane and Seiya Kato for their assistance in the field.

REFERENCES

[1] Yagi, A., “Biological manganese cycle in the oxic and anoxic layers of Lake Fukami-ike”, Limnology in Tokai Region of Japan, Vol. 43, 2010, pp. 51-60.

[2] Yagi A, Funahashi J, Nishio N, and Umemura M, “Seasonal changes of methane and organic acid in Lake Fukami-ike”, Verh. Internat. Verein. Limnol., Vol.30, 2009, pp.878-883.
[3] Murphy J, J.P. Riley, “A modified single solution method for the determination of phosphate in natural waters”, Analytica Chimica Acta, Vol.27, 1962, p.36.
[4] Holm-Hansen O., et al., “Fluorometric determination of Chlorophyll”, J. of Cons. Perm. Int. Explor. Mer, Vol.30, pp.3-15.

First International Conference on Science, Engineering & Environment,
Tsu City, Mie, Japan, Nov.19-21, 2015, ISBN: 978-4-9905958-5-2 C3051

SUCCESSION OF EXOTIC GRASSES USED AS COVER PLANTS FOR EROSION CONTROL ON CUT SLOPES, MT. SAKURAJIMA

Kentaro KONDO[1], Taizo UCHIDA[2], Daisuke HAYASAKA[3], Jun TANAKA[4], Akio SATO[4] and Teruo ARASE[5]
[1]Graduate School of Engineering, Kyushu Sangyo University, Japan; [2]Faculty of Engineering, Kyushu Sangyo University, Japan; [3]Faculty of Agriculture, Kinki University, Japan; [4]Japan Conservation Engineers Co., Ltd., Japan; [5]Faculty of Agriculture, Shinshu University, Japan

ABSTRACT

The utilization of exotic grasses as cover plants for erosion control has received considerable attention in recent years, particularly because these exotic grasses have the potential to become invasive. This study examined succession of exotic grass communities that have been established on the cut slopes of the volcano, Mt. Sakurajima. The results showed that although the exotic grasses, such as *Cynodon dactylon*, *Festuca rubra* and *Dactylis glomerata*, that have been used for erosion control on the cut slopes were dominant for the first two years, marked decreases were observed as the native herbaceous plant, *Miscanthus sinensis*, became dominant after three years. By the sixth year, all of the exotic grasses vanished completely. This high rate of succession would result in the suppression of exotic grass dispersal on Mt. Sakurajima. It was also suggested that the chemical properties of volcanic soils, and the bio-engineering technique employed on Mt. Sakurajima may facilitate this high rate of succession.

Keywords: Cut slope, Erosion, Exotic grass, Succession, Volcano

INTRODUCTION

There are 110 active volcanoes on the islands of Japan, which is located on the Pacific Ring of Fire [17]. Among these volcanoes, Mt. Sakurajima in Kagoshima Prefecture in southwestern Japan is very active, periodically erupting pumice, scoria and ash, and emitting volcanic gases [23], [30], [40]. As a result of this activity, natural vegetation from the summit to halfway down the slopes of the mountain is poorly established, causing soil erosion and the development of rills and gullies, and frequent debris- and mud-flows down the mountain [18-19], [27], [38]. To prevent and mitigate damage caused by erosion, and debris- and mud-flows, a large number of check dams have been constructed from the foothills to halfway up Mt. Sakurajima. In addition, cut slopes resulting from the construction of the check dams have been covered with exotic grasses, such as *Festuca arundinacea*, *Cynodon dactylon*, *Agrostis alba* and *Dactylis glomerata*, for erosion control. However, given the emphasis on conserving biodiversity in recent years, concerns have arisen regarding the utilization of these exotic grasses for erosion control, particularly because they may become invasive.

Numerous case studies have been conducted on the application of exotic grasses to erosion control on volcanic slopes (e.g. Mt. Sakurajima, Mt. Unzen and Mt. Usu) [14], [19], [33-34]. However, relatively few studies have examined the plant biodiversity on volcanoes, particularly in the area of succession and dispersal of exotic grasses used for erosion control. The aim of this study was therefore to examine the succession of exotic grasses that have been applied as cover plants for erosion control on Mt. Sakurajima by surveying the vegetation and environmental characteristics of the cut slopes in four different districts.

MATERIALS AND METHODS

Study Site

A total of 40 cut slopes of check dams were surveyed in the four districts of Hattani-Sawa, Saidou-Gawa, Hikinohira-Sawa and Matsuura-Gawa on Mt. Sakurajima. Permission for the study was obtained from the Forestry Agency, Ministry of Agriculture, Forestry and Fisheries. The slopes in the study area were located at 366 to 655 m above sea level and their angles of inclination ranged from 25 to 70°. The geological features of the slopes were classified as "Recent Ejecta", "Hikinohira Lava Dome" or "Taisho I Lava Flow" [7]. Exotic grasses, such as *Eragrostis curvula*, *Festuca rubra*, *F. arundinacea*, *C. dactylon*, *A. alba* and *D. glomerata*, have been introduced in this area for use as cover plants for erosion control on cut slopes using a bio-engineering technique known as the Stabilization Method (*Stabila Kouhou* in Japanese), which is a method employed for aerial seeding work.

According to data from the Automated Meteorological Data Acquisition System (AMEDAS) for the years 2005 to 2014, the surveyed area is situated in the laurel forest zone (warm temperature zone); values of Kira's Warmth Index [24] ranged from 158.9 to 172.0, and annual precipitation ranged between 1,530 and 2,942 mm.

Vegetation Survey

Surveys of the vegetation on cut slopes were performed at the end of September in 2013 and 2014. Three survey quadrats (10,000 or 40,000 cm^2) were randomly placed on each cut slope. The species composition of the plants in each quadrat was recorded and then scored using the Braun-Blanquet cover-abundance scale [3]. The plant nomenclature used in this paper followed that of Iwatsuki (1992), Miyawaki (1994), Baba (1999) and Shimizu (2003). All of the recorded plant species were categorized as native or non-native, and herbaceous or woody plants based on published literature [2], [16], [32], [35].

In addition, environmental variables considered likely to affect the succession of vegetation on cut slopes were also investigated, containing the number of years that had elapsed since the *Stabila Kouhou* bio-engineering technique had been undertaken on the slope (NYE), and soil chemistries on the slopes. The NYE was calculated as shown in Eq. (1).

$$NYE=YVS - FY \quad (1)$$

Where, YVS and FY are the year of the vegetation survey and the fiscal year in which the bio-engineering technique was implemented, respectively. The soil chemistries (pH, EC, carbon-to-nitrogen ratio (C/N), cation exchange capacity (CEC), ignition loss (IL), NH_4-N, NO_3-N and P_2O_5) were analyzed on soil samples that were collected in each quadrat (approx. 500 ml of soil around the roots of the dominant plant species).

Data Analysis

The Braun-Blanquet cover-abundance scale (r, +, I, II, III, IV, and V) was transformed as follows: r and + were taken as 0.1%; I as 5.0%; II as 17.5%; III as 37.5%; IV as 62.5%, and V as 87.5%.

The cut slopes were classified into vegetation types based on their species composition and two-way indicator species analysis (TWINSPAN). In addition, a canonical correlation analysis (CCA) was performed to clarify the relationship between the

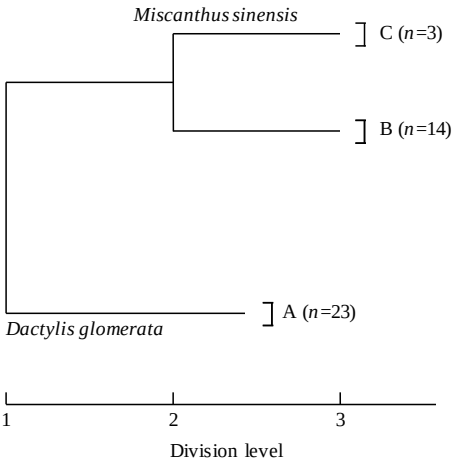

Fig. 1 Classification of vegetation on cut slopes by TWINSPAN using species composition (plant coverage data, %).

Cut levels of 0, 20, 40, 60 and 80 were employed in the analysis.

Table 1 Plant coverage for each type classified by TWINSPAN.

	Vegetation types		
	A	B	C
Species	*n* =23	*n* =14	*n* =3
<Non-native herbaceous plants>			
Trifolium repens	r		
Erigeron annuus	r		
Cynodon dactylon †	I	r	
Festuca rubra †	I	r	
Dactylis glomerata †	II		
<Native herbaceous plants>			
Fallopia japonica	r	r	r
Artemisia indica	r	r	r
Lespedeza juncea	r		
Dennstaedtia hirsuta #		r	
Miscanthus sinensis	+	III	V
<Native woody plants>			
Rhaphiolepis indica		r	
Eurya japonica		r	r
Pinus thunbergii		r	
Ligustrum japonicum		r	
Rhododendron kaempferi		r	r
Duschekia firma	r	r	r
Indigofera pseudotinctoria		r	
Albizia julibrissin			r
Boehmeria spicata			r
NYE ‡	2.0 ± 1.1	5.8 ± 1.6	6.7 ± 2.9

†, exotic grasses as cover plants for erosion control; #, fern, and ‡, mean and standard deviation. In vegetation types Roman numerals and other symbols for each species indicate plant coverage classes, defined as follows: r, under 5%; +, under 10%; I, under 20%; II, under 40%; III, under 60%; IV, under 80%, and V, above 80%.

Table 2 Summary of CCA on Axes 1 and 2.

	Axis 1	Axis 2
Eigenvalues	0.59	0.39
Cumulative percentage of species variance	22.4	37.2
Species-environment correlations	0.81	0.72
P-values by Monte Carlo permutation test	0.02	0.01

vegetation types and environmental variables, such as pH, C/N and P_2O_5 of soil, excluding NYE. The statistical software package PC-ORD (ver. 4.0 for Windows, MjM Software Design, USA) was used for TWINSPAN and CCA.

RESULTS

Vegetation Type on Cut Slope

The TWINSPAN classified the vegetation on 40 cut slopes into three vegetation types, based on their species composition (Fig. 1). Type A, which was found on 23 cut slopes, could be separated from other types by the indicator species, *D. glomerata*. At the second division level, the remaining types were separated into Type B (n=14) and Type C (n=3), respectively, based on the indicator species, *M. sinensis*.

The species that dominated Type A were the exotic grasses, *C. dactylon*, *F. rubra* and *D. glomerata* that had been used as cover plants for erosion control (Table 1). Conversely, *M. sinensis*, which is a native herbaceous species, was dominant in Types B and C. However, the coverage of *M. sinensis* in Type C was larger than that in Type B, and also exotic grasses were not observed in Type C.

The average NYE was 2.0 years for Type A, 5.8 years for Type B, 6.7 years for Type C.

Relation between Vegetation Types and Environmental Variables

A total of 37.2% of the variance in the CCA was explained by Axes 1 and 2, whose eigenvalues indicated 0.59 and 0.39, respectively (Table 2). Monte Carlo permutation test showed that each axis was significantly affected by environmental variables (P<0.05).

Axis 1 approximately divided vegetation types into Type A and the others; Type A was characterized by mostly positive scores, while Types B and C had negative scores (Fig. 2). Meanwhile, Axis 1 showed a strong correlation with positive environmental variables such as NO_3-N, IL, P_2O_5 and CEC, and negative environmental variables such as NH_4-N.

Incidentally, no obvious relationship between vegetation types and Axis 2 was observed.

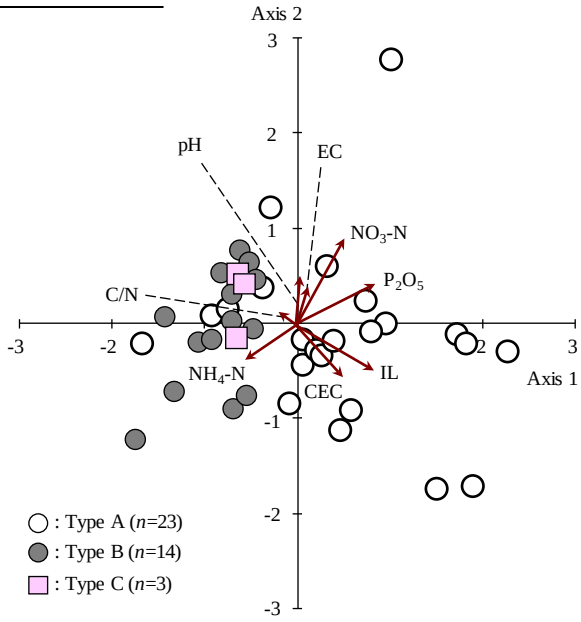

Fig. 2 CCA biplot of vegetation types. Arrows indicate the direction and relative influence of environmental variables in the ordination.

NYE vs. Component Species

The relationship between NYE and component species is shown in Fig. 3. Within two years of the bio-engineering technique, most of the species on cut slopes were exotic grasses used as cover plants for erosion control, such as *C. dactylon*, *F. rubra* and *D. glomerata* (96.9% of total). However, these species decreased remarkably after the third year, and native herbaceous plants, mostly *M. sinensis* (98.7% of total), were dominant. Native woody plants were also observed after about three years, and non-native herbaceous plants including exotic grasses for erosion control vanished totally after six years.

DISCUSSION

Succession of Cut Slope Vegetation

Despite the large number of studies that have been published on succession after volcanic eruptions [1], [4], [8], [22], [29], [36-37], [41],

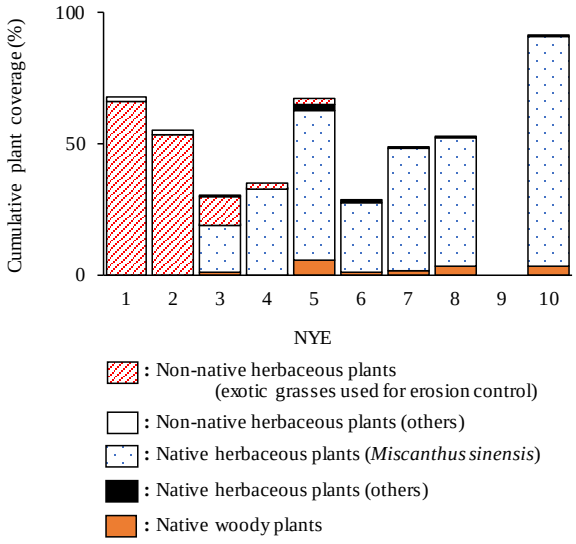

Fig. 3 Relationship between NYE and component species.

relatively little research has been conducted on the succession of exotic grasses used for erosion control on volcanoes.

The findings of this study showed that the vegetation on volcanic slopes consisted of three types (Types A, B and C), which had average NYE values of 2.0, 5.8 and 6.7 years, respectively (Fig. 1 and Table 1). This indicates that the succession of cut slope vegetation after the bio-engineering technique on Mt. Sakurajima is likely to occur in the order of Type A, Type B and then Type C, which means that exotic grasses used for erosion control on cut slopes on Mt. Sakurajima would be replaced by native plant communities dominated by *M. sinensis*.

The high NO_3-N, P_2O_5, CEC and IL levels observed at the study sites may have facilitated the growth of Type A plants compared to Type B and Type C plants (Fig. 2). Indeed, the demand of exotic grasses for nutrients is typically very high, and soil nutrients are major growth limiting factors in these species [5-6], [9], [11], [42-43], [46]. Conversely, *M. sinensis*-dominated grasslands can be maintained under oligotrophic conditions without fertilizer application [10], [13], [25], [39].

We consider that the succession of cut slope vegetation after the bio-engineering technique on Mt. Sakurajima is driven by a progressive decrease in soil nutrients. This decrease in soil nutrients would result from chemical properties of volcanic soils, e.g. N, CaO and K_2O leaching, and fixation of P_2O_5 [9], [12], [15], [28]. In addition, typically, the *Stabila Kouhou* bio-engineering technique requires the repeated application of additional fertilizer [31], [34]; however, no additional fertilizer has been applied to the cut slopes of Mt. Sakurajima.

Decline of Exotic Grasses

The exotic grasses that have been used as cover plants for erosion control were dominant for the first two years after the bio-engineering technique (Fig. 3). However, these plants declined rapidly thereafter and native herbaceous plants became dominant from the third year onward. By the sixth year, the exotic grasses vanished completely. Typically, exotic grasses on slopes start to decline six to ten years after the bio-engineering technique [11], [20-21], [46], but they can remain dominant for more than ten years, occasionally persisting for more than 20 years on slopes [26], [44-46].

Consequently, the disappearance of the exotic grasses on the cut slopes of Mt. Sakurajima is considered to have occurred in quite a short period of time.

CONCLUSION

Balancing the application of exotic grasses to erosion control against the need for the conservation of biodiversity is important. We consider that an optimal balance was achieved in this regard on the slopes of Mt. Sakurajima; coverage of exotic grasses used as cover plants was high shortly after the bio-engineering technique, which would be effective for erosion prevention. However, these exotic grasses declined and vanished much earlier than was expected, and then native plants became established at these sites, which would also result in the suppression of exotic grass dispersal.

It is proposed that, in combination with the chemical properties of volcanic soils, the bio-engineering technique "with little or no nutrient (fertilizer)" is well suited to using exotic grasses for erosion control on volcanoes such as Mt. Sakurajima.

ACKNOWLEDGEMENTS

We are grateful for the assistance of the staff of Kyushu Regional Forest Office. We also thank the members of Laboratory of Plant Ecology at Kyushu Sangyo University.

REFERENCES

[1] Anderson-Teixeira K.J., Vitousek P.M. and Brown J.H., 2008. Amplified temperature dependence in ecosystems developing on the lava flows of Mauna Loa, Hawai'i. PNAS 105, 228-233.

[2] Baba T., 1999. Identifying woody species by their leaf appearances. Shinano Mainichi Shinbunsha, Nagano. 396 pp. *In Japanese*

[3] Braun-Blanquet J., 1964. Pflanzensoziologie. Grundzüge der Vegetationskunde, 3rd ed. Springer-Verlag, Vienna. 865 pp.
[4] Dimopoulos P., Raus T., Mucina L. and Tsiripidis I., 2010. Vegetation patterns and primary succession on sea-born volcanic islands (Santorini archipelago, Aegean Sea, Greece). Phytocoenologia 40, 1-14.
[5] Ehara K., 1971. Research of feed crop and grassland. Yokendo, Tokyo. 402 pp. *In Japanese*
[6] Fukuda E., 2015. The silk tree, *Albizia julibrissin* Durazz. fosters dry matter production and nutritional composition of *Dactylis glomerata* L. Jpn. J. Grassl. Sci. 61, 1-11. *In Japanese*
[7] Fukuyama H., 1978. Geology of Sakurajima Volcano, southern Kyushu. Jour. Geol. Soc. Japan 84, 309-316. *In Japanese*
[8] Grishin S.Y., 2010. Vegetation changes under the impact of volcanic ashfall (Tolbachinsky Dol, Kamchatka). Russian Journal of Ecology 41, 436-439.
[9] Harada I., 1977. Nutrition of pasture and fertilization. Yokendo, Tokyo. 272 pp. *In Japanese*
[10] Horie H. and Nemoto M., 1990. Nutrient absorption characteristics of *Miscanthus sinensis*. Abstracts of the meeting, the Weed Science Society of Japan 29, 149-150. *In Japanese*
[11] Hoshiko T., 1999. A study on the invasions of woody-plants and seed dispersal form on man-made expressway slopes. J. Jpn. Soc. Reveget. Tech. 25, 102-114. *In Japanese*
[12] Ichiki M., Obaru H. and Morita S., 1982. Influence of volcanic ash-fall erupted from Mt. Sakurajima on the physico-chemical properties of agricultural cultivated soil. Bulletin of the Kagoshima Agricultural Experiment Station 10, 1-45. *In Japanese*
[13] Itano S., Sakanoue S., Nakagami K. and Tsutsumi M., 2013. Effects of fire and harvest management on carbon and nitrogen composition of the aboveground plant community in a *Miscanthus sinensis*-dominated grassland. Jpn. J. Grassl. Sci. 59, 29-32. *In Japanese*
[14] Ito J., Narita S., Usui G., Yanai S., Shimizu H. and Sato T., 1984. Aerial seeding work and vegetation on Mt. Usu. Koushunai Kihou 60, 12-16. *In Japanese*
[15] Iwata S., 1991. Roll of soil. Ienohikari-Kyoukai, Tokyo. 191 pp. *In Japanese*
[16] Iwatsuki K., 1992. Ferns and fern allies of Japan. Heibonsha, Tokyo. 311 pp. *In Japanese*
[17] Japan Meteorological Agency, 2015. Volcano. http://www.data.jma.go.jp/svd/vois/data/tokyo/STOCK/kaisetsu/vol_know.html. *In Japanese*
[18] Jitousono T., Simokawa E. and Teramoto Y., 1997. Runoff characteristics of debris flows and floods surrounding Mt. Sakurajima. Res. Bull. Kagoshima Univ. For. 25, 9-20. *In Japanese*
[19] Kagoshima Branch, Kyushu Regional Forest Office, 2002. Experimental aerial seeding works on Mt. Sakurajima. Chisan 47, 10-13. *In Japanese*
[20] Kameyama A., 1981. Succession of the slope vegetation of expressways-V: a case study on the slope vegetation of Kyushu Expressway. Journal of the Faculty of Agriculture, Shinshu University 18, 155-170. *In Japanese*
[21] Kameyama A., 1983. Succession of the slope vegetation of expressways. J. JILA 47, 52-55. *In Japanese*
[22] Kamijo T., Kitayama K., Sugawara A., Urushimichi S. and Sasai K., 2002. Primary succession of the warm-temperate broad-leaved forest on a volcanic island, Miyake-jima, Japan. Folia Geobotanica 37, 71-91.
[23] Kazahaya R., Mori T. and Yamamoto K., 2013. Separate quantification of volcanic gas fluxes from Showa and Minamidake Craters at Sakurajima Volcano, Japan. Bull. Volcanol. Soc. Japan 58, 183-189.
[24] Kira T., 1977. A climatological interpretation of Japanese vegetation zones. In: Miyawaki A. and Tüxen R. (eds.), Vegetation science and environmental protection. Maruzen, Tokyo. pp. 21-30.
[25] Kondo H., Takahashi S., Harada H., Kitahara N., Harashima N. and Nishida T., 2002. Phosphorus dynamics in semi-natural grassland. Bull. Natl. Inst. Livest. Grassl. Sci. 1, 55-64.
[26] Kubo M. and Hayashi A., 2012. Revegetation by sowing alien seeds on cut slopes of forest roads in Yamanashi. J. Jpn. Soc. Reveget. Tech. 37, 478-481. *In Japanese*
[27] Kudo S., Kawahara A., Kikuchi Y. Arakawa R., Tanaka J., Sato A. and Ezawa T., 2013. Vegetation development and tolerance of arbuscule to disturbance, Mt. Sakurajima. Abstracts of the meeting, Japanese Society of Soil Science and Plant Nutrition 59, p. 37. *In Japanese*
[28] Kusano S, Ichiki H. and Tagami M., 1964. Effect of physical property of volcanic ash and fertilizer application on vegetation. Abstracts of the meeting, Japanese Society of Soil Science and Plant Nutrition 10, p. 25. *In Japanese*
[29] Marler T.E. and del Moral R., 2013. Primary succession in Mount Pinatubo: habitat availability and ordination analysis. Communicative & Integrative Biology 6, e25924 [online].
[30] Matsumoto A., Nakagawa M., Amma-Miyasaka M. and Iguchi M., 2013. Temporal variations of the petrological features of the juvenile

materials during 2006 to 2010 from Showa Crater, Sakurajima Volcano, Kyushu, Japan. Bull. Volcanol. Soc. Japan 58, 191-212.

[31] Miyasihita S. and Yamada M., 2010. Succession of vegetation on the southern slope of Mount Usu after aerial seeding work. Forest Consultant 122, 8-14. *In Japanese*

[32] Miyawaki A., Okuda S. and Fujiwra R., 1994. Handbook of Japanese vegetation. Shibundo, Tokyo. 646 pp. *In Japanese*

[33] Nishida K., Kobashi S. and Mizuyama T., 1998. How has revegetation changed surface runoff and sediment discharge on pyroclastic sediments in Unzen Volcano? J. Jpn. Soc. Reveget. Tech. 23, 249-255. *In Japanese*

[34] Ogawa Y., Shimizu A., Shimizu T., Daimaru H. and Miyabuchi I., 2002. Surface runoff and sediment discharge for three years on a slope revegetated by aerial seeding work at Unzen Volcano. J. Jpn. Soc. Reveget. Tech. 28, 255-258. *In Japanese*

[35] Shimizu T., 2003. Naturalized plants of Japan. Heibonsha, Tokyo. 337 pp. *In Japanese*

[36] Swanson F.J., Jones J.A., Crisafulli C.M. and Lara A., 2013. Effects of volcanic and hydrologic processes on forest vegetation: Chaiten Volcano, Chile. Andean Geology 40, 359-391.

[37] Tagawa H., 1964. A study of the volcanic vegetation in Sakurajima, south-west Japan. I. Dynamics of vegetation. Mem. Fac. Sci. Kyushu Univ. Ser. E (Biol.) 3, 165-228.

[38] Teramoto Y., Shimokawa E., Jitousono T. and Fukuno N., 2004. The effects of revegetation on rainwater runoff and sediment discharge from the slopes of Sakurajima Volcano. Res. Bull. Kagoshima Univ. For. 31, 15-20. *In Japanese*

[39] Toma Y., Sato S., Izumi M., Fernández F.G., Stewart J.R., Hatano R., Nishiwaki A. and Yamada T., 2012. Response of fertilization to aboveground biomass production of *Miscanthus sinensis* on poor fertility soil: case study in Tomakomai, Hokkaido Japan. Hokunou 79, 162-169. *In Japanese*

[40] Tomiyama N., Koike K., Iguchi M. and Omura M., 2011. Analysis of topographic change at Mount Sakurajima, South Kyushu, Japan, using JERS-1 SAR interferometry. Geoinformatics 22, 17-24.

[41] Velázquez E. and Gómez-Sal A., 2009. Changes in the herbaceous communities on the landslide of the Casita Volcano, Nicaragua, during early succession. Folia Geobotanica 44, 1-18.

[42] Watanabe K., Katsura I., Sekimura S. and Kumano S., 1968. The effects of fertilization and cutting on the growth of grasses in mixed sward and the chemical properties of soil: the effects of soil improvement, nitrogen fertilizers and cutting height on the growth of grasses. Bull. Tohoku Agric. Res. Cent. 36, 97-111. *In Japanese*

[43] Yamamoto Y., Deguchi Y., Tsukada H., Sato S., Kitagawa M., Nishida T., Terada Y., Matoba K., Ikeda K., Sato S. and Hirano K., 2010. Vegetation, dry matter production and consumption of established pasture for gathering cattle in a vast forest grazing land. Jpn. J. Grassl. Sci. 56, 137-143. *In Japanese*

[44] Yoshida H., 2003. Characteristics of succession in plant communities revegetated by spraying with plant cultivative base. J. Jpn. Soc. Reveget. Tech. 29, 331-342. *In Japanese*

[45] Yoshida H., 2007. Studies of the effectiveness of rapid reforestation systems and the development of seeding design techniques for natural restoration of slopes. J. Jpn. Soc. Reveget. Tech. 33, 389-390. *In Japanese*

[46] Yoshida H. and Kikuchi T., 1993. Research of the variation on spraying thick cultivation method: the transition of 17 years after application. J. Jpn. Soc. Reveget. Tech. 18, 219-226. *In Japanese*

First International Conference on Science, Engineering & Environment,
Tsu City, Mie, Japan, Nov.19-21, 2015, ISBN: 978-4-9905958-5-2 C3051

ASSIMILATIVE CAPACITY OF AIR POLLUTANTS IN AN AREA OF THE LARGEST PETROCHEMICAL COMPLEX IN THAILAND

Apiwat Thawonkaew[1,2], Sarawut Thepanondh[1,2], Duanpen Sirithian[1,2] and Lasita Jinawa[1,2]
[1]Faculty of Public Health, Mahidol University, Thailand,
[2]Center of Excellence on Environmental Health and Toxicology, Bangkok, Thailand.

ABSTRACT

Assimilative capacities of sulfur dioxide (SO_2) and oxides of nitrogen (NOx) in the largest petrochemical industrial complex in Thailand were evaluated in this study. AERMOD dispersion model was simulated to compute for ground level concentrations and spatial distributions of SO_2 and nitrogen dioxide (NO_2) within a radius of 5 km from Maptaphut industrial area. Emission input consisted of 419 stacks which total amount of 2,071.82 and 2,163.66 g/s of SO_2 and NOx were used as baseline emissions. Maximum hourly average and annual concentrations predicted at 8 ambient air quality monitoring stations in the study domain were used to evaluate an assimilative capacity of these pollutants. Emissions of SO_2 and NOx were adjusted to the limit that predicted concentrations will not exceed their ambient air quality standards. Results indicated that in order to achieve both hourly and annual standards, NOx emissions must be reduced by at least 40% from its baseline value. As for SO_2, emissions can be increased up to about 130% from current level. Results of this study indicated that an existing regulation in controlling individual emission source by using emission standard is insufficient. Analysis of air pollution as area-based approach by taking into consideration entire emission sources can support for better planning and management of pollution.

Keywords: AERMOD, Emission rate, Maptaphut, Assimilative capacity, NO_x, SO_2

INTRODUCTION

Maptaphut industrial area (MA) in Rayong province, Eastern region of Thailand. It was established in 1988 as part of the Thai's government policy to develop the eastern seaboard [1]. Main industries found in the Maptaphut industrial area are petrochemical industry, metal processing, oil refining, gas separation, electricity generation, and seaport [2]. The development and operation of the MA has occasionally brought out local environmental problems (e.g., air, wastewater, groundwater contamination, hazardous wastes), among which air pollution appears seriously perceived [3]. Importance is air Pollutant the such, including nitrogen dioxide (NO_2), sulfur dioxide (SO_2), carbon monoxide (CO), particulate matter, volatile organic compounds (VOC), and others.

In order to support air quality management in the MA, the Thai's government declared the MA as a pollution controlled zone in 2009 [4]. This designation requires the Industrial Estate Authority of Thailand and entrepreneurs to seek for proper measures to limit and control emissions to the environment [5]. NO_2 and SO_2 are air pollutants required by the government for consideration when assessing the impacts of an industrial facility in order to acquire a permit for operation in the MA. Furthermore, they are also required parameters to be assessed when planning for future expansion of industrial activities of the MA [6]. NO_2 and SO_2 are generally two main air pollutants well known to have adverse effects on human health, particularly on the respiratory system.

The government has encouraged the studying on the air emissions assimilative capacity using air dispersion model in this area [7]. Efforts have been made to assess status of air quality using both direct measurement and predicted data from air quality model [8]. Evaluation of assimilative capacity of air pollution in this area can assist in area-based management of pollution problems together with individual emission source control through the implementation of emission standards.

This study evaluated assimilative capacities of sulfur dioxide (SO_2) and oxides of nitrogen (NOx). AERMOD dispersion model was simulated to compute for ground level concentrations and spatial distributions of these pollutants within study area. Emission input consisted of stacks which total amounts of emission rate were used as baseline emissions. The maximum hourly average and annual ground level concentrations were predicted and were compared with the Thai's ambient air quality standards for SO_2 and NO_2. Predicted data at 8 ambient air quality monitoring stations in the study domain were used to evaluate an assimilative capacity of these pollutants. Emissions of SO_2 and NO_x were adjusted to the limit that predicted concentrations will not

exceed their ambient air quality standards.

METHODOLOGY

The study domain was designed to encompass the entire Maptaphut industrial area (MA) and its vicinity in Rayong province Thailand, covering an area of 10 × 10 km^2 with a horizontal grid spacing of 500 m. This modeling domain currently includes five industrial estates namely Map Ta Phut, East Hemaraj, Asia, Padaeng and RIl industrial estates[9]. Spatial distribution of these industrial estates in the study area was as shown in Fig 1.

AERMOD is a steady-state Gaussian plume model. It is a refined dispersion model for simple and complex terrain for receptors within 50 km of a modelled source. The AERMOD modelling system used in this study was run with a commercial interface, AERMOD View (Version 8.7). This model was intensively validated for its ability in predicting ground level concentration of SO_2 and NO_2 in this study area [10], [11].

The meteorological parameters data input were prepared over one years (1st January 2013 to 31th December 2013). Data used in this study were generated by Mesoscale Meteorological Model (MM5) in TD-6201 format file. Data were then pre-processed using AERMET processor. The required meteorology data for AERMOD are surface data (hourly values) which describe conditions at the level closed to ground level. Upper air data (daily values) which describe conditions at higher altitude in the atmosphere also be used in the model. Boundary layer parameters used by AERMOD, which are required as input to the AERMET processor, include albedo, Bowen ratio, and surface roughness [12]. The gridded data needed by AERMAP was selected from Digital Elevation Model (DEM) data and the terrain data was collected during the Shuttle Radar Topography Mission (SRTM3). The terrain data were pre-processed with AERMAP prior to modelling in AERMOD.

In this study, a comprehensive Cartesian receptor grid extending to 5 km from the center of the emission source was used in the AERMOD modeling to assess the maximum ground-level pollutant concentrations. The Cartesian receptors grid (14.5 km × 14.5 km domain) has a uniform spacing of 500 m. Eight discrete receptors were set in the modelling domain. The receptors were labelled as Health Promotion Hospital Maptaphut (HMTP), Field Crops Research Center (FCRC), Ban Ta Kuan Public Health Center (BTKH), Wat Nong Fap School (WNFS), Muang Mai Maptaphut (MMTP) , Map Chalut Temple (MCLT), Ta Kuan Temple (TKTP) and Chum Chon Islam (CCIL) as shown in Fig 1. The receptors were randomly selected to represent sensitive receptors such as residential area, schools, health care centers etc.

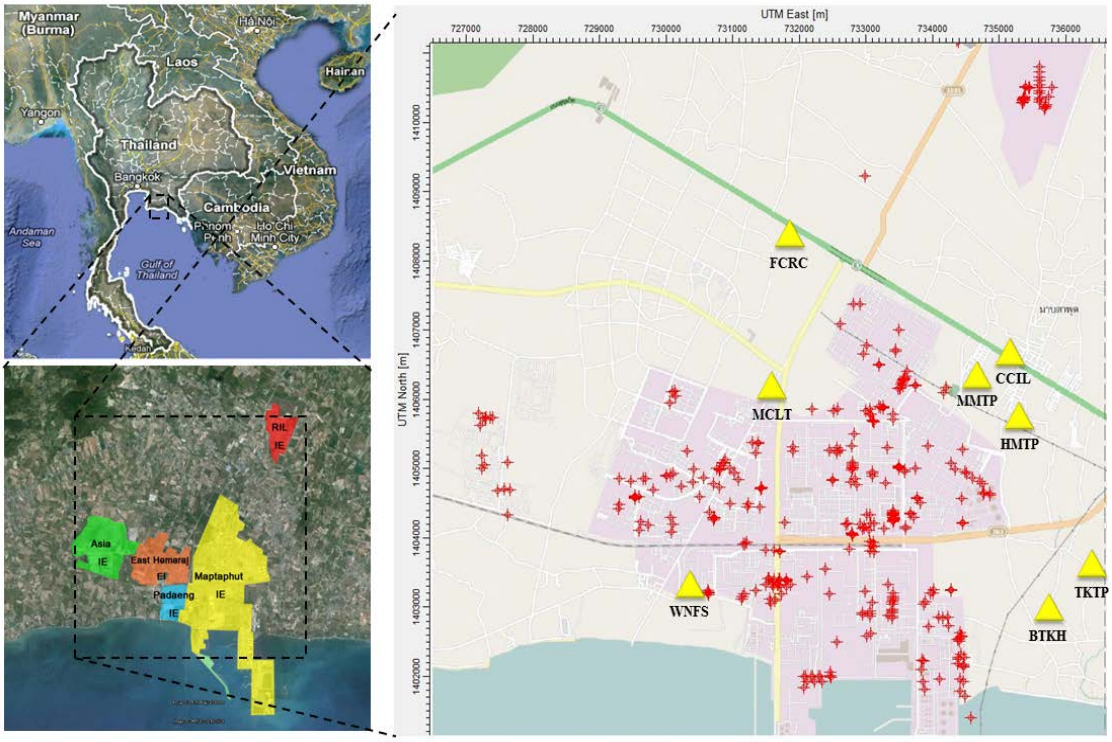

Fig. 1 Study domain in a radius of 5 km from Maptaphut industrial area
(yellow dots represent the position of receptors; red dots represent the position of point sources)

Stack emission data (Table 1 and Table 2) were obtained from the database for MA, which was compiled and reported by the Office of Natural Resource and Environment Policy and Planning [13]. These data consisted of stack height, stack diameter, stack exit temperature (Kelvin), stack exit velocity (m/s) and emission rate (g/s). These emission data comprised of 419 stacks covering entire stacks in the study area.

Determination of assimilative capacities of sulfur dioxide (SO_2) and oxides of nitrogen (NO_x) were carried out by simulation of AERMOD dispersion model. Ground level concentrations and spatial distributions of these pollutants were analyzed as outputs of the simulation. Maximum hourly average and annual concentrations predicted at 8 ambient air quality monitoring stations in the study domain were used to evaluate an assimilative capacity of these pollutants. Emissions of SO_2 and NOx were adjusted to the limit that predicted concentrations will not exceed their ambient air quality standards.

RESULTS

Assimilative capacities of sulfur dioxide (SO_2) and oxides of nitrogen (NO_x) in this study were determined as value of total emission of air pollutant which its predicted ground level concentration was not higher than the Thai's ambient air quality standard [14]. The values of 780 and 100 $\mu g/m^3$ which are designated ambient air quality standard of SO_2 were used to compare with predicted one hour and annual concentration, respectively. As for NO_2, predicted 1 hr and annual concentrations were compared with the values of 320 and 57 $\mu g/m^3$ (ambient air quality standards for NO_2), respectively. Simulated results in an existing condition and predicting assimilative capacities of these pollutants were summarized in Table 3.

Table 1 Physical parameters of stacks

Stack emission group	Number of stacks	Height Mean±SD (m)	Diameter Mean±SD (m)	Exit Temperature Mean±SD (K)	Exit Velocity Mean±SD (m/s)
Petrochemical industry (PETROCHEM)	307	33.30 ± 16.02	1.28 ± 0.88	450.44 ± 150.94	11.76 ± 8.13
Power plant (PP)	45	48.78 ± 33.00	3.91 ± 1.65	408.31 ± 33.97	20.45 ± 6.15
Oil refinery (Refinery)	26	21.60 ± 27.81	0.75 ± 0.92	74.21 ± 102.01	4.11 ± 4.80
Metal industry (Metal)	28	32.83 ± 17.23	1.59 ± 1.46	553.32 ± 233.06	11.4 ± 6.45
Gas Separate Plant (GSP)	13	59.31 ± 47.80	2.69 ± 0.77	460.68 ± 27.37	24.48 ± 12.12

Table 2 Emission rates of SO_2 and NOx

Stack emission group	SO_2[a] (g/s)		NO_x[a] (g/s)	
	Mean±SD	Total	Mean±SD	Total
Petrochemical industry (PETROCHEM)	1.14 ± 4.06	349.24	1.38 ± 2.25	428.98
Power plant (PP)	29.88 ± 153.67	1344.48	34.26 ± 100.12	1541.74
Oil refinery (REFINERY)	19.64 ± 37.67	309.77	4.09 ± 6.86	109.49
Metal industry (METAL)	1.91 ± 4.77	53.5	0.74 ± 0.96	20.73
Gas Separate Plant (GSP)	1.14 ± 0.83	14.83	4.82 ± 1.73	62.72
Total	-	2071.82	-	2163.66

notes : [a] maximum measured/estimated emission rates

SO_2

In an existing condition, there were about 2071.82 g/s of SO_2 emitted from entire study area. The maximum 1 hr and annual average concentration were predicted as about 339 and 28.35 μg/m^3 at MCLT and HTMP, respectively. These values were not exceed ambient air quality standard of SO_2. Therefore, there are still rooms for increasing of emissions of SO_2 in this area. It was found that in this case, emission rate of SO_2 could be increased up to about 4765.19 g/s or about 130 % from its existing condition. At this level, the maximum 1 hr average ground level concentration was predicted as 779.70 μg/m^3. The maximum annual concentration at HTMP station was predicted as 62.22 μg/m^3. These predicted concentrations were not exceeded their ambient air quality standards. Comparisons of pollution maps of SO_2 annual average concentration in an existing condition (total emission rate of 2071.82 g/s) with its predicted assimilative capacity (total emission rate of 4765.19 g/s) were as illustrated in Fig 2.

NO_X

Modeled results indicated that annul average concentrations of NO_2 at every receptor points were not exceed its annual standard in the existing emission rate. However, predicted maximum 1-hr average concentrations at FCRC, WNFS and MCLT stations were higher than 320 μg/m^3 which is set as ambient standard for 1-hr average of NO_2. These predicted values were about 488, 392 and 364 μg/m^3 at WNFS, MCLT and FCRC, respectively. Therefore, in order to achieve attainment of air quality in this area, emissions of NOx must be decreased from its current level. Results from model simulation indicated that at emission rate of about 1296.54 g/s, predicted 1-hr average ground level concentration of NO_2 at every receptor points will be compiled with its environmental standard. Predicted maximum 1-hr average can be achieved by about 44 % reduction from current emission rate of NOx from petrochemical and Power plant (formerly 1970.72 g/s as 1103.60 g/s). This value was corresponded to about 40 % reduction from current emission rate of NOx (2163.66 g/s). Comparisons of pollution maps of NO_2 annual average concentration in an existing condition with its predicted assimilative capacity (total emission rate of 1296.54 g/s) were as presented in Fig 3.

Table 3 Predicted maximum hourly and annual average concentrations at receptor sites in the study domain

Receptor	SO_2				NO_2			
	Hourly std. ≤ 780 (μg/m^3)		Annual std. ≤ 100 (μg/m^3)		Hourly std. ≤ 320 (μg/m^3)		Annual std. ≤ 57 (μg/m^3)	
	current	130% increased	current	130% increased	current	40% reduced	current	40% reduced
HMTP	236.14	543.13	28.35	65.22	290.00	184.60	31.91	21.27
FCRC	337.85	777.05	9.29	21.37	364.00	239.65	13.16	7.89
BTKH	235.90	542.57	20.08	46.18	238.00	150.39	17.67	11.53
WNFS	330.43	760.00	7.91	18.19	488.00	300.29	10.66	6.47
MMTP	304.56	700.48	21.18	48.70	312.00	197.35	38.44	24.17
MCLT	339.00	779.70	9.50	21.85	392.00	250.19	17.12	10.57
TKTP	208.43	479.39	16.59	38.16	228.00	144.58	15.27	9.76
CCIL	261.04	600.39	20.25	46.57	287.00	181.34	33.70	21.59

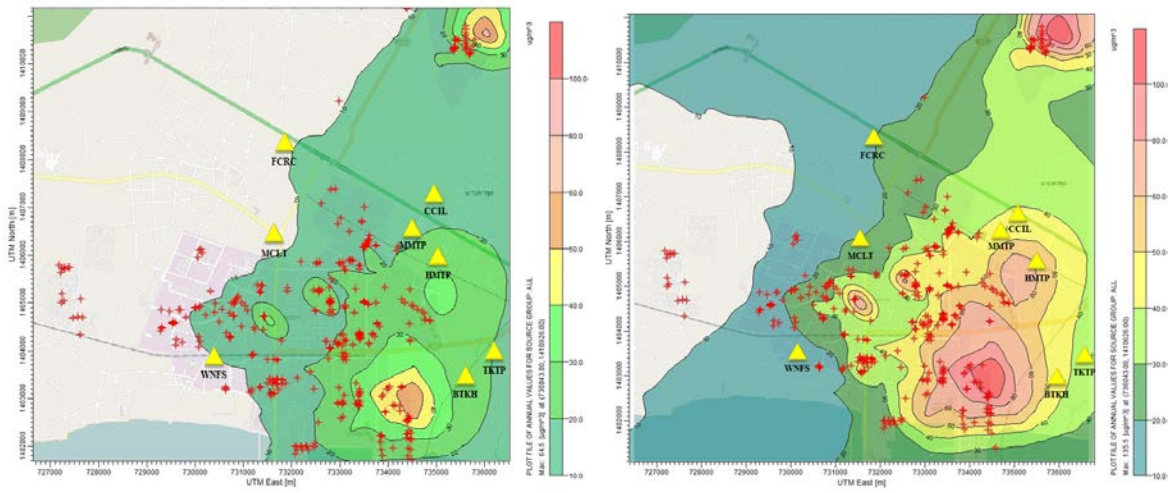

Fig. 2 Annual average concentration of SO_2 for normal emission rate and 130% emission rate increasing

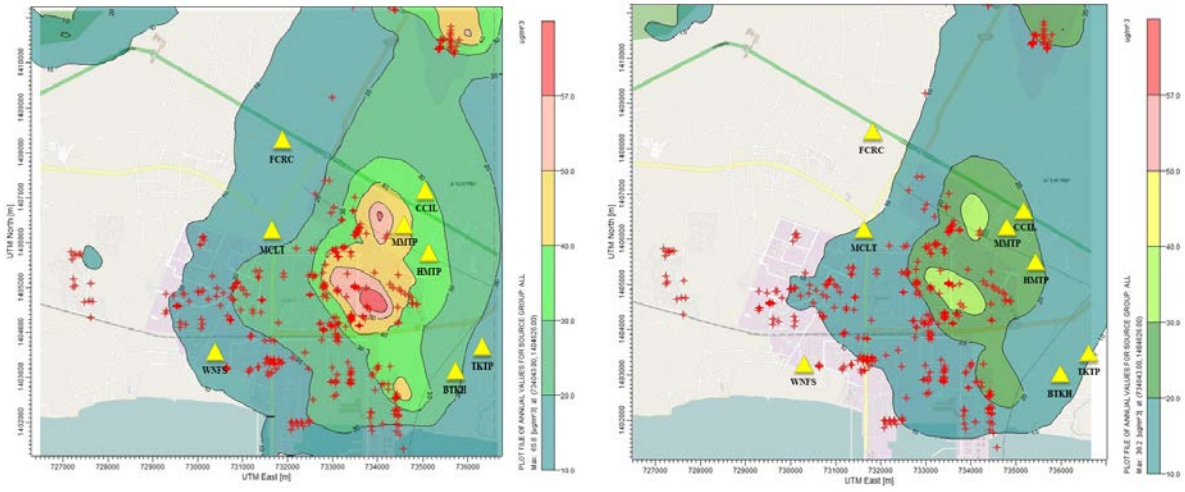

Fig. 3 Annual average concentration of NO_x for normal emission rate and 40% emission rate decreasing from petrochemical & chemical industries and power plant

DISCUSSION AND CONCLUSION

This study focused on analysis of assimilative capacities of sulfur dioxide (SO_2) and oxides of nitrogen (NO_x) in the largest petrochemical industrial complex in Thailand. AERMOD dispersion model was simulated to compute for ground level concentrations and spatial distributions of SO_2 and nitrogen dioxide (NO_2). Results indicated that under current emission rate, predicted maximum NO_2 concentration (1-hr average) was higher than its ambient air quality standard. Therefore, emissions of NO_x must be reduced from its existing level. Evaluation of carrying capacity indicated that emission rate of NOx in the entire area must be reduced to the level of about 1296.54 g/s in order to attain NO_2 ground level concentrations within the environmental quality standard. This amount corresponded to about 40% decreased from current total emission rate. A study on source contribution of NO_2 concentration in Maptaphut area indicated that mostly of NO_2 at WNSF were contributed by petrochemical industrial and Power plant group (about 91 %) [9], [15]. Therefore, efforts in reducing NOx emissions should be given to those petrochemical factories in this industrial complex. As for SO_2, the values of maximum 1-hr and annual average concentrations at receptors predicted under current emission rate were below the Thai ambient standard for SO_2. It was estimated that emission rate of SO_2 could be increased up to 4765.19 g/s in order to attain ground level concentration of SO_2 within its environmental standard. These emission amounts corresponded to about 130 % increasing from current SO_2 emissions in this study area. Results of this study revealed that an existing regulation in controlling individual emission source by using emission standard may insufficient. Analysis of air pollution as area-based approach by taking into consideration entire emission sources can support for better planning and management of

pollution in the study area as well as can be used for further implementation in other industrial complex areas.

ACKNOWLEDGEMENTS

The authors sincerely thank the Pollution Control Department, the Thai Meteorological Department, the Industrial Estate Authority of Thailand and the Office of Natural Resources and Environmental Policy and Planning for providing input data used in this study. This study was partially supported for publication by the China Medical Board (CMB), Center of Excellence on Environmental Health and Toxicology (EHT), Faculty of Public Health, Mahidol University, Thailand.

REFERENCES

[1] Thepanondh S, Toruksa W. Proximity analysis of air pollution exposure and its potential risk. J. of Environmental Monitoring. Vol. 13, 2011, pp. 1264-1270.

[2] Industrial Estate Authority of Thailand. 2015. http://www.ieat.go.th/ieat/index.php/en/ and http://ereport.ieat.go.th/main/default/index. Accessed April 23,2015

[3] SST, Current Situation, Important Pollutions Issues, and Solutions and Additions in Map Ta Phut and Neighboring Areas Solving the Problem in Following Paragraph 2, Article 67 of the Thai Constitution (in Thai). Subcommittee on the Study of Pollutions and the Technical Addition to the Reduction and Elimination of Pollutions in Map Ta Phut and Neighboring Areas. 2010. http://www.publicconsultation.op-m.go.th/rubfung67/proposal6.pdf . Accessed May 8, 2015.

[4] ONEP. Pollution controlled zone in 2009, Thailand. 2009. http://www.onep.go.th/neb/6.%20Laws/data/annoucement_neb/neb_annoucement32.pdf Accessed January 10, 2015.

[5] PCD. Thailand State of Pollution Report 2007. Bangkok, Thailand, 2008. http://infofile.pcd.go.th/mgt/Report_Eng2550.pdf?CFID=40597&CFTOKEN=13393920 Accessed May 8, 2015.

[6] Vassana dumrongdee S, A Final Report, Development of a Strategic Environmental Framework towards Eco Industrial Town : A Case Study of Map Ta Phut, Rayong Province, Thai Health Promotion Foundation (Thai Health), September 2011. http://www.tuhpp.net/files/SEF.pdf. Accessed July 11, 2015.

[7] Thepanondh S, Jitbantoung N, Assimilative capacity analysis of air pollutants over the Dawai industrial complex. International journal of environmental science and development. 2014. pp. 161-164.

[8] NESDB. The studying on the Assimilative Capacity on the Map Ta phut Industrial area, 2011 edition. Bangkok, Thailand. 2011. http://www.nesdb.go.th/Portals/0/eco_datas/area/data/data_0135200511.pdf. Accessed May 5, 2015.

[9] Chusai C, Manomaiphiboon K, Saiyasitpanich P, Thepanondh S. NO_2 and SO_2 dispersion modeling and relative roles of emission sources over Map Ta Phut industrial area,Thailand. Journal of the Air & Waste Management Association. 2012. 62(8). pp.932-45.

[10] Jittra N, Thepanondh S. Performance evaluation of AERMOD air dispersion model in Maptaphut industrial area, Thailand, Environmental Science and Information Application Technology. Conference. 2015, pp. 225-228.

[11] Tunlathorntham S, Thepanondh S. A study of AERMOD tiering approach for prediction of nitrogen dioxide in Maptaphut industrial area, Thailand, Environmental Science and Information Application Technology. Conference. 2015, pp. 230-233.

[12] US EPA, AERMOD: Description of Model Formulation; Final technical report, 2004, pp. 1-91.

[13] ONEP. Stack Emission Database for the Map Ta Phut Industrial Area. Bangkok, Thailand. 2013. http://www.onep.go.th/eia/. Accessed January 7, 2015.

[14] PCD. Ambient Air Standards of Thailand. 2015. http://www.pcd.go.th/info_serv/en_reg_std_airsnd01.html. Accessed January 12, 2015.

[15] Khamyingkert L, Thepanondh S. Source Contribution Analysis of ambient NO_2 concentration in Maptaphut industrial complex Thailand. International Conference on Environmental Research and Technology. Conference. 2015, pp. 44-48.

First International Conference on Science, Engineering & Environment,
Tsu City, Mie, Japan, Nov.19-21, 2015, ISBN: 978-4-9905958-5-2 C3051

SMALL-SCALE IRRIGATION PRACTICES AND TRADITIONAL COMMUNITY WATER MANAGEMENT IN TAKHAR, AFGHANISTAN

Asim Ayoub and Shigeko Haruyama
Graduate School of Bioresources, Mie University, Japan

ABSTRACT

In the result of irrigation infrastructures destruction and the existence of 90% traditional irrigation system, while the efficiency of irrigation network system is workable in only 25-35% of all system, the usage potential irrigation water for agriculture is less than potentiality volume of water resource in Takhar, Afghanistan. This study aims to find out the condition and problems of traditional community water management in northeastern part of Afghanistan and find out the relationship and deference between government and traditional irrigation community management in the area. In-depth interview and fill-up questionnaire survey with water masters (*Mirabs*) and farmers was done respectively in the two districts, and we found that some efforts in recent years have been done to rehabilitate irrigation infrastructures and reforming the social institutions aiming to improve the efficiency of water management and distribution systems, but the results of field survey are not efficient because only those are fully controlled by government having the Water User Associations is a little improved, and the rest of private local Water User Associations are still suffering from technical, social and managerial constraints. We clarified that water shortage, unfair water allocation and management and conflict over water use are the major problems, especially for middle and downstream users of traditional system. In the study area the irrigation has been using for long time in the area, but management of water and irrigation system is still old, due to wasting water and non-efficient water management water shortage is common in most areas. Thus, to save water and use it efficiently to insure sustainable agriculture development, appropriate irrigation practices and water harvesting is necessary to minimize the water use.

Keywords; Irrigation system, community water management, water resources, Afghanistan

INTRODUCTION

From Afghanistan's 26 million population, 80% living in rural area depending on agriculture sector for managing their livelihoods in an arid/semi-arid climatic zone, development and stability of agriculture, water resources and water management have been given high importance in Afghanistan's National Development Strategy [1]. Afghanistan has 65 million ha but only 12% or 7.9 million ha is arable land, which by considering the population growth and cultivated area from 1980 to 2013, population has been increased almost by double from 14 to 26 million and the cultivated area has been decreased from 3.3 to 3.2 million ha, beside that irrigated crop area has been decreased from 2.5 to 2.01 million ha [2].

Generally, Afghanistan has two kinds of irrigation water management, as the existing law on the use of water describes, the traditional or private irrigation system, which is called *Mirab* locally, and the other is government irrigation system. A relatively simple classification system for developing more detailed analysis through describing of system types and providing case study examples in Herat and Kunduz provinces of Afghanistan is done by Afghanistan Research and Evaluation Unit, which is an important start for environmental problems [3].

Variety in irrigation system and the management of water is dependent to the social and geographical condition of the area in Afghanistan. For example; in Nangarhar province, Janikhel canal, have no official water management system, but the *Mirab* system, and the irrigation water is managed in the group of canals by *Mirab* and support from *shora* which is the village council of elders. A *Mirab* is used only, when water shortage occurs and disputes likely to happen in use of water for summer crops. Unsuitable irrigation method in drought years, the limited water resource in summer, water shortages due to intake and conveyance losses are the problems in Tuyan and Ghorak canals of Herat province in west of Afghanistan.

In Ghazni province, there is no *Mirabs* available except in lower Ghazni River valley, where water shortage used to occur. Instead of *Mirab*, *shora* of elders manage the distribution of water in 24-hr (*shab o roz*) turns, the water in upstream areas rotate in every 4–5 days and downstream 1–2 times/month at peak [4]. In all part of Afghanistan in spring as water is a constraint, allocation of water is traditional and known by all population, but the old water allocation and distribution system, water stealing and wasting water during applying irrigation lead to water shortage and conflict. In study area 70% of irrigation canals, irrigate area less than 500 ha. There for clarifying and finding the problems of these systems would help to take a further step in

improving the irrigation system efficiency.

The importance of large-scale irrigation is obvious and comparatively is more profitable than small ones. But, in terms of empowering the local community, small-scale irrigation is suitable as it covers small land available in the rural areas. Access to small scale irrigation enables the households to insure increased and stable production, consumption and improve the food security status [5].

In the study area, limited access to water resources and conflicts over water likely to happen, during the dry years are important problem. This study aims to clarify irrigation system both government irrigation system and the local traditional irrigation system, and to find the community water management problems in the study area.

STUDY AREA

Afghanistan is located in central Asia and due to the rugged mountainous relief, the climate ranges from arid in the south and southwest to semi-arid in the other parts, the Mt.Hindu-Kush and Pamir are moderately humid. Precipitation ranges from less than 100 to 500mm and the annual temperature ranges from -20 to 45 ℃, the evapotranspiration rate is between 5 to 10 mm/day [1]. Takhar province (Fig. 1) is a part of the north-eastern fluvial plains of Afghanistan with permanent rivers and fertile lowlands. The population was 933,000 in 2012, and 85% of population is in agriculture sector and poverty rate is 39 %. The climate differ from cold winters (-23℃) to hot summers (35-40℃). The total area of Takhar province is 1,245,700 ha, from the all area 473,817 ha is agriculture land dividing by 185,268 ha irrigated land and 288,549 ha rain-fed land. However the average yearly precipitation in this province is 415mm.

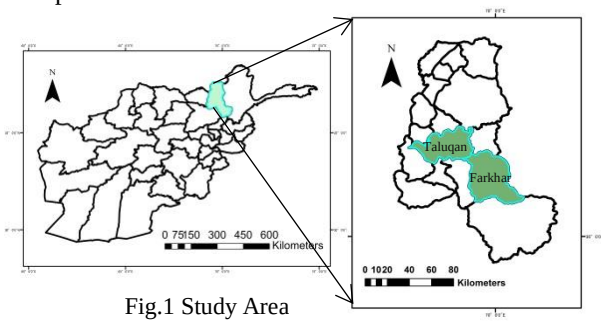

Fig.1 Study Area

More than 80% of the Afghanistan's water comes from Snow-melt of the Mt. Hindu-Kush in summer. Water resources in the country are divided into five major river basins which every basin consist of several watersheds. The Amu basin accounts 48.12million m^3/y (57%), the Kabul River 21.6million m^3/y (26%), the Northern 1.88million m^3/y (2%), the Harirud-Murghab 3million m^3/y (4 %), and the Helmand 9.3million m^3/y (11 %) Fig.2, of the annual water discharge [6].

The study area is located in Taluqan Sub-Basin one of the Panj-Amu River Basin which has the highest storage volume of water resource in Afghanistan. Taluqan Sub-Basin covers 1,300,000 ha of catchment area. From the four rivers which drain in Takhar province, the Kokcha River has the highest volume of water followed by the Taluqan River shown in (Fig.3). Accordingly, it's found that Taluqan River having 51.4 m^3/sec mean yearly discharge is used the most in irrigating agriculture lands, which irrigate 78,437 ha in Taluqan and other neighbouring districts of Takhar province (Fig.3).

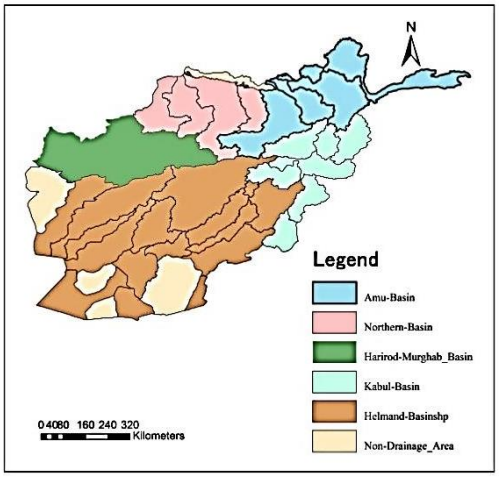

Fig.2.1 Afghanistan Major River Basins

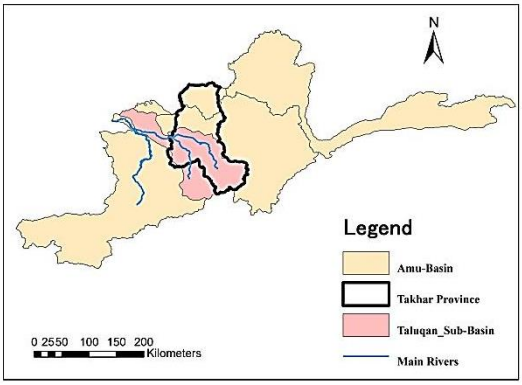

Fig.2.2 Location of Taluqan Sub-Basin in Panj-Amu River Basin

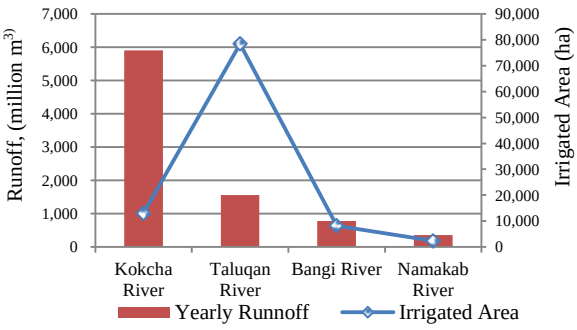

Fig.3 Water Resources and Irrigated Land in Takhar

METHODOLOGY AND DATA

We used the following two methodologies as, questionnaire survey in the field and statistical data analysis, the statistical data, such as, water resources including river discharge and precipitation from 2006 to 2013, and canals structure condition and irrigation system were collected from Irrigation and Agriculture Department of Takhar province. For primary data, we visited field from 10 to 25 May 2015 conducting questionnaire survey in commanding area of Nahr Said, Shorab, Nahr Chaman and Shengan canals in Taluqan and Farkhar districts of Takhar province. Table.1 is showing data for analysis of our study. In the study area, there are quite few written data and we asked the local offices to collect manual data.

The field survey was conducted by using two method of data collection, in-depth interview with key informants (*Mirabs*) and fill-up 50 questionnaire sheets with farmers, the questions include personnel information, irrigation and agriculture practices which covers problems of irrigation, agriculture and water management system in the area. Even the security and lack of database in local government organizations were important constraint for data collection. Data entry and analysis; the collected data was entered to the datasheets and Arc GIS version 9.3 is used for analysis the condition and the geographical distribution maps.

Table.1 Data

Number	Data	Period	Source
1	Mean Monthly River Discharge	2008-2013	Ministry of Energy and Water
2	Cultivated and Irrigated Area	1980-2013	Central Statistics Office
3	Precipitation and Temprature	2006-2014	Ministry of Agriculture
4	Population	1980-2013	Central Statistics Office
5	Sattelite Image	2004	Google
6	50 questionnaire sheets	2015	Questionnaire survey

Flow chart of study

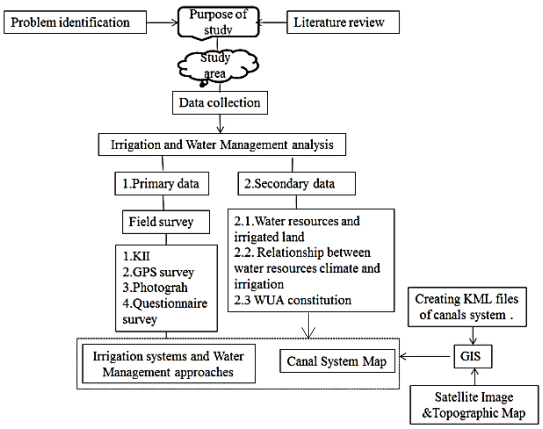

RESULTS

We got the four results from our study, which is explained such as; Irrigation Scheme in the River Morphology, The Irrigation System Canal, Management of Irrigation System and System Operation and Maintenance

A-Irrigation Scheme in the River Morphology

Irrigation water for surveyed canals is obtained from the Taluqan River unless the Shorab Canal from Namak ab River, both tributaries has different mean monthly flows. The average monthly flow data masks the pattern of daily and flood flows and more particularly the water availability for abstraction for irrigation.

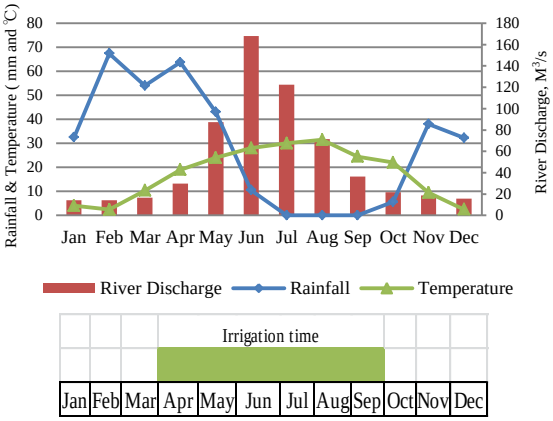

Fig.4 Relationship between river discharge, temperature rainfall and Irrigation Time

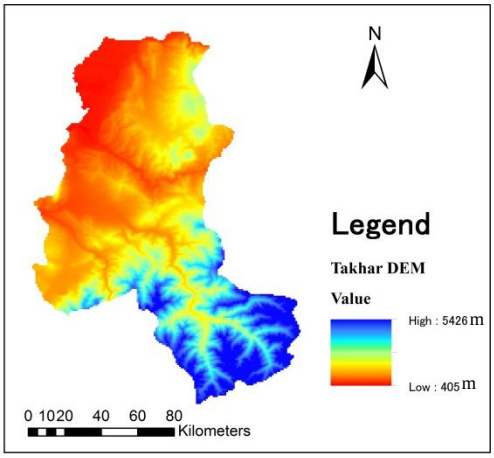

Fig.5 DEM of Takhar Province

The average precipitation is 415mm/year, rainfall is moderate mostly in winter and decreases dramatically in mid spring-summer, while the agriculture crops require water in start of spring and whole summer, specially rice paddy need water where, there is no rainfall in summer (Fig.4). Therefore, the only water resource which is available for agriculture especially for rice paddy is surface water resources by means of irrigation.

Fig.5 is DEM data analysis and this data showing the morphology of the study area. The north part is fluvial plain and the south part is mountains and the rivers water source point's starts from the top of

mountains as result of snow in summer time.

B-The Irrigation Canal System

The irrigation system is divided into private or traditional and government systems; private irrigation systems in most cases have existed for generations and have withstand many social and physical changes, in Takhar province there is 208 private system and 1 government irrigation system. The traditional water management system is characterized by the following key features; A) the local community-based irrigation structures which the construction and maintenance is done by the local community financial and social capital. B) The management and distribution is done by local water masters (locally called *Mirab*) whom they are elected or selected by the community as per their experience and trust at water management in local level and who is responsible for maintenance, enforcement of local norms, and conflict resolution too. C) The water allocation regime is primarily based on landownership and share of contribution to the infrastructure maintenance.

The survey result shows that land slopes in the Taluqan plain have the gradient of 0.03 resulting flat area, giving large river meandering formation that affects large areas of agriculture land each year continually. The conveyance distances from canal intake to command area are quite short, just along the canal. almost all canals supply more than one village, and some similar intakes are used for most of canals in study area unless those are improved such as Said and Chaman canals, but only the Shorab canal which is destroyed by flood, water being abstracted by means of traditional temporary diversion weirs built from soil, stones, timber and grass that extend at a flat angle into the river (Fig 6).

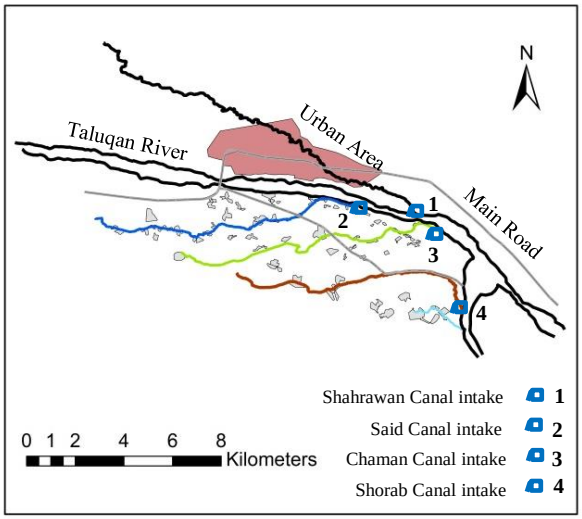

Fig.6 Map of canal system in surveyed area

These weirs are reconstructed every year or when they are damaged by floods. And suitable intake sites are utilized by a number of canals with their intakes running parallel to each other. In Takhar province almost all of irrigation infrastructures have old traditional foundation, which has been constructed more than 100 years ago by local people. Unless in recent years, some irrigation intakes have been constructed or rehabilitated by foreign donors, in the surveyed area we found that 53% of canal intakes mean 25 out of 47 irrigation canals still have the traditional foundation. The largest and modern one of the canals is named Shahrawan Canal having concrete intake and 6 modern controlling gates (Photo.1), is one of the government irrigation system canals which have 38.6 m^3/sec discharge and irrigate 19,325ha in Taluqan district, this canal is managed by Irrigation Department, as the result of survey shows that there is no problem of water shortage because its command area is calculated and the enough water resource is provided (Fig. 7).

From the surveyed area in Taluqan district, villages covered by Shorab canal have the worst condition and the survey result shows that those using the Shorab irrigation canal, Fig. 7 give the highest positive answer to the problems during applying of irrigation water including water shortage and over flooding of farm. As photo (1) shows the condition of Shahrawan canal and photo (2) shows the condition of Shorab canal. But still in both traditional and government owned canals the transition of water from diversion weirs/intakes to farm fields is one of the important matters, because large water losses and soil losses are experienced. For the long canal systems losses, flow duration, interval and rates; result in poor water distribution, also the zigzag shaped canals and streams results lots of water wastage, it's also found that almost all of respondent give negative answer to the irrigation training participation.

Photo 1 Shahrawan intake

Photo 2 Sorab Intake

Photo 4 The boy provide water from Chaman canal to Shorab canal commanded area

Photo 3 Shorab Main canal

Although flow data would indicate that sufficient water is available within the source river for irrigation throughout the year, but water availability in the canals is affected by following hydrological factors that reduce the amount of water that can be diverted into the canals and farms. Low flows at start of spring irrigation season between March and April and the high flows of longer duration with diurnal variations due to snow melt between May and August affecting by too much water in the mid spring, and frequent damage to diversion weirs and intakes at peak demand times, which necessitate continual rebuilding and repair intakes and canals to keep water flowing to the field at a time when farmers need. Even the double-cropping pattern "winter wheat / summer rice" is by far common in the study area, due to agro-ecological constraints (insecure water flow in summer, often heightened by salinity) a large number of farmers specially Shorab Canal users grow rice or wheat as single crops and to a lesser extent, other crops such as mung bean.

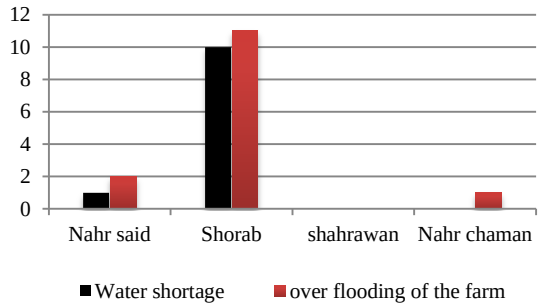

Fig. 7 Problems during irrigation in surveyed area

C-Management of Irrigation Systems

Prior to publishing the water law in 2009, irrigation systems has been managed and controlled by central government and its agencies as a centralized method through *Mirab* system. Although in most of the villages and canals arrangement of water right and water management was done only by *Mirabs* whom they were appointed by local people and completely were dependent to people. The 2009 water law of Afghanistan is based about the Integrated Water Resources Management (IWRM) for reforming the water sector by decentralized decision-making via multi-stakeholder platform, aiming to develop the irrigation system, as far *Mirabs* also take an important role in the operation and management of water. Later, the participatory water management programed and the Water User Associations has established in 2006. The survey show that 25% of canals in Takahr province have the WUA, which have an important role in operation and maintenance, water allocation, water distribution and conflict resolution. As a result of establishing WUA, the number of reported cases of conflict on water use in the study area is decreased. As decreasing the number of conflict in Said Canal from 2006 to 2012, is a good result of WUA (Fig.8), as well Figure.9 shows the organizational chart of the recently established Water User Association. Hierarchically, the *Mirab* is positioned in a lower level of WUA, but still have an important role in water management, operation and maintenance of the system under the supervision of WUA members and or the Taluqan Sub-Basin authority.

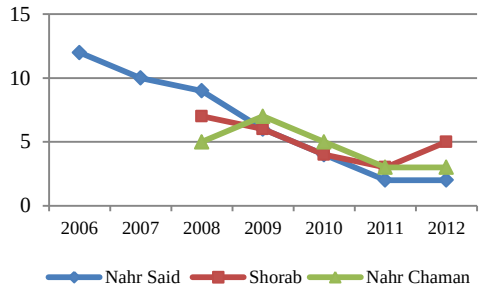

Fig.8 Reported case of conflict on water

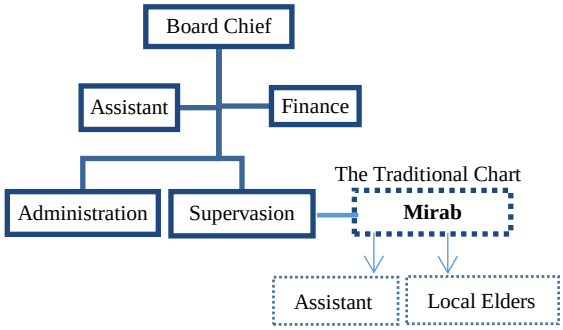

Fig. 9 The Organizational chart of WUA in Takhar

D-System Operation and Maintenance

In the *Mirab* system, each main canal has a *Mirab*, and most communities elect their own *kok bashi* as an assistant of *Mirab* to handle on-farm water distribution. Farmers and villagers are aware of their water rights and *Mirabs* are traditionally elected in late March or early April. On-farm water is allocated on the basis of a local measure, *Paw-ab* or *Qulba*, which relates seed application to land area, similar to the *juftgaw* system in Herat. The presence of this system of measurement indicates old established irrigation systems. Routine cleaning is carried out annually before the start of the irrigation season in (February/March). But in the government irrigation system canals and those have Water User Association the discharge and catchment area is measured in fixed places, and the irrigation water distributes as per 3-3.5 litter/ha, in the times water is excess or water shortage occurs, the water is allocated according to the area considering the above norm.

CONCLUSION

By the following four results from our study, which is explained such as; Irrigation Scheme in the River Morphology, The Irrigation System Canal, Management of Irrigation System and System Operation and Maintenance, we conclude the study.

Due to a high dependency of agriculture to irrigation, irregular river regime and practicing 90% traditional irrigation system and non-mechanized agriculture, Afghanistan is facing deficit in agriculture production every year. However the government and foreign policy makers are trying to introduce and to practice modern irrigation and agriculture methods, but still the results are not efficient, view points and practices in agriculture and irrigation systems are still old and traditional. The major use of water is for irrigation and its supplying need is increasing steadily due to population growth and climate change. This study showed that the irrigation has been using for long time in the area but management of water and irrigation system is still old, which results water shortage due to wasting water and non-efficient water management. In the surveyed area 53% of canal intakes mean 25 out of 47 irrigation canals still have the traditional foundations. The survey shown that only 25% of canals in Takahr province have the Water User Association, which have an important role in operation and maintenance, water allocation, water distribution and conflict resolution. For example, the conflict on water cases is decreased by 75% in Said Canal.

Thus, to save water and use it efficiently to insure sustainable agriculture development we recommend to appropriate irrigation practices and water harvesting is necessary to minimize the water use. Sustainable water management for agriculture aims to consider water availability and water demand in quantity and quality and should have a friendly impact to the environment. To achieve these goal technical facility, sociology of local people, economic and agriculture practices are important matters to be considered. Technical support and construction of modern foundations in addition to introduce modern irrigation systems and the water management are necessary to be considered for sustainable and appropriate use of water in Takhar province.

References;

[1] Afghanistan National Development Strategy Secretariat, Afghanistan National Development Strategy, 2007, pg# 508

[2] Afghanistan Central Statistics Organisation, Afghanistan Statistical Year Book, 1980 and 2013.

[3] Bob Rout, How the Water Flows: A Typology of Irrigation Systems in Afghanistan, Afghanistan Research and Evaluation Unit, 2008, pg#80

[4] Ian McAllister Anderson, Water Management, Livestock and the Opium Economy, Afghanistan Research and Evaluation Unit, 2006, pg#99

[5] Abonesh Tesfaye, The impact of small-scale irrigation on household food security: The case of Filtino and Godino irrigation schemes in Ethiopia, Irrigation and Drainage Systems 2008, Volume 22, Issue 2, pp 145-158

[6] Favre and Kamal, Watershed Atlas of Afghanistan, first edition, 2004, Government of Afghanistan, pg#59

[7] Ministry of Agriculture and Livestock, Kabul, Afghanistan, http://mail.gov.af/en

[8] Ministry of Energy and Water, Kabul, Afghanistan, http://mew.gov.af/en

[9] Constitution of Water Users Association, Drafted by Taluqan Sub-Basin Department office, Takhar, Afghanistan, 2006

First International Conference on Science, Engineering & Environment,
Tsu City, Mie, Japan, Nov.19-21, 2015, ISBN: 978-4-9905958-5-2 C3051

EVALUATING ON THE DEFORMATION OF TIDAL REGIME INDUCED BY SEA LEVEL RISING IN COAST ON MEKONG RIVER DELTA

Nguyen Huu Nhan[1], Shigeko Haruyama [2]
[1] Institute of coastal and offshore Engineering, Vietnam Academy for water Resources, Vietnam;
[2] Graduate School of Bioresources, Mie University, Japan

ABSTRACT

The problem of deformation tidal regime at coast of Mekong Delta induced by sea level rising (SLR) had not studied, while its solving is urgent need for explaining real changes of inundated regime here and for building databases for studying many processes in Mekong Delta impacted by climate change (CC) and SLR. The statistical method had used for analyzing hourly water level records with 27 years long for evaluating real SLR, changes of amplitude and phase of 67 tidal waves at 9 points in coast of Mekong Delta. The shallow water hydrodynamic numerical model with flexible mesh had used for evaluating deformation of main tidal waves (M2, S2, K1, O1) in space. The study results show that: (1) SLR is causing severely negative impacts on Mekong River Delta; (2) The average rate of real SLR here is 3,4-4,1 mm/year; (3) The semi-diurnal tidal waves and shorter are more sensitive to SLR than diurnal tidal waves and longer; (4) The deformation rate of amplitude of semi-diurnal tidal waves is 1-2mm/year; (5) The phase of all tidal wave is more early with rate is 2 minutes/year; (6)The real water level here have been impacted by "double" effects of SLR: rise of mean level and deformation of tidal waves, so the tidal peak is rising larger than tidal foot and mean level, and inundation in Mekong Delta is becoming deeper and longer. The results are bases to explain changes in inundated regime and generating databases to predict SLR impacts in Mekong Delta.

Keyword: Mekong delta, Sea level rising, Deformation of tidal regime, Tidal wave, Numerical Model

INTRODUCTION

Sea level rise (SLR) increases the mean water level (*Z)* by value of SLR. For depth water area, D>>SLR, where D is sea depth, the SLR hardly affects on all kinds of sea current and sea wave, including tidal waves. However, in shallow water as coast and estuaries of Mekong Delta (MD), SLR significant impacts on them by mechanisms: (1) increasing phase speed of tidal wave; (2) Changing its direction; (3) Reducing the impact of tidal current resistance; (4) Causing flooding in the formerly dry coastal areas, leading to change the resonance and spatial interference of the tidal waves in river estuaries, shallow bays, lagoons, mangrove forests, delta and sub-delta geomorphology, etc. In other words, SLR will induce to deformation of tidal regime related with many other processes in coast of MD. Therefore, study tidal deformation induced by SLR is a very important issue. Some studies [1, 5] have given the compelling evidence of the deformation of the tidal regime by SLR. In recent years in Vietnam (VN), phenomena of SLR has been mentioned extensively [3, 4, 5], but the deformation of the tidal regime due to SLR timetable has not been sufficient attention level. The quantitative evaluation of tidal deformation by SLR for coast and estuaries of MD, has not been studied. The quantifying the tidal deformation by SLR is needed to have the scientific basis to: (1) Explain the real pictures of *Z* fluctuations and flooding dynamics in MD and its coast (and another processes as: inundation, erosion, salinity intrusion, distortion of ecosystems, destroy of mangrove, changing micro landform, etc.); (2) Prepare model detailing (down-scaling) SLR scenarios in MD.

METHODOLOGY

There are 2 basic models [2, 5] for evaluating SLR impact on tidal regime: The harmonic analysis model (HAM) and shallow hydrodynamic model (HDM). HAM is the main method of study. HDM has overcomes some disadvantages of HAM, but it is limited in accuracy. It is considered auxiliary method. Optimal method is combining both methods to eliminate the disadvantages of each model in separately application [1, 5]. HAM will used to analyzing series of measured *Z* data to study tidal regime and evaluating impact of SLR on it with the basic advantages are: (1) it has high authenticity in results; (2) it has able to remove non-tidal factors in measured *Z* records (*subsidence, error in benchmark of measured datum, rainfall, flooding of Mekong River, evaporation, wind surges...*) because these evaluations are based only on ranges of *Z* fluctuations with fixed given tidal periods. HDM had used for predicting *Z* fields separately for main tidal waves M2, S2, K1 and O1 for background scenario (1990) and some B2 scenarios of SLR for

finding differences between them used to evaluate SLR impact on tidal regime too.

HAM uses assumptions that *Z(x,y,t)* at each location *(x, y)* and time *t* is a linear superposition of tidal waves and other non-tidal components, so:

$$Z(x,y,t) = a_0(x,y) + Z_0(x,y,t) + \sum_{i=1}^{N} f_i(t) H_i(x,y) \cos[(\Omega_i t + \theta_i(t) - \delta_i(x,y)] \quad (1)$$

Where:

- $\Omega_i = 2\pi/T_i$ is frequency of the tidal wave *i* with period T_i (*from 3 hours to 1 year*)
- *N* is number of tidal waves, N=67;
- H_i and δ_i are amplitude and initial phase of tidal wave i, called tidal harmonic constants;
- a_0 is the average water level at position (x, y) above datum;
- Z_0 is combine sum from non-tidal water level fluctuations;
- f_i and θ_i are the astronomical constants.

For given location *(x, y)* with unchanged conditions, *H* and δ are true constant. However, these parameters may be deformed due to the changes of terrain, location depth, current regime and SLR this deformation is objective of present study. Tidal constants *H* and δ had been found by invert problem from eq. (1), when there are needed records of *Z* (left side) continued for enough long time period. This is the content of the HAM to study changes of (H, δ, a_0) over time, thus quantitative assessing the change of a_0 (relating with SLR) and changes of *H*, δ (deformation of tidal regime). HAM is actually a kind of statistical model. HAM has following features: (1) reliability high in evaluation of parameters *H* and δ; (2) objectivity because results are not dependent on the *Z* fluctuations caused by non-tidal reasons and landmark status of measuring stations. The invert problem of eq. (1), HAM, can be solved by many methods, of which least square algorithm had applied because it is a classic and standard method [5].

The HDM is one module of DHI's model MIKE21/3 coupled model FM [1], which two horizontal momentum equations for the *x*- and *y*-component (*u*,*v*), respectively

$$\frac{\partial hu}{\partial t} + \frac{\partial hu^2}{\partial x} + \frac{\partial hvu}{\partial y} = fvh - gh\frac{\partial \eta}{\partial x} - \frac{\tau_{bx}}{\rho_0} + \frac{\partial}{\partial x}\left(hT_{xx}\right) + \frac{\partial}{\partial y}\left(hT_{xy}\right) \quad (2)$$

$$\frac{\partial hv}{\partial t} + \frac{\partial huv}{\partial x} + \frac{\partial hv^2}{\partial y} = -fuh - gh\frac{\partial \eta}{\partial y} - \frac{\tau_{by}}{\rho_0} + \frac{\partial}{\partial x}\left(hT_{xy}\right) + \frac{\partial}{\partial y}\left(hT_{yy}\right) \quad (3)$$

and continuity equation is written as

$$\frac{\partial h}{\partial t} + \frac{\partial u}{\partial x} + \frac{\partial hv}{\partial y} = 0 \quad (4)$$

with following notes:

$$\frac{\vec{\tau}_b}{\rho_0} = c_f \vec{u}_b \left|\vec{u}_b\right|, \vec{\tau}_b = (\tau_{bx}, \tau_{by}), \quad \vec{u}_b = (u,v), c_f = \frac{g}{\left(Mh^{1/6}\right)^2} \quad (6)$$

$$T_{xx} = 2A\frac{\partial u}{\partial x}, T_{xy} = A\left(\frac{\partial u}{\partial y} + \frac{\partial v}{\partial x}\right), \; T_{yy} = 2A\frac{\partial v}{\partial y} \quad (7)$$

Where η is the surface elevation; *d* is the still water depth; $h=\eta+d$ is the total water depth; *u* and *v* are the depth average velocity components in the *x* and *y* direction; $f=2\omega\sin(\varphi)$ is the Coriolis parameter (ω is the angular speed of earth and φ the geographic latitude); *g* is the gravitational acceleration; A is horizontal eddy viscosity; c_f is the drag coefficient with *M* is Manning coefficient in DHI's meaning [1].

The boundary conditions are following:

- At ocean open boundary lines: *Z* varied along boundary lines will be given;
- At closed boundary lines: set normal depth average velocity component to zero;
- At open cross-sections of Mekong and Bassac rivers: will be given the discharges;
- At open cross-sections of other small rivers: *Z* will be given.

Initial condition is given *(u,v)* and *Z* fields over whole computed domain at moment *t*=0.

The above HDM had solved by numerical finite volume method on flexible mesh. An explicit Euler scheme is used for time integration with time step Δt. There is approach for treatment of the moving boundary problem [1, 5] with 3 parameters Δd_1, Δd_2 and Δd_3 are depths defined the element of computed mesh is drying, flooding or wetting. The procedure for solving the HDM includes 5 steps:

- Generate computed flexible mesh
- Update all input data on computed mesh;
- Calibrate parameters and input data.
- Valid outputs.
- Apply HDM to simulate needed scenarios for evaluating deformation tidal waves induced by SLR

INPUT DATABASE

HAM used 9 series of measured hourly *Z* database from 1984 to 2010 at stations: Vung Tau, Vam Kenh, Binh Dai, An Thuan, Ben Trai, My Thanh, Ganh Hao (in east coast), Ong Doc and Xeo Ro (in west coast). Their locations are shown on fig. 1. The quality of measured data at very good for applying HAM by all aspects as: measured frequency, completeness, continuity, length of the string data and accuracy.

The HDM is working the computed domain covered whole East Sea (see fig. 1) with following (natural) boundaries:

- The closed land boundary is shorelines;
- The open ocean boundaries consist: (1) the Taiwan Strait (O5) in north side; (2) Luzon Strait (O4), North Palawan Strait (O3), South Palawan Strait (O2) in east side; (3) the Singapore-Singkawang Strait (O1) in south side.
- The river ocean boundaries consist (1) Cross-sections of Mekong River at My Thuan Bridge (R1), (2) cross-section of Bassac river at Can Tho (R2); (3) cross-section Nha Be Port (R3).

Their locations are shown at fig.1.

The computed flexible mesh had been generated by Mike zero tool. It had been corrected by model calibration to have final computed mesh at fig. 1.

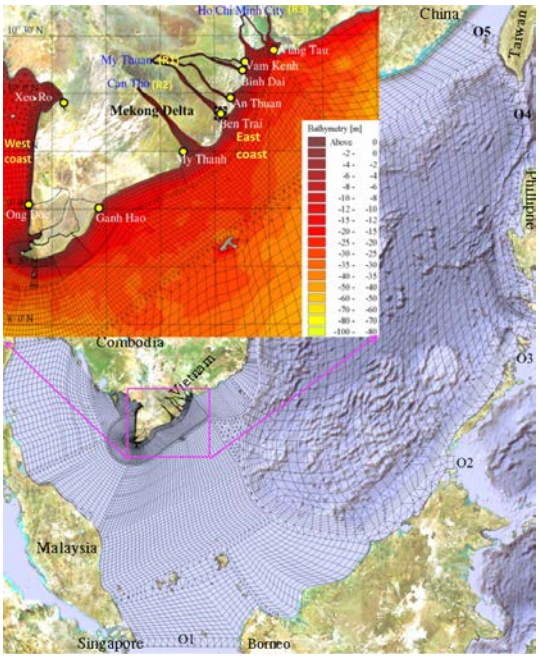

Figure 1. Computed domain; Flexible mesh; bathymetry data; Location of open boundaries; Location of measured Stations in coast of MD.

All kinds of input database should be digitized on computed mesh. The original bathymetric data for depth of sea includes: (1) Digital terrain model (DTM) on grid 0,25 minutes from U.S. Oceanographic Administration (NOAA) provided at: www.ngdc.noaa.gov/mgg/global/relief; (2) DTM database from some Vietnamese agencies and scientific research organizations; (3) Vietnamese Navy maps of scale 1:100,000. For area closed to coast and river branches, the original bathymetric data includes many bathymetric survey maps of scale 1:10,000 and 1:25,000 for all branches of the Dong Nai and Mekong rivers included their mouths and coastal zone. All coastlines of computed domain had defined by the set of present GIS maps and satellite Landsat and Google Earth images. All input data at ocean boundaries O1, O2, O3, O4 and O5 had been generated by tool for predicting tidal water level combined from 67 tidal waves or separated for only one tidal wave. Input data at R1 and R2 includes measured water discharge (Q) data through cross-section at My Thuan bridge and cross-section at Can Tho bridge. Input data at R3 is measured *Z* at Nha Be station (Ho Chi Minh City). Data for model calibration and validation are measured data included: *Q*, *(u,v)* and *Z* at all Mekong River mouths and coast of MD [5].

MODEL CALIBRATION AND VALIDATION

HAM has no parameters, so there is no need in calibration. The accuracy of the harmonic constant data generated by HAM are validated by comparing *Z* calculated by the eq. (1) *without* Z_0 with measured *Z* in September, 2009 and January, 2010 at 9 stations shown above. The comparison shows that: (1) The correlation coefficient between them > 0.94 at the 7 stations on east coast and closed to 0.85 at 2 stations on west coast; (2) There is a pretty good fit between calculated and measured data. The reason of discrepancy between calculated and measured data is mainly due to the measured *Z* is combined, while computed data is pure tide (not including Z_0).

HDM has 7 parameters needed calibration included: *M*, *A*, Δt, Δd_1, Δd_1 and Δd_3 and *mesh*. The measured data (September 14-23, 2009) included Q through cross-sections at main 7 river mouths, (*u, v)* at 6 point and *Z* at 9 stations in coastal zone of MD used for comparing with HDM computed data during calibration. The results of their comparison had given in [5]. The comparison shows that there is a fine agreement between the measured and simulated combined *Z*, *Q* and (*u,v*) in range, phase and direction. The correlation coefficients between the measured and simulated Z are > 0.92 at the 7 stations on east coast and near 0.83 at 2 stations on west coast, between the measured and simulated *Q* are closed to 0.86 at main 7 river mouths and between the measured and simulated (*u,v*) are >0.81 at 6 point in MD. The reasons of discrepancy between them are mainly due to the measured data is full combined, while computed data is not included impacts of some facts, especially, the baroclinic

effect of seawater at estuarine and coastal zone. Also, computer numerical model is always only approximate real world.

The results of model calibration are set of values of parameters of configured model as following:

- M is 44 for depth domain. M is varying from 44 to 48 in coast zone with fine sand with simply terrain. It changes from 33 to 44 in area closed to shoreline zone and river regions. In mangrove area and area closed to it, M is varying in range of 20-33.
- Δt is 2s, that number CLF is always <1;
- A has range of 100-400 m^2/s for depth domain and 1-100 for coast shallow zone and river regions;
- Δd_1=0.005m, Δd_2=0.05m and Δd_3=0.10m are optimal values;
- The computed domain and mesh are presented at fig.1 are optimal for running HDM on PC;
- Initial condition: (u,v) and Z fields over whole computed domain are set to zero.

The measured Z data (January 1-31, 2010) at 9 stations (see fig. 1) in coastal zone of MD is used to compare with HDM computed data for model validation. The detail results of comparison between the measured and simulated data had given in [5] and show that there is a fine agreement between the measured and simulated data in ranges and phase with correlation coefficient is > 0.91 in east coast and 0.81 in west coast. The reasons of differences between them are the same as described above.

The calculated data Z by both model, HAM and HDM, are agreed each together [5].

REULTS

The average speeds (mm/year): ΔZ_{mx}, ΔZ_{avg} and ΔZ_{mn} of changes in yearly maximum, average and minimum of Z for full measured period of length L (year) had been evaluated and presented in table 1.

Table 1. The average speeds of changes yearly maximal, average and minimal Z at 9 stations.

Station name	Mesuared period	L, year	ΔZ_{mx}	ΔZ_{avg}	ΔZ_{mn}
Vung Tau	1984-2011	27	8.1	3.2	1.4
Vam Kenh	1984-2011	27	9.5	7.7	5.6
Binh Dai	1984-2011	27	9.6	5.8	4.1
An thuan	1984-2011	27	11.2	11.2	8.3
Ben Trai	1984-2011	27	11.9	5.2	4.5
My Thanh	1987-2008	20	12.7	11.8	8.1
Ganh Hao	1987-2011	24	13.8	7.9	5.8
Ong Doc	1996-2011	14	4.3	4.3	3.8
Xeo Ro	1984-2011	27	4.6	4.4	4.2

All measured Z data have been processed by HAM for finding (H, δ) of 67 significant tidal waves at 9 stations and 27 years. On fig. 2 and fig. 3 are shown typical picture on changes of (H, δ) of tidal wave M2 during time.

The space changes of H of tidal wave M2 induced by SLR are known by comparison the its maps in 2009 and 2050 (for SLR of scenario B2) presented on fig. 4 and fig. 5. Using these evaluations, we had built the tool for down-scaling Z for a scenario of SLR as that is shown on fig. 6 and fig. 7.

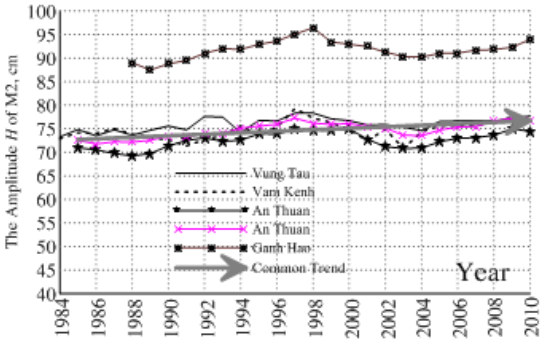

Figure 2. The trends of changes of H of tidal wave M2 with time (year) at east coast of MD

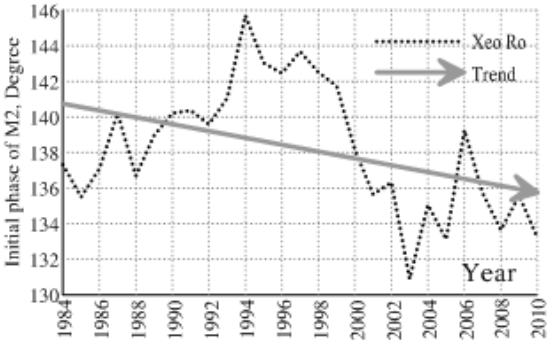

Figure 3. The trends of changes of δ of tidal wave M2 with time (year) at west coast of MD

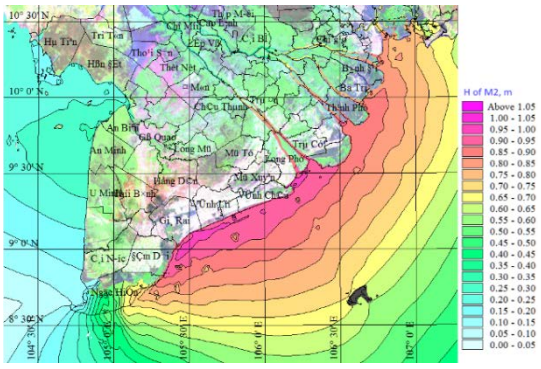

Figure 4. The map of H of tidal wave M2 in 2009

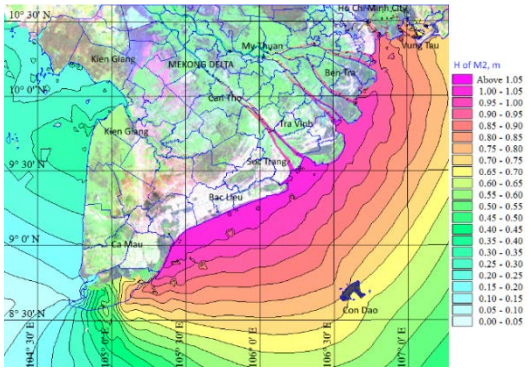

Figure 5. The map of *H* of tidal wave M2 in 2050

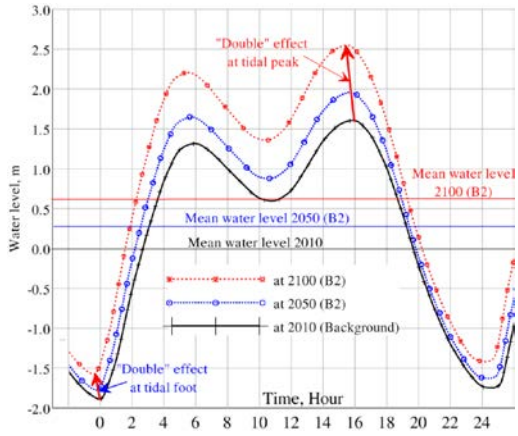

Figure 6. The "double" effect of SLR on tidal regime in east coast of MD

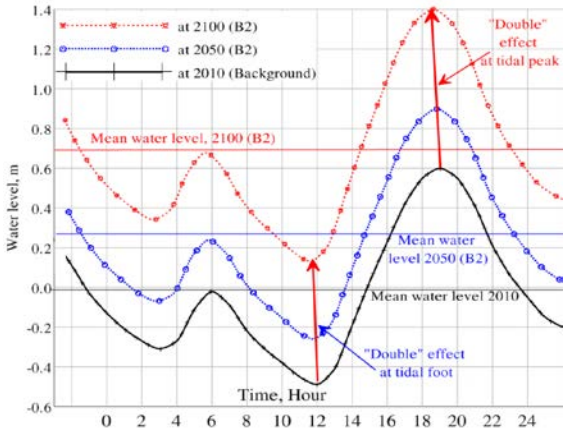

Figure 7. The "double" effect of SLR on tidal regime in west coast of MD

The values of coefficients α and β in linear regression equations for predicting *H* of M2 (from 1990 year) in time. Example, Some computed values of *H* of M2 in 1075 (past time), in 1990 (backround scienario) in 2050 (fulutre time with Scenario B2) are shown in table 2.

Table 2. The coefficients α and β of linear regression equations for predicting *H* of M2 (related from 1990) and its computed values in some years

Station name	Coefficients in regression equations		H, cm		
	α	β	1975	1990	2050
Vung Tau	0.117	75	73	75	82
Ganh Hao	0.119	91	89	91	98
Vam Kenh	0.118	74	72	74	81
My Thanh	0.119	89	87	89	96
Binh Dai	0.118	72	70	72	79
Ben Trai	0.118	78	76	78	85
An Thuan	0.119	74	72	74	81
Xeo Ro	0.046	15	14	15	18
Ong Doc	0.045	11	10	11	14

DISCUSION

Measured data for 27 past years show that Z has trend increased over time and tidal peak is coming earlier than past time. The ΔZ_{mx}, ΔZ_{avg} and ΔZ_{mn} in table 1 are combined by many effects, included SLR. Among 9 stations, the Vung Tau and Ong Doc are located outside space impacted by Mekong River floods, infrastructural development and urbanization in MD, therefore ΔZ_{mx}, ΔZ_{avg} and ΔZ_{mn} here had induced mostly by pure SLR. So, ΔZ_{mx} is 8.1mm/year in east coast and 4.3 mm/year in west coast; ΔZ_{avg} is 3.2 mm/year in east coast and 4.3 mm/year in west coast; Z_{mn} is 1.4mm/year in east coast and 3.8 mm/year in west coast. The differences of ΔZ_{mx}, ΔZ_{avg} and ΔZ_{mn} here mean that tidal regime in coast of MD is deformed by SLR. And, power of these differences in east coast is bigger than in west coast.

It is synthesized as a result of the impact called "double" effect of SLR on tidal regime: it raises the mean sea level together increases range of Z fluctuation (see fig. 6). This effect at east coast with semi-diurnal tidal regime of big range is bigger than west coast with diurnal tidal regime of small range (compare data on fig.6 and fig.7). The tidal phase speed increases too. With these effects, the risk of coastal flooding (depth, scope and duration of flooding) in coastal zone of MD is stronger over time, leading to many other negative impacts. To quantify the impact of SLR on the tidal regime, need to establish its impact separately for each tide component with removing influence of all non-tidal factors by combined using HAM and HDM.

The analysis results give following comments:

- The semi-diurnal waves M2, S2, N2, K2 are quite sensitive to SLR.
- In east coast of MD, the *H* of these tidal waves is increasing with rate of about 0.3% per year. For example, the this rate for *H* of M2, S2, N2 and K2 respectively is 1.2-2.0 mm, 0.5-0.7mm, 0.4-0.5 mm and 0.2-0.4 mm, per year.
- In west coast, their *H* is increased with relative

speed of 0.4%, specifically for wave M2: 0.4-0.5mm per year, S2: 0.2-0.3mm per year, N2: 0.1 mm per year and K2: 0.1 mm, per year.

- The diurnal waves K1, O1, P1, Q1 is insensitive to SLR. Their amplitude *H* virtually unchanged. Especially, in west coast, *H* of K1 is declining at a rate 0.15 mm per year.
- The *H* of the tidal waves with period <14 hours will increase over time, in meanwhile, the tidal wave with period > 20 hours will be little changing, in particular, on the west coast of MD, *H* is reduced.
- The features of impact SLR on tidal regime in west coast may shift nature of tidal regime in future: from diurnal tide now to semi-diurnal tide in 2050, because the range of tidal fluctuations is very small and *H* of K1, O1, P1, Q1 is decreasing over time, while *H* of M2, S1, N2, K2 is increasing with time.
- δ of all tidal waves is earlier with increasing SLR
- The changes of δ at west coast bigger than east coast. Reason of this picture is: the tidal phase speed at west coast is increased more quickly than east coast, because the tidal waves are propagating from East sea to west coast have to pass wide shallow zone, so SLR impact on tidal phase longer and stronger, therefore changes in δ in west coast are bigger than east coast.
- In east coast of MD, δ decrease 0.25-0.31^o per year for the semi-diurnal waves and 0.15-0.2^o per year for the diurnal waves. Thus, after 50 years, the δ would be earlier about 16-17^o (>1 hour)
- In west coast of MD, δ decrease 0.4-0.6^o per year of semi-diurnal and around 0.15-0.3^o per year. So, after 50 years, the tidal peak will come to west coast sooner than currently about 2 hours.

So, the impacts of SLR on tidal regime in coast of MD include 3 main mechanisms: raising mean water level on value of SLR, changing the range of water level fluctuations and increasing phase speed of tidal propagation in shallow water of coastal zone and river mouths of MD. These effects are different for east and west coasts of MD. They generate "double" effects on water level regime as shown on fig. 6 and fig.7. These facts are scientific base for detail down-scaling water level database SLR scenarios for MD.

CONCLUSION

The sea level rise is causing severely negative impacts on coastal zone of South Vietnam with increase of its power over time. The study shows that SLR impacts on the water level fluctuations in coast of MD is not simple. The both measured data and modeled data evidence that this impact generates "double" effect: raising the mean level higher, increasing range of water level fluctuations bigger and decreasing its initial phase earlier. It is become clear that semi-diurnal waves and shallow tidal waves are more sensitive to SLR than diurnal waves and long tidal waves (include storm surge wave). These mechanisms may change tidal regime at shallow water region with small range of water level fluctuations as west coast of MD.

The results are scientific bases for explaining real situations of water level regime and negative changes in inundated regime induced by sea flooding in coastal zone and river basins in MD. They are also scientific bases for "down-scaling" and generating needed boundary water level databases at Mekong river estuaries and coastal zone in modeling processes in MD with CC conditions.

In short word, the impacts of SLR on tidal regime in coast of MD are deforming it leaded to "double" effects on water level regime. Based on results of this study, we can build tool for downscaling water level database with any SLR scenarios. Generally, the evaluations established by both model HAM and HDM are trusted to apply practice. However, these models had used without any changes of study domain topography for long time. So, in this meaning, the study results have some limits. It is problem for next study step.

ACKNOWLEDGEMENTS

Authors express kind thank to Vietnam Academy of Water Resources for support in using computer model MIKE 21/3 coupled Model FM for running many simulations and some measured data for model configuration.

REFERENCES

[1] DHI. MIKE 21/3 Coupled Model FM. User Guide. Published by Danish Hydraulic Institute with software MIKE 21. 2009. 65pp.

[2] Ferla M. Long time variation on sea level and tidal regime in the lagoon of Venive. J. Coastal Engineering. Vol. 57, Apr., 2006, pp. 1279-1399.

[3] Le Thi Viet Hoa, Nguyen Huu Nhan, Eric Wolanski, Tran Thanh Cong, Haruyama Shigeko. The combined impact on flooding in Vietnam's Mekong river delta of local man-made structures, sea level rise, and dams upstream in the river catchment. J. of Estuarine Coastal and Shelf Science,. Vol. 71, Feb., 2007, p. 110-116.

[4] MONRE of Vietnam. The Vietnamese scenarios of climate change and sea level rise. Published by Vietnamese Government. 2012. 120 pp. (in Vietnamese).

[5] Nguyen Huu Nhan. A research on tidal deformation induced by sea level rising in coastal zone of South Vietnam. Project final report of Vietnam Academy of water resources. 2012, 428 pp (in Vietnamese).

[6] Wolanski, E. and Nguyen Huu Nhan. Oceanography of the Mekong River Estuary. pp. 113-115 in Chen, Z., Saito, Y. and Goodbred, S.L., Mega-deltas of Asia-Geological evolution and human impact. China Ocean Press, Beijing, 2005, 268 pp.

First International Conference on Science, Engineering & Environment,
Tsu City, Mie, Japan, Nov.19-21, 2015, ISBN: 978-4-9905958-5-2 C3051

SOLIDIFICATION/STABILIZATION OF NONVALUABLE RESIDUE FROM WASTE PRINTED CIRCUIT BOARD ASSEMBLY

Sunisa Tesanan[1], Suphaphat Kwonpongsagoon[1*], and Premrudee Kanchanapiya[2]
[1] Department of Sanitary Engineering, Faculty of Public Health, Mahidol University, 420/1 Ratchathewi, Bangkok 10400 Thailand; Center of Excellence on Environmental Health and Toxicology (EHT), Bangkok 10400 Thailand
[2] National Metal and Materials Technology Center, National Science and Technology Development Agency, Ministry of Science and Technology, 114 Phahonyothin Rd., Klong 1, Klong Luang, Pathumthani 12120 Thailand

ABSTRACT

The process of copper recovery from waste printed circuit board assembly (PCBA) has remained a large fraction of solid waste called "NonValuable Residue (NVR)". This residue is considered to be a hazardous waste because Pb, Cu, and Sb exceed the regulatory levels. Solidification/Stabilization (S/S) treatment technique is selected to improve waste characteristics before disposal of in hazardous waste landfills. In this study, a cement-based solidification/stabilization was used to treat NVR. Unconfined compression strength test (UCS) and toxicity characteristic leaching procedure (TCLP) were mainly used for physical and chemical characterization of the solidified/stabilized products. After curing for 28 days, the compressive strength and heavy metal leachability (Pb, Cu, Sb) were tested. The results showed that the compressive strength of blank sample was 20.75 MPa while compressive strengths of the solidified/stabilized NVR products were 7.36, 4.17 and 1.35 MPa for 20%, 30% and 40 wt% of NVR, respectively. All experimental mixture ratios satisfied the UCS requirements (0.35 MPa). In addition, the concentrations of Pb, Cu, and Sb in the TCLP leachate of all solidified/stabilized NVR products were lower than the limit value and the original waste. This study indicated that cement-based S/S treatment process was able to improve heavy metal immobilization and subsequently minimize potential environmental impacts in landfill disposal.

Keywords: NonValuable Residue (NVR), Waste Printed Circuit Board Assembly (PCBA), Heavy Metals, Solidification/Stabilization

INTRODUCTION

Nowadays the growing demand for technology and innovation has caused an immense amount of waste generation. Besides demand, one fact is that the lifespan of more products is decreasing; therefore, the large volume of waste stream is rapidly increasing. Waste electrical and electronic equipment (WEEE) or electronic waste such as computers, TVs, fridges, washing machines and cell phones is one of the fastest growing waste streams in many countries. According to the Department of Industrial Works report, in 2014 WEEE in Thailand generated over 20 million units, and had a trend to increase about 10% every year [1]. A main component in the electrical and electronic equipment (EEE) is printed circuit board assembly (PCBA) described as printed circuit boards mounted with various components such as semiconductor chips and capacitors. Although the proportion of PCBA is present only 3 to 6% of the WEEE total weight [2], [3], it has been discarded as waste in large amounts followed by an immense consumption of EEE products.

In general, the waste PCBA comprises about 40 wt.% metallic fractions (MF) and 60 wt.% non-metallic fractions (NMF) [4]. Several precious metals such as copper, gold, and silver are found in these wastes [5]. For nonmetallic fraction (NMF) the material compositions varies with the source and type of waste PCBA [6]. According to Yokoyama and Iji [7], the NMF consisted of glass fiber (65 wt%), cued epoxy resin (32 wt%), and impurities, e.g., copper and solder. The major economic force for recycling waste PCBA is the value of the MF, especially copper, gold, and silver [6]. At present, Thailand can recover only copper from waste PCBA [8]. The process of copper recovery from waste PCBA has remained a large fraction of solid waste residues. In this study, so called "NonValuable Residue (NVR)," which contains a variety of metals, e.g., gold, silver, lead and nickel and other toxic substances, including Brominated Flame Retardants (BFRs), could contaminate and is consequently harmful to the environment and humans. Most hazardous/industrial solid wastes are treated by combustion or secured landfilling. These waste management methods can cause enormous damage

to the environment if not properly treated. The combustion of the NVR could cause the formation of highly toxic polybrominated dibenzodioxins and dibenzofurans while landfilling of the NVR would lead to secondary pollution caused by heavy metals leaching to the groundwater [4], [9]. Therefore, before disposing NVR as hazardous waste by landfilling, it must be stabilized and solidified.

The solidification/stabilization (S/S) is a widely accepted technology for the immobilization of hazardous substances before their disposal such as heavy metals contained in waste. Cement stabilization/solidification is one of the most popular S/S techniques due to its low cost and wide availability [10], [11]. As can be found in other studies, the cement-based S/S is used to immobilize heavy metals in different waste types, for example, Pb and Zn in metallurgical dust [12], Cu, Zn and Ni in plating sludge [13], and Ba in sludge [14]. To date few studies have been conducted on the solidification/stabilization of electronic waste or waste PCBA. To reduce the leachability of the heavy metals contained in NVR and minimize the potential of environmental impacts, this paper aims to study the efficiency of the stabilization and solidification of heavy metals contained in NVR from the waste PCBA using Portland cement.

MATERIALS AND METHODS

Materials and Sample Preparation

The powder material of NVR carried out in this study was obtained from the electronic waste recycling plant in Thailand. This powder remained from the copper recovery process of waste printed circuit board assembly using mechanical and physical methods. The PCBAs were mainly dismantled from waste televisions and computers from a wide range of models and manufacturers. These derived PCBAs were single-sided boards with single-sided layer of copper. According to the recycling process using mechanical and physical methods of this plant, the size of PCBA was reduced by primary and secondary roll crushers and rod mill, respectively. After that, copper was separated from the material using a shaking table. PCBA scrap from the shaking table was divided in three parts: head (high density, medium (medium density), and tail parts (low density). A large fraction of fine particles coming from the tail part was NVR, waiting for further treatment and disposal. This NVR material was collected and used in this study.

In this study, the NVR powder was used to replace ordinary Portland cement (OPC) at a rate of 0, 20, 30 and 40% by weight of the binder. All four mixtures used a water to cement ratio of 0.75, and the ratio of sand to cement was 2.75. Each mix proportion was simply blended in a mechanical mixer and was cast in steel cubical molds at the dimension of 5x5x5 cm. Each mixture gave three cubical samples. After casting for 24 hours, the samples were removed from the molds and cured in water for 28 days. After curing 28 days, the cubical samples were ready for further analyses, e.g., unconfined compressive strength. For X-ray diffraction analysis, all blank samples and solidified/stabilized products had to be crushed to powder before the process of analysis.

Methods of Analysis

The chemical composition of the NVR powder was analyzed by X-ray fluorescence (XRF) and particle size of NVR was measured using laser particle size analysis (Mastersizer). Moreover, the crystalline phases and microstructures in the blank sample and solidified/stabilized NVR products were identified using X-ray diffraction (Rigaku) and Scanning electron microscopy (Hitachi SU8030).

Unconfined compressive strength analysis

The compressive strength of solidified/stabilized products was tested in accordance with ASTM C109 [15]. After curing 28 days, three cubical samples of each mixture were tested using the unconfined compression machine (ADR-Auto V.2.0, ELE International) and average value of compressive strength was reported.

Toxicity characteristic leaching procedure (TCLP)

The metal leaching of solidified/stabilized NVR products at curing time for 28 days was assessed using the toxicity characteristic leaching procedure as defined by the U.S. EPA [16]. The sample was crushed to reduce the particle size to less than 9.5 mm. The crushed sample was extracted using acetic acid solution (pH 2.88$\pm$0.05) at a liquid to solid ratio of 20:1. The extraction vessels were rotated in an end-over-end fashion at 30$\pm$2 rpm for 18$\pm$2 h. The leachate was filtered through a 0.8 µm membrane filter to remove suspended solids and was used to analyze Pb, Cu and Sb present in the leachate by Inductively Coupled Plasma Mass Spectrometry (ICP-MS) following the method 3010 [17].

RESULTS AND DISCUSSION

Fig. 1 shows the particle size distributions of ordinary Portland cement and NVR. The particle size analysis showed specific surface area was 1.17 m^2/g of OPC and 0.28 m^2/g of NVR. The mean particle size of OPC and NVR was approximately 21 µm and 208 µm, respectively. In addition, 90% of OPC and NVR particles size were smaller than 48.7 µm and 475 µm, respectively. The results of the

particle size analysis showed that the actual fineness and specific surface areas of OPC were much more than the NVR powder. This indicated that the reaction of NVR powder could occur slowly when compared with the reaction of cement powder. The result of chemical compositions of the NVR in this study is presented in Table 1. It is obvious that the highest concentration was bromine (Br). Many heavy metals were found in NVR powder; with the highest concentrations being Pb, Sn, and Cu, in order. According to Thailand Notification of the Ministry of Industry B.E. 2548 (2005) on Disposal of Wastes or Unusable Materials [18], any waste or unusable material that contains or contaminates hazardous materials or exhibits hazardous characteristics including flammable, corrosive, reactive, toxic or having the specified constituents equal or exceeding the Total Threshold Limit Concentration (TTLC) as listed in the Annex 2, is defined as "Hazardous Waste". The results of chemical compositions of NVR powder in Table 1 show that the concentration of Pb, Cu and Sb exceeded the limit values. Therefore, the NVR powder in this study was identified as a hazardous waste.

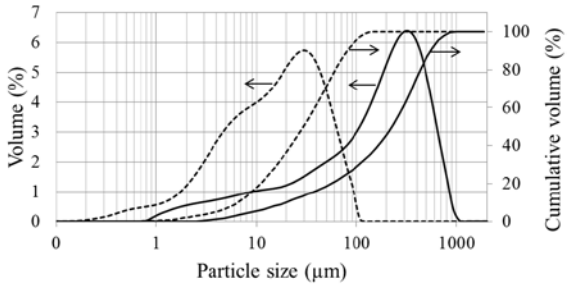

Fig. 1 The distribution of NVR particle size Dashed line: OPC and solid line: NVR

According to many other studies on the improvement of the quality of concrete in terms of strength, durability, and cost reduction, many waste products from natural and industrial process, e.g., silica fume, pulverized fuel ash, blast furnace slag, bagasse ash, rice husk ash, and sheanut shell ash, have been tested and are suggested to be pozzolanic materials or having pozzolanic properties that can be used in concrete paste and mortar [19]-[21]. Pozzolan is defined as a material with an amorphous siliceous or siliceous and aluminous content that reacts with calcium hydroxide in the presence of water to form cementitious hydration products [22]. Based on the ASTM C 618 standard [23] and related research [20], [21], a good pozzolanic performance is likely to contain high SiO_2 or SiO_2+Al_2O_3 or SiO_2+Al_2O_3+Fe_2O_3 content, at least 70 wt%. As seen in Table 1, among all oxide compounds, the presence of Al_2O_3, SiO_2, and Fe_2O_3 is low. Hence, the NVR powder from waste PCBA of this study was not a potential pozzolanic material. This may result in the worst performances of solidified/stabilized cubes.

Table 1 Chemical compositions of NVR powder

Compositions	NVR	Regulation limit*
Elements (mg/kg)		
Br	32,800	n/a
Pb	12,300	1,000
Sn	12,100	n/a
Cu	11,800	2,500
Zn	3,250	5,000
Sb	2,760	500
Ba	2,730	10,000
Ni	966	2,000
Ag	164	500
Co	43	8,000
Oxides (%)		
Al_2O_3	9.62	
SiO_2	6.35	
Fe_2O_3	1.63	
CaO	0.97	
MgO	0.40	
SO_3	0.12	

Note: *Thailand Notification of the Ministry of Industry B.E. 2548 (2005) on Disposal of Wastes or Unusable Materials: Annex 2
n/a: not available

Unconfined Compressive Strength

The average compressive strength of solidified/ stabilized products compared with blank samples after curing 28 days is shown in Fig. 2. Blank samples (without NVR) exhibited compressive strength of 20.75 MPa while compressive strength of 20%NVR, 30%NVR and 40%NVR products were 7.36, 4.17 and 1.35 MPa, respectively. The results indicated that the percentage of NVR loading affected compressive strength. The compressive strength decreased when the amount of NVR increased. This was similar to several studies that investigated the effect of cement-waste ratio on compressive strength of solidified/ stabilized waste [19], [24]. According to Malviya and Chaudhary [25], the solidified products with a compressive strength less than 1 MPa were weak because they contained importantly less cementitious materials. In Fig. 2, compressive strength of all solidified/stabilized NVR products was more than 1 MPa. This indicated that all solidified/stabilized samples of this study were relatively strong.

Replacement of cement with NVR powder at the rate of 20 wt.% had the highest compressive strength when compared with 30 and 40 wt.% replacement. The decrease of cement proportion in the mixture

causes a decrease of main products of the hydration reaction from Portland cement. This can be explained in that the main products of the hydration, calcium silicate hydrate (C-S-H) and calcium hydroxide ($Ca(OH)_2$), are the main carriers of strength in hardened cement [19], [26]. This is in accordance with the following peaks of portlandite ($Ca(OH)_2$) by XRD analysis in Fig. 3.

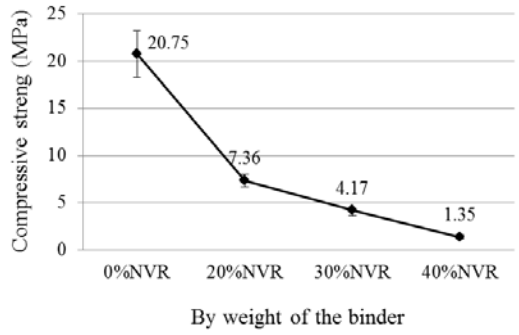

Fig. 2 Average compressive strength of solidified/stabilized NVR products compared with blank sample

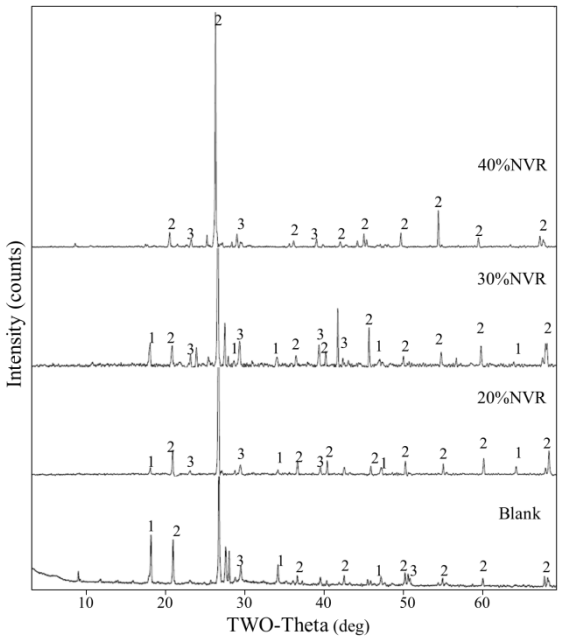

Fig. 3 XRD result for blank and solidified/stabilized products after curing 28 days.1: Portlandite (Ca $(OH)_2$), 2: Quartz (SiO_2), and 3: Calcite ($Ca(CO)_3$)

The XRD patterns of blank and solidified/stabilized samples are shown in Fig. 3. Characteristic peaks of quartz (SiO_2), portlandite ($Ca(OH)_2$) and calcite ($CaCO_3$), which can be found in mortar structure, are present in the XRD result. It can be seen that quartz (SiO_2) and portlandite ($Ca(OH)_2$) are major crystalline phases in blank samples. Similarly, XRD patterns also appear in solidified/stabilized samples but the peak of portlandite ($Ca(OH)_2$) was lower when the NVR was added at a higher rate. The highest peak was SiO_2, which is found in all samples because SiO_2 is a main component of ordinary Portland cement and sand [10], and the NVR powder in this study. In addition, Scanning Electron Microscope (SEM) investigation illustrated another microstructure to improve strength development, called "ettringite", a small needle-like crystal, in both cement paste and NVR paste (see Fig.4). It is obvious that ettringite was formed and observed in cement paste more than in NVR paste. This confirmed less stiff and less durable solidified/stabilized NVR products in this study.

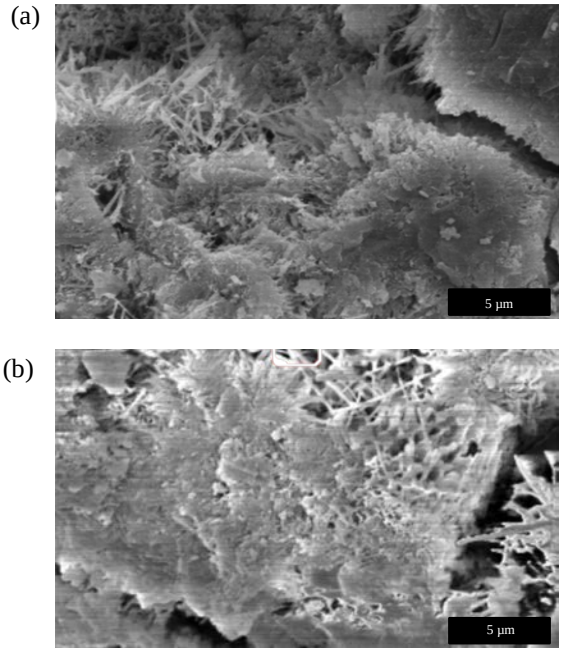

Fig. 4 SEM micrographs of samples at magnification of x10,000: (a) cement paste and (b) NVR paste

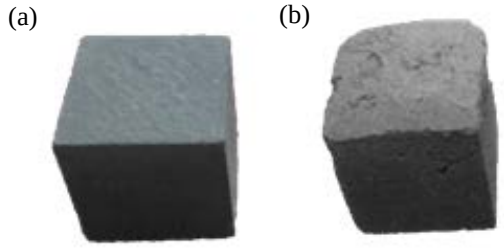

Fig. 5 Solidified/stabilized products. (a) blank sample and (b) solidified/stabilized NVR product

Moreover, all cubical samples containing NVR powder were observed to begin swelling and cracking during casting for 24 hours. (as seen in Fig. 5), and stopped afterwards. Regarding the swelling of those cubical samples, it was found that the height

of these samples increased between 0.5 and 1.1 cm (or 10 to 22%) when compared with the blank sample. According to Aubert et al. [27], swelling and cracking can lead to loss of compressive strength for solidified/stabilized waste. This can be explained in that the swelling and cracking resulted from air voids in solidified/stabilized waste. In this study, 40% NVR powder replacement was the highest content that could be added in the mixture because it revealed a very poor performance of mortar setting. However, the compressive strength of all solidified/stabilized NVR products meets the U.S. EPA requirements of unconfined compressive strength at 0.35 MPa for disposed solidified/ stabilized waste in landfills [28].

Toxicity Characteristic Leaching Procedure Test (TCLP)

TCLP test was generally used for chemical characterization of the solidified/stabilized NVR products, and to determine the efficiency of immobilization of heavy metals in the solidified/stabilized products. In this study, Pb, Cu and Sb were selected as target substances for measurement because these heavy metals were detected at high concentrations in the original material and exceeded the regulation limits as mentioned above. Table 2 shows the metal concentrations in TCLP leachates of solidified/ stabilized NVR samples after curing for 28 days. The results showed that the concentration of Pb in the leachate of all solidified/stabilized NVR samples was lower than the limit value specified by the standard of the U.S. EPA [29]. This means that the cement-based solidification/stabilization technique is effective for immobilization of heavy metals in NVR powder. For Cu and Sb, the U.S.EPA does not specify in the TCLP leachate.

Table 2 Metal concentrations in TCLP leachates

Sample	Concentration (mg/L)		
	Pb	Cu*	Sb*
Regulatory limit	5	-	-
Blank	ND	0.13	ND
20%NVR	0.20	0.60	0.24
30%NVR	0.71	1.26	0.27
40%NVR	0.11	2.26	0.14

Note: * Not specified in the leachate from TCLP test by the U.S.EPA
ND: Not detected

According to Ucaroglu and Talinli [24], when the amount of waste in the mortars increased, the heavy metal concentrations in leachate from the solidified/ stabilized products increased. In Table 2, it can be seen that the more amount of NVR in the mixture, the higher the level of Pb, Cu and Sb concentrations in the leachate extract, except Pb and Sb in the leachate from 40%NVR replacement.

CONCLUSION

The NVR powder from waste PCBA in this study was considered to be a hazardous waste because Pb, Cu, and Sb exceeded the regulatory levels, specified by Thailand Notification of the Ministry of Industry B.E. 2548 (2005) on Disposal of Wastes or Unusable Materials. This study primarily showed that the maximum amount of NVR powder that could be added in the mixture was 40% by weight of binder. After curing for 28 days, the compressive strength and heavy metal leachability (Pb, Cu, Sb) were tested. The results showed that all experimental mixture ratios satisfied the UCS requirements (0.35 MPa). Moreover, concentrations of heavy metals in TCLP leachates for all solidified/stabilized NVR products were below the regulation level specified by the U.S.EPA. It can be concluded that the cement-based solidification/ stabilization treatment technique is effective for immobilization of heavy metals in NVR powder from waste PCBA.

ACKNOWLEDGEMENTS

This research work was supported in part by a grant from the Center of Excellence on Environmental Health and Toxicology, Science & Technology, Postgraduate Education and Research Development Office (PERDO), Ministry of Education. Moreover, this study was supported for publication by the China Medical Board (CMB), Faculty of Public Health, Mahidol University, Bangkok, Thailand.

REFERENCES

[1] Bureau of Policy and Strategy, “Electronic waste”, J. of Health Fact sheet, Vol. 8, 2015, unpaged.

[2] Bernardes A, Bohlinger I, Rodriguez D, Milbrandt H, and Wuth W, “Recycling of printed circuit boards by melting with oxidising/reducing top blowing process”, in Proc. 126th TMS Annual, 1997, pp. 363–375.

[3] Das A, Vidyadhar A, and Mehrotra SP, “A novel flowsheet for the recovery of metal values from waste printed circuit boards”, J. of Resources Conservation and Recycling, Vol. 53, 2009, pp. 464-469.

[4] He W, Li G, Ma X, Wang H, Huang J, Xu M, and Huang C, “WEEE recovery strategies and the WEEE treatment status in China”, J. of Hazardous Materials, Vol. 136, 2006, pp. 502-512.

[5] Wang X, and Gaustad G, "Prioritizing material recovery for end-of-life printed circuit boards", J. of Waste Management, Vol. 32, 2012, pp. 1903-1913.

[6] Guo J, Guo J, and Xu Z,"Recycling of non-metallic fractions from waste printed circuit boards: A review", J. of Hazardous Materials, Vol. 168, 2009, pp. 567–590.

[7] Yokoyama S, and Iji M, "Recycling of printed wiring boards with mounted electronic parts", in Proc. Int. Symp. on IEEE, 1997, pp. 109–114.

[8] Kanchanapiya P, E-waste: technology of printed circuit board management. Bangkok: Thai effect studio, 2011.

[9] Sepulveda A, Schluep M, Renaud FG, Streicher M, Kuehr R, Hageluken C, and Gerecke AC, "A review of the environmental fate and effects of hazardous substances released from electrical and electronic equipment during recycling: Examples from China and India", J. of Environmental Impact Assessment Review, Vol. 30, 2010, pp. 28-4.

[10] Gollmann MAC, da Silva MM, Masuero AB, and dos Santos JHZ. "Stabilization and solidification of Pb in cement matrices", J. of Hazardous Materials, Vol. 179, 2010, pp. 507-514.

[11] Malliou O, Katsioti M, Georgiadis A, and Katsiri A, "Properties of stabilized/solidified admixtures of cement and sewage sludge", J. of Cement & Concrete Composites, Vol. 29, 2013, pp. 55–61.

[12] Giergiczny Z, and Kro A, "Review: Immobilization of heavy metals (Pb, Cu, Cr, Zn, Cd, Mn) in the mineral additions containing concrete composites", J. of Hazardous Materials, Vol.160, 2008, pp.247–255.

[13] Chindaprasirt P, Sinsiri T, Napia C, and Jaturapitakkul C, "Solidification of heavy metal sludge using cement, fly ash and silica fume", Indian J. of Engineering and Materials Sciences, Vol. 20, 2013, pp. 405-414.

[14] Silva MAR, Mater L, Souza-Sierra MM, Correa AXR, Sperb R, and Radetski CM, "Small hazardous waste generators in developing countries: use of stabilization/solidification process as an economic tool for metal wastewater treatment and appropriate sludge disposal", J. of Hazardous Materials, Vol. 147, 2007, pp. 986–990.

[15] ASTM C109/C 109M-95, Test Method for Compressive Strength of Hydraulic Cement Mortars, American Society of Testing and Materials, West Conshohocken, PA, 1995.

[16] U.S.EPA, "Method 1311 Toxicity Characteristic leaching Procedure", U.S.EPA, Jul.1992, http://www.epa.gov/osw/hazard/testmethods/sw846/pdfs/1311.pdf

[17] U.S.EPA, "Method 3010a Acid digestion of aqueous samples and extracts for total metals for analysis by FLAA or ICP spectroscopy", U.S.EPA, Jul.1992, http://www.epa.gov/solidwaste/hazard/testmethods/sw846/pdfs/3010a.pdf

[18] Notification of Ministry of Industry on disposal of wastes or unusable, B.E. 2548 (2005).

[19] Saiwarin W, Napia C, and Sinsiri T, "The study of leaching of heavy metals contaminant in cement pastes containing bagasse ashes", KKU Engineering, Vol.41, 2014, pp. 181-190.

[20] Bui DD, Hu J, and Stroeven P, "Particle size effect on the strength of rice husk ash blended gap-graded Portland cement concrete", J. of Cement & Concrete Composites, Vol. 27, 2005, pp. 357-366.

[21] Tsado TY, Yewa M, Yaman S and Yewa F, "Effect of sheanut shell ash as a partial replacement of ordinary Portland cement in mortar", International J. of Engineering Science Invention, Vol. 3, 2014, pp. 1-5.

[22] American Concrete Institute, ACI Concrete Terminology. Farmington Hills, 2013.

[23] ASTM C 618-12, Standard Specification for Coal Fly Ash and Raw or Calcined Natural Pozzolan for Use in Concrete, American Society of Testing and Materials, West Conshohocken, PA, 2012.

[24] Ucaroglu S, and Talinli I, "Recovery and safer disposal of phosphate coating sludge by solidification/stabilization", j. of Environmental Management, Vol. 105, 2012, pp. 131-137.

[25] Malviya R, and Chaudhary R, "Factors affecting hazardous waste solidification/stabilization: A review", j. of Hazardous Materials, Vol. 137, 2006, pp. 267–276.

[26] Antiohos SK, Papadakis VG, and Tsimas S, "Rice husk ash (RHA) effectiveness in cement and concrete as a function of reactive silica and fineness", j. of Cement and Concrete Research, Vol.61-62, 2014, pp. 20-27.

[27] Aubert JE, Husson B, and Vaquier A, "Metallic aluminum in MSWI fly ash: quantification and influence on the properties of cement-based products", j. of Waste Management, Vol. 24, 2004, pp. 589-596.

[28] U.S.EPA, Stabilization/solidification of CERCLA and RCRA wastes, EPA/625/6-89/022, May 1989.

[29] Federal Register, Environmental Protection Agency-40 CFR Parts 261, 1986.

First International Conference on Science, Engineering & Environment,
Tsu City, Mie, Japan, Nov.19-21, 2015, ISBN: 978-4-9905958-5-2 C3051

SUCCESS OF FUEL QUALITY IMPROVING POLICY IN REDUCING EMISSIONS AND AMBIENT CONCENTRATIONS OF BENZENE: CASE STUDY OF BANGKOK, THAILAND

Lasita Jinawa[1,2] and Sarawut Thepanondh[1,2]
[1]Faculty of Public Health, Mahidol University, Thailand,
[2] Center of Excellence on Environmental Health and Toxicology (EHT), Bangkok, Thailand.

ABSTRACT

The Thai's policy in improving of fuel quality to the changing of emissions and concentrations of air pollutants in Bangkok is evaluated in this study. Benzene content in gasoline had been decreased from 3.5% (EURO II standard) to less than 1.0% (EURO IV standard) since the year 2012. The IVE (International Vehicle Emission) model was applied to develop emission factor of benzene taking into consideration actual fleets and characteristics of vehicles in Bangkok. These vehicles consisted of passenger car, motorcycle, van and pick up, taxi, bus and truck. Then, emission inventory of benzene emitted from mobile sources was calculated. It was found that about 83% of total emissions of benzene were contributed from motorcycle (43%) and passenger car (40%). Emission amounts were reduced from 1.32 x 10^3 ton/year to 0.57 x 10^3 ton/year as resulted from changing of fuel quality from EURO II to EURO IV standard. AERMOD dispersion model was used to simulate ambient ground level concentration of benzene prior and after implementing this policy. Results revealed significantly reduction of benzene concentrations in Bangkok's environment. Spatial distribution of benzene pollution map illustrated that areas having annual concentration higher than 1.7 μg/m^3 (the Thai's air quality standard for benzene) were still only found in traffic-congested zone of the central business district in the metropolitan area.

Keywords: Benzene, IVE, AERMOD, Emission rate, Bangkok

INTRODUCTION

Information from the Department of Land Transport, Ministry of Transport indicated that the cumulative number of vehicles in Thailand, registered in December 31, 2013 were 34,624,406. Among these, the numbers of cumulative registered vehicles in Bangkok were 8,216,859 or approximately 23.7% of the cumulative number of vehicles registered nationwide [1].

Benzene is carcinogenic to human (Group1) [2]. Benzene generally found in petroleum products, such as gasoline and diesel fuel. This air toxic is emitted from gasoline service stations, motor vehicle exhaust and fuel evaporation, the burning of coal and oil, and various other sources. Mobile (i.e., cars, trucks, motorcycles and airplanes) are a major source of benzene. The increasing numbers of motor vehicles are the major cause of the high roadside benzene levels along the busy road [3].

Status of benzene measured in Bangkok indicated that benzene concentrations were higher than its annual ambient air quality standard (1.7 μg/m^3). In addition, it is found that level of air pollution is generally higher than other area of the country. It is well known that the major emission source of air pollution in Bangkok areas is from mobile source since traffic emissions dominate as major source in the city [4].

This study assessed amount of benzene emissions and concentrations from mobile sources in traffic-congested zone of the central business district in the Bangkok metropolitan area, Thailand. Fuel quality in Thailand has been improved from EURO II to EURO IV standard since the year 2012. Major improvement was reducing benzene content in gasoline from 3.5% (EURO II) to less than 1.0% (EURO IV). Therefore, the years 2011 and 2013 were selected as reference years for comparison in this study. Emission factors of benzene of each type of vehicle in these years were derived from the study by Thepanondh S. [5]. This study developed dynamic emission factors, based on travel distance information, for air toxic compounds from vehicles using the IVE (International Vehicle Emission) model. Then, emission inventories, based on dynamic emission factors, were developed using a bottom up approach for the period from the year 2009 to 2024. Emission factors of benzene emitted from each type of vehicle driven in Bangkok area were developed using their current and planned fleet and fuel characteristics of vehicles [6]. Emission factors of each type of vehicle in the EURO II and EURO IV scenarios were as presented in Table 1.

Table 1 Emission factor of benzene used in this study

Type of vehicle	Emission factor (g/km)	
	EURO II	EURO IV
passenger car	0.0151	0.0072
motorcycle	0.0401	0.0048
van and pick up	0.000445	0.000407
taxi	0.0182	0.0162
bus	0.0043	0.0044
truck	0.0096	0.0095

Remarks: These emission factors were calculated from IVE model [5]

These emission rates were used as input data to predict its ground level concentration using air quality dispersion model. AERMOD dispersion model version 8.8.9 was used to simulate ambient ground level concentration of benzene prior and after implementing the Thai's policy in improving of fuel quality in the year 2012 (changing of fuel quality from Euro II to Euro IV standard). Spatial distributions of benzene concentration in the study area were illustrated as pollution map. Sensitivity analysis of effectiveness of implementing fuel quality improvement policy was carried out by identifying differences of modeled results from simulation of with and without this policy.

METHODOLOGY

In this study, the study domain covered area 4×4 km^2 in the traffic-congested zone of the central business district in the Bangkok metropolitan area, Thailand. Six major roads located within the modelling domain were included in this study. They were Phahonyothin road, Phayathai road, Dindaeng road, Rachawithi road, Rama-VI road and Makkasan road. Figure 1 illustrated a map of the study area. Characteristics of each road in study area were presented in Table 2.

Table 2 Characteristics of each major road in study area in 2013.

Road	Length (km)	Width of the road (m)	Traffic density (vehicle per day)
Phahonyothin	1.65	21	60,400
Phayathai	1.82	21	72,033
Dindaeng	2.01	28	64,557
Rachawithi	1.61	21	20,357
Rama-VI	1.26	17.5	56,067
Makkasan	1.15	21	403

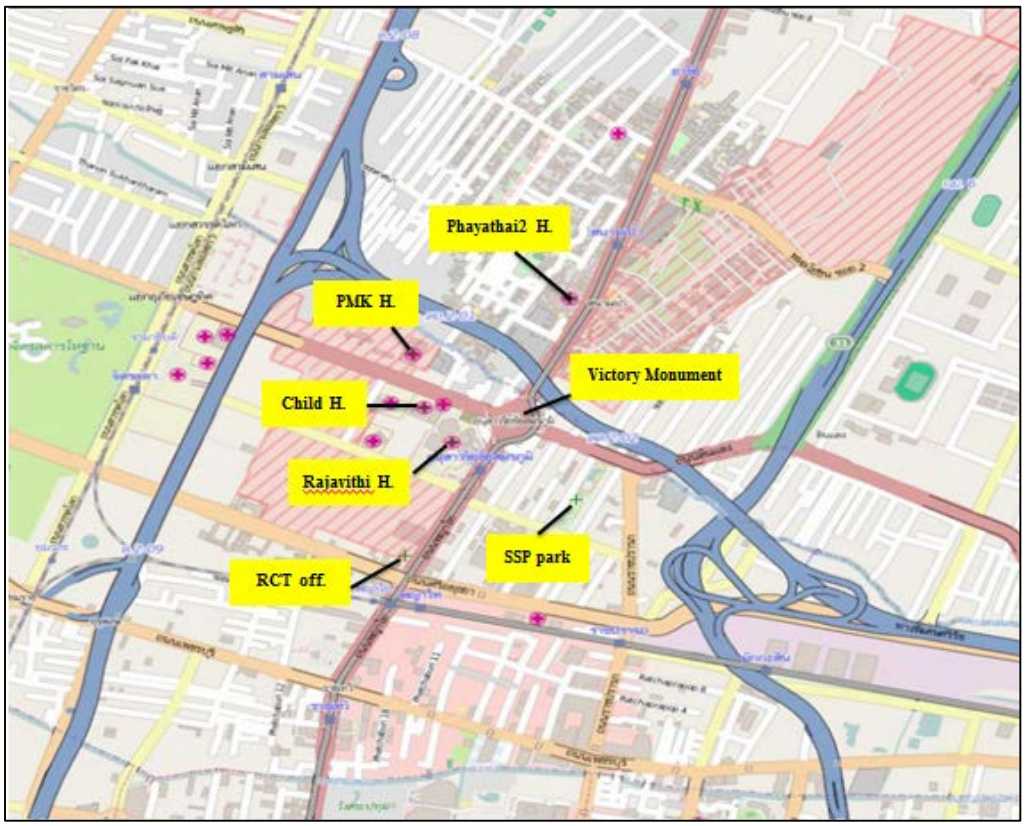

Fig.1 Map of the study area.

Emissions and concentrations of benzene from vehicles in the study area were evaluated. These vehicles consisted of passenger car, motorcycle, van and pick up, taxi, bus and truck. The receptor used as locations to predict ground level concentration of benzene consisted of 6 receptors. They were Phramongkutklao hospital (PMK H.), Queen Sirikit National Institute of Child Health (Child H.), Suan Sunti Phap Park (SSP park), Phayathai 2 hospital, Ratchathewi District Office (RCT off.) and Rajavithi hospital as shown in Fig.1.

Composited emission factor of vehicles were derived from calculation of the IVE model using an actual fleet and fuel characteristic of each type of vehicles in Bangkok. The International Vehicle Emissions (IVE) model is a computer model designned to estimate emissions from motor vehicles. Its prime purpose is for use in developing countries. The model predicts local air pollutants, greenhouse gas emissions, and toxic pollutants. The IVE model has been developed as a joint effort of the University of California at Riverside, College of Engineering–Center for Environmental Research and Technology (CE-CERT), Global Sustainable System Research (GSSR), and the International Sustainable Systems Research Center (ISSRC). Funding for model development was provided by the U.S. Environmental Protection Agency [5].

Numbers of each type of vehicles driven on each road in the year 2013 were summarized in Fig.2. These data were obtained from direct vehicle counting from these streets [7],[8]. It was found that motorcycle and passenger car were dominant types of vehicle within the study area.

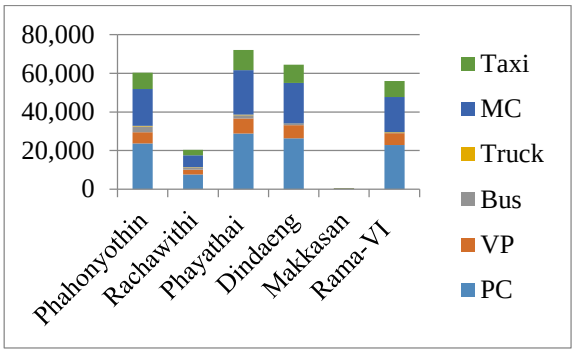

Fig. 2 Proportion of each type of vehicle in study street (vehicle per day)

Data were then used to predict ambient air concentrations of benzene by using the AERMOD dispersion model version 8.8.9. AERMOD model (AMS/EPA Regulatory model) is a steady-state model which assumes that a plume disperses in the vertical and horizontal directions resulting in Gaussian concentration distributions [9]. Model was simulated taking into consideration diurnal variation of number of vehicles on the road. The weekday-weekend profiles were also considered in this simulation.

RESULTS AND DISCUSSION

As for estimation of emission amount of benzene, results indicated that its total emissions were decreased from 1.32×10^3 ton/year (using emission factor of the year 2011) to 0.57×10^3 ton/year (using emission factor of the year 2013). This amount was about 43% reduced from its EURO II fuel quality standard scenario. About 83% of total emissions of benzene were contributed from motorcycle (43%) and passenger car (40%).

AERMOD was used to simulate ambient ground level concentration of benzene prior and after implementing of measures to change the fuel quality from Euro II to Euro IV standard. Model was simulated covering the whole period of the year 2013. Annual concentrations of benzene at each receptor sites were computed. Figure 3-4 illustrated the spatial distribution of areas having benzene annual concentration higher than 1.7 $\mu g/m^3$ (the Thai's air quality standard for benzene). Results clearly indicated significant reduction of benzene ground level concentration within study area from implementation of fuel quality improvement policy.

Predicted results of annual concentration of benzene at receptor positions also revealed the decreasing trend when EURO IV standard had been implemented. Annual benzene concentrations at every receptor were predicted to be within the level of benzene air quality standard. Results from this study were coincided with significantly reduction of benzene concentrations obtained from direct measurement in Bangkok's environment. The maximum benzene annual concentration measured as 11.1 $\mu g/m^3$ in 2011 was dramatically decreased to 3.58 $\mu g/m^3$ in 2013 at the same location [10]. These findings strongly supported that the implementation of measures to improve the fuel quality from Euro II to Euro IV standard was one of a success policy in reducing both emission and concentrations of airborne benzene in Bangkok metropolitan area.

In addition, ozone and photochemical oxidants are one of the major air pollutants which Bangkok is faced at present. These pollutants together with variation of meteorological conditions can affect to temporal distribution and dissipation of benzene. Evaluation of natural dissipation of benzene is also interested to identify natural contribution of this compound. Therefore future study to evaluate influences of these factors and relationship between air toxics and photochemical oxidants are very much interested. These further studies can assist in elucidating atmospheric chemistry of air pollutants for better management of policy to tackle this problem.

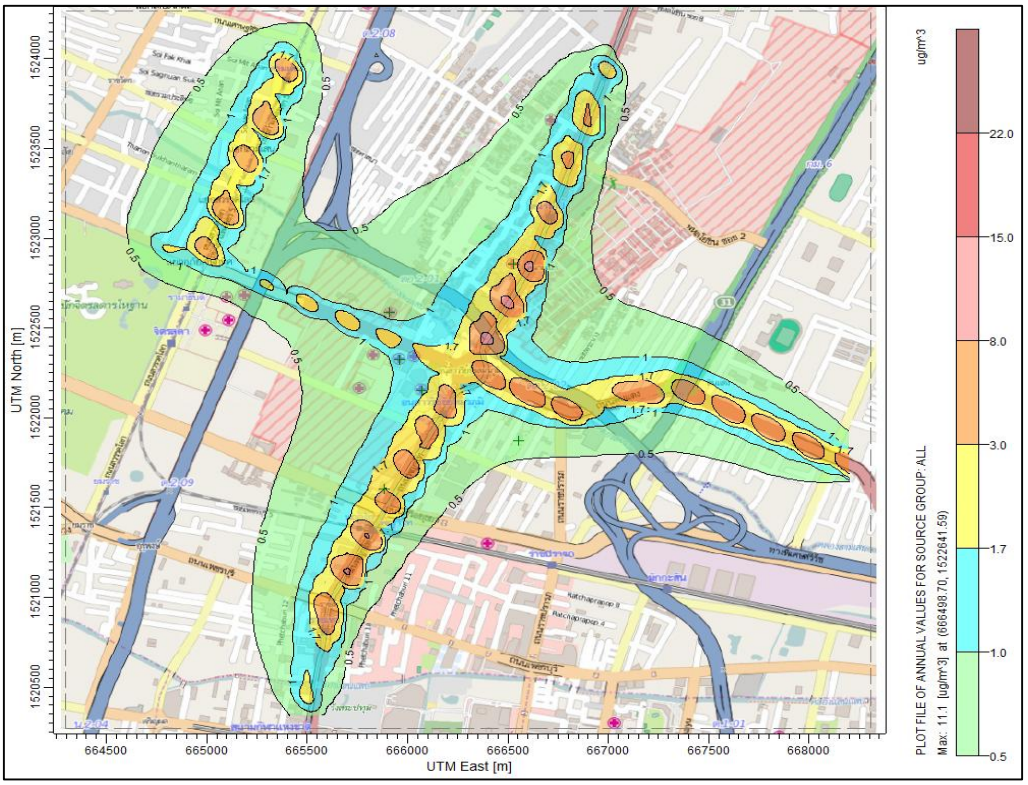

Fig. 3 Spatial distribution of benzene pollution map (EURO II scenario)

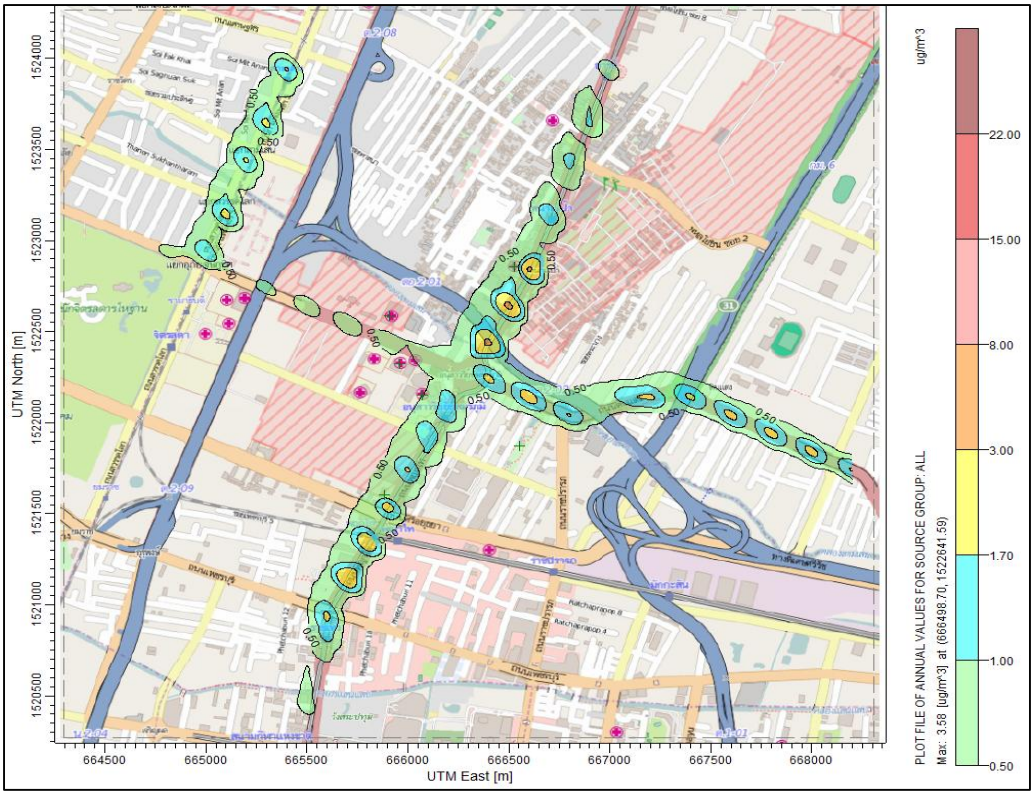

Fig. 4 Spatial distribution of benzene pollution map (EURO IV scenario)

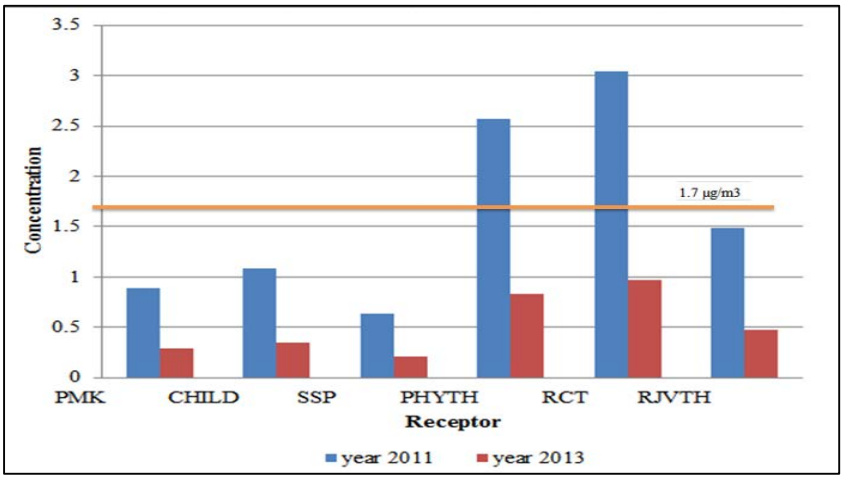

Fig. 5 Comparison of predicted annual concentrations of benzene (µg/m^3)

CONCLUSIONS

The Thai's policy in improving of fuel quality was evaluated to elaborate for its success in reducing emissions and concentrations of benzene in Bangkok's air. Benzene content in gasoline had been decreased from 3.5% (EURO II standard) to less than 1.0% (EURO IV standard) since the year 2012. The IVE model was applied to develop emission factor of benzene using actual fleet and fuel characteristics of vehicles in Bangkok. These vehicles consisted of passenger car, motorcycle, van and pick up, taxi, bus and truck. Then, emission inventory of benzene emitted from mobile sources was calculated. It was found that about 83% of total emissions of benzene were contributed from motorcycle (43%) and passenger car (40%). Emission amounts were reduced from 1.32 x 10^3 ton/year in the EURO II scenario to about 0.57 x 10^3 ton/year in the EURO IV scenario. Annual ground level concentrations of benzene emitted from mobile sources were predicted using AERMOD dispersion model. A traffic-congested zone of the central business district in the Bangkok metropolitan area was selected for this evaluation. AERMOD model was simulated to predict ambient ground level concentration of benzene prior and after implementing the EURO IV policy. Results revealed significantly reduction of benzene concentrations in Bangkok's environment. This study indicated the success and effectiveness of implementing fuel quality improvement policy in managing benzene pollution in Bangkok metropolitan area.

ACKNOWLEDGEMENTS

The authors greatly appreciate the support with data from the Department of Land Transport and the Department Traffic and Transportation, Bangkok Metropolitan Administration, Thailand. This study was partially supported for publication by the China Medical Board (CMB) and Center of Excellence on Environmental Health and Toxicology (EHT), Faculty of Public Health, Mahidol University, Thailand.

REFERENCES

[1] Department of Land Transport. Transport statistics sub-division, Planning division: Transport statistics.2013. http://apps.dlt.go.th/statistics_web/statistics.html. Accessed January 3, 2015.

[2] International Agency for Research on Cancer. Agents classified by the IARC Monographs, Volumes 1-112. 2012. Retrieved January 26, 2015,from http://monographs.iarc.fr/ENG/Classification/List_of_Classifications_Vol1-112.pdf.

[3] Truc, V. T. Q., and Oanh, N. T. K., "Roadside BTEX and other gaseous air pollutants in relation to emission sources", J. of Atmospheric Environment, Vol. 41, Nov. 2007, pp.7685-7697.

[4] Ongwandee, M. and Chavalparit, O., "Commuter exposure to BTEX in public transportation modes in Bangkok, Thailand", J. of Environmental Sciences, Vol. 22, Mar. 2010, pp. 397-404.

[5] Thepanondh S., "Development of emission factors for air pollutants and greenhouse gases from vehicle for establishment of appropriate mitigation policy and measures in the transportation sector in Thailand", 2009, pp. 4(1)-6(27).

[6] Outapa P. and Thepanondh S., "Development of Air Toxic Emission Factor and Inventory of On-road Mobile Sources", J. of Air, Soil and Water Research, Vol. 7, December. 2014, pp. 1-10.

[7] Department of Traffic and Transportation, Bangkok Metropolitan Administration, Thailand. Traffic density at road junctions in Bangkok. 2013.

[8] The Environmental Impact Assessment (EIA) report; MRTA-PURPLE line Bang Sue-Samsen section project, (2013). http://dzygroup.com/demo/eia/projectdetail.php?id=6962. Accessed April 20, 2015.

[9] U.S. Environmental Protection Agency (USEPA), 2004. AERMOD: DESCRIPTION OF MODEL FORMULATION (EPA-454/R-03-004), Office of Air Quality Planning and Standards Emissions Monitoring and Analysis Division Research Triangle Park, North Carolina.

[10] Pollution Control Department. Report on situation and management of air pollution and noise problems year 2013. Pollution Prevention Department, Ministry of Natural Resources and Environment, Bangkok, Thailand.

[11] Saeaw N. and Thepanondh S., "Source apportionment analysis of airborne VOCs using positive matrix factorization in industrial and urban areas in Thailand", J. of Atmospheric Pollution Research, Vol. 6, Jan. 2015.

First International Conference on Science, Engineering & Environment,
Tsu City, Mie, Japan, Nov.19-21, 2015, ISBN: 978-4-9905958-5-2 C3051

WINTER URBAN HEAT ISLAND MAGNITUDES OF MAJOR AUSTRALIAN CITIES

Melissa Neave[1], Scott Rayburg[2],
[1]Centre for Urban Research, RMIT University, [2]Swinburne University of Technology

ABSTRACT

The Urban Heat Island (UHI) effect is a common phenomenon observed in cities around the world. This phenomenon can best be described as an increase in the temperature of urban areas relative to their surroundings. This effect ranges from 1 or 2ºC up to 11ºC or more depending on a variety of factors. This study seeks to determine the relative magnitude of the UHI effect in five major Australian cities during the winter season. To achieve this, the study considers three weather stations in each city: one in a high density urban area, one in a medium density urban area and one in a nearby very low density urban/rural area. In all cases, the elevation was kept approximately constant (within 100 m) to ensure that observed temperature differences could be largely attributed to urban heat variations alone. For each station, temperature data were collected every 30 minutes over a three day period. The data where then plotted and maximum, minimum, and average temperature differences (and the times of those differences) were recorded. The data show that all of the cities investigated showed a strong winter heat island effect with the magnitude ranging from about 3ºC up to 8ºC. The largest temperature differences typically occurred near dawn (about 6 am) and overnight. It was also observed that during the day, the high and moderate density urban areas could have temperatures either higher or lower than the rural areas, a condition consistent with other global observations of the UHI effect.

Keywords: UHI; climate change; weather stations; daily temperature

INTRODUCTION

Globally, cities and urban populations are growing rapidly. As cities expand and develop, they become increasingly warm relative to surrounding areas. This phenomenon is known as the "urban heat island" (UHI) effect [1]-[2]. This temperature difference can lead to significant complications in urban areas including an increase in the magnitude and frequency of heat waves, an increase in urban pollution and energy use, and heat related illnesses and fatalities. These problems are likely to be exacerbated by global warming, which is likely to see Earth warm by an additional 2ºC or more by the end of this century [3].

The causes of this temperature difference between urban areas and adjacent and/or surrounding non-urban areas are multifaceted. These include: a high percentage of low albedo and impermeable surfaces (such as roads, footpaths and buildings); a loss of vegetation (which would normally help to cool the area via shading and evapotranspiration); the geometry of the urban landscape which creates a canyon effect that traps heat and prevents it from escaping; and higher mean pollution levels (than surrounding areas) which can also promote warming and/or trap heat [4]-[7].

As previously mentioned, UHIs can cause numerous problems in cities. These include both social and environmental impacts. In terms of social impacts, perhaps the most significant is a rise in heat related illnesses. Indeed many illnesses have been shown to be related to heat ranging from the relatively benign (e.g., heat rash) to the potentially fatal (e.g., heat stroke). These heat related illnesses are most dangerous for the young and old and those with compromised immune systems. In addition, those without access to cooling are also particularly susceptible, which can make this an environmental justice issue [8]-[9]. The environmental impacts of UHIs can also be significant and include an increase in energy demand in cities (predominantly as a result of increased demand for cooling energy), an increase in pollution (associated with the rise in energy use), and heightened chemical weathering rates [10].

The magnitude of UHIs vary from place to place and according to a variety of climatic and other factors. Observed UHIs magnitudes from around the world range from 0.4°C to as high as 14°C [11]-[12]. These values are strongly influenced by the degree of urbanization, the amount of greenspace, seasonality, time of day and other factors (so that, for example, the highest observed UHI values may have only occurred for a brief period of time on a single day during a particular season). According to current research, the highest UHI magnitudes occur overnight and during summer when conditions are clear and winds are low [13]-[18]. A limitation of most of the studies on the UHI phenomenon is a focus on only one city at a time. In addition, most

studies focus on collecting data in summer alone. This limits our ability to compare the relative strength of the UHI phenomenon during winter and between cities.

To address these problems, this study considers the magnitude of the UHI in five Australian cities over a three day period in the winter of 2015. Data are considered in terms of urban density, city size, and geographic position within Australia. The results of this study will help to clarify the magnitude of UHIs in winter and what might be driving observed patterns in UHI intensity.

SITE DESCRIPTION AND METHODS

This study was undertaken in Australia's five largest cities, namely Adelaide, Brisbane, Melbourne, Perth and Sydney (Fig. 1). These cities were chosen because of their large populations and high urban densities. As of June 2014, the population, from largest to smallest of these cities was: Sydney with 4.8 million (density = 9,295 per km^2); Melbourne with 4.4 million (density = 14,105 per km^2); Brisbane with 2.3 million (density = 7,188 per km^2); Perth with 2.0 million (density = 3,112 per km^2) and Adelaide with 1.3 million (density = 1,814 per km^2).

Fig. 1 The locations of the five largest Australian cities that were sampled in this study.

In terms of average climate, Adelaide and Perth are classified as having hot dry summer or Mediterranean climates (Koppen classification of Csa), Melbourne is classified as having a temperate oceanic climate (Koppen classification of Cfb), and Brisbane and Sydney are classified as having warm temperate/humid subtropical climates (Koppen classification of Cfa).

The average annual rainfall for Adelaide is 545 mm and the average maximum and minimum temperatures are 22.3 ºC and 12.2 ºC, respectively. The average annual rainfall for Perth is 850 mm and the average maximum and minimum temperatures are 24.6 ºC and 18.7 ºC, respectively. The average annual rainfall for Melbourne is 650 mm and the average maximum and minimum temperatures are 19.9 ºC and 10.2 ºC, respectively. The average annual rainfall for Brisbane is 900 mm and the average maximum and minimum temperatures are 26.5 ºC and 16.3 ºC, respectively. The average annual rainfall for Sydney is 1200 mm and the average maximum and minimum temperatures are 21.7 ºC and 13.8 ºC, respectively.

In each city, three Bureau of Meteorology weather stations were selected. These included one in a high density part of the city (population density greater than 2,000 persons per km^2), one in a medium density part of the city (population density approximately 500 persons per km^2), and one in a low density part of the city or its surroundings (population density less than 50 persons per km^2) (Table 1). Stations were also selected to minimise elevation differences between them (as elevation can have a strong control on temperature independent of urbanization influences). Consequently, stations from all cities had elevation differences of less than 40 m except Melbourne where the maximum elevation difference was 100 m (Table 1). From these stations, temperature data were collected every 30 minutes over a period of three days in early August 2015.

Table 1. Weather station characteristics for the 15 locations included in this study.

Stations	Density	Elevation (m)	Lat.	Long.
Adelaide				
Noarlunga	High	55.0	-35.16	138.51
Adelaide	Medium	48.0	-34.92	138.62
Edinburgh	Low	16.5	-34.71	138.62
Brisbane				
Brisbane	High	8.1	-27.48	153.04
Archerfield	Medium	12.5	-27.57	153.01
Amberley	Low	24.2	-27.63	152.71
Melbourne				
Melbourne Olympic Park	High	7.5	-37.83	144.98
Viewbank	Medium	66.1	-37.74	145.10
Melbourne Airport	Low	113.4	-37.67	144.83
Perth				
Perth	High	24.9	-31.92	115.87
Pearce	Medium	40.0	-31.67	116.02
Jandakot	Low	30.0	-32.1	115.88
Sydney				
Observatory Hill	High	39.0	-33.86	151.21
Bankstown	Medium	6.5	-33.92	150.99
Richmond	Low	19.0	-33.6	150.78

For each city, temperature data were plotted on a single graph to compare temporal differences between stations. Then temperatures were compared across stations by subtracting the temperature from each station from that of the other two stations in the same city. This allowed for computations of average, maximum and minimum temperature differences (and the time that the maximum and minimum temperature difference occurred) between stations. Note: for the purposes of this study, night was classed as the hours between 6:00 pm and 6:00 am.

RESULTS AND DISCUSSION

Temperature data for each city and summary differences between stations are presented in Figs. 2-6 and Table 2. For Adelaide (Fig. 2), the temperatures for all three stations are very similar during the day while at night some separation becomes apparent. Generally speaking, the low urban density weather station shows the coolest nighttime temperatures, although at times it has temperatures similar to the medium urban density station. According to Table 2 the highest daytime temperature differences occur between the high and low urban density sites and equate to 3.7ºC and 4.3ºC for daytime and nighttime temperatures, respectively. The maximum temperature difference was observed at 9:00 pm.

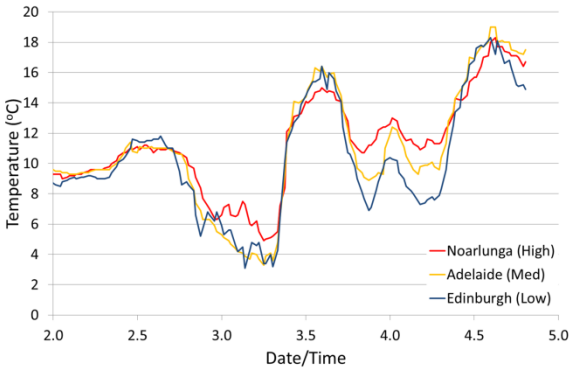

Fig. 2 Temperature comparison for three weather stations in Adelaide in the winter of 2015.

For Brisbane (Fig. 3) the separation between stations was much more pronounced. Here daytime temperatures remain similar but nighttime temperatures display a clear trend with the highest urban density site being the warmest and the low urban density site the coolest. The maximum daytime and nighttime temperature differences were both 9.1ºC which were recorded at 6:30 am and 18:30 pm, respectively (Table 2).

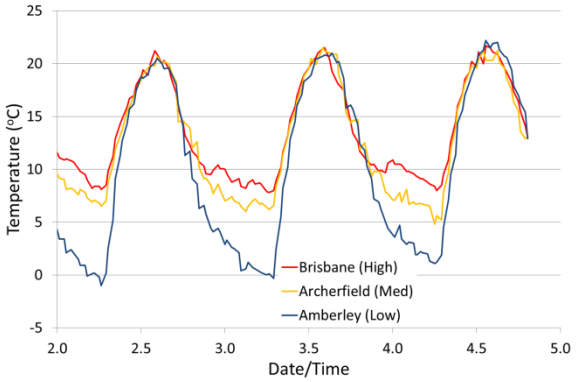

Fig. 3 Temperature comparison for three weather stations in Brisbane in the winter of 2015.

Melbourne temperature patterns are presented in Fig. 4. In Melbourne, the medium urban density and low urban density sites typically plot very close to one another and only clearly separate over one nighttime period (with the low density site showing cooler temperatures for this particular instance). Meanwhile, the high urban density site tends to plot higher that the other two sites, indicating it is warmer overnight but with similar daytime temperatures to the other two. The maximum daytime and nighttime temperature differences were 3.0ºC and 2.7ºC, respectively, with these occurring at 6:30 am and 1:30 am, respectively (Table 2).

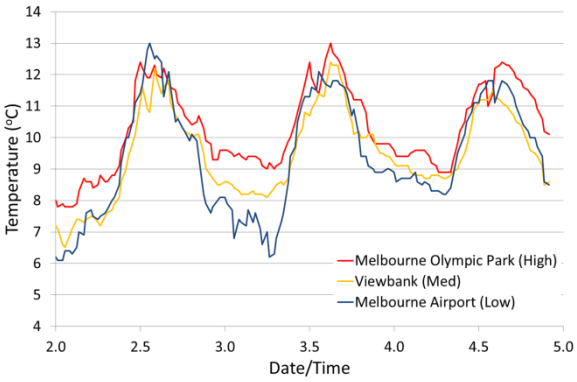

Fig. 4 Temperature comparison for three weather stations in Melbourne in the winter of 2015.

In Perth (Fig. 5) there is little separation between the three stations during the day or overnight. However, some minor nighttime temperature variations are apparent on one of the study nights. The maximum daytime and nighttime temperature differences are 3.7ºC and 3.6ºC, respectively (Table 2) and these occur at 7:00 am and 3:00 am, respectively.

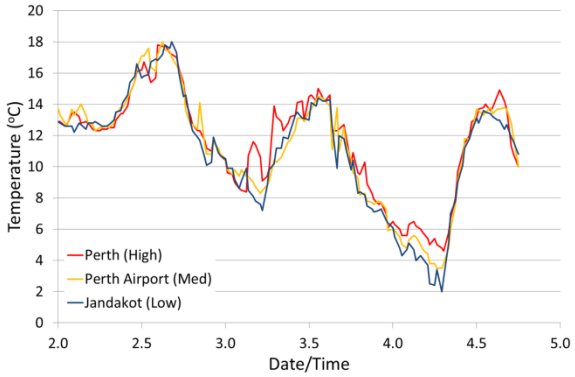

Fig. 5 Temperature comparison for three weather stations in Perth in the winter of 2015.

The final city investigated was Sydney and these data are presented in Fig. 6. Here very clear differences between stations can be observed, with the highest urban density site being warmest at night and the lowest urban density site being coolest at night. The medium urban density site plots in the middle of the other two. During the day, temperatures are generally similar for all sites, although there is some tendency for the high urban density site to be cooler than the other two sites during the hottest part of the day. According to Table 2, the maximum daytime temperature difference is 7.5°C and this occurs at 11:30 am while the maximum nighttime temperature difference is 8.0°C which occurs at 6:00 am.

The results of this study clearly show that there is an obvious and apparent winter UHI effect evident in all five major Australian cities. The UHI magnitude varied from a high of 9.1°C in Brisbane to a low of 2.6°C in Melbourne. In terms of the magnitude alone, Sydney and Brisbane displayed very similar patterns, exhibiting obvious differences between sites and high absolute temperature differences between sites. In contrast, Adelaide, Perth and Melbourne were similar to one another, exhibiting more similar temperatures throughout the day and comparatively minor absolute temperature differences.

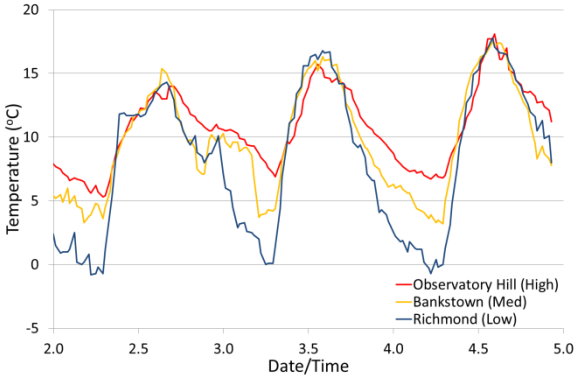

Fig. 6 Temperature comparison for three weather stations in Sydney in the winter of 2015.

For the five cities that were studied in this research the maximum temperature differences tended to occur either overnight or in the very early morning (around 6:00 am being the most common time). In most cases, the maximum daytime and nighttime temperature differences were similar to each other but occurred at similar times (again being very close to the segregation time between day and night as adopted in this study which was 6:00 am). Perhaps, then, it is more useful to say that the maximum temperature differences for all cities occurred during the coolest parts of the day while temperatures were mostly similar during the hottest parts of the day.

Table 2. Summary statistics for the comparisons between the high, medium and low urban density weather stations for each of the five largest cities in Australia.

	Day			Night		
Adelaide	**Avg**	**Max**	**Min**	**Avg**	**Max**	**Min**
High - Med	-0.25	1.70	-1.60	0.94	3.40	-0.80
High - Low	0.19	3.70	-1.90	1.69	4.30	-0.50
Med - Low	0.44	2.20	-0.90	0.75	2.60	-1.30
Brisbane						
High - Med	0.51	3.60	-2.60	1.55	3.80	-2.10
High - Low	1.84	9.10	-2.20	5.10	9.10	-2.30
Med - Low	1.33	7.50	-2.00	3.55	7.40	-2.70
Melbourne						
High - Med	0.76	1.70	-0.20	0.86	1.80	-0.20
High - Low	0.57	3.00	-1.10	1.33	2.60	0.30
Med - Low	-0.19	2.10	-2.20	0.46	1.60	-0.80
Perth						
High - Med	0.33	3.50	-1.70	0.28	2.70	-1.80
High - Low	0.43	3.70	-1.30	0.71	3.60	-1.50
Med - Low	0.10	3.90	-1.50	0.43	2.40	-1.00
Sydney						
High - Med	-0.01	3.60	-2.80	2.27	5.00	0.20
High - Low	0.74	7.50	-2.70	4.65	8.00	0.20
Med - Low	0.75	4.90	-2.70	2.38	6.70	-2.20

CONCLUSION

This study investigated 30-min temperature data for five Australian cities over a three day period in winter. Within each city three sites, representing high-, medium- and low-urban densities, were examined. All five cities exhibit evidence of the urban heat island phenomenon, with the high-density regions routinely recording the highest temperatures. This result was most pronounced for the more northerly cities of Brisbane and Sydney, but was also evident in the more southerly cities of Adelaide, Melbourne and Perth.

In all five cities, the maximum differences between high- and low-urban density settings were observed to occur in the coldest part of the day

(overnight or early morning). In comparison, during the warmest time of the day, temperatures between sites tended to converge. These findings indicate that the urban heat island phenomenon is evident even during winter months but that the impacts reflect lower rates of overnight cooling. This suggests that the urban fabric is retaining heat more effectively than non-urban landscapes and may help to explain why summer temperatures in urban settings are often comparatively high. It is not just a matter of increased rates of energy capture during the daylight hours, but also retention of that energy overnight.

ACKNOWLEDGEMENTS

The authors gratefully acknowledge the Australian Bureau of Meteorology for providing data for this project.

REFERENCES

[1] Meehl, GA & Tebaldi, C 2004, “More intense, more frequent, and longer lasting heat waves in the 21st century”, Science, Vol. 305, no. 5686, pp. 994-997.

[2] Kinney, PL, O'Neill, MS, Bell, ML & Schwartz, J 2008, “Approaches for estimating effects of climate change on heat-related deaths: challenges and opportunities”, Environmental Science and Policy, Vol. 11, no. 1, pp. 87-96.

[3] Chen, X-L, Zhao, H-M, Li, P-X & Yin, Z-Y 2006, “Remote sensing image-based analysis of the relationship between urban heat island and land use/cover changes”, Remote sensing of environment, Vol. 104, no. 2, pp. 133-146.

[4] Kim, Y-H & Baik, J-J 2005, “Spatial and temporal structure of the urban heat island in Seoul”, Journal of Applied Meteorology, Vol. 44, no. 5, pp. 591-605.

[5] Kleerekoper, L, van Esch, M & Salcedo, TB 2012, “How to make a city climate-proof, addressing the urban heat island effect”, Resources, Conservation and Recycling, Vol. 64, pp. 30-38.

[6] Qiu, G-y, Li, H-y, Zhang, Q-t, Chen, W, Liang, X-j & LI, X-z 2013, “Effects of Evapotranspiration on Mitigation of Urban Temperature by Vegetation and Urban Agriculture”, Journal of Integrative Agriculture, Vol. 12, no. 8, pp. 1307-1315.

[7] Rosenfeld, AH, Akbari, H, Bretz, S, Fishman, BL, Kurn, DM, Sailor, D & Taha, H 1995, “Mitigation of urban heat islands: materials, utility programs, updates”, Energy and Buildings, Vol. 22, no. 3, pp. 255-265.

[8] Bai, L, Ding, G, Gu, S, Bi, P, Su, B, Qin, D, Xu, G & Liu, Q 2014, “The effects of summer temperature and heat waves on heat-related illness in a coastal city of China, 2011-2013”, Environmental Research, Vol. 132, pp. 212-219.

[9] Williams, S, Nitschke, M, Sullivan, T, Tucker, GR, Weinstein, P, Pisaniello, DL, Parton, KA & Bi, P 2012, “Heat and health in Adelaide, South Australia: Assessment of heat thresholds and temperature relationships”, Science of the Total Environment, Vol. 414, pp. 126-133.

[10] Tumanov, S, Stan-Sion, A, Lupu, A, Soci, C & Oprea, C 1999, “Influences of the city of Bucharest on weather and climate parameters”, Atmospheric Environment, Vol. 33, no. 24, pp. 4173-4183.

[11] Lokoshchenko, MA 2014, “Urban 'heat island' in Moscow”, Urban Climate, Vol. 10, no. P3, pp. 550-562.

[12] Santamouris, M 2015, “Analyzing the heat island magnitude and characteristics in one hundred Asian and Australian cities and regions”, Science of the Total Environment, Vol. 512-513, pp. 582-598.

[13] Figuerola, PI & Mazzeo, NA 1998, “Urban-rural temperature differences in Buenos Aires”, International Journal of Climatology, Vol. 18, no. 15, pp. 1709-1723.

[14] Magee, N, Curtis, J & Wendler, G 1999, “The urban heat island effect at Fairbanks, Alaska”, Theoretical and Applied Climatology, Vol. 64, no. 1-2, pp. 39-47.

[15] Morris, C & Simmonds, I 2000, “Associations between varying magnitudes of the urban heat island and the synoptic climatology in Melbourne, Australia”, International Journal of Climatology, Vol. 20, no. 15, pp. 1931-1954.

[16] Unger, J, Sümeghy, Z & Zoboki, J 2001, “Temperature cross-section features in an urban area”, Atmospheric Research, Vol. 58, no. 2, pp. 117-127.

[17] Pal, S, Xueref-Remy, I, Ammoura, L, Chazette, P, Gibert, F, Royer, P, Dieudonné, E, Dupont, JC, Haeffelin, M, Lac, C, Lopez, M, Morille, Y & Ravetta, F 2012, “Spatio-temporal variability of the atmospheric boundary layer depth over the Paris agglomeration: An assessment of the impact of the urban heat island intensity”, Atmospheric Environment, Vol. 63, pp. 261-275.

[18] Vardoulakis, E, Karamanis, D, Fotiadi, A & Mihalakakou, G 2013, “The urban heat island effect in a small Mediterranean city of high summer temperatures and cooling energy demands”, Solar Energy, Vol. 94, pp. 128-144.

First International Conference on Science, Engineering & Environment,
Tsu City, Mie, Japan, Nov.19-21, 2015, ISBN: 978-4-9905958-5-2 C3051

MULTIVARIATE GEOSTATISTICAL MODELING OF THE SOIL SPECTROMETRY AND CHEMISTRY FOR CHARACTERIZING THE SOIL SALINIZATION IN EAST DAKHLA OASIS, EGYPT

Alaa A. Masoud [a], Mohamed M. El-Horiny [a,b], Mohamed G. Atwia[a], Katsuaki Koike [b]
[a] Geology Department, Faculty of Science, Tanta University, 31527 Tanta, Egypt
[b] Department of Urban Management, Graduate School of Engineering, Kyoto University, Japan

ABSTRACT

Periodic monitoring of soil salinity levels is necessary for preventing and mitigating land degradation in arid environments. Twenty-five topsoil samples (0–20 cm) were collected in the study area. Soils were highly salt-affected that ranged from 0.523 to 53.9 dSm^{-1} The soil pH ranged between 4.2 and 8.91, with an average of 7.718, suggesting slightly alkaline soils. Soil reflectance curves show two deep absorption features at 1415 nm and 1915 nm. As the salinity levels increase, the absorption features become deeper, broader, and more asymmetrical. This suggests an increase in the soil moisture content with increasing salinization. This relationship is confirmed from the parameters (depth and width) of the absorption band centered at 1415 and 1915 nm and the soil EC. The best coefficient of determination of the soil salinity can be achieved for depth (R^2 = 0.57 & 0.52) and for width (R^2 = 0.70 & 0.56) at 1415 and 1915 wavelengths. Multivariate statistical techniques showed that two main factors accounted for 75.57% of the data variance governed the variability of the soils. The first and second factors accounted for 54.94% and 13.36% of the total variance respectively. Cluster analysis recognized three distinctive soil salinity patterns; their spatial distribution is consistent with the geology, and the urban and agricultural practices. The first class (14 observations) exhibited non saline soils (<2 dS m^{-1}) to slightly saline (2–4 dS m^{-1}) that dominated in the northern zone. The southern zone included the second (6 observations) and third (13 observations) classes which exhibited saline to highly saline soils (> 4 dS m^{-1}). The southern zone is dominated by intensive evaporation/evapotranspiration, unmanaged sewage trenching, extensive land use changes and hence prevailing salinization processes.

Keywords*: Soil Spectrometry, Salinization, Factor analysis, K-means Clustering; Dakhla Oasis, Egypt*

INTRODUCTION

Soil degradation by salinization in Egypt's vast deserts is one of the problems that has recently received attention for research [11]. Drought, which is a natural phenomenon, is a significant driving force for soil degradation in the Western Desert of Egypt as precipitation is much less than evapotranspiration rates.

Salinization has a very bad effect on soil conditions and made many productive areas infertile in arid and semi-arid regions, posing serious socio-economic and environmental implications. In these regions, evapotranspiration commonly exceeds the precipitation that is already insufficient to maintain a regular percolation of the rainwater through the soil. This is in addition to the irrigation with salt-laden water of soils with low permeability that mostly leads to a slow but progressive and excessive accumulation of salts [6]. This accumulation brings drastic changes in soil physical and chemical properties [12] and affects directly the soil salinity and pH levels and hence adversely influences the plant productivity. Some areas of Dakhla Oasis contain enough salts so that they can significantly alter the physical and chemical soil properties and could even make growing the crops rather difficult. This research focuses on the use of the multivariate statistics; factor analysis and K-means clustering, and the geostatistical semi-variogram modeling of soil chemistry data to identify the most influential factors controlling soil salinization, with a special emphasis on the relationships among soil properties and major and trace element concentrations in the eastern part of Dakhla Oasis, Egypt.

DATA AND METHODS

Study Area

The study area is located in the central part of the Western Desert of Egypt (Fig.1). It lies between latitudes 25◦ 24' &25◦ 36' N and longitudes 29◦ 10' & 29◦ 23' E, 190 km to the West of Kharga Oasis. It contains highly fertile lands, it is rich with water and it supports a higher population than Kharga Oasis. The present work focused on the east of Dakhla (Teneida and Balat villages).

The climate of Dakhla Oasis is hot and dry, with a high rate of evaporation, a high level of solar radiation (sunshine), and no rainfall. The aridity index used by the United Nations Environment

Program [14], indicates that this district lies in a hyper-arid region, with an annual rainfall close to 0.0 mm.

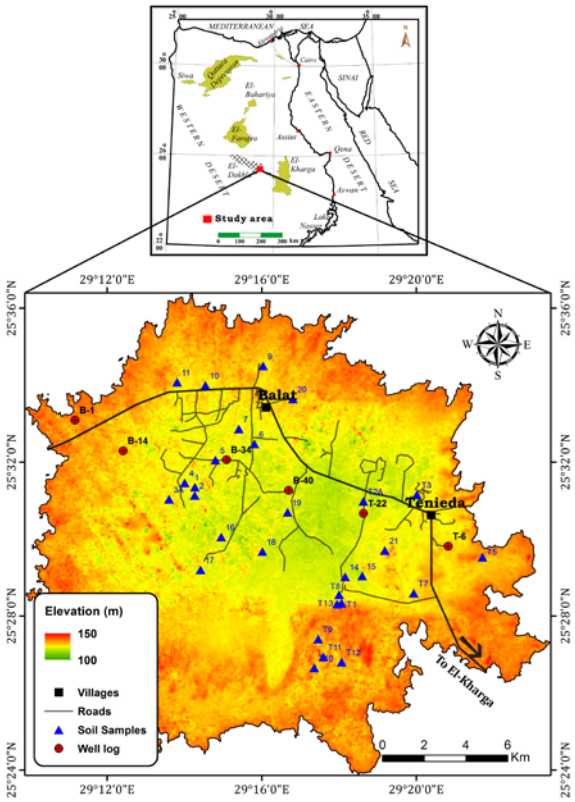

Fig. 1. Map showing the location of study area, topography, and soil samples.

Geomorphologically, the investigated area exhibited three main geomorphologic units [7]. These units are the high plateau, the depression and the structural plain. The high plateau bounds the Dakhla depression from the north, and includes the plateau surface and the escarpments subunits. The depression represents controlled structurally and erosionally low topographic area. The structural plain results from the merging of the Dakhla depression gradually to the south into an extensive elevated plain.

Geologically, the exposed sedimentary rocks ranging in age from Late Cretaceous to Quaternary [4]. The Upper Jurassic–Campanian sequence is represented by sandstone and clay, known by the Nubia Sandstone [13].The Nubia Sandstone overlies directly the basement rocks. It is subdivided into different rock units which can be described from older to younger as following; Six Hills Formation, Abu Ballas Formation; Sabaya Formation; Maghrabi Formation and Taref Formation. The Campanian Transgression include from the base Mut formation, it is composed of variegated shale, siltstone and claystone. Quaternary deposits are of continental origin and varying from fresh deposits to eolian sediments. These deposits include sand dune, alluvial, playa and inland sabkha deposits [5].

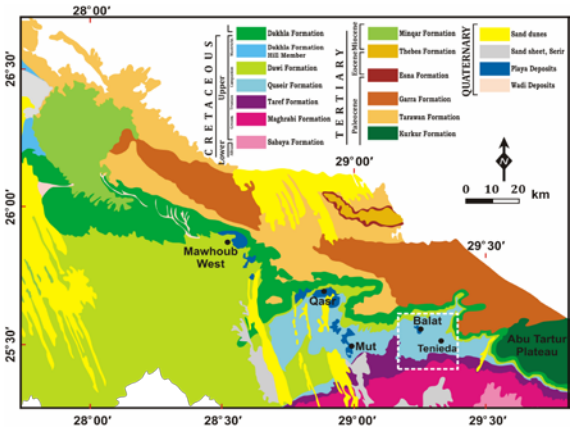

Fig. 2. Geological map of Dakhla oasis [4].

Hydrogeologically, the Nubian Sandstone Aquifer System is composed of different water bearing strata laterally and/or vertically interconnected. Dakhla Basin is the largest and most important basin in Egypt. It consists of three water bearing formations with confining layers in-between. These aquifers, from top to bottom, are Taref, Sabaya and Six Hills Sandstone aquifers. (Fig. 3).

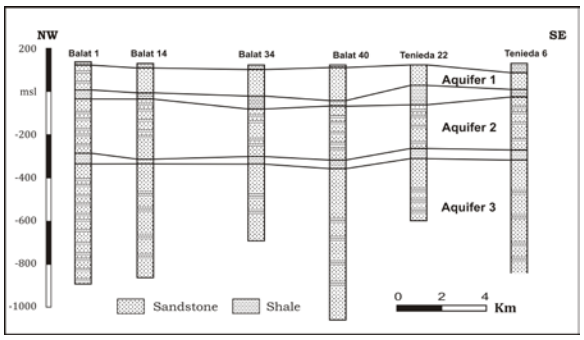

Fig. 3. Simplified cross sections of selected locations in the east of the Dakhla oasis based on the well logs. Location of boreholes are shown on figure 1.

Sampling and Chemical Analytical Techniques

Thirty three soil samples were collected during a field campaign carried out February 2014. At each sampling site, a composite surface sample was formed by mixing five sub-samples taken at 30-m square corners and the mid-point of the square from the top soil (0–20 cm) and was analyzed. The electrical conductivity (EC) was measured for the soil saturated paste extracts (1:2 by weight) using. Direct Soil Conductivity meter model HI 98331. Soil pH was measured in a 1:2 soil/distilled water

suspension using a pre-calibrated glass electrode of HORIBA D-53 pH meter at a resolution of 0.01. Some major and trace elements concentrations (wt %) were measured by using the XRF.

Soil Spectrometry

Soil samples were scanned and absolute reflectances were recorded in the region 400–2500 nm at 0.1 nm spectral resolution, using FieldSpec-3 spectroradiometer (Analytical Spectral Devices, Boulder, Colorado USA) at room temperature. Reflectance is calibrated against a white panel of known reflectance. All spectral measurements were carried out in a dark room to avoid contamination by stray light. For better inter-comparison and spectral identification the raw spectra were subjected to continuum-removal.

Factor Analysis

Factor analysis (FA) using principal component was applied to the datasets. Successful multivariate statistical analyses rely greatly on the optimal selection of variables, particularly their independence and comparable relevance [6]. The selection of variables in the present study was primarily directed towards achieving a compromise between including a sufficient number of variables to ensure an accurate representation of soil quality whilst selecting a representative subset of variables that is large enough to capture the spatial variability of soil chemistry and the processes that control it. Twenty two variables (EC, pH, Cl, Ca, K, Zn, Zr, Ag, Cd, Sn, Sb, Ti, Mn, Fe, Al, Si, P, S, V, Cr, Ni and Pb) were selected for FA.

K-means Cluster Analysis

K-means clustering is applied to the soil chemitry datasets (Table 1). Cluster analysis helps in grouping objects (cases) into classes (clusters) on the basis of similarities within a class and dissimilarities between different classes. It is an iterative process whereby the data are initially partitioned randomly, and iteratively reassigned to a cluster based on the nearest distance to the cluster's centre. The procedure terminates when there is no reassignment of any data from one cluster to another [16]. Setting the optimal number of clusters is a challenging task in using a partition algorithm, like K-means [16].

Geostatistical Modeling

For the estimation of the spatial distribution of the soil electrical conductivity and some trace elements concentrations to soil quality, ordinary kriging (OK) and semi-variogram modeling was applied. Kriging is appraised for building the attribute data layers as it adequately model the low sampling density in an efficient way compared with the simpler methods as well as it provide a probabilistic estimate of the interpolation quality itself [2].

Table 1: Descriptive summary statistics for the soil chemistry data.

Variable	Min.	Max.	Mean	St. Dev.
EC	**0.523**	**53.900**	**15.202**	**14.876**
pH	**4.210**	**8.910**	**7.718**	**0.822**
Zn	**0.002**	**0.010**	**0.004**	**0.002**
Zr	**0.001**	**0.032**	**0.017**	**0.007**
Ag	**0.007**	**0.019**	**0.013**	**0.004**
Cd	**0.009**	**0.024**	**0.017**	**0.005**
Sn	**0.011**	**0.032**	**0.022**	**0.006**
Sb	**0.011**	**0.035**	**0.024**	**0.007**
Ti	**0.021**	**0.471**	**0.250**	**0.120**
Mn	**0.008**	**0.196**	**0.058**	**0.043**
Fe	**0.051**	**5.243**	**2.308**	**1.218**
Cl	**9.040**	**52.030**	**27.179**	**12.408**
Al	**0.160**	**5.440**	**2.427**	**1.607**
Si	**0.223**	**22.130**	**10.111**	**7.473**
P	**0.006**	**0.138**	**0.039**	**0.030**
S	**0.050**	**2.690**	**0.512**	**0.531**
K	**0.357**	**2.646**	**1.347**	**0.638**
Ca	**0.383**	**4.654**	**2.892**	**1.060**
V	**0.007**	**0.040**	**0.025**	**0.008**
Cr	**0.005**	**0.019**	**0.012**	**0.003**
Ni	**0.001**	**0.011**	**0.004**	**0.002**
Pb	**0.000**	**0.001**	**0.001**	**0.000**

RESULTS AND DISCUSSIONS

Soil Chemistry

Soil salinity across the depression ranges from 0.52 dS/m to 53.9 dS/m with an average of 15.2 dS/m indicating highly salt-affected soils. EC distribution map, showed a gradual southward salinization (Fig. 4). The majority of the collected soils have sandy texture; however, little samples have silty and clayey sandy texture. The samples that had the highest salinity levels had clay loam textures, indicating that salinity increases with increasing clay content, which may increase the crusting potential of the soils [10], decrease soil permeability, and lead to poor aeration of the soil. According to the classification of arid lands [15], hyper-arid regions have aridity index (P/ETP) of <0.03, where P is the precipitation and ETP is the evapotranspiration. Dakhla region has an aridity index of <0.001 [8], which is far less than the limit of hyper-arid regions (P/ETP < 0.03). The high groundwater table could be another reason triggering soil salinization [3]. Soil salinization is also attributed to human activities, notably the abuse of water resources. The irrigation practice in Dakhla is one important reason for human-induced (secondary) salinization. The lack of

a well-developed drainage system leads to recharging groundwater with agricultural drainage to the degree that the water table occurs at the surface (Fig. 5). Impacts of this severe salinization involve not only the destruction of soil physical structure but also impairing the soil ecosystem as well.

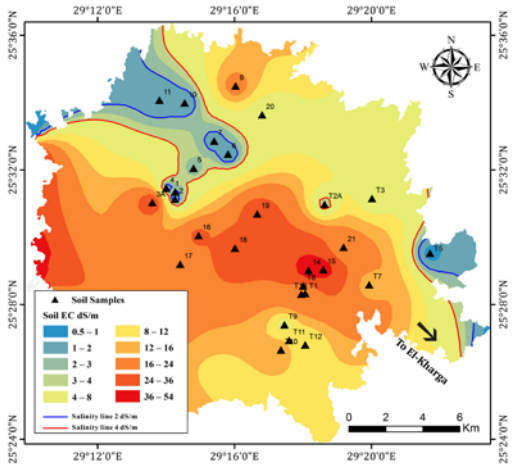

Fig. 4. The electric conductivity, (EC) of soil samples in Dakhla oasis.

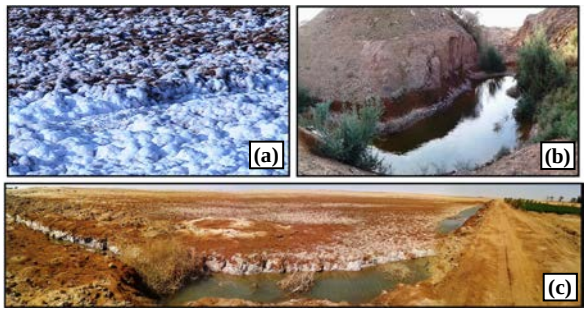

Fig. 5. Ground pictures of Dakhla depression; a) a salt crust at a barren soil area, b and c) drainage water seeps to low-land regions in the depression forming artificial canals and their margins affected by salinization.

Spectral Characteristics of Soils

The basic constituents that strongly affect soil reflectance characteristics are the clay content, Fe-Al oxides, organic matter, moisture, and the clay type [1]. Reflectance and the continuum-removed spectra of the studied soil samples are shown on Fig. 6. The absorptions of iron oxide are prominent at 425-500 nm and 850-900 nm. The absorption peaks were strongly associated with OH features of free water at 1415 and 1915 nm and clay lattice OH features at 1425 and 2200 nm. As the salinity levels increase the magnitude of the relative reflectances decreases (Fig. 6a). Also, the water absorption features become deeper, broader, and more asymmetrical. This suggests an increase in the soil moisture content [1], [9] with increasing salinization. This relationship is confirmed on Fig. 7 from the parameters (depth and width) of the absorption band centered at 1415 and 1915 nm and the soil EC. The depth versus width variation and hence the shape of the absorption feature can be best determined (R^2 = 0.76) at 1415 nm with varying salinity levels (Fig. 7). Also, the best coefficient of determination of the soil salinity can be achieved for depth (R^2 = 0.57) and for width (R^2 = 0.7) at this 1415 nm (Fig. 8). The results therefore confirm that the salt abundances of the studied slightly saline soils of the silty clay loam and sandy loam textures can be spectrally differentiated by the magnitude of the reflectance spectra and specifically by the shape of the OH absorption feature at 1915 nm.

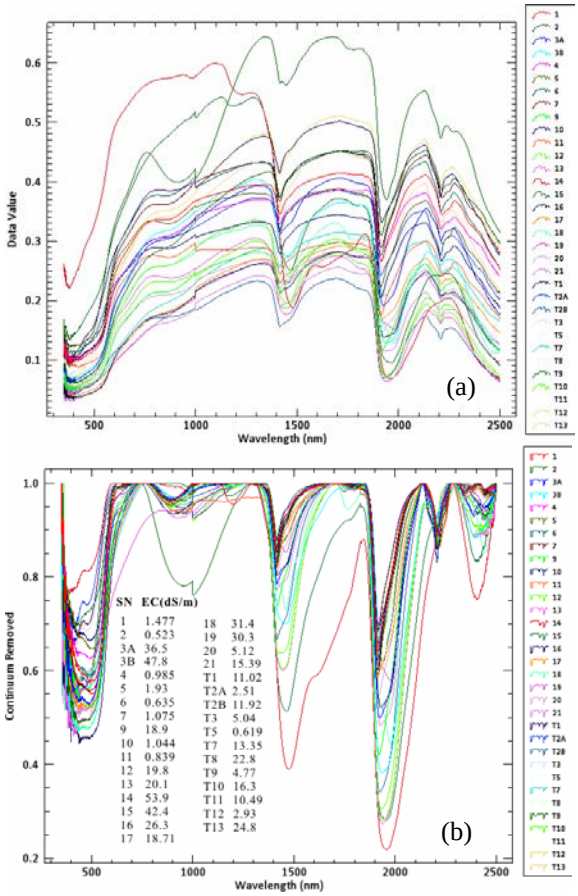

Fig. 6. Raw spectra of soil reflectance (up) and the continuum-removed (down) with their sample number (SN) and corresponding EC (dS/m).

Factor analysis

The results of the factor analysis using the principal components and varimax rotation are presented in Table 2. The first three factors with eigenvalues exceeding 1.6 were selected since they account for 75.57% of the total variance, which is sufficient to give a good idea of data structure. Variables attained the largest squared cosines of the

selected factors are chosen. Therefore, FA is assumed to adequately represent the overall variance of the dataset. F1 accounted for 54.94% of the variance strongly negatively loaded with EC (-0.88) and Cl (-0.59), and positively loaded with Sb (0.95), Sn (0.97), Cd (0.98), Ag (0.96), Si (0.93), Ti (0.87), Al (0.88), Zr (0.85), Fe (0.88), Mn (0.52), Ca (0.68), P (0.63), V (0.83), Cr (0.53), Ni (0.67) and Pb (0.47).

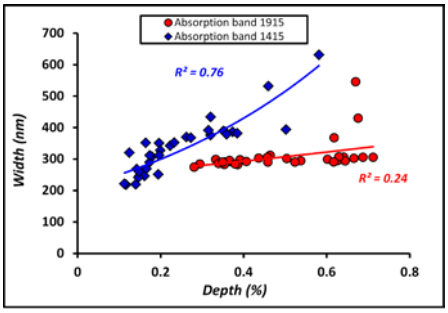

Fig. 7. Spectral depth versus width of the water absorption band centered at 1415 and 1915 nm.

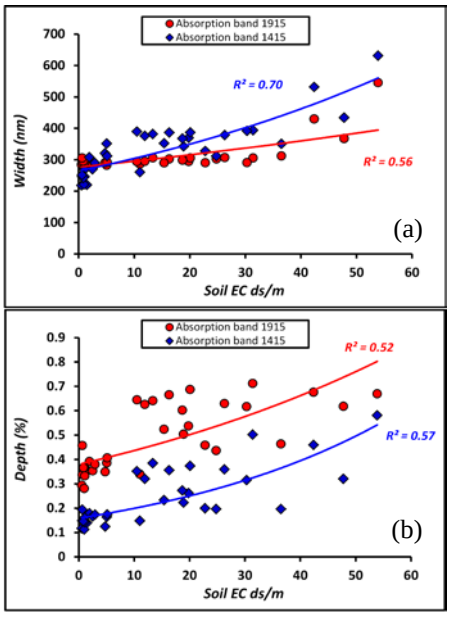

Fig. 8. Soil salinity versus a) width and b) depth of the water absorption band centered at 1415 and 1915 nm.

This clustering of variables associated with F1 signifies that contamination and salinization is the major process controlling the soil chemical variability and connotes salinity enhancement arising most likely from mineral dissolution. The second factor explained 13.36% of the total variance is found to be strongly negatively loaded with Zinc Zn (-0.61) and sulfur S (-0.77) and positively loaded with pH (0.77). Spatial distribution of the variables in the spaces defined by F1 and F2 confirms the grouping of factors affecting the variability (Fig. 9).

Table 2: Factor analysis of the studied soil chemistry parameters (observations = 33).

Variable	F1	F2	F3	communality
EC	-0.88	**-0.06**	**0.28**	**0.95**
pH	**-0.46**	0.77	**0.16**	**0.95**
Zn	**0.54**	-0.61	**0.19**	**0.91**
Zr	0.85	**-0.10**	**-0.28**	**0.92**
Ag	0.96	**0.13**	**0.05**	**0.99**
Cd	0.98	**0.11**	**0.01**	**0.99**
Sn	0.97	**0.16**	**0.02**	**0.99**
Sb	0.95	**0.16**	**0.02**	**0.99**
Ti	0.87	**0.36**	**-0.02**	**0.99**
Mn	0.52	**0.23**	**0.22**	**0.88**
Fe	0.88	**-0.20**	**0.11**	**0.99**
Cl	-0.59	**0.43**	**0.38**	**0.88**
Al	0.88	**0.24**	**0.18**	**0.98**
Si	0.93	**0.28**	**0.16**	**0.99**
P	0.63	**-0.43**	**0.36**	**0.95**
S	**-0.18**	-0.77	**0.43**	**0.95**
K	**0.22**	**0.54**	0.68	**0.96**
Ca	0.68	**0.08**	**-0.51**	**0.89**
V	0.83	**-0.08**	**-0.03**	**0.87**
Cr	0.53	**0.10**	**-0.07**	**0.78**
Ni	0.67	**-0.49**	**0.27**	**0.90**
Pb	0.47	**-0.02**	**0.04**	**0.79**
Eigenvalue	**12.09**	**2.94**	**1.60**	
Variability (%)	**54.94**	**13.36**	**7.28**	
Cumulative %	**54.94**	**68.30**	**75.57**	

NB:Values in bold correspond for each variable to the factor for which the squared cosine is the largest

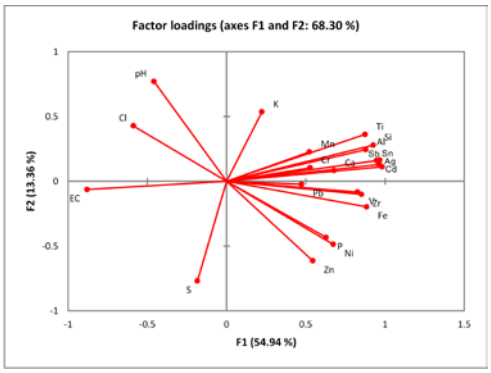

Fig. 9. Spatial distribution of variables in the space defined by F1 versus F2 of the factor loadings.

Cluster Analysis

The results of the Cluster analysis recognized three distinctive soil chemical patterns; their spatial distribution is consistent with the geology, and the urban and agricultural practices. The spatial distribution (Fig. 10) and the descriptive statistics (Table 3) of the three detected classes signify the spatial variability of the soil chemistry among the classes. The first class (14 observations) exhibited non saline soils (<2 dS m^{-1}) to slightly saline (2–4 dS m^{-1}) that dominated in the northern zone. The

southern zone included the second (6 observations) and third (13 observations) classes which exhibited saline to highly saline soils (> 4 dS m^{-1}). The southern zone is dominated by intensive evaporation/evapotranspiration, unmanaged sewage trenching, extensive land use changes and hence prevailing salinization processes.

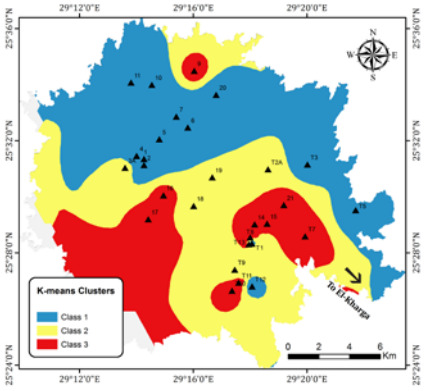

Fig. 10. Map showing the soil chemistry patterns of the Dakhla oasis.

Table 3: Statistics of the three classes detected from the k-means clustering analysis.

	Class 1 (n=14)				Class 2 (n=6)				Class 3 (n=13)			
	Mini.	Max.	Mean	St. dev.	Mini.	Max.	Mean	St. dev.	Mini.	Max.	Mean	St. dev.
EC	0.5230	5.1200	2.1069	1.7095	30.3	53.9	**40.38333**	9.372602	10.4900	26.3000	18.2383	4.9648
pH	4.2100	8.3100	7.4379	1.0078	7.96	53.9	**8.331667**	0.405385	6.9900	8.8500	7.7908	0.5888
Zn	0.0028	0.0098	**0.0050**	0.0018	0.0018	0.0031	0.002467	0.000651	0.0017	0.0053	0.0033	0.0011
Zr	0.0089	0.0316	**0.0221**	0.0054	0.0014	0.0127	0.00705	0.004367	0.0085	0.0203	0.0142	0.0033
Ag	0.0136	0.0186	**0.0169**	0.0013	0.0071	0.0127	0.008825	0.001333	0.0089	0.0123	0.0107	0.0010
Cd	0.0183	0.0241	**0.0216**	0.0016	0.009	0.0135	0.011408	0.0019	0.0115	0.0170	0.0141	0.0016
Sn	0.0236	0.0323	**0.0281**	0.0028	0.0109	0.0184	0.01415	0.002983	0.0146	0.0212	0.0176	0.0018
Sb	0.0274	0.0346	**0.0312**	0.0023	0.0111	0.0193	0.0153	0.003477	0.0162	0.0226	0.0188	0.0019
Ti	0.1415	0.4706	**0.3477**	0.0978	0.0206	0.22695	0.119492	0.081143	0.1289	0.2902	0.1965	0.0499
Mn	0.0357	0.1961	**0.0817**	0.0437	0.0083	0.04325	0.02609	0.012705	0.0207	0.1516	0.0470	0.0410
Fe	1.4737	5.2433	**3.2623**	1.0073	0.0505	1.9626	1.009867	0.791317	0.8480	2.6668	1.7717	0.6098
Cl	9.0400	15.6500	11.9650	2.9681	34.49	52.03	**42.80167**	6.485117	24.6100	47.1500	34.0642	6.8658
Al	1.8200	5.4400	**4.0079**	1.0371	0.1595	1.2521	0.79088	0.425039	0.6208	1.9153	1.2505	0.4524
Si	9.4400	22.1300	**17.7757**	4.3708	0.2225	4.6282	2.51535	1.689343	2.7683	7.0500	4.8400	1.3576
P	0.0383	0.1382	**0.0651**	0.0277	0.013	0.014	0.0135	0.000707	0.0062	0.0389	0.0171	0.0090
S	0.0511	2.6900	0.4456	0.6606	0.1306	1.3625	**0.865633**	0.518203	0.0498	0.8694	0.4028	0.3092
K	0.5281	2.6458	1.6117	0.7155	1.1317	2.3386	**1.6595**	0.392494	0.3573	1.5243	0.9275	0.3818
Ca	2.2655	4.6537	**3.5070**	0.7541	0.3831	2.4781	1.4607	0.836451	1.7314	4.1569	2.7961	0.7426
V	0.0204	0.0400	**0.0319**	0.0051	0.0068	0.0219	0.0154	0.00551	0.0143	0.0314	0.0204	0.0058
Cr	0.0092	0.0192	**0.0130**	0.0032	0.0049	0.0123	0.00879	0.003229	0.0069	0.0169	0.0112	0.0029
Ni	0.0032	0.0105	**0.0048**	0.0018	0.0012	0.0026	0.00198	0.000545	0.0015	0.0063	0.0028	0.0013
Pb	0.0005	0.0013	**0.0008**	0.0002	0.0003	0.00045	0.000375	0.000106	0.0004	0.0008	0.0006	0.0001

NB: Values in bold correspond for the largest mean of each variable among the clusters.

CONCLUSIONS

Physical and chemical properties of soils play a major role in the evaluation of different geochemical signature, soil quality, discrimination of land use type, soil provenance and soil degradation. Thirty three topsoil samples (0–20cm) were collected in the study area. The EC ranged from 0.5 to 53.9 dSm^{-1}; with an average of 15.2 dS/m indicating highly salt-affected soils. Reflectance of the studied soil samples show two deep absorption features at 1415 nm and 1915 nm, which were strongly associated with OH features of water. As the salinity levels increase, the absorption features become deeper, broader, and more asymmetrical. This suggests an increase in the soil moisture content. This relationship is confirmed from the parameters (depth and width) of the absorption band centered at 1415 and 1915 nm and the soil EC. The best coefficient of determination of the soil salinity can be achieved for depth (R2 = 0.57 & 0.52) and for width (R2 = 0.70 & 0.56) at 1415 and 1915 wavelengths.

Two main factors accounted for 75.57% of the data variance governed the variability of the soils.

The first factor accounted for 54.94% of the variance strongly negatively loaded with EC (-0.88) and Cl (-0.59), and positively loaded with Sb (0.95), Sn (0.97), Cd (0.98), Ag (0.96), Si (0.93), Ti (0.87), Al (0.88), Zr (0.85), Fe (0.88), Mn (0.52), Ca (0.68), P (0.63), V (0.83), Cr (0.53), Ni (0.67) and Pb (0.47). The second factor explained 13.36% of the total variance is found to be strongly negatively loaded with Zinc Zn (-0.61) and sulfur S (-0.77) and positively loaded with pH (0.77). Results clarified soil quality degradation due to salinization and contamination consequently resulted from the traditional irrigation practices (Flooding irrigation system) in Dakhla oasis which are not quite suitable due to the arid climate.

Cluster analysis recognized three distinctive soil chemical patterns; their spatial distribution is consistent with the geology, and the urban and agricultural practices. The clustering technique provides a context for better and easier decision making by managers with guidelines for optimal soil resource planning activities. The results of this research could help to prioritize areas where future sustainable development plans should be focused by altering the agricultural and irrigation management practices.

REFERENCES

[1] Bowers S, Hanks RJ, “Reflectance of radiant energy from soils”. Soil Sci. Vol.100, 1965, pp.130–138.

[2] Burrough PA, McDonnell RA. “Principles of Geographical Information Systems”. 1998, Oxford University Press, Oxford.

[3] Chhabra R. “Soil salinity and water quality”. Balkema Pub., 1996, VT, USA.

[4] Conoco, “Geologic Map of Egypt. Egyptian General Authority for Petroleum (UNESCO joint map project) ”, 20 sheets, scale 1:500 000, 1987,Cairo, Egypt.

[5] Ebraheem MA, Riad S, Wycisk P and Sefelnasr AM. “A local-scale groundwater flow model for groundwater resources management in Dakhla Oasis, SW Egypt”. J. of Hydrogeology. Vol.12, 2004, pp.714–722.

[6] Fovell RG, “Consensus clustering of US temperature and precipitation data”. J. Clim. Vol.10 (6), 1997, pp.1405–1427.

[7] Ghoubachi S Y, “Hydrogeological characteristics of the Nubia sandstone aquifer system in Dakhla depression, Western Desert Egypt” M.Sc Thesis, Faculty of Science , Ain Shams Univ., 2001, p260

[8] Hereher ME, Ismael H.“The application of remote sensing data to diagnose soil degradation in the Dakhla depression - Western Desert, Egypt“ J. of Journal of Geocarto International, Vol.30 (2), 2015, pp. 1-26.

[9] Masoud AA,“Predicting salt abundance in slightly saline soils from Landsat ETM+ imagery using Spectral Mixture Analysis and soil spectrometry”.Geoderma Vol.217-218, 2014, pp.45–56.

[10] Mills AJ, Fey MV, Grongroft A, Petersen A, Medinski TV, “Unravelling the effects of soil properties on water infiltration: segmented quantile regression on a large data set from arid south-west Africa”. Aust. J. Soil Res. Vol.44, 2006, pp.783–797.

[11] Nawar S, Buddenbaum H, Hill J, Kozak J, “Modeling and Mapping of Soil Salinity with Reflectance Spectroscopy and Landsat Data Using Two Quantitative Methods (PLSR and MARS) ”. Rem Sens. Vol.6, 2014, pp. 10813-10834.

[12] Qadir M, Ghafoor A, Murtaza G, “Amelioration strategies for saline soils”: a review. Land Degrad. Dev. Vol.11, 2000, pp.501–521.

[13] Russeger J,“Kreide und Sandstein” Einfluss on Granit antfletzteren, Neues Jahrb. Mineralogi ABd., 1837, pp. 665-669.

[14] UNEP (United Nations Environment Programme),“World Atlas of Desertification” 2ED. UNEP, 1997, London.

[15] UNESCO. “Map of the World Distribution of Arid Regions”. MAB Technical Note 7, 1979.

[16] Weatherill G, Burton PW, “Delineation of shallow seismic source zones using K-means cluster analysis, with application to the Aegean region”. Geophys. J. Int. Vol.176 (2), 2008, pp.565–588.

First International Conference on Science, Engineering & Environment,
Tsu City, Mie, Japan, Nov.19-21, 2015, ISBN: 978-4-9905958-5-2 C3051

NUMERICAL ANALYSES ON OCCURRENCE OF THERMAL CONVECTION IN A FLOWING SHALLOW GROUNDWATER

Junichiro Takeuchi, Makoto Kawabata, and Masayuki Fujihara
Graduate School of Agriculture, Kyoto University, Japan

ABSTRACT

Occurrence of thermal convection could change groundwater flows significantly, and the phenomena also alter solute transport. Especially, in a case of a shallow groundwater, it might affect surface water quality since it interacts surface waters such as lakes and marshes directly. Hence, it is important to grasp conditions that induce thermal convection for groundwater management. In this study, the conditions for the onset and decay of thermal convection in a flowing shallow groundwater are investigated with numerical experiments. Through the analyses on the computed results by using the attractor reconstruction technique, three types of flow regime were found. It was indicated that not only the Rayleigh number, which is a well-known influential factor, but also groundwater flow rate affects flow regime.

Keywords: Density-Driven Flow, Rayleigh Number, Bifurcation, Fixed Point, Limit Cycle

INTRODUCTION

In a field of geothermal dynamics, spatially and temporally large scale phenomena in groundwater such as thermal convection and circulation rooted in magmatic heat sources have been main target of research interest. Typically, its objective domain ranges from a few kilometers to tens of kilometers, and the time scale ranges from hundreds to thousands of years e.g., [1], [2]. Recently, thermal dynamics in a relatively shallow groundwater is actively investigated for the following reasons. One reason is that temperature distribution in a shallow ground-water could be an important clue for understanding subsurface structure and groundwater flow, e.g., [3]. Another is that attention is increasing to the geothermal heat pump technology as one of alternatives for clean energy [4]. Generally, it is considered that thermal convection rarely happens in a shallow groundwater except for around heat sources such as hot springs. However, it is reported that few weeks or months scale thermal convection could occur under some conditions such as a groundwater under snow coverage and intrusion of snowmelt water into groundwater [5]. Tortuous groundwater flows by density-driven flow could change solute and heat transports drastically, and so it is essential to grasp the onset, growth, and decay of the density-driven flow for groundwater management. When a certain physical condition varies continuously, occurrence of such qualitative changes in groundwater flow regime is considered as bifurcation in the nonlinear dynamics [6], and hydrodynamic stability has been one of the central problems of fluid mechanics [7].

In this study, two situations which could set up thermal convection are targeted: one is snow coverage and the other is cold water intrusion. Then, this study is aimed at identifying conditions for occurrence of thermal convection under those two situations through systematic numerical experiments and subsequent analyses.

MODEL DESCRIPTION

Governing equations

A vertical two dimensional coordinate system where x and z are the horizontal and vertically upward directions, respectively, are used in this study. To reduce the number of parameters included in the governing equations, a dimensionless version is employed here. The major part of the derivation of the dimensionless equations for groundwater flow and thermal transport is based on Holzbecher (1998) [6] and Kawabata et al. (2015) [8].

The final version of the governing equation for groundwater flow with variable water density is described with the stream function under following assumptions: incompressibility of water, rigidity of the aquifer, absence of sources or sinks, and the Boussinesq approximation.

$$\frac{\partial}{\partial X}\left(\frac{\mu^r}{\kappa_z^r}\frac{\partial \Psi}{\partial X}\right)+\frac{\partial}{\partial Z}\left(\frac{\mu^r}{\kappa_x^r}\frac{\partial \Psi}{\partial Z}\right)=-Ra\frac{\partial \theta}{\partial X} \qquad (1)$$

with

$$Ra=\frac{\gamma Hg\kappa_0\Delta\rho}{\mu_0 D}, \qquad (2)$$

$$\left(U,W\right)^T=\left(\frac{\partial \Psi}{\partial Z},-\frac{\partial \Psi}{\partial X}\right)^T, \qquad (3)$$

$$\theta=\frac{T-T_{\min}}{T_{\max}-T_{\min}}, \qquad (4)$$

$$\rho(\theta) = \rho(T_{\min}) - \Delta\rho\theta, \quad (5)$$

$$\mu(\theta) = \mu^r(\theta)\mu_0, \quad (6)$$

$$\kappa_x = \kappa_x^r \kappa_0, \quad (7)$$

$$\kappa_z = \kappa_z^r \kappa_0 \quad (8)$$

where X and Z are the dimensionless coordinates for x and z, respectively; Ψ is the dimensionless stream function; Ra is the Rayleigh number; ρ is the water density, which is assumed to be represented as a proportional relationship with the dimensionless temperature θ; μ is the viscosity of water; μ^r is a relative value based on the representative viscosity μ_0; κ_x and κ_z are the intrinsic permeability in the x and z directions, respectively; κ_x^r and κ_z^r are relative values based on the representative intrinsic permeability κ_0; H is the representative length, which is the height of an objective domain in this study; g is the gravitational acceleration; γ is the ratio between water and bulk thermal capacities; D is the thermal diffusivity; U and W are the dimensionless velocity in the X and Z directions, respectively; T is the temperature, $T_{\max}$ and $T_{\min}$ are the maximum and minimum temperatures in the domain.

The dimensionless version of the governing equation for thermal transport is described as follows.

$$\frac{\partial\theta}{\partial\tau} = \frac{\partial}{\partial X}\left(\frac{\partial\theta}{\partial X}\right) + \frac{\partial}{\partial Z}\left(\frac{\partial\theta}{\partial Z}\right) - \left(U\frac{\partial\theta}{\partial X} + W\frac{\partial\theta}{\partial Z}\right) \quad (9)$$

where τ is the dimensionless time.

In addition to the governing equations (1) and (9), auxiliary boundary and initial conditions for the dimensionless stream function and temperature are imposed. In this study, a rectangle domain in which groundwater is flowing horizontally unless thermal convections occur is considered. From a part of the top Γ_2 of the domain, cold water intrudes into the aquifer as illustrated in Fig. 1. For both of the stream function and temperature, the Dirichlet-type boundary conditions are given to the top and bottom of the domain, and the Neumann-type boundary condition in which $\partial\Psi/\partial\boldsymbol{\nu} = 0$ and $\partial\theta/\partial\boldsymbol{\nu} = 0$, where $\boldsymbol{\nu}$ is the outward normal unit vector to the boundary, are given to the sides of the domain (Fig. 1). The values of the stream function on the top are constant Ψ_{top} and $\Psi_{top} + \Psi_{ent}$ on Γ_1 and Γ_3, respectively, except for the cold water intruding zone Γ_2, where the value changes linearly from Ψ_{top} to $\Psi_{top} + \Psi_{ent}$. With respect to the temperature, θ_{ent} is given to the water intruding zone Γ_2, and θ_{top} is given to the others Γ_1 and Γ_3 in the top. To the bottom boundary Γ_0, constant values of Ψ_{btm} and θ_{btm} are given to the stream function and temperature, respectively.

As an initial condition for the stream function, a horizontal flow condition where the stream function changes linearly from Ψ_{btm} to Ψ_{top} is given. Regarding the temperature, initial conditions in which some perturbation is added on the linear change from θ_{btm} to θ_{top} are given as illustrated in Fig. 2. When the Rayleigh number is smaller than $4\pi^2$, which is the critical number for the onset of the Benard convection [5], relatively large perturbation is given to confirm convergence to a stable fixed point. On the other hand, when the Rayleigh number is greater than or equal to $4\pi^2$, relatively small perturbation is given to avoid persistence to an unstable fixed point.

Numerical model

The standard Galerkin finite element method is employed for spatial discretization of the governing equations (1) and (9), and the Crank-Nicolson method is used for the time evolution of the governing equation (9), in which the lumped mass matrix approximation is used. The validity of the numerical model was confirmed [8] by the Benard convection, and Henry and Elder problems, which are standard benchmark problems for density-driven flow [9]. When the flow velocity is large compared with the diffusivity, finer computational meshes are used so as to limit the maximum local Peclet number in the domain to unit.

NUMERICAL EXPERIMENTS

Computational settings

To investigate the onset of the instability and the subsequent growth and decay, numerical experiments are conducted under various physical conditions regarding the Rayleigh number and the basal groundwater flow velocity. Here, two cases are considered: one is groundwater flow without cold water intrusion, which is referred to as Case 1, and the other is case with cold water intrusion, which is

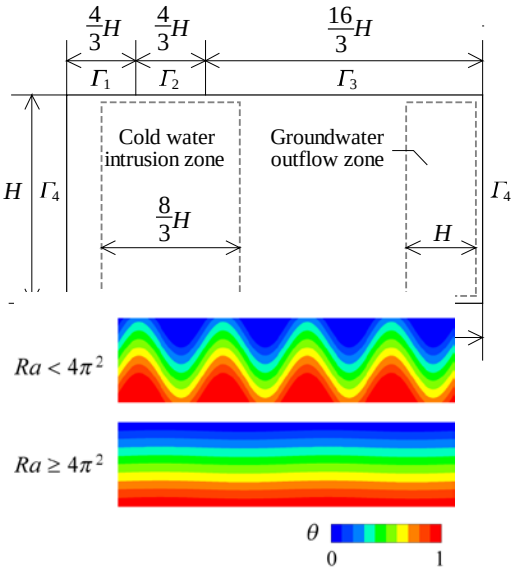

Fig. 2 Initial conditions for temperature

referred to as Case 2. Case 1 is supposed to be snow coverage on saturated ground, and Case 2 is supposed to be waterlogging for soil puddling in spring. The Rayleigh number Ra ranges from 0 to 100, and Ψ_{top} ranges from 0 to 20. As the combination of these two variables varies, simulations are conducted to investigate whether some instabilities such as thermal convection and fluctuation occur or not. For Case 1, Ψ_{ent} is set as 0; and θ_{btm}, θ_{top}, and θ_{ent} are set as 1.0, 0.0, and 0.0, respectively. For Case 2, Ψ_{ent} is set as 2; and θ_{btm}, θ_{top}, and θ_{ent} are set as 1.0, 0.5, and 0.0, respectively.

The domain is assumed to be homogeneous and isotropic, and so the relative values κ_x^r and κ_z^r for the intrinsic permeability are given as unit. The relative value μ^r for the viscosity is determined from the following functional relationship to temperature in unit °K [5].

$$\mu(T) = 10^{-3}\left\{1 + 0.015512\left(T - 293.15\right)\right\} \qquad (10)$$

Analysis on computed solutions

To evaluate computed results quantitatively whether the stream function and/or the temperature in a certain point fluctuate or not, moving variance is calculated on each node in the two sampling zones, the cold water intrusion zone and the groundwater outflow zone (Fig. 1). The number of time series data used to obtain the variance is 400, which is sufficiently-long data compared with the cycle length obtained from our preliminary simulations. When the solution converges to a steady state, the variance decreases and asympotically becomes zero. By contrast, if the solution fluctuates regularly or irregularly, the variance does not converge to zero.

In addition to the moving variance, behaviors of the stream function and temperature in a node are analyzed with the attractor reconstruction, which is one of non-linear-data analysis techniques, and a time series data is transformed into a trajectory in a 2-D phase space [10]. In the attractor reconstruction, the coordinates of each point in the trajectory is generated from a time series data as $\left(\chi(\tau), \chi(\tau + \tau_D)\right)$ with the time delay τ_D, where $\chi(\tau)$ is a time series data of the stream function or the temperature in the node. If a time series data oscillates like a sinusoidal wave, the trajectory becomes a circle when the time delay is given as a quarter of the cycle.

Results

Firstly, the computed results for Case 1 are discussed. The temperature distributions when

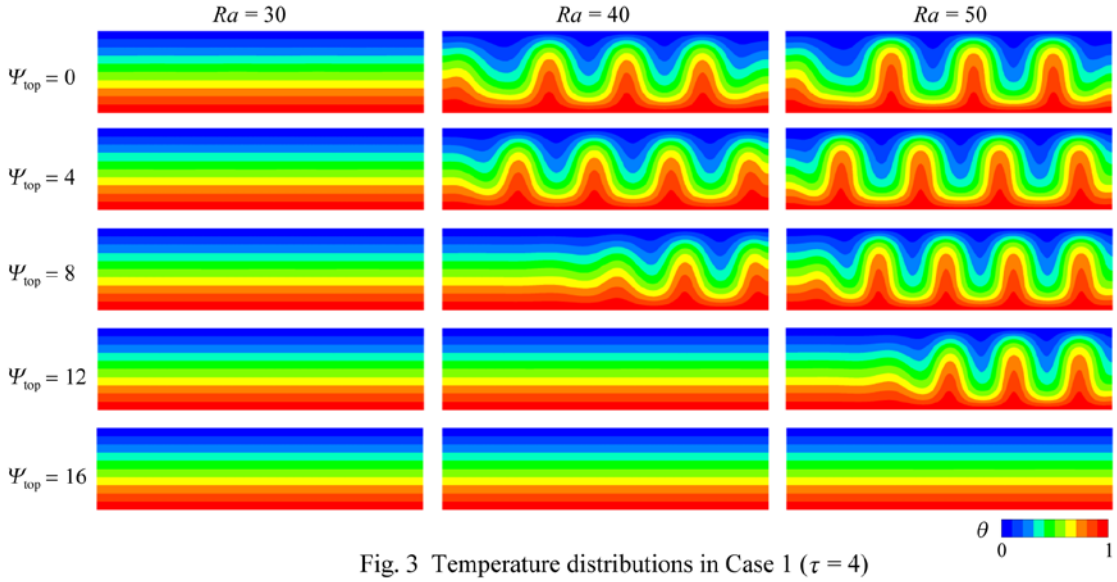

Fig. 3 Temperature distributions in Case 1 ($\tau = 4$)

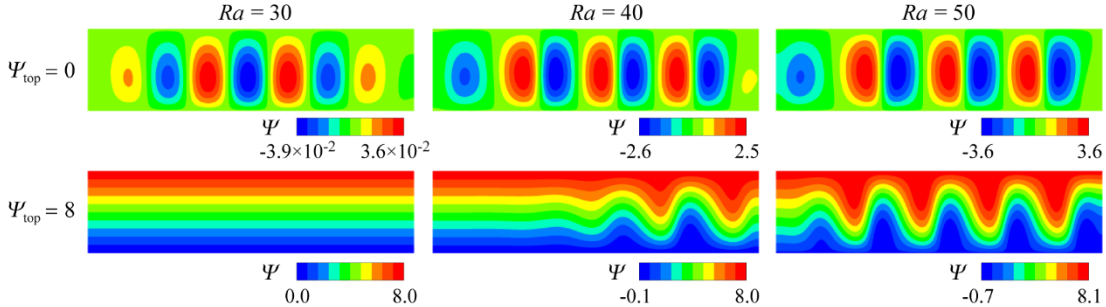

Fig. 4 Stream functions in Case 1 ($\tau = 4$)

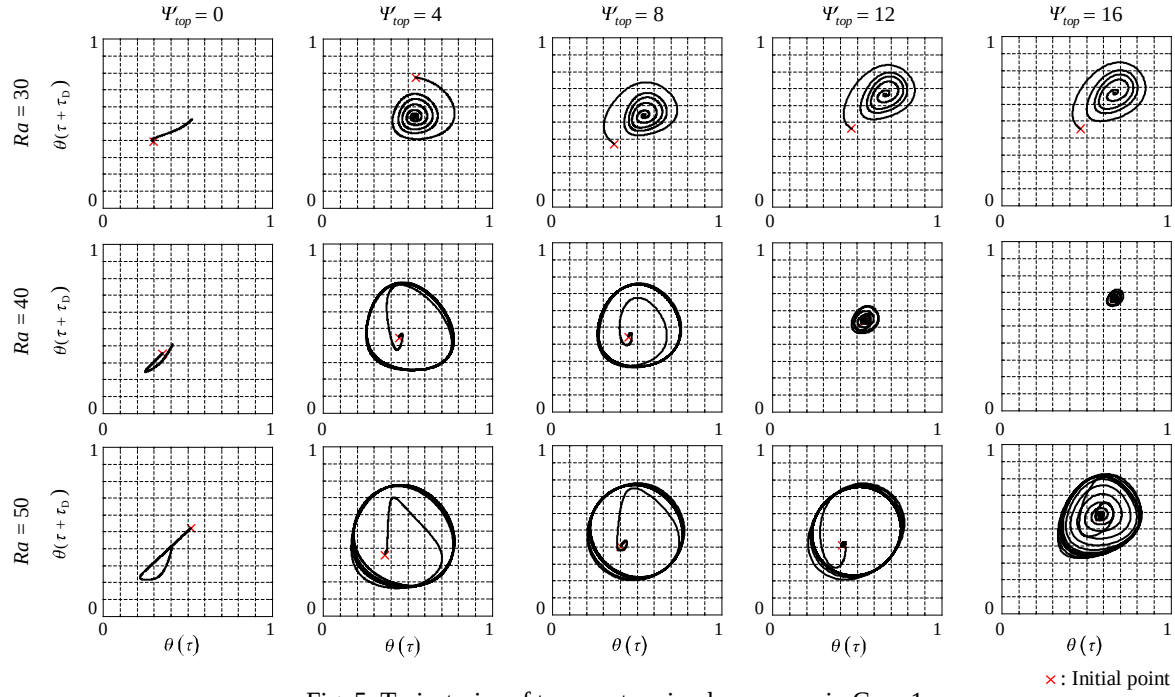

Fig. 5 Trajectories of temperature in phase space in Case 1

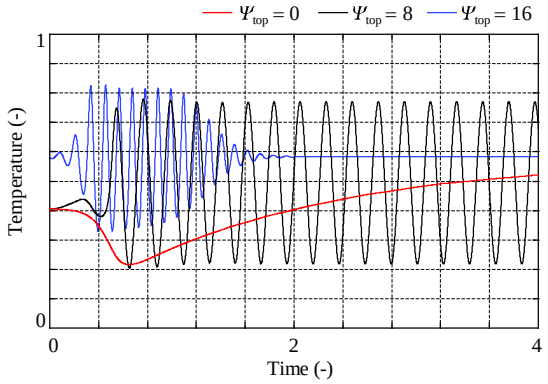

Fig. 6 Temporal changes of temperature in Case 1 ($Ra = 50$)

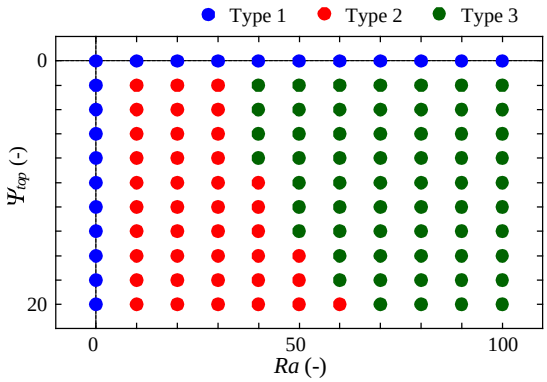

Fig. 7 Classification of computed conditions in Case 1

$\tau = 4$ are shown in Fig. 3, and the corresponding stream functions are shown in Fig. 4. The condition where $\Psi_{top} = 0$ corresponds to the one for the Benard convection, and so thermal convection occurs if the Rayleigh number is greater than $4\pi^2$, 40 and 50 in this case. From Fig. 4, it is found that weak circulations occur even in the condition where $Ra = 30$ and $\Psi_{top} = 0$. It is considered that the obtained result is in the middle of the convergence to the steady state. When the horizontal groundwater flow is given, the waves by thermal convection are carried by the horizontal flow and new waves arise at the upstream end continuously. It is found that larger Rayleigh number is required to keep thermal convection as the basal groundwater flow (Ψ_{top}) increases. Figure 5 shows the trajectories of temperature on the node where the moving variance is maximum in the groundwater outflow zone under each condition. Three types of trajectory are found: convergence to a point without a spiral e.g., in a case of $Ra = 50$ and $\Psi_{top} = 0$; convergence to a point with a spiral, e.g., in a case of $Ra = 50$ and $\Psi_{top} = 16$; and asymptotic approach to a limit cycle with a spiral, e.g., in a case of $Ra = 50$ and $\Psi_{top} = 8$. Here these three flow regimes are referred to Type1, Type 2, and Type 3, respectively. Figure 6 shows the temporal change of temperatures of the above typical three cases. The temporally fluctuating graphs of $\Psi_{top} = 8$ and $\Psi_{top} = 16$ correspond to the spirals in Fig. 5. These qualitative transformations of the trajectories imply bifurcations. In the case of $Ra = 30$, which is under the critical value $4\pi^2$, the stable fixed point in $\Psi_{top} = 0$ transforms to a stable spiral, when some non-zero value is given to Ψ_{top}. In the cases of $Ra = 40$ and 50, which are over the critical value, the stable fixed point transforms to an unstable spiral and a limit cycle is formed, when a small non-zero value that does not exceed a threshold is given to Ψ_{top}. If a value beyond the threshold is given to Ψ_{top}, the unstable spiral transforms to a stable spiral and the limit cycle also disappears. It is found that the threshold depends on

the Rayleigh number. Figure 7 shows the classification of each computed condition into these three types.

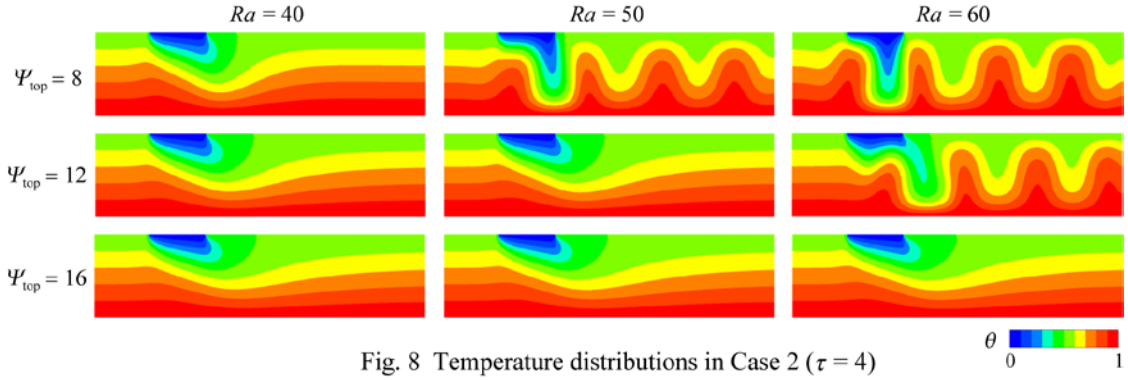

Fig. 8 Temperature distributions in Case 2 ($\tau = 4$)

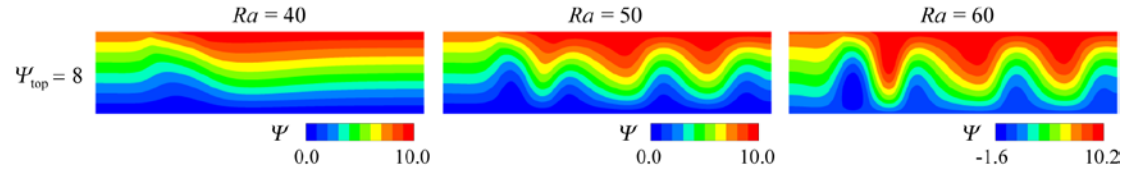

Fig. 9 Stream functions in Case 2 ($\tau = 4$)

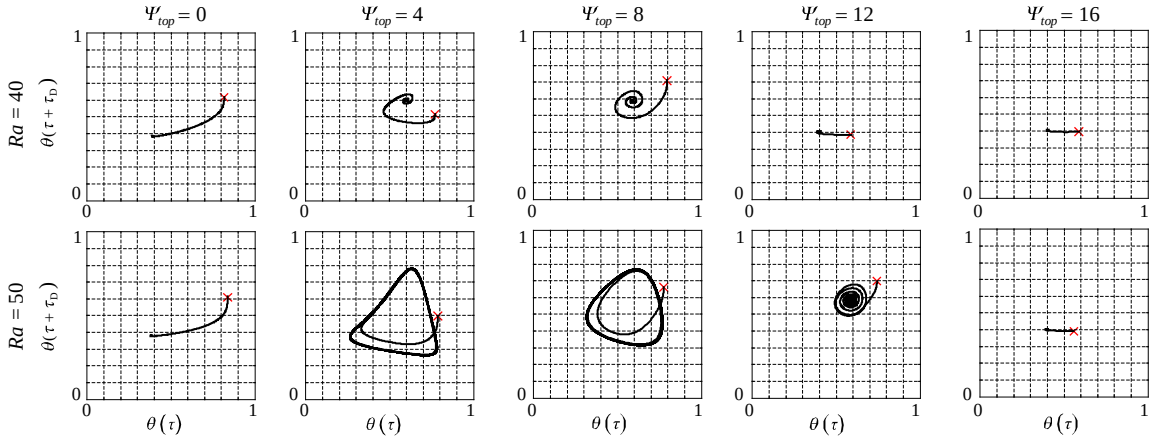

(a) Cold water intrusion zone

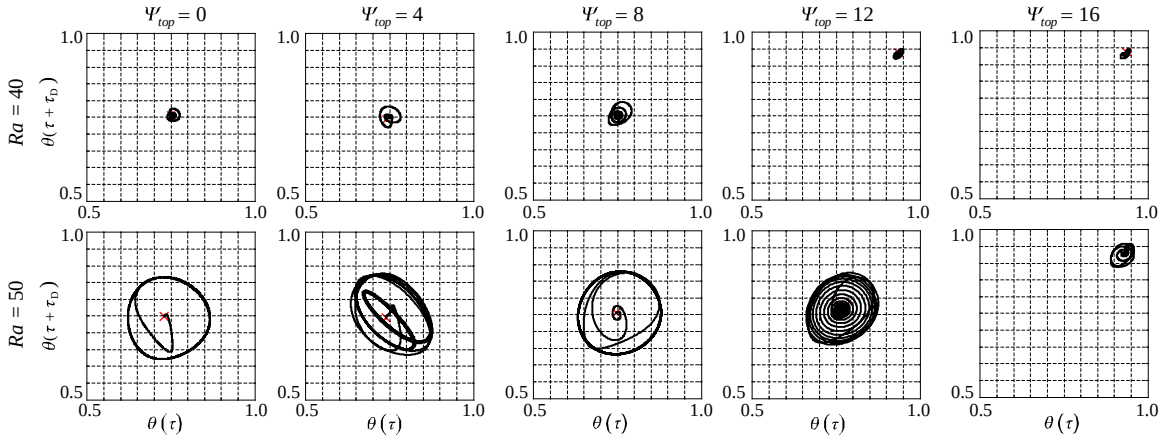

(b) Groundwater outflow zone

×: Initial point

Fig. 10 Trajectories of temperature in phase space in Case 2

Secondly, the obtained results of Case 2, which is the case of the cold water intrusion into flowing groundwater, are discussed in the same way with Case 1. Figures 8 and 9 show the temperature and stream function distributions of typical patterns after a sufficient time in Case 2. From these figures, two patterns of flow regimes are found: steady and unsteady flow regimes. The steady ones are found when the Rayleigh number is smaller than or equal to 40, or when basal groundwater flow is large even in higher Rayleigh number. Under such conditions, Fig. 10 indicates the trajectories converging to a point without a spiral (Type 1) and with a spiral (Type 2). The unsteady flow regimes, in which

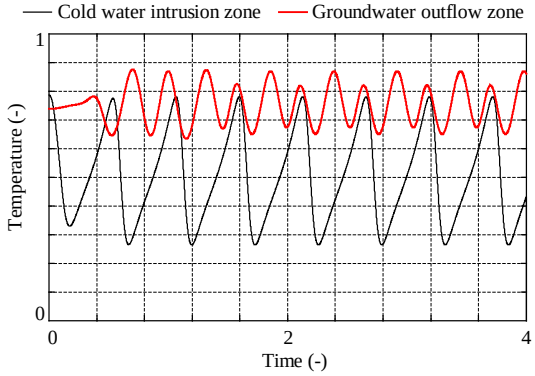

Fig. 11 Temporal changes of temperature in Case 2 ($Ra = 50$, $\Psi_{top} = 8$)

waves are carried by the basal groundwater flow, are found in the remaining conditions. In addition, different types of fluctuation are found in the cold water intrusion zone and the groundwater outflow zone as shown in Figs. 10 and 11. For instance, in the cases of $Ra = 50$ and $\Psi_{top} = 8$ the trajectory approaches toward a single loop and traces it in the cold water intrusion zone (Fig. 10 (a)), while the trajectory traces a double loop in the groundwater outflow zone (Fig. 10 (b)). Figure 11 also shows that the temporal change in the cold water intrusion zone is a periodic function which has a single peak in one cycle, and that in the groundwater outflow zone is a periodic function which has two peaks in one cycle. The classification of the computed conditions is shown in Fig. 12. It is found that flow regimes change from Type 3 to Type 2 as Ψ_{top} increases in the same way with Case 1.

CONCLUSION

In this study, conditions for onset and decay of thermal convection induced by temperature differences between the top and bottom of domain and cold water intrusion from the ground surface in a shallow groundwater were investigated through numerical experiments. The computed results were analyzed with the attractor reconstruction, which visualizes a time series data in a 2-D phase space as a trajectory. From the obtained trajectories, three types of behavior were found: convergence to a point without a spiral, convergence to a point with a spiral, and asymptotical approach toward a loop. These correspond to a stable fixed point, a stable spiral, and a limit cycle, respectively, and the transformation from one state to another corresponds to bifurcation when some parameter (condition) varies continuously. In this study, it is found that flow regime changes from a stable spiral to a limit cycle when the Rayleigh number increases, and that it changes from a limit cycle to a stable spiral when the basal groundwater flow rate increases. From these results, it is indicated that groundwater flow rate is an important factor that determines flow regime as well as the Rayleigh number.

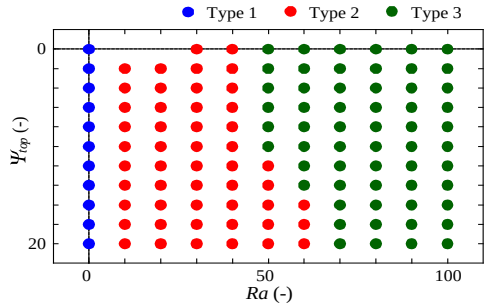

Fig. 12 Classification of computed conditions in Case 2

REFERENCES

[1] Yusa Y, “Numerical experiment of groundwater motion under geothermal condition –Vying between potential flow and thermal convective flow-”, J. Geothemal Res. Society Japan, Vol. 5, 1983, pp. 23–38 (in Japanese).

[2] Travi Y, Pizard P, and Betton M, “Temperatures and thermal gradients in the Senegalese Maastrichtian aquifer: simulated test on their effect on flow discharge”, J. Hydrology, Vol. 187, 1996, pp. 333-350.

[3] Uchida Y and Sakura Y, “Subsurface temperature profiles in the Nobi Plain, central Japan”, Bull. Geol. Surv. Japan, Vo1. 50, pp. 635-659 (in Japanese).

[4] Fujii H, Inatomi T, Itoi R, and Uchida Y, “Development of suitability maps for ground-coupled heat pump systems using groundwater and heat transport models”, Geothermics, 36, 2007, pp. 459-472.

[5] Yoshimura Y, Takeuchi J, Buma N, and Fujihara M, “Analysis of effects on groundwater flow by infiltration-water temperature”, in Proc. JSIDRE, 2013, pp. 402-403 (in Japanese).

[6] Holzbecher E, Modeling Density-Driven Flow in Porous Media, Springer, 1998, p. 286.

[7] Drazin PG and Reid WH, Hydrodynamic Stability 2nd ed., Cambridge University Press, 2004, p. 605.

[8] Kawabata M, Takeuchi J, and Fujihara M, “Numerical analysis of density-driven fluctuation in groundwater caused by saltwater intrusion”, in Proc. PAWEES-INWEPF2015, in print.

[9] Ackerer PH, Younes A, and Mose R, “Modeling variable desity flow and solute transport in porous medium: 1. Numerical model and verification”, Transport in Porous Media, Vol. 35, 1999, pp. 345-373.

[10] Strogatz SH, Nonlinear Dynamics and Chaos 2nd ed., Westview Press, 2015, p. 513.

First International Conference on Science, Engineering & Environment,
Tsu City, Mie, Japan, Nov.19-21, 2015, ISBN: 978-4-9905958-5-2 C3051

UTILIZATION OF RICE STRAW BIOMASS IN THE PRODUCTION OF BIODEGRABLE GEOTEXTILE

Rolando P. Javellonar[1] and Victorino T. Taylan[2]
[1]Faculty, College of Engineering and Technology, Romblon State University
Odiongan, Romblon, Philippines
[2]Faculty, College of Engineering, Central Luzon State University
Science City of Munoz, Nueva Ecija, Philippines

ABSTRACT

The Philippines produces about 18.52 billion kilograms of rice straw annually. Of this amount, about 95% or 17.1 billion kg is left and burned in the field which emits greenhouse gases that contributes to global warming and climate change. Rice straw can be recycled and converted into geotextile like rice straw mat and net to enhance its environmental importance and economic potential. Rice straw mat was prepared using a binder while rice straw net was prepared by making a straw twine and then into rope by spinning two twines. Finally, rice straw rope was weaved to form a net. Physical properties of the developed rice straw geotextile revealed that the developed rice straw mat had higher water absorption capacity (328.5%) and percentage swelling (17.5%) compared to rice straw net with only 167.3% and 1.8%, respectively. On the contrary, rice straw net recorded higher tensile strength of 2.0 kN/sq. cm when wet and 1.95 kN/sq. cm when dry as compared to rice straw mat with 1.08 kN/sq. cm when wet and 1.02 kN/sq. cm when dry. The observed water absorption capacity of rice straw mat and rice straw net as well as tensile strength of rice straw net exceeded the standard generic specification values set by the Department of Public Works and Highways for geotextile as erosion control material. Hence, both the developed rice straw geotextiles can be utilized as ground cover for soil erosion mitigation or an alternate erosion control material in areas where coco coir net is not available.

Keywords: Rice Straw, Rice Straw Mat, Rice Straw Net, Biomass, Geotextile

INTRODUCTION

In the Philippines, about 18.52 billion kilograms of rice straw is generated annually [1]. Of this amount, about 95% or 17.1 billion kg rice straw is left and burned in the field [2] which emits greenhouse gases (GHG) that contributes to global warming and eventually, climate change. The remaining portion is either utilized as feed for livestock, mulching material, substrate for bio-fertilizer production, bedding for mushroom culture and others. Most farmers consider rice straw as nuisance in the field because it does not rot easily rot, thus causes obstruction during farm operations. It then became a traditional practice of the farmers to burn their rice straw after harvest as an easy means of disposal. However, burning of rice straws emit greenhouse gases (GHG) and pollutes the atmosphere [3].

Rice straw is an agro-waste material which when recycled and utilized in the production of rice straw geotextile (RSGT) will enhance its environmental importance and economic potential. Moreover, RSGT can be utilized as ground cover for slope stabilization and erosion control. Just like the coco coir and other biomass, rice straw can be developed into geotextile mat and net for erosion control. Rice straw geotextiles are the most effective geotextiles in reducing relative runoff and soil loss rate [4]. Therefore, considering its abundance, being inexpensive and biodegrable agro-waste resource, rice straw is most appropriate material in the production of geotextile like rice straw mat (RSM) and rice straw net (RSN). With the conversion of rice straw into geotextile products, it can not only be utilized as ground cover for mitigation of soil erosion but likewise, environmental degradation brought about by pollution and climate change can be minimized if not totally eliminated.

Rice straw mat and net are cost effective, environmentally and eco-friendly material as ground cover for erosion control. When used as ground cover, it will not only stabilize the top soil but also helps in the establishment of vegetation for surface cover and improves soil physical structure and condition when decomposed into organic matter. Furthermore, when used as mulch for upland crops, RSM is perceived to have a better soil moisture retention capability as compared to raw rice straw as mulching material because RSM is more dense and compact. Most importantly, the development of this technology will open a new opportunity to small farmers as they can sell their rice straw to augment their income or process into geotextile as means of

livelihood project to alleviate unemployment in the countryside.

Additionally, the utilization of rice straw in the production of geotextile mat and net will likewise pave the way for the development and introduction of new technology out of rice farming by-product. It is in this context that this study was undertaken to demonstrate the potential of rice straw biomass as material in the production of biodegrable geotextile.

Objectives of the Study

Generally, the study aimed to utilize rice straw biomass in the production of biodegrable geotextile as slope protection for soil erosion mitigation. Specifically, it attempted to: 1) develop RSM and RSN geotextile as slope protection for soil erosion mitigation; 2) Determine the technical specifications and physical properties of the developed RSM and RSN, and; 3) Determine the life span of RSM and RSN geotextiles.

MATERIALS AND METHODS

Preparation of Rice Straw Mat

Rice straw mat was prepared using an approximate mass of 600g of dried rice straw/sq m. This quantity was based on the amount of rice straw as mulching material for garlic which is about 6 tons/ha or equivalent to a thickness of 5-12 centimeters of straw mulch [5]. Rice straw mat was prepared manually using centrifuged rubber latex as binder. Rubber latex is a protective fluid contained beneath the bark of the *Hevea brasilienesis* rubber tree. It is a cloudy white liquid similar in appearance to cow milk.

Rice straw was spreaded evenly in a clean concrete pavement or board. Spreading of rice straw was done so that individual grid of straw interlaid with each other at random direction. It was reported that random fiber architecture was the most effective in reducing sediment concentrations, sediment yields, and frequency of rill initiation [6]. While spreading the rice straw, rubber latex as binder was sprayed evenly at the rate of 750 ml/sq. m. After which, the rice straw was immediately covered with board and densified by applying a pressure approximately 100 kg/m^2 atop the board for 12-24 hours. Densification was done so that individual rice straw will be bound properly and achieves an even flat surface.

Preparation of Rice Straw Net

In the preparation of rice straw net, straw twine was first made by manually spinning two or more straws together. Straw was continuously added until a twine of desired length was produced. After twining, a straw rope was likewise made by manually spinning two twines together. The size of straw rope produced approximated the coco coir net (CCN) which has an average thickness of 7.0 mm. After the roping process, the straw rope was weaved into net following the conventional open weave pattern. The approximate mesh size of the developed rice straw net was 2.0 x 2.0 cm. In a related study on coco coir net, mesh opening of 2.0 x 2.0 cm was found to be the most effective in minimizing top soil erosion [7].

Physical Property and Technical Specification

After the development of RSM and RSN geotextiles, samples were characterized and then subjected to laboratory testing to determine its physical properties and technical specifications. The physical property tests undertaken were: swelling percentage (S_p), water absorption (W_a) and tensile strength (T_s). Tensile strength is defined as a stress measured as force per unit area or the maximum load that a material can support without fracture when being stretched, divided by the original cross-sectional area of the material; S_p describes the amount of increase or degree of expansion on the size of the material when wet while W_a relates to the capability of the geotextile to absorb water. Of the three properties, W_a plays a vital role in the selection of geotextile. Geotextile with higher W_a is more preferred as erosion control material since it can absorb and hold more water.

The formula for the determination of T_s and W_a of both the RSM and RSN were adopted from the methods set by the Philippine Standard Association (PhilSA) of 1980. On the other hand, measurement of thickness of rice straw mat and rice straw net was undertaken before and after soaking in tap water at room temperature for 24 hours using a caliper. Measurement of each property was done in three trials.

Swelling Percentage (S_p) was computed using Eq. (1):

$$S_p = [(df - di)/di]100 \quad (1)$$

where: S_p = swelling percentage, %
di = initial thickness, mm
df = final thickness, mm

Water absorption (W_a) was calculated using Eq. (2):

$$W_a = [(wf - wi)/wi]100 \quad (2)$$

where: W_a = water absorption, %
wi = initial weight, g
wf = final weight, g

The physical properties and technical specifications of the developed RSGT were compared to the commercial coco-coir geotextile based on the criteria for geotextile as erosion control material set by the Department of Public Works and Highways (DPWH).

Life Span of the Rice Straw Geotextile

Rice straw mat and net were subjected into actual field condition to determine its life span as ground cover. Life span refers to the life expectancy or length of serviceable life of the RSGT when exposed in adverse weather condition as surface cover. Before the onset of rainy season, samples of RSM and RSN geotextiles were laid out on the side slope of a mountain as ground cover and allowed to undergo the natural process of degradation.

Life span was determined by means of monthly monitoring starting from the first month of installation and onward. Ocular inspection was undertaken to assess qualitatively the physical appearance and condition of the RSM and RSN.

RESULTS AND DISCUSSION

Two types of rice straw geotextile were developed, namely: RSM and RSN (Figs. 1a and 1b). Rice straw mat is a nonwoven mat. It was prepared using rubber latex as binder. On the other hand, RSN was prepared following the three steps: twining, roping and weaving or netting.

a b

Fig. 1 The developed rice straw geotextile, a) RSM and, b) RSN.

Technical Specifications of Rice Straw Mat and Rice Straw Net

The technical specification of the rice straw mat and net is presented in Table 1. The developed RSM has a thickness (t) of 4.1 mm while RSN has rope diameter (d_r) and twine diameter (d_t) of 7.2 and 3.6 mm, respectively. The rope thickness or diameter of RSN was based on the average thickness of the commercial CCN while RSM was based primarily on the recommended amount of rice straw (6 tons/ha) as mulching material.

The developed RSN had higher mass (m) and density (d) of 1,078 g/sq. m and 0.30 g/cu cm, respectively as compared to RSM with mass of only 641.6 g/sq. m and a density of 0.16 g/cu cm. The higher mass and density of RSN were attributed to its thickness and the manner the rice straw rope was prepared wherein a pair of twine was tightly twisted to form a rope. When twisted, it becomes more dense, and heavier.

The mesh opening of RSN was based on the commercially available CCN. Though it might not be as effective as the RSM in intercepting and dissipating the kinetic energy of falling rain because of the presence of openings, its design is perceived to be more appropriate as ground cover for soil erosion mitigation in combination with hydro-seeding. The mesh openings in between rope serve as spaces for weeds to grow. Further, when laid on the ground as surface cover, these openings in between ropes will act as miniature dams or reservoirs to collect rainwater and trap sediment. As a result, the occurrence of surface runoff and the eventual transport of soil particles downhill will be greatly delayed and reduced.

Table 1 Technical specifications of rice straw geotextile

Item	RSGT**		CCN Geotextile*		
	RSM	RSN	400	700	900
t	4.1	7.2	10	10	10
d_r	n/a	7.2	5	5	5
d_t	n/a	3.6	n/d	n/d	n/d
m	642.6	1,078	400	700	900
d	0.16	0.30	0.11	0.19	0.25
M_s	n/a	2 x 2	2 x 2	2 x 2	2 x 2

t- Thickness, mm
d_r - Diameter of rope, mm
d_t- Diameter of twine, mm
m- Mass, g/sq m
d - Density, g/cu cm
M_s - Mesh size, cm x cm
* - Adopted from DPWH Standard Generic Specification for Coconet Bio-Engineering Solutions, Item 622
** - average of three trials
n/a - not applicable
n/d - no data

Physical Properties of Rice Straw Mat and Rice Straw Net

Table 2 shows the physical properties of the RSM and RSN geotextiles. In terms of water absorption (W_a) capacity, it was noted that RSM absorbed more water at 328.5% of its dry weight while RSN absorbed lesser amount at 167.3% of its dry weight. The relatively higher water absorption capacity of RSM could be attributed to its lower density.

Less dense material tends to absorb more water because it has more void spaces to accommodate greater amount of water. Since RSN is denser, it has lesser void spaces, hence, absorbed lesser amount of water. The capability of geotextile to absorb more water is an important factor to be considered in the selection of erosion control material as ground cover. When water absorption capacity of geotextile is high, more water will be held. When more water is held by a certain geotextile, it greatly helps in delaying the occurrence of surface runoff.

As to swelling percentage (S_p), RSM registered a higher swelling of 17.5% as compared to RSN with only 1.8%. Percent swelling is a property associated with water absorption such that when a certain geotextile has a higher water absorption capacity then it follows that its swelling percentage is also higher and vice versa. As explained earlier, the lesser swelling percentage on RSN was attributed to the nature of preparation of rice straw rope.

Table 2 Physical properties of rice straw geotextile

Item	RSGT		CCN GEOTEXTILE*		
	RSM	RSN	400	700	900
W_a	328.5	167.3	163	146	132
S_p	17.5	1.8	n/d	n/d	n/d
T_s					
dry	1.02	1.95	1.6	1.6	1.6
wet	1.08	2.0	n/d	n/d	n/d

W_a - Water absorption, %
S_p – Swelling percentage, %
T_s - Tensile strength, kN/cm^2
* - Data adopted from DPWH Standard Generic Specification for Coconet Bio-Engineering Solutions, Item 622. Note the CCN data are the standards set by DPWH
- no data

Furthermore, it was observed that both rice straw geotextiles exhibited higher tensile strength (T_s) when wet. Rice straw mat had tensile strength of 1.08 kN/cm^2 when wet while 2.0 kN/cm^2 for RSN. When dry, RSM and RSN had tensile strength of 1.02 and 1.95 kN/cm^2, respectively. It can be noted that water absorption of RSM and RSN as well as tensile strength of RSN exceeded the standard generic specification values set by DPWH for coconet geotextile (Table 2).

The observed increase in the breaking resistance of the rice straw geotextile when wet could be due to the effect of moisture that makes the rice straw fibers more firm, strong and resilient when wet. Moreover, the variation in strength between RSM and RSN was due mainly on the method of preparation.

Although tensile strength has less bearing in influencing erosional effectiveness, this property of geotextile however is very important on the aspect of serviceable life. Life span depends largely on the durability and strength of the material. When the geotextile is durable and strong, then it follows that it can withstand adverse weather condition and can stay longer. Other considerations for tensile strength is whether the material is strong enough so as not to break during the installation process and can be used in very high flow velocity conditions.

Percentage of Ground Cover

Table 3 presents the percentage of ground cover of the rice straw and coco coir geotextiles. It can be noted that RSM had the highest percentage of ground cover (99.16%) followed by RSN (51.8%) and the least was coco coir net (48.9%).

The higher percentage of ground cover for the RSM was due mainly to the method of preparation wherein a mass of individual straw was randomly arranged to form a bonded-rice straw matrix mat with almost no opening. On the other hand, the lower percentage of ground cover for the RSN and CCN was attributed to its physical characteristics as net with a designed mess opening of 2 cm x 2 cm.

Table 3 Percentage of ground cover of rice straw mat, rice straw net and coco coir net

Geo-textile	Area of the Soil Test Box sq cm	Area of Covered surface sq cm	Area with-out Cover sq cm	Covered Surf-ace* %
RSM	800	793.3	6.7	99.1
RSN	800	414.4	385.6	51.8
CCN	800	391.2	408.8	48.9

* - average of three trials

The percentage of ground cover of any geotextile plays a vital role in minimizing soil losses. The greater the percentage of ground covers of geotextiles, the lesser the impact of falling rain to the soil. With greater coverage, it becomes more effective in intercepting and dissipating the kinetic energy of rain drops which is responsible in detaching and splashing away soil particles. In a related study on loosely woven rice straw mat, it was

observed that once runoff occurred, even with good mulching, a certain degree of suspended solids was likely to remain because small particulates in suspension were neither filtered nor deposited easily [8].

Life Span of Rice Straw Mat and Net

Based on the actual field condition, it was observed that RSM and RSN can last up to 3 and 4 months, respectively. After these periods, RSM and RSN started to deteriorate. It should be noted however that by the time RSGTs deteriorated, surface vegetation is already established.

The relatively short life span of rice straw geotextile could be due to its very low lignin content which ranges only from 3-4.4% [9]. Lignin is a complex chemical compound most commonly found in plant tissues making them rigid and woody and is believed to be responsible in slowing down decomposition process. Nevertheless, for immediate surface protection, this seemingly shorter life span of RSM and RSN is just enough to serve its purpose as ground cover to prevent erosion especially when they are utilized in combination with hydro-seeding. It was reported that short-term erosion control is frequently achieved by using erosion control blankets, spray-emulsion products, and straw mulches while long-term control is best done by well-established vegetation [10].

In some aspect, the early degradation of RSGT can be advantageous. When decomposed and converted into organic fertilizer, it will serve as plant nutrient to boost the growth and development of surface vegetation.

CONCLUSION

Rice straw is a potential biomass material that can be utilized in the production of geotextile products like rice straw mat and rice straw net because it is abundant and readily available, biodegrable and environment-friendly. When converted into geotextile, rice straw will enhance its economic value and environmental importance.

Rice straw mat has higher water absorption capacity of 328.5% and swelling thickness of 17.5% than rice straw net with absorption capacity of 167.3% and swelling thickness of 1.8%. As to tensile strength RSN has higher with 2.0 kN/cm^2 when wet and 1.95 kN/cm^2 when dry as compared to RSM with 1.08 kN/cm^2 and 1.02 kN/cm^2 when wet and dry, respectively.

Based on the observed physical properties and characteristics, both RSM and RSN are highly recommended as surface cover for soil erosion mitigation. In addition, it exceeded the standard generic specification values set by DPWH for coconet geotextile. However, a follow-up study under actual field condition should be undertaken using RSM and RSN as ground cover for soil erosion control vis-à-vis other erosion control materials being used by DPWH.

ACKNOWLEDGEMENT

The financial and technical support from the Department of Science and Technology (DOST) through the Engineering Research and Development for Technology (ERDT) Scholarship Program are gratefully acknowledged.

REFERENCES

[1] Elauria JC, Quejas RET, Cabrera MI, Liganor RV, Bhattacharya SC and Predicala NIJ. 1999. Biomass as energy source in the Philippines. RERIC International Energy Journal: Vol. 21, No. 1, June 1999.

[2] Gadde B, Menke C, and Wassmann R. 2009. Rice straw as a renewable energy source in India, Thailand, and the Philippines: Overall potential and limitations for energy contribution and greenhouse gas mitigation. Retrieved August 8, 2011 from http://wenku.baidu.com/view/35743feb998fcc22bcd10d52.html.

[3] Magcale-Macandog DB. 2007. Methane emission from major rice ecosystem in Asia. Paper presented during the 4th Workshop on GHG Inventory in Asia (WGIA), Jakarta Indonesia, February 13-14, 2007.

[4] Smets T. 2009. Effectiveness of biological geotextiles in reducing runoff and soil loss under different environmental conditions using laboratory and field plot data. Geophysical Research Abstracts,Vol. 11, EGU2009-1564-1, 2009. EGU General Assembly 2009.

[5] http://www.da.gov.ph/tips/garlic.html. Garlic. Retrieved, May 18, 2011.

[6] Sutherland RA and Ziegler AD. 2007. Effectiveness of coir-based rolled erosion control systems in reducing sediment transport from hill slopes. Geomorphology Laboratory, Department of Geography, University of Hawaii,2424 Maile Way, Honolulu, HI 96822-2223, USA.

[7] Angara EV, Escueta SC, Rotaquio EL, Barrogo LH, Gallego RJ, Resueño MA, Agbayani EA, Teňoso KD and Sagabain KJDL. 2010. Field testing of bio-engineering techniques using geo-textile and bio-logs to mitigate soil slope erosion in Maria Aurora National Highway. ASCOT Research International Journal, Volume 3, December 2010. Aurora State College of Technology, Baler Aurora 3200 Philippines.

[8] Won CH, Choi YH, Shin MH, Lim KJ, Choi JD. Effects of rice straw mats on runoff and sediment discharge in a laboratory rainfall simulation. Retrieved, August 10, 2012 from http://dx.doi.org/10.1016/j.geoderma.2012.06.017.

[9] http://www.carrb.com/94rpt/ RiceStraw.htm).

[10] Benik SR, Wilson BN, Biesboer DD, Hansen B and Stenlund D. 2003. Performance of erosion control products on a highway embankment. Transaction of the ASAE, 46(4): 1113-1119.

First International Conference on Science, Engineering & Environment,
Tsu City, Mie, Japan, Nov.19-21, 2015, ISBN: 978-4-9905958-5-2 C3051

THE SEVERAL TYPES OF INVOLUNTARY BODY MOVEMENT CAUSED BY THE ELECTROMAGNETIC WAVES EMITTED BY CELL PHONES

Yoshiro Fujii
Shin Kobe Dental Clinic, Hyogo, Japan

ABSTRACT

Cell phone use has increased considerably in recent years. These devices have facilitated communication on a global scale. However, there have been a number of reports of health problems related to the electromagnetic waves emitted by such electronic devices. A long list of both general and severe symptoms, including headaches, fatigue, tinnitus, dizziness, memory loss, irregular heartbeat, and whole-body skin lesions, have been reported. These are reportedly associated with the condition known as electromagnetic hypersensitivity (EHS). The subjects' abnormal involuntary body movements, caused by electromagnetic waves emitted by cell phones are sometimes observed. Such movements can lead to a severe accident, e.g. falling from a platform. The movements are classified into several types, i.e. the subject's leaning away from the cell phones, subject's leaning close to them, subject's spine bending and subject's body moving right and left, or back and forth. The underlying mechanism remains unknown but decreased blood flow within the brain has been proposed. The author has often reported prevention of such symptoms using dental techniques, e.g. replacing the dental materials which attract harmful electromagnetic waves with safer materials. However, the reasons why these treatments were so successful remain unknown. The mechanism behind such involuntary movement should be researched immediately, and the regulation of using electronic devices should be considered to prevent severe issues e.g. falling from train platforms onto the rails.

Keywords: Cell phone, Personal computer, Electromagnetic waves, Electromagnetic hypersensitivity, Involuntary body movement

INTRODUCTION

With the development of a technology-based society, the opportunity to use electronic devices, such as cell phones and personal computers, has become increasingly widespread and has enabled communication on a global scale [1, 2]. However, there have been many reports pertaining to health problems resulting from the electromagnetic waves emitted by such electronic devices [3-10]. Physically unpleasant symptoms including headache, fatigue, tinnitus, dizziness, memory loss, irregular heartbeat, and whole-body skin lesions caused by exposure to electromagnetic waves are recognized as electromagnetic hypersensitivity (EHS) [11-15]. The author reported that scoliosis could develop by exposure to electromagnetic waves [16]. The author also reported how a subject's involuntary movements, caused by electromagnetic waves, were treated using a gold alloy dental inlay [17]. In current report, the author has tried to classify the subjects' abnormal involuntary body movements, caused by electromagnetic waves emitted by an active cell phone.

METHOD

One hundred subjects (20 male and 80 female) were seen in the author's dental clinic. The subjects were irradiated by electromagnetic waves emitted by a cell phone which the subject had. If the subject shows an involuntary body movement, it will be classified.

Result

15 subjects out of 100 showed an involuntary body movement. They could be classified into 5 different types (Type 1~5). Type 1 defined as the subject's leaning away from the electronic devices (Figure 1), Type 2 as subject's leaning close to them (Fig.2), Type 3 as subject's spine bending (Fig.3), and Type 4 as subject's body moving right and left, or back and forth (Fig. 4,5).

10 subjects (66.7%) showed Type 1, one subject showed Type 2 (6.7%), one subject showed Type 3 (6.7%), and two subjects showed Type 4 (13.3%). One subject (6.7%) showed irregular movement, for example, sometimes showed Type 1 but sometimes Type 2, which was defined as Type 5. The difference between the sexes wasn't clear.

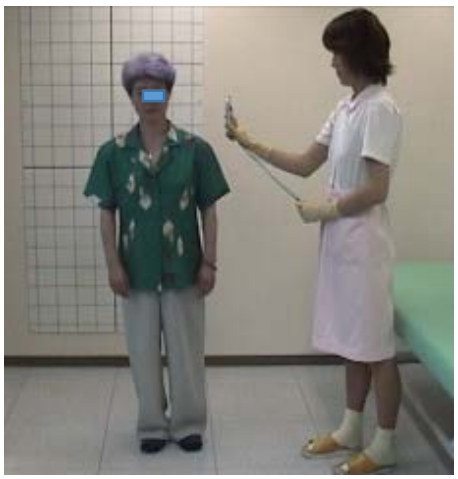

Fig.1 Type 1 defined as the subject's leaning away from the cell phone.

Fig.2 Type 2 as subject's leaning close to the cell phone.

Fig.3 Type 3 as subject's spine bending (The cell phone is not shown in this picture. There is an active cell phone about 2m away from the left side of the subject.

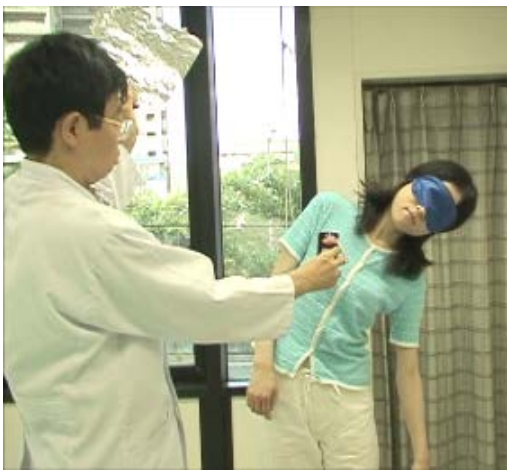

Fig.4a

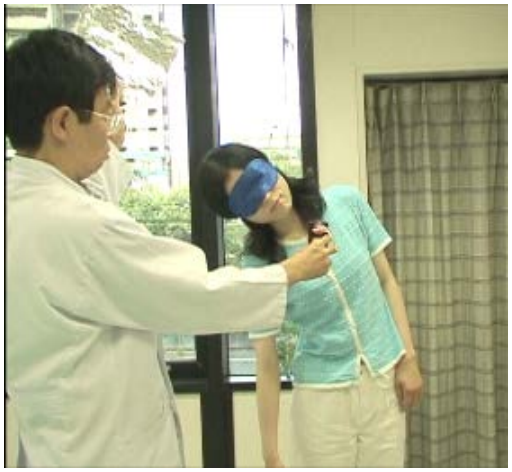

Fig.4b

Fig.4a, b Type 4 as subject's body moving right and left, or forth and back

Discussion

15% of subjects showed an involuntary movement. It seemed to be one of the symptoms of EHS. The underlying mechanism remains unknown so further studies are required but decreased blood flow within the brain has been proposed [4]. The current result shows that 15 people out of 100 (15.0%) showed an involuntary movement. The group which showed involuntary body movement was able to be classified to Type 1 (6.7%), Type 2 (6.7%), Type 3 (6.7%), Type 4 (13.3%), and Type 5 (6.7%) respectively. However, confidence over such ratios are debatable because the cell phones which were used in this experiment

were varied, so electromagnetic waves emitted by the cell phones were also varied. It's different in the strength of the radio wave and the quality depending on the models of the cell phones. Moreover, the environment of electromagnetic waves also changes based on the place where the experiment is performed and the position of the corresponding relay station. The number of subjects was also small. More research is required. Such movements sometimes occur in front of personal computers or other electronic devices. Although, there are a lot of indefinite factors for this field, the mechanism behind such involuntary movement should be researched immediately, and the regulation of using electronic devices should be considered to prevent severe issues e.g. falling from train platform.

CONCLUSION

Involuntary movement due to the electromagnetic waves emitted by cell phones classified 4 types mainly. Although the reason why such involuntary movements occur has not clarified yet, revealing it may be very important to research the mechanism of EHS. The regulation of using electronic devices should be considered to prevent severe issues e.g. falling from train platform.

REFERENCES

[1] Geser, H. Towards a Sociological Theory of the Mobile Phone, Release 3.0, University of Zurich, 2004,(http://socio.ch/mobile/t_geser1.htm/).

[2] Van Dijk, J. and Hacker, K. The Digital Divide as a Complex and Dynamic Phenomenon, The Information Society, 19, 2003, pp. 315-326.

[3]http://www.holisticdentistry.net/blog/2013/07/entry_242/ (last accessed, 2 May 2014).

[4] Aalto, S., Haarala, C., Brück, A., Sipilä, H., Hämäläinen, H. and Rinne, J.O. Mobile Phone Affects Cerebral Blood Flow in Humans. J Cereb Blood Flow Metab, 26, 2006, pp. 885-900.

[5] Feychting, M., Jonsson, F., Pedersen, N.L. and Ahlbom, A. Occupational Magnetic Field Exposure and Neurodegenerative Disease. Epidemiology, 14, 2003, pp. 413-419.

[6] Håkansson, N., Gustavsson, P., Johansen, C. and Floderus, B. Neurodegenerative Diseases in Welders and Other Workers Exposed to High Levels of Magnetic Fields. Epidemiology, 14, 2003, pp. 420-426.

[7] Ahlbom, A. Neurodegenerative Diseases, Suicide and Depressive Symptoms in Relation to EMF. Bioelectromagnetics, Suppl 5, 2001, pp.132-143.

[8] Linet, M.S., Hatch, E.E., Kleinerman, R.A., Robison, L.L., Kaune, W.T., Friedman, D.R., Severson, R.K., Haines, C.M., Hartsock, C.T., Niwa, S., Wacholder, S. and Tarone, R.E. Residential Exposure to Magnetic Fields and Acute Lymphoblastic Leukemia in Children. N Engl J Med, 337, 1997, pp. 1-7.

[9] Röösli, M., Moser, M., Baldinini, Y., Meier, M. and Braun-Fahrländer, C. Symptoms of ill health ascribed to electromagnetic field exposure--a questionnaire survey. Int J Hyg Environ Health, 207, 2007, pp. 141-150.

[10] Edelstyn, N. and Oldershaw, A. The acute effects of exposure to the electromagnetic field emitted by mobile phones on human attention. Neuroreport, 13, 2002, pp. 119-121.

[11] Rea, W., Pan, Y., Yenyves, E., Sujisawa, I., Suyama, H., Samadi, N. and Ross, G. Electromagnetic Field Sensitivity. J Bioelectricity, 10, 1991, pp.241-256.

[12] Rubin, G.J., Das Munshi, J. and Wessely, S. (2005) Electromagnetic Hypersensitivity: A Systematic Review of Provocation Studies. Psychosom Med, 67, 224-232.

[13] Rubin, G.J., Das Munshi, J. and Wessely, S. A Systematic Review of Treatments for Electromagnetic Hypersensitivity. Psychother Psychosom, 75, 2006, 12-18.

[14] Norbert, L. Electromagnetic Hypersensitivity. Advances in Electromagnetic Fields in Living Systems, 5, 2009, pp. 167-197.

[15] Kimata, H. Microwave Radiation from Cellular Phones Increases Allergen-specific IgE Production. Allergy, 60, 2005, pp. 838-839.

[16] Fujii, Y. Do dental implants cause scoliosis?: A case report. Personalized Medicine Universe, 1, 2012, pp. 79-80.

[17] Fujii, Y. Gold alloy dental inlay for preventing involuntary body movements caused by electromagnetic waves emitted by a cell phone. OJAPr, 2, 2014,37-43.

First International Conference on Science, Engineering & Environment,
Tsu City, Mie, Japan, Nov.19-21, 2015, ISBN: 978-4-9905958-5-2 C3051

STATE OF AMBIENT AIR QUALITY IN MARRAKECH CITY (MOROCCO) OVER THE PERIOD 2009 – 2012

Manal Inchaouh[1]; Mohamed Tahiri[1;] Bouchra El Johra[2] and Rachid Abboubi[2]
[1] Faculty of Science Ain chock; University Hassan II of Casablanca; Morocco;
[2] National directorate of Meteorology of Casablanca; Morocco

ABSTRACT

The strong urbanization and the socio-economic development of a city causes potential effects on its environment ; Our study focuses on air quality in the city of Marrakech, it's the first integral study done for that city. We will give a synthesis of air pollutants measurement results; conducted in the city over the period 2009-2012; in order to determine the spatial and temporal variations of major pollutants (NO_x; SO_2; O_3; PM_{10}) measured at the air quality monitoring stations; as well as weather parameters which are essential to understand the dispersion of the pollution. The results showed that the NO_x levels are depending on the local emissions density and the nature of the road network. The concentrations of SO_2 are low compared to the Emission Limit values (ELV) admitted; this is owing to the weak industrial activity and the use of less polluting fuel (350 ppm diesel).As of the particles (PM_{10}); specially related to traffic; industry and natural sources; their levels exceed the thresholds limits on all sites. The city is also subject to photochemical pollution mainly due to its geographical location (strong sunlight). During the spring and summer;the concentrations of O_3 reachs alarming levels with significant overshoot periods for the permitted limits. This study allows us to establish a first approach of the state of Marrakech air quality without assessing the contribution of each source; which requires further study to identify the phenomenon.

Keywords: Atmospheric Pollution; Marrakech City; Air Quality; Atmo-Maroc Index

INTRODUCTION

Man introduced substances in the atmosphere (gas or dust) that create a disturbance in the chemical balance of the air components. Air pollution is a sensitive issue; since it affects the health; the environment and economic interests. Morocco's socio-economic development has resulted from the increase of its gross domestic product (GDP); population growth and modernization and extension of cities that required the increase of the industrial fabric; sustained energy consumption and intensification of transport. This situation has created serious impacts on the air quality. Air pollution is also a complex issue; firstly; the various pollutants have heterogeneous sources ; different effects and requires different solutions and; secondly; their sources and locations are inherently variable. Marrakech city known for its pleasant climate; begins to suffer from the problem of air pollution; the emissions generated on the main roads; by industrie or craft units; is increasingly feeling ; pollution peaks are often recorded in some neighborhoods. This study aims to assess the overall state of air quality in Marrakech and to identify the main pollutants responsible for its deterioration.

STUDY AREA

Marrakech city (31° 37 'North; 8° 02' West) ; the fourth largest city and first tourist destination in Morocco (official population of 1070838 people in 2010); is located in the central Haouz plain bounded by the mountains of the High Atlas in the south; the province of Safi north; Chichaoua and Safi in the east and El Kelaa des Sraghna west. The area represents uniform moderate altitude topography; the only reliefs are formed by the hills of Gueliz and Koudiat Al Abid north. The average altitude is at 465 m. the climate is semi-arid; Annual average of temperature is 22°C with ranges of -7°C and 46.6°C observed over several years. The height of annual rainfall is estimated at 240 mm with an uneven distribution (related to reliefs). Relative humidity is of 73% in January and 33% in July and may cancel during this month when dry winds blow. winds are usually calm; from the west and northwest. In summer ; there is drying winds Chergui and Sirocco from the east and the south; with an annual cumul of about 39 days centered on July.Known for its golf courses; parks and monuments; the city experience rapid industrial expansion and population growth due to rural exodus. The economy of the region is mainly based on the agriculture and livestock; tourism (550000 tourists in January 2013); craft (45% of national handicrafts exports); industrial sector witch is mainly composed of agro-industries; chemical; Para chemical and processing industries.

Consumption of fuels

Table 1 and 2 represents annual consumption of

different fuels and the volumes distributed by the service stations in Marrakech city .

Table 1 Annual consumption of fuel in Marrakech

fuels	Annual consumption
propane	5;29 Ktoe*
butane	64 Ktoe
fuel oil	58;6 Ktoe
wood	360 000 T

Source: Ministry of Energy and Mines (MEM) 2009
*Ktoe: Thousand tons of oil equivalents

Table 2 Volumes distributed by service stations

consumption (m^3)	Afriquia	Total	Shell	ZIZ	Petrom	Total (m^3)
Unleaded	15329	9072	9166	96	3650	37313
Gasoil	40800	24408	26560	1940	13381	107089

Source: Ministry of Energy and Mines (MEM) 2009

Road infrastructures

Table 3 Road network in Marrakech

National roads	Regional roads	Provincial roads
152;706	67;786	313;715

Source: Regional Directorate of Public Works

Table 4 Distribution of vehicles by type

Type of Vehicle	Number
motorcycle	236
Passenger car	6104
Commercial vehicles	2486

Source: Regional transport Delegation

MATERIALS AND METHODS

Monitoring network Description

Air quality monitoring network in Marrakech has three permanent fixed stations; ST_1 (Jamae Lafnae) located in the center of the town; ST_2 (Mhamid) located at about 2km from Marrakech-Menara airport and ST_3 (Daoudiat) located in a residential area. These stations are equipped with automatic physical-chemical analyzers enable to provid real-time concentrations of pollutants in hourly time steps. The information is then transmitted to the central station and processed in the air quality data base through the XR software.

Pollutants studied

To assess the impact of emissions on air quality; we consider the following pollutants: NO_2; SO_2; PM_{10} and O_3; these latter are regulated by the decree setting down the air quality standards and air monitoring arrangements. The developments of pollutants will be presented by temporal profiles for each pollutant and the air quality index (Atmo-Maroc index) for each site for the period 2009-2012.

RESULTS AND DISCUSSIONS

Meteorological data

The dispersion of pollutants depends on weather conditions. The strongest winds favor the dispersion of pollutants and low winds favor their accumulation at local levels [1]. Figure 1 represents the average of wind frequency and speed over the period 2009-2012. Wind roses shows a clear predominance of westerly winds with a high speed (above 9 m/s); which are the most dispersive winds; followed by medium-speed winds (4-9 m/s) and moderate-speed winds (2-4 m/s) mainly from the east and which promotes the accumulation of pollutants.

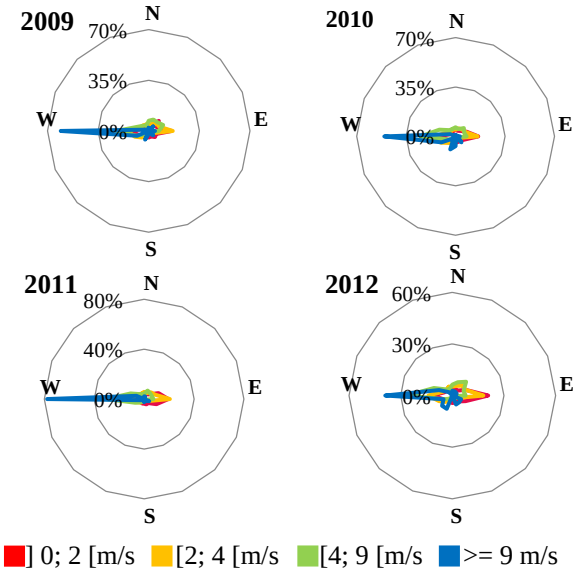

Fig. 1 Wind roses of Marrakech (2009 – 2012)

Temperature influences the vertical dispersion of pollutants. When the air in the ground becomes colder than at altitude then it is a "thermal inversion" situation; cold air remains trapped under the warm air mass that form an atmospheric cover and prevents vertical dispersion of pollutants and favors their concentration near the ground [2]. Temperature also affects the chemistry of pollutants; cold reduces the volatility of some gas and the summer heat promotes the photochemical formation of ozone . humidity plays an important role in the formation process of some pollutants such sulfuric and nitric acids (acid mist) and their elimination (wet deposition).a study [4] showed that the highest concentrations of ions SO_4^{2-}; NO^{3-}; NH^{4+} and H^+ are observed during high humidity periods. Figure 2

shows the monthly average evolution of temperature and relative humidity; overall sites; the temperature increases gradually to a maximum during the summer while relative humidity decrease. The highest values are shown in Daoudiat site given to its geographical nature (elevation of 450 m).

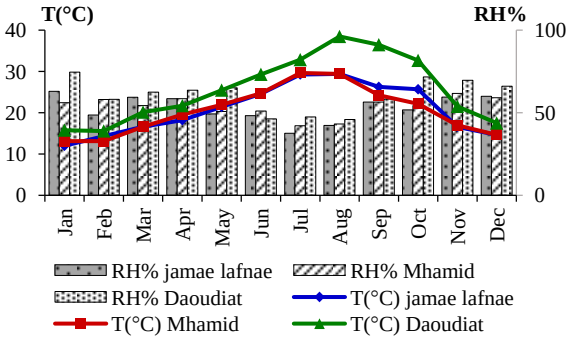

Fig. 2 Monthly mean of Temperature and Relative Humidity for the period (2009- 2012)

Precipitation allows atmospheric leaching of soluble particles and gases by folding them down to the ground and diminishing the concentrations of pollutants [3]. When rainfalls are short and intense; leaching effects is reversible and the levels of pollutants increase rapidly when the rain stops. However; when it rains for several hours this effects is quite significant and pollutant levels remain low long time before recovering. The annual accumulation (Fig.3) experienced a significant drop (about 40%) in 2012 compared to 2009 .

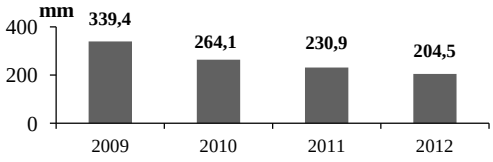

Fig. 3 Total annual Precipitation

Pollutants data analysis

Nitrogen oxides (NO_x)

NO_x includes nitrogen dioxide (NO_2) and monoxide (NO); these precursors of photochemical smog comes mainly from combustion processes (industry; transport…); it is generally accepted that 70-75% of emissions in urban areas comes from vehicles [5]. Near the emission sources the concentrations of NO are larger than those of NO_2 but NO is rapidly oxidized into NO_2 here the emissions are expressed as NO_2-equivalent. Figure 4 (a) and (b) demonstrates that the situation has evolved during the study period. In Jamae lafnae sites directly affected by vehicle emissions and Mhamid affected by Marrakech-Menara Airport traffic; annual levels have increased since 2009; local weather conditions; especially in winter; may explain the most significant changes. limit values for health protection in Mhamid and the annual limit value P98 (200 ug / m3) in Jamae lafnae are exceeded in 2012.The Daoudiat site is the least polluted site given its distance from major roads.

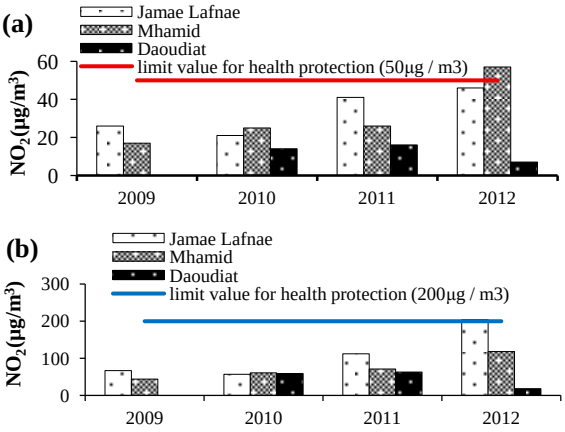

Fig. 4 NO_2 - Annual trends of **(a)** hourly averages and **(b)** 98 percentile of hourly average

In normal situations; NO_2 levels increases during the cold season; This is due to many emissions (heating + frequent use of vehicles). The seasonal averages (Fig. 5) are significantly higher during the winter; with low and variable winds. And also during the summer because of the importance of traffic and tourist activities over the area; associated with the increase of temperature and solar radiations that promotes NO_2 formation.

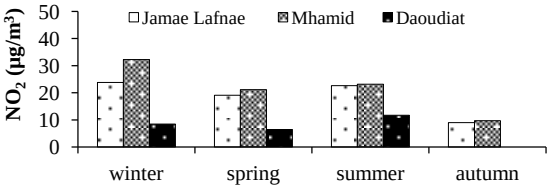

Fig.5 NO_2 - Seasonal averages (2009-2012)

Figures 6 and 7 shows the weekly and daily profiles of NO_2. levels are rather higher on weekdays than weekends with pollution tip in midweek. On the daily profile; the morning peak observed between 8 and 10am is characteristic of the human activity resumption. The decline in the afternoon could be explained by the formation of ozone from the interaction of NO_2 with solar radiations. A second peak is observed between 7 and 9pm corresponding to the evening returns.

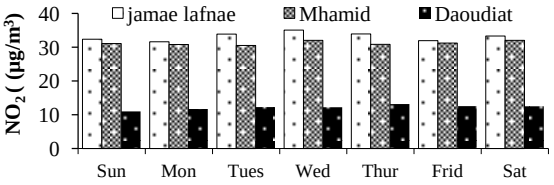

Fig.6 NO_2 - Weekly profil (2009-2012).

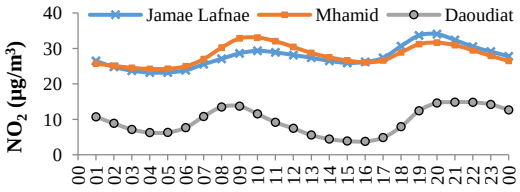

Fig.7 NO_2 - Daily profil (2009-2012)

Sulfur dioxide (SO_2)

SO_2 is mainly emitted by using sulfur-containing fossil fuels and some industrial processes. Emissions of SO_2 in fossil fuels burning represent around 70 to 80 million tons per year at the world level [6]. This gas is transformed in contact with air humidity to sulfuric acid and contributs to acidification; depletion of natural environment and deterioration of buildings. Figure 9 (a) and (b) represent the annual evolution of SO_2; levels tends to increase since 2009 over all measurement sites but remain relatively low compared to the regulatory thresholds.

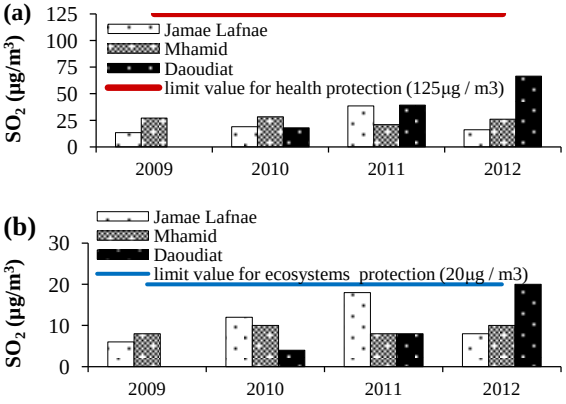

Fig. 8 SO_2 - Annual trends of **(a)** hourly averages and **(b)** 99;2 percentile of hourly average

The levels of SO_2 vary with the seasons; seasonal profil (Fig.9) show increases levels during the cold season. episodes of high concentrations are usually met in winter ;firstly; the weather conditions are less dispersive and; secondly; energy needs and therefore emissions are higher (domestic heating…).

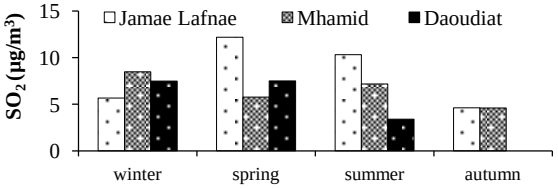

Fig.9 SO_2 - Seasonal averages (2009-2012)

On the weekly profile (fig.10);a slight decrease is observed during the weekend similarly to the reduction of traffic.The daily profile (fig.11) reveals morning and evening increases related to human activity. morning peak is observed between 8 to 10 am and a second strongest peak between 8 and 9pm.

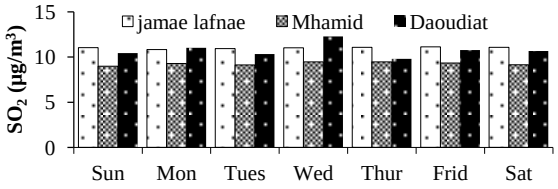

Fig.10 SO_2 - weekly profil (2009-2012)

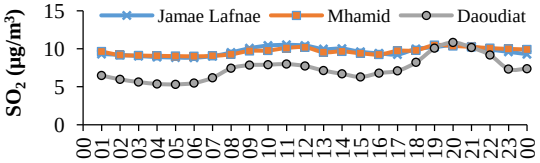

Fig.11 SO_2 - Daily profil (2009-2012)

Ozone O_3

O_3 is a secondary pollutant that depends in its formation and evolution on both of the state of the original primary pollution in the atmosphere and ambient weather conditions [2]; O_3 is formed from precursors during the movement of polluted air masses under the effect of solar radiations; it follows that in general; the highest values are not recorded in areas where primary pollutants are emitted (cities and industrial areas); but in the surrounding and the near rural areas and downwind of agglomerations [7;8]. This pollutant is harmful for the health it causes in high concentrations inflammation and bronchial hyperreactivity ;irritation of nose and throat usually occur; accompanied by breathing difficulty. Eye irritation are also observed. Sensitive subjects (children; chronic bronchitis; asthma ...) are more sensitive to ozone pollution [9] . Annual average of O_3 are presented in Figure 12.the levels decrease gradually in 2010 and 2011; the year 2012 saw a significant increase; this is mainly due to climatic variations; particularly to sunlight (high temperatures). Table 6 presents; in chronological order; overtaking reference values for O_3.

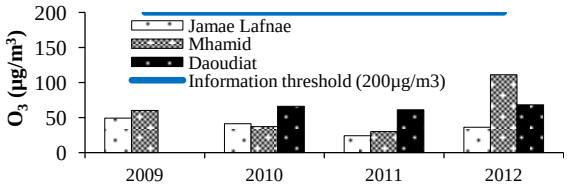

Fig. 12 O_3 - Annual trends (2009-2012)

Tab 6. Number of exceedences of regulatory values

	Number of days exceeding averages on 8 hours **(1)**			Number of 3 consecutive days exceeding the daily average **(2)**		
	jamae lafnae	**Mhamid**	**Daoudiat**	**jamae lafnae**	**Mhamid**	**Daoudiat**
2009	**8**	**42**	**-**	**14**	**62**	**-**
2010	**4**	**1**	**58**	**14**	**20**	**58**
2011	**-**	**-**	**7**	**-**	**20**	**91**
2012	**12**	**118**	**26**	**11**	**112**	**54**

(1) Limit value for health protection: 110µg / m^3
(2) Limit value for vegetation protection : 65µg / m^3

O_3 levels depends on the weather conditions (temperature and irradiation; prolonged sunshine; low humidity and wind speed).these conditions are met in summer. Figure 13 shows that the levels were higher during the warm season. O_3 has a life span of a few days; so it can be transported far from its production area; during the weekend it accumulates significantly in the lower troposphere where it reaches a maximum of about 10% more than during weekdays. This phenomenon; known under the term "sunday effect" was already mentioned in some studies; including one on Long Beach in Los Angeles [10].O_3 levels in air layers near the ground is always determined by the formation-degradation process.Figures 14 and 15 illustrates the weekly and daily profils ; the week is marked by an increase of O_3 during the weekend while the daily profile shows a single typical peak as "bell" in the afternoon (around 2 pm) that persists at high levels for several hours before decreasing at 5 pm.diurnal evolution is generally less pronounced because of the absence of night degradation processes.

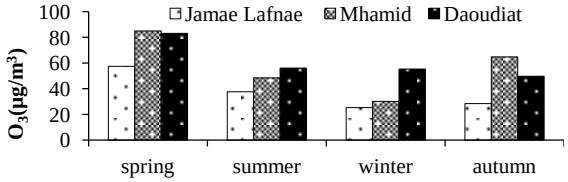

Fig.13 O_3 - Seasonal averages (2009-2012)

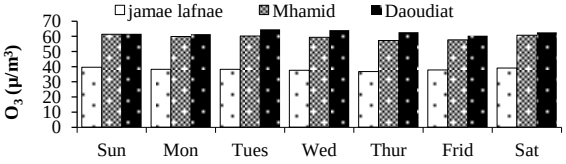

Fig.14 O_3 - weekly profil (2009-2012)

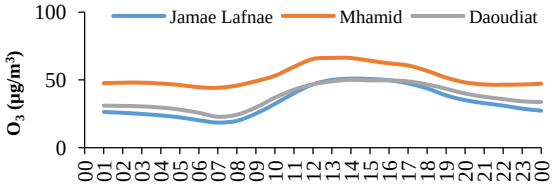

Fig.15 O_3 - Daily profile (2009-2012)

Particulate matter PM_{10}

PM_{10} comes mainly from combustion.in urban areas it comes from traffic (emissions ; tires wear..) and domestic heating; their levels are also linked to physical mechanisms such as resuspension (strong wind) or accumulation during stable weather periods. in Marrakech; the resuspension is responsible for a large share of PM_{10} emissions owing to the dry and windy atmosphere of the area. Due to their small size; fine particles are able to penetrate deep into the respiratory tract and reach the lungs.Short exposures may cause coughing; bronchial irritation and inflammation. particles can also affect lung function and suddenly worsen diseases such as asthma and cardiovascular events [11]. Annual average (Fig.16) shows a very high values over all sites. limit value for health protection is greatly exceeded.

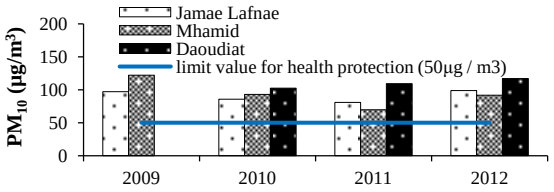

Fig. 16 PM_{10} - Annual trends of 99;2 percentile of hourly average

Seasonal evolution of PM_{10} (Fig.17) shows a great difference between the cold and warm seasons .in winter the rain allows the leaching of the atmosphere causing a drop of levels; while the dry and hot summer favors the accumulation and formation of secondary particles. This often results in reduced visibility; the atmosphere becoming more "opaque". Wind also promotes the dispersion of the pollution but depending on its strength; can recover the suspended particles in the air. weekly profile (Fig.18) is characterized by a decline on the weekend related to the reduction of traffic ;an advanced pollution observed on Thursday.

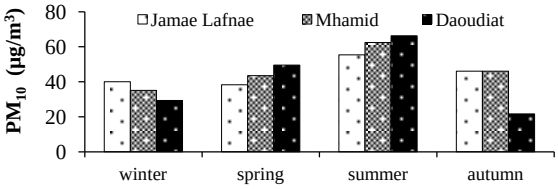

Fig. 17 PM_{10} - Seasonal averages (2009-2012)

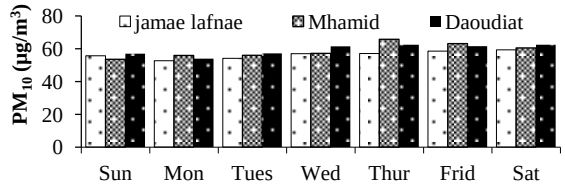

Fig. 18 PM_{10} - weekly profil of (2009-2012)

The daily profile (Fig.19) is marked by a "double-hump curve"; morning peak (from 9 to 11am) and evening peak (from 6 to 8pm). At Daoudiat site the peaks are shifted by about 2 hours from those of other sites; it seems that other sources of pollution than traffic are attributable to this observation (Industrial activity in surrounding areas).

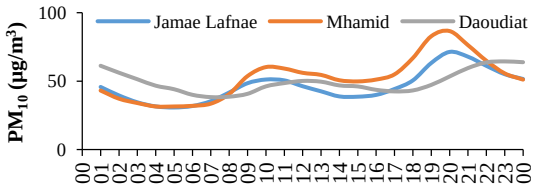

Fig. 19 PM_{10} - weekly profil (2009-2012)

Atmo-Maroc Index

Air pollution can result from a several substances; what makes complex the issue and the understanding of synthetic information .air quality Index is a function that transforms the air quality data (expressed as concentrations of several pollutants measured over different time; in different stations) in a single value and generally single dimensionless which represents or characterizes the air quality of a homogeneous area [12]. Atmo-Maroc Index is an air quality indicator developed by the National directorate of Meteorology in order to have a synthetic information of air pollution in towns with over 100 000 inhabs. This index is compiled from the daily concentrations of four typical pollutants for air pollution phenomenon: SO_2; NO_2; O_3 and PM_{10}. For each of the above pollutants; an air quality sub-index (from 1 to 10) is daily calculated from the recorded data.

Tab 7. sub-indices Scale for Atmo-Maroc Index

index	1	2 ; 3	4 ; 5	6 ; 7	8 ; 9	10
quality	very good	good	mean	mediocre	bad	very Bad

General trends

Figure 20 represent the average trends of the air quality index for each site in 2012.

Air Quality in Jamae Lafnae is generally good (over 60%);in Mhamid the index reflect the observations made on the various pollutants (PM_{10} and NO_2). The year 2012 recorded much higher concentrations of NO_2 than normal and induces bad air quality (37%). at Daoudiat air quality is mean and sometimes bad because of the high levels of particulates and photochemical pollution (O_3).

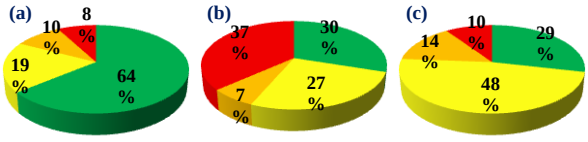

Fig 20. Air quality indices for (a) jamae lafnae ;(b) Mhamid and (c) Daoudiat in 2012

CONCLUSION

The present study has highlighted the pollutants mainly related to traffic.The air quality can be described as generally good for certain pollution indicators (NO_2 and SO_2), but remains worrying for PM_{10} and O_3, although the traffic is not the only parameter that may affect the pollutant concentrations, it still seems to have a major impact since the difference between measured values in the three measurement sites. Temporal trends also shows this influence especially on daily profiles where departure and returns hours are marked overall sites. This shows that the surroundings areas are subject to a very importante road activity both in winter (domestic traffic) than in summer (tourist traffic).The results of this study highlights on the agglomeration scale, the reciprocity of background pollution and traffic proximity phenomena particularly due to the density of the structuring road network. It also highlights the geographical areas where efforts shall be particularly made to clip the higher levels of the air pollution.

References

[1] Diaf, N., Bouchaour, M., Merad, L., Benyoucef, B., 2003. "Parameters affecting the dispersion of gaseous pollutants". Tlemcen University Rev. Energ. Ren ICPWE: (2003) pp.139-142.

[2] El MELKI, Taoufik. "Thermal inversions and air pollutant concentrations in ground-level base of Tunis" (2007): pp.105-129.

[3] Arnaud Q, Leaching of the atmosphere by rain: microphysical approach. Diss. Blaise Pascal University -Clermont-Ferrand II, (2012).

[4] Munger, William J., Jacob, Daniel J., Waldman, Jed M., et al. Fog water chemistry in an urban atmosphere. Journal of Geophysical Research: Oceans (1978-2012), 1983,88.C9,pp.5109-5121.

[5] Lal, Shishir, and R. S. Patil. "Monitoring of atmospheric behavior of NO_x from vehicular traffic." Environmental monitoring and assessment 68.1 (2001): pp.37-50.

[6] Guy L."Impact of fossil energies on the environment". 5. Villette Meetings "energy: a concept of the uses of the issues", (1994), Paris.

[7] Ballaman, Richard. "The Transport and Ozone Pollution as in Switzerland». Science of the total environment 134.1 (1993): pp.103-115.

[8] Brönnimann, Stefan, and Urs Neu. "Weekend-weekday differences of near-surface ozone concentrations in Switzerland for different meteorological conditions." Atmospheric Environment 31.8 (1997): pp.1127-1135.

[9] Doumont, D., and F. Libion. "Health impact of different pollutants: what effects on short, medium and long term?" RESO-UCL Unit of Health Education (2006).

[10] Elkus, Barbara, and Kent R. Wilson. "Photochemical air pollution: weekend-weekday differences."Atmospheric environment (1967) 11.6 (1977): pp509-515.

[11] Reddy, M. K., & Sumathi, M."Air quality status of respirable particulate levels at selected traffic junctions along the section of lateral highway in Hyderabad." Journal of Environmental Protection 2.05 (2011): p.662.

[12] Garcia, J., Colosio, J., & Jamet, P. "Air quality indexes", Ecole des Mines de Paris, (2001)

First International Conference on Science, Engineering & Environment,
Tsu City, Mie, Japan, Nov.19-21, 2015, ISBN: 978-4-9905958-5-2 C3051

STUDY ON REMOVAL OF RADIOACTIVE MATERIAL FROM MARINE AND LAKE MUD

Keiichiro Shibata[1], Hidenori Yoshida[2] and Naomichi Matsumoto[3]
[1]Faculty of technology, Kagawa University, Japan; [2,3] Kagawa University, Japan

ABSTRACT

The serious nuclear disaster in the Fukushima Daiichi nuclear energy plant of the Tokyo Electricity Power Company was occurred by the tsunami which was caused by the Great East Japan Earthquake on March 11, 2011. The radioactive materials emitted by the disaster were widely diffused in and around Fukushima prefecture including the Pacific Ocean by wind, rain and a flow of river. It can't be always said that there is no risk of the condensation of radioactive materials in human's body by ecological chain if fish take in radiation in the ocean contaminated by the radioactive materials. However the effective decontamination methods of the radioactive materials are not developed and the decontamination is less-advanced. The establishment of a new decontamination method is urgent need and indispensable in light of disadvantageous effect on ecological system. Thus, in this study, it is aimed to establish a new decontamination technology of radioactive materials deposited on seabed or lake bed. In particular, the new adsorption material which can adsorb radioactive materials is developed and the new method which can move them from the bottom sediment is proposed. The results obtained from various tests with or without the water circulation and the adsorption material indicate that the water circulation is effective and that the adsorption material has a great deal of potential in the decontamination of radioactive materials. It is expected that the proposed method and the developed adsorption material are efficient to remove radioactive materials from seabed or lake bed when they are expansively applied to the real decontamination.

Keywords: aeration, adsorbent, decontamination, radioactive material

INTRODUCTION

The serious nuclear disaster in the Fukushima Daiichi nuclear energy plant of the Tokyo Electricity Power Company was occurred by the tsunami which was caused by the Great East Japan Earthquake on March 11, 2011. The decontamination of radioactive materials which were emitted and spread by the disaster is urgent business(Ref. [2]). However an efficient and effective technique of decontamination has not been established.

As for a past study in terms of decontamination in hydrosphere, for example, there is the method in which the polluted mud is dredged. Concretely speaking, the bottom deposit is resuspended by a jet blast. The resuspended solids which is stirred up by the jet blast is collected in fluid. At the same time, aerobic is promoted by the stirring. However, in this method, there is the view that the radioactive materials can be diffused widely in hydrosphere. Additionally, it will be difficult to secure intermediate storage facilities enough for hydrosphere. Basically, in a factual issue, the present situation is that the decontamination is nowhere in sight. The decontamination situation for marine and lake is more or less same as that for land. Especially, in hydrosphere, it is possible that human take in radioactive materials by ecological chain in case ecological system is exposed to radiation. If marine and lake were polluted by radioactive materials, the decontamination for them should be urgent. Thus, in this study, the decontamination method for radioactive materials without dredging mud in marine and lake is proposed with keeping in mind of the shortage of the intermediate storage facilities for the sand polluted by radioactive materials.

EXPERIMENT AND ANALYSIS

There are two issues in terms of the decontamination in hydrosphere, the non-proliferation and volume-reduction of radioactive materials. In this study, the new adsorption material which can adsorb radioactive materials is developed and the new method which can move them from the bottom sediment is proposed so as to solve the issues. To be more precise, the new adsorption sheet which consists primarily of hydroxyapatite (HAp) is developed and the aeration is employed for the convection of fluid. The HAp is made of burnt fish bones. The adsorption tests were conducted to confirm the adsorption property of the HAp. First, 5.0 mg of strontium is added into 300 ml of pure water or sodium chloride fluid. The sodium chloride is 3 % concentration in the solution to be close to

that in seawater. Secondly, 6~7g of the HAp which is set in the net for drain is soaked in the pure water or the sodium chloride fluid. There is two types of specimens; one is uncontrolled immersion test and

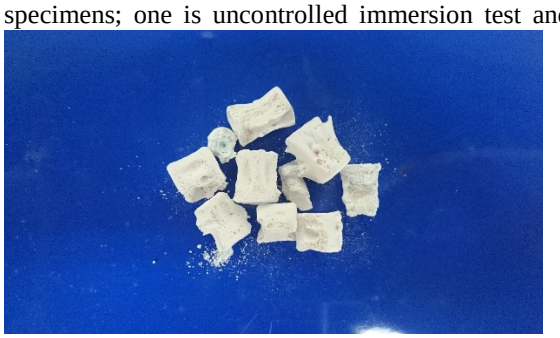

Fig. 1 Hydroxyapatite (HAp).

another is stirred by a screw agitator during the immersion so as to take the flow in river or marine into account. The immersion time is 24 hours. It is noted that same tests for cesium were not conducted since both cesium and sodium belong to alkali metal which makes it difficult to analyze the quantity of cesium by AAS (Atomic Absorption Spectrometer). Table 1 shows the test results of adsorption test for HAp, respectively. The HAp was employed as an adsorbent because it is confirmed that the HAp has

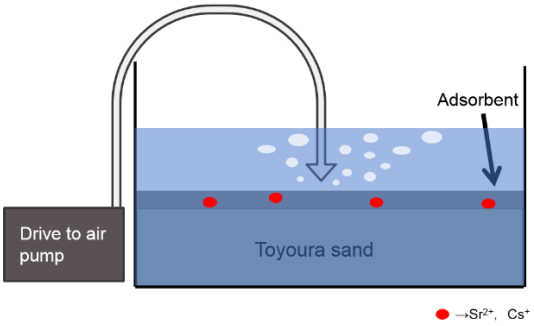

Fig.2 Schematic of aeration test.

enough adsorption performance. The adsorption tests by which cesium and strontium are adsorbed are conducted with the developed sheet and the proposed method to examine their validity and availability.

First, Toyoura sand is laid at the bottom of cylindrical chamber to simulate the decontamination in marine or lake. In the test, 200 g of Toyoura sand which has uniform size of grains is utilized so as to keep the reproducibility of tests. Secondly, 38.1 mg of cesium or 5.0 mg of strontium is added into the sand, and the adsorption sheet and the convection device are set on the sand (see Fig.2). Subsequently, pure water is poured into the chamber to simulate the decontamination in lake, and sodium chloride fluid is poured into the chamber to simulate the decontamination in marine. As for specimens, three types of the specimen are prepared to evaluate the validity and availability of contamination; one is the specimen in which only the sheet is set, another is the specimen in which the sheet and the convective device are set, and the other is the specimen in which nothing is set. And they are left for a given length of time. After the tests, the cesium or strontium contained in Toyoura sand is extracted by washing the sand. For the extracted water solution, cesium is analyzed by AAS to measure its remained amount of the pure water, and the strontium is analyzed by ICP-AES (Inductively-coupled Plasma Atomic Emission Spectrometry) to measure its remained amount of the sodium chloride solution. The availability of convective method and adsorption sheet are examined by the comparison of remained amount of three type specimens.

Table 1. Results of adsorption test for HAp(1 day)

	Residual ratio(%)	
	Pure water	Sodium chloride fluid
Screw	4.39	26.51
Immersion	16.87	17.81

TEST FOR CESIUM ADSORPTION

The results of the immersion tests in which the adsorption performance of cesium by the HAp sheet is examined with changing the immersion time are shown and are discussed. In the tests for cesium,

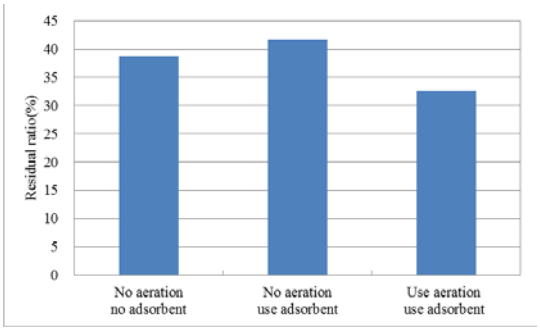

Fig.3 Residual ratio of cesium for 4 weeks.

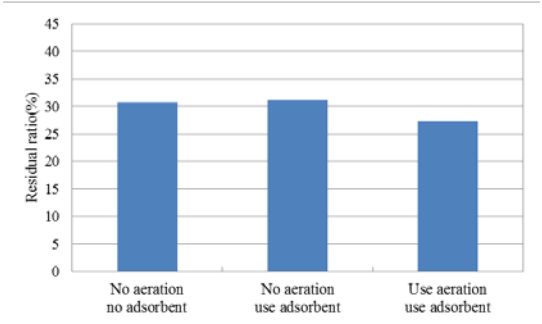

Fig.4 Residual ratio of cesium for 13 weeks.

only pure water is utilized as for the solution. The remained amount of cesium in the water after 4 weeks and 13 weeks from the start of immersion are shown in Table 2. Figs. 3 and 4 show the ratio of the remained amount of cesium to the initial additive amount of cesium after 4 weeks and 13 weeks from the start of immersion, respectively. The ratio is decreased during 9 weeks of their interval. However, not only the test with both the sheet and the aeration but also the test with neither of them show the similar tendency in terms of the decrease of the ratio. Such a phenomenon as the decrease of ratio may be caused by the change of temperature and humidity. Since the reason why the remained amount of cesium in the water for the specimen left uncontrolled is decreased with time is unclear, the effectiveness and availability of the sheet or the aeration are not discussed. Hereafter, the additional tests such as the increase of specimens under varied conditions and the extension of immersion time are required.

Table 2 Test results for cesium

	4 weeks	
	Remained amount(mg)	Residual ratio(%)
No aeration no adsorbent	14.76	38.74
No aeration use adsorbent	15.85	41.61
Use aeration use adsorbent	12.42	32.60
	13 weeks	
No aeration no adsorbent	11.70	30.70
No aeration use adsorbent	11.87	31.15
Use aeration use adsorbent	10.44	27.40

TEST FOR STRONTIUM ADSORPTION

The results of immersion tests in which the adsorption performance of strontium by the HAp sheet is examined with changing the immersion time are shown and are discussed. In the test for strontium, pure water and sodium chloride solution

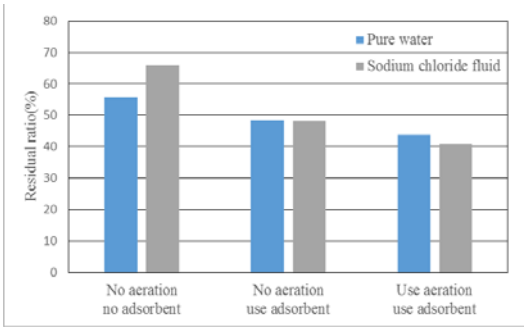

Fig.5 Residual ratio of strontium for 1 week.

are utilized as the solution. The tests time are 1 week, 4 weeks and 13 weeks. The other conditions of

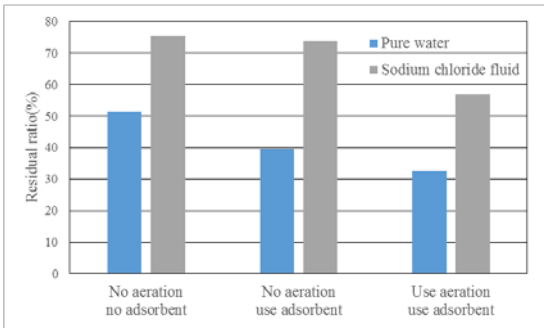

Fig.6 Residual ratio of strontium for 4 weeks.

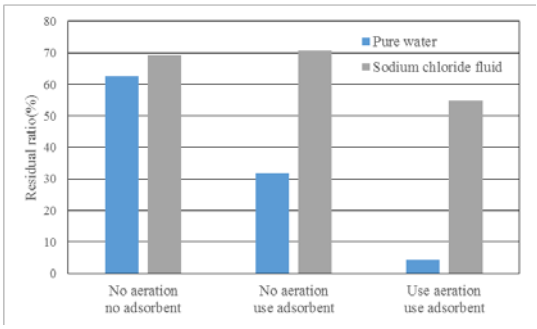

Fig.7 Residual ratio of strontium for 13 weeks.

strontium adsorption test are same as those of cesium adsorption test. The remained amount of strontium in the solution after 1 week, 4 weeks and 13 weeks from the start of immersion are shown in Tables 3, 4 and 5. Figs. 5, 6 and 7 show the ratio of the remained amount of strontium to the initial additive amount of solution after 1week, 4 weeks and 13 weeks from the start of immersion, respectively. According to the figures, the residual ratio of strontium is relatively low in the case of 4 weeks immersion test with pure water and extremely low in the case of 13 weeks immersion test with pure water. The residual ratio decreases with increasing test time in the pure water case. On the other hand, that is relatively low in the case of 1 week immersion test with sodium chloride solution. As the reason, it is possible that the strontium which firmly adhered to the soil is liberated from the soil into the solution. This phenomenon occurs in the case of abundant Na ion (Na^+). Additionally, the convective method may have the space to be improved. The strontium liberated from soil passes through the HAp sheet when the aeration is performed on the sheet. However, the strontium liberated into sodium chloride solution has less chance to pass through the HAp sheet. Therefore, it is needed to exam the setting method for the HAp sheet so as to adsorb cesium or strontium in not only soil but also solution effectively.

Table 3 Test results for strontium for 1 week

	Pure water	
	Remained amount(mg)	Residual ratio(%)
No aeration no adsorbent	2.79	55.74
No aeration use adsorbent	2.42	48.47
Use aeration use adsorbent	2.19	43.86
	Sodium chloride solution	
No aeration no adsorbent	3.29	65.81
No aeration use adsorbent	2.41	48.20
Use aeration use adsorbent	2.05	40.93

Table 4 Test results for strontium for 4 weeks

	Pure water	
	Remained amount(mg)	Residual ratio(%)
No aeration no adsorbent	2.58	51.56
No aeration use adsorbent	1.98	39.66
Use aeration use adsorbent	1.62	32.47
	Sodium chloride solution	
No aeration no adsorbent	3.76	75.29
No aeration use adsorbent	3.69	73.82
Use aeration use adsorbent	2.85	57.00

Table 5 Test results for strontium for 13 weeks

	Pure water	
	Remained amount(mg)	Residual ratio(%)
No aeration no adsorbent	3.13	62.67
No aeration use adsorbent	1.60	31.93
Use aeration use adsorbent	0.22	4.40
	Sodium chloride solution	
No aeration no adsorbent	3.47	69.42
No aeration use adsorbent	3.53	70.69
Use aeration	2.74	54.82

use adsorbent

CONCLUSIONS

In this study, a new decontamination method is proposed without dredging mud in marine and lake with considering the shortage of the intermediate storage facilities for the sand polluted by radioactive materials. To examine the validity and availability of the developed material and the proposed method, the adsorption tests by which cesium and strontium are adsorbed by the developed adsorption sheet are conducted. From the test results, it is found that the difference between the residual ratio of strontium in the tests with the HAp sheet and the convective device and the residual ratio of strontium in the test with nothing is larger than the difference of the residual ratios of cesium in the both tests. From here onwards, the following two knowledge are obtained. One is that most of strontium are existed in the fluid; pure water and sodium chloride solution. Another is that cesium is strongly adhering to Toyoura Sand. As has already stated, the possibility that the strontium is not effectively adsorbed in the experimental environment in this study is not denied. Therefore, the additional issues such as the extension of immersion time and the increase of test specimen should be examined in near future. While at the same time, the settings of the HAp sheet should be also discussed. More to the point, in this study, the number of test is not enough since the longest terms of immersion test are 13 weeks for cesium and strontium. In concrete terms, the longer immersion test, 26 and 52 weeks immersion tests, are required. Alternatively, the residual ratios of strontium in the pure water case and the sodium chloride fluid vary with time Therefore, the different methods for each should be examined as future tasks.
This work was supported by JSPS KAKENHI Grant Number 24520507.

REFERENCES

[1] Ishibashi, M., Ueda, S. and Yamamoto, Y. (1969): The Contents of Strontium and Strontium-90 in Shallow-water Deposits, Journal of the Oceanographical Society of Japan, 25(5), 233-238.

[2] Ishiyama, S. and Yamaguchi, K. (2013): Investigation of Actual Condition of Contaminated Soil in Regulation Pond Conducted by Underwater Radiation Measuring Instrument Installed in Remotely-Operated Vehicle(Second Field Test in Fukushima), The Japan Society of Mechanical Engineers, 79(799), 269-276.

[3] Shigeta, H., Enomoto, T. and Sugihara, T. (2013): Development of a Medical Grinding

Tool Considering Material Properties of Wet Bone for Minimally Invasive Surgery, The Japan Society of Mechanical Engineers, 79(804), 258.

First International Conference on Science, Engineering & Environment,
Tsu City, Mie, Japan, Nov.19-21, 2015, ISBN: 978-4-9905958-5-2 C3051

A COMPARISON OF THE SHADING EFFECTIVENESS OF TWO TYPES OF TREE CANOPY SHAPE IN PENANG, MALAYSIA

Julia Md. Tukiran[1], Jamel Ariffin[2] and Abdul Naser Abdul Ghani[3]
[1,2,3]School of Housing, Building and Planning, Universiti Sains Malaysia, Malaysia

ABSTRACT

Shade trees provide a cooling effect by blocking sunlight, increased ambient air humidity and provide shade during the day. All trees cannot offer relief from the heat in the same amount. This study compared the shading effectiveness of two types of canopy shape (rounded and spreading) in the landscape of Universiti Sains Malaysia, Penang. There are four species selected for this study. Field measurement of microclimate conditions under the tree canopy and open spaces were repeated on a sunny day. The effect of trees shade on air temperature, surface temperature, relative humidity, solar radiation and solar transmission were also compared and related to the leaf area index (LAI). It was found that the air temperature under the canopy could be reduced between 0.67 °C to 2.55 °C, while the surface-soil temperature can be reduced between 3.23 °C to 8.15 °C. Tree species with higher LAI values, *Swietenia macrophylla* (Big leaf mahagony) and *Tabebuia rosea* (Tecoma) provide significantly more cooling than the other species. Reduction of surface temperature is positively correlated with leaf area index. This study shows that shade tree in tropical climates are helpful in improving the outdoor thermal comfort, cooling ground surface by encouraging more latent heat and reduces air temperature by encouraging more evapotranspiration. Thus, the selection of tree species with higher leaf area index value can maximize the benefits they provide to the surrounding area.

Keywords: Shade trees, Tree canopy, Microclimate, Cooling effect, Heat island mitigation

INTRODUCTION

Shade tree planting is one of strategy to reduce heat islands and improve community comfort in three ways such as through shading, evapotranspiration and wind shielding [1][2]. Trees in the urban environment have great potential with many functions such as modulating the microclimate, reducing air and noise pollution, providing a habitat for urban wildlife and improving aesthetic values of urban area. In hot humid climate, high intensity of solar radiation and low wind velocity are the problems experienced by users of open space. Tree can provide relief from high temperature at two spatial scales. Firstly at the microscale through a direct shading effect below canopy, where by incoming solar radiation is intercepted by the canopy and may be either absorbed or reflected. Secondly at the local scale through evaporative cooling, where energy is used for dominated by larger scale warmer and drier surroundings [3].

Many studies have been reported about the measurement and evaluation to tree design aspects in providing significant impact to landscape character, improving the microclimatic performance of built environments, adapting patterns to climate change, and reducing energy consumption and temperature control [4][5][6][7][8]. During the day, shade trees also indirectly reduce heat gain in buildings by altering terrestrial radiation and ultimately reducing ground surface temperatures [9][10][11]. Previous study it was found that constant tree shade can reduce mean radiant temperatures by 5°C – 7°C and concrete surface shaded permanently by a bank of trees can be cooled by up to 20°C in the summer in Manchester, UK [12]. Study by numerical simulations suggest that increasing tree cover by 25% would increase summer temperature by 3.3°-5.6°C in Sacramento and Phoenix [13]. A single layer of leaves allow some visible and infrared radiation to be absorb 50%, whilst reflecting 30% and transmitting the other 20%. Meanwhile, all trees can filter approximately 80-90% of incoming radiation, referring on their leaf density, arrangement and type of leaf [14]. Study reported a comparison of two type of tropical tree species found that the average heat infiltration of *Messua ferrea L.* is 97% whilst that of *Hura crepitans L.* is 86% [14]. Thus, this will affect comfort of people sitting or walking in the shade, namely that most affects a person's thermal comfort as quantified by measures such as their perceived or physiologically equivalent temperature (PET) [15].

The effect of shade trees on urban microclimate can divided in five major effects such as shading effect, ground temperature effect, surface temperature effect, wind effect and reflection effect [16]. Vegetations that have more density value have a greater heat infiltration value [14]. Shading effect of shade trees depends on tree characteristic and

configuration. Physical aspects such as geometry of the canopy, height, density and branching structure, colour of tree leaves and leaf covers are the main components that create shade as well as moderate the microclimate [7][17][18][19]. Moreover for roundhead and pyramidal canopy have a greater shade area than columnar [16]. Shade effectiveness is also related to the leaf area index (LAI), which is defined as a dimension less value of the leaf area per unit ground area. It is the key measure used to understand and compare plant canopies [20]. The shade performance of each species is different, and their effectiveness in filtering radiation will influence microclimate modification. Thus, it is important to investigate the differences between species to understand the impact of each tree species on outdoor comfort [7][17][19].

This study is set out to evaluate the differences in cooling effect of two types of tree canopy shape trees in Penang, Malaysia and to investigate how physical characteristics of trees might affect their performance on a sunny day. The objective of the study are to evaluate the relationship between physical characteristic (tree height, crown height, crown area, crown diameter and LAI) of tree, and observed differences in microclimate conditions under the tree canopy and open space.

METHODS

Tree and Site Selection

One of criteria for the choice of species was those among the most used in tree planting programs by the city council in Penang, Malaysia. The study focused on two types of tree canopies such as roundhead and spreading canopy. All data on trees within the Universiti Sains Malaysia campus were gathered according to tree selection criteria. The selection parameters were divided into two parts, (i) tree physical characteristic and (ii) microclimate condition. The first part comprises several sub parts considered in defining the parameters; tree types, foliage and structural geometry, tree crown and tree maturity. Second part for microclimate condition divided to sub parts namely; site condition with equal environment, ground surfaces and no shading by other trees or buildings.

There four species were identified these were divided into two categories of shape; two species of roundhead, i.e., *Swietenia macrophylla* (big leaf mahagony) and *Filicium decipiens* (fern tree), and two species of spreading canopy, i.e., *Tabebuia Rosea* (tecoma) and *Dalbergia oliveri* (tamalan) (Fig. 1). All tree samples were selected based on the following criteria which is similar height, tree size (medium size), age ranging from 10 to 20 years, evergreen, similar microclimatic condition, ground space cover at least 60-70% turf and 30-40% other materials and open space and not interfered by shade of any buildings.

The trees studied were localized at the Universiti Sains Malaysia, Gelugor, Penang, Malaysia (latitude 5.3569°N, longitude 100.3014°E). Samples of the selected *S. macrophylla* were located at an open space near to the Desasiswa Tekun building. These trees were 10-15 years old and planted randomly. The location of the selected *T. Rosea* species was at a green space near to the Dewan Tuanku Syed Putra, Lecturer Theatres S, T, U & V and the School of Biological Sciences buildings. The trees were 10-15 years old and planted in row. Meanwhile, samples of the selected *F. decipiens* were located at an open space near to the Desasiswa Restu building. The trees were 10 years old and planted in a row. Lastly, the location of the selected *D. oliveri* species was along Desasiswa Tekun Avenue. The trees were 10 years old and planted in row.

Measurement Procedure of Solar Radiation, Solar Transmission, Air Temperature, Relative Humidity and Surface Temperature

All measurements were carried out for each tree at 10.00 am, 12.00 pm and 2.00 pm during the stated period. Only five samples for each type of tree were used and a total tree for measurement was about 20 samples. All measurements were taken over a four day period, namely 14th and 28th of February and 3rd and 5th of March 2015.

The measurements under the tree canopy were taken first. Solar radiation and solar transmission were done using the solar power meter (TES-1333). Air temperature and relative humidity measurements were taken using the (Extech's 45160) 3-in-1 Pocket Hygro-Thermometer-Anemometer. Infrared thermometer (IRtek IR60) was used in measuring ground surface temperature in each tree sample and measurement were taken at 1m height. Solar power meter (TES-1333) and (Extech's 45160) 3-in-1 Pocket Hygro-Thermometer-Anemometer attached to a tripod stand 1m above the ground. All measurements were carried out under the tree canopies and the data were recorded manually. All instruments were placed equidistant from the tree trunk and canopy drip line along each of the four main compass points (north, south, east and west).

The measurements in the open were taken after each set of measurements under the canopy had been completed. The measurements were done using the same set of instruments, approximately 2 m away from the canopy drip line and taken at one point for each tree.

Measurement Procedure of Leaf Area Index

The measurement of LAI using indirect method

which is canopy analysis systems based hemispherical image analysis. It involves a lot of steps from photography to LAI calculation. Hemispherical photographs of a single tree were capture using a digital camera high resolution, Canon EOS 60D Kit with fish eye lens with a field of view of 180° was used. The camera was mounted on a sturdy tripod at 1.0 m height to characterize the canopy without the interfering presence of understory vegetation. The camera was leveled to face exactly the vertical using a bubble level. The top of the camera (position of the flash socket) was orientated to magnetic north using a compass. Photographs were taken without direct sunlight entering the lens in the early morning, late afternoon or on overcast days [21][22]. Therefore, all measurements were done early morning before 9.00 am and it's taken over a one day, namely the 18th of May 2015. This study is using free software for computing LAI from hemispherical photograph, namely WINPHOT by Hans ter Steege [20][23]. The hemispherical photograph was then imported to Paint program to convert from format (.jpeg) to 256 Color Bitmap (*.bmp,*.dib). Finally, the image was then opened in WINPHOT to compute and analyze for getting LAI value.

Measurement Procedure of Shaded Area

To measure amount of shaded area by using computer simulation, main thing need create 3 dimensional of the tree form. Firstly, digital photographs of a single tree were capture using a digital camera. It was taken at 10 m away from the centre of the tree and held at the eye level of the photographer. Snap point were done in two option either from north, northwest and northeast or south, southeast and southwest according to the site conditions. The image was transferred to a computer and by using AutoCAD 2011 software to generate the skeleton of the tree. This skeletal drawing was then imported to SketchUp software to convert from format AutoCAD files (.dwg) to 3DS file (.3ds). The skeletal drawing was then transferred to ECOTECT 2011 to generate a 3D modelling of the tree and also conduct Shadow Analysis for each tree. Simulated shaded area for all trees was running on the 4th of May 2015 at 10.00 am, 12.00pm and 14.00 pm. Thus, this was the best time to compare all measurements.

RESULTS

The four species had quite different physical characteristic, one-way ANOVA showings significant differences between the species in tree height ($F_{(3,16)}$=39.142, P=0.000), crown height ($F_{(3,16)}$=35.580, P=0.000), crown diameter ($F_{(3,16)}$ =6.363, P=0.005) and crown area ($F_{(3,\ 16)}$=5.203, P=0.011). Post hoc analysis shows that of all species, *D. oliveri* had the shortest but widest canopy. Mean air temperature reduction was 3.697% (StD=0.850). One-way ANOVA showed that there were no significant differences between the species in air temperature reduction ($F_{(3,16)}$=1.931, P=0.165). The mean surface temperature reductions were 16.507% (StD=1.340). One-way ANOVA showed that there were not significant differences between the species ($F_{(3,16)}$=1.032, P=0.405). The mean solar radiation filtrations were 81.892% (StD=1.848). One-way ANOVA showed that there were not significant differences between the species ($F_{(3,16)}$=1.544, P=0.242). The mean leaf area indexes were 2.096 m^2/ m^2 (StD=0.508). One-way ANOVA analysis showed that there were significant difference between species ($F_{(3,16)}$=13.481, P=0.000). Post-hoc analysis showed that the *S. macrophylla* had significantly higher leaf area index than *T. rosea*, *F. decipiens* and *D. oliveri*. The mean transmissivity were 12.206% (StD=1.317). One-way ANOVA showed that there were not significant differences between the species ($F_{(3,16)}$=1.762, P=0.195). The mean shade areas were 104.80m^2 (StD=29.579). One-way ANOVA showings significant differences between the species in shade area ($F_{(3,16)}$=5.254, P=0.010). Post-hoc analysis showed that the *S. macrophylla* shade area significantly more than other species.

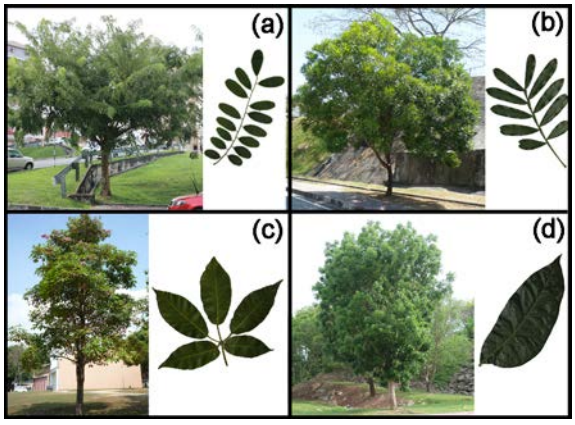

Fig. 1 Tree species (a) *D. oliver*, (b) *F. decipiens*, (c) *T. rosea* and (d) *S. macrophylla*.

Relationship between solar radiation filtration and (transmissivity, leaf area index, shade area, air temperature and surface temperature)

Dalbergia oliveri

The results show that tranmissivity (t= -19.585, P=0.000, R^2=0.992, SEE=0.123), shade area (t=5.080, P=0.015, R^2=0.896, SEE=0.449) and air temperature reduction (t=5.652, P=0.011, R^2=0.914, SEE=0.408) are significant factors for solar radiation filtration but no significant for LAI (t=1.946,

P=0.147, R^2=0.558, SEE=0.925) and surface temperature reduction (t=1.911, P=0.152, R^2=0.549, SEE=0.935). The increase solar radiation filtration percentage corresponds to the decrease transmissivity percentage value of *D. oliveri* canopy. In addition, the increase solar radiation filtration percentage corresponds to the increase value of shade area, LAI, air temperature reduction and surface temperature reduction of *D. oliveri* canopy.

Filicium decipiens

The results show that tranmissivity (t=-14.755, P=0.001, R^2=0.986, SEE=0.227), LAI (t=3.434, P=0.041, R^2=0.797, SEE=0.878), air temperature reduction (t=34.913, P=0.000, R^2=0.998, SEE=0.097) and surface temperature reduction (t=3.454, P=0.041, R^2=0.799, SEE=0.874) are significant factors for solar radiation filtration but no significant for shade area (t=2.144, P=0.121, R^2=0.605, SEE=1.225). The increase solar radiation filtration percentage corresponds to the decrease transmissivity percentage value of *F. decipiens* canopy. In addition, the increase solar radiation filtration percentage corresponds to the increase value of LAI, shade area, air temperature reduction and surface temperature reduction of *F. decipiens* canopy.

Tabebuia rosea

The results show that tranmissivity (t=-13.039, P=0.001, R^2=0.983, SEE=0.385), LAI (t=15.869, P=0.001, R^2=0.988, SEE=0.317), shade area (t=5.136, P=0.014, R^2=0.898, SEE=0.935), air temperature reduction (t=7.679, P=0.005, R^2=0.952, SEE=0.644) and surface temperature reduction (t=7.993, P=0.004, R^2=0.940, SEE=0.619) are significant factors for solar radiation filtration. The increase solar radiation filtration percentage corresponds to the decrease transmissivity percentage value of *T. rosea* canopy. In addition, the increase solar radiation filtration percentage corresponds to the increase value of LAI, shade area, air temperature reduction and surface temperature reduction of *T. rosea* canopy.

Swietenia macrophylla

The results show that tranmissivity (t=-10.313, P=0.002, R^2=0.973, SEE=0.261), LAI (t=10.521, P=0.002, R^2=0.974, SEE=0.256), shade area (t=7.269, P=0.005, R^2=0.946, SEE=0.946) and air temperature reduction (t=6.036, P=0.009, R^2=0.924, SEE=0.434) are significant factors for solar radiation filtration but no significant for surface temperature reduction (t=2.463,P=0.091, R^2=0.669, SEE=0.905). The increase solar radiation filtration percentage corresponds to the decrease transmissivity percentage value of *S. macrophylla* canopy. In addition, the increase solar radiation filtration percentage corresponds to the increase value of LAI, shade area, air temperature reduction and surface temperature reduction of *S. macrophylla* canopy.

DISSCUSSION

Tree physical characteristic and shade area

The sampled tree species showed significant differences in their canopy size and shape, and these differences also show in significant differences between the shade areas produced by the tree canopies. This because the taller trees, such as *S. macrophylla* had narrower canopies, while the shorter trees such as *D. oliveri* had wider canopies. Statically relationship through the correlation between the amount of shaded areas and radiation filtration is not significant (r=0.289, P=0.217). The results indicated that there is significant difference in the mean amount of shaded area of *D. oliveri* (103.732m²), *F. decipiens* (83.340m²), *T. rosea* (94.452m²) and *S. macrophylla* (137.680m²). Based on ECOTECT analysis results and observation, the roundhead canopy of *S. macrophylla* and the spreading canopy of *D. oliveri* provide a broader shaded area than that of *T. rosea* and *F. decipiens*. Shade coverage is important especially in tropical environments during the middle of the day when the sun position overhead for longer duration and it is hottest. Shade characteristics for each tree depend on the form of the canopy and branching of the species, the amount of leaf cover, growing location and the angle of the sun.

Air temperature and surface temperature

The outcome shows that the mean air temperature reduction of *D. oliveri* (3.070%), *F. decipiens* (3.574%), *T. rosea* (3.930%) and *S. macrophylla* (4.214%). Meanwhile, results for the mean surface temperature reduction of *D. oliveri* (16.126%), *F. decipiens* (15.858%), *T. rosea* (16.964%) and *S. macrophylla* (17.082%). Meaning that, SM and *T. rosea* are more reduction in air temperature and surface temperature than *F. decipiens* and *D. oliveri*. Air temperature reduction (r=0.778, P=0.000) and surface temperature reduction (r=0.690, P=0.001) are show positive relationship and significant factors for LAI. Meaning that, *S. macrophylla* and *T. rosea* has thicker branching, twigs and leaves that can create a higher LAI value provide greater surface cooling. Shade trees can contribute to significant reductions in surface temperatures and this will have effect of reducing heat storage in the paved surface. This condition will increase latent heat, promote more evapotranspiration and reduce surrounding air

temperature, this should help improved the urban heat island effect.

Solar radiation

All trees have the ability to filter solar radiation. The results indicated that the mean solar radiation filtration of *D. oliveri* (81.052%), *F. decipiens* (81.266%), *T. rosea* (82.016%) and SM (83.234%). Thus, *S. macrophylla* and *T. rosea* are more effective in solar radiation than *F. decipiens* and *D. oliveri*. Meaning that, *S. macrophylla* and *T. rosea* has thicker branching, twigs and leaves that can create a higher LAI value, less canopy transmissivity and made the best contribution in blocking radiation from reaching the ground surface. On the other hand, *D. oliveri* have spreading and an open crown with droopy and feathery compound leaves, this condition will allow more radiant heat passed through the canopy. That means, *D. oliveri* provide some shade from solar radiation, but the effect is not sufficient due to higher radiation transmission and reflection when compared to *S. macrophylla*.

Transmissivity

The results indicated that the mean transmissivity of *D. oliveri* (12.920%), *F. decipiens* (12.482%), *T. rosea* (12.242%) and *S. macrophylla* (11.182%). There was a significant negative correlation between solar radiation filtration and transmissivity (t=-22.500, P=0.000, R^2=0.966). The increase solar radiation filtration value corresponds to the decrease transmissivity value. A lower value of transmissivity is considered a suitable condition. This means that the transmissivity of the *S. macrophylla* and *T. rosea* canopy is better than *F. decipiens* and *D. oliveri*. This indicated that the *S. macrophylla* and *T. rosea* canopy provides greater density of branching and twigs than *F. decipiens* and *D. oliveri*. A higher reduction of light intensity and glare due to obstruction from branching will create better shade and could increase human comfort.

Leaf area index (LAI)

The outcome shows that the mean LAI of *D. oliveri* (1.702m^2/m^2), *F. decipiens* (1.842m^2/m^2), *T. rosea* (2.052m^2/m^2) and *S. macrophylla* (2.790m^2/m^2). This means that the foliage cover and surface area of *S. macrophylla* and *T. rosea* is denser and higher than *F. decipiens* and *D. oliveri*. Correlation results show positive relationships are strong and significant between solar radiation filtration and LAI for *S. macrophylla* and *T. rosea*. Therefore, it can filter solar radiation and light more effectively than the latter. Based on images of leaf sizes and branching, it is evident the most of the *S. macrophylla* canopy has dense rounded crown with leaves are usually paripinnate (12–45cm long) and are made up of 3–6 pairs of lanceolate or ovate leaflets are asymmetrical (5–12cm long x 2–5cm wide). This provide more multiple layers of leaf throughout the branching and twigs will promote more reflection and absorption of incoming solar radiation and helps in reducing transmission of radiant heat under the canopies. Shaded trees with a higher LAI should contribute more of reducing the urban heat island. In addition, for *F. decipiens* canopy has a dense spreading crown with leaves (13-17cm long) and small oval leaflets (1.8-3.0 long x 1.2-1.8cm wide) that are alternately arranged, and it provides a less multiple layer and low density of leaf cover. So for the tree with better radiation filtrations are significantly relate with branching habits and leaf distributions characteristics.

CONCLUSION

This paper set out to illustrate the shading effectiveness of two types of tree canopy shape in hot humid regions. All trees, namely *D. oliveri, F. decipiens, T. rosea and S. macrophylla* have ability to vary solar radiation due to their physical characteristic. Physical characteristics related to higher LAI values contribute to tapping more incoming solar radiation. Study have shown that some physical characteristics likes foliage cover, branching habit and types, size and arrangement of leaves play important roles in improving efficiency in radiation reflection and absorption. Study find that species with a higher LAI, higher solar radiation filtration, less transmissivity, such as *S. macrophylla* and *T. rosea*, do reduce air temperature and surface temperature and increase relative humidity more because they cast a denser shade. These effect is thought to increase when this species is planted in clusters and its will help in producing cool island effects in city areas. Meanwhile for species provides less LAI value, less solar radiation filtration and higher transmissivity, such as *D. oliveri*, due to the less dense branch habit and small size of leaves. However, physical characteristic of *D. oliveri* with spreading structure of the canopy create more shade, especially during overhead sun. Thus, the study suggest that *D. oliveri* is suitable for planting in parking area or open space because this tree require a wider shade but can tolerant moderately reduced radiant heat. Finally, this knowledge can be implementing by professionals in urban planning and design to offer better outdoor thermal comfort and contribute to energy budgets of buildings and humans in tropical urban climate environments.

ACKNOWLEDGEMENTS

Our sincere appreciation goes to lab assistance Mohd. Faizal Md. Nasir and Nurulhuda Zakaria

from Environmental Lab at School of Housing, Building and Planning, USM for providing instruments and services during the field measurement process.

REFERENCES

[1] Y. J. Huang, H. Akbari, and H. Taha, "The wind-shielding and shading effects of trees on residential heating and cooling requirements," in *Proceedings of the ASHRAE Winter Conference*, 1990, pp. 1403–1411.

[2] R. A. Nasir, S. S. Ahmad, A. Zain-Ahmed, and N. Ibrahim, "Adapting human comfort in an urban area: The role of tree shades towards urban regeneration," *Procedia - Soc. Behav. Sci.*, vol. 170, pp. 369–380, 2015.

[3] T. R. Oke, *Boundary Layer Climates_2nd ed.*, Taylor & F. Routledge, London, 1987.

[4] H. Akbari, D. M. Kurn, S. E. Bretz, and J. W. Hanford, "Peak power and cooling energy savings of shade trees," *Energy Build.*, vol. 25, no. 2, pp. 139–148, 1997.

[5] S. Klaus I, S. James R, and M. E Gregory, "Effetcs of tree cover on parking lot microclimate and vehicle emissions," *J. Arboric.*, vol. 25, no. 3, pp. 129–142, 1999.

[6] S. Streiling and A. Matzarakis, "Influence of single and small clusters of trees on the bioclimate of a city: a case study," *J. Arboric.*, vol. 29, no. 6, pp. 309–316, 2003.

[7] B. Kotzen, "An investigation of shade under six different tree species of the Negev desert towards their potential use for enhancing micro-climatic conditions in landscape architectural development," *J. Arid Environ.*, vol. 55, no. 2, pp. 231–274, Oct. 2003.

[8] X. Picot, "Thermal comfort in urban spaces: Impact of vegetation growth. Case study: Piazza della Scienza, Milan, Italy," *Energy Build.*, vol. 36, no. 4, pp. 329–334, 2004.

[9] H. Akbari, M. Pomerantz, and H. Taha, "Cool surfaces and shade trees to reduce energy use and improve air quality in urban areas," *Sol. Energy*, vol. 70, no. 3, pp. 295–310, Jan. 2001.

[10] R. Pandit and D. N. Laband, "Energy savings from tree shade," *Ecol. Econ.*, vol. 69, no. 6, pp. 1324–1329, 2010.

[11] S. Leuzinger, R. Vogt, and C. Körner, "Tree surface temperature in an urban environment," *Agric. For. Meteorol.*, vol. 150, no. 1, pp. 56–62, 2010.

[12] D. Armson, P. Stringer, and a. R. Ennos, "The effect of tree shade and grass on surface and globe temperatures in an urban area," *Urban For. Urban Green.*, vol. 11, no. 3, pp. 245–255, 2012.

[13] H. Akbari, S. Davis, S. Dorsano, J. Huang, and S. Winnett, "Cooling our communities. A guidebook on tree planting and light-colored surfacing," Washington, D.C., 1992.

[14] M. F. Shahidan, M. K. M. Shariff, P. Jones, E. Salleh, and A. M. Abdullah, "A comparison of Mesua ferrea L. and Hura crepitans L. for shade creation and radiation modification in improving thermal comfort," *Landsc. Urban Plan.*, vol. 97, no. 3, pp. 168–181, Sep. 2010.

[15] a Matzarakis, H. Mayer, and M. G. Iziomon, "Applications of a universal thermal index: physiological equivalent temperature.," *Int. J. Biometeorol.*, vol. 43, no. 2, pp. 76–84, 1999.

[16] G. Scudo, "Thermal comfort in greenspaces," in *Proceeding COST C 11 "Green structures and urban planning,"* 2002.

[17] B. S. Lin and Y. J. Lin, "Cooling effect of shade trees with different characteristics in a subtropical urban park," *HortScience*, vol. 45, no. 1, pp. 83–86, 2010.

[18] L. Vieira de Abreu and L. Chebel Labaki, "Trees and heat fluxes: how much do they contribute to the energy balance at urban spaces?," in *27th International Conference on Passive and Low Energy Architecture*, 2011, vol. 1, pp. 245–250.

[19] D. Armson, M. A. Rahman, and A. R. Ennos, "A comparison of the shading effectiveness of five different street tree species in Manchester, UK," *Arboric. Urban For.*, vol. 39, no. 4, pp. 157–164, 2013.

[20] N. J. J. Bréda, "Ground-based measurements of leaf area index: a review of methods, instruments and current controversies.," *J. Exp. Bot.*, vol. 54, no. 392, pp. 2403–17, Nov. 2003.

[21] G. Frazer, J. Trofynow, and K. Lertzman, "A method for estimating canopy opennes, effective leaf area index, and photosynthetically active photon flux density using hemispherical photography and computerized image analysis techniques.," 1997.

[22] J. Glatthorn and P. Beckschäfer, "Standardizing the Protocol for Hemispherical Photographs: Accuracy Assessment of Binarization Algorithms," *PLoS One*, vol. 9, no. 11, pp. 1–19, 2014.

[23] H. ter Steege, "Winphot 5.0: A Programme to Analyze Vegetation Indices, Light and Light Quality From Hemispherical Photographs," 1997.

First International Conference on Science & Environment,
Tsu City, Nov. 19-21, 2015, ISBN: 978-4-9905958-3-8 C3051

EXAMINING THE SIX WELL KNOWN EQUATIONS FOR ESTIMATING REFERENCE EVAPOTRANSPIRATION IN HERAT, AFGHANISTAN

Homayoon Ganji[1] Takamitsu Kajisa[1] Masaaki Kondo[1] Behroze Rostami[1]
[1]Graduate School of Bioresources, Mie University, 514-8507 Kurima-machiya-cho 1577, Tsu, Japan

ABSTRACT

Herat province as a semi-arid area, having strong winds which are known as "120-day winds" needs to be investigated with aim for discovering the best method for estimating the reference evapotranspiration (ET_0) which has the most accuracy and is adaptable in the area. In this research, an examining has been done between six well known methods based on their performances under the given climatic condition in the Herat provinces. Pan evaporation (E_{pan}) is considered as indicator to compare with Penman-Monteith, which is the only method that includes a variable of wind, Thornthwaite, and Hargreaves, and Hamon, Net radiation and solar radiation methods. 8 years data from 2006 to 2013 is used to show the seasonal climatic variations as well the year 2009 data is used to compare the six methods between each other. The ET_0 estimated values by six methods have been correlated with E_{pan} estimated value, using Pearson's correlation (R) methods. Based on p-value, all of the six methods are found significant to be used for measuring the ET_0. The Penman-Monteith method is showing the highest R. Hence, by considering the Mean Squire Error (*MSE*) calculation, the Penman-Monteith method has the lowest value which suggests the best measuring of the ET_0. The secondary smallest *MSE* was shown for Hargreaves. The yearly ET_0 of Hargreaves was larger than the E_{pan}, while the yearly ET_0 of Penman-Monteith was smaller than E_{pan}. Therefore, in a case the aim is not accuracy but design, the Hargreaves might not be ignored.

Keyword: 120-day winds, Pan Evaporation, Reference Evapotranspiration, Herat, Afghanistan

INTRODUCTION

Evapotranspiration (*ET*) is defined as physical processes whereby liquid water vaporized into the atmosphere from evaporating surfaces [2], [11] and [15]

ET is the most significant component of the hydrologic budget, apart from precipitation [7]. Accordingly, in arid and semi-arid areas, *ET* is important as well. The *ET* varies according to weather and wind conditions. Because of this variability, water managers who are responsible for planning and adjudicating the distribution of water resources need to have a thorough understanding of the *ET* process, and knowledge about the spatial and temporal rates of it.

ET is defined in different concepts as one of the concepts is called potential or reference evapotranspiration (ET_0). The concept of the ET_0 is used to introduce the evaporative demand of the atmosphere apart from the crop type, crop development and management practice [2].

Many different methods for measuring the ET_0 have been developed based on their daily performances under the given climatic condition in the world. In this study, only six models are selected to estimate the ET_0 for Herat, Afghanistan.

Penman-Monteith, the United Nations Food and Agriculture Organization (FAO) has introduced a model for estimating of the standard ET_0 which is known as Penman-Monteith model Eq. (1) Table 1 [2]. The accuracy of the FAO model is as high as recommended sole method of calculating ET_0, if the requirement set of data are available [2]. The only limitation to the Penman family of models, they require many meteorological inputs, thereby limiting their utility in data-sparse areas [7], [4].

Thornthwaite (1944) defines ET_0 as "the water loss which will occur if at no time there is a deficiency of water in the soil for use of vegetation" [16]. As this method requires only monthly average temperature, is considered to be popular method [13] According to the Mintz and Walker (1993), the Thornthwaite method has been developed to temperature measured under potential conditions and in only overestimate the potential evaporation in arid regions if air surface temperature is applied Eq. (2) Table 1.

The Hargreaves-Samani (1985) is one of the older *ET* models which are introduced by Allen and Hargreaves Eq. (3) [9] Table 1. The requirement component for this model is simpler than the Penman-Monteith. The Hargreaves's ET_0 model requires only measured temperature data. This model is seen to be less impacted than Penman-type methods when data are collected from arid or semi-arid and non-irrigated sites.

A method was described by Doorenbos and Pruitt (1977) through which evaporation is converted to ET_0. This method described by Allen et al. (1991), known as FAO 24 Pan Evaporation (24PAN). In order to estimate ET_0, the measured pan evaporation is adjusted by a coefficient K_p Eq. (4). This method is the basic form of the 24PAN model, which is also described by Fontenot, R. L. (2004) Table 1.

Homan Method is also known as one of the simplest methods that are applicable for estimating the ET_0 in monthly base or yearly bases. According to the Haith and Shoemaker (1987), this method requires only average number of daylight hours per day and saturated vapor pressure. The Eq. (5) is used for this method which was given by [8] Table 1.

Finally, FAO-56PM was simplified by Irmak et al. (2003) as expressing a multi-linear regression function that only net radiation (R_n) and solar radiation (R_s) are needed as requires input parameters for estimation Eq. (6)-(7) Table 1.

Table 1 Deferent models' equations

Model	Equation	No
FAO Penman-Monteith (56PM)	$$ET_0 = \frac{0.408\Delta(R_n - G) + \gamma \frac{900}{T+273} u_2 (e_s - e_a)}{\Delta + \gamma(1 + 0.34u_2)}$$	1
Thornthwaite	$$ET_0 = 16 \times \left(\frac{10\,Ti}{I}\right)^a \left(\frac{N}{12}\right)\left(\frac{I}{30}\right)$$ $$I = \sum_{i=1}^{12} \left(\frac{Ti}{5}\right)^{1.514}$$ $$a = (492390 + 17920I - 77.1I^2 + 0.675I^3) \times 10^{-6}$$	2
Hargreaves-Samani 1985 (H-S)	$$ET_0 = 0.0023\,(T_{mean} + 17.8)(T_{max} - T_{mix})^{0.5} R_a$$	3
Pan Evaporation	$$ET_0 = K_p \times E_{pan}$$	4
Homan Method	$$ET_0 = \frac{2.1 \times H_t^{\,2} e_s}{(T_{mean} + 273.3)}$$	5
Net radiation (R_n)	$$ET_0 = 0.489 + 0.289R_n + 0.023T_{mean}$$	6
Solar radiation (R_s)	$$ET_0 = 0.611 + 0.149\,R_s + 0.079T_{mean}$$	7

Where:
ET_0 *is* grass reference evapotranspiration (mm day^{-1}), R_n is net radiation *(*MJ m^{-2} day^{-1}*)*, G is soil heat flux (MJ m^{-2} day^{-1}), γ *i*s the psychometric constant (kPa °C^{-1}), *es* is the saturation vapor pressure (kPa), *ea is th*e actual vapor pressure (kPa), Δ is the slope of the saturation vapor pressure - temperature curve (kPa °C^{-1}), T is the average daily air temperature (°C), u_2 is the mean daily wind speed at 2 m (m s^{-1}) [2]. T_i is the mean monthly temperature (°C); N is the mean monthly sunshine hour, T_{max} is the daily maximum temperature (°C), T_{min} is the daily minimum temperature (°C), *Ra* is the daily extraterrestrial radiation (mm day^{-1}), K_P is the pan coefficient, E_{pan} is the pan evaporation (mm day^{-1}), H_t is average number of daylight hours per day [day], *Rs* is solar shortwave radiation (MJ m^{-2} day^{-1}).

The available ET_0 date with different organization in Herat province is calculated through software developed by FAO, called CLIMWAT and CROPWAT software. Except that, there is no any method has been recommended for estimating the

ET_0 in Herat province yet, it means that, still no any research has been done to compare different methods in this regards so far. Thus, in order to establish a common method which can provide a more accurate ET_0, this research has been done with following hypothesis:

1) E_{pan} can be a good indicator for ET_0 estimation through different methods.

2) The ET_0 estimation value is more accurate with the methods those require wind factor than the dose do not require wind factor.

ESTIMITION METHODS

For estimating the ET_0 rate, six well known methods are used as shown in Table 1. Climatic parameters that is important for estimation of the six different methods, shown in Table 2.

Table 2 Metrological parameters for different methods.

Methods	Variables					
	Temperature	Humidity	Wind speed	Radiation	No. of Daylight hours	Saturated vapour pressure
FAO56-PM	necessary	necessary	necessary	necessary		necessary
Thornthwaite	necessary	-	-		necessary	
Hargreaves	necessary	-	-	necessary	-	-
Hamon	necessary	-	-		necessary	-
Rs- based radiation	necessary	necessary	-	necessary	necessary	-
Rn- based radiation	necessary	necessary	-	necessary	necessary	-

Due to lack of enough E_{pan} data, only the data from year 2009 is used to estimate the ET_0.

Collecting the metrological data is still a challenge in Afghanistan, but recently the ministry of Agriculture and livestock with support of FAO organization could reestablish the metrological stations in each province of Afghanistan.

There is a metrological station in Herat province which belongs to the department of Agriculture and livestock. This station is called Urdu Khan Research Center.

Urdu khan Regional Agricultural Research Station with a total area of 225 hectares is located in latitude of 39° 11' N and a longitude of 68° 13' E with an elevation of 964 meters in Urdu khan village, at 5.8 kilometers southeast of Herat city. The maximum mean annual temperature is around 28.9°C and minimum mean temperature -0.6 °C. Precipitation is reported 220 mm in average base yearly. The first frost almost occurs around November 4th whereas the last frost is seen about March 28th. The total frost-free days are 226 day during the summer season [14]. A strong wind which is called the “120-day winds” persists from early June until late September with a strong average force (7.01 m/sec) [6].

RESULT AND DISCUSSION

Strong winds as a metrological factor, influences the ET_0 which is estimated by different methods. The ET_0 rate is shown different according to the different methods because all applied methods require different metrological factors in estimation of the ET_0.

Among the applied methods in this study, Penman-Monteith is the only method which requires wind factor directly for estimating the ET_0 including of the temperature, relative humidity and sun shine hours. E_{pan} which is measured directly from A-class pan and Hargreaves methods, which requires temperature only, are influenced by wind speed whereas the other methods are seemed not influenced by wind factor.

1. Seasonal difference among the metrological variables is shown in Fig. 1. The monthly average variation of temperature, wind speed, humidity, solar radiation and net radiation which are necessary for ET_0 estimation has been measured for 8 years.

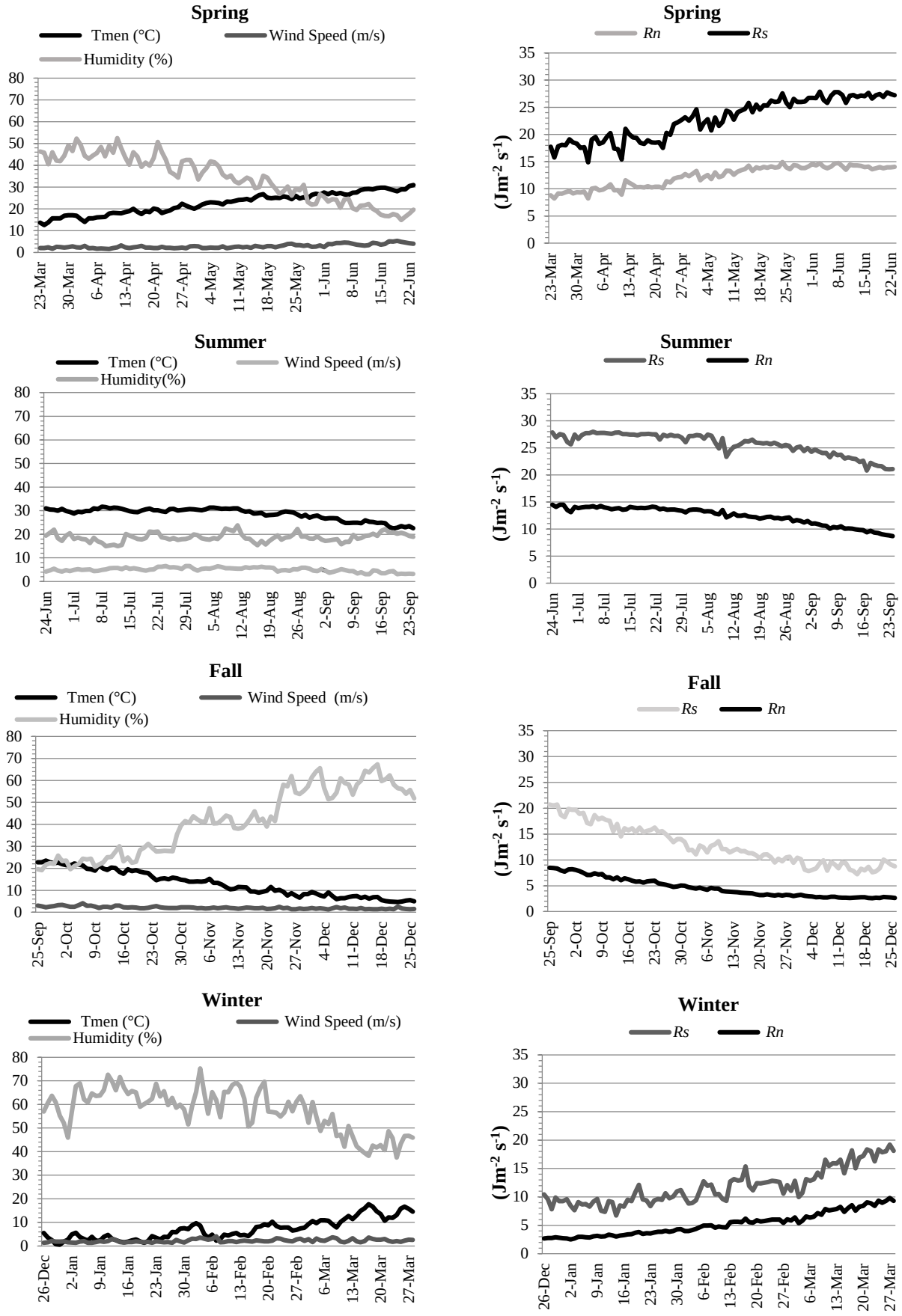

Fig 1 Daily average temperature, wind speed and humidity of four seasons

Humidity is seen high in the early spring, entire the winter and late fall whereas the summer season is characterized with low humidity, due to low precipitation.

The entire of the summer season, wind speed is seen faster, almost more than 5 m/s averagely than the other seasons. Similarly, temperature is high in the summer, but since early of fall the temperature drops till medal of spring.

Net radiation is decreasing by early of fall and again increasing from late winter on.

2. Compression of the daily average ET_0 value, estimated through the different six methods such as; Thornthwaite, Hargreaves, Hamon, Solar radiation and Net radiation, E_{pan} and FAO-56PM between each other is shown by (Fig. 2 to 7),using data of year 2009. All methods show a higher rate of ET_0 from the early summer until late fall.

The Penman-Monteith and Hargreaves methods show closer ET_0 value to the E_{pan} entire of the year, especially at early of summer until late fall seasons (Fig 2 and 3). The reason might be referred to the strong wind "120-day winds" which blows all the summer season with high speed. This is why the ET_0 estimated through penman-Monteith, which requires wind velocity and Hargreaves method, which is recommended at the arid area are closer in volume with E_{pan}.

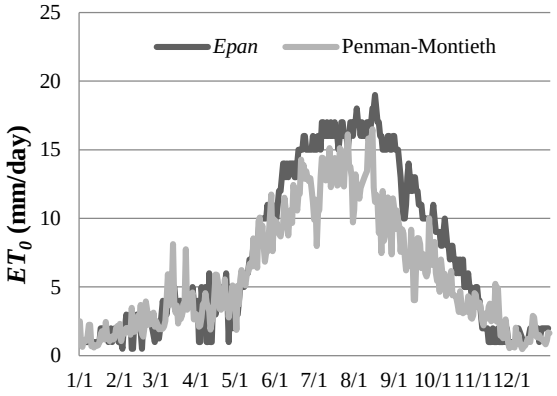

Fig. 2 Daily average estimated ET_0 through *E*pan and Penman-Monteith methods

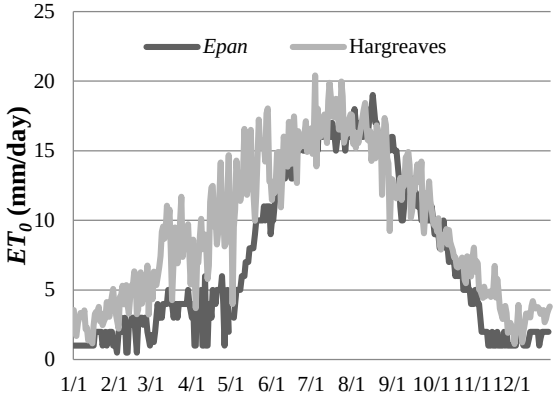

Fig. 3 Daily average estimated ET_0 through *E*pan and Hargreaves methods

It is shown in Fig. 2 that, there is deference between Penman-Monteith ET_0 value and E_{pan} value since early of summer until end of summer season; as well, the deference is seen between Hargreaves ET_0 value and E_{pan} value from January until June shown in Fig. 3.

The other four methods show lower ET_0 value than the E_{pan}, as there is a big deference between each method and E_{pan}, especially form around May until late November (Fig. 4 to 7).

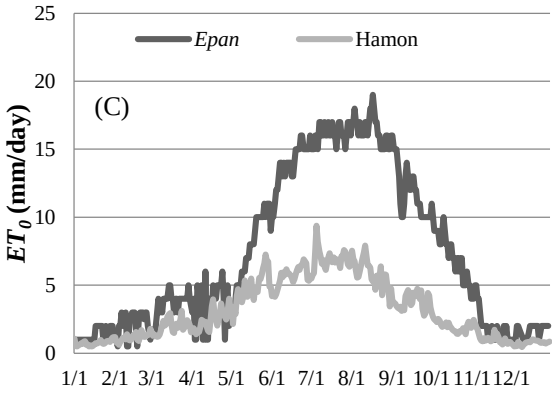

Fig. 4 Daily average estimated ET_0 through *E*pan and Hamon methods

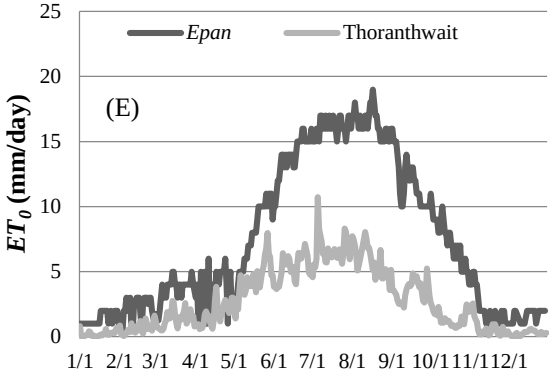

Fig. 5 Daily average estimated ET_0 through *E*pan and Thornthwaite methods

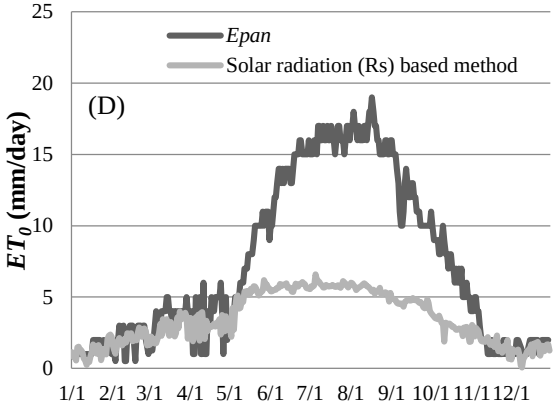

Fig. 6 Daily average estimated ET_0 through *E*pan and Solar radiation methods

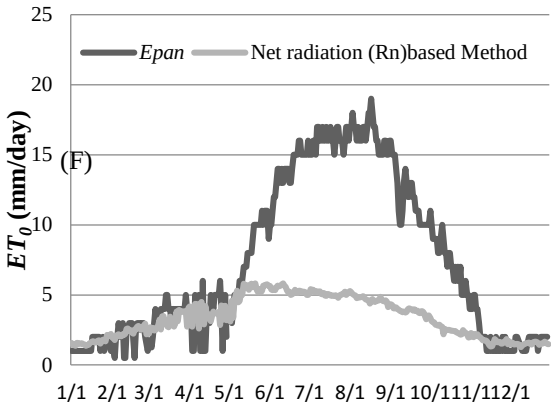

(F)

Fig. 7 Daily average estimated ET_0 through *E*pan and Net radiation methods

3. Yearly estimated ET_0 value by using the six well known methods is shown by Fig. 8.

The Hargreaves, E_{pan} and Penman- Monteith show higher total annual ET_0 value than the four others. Variations in the ET_0 estimation reflect the differences in the variables applied in each method.

According to the Fig. 3, Hargreaves shows the highest total annual ET_0 value that is 3500 mm/year, whereas the Thornthwaite, Homan, Solar radiation based method and Net radiation based methods show the lower value of total annual ET_0 of which Thornthwaite method shows the lowest total annual value that is 1000 mm/year.

As the E_{pan} is considered as indicator, the estimated ET_0 through Penman-Monteith and Hargreaves methods are closer to the E_{pan} value. Therefore, the Penman-Monteith methods can be considered the most accurate method, whereas the Hargreaves methods as the second accurate method is useful to apply for designing of irrigation plan.

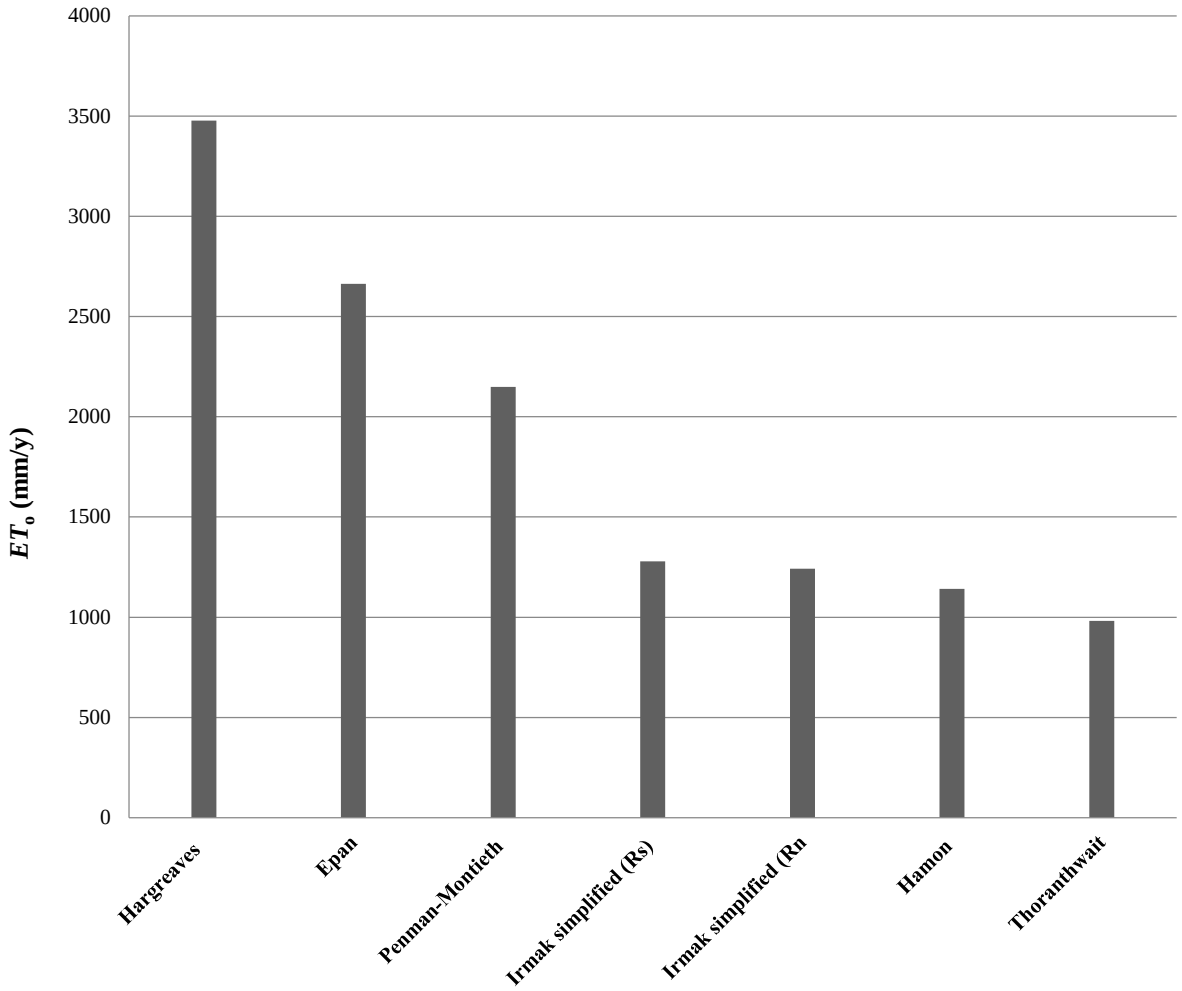

Fig. 8 Total annual ET_0 estimates given by different methods covering 2009 year metrological data

4. Brutsaert and Parlange (1998) indicated that, E_{pan} is often taken as a good indicator of ET_0 [3]. Therefore Fig. 9 shows a strong correlation between penman-Monteith method and E_{pan}. This correlation is found by Zhang et al., 2007. Zhang considered E_{pan} as indicator for reference evapotranspiration and

potential evapotranspiration [17].

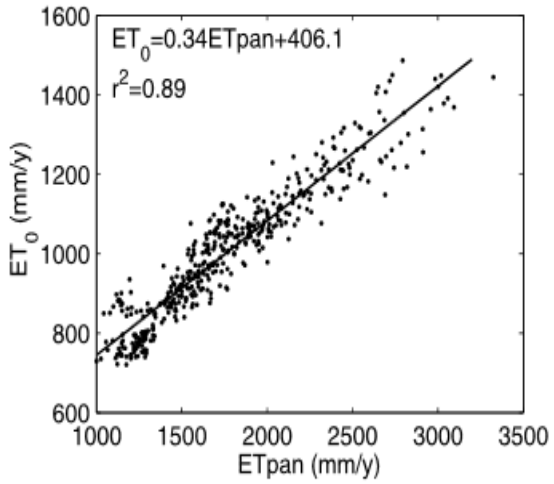

Fig. 9 Relationships between yearly Penman-Monteith ET_0 and evaporation E_{pan} calculated by the Penman equation (source: Zhang et al., 2007).

Therefore, The Hargreaves, Thornthwaite, Hamon, solar radiation and net radiation-based methods, Penman-Monteith are correlated with E_{pan} as the value of (R^2), (a) coefficients and Total yearly ET_0 is shown by Table 4. By considering the (R^2) and (a) value, in a case if the (R^2) value is the same between two methods, the most accurate and significant method is the one which has the (a) nearest to the 1.

The Penman-Monteith method with having (R_2 = 0.8& a = 0.69) is shown the highest correlation with E_{pan} as well as shows the closest ET_0 value to the E_{pan}.

Table 3 Correlated coefficient and mean error square of six well known methods

Models	coefficients				*MSE*	*P*-value
	R^2	*a*	*b*	*n*		
Hargreaves	0.8	0.8	3.6	365	3.32	0.00
FAO-56PM	0.8	0.6	0.7	365	2.70	0.00
Solar-radiation	0.8	0.2	1.4	365	5.70	0.00
Net radiation	0.6	0.2	1.9	365	6.11	0.00
Hamon	0.8	0.3	0.5	365	5.71	0.00
Thornthwaite	0.8	0.3	0.0	365	5.97	0.00

PM is Penman-Monteith method

The relationship between the six methods is shown in (Fig. 10 to 15). Based on *P*-value all the methods have significant correlation with E_{pan}, but by considering the (*a*) value, except the Hargreaves which has (R_2 = 0.8 & a = 0.80), all the others have the low value of (*a)* coefficient. Furthermore, Penman–Monteith requires the wind as a main factor for estimating the ET_0 and in other hand, Herat is characterized with strong wind velocity, the Penman–Monteith is recommended as the most accurate model for estimating the ET_0.

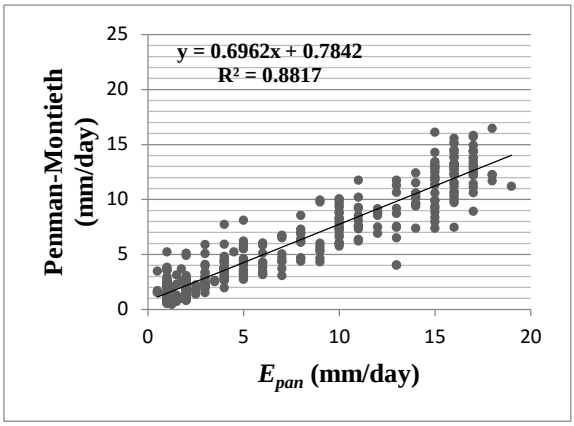

Fig. 10 Relationships between daily average *Epan* evaporation and Penman-Monteith methods

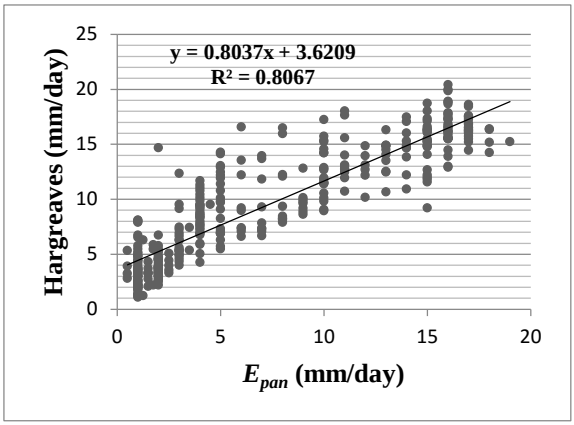

Fig. 11 Relationships between daily average *Epan* evaporation and Hargreaves methods

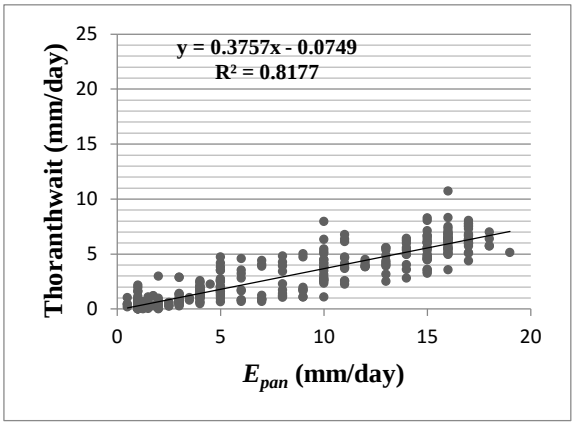

Fig. 12 Relationships between daily average *Epan* evaporation and Thornthwaite methods

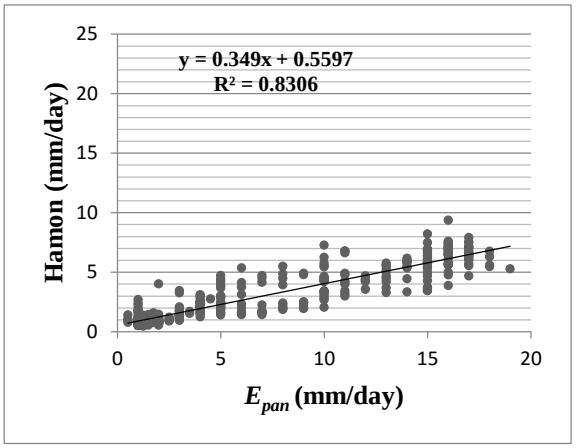

Fig. 13 Relationships between daily average *Epan* evaporation and Hamon methods

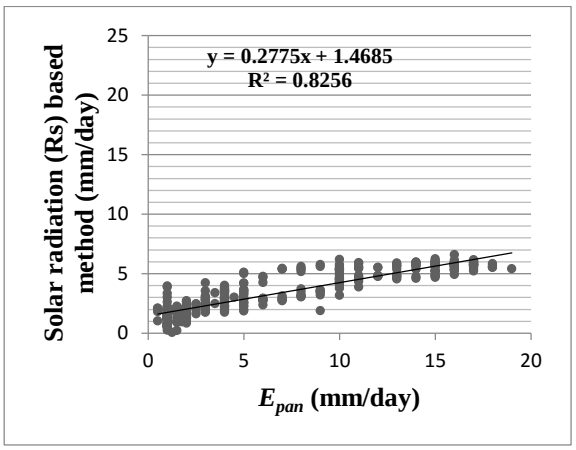

Fig. 14 Relationships between daily average *Epan* evaporation and Solar-radiation methods

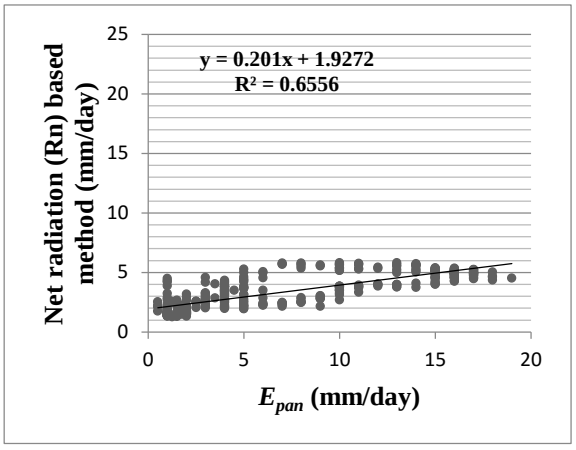

Fig. 15 Relationships between daily average *Epan* evaporation and Net radiation Methods

In a case if the requirement factors for penman-Monteith is not available, the Hargreaves with (R_2 = 0.8067 & a = 0.8037) method, which only requires temperature and radiation for calculation, is recommended for estimating the ET_0 as it shows high correlation with E_{pan}.

CONCLUSION

In Herat province, the ET_0 rate is shown different according to the different methods because all applied methods require different metrological factors for estimation of the ET_0. Among the applied methods in this study, Penman-Monteith is the only method which requires wind factor directly for estimating the ET_0 including the temperature, relative humidity and sun shine hours.

E_{pan} evaporation which is measured directly from A-class pan and Hargreaves methods, which requires temperature only, is also influenced by wind factor whereas the other methods are not influenced.

1. Humidity is high in the early spring, entire the winter and late fall whereas the summer season is characterized with low humidity due to low precipitation.

The entire of the summer season, wind speed is seen faster almost more than 5 m/s averagely than the other seasons. Similarly, temperature also is high in the summer, but since early of fall season the temperature decreases till middle of spring.

Net radiation is decreasing by early of fall and again increasing from late winter on.

2. All methods show a higher rate of ET_0 from the early summer until late fall. The Penman-Monteith and Hargreaves show closer ET_0 to the E_{pan} entire of the year, whereas the other four methods are different especially at early of summer until late fall seasons. The reason is referred to the strong wind "120-day winds" which blows all the summer season with high speed. This is why the estimated ET_0 through penman-Monteith, which requires wind velocity and Hargreaves method, which is recommended at the arid area, are closer to the measured evaporation through E_{pan}.

3. Hargreaves, Penman-Monteith and E_{pan} methods show the higher value of ET_0 as the Hargreaves shows the highest total annual value of ET_0 3500 mm/year, whereas the Thornthwaite, Homan, Solar radiation based method and Net radiation based methods, show the lower value of ET_0 as Thornthwaite has the lowest total annual value of 1000 mm/year.

4. As the E_{pan} is considered as indicator, the estimated ET_0 through Penman-Monteith and Hargreaves methods are closer to the E_{pan} value. Therefore, those methods are applicable than the other four methods in Herat, Afghanistan.

ACKNOWLEDGEMENT

REFERENCES

[1] Allen, Richard G., and William O. Pruitt. "FAO-24 reference evapotranspiration factors." J. of irrigation and drainage engineering, Vol. 117(5), Sep. 1991, pp. 758-773.

[2] Allen, Richard G., et al. "Crop evapotranspiration-Guidelines for computing crop water requirements-FAO Irrigation and drainage paper 56" FAO, Rome , Vol. 300(9), year 1998.

[3] Brutsaert, W., and M. B. Parlange. "Hydrologic cycle explains the evaporation paradox", J. of Nature, Vol. 396.6706, Nov. 1998, pp. 30-30.

[4] Dingman, S.L.1994. Physical Hydrology. Upper Saddle River, NJ: Prentice Hall

[5] Fontenot, R. L., An evaluation of reference evapotranspiration models in Louisiana. Diss. Faculty of the Louisiana State University and Agricultural and Mechanical College in partial fulfillment of the requirements for the degree of Master of Natural Sciences In The Interdepartmental Program of Natural Sciences by Royce Landon Fontenot BS, Louisiana State University, 2004.

[6] Ganji H, Rahmany Ab. S, Kajisa T, Kondo M, Hajime N, "Comparison of the Crop Water Need between Actual Wind Condition and Zero Wind Simulation; Wind Velocity within 24-Hour Interval in Herat, Afghanistan". In Tokyo University of Agriculture. 20th Int. Conf. on ISSAAS, 2014, pp. 91.

[7] Hanson, Ronald L. "Evapotranspiration and droughts." Paulson, RW, Chase, EB, Roberts, RS, and Moody, DW, Compilers, National Water Summary (1988), pp. 99-104.

[8] Haith, Douglas A., and Leslie L. Shoenaker. "Generalized Watershed Loading Functions for Stream Flow Nutrients1", J. JAWRA, Vol. 23(3), Jun. 1987, pp. 471-478.

[9] Hargreaves, George H., and Richard G. Allen. "History and evaluation of Hargreaves evapotranspiration equation." J. of Irrigation and Drainage Engineering, Vol. 129(1), Feb. 2003, pp. 53-63.

[10] Irmak, S., et al. "Solar and net radiation-based equations to estimate reference evapotranspiration in humid climates", J. of irrigation and drainage engineering, Vol. 129(5), Oct. 2003, pp. 336-347.

[11] Li, F., Lyons, T.J., 1999. Estimation of regional evapotranspiration through remote sensing. J. Appl. Meteorol.38, 1644-1654.

[12] Mintz, Y., and Walker, G. K. "Global fields of soil moisture and land surface evapotranspiration derived from observed precipitation and surface air temperature." J. of Meteorology, Vol. 32, Aug. 1993, pp. 1305-12334.

[13] O. Alkaeed, C. Flores, K. Jinno and A. Tsutsumi. 2006. Comparison of Several Reference Evapotranspiration Methods for Itoshima Peninsula Area, Fukuoka, Japan. Kyushu University, Vol. 66, No.1.

[14] Osmanzai, M. 2009. Annual Report. CIMMYT, Afghanistan.

[15] Penman, H.L. 1948. Natural evapotranspiration from open-water, bare soil and grass. Proc. R. Soc. Acad., 193: 120-145.

[16] Thornthwaite, C. W. 1948. "An approach toward a rational classification of climate." Geography. Rev. 38.

[17] Zhang, Yongqiang, et al. "Trends in pan evaporation and reference and actual evapotranspiration across the Tibetan Plateau", J. of Geophysical Research: Atmospheres, Vol. 112.D12. Jun. 2007.

First International Conference on Science, Engineering & Environment,
Tsu City, Mie, Japan, Nov.19-21, 2015, ISBN: 978-4-9905958-5-2 C3051

USE OF FLU GAS DESULFURIZING GYPSUM FOR REMOVAL OF OFF-FLAVOR COMPOUNDS IN FISH PONDS WATER

Niwooti Whangchai[1*], Redel Gutierrez[2], Udomluk Sompong[1], Supannee Suwanpakdee[1], Pornpimol Pimolrat[3] and Kanda Whangchai[4]

[1]Faculty of Fisheries Technology and Aquatic Resources, Maejo University, Sansai, Chiang Mai, Thailand; [2]College of Arts and Sciences, Central Luzon State University, Science City of Munoz, Nueva Ecija, 3120, Philippines; [3]Program in Fisheries, Maejo University, Chumphon Campus, La Mae, Chumphon, Thailand; [4]Department of Biology, Faculty of Science, Chiangmai University, Thailand
*Email: niwooti@hotmail.co.th

ABSTRACT

Accumulation of off-flavor in fish flesh caused by the presence of geosmin and 2-methylisoborneol (MIB) in pond water is a worldwide quality problem in aquaculture. This study investigated the effectiveness of commercial flue gas desulfurizing gypsum (CFG), a cheap and readily soluble material, for the removal of off flavor substances: geosmin and MIB, in fish pond water. Water samples from fish ponds were spiked with known concentrations of geosmin and MIB and varying amounts of CFG (0, 200, 400 and 600 mg/L) were added to compare the removal rate of geosmin and MIB, chlorophyll *a* levels and orthophosphate. The experiment was conducted for 9 days. It was revealed that CFG had significantly reduced both geosmin and MIB in spiked ponds water when compared with the control (0 mg/L) ($P<0.05$). The highest removal rates of geosmin (63.41%) were found when 600 mg/L of CFG was used after 9 days. However, the removal rate of geosmin at 200 and 400 mg/L CFG was not significantly ($P>0.05$) different from 600 mg/L. The highest removal rates of MIB (75.63%) were found with the treatment with 400 mg/L CFG after 6 days. In addition, 200 mg/L CFG was also highly effective in reducing chlorophyll a and orthophosphate concentration through calcium phosphate precipitation. It was suggested that 200 mg/L CFG is the suitable dose to apply for removal of off flavor compounds in fish ponds water.

Keywords: Off-flavor, Removal, Gypsum, Fish pond water, Geosmin, MIB

INTRODUCTION

Increase in population resulting in increased demand has pushed extensive aquaculture towards intensively operated production systems and commonly resulting in eutrophic conditions and cyanobacterial blooms. Cyanobacterial secondary metabolites can cause undesirable tastes and odors leading to acceptability in aquaculture products [1], [2]. Off-flavors especially earthy-musty off-flavors in drinking water supplies and aquatic animals for human consumption are world-wide problems. 2-methylisoborneol (MIB) and geosmin are the two most common earthy/musty-causing compounds. These off-flavors metabolites can be detected by consumers at the concentrations as low as 5–10 ng/L [3]. Some studies have shown that earthy/musty aromas were excreted by cyanobacteria such as *Anabaena* sp., *Oscillatoria* sp., *Lyngbya* sp. [4]-[6]. The conventional methods for controlling cyanobacterial bloom (sources of metabolites) are coagulation, clarification, filtration, algaecide and ozone [7], [8]. These methods, except coagulation, are usually expensive, complicated and can cause further pollution due to the use of chemicals.

Commercial flue gas desulfurizing gypsum has been used in agriculture purposes for soil amendment. Because it is a cheap and readily available source of calcium and sulfur that has been widely used in agriculture for recovery of alkali soils and as a source of calcium and sulfate in fertilizer [9]-[11]. Some studied suggested that natural rock gypsum powder could be used as a pond treatment in aquaculture for: flocculation of clay particles, increasing the concentration of calcium and total hardness, precipitation of phosphate and reducing in water pH [12]. However, the information on using CFG for water treatment in aquaculture especially in algal rich ponds water is limited. So, this study aimed to evaluate and the effectiveness of CFG in removing off-flavors compounds. The changes of phytoplankton cells and water qualities were also observed.

MATERIALS AND METHODS

Experimental Protocol

Algal-rich water samples collected from fish ponds were spiked with known concentrations of geosmin and MIB and varying amounts of CFG (0, 200, 400 and 600 mg/L) were added. Three replications of each group were performed. Commercial flue gas desulfurizing gypsum used in this study was purchased from local company.

The removal rate of geosmin and MIB, chlorophyll a

levels and water quality were monitored for 9 days. The production of hardness of each concentration was analyzed to compare with analytical grade gypsum.

Analysis of Geosmin and MIB in Water

Off flavor analysis was conducted by headspace solid phase microextraction (HS SPME) and gas chromatography-mass spectrometry (GC/MS) model Agilent Technology, USA [13]. A Geosmin and MIB standard from Sigma were used as source of off flavor.

Water Quality and Nutrient Analysis

Standard methods [14] were used for the analysis of total hardness, and orthophosphate-phosphorus in the laboratory.

Hydro-biological Analysis

Chlorophyll-*a* in the water samples was extracted with 10 mL of hot methanol (60^{o}C in water bath) and quantified with a spectrometer (Hach DR4000, USA) [14]. Chlorophyll-*a* concentration was calculated as described by Wintermans and de Mots [15] and Saijo [16].

Data Analysis

Analysis of variance (ANOVA) was used to test for difference between means of observed parameters in each treatment. Duncan Multiple Range Test (DMRT) at 95% confidence level was used for treatment comparison.

RESULTS AND DISCUSSION

1. Effect of gypsum on total hardness

In this study, it was founded that gypsum from different sources (analytical grade and CFG) gave different concentrations of total hardness (Fig. 1). The analytical grade showed higher total hardness than commercial grade and positive correlation between total hardness and gypsum concentration in both analytical and commercial grade. The total hardness per 1 mg of analytical and commercial grade gypsum was 0.546 and 0.329 mg/L of $CaCO_3$, respectively (Fig. 2). In this study, CFG could dissolve easily and provide harness in to the water. Some studies reported that gypsum is more soluble than liming materials and has been widely used in agriculture for increasing concentration of calcium and total hardness [11], [12]. However CFG: available and cheap material is suggested to use as hardness source in aquaculture.

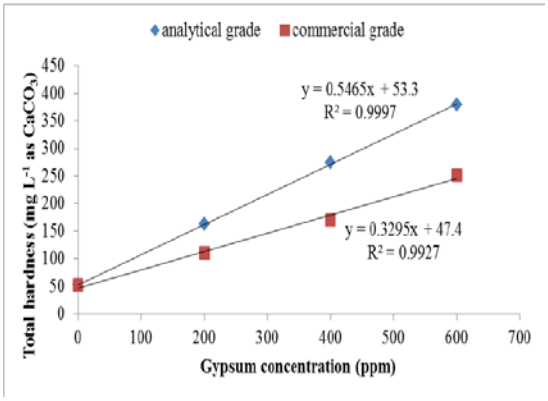

Fig. 1 Relation between total hardness and gypsum concentration

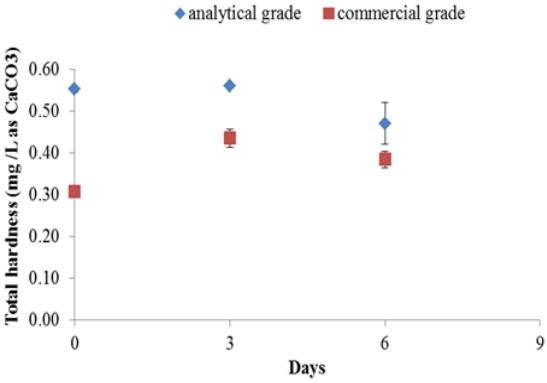

Fig. 2 Total hardness concentration from 1 mg/L analytical and commercial grade gypsum

2. Effect of CFG on geosmin and MIB removal in fish ponds water

In this study, CFG could reduce both geosmin and MIB in ponds water when compared with the control (0 mg/L). Geosmin could be reduced since 3 days when treated with different concentrations of CFG (Fig. 3a). The highest removal rates of geosmin (63.41%) were found in the treatment using 600 mg/L CFG (Table 1). However, the removal rate of geosmin in the groups that use 400 and 200 mg/L CFG was not significantly different from 600 mg/L (Fig. 3b-c, Table 2). It is possibly due to the solubility of different gypsum concentrations in water. The solubility of calcium sulfate (in pond water) at the concentrations of 50-1,600 mg/L at 25 °C ranged from 88.6 to 95% and dissolution increased with decreasing concentration and with increasing temperature [11]. In addition, it was also founded that the intracellular forms of both compounds showed better removal rate than the dissolved forms. It can be assumed that the negatively charged of cyanobacteria cells aggregated, and then settled, due to surface charge neutralization with the positively

charged colloidal formed by coagulant gypsum [19].

MIB concentration decreased slightly with the different concentrations of CFG added on 3 days (Figure. 3d). However, after 6 days the removal rate of MIB showed sharply decrease when treated with CFG (Fig. 3e-f). The highest removal rates of MIB (75.63%) were found when 400 mg/L CFG was used (Table 1).

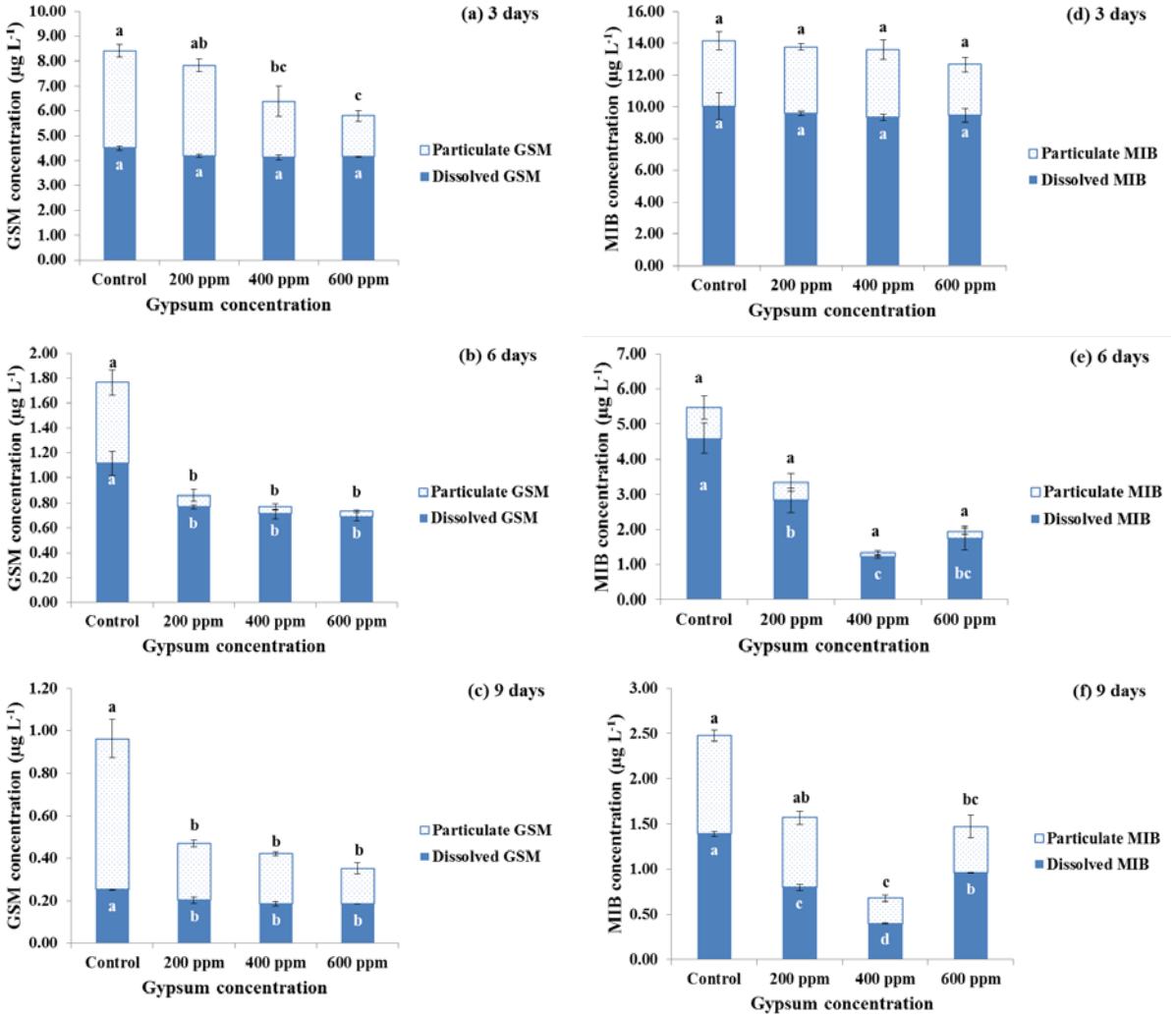

Fig. 3 Effect of CFG on particulate and dissolved geosmin (a-c) and particulate and dissolved MIB (d-e) concentrations at different times

Table 1 Removal rate (%) of geosmin and MIB at different CFG concentrations

Days	Removal rate (%)					
	Total GSM			Total MIB		
	200 mg/L	400 mg/L	600 mg/L	200 mg/L	400 mg/L	600 mg/L
3	6.92	24.25	31.11	2.62	3.89	10.43
6	51.32	56.50	58.47	39.15	75.63	64.64
9	51.14	56.14	63.41	36.67	72.68	40.79

Table 2 Effectiveness of CFG in removing off-flavor compounds (geosmin and MIB) (mean ±SD)

CFG concentration (mg/l)	Effectiveness in removing off-flavor compounds	
	geosmin (ng/l)/ CFG 1 mg/l	MIB (ng/l)/CFG 1 mg/l
200	3.30 ± 0.63	5.71 ± 2.63
400	2.98 ± 1.11	5.42 ± 2.64
600	2.37 ± 1.02	3.35 ± 1.30

In general some filamentous cyanobacteria and actinomycetes released geosmin and MIB to the water. When algal die and decompose, these metabolites consisted both particulate and dissolved forms and have been shown to be somewhat recalcitrant to conventional water treatment [17], [18].

Base on this study, CFG could apply for off flavor removal in fish pond. The recommendation level is 200 mg/l

3. Effect of CFG on chlorophyll a concentrations

Increasing of cyanobacteria and the release of their secondary metabolite, including geosmin and MIB, present an enormous risk to fish pond water. Chlorophyll a is generally considered as an important indicator of algal biomass [20].

In this study, the application of CFG to reduce the algal biomass was evaluated in the laboratory conditions. it was shown that all the three concentrations of CFG (200, 400 and 600 mg/L) could reduce chlorophyll *a* level when compared with the control treatments (Table 3). The highest effectiveness of 1 mg/L CFG that could reduce chlorophyll a was obtained in the treatment using 200 mg/L CFG (Table 3). The reduction of Chlorophyll *a* occurred by coagulation mechanism. Coagulation is a key step in conventional drinking water treatment for algal removal through colloidal charge neutralization followed by aggregation into floc [8]. In general, the effectiveness of coagulants increases with the charge on the metal ion. The calcium (Ca^{2+}) in gypsum ($CaSO_4$) is more effective because it carries a +2 charge [21]. Wu and Boyd [11] also reported that treatment of ponds at Auburn University with 250-500 mg/L of agricultural gypsum affected turbidity: many substances suspended in water including phytoplankton. Removal is similar to that achieved with 15-25 mg/L alum but gypsum has the advantage of a longer residual life than alum, and it is safer to use. Another possible mechanism of gypsum treatment is the reduction of phytoplankton abundance by lowering dissolved orthophosphate concentration through calcium phosphate precipitation in water. [11].

Table 3 Removal of chlorophyll a by different CFG concentrations

Gypsum (mg/l)	Effective removal of chlorophyll a (µg chlorophyll a/ mg CFG)
200	1.26
400	1.16
600	0.74

4. Effectiveness of CFG on orthophosphate removal

Phosphorus is an essential phytoplankton nutrient. In the commercial fish culture most phosphate gets into the water from metabolic waste of fish and from decomposition of uneaten feed [6], [22]. As feeding rate increases, nutrient concentration rises then the phytoplankton become more abundant.

In this experiment, the effect of CFG on dissolved orthophosphate concentration was investigated. The CFG treated water showed higher reduction in orthophosphate concentration than the control group (Figs. 4 and 5). The highest effect of CFG that could reduce orthophosphate concentration was observed in the treatment using 600 mg/L CFG after 9 days. However, the removal rate of orthophosphate in the groups that use 200 and 400 mg/L CFG was not significantly different ($P>0.05$) from the 600 mg/L group.

CFG treatment reduced orthophosphate concentration through calcium phosphate precipitation. Wu and Boyd [11] reported that in the water with low calcium concentration, gypsum application would precipitate phosphate. Additionally, gypsum is safe for human and aquatic life; its residual time in the pond depends on water flocculant retention time. Therefore, CFG is a suitable for use in aquaculture ponds.

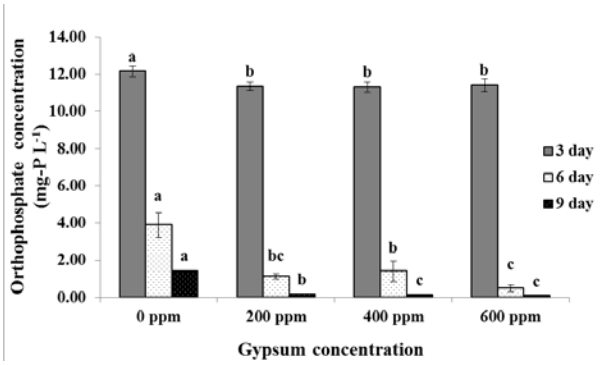

Fig. 4 Orthophosphate concentration in fish pond water

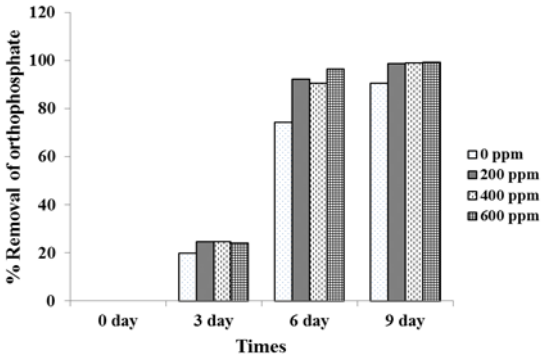

Fig. 5 Removal rate of orthophosphate with different CFG concentrations

CONCLUSION

It was confirmed that CFG at 200 mg/L was suitable for the reduction of geosmin and MIB especially in the particulate form. It also reduce phytoplankton in algal rich pond water because it is shown to be effective in reducing chlorophyll a In addition, CFG could also remove orthophosphate in fish ponds water through calcium phosphate precipitation which is an alternative way to control the problem from phytoplankton in fish culture. Finally it was recommend that CFG can use for water improvement in aquaculture pond.

ACKNOWLEDGEMENT

The work was carried out with the aid of a grant from the Thailand Research Fund (RDG5620050) and Maejo University for the laboratory instruments and research facilities.

REFERENCES

[1] Smith JL, Boyer GL and Zimba, PV, "A review of cyanobacterial odorous and bioactive metabolites: Impacts and management alternatives in aquaculture", Aquaculture, Vol. 280,bNo.1-4, 2008, pp. 5-20.

[2] Han J, Jeon BS, Futatsugi N and Park HD, "The effect of alum coagulation for in-lake treatment of toxic *Microcystis* and other cyanobacteria related organisms in microcosm experiments", Ecotoxicology and Environmental Safety, Vol. 96, 2013, pp. 17-23.

[3] Zhou B, Yuan R, Shi C, Yu L, Gu J and Zhang C, "Biodegradation of geosmin in drinking water by novel bacteria isolated from biologically active carbon", J. Environmental Sciences, Vol. 23, No.5, 2011, pp. 816-823.

[4] Tabachek JL and Yurkowski M, "Isolation and identification of blue-green algae producing muddy odor metabolites and 2-methylisoborneol in saline lake in Monitoba", J. Fish Res. Board Can., Vol. 33, 1976, pp. 25-35.

[5] Lovell RT and Broce D, "Cause of musty flavor in pond culture penaeid shrimp", Aquaculture penaeid shrimp, Aquaculture, Vol. 50, 1985, pp. 169-174.

[6] Pimolrat P, Whangchai N, Chitmanat C, Itayama T and Lebel L, "Off-flavor Characterization in High Nutrient Load Tilapia Ponds in Northern Thailand", Turkish J. of Fisheries and Aquatic Sciences, Vol. 15, No.2, 2015, pp. 275-283.

[7] Cooke GD, Welch EB, Peterson SA and Nichols SA, Restoration and Management of lakes and reservoirs. CRC Press, Inc., Boca Raton, Florida: USA, 2005.

[8] Sun F, Pei HY, Hu WR, Li XQ, Ma CX and Pei RT, "The cell damage of *Microcystis aeruginosa* in PACl coagulation and floc storage processes", Separation and Purification Technology, Vol. 115, 2013, pp. 123-128.

[9] Jackson ML, Soil chemical analysis. Prentice Hall, Englewood Cliffs, New Jersey, 1958.

[10] Jones US, Fertilizers and soil fertility. Reston Publishing, Reston, Virginia. 1979.

[11] Wu R and Boyd CE, "Evaluation of calcium sulfate for use in aquaculture ponds", The Progressive Fish-Culturist, Vol. 52, 1990, pp. 26-31.

[12] Boyd CE, Water quality management for pond fish culture. Elsevier Scientific, Amsterdam, USA, 1982.

[13] Gutierrez R, Whangchai1 N, Sompong U, Prarom W, Iwami N, Itayama T, Nomura N and Sugiura N, "Off-flavour in Nile tilapia (*Oreochromis niloticus*) cultured in an integrated pond-cage culture system", Maejo Int. J. Sci. Technol., Vol. 7(Special Issue), 2013, pp. S1-13.

[14] APHA, Standard Method for the Examination of Water and Wastewater. 15th Edition, Washington DC: American Public Health Association, USA, 1980.

[15] Wintermans JFGM and de Mots A, "Spectrophotometric characteristics of chlorophyll *a* and b and their pheophytins in ethanol", Biochim. Biophys. Acta., Vol. 109, 1965, pp. 448-453.

[16] Saijo Y, "A method for determination of chlorophyll", Jpn J. Limnol., Vol 36, No.3, 1975, pp. 103-109.

[17] Nerenberg R, Rittmann BE and Soucie WJ, "Ozone/biofiltration for removing MIB and geosmin", J. Am. Water Work Ass., Vol. 92, 2000, pp. 85-95.

[18] Ho L, Hoefel D, Bock F, Saint PC and Newcombe G, "Biodegradation rates of 2-methlyisoborneol (MIB) and geosmin through sand filters and in bioreactors", Chemosphere, Vol. 66, 2007, pp. 2210-2218.

[19] He W, Zhu Y, Xiao QH, Yang J, Lei LM, Han BP and. Zhang YM, "Study of removal of water bloom cells by red earth modified with polyaluminium chloride and ferric chloride", Ecol. Environ. Sci., Vol. 19, 2010, pp. 550-555.

[20] Izydorczyk K, Carpentier C, Mrówczyń ski J, Wagenvoort A, Jurczak T, and Tarczyń ska M, "Establishment of an alert level framework for cyanobacteria in drinking water resources by using the algae online analyser for monitoring cyanobacteria chlorophyll a", Water Res., Vol. 43, 2009, pp. 989-996.

[21] Bockris JOM and Reddy AKN, Modern Electrochemistry. New York: Plenum Press, 1973, 622pp.

[22] Boyd CE, "Chemical budgets for channel catfish ponds", Transactions of the American Fisheries Society, Vol. 114, 1985, pp. 291-298.

First International Conference on Science, Engineering & Environment,
Tsu City, Mie, Japan, Nov.19-21, 2015, ISBN: 978-4-9905958-5-2 C3051

KNOWLEDGE, ATTITUDE, AND SELF-CARE PRACTICE AMONG HYPERTENSIVE PATIENTS IN PATHUM THANI, THAILAND.

Chotisiri L.[1], Yamarat K. [1], Trongskul T.[2], Taneepanichskul S.[1]
[1]College of Public Health Sciences, Chulalongkorn University, Bangkok, Thailand
[2]Bueng KhamPhroi Health Promoting Hospital, Ministry of Public Health, Thailand

ABSTRACT

Hypertension is a major risk factor for cardiovascular disease (CVD). The purpose of this study was to explore knowledge, attitude and, self-care among hypertensive patients in Pathum Thani Province, Thailand.
A cross-sectional study was conducted at Bueng Kham Phroi Hospital between January and March 2015. One hundred and forty four cases were recruited. The data were collected by using NCD screening and a structure questionnaire. Descriptive statistics and Chi square were used to analyze the data. Most of respondents were women (74.3%), age 66.1 years old (±9.0 years), married (66.7%), housekeeper/retirement (67.4%), and with an elementary education (79.2%). NCD screening found that blood pressure was 136.4 (±14.4)/79.2 (±10.1) mmHg, body mass index was 24.9 Kg/m^2 (± 3.6 Kg/m^2), waist circumference was 88.6 cm (±7.1 cm) for men and 85.7 cm (±6.8 cm) for women. The knowledge of hypertension score was moderate to high. Most of respondents had a neutral attitude towards the overall score. Self-care practice to control blood pressure was low. In addition, self-care practice in term of healthy diet and physical activity was inadequate.

Keywords: Knowledge, Attitude, Self-care practice, Hypertensive patients.

INTRODUCTION

Hypertension is a major global health problem, the Global Burden of Disease Study (GBDS) stated that premature deaths, disability, stroke, and heart disease are related to increased blood pressure [1]. Higher incidence rates of hypertension are attributed to population growth, ageing, and behavioral risk factors such as unhealthy food intake, physical inactivity, obesity, smoking, excessive alcohol drinking, and chronic stress [2]. Uncontrolled blood pressure is associated with an increased risk of heart disease, stroke, and kidney disease [3], [4].

In all regions of Thailand, there is a high prevalence of newly diagnosed hypertension cases [5], [6]. High blood pressure is associated with many factors including age, gender, body mass index (BMI), family history of hypertension, and sedentary habits. Furthermore, lifestyle choices such as unhealthy food intake, physical inactivity, tobacco, alcohol use, stressful conditions, and insufficient sleep also increase the risk of hypertension [7]-[9]. Both pharmacotherapy and lifestyle modification are recommended treatments for high blood pressure. However, in order to prevent high blood pressure and concomitant cardiovascular disease, changes to medication adherence and lifestyle therapy must be made based on knowledge, awareness, and understanding of changes [10], [11]. As a result, it is necessary to find out knowledge, attitude, and self-care practice in hypertensive patients who are at increased risk of failing to reach blood pressure control treatment. The purpose of this study was to explore knowledge, attitude, and self-care practice among hypertensive patients in Pathum Thani Province, Thailand.

MATERIALS AND METHODS

Participants

A cross-sectional study was conducted at the Buerng Kham Phroi Health Promoting Hospital (HPH), Lam Luk ka district, Pathum Thani, Thailand. The sample size was of 144 cases. Study participants were aged 20 years and older, both male and female, currently diagnosed with hypertension, with regular appointment at Hypertension clinic of HPH. Individuals suffering from serious chronic illness or who were not willing to participate were excluded. The survey was carried out between January 13 and February 23, 2015.

Instruments and Procedures

Measurement tools consisted of digital blood pressure measurement devices, scales for measuring height and weight, and a measuring tape to determine waist circumference. A five part questionnaire was used to collect the following information: 1) general demographics; 2) knowledge of hypertension; 3) attitude towards high blood pressure; 4) self-care practice to control blood pressure; and 5) past medical history and other risk factors. Data collection was divided in to several phases.
The preparation phase began with the validation of the questionnaire by three public health experts. The

Items-Objective Congruence Index (IOC) was of 0.73. A pilot study was examined to test the reliability of the questionnaire and showed Kuder-Richardson (KR) 0.87. The Cronbach's Coefficient Alpha for attitude towards high blood pressure was 0.74. Data were collected by well-trained village health volunteers and trained nurses from HPH.

The collection phase consisted of introducing the research team, explaining the objective of the study, and obtaining written consent from participants that met the inclusion criteria and were willing to participate. Participants went through a complete physical examination including measurement of body weight and height. Body mass index (BMI) was calculated as weight/height (kg/m^2) and waist circumference (WC) was measured [12], [13]. This study defined high blood pressure by diagnosing hypertension under physician's treatment. Blood pressure was taken after a 10 minutes rest in a sitting position using a digital blood pressure measurement device and following a standardized procedure. Two readings of mean measures were used for the analysis. However, if a high systolic blood pressure measurement was greater than 5 mmHg a third reading was taken.

Following this procedure, the lowest of the three readings was taken as the blood pressure measurement. Using the Seventh Report of the Joint National Committee on Prevention, Detection, Evaluation, and Treatment of High Blood Pressure (JNC7), pre-hypertension was read when SBP was 120-139 mmHg and DBP was 80-89 mmHg. Hypertension stage 1 was read when SBP was 140-159 mmHg and DBP was 90-99 mmHg. Hypertension stage 2 when SBP was ≥ 160 mmHg and DBP was ≥ 100 mmHg. In addition, the lowest and highest group from those categories were noted [3].

The operation phase, trained by the researchers began when the nurses at HPH and village health volunteers interviewed all participants using the questionnaire. Interviews lasted an estimated 30 minutes each.

Statistical analysis

SPSS statistical package (Version16.0. Chicago, SPSS Inc) was used for data analysis. Descriptive statistic including frequency distribution, percentage, mean, and standard of deviation were used to describe the following general characteristics: chronic conditions and risk factors, clinical assessment, biological parameters, knowledge, attitude, and self-care practice of hypertension. The total score for knowledge was 10 points. The total score for attitude was 30 points. The total score for self-care practice was 30 points. The mean standard of deviation of knowledge was used to categorize the score as high, moderate, or low, respectively.

High level of knowledge was defined as a score ≥ to the mean +SD, moderate level of knowledge was defined as the score between mean – SD and mean + SD, and low level of knowledge was defined as a score ≤ to the mean – SD. Mean and standard deviation of attitude was also used to categorize the score as positive, neutral, and negative. Positive attitude was defined as a score ≥ mean +SD. A neutral attitude was defined as the score between mean –SD and mean + SD. Negative attitude was defined as a score ≤ mean –SD.

The score of self-care practice was categorized into 3 subgroups: unhealthy dietary intake, physical activity, and social activity. Unhealthy dietary intake was defined as frequent weekly consumption of high salt, high fat, high-energy foods. Participants were considered physically active when they engaged in any form of exercise for 30 minutes a day, at least three times a week. Social activity, emotional status, stress, and sleep were categorized as stressful condition. Similarly, the mean and standard deviations of self-care practice were used to categorize the score from low to high. High level scores of self-care practice were defined as a score ≥ mean +SD, moderate level of self-care practice was defined as a score between mean – SD and mean + SD, and low level of self-care practice was defined as a score ≤ mean – SD.

Ethical Consideration

Ethics approval was sought from the Ethics Review Committee for Research Involving Human Research Subjects, Health Sciences Group from Chulalongkorn University(COA No.178/2557). Prior to participation, the purpose and procedures of the study were fully made clear and all participants gave written, informed, consent.

RESULTS

General characteristics

The majority of the 144 respondents, 74.3%, were women. The average age was 66.1 years old (±9.0 years) with ages ranging from 33 to 80 years old. 66.7% of respondents were married, 79.2% had completed elementary school, and 67.6% were not employed (housekeeper/retirement). Most of the respondents were not cigarette smokers or alcohol drinkers. Over 50% were unaware of family history regarding hypertension. Over 80% of respondents had been diagnosed with hypertension and had been taking antihypertensive drugs for over five years. Nearly 30.0% of patients had other health issues such as diabetes, blurred vision, and hearing loss. As Table 1 shows, the clinical assessment found blood pressure to be 136.4 (±14.4)/79.2 (±10.1) mmHg (43.1%), BMI was 24.9 Kg/m^2 (±3.6 Kg/m^2)

(43.1%), waist circumference was 88.6 cm (±7.1 cm) for men (13.9%) and 85.7 cm (±6.8 cm) for women (53.5%), as shown in Table I.

Knowledge attitude and self-care practice to control blood pressure.

Of the 144 respondents, 62.5% present a high knowledge score for hypertension while the overall score of attitude towards hypertension was neutral for 77.8% of respondents. However, positive attitudes and negative attitudes were equal. The score for self-care practice to control blood pressure showed unhealthy eating habits 3 to 4 days of the week (72.9%) and physical activity less than 3 days a week (66.0%). Results for stressful conditions showed low stress (72.2%), as shown in Table II.

Table I Distribution of general characteristics, chronic condition &risk factors, clinical assessment parameters.

Parameters	N (144)	%
Age 61-70 year (66.1± 9.0)	58	(40.3)
Women	107	(74.3)
Married	96	(66.7)
Elementary school	114	(79.2)
Housework/retirement	106	(67.6)
Chronic conditions		
Non-cigarette smoker	108	(75.0)
Non-alcohol drinker	109	(75.7)
No Family history of HTN	82	(56.9)
Duration of HTN ≥5 years (9.0 ± 3.4)	120	(83.3)
Taking medication ≥ 5 years (8.7 ± 3.5)	118	(81.9)
HTN with other problems	43.3	(29.9)
Blood pressure (mmHg)		
SBP 120-139 (136.4 ±14.4)	62	(43.1)
DBP <80 (79.2 ±10.1)	77	(53.5)
BMI > 25Kg/m^2(24.9 ±3.6)	63	(43.8)
WC (M =37, W=107)		
>90 cm in men (88.6 ±7.1)	17	(13.9)
>80 cm in women(85.7 ±6.8)	77	(53.5)

Note: HTN; hypertension, SBP; systolic blood pressure, DBP; diastolic blood pressure, BMI; body mass index, WC; waist circumference.

Table II Distribution of knowledge, attitude and self-care practice to control blood pressure.

Variables	N(144)	%
score of knowledge: high	90	(62.5)
Score of attitude: neutral	112	(77.8)
Score of self-care practice		
- Unhealthy food: moderate	105	(72.9)
- Physical activity: moderate	95	(66.0)
- Stressful condition: low	104	(72.2)

DISCUSSION

The result findings in the present study had shown that the majority of the respondents were women, had hypertension with taking medication greater than 5 years, control blood pressure less than 140/90 mmHg, BMI 24.9±3.6 Kg/m^2. There were observed in proportions of overweight (BMI> 25 Kg/m^2) and waist circumferences (> 90 cm for men and > 80 cm for women) particular for women were greater than Tiptaradol, S. and W. Aekplakorn study [6]. Similarly, a previous study found that the average BMI and waist circumferences in both sex and socioeconomic factors had also increased a past decade [5], [14]. Furthermore, most of respondents in this study were women, average aged 66.1± 9.0 years might more correlate with cardiovascular, metabolic abnormality and menopausal change [5], [6], [15]. The results finding showed high score of knowledge for hypertension and neutral score of attitude to hypertension, it is possible to explain that Ministry of public health has launched health promoting activities to primary care settings overall regions such as Thailand healthy lifestyle strategic plan 2010-2020 to promote Thai people particular in patients with chronic diseases including hypertension for sufficient lifestyle by balance diet, adequate physical exercise and suitable emotion management as national health campaign into primary health care level over all regions in country [16]. Therefore, patients might more gain a lot of knowledge as same as changing some parts of attitude about diseases than the previous time due to giving education by mass media or communication from health care services [17]. However, we found that the score of self- care practice particular in a part of healthy diet and physical activity in Thai context, socio-geography and individual lifestyle were not adequate. One of reasons was individual factors such as age group and sex, as in [16], [18].

LIMITATION

The results of the study did not representative due to the convenience samples of hypertensive patients utilized for this study. Secondly, the number was not large enough. Finally, we were not able to control others factors such as public health information from outside the center or elsewhere that might effect to perceptions of illness, such as patient utilization, taking herbal supplements, etc. It is also possible that different results may have been obtained among a more homogeneous patient sample having a specific chronic illness, such as kidney disease.

RECOMMENDATION

The results from this study present a high score of knowledge and neutral attitude for hypertension.

However, self-care practice score to control blood pressure did not high. Therefore, it indicates a compelling need for the specific activities to encourage them for better health.

CONCLUSIONS

The knowledge score of hypertension showed moderate to high. The overall score of attitude toward high blood pressure showed neutral level. However, self-care practice to control blood pressure in term of healthy diet and physical activity was inadequate.

ACKNOWLEDGEMENTS

The author specially thank Asst. Prof. Dr. Khemika Yamarat, Assoc. Prof. Dr. Wiroj Jiamjarasransi, Dr. Pornpun Vorasiha, and the healthcare team from Bueng Kam Phroi health promoting hospital and Lam Lukka community hospital, Pathum Thani.

The study has been supported by the Higher Education Promotion and National Research University Project of Thailand, Office of Higher Education Commission (AS1148A-55) and the Ratchada-phiseksomphot Endowment Fund of Chulalongkorn University (RES560530243-AS).

REFERENCES

[1] Campbell, N.R., et al., Using the Global Burden of Disease Study to Assist Development of Nation-Specific Fact Sheets to Promote Prevention and Control of Hypertension and Reduction in Dietary Salt: A Resource From the World Hypertension League. The Journal of Clinical Hypertension, 2015. 17(3): p. 165-167.

[2] Organization, W.H., A global brief on Hypertension, Silent killer, global public health crisis. 2013. URL: http://apps. who. int/iris/bitstream/10665/79059/1/WHO_DCO_ WHD_2013. 2_eng. pdf [accessed 2013-07-17][WebCite Cache ID 6IBqAI2eN], 2014.

[3] Chobanian, A.V., et al., The seventh report of the joint national committee on prevention, detection, evaluation, and treatment of high blood pressure: the JNC 7 report. Jama, 2003. 289(19): p. 2560-2571.

[4] Forman, J.P., M.J. Stampfer, and G.C. Curhan, Diet and lifestyle risk factors associated with incident hypertension in women. Jama, 2009. 302(4): p. 401-411.

[5] Aekplakorn, W., et al., Changes in prevalence, awareness, treatment and control of hypertension in Thai population, 2004–2009: Thai National Health Examination Survey III–IV. Journal of hypertension, 2012. 30(9): p. 1734-1742.

[6] Tiptaradol, S. and W. Aekplakorn, Prevalence, awareness, treatment and control of coexistence of diabetes and hypertension in Thai population. International journal of hypertension, 2012. 2012.

[7] Chongthawonsatid, S., Demographic Factors and Health Care Behavior of Hypertension Disease in Thailand. Silapakorn University Sciences and Technology Journal, 2015. 9(1).

[8] Gangwisch, J.E., et al., Short sleep duration as a risk factor for hypertension analyses of the first national health and nutrition examination survey. hypertension, 2006. 47(5): p. 833-839.

[9] Koti, A. and R.G. Roetzheim, Patient factors associated with documented provision of JNC 7–recommended hypertension care at an academic family medicine office. The Journal of the American Board of Family Medicine, 2015. 28(1): p. 97-104.

[10] Rahman, A.R.A., et al., Perception of hypertension management by patients and doctors in Asia: potential to improve blood pressure control. Asia Pacific family medicine, 2015. 14(1): p. 2.

[11] Barr, P.J., et al., Public knowledge and perceptions of connected health. Journal of evaluation in clinical practice, 2014. 20(3): p. 246-254.

[12] WHO, E.C., Appropriate body-mass index for Asian populations and its implications for policy and intervention strategies. Lancet, 2004. 363(9403): p. 157.

[13] Wildman, R.P., et al., Appropriate body mass index and waist circumference cutoffs for categorization of overweight and central adiposity among Chinese adults. The American journal of clinical nutrition, 2004. 80(5): p. 1129-1136.

[14] Aekplakorn, W., et al., Prevalence and trends of obesity and association with socioeconomic status in Thai adults: national health examination surveys, 1991–2009. Journal of obesity, 2014. 2014.

[15] Chen, S.C., et al., Variations in Aging, Gender, Menopause, and Obesity and Their Effects on Hypertension in Taiwan. International journal of hypertension, 2014. 2014.

[16] Bureau of Policy and Strategy, M.o. Public, and Health., Thailand healthy lifestyle strategic plan,B.E.2554-2563 [2011-2020]. 2011: p.1-61.

[17] Geaney, F., et al., Nutrition knowledge, diet quality and hypertension in a working population. Preventive Medicine Reports, 2015. 2: p. 105-113.

[18] Lee, J.-E., et al., Correlates of self-care behaviors for managing hypertension among

Korean Americans: a questionnaire survey. International journal of nursing studies, 2010. 47(4): p. 411-417.

First International Conference on Science, Engineering & Environment,
Tsu City, Mie, Japan, Nov.19-21, 2015, ISBN: 978-4-9905958-5-2 C3051

THE EFFECTS OF TRADITIONAL THAI SELF-MASSAGE USING WILAI MASSAGE STICK™ IN PATIENTS ON UPPER TRAPEZIUS WITH MYOFASCIAL TRIGGER POINTS: A RANDOMIZED CONTROLLED TRIAL

Phanida Wamontree[1], Naowarat Kanchanakhan[1] Wichai Eungpinichpong[2] and Apichon Jeensawek[3]
[1]College of Public Health Sciences, Chulalongkorn University, Thailand; [2]Research Center in Back, Neck, and Other Joint Pain, and Human Performance, Khon Kaen University, Khon Kaen, Thailand; [3]Lat Lum Kaew Hospital, Pathumthani, Thailand

The purpose of this study was to investigate the effects of traditional Thai self-massage using Wilai massage stick™ in patient with upper trapezius with myofascial trigger points. Sixty patients were randomly allocated to either a massage group using Wilai massage stick™ or a medication group. Both groups were advised to have the same daily stretching exercise. Pain intensity, pressure pain threshold (PPT) and tissue hardness were assessed at baseline, and the fifth day after the last treatment session. The results showed that after 5 days of treatment, there are significant improvement in all assessment time points ($p<0.05$). The adjusted post-test mean values for pain intensity, PPT and tissue hardness were significantly better in the massage group than medication group ($p<0.05$). We conclude that traditional Thai self-massage using Wilai massage stick™ provides better results than taking medication for patients who have upper trapezius pain associated with MTrPs.

Keywords:Massage stick, Myofascial trigger point, Upper trapezius,

INTRODUCTION

Myofascial trigger points (MTrPs) could result from various causes, including muscle overload, severe muscle injury from accident, post-operative conditions leading to the stiffness or immobility of the affected muscles, mental stress, mild injury that left untreated for a long time [1]. The common treatments are either medication and/or massage. In some patients, drug treatment results in gastrointestinal tract side effects. In the past 10 years, non-drug treatment such as massage, chiropractice and acupuncture have become more popular [2]-[3].

Traditional Thai massage (TTM) is one of the oldest forms of Thai remedies. TTM is promoted as an effective means of alleviating pain. In a study in the therapeutic effects of TTM on patients with scapulocostal syndrome, it was found that was effective in alleviating pain, muscle tension, and anxiety [4]. A study comparing the effects of TTM and Swedish massage on patients with back pain also indicated that both type of massage resulted in pain alleviation [5]. Despite it proven benefits, massage was done mainly by therapist. Self-massage is generally use for people but there are some limitations of use for back region. Therefore, a self-massage device to serve people's need for use to relieve muscle tension and pain. Wilai massage stick was a device under investigation because it can be used to determine the location of trigger points (TrPs) and to apply pressure massage line according to TTM principle. A pilot study suggested that it could decrease pain and increase AROM [6]. Our aim to evaluated the effects of Wilai massage stick™ (TTMW) on pain intensity, pressure pain threshold, and tissue hardness in patients with upper trapezius muscle pain associated MTrPs.

SUBJECTS AND METHODS

A randomized controlled trial, was conducted at Lad Lum Kaew Hospital, Thailand. The study was approved by Ethics Review Committee for Research Involving Human Research Subjects of Health Science Group of Chulalongkorn University (COA No.082/2557).

The main inclusion criteria were, aged 18-60 year, VAS pain ≥ 3, suffered from upper trapezius pain for longer than 3 months. Had with diagnosis 1) taut band, 2) nodules, and 3) spot tenderness. Patients should not have received any analgesic or anti-inflammatory drug within two days of entering the study. Those individual, who had undergone surgery, and those with dislocation, fractures, neurological deficits, systemic disorders, or contraindication to treatment were excluded. Informed consent was obtained. Patients who met the inclusion criteria were randomly allocated to either the massage treatment or drug treatment group. Outcome measures:

Pain intensity by visual analogue scale (VAS): Patients were asked to indicate the average intensity of pain by pointing to a point along a 10-cm line; 0-cm indicating no pain and 10-cm severe pain. The pressure pain threshold (PPT) was the point where the patient started to experience pain by using a

tissue hardness meter/algometer (OE-220, Japan). The measurement of tissue hardness meter/algometer (OE-220, ITO, Japan) equipped with a 10-cm diameter plastic disc. Pressure was exerted vertically on the painful pressure point to be examined, and tissue hardness was automatically recorded.

All outcome measures were evaluated by physio therapist who was not informed of subject's group assignment. Assessments were done pre-test the first day and post-test the fifth day treatment sessions.

Statistical analysis: Characteristic data were as mean±(SD) and percentage. An unpaired t-test was used to compare differences of massage group and drug group. The significance was set at an alpha level of 0.05.

In the Wilai massage stick^{TM} group, provided with instructions regarding self-massage according to TTM principles. The back was to be divided into the left side and the right side using the spinal processes as the points of reference [Fig.1] For each side, there are two massage lines. The first one was about the width of a finger from the spinous processes, and the second line was about the width of three fingers from the spinous processes. Each line is further comprised of eight on the back region. Then self-massage was done in a self-massage was done in a sitting or standing posture, starting from the first point along the massage line on the left side of the back. The pressure was gradually increased until mild pain was felt, maintained for 5 seconds, and then releases. This was performed for all the eight points and then repeated 5 times. The procedures were performed for all the massage lines of both sides, lasting approximately 10 minutes. Medication group took a 400 mg. Ibuprofen tablet three times a day after each meal. For the both group did muscle stretching 2 minutes every day for 5 days.

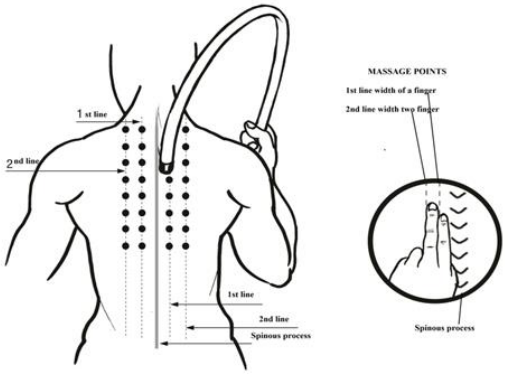

Fig. 1 The massage of TTM [8]

RESULTS

Details of demographic data and health characteristics were shown in (Table 1). The average age of TTMW were 42.85±10.06 and 41.67±11.72 years, respectively. The data demographic data were equally balanced between two groups. Clinical characteristics of patients upper trapezius pain shown that no significant differences were found between the groups on any of these measures.

Table 1 Demographic and characteristic

	Massage group (N=30)		Control group (N=30)	
	Mean	SD	Mean	SD
Age (years)	42.85	10.06	41.67	11.72
Weight (kg)	59.73	14.77	62.46	11.37
Height (cm)	159.79	7.90	159.30	7.44
VAS	5.43	1.45	5.20	1.51
PPT	1.96	0.58	1.77	0.52
Tissue hardness	47.74	6.78	46.09	6.36

Table 2 Comparison of the outcome measure between pre-test and post-test assessments in the TTMW and control group (paired t-test) (Mean±SD)

Outcome	Group	Pretest	Post-test	P-value
Pain intensity (VAS)	TTMW	5.4±1.4	0.8 ±0.5	0.5
	Control	5.2±1.5	1.87 ±1.3	0.5
Pressure pain threshold (kg/cm2)	TTMW	1.9 ±0.5	3.96 ±0.6	0.5
	Control	1.7±0.5	2.5±0.4	0.5
Tissue Hardness	TTMW	47.7±6.7	38.1±7.6	0.5
	Control	46.0±6.3	44.5±6.5	0.5

Note: TTMW = Wilai massage stick^{TM}, Control= Ibuprofen. P < 0.05 statistically differences from pretest

Table 3 Comparison of the adjusted mean and 95% CI outcome measures (adjusted for pretest using ANCOVA

Outcome	Post-test (Mean±SD)			
	TTMW	Control	Difference (95%CI)	P-value
Pain intensity (VAS)	0.8±0.8	1.8±1.3	-1.1(-1.6 to 0.6)	<0.05
Pressure pain threshold (kg/cm2)	3.9±0.6	2.5±0.4	1.3 (1.1 to 1.5)	<0.05
Tissue hardness (%)	38.13±7.67	44.5±6.5	-7.9(-9.7 to -6.1)	<0.05

Note: TTMW = Wilai massage stick^{TM}, Control= Ibuprofen. P < 0.05 statistically differences from pretest

DISCUSSION

This results of this study provide evidence that TTMW is effectiveness treatment reducing pain and improving upper trapezuis muscle pain in patients with MTrPs. The finding of this study suggest that TTMW on the trapezius area was effective in decreasing pain intensity with MTrPs can reduce after 5 days of treatment with either TTMW or control group. This finding consistent with previous studies ischemic pressure using Thera cane and stretching exercise found comparable results. They used the combination of ischemic pressure followed by sustained stretching to treat neck and upper back pain. The author reported reducing in pain intensity after 5 days of treatment [9]. In addition the study of Buttagate used the TTM and stretch exercise to treat upper back pain, and reported a reduction in present pain of treatment. After the patients received treatment with TTMW on the upper trapezius area, PPT was significantly increased at the end of 5 days of treatment. This results similarity from the study of Hantan who applied ischemic pressure localized at the MTrPs and found an improvement in the PPT at the end of a 5 days home program for patients with neck and upper back [10]. Moreover, the present finding support the study of Gulick used ischemic pressure with Backnobber II device on discomfort with MTrPs. at which revealed PPT from 31.74±12.8 at baseline to 44.20±13.33 at the end of a week [43]. The present study demonstrated that tissue hardness was reduced after treatment compare baseline. This indicated that the treatment by TTMW was effective in decreasing tissue hardness, consistent with the results of a previous study which found that use of deep massage on low back pain. The authors reported reduction in tissue hardness after treatment.

CONCLUSION

The results of this study indicated that a traditional Thai self-massage using a Wilai massage stick^{TM} to the upper trapezius area for the effective in reducing pain, tissue hardness increasing PPT in patients associated with myofascial trigger point. This treatment technique is a non-pharmacological management with no side effects. A Wilai massage stick^{TM} can therefore, be promoted as an alternative treatment in cases of limited number of therapists and those patients who have risk effects from medication

ACKNOWLEDGEMENTS

The study was supported by the Higher Education Research Promotion and Nation Research University Project of Thailand, Office of the Higher Education Commission, and the 90th Anniversary of Chulalongkorn University (Ratchadaphiseksomphot) Endowment)Fund. Office of the Higher Education Commission, University Staff Development under Higher Education Research Promotion(USD-HERP), Office of Thai Traditional Medical Knowledge Fund.

REFERENCES

[1] Armstrong RB, Warren GL, Warren JA: Mecchanism of exercise-induce muscle fiber injury. Am J Sports Med, 1991,12: 184-207.

[2] Eisenber DM, Davis RB,and Ettner SL.Trends in alternative medicine use in the United States, 1990-1997: results of a follow-up national survey.JAMA 1998;280: 1569-1575.

[3] Ernes E. Massage therapy for low back pain: a systemic review. J Pain Symptom Manage 1999;17:65.

[4] Buttagat V, Eungpinichpong W, David K, Chatchawan U, Arayawichanon P. Acute effects of traditional Thai massage on electroencephalogram in patients with scapulacostal syndrome. Comp Ther Med 2012; 20: 167-74

[5] Chatchawan U, Thinkhamrop B, Kharmwan S, Knowles J, Eungpinichpong W. Effectiveness of traditional Thai massage versus Swedish massage among patients with back pain associated with myofascial trigger points. J bodywork Mov Ther 2005; 9 (4) : 298-309.

[6] Wamontree P, Kanchanakhan K and Eungpinichpong W. Effects of traditional Thai self-massage using a massage stick versus Ibuprofen on upper back pain associated with myofascial trigger points: A pilot study. JHR 2015; 29(6) (In press)

[7] Hanten WP, Olson SL, Butts NL, Nowicki AL. Effectiveness of a home program of ischemic pressure followed by sustained stretch for treatment of myofascial trigger points. Phys Ther 2000; 80(10): 997-1003.

[8] Eungpinichpong W. Manual of Stick Wilai ; Bongkok, Suweeriyqwqrn,2008.

[9]Gulick DT, Palombaro K, Lattanzi JB. Effect of ischemic pressure using a Backnobber II device on discomfort associated with myofascial trigger points. J bodywork Mov Ther 2011; 15: 319-25.

First International Conference on Science, Engineering & Environment,
Tsu City, Mie, Japan, Nov.19-21, 2015, ISBN: 978-4-9905958-5-2 C3051

ENGLISH LEARNING DEVELOPMENT OF AGRICULTURAL STUDENT IN AGRICULTURAL MACHINERY SUBJECT

Dowroong Watcharinrat[1] and Fathiyyah[2]
[1]Faculty of Agricultural Technology, Rajamangala University of Technology Thanyaburi, Thailand; [2]Faculty of Agricultural Technology, 17 Agustus 1945 University of Banyuwangi, Indonesia

ABSTRACT

This research for developing english ability of agricultural student in agricultural machinery subject. They were the second year of crop production students of Agricultural Technology Faculty, Rajamangala University of Technology Thanyaburi, Thailand in academic year 2/2014. This research was on January – April 2015. There were forty five students in agricultural machinery subject. The first meeting, they got pre-test an hour to know their ability in English. There were 100 questions and picture. The same questions and pictures of pre-test and next post-test was made by researcher. The question also has been recommended by three lecturers who expert in agricultural machinery, research and english. Every questions, there were picture with thai name. Students should write in English name. Those question included about tillage, planting, crop protection and fertilizing, harvesting and processing equipment. The question divided into three part; multiple choice, check list and essay.This class was twice and two hour every meeting . At the end meeting, they got post-test to know their improvements. After that, Lecturer gave the answer of question to the student. The statistical in this research were frequency, presentage and mean.There were forty five students those are sixteen male and twenty nine female. The all student average mean of pre-test was 20.36, they improved 61.24 for post-test 81.6.The average mean improved were 62.06 of male and 60.79 for female and there was a significant difference between pre-test and post- test at .05 level of significance.

Keywords: English Learning, English Picture, Machinery Picture, Machinery English

INTRODUCTION

Our world is large as our language. Because by language we can communicated in many place as that language used. Language is important to survive in communication as way in all part. Asean Economic Community(AEC) is one of part business that need more language to know. Also, english language as international language.

English language have many method to learn it. Here we need try to know more vocabulary also grammar. but, in daily conversation that only need understanding for speaker and listener. But, english character is different with thai character. Because of this, need method that can make thai student easier to know and increase their ability in english.From one of the policy of Rajamangala University of Technology Thanyaburi [8], Faculty of Agricultural Technology is improve an english for the students with going to international in the future.

One of the best way for lecturer to increase their students english is study with picture, the student can quickly learning and easy to remember. Agricultural machinery subject course descriptions are study and practice on use of tractor and agricultural machinery,tillage equipment, planter, maintenance equipment for crop production ,pre and post harvester, selecting and buying of farm Tractor and agricultural machinery. This subject one of the requirement for crop production major in faculty, the students should learn, know and remember farm machinery equipment name in English. From above mention the research is use lecture with picture for methodology to improving their English.

METHODOLOGY

This research aim to development english ability of agricultural student. They were the second year of Crop Production Major students of Agricultural Technology Faculty, Rajamangala University of Technology Thanyaburi, Thailand in Academic Year 2/2014. This research was on January – April 2015. There were forty five students in agricultural machinery subject. The first meeting, they got pre-test a hour to know their ability in English. There were 100 questions and picture. They have one score every question. Totally they have 100 score of all question.

The pre-test and next post-test was made by researcher. The question also has been recommended by three lecturers who expert in agricultural machinery, research and english. Every questions, there were picture [3][4]][5][6][7][9] with thai name. Students should write in English name. Those question included about tillage, planting, crop protection and fertilizing, harvesting and processing equipment[1][2]. The question was

multiple choice. This class was twice and two hour every meeting. At the end meeting, they got post-test to know their improvements. After that, Lecturer gave the answer of question to the student. The statistical in this research were frequency, presentage, mean, t-test and independent t-test.

RESULT

This chapter showed the result of all score of forty five students in agricultural machinery subject in pre-test and post-test. it showed they improvement of their ability in english. It showed the statistical analysis of all student average mean, standard deviation, t-test and independent t-test of their pre-test and post test. it also compared between male and female improvement**.**

Table 1 Pre-test and post-test score of student in learning english of agricultural machinery subject

No	Gender	Pre-Test	Post-Test	Improvement
1	M	23	87	64
2	M	21	89	68
3	M	14	80	66
4	F	20	91	71
5	M	11	73	62
6	F	21	86	65
7	M	15	72	57
8	M	23	83	60
9	F	25	88	63
10	F	24	85	61
11	F	21	83	62
12	F	23	84	61
13	F	21	78	57
14	F	26	90	64
15	F	22	83	61
16	F	23	85	62
17	F	23	81	58
18	F	21	79	58
19	F	20	88	68
20	M	17	77	60
21	F	19	75	56
22	F	13	72	59
23	M	21	74	53
24	F	25	86	61
25	F	23	78	55
26	F	13	61	48
27	F	21	73	52
28	F	26	80	54
29	M	20	88	68
30	F	19	78	59
31	M	24	82	58
32	M	21	81	60
33	F	22	86	64
34	F	24	87	63
35	F	21	81	60
36	M	15	79	64
37	F	20	81	61
38	M	25	92	67
39	M	23	88	65
40	M	20	78	58
41	M	19	82	63
42	F	21	81	60
43	F	19	88	69
44	F	12	76	64
45	F	16	83	67
$\overline{X}$		20.36	81.6	61.24
S.D.		3.78	6.15	4.77

The table above explain the final score of pre-test and post-test from forty five students in agricultural machinery subject to development english. Three highest scores of pre-test score 26, 25 and 24. There were two students of score 26, three students of score 25 and three students of score 24. Three highest scores of post-test scores 92,91 and 90. There were one each of them. Three highest scores of improvement score 71, 69 and 68. There were one student of score 71 and 69 score and three student of score 68. The $\overline{X}$ of pre-test was 20.36 and the standard deviation was 3.78. The $\overline{X}$ of post-test was 81.6 with standard deviation 6.15. They improved in $\overline{X}$ 61.24 and the standard deviation 4.77.

Table 2 Pre-test and post-test score of male student in learning english of agricultural machinery subject

NO	Gender	Pre-Test	Post-Test	Improvement
1	M	23	87	64
2	M	21	89	68
3	M	14	80	66
4	M	11	73	62
5	M	15	72	57
6	M	23	83	60
7	M	17	77	60
8	M	21	74	53
9	M	20	88	68
10	M	24	82	58
11	M	21	81	60
12	M	15	79	64
13	M	25	92	67
14	M	23	88	65
15	M	20	78	58
16	M	19	82	63
$\overline{X}$		19.50	81.56	62.06
S.D.		4.03	6.02	4.33

Table 2 explain the male score in all parts. There were six teen male in this course. The highest pre-

test score were 25 of one male student, 24 of one male student and 23 of three male students. There were one student in each highest score of post-test, that was 92 and 89 and two students in 88. There were two students on 68 score in improvement part as the highest score and one student in each score 67 and 66. The $\overline{X}$ of pre-test from 16 male students was 19.50 and standard deviation 4.03. The $\overline{X}$ of their post-test was 81.56 and standard deviation was 6.02. they have improved by $\overline{X}$ 62.06 and standard deviation 4.33.

Table 3 Pre-test and post-test score of female student in learning english of agricultural machinery subject

No	Gender	Pre-Test	Post-Test	Improvement
1	F	20	91	71
2	F	21	86	65
3	F	25	88	63
4	F	24	85	61
5	F	21	83	62
6	F	23	84	61
7	F	21	78	57
8	F	26	90	64
9	F	22	83	61
10	F	23	85	62
11	F	23	81	58
12	F	21	79	58
13	F	20	88	68
14	F	19	75	56
15	F	13	72	59
16	F	25	86	61
17	F	23	78	55
18	F	13	61	48
19	F	21	73	52
20	F	26	80	54
21	F	19	78	59
22	F	22	86	64
23	F	24	87	63
24	F	21	81	60
25	F	20	81	61
26	F	21	81	60
27	F	19	88	69
28	F	12	76	64
29	F	16	83	67
$\overline{X}$		20.83	81.62	60.79
S.D.		3.62	6.32	5.02

Female score in each part explain in Table 3. There were two student of each highest pre-test score 26, 25 and 24. There were one student of each highest post-test score 91 and 90 and three students of score 83. There were one student of each highest improvement score 71, 69 and 68. From twenty nine female student they have $\overline{X}$ for pre-test 20.83 and the standard deviation 3.62. They have $\overline{X}$ of post-test 81.62 and the standard deviation 6.32. They improved by $\overline{X}$ 60.79 and standard deviation 5.02.

Table 4 The Compared of average mean between Pre-test and post-test score of all student in learning english of agricultural machinery subject by using paired samples t-test

Test	$\overline{X}$	S.D.	t-value	Probability
Pre-Test	20.36	3.78	86.079*	.000
Post-Test	81.6	6.15		

*significant at .05

From the table 4 the result showed that there were significant different between average mean of pre-test and post-test of english learning in agricultural machinery subject. That showed by the $\overline{X}$ pre-test was 20.36 and $\overline{X}$ post-test was 81.6 by t-value 86.079* and probability .000 with statistical significant different .05. Post-test was higher score than pre-test.

Table 5 The Compared of average mean between male and female post-test in learning english of agricultural machinery subject by using independent samples t-test

Group	$\overline{X}$	S.D.	t-value	Probability
Male	81.56	6.02	-.030	.976
Female	81.62	6.32		

*significant at .05

This final table compared of average mean of male and female post-test score english learning in agricultural machinery subject. That showed $\overline{X}$ of male post-test was 81.56 and the S.D. 6.02. The male $\overline{X}$ post-test was 81.62 and S.D. 6.32. The t-value was -.030 and the probability was .976. There were no significant different both of them of their achievement or knowledge that showed by independent sample t-test of the post-test with statistical different 0.5.

DISCUSSION

There were forty five students those are sixteen male and twenty nine female. They were second year of Crop Production Major Agricultural Technology Faculty Rajamangala University of Technology Thanyaburi Thailand 2014. The all student average mean of pre-test of learning english in agricultural machinery subject was 20.36, they improved 61.24 for post-test 81.6. The average mean improved were 62.06 of male and 60.79 for female. The best score on the final grade of Agricultural machinery subject was grade 4 from twenty three students, five students for grade 3.5 and eleven students for grade 3. This grade related with their improving in english.

From the statistical analysis has result that there was significant different between pre-test and post-test score. Because the all student improved about English in agricultural machinery subject. But, there was no significant different between male and female. Because both of them have same ability in english in agricultural machinery subject.

ACKNOWLEDGEMENTS

The authors would like to express their sincere thanks for the participated of Faculty of Agricultural Technology,Rajamangala University of Technology Thanyaburi and other. We would also say thanks for who could not be mentioned here for their kindness and encouragement

REFERENCES

[1] Dowroong Watcharinrat. 2013. Agricultural Machinery (Handout Teory). Rajamangala University Of Technology Thanyaburi Faculty of Agricultural Technology. Pathumtani Province, Thailand. 123 p.

[2] Dowroong Watcharinrat. 2013. Agricultural Machinery (Handout Labratory). Rajamangala University Of Technology Thanyaburi Faculty of Agricultural Technology. Pathumtani Province, Thailand. 35 p.

[3] Goering, C.E. 1986. Engine and Tractor Power. University of Illinois, United States of America. 404 p.

[4] Hunt, D. 1973. Farm Power and Machinery Management. Iowa State University Press, Ames. Iowa. 324 p.

[5] John Deere Publications. 1976. Fundamentals of Machine Operation, Tillage. John Deere Service Training Dept. F.,Moline, Illinois. 368 p.

[6] John Deere Publications. 1974. Fundamentals of Machine Operation, Agricultural Machinery Safety. John Deere Service Training Dept. F.,Moline, Illinois. 334 p.

[7] Patthipa Intarawichai. 1992. Farm Machinery Part 2. Agricultural Engineering Training Center. Pathumthani Province, Thailand. 135 p.

[8] Policy and Planning Division. 2014. Policy of RMUTT. Rajamangala University Of Technology Thanyaburi. Pathumtani Province, Thailand. 33 p.

[9] Smith, H.P., and Wilkes, L.H. Farm Machinery and Equipment. McGraw-Hill Book Company.488 p.

First International Conference on Science, Engineering & Environment,
Tsu City, Mie, Japan, Nov.19-21, 2015, ISBN: 978-4-9905958-5-2 C3051

A PARAMETRIC STUDY OF CLIMATIC-HYDROLOGIC FACTORS IMPACT ON WATER QUALITY IN KHLONG U-TAPAO RIVER BASIN, THAILAND

Saudee Maprasit[1], Chaisri Suksaroj[2] and Rotchanatch Darnsawasdi[3]
[1]Faculty of Environmental management, Prince of songkhla University, Hatyai, Songkhla 90110, Thailand;
[2,3] Prince of Songkhla University, Hatyai, Songkhla 90110, Thailand

ABSTRACT

Water quality degradation in Khlong U-Tapao river basin is come from various factors of land use. Out of this is effect from natural processes. This research objective is to study correlation of water quality by spatial-temporal change of climatic-hydrology in years of 2007-2013. Using multivariate statistical analysis to analyze water quality dataset 9 parameters such as pH, water temperature (WT), turbidity (TB), conductivity (CD), dissolved oxygen, (DO) biochemical oxygen demand (BOD), total coliform bacteria (TCB), fecal coliform bacteria (FCB), Ammonia Nitrogen (NH_3-N). The results show that seasonal change has affected to water quality by climatic-hydrologic factors influence. The climatic-climate relationship is humidity had positive correlations with temperature. The climatic-hydrology relationship is precipitation had positive with humidity but negative with temperature. The climatic-water quality relationship is temperature had positive with WT but negative with NH_3-N. The temporal hydrologic-water quality relationship is precipitation had positive with TB but negative with WT, pH and DO. Water inflow had positive with TB but negative with WT and CD. Water outflow had positive with TB and DO but negative with WT. Water level had positive with TB, BOD and TCB. The spatial hydrologic-water quality relationship is river cross-section had positive with WT and CD but negative with DO. The assessment from multiple linear regression equations can explain water quality variations. Therefore, water quality management should be consideration climatic-hydrologic change to provide basal information for developing improved water pollution control procedures of Khlong U-Tapao river basin.

Keywords: Water quality, Climatic-hydrologic factors, Multivariate analysis, Khlong U-Tapao river basin

INTRODUCTION

There are large scale and plenty of factors in water quality management, including population growth and density, land use in each pattern and practice of urbanization, agriculture, aquaculture and industry comprehensive all activity in water supply system [1]. The unpredictability in the water quality management is physical characteristics and phenomena change of nature. These are impact from geological attribute for example drainage pattern, land slope and soil property, hydrodynamic processes for example rainfall, runoff, river flow and discharge and climate for example temperature and solar radiation [2], [3].

The problem of water quality management in Thailand has uncertainty factors from natural change, for example in coastal zone of Phuket, wet season increasing water level and flow rate to making problem with wastewater discharge control from domestic and household. Geographic characteristics such as land slope and soils properties are aggravate to water quality degradation [4]. Rainfall, the cause of water level and water flow are higher than dry season to increase nutrients in river especially in agricultural zone of the Mun river basin [5]. Agricultural practice in Nakhon Nayok province in off-season is the problem for water quality management because of nutrients carried out to river by rain [6]. Wet season and rain fall make crisis with wastewater from industry and surface water in Lahan swamp of Chaiyaphum [7] and increasing nutrients in Ayutthaya watershed because of water level and water flow increased [8].

Accordingly, water quality study and management in Khlong U-Tapao river basin should be operation in system by consideration quantity of system components and interrelationship behavior with fluctuate and uncertainty variables. The relationship between climatic and hydrologic factors and all those variables have direct impact to water quality or not, because water quality management projects are determined and operated. Even if water quality continuing deterioration, therefore the management should be consideration in other factors such as climate and hydrology change [9]. Seasonal change is temporal effected from climate and can affect to hydrological processes [10]. Which it can induce water quality variation by rainfall increase is the main driver for water level and water flow change [10].

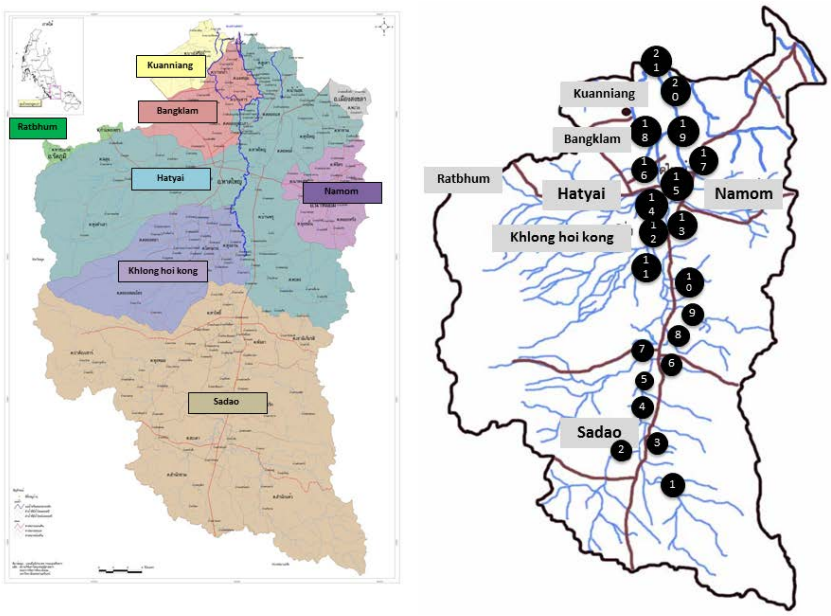

Fig. 1 Map of the Khlong U-Tapao river basin and water quality monitoring station

There are more researches to study impact from hydrology to water quality, from hydrology to water quality and from land use change to water quality. But there is incomplete understanding of the complex influence relationship among climate change in maximum and minimum value with spatial-temporal hydrology especially in Khlong U-Tapao river basin.

So, the conclusion of the study and implication for water quality management in Khlong U-Tapao river basin are complex system education and problem solving. The management should be administrative based on temporal-spatial change by considered human activity change and behavior of natural dynamic change including the assessment under different scenarios. This research objective is to study correlation of water quality by spatial-temporal change of climatic-hydrology.

STUDY AREA

Khlong U-Tapao river basin (KUT) is a main Songkhla lake sub-basin which located at southern part of Thailand. There are about 40 km wide (west to east) and 60 km long (north to south). It is important water resource for people living in Songkhla province and Hatyai district which is economic significance [11], [12]. There are 2,840 square kilometer and 7 district (fig.1) such as Sadao, Namom, Hatyai, Khlong hoi kong, Bangklam, Ratpum and Kuanniang. Land use-land cover (LULC) in the area of Khlong U-Tapao can classify in 8 main groups [12]. There are residential land uses, agricultural land uses, forestry land uses, industrial land uses, shrimp farming, water resources both of natural and manmade, lowland and other land uses for example fields, waste landfills, recreation zone, golf court, airport, graveyard and others.

MATERIALS AND METHODS

Data

Data gathering: to collect secondary data for water quality such as, pH, water temperature (WT), turbidity (TB), dissolved-oxygen (DO), conductivity (CD), biochemical-oxygen-demand (BOD), Total-Coliform-Bacteria (TCB), Nitrogen-Ammonia (NH_3-N) and Fecal-Coliform-Bacteria (FCB) from Regional Environmental Office 16, Songkhla from 2007-2013. The secondary data of water quality come from 21 stations along the Khlong U-Tapo river basin (Fig.1, table 1) and cover 13 administrative districts, there are 4 sub-district administration organization (SAO), 6 sub-district municipality (SM) and 3 town municipalities (TM).

Climate variables; there are maximum, minimum and mean of temperature (MAXT, MINT and MEANT respectively), humidity (MAXH, MINH and MEANH respectively) and wind flow from Songkhla Meteorological department.

Hydrology; there are precipitation (PRECI), inflow (IF) and outflow (OF) from Regional Irrigation Office 16, Songkhla. In the space parameter, there are cross-section (C-SECT) is computed by river width (RW) and depth (RD) from data of REO 16.

Table 1 water quality stations monitoring in KUT river basin

station	Station name	Geographic co-system		Canal	Location area
		x	y		
UT01	The bridge of huiku temple	664730.0	729095.0	Sadao	Samnak Taeo SAO
UT02	Sadao water supply office	659083.0	733842.0	Sadao	
UT03	the bridge of mitrsampan community	655884.0	729678.0	Krob	
UT04	The bridge of Saenpong school	656722.0	733392.0	Krob	Sadao TM
UT05	The bridge of Ban Namhua	654394.0	733327.0	Laeh	
UT06	The back of Safe skin medical factory	658130.0	736990.0	Laeh	
UT07	The bridge of Ban Huatanon	658774.0	737533.0	U-tapao	
UT08	the bridge of Ban Takianpao	658731.0	741088.0	U-tapao	Prik SM
UT09	the bridge of Ban thapohoak	659883.0	749279.0	U-tapao	Tha Poh SAO
UT10	the bridge of Muangkong temple	659264.0	754133.0	U-tapao	Phang La SM
UT11	the bridge of Ban Prao	662071.0	757846.0	U-tapao	
UT12	the bridge of Siam fiber board factory	661236.0	759087.0	U-tapao	Phatong SM
UT13	the bridge of Ban Khlongpom	661418.0	760892.0	U-tapao	
UT14	the bridge of Khlong Phla-Kokphyom	661033.0	762692.0	U-tapao	Ban Phru TM
UT15	The bridge of Bangsala temple	659416.0	766076.0	U-tapao	
UT16	the bridge of Hatyai university	661984.0	771489.0	U-tapao	Khohong SM
UT17	Water gate of Khlong U-tapao	661851.0	772341.0	U-tapao	Khuan Lang SM
UT18	the bridge of thasae temple	660804.0	777315.0	U-tapao	Khlong Hae TM
UT19	the bridge of Narungnok temple	662471.0	781796.0	U-tapao	Mae Tom SAO
UT20	the bridge of Kutao temple	662140.0	785665.0	U-tapao	Ku Tao SM
UT21	the bridge of Songkhla lagoon	661073.0	787729.0	U-tapao	

Note: SAO: Subdistrict Administration Organization, SM: Subdistrict Municipality, TM: Town Municipality (Department of Provincial Administration, Ministry of Interior, 2013).

Statistical analysis

A parametric study is a study process about parametric statistics for a normal distribution statistical data. There are several statistical procedures in this study such as two-sample t-test for compare the different of average value between two groups variable of dependent and independent, one-way-ANOVA is relationship test for more than 2 groups of in/dependent variables. Correlation and regression analysis is for related variables and water quality variation equations to explain trends of dependent variable by multiple independents [13], [14].

RESULT AND DISCUSSION

Relationship analysis of water quality by spatial-temporal patterns

Results in table 2 reveal the significance correlations of climatic-climate and climatic-hydrology. The correlation results show water quality change depends on temporal patterns such as time-period and season [15], [16]. In case of TCB and FCB are not changed by time because average value in each year not different (higher than standard value but increased a few in every year). CD is not depends on season that mean soluble matters is not different by seasonal change. Spatial patterns such as station or area of land use is related to water quality which WT and CD maybe because of wastewater characteristic, DO and TCB from the different of land use such as agricultural, industrial and urbanized zone [17].

Relationship analysis of climatic-climate and climatic-hydrology

From table 3-4, the result shows that, climate temperature in KUT river basin is affected by humidity and wind change. Almost climate temperature had positive correlation with humidity but negative with wind flow because wind flow can reduce temperature by dispersed but humidity can increase temperature by expanded heat energy. Climate MAXT had negative correlation with PRECI, W-level, Inflow, and river depth so MINT had positive correlation [18], [10]. All humidity change had positive correlation with hydrological variables. The phenomenon of precipitation into rainfall have affected by maximum climate temperature, the higher change can reduce occurred raining but higher humidity especially minimum value can support precipitation and hydrological parameters such as rainfall, water level and water flow.

Relationship analysis of climatic-hydrologic water quality

Results of significance correlation of climate change, hydrological processes and water quality of KUT river basin in table 5, explain the impact of water quality change based on climatic-hydrologic change by follows;

Table 2 Significant t-test/ F-test of spatial-temporal water quality

Parameters	WT	pH	TB	CD	DO	BOD	TCB	FCB	NH_3-N
Time (year)	0.000 **	0.000 **	0.000 **	0.025 **	0.002 **	0.000 **	0.886	0.715	0.000 **
Season (SS)	0.000 **	0.000 **	0.000 **	0.095	0.000 **	0.002 **	0.019 **	0.035 **	0.000 **
Station (St)	0.000 **	0.391	0.152	0.000 **	0.000 **	0.421	0.038 **	0.111	0.217

Note: **Significant at 0.01 level (2-tailed) / * Significant at 0.05 level (2-tailed)

Table 3 correlation analysis of Climatic-climate

Parameters		Climate					
		MAXT	MINT	MEANT	MAXH	MINH	MEANH
Climate	MAXT	-	-	-	-	-	-
	MINT	0.541**	-	-	-	-	-
	MEANT	0.926**	0.695**	-	-	-	-
	MAXH	0.506**	0.653**	0.743**	-	-	-
	MINH	-0.101*	0.506**	0.256**	0.634**	-	-
	MEANH	-	0.534**	0.356**	0.746**	0.951**	-
	Wind	-	-0.337**	-0.169**	-	-0.350**	-0.275**

Note: **Significant at 0.01 level (2-tailed) / * Significant at 0.05 level (2-tailed)

Table 4 correlation analysis of Climatic-hydrology

Parameters		Climate					
		MAXT	MINT	MEANT	MAXH	MINH	MEANH
Hydrology	PRECI	-0.244**	0.231**	-	0.383**	0.699**	0.660**
	W-level	-0.109*	-	-	-	0.154**	0.138**
	Inflow	-0.250**	0.141**	-	0.187**	0.427**	0.391**
	Outflow	-	-	-	-	0.116*	-
	Width	-	-	-	-	-	-
	Depth	-0.177**	-	-	0.118*	0.259**	0.221**

Note: **Significant at 0.01 level (2-tailed) / * Significant at 0.05 level (2-tailed)

Table 5 correlation analysis of Climatic-hydrologic water quality

Parameters		Water quality								
		WT	pH	TB	CD	DO	BOD	TCB	FCB	NH_3-N
Climate	MAXT	0.582**	0.249**	-	0.206**		-	-	-	-0.540**
	MINT	0.196**	0.220**	0.255**	-	-0.106*	-	-	-	-0.494**
	MEANT	0.507**	0.154**	-	0.163**		-	-	-	-0.558**
	MAXH	0.107*	-0.107*	0.288**	-	-0.236**	-	-	-	-0.505**
	MINH	-0.209**	-0.274**	0.574**	-0.121*	-0.209**	-	-	-	-0.208**
	MEANH	-0.114*	-0.266**	0.497**	-0.096*	-0.244**	-	-	-	-0.346**
Hydrology	PRECI	-0.145**	-0.328**	0.591**	-	-0.098*	-	-	-	-
	Inflow	-0.248**	-	0.434**	-0.144*	0.131*	-	-	-	0.188*
	Outflow	-0.167**	-	0.301**	-	0.278**	-	-	-	-
	Width	0.350**	0.184**	-	0.211**	-	-	-	-	-
	Depth	-	-	0.558**	-	-0.194**	0.150**	0.273*	0.277*	-

Note: **Significant at 0.01 level (2-tailed) / * Significant at 0.05 level (2-tailed)

Climate temperature had positive correlation with WT, pH, TB and CD but negative correlation with DO and NH_3-N. It is possibly explained, water temperature is directly impacted by climate temperature (MAXT) [10], [2] and increased pH is comes from increased chemical change form high climate temperature and induce to alkalinity in water. So, dissolved oxygen and nutrients is reduced from biological and chemical process [19], [10].

Climate humidity had negative correlation with WT, pH, CD, DO and NH_3-N but positive correlation with TB. Humidity can expand climate temperature, therefore water temperature is decreased can induce to decline the biological-chemical process [19], [10] and for turbidity may come from the after-effect from water flushed on surface soils [10], [20].

Hydrological process is showed by precipitation (PRECI) had negative correlation with WT, pH and DO but positive with TB. Results mean water temperature is affected by precipitation.

Table 6 multiple linear regression equations

Parameter	Multiple linear regression equations	R	R^2	Sig	Multi-collinearity
WT	8.754- 0.209(DO) +0.625(MAXT) -0.018(OF) +0.026(RW)	0.757	0.573	**	0.70-0.99
pH	5.304+ 0.009(RW) -0.056(WT) +0.136(MINT) -0.002(PRECI)	0.424	0.180	**	
TB	86.794 +38.826(RD) -3.716(WT) +5.164(OF)	0.797	0.635	**	
CD	-408.04 -0.764(RW) +67.736(pH) -1.756(IF) +2.187(MAXT) +1.244(DO)	0.380	0.144	**	
DO	13.131- 0.083(RD) -0.258(WT) -0.136(BOD) -1.227(Wind) +0.002(PRECI) +0.064(OF) +0.034(MAXH) -0.018(IF) -0.098(MINT)	0.739	0.545	**	
BOD	4.431 -1.124(DO) +0.126(MAXT) -0.022(RW) +0.411(RD)	0.459	0.211	**	
TCB	6984.179 -3030.444(RD) -345.027(SS) +85.830(TB) -835.662(DO) +1.002(FCB)	0.988	0.976	**	
NH_3-N	1.498 -0.001(TB) +0.004(BOD) -0.042(MAXT)	0.603	0.364	**	

Note: **Significant at 0.01 level

Which lower temperature is leading pH and DO decreased by TB increase can reduce absorbed DO and biological-chemical process [10], [19].

Water flow (inflow and outflow from reservoirs) had positive correlation with TB, DO and NH_3-N and negative with TEMP and CD. Water flow is a driver for turbidity increase [21] and soluble matter decrease. The increase of water flow can flushed erosive soils and nutrients from land surface and increase sediments in river [10], [20], [22] but in other words it can decrease conductivity by carried soluble matters along the river that not similar to the study of [10], [19] but similar with the study of [20].

River cross-section in terms of river width had positive correlation with WT, pH and CD and depth had positive correlation with TB, BOD, TCB and FCB but negative with DO. The river width can increase water temperature and leading to rising pH and conductivity by increased chemical change. The river depth is depends on water level, therefore turbidity and waste-matter is increased by flushed water [10], [21], [22] and large amount at river bottom.

Multiple linear regression analysis

Water quality variation is impacted by climatic-hydrologic change can explained by regression equations in table 6;

Water temperature (WT) variation is depend on MAXT, DO, OF and RW with moderate coefficient of determination values (R^2). Maximum climate temperature is a main driver to increase water temperature.

Turbidity (TB) variation is can description by climatic-hydrologic change. River depth and outflow are major factors to impact on turbidity with moderate coefficient of determination values (R^2).

Dissolved Oxygen (DO) variation is impacted by climate variables such as wind flow, MINT, MAXH and hydrology by PRECI, water flow and river depth with moderate coefficient of determination values (R^2).

Total coliform-bacteria (TCB) is affected by river depth, the driving source of this parameter with high coefficient of determination values (R^2).

The variations of pH, Conductivity (CD), BOD and NH_3-N is a few explanation by climatic and hydrology with multi-collinearity conditions. This suggests that other factors should be consideration in the regression equations to explain the variation of water quality with good coefficient of determination values (R^2)

CONCLUSION

There were significant correlations between climatic-hydrologic factors with water quality of Khlong U-Tapao river basin. Climate temperature, precipitation, water level, water flow and cross-section are main drivers to impact water quality. Water temperature and NH_3-N are as sensitive for monitoring impact from climate and turbidity as for hydrology. Therefore, water quality management planning should be consideration climatic-

hydrologic change for developing improved in protection and control wastewater discharge from various land use.

ACKNOWLEDGEMENTS

This study was supported by Office of the Higher Education Commission, Ministry of Education, Thailand.

REFERENCES

[1] UNICEF/WHO, "UNICEF Handbook on Water Quality", New York, 2008, pp. 1-2.

[2] Rehana S and Mujumdar PP, "River water quality response under hypothetical climate change scenarios in Tunga-Bhadra river,India", Hydrological Process, Vol. 25 (23), 2011, pp. 3373-3386.

[3] Tsakiris G and Alexakis D, "Water quality models: An overview", European Water 37, 2012, pp. 33-46.

[4] Pasinee R, Carter RW, Suchai W and Crossland CJ, "Wastewater discharge degrades coastal waters and reef communities in southern Thailand", Marine Environmental Research Vol.69, 2010, pp. 287-296.

[5] Akter A and Babel MS, "Hydrology modeling of the Mun River basin in Thailand", J. of Hydrology Vol.452, 2012, pp. 232-246.

[6] Seeboonruang U, "A statistic assessment of the impact of land uses on surface water quality indexs", J. of Environmental Management Vol.101, 2012, pp. 134-142.

[7] Pongpetch N and Suwanwaree P, "Spatial Water Quality Assessment and Mapping of Lahan Swamp, Chaiyaphum, Thailand", Procedia Environmental Science Vol.13, 2012, pp. 655-659.

[8] Supatimusro D, Areerachakul N and Poomsripanon J, "The Applied Geographic Information System and the Relation of Mollusk with Water quality in Ayutthaya Province, Thailand", Energy Procedia Vol. 34, 2013, pp. 99-108.

[9] Li YP and Huang GH, "Two-stage planning for sustainable water-quality management under uncertainty", J. of Environmental Management, Vol.8, 2009, pp. 2402–2413.

[10] Prathumratana L, Sthiannopkao S, Kim KW, "The relationship of climatic and hydrological parameters to surface water quality in the lower Mekong river", Environment International, Vol.34, 2008, pp. 860-866.

[11] Gyawali S, Techato K, Yuangyai C and Monprapussom S, "Assessment of Surface Water Quality Parameters and Their Variations for Effective River Monitoring System: A Case Study of U-Tapao River Basin", J. of Environ. Res. Vol.34 (2), 2012, pp. 89-106.

[12] Regional Environmental Office 16, Songkhla, "Water quality in Khlong U-Tapao river basin", year reports of 2006-2014.

[13] Ethington B., "Things To Know About Regression:, Edpr 7/8542, Spring, Retrieved on 07 June 2013 from https://umdrive.memphis.edu/yxu/public/Bunty's%20REGKNOW.pdf

[14] Patrasinee P, "chapter7: multiple linear regression analysis", Statistics for Scientific research, 1st ed. Bangkok: Chulalongkorn University, 2007, pp. 279-302.

[15] Karakoc G, Erkoc FU, Katircioglu H, "Water quality and impacts of pollution sources for Eymir and Mogsn lakes (Turkey)", Environment International, Vol.29, 2003, pp. 21-27.

[16] Kannel PR, Lee S, Lee YS, "Assessment of spatial-temporal patterns of surface and ground water qualities and factors influencing management strategy of groundwater system in an urban river corridor of Nepal", J. of Environmental Management, Vol.86, 2008, pp. 595-604.

[17] Xia LL, Liu RZ, Zao YW, "Correlation analysis of landscape pattern and water quality in Baiyangdian watershed", Procedia Environmental Sciences, Vol.13, 2012, pp. 2188-2196.

[18] McCarthy JJ, Canziani OF, Leary NA., "Climate change 2001; Impact, adaptation, and vulnerability", Cambridge University Press; 2001, pp. 195-233.

[19] Welsch DL, Cosby BJ, Hornberger GM, "Simulation of future stream alkalinity under changing deposition and climate scenarios", J. of Sci Total Environ, Vol.367, 2006, pp. 800–810.

[20] Zhao J, Fu G, Lei K, Li Y, "Multivariate analysis of surface water quality in the Three Georges area of China and implications for water management", J. of Environmental Sciences, Vol.23 (9), 2011, pp. 1460-1471.

[21] Chang H, "Spatial analysis of water quality trends in the Han river basin, South Korea", Water Research, Vol.42, 2008, pp. 3285-3304.

[22] Teeraphol S, Veerasak U. and Nuchanata M, "The specific hydro meteorological characteristics on soil loss and sediment transportation of the upper Lam Phra Ploeng watershed, Wang Nam Khieo subdistrict, Wang Nam Khieo district, Nakhon Ratchasima Province", in Proc.1st sustainable land use and natural resource management, Conf. on Bangkok, Thailand, 2004, pp. 33-42.

First International Conference on Science, Engineering & Environment,
Tsu City, Mie, Japan, Nov.19-21, 2015, ISBN: 978-4-9905958-5-2 C3051

A SIMULATION MODEL FOR COUPLED GROUNDWATER AND OPEN-CHANNEL FLOW IN RECLAIMED TIDAL PEATSWAMP

Aswandi[1], Robiyanto. H. Susanto[1], Edward Saleh[1], Iskhaq Iskandar[1] and M. RaisAbdillah[2]
[1]Department of Environmental Sciences, Sriwijaya University, South Sumatra, Indonesia
[2]Department of Geophysics, Graduate School of Science, Tohoku University, Sendai, Japan

ABSTRACT

A three-dimensional (x,y,t) model of coupled groundwater and open-channel flow is developed for simulating irrigated tidal peat swamp land in Berbak Delta, Jambi, Indonesia. It exhibits spatial feature and coupling ability which are rarely used in groundwater analysis in this region. The model uses Saint-Venant and Manning equations for open-channel flow and Darcy equation for groundwater flow. On the canal boundary, the water height data is simply assimilated on the previous day to reflect the tidal influence. Model performance is investigated in a small irrigated area for two periods during 2012/13 and 2013/2014.The simulated water table show coherent result with the observation. The model is expected to be useful for not only groundwater and irrigation application, but also broader analysis related subsidence and carbon loss in local area. It facilitates consumer (user) and policy makers (decision maker) in deciding on land-use planning and water management scenarios in the reclaimed area of tidal peat swamps.

Keywords: Modeling, Canal, Groundwater, Spatial, and Management

INTRODUCTION

For a complex environment system, not all driving factors could be identified or measured directly by people. A computer model helps us to represent the complex system and gives approximate solutions for users. In South Sumatera and Jambi Province, Indonesia, hydrology models have been used for water management system in irrigated lands. So far, the model applications were often limited to 2-dimensional (x,t) analysis for water flow in the canals only or soils only. For instance, Imanudin, M.S (2010) performed groundwater simulation using Drainmod model in a crop land. Damayanti, Evi (2013) used DUFLOW to study the water flow on the canals. To obtain more detail and more reliable results, we develop a 3-D (x,y,t) model that is able to reflect both groundwater and open-channel flow simultaneously. The model is named as Groundwater-Canal Flow (GCFlow) model. GCFlow has features that highlight the easiness for users. Therefore, it can be easily utilized by local institution and be developed for further analysis related to water management system.

MODEL DESIGN

Flowchart of the model

Fig. 1 exhibits the general flowchart of GCFlow model. The model needs daily rainfall and evapotranspiration dataset, soil and canal parameters data, and initial water table in the land and canal as initial condition. These dataset are then calculated in the model cores which consist of two systems: open-channel flow and groundwater flow. Finally, the predicted water table is produced. It can be used for the next iteration in the next day.

Basic Equations

Open-channel system simulates the behavior of water in the canal (open-canal type). The groundwater system simulates the flow of water in soil pores. Both components interact with each other in the model.

.

System of Open Channel Flow

Two equations in an open flow component are Saint-Venant equation and the Manning equation. The Saint-Venant equation is given by

$$\frac{\partial h}{\partial t} = \frac{\partial q}{\partial x} \tag{1}$$

where ∂h and ∂q are the change in water height (L) and change in discharge per cross-sectional width (L^2T^{-1}), respectively. ∂t and ∂x denote change in time and space, respectively. In finite difference approach, Eq. (1) can be written into

$$\frac{\Delta h}{\Delta t} = \frac{1}{w}\frac{Q_{in} - Q_{out}}{\Delta x} \tag{2}$$

$$h_i^{k+1} = h_i^k + \frac{1}{w}\frac{Q_{in} - Q_{out}}{\Delta x}\Delta t \tag{3}$$

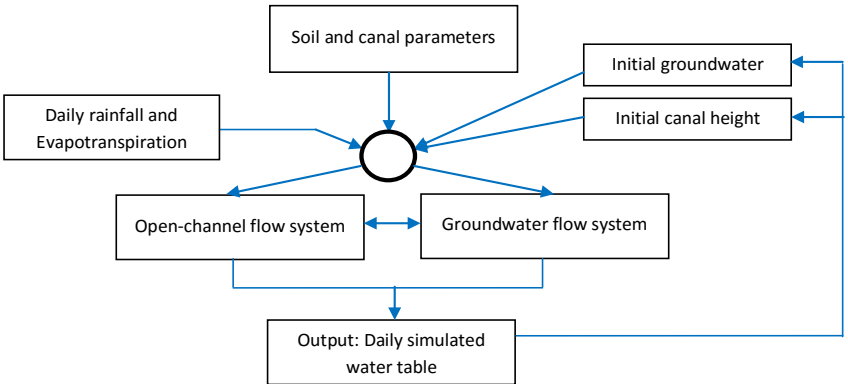

Fig. 1 Flowchart of GCFlow model

where w, Q_{in} and Q_{out} denote width of channel (L), total discharge entering and exiting a segment (L^3T^{-1}), respectively. h_i^{k+1}denotes simulated water height at time step $(k+1)$. The total discharge is estimated based on Manning equation as follow

$$Q = \frac{A}{n} R^{2/3} |S|^{1/2} \quad (4)$$

where A is cross section of the segment (L^2), n is Manning roughness coefficient ($L^{-1/3}T^{-1}$), R is hydraulic radius (L) and S is energy slope in the upstream and downstream of the segment, simplified to the slope of the surface water between segments (LL^{-1}). If S > 0 (S < 0), then the computed Q is classified as $Q_{in}(Q_{out})$, respectively.

In model, the canal is represented as grids that distributed spatially (Fig. 2). To measure the discharge Q_{in} and Q_{out}, model evaluates every energy slope S in all surrounding canal-type grids as illustrated in Fig. 2 (right). Note that to obtain Q, model uses the actual width of the canals, not the width of the simplified canal in the box.

System of Groundwater Flow

GCFlow assumes 1-layer aquifer system because characteristic of vertical hydraulic variation in peat soils is more uniform compared in mineral soils. The vertical hydraulic conductivity value is observed very low and can be neglected.

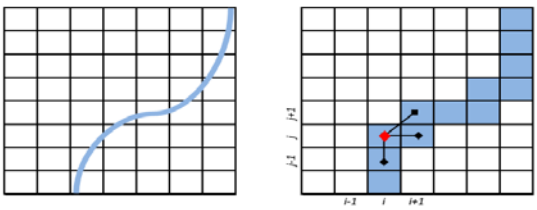

Fig.2 Canal schematization. (left) blue line denotes real position of water body. (right) blue boxes denote canal in the model. See text for details.

Aquifer system is simplified into a number of grids that have the same width (ΔX). Each grid is a three-dimensional body whose depth dimension is represented by the thickness of the aquifer. The flow is assumed to occur in the direction of the X-axis and Y-called flow between grids. Flow between grids occurs following the hydraulic gradient (dH/dX) formulated in finite difference method as ΔH/ΔX. The groundwater flow direction is determined by five neighboring cells.

Based on the principle of conservation of mass, we can derive the following equations:

$$\frac{\boldsymbol{dV}}{\boldsymbol{dt}} = \sum \boldsymbol{Q_{in}} - \sum \boldsymbol{Q_{out}} \quad (5)$$

$$\frac{\boldsymbol{\Delta H}}{\boldsymbol{\Delta t}} = \frac{\sum \boldsymbol{Q_{in}} - \sum \boldsymbol{Q_{out}}}{(\boldsymbol{\Delta X})^2} \quad (6)$$

$$\frac{\boldsymbol{\Delta H_{i,j}}}{\boldsymbol{\Delta t}} = \frac{\boldsymbol{KA_{i,j}}}{\boldsymbol{f_{i,j}}(\boldsymbol{\Delta X})^2} \frac{\left(\sum_{N=1}^{4} \boldsymbol{H_N^k}\right) - \boldsymbol{4H_{i,j}}}{\boldsymbol{\Delta X}} \quad (7)$$

$$\sum_{N=1}^{4} \boldsymbol{H_N^k} = \boldsymbol{H_{i+1,j}} + \boldsymbol{H_{i-1,j}} + \boldsymbol{H_{i,j+1}} + \boldsymbol{H_{i,j-1}}$$

In Eq. 5, $\boldsymbol{V}$ is the volume occupied by groundwater in a grid integrated from aquifer until the water table position (L^3). $\boldsymbol{Q_{in}}$ and $\boldsymbol{Q_{out}}$ are flow entering and exiting a grid (L^3T^{-1}). Eq. 6 shows the finite difference form of Eq. 5.

We then can break down the parameter of $\boldsymbol{Q}$ into water table height (**H**), saturated hydraulic conductivity ($\boldsymbol{K}$), storage coefficient ($\boldsymbol{f}$), and cross-sectional area of flow ($\boldsymbol{A}$). By adding Darcy equation, we obtain Eq. 7 where $\sum \boldsymbol{H_N^k}$ is sum of surrounding cells height, $\boldsymbol{N}$ = (1,2,3,4) is an index for the water height **H** in four neighboring cells:{(i-1,j), (i+1,j), (i,j+1), (i,j-1)}. Notation i and j denote the indices of grids/boxes. Notation $\boldsymbol{k}$ denotes the time step of the model. The cross-sectional area ($\boldsymbol{A}$) is a scalar product of water table depth ($\boldsymbol{D}$) with width of the grid ($\boldsymbol{\Delta X}$),

$$A_{i,j} = D_{i,j}\Delta X \quad (8)$$

The Eq. 8 is then modified after including net precipitation (***P***):

$$H_{i,j}^{k+1} = H_{i,j}^{k} + \frac{P_{i,j}^{k}}{f_{i,j}} + \frac{KD_{i,j}}{f_{i,j}}\left[\frac{\left(\sum_{N=1}^{4} H_N^k\right) - 4H_{i,j}^k}{(\Delta X)^2}\right]\Delta t \quad (9)$$

The net precipitation is raw precipitation measured in meteorological station minus evapotranspiration. Basic depth of groundwater flow (***D***) is calculated by Hooghoudt principle as shown in Eq. 10, where **L** is the distance between the canals (L), r_0 is the specific radius of flow (L), **m** is a function of aquiver thickness ratio and distance between canals (L/L), ***T*** is the thickness of the aquifer (L), ***w*** is the flow width in the canal (L) and ***l*** is the flow depth in the canal (L).

$$D = \frac{\frac{\pi L}{8}}{ln\frac{L}{\pi r_0} + F(m)} \quad (10)$$

$$m = \frac{2\pi T}{L}$$

$$F(m) = 2\sum_{n=1}^{\infty} ln(\coth(nm))$$

$$r_0 = \frac{wl}{\pi(w+2l)}$$

Initial condition

Model uses UTM coordinate for identifying grid location. The dataset is compatible with GIS software such as ArcView/ArcGIS. Table 1 shows the data parameters needed by the model. For canal parameters, it should be provided in a *shape file* (shp) line-type vector format that consist geographical location of actual canal, depth and width of the canal segment. GCFlow will discrete the canal segments into grids/cells (Fig. 2). Model also needs soils parameter, DEM, and net-precipitation dataset.

To prepare the initial condition, the model calculates initial water table in the canal first and adjusts initial water table in the land afterwards. There are two methods to prepare the initial condition of water table: method of uniform and data-logger. Both control the initiation in the canal.

In uniform method, user will be asked to input a value for average water table depth in the canals relative to surface topography. The open-channel flow equation is then applied to *smoothing* the initial water table in a short period.

Table 1. The parameters used in GCFlow model

Data Input	Unit (dimension)
Canal system:	
• Map of canal	-
• Depth of canal	m
• Top width of canal	m
• Bottom width of canal	m
• Manning coefficient	-
• Initial water table	m
Soil characteristics:	
Hydraulic conductivity	m day^{-1}
Coefficient storage	m^3 m^{-3}
Elevation (DEM)	m
Net-precipitation	mmday^{-1}

After that, the groundwater flow equation is used to represent initial water table in the land. This option is suitable for simulations of various scenarios assuming a uniform averaged canal water height.

The method of data logger is similar with the uniform, except user must input real observation data in canal. If the user wants to perform simulations of real-case for a certain time span, the user must prepare the water level observation data canal on the first day. The data logger is expected to spread across all segments of the canal in order to accurately form the water table surface.

Model codes, layouts and features

The GCFlow codes are written in MATLAB programming language (www.mathworks.com). The model is designed with GUI feature for easiness to user. A snapshot of the model interface is shown in Fig. 3. GCFlow provide interesting features for visualization of ground water. In addition to displaying spatial map of groundwater, user can see the cross-section of water level from various locations. Users can also view time-series water level in any cell selected by the user. The model output can be saved in a format ArcView/ArcGIS, Ms. Excel, or ASCII.

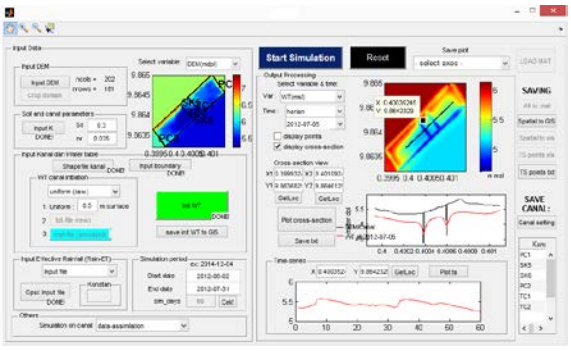

Fig.3 A snapshot of GCFlow model.

CASE STUDY IN RANTAUMAKMUR

Model performance is investigated in small irrigated land in Rantau Makmur village, Jambi, Indonesia from 1 April 2012 to 31 March 2013 (Fig. 4). The domain has two primary canals (PC), two secondary canals (SK), and two tertiary canals (TC). Total grids simulated in the model are 202 × 181 or 36 562 grids with 10 m resolution. The topography of the study area is presented in Fig. 5.

Preparation of soil and canal data

To make 2-dimensional datasets of soil and canal parameter, we perform interpolation technique and simple calibration. The former one is used when the observations are considerably much and scattered. The latter one is used when data observations are less.

Spatial interpolation

We consider the topography (DEM) and hydraulic conductivity (K) datasets are appropriate for interpolation. Interpolations are done using ArcView/ ArcGIS program using natural neighbor method for DEM data and hydraulic conductivity (K). The observation of K is constrained in the inner part of domain where the main analysis is conducted.

Calibration

Storage coefficient (S) and the manning coefficient parameter are calibrated. This is because these parameters are considered uncertainty great value but less observation point. To obtain appropriate value for S and n, GCFlow runs several times with different initial conditions. The range of initial values is based on previous measurement in Berbak Delta. The simulated water table for all experiments are assessed by finding the highest correlation coefficient with the observation. For S, the calibration result shows that 0.3 m^3m^{-3} is the best so far for our calculation. While the results of the calibration for manning coefficient is 0.03.

Inserting tidal influence

Water canals in Rantau Makmur village are strongly affected by sea tidal force thus it is important to include tidal force in the model. However, we do not use basic dynamic equations of tidal force. In GCFlow, we simply assimilate the tidal force by a proxy of WT canal observation at the previous day of simulated WT in every outer boundary of PC canals (water table observation is held every 24-hours). In details, if number of time

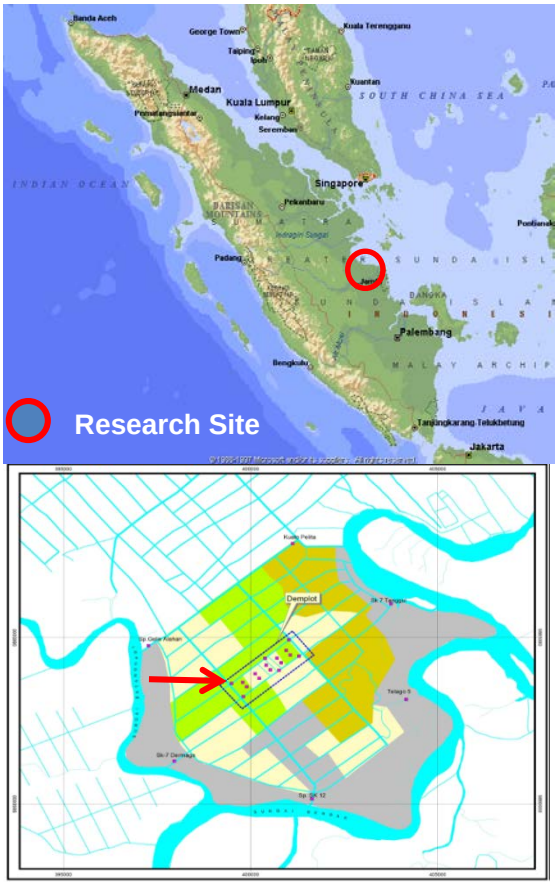

Fig. 4 (Top) Sumatra Island, Indonesia and (bottom) the location of the research site for case study in Rantau Makmur village, Jambi Province, Indonesia (depicted by red circle in (top) and pointed by red arrow in (bottom)).

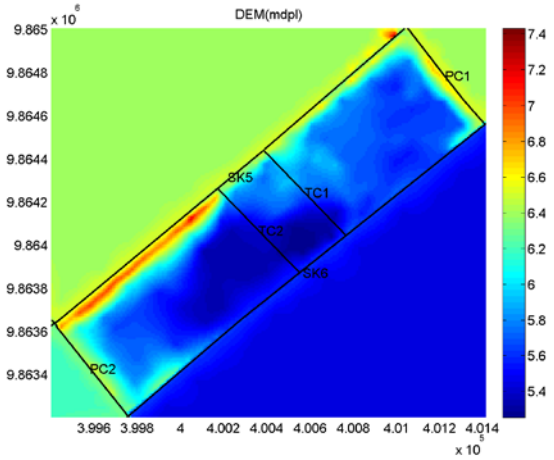

Fig. 5 Topography (m msl) and canals location that used in case study (projection in UTM 48S)

step for each day is 12 steps (2 hour), the initial water height for calculating water height at step 1 is obtained by modifying simulated water height at 24th step in previous day. The modified simulated water height is

$$h_{i,j}^{k} = (1-\alpha)h_{i,j}^{k} + \alpha\overline{h_{obs}} \qquad (11)$$

where $h_{i,j}^{k}$ is raw simulated water height at last step k for previous day. $\overline{h_{obs}}$ is the average of canal water height observations on previous day. α is assimilation factor which has a value between 0 to 1 depending on user's demand. In our case, we simply use α of 0.5.

Simulation for year 2012/2013

In this period, GCFlow simulates water table from April 1, 2012 to March 31, 2013. Fig. 6 exhibits spatial simulation result on 30 April 2012. This model provides a feature for analyzing the cross-section of water table from any locations.

Fig. 7 shows daily time-series of simulated and observed canal water and groundwater height. In the canal, the model simulates good in-phase relationship (Fig. 7 top). The model succeeds to show the fluctuation affected by tidal although the amplitude seems a bit suppressed. The model shows surprisingly great result after November 2012 when the canal water is observed on the surface. In general, the R^2 values on the canal points of P8, P9, S5 and S2 are considerably good (Table 2), indicating good performance of the model. The difference on R2 value may be caused by assimilation process which includes only averaged value of observational data.

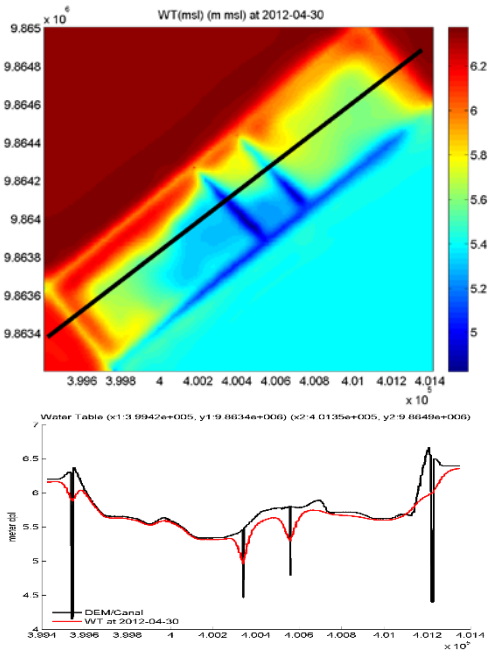

Fig. 6 (top) Result of simulated water table on 30 April 2012. Black line denotes location for cross-section. (bottom) the cross-section of water table. Black (red) line indicate DEM (water) height.

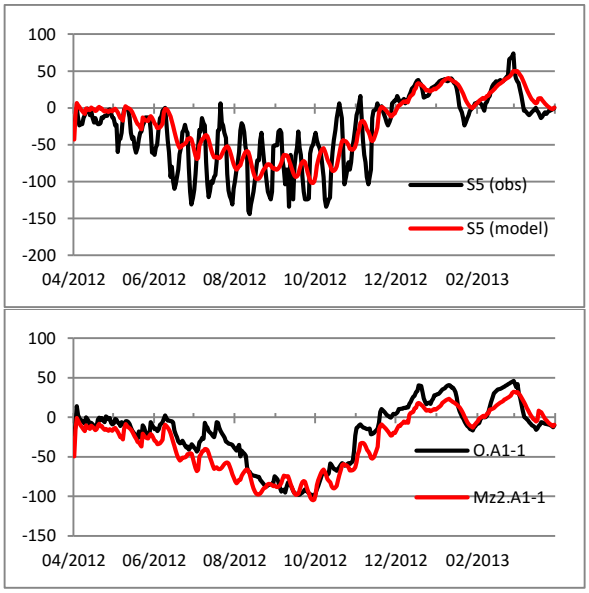

Fig. 7 Daily time-series of simulated water table (black line) versus observation (red line) on the secondary canal (top) and on the land (bottom) during 1 April 2012 to 31 March 2013. Y-axis is in cm relative to ground surface.

Table 2. R^2-value of observational data and model results for the period 1 April 2012 - May 31, 2013 in available observation points on canal and land

Canals	P8	P9	S2	S5		
R^2	0.82	0.90	0.73	0.62		
Lands	A1-1	A1-2	A1-3	A1-4	A2-1	A2-3
R2	0.87	0.85	0.81	0.87	0.68	0.77

Simulated water depth on the land is presented on Fig. 7 (bottom). In A1-1, the simulation shows very coherent result. It is also shown on the R^2 of secondary block of A1-2, A1-3, and A1-4 (Table 2). In addition, the simulated and observed water table on tertiary block (A2-1 & A2-3) is not as good as secondary block, particularly starting the dry season (July) which led under-estimation (figure not shown).

Simulation for year 2014/2015

In the second case, the model produces high correlation of water table on the canals (Fig. 8 top). It seems that the consistency of observational data used for assimilation in this period is better than previous period (Fig. 7 top). The values of R^2 on the canal exceed 0.9 (Table 3). In the land, the model can also produce coherent result as shown in Fig. 8 (bottom) and Table 3 of AP12 and AP13. However, some variations are not captured by the model in the middle of period (July-October).

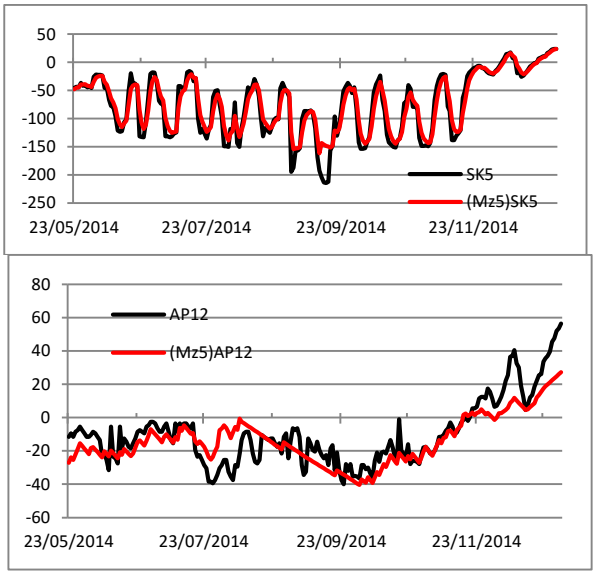

Fig. 8 As in Fig. 7, but for the simulation period of 23 May 2014 to 31 December 2014.

Table 3.Value R^2 of observational data and model results in the period 23 May to 31 December 2014

Point of obs	Canals		Lands	
	TC1	SK5	AP12	AP13
R^2	0.95	0.91	0.73	0.81

CONCLUDING REMARKS

Model GCFlow is 3D models that simulate the movement of water in the canal and on land as well. The model can calculate the movement of water in primary canal, secondary canal, tertiary canal and land for water management planning in tidal land reclaimed, with the data observation period in 2012/2013 and 2014 in Block-A Rantau Makmur, Tanjabtim-Jambi. Testing results of the simulation WL (water level) in all canals and on land has been very good, with the R^2 value reaches 0.95.

From the results, the model can be used for next simulation of CO_2 emissions and subsidence prediction using yearly predicted groundwater. The hope is to be found the optimum water level predictions for crop cultivation, and minimum damage to the environment (CO_2 emissions and subsidence) in the peat swamps tidal reclamation results in Delta Berbak in particular, or in other tropical tidal areas.

This model is newly made for developing Berbak Delta in Jambi, Indonesia. We started from simple calculations that at least can produce coherent result. However, there are still some lacks and many assumptions in the model that needs to be improved and evaluated, for example the tidal forcing and the existence of water gate.

REFERENCES

[1] Christian, Aswandi, and Dipa. 2004. Hydrological Modelling. "Promoting the river basin and ecosystem approach for sustainable management of SE Asian lowland peatswamp forests" Case study Air Hitam Laut river basin, Jambi Province, Indonesia

[2] Damayannti, Evi. 2016. Improving Water Management for Increasing Production and Conserving Peat Land Areas. Case StudyMuaro Jambi, Indonesia. Unesco-IHE. Case Study Muaro Jambi, Indonesia . MSc Thesis (WSE-HELWD.13.3.

[3] Dipa.S.R. 2011. Drainage-driven subsidence and carbon emission in Air Hitam Forest Reserve and its surrounding area, Johor-Malaysia.

[4] Hooijer. A, S. Page, J.Jauhiainen, W.A.Lee, Aswandi, and G. Anshari. 2011. Subsidence and carbon loss in drained tropical peatlands. Journal Biogeosciences 9, 1053-1071.

[5] Imanuddin, M.S. 2010. Strategi pengendalian muka air untuk pertanian daerah rawa pasang surut Sumatera Selatan, Indonesia.

[6] Susanto, R.H. 1998. Water status evaluation in tertiary and secondary blocks of South Sumatra reclaimed tidal lowlands using the hidrotopography and SEW-30 concepts. Proceeding of the Young Professional Forum-International Commission on Irrigation and Drainage Seminar (B3). Bali July 23, 1998.

[7] Susanto, R.H. 1994. METODE AUGER: Pengukuran Keterhantaran Hidrolik Tanah di Bawah Muka Air Tanah. Terjemahandari THE AUGER HOLE METHOD: A Field Measurement of the Hydraulic Conductivity of Soil below the Water Table. W.F.J. Van Beers. 1983. ILRI, the Netherlands. Jurusan Tanah Fakultas Pertanian. Universitas Sriwijaya.

[8] Susanto, R.H. dan R.H. Purnomo. 1996. Pengantar Fisika Tanah. Terjemahan. Fakultas Pertanian. Universitas Sriwijaya.

[9] www.clarklabs.org . Clark University, USA:

[10] www. Viva. Co. id. 2015. file:///E:/PBB%20Perubahan%20Iklim%20Dunia%20Bergantung%20Hutan%20Indonesia.html

[11] http://redmonk.com/sogrady/2014/06/13/language-rankings-6-14/).

[12] http://www.mathworks.com

Acknowledgement: The authors appreciatively acknowledge funding from DP_3M project, Directorate of High Education, Department of National Education of Republic of Indonesia.

First International Conference on Science, Engineering & Environment,
Tsu City, Mie, Japan, Nov.19-21, 2015, ISBN: 978-4-9905958-5-2 C3051

A METHOD OF PARTNERSHIP BETWEEN GOVERNMENTS AND CITIZEN'S COMMUNITY GROUPS FOR ACHIEVING ENVIRONMENTAL SUSTAINABILITY: FOCUSING ON THE LANDCARE MOVEMENT IN AUSTRALIA

Tomomi Maekawa
Department of Value and Decision Science, Graduate School of Decision Science and Technology,
Tokyo Institute of Technology, Japan

ABSTRACT

With regard to achieving environmental sustainability, it has long been recognised that partnership between citizens and governments is important for conservation and for solving environmental problems. It has also been recognised that what form that partnership takes makes a difference. However we are still in the process of seeking out a methodology for an ideal form of partnership between citizens and governments. This study will focus on the partnership between citizen's community groups and governments in an Australian community-based approach to natural resource management called Landcare, which has been recognised as a successful approach for natural resource management through multi-party partnership. In the Landcare movement, local voluntary groups care for the local environment, including such things as parks, creeks, forests and farms. In order to clarify the nature of the partnership between citizen's community groups and governments in the Landcare movement, documention analysis and in-field research in the State of Victoria, Australia, were undertaken. The in-field research included observations through participation and interviews with individuals participating in the Landcare movement as volunteers or staff members. As a conclusion, the partnership between citizen's community groups and governments in the Landcare movement has been found to include respect for the voluntary and autonomous nature of the local groups that carry out the activities for improving local environments with informational, financial, technical, and motivational support from the state and federal government.

Keywords: Partnership between Governments and Citizen's Community Groups, Environmental Sustainability, Landcare Movement in Australia, respect for voluntary and autonomous nature of the local groups, supports from the state governments and the federal government

INTRODUCTION

What the Partnership Should be?

Research in Japan has shown that partnership between citizens and governments has been significant for conservation and for solving environmental problems, and also that the form the partnership takes is important [1], [2].

Reference [1] points out that "For the creation of environmental capital grounded in a partnership between governments and citizens, it is important that, through making clear the roles expected of and actually performed by each, a relationship that is well suited to the needs of both be established, and that the tasks apportioned to each be made clear in order for projects to progress effectively. In case studies too, this has been a central issue." [3]. [2] also points out that "From now on, to address environmental issues, it will be important to make clear the respective roles of governments and citizens and the form that networking between these should take." [4]. As [2] points out, "Agenda 21 adopted at the United Nation's Conference on Environment and Development (UNCED) in 1992, lists women, children, youth, non-governmental organisations, local governments, labourers, labour unions, the industrial world, etc., as actors who play primary roles for environment and development, and suggests the establishment of a genuine social partnership among them. This is true in conservation of the local environments." [5]. With regard to what is required for building partnerships for conservation and for dealing with environmental issues, [2] suggests the establishment of groups or organisations where people can find worthwhile activities in given local areas across Japan, and also suggests the distribution and sharing of information among citizens, businesses, and governments.

Clearly, there is a strongly sensed need for a means of partnership between citizens and governments. However, a truly effective methodology remains to be discovered.

Purpose of this Study

Keeping in mind the indications and the suggestions provided by the research mentioned in the previous section, this study will aim to clarify the nature of the partnership between citizen's community groups and governments in an Australian community-based approach to natural resource management called Landcare, as a successful model that may be relevant to Japan. The reasons for focusing on the partnership in Landcare as a model in this study are the following:

Various stakeholders have participated in Landcare and it has been recognised as "effective" and "successful". It "has been embraced by governments, farmer organizations, and conservation groups throughout Australia as a model for effective community action to assist the move to more sustainable resource use [6]" and is "a highly successful community-based volunteer movement that facilitates and coordinates actions to care for our environment" where people "come together to discuss shared land management issues, and to action to address these issues" [7].

Landcare has had over twenty-five years of history since its inception in 1986 in Victoria and has spread across the nation. There are more than 630 groups in Victoria alone [8] and over 5,000 groups across Australia [9].

These facts indicate that Landcare is highly regarded and that it is successfully provided a stable form of partnership between citizens' community groups and governments.

METHODOLOGY

The methodologies used to clarify the nature of the partnership between citizen's community groups and governments in Landcare, were documentation analysis (including gathering information from the webpages of the related organisations on the internet), observation through participation, and interviews with individuals participating in the Landcare movement as volunteers or staff members. The in-field research, the observation through participation and the interviews with individuals, was carried out in the state of Victoria, Australia, with support from the chair of Australian Landcare International, who has been involved in Landcare since its beginning and has a broad range of contacts with individuals related to Landcare in Victoria and across Australia. The in-field research was carried out during the period from 18 March 2014 to 24 March 2014.

In this study, at first I identified the main existing institutions and the other forms of support for Landcare provided by governments, focusing on the case of the State of Victoria. I then undertook documentation analyses, observation through participation, and interviews with individuals to determine how the institutional and other forms of support identified have been working in field.

In order to identify main existing institutions and other forms of support, information was gathered from the websites of the Department of Environment and Primary Industries in the State of Victoria, the Department of Agriculture in the Australian Government, and other related organisations.

FINDINGS

Identifying and Categorising Institutional and other Forms of Government Support

The institutions and the other forms of support identified for the citizen's community groups collectively called Landcare groups or Landcare networks from the State Government of Victoria and the federal government of Australia can be categorised into four different groupings. There are informational, financial, technical, and motivational. (See Table 1)

Table 1 Institutions and the other forms of support provided by the State Government of Victoria and the federal government

Category	institution	source	deliverer
informational	Victorian Landcare Gateway	the State Government of Victoria	DEPI
	The Victorian Landcare & Catchment Management Magazines	the State Government of Victoria (DEPI)	Available through the Victorian Landcare Gateway
	National Landcare Directory	the federal government and other organisations	Landcare Australia Limited
financial	Victorian Landcare Grants	the State Government of Victoria	10 CMAs in Victoria
	National Landcare Program Regional Funding	the federal government	56 natural resource management organisations

			across Australia
	Landcare tax benefits	the federal government (Department of Agriculture)	Deduction claim available via Australian Taxation Office
technical	Regional Landcare Coordinators	the State Government of Victoria (DEPI)	10 CMAs in Victoria
	Regional Landcare Facilitators	the federal government	56 natural resource management organisations across Australia
motivational	States and Territory / National Landcare Awards	the federal government	Nominations available on the internet
	Victorian Landcare Awards	the State Government of Victoria	Nominations available on the internet

Note: in Table 1, "institution" means institution and the other forms of support by the State Government of Victoria or the federal government of Australia; "source" refers to the original source or provider of the information/funding/assistance; "deliverer" refers to the institution or individuals that mediate this to the recipient. "DEPI" is for the Department of Environment and primary Industries in the State Government of Victoria, and "CMAs" is for the Catchment and Management Authorities.

Institutions and the other Forms of Support Identified

Informational Support

With regard to informational support, in the state of Victoria, the State Government of Victoria provides information related to Landcare through managing a website called Victorian Landcare Gateway and through a magazine called *Victorian Landcare & Catchment Management*. At the national level, Landcare Australia Limited which is a non-profit private company formed and funded by the federal government of Australia in order to "raise awareness and generate corporate support for Landcare" [10] provides information on its website which includes a National Landcare Directory.

With regard to the institutional support provided by the State Government of Victoria, "The Victorian Landcare Gateway is the central point of contact for Landcare in Victoria" and in this system people "can find news from Landcare groups and networks, including up-coming volunteer activities and events, resources and toolkits for groups, information on grants and projects, as well as group and network contacts" [11]. The magazines *Victorian Landcare & Catchment Management* features stories that are "primarily contributed by community Landcarers" on broad natural resource management issues and is available through the Victorian Landcare Gateway (Department of Environment and Primary Industries, the State of Victoria. Available online at http://www.depi.vic.gov.au/environment-and-wildlife/community-programs/landcare/victorian-landcare-gateway. Accessed 20 July 2015).

On the other hand, with regard to support at the national level, there is the National Landcare Directory managed by Landcare Australia Limited. Through this directory, people can find Landcare groups "to volunteer and learn about Landcare activities" in given areas, related events in which people can get involved such as special events, "regular activities,…environmental workshops, and training" in given areas, and projects "that Landcare Australia has funded in partnership with our Corporate Partners" [12].

Financial Support

With regard to financial support, in the state of Victoria, the State Government of Victoria provides funding in the form of Victorian Landcare Grants. At the national level, the federal government provides funding through National Landcare Program Regional Funding and also provides the possibility of tax deductions for landowners incurring capital expenditures for their property improvements (known as a Landcare tax benefit).

The Victorian Landcare Grants are provided through 10 Catchment Management Authorities (CMAs) to "on-ground works that deliver on local, regional and State priorities, capacity building activities for land stewardship and on-ground change, projects that promote innovation through experimental trials and pilot programs, start-up funding (for new groups & networks) and maintenance grants to ensure a strong Landcare base across the State, and opportunities to promote Landcare and increase membership and volunteer numbers" [13].

On the other hand, the delivery of the National Landcare Program Regional Funding, which is available only to the 56 regional natural resource management organisations across Australia, "should be designed to maintain or build upon current engagement in landcare and practice change

activities, while increasing the engagement and participation rates in natural resource management and sustainable agricultural activities of a wide variety of groups" with of the stipulation that at a "minimum 20 per cent of their annual regional allocation [should go] to small, on ground projects and related activities that are delivered by, or directly engage with, the local landcare community" [14]. At the national level, specific landholders with approved land management plans, who "incur capital expenditure on a landcare operation" such as "exterminating "animal pests from the land" and "combating land degradation other than by the use of fences", can claim a tax deduction [15], [16].

Technical Support

With regard to technical support, in the state of Victoria, the State Government of Victoria invests in what are called Regional Landcare Coordinators. There is one based in each region in Victoria. Likewise, the federal government invests in what are called Regional Landcare Facilitators, with one based in each of 56 natural resource management organisations across Australia.

Regional Landcare Coordinators facilitate "communication through newsletters and through the Victorian Landcare Gateway", "conduct annual regional forum", "assist with funding", "managing the annual Victorian Landcare Grants program", and "represent the region's interests at the state level" (based on an interview with staff members at Glenelg Hopkins Catchment Management Authority, 24 March 2014).

Regional Landcare Facilitators assist Landcare and other community groups in seeking funding, membership, and resources for natural resource management activities, for the development, delivery, monitoring, and evaluation of regional plans, and for building and strengthening partnership between Landcare, community, grower groups, industry groups and each CMA (based on an interview with staff members at Glenelg Hopkins Catchment Management Authority, 24 March 2014).

Motivational Support

With regard to motivational support, the State Government of Victoria provides Victorian Landcare Awards, and the federal government provides States & Territory Landcare Awards and National Landcare Awards.

State & Territory Landcare Awards, which include Victorian Landcare Awards, are held every two years "to acknowledge the success and achievements of community Landcarers, groups, networks, and organisations who have been working to protect and restore our environment" and the winners of some national awards categories "will go on to represent their state or territory" at the National Landcare Awards which are held following the State & Territory Landcare Awards [17]. In these Awards, there are categories such as "individual Landcarer Award", "Landcare Facilitator or Coordinator Award", and "Qantas Landcare Innovative Community Group Award" [18] which are sponsored by governments, private companies, and other organisations [19].

How the Institutions and the other Forms of Support by Governments Work in-field?

Making Farms Sustainable and Better Environment for Farmers

Through participation in an event held at a member's farm of one Landcare group in Drouin South, it has been found that grants, volunteers, and staff have, through Landcare, been supporting the farmer in carrying out more sustainable farming practices and other farmers have also used this as a point of reference.

According to the document distributed to the participants at the event, the member who is the owner of the farm where the event was held "started to planting indigenous plants on his property in the late 80s… He initially started by fencing off and planting the steep embankment at the back of the property where small landslips were occurring". He "has been involved in Landcare since the 1980s and is an inaugural committee member of Lardner and District Landcare Group. He has hosted and supported many Landcare plantings and field days on his property and has inspired others to also become involved." He "believes the farm is a better environment now for his family to live and work. Some of the benefits to the farm" that he "has observed include; more shade for cows resulting in less stressed cows and improved milk quality, increased production, improved cow condition, and better quality of pastures. He believes that their farm is more drought resilient and observed that during the height of the drought his farm had a tinge of green whereas other areas were brown." (based on documentation entitled *Demonstrating Sustainable Farm Practices Field day - Drouin Sth*).

At the event he gave a presentation on his farm's history and what he has done to make its environment better and showed the participants around his farm. According to the documentation distributed, the event was a project launch event. The project, entitled "Demonstrating Sustainable Farm Practices in Western Port, Port Phillip and Yarra catchment" is "managed by the Western Port Catchment Landcare Network and supported by Port Phillip & Western CMA through funding from the Australian Government". The "aim of this project is to work with farmers from all enterprises to promote

and support the uptake of sustainable farming practices. Landcare staff will primarily deliver the project but we will utilise the services of farm consultants, agronomists, DEPI and soil scientists when required."

A Bushfire Recovery Project as a Model Restoration

Through visiting and through interviews with the members of one Landcare network in Flowerdale, it has been found that, through Landcare, the grants, volunteers, and staff have been supporting the landowners and local community in the Murrindindi Shire and Mitchell Shire with rebuilding and rehabilitating the local environment on private properties that were destroyed by the bush-fire in 2009, known as the Black Saturday Bushfire.

Based on interviews with the members of one Landcare network which has been carrying out a project for achieving bushfire recovery, and also according to the documentation provided by them, after the Black Saturday bushfire, the Upper Goulburn Landcare Network (UGLN) "recognised that recovery, support, direction needed to happen to assist landholders". The network started a project with support from the Goulburn Broken CMA and a program of the federal government for "developing a community driven fire recovery program operating within the fire affected areas of the upper Goulburn catchment". In the recovery project, "soil retention", "revegetation", "implementation of threatened species action plans", etc., were the topics to be considered, and in the implementation of the project, the activities required were assessments of burnt and non-burnt resources, "seed collection", fencing, coordination of "volunteer and paid labour", "management of finances from government coffers", etc. Volunteers from private companies, public sectors, schools, and other organisations have joined field days of tree plantings, building nest boxes for birds and animals, or supplying seedlings for plantings.

According to the members of the network interviewed and the documentation provided by them, the volunteers have supported the network continuously since the Black Saturday Bushfire of 2009, and the network has a wide range of achievements such as a "weed ID & control workshop for landholders", "revegetation" (See Fig. 1) and coordination of "remnant vegetation surveys", "harnessing volunteer labour [to] remove burnt fences, [and] build new ones", "seed collection", the purchase of a trailer and protective gear, and "communication; media release, calendar of events, website, brochures, pamphlets, branding, logos". The process and achievements of the project were passed on to Landcare Queensland "after floods to help them with restoration using UGLN model" (based on an interview with members of Upper Goulburn Landcare Network at Flowerdale, 19 March 2014).

Fig. 1 Property of a Landcare group's member where the fire recovery project has been carried out (at Strath Creek on 5 September 2012).

Discussion on the Nature of Partnership between Citizen's Community Groups and Governments in Landcare Movement

Two examples of institutional and the other forms of support by governments operate in-field in the previous section show that they promote the sustainability of both farms and farming through encouraging voluntary activities by farmers and through promoting recovery from natural disasters by supporting community driven projects. This shows that institutional and other forms of support by governments work in-field to respect for the voluntary and autonomous nature of the local groups/networks and their activities.

The possible benefits of this institutional support, and of the other forms of support from governments are the following: the grants from governments are allocated to projects proposed by local groups or networks or regional natural resource management organisations who know what the local or regional environment and people need in each area. Therefore, the money can be used effectively for local or regional priorities: technical support provided through Regional Landcare Coordinators and Regional Landcare Facilitators to local groups and networks help the groups and networks to be sustainable. Choosing awardees and celebrating awards from the states and from the nation encourage diversity which increases the chance of cross-reference among local groups and networks. Delivery systems of information on the internet which promote interaction among individuals, local groups, and networks make it easier for farmers in rural areas isolated from towns to access related information and to join specific local groups or networks.

CONCLUSION

The partnership between citizen's community groups and governments in the Landcare movement in Australia has been found to include respect for the voluntary and autonomous nature of the local groups/networks and their activities, which enables to keep them independent from each other without indifference. It has been also found that this nature has been realized in the informational, financial, technical, and motivational institutions and other supports from the governments across the state and the nation.

ACKNOWLEDGEMENTS

This work was highly supported by Charles Sturt University Institute for Land, Water and Society, and Mr. Rob Youl, chair of the Australian Landcare International, and his family and colleagues who are engaged in Landcare or other activities tackling environmental issues, and by administrative officers who support these individuals and groups. I would like to express my appreciation to all the people who kindly helped the in-field research in Australia, and to the support from the members of the Secretariat to Promote the Establishment of Landcare in Japan and from the members of Kuwako Lab at the Tokyo Institute of Technology.

REFERENCES

[1] Matsumoto Y, "Kankyoushisandukuri to partnership", Kankyoukeikaku, seisakukenkyu no tenkai – jizokukanounashakaidukuri heno gouikeisei-, Harashina, Ed. Tokyo: Iwanami Shoten, 2007, pp. 177-210.
[2] Utsunomiya F, Kankyougyousei no rinen to jissen – kankyoubunmeishakai no jitsugen wo mezashite-, Kanagawa: Toukaidaigaku shuppankai, 2006.
[3] p182 in [1].
[4] p268 in [2].
[5] p268 in [2].
[6] Curtis A, Birckhead J, and De Lacy T "Community Participation in Landcare Policy in Australia: The Victorian Experience with Regional Landcare Plans", Society and Natural Resources, Vol.8, 1995, p415.
[7] Department of Environment and Primary Industries, the State of Victoria. [online] Available at http://www.depi.vic.gov.au/environment-and-wildlife/community-programs/landcare/about-the-victorian-landcare-program. Accessed 20 July 2015.
[8] See [7].
[9] Landcare Australia Limited, Annual Report 2013, Landcare Australia Limited, 2013. Available at http://www.landcareonline.com.au/?page_id=1178. Accessed 20 July 2015.
[10] Johnson M, Poussard H, and Youl R, "Landcare in Australia", Landcare: Local action – global progress. Catacutan, Neely, Johnson, Poussard, and Youl, Ed. Nairobi: World Agroforestry Centre, 2009, p16.
[11] Department of Environment and Primary Industries, the State of Victoria. [online] Available at http://www.depi.vic.gov.au/environment-and-wildlife/community-programs/landcare/victorian-landcare-gateway. Accessed 20 July 2015.
[12] Landcare Australia Limited. [online] Available at http://nld.landcareaustralia.com.au/. Accessed 20 July 2015.
[13] Department of Environment and Primary Industries, the State of Victoria. [online] Available at http://www.depi.vic.gov.au/environment-and-wildlife/community-programs/landcare/victorian-landcare-program. Accessed 20 July 2015.
[14] The Commonwealth of Australia, The National Landcare Programme Regional Funding 2014-15 to 2017-18 Applicant Guidelines Commonwealth of Australia, 2014. Available at http://www.nrm.gov.au/regional/regional-funding. Accessed 20 July 2015.
[15] Australian Government, Department of Agriculture. [online] http://www.daff.gov.au/ag-farm-food/natural-resources/landcare/tax. Accessed 20 July 2015.
[16] Australian Government, Australian Taxation Office. [online] https://www.ato.gov.au/business/primary-producers/in-detail/capital-expenditure/landcare-operations/. Accessed 20 July 2015.
[17] The State of Victoria Department of Environment and Primary Industries, 2013 Victorian Landcare Awards Winners' Booklet. Melbourne: The State Government of Victoria Department of Environment and Primary Industries, August 2013, p2.
[18] pp.3-7 in [17].
[19] Australian Government, Department of Agriculture. [online] http://www.agriculture.gov.au/ag-farm-food/natural-resources/landcare/national-landcare-programme/landcare-awards. Accessed 20 July 2015.

First International Conference on Science, Engineering & Environment,
Tsu City, Mie, Japan, Nov.19-21, 2015, ISBN: 978-4-9905958-5-2 C3051

DEVELOPMENT OF ANTHROPOMETRIC CHAIR BASED ON ARM SPAN, KNEE HEIGHT, AND SITTING HEIGHT FOR ELDERLY

Fatmah[1], Erwin[2]
[1]Public Health Nutrition Department, Faculty of Public Health,
University of Indonesia, Depok City, West Java Province, Indonesia; [2]Sultan Ageng Tirtayasa University,
Banten Province, Indonesia

Elderly with less nutritional status would be susceptible to get infectious disease, immune deficiencies, reduced productivity, high risk of various complications of disease, and can even cause death. Height as the one indicator of nutritional status assessment in elderly is difficult to measured due to such conditions as osteoporosis, scoliosis, kyphosis, etc. Arm span, knee height and sitting height can be used to predict the height. However, some anthropometric measurements with different positions are not effective because of discomfort. Three anthropometric measurements in one tool like a chair can overcome the problems. The study aimed to develop the anthropometric chair (Body Mass Index/BMI Meter) for elder's nutritional status assessment with an easy, practical measurement. The study design was cross sectional using survey method toward 300 healthy older people. Upper leg length, lower leg length, pelvic width, shoulder width, elbow height, shoulder height and patellar height were measured to design the chair. The study revealed that the male elderly had higher data anthropometric than female. The mean of anthropometric data decreased with age. The validity of anthropometric chair from the sensitivity (85-100%), specificity (70-80%), Positive Predictive Value (80-90%) and Negative Predictive Value (80-100%). The anthropometric chair can be used for assessing elders nutritional status.

Keywords: Anthropometric Chair, Arm Span, Knee Height, Sitting Height, Elderly

INTRODUCTION

Malnutrition remains a major nutritional problem commonly found in groups of elderly such as undernutrition and overnutrition. Combination of changes in physiology and psychology also contributes in the development of malnutrition cases in the elderly. Therefore, early screening of elderly malnutrition is urgently needed in assessing nutritional status through the calculation of Body Mass Index (BMI) with height and weight as indicators [1]. However, height in elderly is difficult to measured because changes in posture due to aging; abnormalities of the spine due to osteoporosis, kyphosis, or wheelchair-bound or bedridden Inappropriate height measurements may lead to inaccurate assessment of the nutritional status in elderly [2]. Currently, geriatric service workers in health centers and hospitals in Indonesia has difficulty in measuring height in elderly who are unable to stand up. They are still using a device made by wood and aluminum to measure knee height. The results then are to be converted to height prediction with Eleanor's formula as defined in The Guidance of Elderly Management for Dietitian at the Health Center [3]. Meanwhile, this formula developed in Caucasian elderly who have differences in posture and height with Indonesian, so that the results are not accurate. One recent and sophisticated discovery to assess the nutritional status of elderly who can not be measured in upright position is the use of Nutrition Status Assessment (NSA) Card from predicted height using arm span, knee height and sitting height [4]. This card has been developed and validated in 2009 towards 560 elderly in Depok, Jakarta, and Bogor respectively [5]. Validation test for predictive HB model of this card revealed that all three aspects had the highest sensitivity and specificity rather than Eleanor S. and Chumlea model so it is accurate enough in determining the predicted height in elderly. As many as 33 cadres of integrated training post (as called *"Pos Pembinaan Terpadu"* or *Posbindu*) and nutrition workers of health center or hospital in the District of Pancoran Mas Depok in 2009 had previously been trained. The aims of this training were to measure and interprete anthropometric nutritional status in elderly with NSA cards, as well as to provide a set of anthropometric tool for several integrated training posts selected to be applied in the field. However, the study showed that elderly cadres of integrated service post and nutrition workers or clinic midwifes in Depok still have problems using anthropometric predictors for all models with tool made by wood. While using the tool, the elderly have to undergo three times

measurement in two different positions i.e. standing and lying down. This anthropometric tool is also quite heavy when taken to a field that is not practical to use and requires four people to operate it. Whereas the elderly activities in integrated training post were in high level of mobility that was often moved from one place to another with the same tools and different schedules, even in a limited number of field workers. Therefore, there should be a study available in designing or developing the tools of anthropometric which may cover all of three predictors of height for elderly with ergonomic beneficial and practical on hand. The aim of this study was to develop a digitally anthropometric tool which capable to analyze (integrated analysis) of arm span, sitting height and knee height, namely BMI Meter in assessing the nutritional status in elderly to meet the ergonomic value as needed based on physical condition of them.

MATERIAL AND METHODS

Study Design

This descriptive analytical study described the relationship inter-variables. Hypothesis was tested to assess the association between anthropometric chair ergonomically with the validity of the nutritional status of elderly based on height prediction of arm span, knee height and sitting height. The study was cross sectional method using observation approaches [6].

Subject and Data Collection

The subject was elders (senior citizens) with the inclusion criteria: men and women, aged over 60 years, able-bodied, stand still and resided in Jakarta and Depok. At the beginning, anthropometric database was collected using a form that embraces measurement of upper and lower legs length, shoulder width and height, hip width, elbow and patella height. The anthropometric data collection was conducted to determine the shape, size and exact dimensions related to product designed and to specify individuals who will operate or use the product. As many as 200 elderly in Jakarta and Depok have been chose as samples for this study. The chair will be designed within 6 months based on anthropometric dimensions of data. Validity test for the chair conducted on 100 elderly whom resided in Jelambar district, Grogol Petamburan subdistrict, West Jakarta. The test included the measurement of body weight, sitting height, knee height, and arm span using the form. The measurement of anthropometric data conducted by five students who had been trained for using anthropometer.

Data Analysis

Furthermore, data(s) were analyzed and processed with SPSS for Windows 13rd version. Univariate analysis of data was presented to describe the frequency distribution, maximum-minimum value and the mean value of all variables studied. The data(s) resulted from validation test of the chair were analyzed with the chair sensitivity, specificity, Positive Predictive Value (PPV) and Negative Predictive Value (NPV).

RESULT AND DISCUSSION

Mean age of respondents was 61.6 years with 87 years age as the highest while 48 years age as the lowest. Elderly women had a mean of age slightly less than men. The anthropometric data for appropriate chair design was depicted in Table 1. It showed that elderly men have greater results than women related to the upper and lower legs length, shoulder width and height, and patellar and elbow height. The mean of anthropometric parameters measured in elderly men had a value greater than the elderly women, unless the width of the pelvis. Male posture was higher and larger than female. Since body dimensions was took into account, male generally larger than women, except for several particular parts such as hip, etc. [7]. Table 2 showed the distribution of anthropometric measures decreased with age. The size of the human body varies according to age. As advanced age, the value of anthropometric parameters measured in the elderly is low. Physical development in both men and women continued to increase until adolescence. However, around aged of 40, it tends to decrease or depreciate until old age. BMI is an indicator for assessing obesity and CED (Chronic Energy Deficiency) risks in elderly. However, it is difficult to measure stature of elderly due to kyphosis and scoliosis. To overcome the problem, we can measure the predicted height of elderly using arm span, knee height, and sitting height [8, 9]. Table 3 showed that the mean of height and weight, arm span, knee height and sitting height in elderly men were greater than women. This result supported the studies conducted in elderly Chinese in South America [10] and Chile [11]. Elderly men were taller and heavier than women because both groups experienced a loss of fat-free mass is greater. Reduction in height of men is lower than female. The decreasing of height in

elderly associated with posture, osteoporosis, spinal damage, kyphosis and scoliosis. Male commonly have mean knee height, arm span, and sitting height higher than female. It is consistent with two studies who found that the mean height of the three predictors in elderly male was larger than the female [12], [13]. It may be caused by the differences in posture and physical activity between them. Mean difference of prediction height for the three predictors with actual height is presented in Table 4. Sitting height has the lowest distinction rather than arm span and knee by gender and wholly, as followed by knee height in elderly men and arm span in elderly women. Table 5 showed the validity of the test is based on four indicators of anthropometric chair i.e. the sensitivity, specificity, PPV (Positive Predictive Value), and NPV (Negative Predictive Value). Sitting height is a predictor that has the highest sensitivity in the group of elderly men and women which subsequently followed by a knee height and arm span. Moreover, that predictor may become a filter to screen whether elderly are under nutrition or over nutrition among those with normal status nutrition during assessment. In contrast, knee height has the greatest level of specificity rather than arm span and commonly sitting height. It means that the first predictor is able to recognize the elders with normal nutritional status among those with malnutrition. Positive Predictive Value (PPV) is the measurement parameter to find the likelihood that the patients were 'true positive' disease [14] Knee height is the most precise predictor to assess the probability of elderly malnutrition whether in over nutrition and under nutrition to both elderly men and women. Afterwards, the sequential predictors are sitting height and arm span. In elderly men, sitting height more precisely measure the likelihood of malnutrition cases in well-nourished elderly. Meanwhile knee height becomes the most accurate predictor to assess the likelihood of malnutrition status among elderly women with normal nutritional status. Negative Predictive Value (NPV) describes the likelihood that the patients are really free from disease or in healthy status [14]. Sitting height has the largest NPV value among all elderly and as gender accordingly. It is the most accurate way to assess the likelihood of elderly people with actually normal nutritional status. Based on the results of validity test above, it can be concluded that the anthropometric chair has been tested and valid in assessing the nutritional status of elderly people whom their actual height was unmeasured manually by measuring arm span, knee height, and sitting height. Thus, it was practical tool to measure the nutritional status of the elderly at once without the need to change the measurement in varying position, as it merely done while sitting. The reading of the NSA can be seen in BMI meter which denotes the value of IMT elderly of all three predictors. In addition, over 300 grams *Load Cell* can be used to solve the difficulty of weighing the elderly who unable to stand up during weighing due to disability or paralysis. All tool components such as sensor at the three-point anthropometric measurements, BMI meter and load cell have been calibrated to obtain the exact value of BMI.

CONCLUSION AND SUGGESTION

The type of chair as an anthropometric tool for assessing nutritional status in elderly was selected based on practical reasons i.e. it measured nutritional status in elderly at once in sitting position since the convenience of the elderly was also considered. The verification of the estimating body height of such predictors, as arm span, knee height, and sitting height with anthropometric chair to nutritional status of elderly people showed that the results of nutritional status of older adults extracted from the three predictors as measured proved to be representative or may represent the BMI value of the actual body height. It is suggested that the validity test of anthropometric chair for elderly can be performed widely with greater number of elderly either in urban and rural for the variances of the sensitivity, specificity, PPV, and NPV.

REFERENCES

[1]Gibson R. Principles of Nutritional Assessment 2nd edition. USA: Oxford University Press, 2005, pp 15-20.

[2]Fatmah. Nutrition in Elderly. Jakarta: Erlangga, 2010, pp. 25-30.

[3]Indonesian Ministry of Health (MOH). Manual on Geriatric Nutrition Management for Health Staffs Jakarta: Community Nutrition Directorate – MOH, 2006, pp. 19-22.

[4] Fatmah. Developing predicted height model of Javanese Elderly based on knee height, arm span, and sitting height. Indonesian Medical Journal Vol. 58, 2008, pp 509-516.

[5] Fatmah. Validation span, knee height and sitting height in Indonesian elderly people. Journal of Clinical and Medicine Research Vol. 2, 2010, pp, 67-73.

[6] Sastroasmoro S. Basics on Clinical Research Methodology. Jakarta: Sagung Seto, 2006, pp. 101-105.
[7] Pheasant S. Body Space Anthropometry, Ergonomics and the Design of Work Second Edition. Taylor & Francis, 2000, pp, 36-42.
[8] Jarzem PF., Gledhill RB. Predicting height from arm span measurement. J. Pediat. Orthopedy Vol. 13, 1993, pp. 761-765.
[9] Myers T. Stature estimated from knee height in Elderly Japanese Americans. Am J Geriatric Soc Vol 42, 1994, pp 157-160.
[10]Edmun L.T.S., Emily K.T., Cora Y.W., Susan S. L. Predicting stature from knee height in Chinese elderly subjects. Asia Pacific J. Clinical Nutrition, Vol. 9, 2000, pp. 252-255.
[11]Santos J.L., Albala C., Lera L. Garcia C., Arroyo P., Perez-Bravo F. Anthropometric measurements in the elderly population of Santiago, Chile. Nutrition, Vol. 20, 2004, pp. 452-457.
[12] Fatmah. Predictive equations for estimation of stature from knee height, arm span, and sitting height in Indonesian Javanese elderly people. International Journal of Medicine and Medical Sciences, Vol 1, Oct 2009, pp. 456-461.
[13]Tancocho C, Charmain AD, Edna SL. Arm span and knee height as proxy indicators for height FNRI, Jan 2007.
[14]Altman DG and J.M. Bland. Statistics Notes: Diagnostic tests 2: predictive values. British Medical Journal, Vol. 309, 1994, pp.102.

Table 1. Anthropometric data for appropriate chair design according to gender

Sex	Statistic	Age (years)	Knee height (cm)	Lower leg length (cm)	Pelvis width (cm)	Shoulder width (cm)	Shoulder height (cm)	Pat hei (c
Male	Mean	62.8	39.5	48.7	29.8	39.0	57.9	49
	Median	64.0	39.0	49.1	29.9	39.1	58.4	49
	Minimum	49.0	32.0	36.0	24.1	32.5	43.5	43
	Maximum	81.0	50.0	53.0	32.7	43.3	65.5	58
	SD	7.1	3.8	2.7	1.7	2.0	3.9	3
	n	68	68	68	68	68	66	6
Female	Mean	61.0	38.1	45.1	30.3	35.4	52.9	45
	Median	60.0	38.1	45.0	30.1	35.5	53.3	46
	Minimum	48.0	30.2	38.8	25.5	30.9	43.0	39
	Maximum	87.0	55.0	52.5	35.5	39.0	60.5	52
	SD	7.3	3.4	2.2	2.1	1.8	3.4	2
	n	141	141	141	141	141	134	13
Total	Mean	61.6	38.6	46.2	30.2	36.6	54.6	47
	Median	61.0	38.2	46.0	30.0	36.5	54.2	46
	Minimum	48.0	30.2	36.0	24.1	30.9	43.0	39
	Maximum	87.0	55.0	53.0	35.5	43.3	65.5	58
	SD	7.3	3.6	2.9	2.0	2.5	4.3	3
	n	209	209	209	209	209	200	20

Table 2. Anthropometric data for ergonomically design of chair according to age group

Age group	Statistic	Knee height (cm)	Lower leg length (cm)	Pelvis width (cm)	Shoulder width (cm)	Shoulder height (cm)	Patella height (cm)	Elbow height (cm)
45-59 y.o	Mean	38.8	45.9	30.2	36.6	55.5	46.6	23.2
	Median	38.5	46.0	29.9	36.7	55.0	46.0	23.0
	Minimum	30.6	36.0	24.1	31.1	45.8	39.0	16.2
	Maximum	55.0	53.0	35.0	43.3	65.5	58.6	53.0
	SD	3.8	2.7	2.1	2.2	3.6	3.3	4.4
	n	89	89	89	89	85	85	85
60-74 y.o.	Mean	38.4	46.7	30.2	36.8	53.9	47.4	21.1
	Median	38.0	46.1	30.1	36.6	53.7	47.0	21.1
	Minimum	30.2	41.2	26.0	31.7	43.0	40.0	2.0
	Maximum	50.0	53.0	35.5	43.3	64.0	58.9	29.5
	SD	3.3	2.9	1.9	2.7	4.7	3.3	3.2
	n	112	112	112	112	107	107	107
75-89 y.o	Mean	37.3	44.7	29.6	34.0	52.6	45.8	22.6
	Median	38.0	45.5	30.0	34.2	51.1	45.5	22.0
	Minimum	31.1	38.8	25.5	30.9	49.8	42.0	20.0
	Maximum	41.8	49.0	31.4	37.3	61.5	50.0	26.0
	SD	3.8	3.4	1.8	2.0	3.9	2.5	2.0
	n	8	8	8	8	8	8	8
Total	Mean	38.6	46.2	30.2	36.6	54.6	47.0	22.0
	Median	38.2	46.0	30.0	36.5	54.2	46.8	22.0
	Minimum	30.2	36.0	24.1	30.9	43.0	39.0	2.0
	Maximum	55.0	53.0	35.5	43.3	65.5	58.9	53.0
	SD	3.6	2.9	2.0	2.5	4.3	3.3	3.8
	n	209	209	209	209	200	200	200

Table 3. Mean of height (H), weight (W), arm span (AS), knee height (KH) and sitting height (SH) in centimeter

Sex	**Statistic**	**H**	**W**	**AS**	**KH**	**SH**
Male	Mean	159.,2	61.9	161.4	48.7	83.3
	Minimum	150.,0	43.1	130.5	45.0	76.0.
	Maximum	170.,5	81.0	183.0	53.0	88.5
	SD	5.3	9.4	11.6	2.5	3.0
Female	Mean	149.1	58.5	152.9	44.9	78.4
	Minimum	136.5	34.0	134.4	38.0	72.0
	Maximum	166.0	88.4	170.0	50.5	85.2
	SD	6.2	11.6	7.9	2.6	3.5
	n	72	72	72	72	72
Total	Mean	151.9	59.5	1553	46.0	79.8
	Minimum	136.5	34.0	130.5	38.0	72.0
	Maximum	170.5	88.4	183.0	53.0	88.5
	SD	7.5	11.1	9.8	3.1	4,0
	n	100	100	100	100	100

Table 4. Mean difference of predicted height of arm span (AS), knee height (KH), sitting height (SH) with actual height according to gender (in centimeter)

Sex	Statistic	AS	KH	SH
Male	Mean	2.6	0.5	0.3
	Minimum	-14.5	-15.6	-7.8
	Maximum	24.1	10.4	6.6
	SD	9.1	5.0	3.4
	n	28	28	28
Female	Mean	0.9	1.6	-0.1
	Minimum	-16.8	-8.8	-6.7
	Maximum	23.2	12.1	12.6
	SD	5.4	4.1	3.7
	n	72	72	72
Total	Mean	1.4	1.3	0.1
	Minimum	-16.8	-15.6	-7.8
	Maximum	24.1	12.1	12.6
	SD	6.7	4.4	3.6
	n	100	100	100

Table 5. Sensitivity, specificity and predictive value of estimating heght in elderly according to anthropometric chair (arm span, knee height and sitting height)

Indicator	Normal nutrition			
	Sensitivity	Specificity	PPV	NPV
Male				
Arm span	75.0	41,7	63.2	55.6
Knee height	87.5	58.3	73.7	77.8
Sitting height	100.0	75.0	84.2	100.0
Female				
Arm span	93.2	82.1	89.1	88.5
Knee height	93.2	85.7	91.1	88.9
Sitting height	97.7	75.0	86.0	95.5
Total				
Arm span	88.3	70.0	81.5	80,0
Knee height	91.7	77.5	85.9	86,1
Sitting height	98.3	75.0	85.5	96,8

Note:
PPV : *Positive Predictive Value*
NPV: *Negative Predictive Value*

Fig.1 Anthropometric chair for elderly

First International Conference on Science, Engineering & Environment,
Tsu City, Mie, Japan, Nov.19-21, 2015, ISBN: 978-4-9905958-5-2 C3051

HIGHLY EFFICIENT OXIDATION AND SIMULTANEOUS REMOVAL OF ARSENITE WITH CuO/ZnO PHOTOCATALYST

Abdus Samad [1,*], Hideyuki Katsumata[1], Tohru Suzuki[2] and Satoshi Kaneco[1,2]

[1] Department of Chemistry for Materials, Graduate School of Engineering, Mie University, Tsu, Mie 514-8507, Japan
[2] Mie Global Environment Center for Education & Research, Mie University, Tsu, Mie 514-8507, Japan

ABSTRACT

Pre-oxidation of arsenite to arsenate is a crucial step for its removal from aqueous solution as As(V) shows higher affinity towards adsorbent. The photocatalytic oxidation of trivalent arsenic to pentavalent arsenic and simultaneous removal through adsorption on CuO/ZnO photocatalyst surface under UV irradiation at mild condition was evaluated in this study. Mechanical mixing technique was used to prepare catalyst mixture of various weight ratios. Experiments were carried out using 30 mg L^{-1} of As(III) solution containing 0.33 g L^{-1} catalyst at pH of about 7. As(III) oxidation was negligible with bare CuO. Oxidation efficiency with pure ZnO was low. The results were significantly improved by the addition of CuO. The various weight ratio was evaluated, and CuO(20%)/ZnO exhibited highest oxidation efficiency. As(III) was completely oxidized within 4 hours of irradiation time. Simultaneous oxidation and removal study with various initial concentration of As(III) was checked. About 85% of 5 mg L^{-1} As(III) can be removed using this technique. The adsorption efficiency of As(III) with ZnO was very low. Although both ZnO and CuO showed preferential adsorption tendency towards As(V), ZnO demonstrated higher adsorption efficiency to As(V). This technique might be a potential one step arsenic removal method for the highly contaminated water.

Keywords: Photocatalyst, Arsenic, Oxidation, Adsorption, Removal.

INTRODUCTION

Arsenic contaminated water poses serious toxic effect on human health and is termed as the biggest natural calamity in the world. Over 20 million people in Bangladesh [1] and 144 million over the world [2] are at health risk from drinking arsenic contaminated water. Arsenic in ground water exists as arsenite (As(III)) and arsenate As(V). Arsenite is 25-60 times more toxic than arsenate [3]. Typically, arsenite is removed by first oxidizing to As(V) either by chemical oxidation or by photocatalytic oxidation using various photocatalyst, then As(V) is removed through adsorption, coagulation, ion exchange or membrane process. ZnO is one of the widely used photocatalyst due to its high photosensitivity, physical and chemical stability, low cost, ease of availability and non-toxicity [4]. It is an alternative to TiO_2, as they have similar bandgap energy and photocatalytic mechanism [5]. Furthermore, recent study demonstrates that ZnO is a potential adsorbent for heavy metals [6]. Nevertheless, the low photocatalytic efficiency has been recognized as a major obstacle for its application as a photocatalyst in large-scale. The photocatalytic activity of ZnO can be enhanced by various techniques such as modification of ZnO by non-metal [7], addition of transition metal [8] as well as use of compound with lower bandgap.

Previous researches have demonstrated that the recombination rate of the photo-induced electron–hole pairs in ZnO plays an important role in the photocatalytic reaction process [9], which is usually faster than surface redox reactions [10]. Therefore, the incorporation of charge-accepting nanomaterials is considered to be one of the most effective strategies to suppress the electron–hole recombination, leading to high photocatalytic efficiency.

Recently, the nanocomposites based on ZnO and other metal oxides have been studied and demonstrated that a higher photocatalytic activity can be obtained due to the effective transfer of charge carriers [11]-[13]. Copper oxide (CuO) is a semiconductor material with a narrow band gap (1.7 eV). Enhanced photocatalytic activity of ZnO coupled with CuO, synthesized by various techniques has been reported in recent times for the degradation of dyes and oxidation of metals [14]-[16]. Nonetheless, photocatalytic treatment of arsenite on ZnO and CuO mixture is not available in literature. The photocatalytic oxidation of As(III) on CuO/ZnO under UV irradiation and its simultaneous

removal by adsorption on catalyst surface was investigated in this research.

EXPERIMENTAL

Chemicals

ZnO; Particle size 50 ~ 70 nm, surface area 15 ~ 25 m^2/g and CuO; Particle size 33 nm, surface area 29 m^2/g were used as received. Potassium arsenite ($KAsO_2$, 90%, nakarai), Potassium arsenate (KH_2AsO_4, extra pure, nakarai) were used for the preparation of As(III) and As(V) stock solution respectively. Ammonium molybdate ($(NH_4)_6Mo_7O_{24}\cdot 4H_2O$, nakarai), L-ascorbic acid ($C_6H_8O_6$, 99%, nacalai), antimony potassium tartrate ($C_4H_4KO_7Sb\cdot 1/2H_2O$, 99.8%, nacalai), sulphuric acid (H_2SO_4), potassium permanganate ($KMnO_4$, 99.3%, chameleon) were also used as reagent. Stock solution of 1000 mg L^{-1} for both As(III) and As(V) were prepared from estimated amount of solid $KAsO_2$ and KH_2AsO_4. Dilute solutions were prepared daily before experiment. Pure water was further purified with an ultrapure water system (Advantec MFS, Inc., Tokyo, Japan) having resistivity > 18 MΩ cm.

Preparation of photootocatalyst

Commercially available ZnO and CuO was used for experiment. Mechanical mixing method was used for the preparation of photocatalyst mixture. The different weight ratios of mixture were prepared by adding calculated amount of ZnO and CuO.

Photocatalytic oxidation and removal experiment

UV irradiation was performed in a cylindrical quartz photoreactor cell of 50 mL with black light as irradiation source. Photon flux of the light source was measured as 2.0 mW cm^{-2} with actinometer. Reactor with CuO/ZnO suspension was positioned on the top of a magnetic stirrer for agitation. Prior to irradiation, suspension was stirred 30 minute in dark to allow sufficient time for arsenic to establish adsorption equilibrium. The decrease in As(III) concentration before placing UV cell was calculated and subtracted from starting concentration to take into account the change of concentration due to photocatalytic treatment only. Each experiment was performed with 30 mg L^{-1} 30 mL As(III) solution. Initial pH was about 7 and loading of CuO/ZnO was always 0.33 g L^{-1}. After treatment, solution was filtered with 0.20 μm Millipore filter. Concentration of arsenic was measured by UV-Visible spectrophotometry using arseno-molybdate technique [17].

RESULTS AND DISCUSSION

The effect of CuO on the photocatalytic oxidation of As(III) to As(V) and simultaneous adsorption on photocatalyt surface was investigated. Pure CuO, pure ZnO, CuO(5%)/ZnO, CuO(10%)/ZnO and CuO(20%)/ZnO were tested and the results are presented in Fig. 1. Arsenic oxidation was negligible with bare CuO (Fig.1a). Although oxidation of As(III) with pure ZnO was possible, its oxidizing efficiency was low. It was observed that the CuO/ZnO mixture exhibited faster photooxidation rate than pure ZnO. Experiment with CuO/ZnO mixture showed that the photocatalytic efficiency was enhanced with the increase of proportion of CuO in the CuO/ZnO mixture. Among the various ratios of CuO/ZnO analyzed, CuO(20%)/ZnO showed highest oxidization efficiency. With CuO(20%)/ZnO, complete oxidation of 30 mg L^{-1} of As(III) was observed within 4 hours. The higher oxidation efficiency of ZnO in presence of CuO was due to the effective separation of photogenerated electron and hole. During photocatalytic oxidation reaction, a fraction of arsenic was also adsorbed on catalyst surface which was evidenced by the decrease of total arsenic with reaction time. As shown in Fig. 1, the total arsenic was also decreased with the increase of CuO content in the mixture. Decrease of total arsenic concentration in solution was found proportional to the photocatalytic efficiency of oxidation of arsenite to arsenate. These results suggested that the conversion of As(III) to As(V) facilitate the adsorption of arsenic on catalyst surface; As(V) was preferentially adsorbed on catalyst surface. We performed further analysis with CuO(20%)/ZnO as it showed highest oxidation efficiency.

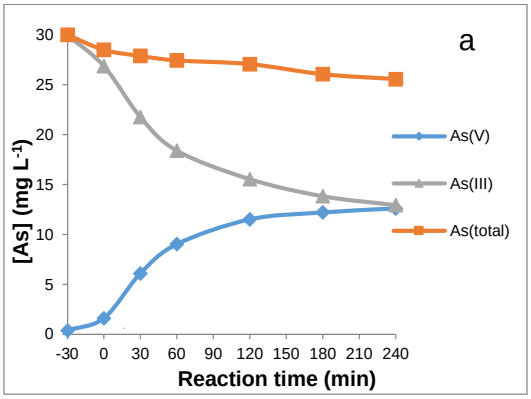

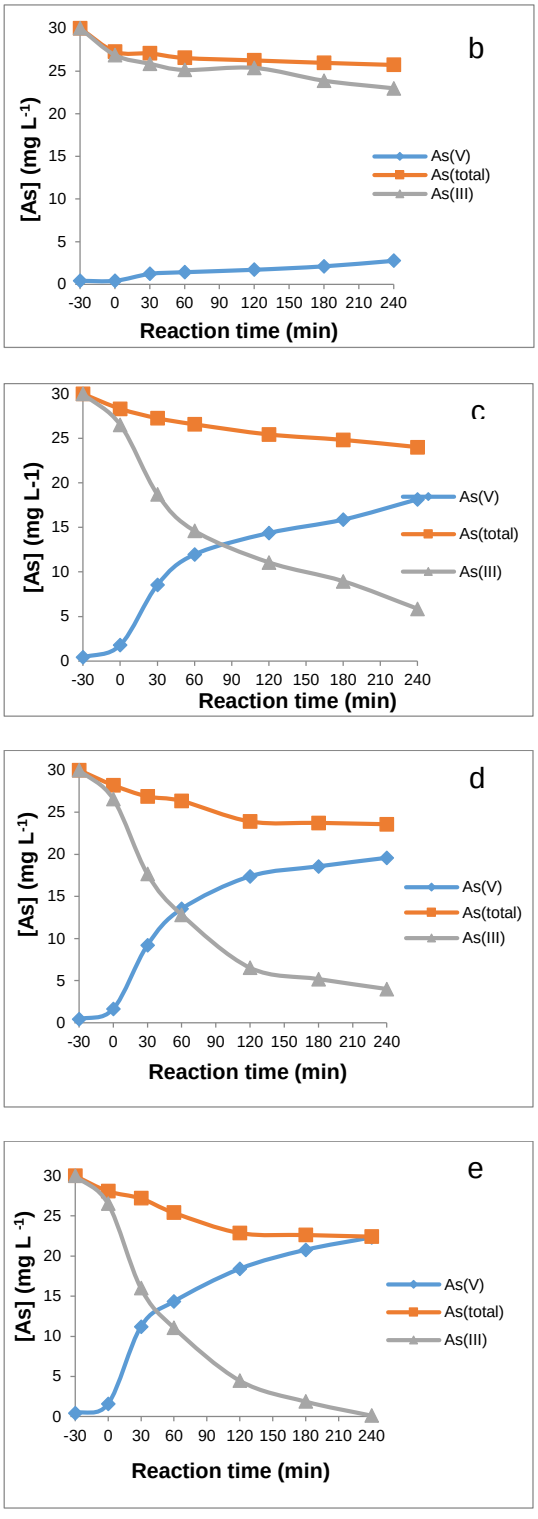

Fig. 1 Effect of CuO on the oxidation and simultaneous removal of As(III).
(a) pure ZnO, (b) pure CuO, (c) CuO(5%)/ZnO, (d) CuO(10%)/ZnO (e) CuO(20%)/ZnO.

Effect of initial concentration on simultaneous oxidation and removal of arsenite to arsenate was examined. For each treatment, irradiation time was four hour. Fig. 2 describes the efficiency of photocatalytic oxidation of As(III) with various initial concentrations. It shows that, C/C*i* curve for both As(V) and As(total) is almost same which indicates that for all the initial concentrations, As(III) almost completely converted to As(V) within the treatment period except for 40 mg L^{-1}. About 94% of As(III) was oxidized for the initial concentration 40 mg L^{-1}. These data demonstrates the high oxidation efficiency of CuO(20%)/ZnO mixture. During UV light irradiation, As(III) was converted to As(V) and part of them was simultaneously removed via adsorption on the surface of the photocatalyst. For low initial concentration, major portion of arsenic was adsorbed on the catalyst surface. With the increase in the initial concentration, percentage of arsenic adsorbed was decreased. Removal efficiency was 84.5%, 67.7%, 44.0%. 31.4%, 25.3% and 22.8% for the initial concentration of 5, 10, 15, 20, 30, and 40 mg L^{-1}. However, with the increase in the initial concentration, the total amount of arsenic removed (mg g^{-1}) was increased. Amount of arsenic removed was 12.7 mg g^{-1} when the initial concentration was 5 mg L^{-1} and 27.6 mg g^{-1} when the initial concentration was 40 mg L^{-1}. The decrease in the percentage removal of arsenic can be explained with the fact that all adsorbents had a limited number of active sites, which would have become saturated above a certain concentration.

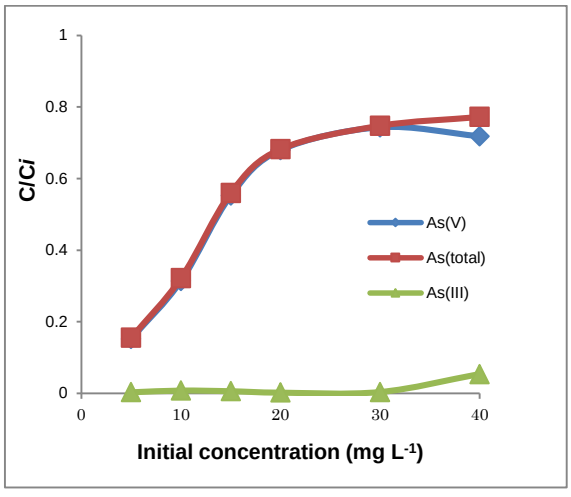

Fig. 2 Effect of Initial concentration on the photocatalytic oxidation and removal of As(III).

The preferential adsorption of As(V) over As(III) by photocatalyst was examined. The adsorption of both As(III) and As(V) on ZnO, CuO and CuO(20%)/ZnO was evaluated and the results

are depicted in Fig. 3. It is clear that the adsorption efficiency of As(V) on ZnO was higher than As(III). CuO also had higher affinity to As(V) than As(III) but CuO has higher adsorption efficiency of As(III) than ZnO. Meanwhile ZnO showed higher affinity to As(V) than CuO. CuO(20%)/ZnO mixture also showed higher adsorption efficiency to As(V) than As(III). These properties explain the higher removal efficiency during simultaneous oxidation and removal experiments.

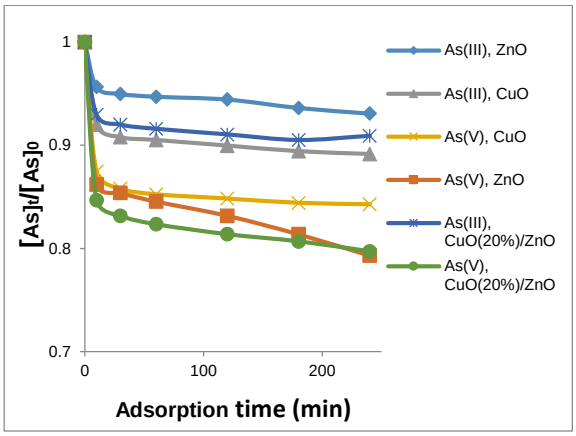

Fig. 3 Adsorption of arsenic species on ZnO, CuO and CuO(20%)/ZnO.

MECHANISM

The schematic band structure and charge transfer process of the CuO/ZnO photocatalyst are illustrated in Fig. 4. The photo-induced electron–hole pairs are separated from each other in ZnO under UV irradiation. The electrons transit from the valence band (VB) to the conduction band (CB) and leave positive holes (h^+) in VB. After separation of electrons and holes, the dissolved oxygen (O_2) adsorbed on ZnO surface will react with photo-induced electrons to form superoxide radical ($\cdot O_2^-$). Considering the band structures of ZnO and CuO, direct transfer of photo-induced holes from ZnO to CuO thermodynamically occurs in the CuO/ZnO composite [15], leading to low recombination rate of the photo-induced electron-hole pairs. The hydroxyl ions (OH^-) will be oxidized into hydroxyl radicals ($\cdot OH$) by photo-induced holes [18]. The As(III) species can be oxidized by both superoxide and hydroxide radicals by the continuous generated reactive oxidation species. Therefore, the enhanced photocatalytic oxidation of the CuO/ZnO photocatalyst should be attributed to the effective charge-transfer between ZnO and CuO.

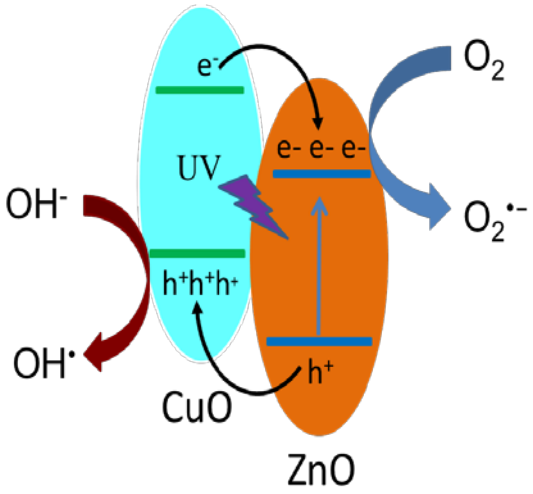

Fig. 4 Schematic diagram of the band structure and charge transfer process in the CuO/ZnO photo-catalyst.

CONCLUSIONS

This method utilizes simultaneously the higher oxidizing efficiency of Zinc oxide and Cupper oxide mixture and the higher adsorption capacity of ZnO for As(V).Commercial ZnO and CuO was used for treatment which are cheap and usually available in large amount. It is effective for the removal of arsenic from highly contaminated aqueous solution. As both the oxidation and removal is simultaneous process, it is less time consuming as compared to contemporary available techniques. Arsenic removal is possible at pH about 7 that is the pH of natural water indicating that pH adjustment is not necessary during the use of this technique for typical water.

ACKNOWLEDGEMENTS

The present research was partly supported by Grant-in-Aid for Scientific Research (C) 15K00602 from the Ministry of Education, Culture, Sports, Science, and Technology of Japan. All experiments were conducted at Mie University. Any opinions, findings, conclusions or recommendations expressed in this paper are those of the authors and do not necessarily reflect the view of the supporting organizations.

REFERENCES

[1] Caldwell BK, "Tubewells and arsenic in Bangladesh: Challenging a Public Health Success Story", International Journal of Population Geography, Vol. 9, 2003, pp. 23–38.
[2] Clancy TM, "Arsenic Waste Management: A Critical Review of testing and disposal of arsenic-bearing solid wastes generated during

arsenic removal from drinking water", Environ. Sci. Technol, Vol. 47, 2013, pp. 10799−10812.

[3] Korte NE, "A review of arsenic(III) in groundwater", Crit**.** Rev**.** Environ**.** Control, Vol. 21, 1991, PP. 1–39**.**

[4] Xu F**,** "Enhanced photocatalytic activity of hierarchical ZnO nanoplate-nanowire architecture as environmentally safe and facilely recyclable photocatalyst**",** Nanoscale, Vol. 3, 2011, pp. 5020-5025.

[5] Daneshvar N, "Photocatalytic degradation of azo dye acid red 14 in water on ZnO as an alternative catalyst to TiO_2", J. Photochem. Photobiol. A: Chem, Vol. 16, 2004 pp. 317–322.

[6] Madhavi S, "Removal of heavy metals from aqueous solutions using Fe_3O_4, ZnO, and CuO nanoparticles" J. Nanopart Res, Vol 14, 2012, pp. 1-18.

[7] Shifu C, "Preparation, characterization and photocatalytic activity of N-containing ZnO powder", Chem. Eng. J, Vol. 148, 200, pp. 263–269.

[8] Kanade KG, Self-assembled aligned Cu doped ZnO nanoparticles for photocatalytic hydrogen production under visible light irradiation, Mater. Chem. Phys, Vol. 102, 2007, pp. 98-104.

[9] Li B, "Facile synthesis and photocatalytic activity of ZnO-CuO nanocomposite", Superlattices and Microstructures, Vol. 47, 2010, pp. 615-623.

[10] Li BJ, "ZnO@graphene composite with enhanced performance for the removal of dye from water", J. Mater. Chem, Vol. 21, 2011, pp. 3346–3349.

[11] Zhang C, "Preparation and photocatalytic activity of hollow ZnO and ZnO–CuO composite spheres", Mater. Lett, Vol. 67, 2012, pp. 303–307.

[12] Wei A, "CuO nanoparticle modified ZnO nanorods with improved photocatalytic activity", Chin. Phys. Lett, Vol. 30, 2013, pp. 046202–5.

[13] Wang C, "Enhanced photocatalytic performance of nanosized coupled ZnO/SnO_2 photocatalysts for methyl orange degradation", J. Photochem. Photobio. A: Chem, Vol. 168, 2004, pp. 47–52.

[14] Xu T, "Significantly enhanced photocatalytic performance of ZnO via graphene hybridization and the mechanism study", Appl. Catal. B: Environmental, Vol. 101, 2011, pp. 382–387.

[15] Wang J, "Fabrication of CuO/T-ZnO nanocomposites using photo-deposition and their photocatalytic property", Appl. Surf. Sci. Vol. 258, 2011, pp. 1797-1805.

[16] Saravanan R, "Enhanced photocatalytic activity of ZnO/CuO nanocomposite for the degradation of textile dye on visible light illumination", Mater. Sci. Eng. C, Vol. 33, 2013, pp. 91–98.

[17] Tsang S, "Determination of phosphate/arsenate by a modified molybdenum blue method and reduction of arsenate by $S_2O_4^{2-}$", Talanta, Vol. 71, 2007, pp. 1560-68.

[18] Xiang QJ, Quantitative characterization of hydroxyl radicals produced by various photo-catalysts", J. Colloid Interf. Sci, Vol. 357, 2011, pp. 163–167.

First International Conference on Science, Engineering & Environment,
Tsu City, Mie, Japan, Nov.19-21, 2015, ISBN: 978-4-9905958-5-2 C3051

VISIBLE WEAK FLUORESCENT LIGHT PHOTOCATALYTIC DEGRADATION OF ORANGE II AND METHYL ORANGE WITH DYE-SENSITIZED TIO_2

Md. Ashraful Islam Molla[1], Hideyuki Katsumata[1], Tohru Suzuki[2], Satoshi Kaneco[1,2]
[1]Department of Chemistry for Materials, Graduate School of Engineering, Mie University, Japan
[2] Mie Global Environment Center for Education & Research, Mie University, Japan

ABSTRACT

Wastewaters containing azo-dyes from the textile industries raise much concern because of the harmful environmental and toxic effects they cause on ecological systems. In this study, we applied the dye-sensitization technique to TiO_2 catalyst and used it under visible light generated from a LED lamp (λ = 450 nm) and visible weak room (fluorescent) light for Orange II (O II) and Methyl Orange (MO) degradation. The photodegradation experiments were carried out at different periods of time using 20 mg of TiO_2 and 30 mL of 5 mg/L of initial concentration of O II and MO at room temperature and at natural pH values of the solution without the adjustment of pH. The percentage of MO and O II removal increases with an increase of irradiation time and reached up to 23.9% and 60.8% for room light and 41.1% and 88.4% for LED light, respectively, after 6 h irradiation time. The adsorption (removal) percentage on TiO_2 particles in the dark was found to be large for of O (II) and very little for MO, respectively, up to 30 min. There were no visible changes in the O II and MO solutions during photolysis. The kinetic behavior was described in terms of the Langmuir-Hinshelwood model. The possible mechanism of photodegradation under visible light was proposed.

Key words: Photodegradation, Visible Light, Dye-sensitization, Irradiation time

INTRODUCTION

Azo-dyes are an abundant class of synthetic, colored, organic compounds that comprise about half of the textile dyestuffs used today [1]. Wastewaters containing azo-dyes from the textile industries raise much concern because of the harmful environmental and toxic effects they cause on ecological systems [2]. Orange II (O II) is a textile azo-dye resistant to light degradation and the action of O_2 and common acids and bases. The high stability of O II is useful in textile applications make them difficult to degrade. Moreover, O II does not undergo biological degradation in wastewater treatment plants [3,4]. Methyl Orange (MO) is a commonly used water-soluble azo-dye. Its production and use as a pH indicator and as a dye for textiles may result in its release into the environment through various waste streams. MO dye in water is highly visible, even at very low concentrations, which hinders the penetration of light and therefore causes adverse effects on photosynthesis [5]. Therefore, the effective decolorization of dye-containing wastewater is an important and challenging task that must be approached.

In the solar spectrum, the range of wavelengths is broad, spanning from 250 to 2500 nm, but only 3.5−8% of it is in the UV range [6]. Hence, TiO_2 can make use of only a small fraction of solar light for photodegradation. This problem can be solved only by extending the light absorption capacity of TiO_2 catalysts. Semiconductor photocatalysts can be modified to expand their photoresponse to the visible region for dyes degradation in several ways. Most of these methods, however, are quite expensive and time-consuming. Dye sensitization, on the other hand, is new and simpler methods that can extend TiO_2 activation to wavelengths longer than those corresponding to its band gap.

The dye-sensitization technique has been reported as an innovative technology that could play an important role in developing efficient and cost-effective semiconductor photocatalyst in the near future [7]. Dye sensitization begins with electron injection from the excited dye into the conduction band (CB) of TiO_2, followed by interfacial electron transfer [8-12].

In this study, we applied the dye-sensitization technique to TiO_2 catalyst and used it under visible light generated from a LED lamp (λ = 450 nm) and visible room light for orange II and methyl orange degradation. The degradation of dyes was achieved at room temperature and at natural pH values of the solution, without the adjustment of pH. In the present experiment, the visible weak room (fluorescent) light was effective for the self-sensitized photocatalytic degradation of dyes with TiO_2.

EXPERIMENTAL

All reagents were of analytical grade and were used without further treatment. Orange II and methyl orange used in this study was purchased from Nacalai Tesque Inc., Kyoto, Japan (grade >99%) and used to make standards and aqueous solutions for the photocatalytic reactions. Ultrapure water (18 MΩ) was prepared by an ultrapure water system (Advantec MFS Inc., Tokyo, Japan). TiO_2 powder (Degussa P25, 80%:20% anatase/rutile, purity 99.9%) was added to the solution to produce a given concentration of TiO_2 suspension. The detailed experimental conditions were shown in Table 1. The dye concentration was measured by UV-Visible spectrometry.

Table 1 Experimental conditions

Samples	:	Orange II, 5 ppm (30 mL) Methyl orange, 5 ppm (30 mL)
Temperature	:	Room temperature
TiO_2	:	20 mg
Light source	:	LED lamp (450 nm) and room light
Instrument	:	UV-Visible spectrometry
λ_{max}	:	Orange II (485 nm) Methyl orange (464 nm)
Illumination time	:	6 h

RESULTS AND DISCUSSION

The effect of irradiation time on photodegradation of O II was carried out by measuring the percentage of O II removal at different periods of time under LED light (450 nm) and room light at ambient temperature (Fig. 1). The results revealed that the percentage of O II removal increases with an increase of irradiation time and reached up to 60.8% for room light and 88.4% for LED light, respectively, after 6 h irradiation time. The adsorption experiment of O II at different periods of time using 20 mg of TiO_2 and 30 mL of 5 mg/L of initial concentration of O II was conducted with aluminum foil coverage to block the impact of radiation. The adsorption (removal) percentage of O II on TiO_2 particles was found to be large up to 30 min, and after the time it was almost flat. The O II solutions with the photocatalysts were stirred in the dark for 30 min, prior to the exposure to the visible light radiation, which is expressed as the "negative time" in Fig. 1 and the "positive time" starts when the radiation exposure of the O II solution was initiated. There were no visible changes in the O II solutions during photolysis (without the photocatalyst).

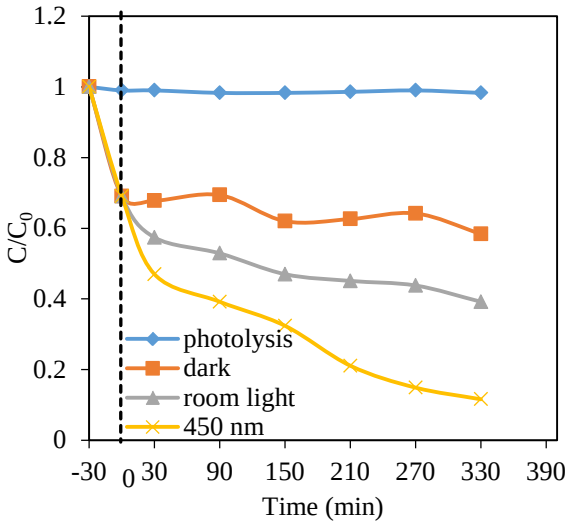

Fig. 1 Time courses of concentration of orange II in the dispersions containing TiO_2 under dark, LED light, room light and during the photolysis (without TiO_2).

The effect of irradiation time on photodegradation of MO was carried out by measuring the percentage of MO removal at different periods of time under LED light (450 nm) and room light (Fig. 2). The results revealed that the percentage of MO removal increases with an increase of irradiation time and reached up to 23.9% for room light and 41.1% for LED light, respectively, after 6 h irradiation time.

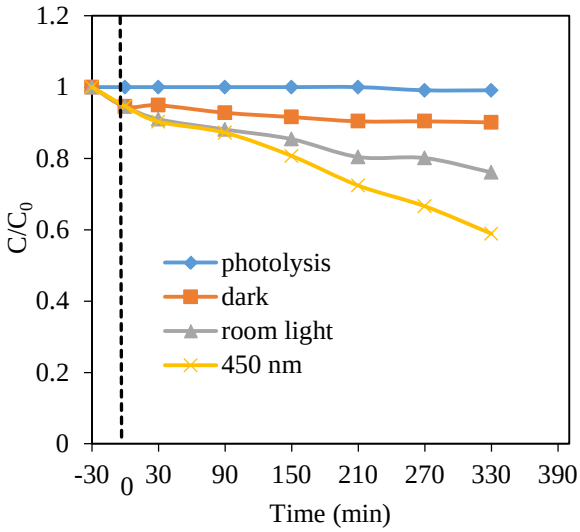

Fig. 2 Time courses of concentration of methyl orange in the dispersions containing TiO_2 under dark, LED light, room light and during photolysis (without TiO_2).

The adsorption experiment of MO at different periods of time using 20 mg of TiO_2 and 30 mL of 5 mg/L of initial concentration of MO was carried out in the dark. The adsorption (removal) percentage of MO on TiO_2 particles was found to be very little up to 30 min, and after the time the appreciable change was not observed in the time range. This weaker adsorption process of methyl orange compared to the orange II dye could be due to it that the MO molecule has the only one SO_3^- group while the O II molecule has one SO_3^- and one OH^- groups. There were no visible changes in the MO solutions in presence of visible light without any catalyst. These observations revel that visible light and photocatalyst are needed for effective destruction of both dyes.

The efficiency of the photocatalytic degradation process of both dyes under LED light was more effective than room light radiation. Since the catalyst powders are suspended in a stirred solution, the light intensity will affect the degree of absorption of light by the catalyst surface.

Kinetic Analysis

The heterogeneous photocatalytic degradation of dyes selected for the study viz., O II and MO, containing TiO_2 obeys apparently pseudo-first order kinetics at low initial substrate concentration and the rate expression is given by the equation:

$$r = - dC/dt = kC \quad (1)$$

where k is the pseudo-first order rate constant. Integration of the above equation with the limit of $C = C_0$ at $t = 0$ with C_0 being the equilibrium concentration of the bulk solution gives the following equation:

$$Ln(C_0/C_t) = kt \quad (2)$$

where C_0 is the equilibrium concentration of amitrole and C_t is the concentration at time t.

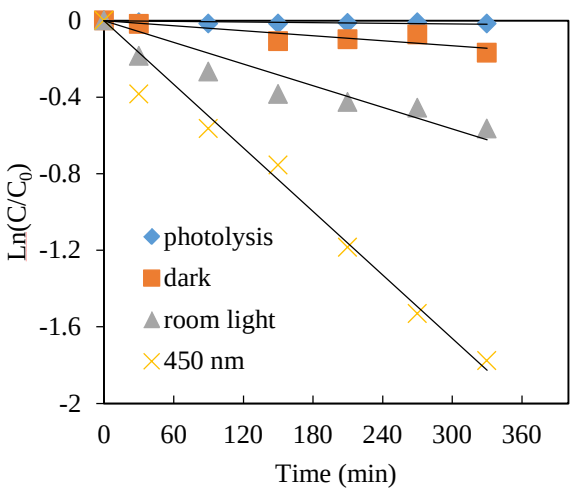

Fig. 3 Plot of $Ln(C/C_0)$ versus irradiation time for orange II.

$Ln(C/C_0)$ was plotted as a function of the visible light illumination time for O II and MO shown in fig. 3 and fig. 4, respectively. Since the linear plots were observed, the primary photocatalytic degradation dynamics of O II and MO may be pseudo first-order kinetics.

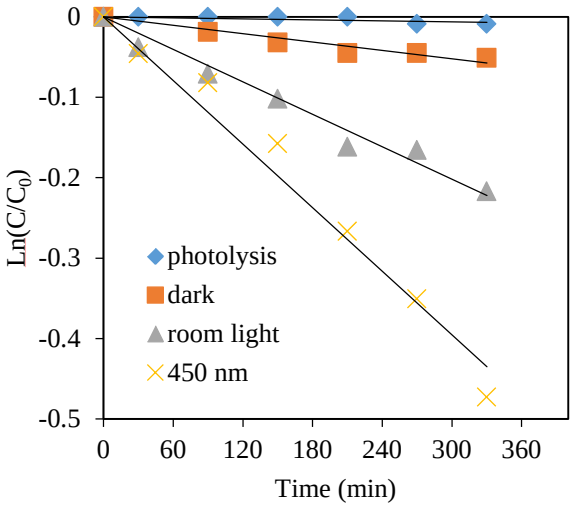

Fig. 4 Plot of $Ln(C/C_0)$ versus irradiation time for methyl orange.

The values of rate constants have been determined from the slope and intercept of these plots. As shown in Table 2, the rate constant values k (min^{-1}) were found to be decrease in room light than LED light for both dyes, when other parameters are kept unchanged. During the photodegradation experiment, the substrate half-life $t_{1/2}$ of O II and MO were about 125 min and 525 min for LED light and 367 min and 1029 min for room light, respectively.

Table 2 Rate constants, R^2 and half-life values of O II and MO dyes using TiO_2

Light source	*k* (min^{-1})		R^2		$t_{1/2}$ (min)	
	O II	MO	O II	MO	O II	MO
LED Light	0.0055	0.0013	0.974	0.975	125	525
Room light	0.0019	0.0007	0.801	0.968	367	1029

Proposed Degradation Mechanisms

Dye-sensitized photodegradation of orange II and methyl orange under visible light (LED light and room light) is initiated through excitation of the dyes molecule from its ground state to the excited state, which finally facilitates electron transfer to the conduction band of the semiconductor (TiO_2). A possible degradation reaction mechanism is proposed below.

$$\text{Dye} + h\nu \rightarrow \text{Dye}^* \quad (3)$$

$$\text{Dye}^* + TiO_2 \rightarrow \text{Dye}^{+\bullet} + TiO_2\,(e) \quad (4)$$

$$TiO_2\,(e) + O_2 \rightarrow TiO_2 + O_2^{-\bullet} \quad (5)$$

$$O_2^{-\bullet} + TiO_2\,(e) + 2H^+ \rightarrow H_2O_2 \quad (6)$$

$$H_2O_2 + TiO_2\,(e) \rightarrow \bullet OH + OH^- \quad (7)$$

$$\text{Dye}^{+\bullet} + O_2 \text{ (or } O_2^{-\bullet} \text{ or } \bullet OH) \rightarrow \text{peroxylated or hydroxylated intermediates} \rightarrow\rightarrow \text{degraded or mineralized products} \quad (8)$$

CONCLUSIONS

The degradation of dyes was achieved at constant ambient temperature, pressure, and natural pH values of the solution, without the necessity to adjust the pH values. O II adsorbs better onto P25 TiO_2 than MO does. The photodegradation of both dyes were less effective in room light radiation than the radiation created by the lamp. Negligible degradation occurred for both dyes in presence of visible light without any photocatalyst. The kinetics of O II and MO photodegradation were found to follow the pseudo-first order rate law and could be described in terms of Langmuir–Hinshelwood model. The visible weak room (fluorescent) light was effective for the self-sensitized photocatalytic degradation of dyes with TiO_2.

ACKNOWLEDGEMENTS

The present research was partly supported by Grant-in-Aid for Scientific Research (C) 15K00602 from the Ministry of Education, Culture, Sports, Science, and Technology of Japan. All experiments were conducted at Mie University.

REFERENCES

[1] Zollinger H, Color Chemistry, Properties and Applications of Organic Dyes and Pigments. New York: Publishers VCH, 1987.
[2] Combes R. D' Havelandsmith R. B, A review of the genotoxicity of food, drug and cosmetic colors and other azo, triphenylmethane, and xanthene dyes, Mutat. Res. , 98, 1982, 101–243.
[3] Helz G, Zepp R, Crosby D, Aquatic and Surface Chemistry. Boca Raton, FL: Lewis Publishers, 1995.
[4] Halmann M, Photodegradation of Water Pollutants, Boca Raton, FL: CRC Press, 1996.
[5] Liu Q, Zheng Z, Yang X, Luo X, Zhang J, Zheng B, Effect of factors on decolorization of azo dye Methyl Orange by oxone/natural sunlight in aqueous solution, Environ. Sci. Pollut. Res., 19, 2012, 577–584.
[6] Galvez J B, Rodriguez S M, Solar Detoxification, UNESCO: Paris, 19, 2003.
[7] Ni M, Leung M K H, Leung D Y C, Samathy L K, Renewable Sustainable Energy Rev., 11, 2007, 401.
[8] Ellingson R J, Asbury J B, Ferrere S, Ghosh H N, Sprague, J. R.; Lian T, Nozik A J, J. Phys. Chem. B, 102, 1998, 6455.
[9] Elena G, Coord. Chem. Rev., 248, 2004, 1283.
[10] Gratzel M, Inorg. Chem., 44, 2005, 6841.
[11] Duncan W R, Prezhdo O V, Annu. Rev. Phys. Chem., 58, 2007, 143.
[12] Kim W, Tachikawa T, Majima T, Choi W, J. Phys. Chem. C , 113, 2009, 10603.

First International Conference on Science, Engineering & Environment,
Tsu City, Mie, Japan, Nov.19-21, 2015, ISBN: 978-4-9905958-5-2 C3051

GREEN SUPPLY CHAIN IMPLEMENTATION IN MALAYSIA: A PERSPECTIVE

Alina Shamsuddin[1], Eta Wahab[2] and Nor Hazana Abdullah[2]
[1] Center of Academic Development, Universiti Tun Hussein Onn Malaysia, Malaysia [2] Faculty of Technology Management and Business, Universiti Tun Hussein Onn Malaysia

ABSTRACT

This paper is a case study in Malaysia which examines the level of implementation of Green Supply Chain Management (GSCM) practices in Malaysia. The findings serve as an indicator to the future prospects of GSCM in Malaysia. The study was carried out in the manufacturing industry as the manufacturing industry produces more emissions compared to other industries. A quantitative method was adopted. Questionnaires were sent to the employees of the manufacturing companies and the data was analyzed using the Statistical Package for Social Science (SPSS) program. The levels of implementation of the manufacturing companies were determined using a descriptive analysis. The results indicate that the company had a medium implementation level of GSCM practices. From the results, it can be concluded that the manufacturing companies are aware of green practices but are not able to implement it out in each of the supply chain. Despite this, it is reassuring that there is some initiative to implement green practices even it is not required by law.

Keywords: Green Supply Chain, Green Practices, ISO 14001

INTRODUCTION

Manufacturing companies produce more emissions compared to other industries during the manufacturing processes of their products to meet their customer needs and demands. Hence, the manufacturing companies need to be more concerned about the environment and how their processes are influencing the environment. Because of this massive ignorance of the majority of manufacturing companies, manufacturing companies are now accused for the cause of global warming in the form of waste generation, ecosystem disruption, and depletion of natural resources [1]. Nevertheless, manufacturing companies have now begun to be more aware of their processes and how it affects the environment.

Over the years, green supply chain management (GSCM) has gained popularity among Malaysian manufacturing companies although not as popular when compared to developed countries [2]. However, there are still a lot of manufacturing companies which are not adopting green supply chain practices in their manufacturing processes. According to [2], green supply chain management can be considered as closing the loop. The reason for this is because the product's "life" does not end when the consumer is done with it, but instead, it is brought back to the first stages where it can be used as raw materials or be reused, remanufactured, or recycled. This research addresses the level of implementation of GSCM in manufacturing companies that are attained the ISO 14001 certificate. This certification is to certify that a company's processes are green but it does not certify that the whole supply chain is green. According to [4], the ISO 14001 principle provides a framework, which guides firms to implement Environmental Management System (EMS) to improve environment performance only within a firm's operation boundaries instead of throughout the whole supply chain management of the manufacturing company.

In Malaysia, environmental issues have become a priority for the government and the public [2]. The depletion of natural resources has caused a shortage in some raw materials as the population of the world increases while resources start to decrease. Companies are starting to realize that the supply chain must be redesigned [5]. Researchers have now come to the conclusion and claim that the future of supply chain management is sustainability [5,6]. Concept of GSM is gaining more attention among the public as it enables companies to minimize the negative impact of the industries while enhancing their competitiveness [7]. Fully owned Malaysian companies have the lowest level of participation in green supply chain initiatives as compared to foreign based companies [2]. Various reasons have been identified such as difficulties and barriers to adopt green supply chain initiatives low involvement in green initiatives as compared to multinational

companies (MNC) [8,2]. This supports the fact that there are definitely barriers and obstacles that are hindering the local manufacturing companies from converting and start practicing GSCM. Greening supply chain not only allow firms to achieve substantial cost saving, it would also enhance sales, market share, exploit new market opportunities, which lead to greater profit margins [9].

Putting GSCM into context

The traditional supply chain is an integrated manufacturing process wherein raw materials are manufactured into final products, then delivered to customers via distribution, retail, or both [10]. The focus of the definition of supply chain has shifted over the years; early definition took into consideration the integration of a firm's internal functional groups such as purchasing, manufacturing, and distribution but the current definition pays attention to the interdependence in a broader sense, a global perspective. Definitions of GSCM have ranged from green purchasing to integrated supply chains flowing from supplier, to manufacturer, to customer and reverse logistics, which is closing the loop [10]. GSCM improves environmental performances as measured by reductions in air emissions, effluent waste, solid waste, and the consumption of toxic materials. In a nutshell, unlike traditional environmental management, green supply chain assumes full responsibility of a firm towards its products from the extraction or acquisition of raw materials up to final use and disposal of products.

Fully owned Malaysian firms have the lowest participation of green supply chain initiatives compared to foreign based companies or MNCs (Multinational Companies) [2]. The reason for this is that the concept of green purchasing is still new in Malaysia. In addition firm size plays an important role too in influencing GSCM, the bigger the firm size, the more willing to participate in green supply chain initiatives [2]. Nine influencing factors of GSCM, they are Information Technology (IT) implementation, Technology Advancement and Organization Adoption, Quality of Human Resources, Government Support systems, Innovative Green Practices, Top Management Commitment, International Environment Agreements, and Supplier Motivation [11]. IT implementation refers to efficient information technological system is necessary for effective communication and supporting the GSCM. Technology advancement and organization adoption is advancements in machinery and equipment to improve the products and services to increase the environmental performance to achieve GSCM. Organization Encouragement is to motivate the employees to achieve efficient GSCM. Quality of human resources means well qualified and professionals to implement effective green practices. Government support systems are industry friendly policies to promote GSCM. Innovative Green Practices involves hazardous solid waste disposal, energy conservation, reusing and recycling materials. Top management commitment is a dedication to empower people to change, the progress to ensure core manufacturing strategies and business strategies. An international environment agreement means green practices should be promoted at international platforms. Supplier motivation involves involving the suppliers in design process and technology affects overall performance of whole chain. All these factors were identified by the researcher using existing literature review and expert opinion.

In a summary, GSCM is best described as the firms full responsibility towards a product from the beginning of the supply chain process (acquisition of raw materials), until the end of the product life cycle (disposal of product). The level of implementation is influenced by IT implementation, Technology Advancement and Organization Adoption, Quality of Human Resources, Government Support systems, Innovative Green Practices, Top Management Commitment, International Environment Agreements, and Supplier Motivation, new concept, and firm size. By realizing the factors and level of implementation of GSCM practices in manufacturing companies, this study is able to not only get an idea of GSCM in Malaysia, but also to propose an action plan for future companies to follow.

METHODOLOGY

This study adopts a quantitative approach in gathering and analyzing the data. Quantitative research methods attempt to maximize objectivity, the ability to replicate it, and the generalization of findings, which are normally interested in prediction. In this study, purposive sampling is applied. This type of sampling is the purest form of probability sampling with each member of the population has an equal and known chance of being selected. The population of this study is the employees in a manufacturing company with the ISO 14001 certification. The sample of this study is taken from different levels of employees within a company with the ISO 14001 certification. The primary method for collecting data for this study is through questionnaires. The questions are adopted from a journal "The Implementation of Green Supply Chain Management Practices in Electronics Industry" by Ninlawan et al. (2010). The type of data analysis used in this study is descriptive analysis. The data collected will be analyzed using the Statistical Package for Social Science (SPSS) program. This program calculates the frequency,

percentage, and mean are determined.

DATA ANALYSIS AND DISCUSSIONS

This study analyses the data collected via questionnaires distributed and uses the aid of Statistical Package Social Science (SPSS) to analyze and determine the level of GSCM in this Malaysian manufacturing company. Instrument reliability analysis, demographic analysis, and also descriptive analysis was conducted in order to give a clearer picture and better understanding of the data collected using the questionnaire. The population size of the company was 600 and according to the table done by Krejcie and Morgan (1970) on population and sample size, a population of 600 required a sample size of 234, thus to be on the safe side, 250 questionnaires were distributed and only 200 were returned.

To ensure that the questions contained in the questionnaire are valid and reliable, pilot testing was carried out before distributing the questionnaire for the masses. The people chosen for the pilot test were supervisors and executives who in general know more about GSCM. The number of questionnaires used in the pilot test was 20. According to Sekaran (2003), the coefficient of Cronbach's Alpha should be higher than 0.6 to considered an acceptable, good and valid question. If the question scores lower than 0.6, then the question may contain a few problems like vagueness or appropriateness. The table below shows a summary of the results of the pilot test.

Table 1 Pilot Test (Reliability)

Item	Cronbach's Alpha
Internal environment assessment	0.748
Green purchasing	0.748
Eco design	0.895
Cooperation with customers	0.881
Investment recovery	0.603
Total	0.910

The results of the test clearly show that the questionnaire is valid and can be used for the research and is ready to be distributed. In addition to the validity of the questionnaire, previous researchers have used these questions in their research such as Ninlawan et.al., (2010).

After collecting the data from the respondents, the data was analyzed again for its reliability. The table below shows the results of the analysis.

Table 2 Actual Test (Reliability)

Item	Cronbach's Alpha
Internal environment assessment	0.648
Green purchasing	0.707
Eco design	0.837
Cooperation with customers	0.656
Investment recovery	0.774
Total	0.906

The total of the Cronbach's Alpha for the actual test is 0.906 which indicates that the questions are valid and are appropriate for the research.

Descriptive Analysis

Descriptive analysis can be used to generalize the sample to the population. This research will use descriptive analysis on each section to analyze the data collected.

The discussions continues with the personal information of the respondents such as their gender, age, position held, and department their attached to. Frequency and percentage will be used to explain the data collected. Out of the 200 samples analyzed, there were 102 males and 98 females or 51% and 49% respectively that took part in this study. This showed that there is almost a balanced number of respondents between males and females in this research. The results are shown in Table 3.

Table 3 Gender analysis

Item	Frequency	Percentage
Male	102	51%
Female	98	49%
Total	200	100%

In this study, age was divided into four categories. Below 30, between 31 to 40, between 41 to 50, and above 50. The ages between 31 to 40 has 96 respondents which is the highest followed by ages 41 to 50 with 71 respondents and then the below 30 category with 26 respondents and finally those above the age 50 with 7 respondents. Table 4 below shows the tabulation and the percentage of each category.

Table 4 Age analysis

Item	Frequency	Percentage
<30	26	13%
31-40	96	48%
41-50	71	35.5%
>50	7	3.5%
Total	200	100%

The positions held by the respondents were divided into four categories namely Executives, Supervisors, Managers, and Operational or Staff. Being a

manufacturing company, the labor force dominates the number of respondents with 159 or 79.5% of the respondents. This is followed by supervisors with 17 people or 8.5%, executives with 13 people or 6.5% and lastly by managers with 11 people or 5.5%. Table 5 shows the distribution of the positions held with their frequency and percentage.

Table 5 Position analysis

Item	Frequency	Percentage
Manager	11	5.5%
Executive	13	6.6%
Supervisor	17	8.5%
Operational or Staff	159	79.5%
Total	200	100%

The data collected revealed that there are nine departments that took part in the survey. They are Human Resource, Information Technology, Marketing, Customer Service, General Administration, Finance and Accounting, Production, Engineering, and Quality Control. In keeping in line with the number of positions held, the production department yields the most amount of responders, while at the opposite side of the scale, Engineering, and Finance and Accounting departments yielded the least amount of responders with 10 people each. Table 6 below shows the results collected.

Table 6 Department analysis

Item	Frequency	Percentage
Human Resource	14	7%
Information Technology	15	7.5%
Marketing	12	6.0%
Customer Service	13	6.5%
General Administration	13	6.5%
Finance And Accounting	10	5.0%
Production	100	50%
Engineering	10	5.0%
Quality Control	13	6.5%
Total	200	100%

In order to figure out the level of implementation, the mean of each question and each section is taken into account and based on Chua (2006), the level of implementation can be determined by using the calculated mean. The table 7 shows the central tendency level and the mean range.

Table 7 Agreement level of mean measurement

Central tendency level	Mean range
3.68 – 5.00	High
2.34 – 3.67	Medium
1.00 – 2.33	Low

Internal Environment

Question one to question nine in the questionnaire are indicators for internal environment assessment. Based on the mean results of these nine questions, the level is only medium. It is clear that there are plans to carry out (or even is being carried out) ISO 14001 activities, as the mean is the highest with 4.245. The lowest mean would be plans for eco labeling of products, with a mean of only 3.290. Despite this, the overall level is medium as the overall mean is 3.619. Table 8 shows the mean breakdown of each question

Table 8 Internal environment assessment

No	Item	Mean	Level
1.	Question 1	3.75	High
2.	Question 2	3.66	Medium
3.	Question 3	3.38	Medium
4.	Question 4	3.63	Medium
5.	Question 5	3.71	High
6.	Question 6	4.25	High
7.	Question 7	3.58	Medium
8.	Question 8	3.29	Medium
9.	Question 9	3.34	Medium
	Total Average	3.62	Medium

Green Purchasing

Questions 10 to question 13 discuss on green purchasing. Overall, the level of green purchasing is medium with cooperation with suppliers for environmental regulations receiving the lowest mean with 3.250, and the highest mean of 3.275 goes to certifying suppliers with ISO 14000. This shows that there is indeed intention of applying GSCM. Table 9 below shows each question's mean and level.

Table 9 Green purchasing

No	Item	Mean	Level
1.	Question 10	3.25	Medium
2.	Question 11	3.26	Medium
3.	Question 12	3.28	Medium
4.	Question 13	3.27	Medium
	Total Average	3.26	Medium

Eco Design

The next section starting from question 14 to question 20 indicates the level of eco design. Plans to design products that minimize capacity, time, area stored, and energy between transport has the highest mean with 3.385, while plans to design products for easy set up for users with minimal effort receives the lowest mean which is 3.200. Table 10 below shows

the mean and level of the questions involved.

Table 10 Eco design

No	Item	Mean	Level
1.	Question 14	3.32	Medium
2.	Question 15	3.35	Medium
3.	Question 16	3.30	Medium
4.	Question 17	3.27	Medium
5.	Question 18	3.39	Medium
6.	Question 19	3.20	Medium
7.	Question 20	3.38	Medium
	Total Average	3.31	Medium

Cooperation with Customers

The next three questions show the level of cooperation with customers that the company has. The overall level of cooperation with customers is medium with a mean of 3.223. The lowest mean is shared between plans to cooperate with customers for eco-design, and plans to cooperate with customers for green packaging, with a mean of 3.225. The highest of the three is plans to cooperate with customers for cleaner production with a mean of 3.230. Table 11 below shows the data.

Table 11 Cooperation with customers

No	Item	Mean	Level
1.	Question 21	3.23	Medium
2.	Question 22	3.23	Medium
3.	Question 23	3.23	Medium
	Total Average	3.22	Medium

Investment Recovery

The last three questions of the questionnaire deal with investment recovery and has an overall mean level of 3.291. The lowest mean which is 3.200 belongs to plans for sale of excess inventories or materials; whereas plans to sell excess capital equipment have the highest mean of 3.370. Table 12 below illustrates the collected data.

Table 12 Investment recovery

No	Item	Mean	Level
1.	Question 24	3.20	Medium
2.	Question 25	3.31	Medium
3.	Question 26	3.37	Medium
	Total Average	3.29	Medium

Summary of GSCM Practices

A summary of all the GSCM practice with their respective means and levels are shown in table 13 below. As seen from the table below, it is clear that the company implies a medium level of GSCM across the board and as a result, the overall implementation can be considered as medium level as the total mean average is less than 3.68.

Table 13 Summary of GSCM practices

GSCM Practices	Mean	Level
Internal Environmental Management	3.62	Medium
Green Purchasing	3.26	Medium
Eco Design	3.31	Medium
Cooperation with Customers	3.22	Medium
Investment Recovery	3.29	Medium
Total Mean Average	3.34	Medium

Discussions

The level of GSCM practices implemented by the company had to be measured. The questions that were adopted from Ninlawan et al. (2010) are based on a scale of one to five thus allowing the measurement of the level of implementation. The mean results from the research have revealed that the company has been implementing some of the GSCM practices and according to the agreement level of mean measurement, it can be concluded that as an overall, the company has achieved an implementing level of medium for GSCM practices, which is a mean of 3.34 out of 5.00. To achieve a high level, the mean must be at least 3.68. Despite only achieving a medium level, a closer look at the results show that the company's mean is only 0.34 shy from achieving a high implementation level of GSCM practices. The questions in the questionnaire were analyzed in five categories which were internal environmental management, green purchasing, eco design, cooperation with customers, and investment recovery. Each category was measured with the same agreement level of mean measurement, and all the categories had a medium level of GSCM implementation with 3.62, 3.26, 3.31, 3.22, and 3.29 respectively.

Companies that would want to implement GSCM could start off by fulfilling the conditions of acquiring the ISO 14000 certification. Although this does not make them a fully green supply chain [4], it is a start. From there, companies slowly work their way to a green supply chain by tackling the elements of green supply chain like Internal Environmental Management, Green Purchasing, Eco Design, Cooperation with Customers, and Investment Recovery [13]. It all starts with the companies, after acquiring the ISO certification, they can start by selecting suppliers that not only deliver on quality and affordable prices, but also adhere to environmental standards. They can also design their

products to reduce the need for environmentally hazardous materials. It also needs to be designed for reuse, repairs, reduced energy consumption (APO, 2004), and recycling. They could also introduce reverse logistics which deals with reuse, remanufacturing, and recycling of their products after consumers are done with them.

This study was to examine the implementation level of GSCM practices. To examine the implementation level of GSCM practices, a descriptive analysis was performed on the data collected through purposive sampling. The results from the analyzed data showed that the implementation level of GSCM was a medium level which was based on the mean and it fell in the medium range as described by the agreement level of mean measurement. Overall, the literature supported the results that manufacturing companies in Malaysia were not so keen in GSCM yet. Future research on the topic can be improved dramatically by increasing the sample size of the companies sampled to include manufacturing companies from all over Malaysia. But as far as results go, it is encouraging to see that at least the company sampled was applying some methods of GSCM in:

- Internal Environmental Management
- Green Purchasing
- Eco Design
- Cooperation with Customers
- Investment Recovery

ACKNOWLEDGEMENTS

We would like to thank UTHM for funding this research under vot number MDR 1317/2013

REFERENCES

[1] Fiksel, J. (1996). Design for environment: Creating eco-efficient products and processes. New York, NY and London: McGraw-Hill.

[2] Eltayeb, T. K.; Zailani, S.;. (2009). Going green through green supply chain initiatives towards environmental sustainability. *Operations & Supply Chain Management Vol. 2 No, 2*, 93-110.

[3] Zhu, Q.H.; Sarkis, J.; Geng, Y.;. (2004). Green supply chain management in China: pressures, practices and performance. *Green supply chain management*, 449-465.

[4] Handfield, R. B.; Sroufe, R.; Walton, S. V.;. (2005). Intergrating environmental management and supply chain strategies . *Busines Strategy and the Environment Vol. 14(1)*, 1-19.

[5] Carter, C.R., Jennings, M.M. (2004). The role of purchasing in corporate social responsibility: A structural equation analysis . *Journal of Business Logistics, Vol.25 (1)*, 145-186.

[6] Murphy, P.R. and Poist, R.F. (2002). (2002). Socially responsible logistics: an exploratory study. *Transportation Journal, Vol. 41 (4)*, 23-35.

[7] Rao, P. (2006). Greening of suppliers/In-bound logistics-in the South East Asian context. In J. Sarkis (Ed). *Greening the Supply Chain London: Springer* .

[8] Wycherley, I. (1999). Greening supply chains: the case of The Body Shop International. *Business Strategy and the Environment, Vol. 8 (2)*, 120-127.

[9] Rao, P. & Holt, D. (2005). Do green supply chains lead to competitiveness and economic performance? *International Journal of Operations & Production Management, Vol. 25 No. 9*, 898-916.

[10] Beamon, B. M. (1999). Designing the Green Supply Chain. *Logistics Information Management*, 332-342.

[11] Zhu, Q.H; Sarkis, J.;. (2004). Relationships between operational practices and performance among early adopters of green supply chain management practices in Chinese manufacturing enterprises. *Journal of Operations Management Vol. 22*, 265-289.

[12] Luthra, S.; Garg, D.; Kumar, S.; Haleem, A.;. (2012). Implementaion of the green suply chain management in manufacturing industry in India using interpretive structural modeling technique. *A Journal of Science, Technology & Management* .

[13] Ninlawan, C.; Seksan, P.; Tossapol, K.; Pilada, W.;. (2010). The implementaion of green supply chain management pratices in electronics industry. *Proceedings of the International Multiconference of Engineers and Computer ScientistsVol. 3* .

First International Conference on Science, Engineering & Environment,
Tsu City, Mie, Japan, Nov.19-21, 2015, ISBN: 978-4-9905958-5-2 C3051

INNOVATIVE GREEN EXTRACTION TECHNOLOGY FOR OIL EXTRACTION AND ITS APPLICATION IN DIFFERENT FIELDS

Wael Abdelmoez,
Chemical Engineering Department, Minia University, 61516, Egypt

ABSTRACT

This study presents the extraction of oil using subcritical water technology from different oil containing procurers. The effect of extraction parameters including temperature, water to feed ratio, extraction time and mean particle sizes were studied for different procurers. Cotton seeds and edible oil bleaching powder were presented and compared to explore the efficiency as well as the diversity of the subcritical water technology in oil extraction as a green solvent. In addition, the application of the technology in the field of pharmaceutical active ingredient was also investigated through demonstration of extracting medical oils such as jojoba oil from its seeds. Moreover, the kinetic as well as the thermodynamic of the extraction process were investigated. The obtained results revealed that the increase in both temperature and the time of extraction while a decrease in particle size generally improved the yield of extraction up to certain limits. Both rates of extraction and decomposition were estimated using the reaction rate equations using nonlinear regression method. It was also found that in the case of oil extraction using subcritical water, the reaction kinetics could be correlated well with an irreversible consecutive unimolecular-type first order and the extraction process is mainly diffusion control. The apparent activation energy was calculated to be 46.1 kJ.mol-1. This result indicates a diffusion controlled reaction. For more exploration and deep understanding of the extraction mechanism, other thermodynamic parameters were also calculated and analyzed including, ΔH#, ΔS#, and ΔG# of the extraction step.

Keywords: (Subcritical water, Extraction, waste management, green technology)

1-INTRODUCTION

Extraction always involves a chemical mass transfer from one phase to another. The principles of extraction are used to advantage in everyday life, for example in making juices, coffee and others. The principles of green chemistry are critically important today, and pressurized hot water extraction, as a "solvent less" extraction technique fulfils the criteria of green chemistry well. According to definition, green chemistry involves approaches that reduce or eliminate the use or generation of hazardous substances in the design, manufacture and application of chemical products. The first principle of green chemistry is that it is better to prevent waste than to treat or clean it up after it is formed.

In the move to reduce or eliminate the use of organic solvent and improve the extraction processes, newer sample preparation methods such as microwave assisted extraction (MAE), super-critical fluid extraction (SFE), accelerated solvent extraction (ASE) or pressurized liquid extraction (PLE) and pressurized hot water extraction have been introduced for the extraction of analyses present in plantmaterials [1–3].Water is non-flammable, non-toxic, readily available and an environmentally acceptable solvent. It has not yet received much attention as an analytical extraction solvent for plant materials because water is too polar to efficiently dissolve most organics that are associated with botanicals. It has been demonstrated that raising the temperature with enough pressure to maintain the liquid state allows it to quantitatively extract a wide variety of organic solutes from many different matrixes.

Subcritical water extraction (SWE) is a new and powerful technique at temperatures between 100 and 374o C and pressure high enough to maintain the liquid state (Fig.1) [4]. Unique properties of water are namely its disproportionately high boiling point for its mass, a high dielectric constant and high polarity [4]. As the temperature rises, there is a marked and systematic decrease in permittivity, an increase in the diffusion rate and a decrease in the viscosity and surface tension while the diffusivity increases, allowing a deep penetration of the solvent into the matrix, thus enhancing the efficiency and speed of the extraction process .In addition, increases in vapor pressures and rapid thermal desorption of target compounds from matrices could also enhance the extraction efficiency.

In consequence, more polar target materials with high solubility in water at ambient conditions are extracted most efficiently at lower temperatures, whereas
moderately
polar and non-
polar targets require a less polar medium induced by elevated temperature [5].
For SWE, the extraction times were very short compared with any other conventional extraction techniques. But, a long heating time during the extraction may cause the compound degradation.

Therefore, optimization of time is very important to construct the SWE process.
Based on the research works published in the recent years, it has been shown that the SWE offers a series of important advantages over other techniques: the higher quality of the extracts, a faster process, a reduction in the amount of solvents used, and its cost. Additionally, by using water instead of organic solvents, SWE is a more environmentally friendly extraction process for extracting functional food or pharmaceutical ingredients that are beneficial to health .
This article discusses recent results in the application of SWE to various plants for use in the food and pharmaceutical industries. The first part views the properties of SWE, its mechanism, and its benefits. The second part discusses how the subcritical water technology is applied to plant extraction, and many other applications in different fields.

2. Unique properties of water under subcritical conditions

Water is a natural occurring and abundant substance that exists in solid, liquid, and gas forms on our

planet. The physics and chemistry of water is the backbone of engineering and sciences. The water in the vicinity of the critical point is compressible fluid and, in addition, most of its properties are all totally different in its physics and chemical feature. Working within the critical point which so called the subcritical region has the advantageous of moderating the condition of the reaction media with maintaining some of the distinctive properties of the supercritical region. In this sense, water within its critical point (subcritical water) could be defined as a hot water under sufficient pressure to maintain the liquid state. In the following we will explore briefly the important parameters, including the hydrogen bond, density, dielectric constant, and ion product, which directly affect the waste treatment near or above the critical point.

2. 1.THE HYDROGEN BOND

When two water molecules close to another at ambient temperature, a hydrogen atom on one of the molecule is attracted to the oxygen of the other molecule. Such behavior is attributed to the specific characterization of the covalent bond existing between the oxygen and hydrogen atoms in the water molecule itself. When the distribution of electrons in the water molecule is considered in detail, it becomes apparent that one of the atoms gets "more" of the shared electrons than the other does. As a result, oxygen has a partial negative charge, and the hydrogen has a partial positive charge with forming two different poles. Thus, when water molecules are close together, their positive and negative poles are attracted to the oppositely charged regions of nearby molecules. This polar characteristic of the water results in the hydrogen bond formation. Each water molecule is hydrogen bonded to four others as shown in Fig. 1.

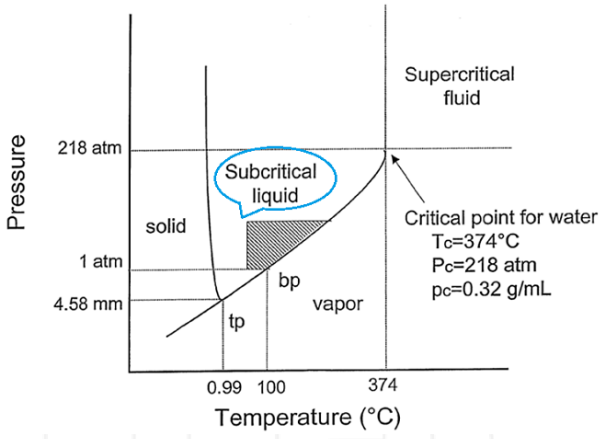

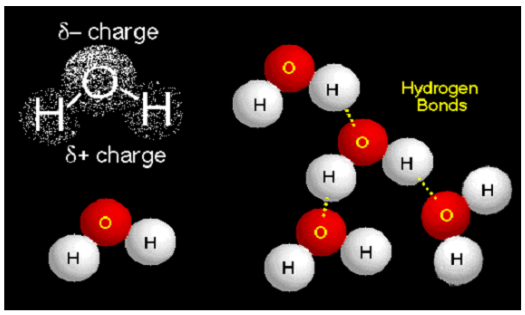

Figure 1 Hydrogen bonding of water molecules

The ability of water molecules to form such hydrogen bond is responsible of the unique properties of water including the solvent ability to polar compounds and on the contrary, the squeezing (the hydrophobic) effect which resulting in the exclusion of non-polar compound [6]. The polarity of the water molecules determines the forces of attraction between the molecules in the liquid state. The high internal-energy of water near and above the critical point keeps farther distances between the water-molecule. As the result the intensity of the hydrogen bond between molecules in closer neighborhood becomes forcedly reduced and consequently the polarity decreased.

2.2. DENSITY AND VISCOISTY

The density of water is extremely sensitive to minor changes in temperature and pressure near the critical point (Fig. 2). The liquid-vapor coexistence curve ends at this point. Upon heating under pressure, as the liquid water expands, many of its molecules become vapor (steam) and rise above the liquid. Vapor density consequently increases, while liquid density decreases. Eventually, when the pressure reaches 220 times or more beyond normal

atmospheric pressure, the liquid and vapor densities are identical. The density under this state is closer to that of organic liquids but the solubility of solids can be 3-10 orders of magnitude higher. A plot of the solubility parameter versus pressure
would resemble that a plot of density versus pressure. This confirms that the solvation strength of the water near or above the critical point is directly related to the density. Similarly, the viscosity of water decreases with increasing temperature, and at 500 °C and 10 bar is only 10% of its magnitude under ambient conditions [7]. Even under more mild conditions the viscosity is still lowered, and thus it may be envisaged that the mobility of dissolved ions and molecules is higher under sub and supercritical conditions than at ambient pressure and temperature. Thus, the solubility of a solid can be manipulated by making slight changes in temperatures and pressures to remote both the density and viscosity of the water.

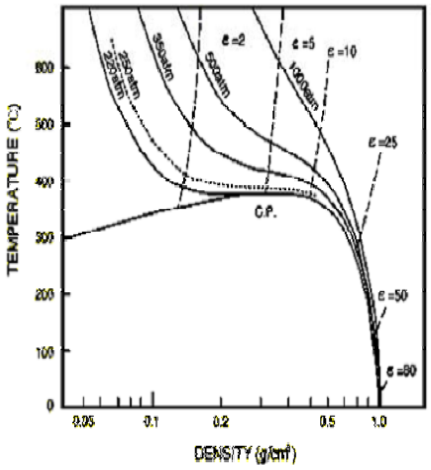

Figure 2 density of water under different conditions

2.3. THE DIELECTRIC CONSTANT

The key properties of water that influences many of the most important interactions are the dipole moment and its ability to both donate and accept protons. This imparts on water the ability to hydrogen bond with itself, to hydrogen bond with both proton donors and proton acceptors, to dissociate, to coordinate with ions and other dipoles. Water has a very high dipole moment due to the electro negativity of oxygen and the fact that hydrogen-oxygen bonds are short which results in a high dielectric constant with a typical value at the standard conditions of 80. In methanol, for instant, one of the hydrogen atoms is replaced by a CH3 group lengthening the bond and so reducing the dipole moment and consequently the dielectric constant by a factor of over 2. So, what implications does the dielectric constant have for chemical interactions? The first thing to note is that the concept of a dielectric constant is an essentially macroscopic concept. Such concept has a direct effect on the solubility properties of solvent materials. Under ambient conditions, liquid water has a high dielectric arising from dipoles of individual molecules and association of molecules due to hydrogen bonding. However, because hydrogen bonding is exothermic, the equilibrium constant decreases with increasing temperature and the intermolecular associations break down causing the dielectric constant to fall down [8,9]. Therefore, organics are much more soluble in supercritical water but there is essentially no ionizing power and salts drop out of solution (precipitate, as we mentioned for the density). However, in the water under the SCW conditions, it has a dielectric constant which is greatly reduced from that of ambient water, but still possesses a degree of ionizing potential (Fig. 3). Thus many of the benefits of working in supercritical water is available in SCW as well, but with many additional advantages. Polar organics of any sort are completely miscible and even hydrocarbons dissolve to a large degree. For example, benzene shows a complete miscibility in supercritical water, whereas in liquid water under ambient conditions the benzene solubility is equal to a few ppms [10]. Moreover, separation after reaction becomes very easy; simply lowering the temperature raises the dielectric constant enough to render organics insoluble, and products can be simply decanted.

Figure (3) Water properties under different conditions of temperatures and pressures

2.4. ION PRODUCT

Pure water is a poor conductor of electricity because it does not ionize to any great extent.
However, a little ionization of water results in the production of H+ and OH-ions. At room temperature, one in a billion water molecules will ionize. Water can react with its own molecules to produce hydronium and hydroxide ions in what so-called ion production process. As shown in Fig. 4, one molecule of water acts as an acid and the other acts as a base to produce a conjugated acid and conjugated base. The equilibrium constant for this reaction can be calculated as follows:

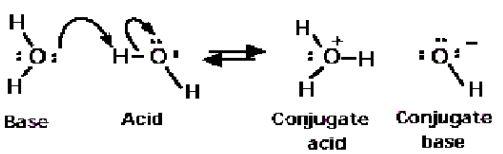

Figure (4) the dissociation of water(a)

The characteristics of water as a reactive catalyst can be evaluated with the value of the ion product (the product of the hydrogen ion concentration and the hydroxyl ion concentration). Increasing in the ion

product value increases the hydrogen ion concentration.

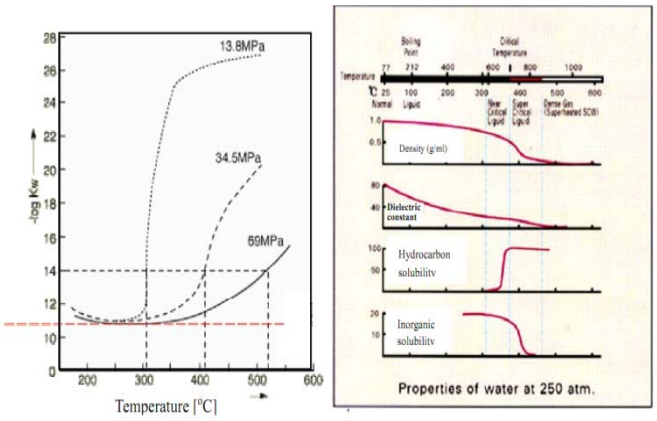

Figure (4) the dissociation of water(b)

Under subcritical conditions, the hydrogen bonding network of water is minimized. The weakening of the hydrogen bonding is thought to induce the evolution of protons, further increasing its acidity. Then, under high ion product values water possesses the effect of an acid catalyst. Such a high ion product value for the subcritical water allows it to catalyze many reactions in the absence of any extra catalyst.

3. Applications of Subcritical Water Technology

3. 1. Hydrolysis of agriculture wastes

Cellulose wastes represent an attractive source of renewable energy. The cellulosic nature of agricultural wastes makes them suitable raw materials for bioconversion processing to produce end products with high value added. They are renewable, available in large quantities, and cheap. The utilization of agricultural wastes as a feedstock has a double effect consequence, environmentally and economically, by minimizing the waste disposal problems, and producing valuable products from low-cost cellulosic wastes. About 26-28 million tons of agriculture wastes are produced annually in Egypt [11]. The amount of wheat straw produced in the year 2004 was estimated to be 4.65 million tons according to data in the report of The Ministry of Agriculture and Land Reclamation [12]. In practice these agriculture wastes are burned, which creates environmental pollution problems [13].

There are several technologies available for the hydrolysis of wheat straw and other cellulosic wastes, such as acid hydrolyses, enzymatic hydrolyses and others. Many researchers studied acid hydrolysis under different operating conditions [14, 15, 16]. The results indicated that acid hydrolysis could produce high yields of hydrolysate.. However, this technique has many drawbacks like using toxic and corrosive chemicals [17]. Also, acid pretreatment is considered too expensive because it requires corrosion resistant materials of construction and some mineral acids produce degradation products [18]. To overcome the drawbacks of the acid hydrolysis and to go through a more environmentally friendly process, enzymatic hydrolysis was thoroughly studied [19, 20]. The results showed that high yields of hydrolysate could be obtained by using enzymatic hydrolysis, but the economic feasibility of the process is uncertain so far.

Cellulose hydrolysis in subcritical and supercritical water was been studied [21, 25]. The results revealed that subcritical water technology is a promising technique and it is strongly advocated to be an alternative route for not only cellulose hydrolysis but also other biomass conversions. This technique has immediate advantages over traditional hydrolysis techniques. It represents a flexible process due to the possibility of continuous changing of the solvent power/selectivity of the subcritical water. Also, it allows the elimination of polluting acid solvents and the expensive post-processing of the hydrolyzates for solvent elimination. Using of subcritical water in hydrolyzing wheat straw to recover available sugars for subsequent fermentation to produce ethanol or other sugar-based fermented products is investigated [26].The results showed under subcritical water condition the value of ion product increases, so water possesses the effect of an acid catalyst and for that particular reason subcritical water was found to be a safe, green, and sustainable alternative for acid hydrolysis.

3.2. Using SWE for extraction of edible oils

Extraction of compounds from natural sources is the most important application of subcritical water. In 1999, Hiroyuki Yoshida, showed that a relatively large amount of oil, organic acids, and amino acids could be extracted from fish, squid entrails and meat wastes by subcritical water treatment [27, 28]. The essential oil from plants has been extracted by using subcritical water. Usually the oil in these plants is traditionally extracted either using steam distillation [29, 30] or solvent extraction [27, 28, 31, 32]. These techniques present some shortcomings, namely losses of volatile compounds, low extraction efficiency, long extraction time, degradation of unsaturated compounds, and toxic solvent residue. That encourages the use of alternative techniques for the extraction of essential oils [33]. Continuous subcritical water extraction presented a powerful alternative for solid sample extraction [34–36]. Its use in the field of essential oils is recent and seems to be very promising [37, 38].

Subcritical water has been used as a new pathway for cottonseed oil extraction. Comparing this technique with the traditional hexane extraction method, it is found that the new technique has a shorter time of extraction providing an environmentally friendly proceeding, since it uses

water as the solvent and no organic solvents are involved [39].
Subcritical water treatment is an emerging technique for extracting useful materials from agricultural by-products or food wastes or for degrading environmental pollutants [40-42]. The subcritical water extraction was applied to soy sauce cake to produce useful materials from it. The properties of the extract were compared with those of the extracts from defatted rice bran and wheat bran. Although hydrolysis and degradation reactions would occur during the treatment, the term of extraction is used for the purpose of the treatment [43].
The extraction of oil from jojoba seed using SCWT for bio-fuel production was investigated to find out the optimum extraction conditions. The oil was extracted directly from the virgin jojoba seed. The results were compared with those obtained by traditional techniques to study the advantages of using subcritical water method for the extraction of jojoba oil [44].

3.3. Production of valued materials from fish processing wastes

Subcritical water hydrolysis was carried out to produce valued materials from squid viscera, the waste product of fish processing industries. These wastes contain a lot of protein, lipid and many kinds of biological active matter. From environmental and economical point of view, it is appreciated to convert these wastes into useful materials. Some works have been carried out for isolation and identification of polyunsaturated fatty acids especially EPA and DHA, enzymes and other bioactive compounds from fish waste [45-49].
Recently the requirement of biomass (aquatic, livestock, bird etc.) products is enormously increasing around the world. Recognition of the limited biological resources and increasing environmental pollution has emphasized the need for better and more value added utilization of the under-utilized fish and the by-products from the fishing industries. Traditionally, much of this material has been converted to powdered fish meal by a combined process of cooking, separation of soluble from insoluble, concentration of the soluble and dehydration of the insoluble [50]. The hydrolysis of waste into value added products (proteins, amino acids, reducing sugar etc.) is an alternative and effective way.
Current industrial hydrolysis methods of biomass waste include chemical (acid, alkali or catalytic) hydrolysis and enzymatic hydrolysis. But the chemical hydrolysis needs violent reaction conditions and often brings serious pollution of the environment. Enzymatic hydrolysis is expensive, and with long production cycle. Most of biomass waste is easily hydrolyzed in super- or subcritical water, which is structurally different from normal liquid water, and possesses some marvelous properties. Without any pollution, hydrolysis in super-or subcritical water is environment-friendly technology [51] .Subcritical water is a promising medium for dissolution of biomass in water. The waste can be hydrolyzed into high value industrial raw material: amino acid, unsaturated fatty acid, oil and polysaccharide [52-55], hydrogen and methane [56] and so on. The thermal protein hydrolysis is gaining in importance in economical as well as **ecological aspects.**

3.4. Using subcritical Technology for Biomass conversion

As energy demands increase and fossil fuels are limited, research is directed towards alternative renewable fuels. Biomass is the most important candidate as a renewable recourse for energy, chemicals, food, and feedstock. This makes cellulose, which is the major component of biomass, an important compound to study for achieving this goal. For the conversion of biomass resources into useful chemicals and bio-energy, three major process types, direct combustion, gasification, and liquefaction are reported to be effective [57]. Theses methods suffer many drawbacks, as low conversion rates and additional purification methods are required for the by-products.
Antal and others [58] investigated the conversion of biomass feedstocks consists of a semisolid gel of 4 % starch in water. Wood sawdust and other particulate biomass were mixed into the starch gel to form a suspension which was delivered to a supercritical flow reactor by a cement pump. The biomass vaporized over a packed bed of carbon within the reactor could be steam reformed to a gas composed of hydrogen, carbon dioxide, methane, carbon monoxide, and traces of ethane. Although the higher yield of hydrogen and other combustible gases obtained by this method, the over all processes suffers many disadvantageous, including the plugging of the reactor due to the cake and ash build up and the sever corrosion of the reactor material.
On the contrary, subcritical water was proved to be effective for the biomass conversion. Arai and his group began a series of fundamental researches on the non- catalytic conversion of cellulose using the SCWH [59]. The results showed that using the SCWH without any catalyst the cellulose was rapidly converted to water-soluble species with a relatively high glucose yield which this yield increased with elevating the temperature. The overall reaction rate was 1 or 2 orders of magnitude higher than of the conventional acid catalytic process.
Another example of biomass conversion was given by Alemán and others [60]. They reported the possibility of the hydrolysis and saponification of carboxlic esters (methyl benzoates) in both water and slightly alkaline solution (2% KOH) under the SCWH (200-300 °C) using a batch reactor. They achieved a partial hydrolysis or quantitative saponification of sterically hindered and p-substituted methyl benzoates in 30 minutes.

King and co-workers reported the hydrolysis of the soybean oil using the SCWH [61]. They used a subcritical water flow reactor in the hydrolysis processes. The results showed that such reactor system represents an effective system for the hydrolysis of the soybean oil to free fatty acids. The hydrolysis of soybean oil; whose fatty acid composition was: palmitic (12.6%), Olic (26.0%), linoleic (51.0%), and linolenic (5.8%), occurred rapidly, within 10 to 15 minutes of residence time. The reactions were carried out at temperatures between 330 and 340oC. The total conversion yield was 97% or better
without the needed for catalysts, emulsifying agents, or any reactor internals . Such rapid hydrolysis rate contrast with the multi-hour conversion utilized industrially to achieve a 96-98% fatty acid yield.

3.5. Hazardous wastes treatment and plastic recycling

Hazardous wastes could be classified into the following categories, (1) Corrosive that damages human tissue, (2) ignitable that catches fire under certain conditions, (3) toxic that causes injury or death if swallowed, absorbed, or inhaled, and (4) reactive that capable of causing an explosion. Such categorization covers a wide area of wastes. Both subcritical water oxidation and hydrolysis showed promising results for being used as a new technology for hazardous waste treatment. Supercritical water oxidation can decontaminate hazardous organic wastes, including mixtures whose constituents vary widely in their susceptibility to oxidation. Many studies reports the complete destruction of many hazardous using both the sub and supercritical water oxidation including, polychlorinated biphenyls (PCBs) [62] and irradiated materials [63] which are facing unusually challenging problems due to the very high chemical stability and low water solubility of these compounds.

Regarding the SCWH, it found many applications in the chemical recycling of waste plastics.Such target becomes more important from the viewpoint of preservation of natural resources and global environmental protection. The decomposition of synthetic polymers with subcritical water has been investigated [64]. Usually the recycling of composite plastics is more difficult than recycling those composed of a single polymer. The SCWH was used for the recycling of the laminate film composed of polyamide and polyethylene. Using subcritical water, the polyamide was hydrolyzed to a monomer, ε-caprolactam, which dissolves in water. However, the polyethylene was not decomposed,
but deposited in water. Therefore, polyamide was recovered as ε-caprolactam and polyethylene as a single-component polymer [64]. Moreover, the decomposition of additional polymerization plastics like polystyrene has been presented.

Another example of plastic recycle is the de-polymerization of Poly Lactic acid (PLA) reported by Sasaki [65]. The optimum condition for the subcritical water technology under the tested conditions were found at temperature of 220°C and reaction time of 20 min. under these conditions, higher optical purity of L-LA is recoverable. Study on the effect of temperature on the optical isomer of lactic acid product demonstrated L-type was dominant at low range temperature of 180-220°C. At higher temperature, optical purity was drop and racemic mixture was observed. Based on the obtained results, the method was found to be a promising technique for recycling of PLA into its monomer, LA. Figure (5) shows a comparison between the tradition recycling method and that uses the subcritical water technology.

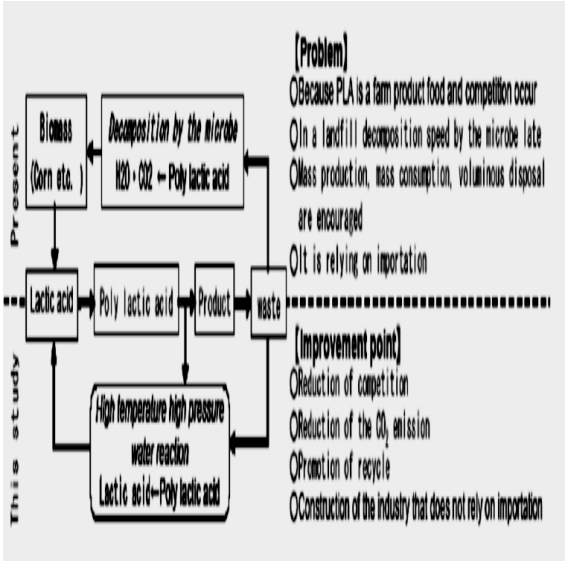

Fig (5) comparison between the tradition plastic recycling method and that uses the subcritical water technology

3. 6. Application of SWE in Pharmaceutical Industry

At present, plant medicine, which mainly comes from plant extraction, has occupied nearly 30 percent to 40 percent among the thousands of worldwide used pharmaceutical products. As a natural healthy protection product, it has incomparable natural advantages, compared with the relative chemical drugs. Extraction and separation of effective pharmaceuticals, looking for leading compounds, is the first and most important step in the new drug development. However, chemical composition of various medicinal plants is very complex, usually containing many kinds of effective ingredients. Numerous methods, including conventional solvent extraction, steam distillation, and sublimation, etc., are known for extracting phytochemicals from plant materials, most based on sequential extraction processes incorporating one or more organic solvents in combination with washing steps. Phytochemical extracts produced by such methods must be further processed to remove all trace of the organic solvents, to remove impurities,

and to separate and purify individual phytochemicals. While such methods are useful for extraction and purification of small quantities of phytochemicals for research purposes, they are difficult to scale to commercial through-put volumes because of the problems associated with cost-effectively, safely and completely removing and recovering the organic solvents from the extracts and spent plant materials. Furthermore, the types and concentrations of organic solvents must be carefully selected in order to avoid structural changes to the target phyto-chemicals during extraction that may adversely affect one or more of their desirable physical, chemical and biological properties [66]. Recently many new technologies and methods, such as ultrasonic extraction, microwave extraction, membrane separation technology, molecular distillation, macroporous resin adsorption and supercritical CO2 extraction technology, are introduced to the extraction and separation of effective components in medicinal plants, promoting the development of plant extracts industry.

Sub-critical water extraction has been extracted the most active compounds from herbs, such as Rosmarinus officinalis (rosemary), Matricaria recutita (German chamomile), Cassia angustifolia (senna), Valeriana officinalis (valerian), Scutellaria baicalensis (Baikal skullcap), Schisandra chinensis (Wuweizu), Zingiber officinale (ginger), Astragalus Membranaceus, etc. [67]. Those extracts were demonstrated to exhibit a composition essentially similar to that of the corresponding methanol or aqueous alcohol, which would show comparable pharmacological activities. The most common application of SWE in the field of pharmaceutical industry is summerised as follows:

3.6.1. Extraction of Volatile Oils

Volatile oil, also known as essential oil, is present in a class of plants with aromatic smell, which is water insoluble and can be distilled with steam. As an important class of active ingredients, essential oils are volatile oil like components of the general, with a variety of pharmacological activities and applications in medicine and food industry. Traditional methods include steam distillation and organic solvent extract, indicating much more shortcomings, such as volatile components loss, low extraction efficiency, heating for a long time, organic solvent residual and so on. In 1998, Basile et al [68] first confirmed that the sub-critical water extraction was a practical method for the essential oil. In their research, the extracts from rosemary was compared with that from steam distillation, the result showed short extraction time, high yield of oxygenated compounds, good quality and lower energy consumption. From that brand-new start, sub-criticalwater extraction has been applied on essential oils of different kinds of herbs, including Fructus Foeniculi [69], Thymbra spicata [70], Marjoram [71], Peppermint [72,73], Laural [74], Eucalyptus [75], and clove buds [76], etc., which were compared with hydro-distillation, supercritical carbon dioxide and extraction. All of the further evidences supported the sub-critical water extraction as a powerful alternative of the extraction of essential oil from herbs with higher oil yield and shorter extraction time.

3.6.2. Extraction of Plant Phenols

Plant phenolic compounds mainly exist in plants, roots, leaves the skin, shell and pulp,

including tannins, flavonoids, anthraquinones, lignin and some simple phenols as a kind of widespread active ingredients of many medicinal plants in nature, could inhibit tumor development in animals and humans, prevent cardiovascular disease, as well as anti-mutation, anti-virus and anti-oxidation, the study of polyphenols has been attracted more and more attention. Sub-critical water has been proved good to extract plant phenolic compounds according to many results of researches. Some examples will be given below

3.6.2.1. Extraction of Tannins

G. M. Matilde [77] studied grape seed extraction in batch and continuous Manners at different temperatures (50˚C, 100˚C, 150˚C), the result showed that a continuous extraction of material is conducive to the dissolution of tannin. Antuon [78], the extraction time has fixed to 20 min, the total polyphenol content of grape seed by sub-critical water extraction is 2 times higher than that of 70% ethanol extraction.

3.6.2.2. Extraction of Anthraquinones

As another subtype of plant polyphenols, anthraquinones which make the potential usefulness in several medical applications. A research [79] of the extraction anthraquinones from dried roots of Morinda citrifolia (Noni)., which possesses several therapeutic properties, such as antiviral, antibacterial, and anticancer, indicated the increase of extraction yield with the rise of temperature, while almost unaffected by pressure. In the extraction of damnacanthal, which is the most valuable anthraquinone compound in the roots of Morinda citrifolia (Noni)., Anekpankul et al [80] studied the extraction yield at different temperatures and flow rates, and suggested that the subcritical water extraction would be a promising method. Also, the extraction of anthraquinones by sub-critical water from the roots of mulberry was also reported [81-83].

3.6.2.3. Extraction of Flavonodis

Flavonoids are widely found in fruits, vegetables, beans, tea and many medical plants. As a type of phytochemicals, they have been applied to treat and inhabit disease and medically functional disorders as healers, antimicrobial agents, as well as antioxidants. However, the poor water solubility and lipid solubility limit their application. With the rise of sub-critical water extraction, a study, focused on the

influence of different pressures, temperatures and flow rates in the water extraction of five isoflavones from defatted soybeans, was started by Chang et al [84]. The results exhibited the best extraction yield of total isoflavones up to 99.7%. Charlotta Turner et al. [85] showed that sub-critical water extraction following by β-glucosidase-catalyzed hydrolysis was a rapid method to determine the content of quercetin and isorhamnetin in onion samples, and environmentally sustainable as the only use of water. Zhi-hong Xu et al. [86] has figured out the influence of temperature, pressure, time, particle size, solvent ratio on the extraction of baicalin from Scutellariae Radix by sub-critical water and compared with the organic solvent extraction method.

3.6.3. Extraction of Lactones

Active ingredients from the roots and rhizomes of piper methysticum forst, named Kavalactones are widely used as medicine and soft drink in Europe and America. Kubatova et al. [87] compared its sub-critical water extraction with that of soxhlet extraction, ultrasonic extraction in boiling water and acetone extraction. The result showed that the extraction rate of the first method, sub-critical water extraction, was much higher than the others, whether the peper was crushed or not.

In conclusion, the use of sub-critical water as available alternative solvent for the extraction of phytochemicals from medical plants has been shown to be feasible.

4. Instruments and basic experimental set-up for SWE

The experimental set-up in most of the previous researches was performed using a laboratory made system [27, 28, 39, 43–44]. The differences in the design of the various instruments used can be seen in (Fig. 6). As seen in Fig. 6A and B, some set-up requires the use of gases, cooling coils and a second high pressure pump. Some groups have **proposed** coupling on-line SWE with microporous membrane liquid–liquid extraction (MMLLE) and gas chromatography (GC) [88]. Instruments for sub-critical water extraction with an on-line solid-phase extraction (SPE) or sorbent trap was proposed [89-91]. All the set-ups consist of a stainless steel preheating coil to ensure that the water is at the operating temperature prior to entering the extraction cell. The stainless steel tubings used were 1/16 in. O.D. and 0.18mm I.D. For the experimental set-up in Fig. 6B, the backpressure was generated using a back pressure regulator by VICI Jour Research (Onsala, Sweden). The system consists of stainless steel extraction cells with 10mmI.D.×150mm (approximately 10ml) or larger. The extraction cell was heated in a gas chromatograph oven and a pump was used to pump the fluid into the extraction cell. By pressurizing the sample cell, it was possible to keep the fluid in liquid phase at the high extraction temperatures used (up to 200 ◦C) [89–90]. For some work, a restrictor was used to generate the back pressure. For certain set-ups, in-order to prevent deposition of the solutes from the water that cools during collection, a second pump is used to inject chloroform/dichloromethane into a fused silica-lined tee placed in the oven between the saturation cell and collection valve (Fig. 6A). A cooling trap is used to cool the fluid coming out from the extraction cell to room temperature (Fig. 6A) [96–100]. From the systems that are built, care must be taken to avoid narrow bore tubing that might be blocked by a precipitate when the botanical extracts leave the oven.

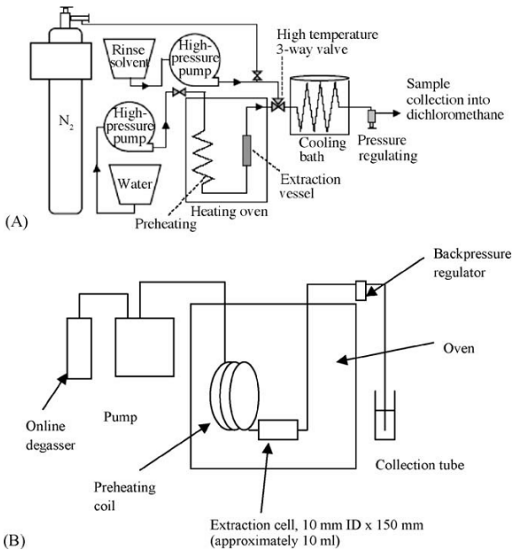

Fig.6. (A) Schemtic diagram of SWE equipment with a cooling coil and a second pump (rinse solvent) delivering dichloromethane [92] and (B) Schematic diagram of an alternative laboratory made SWE system proposed by other group [93–95].

References

[1] C.W. Huie, "A review of modern sample-preparation techniques for the extraction and analysis of medicinal plants," Anal. Bioanal. Chem. 373 (2002) 23-30.

[2] B. Zygmunt, J. Namiesnik, "Preparation of samples of plant material for chromatographic analysis," J. Chromatogr. Sci. 41 (2003) 109-116.

[3] E.S. Ong, "Extraction methods and chemical standardization of botanicals and herbal preparations," J. Chromatogr. B 812 (2004) 23-33.

[4] King, et al., US Patent 7,208,181, B1, 2007.

[5] R. M., Smith, "Superheated water: The ultimate green solvent for separation science", Anal. Bioanal. Chem., 385(3), 419 (2006).

[6] L. Pauling," The Nature of the Chemical Bond," 2nd ed. (Cornell University Press, New York, (1948)).

[7] R. Walton," Subcritical solvothermal synthesis of condensed inorganic materials ," Chem. Soc. Rev., 31, 230–238,2002.

[8] R.H. Tromp, P. Postorino, G.W. Neilson, M.A. Ricci, and A.K. Soper," Neutron diffraction

studies of H2O/D2O at supercritical temperatures: a direct determination of gHH(r),gOH(r) and gOO(r) ," J. Chem. Phys., Vol. 101,PP. 6210-6214, 1994.

[9] H. Ohtaki, T. Radnai, and T. Yamaguchi," Structure of water under the subcritical and supercritical conditions studied by means of solution x-ray diffraction," Chem. Soci. Rev., PP. 41-51, 1997.

[10] J.F. Connelly, "Solubility of hydrocarbons in water near the critical solution temperature". J. Chem. Eng. Data Vol. 11, PP. 13-16, 1966.

[11] Arab Republic of Egypt, Ministry of State for Environmental Affairs – Egyptian Environmental Affairs Agency, "Agricultural wastes recycle".

[12] Arab Republic of Egypt, Ministry of Agriculture and Land Reclamation – Economical Affairs Sector, "Net returns for field crops in A.R.E.".

[13] Monazie A., Comparative study on acid hydrolysis of cellulosic wastes, M.Sc thesis, El Minia University, Egypt, 2007; pp. 44.

[14] Va´zquez M, Oliva M, Te´llez-Luis S, Ramı´rez J. Hydrolysis of sorghum straw using phosphoric acid to evaluation of furfural production. Bioresource Technology, 2007; 98; 3053-3060.

[15] Rahman, S, Choudhury J, Ahmad A. Production of xylose from oil palm empty fruit bunch fiber using sulfuric acid. Biochemical Engineering Journal, 2006; 30; 97-103.

[16] Karimi K, Kheradmandinia S, Taherzadeh M. Conversion of rice straw to sugars by dilute-acid hydrolysis. Biomass and Bioenergy, 2006; 30; 247-253.

[17] Xu Z, Wang Q, Jiang Z, Yang X, Ji Y. Enzymatic hydrolysis of pretreated soybean. Biomass and Bioenergy, 2007; 31; 162-167.

[18] Li Q, He Y, Xian M, Jun G, Xu X, Yang J, Li L, Improving enzymatic hydrolysis of wheat straw using ionic liquid 1-ethyl-3-methyl imidazolium diethyl phosphate pretreatment, Bioresource Technology, 2009; 100(14); 3570-3575.

[19] Fubao Sun, Hongzhang Chen, "Enhanced enzymatic hydrolysis of wheat straw by aqueous glycerol pretreatment", Bioresource Technology, 2008; 99; 6156-6161.

[20] Yoon K, Woodams E, Hang Y. Enzymatic production of pentoses from the hemicellulose fraction of corn residues. LWT- Food Science and Technology, 2006; 39; 388-392.

[21] Matsunaga M, Matsui H, Otsuka Y, Yamamoto S. Chemical conversion of wood by treatment in a semi-batch reactor with subcritical water. J. of Supercritical Fluids, 2008; 44(3); 364-369.

[22] Wiboonsirikul J, Hata S, Tsuno T, Kimura Y, Adachi S. Production of functional substances from black rice bran by its treatment in subcritical water. LWT – Food and Science Technology, 2007; 40; 1732–1740.

[23] Williams P, Onwudili J. Subcritical and supercritical water gasification of cellulose, starch, glucose, and biomass waste. Energy Fuels, 2006; 20(3); 1259–1265.

[24] Yan Zhao, Wen-Jing Lu, Hong-Tao Wang, Jin-Long Yang. Fermentable hexose
production from corn stalks and wheat straw with combined supercritical and subcritical hydrothermal technology. Bioresource Technology, 2009; 100; 5884-5889.

[25] Yan Zhao, Hong-Tao Wang, Wen-Jing Lu, Hao Wang. Combined supercritical and subcritical conversion of cellulose for fermentable hexose production in a flow reaction system. Chemical Engineering Journal; 2011;166; 868–872.

[26] W. Abdelmoez*1, S.M. Nage1, A. Bastawess1, A. Ihab2. H. Yoshida3 .Production of Sugars and Biofuel from Wheat Straw Using Subcritical Technology,

[27]. Yoshida H, Tavakoli Q. Effective recovery of harmful metal ions from squid wastes using subcritical and supercritical water treatment. Environ Sci Technol J. 2005;39:2357–2363.

[28]. Tester J, Holgate H, Armellini F, Webley P, Killilea W, Hong G,Barner, H. Supercritical water oxidation technology. In: Tedder DW, Pohland FG, editors. Emerging Technologies in Hazardous Waste Management III, Washington DC: American Chemical Society, 1993.

[29]. Schneider G. Phase equilibria in fluid mixtures at high pressures. In I. Prigogine and S. A. Rice, eds., Advances in Chemical Physics.1970, Vol 17:39.

[30]. Zosel K. The process for the decaffeination of green coffee beans, Ger. Pat. DBP 2,005,293, 1970.

[31]. Tester J, Pohland F. Supercritical Water Oxidation Technology: A Review of Process Development and Fundamental Research. In: Tedder DW, Pohland FG, editors. Emerging Technologies in Hazardous Waste Management III, ACS Symposium Series #518, Chapter 3, American Chemical Society Symposium Series No. 518, 1993.

[32].Modell M. SCWO Historical Perspective. Supercritical Water Oxidation Achievements and Challenges in Commercial Applications Strategic Analysis, Inc. 2001

[33]. Hutchenson K, Foster N. Innovations in Supercritical Fluids. ACS Symposium, Series 608, Washington, 1995.

[34]. Akgerman A, Madras G. Supercritical Fluids-fundamentals for Application. NATO ASI Ser. E 273, Dordrecht: Kluwer, 1994, 669–695.

[35]. Yoshida H, Terashima M, Takahashi Y. Production of organic acids and amino acids from fish meat bysubcritical water hydrolysis. Bio-technol Prog. 1999; 15:1090–1094.

[36]. Yoshida H, Katayama Y. Production of useful substances from wood wastes by subcritical water hydrolysis. Proceedings of the 10th APCChE Congress. 2004, 3P-03–025, A272.

[37]. McHugh M, Krukonis V. Supercritical Fluid Extraction: Principles and Practice, 1st ed.. Stoneham, MA: Butterworths. April 1986; 2nd ed, 512 January 1994.

[38]. Cansell F, Botella P, Garrabos Y, Six J, Gnanou Y, Tufeu R. Fractionation of polyethylene oxide star samples by supercritical fluids.Polymers J. 1997; 29:910–916.

[39]. W.Abdelmoez, R. Abdelfatah, and A. Tayeb, Extraction of Cottonseed Oil Using Subcritical Water Technology. 2010 American Institute of Chemical Engineers AIChE J, 57: 2353–2359, 2011.

[40] S. Morales-Muñoz, L. Luque-García, M. D. Luque de Castro; Pressurized hot water extraction with on-line fluorescence monitoring: a comparison of the static, dynamic, and staticdynamic modes for the removal of polycyclic aromatic hydrocarbons from environmental solid samples. Anal. Chem., 74, 4213-4219 (2002).

[41] M. García-Marino, J. C. Rivas-Gonzalo, E. Ibáñez, C. GarcíaMoreno; Recovery of catechins and proanthocyanidins from winery by-products using subcritical water extraction. Anal. Chim. Acta, 563, 44-50 (2006).

[42] J. Wiboonsirikul, S. Adachi; Extraction of functional sub-stances from agricultural products or by-products by subcritical water treatment. Food Sci. Technol. Res., 14, 319-328 (2008).

[43] Y. Murym, T. Kobyshi, and S. Adachi, Properties of Extracts from Soy Sauce Cake Using Subcritical Water Treatment. Japan Journal of Food Engineering, Vol. 11, No. 1, pp. 67 - 71, Mar. 2010

[44] W. Abdelmoez, M. Abdelhamid and Hiroyuki Yoshida, Extraction of Jojoba Oil Using Subcritical Water Technology .Recent Patents on Chemical Engineering, 2012, 5, 63-70

[45] Wu, T.H. and P.J. Bechtel: Salmon by-product storage and oil extraction. Food Chemistry, 111, 868-871 (2008).

[46] Guerard, F., L. Guimas and A. Binet: Production of tuna waste hydrolysates by a commercial neutral protease preparation. Journal of Molecular Catalysis B. Enzymatic, 19-20, 489-498 (2002).

[47] Kang, K.Y., D.H. Ahn, S.M. Jung, D.H. Kim and B.S. Chun: Separation of protein and fatty acids from tuna viscera using supercritical carbon dioxide. Biotechnol. Bioprocess Eng., 10, 315-321 (2005).

[48] El-Bel tagy, A.E., T.A. El-Adawy, E.H. Rahma and A.A. El-Bedawey: Purification and characterization of an acidic protease from the viscera of bolti fish (Tilapia nilotica). Food Chem., 86, 33-39 (2004).

[49] Prasertsan, P., S. Jitbunjerdkul, Trairatananukoon and T. Prachumratana: Production of enzyme and protein hydrolysate from fish processing waste In: New horizons in biotechnology (Eds.: S. Roussos, C.R. Soccol, A. Pandey and C. Augur) IRD editions, Kluwer Academic Publisher, India (2001).

[50] Ferreira, N.G. and H.O. Hultinn: Liquefying cod fish frames under acidic conditions with a fungal enzyme. J. Food Process. Preserv., 18, 87-101 (1994).

[51] Cheng, H. , X. Zhu, C. Zhu, J. Qian, N. Zhu, L. Zhao and J. Chen: Hydrolysis technology of biomass was te to produce amino acids in subcr i t ical water. Biores . Technol . , 99, 3337-3341(2008).

[52] Kang, K., A. Quitain, H. Daimon, R. Noda, N. Goto, H.Y. Hu and K. Fujie: Optimization of amino acids production from waste fish entrails by hydrolysis in sub- and supercritical water. Can. J. Chem. Eng., 79,65-71 (2001).

[53]Yoshida, H. and O. Tavakoli: Subcrit ical water hydrolysis treatment for waste squid entrails and production of amino acids, organic acids, and fatty acids. J. Chem. Eng. Jpn., 37, 253-260 (2004).

[54] Tavakoli, O. and H. Yoshida: Squid oil and fat production from squid wastes using subcritical water hydrolysis: Free fat t y acids and transesterification. Ind. Eng. Chem. Res., 45, 5675-5680 (2006).

[55] Toyoji, K.: Synthesis of polysaccharide derivatives in supercritical fluid. Cellulose Communications, 8, 66-70 (2001).

[56] Levin, D.B., H. Zhu, M. Beland, N. Cicek and B.E. Holbein: Potential for hydrogen and methane production from biomass residues in Canada. Biores. Technol., 98, 654-660 (2007).

[57] D. G. B. Boocock and K. M. Sherman," Further aspects of powdered poplar wood liquefaction by aqueous pyrolysis," The can. Of Chem. Eng. 63, 627-633,1985.

[58] M. J. Antal, S. G. Allen, D Schulman, Xu. Xiaodong," Biomass gasification in supercritical water," Ind. Eng. Res., Vol. 39, PP. 4040-4053, 2000.

[59] T. Adschiri, S. Hirose, R. M. Malaluan, and K. Arai, "noncatalytic conversion of cellulose in supercritical and subcritical water," J. Chem. Eng. Jpn., Vol. 26(6), PP. 676-680, 1993.

[60] P. Alemán, C. Boix and M. Poliakoff," Hydrolysis and saponification of methyl benzoates A green procedure in high temperature water,"Green Chem., Vol.1 (2), PP. 65 - 68, 1999.

[61] K. Kang, and B. Chun,"Behavior of hydrothermal decomposition of silk fibroin to amino acids in near-critical water," Korean J. Chem. Eng., Vol. 21(3), PP. 654-659, 2004.

[62] G. Anitescu and L.L. Tavlarides, "Supercritical water oxidation reaction pathway and kinetics of polychlorinated biphenyls," Proceeding of the 2001 conference on Environmental research, 2001.

[63] C. fromonteil, Ph. Bardelle, F. Cansell, " Hydrolysis and Oxidation of an epoxy resin in

sub- and Super critical Water," Ind. Eng. Chem. Res. Vol. 39, PP. 922-925, 2000.

[64] Joint meeting of the chemicals committee and the working party on chemicals, Report of the Organization for Economic Co-operation and Development, Env/Jm/Mono (99)19/part1, 9, Sep 1999.

[65] T. Saeki, "Depolymerization of Poly(L-lactic Acid) under hydrothermal conditions," COE project report at the Department of Ecological Engineering, Toyohashi University of Technology

[66] L. Xiaoxia, F. Qiaojia "Application of Sub-Critical Water Extraction in Pharmaceutical Industry" Materials Science and Chemical Engineering, 2013, 1, 1-6.

[67] W. G. William and D. Kenneth, "Sub-Critical Water Extraction of Medicinal Plants," WO/2010/034971, PCT/ GB2009/002229.

[68] A. Basilea, M. M. Jimenez-Carmona and A. A. Clifford, "Extraction of Rosemary by Superheated Water," Journal of Agricultural and Food Chemistry, Vol. 46, No. 12, 1998, pp. 5205-5209.

[69] G. Gmiz and M. D. Luque de Castro, "Continuous SubCritical Water Extraction of Medicinal Plant Essential Oil Comparison with Conventional Techniques," Talanta, Vol. 51, 2000, pp. 1179-1185.

[70] M. Z. Ozel, F. Gogus and A. C. Lewis, "Sub-Critical Water Extraction of Essential Oil from Thymbra Spicata," Food Chemistry, Vol. 82, No. 3, 2003, pp. 381-386.
http://dx.doi.org/10.1016/S0039-9140(00)00294-0

[71] M. M. Jimnez Carmona, J. L. Ubera, M. D. Luque de Castro, et al., "Comparison of Continuous Sub-Critical Water Extraction and Hydro-Distillation of Marjoram Essential Oil," Journal of Chromatography A, Vol. 855, 1999, pp. 625-632.

[72] A. Kubatova, A. J. M. Lagadec, D. J. Miler, et al., "Selective Extraction of Oxygenates from Savory and Peppermint Using Sub-Critical Water," Flavour and Fragrance Journal, Vol. 16, No. 1, 2001, pp. 64-73. http://dx.doi.org/10.1016/S0021-9673(99)00703-7

[73] A. Ammann, D. C. Hinz, R. S. Addleman, et al., "Super-heated Water Extraction, Steam Distillation and SFE of Peppermint Oil," Fresenius Journal of Analytical Chemi-
stry, Vol. 364, No. 7, 1999, pp. 650-653.

[74] Z. V. Fernandez Pere, M. M. Jimenez Carmona, M. D. Leque de Castro, "An Approach to the Static-Dynamic Sub-Critical Water Extraction of Laurel Essential Oil
Comparison with Conventional Techniques," Analyst,
Vol. 125, 2000, pp. 481-485.

[75] M. M. Jimenez Carmona and M. D. Luque de Castro, "Isolation of Eucalyptus Essential Oil for GC-MS Analysis by Extraction with Sub-Critical Water," Chromatographia, Vol. 50, 1999, pp. 578-582. http://dx.doi.org/10.1039/a907244f

[76] A. A. Clifford, A. Basile and R. Ai-Saidish, "A Comparison of the Extraction of Clove Buds with Supercritical Carbon Dioxide and Superheated Water," Fresenius Jour-
nal Analysis Chemistry, Vol. 364, 1999, pp. 635-637. http://dx.doi.org/10.1007/s002160051400
http://dx.doi.org/10.1007/s002160051400

[77] M. G. Marino, et al., Analytica Chimica Acta, Vol. 563, 2006, pp. 44-50.

[78] I. D. Antuon, "Use of Sub-Critical Water for the Extraction of Natural Antioxidants from By-Products and Wastes of the Food Industry," 14th Workshop on the Developments in the Italian PhD Research on Food Science Technology and Biotechnology, University of Sassari Oristano, 2009, pp. 16-18. http://dx.doi.org/10.1016/j.aca.2005.10.054

[79] A. Shotipruk, J. Kiatsongserm, P. Pavasant, M. Goto and M. Sasaki, "Pressurized Hot Water Extraction of Anthra- quinones from the Roots of Morinda citrifolia," Biotechnology Progress, Vol. 20, 2004, pp. 1872-1875.

[80] T. Anekpankul, M. Goto, I. M. Sasak, et al.,"Extraction of Anticancer Damnacanthal from Roots of Morinda citrifolia by Sub-Critical Water," Separation and Purification Technology, Vol. 55, 2007, pp. 343-349. http://dx.doi.org/10.1021/bp049779x

[81] B. P. Ravane, et al., Journal of Supercritical Fluids, Vol. 37, 2006, pp. 390-396.
http://dx.doi.org/10.1016/j.seppur.2007.01.004

[82] A. Shotipruk, et al., Biotechnology Progress, Vol. 20, 2004, pp. 1872-1875.
http://dx.doi.org/10.1016/j.supflu.2005.12.013

[83] T. Anekpankul, et al., Separation and Purification Technology, Vol. 55, 2007, pp. 343-349. http://dx.doi.org/10.1021/bp049779x
http://dx.doi.org/10.1016/j.seppur.2007.01.004

[84] L. H. Chang, Y. C. Cheng and C. M. Chang, "Extracting and Purifying Isoflavones from Defatted Soybean Flakes Using Superheated Water at Elevated Pressures," Food
Chemistry, Vol. 84, 2004, pp. 279-285.

[85] C. Turner, P. Turner, G. Jacobson, K. Almgren, M. Waldebäck, P. Sjöberg, E. N. Karlssonb and K. E. Markides, "Sub-Critical Water Extraction and b-Glucosidase-Cata-
lyzed Hydrolysis of Quercetin Glycosides in Onion Waste," Green Chemistry, Vol. 8, 2006, pp. 949-959. http://dx.doi.org/10.1016/S0308-8146(03)00212-7

[86] Z. H. Xu, G. S. Qian, S. K. Liu, Z. W. Li and X. Y. Chen, "Study on Subcritical Water Extraction of Baicalin from Radix Scutellariae Coupled to High Performance Liquid Chromatographic Analysis," Chinese Journal of Chromatography, Vol. 22, No. 1, 2004, pp. 44-47. http://dx.doi.org/10.1039/b608011a

[87] A. Kubatova, D. J. Miller and S. B. Hawthorne, "Sub-Critical Water and Organic Solvents for Extracting Kava Lactones from Kava Root," Journal of Chromatography
A, Vol. 923, No. 1, 2001, pp. 187-194.
[88] K. Kuosmanen, T. Hyotylainen, K. Hartonen, J.A. Jonsson, M.L. Riekkola, Anal. Bioanal. Chem. 375 (2003) 389.
[89] Y. Yang, B. Li, Anal. Chem. 71 (1999) 1491.

[90] L.J. Lamm, Y. Yang, Anal. Chem. 75 (2003) 2237.
[91] C. Crescenzi, G. D'Ascenzo, A. Di Corcia, M. Nazzari, S. Marchese, R. Samperi, Anal. Chem. 71 (1999) 2157.
[92] K. Luthje, T. Hyotylainen, M. Rautiainen-Rama, M.L. Riekkola, Analyst 130 (2005) 52.
[93] E.S. Ong, S.M. Len, Anal. Chim. Acta 482 (2003) 81.
[94] E.S. Ong, S.M. Len, J. Sep. Sci. 26 (2003) 1533.
[95] E.S. Ong, S.M. Len, J. Chromatogr. Sci. 42 (2004) 211.
[96] D.J. Miller, S.B. Hawthorne, Anal. Chem. 70 (1998) 1618.
[97] B. van Bavel, K. Hartonen, C. Rappe, M.L. Riekkola, Analyst 124 (1999) 1351.
[98] R.M. Smith, J. Chromatogr. A 975 (2002) 31.
[99] C. Crescenzi, G. D'Ascenzo, A. Di Corcia, M. Nazzari, S. Marchese, R. Samperi, Anal. Chem. 71 (1999) 2157.
[100] K. Kuosmanen, T. Hyotylainen, K. Hartonen, M.L. Riekkola, Analyst 128 (2003) 434.

First International Conference on Science, Engineering & Environment,
Tsu City, Mie, Japan, Nov.19-21, 2015, ISBN: 978-4-9905958-5-2 C3051

DIGITAL HERBARIUM OF THE CROP PLANTS OF BANGLADESH FOR TAXONOMIC STUDIES

*M A Baset Mia, T. Hossain, H. I. Khan and M.M. Uddin
Department of Crop Botany
Bangabandhu Sheikh Mujibur Rahman Agricultural University
Gazipur, Bangladesh

ABSTRACT

Recently, digital herbarium is introduced and gaining prominence for easy use and maintenance. Additionally, digital herbarium along with database on plant characters is being used for quick identification and taxonomic studies of plants. However, digitization in agriculture especially the analyses of plant image for identification of crop plants of Bangladesh are obscure. Image analysis is a modern area of research in biology for generating information on plants in digital mode. Different universities along with the Bangladesh National Herbarium are maintaining the herbaria for plant identification and to dissect the plants in diversified purposes. However, digitization of plant image along with virtual herbarium is new era in Bangladesh. The department of Crop Botany, BSMRAU, Gazipur, Bangladesh has initiated a project for the establishment of digital herbarium for crop, medicinal and forest plants. Under this project images of different crop plants are captured in proper way with desired resolution and processed for database development. A virtual herbarium is being developed for global uses for identification and taxonomic studies of crop plants.

Key words: *Plant taxonomy, Herbarium, Image, Digitization*

INTRODUCTION

A herbarium is a collection of preserved plant specimens where specimens are kept at mainly dried and pressed, although it is often stored 'wet' plant collections preserved in chemicals like in ethanol and formalin. Specimens of herbarium form an important record of plants for different purposes over time. They may have been produced as a voucher for botanical research, and serve as a permanent record allowing anyone to go back and check the identification, re-sample or repeat research. It is a special type of data banks for plants with vast quantities of genuine information and the specimens therein supply a lasting record of the flora of a location or a region [1]. However, maintenance of plant materials in the herbarium is laborious and difficult task which needs alternative approach.

Recently, digital herbaria and online databases are emerging area of plant systematic and biodiversity studies. A conventional herbarium-based database (virtual herbarium), thus maximizes the usefulness of the collection by providing authentic and lasting information [2].
importance many countries like India, Australia, USA have already launched virtual herbaria [1]. Therefore, a project has been initiated to digitize the crop plants of Bangladesh along with their taxonomic attributes.

Bangladesh has an excellent scope of collecting crop specimens for developing database which might be used as source of academic and research purpose. The national agricultural research institutes and agricultural universities have developed and released a large number of crop varieties. Many of those varieties are successfully cultivated throughout the countries and some of them are recognized as mega varieties e.g. rice varieties like BR11, BRRIdhan 28, BRRIdhan29 [3].

However, crop varieties in most cases, not properly indexed and documented following a standard format incorporating the key characteristics of the varieties. Crop herbarium of those varieties are not established which is very essential for identification and demarcation. Therefore, it has become necessary to prepare a consolidated documentation following a standard format incorporating the salient feature with digital image of the crop plants. Digital herbarium of the crop plants in Bangladesh is very much necessary and considering the

METHODOLOGY

The images of different parts of crop plants, both external and internal are being captured by high quality digital camera (EOS70D DSLR Camera). The images and morphological data to be presented on the 'Herbarium' website of crop plant varieties are first recorded into Microsoft Excel spreadsheets. Each entry bears all required information such as the herbarium specimen label, including species name, author citation, sub-species if any, variety if any, family, subfamily, collection number, locations, date of collection, habitat and the collector's name. The data further comprise 'crops' in which the species are described. Additional information includes the nomenclature update according to 'the variety list'. The adaptation of DSpace software, originally for academic repositories, to develop a repository for a Digital Herbarium seems effective, making it possible to give access to a type of collection usually restricted, in an organized and structured manner. Therefore, there is relevant importance of offering an information service that provides a collection of exsiccates, which has aspects of digital data. Thus, it is a structured open data repository, while disseminates information relating to the herbarium [4].

A detailed description in a scanned copy of the crop pages, phenology, distribution, threat status and comments on any special features of the taxon. The digitized herbarium specimens at a minimum resolution of 300 dpi and images of live specimens provided in the database form an information synergy on the species [5].

The focus is on digitization workflow, the sequence of tasks that are performed in order to create digital information that characterizes individual specimens. These tasks typically include photography of specimens and labels, image processing, capture of label information as text. The presentation of workflow characteristics in this paper provides the framework for analyzing the effectiveness and efficiency of workflows and for the development of new effective workflows [2].

RESULTS AND DISCUSSION

The contribution of agricultural research organizations for the improvement of national economy is very significant in Bangladesh. There are six national agricultural research institutes and three agricultural universities which are working with the development of crop varieties in Bangladesh. According to [3] around 594 crop varieties have been developed and are successfully cultivated throughout the country (Table 1 and Table 2).

Table 1. Institute-wise developed crop varieties grown in Bangladesh

Research Institute/Agricultural Universities	No. of varieties developed
Bangladesh Agricultural Research Institute (BARI)	303
Bangladesh Institute of Nuclear Agriculture (BINA)	53
Bangladesh Jute Research Institute (BJRI)	29
Bangladesh Sugarcane Research Institute (BSRI)	57
Bangladesh Tea Research Institute (BTRI)	40
Cotton Development Board (CDB)	22
Bangladesh Agricultural University	64
Bangabandhu Sheikh Mujibur Rahman Agricultural University	24
Shere-e-Bangla Agricultural University	02
Total	**594**

Table 2. Crop-wise variety developed by Bangladesh national agricultural research institute and agricultural universities

Broad crop area	**No. of varieties**
Cereal crops	110
Root and tuber crops	45

Oilseed crops	47
Pulses crops	54
Vegetable crops	92
Fruit crops	121
Spices crops	22
Flowers	32
Sugarcane	40
Tea	22
Total	**594**

Besides this, some traditional crop varieties and varieties developed by private companies like Lal Teer Seed Limited have developed 32 vegetable crops which are being cultivated throughout the country.

Bangladesh National Herbarium (BNH)

Bangladesh National Herbarium is working as a Directorate of the Ministry of Environment and Forest, Bangladesh. The organization has collected nearly 100,000 (one hundred thousand) specimens (having duplicate) of plants of the country. The oldest specimen dates from 1855 but the main bulk of the historic specimens comes from the 20th century. The specimens of BNH stored in the herbarium act as reference for identification of plants, writing of Floras (a description of all the plants in a country or region), monographs (a description of plants within a plant group, such as a family) and the study of plant evolutionary relationships [3]. The most important specimens are called ‘types' which is a specimen chosen by the author of a new species as a reference point for a particular species.

Recently, BNH is starting to digitize the herbarium material involves the process of capturing data and images and storing them in digital form.

Herbarium in University

Besides the NHB, department of botany of universities of Bangladesh like Dhaka University, Rajshahi University, Chittagong University, Jahangirnagar University, Bangladesh Agricultural University, Bangabandhu Sheikh Mujibur Rahman Agriculrural University, Shere-e-Bangla Agricultural University, Patuakhali Science and Technology University, Hajee Danesh Science and Technology University, Sylhet Agricultural University are working with herbaria for academic and research purposes. Among them the department of botany of Dhaka University has a herbarium with over 5000 specimens.

Development of Digital Archives of Crop Varieties

The images of crop variety are being collected and described their morphological characters (both external and internal). The collected images were submitted in Dspace metadata for preparing the digital herbarium. Metadata pages to describe the plant specimen; each page caters to a different category given in specimen metadata; upload step, where file will be uploaded; verify step, where metadata is verified. The data can be browsed by accession number; by collector; by family; by date; by location. The archive can be searched through advanced search by crop variety detail, taxonomy, coverage; contributors; date. The simple search all of DSpace for the nearest match and even provides full text search. This content digital archive system will store individual data structure, metadata standards, management policy and search interface [4].

Design of Website

The website is being developed for using public domain open-source web server Apache and specialized database software like MySQL in back-end which run under windows platform , a scripting language like PHP or HTML,CSS, Javascript in front-end. Plant taxonomic data will be stored in the database, which allows rapid indexed searches to be carried out and the content will be generated dynamically.

Interface of Website User

An image gallery will be provided that allows species to be identified by browsing images. Each image is hyperlinked to the corresponding species webpage. Alphabetically sorted species and family lists allow users to browse by species name and family, respectively. The website will provide basic and advanced search capabilities [5]. Text entered in basic search will be explored in all fields of the herbarium database, while advanced search allows text to be searched in one or more fields like genus, threat status or common name.

Herbarium-based databases

Herbarium-based databases (virtual herbaria) worthy of mention are Herbarium Catalogue of Digitization of existing collections is an enormous undertaking. Initial digitization efforts focused on assembling very complete data records and access to researchers and the public was granted only after extensive quality control [4]. More recently, it has been recognized that not every element of a collection record needs to be recorded in a single digitization event For example, recording of an image and "filed-under" taxon name are sufficient to start the process. Digital capture of useful information can follow at a later stage and be treated as annotations (e.g., a history of taxonomic determinations).

Additionally, collected morphological data will be generally available online, updating nomenclature and taxonomic interpretations and vetting type specimens can occur after the publication of data and images on the internet, providing an opportunity for off-site experts to comment on the specimens [1].

CONCLUSIONS

Development of virtual herbarium of crop plants of Bangladesh will be a new resource of crop varieties for academician, researchers and policy makers. Digitization of crop varieties developed by research institutes and traditional varieties is a tedious job and needs quality control in taking images. Protocols for periodic quality control should be established for all stages in the digitization workflow to ensure data accuracy and the production of high quality digital images. Selection of data entry and imaging technicians should be guided by highly skilled personnel. A well developed digital herbarium will be built which will utilized both academician and researchers.

ACKNOWLEDGEMENTS

The authors are grateful to Higher Education Quality Enhancement Project (HEQEP), UGC, Ministry of Education, Government of Bangladesh for providing the fund for implementing the project entitled "Establishment of Digital Herbarium and Herbal Museum for Increasing the Academic and Research Capability in Crop Botany, BSMRAU", and the present research is the part of the project.

REFERENCES

[1] Morris P J, Relational Database Design and Implementation for Biodiversity Informatics. Phyloinformatics, vol 7, 2005, pp1–66.

[2] Nelson G., Paul D, Riccardi G, Mast A R, Five task clusters that enable efficient and effective digitization of biological collections, Zoo Keys, vol.209, pp19–45.

[3] Afroz D, Kamal MRM and Hossain S M M, Plant varieties developed by the NARS institutes and agricultural universities of Bangladesh, 2011, BARC, Dhaka.

[4] Anonymous, A Guide to Handling and Digitizing of Specimens. In Rapid Digitization Project: Final Report of Australian Museum (http:// ustralianmuseum. net.au/ Uploads/ Documents /22932/ rchive%20Training%20Compressed.pdf), 2011.

[5] Antweb Automontage imaging guidelines, http://www.antweb.org/homepage/Ant-Web%20Imaging%20guidelines%20v01.pdf, 2010.

SEE-Osaka2016

Second International Conference on
Science, Engineering & Environment
21-23 November 2016, Osaka, Japan

Invitation to participate

- The "International Journal of GEOMATE" is a Scientific Journal of the GEOMATE International Society that encompasses a broad area in Geotechnique, Construction Materials and Environment.
- The key objective of this journal is to promote interdisciplinary research from various regions of the globe.
- The editorial board of the journal is comprised of extensively qualified researchers, academicians, scientists from Japan and other countries of the world.
- It is peer-reviewed Journal that is published quarterly till 2015 and now bimonthly. All articles published in this journal are available on line.
- Contributors may download the manuscript preparation template for submitting paper or contact to the Editors-in-Chief

  [editor@geomatejournal.com].